30º Congresso da Sociedade Brasileira de Microscopia e Microanálise

SBMM

PROCEEDINGS

Proceedings of the 30th Meeting of the Brazilian Society for Microscopy and Microanalysis (30th CSBMM)

Maceió, AL
2025

Copyright © 2025 by the authors

Content, textual and grammatical review: Responsibility of the respective authors.

All rights reserved 2025

Unauthorized reproduction of this publication, in whole or in part, constitutes a violation of copyright law (Law No. 9,610/98).

Dados Internacionais de Catalogação na Publicação (CIP)
(Câmara Brasileira do Livro, SP, Brasil)

Proceedings of the 30th Meeting of the Brazilian Society for Microscopy and Microanalysis (30th CSBMM) [livro eletrônico] / [organização Sociedade Brasileira de Microscopia e Microanálise]. -- Maceió, AL : Aptor Sofware, 2025.
PDF

Vários autores.
Vários colaboradores.
ISBN 978-85-63273-85-7

1. Educação profissional 2. Imagens - Análise 3. Materiais 4. Microscopia - Técnica 5. Tecnologias digitais I. Microanálise, Sociedade Brasileira de Microscopia e.

26-337943.1 CDD-371.33

Índices para catálogo sistemático:

1. Tecnologias no ensino : Educação 371.33

Camila Aparecida Rodrigues - Bibliotecária CRB - SP-010133/O

Sponsored

Diamond

Gold

Silver

KOCH ELECTRON MICROSCOPY

REDE DE PLATAFORMAS TECNOLÓGICAS FIOCRUZ

Support

CAPES

CNPq

FAPEAL
FUNDAÇÃO DE AMPARO À PESQUISA DO ESTADO DE ALAGOAS

Institutional Support

Maceió Convention & Visitors Bureau

SBMM
Sociedade Brasileira de Microscopia e Microanálise

Official Travel Agency

follow UP
Turismo & Eventos

Organization

AG EVENTOS®

Summary

Transmission Electron Microscopy of Nanostructures and Engineering Materials, including all techniques associated with TEM, such as STEM, EDS, EELS, electron diffraction, 4DSTEM, in situ experiments, and electron tomography	**1**
Probing Atomic Defects in 2D Materials by Scanning Transmission Electron Microscopy	**2**
Strain Mapping from Sparse 4D STEM Data Using Physics-Informed Neural Networks	**3**
Experimental Detection of Chemical Short-Range Order in Metallic Alloys by Electron Diffraction and HRTEM: Challenges and Advances	**4**
Microscopic and Structural Evaluation of the Effect of High Frequency Sonication on the Obtaining of Heterostructured Monolayers of MoS2.	**6**
Probing Short- and Long-Range Order in Molecular, Mineral, and Oxide Nanomaterials Using 3D Electron Diffraction and Electron PDF	**8**
A Transmission Electron Microscopy Investigation into the Nanoscale Amorphization and Enhanced Conductivity of FIB-Patterned MoS_2 Monolayers	**10**
Characterization of Nb and Mo precipitates in Ferritic\Bainitic steels using HRTEM assisted by EDS	**12**
Characterization of NbC Carbides in Lightweight Fe-Al-Nb-C Steel Using Electron Microscopy	**14**
Evaluation of Ar/O2 and heating under vacuum as protocols for cleaning self-supported thin films based on capped nanoparticles	**16**
Evaluation of Dispersion of Chemical Reagents by SEM-EDS and TEM-EDS	**18**
Fluorescent Nanoparticles based on Mesoporous Silica and Chitosan applied for Latent Fingerprint Development	**20**
Green Nanotechnology Applied to Skin Health: Development of Sustainable Formulation from Apple Industry Co-Products.	**22**
High-Temperature creep behavior of Ti-6Al-4V with TBC characterized by TEM	**24**
Impact of Aging Treatments on the Microstructure and Mechanical Properties in the Ti-24Nb-4Mo-6Zr Alloy	**26**
Investigation on precipitation in Zr-Nb-Mn alloys	**28**
Solute segregation during crystallisation of multicomponent glassy alloys of the system (FeCoNiCrMn)B	**30**
Study of the morphology and characterization of defects in MnBi2Te4/Bi2Te3/CdTe thin films via FIB sample preparation, STEM, and EDS chemical analysis	**32**
Study of thin film of CuZr metallic glass by electron pair distribution function (ePDF)	**34**
Surface Characterization of the TiVNbCr Alloy After Pulsed Laser Activation for Hydrogen Storage	**36**
Surface Oxidation State Analysis of Magnetite (Fe_3O_4) Nanoparticles and Their Magnetic Properties	**38**
Synthesis and Characterization of In2S3Semiconductor Quantum Dots for Potential Photocatalytic Applications in Water Pollution Remediation	**40**
The Role of TiFe Nanostructure as an Additive in Mg/MgH_2 Composites for Hydrogen Storage	**42**
The synthetic pathway of whitlockite nanoparticles elucidated by transmission electron microscopy	**44**
Transmission Electron Microscopy as a Realistic Data Source for the Micromagnetic Simulation of Polycrystalline Nickel Nanowires	**46**
Transmission Electron Microscopy Study of the Martensitic Phase in a MnNiFeCoSiGe Magnetocaloric High-Entropy	**48**
Visualization of Ferroelectric Domains in Bulk Tellurium by Differential Phase Contrast Scanning Transmission Electron Microscopy	**50**
Scanning Electron Microscopy of Nanostructures and Engineering Materials, including all techniques associated with SEM, such as EDS, EBSD, and FIB	**52**
Radiation-Induced Degradation in Halide Perovskite Films	**53**
SEM and FIB in Semiconductor Manufacturing: From Process Development to High-Volume Control	**55**
AIR AND OXYGEN PLASMA PEN TREATMENT ON THE NANOSTRUCTURATION OF CORN STARCH	**56**
A microstructural study of a naturally occurring chrysoberyl encapsulated in beryl	**58**
FIB-SEM characterization of the porous network of cap rocks with potential for long-term and safe sealing	**60**
Hydrothermal growth of grass-like Al_2O_3 nanostructures on 3D-printed Al-based monolith: tailoring iron dispersion for CO2 hydrogenation catalysts	**62**

Morphological effect on electroplated BiVO4films in a range of electrical charge applied	**64**
Segmentation of Interphase Boundaries in Complex-Phase Steels	**66**
Assessment of Fusion Parameters for the Development of Novel Nanostructured Bainitic Steels	**68**
Assessment of Particulate Matter in an Industrial Influence Area by Scanning Electron Microscopy and X-ray Microfluorescence	**70**
Automated Mineralogical Mapping and SEM Analysis of Au-Bearing Rocks from the Tapajós Mineral Province	**72**
Case study of a Multi-detector SEM Approach for Apatite Characterization	**74**
Characterization by SEM and EDS of Construction Waste Containing Asbestos	**76**
Characterization of Layered Double Hydroxides Nanomaterials (LDH)	**78**
Characterization of newly formed bone on TI6AL4V implants subjected to thermochemical treatment combined with cold atmospheric plasma	**80**
Comparative Morphological Analysis of Chemically Modified Graphene Derivatives	**82**
Development of Hardfacing Coatings Using Flux with Recycled Niobium Chips	**84**
EFFECT OF HUMIDITY ON THE SYNTHESIS OF CoTiO3	**86**
Effect of punctual defectsWBi6+3+´´´in the BiVO4morphology and electronic properties.	**88**
Effect of seed layer on the photoelectrochemical performance of WO3thin films	**90**
Electrodeposition of Binary NiCo/NF Alloy for Green Hydrogen Production: Preliminary Results	**92**
Electron Microscopy Characterization of Nb2O5Nanosheets Grown via Planar Confinement on Graphene Oxide	**94**
Exploring Morphological Influence On Nanostructured Nickel Oxides (NiO) Nanofoams Synthesized By Pulsed Laser Deposition (PLD)	**96**
Failure Analysis of Turbine Blades in an Oil Refinery: Insights From SEM/EDX Techniques	**98**
Formation and Microstructure of Electrochemically Induced Niobium Hydrides	**100**
Graphene Nanoplatelets on Silicon Substrates: A Characterization Study for Lubricant Oil Applications	**102**
Humidity Sensing with Manganese Oxide Nanofoam Film Prepared by Pulsed Laser Deposition	**104**
Image Processing Pipeline and Composition Analysis in Mud Rocks using SEM and EDS Images	**106**
Influence of Synthesis Parameters on Hydroxyapatite Morphology and Microstructure.	**108**
Investigation of TNZT Alloy Processed by Spark Plasma Sintering and Coated with TiO_2 Nanotubes	**110**
Lignin nanoparticles produced by ultrasound in a completely green approach	**112**
Microfabrication of Nanostructures by FIB Milling; Parameters Calibration on Si and Si+Au/Pd Substrates	**114**
Microstructural Analysis of Silicon Carbide Parts Printed by FFF with Gyroid Topology	**116**
Microstructural Characterization by SEM of Accelerated Leaching Products in Cement Pastes	**118**
Microstructural Characterization of Thermo-Reactive Diffusion Coating on AISI 1513 Steel Produced with Titanium Chips Recycling	**120**
Morphological Characterization of Piperine-loaded polymeric microparticles using Eudragit RS30D and S100	**122**
Morphological study of ZnO nanorods grown on plasma-etched substrates for spintronic applications	**124**
Nitrogen-doped Carbon Dots Analyzed by SEM and STEM with Blue Spectrum Optical Emission	**126**
Phase Evolution in WAAM Super Duplex Stainless Steel 2594: Thermodynamic Simulation and Microstructural Characterization	**128**
Quantitative Phase Analysis of Martensite and Bainite in the Coarse-Grain Heat-Affected Zone of Welded X80 Steel Using EBSD	**130**
Recycling of Machining residues in the Production of Welding Fluxes for Hardfacing Coatings	**132**
Revealing the microstructural features of cement pastes with limestone filler using SEM-EDS	**134**
Scanning Electron Microscopy Analysis of Flocs Formed by Different Coagulation Mechanisms in Kaolinite-Based Raw Water	**136**
Structural Characterization of Equimolar TiVNbCr Multicomponent Alloy upon Hydrogenation	**138**
Sustainable Hydrogen Storage Using Recycled Ti6Al4V Scraps for Metal Hydride Synthesis	**140**
Sustainable preparation of graphene oxide from sugarcane bagasse via pyrolysis and functionalization for incorporation of Ni nanoparticles	**142**
Synthesis and Characterization of Nickel Selenide Nanowires on Nickel Foam for Green Hydrogen Production: Preliminary Results	**144**

Synthesis Of Superabsorbent Polymers For Harvesting Atmospheric Water For Human Consumption	**146**
Ti/TiCu Multilayer Composites Fabricated by L-PBF and Functionalized with TiO_2 Nanotubes for Photocatalysis	**148**
Tribological Evaluation of Graphene Coatings on ASTM A36 Steel Synthed by Low-Pressure Chemical Vapor Deposition	**150**
Optical microscopy applied to materials science and related techniques such as fluorescence, confocal, and polarized light microscopy	**152**
Dispersion and Stability of CaO Microfluids from Natural Waste in Enhanced Oil Recovery: A Microscopy Study	**153**
Effect of Cathodic Protection under Alternatives Potentials on the Corrosion Morphology of Carbon Steels	**155**
Elemental Characterization of Pigments in a 19th Century Prayer Book Using Portable Milli-XRF	**157**
Immunofluorescence analysis of IL-6 and OPN in the pulp tissue	**159**
Impact of top coat thickness on the integrity of thermal barrier coatings	**161**
Kapok as an Active Morfolological Agente In Emulsion Coalescence: An Optical Microscopy Approach	**163**
Macrophage-mediated apoptosis in LNCaP cells requires functional p53	**165**
Microfossil Analysis by Raman Spectroscopy and Confocal Microscopy	**167**
Microscopy of Paraffinic Gels: A Comparison Between Bright-Field and Polarized Light Techniques	**169**
Morphological Influence of Coconut Shell Fiber Composites on Oil Removal: A Sustainable Agribusiness Solution from Alagoas	**171**
Preclinical Evaluation of the Topical Leishmanicidal Activity of Kojic Acid: An Experimental Study	**173**
Protective Effects Of Resistance Exercise On The Histomorphology Of Retroperitoneal Fat Tissue in a Rheumatoid Arthritis Model	**175**
The overlooked impact of N-terminal acetylation on biomolecular condensation	**177**
X-ray tomography applied to materials science, including lab and synchrotron-based tomography, new equipment setups, improved AI-based reconstruction methods, and 3D image analysis.	**179**
Applications of microCT in Industry and Archaeometry: Case Studies	**180**
Evaluation of Magnetic Nanoparticle Dispersion in NVT Epoxy Adhesive	**181**
Multimodal Imaging of Silica Nanoparticle Distribution: Impact of Concentration and Cell Doubling Time	**183**
Multi-Scale and Multi-Technique microscopy approaches for material characterization: From energy resources to cultural heritage	**185**
Whole-Tissue X-ray Microtomography Reveals 3D Attachment Patterns ofTrichuris murisin Murine Intestine	**187**
3D Characterization of pericarp laticifers inSwartzia langsdorffiiusing synchrotron X-ray nanotomography	**189**
Application of X-ray MicroCT for the Characterization of Defects in Flexible Risers	**191**
Microstructural Tailoring of HYTA Alloys: A Metallographic Investigation of Functionally Graded Titanium Processed by PBF-LB	**193**
Study of the Anti-Caries Action of Silver Nanoparticles by X-ray Microtomography with FIB Sample Preparation	**195**
Scanning electron microscopy (SEM) applied to biological samples, including all techniques associated with SEM, such as EDS and FIB	**197**
Creative views of Toxoplasma gondii in the feline host by SEM and Serial Block Face	**198**
Cryo-Preparation and In Situ Cooling Strategies for Electron Beam-Sensitive Samples in VPSEM	**200**
Internal organization patterns of trabeculae in long bones	**202**
3D reconstruction by slice-and-view FIB-SEM of oriented cell monolayers	**204**
A modified SEM protocol for studying plant secretions	**206**
“In Vivo Evaluation of the Osseointegration of Nanostructured Biomaterials”	**208**
Application of SEM-EDS for detecting metallic nanoparticle incorporation in the shell matrix of Perna perna due to bioaccumulation	**210**
Application of SEM/EDS in the Assessment of Heavy Metals in Marine Cyanobacteria	**212**
Calcium Hydroxyapatite Nanoparticles Functionalized with Luteolin: A Microstructural Approach for Cutaneous Biostimulation	**214**
Characterization of Zinc Oxide Nanoparticles Functionalized for Biomedical Applications	**216**
Decellularized Plant Scaffold: A Sustainable Approach to 3D Cell Culture	**218**

Development and Characterization of Buriti Oil Microparticles (Mauritia flexuosa) Obtained by Complex Coacervation	**220**
Development, Physicochemical and Morphological Characterization by Scanning Electron Microscopy of Alginate-Based Microspheres Containing Red Propolis and Metallic Nanoparticles via Ionic Gelation for Nutraceutical Applications	**222**
Evaluation of Antileishmanial Activity of Silver Nanoparticles via Cassava Starch	**224**
Extracellular Vesicle Secretion by Ependymal Cilia in Rat Brain Ventricles Following Experimental Brain Ischemia: uncovering new roles for a neglected structure	**226**
Floral meristem size influences androecium ontogeny inBauhiniaL. (Fabaceae): Insights from scanning electron microscopy	**228**
Induction and Experimental Characterization of Extracellular Vesicles from Epimastigotes of Trypanosoma cruzi	**230**
Investigation By Microscopy of The Biological Effects of Topoisomerase Inhibitors in Anti-Giardia intestinalis Chemotherapy	**232**
Microscopy Techniques for Investigating the Phytoremediation Potential of Iron by Isoëtes cangae Assisted by Mycorrhizal Fungi	**234**
Morphological Characterization of Terminalia and Spermatozoon ofOrnidia obesa(Fabricius, 1775) (Diptera: Syrphidae)	**236**
Nanostructured Mn-Co Silicates Synthed via Coprecipitation for Biomedical Applications	**238**
Temperature-Controlled Strategies for In Situ Analysis in Scanning Electron Microscopy	**240**
Toxicity of cold plasma processed coconut waterin vivomodels ofArtemia salinaandDanio rerio.	**242**
Ultrastructural Aspects of Melanosomes in Sporothrix brasiliensis	**244**
Use of Hexamethyldisilazane (HMDS) in the Preparation ofPodocnemis expansaEmbryos for Scanning Electron Microscopy	**246**
Use of Natural Deep Eutectic Solvents (NaDES) in the Cryopreservation of Fibroblast Cells in the L-132 Cell Line	**248**
Use of Scanning Electron Microscopy in the Investigation of Atmospheric Particulate Material Contamination inCrassostrea rhizophoraeShells	**250**
Use Of The New Experimental Model Metarhabditis blumi In In Vitro Assays To Test New Anthelmintic Drug Candidates	**252**
Transmission electron microscopy (TEM) applied to biological samples, including all techniques associated with TEM, such as STEM, EDS, in situ experiments, and electron tomography	**254**
Morphological Changes in Vero Cells Infected with Mayaro Virus: An Electron Microscopy Approach	**255**
Transmission electron microscopy applied to the study of eosinophilic diseases	**257**
Beyond Diffraction: EELS as a Quantitative Probe for Electron Beam Damage in Protein Crystals	**258**
Cytopathological effects of a new Lysinibacillus sphaericus isolate from Pernambuco, Brazil, on the midgut of Culex quinquefasciatus larvae susceptible and resistant to biological larvicides.	**260**
Human Lung Cells Toxicity And Detoxification Follow-Up After Internalization Of Environmental Metallurgical Nanoparticles	**262**
Integrative Microscopy Techniques Reveal Floral Reproductive System inBauhinia uruguayensisBenth. (Fabaceae)	**264**
Interfaces in cortical regions of long bovine bones	**266**
Multimodal microscopic and spectroscopic analysis of iron contamination effects on macroalgae from a Brazilian Marine Environmental Protected Area affected by the Fundão dam collapse	**268**
A C-type lectin fromBothrops leucurussnake venom killsLeishmania infantumby inhibiting cell division and mitochondria-dependent pathway cell death	**270**
Aldosterone Excess Alters Mitochondrial Biogenesis and Apoptosis in the Adrenal Gland.	**272**
Amazonian Essential Oil Exhibits Antileishmanial Activity and Induces Morphological Alterations inLeishmaniaspp	**274**
Architecture of Basal Bodies and the Mastigont System in Trichomonas vaginalis	**276**
Characterization of Acidocalcisomes in Plasmodium vivax transmission stages	**278**
Characterization of Chikungunya Virus (CHIKV) Infection in Human Neuroblastoma IMR-32 Cells.	**280**
Characterization of Foamy Macrophages in Oral Inflammatory Lesion: A Microscopic and Ultrastructural Analysis	**282**

Characterization of the structural transition for functional amyloid formation in the context of hormone cellular secretion	**284**
Convergent Microscopy Techniques Confirm the Occurrence of Callose in Laticiferous Cells of a Legume Species	**286**
CULTURE MEDIA IMPACTS HYPHAL DEVELOPMENT IN THE PATHOGENIC FUNGUSCandida albicans	**288**
Effect of Cold Rolling on the Kinetics of Spinodal Decomposition in a Lean Duplex Stainless Steels	**290**
Effect of quinazoline derivatives on theToxoplasma gondiitachyzoite mitochondrion	**292**
Effects of settleable atmospheric particulate matter on cardiac function and metal nanoparticle uptake in bullfrog (Aquarana catesbeiana) tadpoles	**294**
Impacts of settleable atmospheric particulate matter on bullfrog tadpole (Aquarana catesbeiana) gills: morphological and metal bioaccumulation	**296**
Mapping latex compounds in situ and their secretory machinery in figs (Ficus, Moraceae)	**298**
Morphological and Ultrastructural Insights into Nuclear Degeneration Patterns in Oral Squamous Cell Carcinoma	**300**
Multiscale Evaluation of Bone Regeneration Using Granular Hydroxyapatite in an Ovine Model	**302**
Nanoencapsulation of Baculoviruses Using NaDES-Stabilized Lipid Nanocarriers for Enhanced Agricultural Biocontrol	**305**
Oropouche Virus: In Vitro Isolation and Ultrastructural Study from a Human Case in Rio de Janeiro	**307**
Seminiferous tubules ultrastructure after testicular nanoparticle-mediated hyperthermia	**309**
Telemicroscopy: integrating transmission electron microscopy and medical diagnosis in Brazil	**311**
Temperature Interference on ZIKV and CHIKV Cycles in Mosquitoes and Mammalian Cells	**313**
Three-dimensional reconstruction reveals distinct organizational patterns of the intravacuolar network inCyrilia lignieresi	**315**
Titanium Nanotopography Modified by Cold Atmospheric Plasma Influences Mitochondrial Dynamics of Osteoblastic Cells	**317**
Ultrastructural Analysis of the Tegument of Schistosoma mansoni Using HighPressure Freezing and Freeze Substitution (HPF/FS)	**319**
Ultrastructural and Cytochemical Analysis of Secretory Trichomes in Syconia of Ficus citrifolia	**321**
Ultrastructural characterization of spores and crystals from a new isolate of Lysinibacillus sphaericus from Pernambuco (Ls-PE) with larvicidal activity against mosquito vectors.	**323**
Ultrastructural effects of the interaction between titanium dioxide (TiO2) microparticles andLactuca sativa	**325**
Ultrastructural evidence of metal/metalloid nanoparticle internalization in brain and muscle ofOreochromis niloticus	**327**
Ultrastructural Features of Ilhéus Virus Replication and Cytopathology Using In Vitro System	**329**
X-ray Microtomography to understand target organs morphology ofAedes aegypti	**331**
Zika Virus Infection Induces Neurodegeneration and Inflammatory Process During Retinal and Optic Nerve Lesions	**333**
Cryo-EM and Cryo-ET applied to biological samples	**335**
Structural Diversity and Dynamic States of Acidocalcisomes in Trypanosoma cruzi Revealed by In Situ Cryo-EM	**336**
When viruses hunt bacteria: unveiling the E. coli phage O86α	**338**
ACE2 nanoparticles block infection by SARS-CoV-2 variants demonstrated by Cryo-Electron Tomography	**339**
Comparative Characterization of the Three-Dimensional Morphology of P. serpens Using Cryo-Electron Tomography	**341**
Using cryoEM to study ribosome biogenesis in yeast	**343**
Adaptation of a Time-Resolved Vitrification System for (cryo) electron microscopy	**345**
Cryo-EM Structure of VgrG4 from the T6SS ofKlebsiella pneumoniaeReveals a Nucleotide-Binding Site	**347**
Structural and Functional Studies of the Bacteria-Phage Interface by Cryoelectron Tomography	**349**
Optical microscopy applied to biological samples, including confocal and super-resolution microscopy (STED, PALM, STORM) and its applications in bioimaging	**351**
Effects of Amoxicillin and Calcium/Vitamin D Supplementation on Incisor Enamel in Fluorotic Rats: A Morphological, Biochemical, and Immunohistochemical Study	**352**

Integrated Microscopy and Spectroscopy Approaches for Intracellular Localization of a Bioactive Alkaloid in the cyanobacteriumMoorena bouillonii	**354**
Protective Role of an Annexin A1-Derived Peptide in Oxidative Stress Models of Human Retinal Organoids	**356**
Proton-secreting clear cells proliferation and CD8 infiltration in epididymis of SARS-CoV-2 infected K18-hACE2 transgenic mice	**358**
Acethylcholine Receptors (nAChRs) recovery after neurorrhaphy associated with fibrin biopolymer sealant (BHF) on peripheral nerve injury	**360**
Analysis Of Oral Supplementation With Turmeric (Curcuma longa L.) Associated With Stair Climbing Resistance Exercise On The Connective Tissue Of The Extensor Digitorum Longus Muscle In a Rheumatoid Arthritis Model	**362**
Análise bioquímica e avaliação morfométrica de ovários de ratas diabéticas tratadas com lectina da casca de Crataeva tapia (Crata BL)	**364**
Análise Morfométrica dos Pulmões de Ratas Submetidas à Desnutrição Proteica Durante o Período Médio da Gestação e Suplementadas com Nanoemulsão de Canabidiol	**366**
Annexin A1 Deficiency Attenuates Renal Injury in a Streptozotocin-Induced Model of Diabetic Nephropathy	**368**
Annexin A1 Modulates Cardiac and Reproductive Outcomes in Female Mice with Streptozotocin-Induced Diabetes	**370**
Application of multifractal computational methods in the detection of changes in collagen deposition in glomeruli after renal injury due to ureteral obstruction.	**372**
Beneficial Effect Of Treatment With Capybara Oil Nanoemulsion On Liver Tissue Of Obese Mice	**374**
Can Fractal Methods Detect Spatial Changes in Liver Lipid Macro-droplets of Lactating Rats Subjected to Malnutrition and Physical Activity?	**376**
Capybara Oil In Free Form And In Nanoemulsion Improves Morphological Aspects Of Pancreatic Tissue In Obese Mice	**378**
Characterization of Biochemical Parameters by Raman Spectroscopy in Cutaneous Wound Healing in Mice	**380**
Cold Atmospheric Plasma as an Adjunct Therapy in Feline Chronic Gingivostomatitis: Histomorphometric and Immunohistochemical Evidence	**382**
Comparative Analysis of Leishmania braziliensis Infection in Phagocytic and Non-Phagocytic Cells Using 2D and 3D Culture Models	**384**
Comparative Histopathology of Vital Organs from Acute Oral Toxicity Induced by Ethanolic Extract ofRhipsalis bacciferain Swiss Albino Mice.	**386**
Comparison of Synovitis in Arthritis Models	**388**
Confocal Microscopy Analysis of TiO_2 Nanoparticle-Induced Cellular Damage in Zebrafish Embryos	**390**
Distinct Inflammatory and Metabolic Patterns Associated with Auditory Recovery in Sudden Sensorineural Hearing Loss	**392**
Efeito da Nanoemulsão de Canabidiol na Integridade Histopatológica do Miocárdio de Ratas Submetidas à Desnutrição Proteica Durante a Gestação	**394**
Effect of Cannabidiol Nanoemulsion on Cardiac Morphometry ofRats Subjected to Protein Malnutrition During Pregnancy	**396**
Effect Of Maternal Glyphosate Exposure On Neuromuscular Junctions In The Extensor Digitorum Longus Muscle Of Mice	**398**
Effects of Perinatal Exposure to Phthalates on the Extracellular Matrix of Mongolian Gerbil Ovaries	**400**
Estradiol-Induced Changes In The Prostatic Extracellular Matrix In Spontaneously Hypertensive Rats And The Effects Of The Combination With Naringenin	**402**
Estrogenic and antiandrogenic effects of atrazine on the ventral prostate of adult gerbils	**404**
Evaluation Of Cell Proliferation and Histopathological Analysis Of Ovaries From Diabetic Rats Treated With Lectin From The Bark Of Crataeva tapia (Crata BL)	**406**
Evaluation of the Effects of Aspartate-Arginine Dipeptide on the Ventral Prostate of SHR: Analysis of Metalloproteinase Activity and Incidence of Collagen Fibers in the Prostatic Stroma	**408**
Experimental infection of central nervous system cells from mice with CHIKV, in vitro.	**410**
Fractal Evaluation Of Myocardial Nuclear Architecture In Neonatal Rats Exposed To Maternal Protein-Energy Malnutrition Treated With Cannabidiol nanoemulsion	**412**
Galectin-3 as a Modulator of NLRP3 Inflammasome and Ocular Inflammation in Allergic Conjunctivitis	**414**

Histochemical, Morphometric, and Fractal Analysis of the Duodenum in Rats Subjected to Early Weaning and Treated with Melatonin	**416**
Histological and PCNA Analysis of Pregnant Rats' Ovaries Subjected to Different Intensities of Physical Activity and Protein Malnutrition	**418**
Histopathological Analysis Of The Extensor Digitorum Longus Muscle of Rats Induced With Rheumatoid Arthritis And Supplemented With Turmeric (Curcuma longa L.) Associated With Resistance Stair-Climbing Exercise	**420**
Histopathological analysis of the liver of rats induced with Diabetes mellitus and treated with Craetavia tapia lectin.	**422**
Histopathological Analysis Of The Mucosa Of The Dorsum Of The Tongue Of Rats Treated With Botulinum Toxin Type A Injection Into The Submandibular Gland	**424**
Histopathological Analysis Of The Spleen Of Rats Subjected To ProteinMalnutrition During Pregnancy And Supplemented With Cannabidiol	**426**
Histopathological analysis of the uterus of rats subjected to voluntary physical activity and protein malnutrition.	**428**
Histopathological and Histochemical Analysis of the Uterus of Pregnant Rats Subjected to Protein Malnutrition and Treated with Cannabidiol	**430**
Histopathological aspects of epididymis following chronic infection with a newTrypanosoma cruzistrain in mice	**432**
Histopathological Evaluation of the Lungs in Wistar Rats Subjected to Early Weaning and Treated with Melatonin	**434**
Histopathological Evaluation Of The Offspring Lungs Of Rats Subjected To Protein Malnutrition During Pregnancy And Supplemented With Cannabidiol Nanoemulsion	**436**
Immunohistochemical Analysis For Caspase-3 Of The Mucosa Of The Dorsum Of The Tongue Of Rats Treated With Botulinum Toxin Type A Injection Into The Submandibular Gland	**438**
Impact ofTrypanosoma cruzi(Tv Strain) Infection on Incisor Enamel Development inSwissMice.	**440**
Insuficiência hepática em ratas lactantes: efeitos sinérgicos da desnutrição proteica e do exercício físico	**442**
Internalization Of Carbon Dot Derived From Methyl Red In Yeast Cells Verified Via Confocal Microscopy For Application In Antimicrobial Photodynamic Therapy	**444**
Investigation of the Therapeutic Potential of Mesenchymal Stem Cell-Derived Extracellular Vesicles in a 3D Model of Liver Fibrosis	**446**
In VitroAnalysis of Antioxidant potential in Nanostructured Lipid Carrier Derived from Seriguela Byproducts of the Brazilian Cerrado	**448**
Metabolic Programming By Maternal Exposure To Glyphosate And High-Fat Diet: Study Of Neuromuscular Junctions In The Soleus Muscle Of Mice.	**450**
Metabolic Programming By Maternal Exposure To Glyphosate: Morphometric Evaluation Of The Extensor Digitorum Longus Muscle In Mice	**452**
Morphological and behavioral adaptations for milk production in amphibian caecilians	**454**
Morphometric Analysis of Pulmonary Alveoli in Wistar Rats Subjected to Early Weaning and Treated with Melatonin	**456**
Morphometric Analysis Of The Neonate Rats' Myocardium Born To Mothers Subjected To Protein Malnutrition Treated With Cannabidiol Nanoemulsion	**458**
Morphometric Analysis of the Uterus of Pregnant Rats Subjected to Protein Malnutrition and Treated with Cannabidiol (CBD)	**460**
Morphometric analysis of the uterus of rats subjected to voluntary physical activity and protein malnutrition.	**462**
Morphometric And Fractal Evaluation Of The Offspring Lungs Of Pregnant Rats Subjected To Protein Malnutrition And Supplemented With Cannabidiol Nanoemulsion	**464**
Morphometric and Stereological Evaluation in the Ventral Prostate of Spontaneously Hypertensive Senile Rats	**466**
Morphometric Study Of The Spleen Of Rats Subjected To ProteinMalnutrition During Pregnancy And Supplemented With Cannabidiol	**468**
MORPHOPHYSIOLOGICAL ANALYSIS OF CHICKEN EMBRYOS (Gallus gallus domesticus) SUBJECTED TO GRADUAL AND CONTROLLED EXPOSURE TO ACEPHATE	**470**

MORPHOPHYSIOLOGICAL ANALYSIS OF CHICKEN EMBRYOS (Gallus gallus domesticus) SUBJECTED TO GRADUAL AND CONTROLLED EXPOSURE TO GLIPHOSATE	**472**
Nanostructured Lipid Carriers Enhance Antioxidant Delivery of Tapereba's Coproducts in Human Keratinocytes	**474**
Natural Deep Eutectic Systems (NaDES) as Alternative Cryoprotective Agents on the Cryopreservation of SH-4 Melanocytes	**476**
NET Formation Induced by Cr-LAAO Analyzed by Confocal Microscopy in Human Neutrophils	**478**
Nonlinear Analysis by Fractal and Lacunarity of Heterochromatin in Hepatic Cells of Rats Induced with Diabetes Mellitus and Treated with Craetavia tapia Lectin	**480**
Profile Of Prostatic Developmental Markers In Prostate Development Of The Spontaneously Hypertensive Rats	**482**
Protective Role of High-intensity Resistance Training on Neuromuscular Junction in a Rheumatoid Arthritis Rat Model	**484**
Raman Microscopy for Identification of Chemical Substances with Immunotherapeutic Potential inMomordica charantia.	**486**
SARS-CoV-2 Induces Morphological Alterations and Inflammatory Responses in Human Placental Tissues	**488**
Structural and functional changes in the submandibular gland of rats treated with paroxetine	**490**
Study of Annexin A1 in Mouse Diabetic Cardiomyopathy Induced by Streptozotocin	**492**
Study Of Muscle Fibers In The Soleus Muscle Of Obese Mice Exposed To Glyphosate During The Prenatal And Postnatal Periods.	**494**
Systemic Morphological Alterations Induced By Secondary Dengue Infection In BALB/cJ Mice	**496**
Toxic effect of silver nanoparticle to Artemia salina nauplii I	**498**
Scanning probe microscopy and applications in physics, materials science, and life sciences.	**500**
Mapping the Segregation and Micellization of PEG-b-PCL Multiblock Copolymers in PLA/PCL Blends via AFM-IR	**501**
Revisiting the Microstructural Analysis of ZnO Varistors Using Atomic Force Microscopy and Electron Microscopy	**503**
Shedding Light on the Antibacterial Mechanisms of Silver Nanoparticles with Correlative Microscopy	**505**
Caracterização do biofilme de Staphylococcus aureus em vidros contendo óxido de zinco: uma abordagem topográfica e nanomecânica usando microscopia de força atômica	**507**
Comparative study of porous detection by AFM e FIB-SEM	**509**
Exploring Nanomechanical Properties of Pharmaceutical Nanocrystals: An Approach Using Atomic Force Microscopy	**511**
Hierarchical Nanotopographies and Fractal Fingerprints of Anopheles Mosquito Wing Surfaces	**513**
Kapok Fiber Modifications (Ceiba pentandra (L.) Gaerth) for Oil Spill Remediation	**515**
Nanoscale Characterization of Beta Ti processed by Accumulative Roll Bonding and 3D printing alloy for Application as Biomaterials	**517**
Scanning thermal microscopy for nanoscale mapping of thermal properties of epoxy/carbon fiber composite and multiphasic ceramic: a parameters optimization study	**519**
Image processing and alanysis for life science and materials science, including new artificial intelligence, machine learning, and deep learning methods	**521**
Automatic Rock Chip Characterization Combining LIBS and the Segment Anything Model (SAM)	**522**
Automatic Sinter Feed Characterization combining Segment Anything Model and Classification Model	**524**
Development of a Convolutional Neural Network-Based Platform for the Classification of Force Curves Acquired by Atomic Force Microscopy in Pharmaceutical Inputs	**526**
Development of Deep Learning Model for Composition Determination in Mudrocks Using SEM and EDS Images	**528**
Three-dimensional quantification of vacancies through 4DSTEM multislice ptychography	**530**
Advanced Processing of Cryo-EM Data with Modern Mini-PCs	**532**
Analysis and Comparison of the Cryo-EM structures of Togaviridae	**534**
Automated Analysis of Neurons In The Oculomotor Nerve Nucleus InArtibeus planirostris	**536**
Automated morphometry of serotonin-immunoreactive neurons in the raphe nuclei of Artibeus planirostris	**538**

Fractal Methods Applied in Computational Algorithms for Detecting Chromatin Alterations in Basal Cells of Oral Squamous Cell Carcinoma	**540**
Identification of interaction sites between the staphylococcal exfoliative toxin complex and desmoglein 1	**542**
Physicochemical Characterization of Bacterial Cellulose Membrane Functionalized with Strontium Apatite.	**544**
Single-Electron Counting in EM is changing the Foundations of Physics.	**546**
Interface between life and material sciences	**548**
Effect of phosphonate molecules in the nucleation and growth of calcium carbonate nanoparticles revealed by cryo-TEM	**549**
Immunomodulatory action of turmeric extract (Curcuma longa L.) diluted in fish oil associated with resistance exercise in a model of induced rheumatoid arthritis	**550**
Inside the Placenta: Visualizing Microplastic Internalization with Multimodal Microscopy	**552**
Integrated analysis of D-galactose-induced cellular senescence in murine thymic epithelial cells	**553**
Investigation of Nucleation and Crystallization Mechanisms in Hydroxyapatite–Chitosan Nanocomposites	**555**
Magnetic Hyperthermia with Iron Oxide: Oncological Theranostic forOsteosarcoma in Alternative Models to Animal Use	**556**
Microbiological Profile of Natural Seawater from the Brazilian Atlantic Coast and Its Influence on Carbon Steel Corrosion	**558**
Navigating the Bone–Biomaterial Interface: Structural Hierarchy Revealed by Multiscale Imaging	**560**
Raman Spectral Microscopy for the Characterization of 2D and 3D Cultures of Murine Thymic Epithelial Cells	**562**
Synthesis and Characterization of Polysaccharide-Nanozyme Biohybrids for Potential Chemodynamic Therapy of Brain Cancer	**564**

Transmission Electron Microscopy of Nanostructures and Engineering Materials, including all techniques associated with TEM, such as STEM, EDS, EELS, electron diffraction, 4DSTEM, in situ experiments, and electron tomography

30º Congresso da Sociedade Brasileira de Microscopia e Microanálise

Probing Atomic Defects in 2D Materials by Scanning Transmission Electron Microscopy

Paulo Ferreira

International Iberian Nanotechnology Laboratory (INL), 4715-330, Portugal.

Department of Mechanical Engineering and IDMEC, Instituto Superior Técnico, University of Lisbon, 1049-001, Portugal

An ubiquitous challenge in the fabrication of 2D materials and devices is the introduction of defects during synthesis and handling, in addition to the challenging production of large-area monocrystalline structures. Since any defect will have a significant effect in such thin structures, investigating the formation and stability of these defects is a critical issue in 2D materials research. The changes caused by the defects can be detrimental for certain applications, but they may also reveal opportunities for tuneable behaviours that extend the relevance of the materials to other purposes, further justifying the need for comprehensive studies on this topic.

In this paper, the purpose is to monitor the type of defects that occur in $Mo(X)_2$ where X= S or Se, under exposure to the electron beam, including their dynamics and stability. The $Mo(X)_2$ samples analysed were mechanically exfoliated flakes from bulk crystals of the material transferred onto holey SiN grids. Subsequently, single-frame HAADF-STEM images were recorded in order to determine the condition of the sample and its overall behaviour under beam exposure. Next, DPC-STEM data was acquired using fast-scanning series image acquisitions, recording several frames to reduce the rate of damage during the total acquisition time and to improve SNR by alignment and averaging of individual frames. This analysis leverages the heightened sensitivity of iDPC imaging to perform clearer observations of the structure and formation mechanisms of the defects, ultimately providing insights into potential opportunities for defect engineering and structural manipulation of the material at the atomic level.

We have found various types of defected structures, along with observations regarding their formation and equilibrium dynamics, including large vacancy complexes that acted as unstable single-atom switches, 8-fold-ring complexes, point-sharing 4-fold-ring (4|4P) grain boundaries, and the formation of staggered double VSe line (SDVL) defects in the $Mo(X)_2$ structure due to a large depletion of X atoms. These SDVLs were observed to have remarkable stability in their shortest form and were identified as a preferential configuration whenever a large loss of X atoms begins to occur, with a variety of possible formation mechanisms.

Strain Mapping from Sparse 4D STEM Data Using Physics-Informed Neural Networks

Roberto dos Reis[1,2,3]

[1]Department of Materials Science and Engineering, Northwestern University, Evanston, IL, USA
[2]Northwestern University Atomic and Nanoscale Characterization Experimental (NU*ANCE*) Center, Northwestern University, Evanston, IL, USA
[3]International Institute for Nanotechnology, Northwestern University, Evanston, IL 60208, USA

e-mail: roberto.reis@northwestern.edu

Physics-Informed Neural Networks (PINNs) offer a novel approach for strain analysis in 4D Scanning Transmission Electron Microscopy (4D STEM) datasets. By incorporating elasticity equations from continuum mechanics directly into the neural network training process, PINNs overcome limitations of traditional methods that require dense sampling and extensive preprocessing. The implementation utilizes a multilayer neural network architecture with nonlinear activation functions, trained on spatial coordinates and diffraction patterns from 4D STEM data. Unlike conventional neural network approaches, the model employs a composite loss function that simultaneously optimizes experimental data fidelity and compliance with fundamental elasticity equations. This dual optimization ensures predictions satisfy both empirical observations and established mechanical principles.

This approach enables quantitative strain mapping at nanoscale resolution from sparse datasets, overcoming a major bottleneck in high-throughput materials characterization. The method facilitates deeper understanding of mechanical behavior under different loading conditions, temperature gradients, and defect configurations. The integration of physical principles with neural networks represents a significant advancement over conventional analysis methods, particularly for complex microscopy data interpretation where traditional techniques struggle with data sparsity and noise.

Experimental Detection of Chemical Short-Range Order in Metallic Alloys by Electron Diffraction and HRTEM: Challenges and Advances

Francisco G. Coury[1], Angelo Andreolli[1], Vinícius Bacurau[1,2], Michael Kaufman[3]

[1] Department of Materials Engineering, Federal University of São Carlos, São Carlos, SP, Brazil
[2] Graduate Program in Materials Science and Engineering, Federal University of São Carlos, São Carlos, SP, Brazil.
[3] Department of Metallurgical and Materials Engineering, Colorado School of Mines, Golden, CO, USA
Corresponding Author - fgcoury@ufscar.br

Chemical short-range order (CSRO) is expected to play a crucial role in defining the physical and mechanical properties of metallic alloys. However, its experimental detection remains challenging due to the statistical nature of the phenomenon and the subtle structural deviations it causes from a random solid solution. Unlike long-range order, CSRO does not generate sharp superlattice reflections, but instead produces diffuse scattering and slight variations in local contrast, which require careful analysis. Electron diffraction, especially selected-area electron diffraction (SAED), and high-resolution transmission electron microscopy (HRTEM) have emerged as key techniques to investigate CSRO, providing sensitivity to atomic-scale chemical fluctuations that are otherwise difficult to capture [1].

In this work, we explore the application of SAED patterns and HRTEM imaging for the detection and characterization of CSRO in face-centered cubic (FCC) alloys. A major focus is placed on distinguishing true CSRO-related diffuse scattering from artifacts such as higher-order Laue zone (HOLZ) reflections, which can mimic CSRO signatures in electron diffraction patterns [2]. Our experimental approach involves acquiring diffraction patterns along multiple zone axes, combined with systematic tilting experiments to assess the persistence and nature of the observed diffuse features. Dark-field imaging and high-resolution contrast analysis are also employed to gain complementary information about the spatial distribution of chemical heterogeneities.

Our results show that HOLZ effects are universal in FCC materials and can lead to misinterpretations if not properly accounted for [2]. By careful symmetry analysis and comparison with simulations, it is possible to isolate genuine CSRO signatures, as shown in figure 1. Additionally, HRTEM images, when interpreted with the aid of simulations, reveal subtle contrast modulations related to local chemical ordering, although interpretation remains nontrivial due to the projected and statistical nature of the phenomenon [3].

Overall, these findings underscore the necessity of combining multiple electron microscopy techniques with computational modeling to achieve reliable CSRO detection. We also discuss the challenges posed by low atomic number contrast and the need for advanced statistical analysis to distinguish CSRO from random fluctuations. Future work should aim at integrating electron microscopy data with complementary techniques, such as atom probe tomography and synchrotron-based scattering methods, to further improve the understanding of chemical ordering phenomena in complex alloys.

[1] X. Chen et al., Nature 592 (2021) 712.
[2] F.G. Coury et al., Nature 622 (2023) 742.
[3] P. De Meulenaere, D. Van Dyck, G. Van Tendeloo, J. Van Landuyt, Ultramicroscopy 60 (1995) 171.
[4] A.F. Andreoli et al., Mater. Des. 238 (2024) 112724.
[5] V.P. Bacurau et al., Nat. Commun. 15 (2024) 7815.
[6] This research was supported by Laboratório de Caracterização Estrutural, FAPESP Grant 2022/02770-7 (Brazil) and DEVCOM/AFRL Grant W911NF-23-1-0310 (USA).

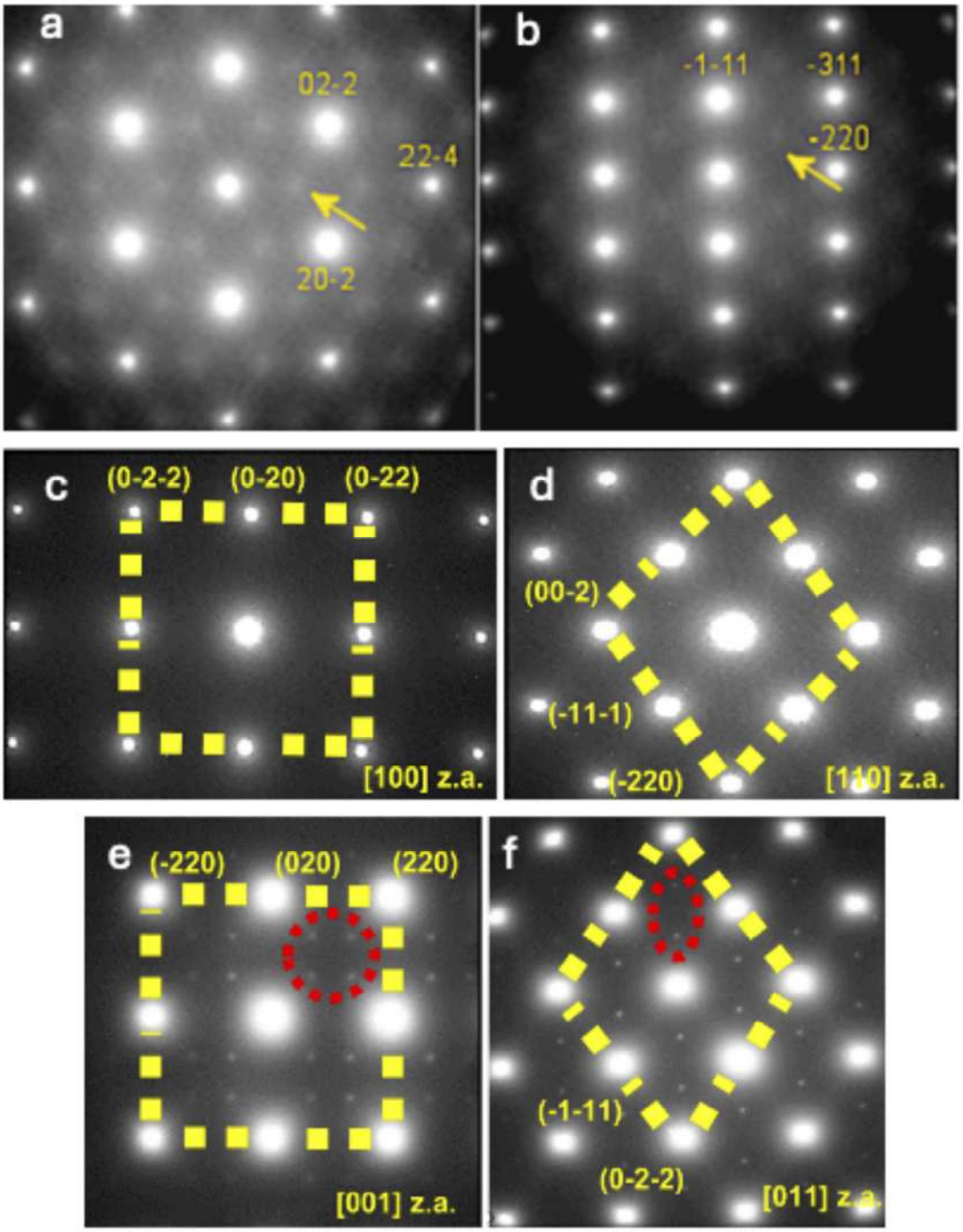

Figure 1 — Selected-area electron diffraction patterns. (a–d) Patterns along the [111], [112], [100], and [110] zone axes of a CrCoNi alloy exhibiting chemical short-range order (CSRO) without long-range order (LRO). The diffuse scattering observed in (a) and (b) are intrinsic to the disordered structure. (e, f) Patterns along the [111] and [112] zone axes of a Cr_2Ni alloy with LRO, showing the appearance of extra superlattice reflections. Adapted from [4] and [5].

Microscopic and Structural Evaluation of the Effect of High Frequency Sonication on the Obtaining of Heterostructured Monolayers of MoS_2

Mariana O. Paes[1]*, Ewellyn S. Souza[2], Johanny D. L. Sousa[2], Dyego M Oliveira[1], Jefferson L. Costa[1], Emanoel L. T. França[1], Juliana G. Restrepo[2], Eduardo Padrón-Hernández[1,2], James C. Melo[3], Adriana S. Carvalho[3]

[1] Department of Physics (DF), UFPE, Recife – PE, Brazil
[2] Postgraduate Program in Materials Science (PGMTR), Federal University of Pernambuco (UFPE), Recife – PE, Brazil.,
[3] Centro de Tecnologias Estratégicas do Nordeste (CETENE), Recife – PE, Brazil. *mariana.odon@ufpe.br

Molybdenum disulfide (MoS_2) is a two-dimensional material belonging to the transition metal dichalcogenides (TMDs) class, with a layered structure. It presents different crystalline phases that influence its electronic and optical properties: 2H (semiconductor), 1T (metallic), and 3R (trigonal semiconductor). Due to these characteristics, it is widely explored in electronic, photonic, spintronic devices, and, more recently, in quantum computing. In this study, heterostructured MoS_2 (Hybrid-MoS_2) was obtained by hydrothermal synthesis [1], followed by sonication-assisted liquid-phase exfoliation (80 kHz). High-frequency sonication is important for preserving the quality and structural characteristics of the material [2]. The coexistence of the 1T/2H phases and the incorporation of oxygen should favor optical-electronic applications. Structural, morphological, and electrical characterizations presented consistent results. Fourier transform infrared spectroscopy (FTIR) revealed bands typical of Mo-S, Mo-O, and S-O bonds, confirming the formation of MoS_2 and the incorporation of oxygen into the structure. Raman spectroscopy provided elucidation of a 1T/2H hybrid structure, with bands at 144, 234, and 333 cm^{-1} (1T phase) and vibrational modes E_{1g} (279 cm^{-1}), E_{2g}^1 (374 cm^{-1}), and A_{1g} (400 cm^{-1}), characteristic of the 2H phase. X-ray diffractometry (XRD) analysis also confirmed the formation of a heterostructure [3]. Scanning electron microscopy (SEM), Figure 1a and 1b, combined with energy-dispersive X-ray spectroscopy (EDS), revealed the production of thin, isolated layers, with good distribution of molybdenum, sulfur, and oxygen. Atomic force microscopy (AFM), Figure 1c, allowed measuring the layer heights, confirming the formation of monolayers. Transmission electron microscopy (TEM), as observed in Figure 2, demonstrated atomic arrangements that follow crystallographic structures corresponding to the 2H and 1T phases, revealing the formation of multilayer domains in regions with fine lamellar structures. Fast Fourier transform (FFT) applied to the images revealed hidden (100) and (101) planes, and interplanar distances were measured at 0.62 nm (002 plane - 2H phase) and 0.91 nm (001 plane - 1T phase). Electrical characterization was performed using the four-tip probe method on films prepared with dilute suspensions of Hybrid-MoS_2 deposited by spin coating on a Si/SiO_2 substrate. In this analysis, the sample demonstrated non-ohmic and semiconductor behavior, with electrical conductivity of 9.6×10^{-5} S/cm.

[1] M. Telkhozhayeva et al., *Langmuir* 36 (2020) 12402.
[2] J. Xie et al., *J. Am. Chem. Soc.* 135 (2013) 17881.
[3] U. Gupta et al., *APL Mater.* 2 (2014) 092802.

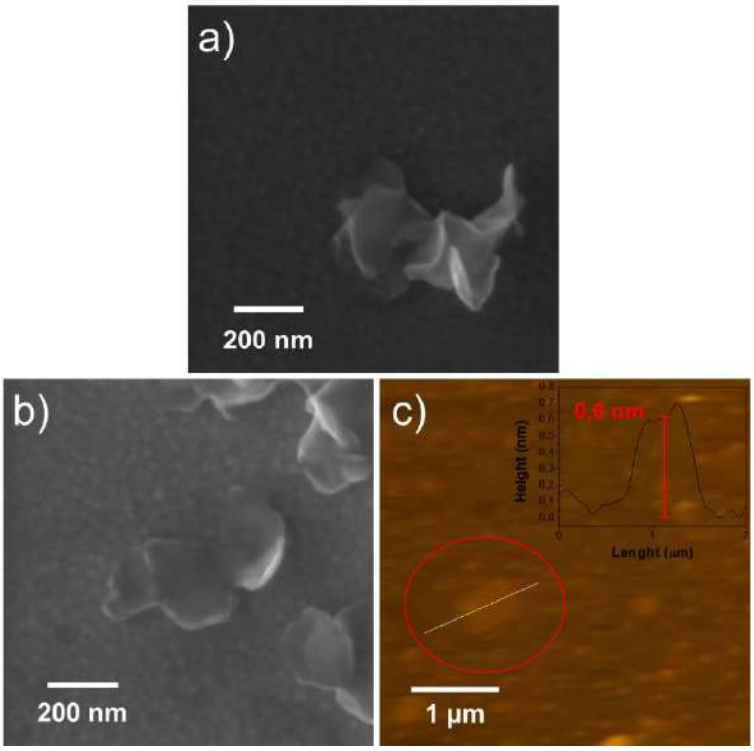

Figure 1. a) b) SEM and c) AFM images of Hybrid-MoS_2 monolayers. Insert in Figure 1c: height profile along the line in the isolated Hybrid-MoS_2 monolayer.

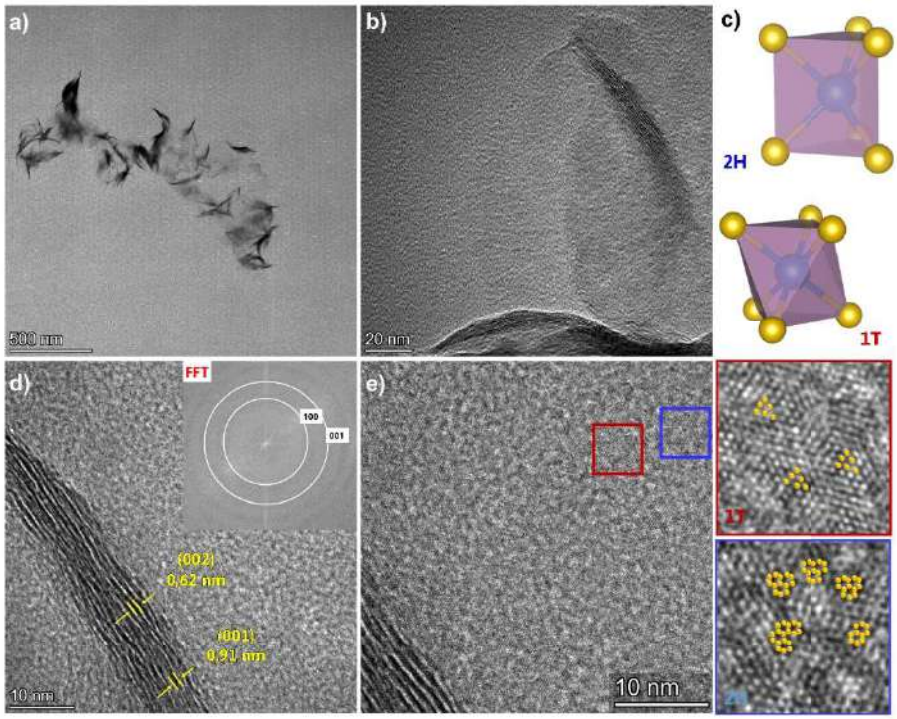

Figure 2. TEM image of a) interlaced layers and b) regions of extensive monolayers and others with lamellar stacking of Hybrid-MoS_2. c) Schematic illustration of the unit cells of the 2T and 1T phases of Hybrid-MoS_2. HR-TEM image d) highlighting the stacking region, indicating the interplanar spacing of the (002) and (001) planes, and e) highlighting the monolayer region with blue and red squares, evidencing the 2H and 1T phases, respectively. Insert in Figure 2d: FFT pattern of the image. Insert in Figure 2e: zoom in the blue region of the trigonal prismatic structure of the 2H phase, and in the red region of the octahedral structure of the 1T phase.

Probing Short- and Long-Range Order in Molecular, Mineral, and Oxide Nanomaterials Using 3D Electron Diffraction and Electron PDF

Naga V. V. Mogili[1*], Derik. T. Machado[1,2], João B. S. Junior[1,3], Jefferson Bettini[1], Edson R. Leite[1,2]

[1]Laboratório Nacional de Nanotecnologia, CNPEM, [2]Departamento de Química, UFSCar, [3]Instituto de Química, UNICAMP.
e-mail: vishnu.mogili@lnnano.cnpem.br

Structural analysis across multiple length scales is essential for understanding the behavior of functional and heterogeneous materials. In this work, we combine two complementary electron diffraction techniques—3D electron diffraction (3D ED) [1] and electron pair distribution function (e-PDF) [2] analysis—to investigate systems with varying degrees of crystallinity, ranging from ordered molecular and mineral structures to disordered oxide nanoparticles. 3D ED was applied to two distinct crystalline samples: paracetamol and jacutingaite (Pt_2HgSe_3) microcrystals synthesized via high temperature solid state reaction. Paracetamol was used as a model molecular system to demonstrate the capability of 3D ED in solving structures of small organic compounds. The known polymorph was successfully identified (Figure – 1), validating the method for pharmaceutical applications. In the case of jacutingaite, the reconstruction of the 3D reciprocal lattice followed by structure refinement provided detailed insights into the crystallographic symmetry and atomic arrangement of this layered mineral phase. In contrast, e-PDF analysis was employed to study barium tin oxide ($BaSnO_3$) nanoparticles, a perovskite-type oxide subjected to ex-situ phase transformation. These nanoparticles, with crystallite sizes in the 1–4 nm range, were analyzed using total scattering data extracted from nano-area electron diffraction patterns. The reduced pair distribution functions revealed short- and medium-range correlations (Figures – 2a, 2b), enabling the assessment of local distortions induced by the transformation—features not accessible via conventional diffraction methods. Together, these results highlight a multimodal approach to electron diffraction-based structural characterization. By combining 3D ED for crystallographic structure solution and e-PDF for local structural analysis in nanoscale and disordered systems, this study demonstrates the broad applicability and complementarity of these techniques for probing structural complexity at the nanoscale.

REFERENCES:

[1] Gemmi, M. *et al.,* ACS Cent. Sci. 5, (2019) 1315−1329.
[2] Mogili N.V.V. *et al.,* Acta Cryst. A79, (2023) 412-426.
[3] This research was supported by FAPESP Grant No. 2021/03321-9, 2023/00906-1 and 2013/07296-2.

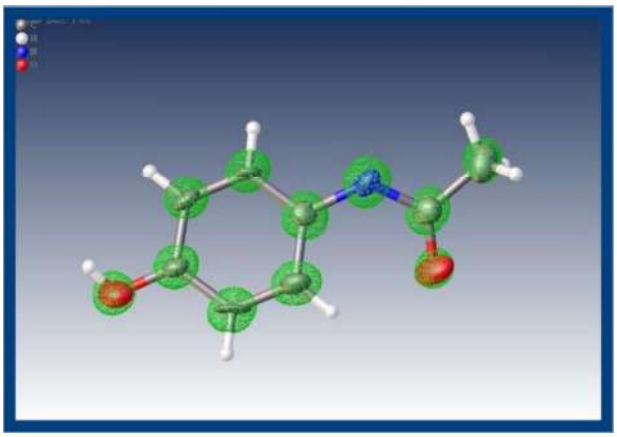

Figure 1. Refined crystal structure of paracetamol obtained from 3D Micro Electron Diffraction (3D ED) data. The molecular model was refined using the SHELXL software suite and visualized in Olex2. The green mesh represents the electron density isosurface at 1.075 $e^{-}/Å^3$, confirming accurate localization of atoms, including light elements such as hydrogen. 3D ED enables structural determination from sub-micron crystals, as demonstrated here. Data were collected on a Thermo Fisher Talos TEM equipped with a CetaD CMOS 4k × 4k camera, operated at 200 kV. The resolution cutoff was set to 0.85 Å.

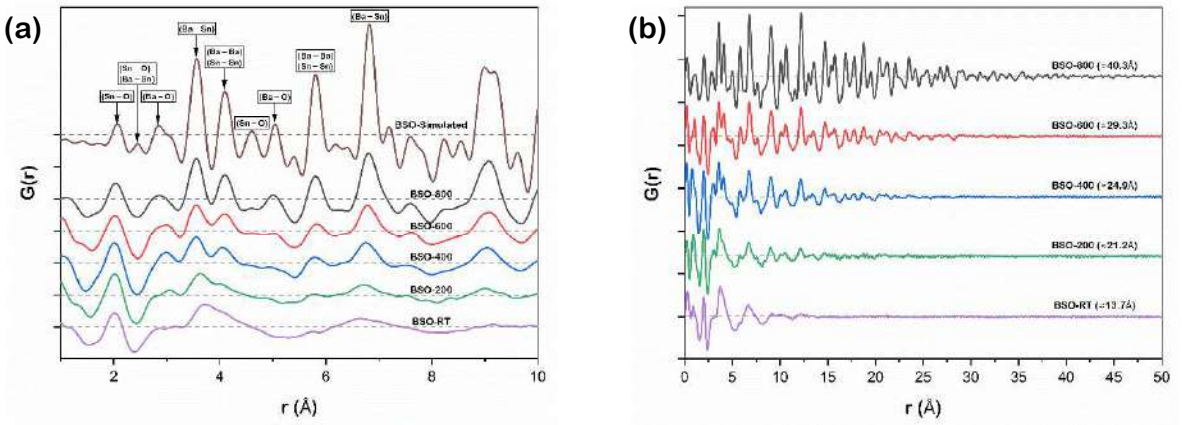

Figure 2. (a, b) show the extracted electron Pair Distribution Function (e-PDF) $G(r)$ profiles from Barium Stannate ($BaSnO_3$, BSO) nanoparticles in the low-r (1–10 Å) and wide-r (1–50 Å) ranges, respectively, derived from the reduced intensity function $\varphi(q)$. Comparison with a simulated $G(r)$ profile (labeled "BSO-Simulated" in **Figure 2a**) reveals the evolution of pairwise bond lengths in BSO nanoparticles that have undergone ex situ phase transformation. The gradual decay of peak intensities in **Figure 2b** reflects the degree of structural coherence, enabling estimation of the effective crystallite size in the BSO sample. Experimental data were acquired using a Thermo Fisher Titan Themis aberration-corrected TEM operated under parallel illumination at 300 kV.

A Transmission Electron Microscopy Investigation into the Nanoscale Amorphization and Enhanced Conductivity of FIB-Patterned MoS_2 Monolayers

Tarcísio M. Perfecto[1]*, Matheus F. F. das Neves[1], Heloísa M. Barêa[1], Jefferson Bettini[1], Felipe Crasto de Lima[2], Rafael F. Oliveira[1], Adalberto Fazzio[1,2,3], Murilo Santhiago[1,3] Edson R. Leite[1]

[1]Brazilian Nanotechnology National Laboratory (LNNano), Brazilian Center for Research in Energy and Materials (CNPEM), Campinas, SP, Brazil. [2]Ilum School of Science, Brazilian Center for Research in Energy and Materials (CNPEM), Campinas, SP, Brazil. [3]Federal University of ABC (UFABC), Santo André, SP, Brazil.

*tarcisio.perfecto@lnnano.cnpem.br

The controlled engineering of defects in two-dimensional materials like molybdenum disulfide (MoS_2) is a promising avenue for tuning their electronic properties for next-generation devices [1]. While methods like Focused Ion Beam (FIB) irradiation can induce significant changes in electrical conductivity, the underlying structural transformations at the atomic scale remain a subject of intense investigation [2, 3]. This work presents a definitive microstructural analysis, centered on advanced aberration-corrected scanning/transmission electron microscopy (S/TEM), to elucidate the mechanisms driving an anomalous, order-of-magnitude increase in conductivity in MoS_2 monolayers following localized Ga^+ FIB irradiation. Our investigation systematically correlated the ion dose with the resulting nanoscale structure, providing direct visual evidence of a dose-dependent lateral damage profile. High-resolution TEM (HR-TEM) and high-angle annular dark-field (HAADF-STEM) imaging revealed that the edges of the FIB-patterned channels undergo complete amorphization, confirmed by the emergence of diffuse halos in their corresponding Fast Fourier Transform (FFT) patterns. In contrast, the central regions of the channels, even when subjected to the highest ion doses, retained a degree of crystallinity, characterized by the presence of randomly oriented nanocrystalline domains within a disordered matrix. This structural dichotomy between the edge and center was directly correlated with spectroscopic and electrical mapping, confirming that the amorphized regions are the primary pathways for enhanced current flow. Furthermore, atomic-resolution STEM analysis allowed for precise measurement of Mo-Mo interatomic distances, which remained consistent at approximately 0.30 nm across all irradiated samples. This critical finding challenges the hypothesis that enhanced conductivity arises from the formation of shorter, metallic-like bonds [4], suggesting instead that the increase in the density of delocalized states within the amorphous structure, as supported by DFT calculations, is the dominant mechanism. Ultimately, this study underscores the indispensable role of state-of-the-art electron microscopy in providing the fundamental structural evidence necessary to understand and engineer the properties of 2D materials at the atomic level.

[1] Liang, Q., Zhang, Q., Zhao, X., Liu, M., & Wee, A. T. S. (2021). Defect Engineering of Two-Dimensional Transition-Metal Dichalcogenides: Applications, Challenges, and Opportunities. ACS Nano, 15(2), 2165–2181.
[2] Telkhozhayeva, M., & Girshevitz, O. (2024). Roadmap toward Controlled Ion Beam-Induced Defects in 2D Materials. Advanced Functional Materials, 34(45).
[3] Florindo, B. R., et al. (2023). Patterning edge-like defects and tuning defective areas on the basal plane of ultra-large MoS2 monolayers toward the hydrogen evolution reaction. Journal of Materials Chemistry A, 11(37), 19890-19899.
[4] Krbal, M., Prikryl, J., Pis, I., Prokop, V., et al. (2023). Anomalous electrical conductivity change in MoS2 during the transition from the amorphous to crystalline phase. Ceramics International, 49(2), 2619–2625.

This research was supported by FAPESP grant number: 2022/14720-4

By employing advanced image processing techniques on the raw STEM data (Figure 1), we can move beyond qualitative observation. Azimuthal integration of FFTs provides a quantitative measure of crystallinity, confirming the trends observed visually. Furthermore, filtered images, generated by inverse FFT of specific Bragg reflections, act as a powerful visualization tool, effectively mapping the areas that retain their original lattice structure. This analysis reinforces the conclusion that the FIB process creates a heterogeneous material, with highly conductive amorphous pathways flanking a less-damaged central region.

Figure 1: Advanced analysis of crystallinity using filtered TEM images

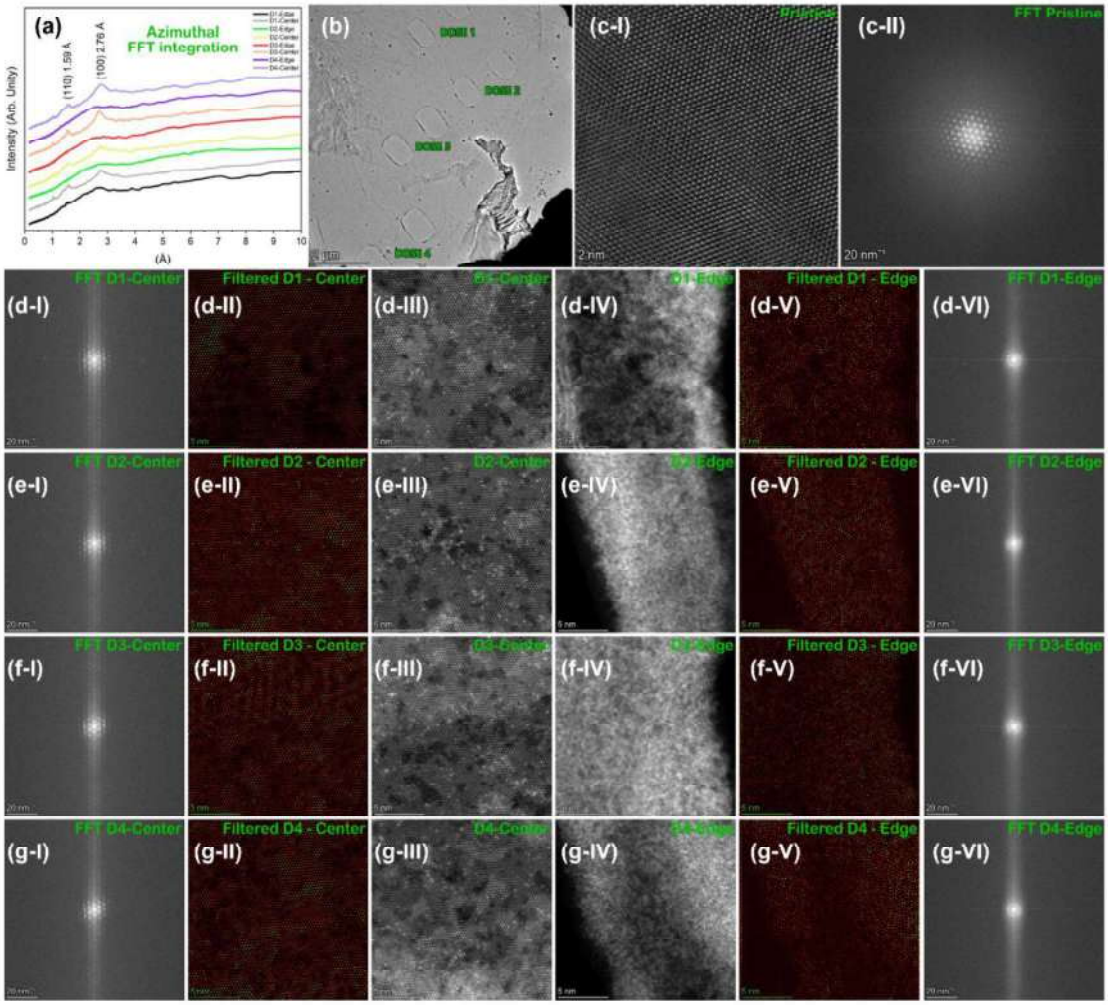

Characterization of Nb and Mo precipitates in Ferritic\Bainitic steels using HRTEM assisted by EDS

Davi Fajardo[1]*; Renan M. C. Lima[1];Adriele A. de Almeida[1]; Evellyn R. N. Silva[1];Cauê S. C. Nogueira[1]; Yutao Xing. [2]

[1]Instituto de Física - UFF, [2] Engenharia Química - UFF
*davifajardo@id.uff.br

High Strength Steels (HSS) and Advanced High Strength Steels (AHSS) are important segments of the automotive market. They include many commercial steels such as *Dual-Phase* (DP), *Complex Phase* (CP), and martensitic (MS) steels, known for their good balance between strength and ductility [1]. Ferritic\Bainitic steels are classified as HSS, but composition in study have been breaking the properties of the AHSS range. They feature a microstructure composed of ferrite and bainite, produced directly by hot-rolling, and are alloyed using elements such as niobium and molybdenum. In the microstructure, ferrite contributes to good ductility and formability, while bainite provides higher mechanical strength. This combination results in an ideal balance between toughness and stiffness [2]. The use of only hot rolling, without the need for complex heat treatments, significantly reduces the manufacturing costs. Due to its higher strength, this steel allows the production of thinner and lighter automotive components, contributing to vehicle energy efficiency [3]. This higher strength comes mainly from the microstructure refining. The alloying using Nb, Mo and V is believed to lead to strain-induced precipitation. The precipitates formed improve the microstructure refining. In this work, an FB steel alloyed with Nb, Mo, and V was studied. For its microstructural characterization, samples were prepared using the *Focused Ion Beam* (FIB). The procedure was carried out in a dual beam column with a scanning electron microscope and an ion beam, in which a region of interest was identified, cut, removed using a nanomanipulator, and welded to a support grid. Subsequently, the sample was polished and prepared for analysis in a transmission electron microscope (TEM) [4]. Using the *Energy Dispersive Spectroscopy* (EDS) technique, it was possible to identify the presence of precipitates containing niobium and molybdenum, confirming the presence of these precipitates and their possible effect on the microstructural distribution of the steel [5].

[1] WorldAutoSteel. (2014). *Advanced High-Strength Steel (AHSS) Application Guidelines, Version 5.0*.
.

[2] Bleck, W., et al. (2010). "New developments in AHSS for automotive applications." *Steel Research International*, 81(9), 812–817.

[3] Kuziak, R., Kawalla, R., & Waengler, S. (2008). "Advanced high strength steels for automotive industry." *Archives of Civil and Mechanical Engineering*, 8(2), 103–117.

[4] Mucha, H., Kato, T., Arai, S., Saka, H., Kuroda, K., & Wielage, B. (2005). Focused ion beam preparation techniques dedicated for the fabrication of TEM lamellae of fibre-reinforced composites. *Journal of Electron Microscopy (Tokyo), 54*(1), 43–49.

[5]Williams, D.B., & Carter, C.B. (2009). *Transmission Electron Microscopy: A Textbook for Materials Science*. Springer.

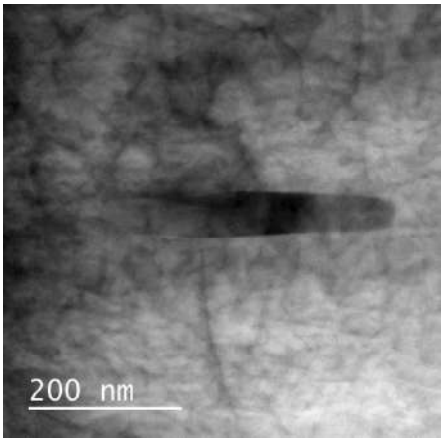

Figure 1. FB on TEM.

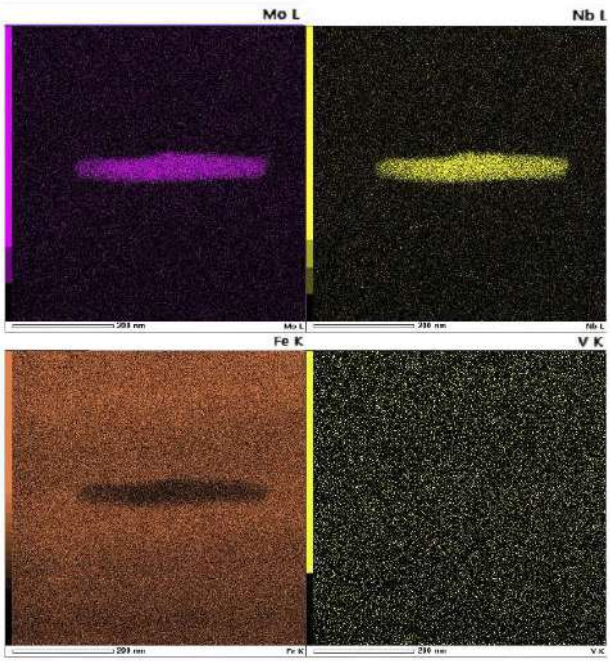

Figure 2.Result of EDS performed in the precipitate region confirming the composition containing Nb and Mo, as well as the proper distribution of V as an alloying element.

Characterization of NbC Carbides in Lightweight Fe-Al-Nb-C Steel Using Electron Microscopy

Kellen Venancio dos Santos[1], Eustáquio de Souza Baêta Júnior[1],Camila Alves Pelicarto da Silva[1], Letícia dos Santos Aguilera[2], José Brant de Campos[1], **Suzana Bottega Peripolli[1*]**

1 - Postgraduate Program in Mechanical Engineering, Faculty of Engineering, State University of Rio de Janeiro.
2 - Postgraduate Program in Science and Technology of Materials, Polytechnic Institute, State University of Rio de Janeiro.
speripolli@eng.uerj.br

The automotive industry has driven material science efforts toward the development of lighter metallic alloys. In this context, aluminum has established itself as a primary candidate for the partial replacement of iron in structural alloys due to a combination of strategic factors [1,2]. The increasing demand for materials with high mechanical strength and low density has further stimulated the development of advanced metallic alloys, such as those in the Fe-Al-Nb-C system. The application of these materials, however, requires precise control of the microstructure, as the presence and distribution of intermetallic phases and precipitates, potentially formed by the addition of alloying elements, can directly influence mechanical performance. Therefore, detailed microstructural characterization is essential, enabling not only the identification of the present phases but also a comprehensive understanding of the relationship between microstructure and properties. In this work, micro- and nanostructural characterization was performed to investigate the distribution, morphology, and semi-quantitative chemical composition of Nb-containing precipitates, with emphasis on electron microscopy analyses using Energy Dispersive Spectroscopy (EDS). Surface regions of interest were initially selected by Scanning Electron Microscopy (SEM), performed on a JEOL JSM-7100FT FEG SEM at NanoFAB/UERJ) (see Figure 1). Subsequently, ultrathin lamellae were prepared using a focused ion beam (FIB) lift-out method, with samples structured as triple windows, as illustrated in Figure 2(A). Scanning Transmission Electron Microscopy (STEM) analyses using a High Angle Annular Dark Field (HAADF) detector were also carried out at the National Nanotechnology Laboratory (LNNano/CNPEM). The obtained images, as shown in Figure 2, combined with the semi-quantitative chemical analyses of the highlighted region summarized in Table 1, allowed for the observation of the morphology and distribution of Nb- and C-enriched precipitates. These precipitates are associated with the presence of NbC-type carbides dispersed throughout the matrix, an important finding considering that their volumetric fraction increases with niobium content, which can significantly impact the material's strength and hardness [3].

[1] RANA, R.; LIU, C.; RAY, R. K. Low-density low-carbon Fe–Al ferritic steels. *Scripta Materialia*, v. 68, p. 354–359, 2013. DOI: 10.1016/j.scriptamat.2012.10.004.
[2] RAWAT, Pankaj; PRAKASH, Ujjwal; PRASAD, V. V. Satya. Microstructure and mechanical behaviour of Nb-containing high Al ferritic low density steels. *Materials Characterization*, v. 204, p. 113176, 2023. DOI: 10.1016/j.matchar.2023.113176.
[3] KHAPLE, S.; PRAKASH, U.; GOLLA, B. R. et al. Effect of niobium addition on microstructure and mechanical properties of Fe–7Al–0.35C low-density steel.

Metallography, Microstructure, and Analysis, v. 9, p. 127–139, 2020. DOI: https://doi.org/10.1007/s13632-020-00622-9.
[4] This research was supported by FAPERJ (Brazil)

Figure 1 – SEM images acquired using secondary electrons, showing NbC precipitates indicated by circles. (A) 2000× magnification; (B) 1000× magnification.

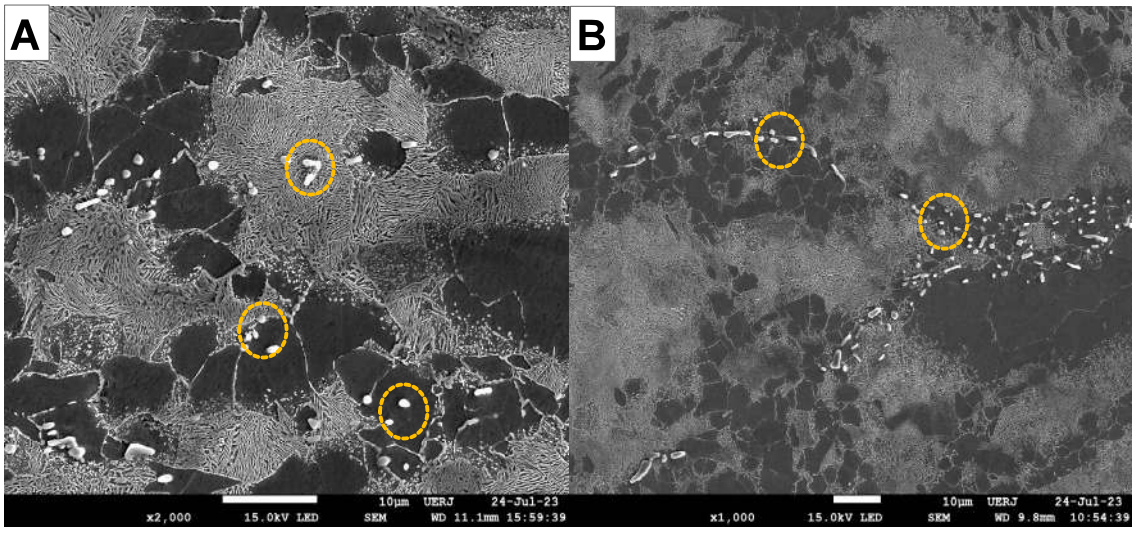

Figure 2 – (A) FIB lamellae in three windows and EDS area mapping performed in the TEM, showing the distribution of Nb, Fe, Al, and C elements (Nb in yellow, Fe in blue, Al in green, and C in red).

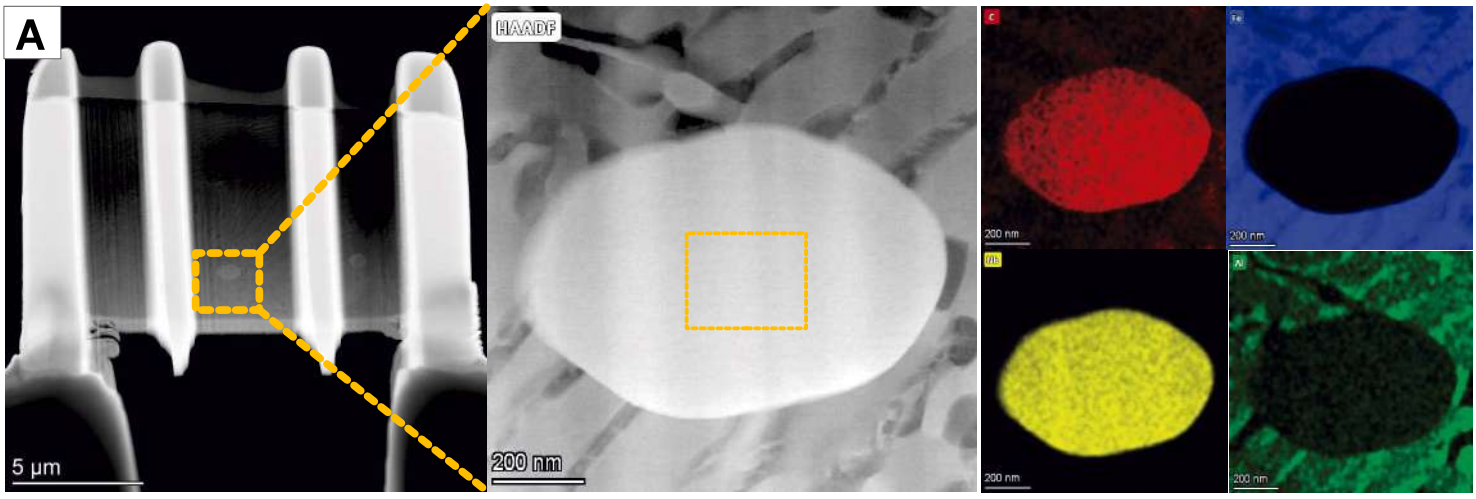

Table 1 – TEM-EDS semi-quantitative mass fractions of Fe, Al, and C in the region outlined by the yellow square on the precipitate shown in Figure 2.

Z	Chemical Element	Mass Fraction (%)	Atomic Fraction (%)
6	Carbon	1.72	11.81
13	Aluminum	0.06	0.17
26	Iron	1.09	1.62
41	Niobium	97.13	86.40

Evaluation of Ar/O_2 and heating under vacuum as protocols for cleaning self-supported thin films based on capped nanoparticles

Tanna E. R. Fiuza[1], Tarcísio M. Perfecto[1], Jefferson Bettini[1], Murillo H. M. Rodrigues[1,2,¥], Danilo B. Janes[1], Edson R. Leite[1,2]

[1] Brazilian Nanotechnology National Laboratory (LNNano), CNPEM, 13083-970 Campinas, São Paulo, Brazil

[2] Department of Chemistry, Federal University of São Carlos, 13565-905 São Carlos, SP, Brazil

[¥] Present address: Chemistry Institute, University of Campinas, Campinas, SP, Brazil

*tanna.fiuza@lnnano.cnpem.br

The study of colloidal nanoparticles by transmission electron microscopy is one of the most important paths to better understand the nanoparticles' synthesis, evolution, and stability for many applications. Also, it is possible to correlate these properties with other characterizations, getting a full picture of the sample. In general, decreasing the nanoparticles' size requires increasing the amount of capping ligands to avoid agglomeration, thereby keeping the dispersion stable for several weeks. Another interesting use of capping ligands is to produce homogeneous thin films from the nanoparticles on substrates or self-supported thin films using the particles directly on TEM grids. In the last case, this approach is interesting to follow processes in which the interaction between the film and the ultrathin carbon layer can affect the process. For instance, to follow the sintering of a nanoparticle-based thin film, the interaction with the ultra-thin carbon layer may decrease the atom movement under the stimulus (i.e., irradiation or heating), or even halt it, making the analysis impossible.

The main issue related to the capped nanoparticles is the deposition of a carbon layer in the analyzed region, particularly in scanning (STEM) mode. For higher resolution imaging and chemical mapping, focusing the electron beam on a small region can lead to the formation of a carbon layer on the sample, making it difficult to refine some alignments (i.e., astigmatism) or, in some cases, preventing the collection of good images or maps. It requires additional steps, such as purification steps to remove excess capping ligands from the nanoparticle surface, or cleaning steps when the sample is already on the grid, such as beam shower, Ar/O_2 plasma, etc.[1] Given that the self-supported thin film contains a large number of capping ligands to maintain its stability within the TEM grid holes, it is reasonable to anticipate that beam showering will require considerable time to clean a small region, making it a secondary step to be performed after other major cleaning steps. For this reason, we investigated the effectiveness of Ar/O_2 plasma and heating under vacuum to clean a self-supported thin film of oleic acid-capped monoclinic ZrO_2 nanoparticles, prepared as described in our previous work. [2] The thin film is only supported by the Holey Carbon layer, without an ultrathin carbon membrane.

The first approach was to clean the sample supported on the TEM grid using Ar/O_2 plasma (Fischione Plasma Cleaner model 1020), and the process was followed by EELS using a Gatan Tridiem 683 detector coupled to a JEOL JEM-2100F microscope operated at 200 kV. Multiple steps of 5s each were carried out, and after 2 minutes (summed cleaning time), there was a decrease in the C-K peak. This decrease leads to the better visualization of the peaks between 330-350 eV, related to $M_{2,3}$ edges of Zr [3]. After the cleaning time, some regions of the ZrO_2 thin film ruptured, and despite still being in the grid, the stability was reduced, and some regions appeared to be moving during the image collection. Figure 1a shows the comparison between the EELS spectra of the fresh and cleaned thin film.

A cleaning using a vacuum furnace was proven to be effective, as seen in our previous work. [2] However, it is not easy to understand the evolution of the film inside the vacuum furnace. Therefore, the evolution of the ZrO_2 thin film under heating in vacuum was followed using a Cs-corrected Titan Cubed Themis microscope operated at 300 kV, while heating using a Gatan 628 single tilt heating holder, from room temperature up to 500 °C, and 30 min of holding time. The evolution was followed using low magnification to have a better look at the average behavior. In general, the cleaning occurred by gradual removal of capping ligands, leading to the formation of some holes due to the contraction of the film. No significant sintering of ZrO_2 nanoparticles was seen at this point. Figure 1 shows the comparison between the EELS spectrum collected after the heating process (JEM-2100F microscope) with the fresh and cleaned with plasma. No significant changes were seen comparing the plasma and heating cleaning spectra. However, the cleaning by heating leads to the rupture of small regions instead of larger areas, contributing to a better stability of the film. Image 1b-c shows the fresh ZrO_2 thin film and the cleaned film using a heating holder. It is important to note that there was a significant difference between the carbon removal closer to the copper grid edge and in the center of the square using the heating holder, which was not observed in the cleaning process using a conventional vacuum furnace. We hypothesize that these differences can be decreased by optimizing the conditions, particularly the holding time during the in situ heating. Despite this, the experiment provided valuable insights into the comprehension of the cleaning process, which will be considered and optimized for future experiments involving self-supported thin films based on capped nanoparticles.

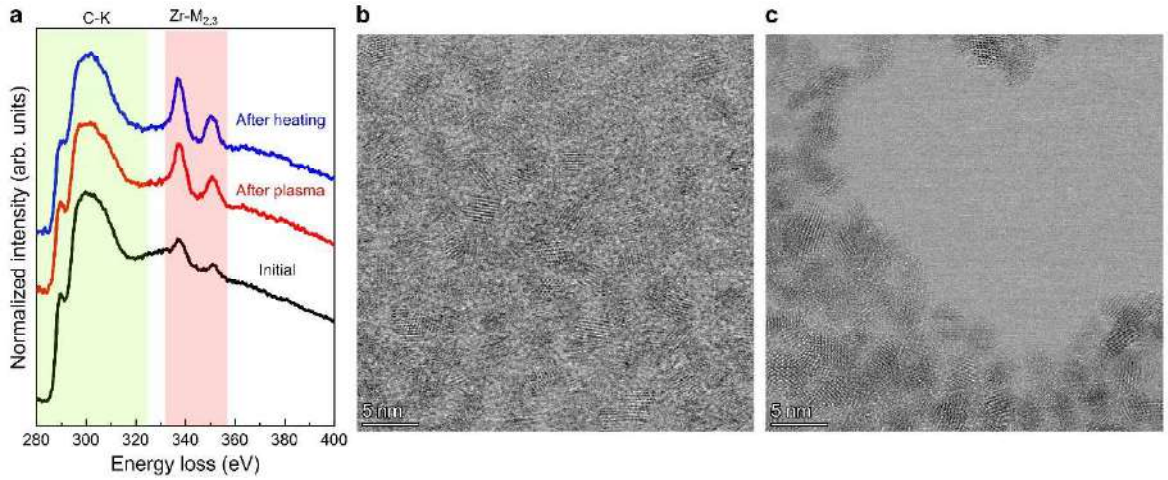

Figure 1. (a) EELS spectra showing the C-K and Zr-$M_{2,3}$ peaks of fresh film, and after Ar/O_2 and heating cleaning protocols. (b-c) High-resolution images of ZrO_2 thin film (b) before and (c) after cleaning using a heating holder, showing the formation of a hole due to the removal of capping ligands and decreasing distance between ZrO_2 nanoparticles without sintering.

[1] Li et al. Ultramicroscopy, 2021, 221, 113195
[2] Fiuza et al. Nano Lett., 2022, 22, 5, 1978-1985.
[3] EELS Atlas, available at https://eels.info/atlas.

Evaluation of Dispersion of Chemical Reagents by SEM-EDS and TEM-EDS

Matheus Costa Ximenes[1], Suzana Bottega Peripolli[1], Jaqueline Dias Senra[2]*, José Brant de Campos[1]*.

[1]Mechanical Engineering Department, Rio de Janeiro State University, 121, Fonseca Teles St, Rio de Janeiro, RJ 20940-200, Brazil, [2]Chemistry Institute, Rio de Janeiro State University, 524, São Francisco Xavier St, Rio de Janeiro, RJ 20550-900, Brazil
* jaqueline.senra@uerj.br, brant@uerj.br

The Suzuki-Miyaura cross-coupling reaction is a widely used tool in the synthesis of biaryl compounds and is especially relevant in the pharmaceutical industry and in the manufacture of optoelectronic materials. In this context, heterogeneous palladium-based catalysts have been increasingly explored due to their high efficiency, ease of recovery, and the possibility of reuse over multiple reaction cycles [1]. In solid-state reactions, the catalytic activity of these systems strongly depends on the spatial distribution of active components deposited as films, such as the metal itself (Pd) and organic reactants [2]. The detailed characterization of the dispersion of these species within supported solid matrices thus becomes essential for predicting reaction performance and optimizing experimental conditions. This work presents a morphological and compositional analysis of a catalytic system applicable to the coupling reaction between carbazole and phenylboronic acid, aiming at obtaining a functionalized carbazole derivative, for this purpose, scanning electron microscopy (SEM) and transmission electron microscopy (TEM), both combined with energy dispersive spectroscopy (EDS) technique [3,4]. These approaches allow the evaluation of surface and internal distribution of reagents and the catalytic metal at different resolution scales, in addition to identifying possible agglomeration or segregation zones that could compromise the catalytic activity [5]. Characterization by energy dispersive spectroscopy coupled to scanning electron microscopy (SEM-EDS) allows a comparative analysis between two widely used techniques in thin film deposition: dip-coating and drop-casting. These methodologies are frequently used in the preparation of functional surfaces for applications in sensors, optoelectronic devices, catalytic systems, and protective coatings [6,7]. On the other hand, characterization by energy dispersive spectroscopy coupled to scanning transmission electron microscopy (STEM-EDS) allows a detailed analysis of the internal structure and elemental distribution in thin films deposited in TEM grids. Through an initial comparison between the aforementioned thin film deposition techniques, it was possible to observe a relatively uniform dispersion of palladium over the substrate used, suggesting a good exposure of the active metallic species. Additionally, it was possible to map the presence and relative location of carbazole and phenylboronic acid adsorbed on the catalyst surface before the reaction, providing valuable information regarding the interaction between the reactants and the solid reaction medium [8]. The combination of SEM-EDS (figure 1) and STEM-EDS (figure 2) techniques proved effective in the accurate detection of both light and heavy elements simultaneously, contributing to the understanding of the micro and nanostructures of the analyzed system.

[1] I. P. Beletskaya, F. Alonso, V. Tyurin, Coord. Chem. Rev. 385 (2019) 137–173.
[2] H. Lin et al. Nanoscale, 16 (2024) 6151–6162.
[3] J.I. Goldstein et al., Scanning Electron Microscopy and X-ray Microanalysis, Springer, New York, 2017.
[4] D. B. Williams, C. B. Carter, Transmission Electron Microscopy: A Textbook for Materials Science, Springer, New York, 2009.
[5] K.E. MacArthur et al., Microsc. Microanal. 22 (2016) 71–81.

[6] X. Tang, X. Yan, J Sol-Gel Sci Technol. 81 (2017) 378–404.
[7] A.K.S. Kumar et al., Electrochem. commun. 121 (2020), 106867.
[8] M.C. Ximenes et al., Angew. Chem. Int. Ed. 64 (2025) e202425591.

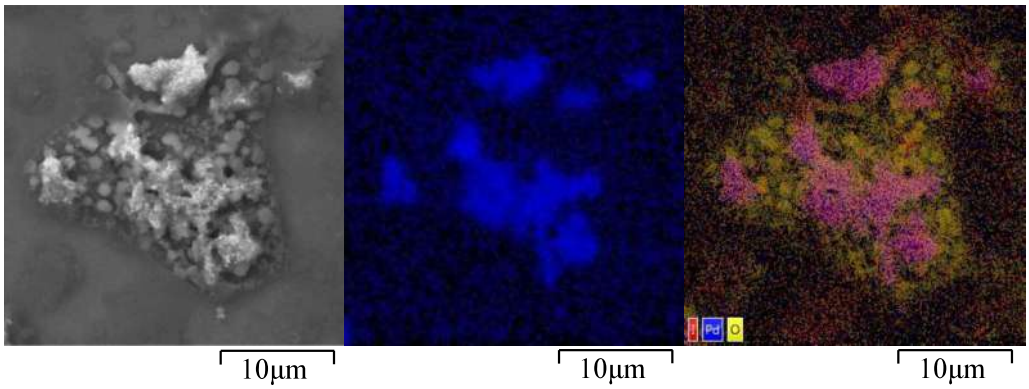

Figure 1. SEM electron image (left), EDS palladium map (center) and EDS layered image (right).

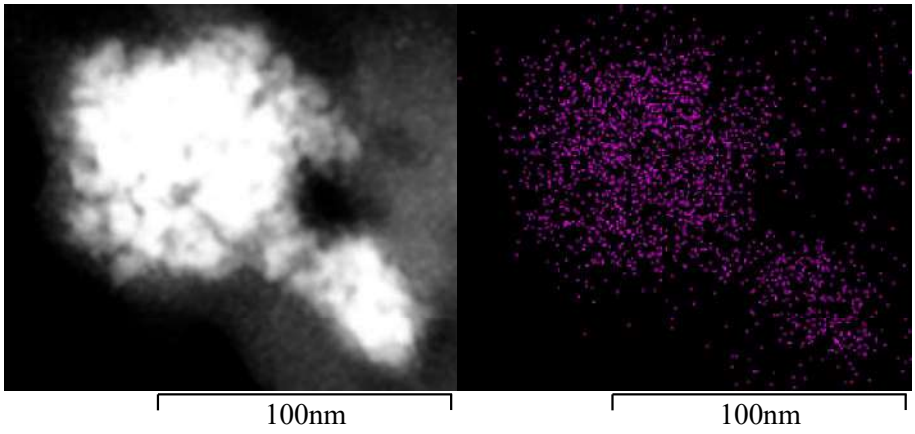

Figure 2. STEM electron image (left) and palladium EDS map (right).

Fluorescent Nanoparticles based on Mesoporous Silica and Chitosan applied for Latent Fingerprint Development

Laís F.A.M. Oliveira[1]*, Lais V.A.T. da Silva[1], Artur F. Sonsin[1], Meclycia S. Alves[1], Cristiane V. Costa[1], Jeane C.S. Melo[1], Nicholas Ross[2], Ticiano G. do Nascimento[1], Eduardo J.S. Fonseca[1], Alexandro M.L. de Assis[145], A. Robert Hillman[2] and Adriana S. Ribeiro[1].

[1]Federal University of Alagoas, Maceió, AL, Brazil, [2]Department of Chemistry, University of Leicester, Leicester, UK and [4]Federal Police, Brazil
*lais.farias@fis.ufal.br

The papillary ridges on human fingertips are unique and permanent, making them fundamental in forensic identification. When a finger touches a surface, sweat and oily substances are transferred, forming marks that are often invisible to the naked eye – the so-called latent fingerprints [1]. To make them visible, physicochemical techniques using colored or fluorescent reagents are employed. Conventional methods include simple powders, cyanoacrylate fuming and ninhydrin. Although effective, these approaches present limitations in terms of sensitivity, selectivity, and toxicity [2]. Therefore, innovative strategies have emerged, such as the use of mass spectrometry, electrochemical techniques, and nanoparticles, offering superior performance in fingerprint development [3]. Mesoporous silica nanoparticles, specially MCM-41, stand out due to their high surface area, stability, and ease of functionalization [4]. However, their tendency to aggregate requires surface modification, usually through polymers. Chitosan, a natural polymer, possesses a polycationic nature that allows electrostatic interaction with lipid and protein residues from fingerprints [5,6]. In this context, fluorescent hybrid MCM-41 nanoparticles functionalized with chitosan (Ch) and the fluorophore dansylglycine (DnsGly), namely MCM-41@Ch@DnsGly, were synthesized and characterized by TEM (Figure 1) and other characterization techniques. This material exhibited excellent high fluorescence and adhesion to the fingermark residue (amino acids and fatty acids) (Figure 2), being very effective for development even in aged fingerprints. The nanoparticles were successfully applied to the visualization of latent fingerprints on various surfaces such as glass, metal, plastic (Figure 3A), and polymer banknotes, which pose additional challenges due to their colors, textures, and holographic elements (Figure 3B). The image quality of the developed fingerprints was evaluated according to the United Kingdom Home Office grading system, with 94% of the images classified as levels 3 or 4 – sufficient for reliable individual identification. Second- and third-level minutiae and details could be readily identified using forensic software (Figure 4). These results indicate a high potential for the immediate forensic application of the MCM-41@Ch@DnsGly nanoparticle, representing a significant advancement in the detection and analysis of latent fingerprints.

[1] C. Lennard, *Fingermark detection and identification: current research efforts.* 52 (2020), 125-145.
[2] O.P. Jouja et al., *Development of latent fingermarks on surfaces submerged in water: Optimization studies for phase transfer catalyst (PTC) based reagents.* 55 (2015) 335-342.
[3] M.S. Alves et al., *Latent fingerprint enhancement by Ag nanoparticles electrodeposition on metal surfaces.* 484 (2024) 143925.
[4] L.F.A.M Oliveira et al., *Antioxidant and antimicrobial activity of red propolis embedded mesoporous silica nanoparticles.* 46 (2020) 1199-1208.
[5] Q. Li et al., *Evaluation of Chitosan Derivatives Modified Mesoporous Silica Nanoparticles as Delivery Carrier.* 26 (2021) 2490.
[6] N. Vučković et al., *A novel chitosan/tripolyphosphate/L-lysine conjugates for latent fingerprints detection and enhancement.* 66 (2020) 149-160.
[7] This research was supported by CNPq (Brazil), CAPES (Brazil) and UFAL (Brazil).

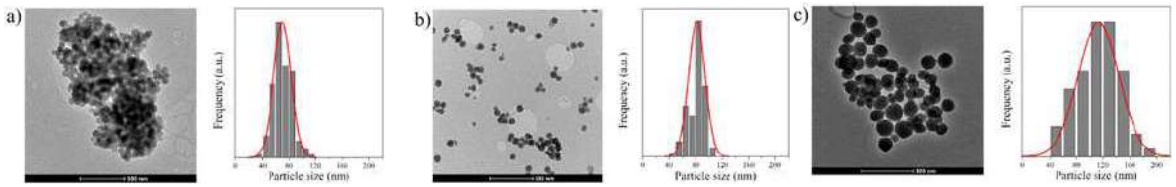

Figure 1. TEM images of (a) MCM-41, (b) MCM-41@Ch and (c) MCM-41@Ch@DnsGly and their particle size distribution histograms.

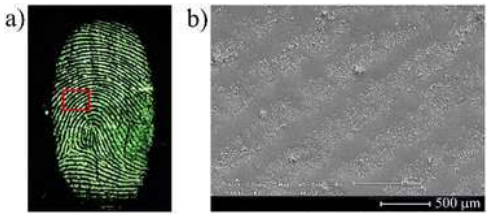

Figure 2. Representative image of (a) 30 day old fingerprint on stainless steel developed by applying MCM-41@Ch@DnsGly NPs together with (b) SEM image showing the NPs (clusters) preferentially deposited on the fingermark ridges.

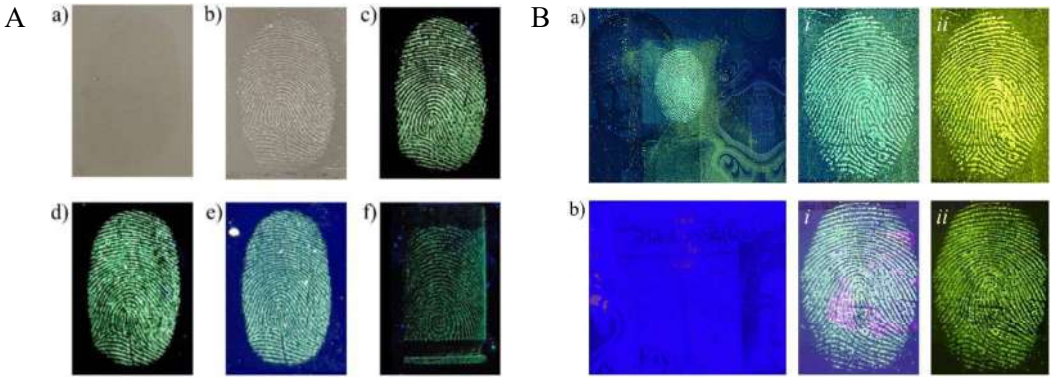

Figure 3. (A) Representative images of latent fingermarks on stainless steel illuminated by and viewed under visible light (a) before development and (b) after development with MCM-41@Ch@DnsGly NPs. Corresponding images generated by illumination with UV light (λ_{ex} = 365 nm) by MCM-41@Ch@DnsGly NP development on (c) stainless steel, (d) glass, (e) plastic and (f) unfired brass cartridge case substrates. (B) Fingerprint developed using MCM-41@Ch@DnsGly NPs on a £5 banknote: (a) back security feature illuminated at 365 nm and viewed with no filter (i) and 510 nm filter (ii) (b) holographic foil illuminated at 365 nm and viewed with no filter (i) and a 510 nm filter (ii).

Figure 4. Representative binarized (B&W) images of developed latent fingerprints on (a) stainless steel, (b) unfired brass cartridge case and (c) UK banknote. In each row, the left hand image shows the whole mark with level 1, 2 and 3 details identified: ridge ending (red), bifurcation (green), delta (blue triangle) and core (blue circle). Images in the right hand column show magnified sections of the mark, similarly annotated using the forensic software.

Green Nanotechnology Applied to Skin Health: Development of Sustainable Formulation from Apple Industry Co-Products

Isadora Florêncio[1]*, Victor Mello[2], Leila Falcão[3], Luana Boron[3], Sônia Nair Báo[1].

[1] Laboratory of Microscopy and Microanalysis, Department of Cell Biology, Institute of Biological Sciences, University of Brasília, Brasília 70910-900, DF, Brazil;
[2] Cooil Cosmetics LTDA, Brasília, DF, Brazil;
[3] Inaturals, Avignon, France.
*isadoraflorenciofs@gmail.com.

The apple tree (*Malus domestica*) stands out as one of the most socioeconomically important fruit crops worldwide, with global production exceeding 100 million tons in 2022, including nearly one million tons from Brazil [1, 2]. This large-scale production is associated with a significant generation of by-products from agro-industrial processing, especially apple pomace—a mixture of seeds, peels, stems, and pulp residues—which is frequently discarded, contributing to environmental concerns related to solid waste accumulation [3]. Nevertheless, these by-products are rich in bioactive compounds, including vitamins, essential fatty acids, and antioxidant molecules. Among them, apple seed oil and peel wax have gained attention due to their promising potential in technological and cosmetic applications [4]. Despite the increasing interest in sustainable ingredients, the incorporation of these compounds into nanotechnology-based systems remains incipient and underexplored [5]. In this context, the present study aims to develop sustainable lipid-based nanoparticles using apple seed oil and apple peel wax as functional constituents of the lipid matrix, with a focus on topical applications targeting skin health. Apple seed oil and apple peel wax were obtained through solvent extraction. Nanoparticles formulation was carried out by testing different ratios of oil, wax, and surfactant, employing low-energy methods. For colloidal characterization, nanoparticles hydrodynamic diameter (HD), polydispersity index (PDI), and zeta potential (ZP) were measured using dynamic light scattering (DLS) and electrophoretic mobility techniques. Morphological characterization was performed by transmission electron microscopy (TEM) using a JEOL 1011 microscope (Tokyo, Japan). To assess UV stability, nanoparticles were exposed to UV-C radiation (0–240 minutes), followed by colloidal parameters evaluation. Antioxidant activity was determined using a colorimetric assay with the free radical 1,1-diphenyl-2-picrylhydrazyl (DPPH). As results, variation in the proportions of apple seed oil and peel wax in the nanoparticle formulation presented distinct colloidal profiles, indicating that compositions with a higher proportion of oil relative to wax provided more appropriated parameters. The optimized formulation exhibited a hydrodynamic diameter (HD) of approximately 60 nm, a polydispersity index (PDI) of 0.192, and a zeta potential (ZP) of -22.8 mV (Figure 1.A). Stability assays under ultraviolet radiation exposure did not indicate significant changes in the colloidal parameters over time, suggesting structural stability of the formulation (Figure 1.B). Antioxidant assays demonstrated antioxidant potential of 60% at a concentration of 37.5 mg/mL for apple active compounds, a performance comparable to that of ascorbic acid, the positive control (Figure 1.C). Transmission electron microscopy (TEM) images showed spheroidal particles with homogeneous morphology and an average diameter of 103 nm (Figure 1.D). The study successfully developed a sustainable lipid nanoparticle using apple seed oil and peel wax, with optimized formulations showing suitable colloidal properties, morphological uniformity, UV stability, and antioxidant activity. These results support the potential of integrating agro-industrial co-products into green nanotechnology for cosmetic applications focused on skin health and sustainability.

[1] V.W. Ruttan, Journal of Economic Perspectives, 16 (2002) 161.
[2] IBGE, Municipal Agricultural Production, Rio de Janeiro, IBGE, 2023. Available at: https://cidades.ibge.gov.br/brasil/pesquisa/15/11979?ano=2022 (accessed January 2024).
[3] S. Bhushan et al., Critical Reviews in Biotechnology, 28 (2008) 285.
[4] P. Górnaś, Food Chemistry, 172 (2015) 129.
[5] W. Johnson et al., International Journal of Toxicology, 42 (2023) 36S.
[6] This research was supported by CAPES, CNPq, FAPDF, FINEP and UnB (Brazil).

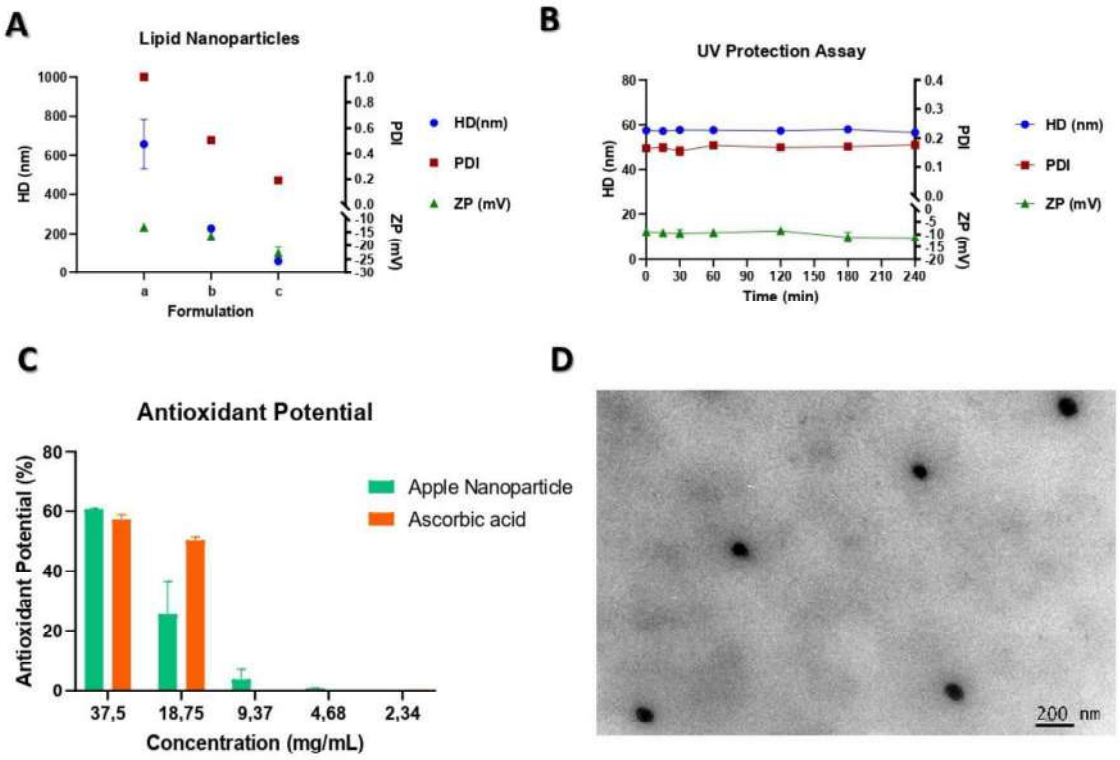

Figure 1. (A) Colloidal characterization of apple-based lipid nanoparticles). The figure shows the hydrodynamic diameter (HD), polydispersity index (PDI), and zeta potential (ZP) of three formulations: *a* (equal oil and wax), *b* (more wax than oil), and *c* (more oil than wax). **(B)** UV stability of apple-based lipid nanoparticles over 240 minutes of UV-C exposure for formulation *c*. **(C)** Percentage of antioxidant potential exhibited by the apple nanoparticle developed compared to ascorbic acid at concentrations of 37.5, 18.75, 9.37, 4.68, and 2.34 mg/mL using a colorimetric assay with DPPH. **(D)** Transmission electron microscopy image of lipid nanoparticles composed of apple seed oil and apple peel wax at 10,000× magnification. The nanoparticles exhibit a homogeneous spheroidal morphology with an average diameter of approximately 103 nm.

High-Temperature creep behavior of Ti-6Al-4V with TBC characterized by TEM

Renata Jesuina Takahashi[1], João Marcos Kruszynski de Assis[2], Bianca Costa Rodrigues[1], Danieli Aparecida Pereira Reis[1]*.

[1] Federal University of São Paulo (UNIFESP), [2] Institute of Aeronautics and Space (IAE).
*danieli.reis@unifesp.br

The Ti-6Al-4V alloy with thermal barrier coatings (TBCs) is widely used in aerospace turbine blades to provide both thermal and chemical protection to the metallic substrate while ensuring high-temperature mechanical strength, low specific density, toughness, and corrosion resistance [1]. Creep deformation is one of the most critical failure mechanisms in components subjected to elevated temperatures for prolonged periods [2]. The application of TBCs to Ti-6Al-4V significantly reduces the creep rate, increases rupture life, and alters fracture mechanisms [3-5]. This study investigates the microstructural evolution of TBC-coated Ti-6Al-4V alloy after creep tests performed at constant temperatures of 500, 600, and 700 °C under stress levels of 125, 250, and 319 MPa. The TBC system consisted of a NiCrAlY bond coat, a thermally grown oxide (TGO) layer, and a ceramic topcoat composed of zirconia stabilized with 16.0% yttria and niobia in equimolar proportions. Both the bond coat and the ceramic layer were deposited using CO_2 laser processing [6]. Microstructural characterization was performed using optical microscopy, scanning electron microscopy, transmission electron microscopy (TEM), energy-dispersive spectroscopy, and X-ray diffraction. Martensitic and Widmanstätten microstructures were identified and remained unchanged after the creep tests. The martensitic structure, observed at the specimen edges, was attributed to the thermal effects during TBC processing, while the Widmanstätten structure, located in the central region of the specimen, remained unchanged from the initial condition. Table 1 shows the main creep test parameters. At 600 °C and 250 MPa, the coated alloy exhibited an approximate 37% increase in creep resistance compared to the uncoated material [7], primarily due to a reduction in the secondary creep rate. Fractographic analysis revealed predominantly ductile failure, confirmed by the presence of dimples. Figure 1 presents a bright-field TEM micrograph in which a high density of dislocations is observed. Supported by TEM observations, a stress exponent of 2.50 and an activation energy of 337.5 kJ/mol indicate that the dominant creep mechanism was dislocation glide along preferred slip planes.

[1] G. Moskal, Journal of Achievements in Materials and Manufacturing Engineering, 37 (2009) 323–31.
[2] R.W. Evans And B. Wilshire, Introduction to Creep, London: Institute of Materials, 1993.
[3] T. Sugahara, et al., Materials Science Forum 636–637 (2010) 657–62.
[4] F.P. Briguente et al., Materials Science Forum 802 (2014) 472–76.
[5] F.E. Freitas et al., Surface and Coatings Technology 369 (2018) 257–64.
[6] R.J. Takahashi et al., Coatings 15 (2025) 47.
[7] D.A.P. Reis et al., Materials Science and Engineering A 399 (1–2) (2005) 276–80.
[8] This research was supported by CNPq (Brazil), FINEP and FAPESP.

Table 1. Creep test data of the Ti-6Al-4V alloy with TBC.

T (°C)	σ (MPa)	t_p [h]	$\dot{\varepsilon}_s$ [1/h]	t_f [h]	ε_f [mm/mm]
500	**125**	31.0	0.00002	-*1	-*1
600	**125**	0.02	0.0568	0.34	0.0487
700	**125**	0.02	0.0568	0.34	0.0487
600	**250**	0.01	0.1496	0.36	0.1371
600	**319**	0.004	0.8358	0.04	0.0622

*1 The creep test was interrupted prior to fracture.
* The secondary creep rate of uncoated Ti-6Al-4V at 600 °C is 0,4030 h^{-1} [7].

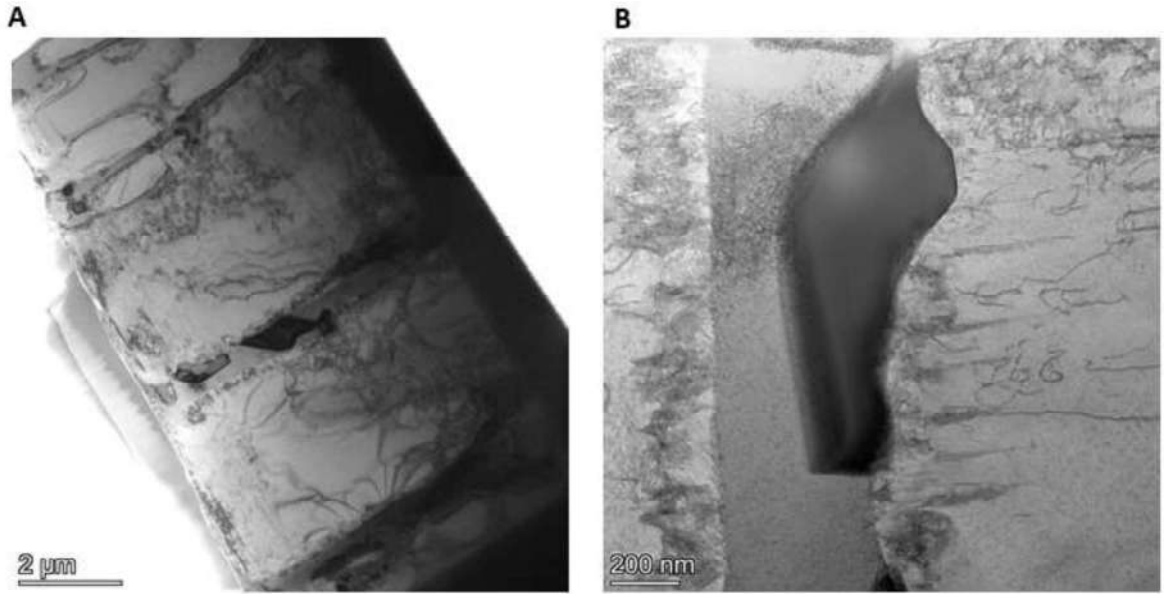

Figure 1. A) Bright-field TEM micrograph of Ti-6Al-4V with TBC. B) Higher magnification.

Impact of Aging Treatments on the Microstructure and Mechanical Properties in the Ti-24Nb-4Mo-6Zr Alloy

Aline Raquel Vieira Nunes [1,2*], Sinara Borborema [2], Ana Isabel de carvalho Santana [2], Jean Dille[3], Luiz Henrique de Almeida [1]

[1]Universidade Federal do Rio de Janeiro, Rio de Janeiro, RJ, Brazil
[2]Universidade do Estado do Rio de Janeiro, Rio de Janeiro, RJ, Brazil
[3]Université Libre de Bruxelles, ULB, Brussels, Belgium
*aline.nunes@uerj.br

Metastable β titanium alloys stabilized with biocompatible elements such as Nb, Mo and Zr are candidates to replace Ti-6Al-4V in orthopedic implants by reducing elastic modulus while retaining high strength, these alloys mitigate stress-shielding and improve osseointegration [1,2]. This study aims to elucidate the effects of aging at 300 °C, 400 °C and 500 °C for 4 h on the microstructural evolution in Ti-24Nb-4Mo-6Zr alloy. This alloy was produced by vacuum arc melting using high-purity raw materials, followed by solution treatment at 1000 °C for 24 h and water quenching, 90% cold rolling and annealing at 950 °C for 1 h. The alloy was then aged isothermally at 300 °C, 400 °C and 500 °C for 4 h and water quenched to evaluate the effects on microstructure and mechanical behavior for biomedical implant applications.

X-ray diffraction indicated a (β + α) alloy after aging at 500 °C and ω phase precipitation in β matrix after aging at 300 °C and 400 °C (Figure 1). Transmission electron microscopy (TEM) on thin foils prepared by focused ion beam confirmed the XRD results (Figure 2). After aging for 4h at 300°C, ultrafine ωiso precipitates of 5–10 nm, uniformly dispersed, in the β matrix are observed whereas after aging for 4h at 400 °C, larger ellipsoidal ωiso particles show a size between 20 and 50 nm. After aging at 500 °C for 4h, TEM analysis showed a bimodal α + β microstructure with no ωiso, indicating its complete dissolution. Energy-dispersive X-ray (EDX) elemental mappings revealed a progressive elemental partitioning and enrichment of the β matrix by β-stabilizing elements with the increase of aging temperature.

Vickers microhardness (HV0.2) increased from 353,4 ± 1,5 HV after aging at 300 °C, peaking at 416,6 ± 3,2 at 400 °C due to maximum ωiso hardening, then decreasing to 311,6 ± 1,7 HV at 500 °C as ωiso dissolved and recovery and α precipitation occurred. The combination of TEM and EDX enables precise correlation of ωiso morphology and solute partitioning with mechanical properties.

These results demonstrate that aging at 400 °C maximizes ωiso-induced hardening, while aging at 500 °C yields an α + β structure suitable for orthopedic implants thereby optimizing load transfer and minimizing stress shielding in bone. Such microstructure and property results underpin the design of β-Ti implants with tailored performance for biomedical applications.

[1] W. Abd-Elaziem et al., Titanium-based alloys and composites for orthopedic implants applications: A comprehensive review, Mater. Des. 241 (2024) 112850.
[2] S.S. Sidhu et al., A review on alloy design, biological response, and strengthening of β-titanium alloys as biomaterials, Materials Science and Engineering C 121 (2021) 111661.
[3] This research was supported by FAPERJ (Brazil).

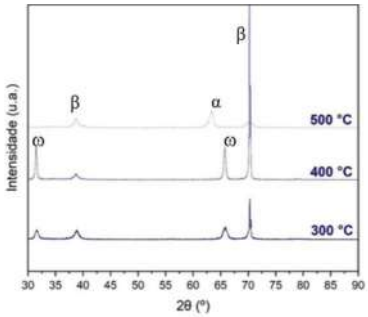

Figure 1: XRD patterns of Ti-24Nb-4Mo-6Zr Alloy after aging.

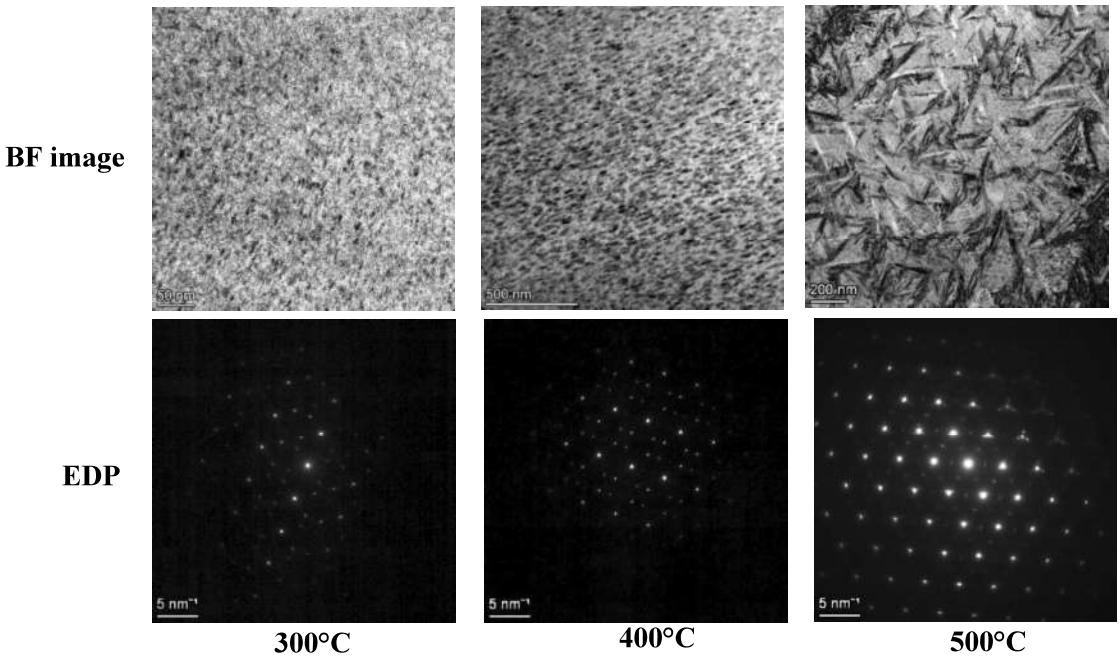

Figure 2: TEM analyses of Ti-24Nb-4Mo-6Zr Alloy.

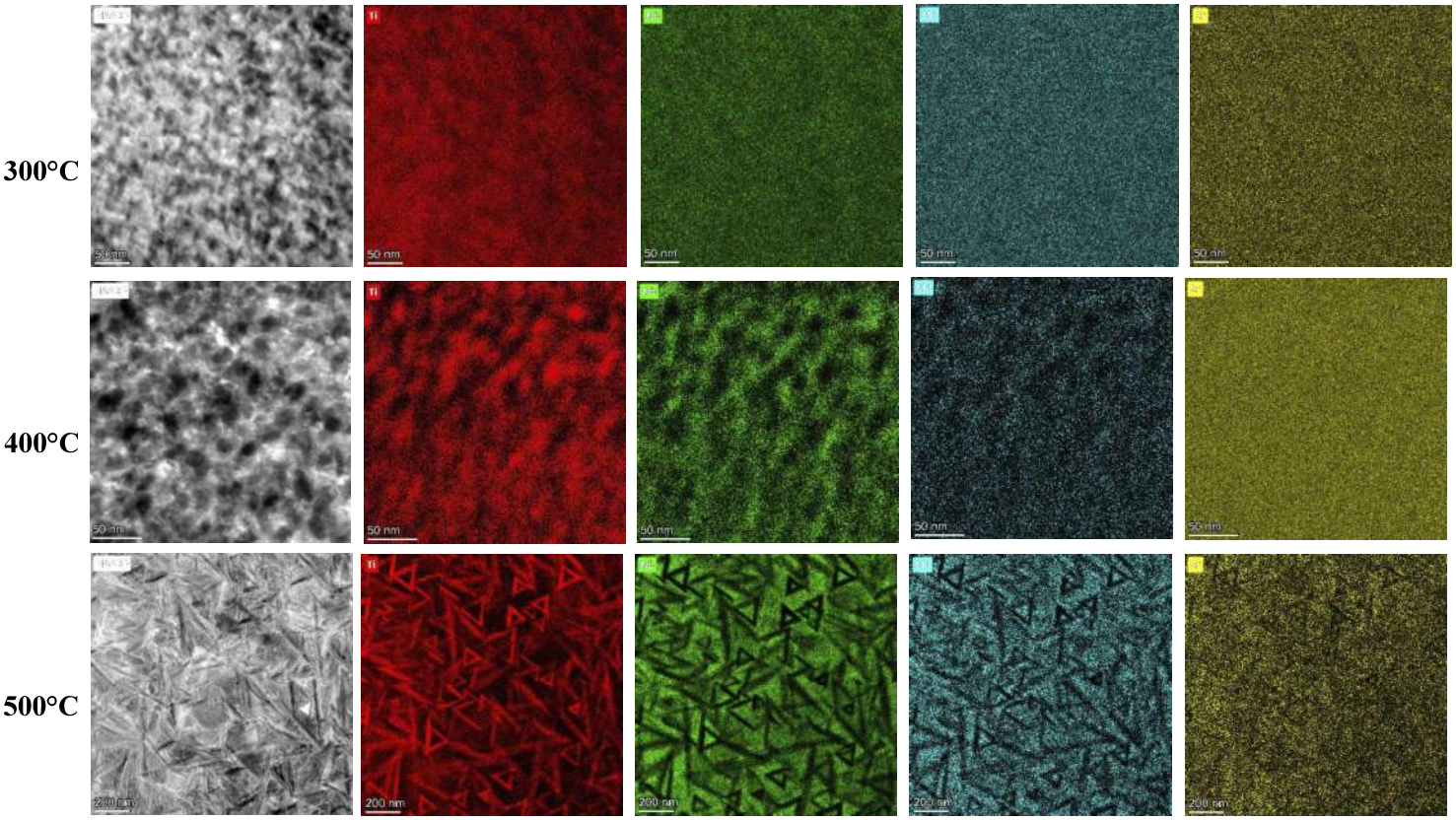

Figure 3: EDX mapping of elemental partitioning in Ti-24Nb-4Mo-6Zr Alloy after aging.

Investigation on precipitation in Zr-Nb-Mn alloys

Bernardo Pompermayer Eduardo[1]*, Paula Mendes Jardim[1], Rafaella Martins Ribeiro[1].

[1] Universidade Federal do Rio de Janeiro – UFRJ /COPPE, Programa de Engenharia Metalúrgica e de Materiais – PEMM.
*bernardopeduardo@metalmat.ufrj.br

Zirconium alloys are widely employed in nuclear reactors for components such as fuel claddings and spacer grids due to their low neutron absorption, high corrosion resistance, and suitable mechanical properties [1]. These characteristics are achieved through the addition of alloying elements and thermomechanical processing. Among these elements, niobium is particularly effective in promoting a fine and uniform dispersion of β-Nb precipitates in fully or partially recrystallized microstructures, contributing to improved creep resistance and dimensional stability under irradiation. Nb also stabilizes the ZrO_2 protective layer, enhancing corrosion resistance [2]. Recent studies [3,4] have proposed the addition of Mn in Zr-Nb alloys, as Mn has demonstrated enhanced formability, increased hydrogen solubility and the corrosion resistance comparable to that of Zr-1Nb. Despite these promising results, the effect of Mn addition on microstructure and precipitation has not yet been investigated. This study investigates the effect of Mn additions in Zr-0.9Nb-0.1Mn, Zr-0.8Nb-0.2Mn, and Zr-0.6Nb-0.4Mn alloys after annealing at 650 °C for 2 hours, focusing on the morphology, distribution, and chemical composition of the precipitates by transmission electron microscopy (TEM). Bright-field TEM analysis of the annealed microstructures revealed an α-Zr matrix containing two distinct types of precipitates: large spherical particles, with diameters on the order of hundreds of nanometers, and smaller square-shaped precipitates ranging from 30 to 100 nm, as shown in Figure 1(a) for the Zr-0.9Nb-0.1Mn alloy. Precipitation was found to be non-uniform across all compositions, with some areas free of precipitates, others exhibiting high concentrations of smaller precipitates, Figure 1 (e) for Zr-0.8Nb-0.2Mn alloy, and regions with sparse distribution, as show in Figure 1 (g) for Zr-0.6Nb-0.4Mn alloy. Selected area electron diffraction (SAED) pattern analysis, Figure 1(c), identified the spherical precipitates shown in Figure 12(a) as the β-Nb phase with a body-centered cubic structure. EDS mapping confirmed their Nb-rich composition (Figure 1d), in agreement with previous reports for Zr-Nb alloys [5]. The square-shaped precipitates were composed of both Mn and Nb, with a Mn/Nb atomic ratio close to 2, suggesting the formation of the Mn_2Nb phase with a hexagonal close-packed (hcp) structure. This was further supported by a diffraction spot indexed to the (100) plane of Mn_2Nb (d = 4.23 Å), marked in orange in Figure 1 (c), consistent with ICSD code 152628. Mn-rich precipitates of similar morphology have been previously reported by Shi et al. [6] in Zr alloys, and the Mn_2Nb phase is also predicted in the Mn-Nb equilibrium phase diagram [7]. EDS mapping for the Zr-0.8Nb-0.2Mn, Figure 1 (f) and Zr-0.6Nb-0.4Mn, Figure 1 (h) alloys confirmed the presence of both precipitate types: larger β-Nb and smaller Mn_2Nb particles. Overall, the precipitation behavior across all compositions revealed a heterogeneous microstructure, with spatial variations in precipitate type and distribution. The Mn_2Nb phase, notably, has not been previously reported in similar alloys annealed at higher temperatures.

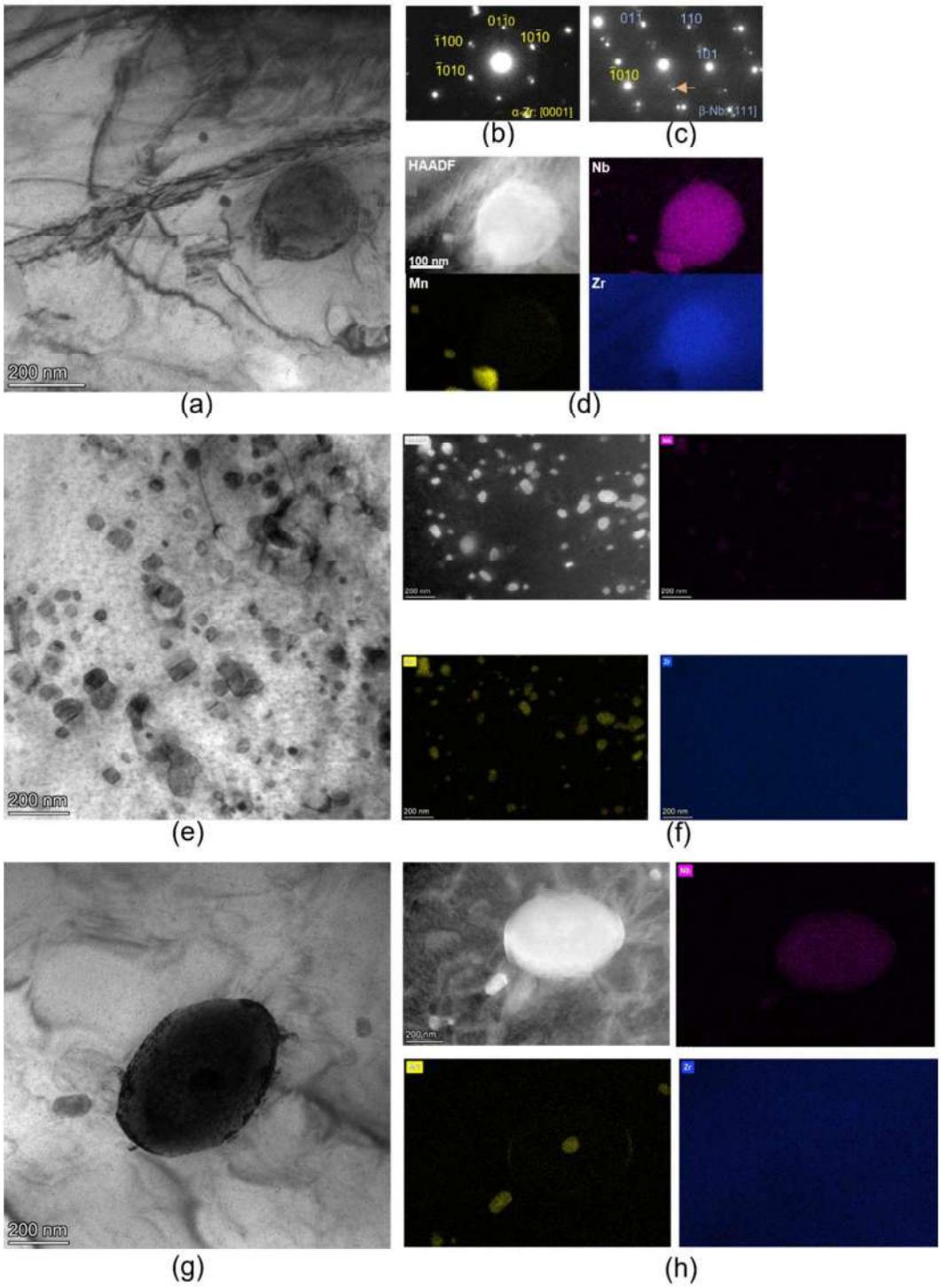

Figure 1. TEM images after annealing at 650°C/2h. (a) Zr-0.9Nb-0.1Mn alloy showing spherical and square-shaped precipitates. (b-c) SAED patterns containg the larger precipitate corresponding to β-Nb (indexed in blue), matrix (indexed in yellow) and the smaller precipitate rich in Mn (spot marked with orange arrow). (d) STEM HAADF image and EDS maps of same region in (a). (e) Smaller precipitates in the Zr-0.8Nb-0.2Mn alloy. (f) STEM HAADF image and EDS maps. (g) Region with β-Nb and Mn_2Nb precipitates in the Zr-0.6Nb-0.4Mn alloy. (h) STEM HAADF image and EDS maps.

[1] S. Deng et al., Int. J. Solids Struct, 213 (2021) 63-72.
[2] S. Neogy et al., Metall. Trans. A, 38A (2007) 485-498.
[3] R.M. Ribeiro et al., Int. J. Hydrogen Energy, 40 (2015) 17118-17127.
[4] T.B. Pintor et al., Mater. Res., 22 (2019) e20190182.
[5] G. Yuan et al., Mater. Chem. Phys., 165 (2015) 87–90.
[6] H. Shi et al., Corros. Sci., 157 (2019) 167-179.
[7] S. Liu et al., Calphad, 38 (2012) 43-58.

Solute segregation during crystallisation of multicomponent glassy alloys of the system (FeCoNiCrMn)B

Coimbrão, Diego[1]*; Zepon, Guilherme[1]; Koga[1], Guilherme; Inoue, Akihisa[2]; Botta, Walter[1]
[1] Universidade Federal de São Carlos, Brazil
[2] Inter. Institute of Green Materials, Josai International University, Togane, 283-8555, Japan
*fdiego@ufscar.br

Multicomponent glassy alloys can crystallise in a variety of different ways, depending on composition which opens the possibilities to form novel nanostructures during partial crystallisation. These structures may include metastable or highly stable phases, resulting from slow atomic diffusion and complex elemental interactions. Such behavior can lead to the initial formation of crystalline multi-principal element (MPE) phases that retain compositional similarity to the parent alloy. These features are particularly advantageous for applications requiring the simultaneous optimisation of corrosion and wear resistance, making these materials promising for multifunctional engineering applications. In the present study, we present a comprehensive investigation of the chemical composition and microstructural evolution that occurs during the crystallisation process of the MPE glassy $(Fe_{0.25}Co_{0.25}Ni_{0.25}Cr_{0.125}Mn_{0.125})_{91\text{-}87}B_{9\text{-}13}$ alloys using advanced characterisation techniques. In this work we will focus on the two limiting compositions with 9at% B and 13at% B, with the alloys being identified a B9 and B13. The crystallisation sequence from the glassy phase in both alloys follows the same pattern as other Fe-based multicomponent alloys [1] with limited solute partitioning during the first crystallisation stages. Such condition can be represented as: [am]→[remaining amorphous (am') + bcc]→[am″ + bcc + fcc]→[fcc + borides]. The data were obtained in a TEM Thermofisher Talos F200X (Cold FEG). Figure 1 shows the microstructural and chemical characterisation of the $(Fe_{0.25}Co_{0.25}Ni_{0.25}Cr_{0.125}Mn_{0.125})_{91}B_9$ alloy in the as-spun and annealed conditions, at the temperatures indicated in the figure. The treatments correspond to the exothermic events as indicated by DSC curves and one relevant aspect of the microstructure evolution can be seen in the EDS line scan of Fig.1 (e) with the composition profile along one crystalline particle in the annealed sample at 420 ºC, with clear depletion of Cr and Mn elements. The other microstructural features are described in the figures legend, including the sequence of XRD patterns with increasing annealing temperatures. Figure 2 shows the equivalent analyses for the $(Fe_{0.25}Co_{0.25}Ni_{0.25}Cr_{0.125}Mn_{0.125})_{87}B_{13}$ alloy, in the as-spun and annealed conditions at the indicated temperatures. The XRD patterns confirms the same mechanism of crystallisation with an initial bcc phase that transforms to an fcc plus borides phases at later stages of crystallisation. The EDS line scan also shows the same feature with the formation of the first bcc crystals, rich in Co and Ni and depleted of Cr and Mn, justifying the later transformation to the fcc phase. These results emphasize the importance of solute segregation in defining the intermediate and final properties of partially and fully crystalline alloys of the system (FeCoNiCrMn)B.

[1] F. Wang et al. Acta Mater. (2019), https://doi.org/10.1016/j.actamat.2019.03.019.
[2] This research was supported by CNPQ, CAPES, FINEP, FAPESP (Brazil).
[3] The authors are grateful for the electron microscopy facilities from the Laboratory of Structural Characterization of Federal University of São Carlos (LCE/DEMa/UFSCar).

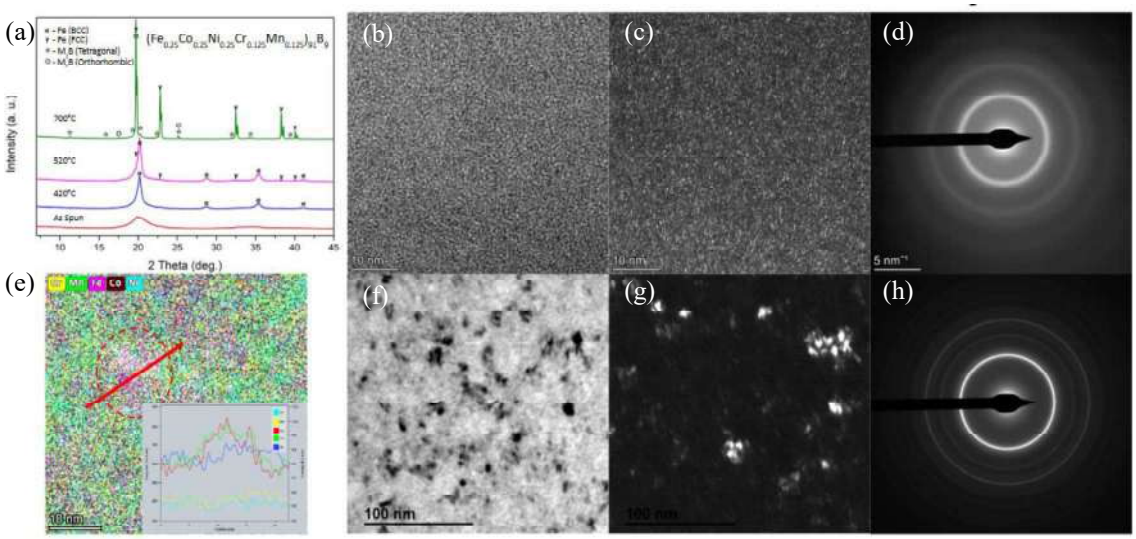

Fig.1 (a) XRD patterns of the $(Fe_{0.25}Co_{0.25}Ni_{0.25}Cr_{0.125}Mn_{0.125})_{91}B_9$ alloy as-spun and annealed at the indicated temperature. The first treatment at 420 ºC corresponds to the first exothermic peak, 520 ºC corresponds to the second exothermic peak and 700 ºC presents a fully crystallized microstructure. (b, c and d) Bright-field, dark-field TEM images and corresponding SAEDP of the fully amorphous as-spun ribbon. (e) Line scan with the chemical composition profile along the line of the sample annealed at 420 ºC. (f, g and h) Bright-field, dark-field TEM image and corresponding SAEDP of the sample annealed at 420 ºC.

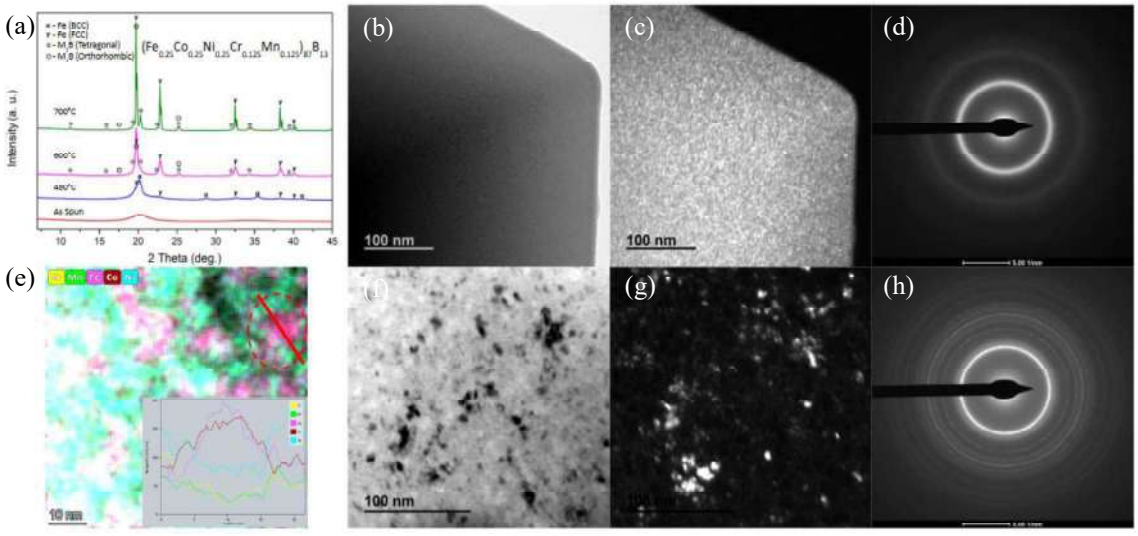

Fig.2 (a) XRD patterns of the $(Fe_{0.25}Co_{0.25}Ni_{0.25}Cr_{0.125}Mn_{0.125})_{87}B_{13}$ alloy as-spun and annealed at the indicated temperature. The first treatment at 480 ºC corresponds to the first exothermic peak, 600 ºC corresponds to the second exothermic peak and 700 ºC presents a fully crystallized microstructure. (b, c and d) Bright-field, dark-field TEM images and corresponding SAEDP of the fully amorphous as-spun ribbon. (e) Line scan with the chemical composition profile along the line of the sample annealed at 480 ºC. (f, g and h) Bright-field, dark-field TEM image and corresponding SAEDP of the sample annealed at 480 ºC.

Study of the morphology and characterization of defects in $MnBi_2Te_4/Bi_2Te_3/CdTe$ thin films via FIB sample preparation, STEM, and EDS chemical analysis

Maybi F. Sampaio[1]*, Olavo T. Neto[1], Wesley F. Inoch[2], Leonarde N. Rodrigues[2], Braulio S. Archanjo[1].

[1]INMETRO, [2] Universidade Federal de Viçosa
*mfalker@colaborador.inmetro.gov.br

Topological quantum materials have been gaining attention due to their topological insulating properties and magnetic ordering [1]. In this work, the characterization by Transmission Electron Microscopy of thin films of the aforementioned materials is presented. This investigation concentrates on the preparation of submicron lamellae, image acquisition, and chemical analysis of $MnBi_2Te_4$, Bi_2Te_3 and CdTe thin films. The objective is to investigate the morphology of the material, with emphasis on epitaxial growth and films integrity, as well as the presence of defects or imperfections in the membranes. The interatomic distances and the chemical composition were also checked. Focused ion beam (FIB) was used to prepare the thin lamellae, High-Resolution Scanning Transmission Electron Microscopy (HSTEM), and EDS (Energy Dispersive Spectroscopy) techniques were employed. The analyses were carried out on a FEI SEM/FIB NOVA NANOLAB 600 electron microscope and a FEI TEM TITAN 80300 transmission electron microscope equipped with an aberration corrector. Two samples with different combinations of film and substrate materials were studied, A714 ($GaAs/MnBi_2Te_4/CdTe$) and A688 ($glass/Bi_2Te_3/CdTe$). During the lamella preparation process, the main challenge was to maintain the integrity of the film, since the deposition of Ga ions could have damaged the top membrane. For this purpose, a 50 nm Pt layer was deposited on the upper membrane in other to protect it (Figure 1(a), 1(c)). At the end of the milling and polishing processes, thicknesses of around 70 nm were achieved (Figure 1(b)) on both samples. Subsequently, the lamellae were observed in TEM, which was maintained in condensed beam mode (STEM). The images were taken at beam accelerating voltages of 200 and 300kV. The high-resolution images show the defects due to CdTe stacking failure (Figure 1(d)), in agreement with what has already been observed in the literature [2]. This defect is due to compact stacking planes that have been removed or added to a perfect crystal (intrinsic or extrinsic stacking fault) [2]. Across stacking faults, there are no dislocations; the Cd and Te atoms bond as in a defect-free area. It is very common to observe twin boundaries or intrinsic/extrinsic stacking faults traversing entire CdTe grains and terminating at GBs (grain boundaries) or interfaces [2]. It was also possible to see the CdTe dumbbells (Figure 1(d)). Furthermore, it can be seen that the integrity of the layers was preserved during the FIB process (Figure 1(c) and Figure 2(a), (b) - electron image). Finally, is concluded that there are no relevant discontinuities observed in the films. The development of these films will allow the researchers to investigate specific topological quantum states and design new spintronic devices for quantum computing applications.

[1] W. F. Inoch et al., Nanoscale, 17 (2025) 10013.
[2] C. Li et al., Materials Science in Semiconductor Processing 65 (2017) 64.

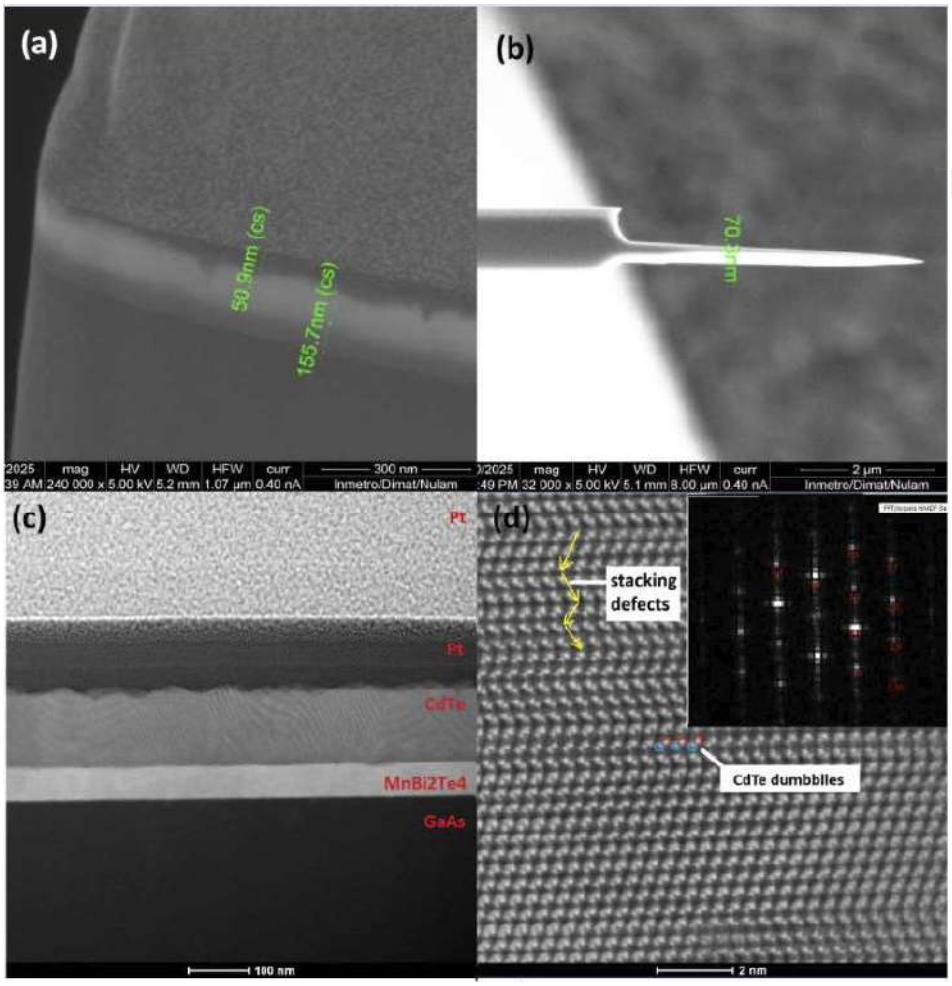

(e)

D-spacing [1/n]	Distance [A]	hkl
5.07	3.94	-111
8.3	2.41	-202
5.94	3.37	020
9.8	2.04	13-1
11.9	1.68	040
10.3	1.94	22-2
12.8	1.56	3-1-3

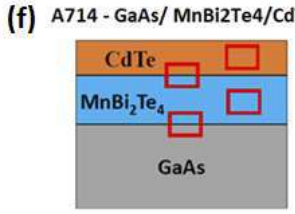

Figure 1. (a) and (b): FIB preparation details of A714 sample; (c) STEM image of A174 layers; (d) HRSTEM image showing stacking defaults and CdTe dumbblles; (e) interatomic distances of CdTe measured by FFT; (f) diagram illustrating the layers.

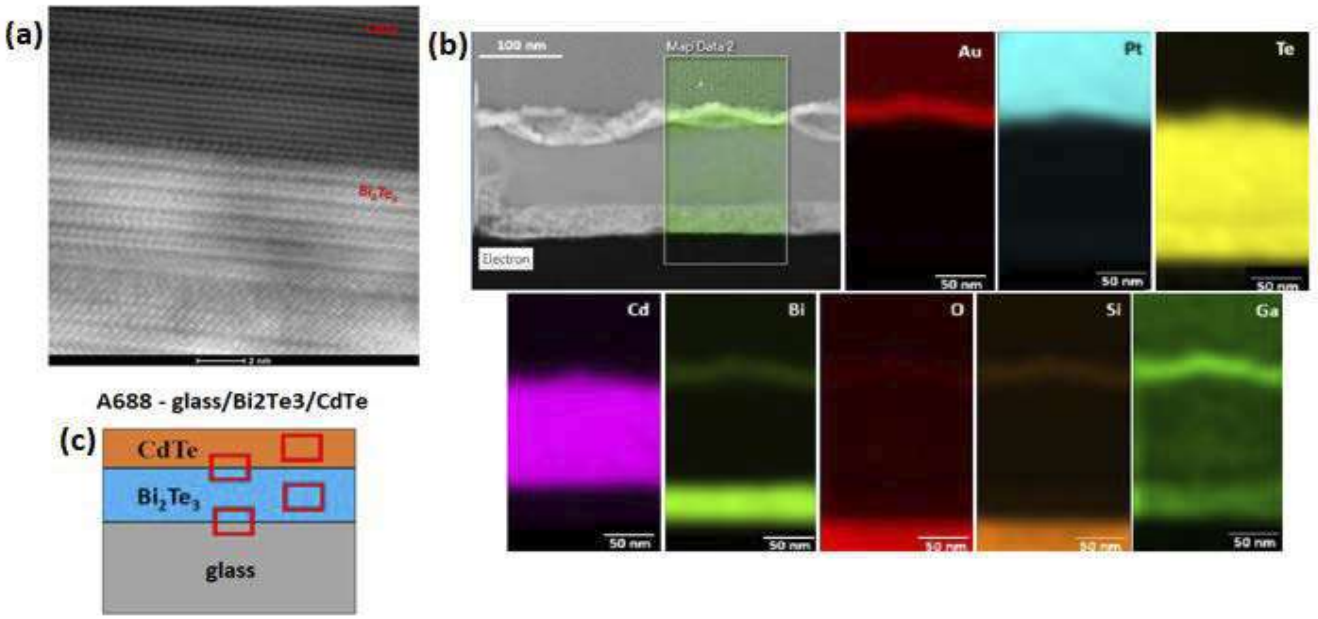

Figure 2. (a) STEM image of A688 sample (glass/Bi_2Te_3/CdTe); (b) EDS maps of A688; (c) diagram illustrating the layers of A688 sample.

Study of thin film of CuZr metallic glass by electron pair distribution function (ePDF)

Jefferson Bettini[1], Heloisa Helena Pereira Silva[1]

[1]Brazilian Center for Research in Energy and Materials, Campinas, Brazil
e-mail: jefferson.bettini@lnnano.cnpem.br

Thin film metallic glasses (TFMG) are coating materials that can enhance the mechanical, thermal, and optical properties of substrates. TFMG can be created by combining different elements and compositions to tailor specific features for use in various applications, from biomedical equipment to electronic devices.

TFMG unique quality, such as increased fracture resistance, reduced corrosion, and minimized strain deformation, distinguish it from its bulk material counterparts. TFMG can be produced through sputtering deposition. The properties of TFMG are closely linked to their low periodicity (degree of amorphization), and understanding how composition influences these properties is a key point for enhancing their applicability. The amorphization degree can be assessed using the electron pair distribution function (ePDF), which describes the likelihood of finding neighboring atoms in relation to a reference atom.

In this study, copper (Cu) and zirconium (Zr) TFMG were grown at different compositions and analyzed their amorphization degree by ePDF [1] using selected area electron diffraction (SAED). Film composition was checked by energy dispersive spectroscopy (EDS) and electron energy loss spectroscopy (EELS), figure 1a. The structure analysis was done by ePDF, see figure 1b. Two important parameters can be directly obtained from ePDF curves: the length of structural coherence (LSC) and the maximum average size of crystals (max r), see figure 1c. The LSC corresponds to the 0.367 (1/e) exponential decay of oscillations (maximum peaks) from the peak of the first neighbor [2,3], and the max r was determined based on the end of structural oscillations.

The CuZr TFMG were grown by sputtering, and the compositions were analyzed by three methods, which had similar results between each other and the theoretical value. We obtained the ePDF of samples to analyze the structure of the film, evaluating the amorphization degree through the LSC coefficient and max r. These parameters showed that a film with 33 at.% Zr has the lowest crystallinity.

[[1] J. Shanmugam; K. B Borisenko; Y.-J. Chou; A. I. Kirkland. eRDF Analyser: An interactive GUI for electron reduced density function analysis, SoftwareX. 6 (2017) 185-192.
[2] S. Ergun; R. R. Schehl. Analysis of the structure of a glassy carbon using the Fourier transform technique, Carbon. 11(1973) 127-138.
[3] V. Petkov; P. D. Cozzoli; R. Bounsanti; R. Cingalani; Y. Ren. Size, shape, and internal atomic ordering of nanocrystals by atomic pair distribution functions: A comparative study of γ-Fe2O3 nanosized spheres and tetrapods. J. Am. Chem. Soc.131 (2009)14264-14266...

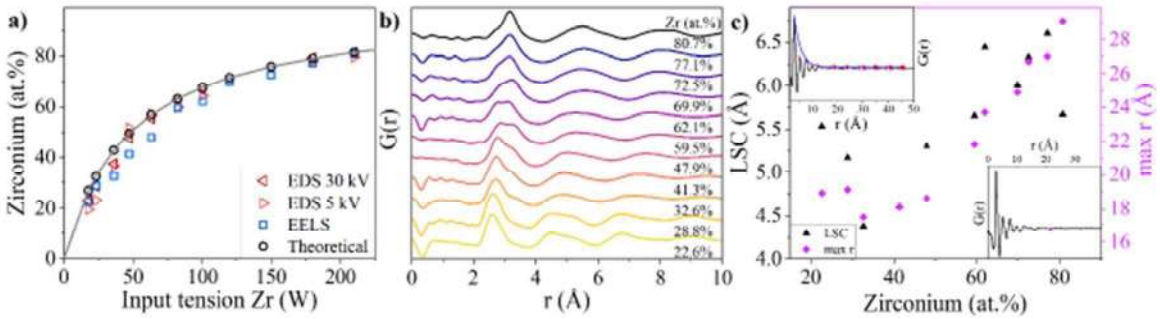

Figure 1: (a) Theoretical composition and experimental composition obtained by EELS, EDS 5 kV, and 30 kV; (b) ePDF of samples; (c) LSC coefficient and max r..

Surface Characterization of the TiVNbCr Alloy After Pulsed Laser Activation for Hydrogen Storage

Ana Rodrigues Cameirão[1], Juliana Mara Pinto de Almeida[1,2], Antonio Carlos Hernandes[3], Diego Davi Coimbrão[1,2], Vitor A. Sacramento Mendes[1], Guilherme Zepon[1,2*].

[1]Federal University of São Carlos, Graduate Program in Materials Science and Engineering (PPGCEM/UFSCar), São Carlos, SP, Brazil.
[2]Federal University of São Carlos, Department of Materials Engineering (DEMa/UFSCar), São Carlos, SP, Brazil.
[3]São Carlos Institute of Physics, University of São Paulo, São Carlos, SP, Brazil.

*zepon@ufscar.br

Hydrogen storage in metal hydrides might play an important role in the energy transition from fossil fuels to a hydrogen-based energy economy. In the last decade, multicomponent alloys that can form multicomponent hydrides with tunable hydrogen storage properties have been reported in literature [1]. New materials capable of reversibly absorbing/desorbing large amounts of hydrogen, with gravimetric capacities as high as 3.0 wt.% of H and volumetric capacities of up to 150 kg/m^3, at mild pressure and temperature conditions have been developed in the last few years [2–6]. The body-centered cubic (BCC) alloys from the Ti-V-Nb-Cr system stand out as hydrogen storage materials because it can form an FCC hydride (CaF2-type structure) that can store up to 2.0 H/M (hydrogen to metal atoms ratio). In addition to the high hydrogen storage capacity, the hydrogen storage properties of these alloys can be finely tuned by varying the ratio between of the metal elements in the alloy. For instance, while the equiatomic $(TiVNb)_{85}Cr_{15}$ alloy absorbs hydrogen at very low pressure forming an FCC hydride that can only desorb hydrogen above 200 ºC [4], the $Ti_{11}V_{30}Nb_{28}Cr_{31}$ alloy can reversibly absorb and desorb hydrogen at room temperature, by forming a less stable hydride that is stable only above 10 bar at room temperature [5]. For this alloy, it was demonstrated that its hydrogen absorption is inhibited when the alloy is exposed to air for 30 days. In most transition metal alloys, surface states impermeable to hydrogen are formed upon exposure to air and only after an activation treatment – i.e., heating the specimen to a specific temperature under dynamic vacuum or H_2 gas – does the surface become permeable to hydrogen. Recently, the Pulsed Laser Activation (PLA) method was proposed as an alternative activation method for hydrogen storage alloys based [7]. The PLA method uses a nanosecond pulsed laser to scan a powder sample of the non-activated alloy, using a constant speed of 400 mm/min. The experimental setup included a Nd:YAG laser (pulses of 10 ns, at 1064 nm, repetition rate of 10 Hz, operating with 0.8W of average power), a focusing lens (f = 15 cm), and a computer-controlled x-y translational stages. It was demonstrated that the hydrogen storage ability of the $Ti_{11}V_{30}Nb_{28}Cr_{31}$ alloy exposed to air for 30 days can be completely restored by the PLA processing. It was shown that during PLA processing, the surface of the fragmented particles is partially melted and XPS analysis indicated that the fraction of oxides near to the surface is increased [7]. The reactivation of the alloy after PLA with the increase of the oxide layer is a counterintuitive result, since it is expected that the oxide layer can be a barrier for the H at the surface. Thus, to better understand this phenomenon, in this work, a sample of the equiatomic TiVNbCr alloy was immersed in deionized water for 24 hours, yielding a non-activated sample. Then, the PLA process was carried out in this sample. Absorption kinetic measurements in Sieverts-type apparatus confirmed that the sample was re-activated after PLA process. To observe the surface of the sample after PLA processing, the particles of the sample were coated with carbon by sputtering to preserve the surface. A lamella of a remelted surface was removed by Focused Ion beam (FIB) as presented in Figure 1 (A) using a ThermoFisher Scios 2 HiVac microscope. EDS measurements of the surface were carried out at the surface of the sample (Figure 1 (B)) using a ThermoFisher Talos F200X with a Super-X EDS. It could be seen that a layer of

less than 10 nm of a Ti oxide was formed in the surface of the sample. Automatic Crystallographic Mapping using the ASTAR system in the same microscope showed that the FCC TiO phase is present in surface of the sample, confirming that the LPA process induces the formation of Ti-rich oxides in the surface. Moreover, it confirms that such oxide layer is not the barrier for hydrogen absorption, given that the PLA samples were completely reactivated.

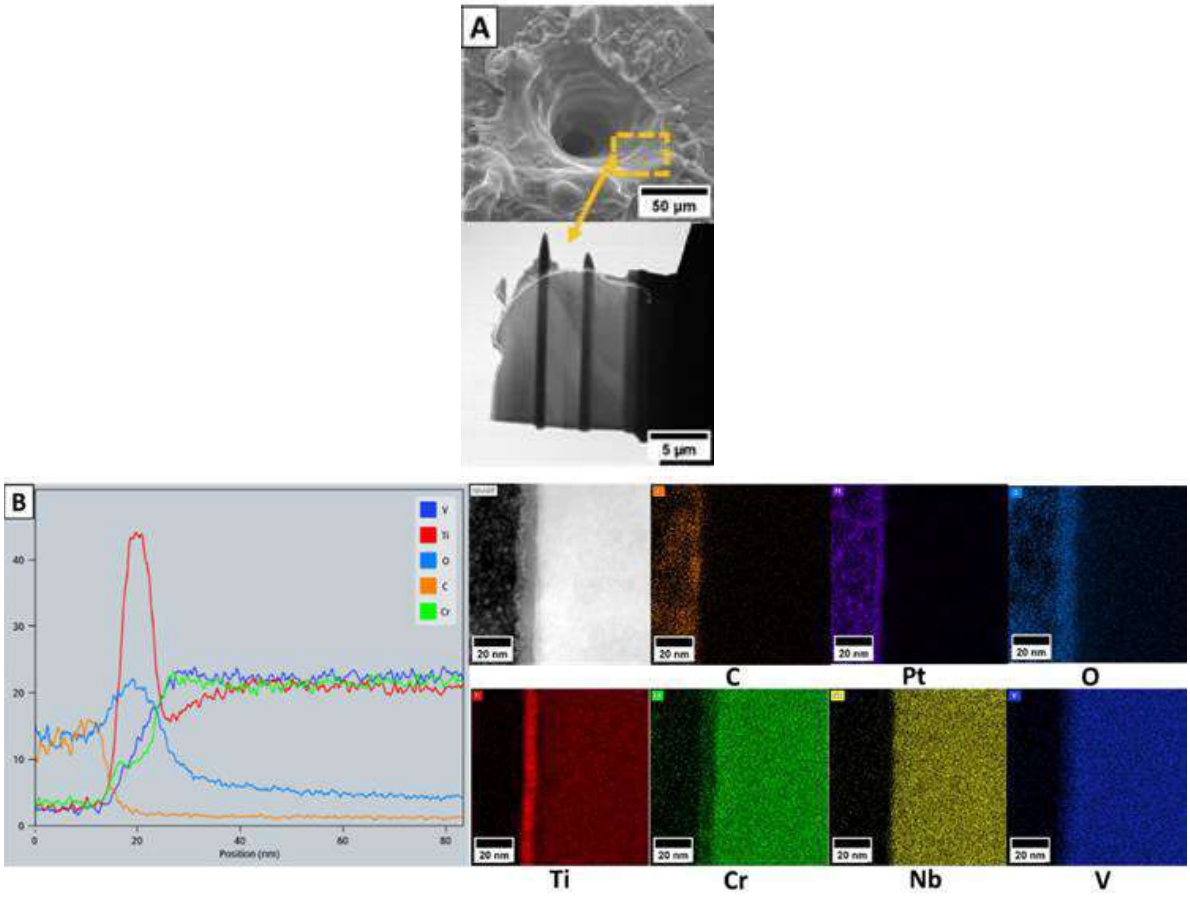

Figure 1. (A) FIB lamella taken from the surface of the TiVNbCr alloy after PLA processing. **(B)** TEM EDS map and quantification confirming the presence of a 10 nm layer of Ti-rich oxide formed in the surface of the sample.

References

[1] F. Marques, et al. Energy Environ Sci 14 (2021) 5191–5227.
[2] R.B. Strozi, et al. Energies (Basel) 14 (2021) 3068.
[3] R.B. Strozi, et al. J Alloys Compd 932 (2023) 167609.
[4] B.H. Silva, et al. J Alloys Compd 901 (2022) 163620.
[5] B. Hessel Silva, et al. Int J Hydrogen Energy 48 (2023) 32813–32825.
[6] M.M. Nygård, et al. Acta Mater 175 (2019) 121–129.
[7] B. H. Silva, et al. Int J Hydrogen Energy 53 (2024) 885–890.

Acknowledgments

This work was financed in part by the by Sao Paulo Research Foundation (FAPESP, process number 2024/03659-8) and in part by the Brazilian National Council for Scientific and Technological Development – CNPq (Grant numbers: 407906- 2022-3 and 309467/2021-7). This study was also financed in part by the Coordenação de Aperfeiçoamento de Pessoal de Nível Superior - Brasil (CAPES) - Finance Code 001, Federal University of Sao Carlos, Graduate Program in Materials Science and Engineering. The authors are grateful to the Laboratory of Structural Characterization (LCE/DEMa/UFSCar) for the electron microscopy facilities.

Surface Oxidation State Analysis of Magnetite (Fe_3O_4) Nanoparticles and Their Magnetic Properties

Douglas M. A. Ferreira[1]*, Adriele A. Almeida[1], Renan M. C. Lima[1], Maria G. F. Vaz[2], Miguel A. Novak[1], Yutao Xing[1].

[1]Instituto de Física – Universidade Federal Fluminense
[2]Instituto de Quimica – Universidade Federal Fluminense
*dmaillard@id.uff.br

Magnetite nanoparticles (Fe_3O_4 NPs) are widely studied due to their physicochemical properties, which strongly depend on particle size, surface-to-volume ratio, and morphology. These nanomaterials are promising for various applications, including biomedical, catalysis, nanotechnology, and environmental remediation. Assuring control of their stability against oxidation and agglomeration is crucial. In this work, we investigated magnetite nanoparticles synthesized via chemical coprecipitation with an average size of approximately 100 nm as observed by Transmission Electron Microscopy (TEM). The main objectives of this study are to confirm the oxidation state of the nanoparticles, their size distribution and suspension stability throughout their entire volume. It is well known that under environmental conditions, they tend to undergo partial or complete oxidation, leading to the formation of maghemite (γ-Fe_2O_3). This transformation can significantly modify the physical properties of the particles, directly impacting their effectiveness in different applications [1,2]. Morphological and structural characterization was performed using Transmission Electron Microscope JEOL JEM 2100F (TEM), allowing observation of particle shape, size distribution, and structure. High-resolution images (HRTEM) enabled the identification of crystalline planes and evaluation of structural order, (Figure 1). Additionally, spectroscopic TEM analysis, including Energy-Dispersive X-ray Spectroscopy (EDS) and Electron Energy Loss Spectroscopy (EELS), will be employed to investigate the elemental composition and electronic structure of the nanoparticles. Magnetic properties were investigated using DC magnetometry with a SQUID Cryogenics SX-700R magnetometer through magnetization curves as a function of field (M×H) and temperature (M×T), (Figure 2). These measurements allowed us to investigate the superparamagnetic behavior, coercivity, and possible magnetic transitions, and served as a complementary indication of the oxidation degree of the samples [1-3]. This study contributes to a better understanding of the correlations between morphology, crystal structure, and magnetic properties in iron oxide nanoparticles, providing valuable insights for controlling structural quality and optimizing performance in technological and biomedical applications.

[1] Lavorato, Gabriel C., et al. "Shell-mediated control of surface chemistry of highly stoichiometric magnetite nanoparticles." Nanoscale 12.25 (2020): 13626-13636.
[2] Bogart, Lara K., Cristina Blanco-Andujar, and Quentin A. Pankhurst. "Environmental oxidative aging of iron oxide nanoparticles." Applied Physics Letters 113.13 (2018).
[3] Lavorato, Gabriel C., et al. "Redox phase transformations in magnetite nanoparticles: impact on their composition, structure and biomedical applications." Nanotechnology 34.19 (2023): 192001.

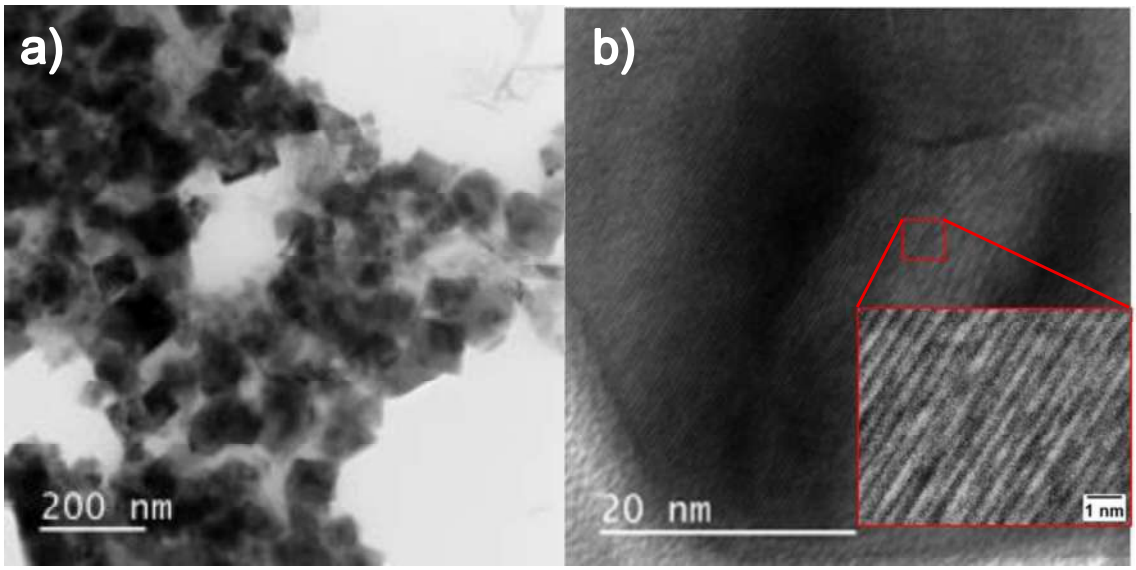

Figure 1. a) Representative TEM bright field images. **b)** HRTEM image of a single nanoparticle of the sample Fe_3O_4, the inset show the particle structure.

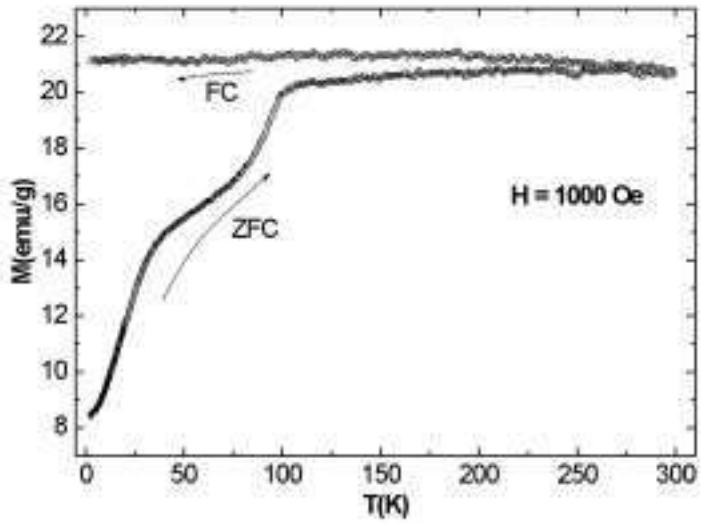

Figure 2. Magnetization curves as function of temperature (MxT) of the sample Fe_3O_4 measurements in zero-field-cooling (ZFC) and field-cooling (FC) protocols with applied field of H = 0.1 Tesla.

Synthesis and Characterization of In_2S_3 Semiconductor Quantum Dots for Potential Photocatalytic Applications in Water Pollution Remediation

Herman S. Mansur[1]*, Thiago L. S. Esteves[1], Alexandra A. P. Mansur[1].

[1]Center of Nanoscience, Nanotechnology, and Innovation – CeNano[2]I, Department of Metallurgical and Materials Engineering, Federal University of Minas Gerais, UFMG, Brazil.
*hmansur@demet.ufmg.br; herman.mansur2016@gmail.com

The threat of toxic organic pollutants to the ecosystem is causing increasing concerns globally due to rapid urbanization, development, and industrial activities. Hence, the progress of effective nanosized photocatalysts to eliminate these hazards from the aquatic system is highly needed [1-4]. Quantum dots (QDs) are an emerging new class of optically active semiconductor nanoparticles with a huge surface-to-volume ratio suitable for numerous environmental applications. Heterogeneous photocatalysis based on QDs is an attractive technology for the advanced treatment of water polluted by organic dyes. Indium sulfide (In_2S_3), an effective visible-light semiconductor absorber, has been broadly investigated for the photodegradation of dyes and organic pollutants due to its remarkable advantages, including a high photo-absorption, a middle bandgap (2.0–2.5 eV) transition for solar light absorption, excellent chemical stability, and minimal toxicity compared to traditional heavy metal-based QDs [1-4]. In this study, In_2S_3 semiconductor QDs (In_2S_3 QDs) were synthesized via a facile single-step colloidal precipitation process using a green aqueous route. These novel In_2S_3 QDs, surface-stabilized by the carboxymethyl cellulose biomolecule (CMC), were extensively characterized for assessing their optical, morphological, and structural properties, aiming at their potential use in photocatalytic applications. The X-ray fluorescence analysis (XRF) confirmed In and S as major elements of the nanoparticles (In-Kα at 2θ = 14.5°; S-Kα at 2θ = 76°, Fig.1A) with an estimated molar ratio of [In:S]=2:4 as compared to the stoichiometry [In_2S_3=2:3]. The UV-Vis spectroscopy results demonstrated that optically active In_2S_3 nanoparticles were formed, showing strong absorption between 250-350 nm, and onset at approximately λ=360 nm (Fig.1B). The Tauc's plot indicates an estimated direct excitonic bandgap value of 3.46 ± 0.04 eV, i.e., *blue shift* of ~1.1 eV (Fig.1B, insert), considering the In_2S_3 bulk bandgap (2.3-2.5 eV) [2,4]. Based on the particle-in-box model, these findings confirmed the formation of In_2S_3 QDs with a strong quantum confinement effect, with a projected size of approximately 3.0 nm, much smaller than the Bohr radius (a_B ~ 33 nm) [1-4]. The X-ray diffraction analysis (XRD) confirmed the formation of nanoparticles compatible with nanocrystalline β-In_2S_3, evidenced by the major peaks at 2θ = 14°, 27.4°, 28.6°, 43.5°, and 59.2°. It also indicated the presence of the CMC macromolecule used as a colloidal ligand by the broad band between 2θ = 15° and 35° (Fig.1C). The high-resolution transmission electron microscopy (HR-TEM) showed the formation of ultrasmall and well-dispersed nanoparticles, with spheroidal morphological shapes, a narrow and uniform size distribution, with an average diameter of 2.9 ± 0.3 nm (Fig.2A, insert). The TEM dimension was well-matched with the estimated size from the UV-vis analysis through Tauc's plot (~3.0 nm). The crystallinity was also assessed using electron diffraction (ED) patterns (Fig.2B), which revealed an interplanar distance of d = 0.27 ± 0.07 nm, compatible with the β-In_2S_3 phase (JCPDS 51-1160). The elemental chemical analysis by EDS confirmed the presence of In and S species in the composition of the nanoparticles (Fig.2C). These In_2S_3 colloidal nanomaterials were further characterized by dynamic laser scattering (DLS), presenting a hydrodynamic diameter H_D = 188 ± 37 nm, and zeta potential analysis (ZP), with value of -57.1 ± 2.2 mV. These results demonstrated that colloidal supramolecular nanostructures were effectively formed, compatible with an inorganic core of In_2S_3 surrounded by an organic shell of CMC biomolecule (*i.e.,* core-shell morphology). Acknowledgments and Funding support [5].

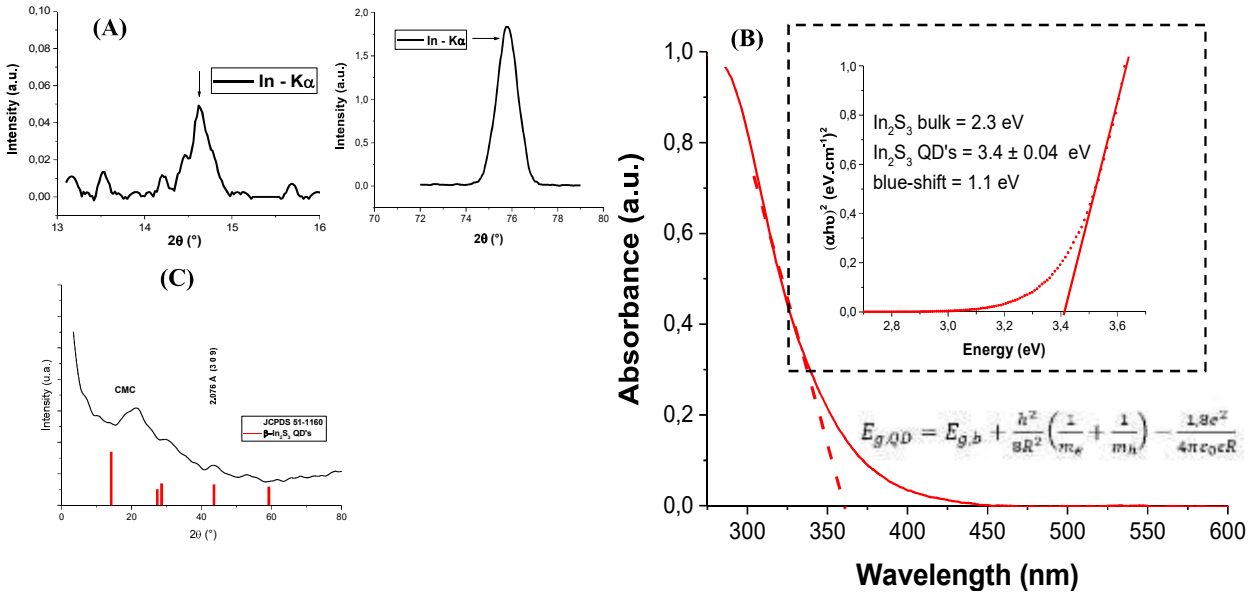

Figure 1. Spectroscopic and structural characterization of In_2S_3 QDs: (A) XRF spectra; (B) UV-Vis spectra, Tauc´s Plot (insert); (C) XRD analysis.

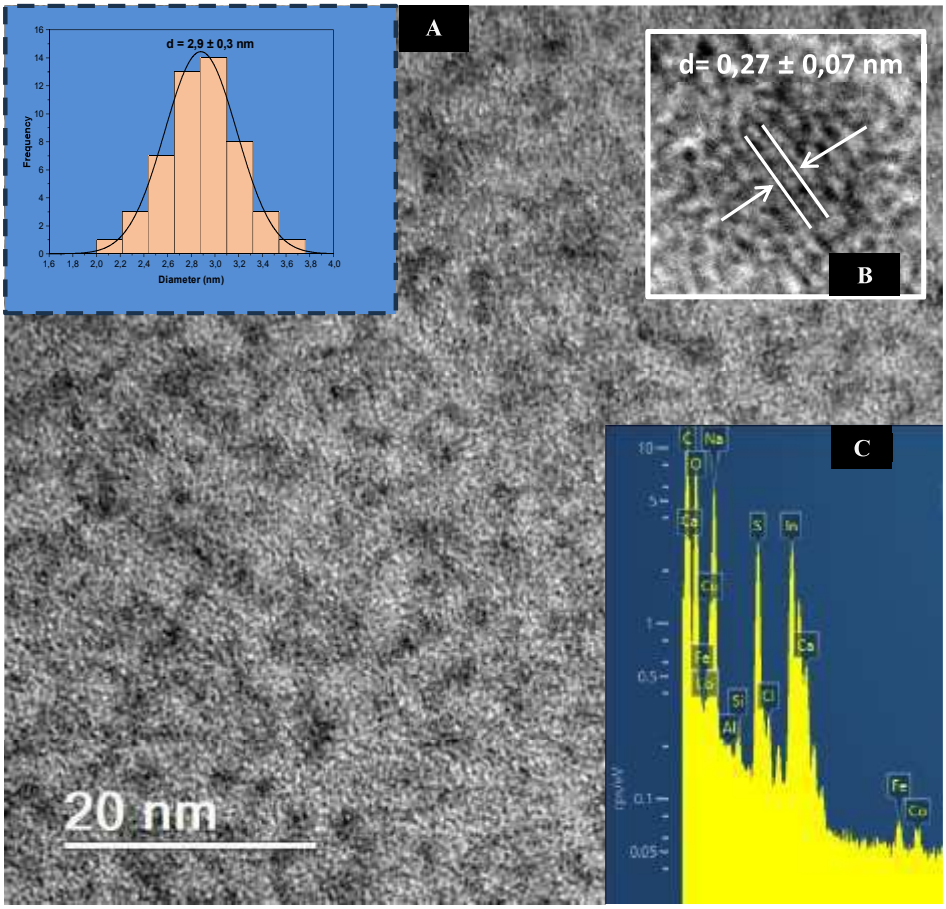

Figure 2. Spectroscopic, morphological, and structural characterization of In_2S_3 QDs: (A) TEM image, size distribution histogram (insert); (B) ED pattern; (C) EDS spectra.

[1] A. A. Mansur et al., *Applied Catalysis B: Environmental*, 158-159 (2014) 269.
[2] S. K. Batabyal et al., *Crystal Growth & Design* 16 (2016) 2231.
[3] A. A. Mansur et al., *International Journal of Biological Macromolecules*, 231 (2023) 123363.
[4] Mishra, S. R., Gadore, V., & Ahmaruzzaman, M. (2024). *Journal of Environmental Chemical Engineering*, 12(5), 113449.
[5] This research was financially supported by FAPEMIG, CAPES, and CNPq (Brazil).

The Role of TiFe Nanostructure as an Additive in Mg/MgH_2 Composites for Hydrogen Storage

F.J. Antiqueira*, D.D. Coimbrão, E. A. de Oliveira, D.R. Leiva, G. Zepon, W.J. Botta
Federal University of São Carlos (UFSCar), Department of Materials Engineering (DEMa), São Carlos – SP, Brazil.
*e-mail: fantiqueira@ppgcem.ufscar.br

In a previous work we aimed to enhance the hydrogen storage properties of Mg by incorporating small amounts (2 mol%) of additives such as Fe, TiFe, TiAl, and Nb_2O_5, processed via reactive milling (RM) under 10 bar of H_2 [1]. The milling was performed in a planetary mill using the following parameters: ~720 mg of sample, 400 rpm, ball-to-powder ratio (BPR) of 100:1, with a total of 20 hours of milling and 20 hours of pauses, both alternated in 20 cycles of 30 minutes each. After milling, each sample was fully desorbed in a Sieverts-type apparatus at 330 °C, then cooled and reabsorbed under 20 bar of H_2 at room temperature (RT) (23 °C). The results indicated that TiFe was the most effective additive in promoting the conversion of Mg to MgH_2, followed by Fe (Figure 1). The present study investigates the influence of higher TiFe fractions (4 mol% = 7.6 wt.%, 15 mol% = 25.8 wt.%, 25 mol% = 39.6 wt.%) in Mg/MgH_2 mixtures. Under the same reactive milling conditions above, the recent results reveal formation of Mg_2FeH_6 when TiFe content reaches or exceeds 15 mol%. The γ-MgH_2 and β-MgH_2 phases are present in both the milled MgH_2 reference sample and the composite with 4 mol% TiFe. However, at TiFe fractions ≥ 15 mol%, the γ-MgH_2 phase is nearly absent, suggesting its participation in the Mg_2FeH_6 formation. Transmission electron microscopy (TEM) analysis of the samples after the first hydrogen absorption cycle at RT revealed the presence of nanometric TiFe, Fe, and Ti particles, as shown in Figures 2 and 3, indicating the formation of nanoclusters with interesting morphology and shapes [2,3]. TEM was carried out in powder samples in a Talos F200X G2 FEG Scanning Transmission Electron Microscope/ Thermo Fisher Scientific, at 200 kV, using conventional TEM, Scanning-TEM (S-TEM) and High-Angle Annular Dark Field (HAADF) mode. These nanostructures are proposed to play a pivotal role in accelerating hydrogen sorption kinetics and destabilizing thermodynamics of MgH_2, thereby improving storage performance [4,5]. The TEM findings underscore the RM route potential to obtain nanoclusters and show its power as a nanoscale characterization tool, providing direct evidence of phase evolution and nanostructural features critical to hydrogen storage mechanisms. These insights highlight the potential of Mg/MgH_2-based materials as safe and efficient solid-state hydrogen storage media.

[1] F. J. Antiqueira et al., International Journal of Hydrogen Energy, (2022) v. 47, n. 1, p. 470-489.
[2] B. Boruah, B. Kalita, Journal of Energy Storage, 72 (2023) 108217.X.
[3] X. Zhang et al. Chemical Communications, 53.99 (2017) 13213-13216.
[4] I. J. T. Jensen et al., Physical Review B—Condensed Matter and Materials Physics, 82.17 (2010) 174121.
[5] R.W. Wagemans et al., Journal of the American Chemical Society, 127.47 (2005) 16675-16680.
[6] This research was supported by CNPQ, CAPES, FINEP, FAPESP (Brazil).
[7] The authors are grateful for the electron microscopy facilities from the Laboratory of Structural Characterization of Federal University of São Carlos (LCE/DEMa/UFSCar).

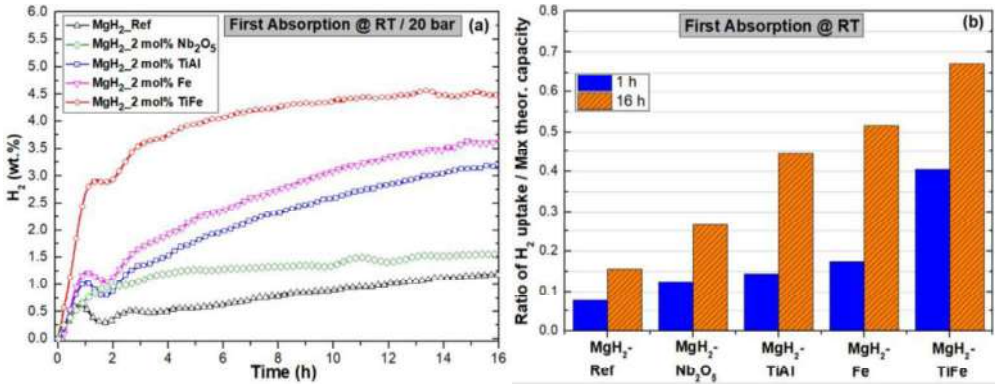

Figure 1. First absorption kinetics at RT (23 °C)/ 20 bar H_2 for MgH_2-Ref and MgH_2-2 mol% X (X = Nb_2O_5, TiAl, Fe and TiFe) after first desorption at 330 °C. a) First absorption at RT/ 20 bar H_2 as H_2 (wt.%) vs time; b) First absorption at RT/ 20 bar H_2 as a Ratio between H_2 uptake and Maximum theoretical H_2 capacity [**1**].

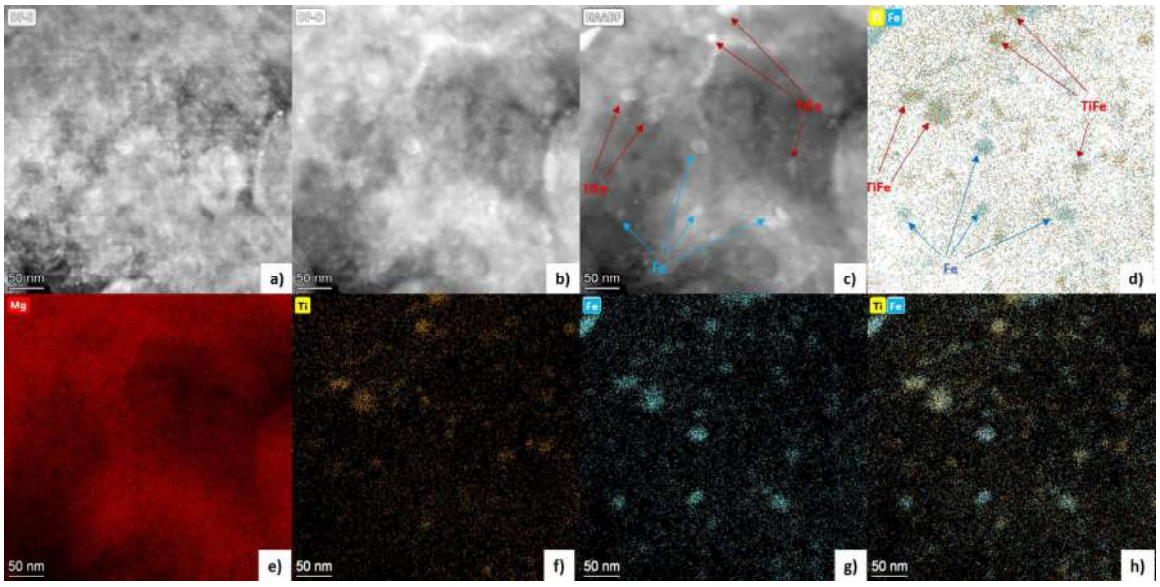

Figure 2. TEM images and Elemental chemical mapping (EDS) from STEM mode for the MgH_2-4 mol% TiFe after first H_2 absorption at RT. a) Dark field-S, b) Dark field-O, c) HAADF, d) Overlapped EDS color mapping with bright matrix, e), f), g), h) EDS color mapping from Mg, Ti, Fe and Ti/Fe in overlap, respectively.

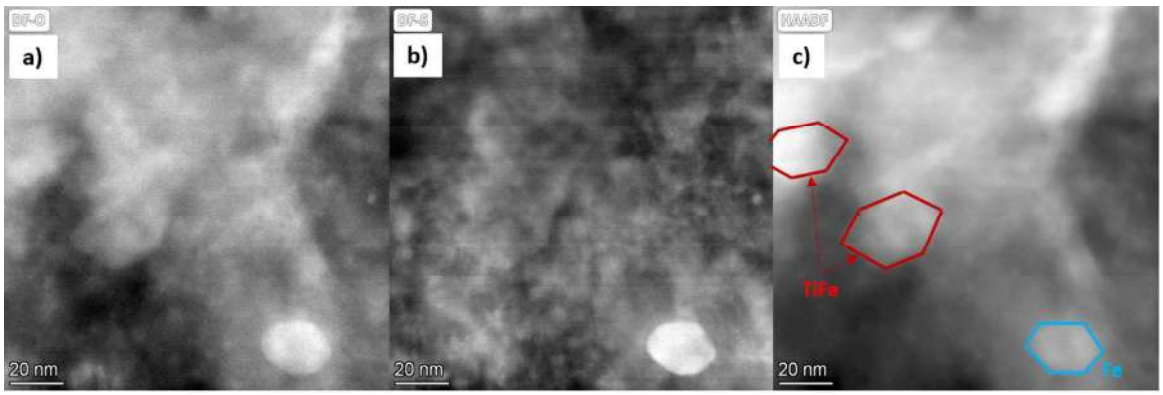

Figure 3. TEM images for the MgH_2-4 mol% TiFe after first H_2 absorption at RT. a) HAADF, b) BF, c) DF (20 nm scale).

The synthetic pathway of whitlockite nanoparticles elucidated by transmission electron microscopy

Laila Maximiano Veras[1], Luelc Souza da Costa[2]*, Pierre B. Almeida Fechine[3], Alan Silva de Menezes[4], Davino M. Andrade Neto[1].

[1] Federal Institute of Education, Science, and Technology of Ceará, Campus Camocim, 62400-000 Camocim, CE, Brazil.
[2] Brazilian Nanotechnology National Laboratory (LNNano), Brazilian Center for Research in Energy and Materials (CNPEM), Campinas, Sao Paulo, Brazil.
[3] Group of Chemistry of Advanced Materials (GQMat)–Department of Analytical Chemistry and Physic-Chemistry, Federal University of Ceará–UFC, Pici Campus, 12100, CP 60451-970 Fortaleza, CE, Brazil;
[4] Department of Physics, Federal University of Maranhão, CEP, 65080-805, São Luís, MA, Brazil
*luelc.costa@lnnano.cnpem.br

Abstract

Whitlockite (WH, $Ca_{18}Mg_2(HPO_4)_2(PO4)_{12}$) has emerged as a promising bone regenerative material due to its abundance in human bones and teeth [1]. However, its practical application has been hindered by the challenge of obtaining pure WH. To facilitate the development of novel and efficient synthesis methods, we present a detailed chemical pathway towards WH nanoparticles. In this work, we propose the mechanism for WH nanoparticle formation using cryo-transmission electron microscopy (TEM) and in situ TEM. Initially, a hydrothermal methodology was developed, leading to the successful synthesis of pure WH nanoparticles after a 4.5-hour treatment. X-ray diffraction (XRD) revealed the crystalline evolution during hydrothermal treatments (Figure 1). After the heating step, the solid phase comprised only brushite ($CaHPO_4 \cdot 2H_2O$) and an amorphous Mg^{2+} phase (Figure 2 A-B). Subsequently, during hydrothermal treatments between 0.17 and 0.45 hours, struvite ($MgNH_4PO_4 \cdot 6H_2O$) formed, followed by the appearance of monetite ($CaHPO_4$) and WH after 1 hour. Ultimately, at 4.5 hours, only WH was observed, as confirmed by XRD and cryo-TEM (Figure 1 and Figure 2 C-D). While evidence of reaction intermediates exists, the specific interconversion process between the compounds remains elusive. To shed light on this aspect, we will perform ex situ TEM experiments with samples at intermediate times and in situ TEM, representing the next phase of this investigation. Anticipating the upcoming event, we expect to present these results and elucidate the complete mechanism. The significance of our work lies in the demonstration of a new synthetic route for nanoparticles, facilitated by the precise identification of reactive intermediates. This advancement paves the way for the effective utilization of WH in bone regeneration. [2]

[1] Cheng et. al. Acta Biomater. 2018, 69, 342-351.
[2] Acknowledgements:LNano for cryo-TEM facilities [Projects IDs: 20210560, 20230286, 20230715]

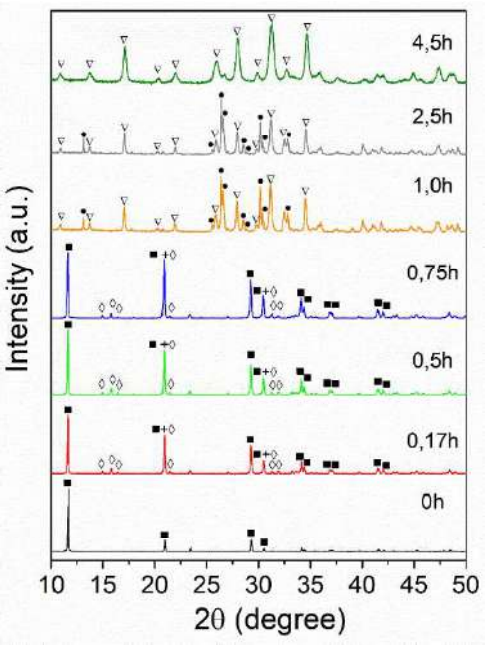

Figure 1 – X-ray diffraction (XRD) patterns of the samples of calcium phosphate powders according to the time of hydrothermal treatment at 190 °C. Identification of the phases: ■ Brushite ($CaHPO_4 \cdot 2H_2O$); ◊ Struvite ($MgNH_4PO_4 \cdot 6H_2O$); ● Monetite ($CaHPO_4$); ∇ Whitlockite ($Ca_{18}Mg_2(HPO_4)_2(PO_4)_{12}$).

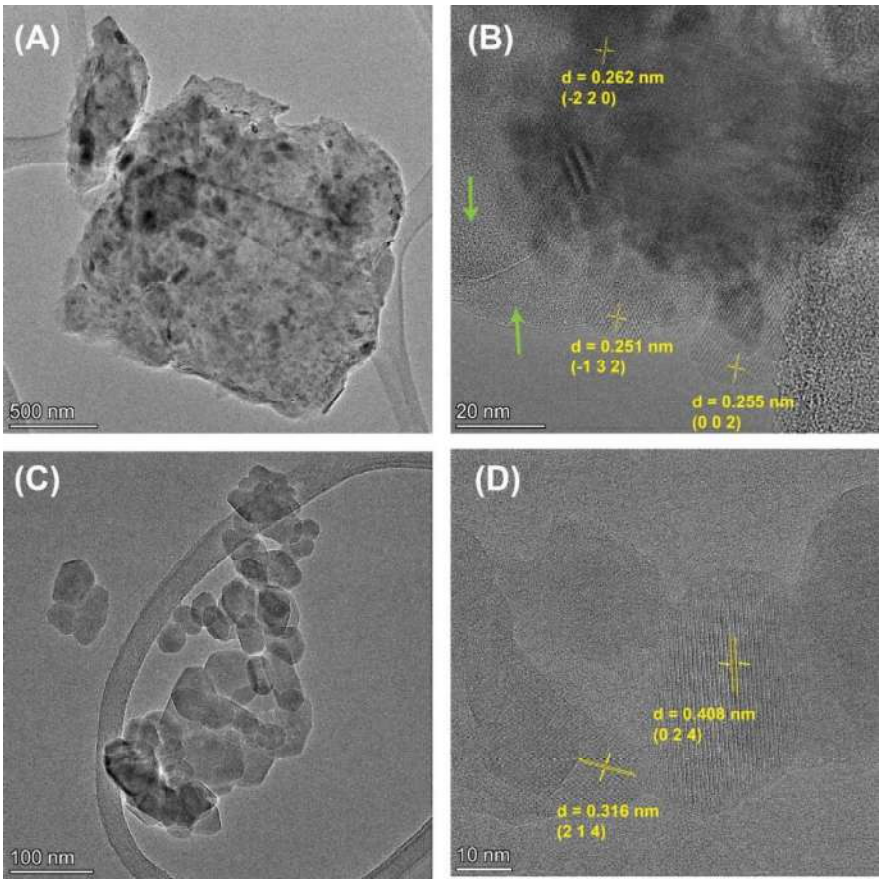

Figure 2 – TEM micrographs of samples A) 0h and C) 4.5h (WH). Micrographs B) and D) show higher magnification views, revealing the interplanar distances and Miller indices of the respective lattice plane families. In B), green arrows highlight the presence of amorphous particles in sample 0h.

Transmission Electron Microscopy as a Realistic Data Source for the Micromagnetic Simulation of Polycrystalline Nickel Nanowires

C.A. França[1]*, Y. Guerra[2], D.R.B. Valadão[3], J. Holanda[4], E. Padrón-Hernández[5]

[1]Centro de Tecnologias Estratégicas do Nordeste, [2] Universidade Federal de Alagoas, [3]Universidade Federal de Lavras, [4]Universidade Federal Rural de Pernambuco, [5]Universidade Federal de Pernambuco
*claudio.franca@cetene.gov.br

Magnetic nanowires in hexagonal arrays have technological and academic importance due to their properties and applications [1,2]. The most popular methodology used to fabricate these systems is the electrochemical route [3] because it is possible to produce ordered arrays into the pores of alumina membranes [4,5]. Research groups investigated the magnetic interactions for this systems [6]. In some works were proposed different modes for the reversion of the magnetization [7]. Landeros et al. [8] observed the predominance of the coherent mode for nanowires constituted by short particles. Hernández et al. [9] showed an alternative for express the magnetic free energy in polycrystalline nanowires. A chain of ellipsoids was proposed for explain the dipolar interactions along the wire. Some studies have attempted to establish a phase diagram for the reversion of the magnetic moments. In other hand, there is not a definitive mathematical equation describing the angular dependence for the coercivity and remanence in these systems. Microstructure is a critical aspect for study this problem and every model will enter the real characteristics of the nanowires. The aim of the present work is to take the great advantages of transmission electron. Sample preparation was using membranes of anodic aluminum oxide (AAO) as a template and electrodeposited the nickel within the cylindrical pores. Magnetization curves were performed with the field in different orientations and were registered the angular dependence of coercivity and remanence. Magnetic measurements were performed in a vibrating sample magnetometer (VSM), Fig. 2 and Fig. 3. Transmission electron microscopy (TEM) images were registered in a TITAN 300 kV. For the micromagnetic model the objects considered were polycrystalline nanowires, composed by twenty cuboctahedron of 30 nm, randomly oriented according to the TEM results, Fig. 1a. In the simulation we considered a hexagonal array of seven nanowires of 450 nm for longitudinal size and the center to center distance was l = 70 nm, Fig. 1b and c. As a conclusion, Micromagnetic simulation is a very strong theory that may be applied starting by the experimental observation of the real object.

[1] R.H. Koch, J.G. Deac, D.W. Abraham, P.L. Trouilloud, R.A. Altman, Y. Lu, W.J. Gallagher, R.E. Scheuerlein, K.P. Roche, S.S.P. Parkin, Phys. Rev. Lett. 81 (1998) 4512.
[2] R.P. Cowburn, D.K. Koltsov, A.O. Adeyeye, M.E. Welland, Phys. Rev. Lett. 83 (1999) 1042.
[3] M. Motoyoma, Y. Fukunaka, T. Sakka, Y.H. Ogata, Electrochim. Acta 53 (2007) 205.
[4] H. Masuda, K. Fukuta, Science 268 (1995) 1466.
[5] K. Nielsch, R.B. Wehrspohn, J. Barthel, J. Kirschner, U. Gosele, S.F. Fischer, H. Kronmuller, Appl. Phys. Lett. 79 (2001) 1360.
[6] J. Escrig, R. Lavín, J.L. Palma, J.C. Denardin, D. Altbir, A. Cortes, H. Gomez, Nanotechnology 19 (2008) 075713.
[7] M. Vazquez, K. Pirota, M. Hernandez-Velez, V.M. Prida, D. Navas, R. Sanz, F. Batallan, J. Velazquez, J. Appl. Phys. 95 (2004) 6642.
[8] Landeros, S. Allende, J. Escrig, E. Salcedo, D. Altbir, E.E. Vogel, Appl. Phys. Lett. 90 (2007) 102501.
[9] E.P. Hernández, S.M. Rezende, A. Azevedo, J. Appl. Phys. 103 (2008) 07D506

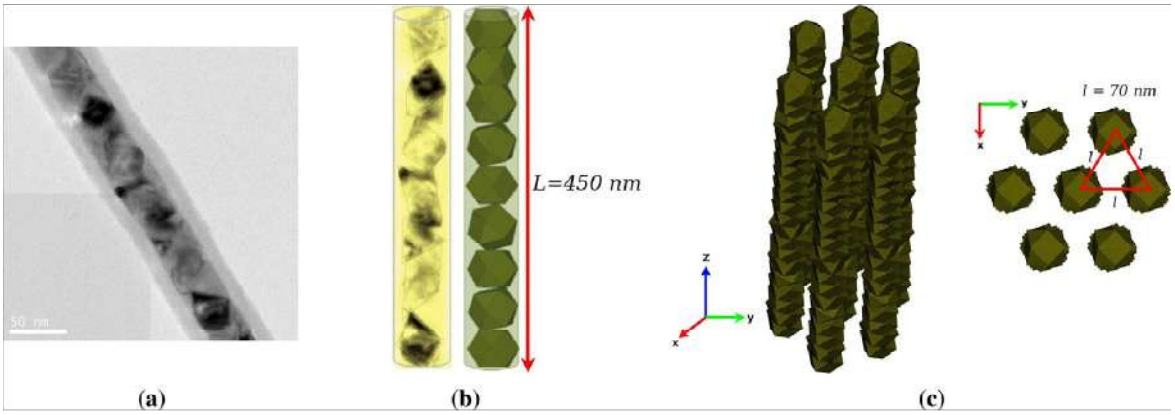

Figure 1. (a) Transmission electron microscopy for the electrodeposited wire, (b) the geometry representing the used parameters for the calculations and the lateral profile of the nanowire and (c) network used for the micromagnetic simulation.

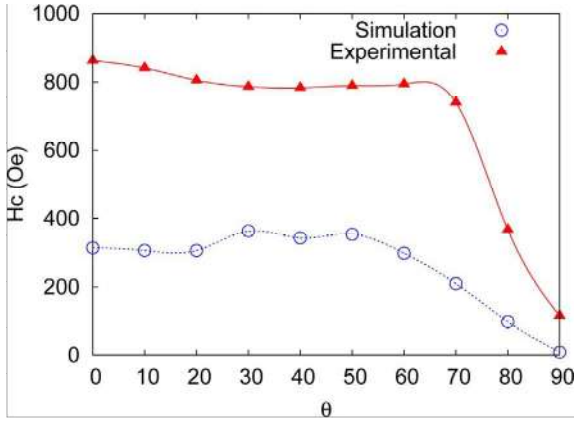

Figure 2. Angular dependence for the coercivity according to the experimental observations (red) and according to the calculated values form the equilibrium configuration of the magnetic moments (blue).

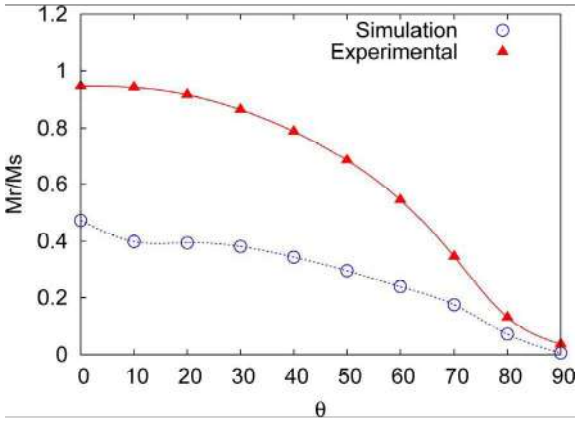

Figure 3. Angular dependence for the remanence according to the experimental observations (red) and according to the calculated values form the equilibrium configuration of the magnetic moments (blue).

Transmission Electron Microscopy Study of the Martensitic Phase in a MnNiFeCoSiGe Magnetocaloric High-Entropy

Pedro Henrique Mancilha[1]*, Diogo de Campos Fernandes[2], Francisco Gil Coury[1,2].

[1]PPGCEM/UFSCar, [2]DEMa/UFSCar
*pedromancilha@estudante.ufscar.br

Observed for the first time by Weiss and Piccard in 1918, the magnetocaloric effect has drawn considerable interest over time due to the potential utilization of this effect in magnetic refrigeration systems, in which a magnetocaloric material is subjected to thermodynamic cycles in order to extract heat from a material or environment that is being cooled and transfer it to a heat sink [1]. Magnetic refrigeration systems offer several compelling benefits over conventional vapor-compression cooling systems, such as (1) higher environmental friendliness, (2) greater energy efficiency, and (3) quieter operation [2]. The magnetocaloric effect results in a temperature change when a magnetocaloric material is adiabatically magnetized or demagnetized, or in an entropy change if the process is carried out isothermally [2]. Due to the prohibitive costs and limited performance of commercially available magnetocaloric materials, large-scale deployment of magnetic refrigeration systems has faced significant obstacles and has yet to be realized; recently, however, the discovery of high-entropy alloys with promising magnetocaloric properties has renewed interest in such materials [3]. The first magnetocaloric high-entropy alloys contained rare-earth elements in their composition, but recently, alloys without these elements have been developed. In particular, the MnNiFeCoSiGe system possesses several compositions of the type $(MnNiFeCo)_2(SiGe)_1$ that exhibit a strong magnetocaloric response due to a magnetostructural transformation in which a hexagonal austenitic and paramagnetic phase transforms into an orthorhombic martensitic and ferromagnetic phase upon cooling, as shown in Figure 1 [4,5]. Some alloys from this system are promising candidates for coolants in magnetic refrigeration systems, as they possess a combination of strong magnetocaloric effect, low thermal hysteresis, and low Curie temperature. However, each thermodynamic cycle is followed by structural transformations in these materials, and studying the evolution of their microstructure and properties is crucial to assess whether these materials can be realistically employed in magnetic refrigeration systems. In this context, this work presents a detailed characterization of the low-temperature martensitic phase in a MnNiFeCoSiGe high-entropy alloy via transmission electron microscopy [6].

[1] A. Smith et al. Materials Challenges for High Performance Magnetocaloric Refrigeration Devices. Advanced Energy Materials, 2, 11, 1288-1318, 2012.
[2] V. Franco et al. Magnetocaloric effect: From materials research to refrigeration devices. Progress in Materials Science, 93, 112-232, 2018.
[3] J. Law et al. Current perspective in magnetocaloric materials research. Journal of Applied Physics, 133, 040903, 1-13, 2022.
[4] J. Law, V. Franco. Review on magnetocaloric high-entropy alloys: Design and analysis methods. Journal of Materials Research, 38, 1, 37-51, 2023.
[5] Z. Zheng at al. Giant magnetocaloric effects of MnNiSi-based high-entropy alloys near room temperature. Journal of Alloys and Compounds, 966, 171483, 1-13, 2023.
[6] This research was supported by FAPESP (Process no. 2025/02882-8) and CAPES (Brazil).

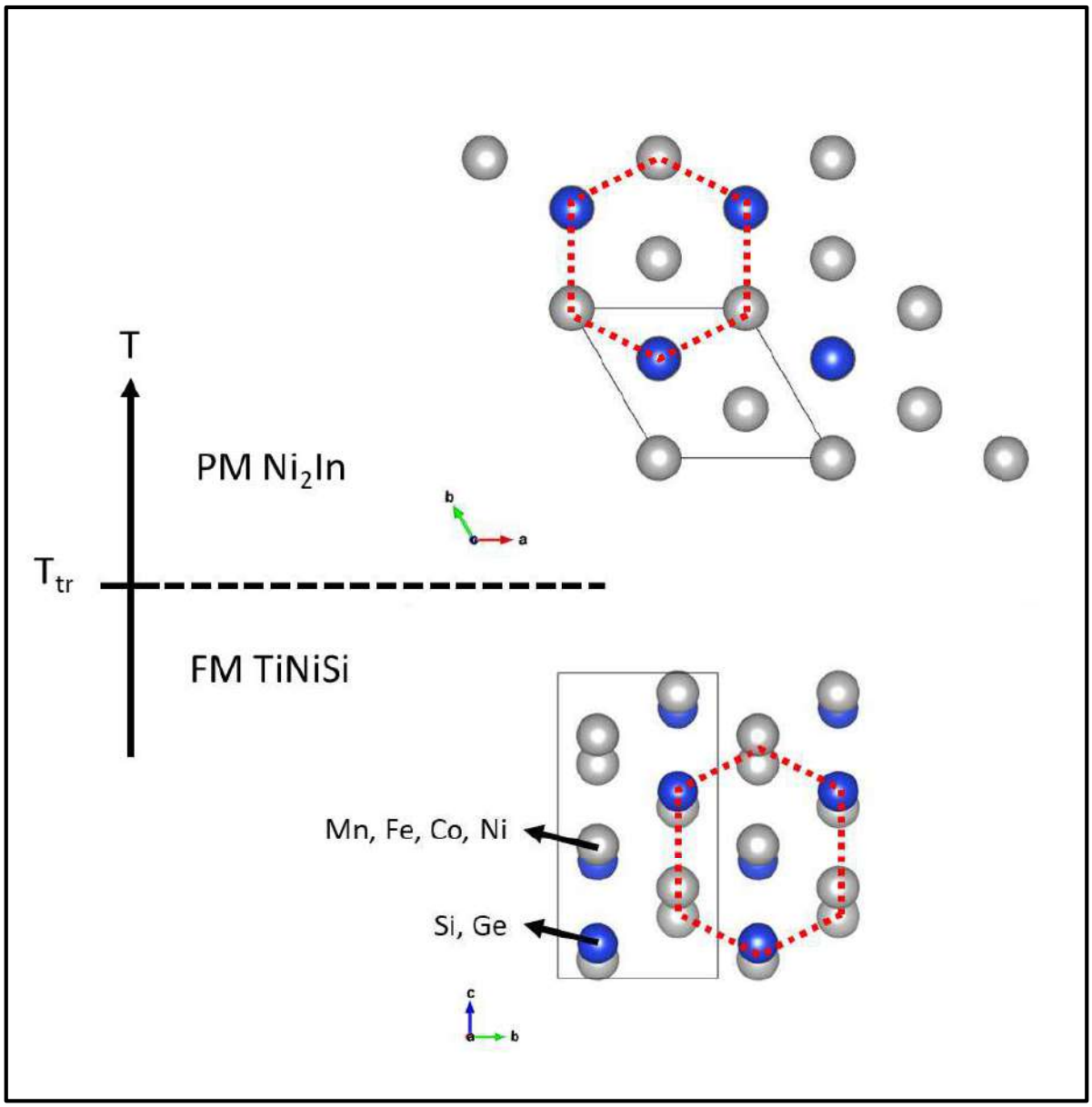

Figure 1 – Top view of the hexagonal and paramagnetic (PM) phase (Ni_2In prototype) and lateral view of the orthorhombic and ferromagnetic (FM) phase (TiNiSi prototype). The transformation starts at temperature T_{tr} (which depends on composition and applied magnetic field) and is a martensitic phase transformation. In the austenite-to-martensite transformation, neighboring atoms in each atomic collum parallel to the $[001]_{hex}$ direction shift in opposite directions.

Visualization of Ferroelectric Domains in Bulk Tellurium by Differential Phase Contrast Scanning Transmission Electron Microscopy

Jaime F. Oliveira[1], Geraldo Cernicchiaro[1], Pedro V. Lopes[2], Magda B. Fontes[1], Carsten Enderlein[3], Elisa Baggio-Saitovich[1], Bruno Focassio[4], Gabriel R. Schleder[4], Rodrigo B. Capaz[2, 4], Saif Ullah[5], Timo Thonhauser[5], Marcos Menezes[2], Fabiano Montoro[4], Carlos Ospina[4], Jefferson Bettini[4], Marcello B. Silva Neto[2*].

[1]CBPF, Rua Xavier Sigaud, 150, Rio de Janeiro, 22290-180, RJ, Brazil, [2]Instituto de Física, UFRJ, Av. Athos da Silveira Ramos, 149, Rio de Janeiro, 21941-909, RJ, Brazil, [3]Instituto de Física, UFRJ, Campus de Duque de Caxias, RJ, Brazil, [4]LNNano, CNPEM, R. Giuseppe Maximo Scolfaro, 10.000, Campinas, 13083-100, SP, Brazil, [5]Wake Forest University, Winston-Salem, North Carolina, US.
*mbsn@if.ufrj.br

Differential Phase Contrast Scanning Transmission Electron Microscopy (DPC-STEM) is one of the most recommended techniques for characterizing intrinsic electric and magnetic fields at sub-ångström resolutions, especially when combined with spherical aberration correction of the electron probe [1]. It is particularly valuable for analyzing technologically relevant materials. Mapping electric and/or magnetic fields in TEM specimens requires a segmented annular detector capable of detecting angular deflections of the electron probe caused by internal fields, such as those associated with ferroelectric domains. A perfectly trigonal phase of bulk tellurium (Te) does not exhibit ferroelectricity, that is, spontaneous electric polarization, due to the C_3 rotational symmetry of its unit cell [2]. However, this symmetry can be broken by structural defects, which induce atomic displacements and lone-pair rearrangements, ultimately leading to spontaneous polarization. This study aimed to analyze the ferroelectric domains at the nanometric and atomic scales in bulk tellurium samples, where C_3 symmetry is broken due to the presence of structural defects. We conducted a series of experimental measurements, as well as theoretical (based on Lewis' octet rule), numerical (Density Functional Theory – DFT, including Electron Localization Function – ELF, and Integrated Local Density of States – ILDOS) and simulation-based (ab-TEM) calculations, to support our findings [3 – 5]. From a hollow, needle-like tellurium sample produced by chemical vapor deposition, TEM specimens were extracted from regions parallel and perpendicular to its axis using Focused Ion Beam (FIB) in a Helios LabNano 660 microscope. We performed High-Resolution STEM (HRSTEM) and DPC-STEM imaging using a High-Angle Annular Dark-Field (HAADF) detector and a four-segment annular dark-field detector for electric field mapping, in a double spherical aberration-corrected Titan Cubed Themis microscope at 300 kV. A high density of structural defects was observed (Figure 1a), along with Voronoi patterns (Figure 1b) and their corresponding polar domains (Figure 1c). At ultra-high resolution, projections of the helical structure of trigonal Te are shown in Figures 1d and 1e, with corresponding electric field maps in Figures 1f and 1g. The Voronoi mosaic appears to be a structural mechanism that energetically compensates for internal deformations caused by defects, rendering the material polar. Notably, the polar domains align well with the Voronoi patterns (Figure 1c). At atomic resolution, lone-pair redistributions give rise to electric fields, as shown in Figure 1f and 1g, which were confirmed by numerical and simulation results (inset in Figure 1g). These findings provide the first evidence of ferroelectricity in bulk materials composed of a single chemical element, where rotational symmetry is broken due to synthesis-induced structural defects. The results pave the way for designing materials with tunable electrical properties through

structural engineering [6].

[1] N. Shibata et al., Nature Physics, 13 (6) (2017), 533.
[2] P.W. Bridgman, Proceedings of the American Academy of Arts and Sciences, 60 (6) (1925) 305.
[2] G. Kresse and J. Furthmuller, Physical Review B, 54 (16) (1996) 11169.
[3] A.D. Becke and K.E. Edgecombe, The Journal of Chemical Physics, 92 (9) (1990) 5397.
[4] Jacob Madsen and Toma Susi, Ultramicroscopy, 197 (2019) 16.
[5] A. Okabe et al., Spatial Tessellations: Concepts and Applications of Voronoi Diagrams. Wiley, 2000.
[6] This research was supported by CAPES, CNPq, FAPESP and INCT – Materials Informatics (Brazil). It was conducted using the Dual Beam Helios NanoLab 660 and Titan Cubed Themis facilities at the Brazilian Nanotechnology National Laboratory (LNNano), part of the Brazilian Centre for Research in Energy and Materials (CNPEM), a private non-profit organization under the supervision of the Brazilian Ministry for Science, Technology, and Innovations (MCTI).

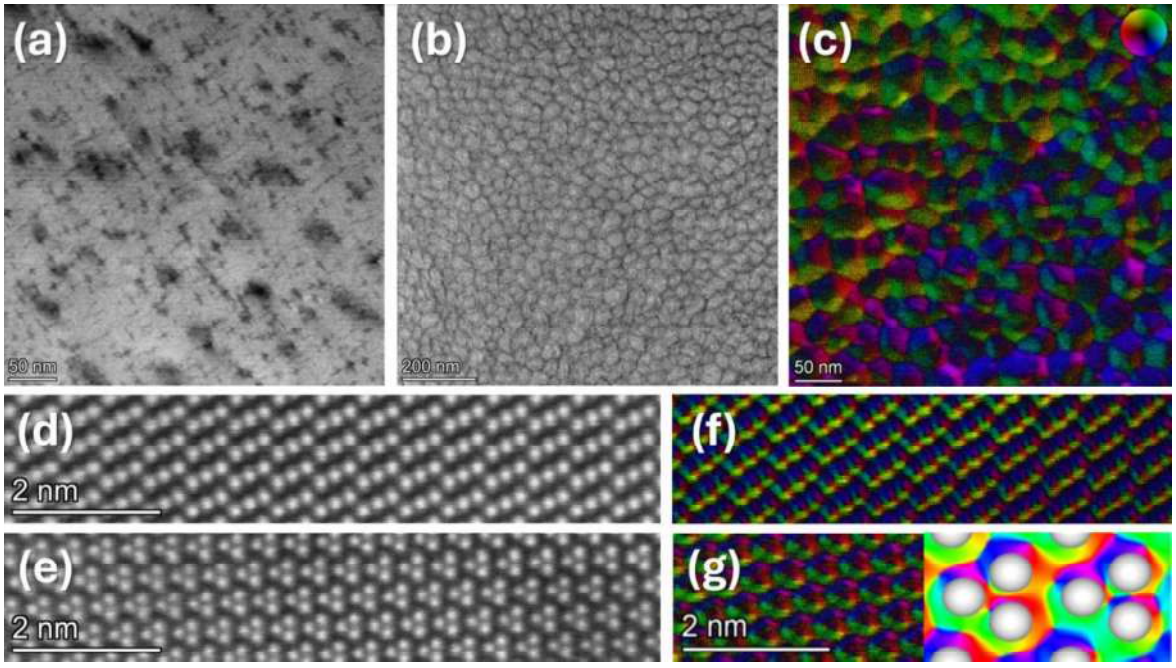

Figure 1. Scanning Transmission Electron Microscopy (STEM) images of lamellae extracted from a region parallel (a) and perpendicular (b) to the axis of the hollow, needle-like tellurium (Te) sample, along with the corresponding ferroelectric domains mapped by DPC-STEM (c). Spherical aberration-corrected High-Angle Annular Dark-Field STEM (HAADF-HRSTEM) images of parallel (d) and perpendicular (e) specimens, and their corresponding electric field maps (f, g). The inset in (g) shows the superposition of the simulated STEM image and the ab-initio electric fields simulations, based on the numerically calculated lone pair distribution.

Scanning Electron Microscopy of Nanostructures and Engineering Materials, including all techniques associated with SEM, such as EDS, EBSD, and FIB

30º Congresso da Sociedade Brasileira de Microscopia e Microanálise

Radiation-Induced Degradation in Halide Perovskite Films

M Josefina Arellano-Jimenez*, Leunam Fernandez-Izquierdo, Zhiyang Qin, Marlon Danny Jerez-Masaquiza, and Manuel Quevedo-Lopez.

The University of Texas at Dallas. 800 W Campbell Road. Richardson, Texas 75080-3021. USA.
*josefina.arellano@utdallas.edu

Perovskite materials are widely utilized because of the adaptable nature of their crystal structure. Key properties such as charge carrier mobility, concentration, bandgap, and overall stability can be tuned by modifying their composition. In metal-halide perovskites, which follow the general formula ABX_3, the A and B positions are filled by metal cations, while the X site is occupied by a halide anion. Although the basic structure is relatively simple, a vast number of combinations are possible since the A and B sites can accommodate nearly any element from the periodic table. Halide perovskites are commonly used in devices like solar cells, photodetectors, and detectors for gamma rays and X-rays. However, exposure to ionizing radiation can degrade the perovskite structure, compromising device stability and performance. A critical area of ongoing research is understanding how variations in composition and structure influence the material's resistance to high doses of ionizing radiation, including X-rays, gamma rays, and alpha and beta particles. Therefore, an exhaustive study of the relationship between the different types of ionizing radiation, energies, and doses to which the devices are exposed and the optoelectronic properties is necessary to obtain the best device performance, assess and predict stability, as well as to identify the best halide perovskite composition for each application. The objective of this study is to systematically examine the mechanisms by which ionizing radiation induces degradation in metal halide perovskites. This work presents experimental data that establishes correlations between radiation-induced damage and the compositional and structural characteristics of the perovskite materials. Furthermore, it evaluates the consequent effects on their stability, optoelectronic properties, and overall device performance. Initially, the experiment focused on the ABX_3 composition. $CsPbBr_3$ is used as a model system to study the correlation between halogen type, halogen combinations, and the resulting radiation tolerance. Given our previous experience, initial perovskite materials are synthesized using a unique method developed in the group, and films are produced using the Closed Space Sublimation method [1-2]. The films are exposed to ionizing radiation, with different exposure doses. Then, a comprehensive characterization of the films is performed. This work focuses on electron microscopy characterization, using supportive results from XPS and XRD analysis. SEM-FIB, TEM, and EDS were used to obtain qualitative and semi-quantitative information and identify changes in the crystalline structure associated with the damage created by the ionizing radiation. $CsPbBr_{3-x}Cl_x$ films showed changes in the diffractograms and photoluminescence spectra after being irradiated. Specimens from those films were observed using SEM-FIB and later prepared for TEM analysis. Figure 1 shows the mechanism of the difference in mobility of halide and cation vacancy leads the material and device to a temporarily unstable state. Complementing the results obtained using a variety of spectroscopic techniques and electron microscopy confirmed the different levels of damage or changes that can be generated in perovskite films. The following step combines this experimental information with theoretical simulations to create a model that allows us to better understand the relationship between the composition of perovskite films and the damage caused by different sources of ionizing radiation [3]. Figure 1 illustrates the mechanism by which differences in the mobility of halide and cation

vacancies lead to a transiently unstable state in the material and device. Complementary results obtained through various spectroscopic techniques and electron microscopy confirm the presence of distinct levels of damage and structural changes in perovskite films. The next phase of the study integrates this experimental data with theoretical simulations to develop a model that enhances our understanding of the relationship between the perovskite composition and the damage caused by different sources of ionizing radiation on the perovskite film. The established correlation will enable the application of modeling methods to guide the experimental optimization of perovskite materials and device performance under ionizing radiation exposure.

References

[1] Fernandez-Izquierdo, L., et al., Adv. Mater. Technol. 2020, 5, 2000534.
https://doi.org/10.1002/admt.202000534
[2] Reyes-Banda, M. G., et al., ACS Applied Electronic Materials. 2021, 3, (3), 1468-1476.
https://doi.org/10.1021/acsaelm.1c00072
[3] Lee, Y., et al., The Journal of Physical Chemistry C. 2021, 125, (19), 10676-10684.
https://doi.org/10.1021/acs.jpcc.1c01439

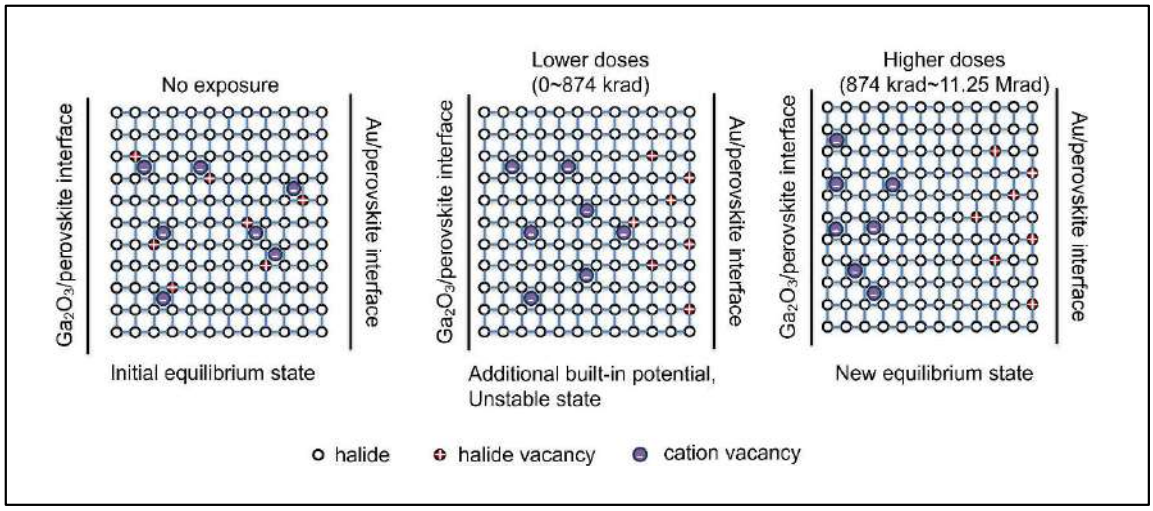

Figure 1. *Schematic illustration of the mechanism by which differences in halide and cation vacancy mobility induce a temporary instability in the device.*

SEM and FIB in Semiconductor Manufacturing: From Process Development to High-Volume Control

Ricardo Cunha Goncalves da Silva

CEITEC S.A. - Semiconductors

This presentation details the fundamental role of advanced metrology, specifically Scanning Electron Microscopy (SEM) and Focused Ion Beam (FIB) technologies, in modern semiconductor fabrication. High-Volume Manufacturing (HVM) relies on a complex, multi-stage sequence of physicochemical processes that demand rigorous control. In this context, SEM metrology is essential for production quality control, ensuring critical dimension (CD) measurements and defect review, thereby optimizing costs and minimizing yield loss. Furthermore, the versatile SEM-FIB dual-beam system proves invaluable during the development and ramp phases, enabling precise material removal for construction analysis (CA), cross-sectioning, and failure analysis. The strategic application of SEM and FIB technology is therefore paramount for scaling new processes and sustaining the high performance demanded by current semiconductor roadmaps.

Air and oxygen plasma pen treatment on the gelatinization of corn starch

Renata Antoun Simao[1], Olavo Teixeira Neto[1], Carlos Eduardo Musa[1], Yuri Ferreira da Silva[1], Felipe Sampaio Alencastro[1]

[1]Programa de Engenharia Metalúrgica e de Materiais – COPPE – UFRJ
*renata@metalmat.ufrj.br

Starch, a widely available and low-cost natural carbohydrate, plays a crucial role in various industrial applications due to its biodegradability and versatility as a biopolymer. The production and modification of starch nanoparticles (SNPs) usually involves a bottom-up approach, where gelatinization and recrystallization processes are employed to form nanoparticles, often through acid precipitation [1]. However, traditional methods like acid hydrolysis and ultrasound tend to take several days and produce significant waste [2,3]. Recently, plasma treatment is being studied as a promising method for starch modification. Studies have demonstrated that plasma treatment can introduce functional groups like carbonyl and carboxyl on starch surfaces, leading to a reduction in crystallinity and a negative surface potential [4]. Plasma-activated water (PAW) represents a novel approach within the field of plasma applications. PAW is generated by treating the surface of a volume of water with a plasma plume; the plasma-activated energetic particles become trapped within the water, reacting with water molecules and leading to a series of reactive species dissolved into the aqueous solution, such as reactive oxygen and nitrogen species (RONS), for instance H_2O_2, NO_2^-, NO_3^- and O_3 [5], which persist for weeks and induce oxidation and a significant drop in pH within liquids. As a relatively low-cost and scalable method, PAW offers a promising alternative for starch modification without generating significant waste. Despite the increasing number of studies on PAW, research focusing on the effects of PAW on the material properties of starch remains limited. In this study, we aim to investigate the effect of PAW on the gelatinization behavior of corn starch and produce SNPs from a suspension of starch on plasma-activated water. For that, a 5% w/v starch slurry was prepared by dissolving 10.7 grams of starch (AMIDEX 3001, Ingredion Brasil Ltda., SP, Brazil) in 200 mL of ultrapure water The slurry was transferred to a 1000 mL beaker with a diameter of 10.8 cm and continuously stirred using a magnetic stirrer throughout the entire treatment process. A Plasma Pen (PVA TePla America, USA) was used for sample treatment. The pen tip was positioned at a fixed distance of 15 mm above the surface of the liquid. PAW was continuously applied for 5 minutes. After treatment, the slurry was allowed to decant and was then filtered using a 0.22 μm filter. The filtered liquid was deposited onto silicon substrates for analysis.

Both scanning electron microscopy (SEM) and atomic force microscopy (AFM) were performed on the granules and on the suspended solution and nanoparticles were observed with different size and shapes. SEM and AFM images of both the granules and nanoparticles formed after PAW are presented in Figure 1. It can be observed a clear degradation pattern of the initial granules with the release of nanoparticles in a top-down formation pattern. AFM images shows that, although particles of 500 nm are observed to be formed and its surface seems intact, phase contrast image shows that granules are irregular in mechanical properties and are composed of a softer external shell surrounding harder nanometric particles .

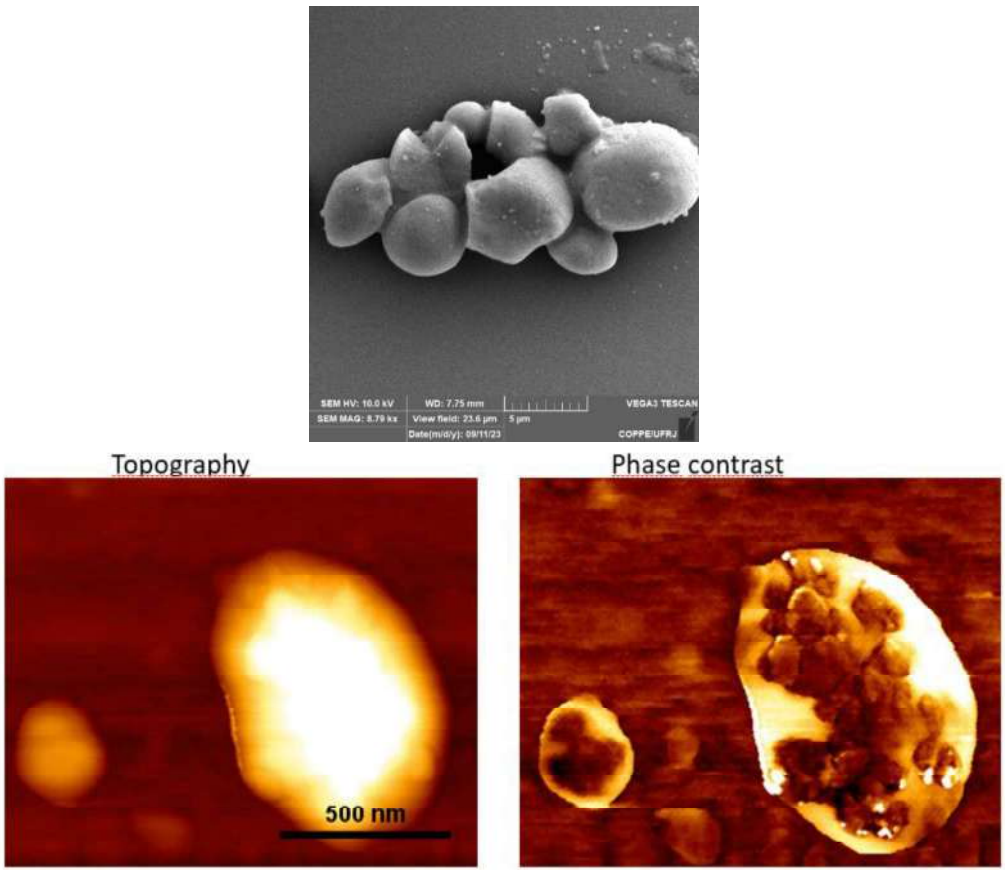

Figure 1 – Granules and nanoparticles observed in PAW after 5 minutes of plasma

The pH of a 6.7 starch slurry in water was measured before and after treatment and it was observed that air plasma led to an increase in medium acidity where solution showed a pH of 3.0 after 5 minutes of treatment. The degradation of the granules is observed and is related to the attach of the amorphous portion of the granule revealing the crystalline blocklets of starch. This process can be very much similar to acid hydrolysis treatment of starch but the time for exposing the granule inner structure is significantly reduced from days to minutes. PAW, as a reactive medium, can disaggregate starch granules into crystalline structures. Here, starch blocklets were isolated using only PAW.

References

[1] Y. Bist et al., Starch, 77 (2024) 2400172.
[2] S. Wang et al., Crit Rev Food Sci Nutr. 55 (2015) 1081.
[3] S. Kumari et al., Food Hydrocolloids 153 (2024) 110008.
[4] S. Ma et al., carbohyd. Pol. 340 (2024) 122254.
[5] R. Thirumdas et al., Trends in Food Sci. and Tech. 77 (2018) 21.

Acknowledgement

This work was supported by FAPERJ and CNPq

A microstructural study of a naturally occurring chrysoberyl encapsulated in beryl

B.B. Moreira[1]*, José Coelho Neto[2], Karla Balzuweit[1,3]*.

[1][1]Centro de Microscopia da Universidade Federal de Minas Gerais, [2] [2]Instituto de Criminalística da Polícia Civil de Minas Gerais, [2] [3]Departamento de Física – ICEx - Universidade Federal de Minas Gerais -- Belo Horizonte – MG - Brasil
*karla@fisica.ufmg.br

Microstructural analysis combining chemical and crystallographic analysis is an important aspect in the study of heterogeneous samples. The study of naturally occurring minerals is important in clarifying questions such as the genesis of the region where the mineral is found, or provenance studies both for cultural heritage and forensics, or in mineral liberation analysis for mining purposes. Alexandrite is a variety of chrysoberyl (BeAl2O4) which can assume a greenish hue when exposed to sun light and becomes red under artificial light. Emerald is a green colored variety of beryl (Be3Al2Si6O18). The main chromophore element in both gem varieties is the presence of chromium. Emeralds, which belong to a beryl group of minerals are quite rare, but present in several countries, in between them Brazil. Chrysoberyl can occur together with emerald deposits but are even rarer. Several studies [1,2] have been performed on hundreds of beryl samples aimed at the classification of the minerals based on trace elements which could explain their probable geological formation. A set of seven samples of chrysoberyl embedded in beryl from the northeast region of Brazil were studied with scanning and electron microscopy and microanalysis with EDS. Figure 1 shows a BSE image of one of the samples where a difference in contrast shows that besides the chrysoberyl in the central left part of the sample other mineral phases are also present. Figure 2 is a chemical map combining only aluminum and silicon showing the distinct regions of the two minerals clearly, as silicon is only present in the emerald. Several types of mica such as muscovite $KAl_2(AlSi_3O_{10})(OH)_2$, phlogopite $KMg_3(AlSi_3O_{10})(OH)_2$, biotite K $(Mg, Fe)_3(AlSi_3O_{10})(OH_2)$, were identified. Semiquantitative point microanalysis was performed in several points of all minerals evidencing a relatively homogeneous composition of all minerals. Chromium and iron were identified and minor elements in alexandrite and chromium, iron , magnesium and sodium were identified in the emeralds.

[1] C. Aurisicchio, et al., Ore Geology Reviews **94** (2018) 351-366.
[2] G. Giuliani, et al., Minerals **9** (2019) 105.
[3] This research was supported by FAPEMIG, FINEP, CAPES, CNPq (Brazil).

Figure 1. Backscattered scanning electron image (BSE) of the encapsulated chrysoberyl in emerald. (b) Al and Si chemical map

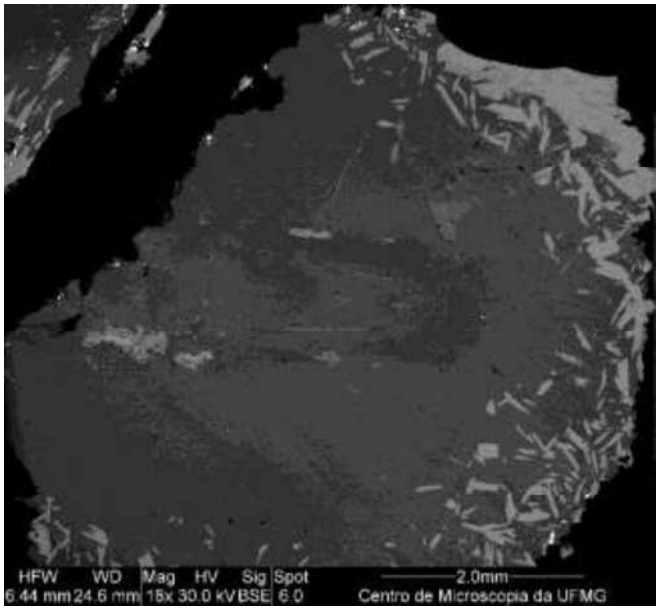

Figure 12. EDS Aluminum and Silicon chemical map

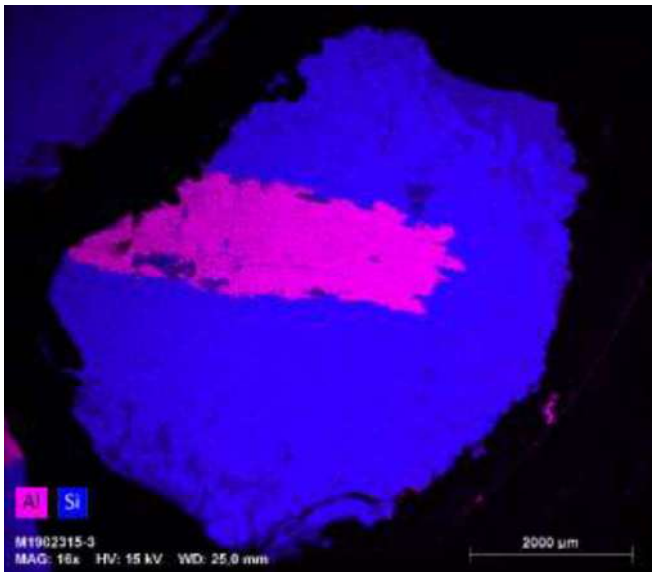

FIB-SEM characterization of the porous network of cap rocks with potential for long-term and safe sealing

Erveton P. Pinto[1,2]*, Carlos A. Senna[1], Thalita D. P. Caldas[1], Gabriel B. Pinheiro[1], Rodrigo Prioli[1], Dorval C. Dias-Filho[3], Marcos K. de Souza[3] and Yaro M. Parizeck[3]

[1]Departamento de Física, Pontifícia Universidade Católica do Rio de Janeiro (PUC-Rio), Rio de Janeiro, Brazil, [2]Departamento de Ciências Exatas e Tecnológicas, Universidade Federal do Amapá (UNIFAP), Macapá, Brazil, [3]Petrobras – Centro de Pesquisas Leopoldo Américo Miguez de Mello (CENPES), Rio de Janeiro, Brazil

*erveton@unifap.br, E. P. Pinto.

Geological carbon storage is seen as a promising and sustainable method to reduce CO_2 emissions and address global climate change [1,2]. However, it's important to ensure that we can capture a significant amount of carbon dioxide and safely store it in the long term within geological formations. To be successful, there should be no leakage from the injection site. Therefore, it is essential to carefully consider the nature of the cap rocks when assessing potential implementation opportunities. Understanding the effectiveness of the cap rocks involves observation of the pore network. For instance, the small pores in clay-rich cap rocks with high specific surface areas result in elevated capillary pressures and viscous drag, which reduces the migration of carbon dioxide [3]. To properly evaluate the porous network of a cap rock, we have developed a new method, using a representativeness-variability plane (Figure 1), for identifying the representative elementary volume (REV) of the rock and have applied it to study muddy rocks (Figure 2) using a Focused Ion Beam Scanning Electron Microscopy (FIB-SEM). With the proper REV, we evaluated the porous system with high-spatial resolution and in three dimensions for various aspects: total and effective porosity, pore and throat size, connectivity, and specific surface. Our analysis revealed that the rocks exhibit noteworthy petrophysical characteristics, such as porosity and pore size distribution, making them suitable for effective CO_2 containment in geological formations. The new method also reduces uncertainty in 3D porosity measurements to as little as 2% (Table 1) by enabling appropriate analysis of the porous networks in three dimensions. The porosity measurements from our representative volumes matched well with those taken from larger, millimeter-sized areas. Furthermore, our method cuts FIB-SEM analysis time by over 30%.

Keywords: cap rock; FIB-SEM; representative elementary volume; representativeness-variability plane.

[1] M. Fleury et al., Evaluating sealing efficiency of caprocks for CO_2 storage: An overview of the geocarbone-integrity program and results, Oil and Gas Science and Technology 65 (2010). https://doi.org/10.2516/ogst/2010007.

[2] R.M. Abraham et al., Assessment of CO_2 storage prospect based on physical properties of Rio Bonito Formation rock units, Energy Geoscience 5 (2024). https://doi.org/10.1016/j.engeos.2023.100163.

[3] D.N. Espinoza and J.C. Santamarina, CO_2 breakthrough—Caprock sealing efficiency and integrity for carbon geological storage, International Journal of Greenhouse Gas Control 66 (2017). https://doi.org/10.1016/j.ijggc.2017.09.019

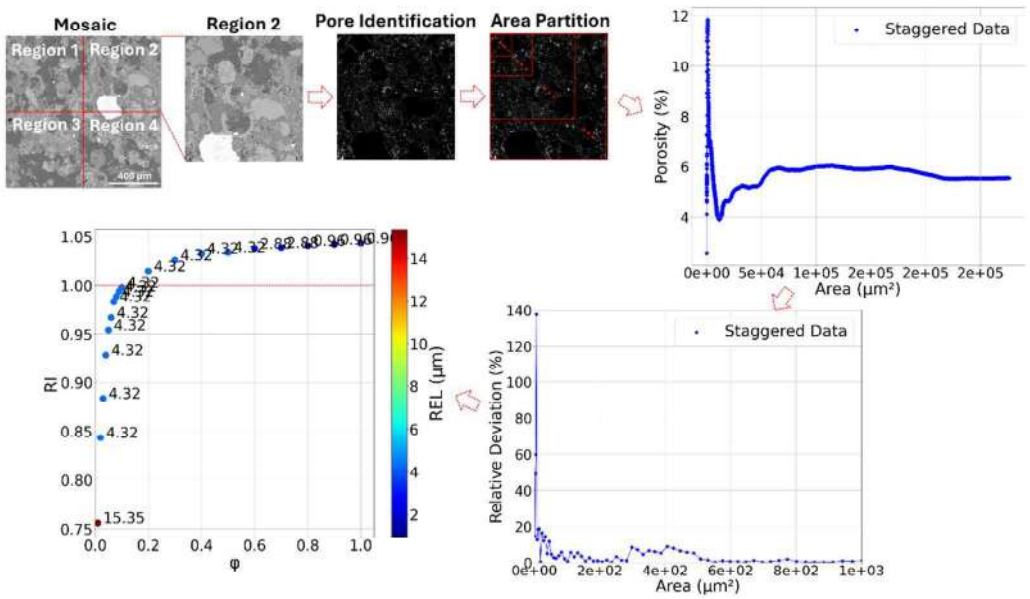

Figure 1. Illustration of the steps for identifying representative elementary area (REA), where RI is the representativeness index and φ is the variability factor. The 2D mosaic of each sample was divided into four parts for analysis due to computational cost. The representative elementary volume (REV) refers to the volume reconstructed from slices that have an area equal to the REA obtained through FIB-sectioning. To facilitate input parameters into FIB-SEM, we define the representative elementary lateral as being $REL = \sqrt{REA}$.

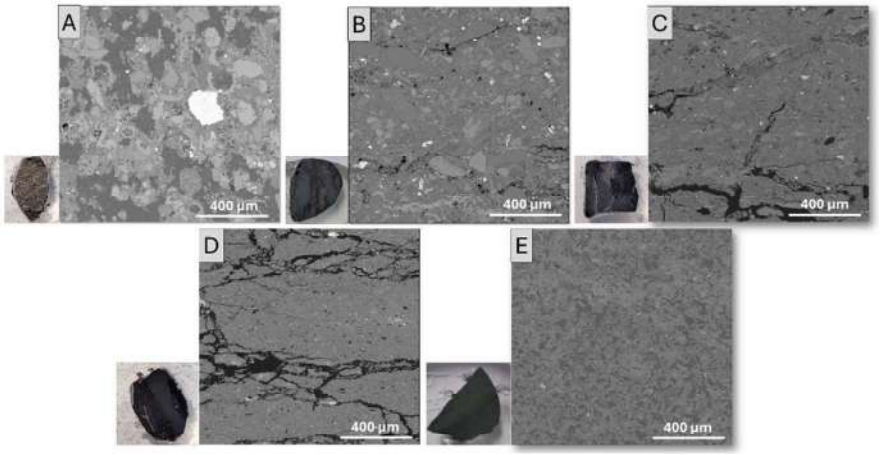

Figure 2. 2D mosaics: (A) sample 1, (B) sample 2, (C) sample 3, (D) sample 4, and (E) sample 5. Within the area of each mosaic, the REVs were sectioned according to the results in Table 1.

Table 1. 2D porosity versus 3D porosity.

Samples	REV (μm^3)	2D mosaic porosity (%)	3D porosity (%)	Inaccuracy (%)
A	$11.25 \times 11.25 \times 4.7$	5.89	5.44	7.64
B	$6.58 \times 6.58 \times 4.3$	7.04	6.90	1.99
C	$12.96 \times 12.96 \times 12.96$	3.62	3.20	11.60
D	$3.84 \times 3.84 \times 4.9$	3.30	1.41	57.27
E	$12.0 \times 12.0 \times 6.0$	1.54	1.30	15.58

Hydrothermal growth of grass-like Al_2O_3 nanostructures on 3D-printed Al-based monolith: tailoring iron dispersion for CO_2 hydrogenation catalysts.

Anna Luiza Ferreira Santos Silva[1], Erika Batista Silveira[1], Lucas Paodjuenas[1], Paula Mendes Jardim[1*], Fabio Souza Toniolo[1], Carla Ramos Moreira[1,2*].

[1]Universidade Federal do Rio de Janeiro, UFRJ; [2] Fundação Oswaldo Cruz, Fiocruz
*carla.moreira@fiocruz.br; pjardim@metalmat.ufrj.br

The production of light olefins (C_2–C_4) from CO_2 offers a sustainable alternative to fossil-based processes, contributing to greenhouse gas mitigation while valorising CO_2 as a feedstock. Iron-based multifunctional catalysts have shown promise for CO_2 conversion to olefins via tandem reaction pathways [1]. Structured supports, such as metallic monoliths produced by additive manufacturing, offer advantages like enhanced mass transfer and structural control [2]. Additionally, grass-like Al_2O_3 nanostructures can be grown on aluminium surfaces via low-temperature hydrothermal treatment [3], increasing surface area and improving the dispersion of active phases, such as iron nanoparticles. This work aims to develop FeOx/Al_2O_3/3D-Al catalysts with enhanced iron dispersion for improved performance in CO_2 hydrogenation. Two hydrothermal conditions were tested on 3D-Al monoliths from ALKIMAT: one at 150 °C for 16 h under autogenous pressure (**H.150**), and another at 100 °C for 1 h under atmospheric pressure (**H.100**). Iron was deposited by dip-coating, varying iron concentration (0.05 and 0.5 mol L^{-1}) and immersion time (30 and 120 min) [4]. The catalyst nomenclature follows Fe.X_Y/H.Z, where **X** is immersion time (min), **Y** is iron concentration (mol L^{-1}), and **Z** the hydrothermal treatment temperature (tab. 1). Samples were analysed by SEM/EDX and STEM-HAADF/EDX. SEM images (Fig. 1) show that H.100 (fig. 1a) produces thinner and shorter grass-like filaments compared to the thicker, rod-like structures from H.150 (fig. 1b). This suggests H.100 leads to the initial growth stage of these structures. In Fe.120_0.5/H.150 and Fe.120_0.5/H.100 (Figs. 1c and 1d, respectively), the monoliths are covered by a thick, cracked iron layer, but the underlying grass-like features remain visible. EDX mapping shows iron is concentrated on cracks in H.150, while it more uniformly covers the structures in H.100. At lower Fe concentration (0.05 mol L^{-1}, Fig. 1e), the grass-like morphology is preserved, and EDX shows good iron dispersion. A shorter immersion time (Fe.30_0.5/H.100, Fig. 1f) also retains the morphology, with minimal agglomeration. To assess iron particle size, the Fe-containing layer was scratched and examined by STEM-HAADF (Fig. 2), revealing well-dispersed nanoparticles throughout the grass-like structures. EDX quantification at 0.5 mol L^{-1} showed that iron content increased with immersion time: 3% after 30 min and up to 12% after 120 min. While higher iron loading may improve activity, excessive deposition (120 min) forms a thick top layer that could mask active sites. Conversely, 30 min may result in insufficient iron content. Therefore, an intermediate immersion time (e.g., 60 min at 0.5 mol L^{-1}) may provide a balanced condition, combining good dispersion with adequate loading for improved catalytic performance.

[1] Q. Yang, Qingxin & E. V. Kondratenko, Acc. Mater. Res. 5 (2024) 1314.
[2] Y. Wang et al., Appl. Catal. B: Environ. 340 (2024) 123211.
[3] S. Ono & H. Asoh, Corros. Sci, 181 (2021) 109221.
[4] L. Villegas et al. Appl. Catal. A: Gen., 320 (2007) 43.

Table 1. Sample nomenclature, hydrothermal treatment conditions for the monoliths and iron dip-coating conditions.

Nomenclature	Hydrothermal treatment (**H**)	Fe dip-coating (**Fe**)
H.150	16 h, 150°C	x
Fe.120_0.5/H.150	16 h, 150°C	$Fe(NO_3)_3$ 0.5M, 120 min.
H.100	1 h, 100°C	x
Fe.30_0.5/H.100	1 h, 100°C	$Fe(NO_3)_3$ 0.5M, 30 min.
Fe.120_0.5/H.100	1 h, 100°C	$Fe(NO_3)_3$ 0.5M, 120 min.
Fe.30_0.05/H.100	1 h, 100°C	$Fe(NO_3)_3$ 0.05M, 30 min.

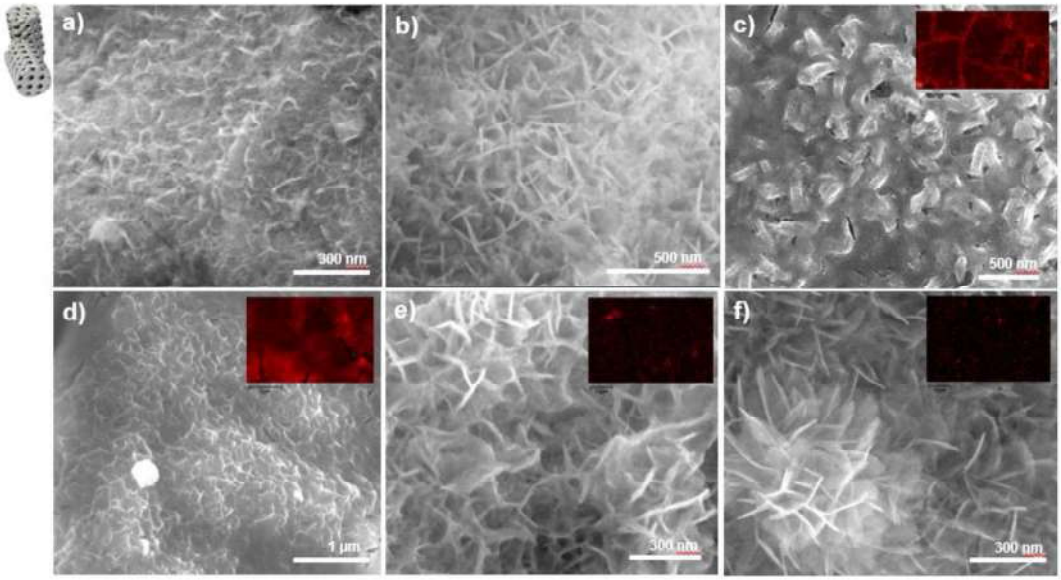

Figure 1. SEM micrographs of a) H.100, b) H.150, c) Fe.120_0.5/H.150, d) Fe.120_0.5/H.100, e) Fe.30_0.05/H.100 and f) Fe.30_0.5/H.100. Insets: EDX Fe elemental mapping.

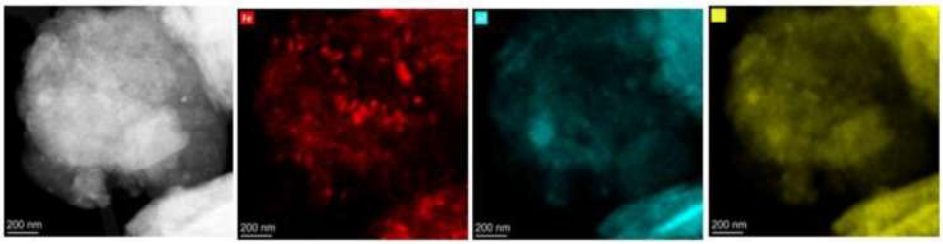

Figure 2. STEM-HAADF image of the Fe.30_0.5/H.100 sample and its corresponding EDX elemental mapping, with Fe represented in red, Al in blue, and O in yellow.

Morphological effect on electroplated $BiVO_4$ films in a range of electrical charge applied

Luana Beatriz Correia de Oliveira[1,2*], Felipe LN Sousa[2], Denilson de Vasconcelos Freitas[2], Lizeth Carolina Mojica Sanchez[2], Ellen Cristovão de Souza[1,2], Iasmin Brandão Cavalcanti[1], Marcelo Navarro[1], Giovanna Machado[2]

[1] Universidade Federal de Pernambuco (UFPE), [2] Centro de Tecnologias Estratégicas do Nordeste (CETENE)
*luana.correia@ufpe.br

$BiVO_4$ is a promising semiconductor due to intrinsic characteristics such as outstanding visible light absorption (~2.3–2.4 eV band gap energy), suitable band potentials, photostability with photocorrosion resistance, low toxicity, and a theoretical photocurrent density of 7.5 mA cm^{-2}, which corresponds to a Solar-To-Hydrogen (STH) efficiency of 9.2% [1]. These attributes make this semiconductor widely used in many fields like pharmaceutical, photocatalytic, sensors and photoelectrochemical [2]. In this work, the authors report the morphological effects of applied electrical charge on $BiVO_4$ photoanodes produced through bismuth oxyiodide (BiOI) films synthesized electrochemically. The BiOI films were electrodeposited onto fluorine-doped tin oxide (FTO) conductive glass (working electrode), using a three-electrode configuration with $Ag|AgCl_{sat}$ as reference electrode, and platinum wire as counter electrode. In the system, a fixed potential of -0,1 V was applied while changing the electrical charge density from -0.2 to -1.0 Ccm^{-2} [3]. After electrodeposition, a solution of 0.4 M vanadyl(III) acetylacetonate ($VO(acac)_2$) in dimethyl sulfoxide (DMSO) was added to the substrate, covering the BiOI film. Subsequently, a thermal conversion of BiOI to $BiVO_4$ was carried out at 500° C for 30 min followed by a chemical treatment in NaOH (0.1 M) for 30 min. Can be observed in Fig 1. SEM images of $BiVO_4$ (a-e) and BiOI (f) thin films obtained by secondary electrons. The $BiVO_4$ films exhibit three-dimensional (3D) agglomerated nanostructures, with thickness increasing from approximately 769.2 nm to 1854.7 (n=250), as the applied electrical charge density decreases from −0.2 C (Fig. 1a) to −1.0 C (Fig. 1e). Furthermore, can be noticed in fig. 1f a morphological change when the conversion of BiOI to $BiVO_4$ happen in the material, with a transformation from 2D to 3D nanostructures. The morphologies of the samples obtained at −0.8 C (Fig. 1d) and −1.0 C (Fig. 1e) differ noticeably from those produced at lower charge densities (−0.2 to −0.6 C), with significant particle agglomeration observed in both cases. Notably, the morphology of the −1.0 C sample (Fig. 1e) appears similar to that of BiOI thin film (Fig. 1f). To investigate this, EDS analysis was performed (Fig. 2), which revealed spectroscopic signals characteristic of iodine (I, Lα transitions). This result suggests that at higher applied electrical charges, complete conversion to $BiVO_4$ did not occur.

[1] G.S. Kamble et al, Nanomater. 13 (9), 1528, (2023)

[2] H.Q. Alijani et al, Catalysts. 13 (1), 59, (2023)

[3] K.J. McDonald and K.S. Choi. Energy Environ. Sci., 5, 8553, (2012)

[4] CNPQ, FACEPE, CAPES, PPGMat (UFPE) and Dr. Nielson Torres by SEM analysis.

Figure 1. SEM Cross Section images of thin films based on $BiVO_4$ electrosynthetized applying -0.2 (a), -0.4 (b), -0.6 (c) -0.8 (d), and -1.0 (e) and BiOI produced using -0.8 C (f). (BiVO4: 5 kV voltage and scale bar of 1 μm in all images. (a) SEM Mag: 60.0 kx, work distance: 15.0 mm; (b) 54.5 kx, 14.01 mm; (c) 60.2 kx, 15,01 mm; (d) 57.7 kx; 14.63 mm; (e) 59.9 kx, 14.93 mm. BiOI (f): 5 kV voltage, 44.0 kx, 16.17 mm, and scale bar of 2 μm).

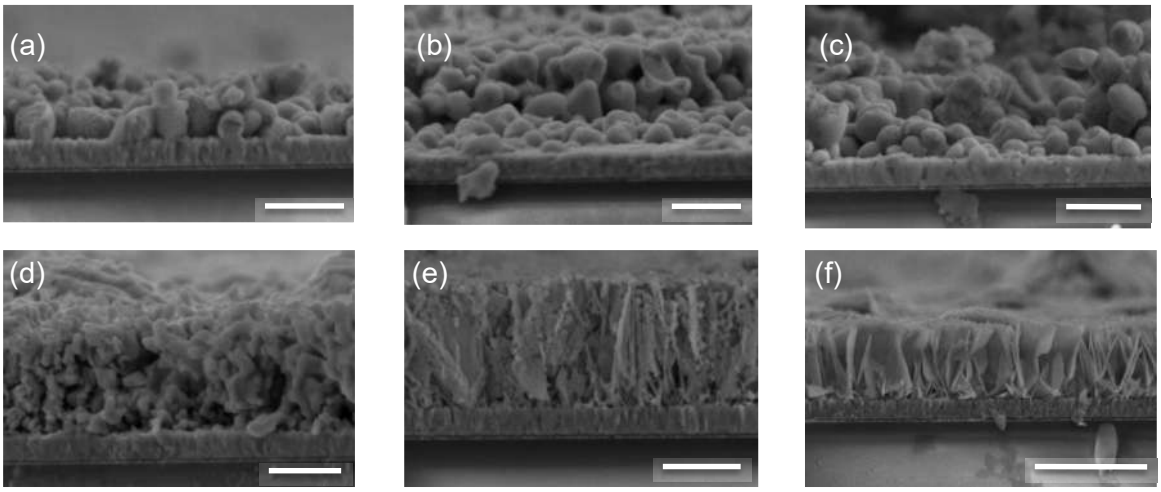

Figure 2. EDS Spectrum (a) and elemental mapping of $BiVO_4$ thin film (b) produced applying -1.0 C.

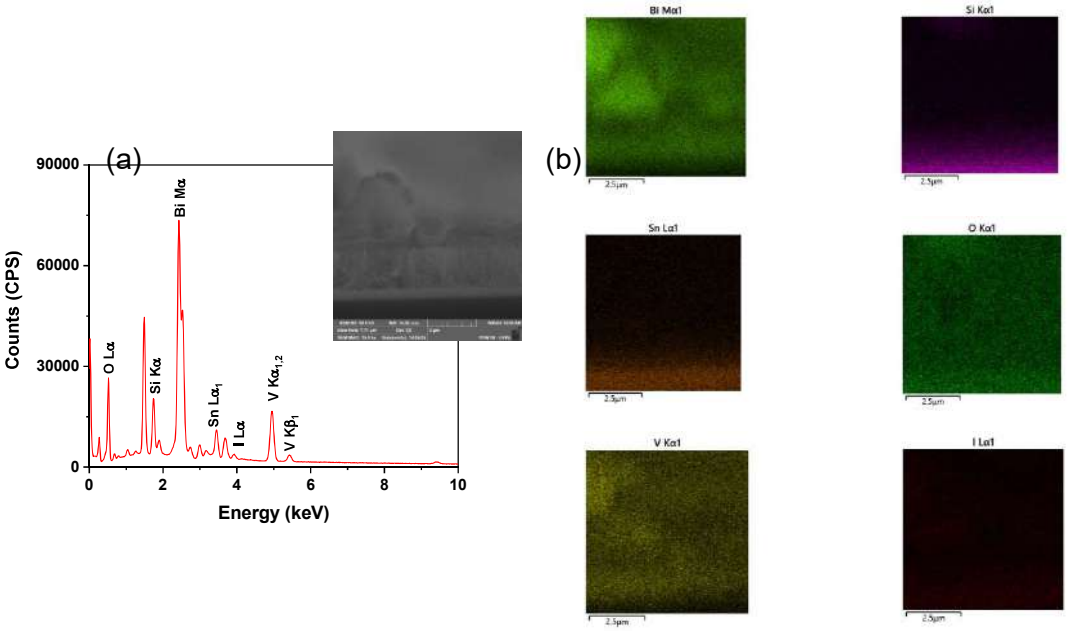

Segmentation of Interphase Boundaries in Complex-Phase Steels

Renan M.C. Lima[1]*, Flávia T.S.F. Tolomelli[2], Yutao Xing[1], Fernando C. Rizzo[3]

[1]Instituto de Física – Universidade Federal Fluminense
[2]Companhia Siderurgica Nacional
[3]DEQM – Pontifícia Universidade Católica do Rio de Janeiro
*rmclima@id.uff.br

The automotive industry is a highly competitive market in which steelmakers must continually improve mechanical properties and damage mitigation strategies to remain viable against aluminum and other alternatives. Void nucleation is the primary mechanism driving damage evolution, ultimately leading to mechanical failure in first-generation Advanced High Strength Steels (AHSS) of the Complex-Phase (CP) class [1–3]. In lower-strength CP steels, their coarser grain structure allows damage evolution to be assessed via μ-tomography. In contrast, the finer grains in higher-strength variants limit the applicability of μ-tomography due to insufficient spatial resolution. Void nucleation is strongly influenced by the distribution of microconstituents, as it predominantly occurs at interphase boundaries with high hardness contrast—such as ferrite/martensite interfaces. Therefore, an alternative approach would be to analyze the distribution of interphase boundaries instead of the voids themselves. In this study, Electron Backscatter Diffraction (EBSD) maps—previously reclassified by the Aztec Crystal software's machine learning tool using band contrast (BC), grain orientation spread (GOS), and kernel average misorientation (KAM) parameters (4,5)—were segmented using image processing techniques to investigate the interphase boundary distribution in industrially produced CP steels. The segmented interfaces were color-coded in RGB: red for ferrite, green for bainite, and blue for martensite. Superimposing boundaries of different phases produced mixed colors: yellow for ferrite/bainite, cyan for bainite/martensite, and purple for ferrite/martensite.

1. Pathak N, Butcher C, Worswick MJ, Bellhouse E, Gao J. Damage evolution in complex-phase and dual-phase steels during edge stretching. Materials. 2017;10(4):1–29.
2. Pathak N, Adrien J, Butcher C, Maire E, Worswick M. Experimental stress state-dependent void nucleation behavior for advanced high strength steels. Int J Mech Sci [Internet]. 2020;179(April):105661. Available from: https://doi.org/10.1016/j.ijmecsci.2020.105661
3. Avramovic-Cingara G, Saleh CAR, Jain MK, Wilkinson DS. Void nucleation and growth in dual-phase steel 600 during uniaxial tensile testing. Metall Mater Trans A Phys Metall Mater Sci. 2009;40(13):3117–27.
4. Lima R de MC, Spadotto J, Rizzo FC. Use of LOM and EBSD to Identify Bainite in Complex Phase Steel. Microscopy and Microanalysis. 2021;27(S1):370–2.
5. Lima R de MC, Tolomelli FT dos S, Clarke AJ, Clarke KD, Spadotto JC, Rizzo FC. Microstructural characterization of A 1100 MPa complex-phase steel. Journal of Materials Research and Technology. 2021;2–9.

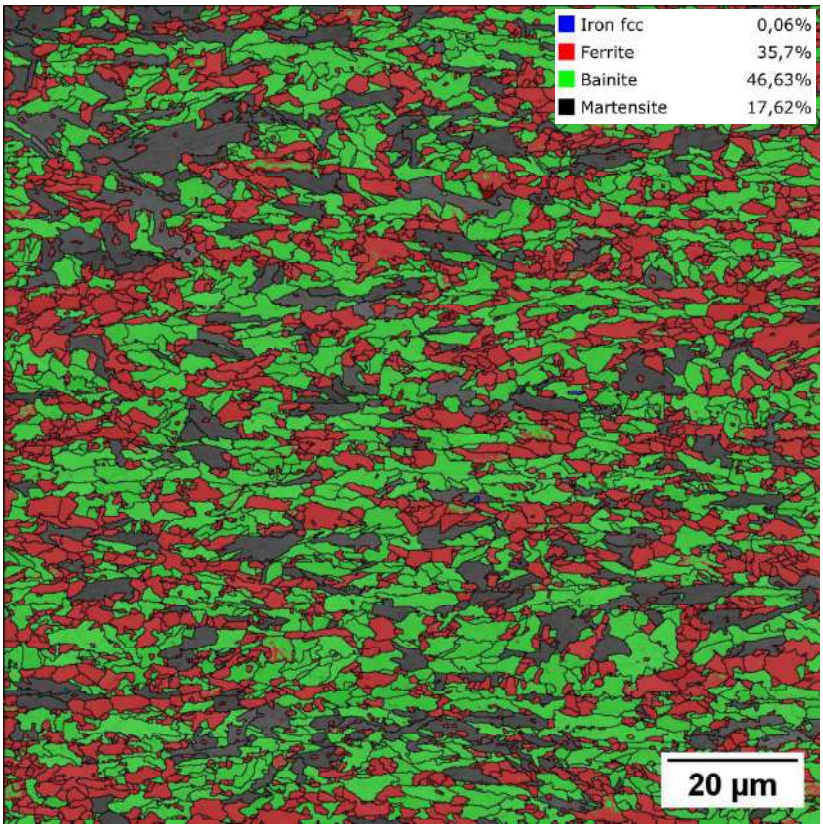

Figure 1. Reclassified EBSD map showing dark martensite, green bainite, red Ferrite, and blue retained austenite.

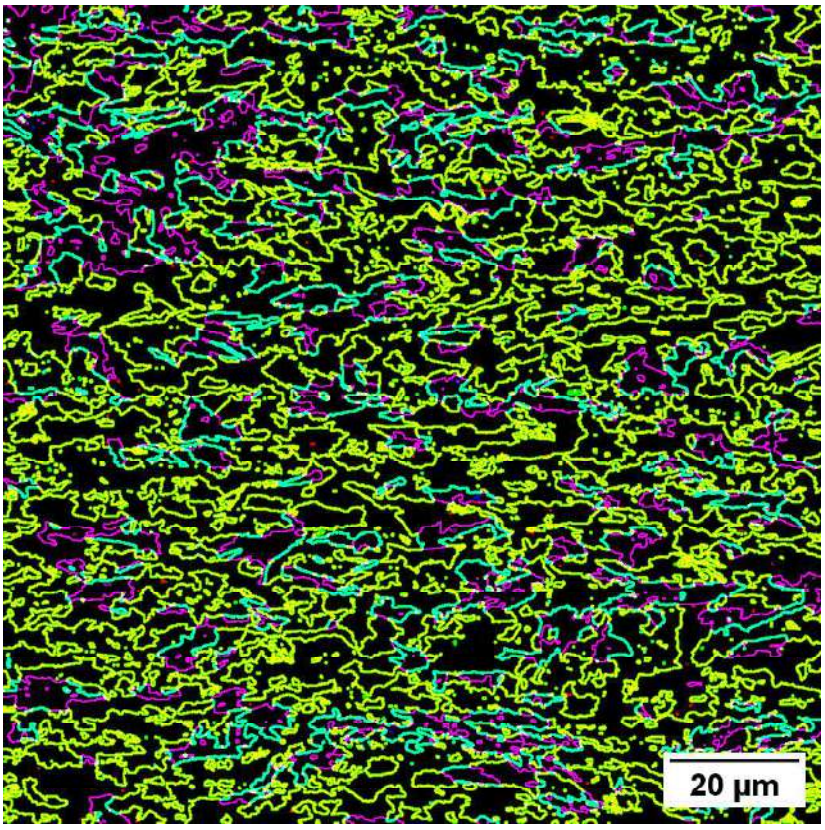

Figure 2. Segmented interphase boundaries. Red ferrite, green bainite, blue martensite, yellow ferrite/bainite, cyan bainite/martensite, purple ferrite/martensite.

Assessment of Fusion Parameters for the Development of Novel Nanostructured Bainitic Steels

Rodrigo Xavier Moraes[1]*, Matheus Campolina Mendes[2], Adriana da Cunha Rocha[1].

[1] Universidade Federal do Rio de Janeiro, [2] Centro Federal de Educação Tecnológica Celso Suckow da Fonseca
*rxmoraes@metalmat.ufrj,br

Bainitic steels offer an excellent balance between mechanical strength and ductility when compared to conventional ferrous alloys [1–3]. The ability to refine their microstructure to the nanometric scale can further enhance these properties, often outperforming martensitic and high-strength steels [4]. Among the most explored processing routes is austempering; however, it typically requires long treatment times, making it less viable for industrial applications [5]. This project aimed to identify alloy compositions with reduced processing times for obtaining nanostructured bainitic steels. A literature review was conducted to select four alloys with favorable characteristics. Using MAP_STEEL_MUCG83, the transformation driving force (−FTO) was estimated, while MAP_STEEL_AC3 was used to predict the Ac_3 temperature for each composition. Based on this analysis, a commercial steel that matched the criteria for a base alloy was selected. A new composition was then proposed by increasing the contents of carbon (C), silicon (Si), and niobium (Nb), guided by strategies reported in the literature. The proposed alloy exhibited a suitable austempering temperature range, with bainite-start (B_s) and martensite-start (M_s) temperatures between 250 °C and 350 °C. The Ac_3 temperature (~800 °C) was also favorable, reducing the risk of austenite grain coarsening. The alloy was produced in an electric arc furnace, hot-rolled, and normalized. Samples were characterized using optical microscopy (OM), scanning electron microscopy (SEM), optical emission spectroscopy, X-ray diffraction (XRD), electron backscatter diffraction (EBSD), and Vickers microhardness testing. JMatPro software was used to simulate the TTT diagram and define austempering parameters. SEM analyses showed a typical pearlitic microstructure with a proeutectoid phase [6]. EBSD confirmed a refined grain structure with low deformation, and XRD, compared to CIF databases, revealed a predominantly ferritic profile [7]. Vickers hardness measurements yielded an average of 296 HV, consistent with similar pearlitic steels [8]. The TTT simulation indicated that 90% bainite could form in just over 2 hours, suggesting the potential for faster heat treatments. Overall, the alloy design and experimental validation showed promising results. Scanning electron microscopy (SEM) micrographs were essential for verifying whether the desired microstructure had been achieved and whether the as-solidified columnar structure had been disrupted. Electron backscatter diffraction (EBSD) images facilitated accurate grain size measurement and revealed the absence of deformation within the microstructure. Future work will focus on performing the austempering treatment and using Rietveld refinement to analyze crystallite evolution and bainite formation kinetics.

[1]H. K. D. H. Bhadeshia, *Bainite in Steels: Transformations, Microstructure and Properties*, 2ª., IOM Communications Ltd, London (2001).
[2]H. K. D. H. Bhadeshia, Mater. Sci. Forum, 284–286, 39 (1998).
[3]H. K. D. H. Bhadeshia, Metall. Mater. Trans. A Phys. Metall. Mater. Sci., 41, 1351 (2010).
[4]H. K. D. H. Bhadeshia, Sci. Technol. Adv. Mater., 14, (2013).
[5]C. Garcia-Mateo et al., Mater. Sci. Technol. (United Kingdom), 30, 1071 (2014).
[6]H. Bhadeshia e R. Honeycombe, *Steels - Microstructure and Properties*, 3 ed., Elsevier, Oxford (2006).
[7]ICSD - Inorganic Crystal Structure Database, https://bdec.dotlib.com.br/bases.
[8]E. Duka et al., in *AIP Conf. Proc.*, (2012), p. 47–51

Table 1 – Base commercial alloy composition and proposed alloy for accelerated kinetics of nanostructured bainite formation (balance in Fe [wt.%])

Liga	C	Mn	Cr	Si	Nb
Base	0,25	1,0	0,25	-	-
Proposed	0,6	1,0	0,25	1,5	0,02

Table 2 - Simulated parameter values for the proposed alloy suggesting potential for faster heat treatments.

-FTO (J/mol)	Ac3 (°C)	Bs (°C)	Ms (°C)
960	828	420	260

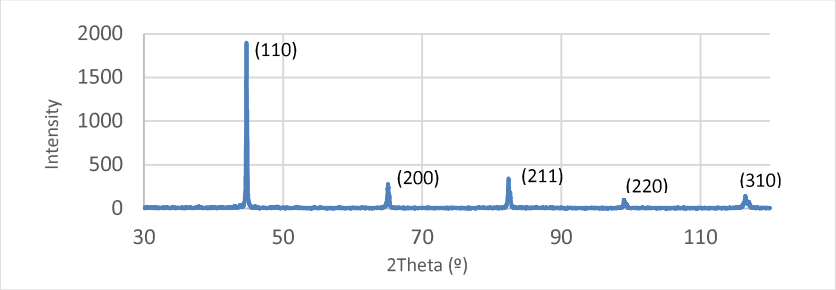

Figure 1 – Diffractogram highlighting the ferritic phase planes.

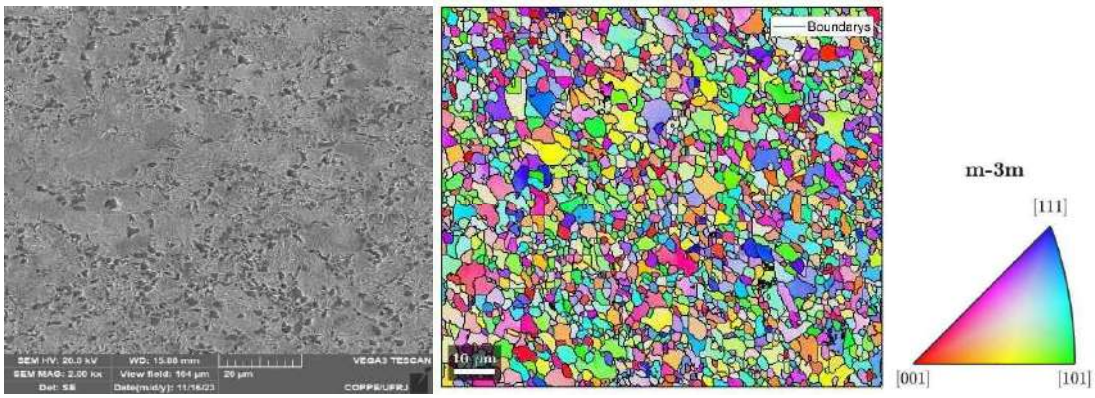

Figure 2 – SEM micrograph showing pearlitic phase profile and proeutectoid ferrite; crystallographic orientation map and inverse pole figure.

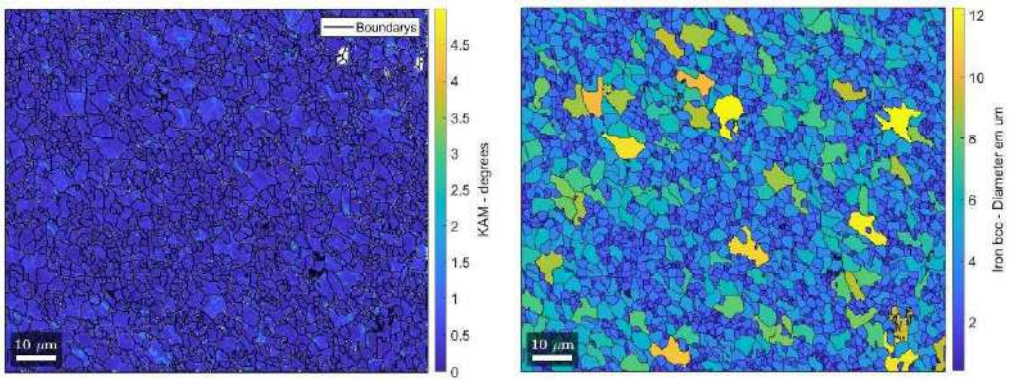

Figure 3 – Kernel Average Misorientation (KAM) map revealing a microstructure with minimal deformation; grain size distribution map showing the majority of grains measuring approximately 2µm.

Assessment of Particulate Matter in an Industrial Influence Area by Scanning Electron Microscopy and X-ray Microfluorescence

Ana Paula F. Almeida[1*], Roberta G. Leitão[1], Áquila R. de Araujo[2], Átila de P. Teles[1, 3], Marcelino J. Anjos[4], Joaquim Assis[5], Ricardo T. Lopes[1], Davi F. Oliveira[1]

[1] Nuclear Instrumentation Laboratory, Federal University of Rio de Janeiro, Brazil,
[2] Multiuser Electron Microscopy Laboratory, Federal University of Rio de Janeiro, Brazil,
[3] Federal Institute of Paraná, Pinhais, Brazil,
[4] Electronic Instrumentation and Analytical Techniques Laboratory, State University of Rio de Janeiro, Brazil,
[5] Polytechnic Institute, State University of Rio de Janeiro, Nova Friburgo, RJ, Brazil.

*anacamiqui@gmail.com

Atmospheric pollution is a global challenge with significant repercussions for ecosystems and human health. According to the World Health Organization (WHO), it is considered the main environmental risk factor for public health [1]. Particulate matter (PM) present in the air is one of the most relevant atmospheric contaminants. PM originates from the release of gaseous precursors into the atmosphere, which can be directly emitted by natural and anthropogenic sources or formed through chemical reactions in the air [2]. Its potentially harmful chemical composition may include substances such as sulfates, nitrates, and trace elements, contributing to the formation of dense haze and negatively impacting health, air quality, and climate balance [3]. Individual particle analysis techniques have provided direct data on the micromorphology and composition of specific particles. These techniques are widely applied in PM research, including the use of scanning and transmission electron microscopy [4, 5], as well as X-ray fluorescence spectroscopy (XRF), which allows for the high-resolution identification of the chemical elements present in the particles [6, 7]. In this context, the aim of this study was to analyze the PM collected in the city of Duque de Caxias, located in the Metropolitan Region of Rio de Janeiro, Brazil—an area influenced by the Duque de Caxias Refinery (REDUC)—focusing on the morphological and compositional characterization of the particles using Scanning Electron Microscopy and X-ray microfluorescence (micro-XRF), in order to better understand their possible sources and health impacts. Particulate matter was collected using a cascade impactor operating for a 24-hour period at three sampling points near the petrochemical complex. The particles were retained on membranes placed inside the equipment. The morphological analysis by scanning electron microscopy (Figure 1) revealed the presence of particles from different sources, including irregular materials likely from industrial origin, biological structures such as pollen grains, and particulate fragments with morphology consistent with urban or mineral dust. XRF elemental maps (Figure 2) showed the presence of Al, S, Fe, Cu, Br and Pb in PM 1.0 – 2.0 μm, with Cu and Pb more concentrated at the outer edge of the membrane. In PM 4.0–8.0 μm, Al, S, Fe, Cr and Zn exhibited a diffuse and heterogeneous distribution, indicating a mineral or industrial origin. Heavy metals confirm anthropogenic influence.

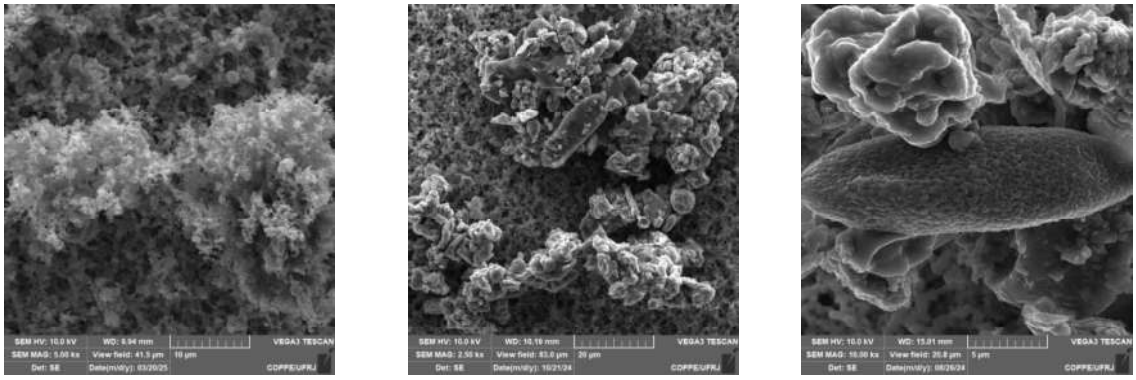

(a) (b) (c)

Figure 1. Particles Associated with Anthropogenic (a), Agglomerates of particles possibly from industrial and crustal origin (b) and Particles associated with biogenic origin (c).

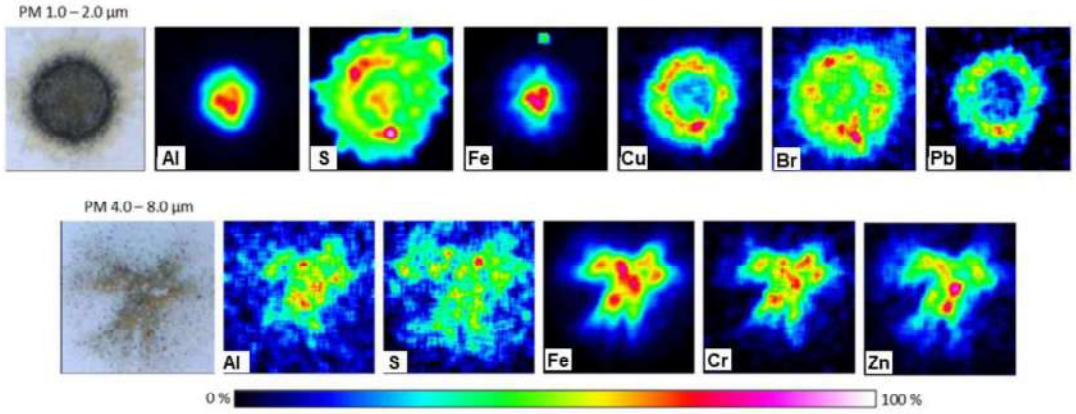

Figure 2. Two-dimensional distribution map of the normalized intensity of elements.

[1] A. Prüss-Üstün, C. Corvalán, *Preventing disease through healthy environments: A global assessment of the burden of disease from environmental risks*, World Health Organization, Geneva, 2016.
[2] R.W. Atkinson *et al.*, *Epidemiology* 21 (2010) 501.
[3] B. Wu *et al.*, *Environ. Pollut.* 259 (2020) 113886.
[4] F. Silval, T. Moreno, X. Query, Sci. Total Environ. 407 (2009) 4972.
[5] D. Salcedo et al., Atmos. Chem. Phys. 6 (2006) 925.
[6] A.P.F. Almeida *et al.*, *X-Ray Spectrom.* 52 (2023) 3378.
[7] F. Bilo, P. Cirelli, L. Borgese, Trends Anal. Chem. 170 (2024) 117427.
[8] This research was supported by the Electron Microscopy Center of COPPE at the Federal University of Rio de Janeiro (UFRJ).

Automated Mineralogical Mapping and SEM Analysis of Au-Bearing Rocks from the Tapajós Mineral Province

Gabriel Fernandes Silva Araujo[1]*, Nilson Francisquini Botelho[1,] Leandro Duarte Campos[2].

[1]University of Brasília, Institute of Geosciences, Graduate Program in Geology.
[2]Geological Survey of Brazil (SGB).
*fernandes.araujo@aluno.unb.br

The Tapajós Mineral Province (TMP) is a major metallogenic district located in the southwestern region of Pará State, Brazil. It is predominantly underlain by extensive felsic magmatic rocks, mainly granites. The region has been historically exploited since the 1950s and was a significant contributor to Brazil's gold production during the 1970s and 1980s through artisanal mining. Official records report more than 225 tons of gold extracted [1], while unofficial estimates suggest over 900 tons [2]. The aim of this work was to validate the use of advanced techniques of automated mineralogical mapping, and SEM, in order to optimize the acquisition of mineralogy and further comprehend the textural relations between gold, ore sulphides and hydrothermal minerals. Currently, gold production in the region is declining due to the depletion of alluvial deposits, which limits the activity of artisanal miners. However, the development of mines such as Palito, Tocantinzinho, and Serrinha/Coringa, along with scientific research initiated in the 1990s, reflects renewed economic interest in gold exploration and exploitation in the region. This study aimed to evaluate the effectiveness of advanced techniques such as automated mineralogical mapping and scanning electron microscopy (SEM) in optimizing mineralogical data acquisition and improving the understanding of textural relationships between gold, ore-related sulphides, and hydrothermal minerals. Analyses were conducted using QEMSCAN (Quantitative Evaluation of Minerals by Scanning Electron Microscopy), with results compared to those obtained through Electron Probe Microanalysis (EPMA) and optical petrography. Gold, chalcopyrite, sphalerite, and galena are found as inclusions within pyrite. Galena is not restricted to inclusions in pyrite; it also occurs filling fractures, often associated with minerals of the aikinite–bismuthinite series. Chalcopyrite is mainly found in fractures, commonly associated with gold. The results demonstrate that automated mineralogical mapping is a reliable and effective technique, capable of revealing fine-scale textures and mineral distributions. However, the use of EDS (Energy Dispersive Spectroscopy) imposes certain limitations. Bismuth and lead sulphides, as well as tellurides, cannot be accurately distinguished by EDS due to significant spectral overlap among Bi, Pb, Te, and S. However, these phases can be reliably differentiated using WDS analysis in EPMA. Despite these limitations, automated mineralogical mapping remains a valuable complementary tool, contributing significantly to ore mineral characterization and to the advancement of geological understanding in the Tapajós Mineral Province.

[1] Faraco M.T.L., Carvalho J.M.A., Klein E.L. 1997. Carta metalogenética da Província Aurífera do Tapajós. In: M.L.C. Costa & R.S. Angélica (Eds.). Contribuições à Geologia da Amazônia. SBG, Belém, 1:423-437.
[2] Santos, J.O.S., Groves, D.I., Hartmann, L.A., Moura, M.A. and McNaughton, N.J., 001. Gold deposits of the Tapajós and Alta Floresta Domains, Tapajós–Parima orogenic belt, Amazon Craton, Brazil. Mineralium deposita, 36, pp.278-299.
[4] This research was supported by CAPES (Brazil).

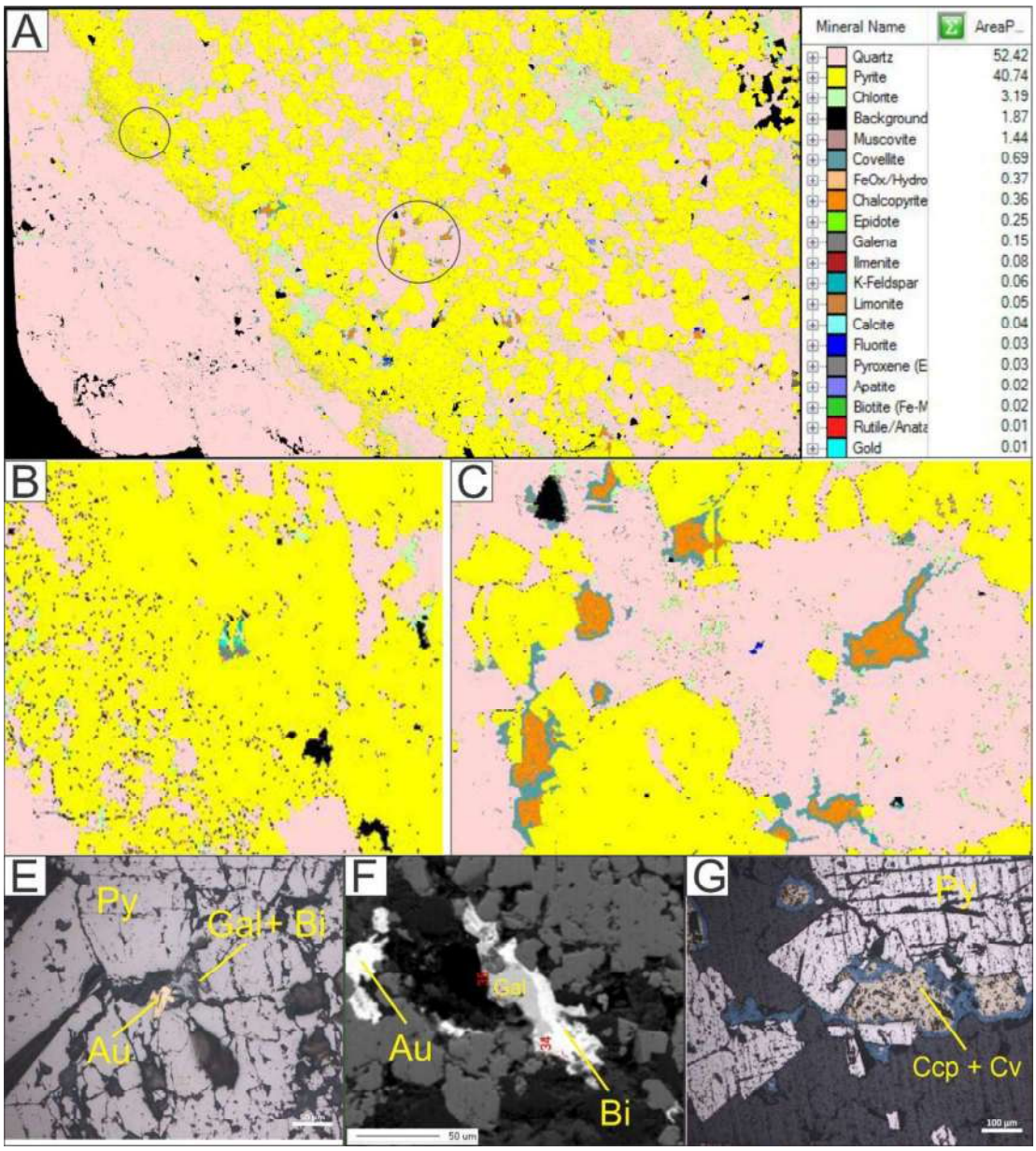

Figure 1. A: Mineralogical and textural map of the thin section from sample LD-45-E, from Palito mine generated by QEMSCAN analysis, with circles highlighting the areas shown in Figures B and C (from left to right). B: Occurrence of gold (light blue), galena and bismuthinite gray), and covellite (dark blue) associated with fractures in pyrite. C: Chalcopyrite (orange) with a "rim" of covellite (dark blue), along with chlorite and fluorite in veinlets. E: Gold and chalcopyrite included in pyrite under reflected light (non-analyzed light). F: Backscattered electron compositional image showing the association of minerals from the aikinite–bismuthinite series, galena, and gold. G: Pyrite associated with chalcopyrite and covellite under reflected light (non-analyzed light).

Case study of a Multi-detector SEM Approach for Apatite Characterization

Ana Maria Afonso Sena[1]*, Daniel Uliana[1], Liz Zanchetta[1], Carina Ulsen[1].

[1]Escola Politécnica da Universidade de São Paulo – Departamento de Engenharia de Minas e Petróleo, Av. Professor Mello Moraes, 2603,05508-030, São Paulo, Brazil

*mev@lct.poli.usp.br

Scanning electron microscopy (SEM) is a powerful analytical tool in materials science, geology, and mineral engineering, due to its ability to analyze materials from micrometer to nanometer scale [1]. It allows the textural analysis and the determination of the association forms of minerals composing samples. These determinations are one of the key points in the description of rock systems, helping to predict how an ore will behave. Apatite, recognized as the primary source of phosphorus ore [2], plays a critical role in human development, being indispensable, for example, in agriculture as the main raw material for phosphate fertilizers, essentials for global food production and food security [3]. The physical, chemical, and crystallographic properties of apatite vary considerably within the various rocks bearing apatitic mineralization, and, within the same deposit, different generations of apatite can coexist [4], making complex its characterization. In this context, SEM equipped with complementary detectors offers a powerful platform for the detailed characterization of apatite and its associated mineral phases. Some of these detectors are BSE-backscattered electron detector which provides phase differentiation based on atomic number contrast, EDS-energy dispersive X-ray spectrometer allows the qualitative and quantitative determination of chemical composition and CL-cathodoluminescence detector aids the recognition of different generations of minerals. This work presents a successful case study of the characterization of apatite embedded in cold-mounted polished resin, through a SEM multi-detector approach. In the first part of the framework, BSE images and EDS compositional maps were collected, aiming at the compositional characterization of the minerals associated with apatite. The analyses were performed using a Quanta 650 FEG (Thermo Fisher Scientific), equipped with an EDS detector XFLASH 6|60 (Silicon Drift Detector technology, SDD) and software Esprit (Bruker) at 20kV. Subsequently, CL images were acquired, to guide the selection of areas of interest (due to differences in the shown signal) for performing chemical microanalyses by EDS. The analyses were performed using a Stereoscan 440 (LEO) scanning electron microscope, equipped with an INCA X-act EDS (Oxford), and a monochromathic CL detector. The multi-dimensional analysis by BSE combined with the EDS elemental maps revealed the association of apatite with phyllosilicates and Fe oxyhydroxides (Figure 1). CL imaging allowed clear differentiation between apatite generations (Figure 2). Primary apatite displayed variable CL signal intensities, while secondary apatite showed no CL response. The chemical results obtained through the EDS analysis showed that the CaO/P_2O_5 ratios of the primary apatite (points 1, 2, and 4 from Table 1) exhibited values close to theoretical fluorine-apatite of 1.33, whereas secondary apatite (point 3 from Table 1) presents intermediate ratios between F-apatite and carbonate-apatite, of 1.58 [4]. This successful case study demonstrates the potential and effectiveness for characterizing textural, compositional and genetic properties of minerals such as apatite, through a multi-detector SEM workflow, highlighting the technique´s value in mineralogical research and ore characterization.

[1] J.I., Goldstein et al., Scanning electron microscopy and X-ray microanalysis, Springer, 3rd edition, 2017. ISBN-10: 149396674X.
[2] F.E.L., Loureiro et al., Rochas e minerais industriais: usos e especificações, CETEM, 2nd edition, Rio de Janeiro, 2005. ISBN-10: 8572272178

[3] E., DESMIDT et al. Global Phosphorus Scarcity and Full-scale P-recovery Techniques: a Review. Critical Review in Environmental Science and Technology, v. 45, p. 336-384, 2015. https://doi.org/10.1080/10643389.2013.866531
[4]M.C.M., Toledo et al., *Variabilidade de composição da apatita associada a carbonatitos*, Revista do Instituto Geológico, São Paulo, 2001. https://doi.org/10.5935/0100-929X.20010002

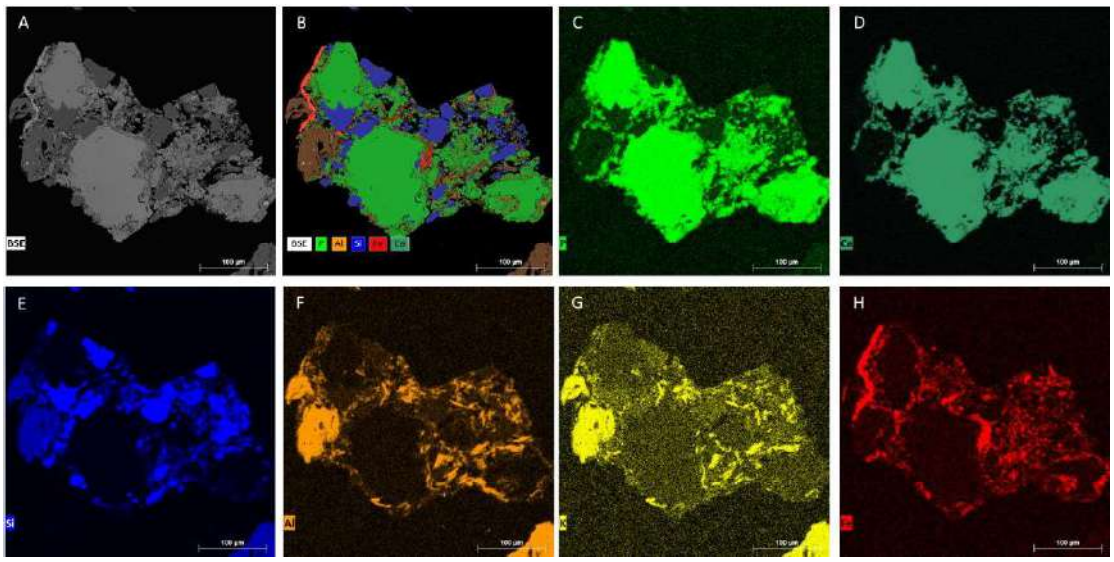

Figure 1. BSE (a) and chemical microanalyses by EDS, showing the mix of elements P, Al, Si, Fe and, Ca (b) and the mapping of individual elements P-Phosphorus (c), Ca-Calcium (d), Si-Silicium (e), Al-Aluminum (f), k-Potassium (g) and Fe-Iron (h).

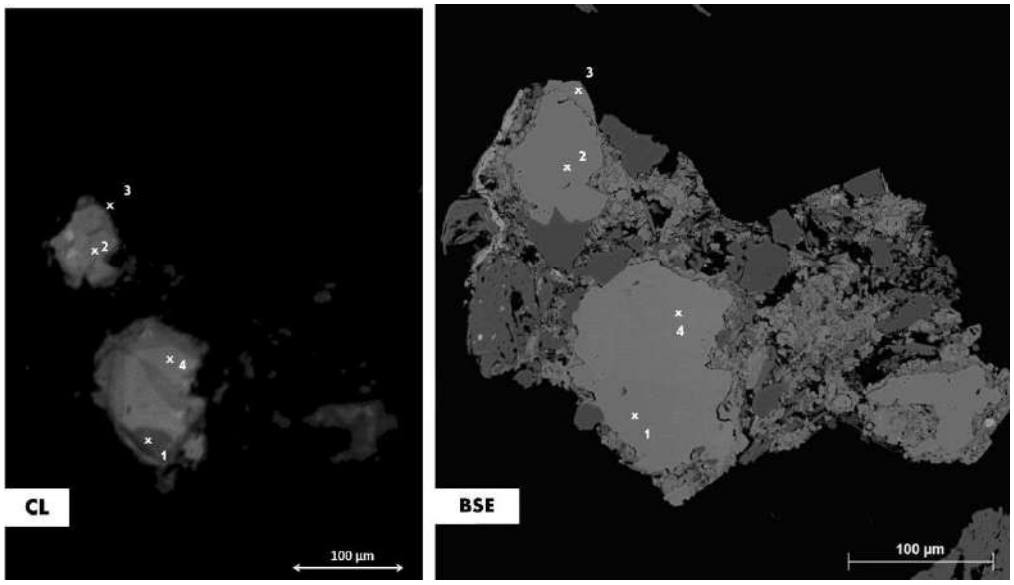

Figure 2. CL and BSE images comparison, showing the 4 selected points which were chosen to be analyzed by EDS.

Table 1. Chemical compositions of the selected points analyzed by EDS.

	Content (% wt)			
EDS	**F**	**P_2O_5**	**CaO**	**CaO/P_2O_5**
1	5,25	44,0	56,7	1,29
2	4,49	42,8	56,3	1,31
3	4,93	38,8	55,1	1,42
4	4,58	38,5	51,6	1,34

Characterization by SEM and EDS of Construction Waste Containing Asbestos

Mauricio Kazuto Ichikawa[1]*, Ricardo Damian Rodriguez Baez[1], Roseli das Graças Padre[1].

[1]Itaipu Binacional.
*maukail@itaipu.gov.br

Asbestos, commonly known as "amianto" in Brazil, was extensively utilized in engineering applications for several decades due to its remarkable properties including high tensile strength, chemical resistance, thermal stability, and flexibility. These characteristics made it particularly valuable in the construction industry, where its combination with Portland cement enabled the manufacturing of various commercial products such as corrugated roofing sheets, water storage tanks, thermal-acoustic insulation panels, and partition walls, leading to the widespread adoption of the term "fiber cement" [1]. In nature, asbestos occurs in two main mineralogical groups: serpentine and amphibole. Within the construction sector, chrysotile - belonging to the serpentine group - was predominantly employed owing to its flexible and soft fibrous structure, in contrast to the straight, rigid, and needle-like amphibole varieties [2]. In Brazil, all activities involving chrysotile including mining, production, industrialization, utilization, commercialization and exportation have been prohibited since 2017 by federal legislation. This prohibition was reaffirmed in 2023 when the Brazilian Supreme Federal Court (SFC) rejected all appeals requesting the suspension of the chrysotile ban, thereby ratifying its 2017 decision [3]. These judicial determinations reflect the well-established correlation between asbestos exposure and severe health deterioration among workers, particularly the elevated incidence of lung cancer and other respiratory malignancies [2,4,5,6]. The “Production Building” of Itaipu Hydroelectric Power Plant, a five-story structure erected above the Powerhouse between Units 9 and 11, recently underwent its first major renovation after thirty years of service. During preliminary inspections, thermal insulation panels composed of cementitious material and expanded polystyrene (EPS) were identified. Given the building's age and the panels' visual characteristics, preliminary assessment suggested possible asbestos content in fiber cement form. These materials were subsequently analyzed at Itaipu's Concrete Technology Laboratory (ICTL) employing scanning electron microscopy (SEM) with secondary electron detection and energy-dispersive X-ray spectroscopy (EDX) for elemental microanalysis. SEM examination revealed fibrous material dispersed within the cement matrix exhibiting variable distribution densities. The fibers displayed considerable length with diverse cross-sectional geometries and thicknesses, morphologically consistent with descriptions found in asbestos literature (Fig 1). EDX spectra showed predominant peaks for silicon (Si) and magnesium (Mg), accompanied by minor iron (Fe) and calcium (Ca) signatures (Fig 2). These elemental profiles correspond precisely with characteristic chrysotile compositions reported in mineralogical studies. Based on these conclusive findings, the renovation consortium will implement specialized protocols to ensure proper handling procedures, temporary storage containment, and ultimate disposal of the asbestos-containing materials in designated facilities.

[1] SILVA, A. L. G.; ETULAIN, C. Avaliação do impacto econômico da proibição do uso do amianto na construção civil no Brasil: relatório final de pesquisa. Campinas: Unicamp, 2010. Disponível em: https://www.cntm.org.br/materias/imagens/%7b2D24E5FE-5D84-4EDB-B880-901E9C712857%7d_EstudoAmianto.pdf. Acessado em 23/07/2025.
[2] SANTOS, G. L.; SANTOS, L. C. M. L.; NETO, J. F. A. Um olhar sobre os minerais de asbesto: aspectos históricos e geológicos e estudo de caso do sítio Xilili (PE), porção central da província Borborema. São Paulo, UNESP, Geociências, v. 41, n. 1, p. 63 - 73, 2022. https://www.periodicos.rc.biblioteca.unesp.br/index.php/geociencias/article/view/16327
[3] STF. STF declara inconstitucionalidade de dispositivo federal que disciplina uso do

amianto crisotila. Disponível em https://portal.stf.jus.br/noticias/verNoticiaDetalhe.asp?idConteudo=353599&ori=1. Acessado em 23/07/2025
[4] PINTO, V. R. S. et.al. O banimento do amianto no Brasil e os desafios para as políticas públicas em desamiantagem. Disponível em: https://repositorio.ipea.gov.br/server/api/core/bitstreams/99e025e7-7156-4601-aa07-d09fc4145101/content
[5] IDES, Institut d'Estudis de la Seguretat. “Prospección sobre la presencia de amianto o de materiales que lo contengan en edificios Identificación práctica de amianto en edificios y metodologías de análisis”. 2003.
[6] FUNDACENTRO. Boas práticas em desamiantagem. Disponível em https://www.gov.br/fundacentro/pt-br/centrais-de-conteudo/faq-desamiantagem/boas-praticas-em-desamiantagem.
[7] This work was supported by Itaipu Binacional.

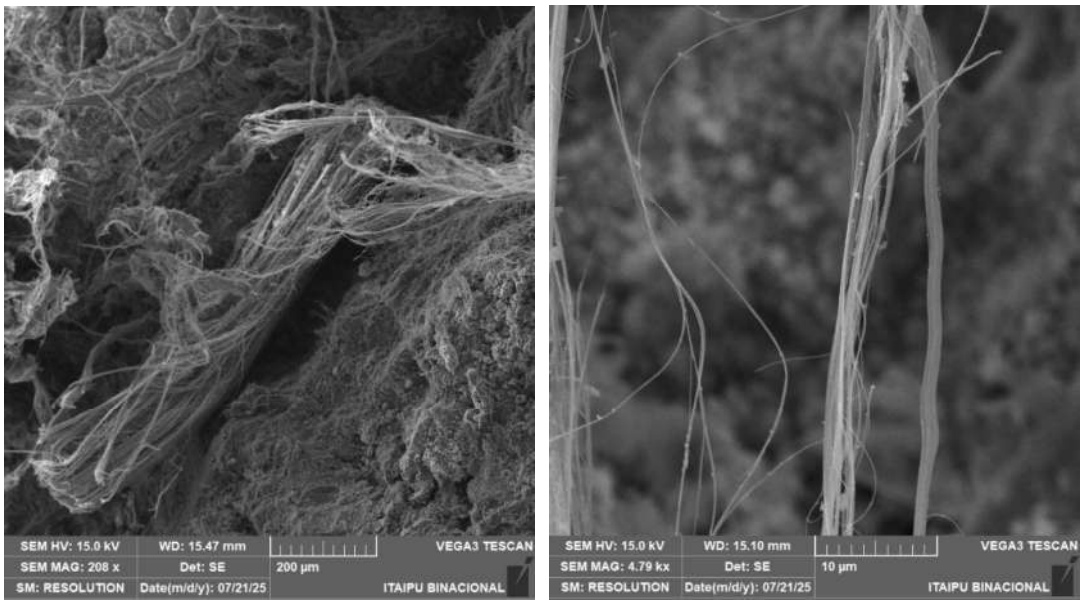

a) Asbestos fibers b) Magnification to observe the fiber diameter

Figure 1. SEM images of asbestos fibers (a) general view; (b) diameter magnification.

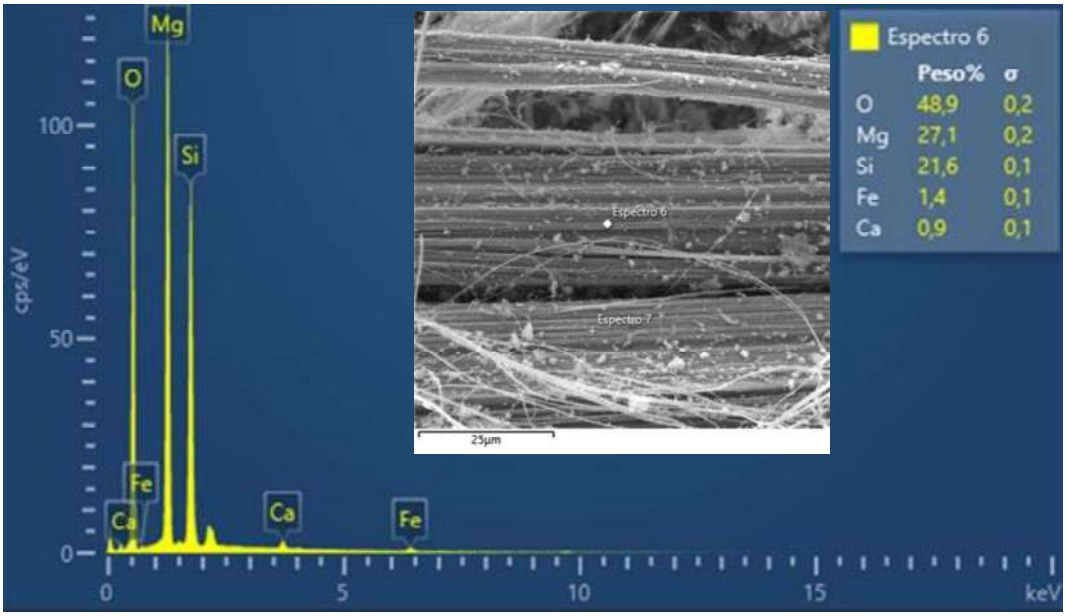

Figure 2. EDS spectrum of asbestos fiber.

Characterization of Layered Double Hydroxides Nanomaterials (LDH)

Patricia Afonso Barbosa[1]*, Raphael Longuinhos Monteiro Lobato[1], Jairo Tronto[2], Leônidas Carrijo Azevedo Melo[1], Jenaina Ribeiro Soares[1].

[1]Universidade Federal de Lavras, [2] Universidade Federal de Viçosa
*patricia.barbosa2@estudante.ufla.br

Layered Double Hydroxides (LDHs) are formed by two metal cations, divalent and trivalent, in double layers of a lamellar structure. Anions such as nitrates, sulfates or carbonaceous substances are found between the metal layers. LDHs come from brucite, or mineral clay, made mainly of $Mg(OH)_2$ [1]. The nanostructure of LDH, the retention of several metal cations in its layers, the hydroxyl groups -OH on its surface, among other aspects, suggest applications for LDHs in areas such as catalysts, catalyst supports, electrodes, adsorbents and drug transport [2]. Knowing their physical and chemical properties is essential to optimize their use in several applications. Therefore, this work aims to characterize a group of seven samples of a LDH-type nanomaterial, composed of Mg, Al and Fe, different from each other in the synthesis process and composition, using Raman Spectroscopy and Scanning Electron Microscopy (Field emission SEM Tescan Clara), with Bruker's X-ray microanalysis system (Quantax EDS). With Raman Spectroscopy, 785 nm laser, it was observed that the spectra have different peaks, possibly indicating the change in composition between layers of the samples. The laminar structural morphology was obtained with SEM (Figure 1), predominantly displaying a plate-like morphology, as expected for these LDH samples [3]. In the EDS, the elemental composition of the sample with Mg, Al, and Fe, in different proportions, shows the aggregation of Al in certain regions of the samples, suggesting a difference in phases of the composition. Thanks for the support for the research [4].

[1] Altalhi, A. A. et al. Recent advances in layered double hydroxide (LDH)-based materials: fabrication, modification strategies, characterization, promising environmental catalytic applications, and prospective aspects. Energy Advances vol. 3 2136–2151 Preprint at https://doi.org/10.1039/d4ya00272e (2024).

[2] Wijitwongwan, R. et al. Preparation of layered double hydroxides toward precisely designed hierarchical organization. *ChemEngineering* vol. 3 1–22 Preprint at https://doi.org/10.3390/chemengineering3030068 (2019).

[3] Olszówka, J. E. et al. New insight into the preferred valency of interlayer anions in hydrotalcite-like compounds: The effect of Mg/Al ratio. Applied Clay Science, v. 155, p. 84–94, 1 abr. 2018.

[4] This research was supported by FAPEMIG, FINEP, CNPq, INCT Nanocarbonos, DFI, LMM and LME - UFLA (Brazil).

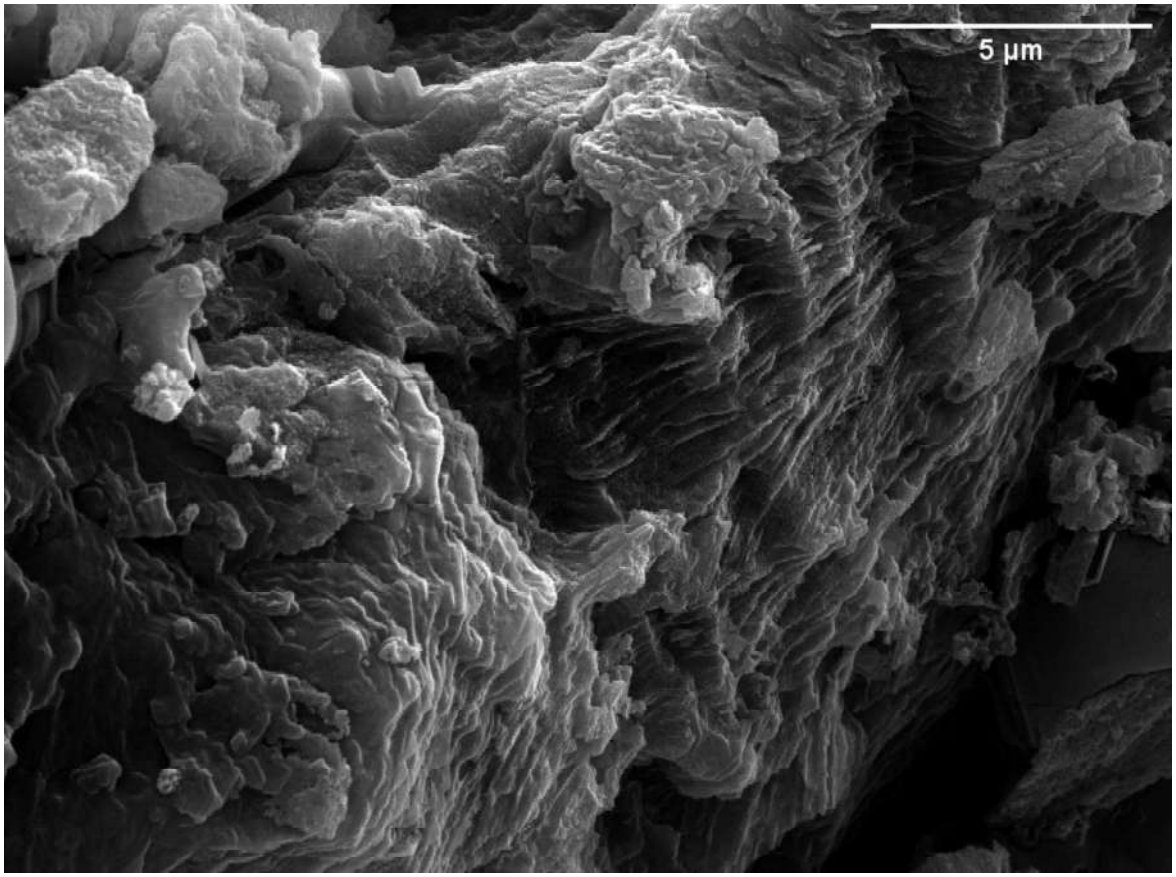

Figure 1. SEM image of hydrotalcite-like material with Mg and Al. Magnification 13.4 kx, white bar corresponds to 5 µm.

Characterization of newly formed bone on TI6AL4V implants subjected to thermochemical treatment combined with cold atmospheric plasma

Kalyne Danielly Silva de Oliveira[1], Giulia Elisa Costa Guimarães[1], Renato Melo Torres[1], Naftali Silva Fernandes[1], Jussier de Oliveira Vitoriano[1], Bruno Caio Chaves Fernandes[1], Moacir Franco de Oliveira[1], Cibele dos Santos Borges[1], Valéria Veras de Paula[1], Clodomiro Alves Júnior[1], Carlos Eduardo Bezerra de Moura[1]*

[1]Federal Rural University of the Semi-Arid Region (UFERSA)
*carlos.moura@ufersa.edu.br

The wettability and presence of TiO_2 biofilm on titanium surfaces are key factors associated with improved osseointegration [1,2]. Studies indicate that thermal plasma treatment at 200 °C promotes the formation of highly stable and biofunctional TiO_2 films, more efficient than those formed at lower temperatures [3]. Cold atmospheric plasma (CAP), although not generating such films, significantly enhances surface hydrophilicity [4]. This study aimed to evaluate the combination of thermochemical treatment of Ti6Al4V alloy surfaces with CAP to enhance osseointegration. New bone formation was characterized using energy-dispersive X-ray spectroscopy (EDS) coupled with scanning electron microscopy (SEM), allowing analysis of mineral composition and the calcium-to-phosphorus (Ca/P) ratio indicative of hydroxyapatite. Fourteen Ti6Al4V screws (1.5 mm × 5 mm) were treated in a custom-designed device comprising a sealed chamber, an electrical discharge source (6.5 kV, 50 kHz), and an argon plasma jet (1 L/min). The samples were placed on a flat electrical resistance platform, functioning as both support and heating element, maintaining a constant temperature of 200 °C for 30 minutes. Temperature stability and process reproducibility were ensured by continuous thermocouple monitoring. For osseointegration assessment, seven adult non-castrated Wistar rats received bilateral proximal tibial implants: one control screw and one treated screw, randomly allocated (UFERSA Animal Ethics Committee approval nº 14/2023). After 30 days, the animals were euthanized, and the tibiae with implants were collected and fixed in 2.5% glutaraldehyde in phosphate buffer for 12 h. The post-fixation was performed in 1% osmium tetroxide in PBS for 2 h. The samples were progressively polished using silicon carbide (SiC) abrasive papers with grits of 100, 220, 400, and 600 MESH, followed by dehydration in increasing ethanol concentrations (25%, 50%, and 75% for 20 min each, and absolute ethanol for 60 min). Samples were then sputter-coated with a 9 nm gold film (Q150R ES, Quorum Technologies Ltd., UK) for SEM analysis (SEM-SSX 550 Superscan, Shimadzu Corporation, Japan). SEM morphological analysis revealed a greater quantity of newly formed bone and closer contact between the treated implant and adjacent bone tissue. The elemental composition at the bone–implant interface was analyzed by SEM-EDS, enabling element identification, quantification, and elemental mapping. Tissues adjacent to treated surfaces exhibited an average Ca/P molar ratio of 1.64 ± 0.18, close to the ideal hydroxyapatite stoichiometry (Ca/P = 1.67), while control surfaces showed a lower average ratio of 1.48 ± 0.08, indicating enhanced mineralized bone matrix formation on treated surfaces. Based on these findings, it is concluded that the combination of 200 °C heating and argon CAP treatment induces beneficial surface modifications that favor osseointegration. This approach represents a promising alternative for improving the performance of orthopedic and dental implants by enhancing bone healing and reducing the risk of implant failure [5].

References:
[1] C. Chen et al., Surf. Coat. Tech. 399 (2020) 126125.
[2] A. Bandyopadhyay et al., Acta Biomater. 96 (2019) 686.
[3] D. Martinez & A. Chourasia, Surf. Coat. Tech. 456 (2022) 129132.
[4] G. M. Martins et al., ACS Biomater. Sci. Eng. 10 (2024) 1765.
[5] Acknowledgment to titanium fix for donating the implants. This research was supported

by CNPq (Brazil) process nº 402536/2021-5.

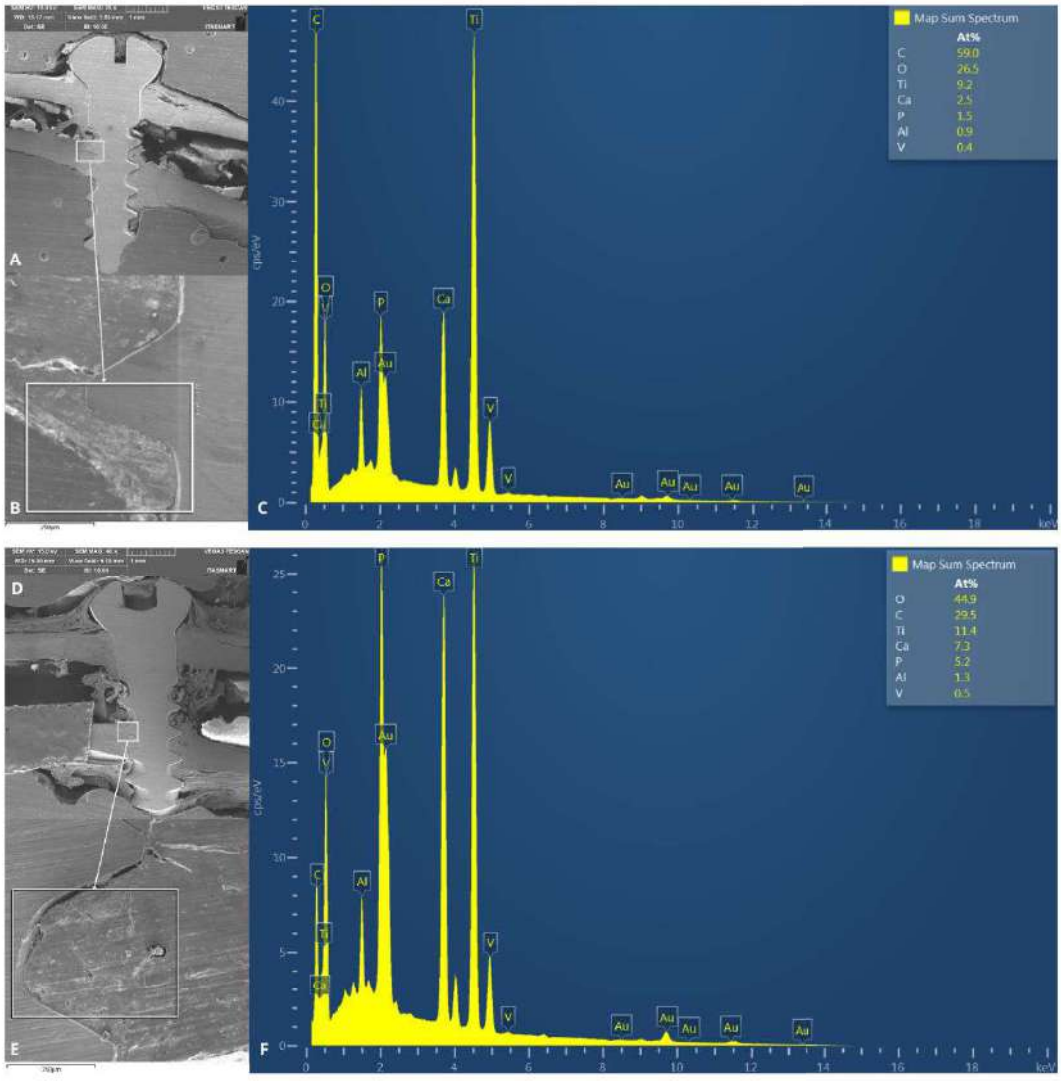

Figure 1. Scanning electron microscopy (SEM) and energy-dispersive X-ray spectroscopy (EDS) images showing the composition of the bone–implant interface after 30 days of implantation. Panels A, B, and C: SEM micrograph, EDS analysis area, and EDS spectrum of the interface from the implant treated with CAP and 200 °C heating, showing a higher Ca/P molar ratio of 1.64, consistent with mineralized bone matrix composed of hydroxyapatite. Panels D, E, and F: Control implant without treatment, with a lower Ca/P molar ratio of 1.48. The spectrum confirms the presence of typical bone elements (Ca and P), implant constituents (Ti, Al, and V), and the gold coating used for conductivity.

Comparative Morphological Analysis of Chemically Modified Graphene Derivatives

Williane Francisco[1]*,Francisco A. S. Ribeiro[1,2,] Denilson V. Freitas[2], Alex Neris[2], Giovanna Machado[1,2].

[1]Universidade Federal de Pernambuco (UFPE), [2]Centro de Tecnologias Estratégicas do Nordeste (CETENE)
*willianedsf@gmail.com

The production of graphene derivatives from natural graphite remains a promising alternative, addressing the limitations associated with large-scale graphene synthesis [1]. In this work, we investigated the synthesis of graphene oxides (GOs) with varying oxidation levels using an improved Hummers method [2]. We achieved this by adjusting the ratio between $KMnO_4$ (oxidizing agent) and $NaNO_3$ (intercalating agent), aiming to analyze the resulting structural and morphological changes in the obtained materials. The samples were characterized by FT-IR, Raman spectroscopy, XRD, and SEM. FT-IR spectra confirmed the presence of hydroxyl, epoxy, and carbonyl groups, with higher intensities observed in the more oxidized samples, especially GO3 (without $NaNO_3$), which exhibited the most intense signals. In a second series of experiments, keeping $KMnO_4$ constant while varying $NaNO_3$, we observed that an excess of the intercalating agent reduced both the interplanar distance (d_{002}) and the crystallite size. This compromised the oxidation process, leading to the reduction or disappearance of bands in the FT-IR spectra. The I_D/I_G ratio from Raman spectroscopy increased with the oxidation degree (GO3 = 1.19 and GO6 = 1.13), suggesting a greater quantity of defects. The broadening of the D band (FWHM) was also associated with the presence of disorder, as observed in GO5 (131 cm^{-1}). XRD analysis showed that GO4 (with a lower intercalator dosage) had a larger d_{002} spacing (0.87 nm) and greater crystallite size, indicating better insertion of functional groups. The d_{002} increased significantly in GO3 and GO4, reaching 0.86 nm and 0.87 nm, respectively. This reinforces the increased insertion of oxygenated groups between the graphitic layers and corroborates the FT-IR results. This occurs because, with a greater interplanar distance, the oxidizing agent can diffuse more easily through the sheets, leading to more effective oxidation. SEM revealed that GO1 exhibited densely agglomerated sheets (Fig. 1A), while GO2 (Fig. 1B) and GO3 (Fig. 1C) showed greater separation and roughness, associated with more intense oxidation. GO4 presented uniformly exfoliated and wrinkled sheets (Fig. 1D), indicating good oxidation without structural collapse. In contrast, GO5 (Fig. 1E) and GO6 (Fig. 1F) displayed regions with excessive stacking and rigid deformations, suggesting damage caused by the excess intercalator [3]. In the series containing an intercalator, GO4 showed exfoliated sheets with homogeneous wrinkling, indicating efficient oxidation without

compromising the structure, unlike GO5 and GO6, which displayed excessive stacking and rigid deformations, attributed to the high usage of $NaNO_3$ [1]. The wrinkling results from the insertion of oxygenated groups, internal stresses, and shrinkage during drying [3]. These morphological effects, related to the oxidation degree, allowed a detailed comparison between GO3 and GO4, revealing that while both exhibit high oxidation, GO4 achieved a better balance between functionalization and morphological preservation [3,4]. Thus, the results reinforce that the intercalator/oxidant ratio is a decisive parameter in obtaining functionally controlled structures.

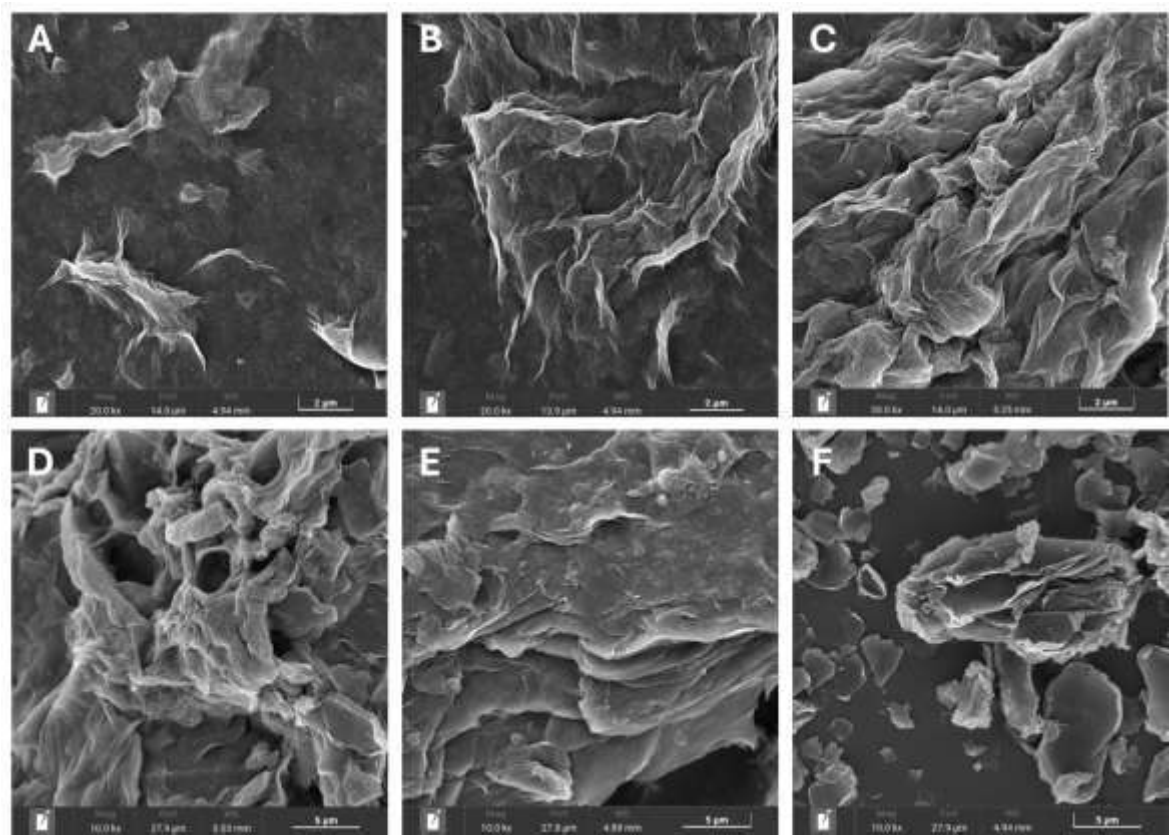

Figure 1. SEM images of graphene oxides produced by the improved Hummers method. Micrographs of GO produced in the absence of $NaNO_3$: (A) GO1, (B) GO2, and (C) GO3; In the presence of $NaNO_3$: (D) GO4, (E) GO5, and (F) GO6.

References

[1] HOU, Yonggang *et al*., *Ceramics International,* v. 46, n. 2, p. 2392-2402, 2020.

[2] SHEN, Xi *et al., Carbon*, v. 66, p. 84-92, 2014.

[3] WANG, Changguo *et al*., *Nanoscale*, v. 5, n. 10, p. 4454-4461, 2013.

AGRADECIMENTOS

PPGMat-UFPE, CETENE, CNPq, FINEP and CAPES.

Development of Hardfacing Coatings Using Flux with Recycled Niobium Chips

Leticia Karolayne Moreira Firmo[1], Vicente Afonso Ventrella [1,] Juno Gallego[1]. José Gedael Fagundes Júnior[1]*

[1] São Paulo State University "Júlio de Mesquita Filho" (UNESP). Department of Mechanical Engineering. Materials and Process Technology Development and Characterization Group (MaProTec)

* gedael.fagundes@unesp.br

Hardfacing coatings play a key role in industry by extending the service life of components subjected to severe wear, reducing maintenance and replacement costs, and enhancing the performance of machines and equipment in aggressive environments. In this context, the pursuit of more efficient and sustainable solutions has driven the development of new approaches for coating deposition, such as the use of recycled materials [1]. This study investigated the use of niobium chips as a component in welding fluxes for the formation of hard coatings reinforced with niobium carbides (NbC), aiming to enhance resistance to abrasive wear. The flux was formulated by mixing 10 g of niobium chips with 1.5 g of graphite, in a proportion determined based on stoichiometric calculations, using sodium silicate as a binder. A layer containing the flux was previously deposited onto the base metal, forming a track with approximate dimensions of 3 × 6 × 65 mm. Subsequently, this layer was fused using the GTAW welding process, with the torch mounted on a portable tractor to ensure precise control of the welding speed. The welding parameters are presented in Table 1. Two experimental conditions were evaluated, one including the addition of silicon and manganese as alloying elements to the mixture and the other without their addition. The results showed that the addition of Si and Mn led to deposits with improved metallurgical quality, exhibiting a lower incidence of porosity, Figure 1. Although the dilution rates were higher than those typically recommended for hardfacing applications, the study suggests that the use of overlapping passes may help mitigate this effect by optimizing the ratio between base metal and deposited material. Microstructural characterization revealed the formation of a matrix enriched with dendritic niobium carbide (NbC) branches, homogeneously distributed throughout the fusion zone, Figure 2. Due to the lower dilution, the volumetric fraction of NbC was higher under the conditions with silicon and manganese. X-ray diffraction tests confirmed the predominance of the NbC phase, with no detection of metallic niobium, indicating that chemical reactions between niobium and carbon occurred during the welding process. The presence of NbC resulted in a significant increase in hardness values in the weld region, demonstrating the effectiveness of niobium chips in generating hard compounds during welding [3]. It is concluded that the use of recycled niobium chips as a flux component represents a viable and sustainable alternative, enabling coatings with good mechanical properties. The addition of Si and Mn proved essential for enhancing the integrity and performance of the deposit, establishing this approach as a promising solution for industrial applications.

Key-words: Hardfacing. Recycling of niobium chips. Carbides.

[1] H.Holleck, Journal of Vac. Sc. Techn. Vol. 5 (1986) DOI: 10.1116/1.573700.
[2] N.G.chaidemenopoulos, et al. Surf. Coat. Technol., v. 357, p. 651–661, 2019.
[3] M.C.Cunha, et al. Int. J. Adv. Manuf. Technol., 136, 1241–1251, 2024.
[4] This research was supported by CAPES (Brazil), 001 Financial Code.

Table 1. Welding condition

Welding Current, A	Welding Voltage, V	Welding Speed, mm/min	Arc Gap, mm	Argon flow rate, l/min
175 - 180	15 - 16	115	3	12 - 14

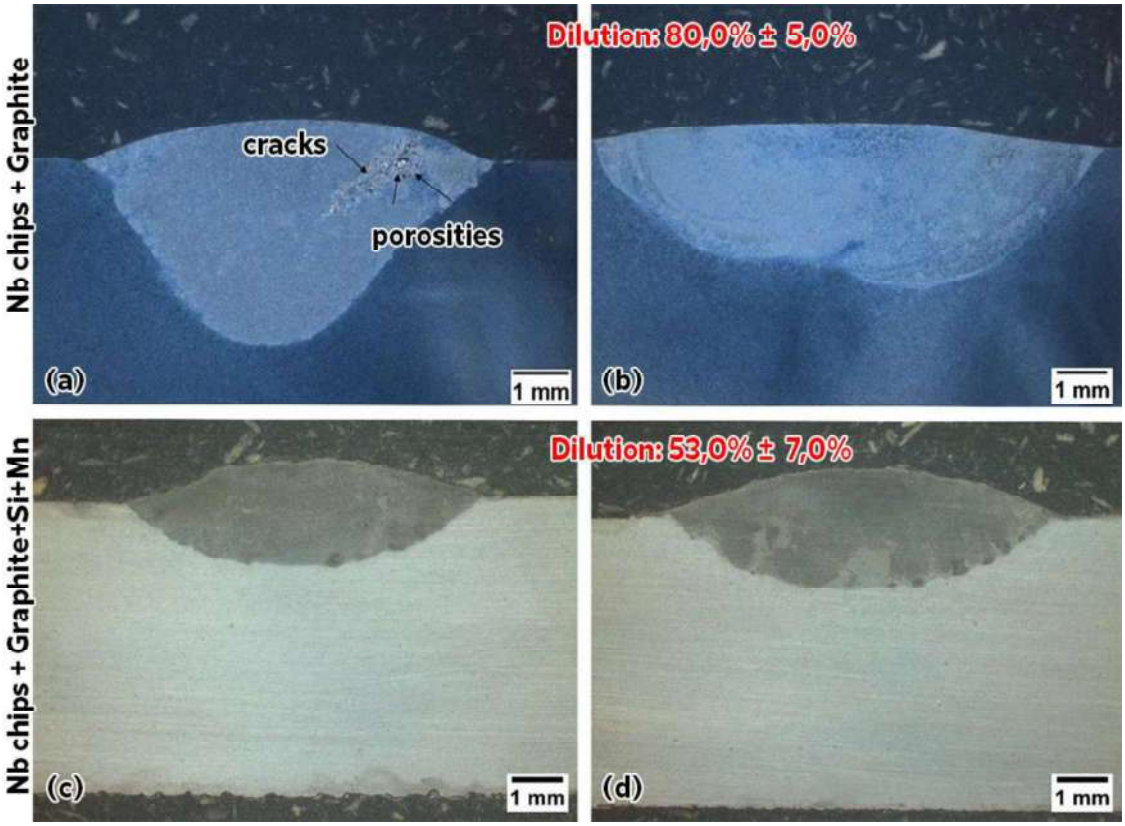

Figure 1. Cross-sectional images of the investigated conditions.

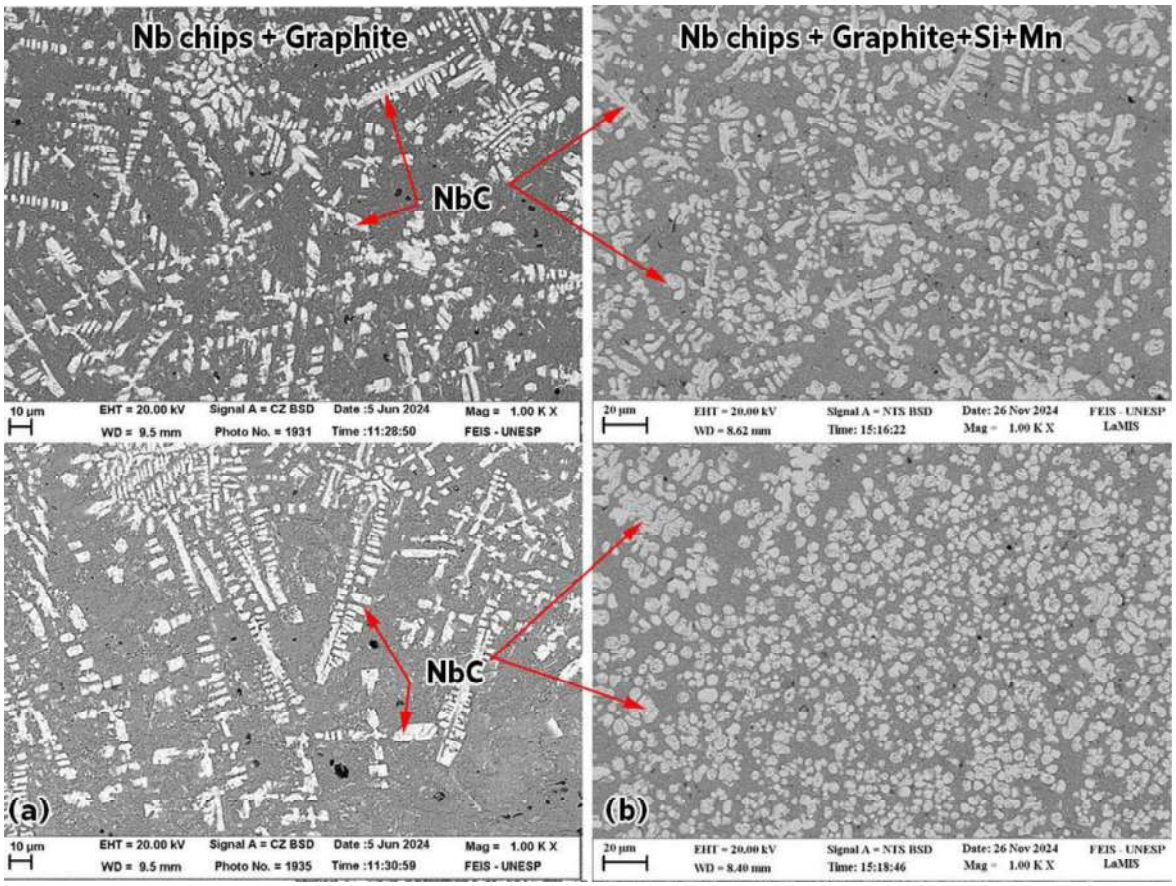

Figure 2. Micrograph of the welded region. (a) Nb + graphite. (b) Nb + graphite + SiMn.

EFFECT OF HUMIDITY ON THE SYNTHESIS OF $CoTiO_3$

Beatriz S. G. Xavier[1]*, Thiago A. S. Soares[2], Giovanna Machado[2].

[1]Universidade Federal de Pernambuco, [2]Centro de Tecnologias Estratégicas do Nordeste
*beatriz.gomesxavier@ufpe.br

Photocatalysis has been widely studied due to its versatility in pollutant degradation and energy production [1, 2]. Currently, most photocatalysts are composed of semiconductors based on binary metal oxides, such as TiO_2 [1]. Perovskite oxides have gained prominence due to their good response to visible light and tunable electronic properties, making them promising for photocatalytic applications, an example is $CoTiO_3$ [3]. However, it has been observed that small variations in synthesis conditions can directly impact the formation of undesired phases [4]. This study aims to investigate the influence of humidity in the synthesis process of $CoTiO_3$, evaluating its correlation with the formation of secondary phases and structural consequences. Through this approach, we sought to optimize synthesis conditions to ensure phase purity of $CoTiO_3$ and maximize its photocatalytic performance. $CoTiO_3$ was synthesized using cobalt(II) acetate and titanium butoxide in ethylene glycol, followed by calcination at 700 °C for 4 h. To assess the impact of humidity, a preheating step was employed to remove water from the samples, which were later characterized by XRD and SEM. During synthesis, a color change was observed in the cobalt acetate solution in ethylene glycol—from magenta to deep purple after heating—which served as the first indication of water evaporation. XRD results confirmed that, without the water removal step, the major phases formed were anatase (56%) and rutile (10%), both crystalline forms of TiO_2. This result indicates that the presence of water in the system favors the hydrolysis of titanium precursors, promoting the formation of TiO_2 instead of enabling the complete reaction with cobalt to form $CoTiO_3$. In the samples that underwent heating, a significant formation of $CoTiO_3$ was obtained, confirming that water removal is essential for the efficient synthesis of this material. Although the crystalline structures of the samples differed, SEM analysis showed that both formed particles with similar size ranges and shapes. Figure 1 shows a morphology predominantly composed of nanorod structures with hexagonal outlines. Samples exposed to moisture displayed a morphology with more cavities/interstices, resulting in a more granular texture. In contrast, the absence of water in the synthesis may have contributed to reduced dispersion of particles aggregated in the nanorods. Figure 1B shows that the nanorods exhibit a more compact surface with larger particle aggregates forming the nanorods. In summary, the results of this study highlight that humidity plays a critical role in the synthesis of $CoTiO_3$ via the ethylene glycol-based route. The absence of water favored the formation of $CoTiO_3$, promoting a more efficient reaction with cobalt. SEM analysis revealed nanorod morphology with hexagonal outlines in both samples. However, $CoTiO_3$ nanorods showed a more compact surface, indicating that synthesis conditions may have also influenced the surface organization of the particles [5].

[1] F. B. Li, and X. Z. Li. The enhancement of photodegradation efficiency using Pt–TiO2 catalyst. (Chemosphere 48.10) (2002) 1103-1111.
[2] D. Cui et al. Synthesis of CoTiO3 nanoparticles with enhanced photocatalytic degradation. (Micro & Nano Letters 14.8) (2019) 840-844.
[3] Y. RongQin et al. Fabrication of CoTiO3/g-C3N4 Hybrid Photocatalysts with Enhanced H2 Evolution: Z-Scheme Photocatalytic Mechanism Insight. (ACS Applied Materials & Interfaces) (2016).
[4] S. Rasalingam, and R. T. Koodali. Visible-light driven oxygen evolution over CoTiO 3 perovskites via a modified Pechini method. (CrystEngComm 18.6) (2016) 868-871.
[5] This research was supported by CNPq, CETENE and UFPE (Brazil).

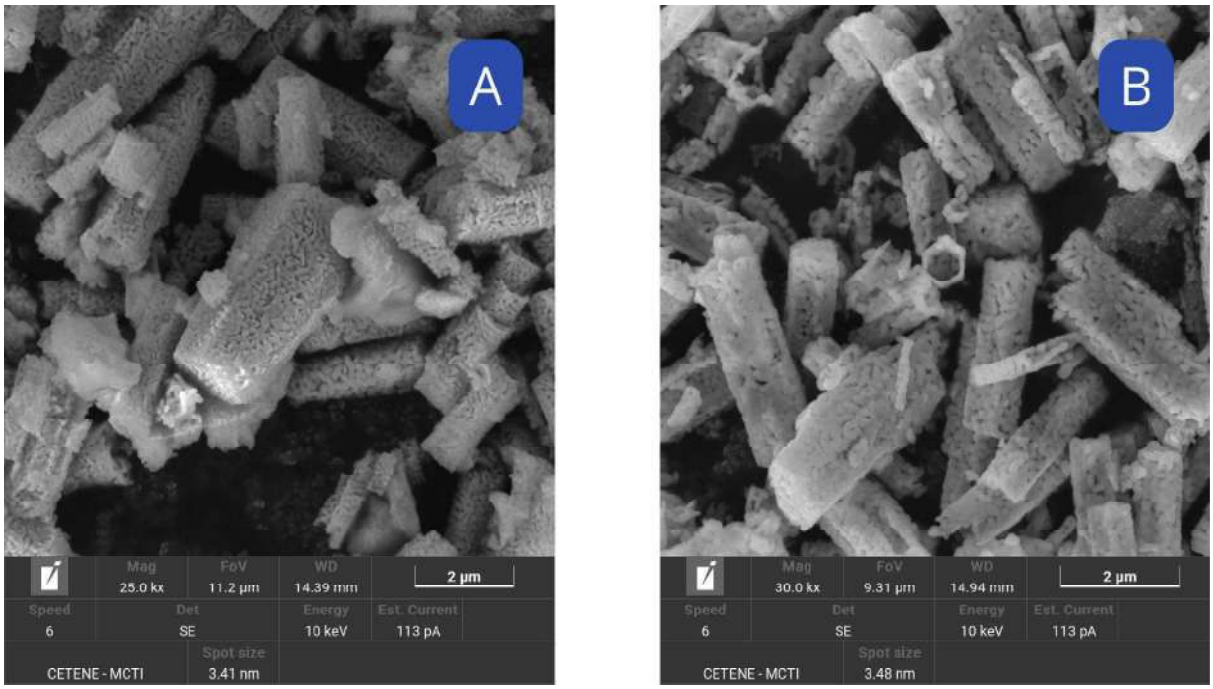

Figure 1. SEM images of the samples: (A) with humidity and (B) without humidity.

Effect of punctual defects $W_{Bi^{3+}}^{6+'''}$ in the $BiVO_4$ morphology and electronic properties

Ellen C. Souza,[1,2]* Luana B. C. Oliveira,[1,2] Felipe LN Sousa,[1] Giovanna Machado[1]

[1]Centro de Tecnologias Estratégicas do Nordeste, [2]Universidade Federal de Pernambuco.
*ellen.souza@cetene.gov.br

Bismuth vanadate ($BiVO_4$) is a promising semiconductor for photoelectrochemical hydrogen generation from water, owing to its narrow bandgap of approximately E_g^{bulk}= 2.4 eV, which allows for light absorption, and its chemical stability. However, its practical performance is limited by a high recombination rate of photogenerated electron-hole pairs and inefficient charge transport [1]. The substitution of VO_4^{3-} groups with WO_4^{2-} can improve the system's efficiency due to the necessary formation of oxygen vacancies ($V_{\ddot{O}}$) to maintain electroneutrality, which implies better charge separation in the system [2, 3]. Nevertheless, ensuring the coexistence of these groups during the thermal conversion step leads to a low concentration of dopant groups. From this perspective, we developed the insertion of W^{6+} ions during the electrodeposition of BiOI, forming point defects of the type $W_{Bi^{3+}}^{6+'''}$. The $Bi_{1-x}W_xOI$ (x = 0, 0.25, 0.5) films were obtained by adding *x*W to a solution containing *p*-benzoquinone, and deposited using a chronoamperometric procedure with an electric charge cutoff. The $(Bi_{1-x}W_x)VO_4$ was obtained in a thermal conversion step in the presence of vanadyl acetylacetonate ($VO(acac)_2$). The structural and morphological modifications of the films were investigated at each stage by X-ray diffraction, electron microscopy, and energy-dispersive X-ray spectroscopy (EDX), and the electronic changes by photoelectrochemical techniques. The $Bi_{1-x}W_xOI$ (Fig. 1a) present as nanoplates, and in the EDX spectra (Fig. 1b), the spectroscopic signals of Bi, W, O and I are verified. The samples of $BiVO_4$ (Fig. 1c) and $(Bi_{1-x}W_x)VO_4$ x = 0.5% (Fig. 1e) show the preservation of the semiconductor's morphology even with doping, where the nanoparticles exhibit similar thicknesses of 0.163 ± 0.036 μm and 0.161 ± 0.034 μm for the doped samples. The incorporation of W into the $BiVO_4$ structure was confirmed by EDX (Fig. 1d). As a consequence of the insertion of crystalline defects from doping, an increase in photocurrent density was observed from 2.0 mA cm^{-2} for BiVO4 to 2.5 mA cm^{-2} with $(Bi_{1-x}W_x)VO_4$. The increase in photocurrent is reflected in the increased hydrogen production rate compared to the pure material, demonstrating the effectiveness of band engineering for advancing green hydrogen production systems.

[1] J. Mater. Chem. A, 2021, 9, 16137–16149.
[2] J. Colloid and Interface Science, 2022, 624, 515-526.
[3] Front. Chem., 2018, 6, 266.
[4] This research was supported by FACEPE (Brazil)

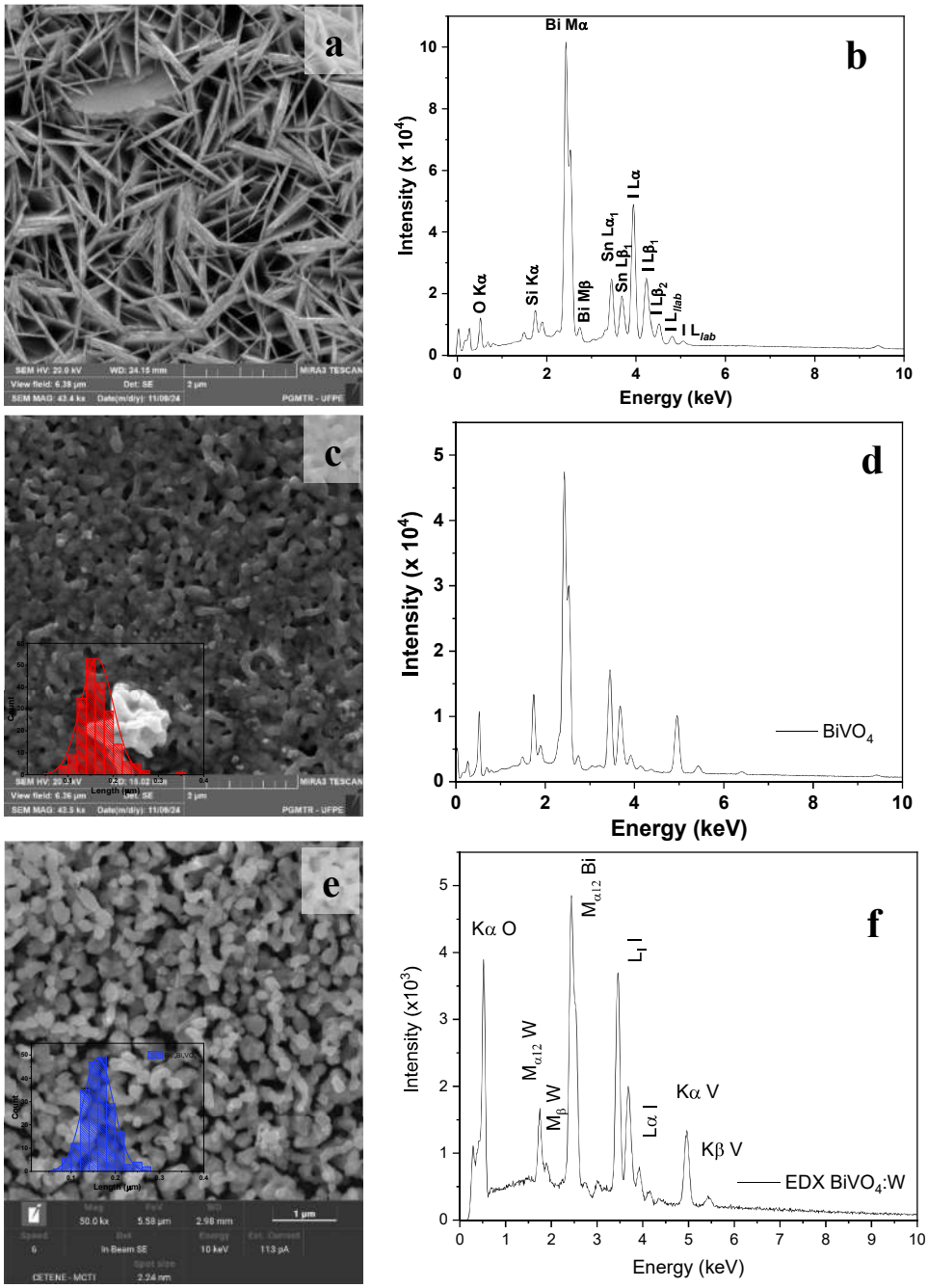

Figure 1. SEM images and EDX spectrum of (a,b) BiOI , (c,d) $BiVO_4$, (e,f) $Bi_{1-x}W_xVO_4$.

Effect of seed layer on the photoelectrochemical performance of WO_3 thin films

Larissa Giovanna Campos Silva[1, 2]*, Denilson de Vasconcelos Freitas[2] , Lizeth Carolina Mojica-Sánchez[2], Giovanna Machado[2].

[1] Universidade Federal de Pernambuco (UFPE), [2] Centro de Tecnologias Estratégicas do Nordeste (CETENE).

*larissa.silva@cetene.gov.br

The excessive use of fossil fuels, driven by high energy demand, significantly increases CO_2 emission levels. In this context, photoelectrocatalysis is considered a sustainable and renewable route to minimize environmental pollution and address the energy crisis, by converting solar energy into chemical energy [1]. To increase the efficiency of solar-to-hydrogen (STH) conversion, semiconductors such as tungsten oxide (WO_3) are used as catalysts because they provide a band gap of 2.7 eV and high electrical conductivity [2]. In this work, we study the effect of the seed layer, deposited by spin-coating, on the photoelectrochemical performance of WO_3 thin films grown by hydrothermal reaction. Films were produced over FTO in two steps. First, a WO_3 seed layer was deposited by spin coating, using a precursor solution containing H_2WO_4, followed by thermal treatment at 500 °C for 60 min. The WO_3 thin films were then grown by hydrothermal reaction at 180 °C for 2 h, and at the end of the process, the photoanode was thermally treated at 550 °C for 2 h. Figure 1 shows scanning electron microscope (SEM) micrographs (obtained by secondary electrons) of WO_3 thin films without a seed layer (Fig. 1a) and with this layer (Fig. 1b). Both systems exhibit the same nanoplate morphology; however, in Figure 1a, there is a large exposure of the FTO, while in Figure 1b, the growth of the nanoplates occurs successfully. The presence of the seed layer favors the adhesion of the material to the substrate, in addition to promoting more controlled growth. The synthesis route based on the seed layer results in thin films with a monoclinic phase, high absorption, and a film thickness of 2.128 ± 0.107 μm (Fig. 2a). The photoanodes better photoelectrochemical performance was dependent on the seed layer, showing a maximum photocurrent density of approximately 0.8 mA cm^{-2} to 1.5 mA cm^{-2} with the seed layer (Fig. 2b). Thus, the seed layer considerably increases the photocurrent density, making the system favorable in applications such as photoelectrochemical hydrogen production.

[1] P. Shandilya et al., J. Hazardous Mat.,428 (2022) 128218.

[2] M. Ade et al., Sust. Energy Fuel, 7 (2023) 4332.

[3] This research was supported by CNPq, CAPES and FINEP.

Figure 1. SEM images of thin films of WO_3 without (a) and with (b) seed layer (Voltage: 10 kV, SEM Mag: 30.0 kx, work distance: 6.16 mm, and scale bar of 2 μm).

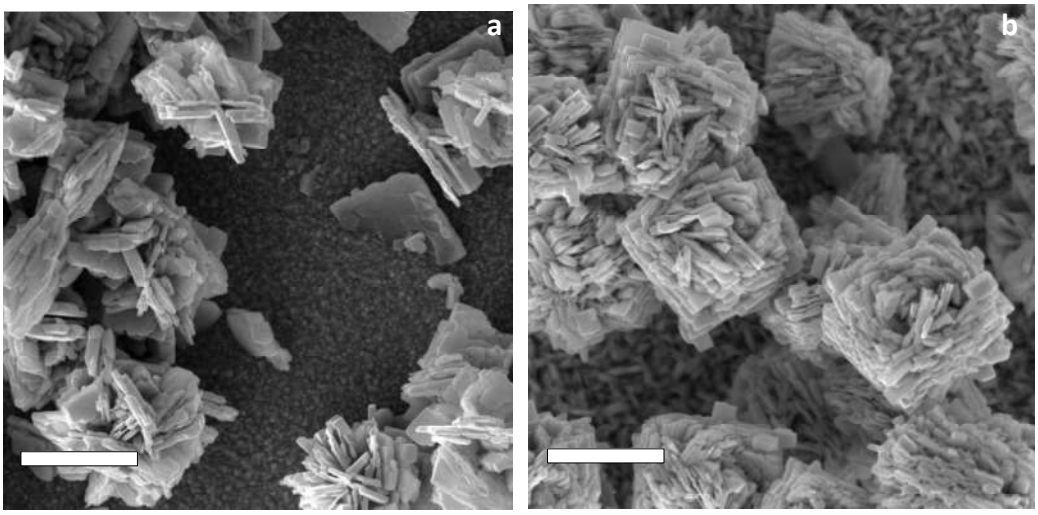

Figure 2. (a) Cross-section of the WO_3 photoanodes and (b) bar graph of photoelectrochemical performance of WO_3 samples measured at 1.23 V *vs.* RHE in 0.5 mol L^{-1} Na_2SO_4/ 1 mol L^{-1} glycerol electrolyte.

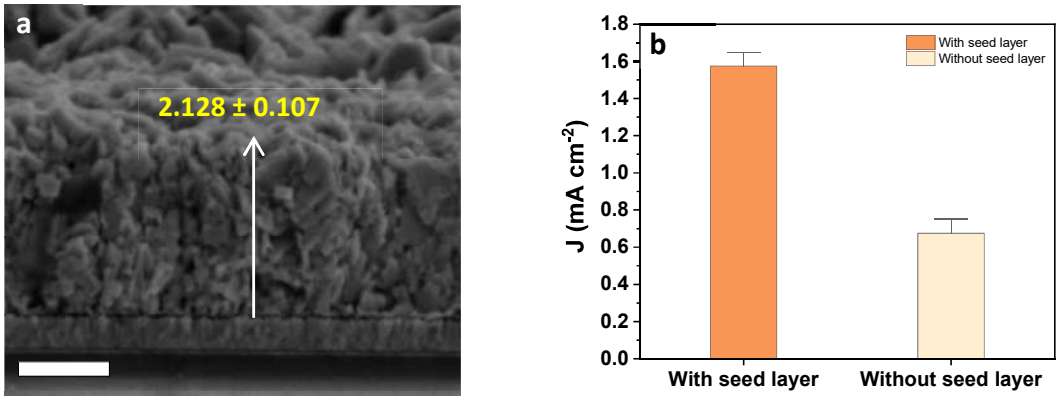

Electrodeposition of Binary NiCo/NF Alloy for Green Hydrogen Production: Preliminary Results

Déboralys Ferreira Passos[1,2]*, Ivani Meneses Costa[2], Katlin Ivon Barrios Eguiluz[1,2], Giancarlo Richard Salazar-Banda[1,2], Amanda de Azevedo Gonçalves[3]*

[1] Programa de Pós-graduação em Engenharia de Processos, Universidade Tiradentes (PEP/Unit), Aracaju, SE, Brasil; [2] Laboratório de Eletroquímica e Nanotecnologia, Instituto de Tecnologia e Pesquisa (LEN/ITP), Aracaju, SE, Brasil; [3] Sergipe Parque Tecnológico (SERGIPETEC), São Cristóvão, SE, Brasil.
*deboralyshp@gmail.com *amanda.goncalves@sergiptec.org.br

The increase in greenhouse gas emissions have driven the search for sustainable energy sources. In this context, hydrogen (H_2) has emerged as a promising alternative, particularly when produced via water electrolysis. However, this pathway faces limitations related to energy efficiency and the sluggish kinetics of the hydrogen evolution reaction (HER) [1]. Key challenges that compromise overall process performance include the high costs of noble metal-based electrolyzers, the low catalytic activity of alternative materials, and the requirement for high overpotentials. Therefore, the development of stable, efficient, and economically viable electrocatalysts is essential. Electrodeposition has emerged as a promising strategy, as it enables the direct deposition of catalytic materials onto the substrate, ensuring better adhesion, process simplicity, and enhanced electrochemical performance [2]. In view of this scenario, this study developed NiCo bimetallic electrocatalysts supported on nickel foam (NiCo/NF) by electrodeposition, aiming at the improvement of efficient catalytic materials for sustainable hydrogen production. For this purpose, nickel foam (0.5 cm^2) was pretreated by sequential sonication in ethanol, acetone, and ultrapure water for 10 minutes in each solvent, followed by drying in an oven at 60 °C for 30 minutes. Simultaneously, the electrolyte solution was prepared by dissolving 0,30 $mol.L^{-1}$ nickel(II) sulfate hexahydrate, 0,03 $mol.L^{-1}$ cobalt(II) sulfate heptahydrate, and 0,20 $mol.L^{-1}$ potassium citrate in ultrapure water (Gehaka MS 2000 system). A sodium carbonate solution (1,0 $mol.L^{-1}$) was then slowly added until the pH reached 10 [3]. Electrodeposition was performed in an one-compartment electrochemical cell (50,0 mL) using a potentiostat (PGSTAT302N, METROHM AUTOLAB) at a constant potential of -1.2 V for 60 minutes. The experiments used an Ag/AgCl reference electrode, a platinum counter electrode (1 cm^2), nickel foam as the working electrode, and a nitrogen (N_2) gas inlet to ensure an inert atmosphere throughout the process. After synthesis, the electrodes were characterized by scanning electron microscopy (SEM) and energy-dispersive X-ray spectroscopy (EDS). The SEM images of the NiCo/NF sample in Figure 1, taken at low magnification, depict the typical three-dimensional microstructure of nickel foam, with interconnected open cells and pores of various sizes. This porosity enhances surface area, promotes improved charge transfer, and reduces diffusion resistance at the electrode–electrolyte interface [4]. At higher magnifications (highlighted with red and yellow dashed lines), the formation of a thin, homogeneous film with "microflower"-like structures is evident, indicating uniform metal deposition on the substrate. The surface irregularities observed can also contribute to an increased contact area with the electrolyte, thereby enhancing electrochemical reactions [5]. EDS analysis, shown in Figure 2, confirmed the presence of nickel and cobalt on the electrode surface indicates efficient metal deposition, which is crucial for high catalytic performance. Nickel originates from both the foam structure and the deposit, while cobalt was incorporated through electrodeposition. These results suggest that the NiCo/NF electrode exhibits structural and compositional features that are favorable for its application as an electrocatalyst in green hydrogen production via water electrolysis [6].

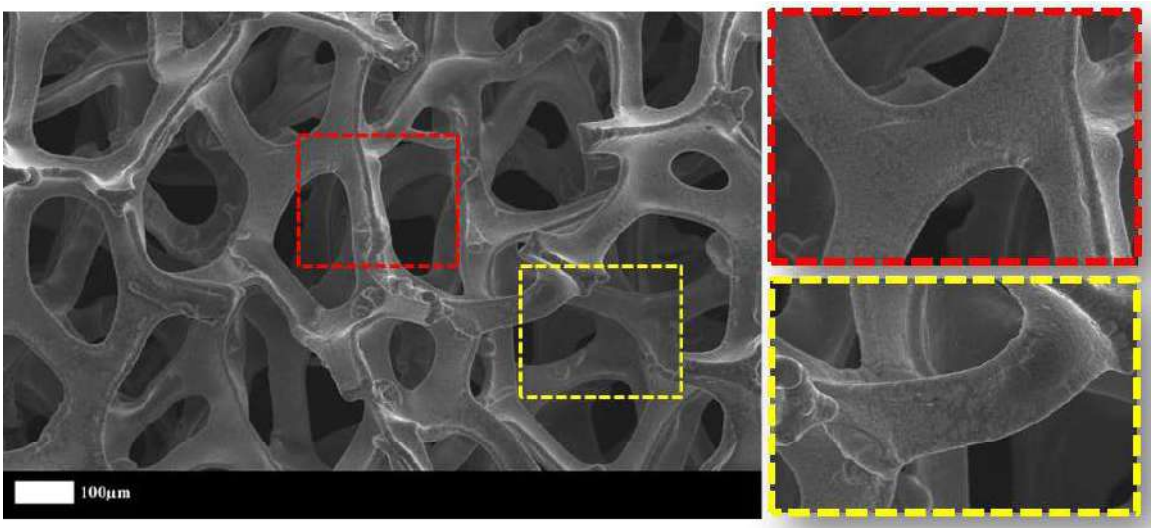

Figure 1. Scanning electron microscopy image of the NiCo/NF electrode, electrodeposited at -1.2 V for 60 minutes, acquired at 100x magnification. Two distinct regions of the sample are highlighted.

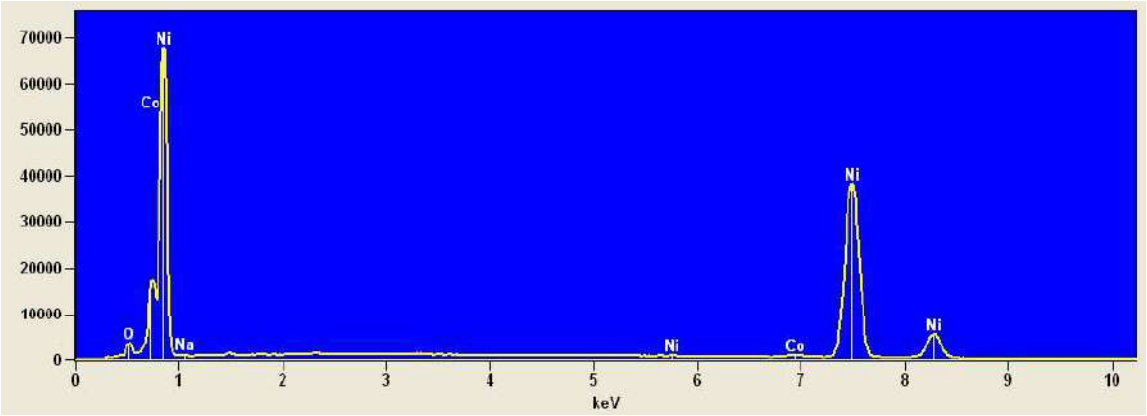

Figure 2. EDS spectrum of the NiCo/NF electrode.

[1] Y. Wen et al., *Preparation of Ni nanocone/Grid electrodes by laser-electrodeposition combined process as an efficient and stable electrocatalyst for hydrogen evolution reaction*. International Journal of Hydrogen Energy, 89 (2024) 518.
[2] M. Molaei, *Nickel-based coatings as highly active electrocatalysts for hydrogen evolution reaction: A review on electroless plating cost-effective technique*, Sustainable Materials and Technologies, 40 (2024) e00991.
[3] H. Roh et al., *Hierarchically nanostructured Ni(Mo, Co)-WOx electrocatalysts for highly eficiente urea electrolysis*, Applied Surface Science, 610 (2023) 155520.
[4] S. Kroy, W. G. Shin, *Understanding the effect of electrode thicknesses on bubble detachment and hydrogen evolution reaction (HER) in water electrolysis using bare nickel foam*, Journal of Power Sources, 613 (2024) 234820.
[5] C. S. Torres, C. F. Malfatti, *Produção de hidrogênio a partir de glicerina em eletrodos de Ni-Zn*, Estudos tecnológicos em engenharia, 10, n° 2 (2014) 71.
[6] This research was supported by the National Council for Scientific and Technological Development – CNPq (307866/2022-0 and 305287/2022-2), the Foundation for Research and Technological Innovation Support of the State of Sergipe - FAPITEC/SE (019203.05926/2023-6) *and the* Sergipe Technological Park (SERGIPETEC).

Electron Microscopy Characterization of Nb_2O_5 Nanosheets Grown via Planar Confinement on Graphene Oxide

Carolina Carvalho de Mello[1]*, Cleybson Kaian Santos Silva[1], Kelly Leite dos Santos Castro Assis[1], Braulio Soares Archanjo[1], Carlos Alberto Achete[1].

[1] Metrology Material's Division, National Institute of Metrology, Quality and Technology, Duque de Caxias, RJ, Brazil
*ccmello@colaborador.inmetro.gov.br

Two-dimensional (2D) nanomaterials have gained attention for their high surface area, ordered structure, and unique physicochemical properties [1]. Although niobium pentoxide (Nb_2O_5) is not inherently 2D, it can be synthesized in ultrathin layers that exhibit similar characteristics. Nb_2O_5 nanosheets show promise for environmental applications, including sensors and photoactive filters [2,3]. Here in this work, the material was synthesized using hydrothermal synthesis, via planar growth on graphene oxide (GO) nanosheets, a method known to promote the formation of nanosheet-like structures. In this study, advanced electron microscopy techniques were employed to perform structural and morphological characterization of Nb_2O_5 nanosheets. The nanosheets were obtained through the hydrolysis of $NbCl_5$ in ethanol, followed by thermal pretreatment under an inert atmosphere and subsequent calcination in an oxidizing atmosphere. This approach promoted the growth of Nb_2O_5 nanosheets on GO, the decomposition of synthesis byproducts, structural reorganization, crystallization of the orthorhombic T-Nb_2O_5 phase. Additionally, it enabled the near-complete removal of GO template, resulting to the morphological stabilization of the final material [4,5]. The obtained nanosheets exhibited mesoporous morphology composed of interconnected nanometric units arranged in a lamellar network, as revealed by scanning electron microscopy (SEM). This architecture enhances surface area and facilitates chemical species diffusion within the material, which is desirable for adsorption and catalysis applications [5,6]. SEM analysis also enabled measurement of the lateral dimensions, with up to 80% of the nanosheets exhibiting dimensions in the 3 to 20 μm range. The lamellar and 2D structure of the nanosheets was further evidenced by transmission electron microscopy (TEM). Their thickness was evaluated by electron energy-loss spectroscopy (EELS), showing that thinner samples (5–10 nm) exhibited discontinuities, whereas thicker samples (30–100 nm) formed more continuous sheets, suggesting multilayer stacking. Atomic force microscopy (AFM) topography profiles corroborated these outcomes, revealing discontinuous thin regions and thicker, uniform and compact regions. The consistency between EELS and AFM data supports the structural interpretation that increased thickness leads to greater continuity and stacking. Energy-dispersive X-ray spectroscopy (EDS) confirmed the presence of Nb and O, with residual carbon signals consistent with GO removal after calcination. The crystalline structure was confirmed by X-ray diffraction (XRD), which revealed well-defined peaks, including the (001), (180), and (181), characteristic planes of the orthorhombic T-Nb_2O_5 phase, in agreement with JCPDS #00-030-0873 [4,7,8,9,10]. These findings highlight the crucial role of electron microscopy techniques in providing detailed morphological and structural insights at the nanoscale, which are essential for understanding the growth mechanism and preservation of the two-dimensional architecture of the Nb_2O_5 nanosheets. These results also underscore the effectiveness of the GO-assisted synthesis approach in producing highly ordered Nb_2O_5 nanosheets.

[1] N. Baig et al., *Compos. Part A Appl. Sci. Manuf.* 165 (2023) 107362.
[2] R. N et al., *Sens. Technol.* 2 (1) (2024) 2299092.
[3] K. Su et al., *Adv. Sci.* 8 (8) (2021) 2003156.
[4] P. Nagaraju et al., *Nanomaterials* 10 (1) (2020) 160.

[5] J. Wan et al., *Chem. Eng. J.* 488 (2024) 150912.
[6] C.L. Ücker et al., *Chem. Phys. Lett.* 764 (2021) 138271.
[7] A.A. AbdelHamid et al., *Adv. Mater.* 29 (32) (2017) 1701427.
[8] J. Jin et al., *FlatChem* 27 (2021) 100236.
[9] D. Cao et al., *Catal. Lett.* 147 (4) (2017) 926–933.
[10] R. Pang et al., *Mater.* 16 (21) (2023) 6956.
[11] This research was supported by CNPq, Faperj, and Inmetro (Brazil).

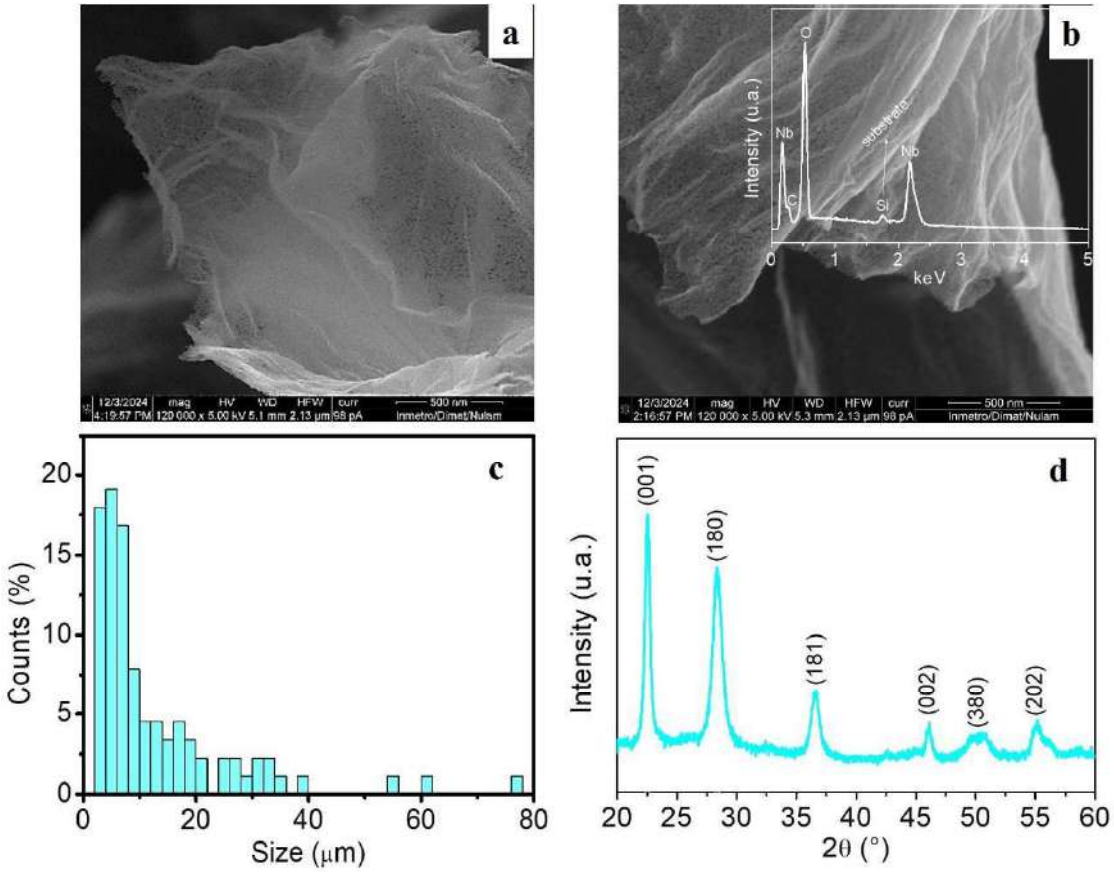

Figure 1. a) SEM image showing Nb2O5 nanosheets morphology. **b)** SEM image and elemental analysis by EDS. **c)** Lateral size distribution. **d)** Crystalline structure by XRD.

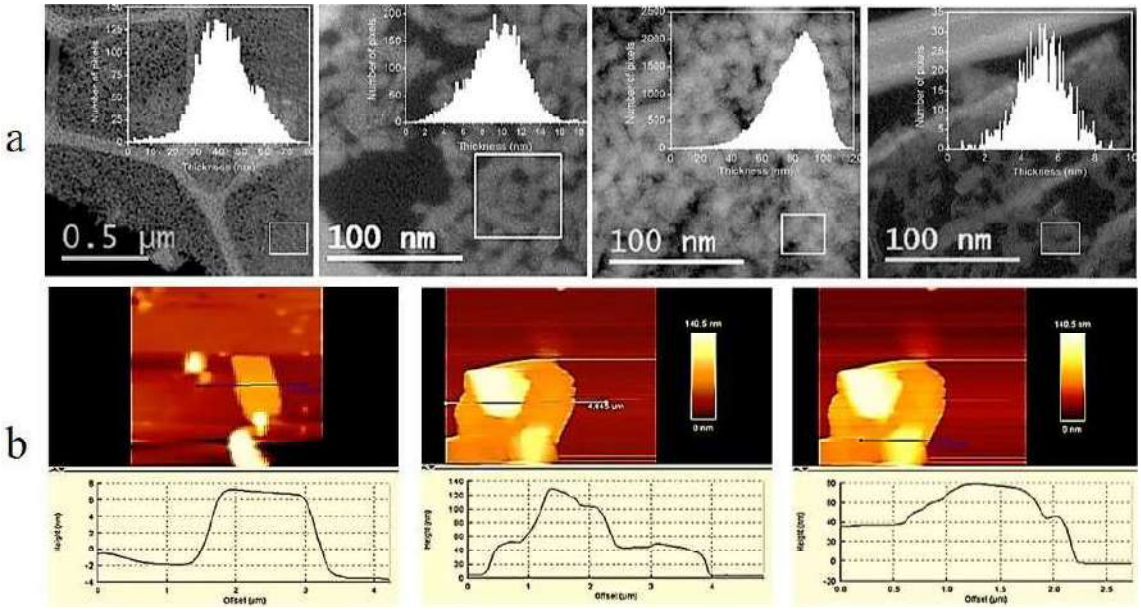

Figure 2. a) Lamellar 2D structures of the Nb_2O_5 nanosheets by TEM and thickness histograms by EELS. **b)** Topography profiles by AFM.

Exploring Morphological Influence On Nanostructured Nickel Oxides (NiO) Nanofoams Synthesized By Pulsed Laser Deposition (PLD)

Luciana Mary Neugedachter[1]*, Adriele Aparecida de Almeida[1], Yutao Xing[1], Fabio Barboza Passos[1].

[1]Universidade Federal Fluminense (UFF)
*lucianamary@id.uff.br

Energy storage devices are essential for the efficient utilization of renewable energy sources, such as solar and wind energy, which often struggle to deliver a consistent power supply. To ensure stable and reliable grid performance, technologies such as supercapacitors have been the focus of ongoing performance enhancements [1]. While the development of novel materials has contributed to more compact storage solutions, it offers only a partial answer [2]. In this context, understanding how nanostructures affect the macroscale efficiency of storage systems has become especially valuable [3]. In this study, we investigate how morphology, specifically porosity and layer thickness, affects the electrochemical behavior of pseudocapacitors. The work focuses on nickel oxide (NiO) materials, aiming to enhance capacitance by leveraging NiO's high chemical stability and large surface area. NiO samples with different morphologies were synthesized using Pulsed Laser Deposition (PLD) with an Nd:YAG laser. The depositions were performed at room temperature with a fixed laser fluence but under varying atmospheric pressures (133.3–333.3 Pa) to control morphology. Two different substrates were used: stainless steels for electrochemistry tests and silicon substrates for morphology investigations. The resulting films were thermally treated to improve the mechanical bonding and then characterized using scanning electron microscopy (SEM) to compare nanoscale morphologies across different pressure (Figure 1). Cyclic voltammetry was employed to evaluate electrochemical performance, including specific capacitance and charge–discharge efficiency. For this analysis, a three-electrode configuration was used, with platinum as the counter electrode, Ag/AgCl as the reference, and a 1 mol/L KOH solution as the electrolyte. Preliminary experiments indicated that the NiO surfaces agree with existing literature: lower pressures produced compressed thin films, while higher pressures led to porous nanofoam structures [4]. The findings demonstrate that, although increased porosity can improve ion diffusion, layer thickness plays a dominant role in determining overall capacitance—an effect similarly observed in manganese oxides [5]. Other characterization techniques, such as Raman spectroscopy, X-ray diffraction (XRD) and transmission electron microscopy (TEM) are used to give more structural information. Based on the results obtained in this study, we plan to choose the sample with the best performance to investigate composite materials as electrodes for supercapacitors, namely, Ni-Si composite materials. The reaction between Ni and Si generates NiSi compound and consequently increase the conductivity of the NiO electrode.

[1] K.Dissanayake, D. K. Abeywardana Jounal of Energy Storage, 96 (2024) 112563.
[2] N. I. Jalal et al., Jounal of Physics Conference Series, 1973 (2021) 012015.
[3]S. Chen et al., J. Mater. Chem. A, 2013, 1 (2013) 2941.
[4] N. A. Shepelin et al., Chem Soc Rev., 52 (2023) 2294.
[5] J. A. Pereira et al., Mater Adv., 1(2020) 2433.

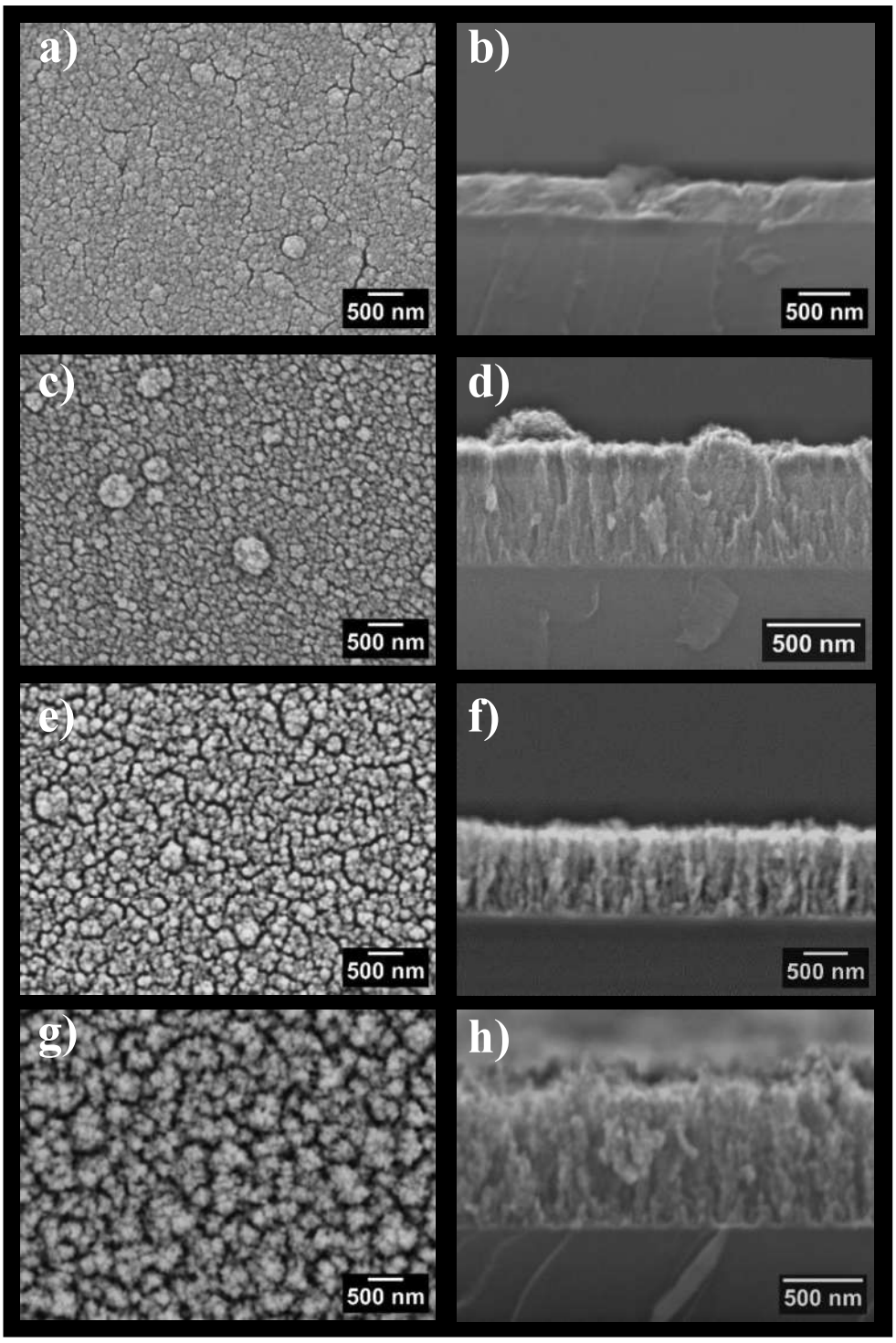

Figure 1. SEM images of NiO nanostructures deposited by PLD on stainless steel substrates at oxygen pressures of 133.3 Pa (a), 199.9 Pa (c), 266.6 Pa (e), and 333.3 Pa (g), along with the corresponding cross-sectional views on silicon substrates at 133.3 Pa (b), 199.9 Pa (d), 266.6 Pa (f), and 333.3 Pa (h).

Failure Analysis of Turbine Blades in an Oil Refinery: Insights From SEM/EDX Techniques

Ricardo Sanson Namur[1]*, Luciano dos Santos Silva[1], Gustavo Spera Alves[2].

[1]Petrobras – Refinaria de Paulínia – REPLAN. Av. Professor Zeferino Vaz, km 132, s/nº, 13147-900, Paulínia – SP – Brazil.
[2]Petrobras – Refinaria Henrique Lage – REVAP. Rod. Presidente Dutra, km 143, s/nº, 12223-900, São José dos Campos – SP – Brazil.
*ricardo.namur@petrobras.com.br

Oil refineries are industrial facilities designed to transform crude oil into a wide range of valuable products, including fuels, petrochemicals, and raw materials essential for various industries, playing a critical role in the global energy supply chain. One of the main processing units in oil refineries is the Fluid Catalytic Cracking (FCC), which is a conversion unit that breaks down heavy hydrocarbons into lighter, more valuable products such as gasoline, LPG (liquified petroleum gas) and propene. Additionally, the FCC enhances the economic value of crude oil while increasing the refinery's flexibility to meet local demand for transportation fuels and petrochemical feedstocks [1,2]. The FCC unit employs zeolite-based catalysts at high temperatures to break down heavy molecules. However, the formation of coke on the catalyst surface leads to its gradual deactivation, requiring regeneration to restore optimal performance. Regeneration takes place in a dedicated chamber, where high-temperature air is injected to burn off the coke accumulated on the catalyst. The injected air burns off the coke deposited on the catalyst surface, restoring its activity for reuse in the cracking process. This regeneration step is crucial for maintaining the efficiency and continuity of the FCC unit, as it ensures the catalyst can be used repeatedly [1,2]. Nonetheless, the partial combustion of coke may produce carbon monoxide, which needs to be further oxidized to carbon dioxide in a CO boiler before exhaustion to the atmosphere. One of the components of the CO boiler is the turbo-expander, which uses the exhaustion of flue gas for power recovery in a generator [3]. In this work, the turbine blades of a turbo-expander were analyzed after the failure of an Inconel 738 blade after operating about 60 days. Inconel 738 is precipitation hardenable nickel-base alloy with substantial adds of Cr, Co, W, Ta, Nb, Al, Ti and Zr for intermetallic precipitation. Such material is an industry standard, since it offers high creep-rupture strength and superior hot corrosion resistance compared to lower-chromium superalloys. It performs reliably at temperatures up to 1255 K, even under prolonged exposure to corrosive environments [4]. The same blades were coated with a proprietary compound by Linde – Advanced Material Technologies (former Praxair Surface Technologies). These coatings were applied to enhance resistance to erosion and corrosion, as small amounts of high-speed catalyst particles and gaseous H_2S can reach the turbo-expander. The fracture surface was analyzed macroscopically using a stereo microscope, revealing two distinct fracture patterns, as shown in Figure 1. The fracture had its onset on the surface, where fatigue beach marks are visible. In a second area, the fracture surface indicates that overload led to the rupture of the blade. The interface between them is indicated with a dashed line. After observing the macroscopic features of the fracture, further analysis was conducted using a Zeiss EVO 10 Scanning Electron Microscope (SEM). SEM images (Figure 2) revealed that the coating layer remained adhered to the surface. Beach marks were visible only on the blade body, suggesting that the fatigue did not happened in the coating. Additionally, cracks were identified within the coating, which may have been critical to the failure of the component. One hypothesis is that these coating cracks propagated several tens of micrometers into the base metal, creating a region of high stress concentration that facilitated the nucleation of a fatigue crack. Moreover, backscattered

PÚBLICA

electron analysis in the SEM revealed a pronounced contrast between the base metal and the surface of certain cracks in the blade body. Since differences in backscattered electron contrast can indicate variations in chemical composition, point analyses using energy-dispersive X-ray spectroscopy (EDX) were performed at these locations. The results showed an elevated concentration of sulfur on the surfaces of the cracks, likely due to a corrosive process. According to API RP 571, nickel-based alloys are susceptible to sulfidation. Above 918 K, high-nickel alloys can experience sulfidation and metal loss due to the formation of nickel sulfides beneath the metal surface - a phenomenon also referred to as hot corrosion. The findings suggest that cracks in the coating allowed the penetration of H_2S, leading to sulfidation and the creation of a stress concentration zone that facilitated fatigue crack nucleation. Although Inconel 738 is known for its excellent corrosion resistance, the evidence suggests that sulfidation occurred and may have played a significant role in the failure of this component. The routine use of SEM/EDX in Brazilian oil refineries is not yet standard practice. However, this equipment has significant potential to enhance failure analysis of process equipment, thereby reducing risks to both the environment and human safety [6].

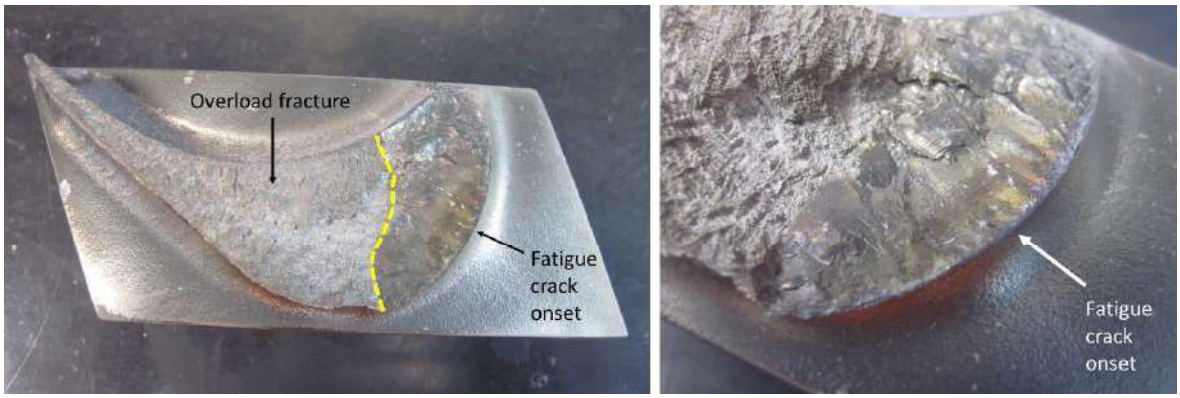

Figure 1: Macroscopic features of the fracture surface.

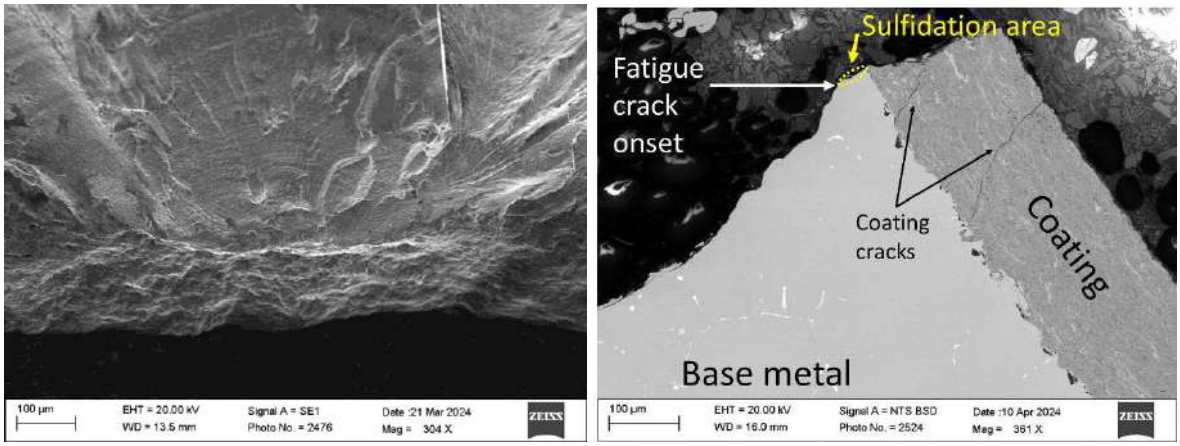

Figure 2: SEM image of the fracture onset. Beach marks can be seen in the blade metal.

[1] S.A. Treese, *et al*. Handbook of Petroleum Processing. Springer, London, 2015.
[2] Y. Chen. Powder Technology. 163 (2006) 2-8.
[3] N.E.G. Fermoselli. Thermal Engineering. 9 (2010) 40-46.
[4] Nickel Institute. Alloy In-738 Technical Data – A practical guide to the use of nickel-containing alloys nº497 (2020).
[5] American Petroleum Institute – API RP 571 - Damage Mechanisms Affecting Fixed Equipment in the Refining Industry, 3ª ed, Washington, 2020.
[6] The authors acknowledge Petrobras for supporting this work.

PÚBLICA

Formation and Microstructure of Electrochemically Induced Niobium Hydrides

Audrey Marie Bedoch[1*], Guilherme Yuuki Koga[1], Guilherme Zepon[1]

.

[1] Federal University of São Carlos, Department of Materials Engineering
*audrey.bedoch@estudante.ufscar.br

Energy storage remains one of the key scientific challenges in enabling the widespread adoption of sustainable energy sources such as solar, tidal, and wind power. Due to their intermittent nature, these sources demand efficient and reliable storage solutions. Metal hydrides have emerged as promising candidates for safe, solid-state hydrogen storage. Certain metals can form hydrides either through direct reaction with hydrogen gas or via electrochemical processes in alkaline media. Gaining a deeper understanding of the electrochemical hydrogenation behavior of various metals and alloys is therefore essential for developing advanced materials for hydrogen storage. Niobium (Nb, α), a body-centered cubic (BCC) metal, is particularly attractive as it forms β-$NbH_{0.89}$ and δ-NbH_2 hydrides. However, the formation of Nb hydrides appears to be irreversible [1]. In this study, the phases formed during electrochemical hydrogenation and those remaining after hydrogen desorption were analyzed using X-ray diffraction (XRD), scanning electron microscopy (SEM), and electron backscatter diffraction (EBSD). The β-phase preferentially nucleates at α-phase grain boundaries, without altering grain size. The growth of the β-phase is governed by nucleation kinetics and interface motion, which accommodate structural expansion and the formation of crystallographic variants. Subsequently, the δ-phase forms as martensite-like plates through a displacive transformation, where nucleation follows isothermal martensitic behavior, and growth is diffusion-controlled, like to the formation of Widmanstätten ferrite. Microstructural analysis reveals δ-phase plates embedded within the surrounding β-phase. Due to hydrogen saturation, the δ-phase becomes trapped inside the β-matrix, rendering its decomposition irreversible at the same temperature. Complete hydride decomposition requires thermal activation to promote niobium atomic mobility and enable reconstructive phase transformations.

[1] A.M. Bedoch, G.Y. Koga, V. Roche, G. Zepon, Electrochemical Hydrogenation of Nb: Unraveling Structural and Surface Dynamics of Hydride Formation, J. Phys. Chem. C. 129 (2025) 8509–8520. https://doi.org/10.1021/acs.jpcc.5c00570.

[2] This research was financially supported by the Instituto Serrapilheira (grant number Serra-1709-17362) and the CNPq - National Council for Scientific and Technological Development (grant numbers 140179/2021-6 and 309467/2021-7). This study was also supported by the Coordination for the Improvement of Higher Education Personnel - Brazil (CAPES) - Finance Code 001. The authors thank the Laboratory of Structural Characterization (LCE/DEMA/UFSCar) for the general facilities and support to this research.

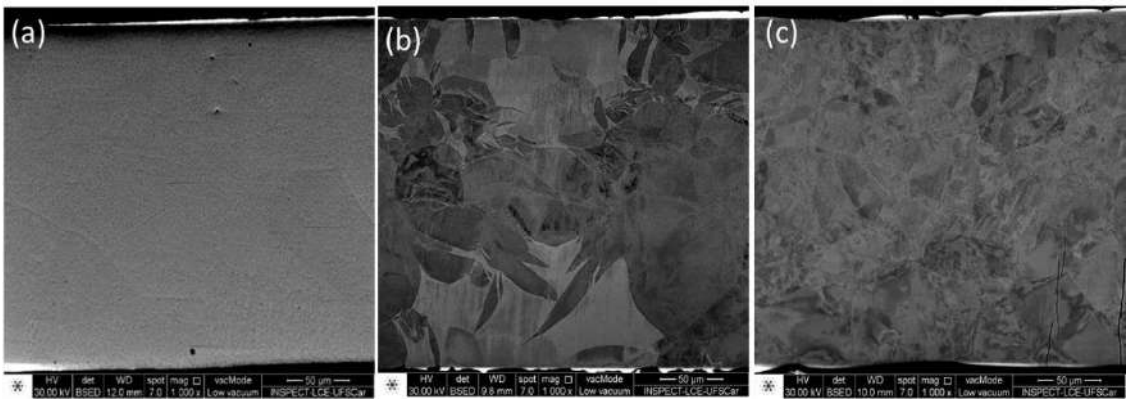

Figure 1. BSE images of **(a)** the Nb electrode in the initial condition; **(b)** the electrode containing both α and β phases (darker regions); and **(c)** the electrode containing only the β phase.

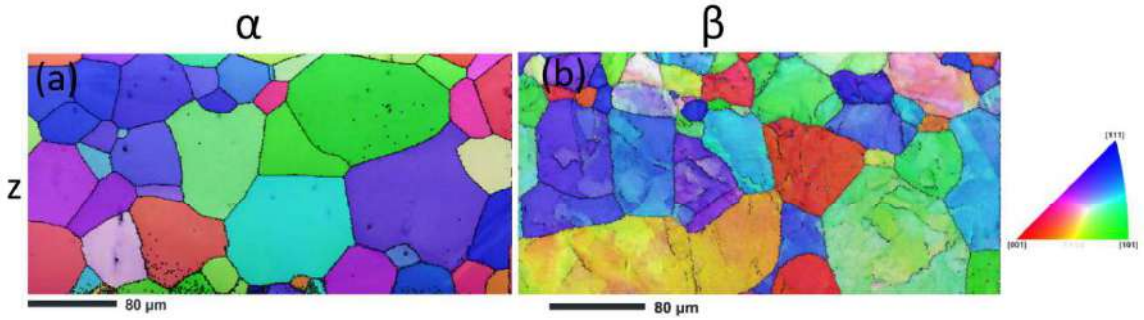

Figure 2. EBSD maps in the Z orientation of the samples: **(a)** initial Nb and **(b)** sample with 100% β-phase

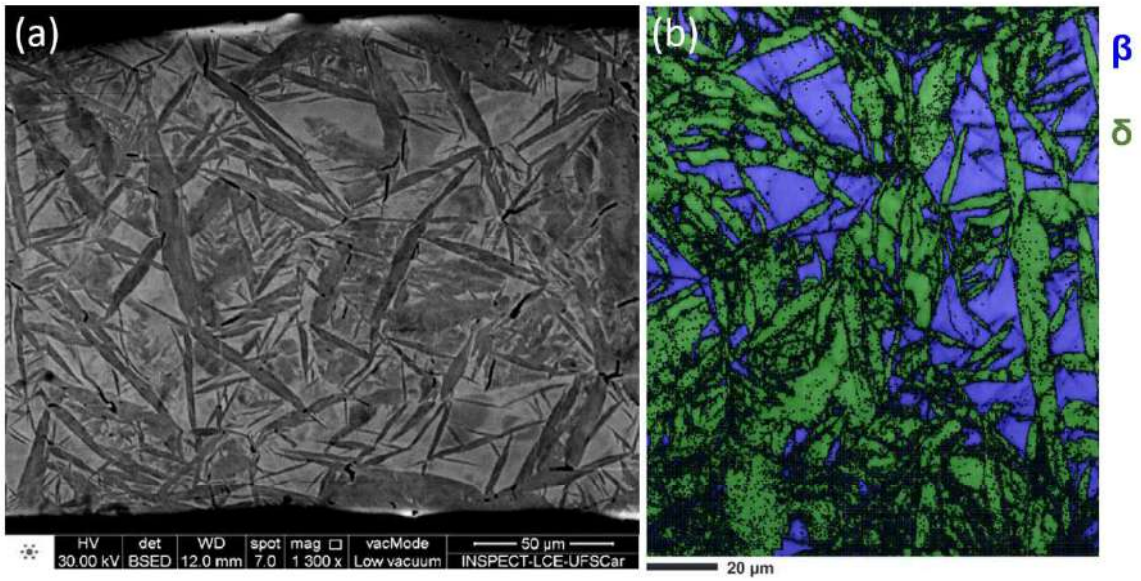

Figure 3. (a) BSE image after complete electrochemical hydrogenation, showing the presence of both β and δ (darker regions) phases. **(b)** Phase map of the same sample obtained by EBSD, indicating 42% of the β-phase (blue) and 58% of the δ-phase (green).

Graphene Nanoplatelets on Silicon Substrates: A Characterization Study for Lubricant Oil Applications

Juliana Ferreira dos Santos[1], Alessandro Dias de Oliveira[3], Alberto Nei Carvalho Costa[3], Matheus Costa Ximenes[1], Carolina Paz Correa Garin[4], Fábio Gatamorta[1] , Jose Brant de Campos[1], Deborah Vargas Cesar[2], Giovanna Machado[5], Mila Rosendahl Avelino[1,6] , Suzana Bottega Peripolli[1]

[1] Mechanical Engineering Department, Rio de Janeiro State University, 121, Fonseca Teles St, Rio de Janeiro, RJ 20940-200, Brazil
[2]Department of Analytical Chemistry, Chemical Institute, Rio de Janeiro State University, 524, São Francisco Xavier St, Rio de Janeiro, RJ 20550-900, Brazil
[3]CSN – Companhia Siderúrgica Nacional, BR 393 – Lúcio Meira Highway, KM 5,001, Santa Cecília Village, Volta Redonda, RJ, 27260-390, Brazil
[4] Labcorr - Corrosion Laboratory from COPPE/UFRJ, Federal University of Rio de Janeiro, Cid. Universitária-Centro de Tecnologia-Bloco I, Ilha do Fundão, 68505, Rio de Janeiro, RJ, 21941-972, Brazil
[5] Northeast Center for Strategic Technologies - CETENE, Technology Center, Avenue Professor Luiz Freire 1, Recife, PE, 50741-495, Brazil
[6] The National Institute of Metrology, Quality and Technology (INMETRO)
*julianafs100@gmail.com , speripolli@eng.uerj.br

This study explores the preparation and characterization of graphene nanoplatelets dispersion on a silicon substrate, which is a crucial step towards their application as additives in lubricating oils to enhance tribological performance. Due to its lamellar structure and exceptional physicochemical properties, including mechanical strength, thermal conductivity, and chemical stability, graphene holds significant promise for reducing friction and wear in mechanical systems. Nanomaterials such as graphene can notably improve key lubricant properties [1]. Previous research has demonstrated that both graphene oxide (GO) and reduced graphene oxide (rGO) are capable of significantly decreasing the coefficient of friction and wear rates, achieving enhancements of up to 51.85% in surface durability. These results are highly encouraging for extending the operational lifespan of moving mechanical components [2,3,4]. In this work, dispersions of three types of rGO - rGO, rGO 4, and rGO Plates, each synthesized via a distinct method, were prepared on silicon substrate and characterized using Scanning Electron Microscopy (SEM) and Energy Dispersive Spectroscopy (EDS) to assess their morphological features and dispersion uniformity. As illustrated in Figure 1, the SEM images provide visual evidence of the distinct structural features among the different rGO samples. Specifically, the rGO sample exhibited thinner and less wrinkled sheets, which is crucial for lubricating fluids, compared to the thicker, more agglomerated structures of the rGO 4 and rGO Plates samples. Previous studies directly link these structural characteristics of rGO to its tribological properties [3]. Preliminary findings suggest that silicon substrates facilitate more homogeneous dispersion compared to carbon tape, likely due to differences in surface energy and roughness [5]. Additionally, SEM-EDS analysis was conducted on the rGO samples deposited on silicon substrates, allowing for both elemental and morphological assessment. EDS mapping results, presented in Figure 2, confirmed the presence of carbon and oxygen from the graphene materials and silicon substrate, the successful application and characterization of the rGO on the substrate. The use of color-coded elemental maps enabled clear visualization of ultrathin graphene layers, as the underlying silicon signal remained partially visible beneath the rGO coatings. This observation is consistent with previous studies reporting that low accelerating voltage (low-kV) SEM-EDS enhances thin film resolution by reducing the interaction volume [1]. A qualitative elemental analysis by EDS confirmed the presence of only carbon, oxygen, and silicon in the samples, indicating the absence of significant contaminants. Overall, this study provides fundamental insights into the detailed characterization (morphological and elemental) of different rGO types when prepared on silicon substrates. This foundational assessment of their behavior lays important groundwork for their future optimization as additives in high-performance, environmentally sustainable lubricants, directly contributing to advancements in the metal-mechanical industry.

[1] Dai, W., Kheireddin, B., Gao, H. and Liang, H., *Roles of nanoparticles in oil lubrication*, *Tribology International*, vol. 102, pp. 88–98, 2016. https://doi.org/10.1016/j.triboint.2016.05.020.
[2] Chen, Z., Liu, Y. and Luo, J., *Tribological properties of few-layer graphene oxide sheets as oil-based lubricant additives*, *Chinese Journal of Mechanical Engineering*, vol. 29, no. 2, pp. 439–444, 2016. https://doi.org/10.3901/CJME.2015.1007.121.
[3] Patel, J., & Kiani, A. (2019). *Effects of reduced graphene oxide (rGO) at different concentrations on tribological properties of liquid base lubricants*. **Lubricants**, 7(2), 13. https://doi.org/10.3390/lubricants7020013
[4] Tang, Q. et al., *Ultrafast and stable dispersion of graphene oxide in lubricant oil toward excellent tribological property*, *Tribology International*, vol. 192, 108260, 2024. https://doi.org/10.1016/j.triboint.2024.108260.
[5] INMETRO. (2024). *Sample Preparation Protocol for Graphene Oxide for SEM and AFM Analyses (1)* [Confidential internal document]. Instituto Nacional de Metrologia, Qualidade e Tecnologia – INMETRO.
[6] This work was supported by the UERJ Extension Scholarship. The authors acknowledge the guidance and support of the Brazilian Center for Research in Physics (CBPF)

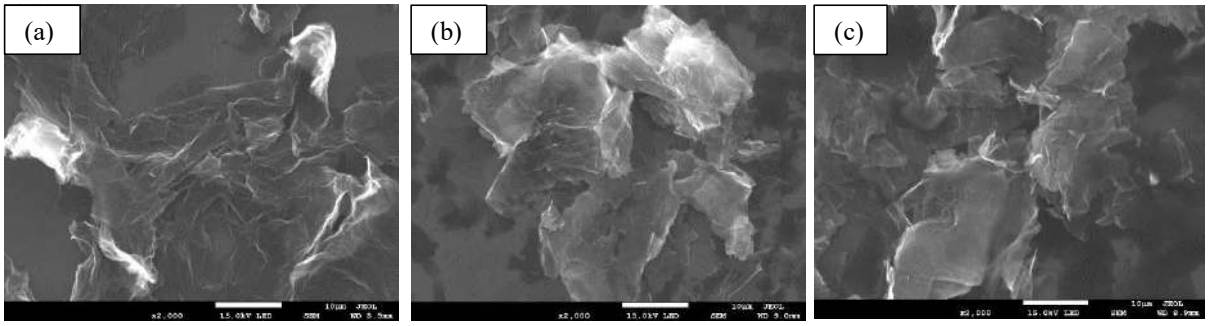

Figure 1. Scanning Electron Microscopy image, (a) rGO, (b) rGO-4, (c) rGO Plates

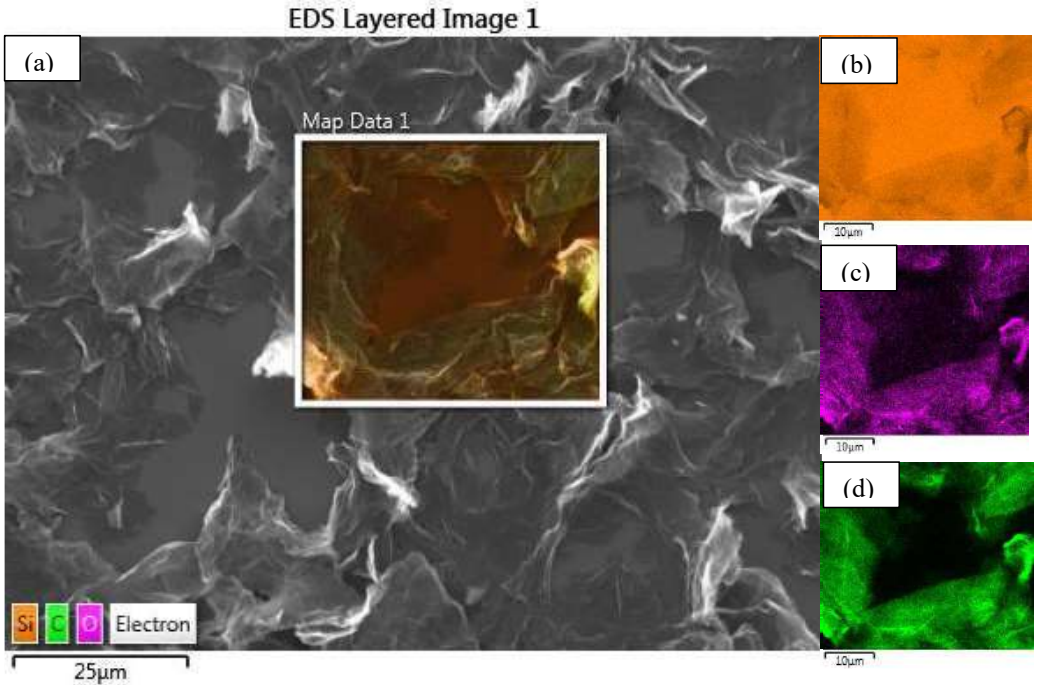

Figure 2. (a) SEM image from rGO and EDS mapping from (b) Silicon, (c) Oxygen and (d) Carbon.

Humidity Sensing with Manganese Oxide Nanofoam Film Prepared by Pulsed Laser Deposition

E.R. Nobre[1*]; D. Fajardo[1] ; C.S.C. Nogueira[1] ; D.F. Franceschini[1] ; Y.T. Xing[2].

[1] Instituto de Física, [2] Engenharia Química ,Universidade Federal Fluminense.
*evellynr@id.uff.br

Manganese oxide (MnOx) nanostructures have been widely investigated for humidity sensing applications due to their high surface reactivity, stability, and tunable electrical conductivity, which can range from 10^{-2} to 10^{2} S/cm depending on phase and structure [1,2]. Among the possible phases, Mn_3O_4 is commonly observed in oxide films deposited under moderate oxygen pressure, and X-ray diffraction (XRD) patterns typically confirm this phase as dominant [3]. Additionally, X-ray photoelectron spectroscopy (XPS) studies often report a Mn^{2+}/Mn^{3+} ratio near 1:2, consistent with the mixed-valence nature of Mn_3O_4 [4]. In this work, MnOx nanofoam films were fabricated using pulsed laser deposition (PLD) from a metallic Mn target (99.99%) in an oxygen atmosphere (~1.5 Torr), as illustrated in Figure 1. A Nd:YAG laser (λ = 1064 nm, 600 mJ/pulse, 10 Hz) was used for ablation, with the substrate kept at room temperature during deposition. Under these conditions, previous studies have reported uniform films with thicknesses around 2 μm and hybrid morphologies that combine nanostructured porosity with film continuity [5,6]. The deposited films have been analyzed using scanning electron microscopy (SEM) and lift-out were prepared with focused ion beam (FIB), for TEM work, in order to, investigate their surface morphology and microstructure, highlighting the nanostructured porosity and surface topology - critical to sensing performance, as shown in Figure 2a–c. The current stage of the study focuses on evaluating the humidity sensing performance of these MnOx films, particularly their sensitivity, response time, and stability in the 40–80% relative humidity (RH) range. Literature data show that MnOx sensors can reach sensitivities on the order of 10–15 kΩ/%RH, with response times below 5 s and hysteresis typically under 3% [7,8]. These values are strongly influenced by film morphology and surface chemistry. Humidity sensing tests will be carried out using interdigitated electrode configurations under constant current, by monitoring resistance changes as a function of humidity. According to previous reports, the sensing mechanism is related to the adsorption of water molecules, which affects both surface conductivity and oxidation states at the MnOx interface [9,10]. By optimizing PLD parameters and film architecture, we aim to develop a low-cost, reproducible sensor platform based on MnOx for environmental humidity monitoring.

Acknowledgements:
Capes, ANP/Petrobras, Faperj, CNPQ.

References:

[1] M.C. Biesinger et al., Appl. Surf. Sci. 257 (2011) 2717–2730.
[2] S. Ghosh et al., J. Phys. Chem. C 125 (2021) 19812–19824.
[3] X. Li et al., Micron 111 (2018) 21–29.
[4] Z. Zhao et al., Mater. Charact. 146 (2018) 43–51.
[5] D. Zhang et al., Sens. Actuators B 304 (2020) 127351.
[6] D. Zhang et al., Sens. Actuators B 304 (2020) 127351.
[7] K. Kim et al., Sens. Actuators B 327 (2021) 128893.
[8] Y. Xing et al., Appl. Surf. Sci. 510 (2020) 145489.
[9] J. Chrisey and G.K. Hubler, Pulsed Laser Deposition of Thin Films, Wiley, 1994.
[10] P.R. Willmott and J.R. Huber, Rev. Mod. Phys. 72 (2000) 315.
[11] W. Wang et al., ACS Appl. Mater. Interfaces 13 (2021) 9876–9887.

Figure 1. Photograph of the MnOx film during fabrication by pulsed laser deposition (PLD).

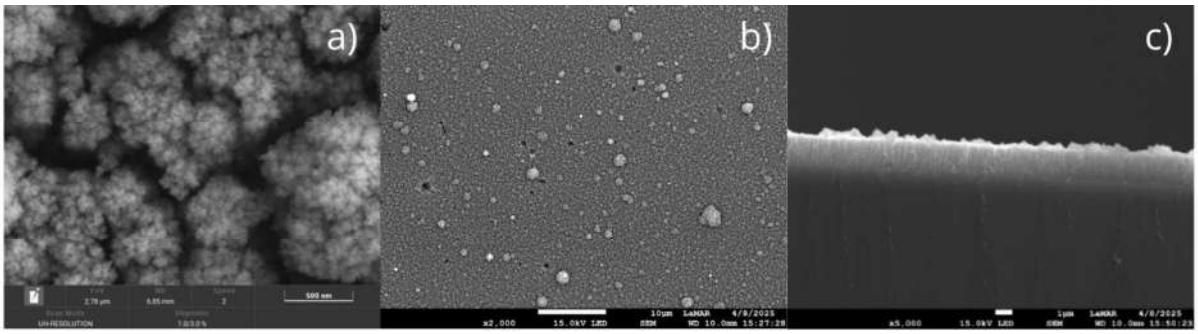

Figure 2a-c. As shown in Figure 2a–c, the MnOx film exhibits a porous and continuous morphology, as observed in the top-view SEM and FIB images (Figures 2a and 2b), and a well-defined interface, as revealed by the cross-sectional SEM image (Figure 2c).

Image Processing Pipeline and Composition Analysis in Mud Rocks using SEM and EDS Images

Maria Vitória Torres Finamore[1]*, Thalita Dias Pinheiro Caldas[1], Carlos Alberto Senna[1], Erveton Pinheiro Pinto[2], Rodrigo Prioli[1], Dorval Carvalho Dias-Filho[3], Marcos Klotz de Souza[3], Yaro M. Parizeck[3].

[1]Departamento de Física, Pontifícia Universidade Católica Do Rio De Janeiro, Rio De Janeiro, Brazil , [2] Universidade Federal do Amapá, [3]Petrobras, Rio De Janeiro, Brazil.
*torresfinamore@aluno.puc-rio.br

Mudrocks present significant challenges for analysis as a consequence of its fine-grained and mineralogically complex nature. This study introduces an image processing workflow and methodology for a quantitative characterization of mineral phases inside mudrocks using elemental maps obtained via Scanning Electron Microscopy (SEM), Energy Dispersive Spectroscopy (EDS), and a database created with an AI-based automated segmentation model. The proposed approach involves a logical routine arranged with the FIJI ImageJ software interface to pre-process the sample images, using tools to reduce noise, and apply Otsu's thresholding, separating mineral spectra from background signals and lessening intra-class variance of the associated histogram[1]. Figure 1 gives a visual example of the process, starting with a grey level image and an elemental map, as shown respectively in Figure 1a and Figure 1b, and after the aforementioned steps, the resulting image resembles Figure 1c. The new processed binary images of each main element identified inside the sample with EDS are then combined using bitwise operators and logic[1] (AND, OR, XOR) and reconstructed into mineral-specific maps of expected compositional phases[2]. Particle analysis is performed on the resulting binary images to quantify pixel percentages per area. Pore spaces and imaging artifacts quantified by the neural-network are then systematically excluded from the final area calculation to ensure an accurate final percentage of the total compound area. A final segmentation step is implemented, classifying the pixel area into three categories: (1) non-clay minerals[2], (2) clay minerals[2], and (3) others. The results are then compared against the results from the AI-based model, for further discussion on method assessment and efficiency. The primary focus of this study is the region classified as "non-clay minerals", as it shows more consistency throughout the process of the constructed workflow and logical routine. As an aim to reduce the region categorized as "others", be it by an optimization of the current pipeline, or by correctly identifying the remaining possible minerals inside the mudrock.

[1] Staib, L.H.,"The image processing handbook", 2nd edition, J. C. Russ. J Nucl Cardiol 5, 451–452, 1998, doi: 10.1016/S1071-3581(98)90154-4
[2] Deer, W. A., Howie, R. A., & Zussman, J., "An Introduction to the Rock-Forming Minerals", 3rd edition, Mineralogical Society of Great Britain and Ireland, 2013, doi: 10.1180/DHZ

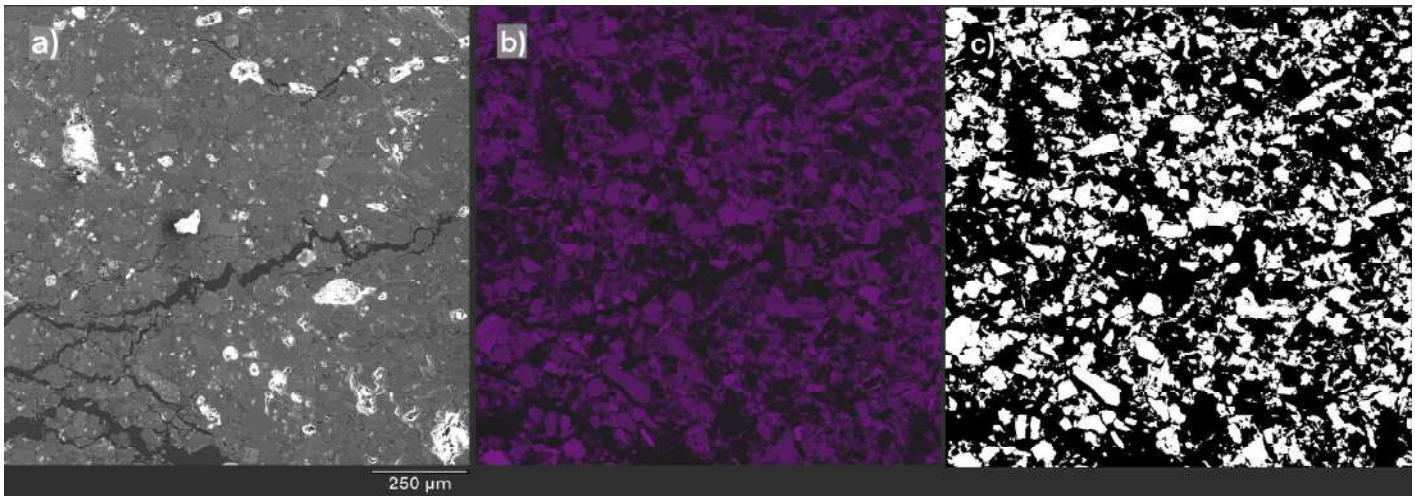

Figure 1. Different Images produced during the routine of the same sample. In a) the Grey level image of the surface, in b) the processed binary image of the Aluminum map, both obtained with SEM-EDS, and in c) the processed binary image.

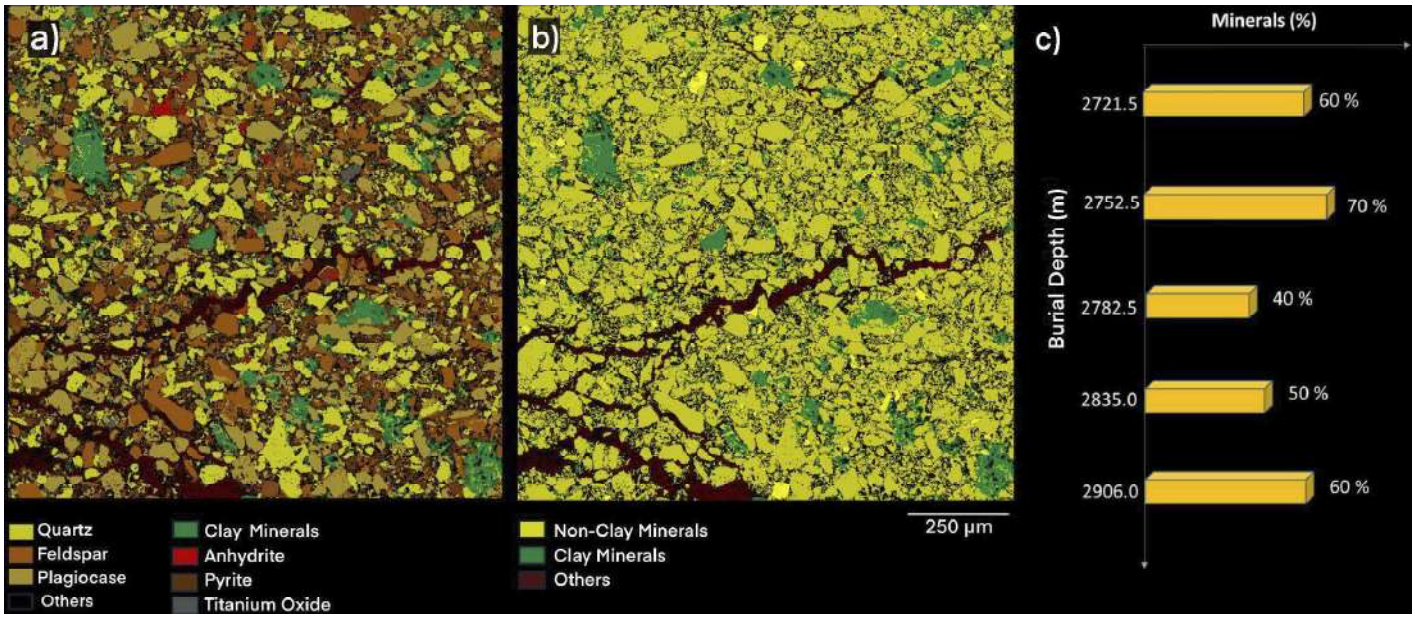

Figure 2. In a) image of the Grey-level map showing each mineral identified in a different color for a better view of the mineral fraction per pixel area, and in b) showing in yellow the phases classified as “non-clay minerals”, in green the phases classified as “clay minerals” and in brown the phases classified as “others”. In c) a graphic of the fraction of minerals per pixel area in function of the burial depth of the mudrock sample containing some of the samples used in the study.

Influence of Synthesis Parameters on Hydroxyapatite Morphology and Microstructure.

Mr. Camila Alves Pelicarto da Silva[1]*, Mr Kelllen Venancio dos Santos[1], Mr. Vinícius de Figueiredo Ilha Alves Pereira, Dr. Marilza Sampaio Aguilar[2], Dr.Francisco José Moura[3], Dr. Suzana Bottega Peripolli[1], Dr. José Brant de Campos[1].

[1] Rio de Janeiro State University, [2] Technical School Support Foundation (FAETEC), [3]Pontifical Catholic University of Rio de Janeiro.
*camilaalvespelicartodasilva@yahoo.com.br

Hydroxyapatite is widely used and recognized, especially in the field of biomaterials, for its properties that allow it not to harm the body, to interact positively with body tissues and to promote the growth of surrounding bone. These characteristics make it a very important material in this area [1]. Hydroxyapatite is also used in other areas, such as the pharmaceutical and cosmetics industries, and in the environmental sector, especially in water and soil treatment [2]. In order to act as a biomaterial, morphology and microstructure are fundamental, as they directly influence cell adhesion and bone tissue growth, favoring regeneration. Due to its wide applicability, hydroxyapatite can be produced in various ways, and for each type of preparation, a material with specific characteristics is obtained [3]. In this study, the synthesis method chosen was precipitation, as it is simple and efficient. This method consists of adding phosphate ions to a suspension containing calcium ions. In order to study the morphology and microstructure of hydroxyapatite from hen's eggshell, in this work we varied the dripping speed of the phosphoric acid, resulting in two types of hydroxyapatite Hap V1 (Phosphoric acid added directly) and Hap V2 (Gradual dripping speed). To analyze the morphology of the hydroxyapatites obtained, Scanning Electron Microscopy and particle size dispersion analyses were carried out, and Transmission Electron Microscopy (TEM) was used to analyze the microstructure. The images in Figure 1 show HapV1 and in Figure 2 Hap V2, both $Ca_{10}(PO_4)_6(OH)_2$ samples showed agglomerations characteristic of the precipitation synthesis method. However, the Hap V1 samples show a heterogeneous morphology, which indicates disordered crystalline growth and the presence of partially organized phases similar to those reported by Goh, et al. 2021. In Figure 2, the HapV2 sample showed a more homogeneous morphology. Figure 3A, referring to HapV1, shows a material with more disorganized planes, characteristic of a high nucleation rate. The particles in the HapV2 sample were larger because they had been aged long enough for the crystals to grow and organize better, as corroborated by the results presented in Tables 1 and 2. For biomaterial applications, HapV2 is more effective, as its greater crystallinity and uniform morphology favor cell adhesion, integration with bone tissue and a more controlled biological response, which are desirable characteristics for bone grafts.

[1] C. Coelho et al, Nano-hydroxyapatite in oral care cosmetics: characterization and cytotoxicity assessment. Scientific Reports, 9 (2019). https://doi.org/10.1038/s41598-019-47491-z.
[2] T. Varadavenkatesan et al, Synthesis, biological and environmental applications of hydroxyapatite and its composites with organic and inorganic coatings. Progress in Organic Coatings, 151 (2021). https://doi.org/10.1016/j.porgcoat.2020.106056.
[3] I. Ielo, G. Calabrese, G. de Luca, & S. Conoci, Recent Advances in Hydroxyapatite-Based Biocomposites for Bone Tissue Regeneration in Orthopedics. International Journal of Molecular Sciences, 23 (2022). https://doi.org/10.3390/ijms23179721.
[4] A.Yelten-Yilmaz & S. Yilmaz, S, Wet chemical precipitation synthesis of hydroxyapatite (HA) powders. Ceramics International, 44 (2018). https://doi.org/10.1016/J.CERAMINT.2018.02.201.
[5] K. W. Goh, et al, Effect of pH on the properties of eggshell-derived hydroxyapatite bioceramic synthesized by wet chemical method assisted by microwave irradiation. *Ceramics International* , (2021):

Figure 1. Scanning electron microscopy images Hap V1 at magnification A) 5 kx B) and C) 15 kx .

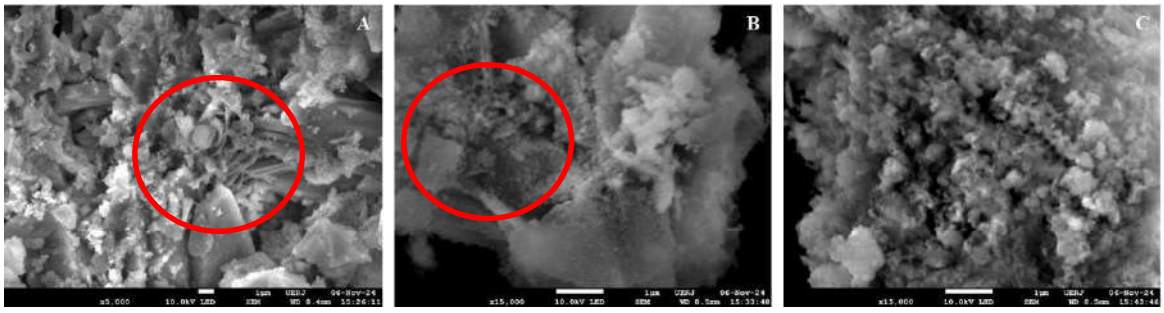

Figure 2. Scanning electron microscopy images Hap V_2 at magnification A) 10 kx B) and C) 15 kx.

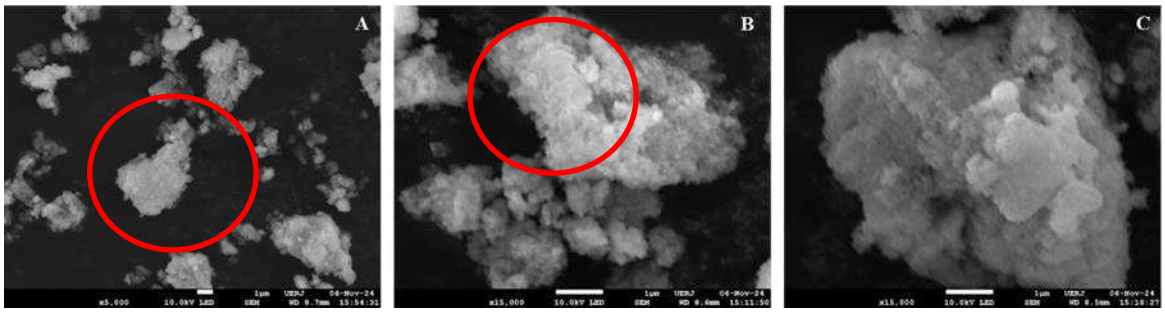

Figure 3. A) Transmission Electron Microscpy images at Hap V1 e B) Hap V2.

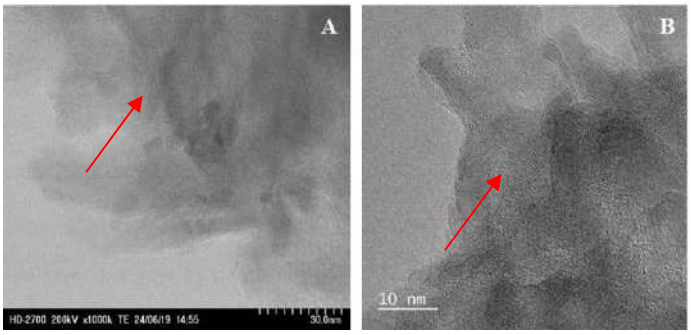

Table 1. Laser Light Scattering HapV1 particle size distribution.

Ultrasound time (s)	D10 (µm)	D50 (µm)	D90 (µm)
0	11,764	113,171	457,373
2	2,8	21,846	52,757
6	2,379	17,849	48,006

Table 2. Laser Light Scattering HapV2particle size distribution.

Tempo de Ultrassom (s)	D10 (µm)	D50 (µm)	D90 (µm)
0	9,750	179,518	613,578
2	2,140	17,497	62,092
6	1,916	11,815	48,566

Investigation of TNZT Alloy Processed by Spark Plasma Sintering and Coated with TiO_2 Nanotubes

Márcia O. Taipina [1*] , Carolina Bertanha Peruchi [2] , Tushar Borkar[3], Rubens Caram [1] , Rodrigo José Contieri [1-2], Alessandra Cremasco [1-2]

[1]University of Campinas (UNICAMP), School of Mechanical Engineering Campinas, SP, 13083- 860, Brazil
[2]University of Campinas (UNICAMP), School of Applied Sciences Limeira, SP, 13484350, Brazil
[3]Cleveland State University, Department of Mechanical Engineering, OH 44115, USA

*taipina@unicamp.br

In the field of orthopedics and orthopedic surgery, where cutting-edge technologies are constantly employed, advances in biocompatible materials have significantly improved surgical practices. Research on materials for orthopedic implants has focused on alloys such as Ti-6Al-4V; however, challenges such as mechanical strength and toxicity to adjacent tissues still persist. The phenomenon of 'stress shielding' [1], in which the transfer of forces between materials with different elastic moduli can lead to bone atrophy, exemplifies complications that remain to be addressed. The search for alloys with lower elastic modulus and improved ductility aims to mitigate these effects, enhancing the longevity and compatibility of implants [2]. The TNZT alloy, based on Ti, Nb, Zr, and Ta, was developed to offer low stiffness and to promote bone healing and remodeling, opening new possibilities for future orthopedic applications. Advanced techniques such as Spark Plasma Sintering (SPS) have created new opportunities for the fabrication of biomedical components, enabling the production of materials with homogeneous microstructures and optimized properties. These techniques are gaining prominence in research and development environments and advancing toward large-scale production applications. Among the surface modification techniques, the formation of nanostructured surface oxides has proven capable of enhancing biocompatibility as well as increasing the cellular activity of osteoblastic cells [3]. The main objective of this project is to characterize TNZT alloys produced by SPS and subsequently subject them to an anodization process to grow a nanostructured TiO_2 layer on the surface, in order to enhance the material's biocompatibility. After the anodization process the results revealed the formation of a nanostructured oxide layer on the surface of all the studied materials.

[1] M. Niinomi, M. Nakai, International Journal of Biomaterials (2011) 2011.
[2] M. Long, H.J. Rack, Biomaterials 19 (18) (1998) 1621.
[3] L. Zhang, T.J. Webster, Nano Today, v. 4, (2009) 66.

This research was supported by FAPESP (Sao Paulo Research Foundation, Grant 2018/18293-8).

Tabela 1. Nominal and measured composition (wt.%) measured by X-ray fluorescence of the studied materials.

Alloy	Nb		Ta		Zr		Ti	
	Nominal	Measured	Nominal	Measured	Nominal	Measured	Nominal	Measured
L1	30	28	20	21	5	5	45	46
L2	35	31	20	21	5	5	40	43
L3	35	31	5	9	7	7	53	53
L4	35	32	5	6	7	7	53	55

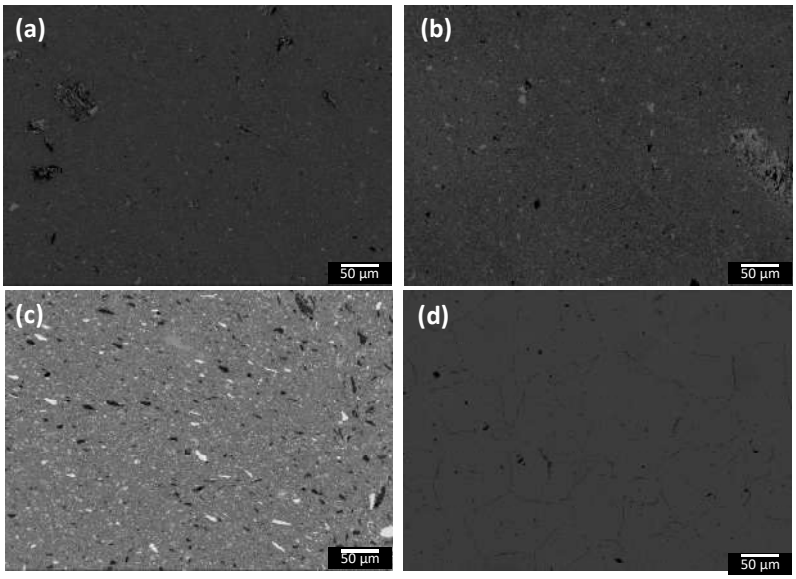

Figure 1. SEM Micrographs of the studied alloys: (a) L1, (b) L2, (c) L3 and (d) L4.

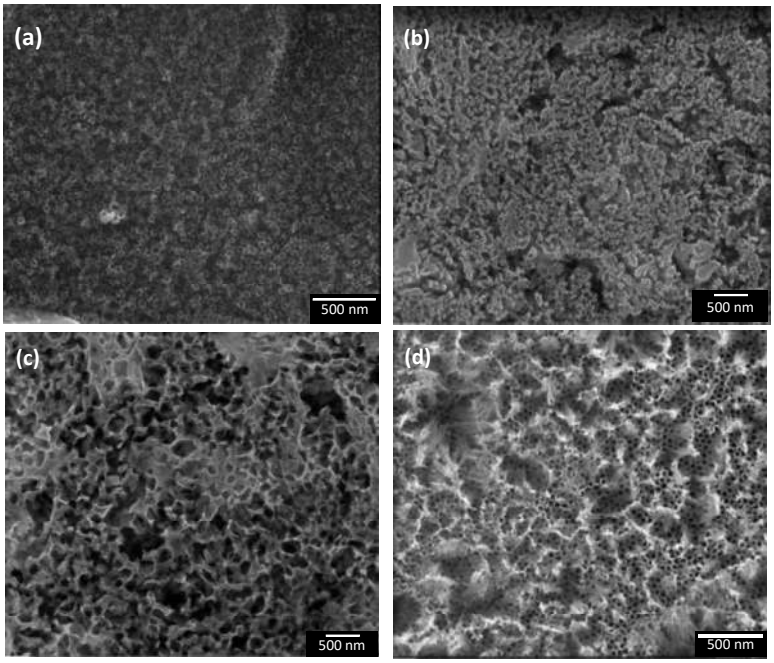

Figure 2: SEM micrographs of the obtained TiO_2 on different alloys: a) L1, (b) L2, (c) L3 and (d) L4.

Simple and green production of lignin nanoparticles using ethanol–water mixtures and ultrasonication

Eduardo Genner Ferreira de Almeida[1], Lucas Galhardo Pimenta Tienne[2], Braulio Soares Archanjo[3], Felipe Sampaio Alencastro[4], Tiago Albertini Balbino[1], and Renata Antoun Simao[4,*],

[1]Programa de Engenharia da Nanotecnologia, UFRJ, [2]Departamento de Ciência e Tecnologia de Polímeros, IMA, UFRJ, [3]Instituto Nacional de Metrologia, Inmetro, [4]Programa de Engenharia Metalúrgica e de Materiais, UFRJ

*renata@metalmat.ufrj.br

Lignin hollow nanoparticles is viewed as a promising pathway for producing green drug delivery systems. Mainly, they are being prepared by solvent shifting (self-assembly), due to their high applicability and potential to afford products in good shape. In a typical solvent shifting process, lignin is dissolved in an organic solvent, followed by mixing it with an excess of anti-solvent, and then lignin nanoparticles are generated where the hydrophobic lignin structure aggregates into micellar structure, where the micelle shell is composed by the hydrophobic end groups while the hydrophilic aliphatic hydroxyl groups form the shell structure. The solvents usually employed are THF, DMSO and acetone [2] and the idea of the use of natural materials does not match with the use of expensive or strong and toxic solvents. In this work, we report the production of lignin round shaped particles sized in the range of hundred nanometers produced by ultrasound sonification in water/ ethanol solutions at different relative concentrations. It was observed that solvent relative concentration is a key factor for determining the solubility and shape of the formed nanostructures. SEM will be used to follow the process of particle formation in different solvents and different sonification times.

Kraft lignin (alkali, low sulfonated), obtained from Sigma-Aldrich, was used without further purification. Ethanol (≥99.5%, analytical grade) was purchased from Vetec and used as received. Ultrapure water (resistivity 18.2 MΩ·cm) was obtained using a Milli-Q purification system. LNPs were synthesized using an environmentally friendly nanoprecipitation approach involving ethanol-water solutions at a volume ratio of 50:50 (ethanol:water, v/v), to investigate the influence of ultrasound stirring on nanoparticle formation. In each experiment, 20 mg of lignin were added to 20mL of ethanol-water solution resulting in a final concentration of 1mg/mL.

For all formulations, the solvent mixture was prepared prior to lignin addition, and the solid lignin powder was directly introduced into the solution. The dispersions were magnetically stirred for 20 min to promote dissolution and partial solubilization of lignin aggregates. No surfactants, pH adjustments, or chemical additives were used throughout the process, distinguishing this procedure from more complex or chemically intensive methods reported previously. The final samples were let to decant for 24 h and then poured in a silicon wafer for SEM analysis.Ultrasonication was employed to assist nanoparticle control and reduce particle size. Samples were subjected to ultrasonic treatment using a sonicator bath Quimis 03/350 operating at 40 kHz and 160 W. Sonication was performed for up to 4 h under ambient temperature, while control samples were maintained under magnetic stirring alone (0 h ultrasonication). All dispersions were subsequently stored in falcon tubes for further analysis. Representative SEM images (Figure 1) reveal the

morphology of LNPs synthesized under selected conditions, specifically, 0.5 h and 1 h of ultrasonication. Hollow lignin nanoparticles were produced in 50% ethanol, the morphology was predominantly spherical with relatively smooth surfaces and after 1 hour of ultrasonication the particles appear to be hollow. This suggests that ultrasonication facilitates disaggregation and fragmentation of lignin clusters, promoting the formation of uniform nanostructures in moderately polar media[10]. This way, we demonstrated a simple, eco-friendly method for producing LNPs using only ethanol–water mixtures and ultrasonication, without the need for surfactants, toxic solvents, or chemical modifications. The results highlight the influence of sonication time on nanoparticle formation, size, and morphology.

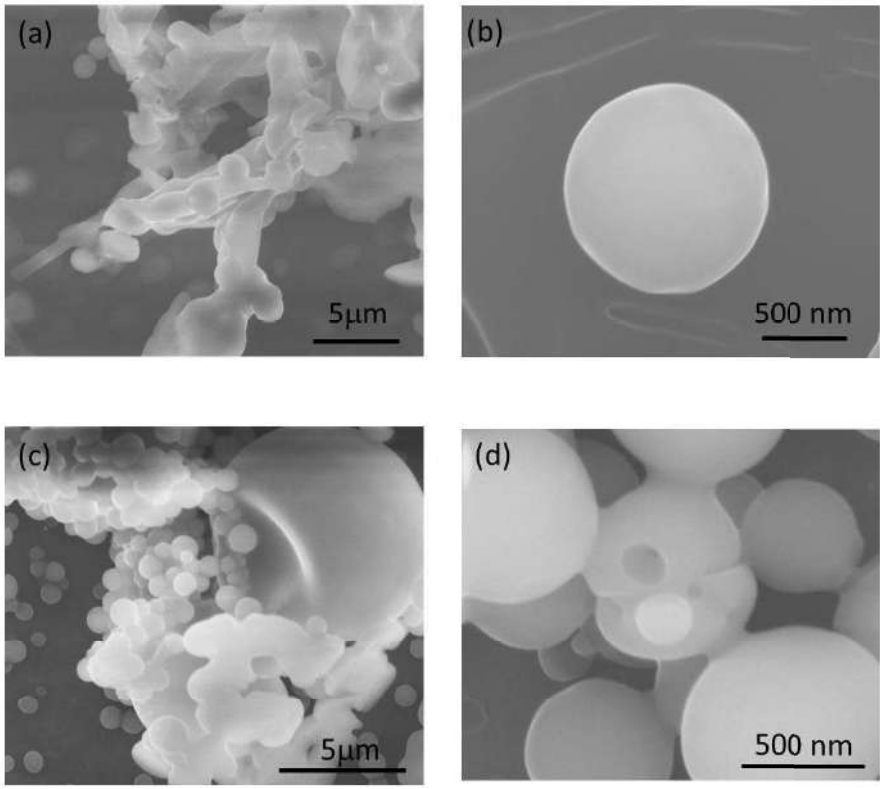

Figure 1. SEM images of lignin nanoparticles (LNPs) synthesized in 50% ethanol at different ultrasonication times (a) and (b) 0.5 h and (c) and (d) 1 h.

References

1. Y. Zhou et al., Nanoparticles 9 2019) 997.
2. S.Li et al., Ind. Crops and prod. 171 (2021) 113860.
3. Q. Tang et al., Polymers 12 (2020) 2471

Authors acknowledge to CNPq and FAPERJ for financial support

Microfabrication of Nanostructures by FIB Milling; Parameters Calibration on Si and Si+Au/Pd Substrates

Vitor M. Bertani[1]*, Yuri H. Isayama [1], Jéssica A. de Paula[2], Henrique Limborço[2], Wesller G. Schmidt[2], Wagner N. Rodrigues[1,2].

[1]Departamento de Física, Universidade Federal de Minas Gerais, Belo Horizonte, MG 31.270-901, Brazil
[2] Centro de Microscopia, Universidade Federal de Minas Gerais, Belo Horizonte, MG 31270-901, Brazil
*vitormbertani@gmail.com

In the pursuit of precision in microfabrication, the predictability of results from fabrication tools is critical. This study presents preliminary milling calibration of Si, SiO2 and Au/Pd coated Si by Ga+ Focused Ion Beam (FIB) aiming the fabrication of templates for nanostructures arrays. Two types of nanostructures will be produced: arrays of gold nanorods and arrays of gold nanopyramids. Both are plasmonic systems that will be used as SERS substrates. For the nanorods the template will consist of an array of cylindrical cavities machined in silicon, that will be subsequently filled with gold by thermal evaporation deposition. The nanopyramids template will be obtained by anisotropic etching of Si (100) oriented wafer. Apertures need to be opened in the silicon dioxide layer that covers the wafer using advanced lithography – as FIB or e-beam – and submitted to KOH etching. The procedure results in an array of nano pyramidal cavities. The deposition of gold by thermal evaporation on the described template will produce the aimed gold nanopyramids arrays. Extraction of the nano-objects arrays by stripping of cured resins applied on the gold film results on the SERS substrate[1]. Here the main motivation is to establish a reliable and predictable fabrication protocol, as the milling parameters programmed in a FIB system hardly reflect the real dimensions, thus requiring calibration. The methodology consisted of milling circular holes with specified diameters and depths using the FIB with different beam parameters, and subsequent evaluation of the produced craters by high-resolution topographical AFM images of the resulting structures. The results obtained for a silicon (Si) substrate and silicon coated with a gold-palladium (Au/Pd) film expose a strong non-linear deviation from the intended parameters. Specifically, for smaller holes with a diameter of 170 nm and spacing of 390 nm in Si, the milling efficiency dropped from 86% for holes with a 30 nm depth to 8% for an 800 nm target. This effect can be attributed to the redeposition of sputtered material inside the milled cavity, which becomes more significant in deeper holes. In contrast, larger holes with a 1.5 μm diameter in Si showed extreme over-milling at shallow depths; a programmed depth of 50 nm resulted in 190 nm (an efficiency of 380%). On the Si+Au/Pd substrate, where smaller holes with a 170 nm diameter and 390 nm spacing were milled, over-milling was present at shallower depths up to 100 nm. The central conclusion is that these preliminary tests demonstrate that there is no direct correlation between the programmed dimensions and the achieved result. To obtain precise and reproducible microfabrication, it is necessary to create calibration curves for each material and for each set of machining parameters. In Figure 1 we show the secondary electrons image of an example of calibration experiment. In Figure 2 the AFM image of the machined apertures is shown.

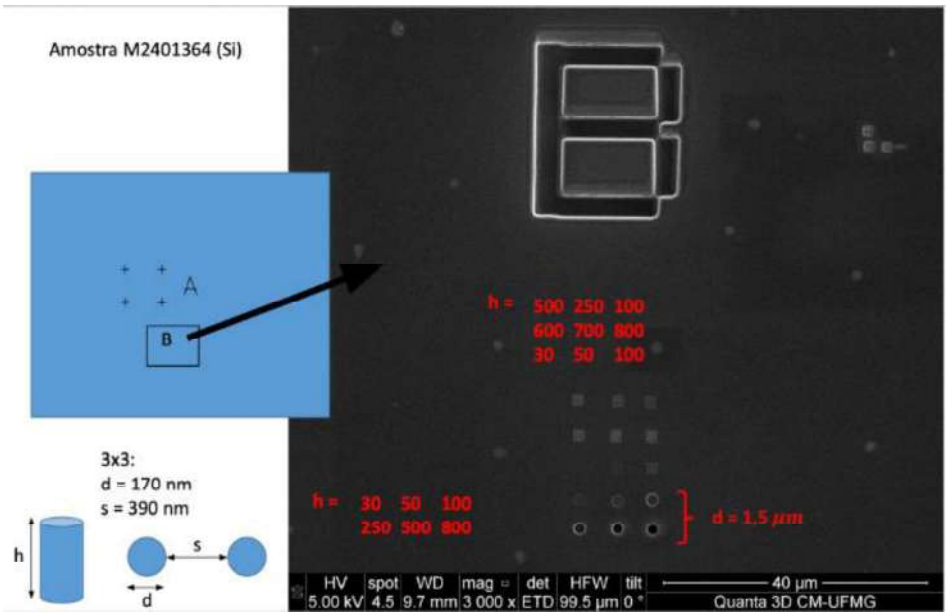

Fig. 1: arrays for determination of etching rates of silicon with different beam parameters.

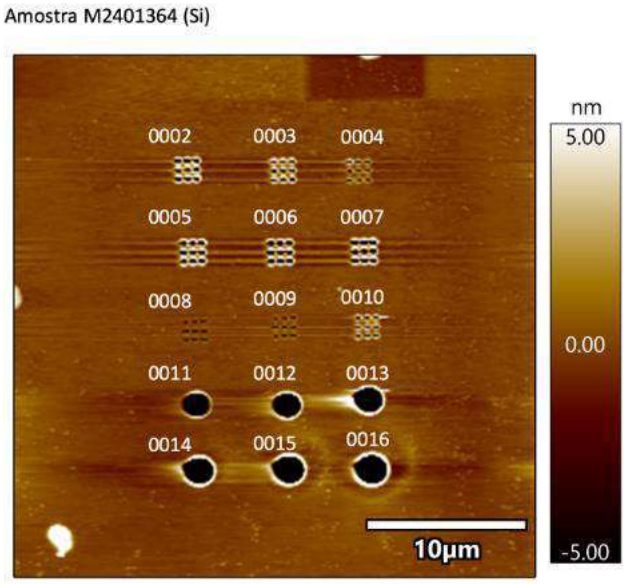

FIB	AFM		
30	25,7	86%	0008
50	27,5	55%	0009
100	34,8	35%	0004
100	34,9	35%	0010
250	46,7	19%	0003
500	59,7	12%	0002
600	56	9%	0005
700	54,2	8%	0006
800	62,8	8%	0007
30	86,7	289%	0011
50	190	380%	0012
100	195	195%	0013
250	302	121%	0014
500	303	61%	0015
800	303	38%	0016

Fig. 2: AFM image of the machined apertures shown in Fig.1.

[1] *Design and Experimental Demonstration of Pyramidal SERS Substrates with High-Throughput Fabrication Method*. Fabiano C. Santana et al., ACS Omega 2025, 10, 22760−22768.

Microstructural Analysis of Silicon Carbide Parts Printed by FFF with Gyroid Topology

Marllon Fraga Silva[1]*, Marcio Celso Fredel[2], Eduardo de Sousa Lima[1].

[1]Military Institute of Engineering - IME, [2] Federal University of Santa Catarina - UFSC
*marllon.1@hotmail.com

This work analyzes the use of additive manufacturing by Fused Filament Fabrication (FFF) for producing silicon carbide (SiC) components with gyroid-type infill, a geometry classified as a triply periodic minimal surface (TPMS) known for promoting mechanical isotropy, stress distribution, and efficient gas flow [1,2]. SiC is widely used in critical applications due to its high hardness, chemical inertness, and thermal stability above 2000 °C, which make it suitable for aerospace, defense, and energy systems [3]. However, its brittleness and processing limitations challenge conventional manufacturing, especially for complex geometries. The FFF process, adapted for ceramic-loaded thermoplastic filaments, allows layer-by-layer construction of intricate green bodies. In this study, SiC filaments were used to print gyroid-infill components (Figure 1), which underwent chemical debinding in acetone, thermal debinding in inert atmosphere, and sintering at 2185 °C, resulting in dense, with minimal defects [4]. The gyroid architecture proved advantageous across all stages. Its continuous curvature aided stress homogenization, while its internal porosity facilitated binder removal and minimized defects such as delamination and shrinkage [5]. Microstructural characterization by Scanning Electron Microscopy (SEM) (Figure 2) showed consolidated layers, strong interfacial bonding, and low porosity. Energy Dispersive Spectroscopy (EDS) confirmed chemical purity, identifying only silicon and carbon (Figure 3) [6]. Studies indicate that gyroid-infill improves compressive strength and energy dissipation compared to conventional infill patterns, enhancing mechanical resilience and damage tolerance [7]. Applications in robotics and aerospace further support its use in lightweight structures demanding both strength and functionality [8]. Thus, the integration of SiC with architected TPMS-type infill via extrusion-based additive manufacturing presents a promising route for the development of high-performance ceramic components, uniting geometric versatility, structural efficiency, and material reliability.

[1] Pelanconi, M.; Ortona, A. Nature-inspired, ultra-lightweight structures with gyroid cores. Materials, v. 12, n. 24, p. 4134, 2019.
[2] Meet the gyroid. Plus Magazine, 2011.
[3] Gibson, I. et al. Additive Manufacturing Technologies. Springer, Cham, 2021.
[4] Mohamed, O. A. et al. Optimization of fused deposition modeling process parameters: a review. Advanced Manufacturing, v. 3, p. 42–53, 2015.
[5] Galha, L.; Gonzales, M. Série estruturas celulares: a engenharia imitando a natureza. UFABC Divulga Ciência, 2023.
[6] Silva, M. F., Fredel, M. C., Lima, E. S. Processo de manufatura aditiva na produção de cerâmicas utilizadas em sistemas de blindagem: uma revisão. Revista Observatorio de la Economia Latinoamericana, 2024.
[7] Yánez, A. et al. Compressive behaviour of gyroid lattice structures. Materials Science and Engineering, v. 68, p. 445–448, 2016.
[8] Stan, A.; Milodin, N. L. Robotic arm structural frame enhancement by gyroid lattice cube integration. International Journal of Mechatronics and Applied Mechanics, v. 2, n. 8, 2020.
[9] Dr. Eduardo de Sousa Lima would like to thank the National Council for Scientific and Technological Development - CNPq (project number 312161/2020-4) for the financial support.

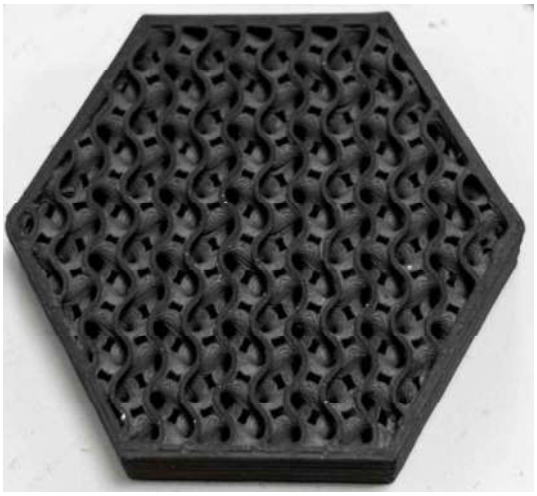

Figure 1. Hexagonal silicon carbide sample printed with gyroid infill via FFF.

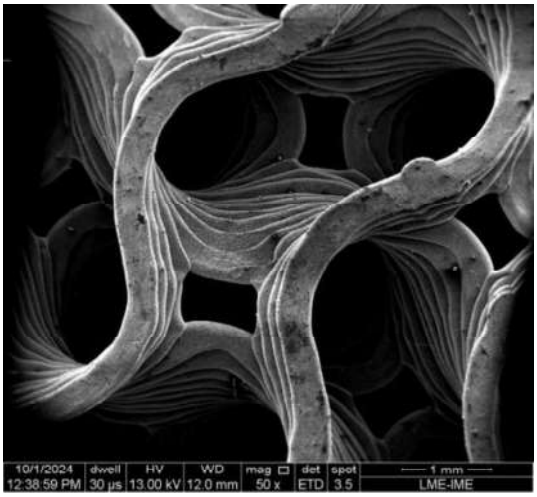

Figure 2. SEM image (50×) showing gyroid architecture and interlayer bonding.

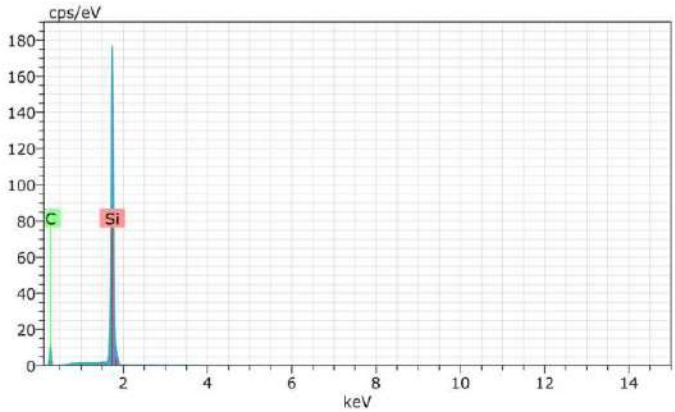

Figure 3. EDS spectrum confirming chemical purity: only Si and C detected.

Microstructural Characterization by SEM of Accelerated Leaching Products in Cement Pastes

Roseli das Graças Padre[1]*, Ricardo Damian Rodriguez Baez[1], Mauricio Kazuto Ichikawa[1].

[1]Itaipu Binacional
*rpadre@itaipu.gov.br

Leaching in concrete is a chemical degradation process that compromises the durability and structural integrity of civil works exposed to pure water or aggressive solutions. This phenomenon occurs mainly due to the dissolution and migration of hydrated compounds from the cementitious matrix, such as calcium hydroxide ($Ca(OH)_2$), leading to increased porosity, reduced mechanical strength, and exposure of metallic reinforcements to corrosion [1]. Accelerated leaching studies have been conducted using ammonium nitrate (NH_4NO_3) and ammonium chloride (NH_4Cl) solutions, which intensify calcium ion extraction and simulate, in less time, the effects of aggressive environments on concrete [2]. Due to its high solubility and ion exchange capacity, ammonium nitrate selectively dissolves portlandite and destabilizes the C-S-H phase, resulting in mass and strength loss [3]. Ammonium chloride, in addition to acting as a leaching agent, introduces chloride ions that can accelerate reinforcement corrosion, making it particularly relevant in durability studies of structures exposed to marine or industrial environments [4]. Scanning electron microscopy (SEM) has proven to be an essential tool for characterizing the microstructure of leached concrete. Through morphological analysis and chemical composition via energy-dispersive X-ray spectroscopy (EDS), it is possible to identify degradation products such as calcium carbonate ($CaCO_3$), silica gel, and secondary ettringite, as well as map zones of chemical attack and evaluate pore connectivity [5,6]. The formation of preferential flow channels and disaggregation of the cement matrix are typical signs observed in samples subjected to accelerated leaching [7]. In this study, cement pastes of CP IV in cubic format (5×5×5 cm) were exposed to leaching solutions of 2N ammonium nitrate and 2N ammonium chloride. After exposure, the concentration of calcium extracted from the cement pastes was determined by complexometric titration using 0.05N EDTA (Ethylenediaminetetraacetic acid). Morphological and microstructural characterization of the resulting products from the accelerated leaching was also carried out using SEM. As a result, the study showed that the ammonium nitrate solution was more aggressive than the ammonium chloride solution, extracting more calcium compounds from the cement pastes. In the pastes attacked with ammonium nitrate, the main degradation product found was ettringite, while in those attacked with ammonium chloride, the predominant product formed was calcium carbonate. Figure 01 presents the images of the cement paste obtained using the Tescan Vega3 SEM model.

[1] H. F. W. Taylor, Cement Chemistry. 2. ed. London: Thomas Telford, 1997.
[2] Q. T. Phung, et al. Effect of ammonium nitrate solution on the degradation of cement paste: Leaching kinetics and microstructural changes. Cement and Concrete Research, v. 79, p. 1–15, 2016.
[3] P. G. Goularte, A. C. P. Santos. Lixiviação acelerada em materiais cimentícios: avaliação da influência dos materiais cimentícios complementares como adições na matriz cimentícia. UNILA, 2024.
[4] F. K. Sell Junior, et al. Avaliação experimental de métodos acelerados de determinação do coeficiente de difusão de cloretos no concreto. Revista IBRACON de Estruturas e Materiais, v. 14, n. 4, 2021.
[5] B. A. Dedavid, C. I. Gomes, G. Machado, Microscopia eletrônica de varredura: aplicações e preparação de amostras. Porto Alegre: EDIPUCRS, 2007.
[6] R. L. Henriques, Utilização da microscopia eletrônica de varredura (MEV) para

avaliação da ação de cloretos em compósitos de matriz cimentícia. UFMG, 2019.
[7] E. Rozièr, et al. Durability of concrete exposed to ammonium nitrate: Influence of cement type and supplementary materials. Materials and Structures, v. 42, p. 1–12, 2009.
[8] This research was supported by Itaipu Binacional.

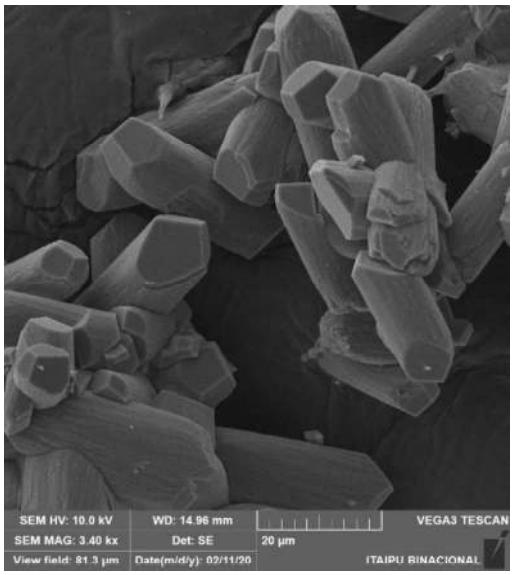

a) Cement paste attacked by NH_4Cl. Calcium carbonate crystals.

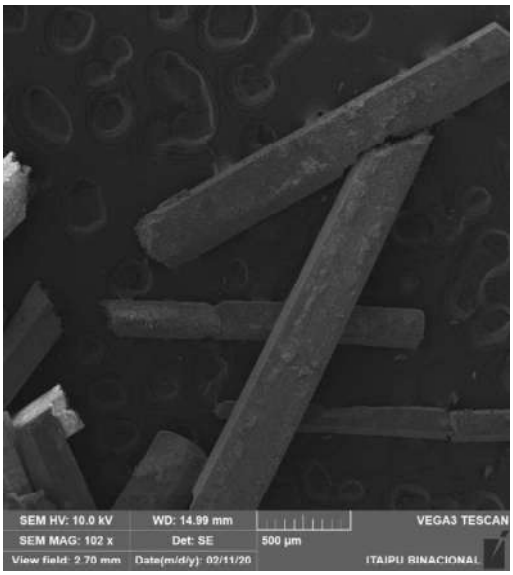

b) Cement paste attacked by NH_4NO_3. Ettringite crystals.

Figure 1. Images obtained by SEM. Pastes attacked by ammonium chloride (a) and ammonium nitrate (b).

Microstructural Characterization of Thermo-Reactive Diffusion Coating on AISI 1513 Steel Produced with Titanium Chips Recycling

Vitor S. Rolin[1], José Gedael Fagundes Jr[2], Vicente A. Ventrella[1,2] and Juno Gallego[1,2*]

[1] Post-Graduate Program in Mechanical Engineering at UNESP – Ilha Solteira.
[2] Department of Mechanical Engineering, São Paulo State University – UNESP, Ilha Solteira, São Paulo, CEP 15.385-007, Brazil.
* juno.gallego@unesp.br

Life of tools and mechanical parts is commonly shortened due to failures caused by wear and corrosion. A solution to reduce these drawbacks is the strengthening of surfaces by thermochemical treatments, such as thermo-reactive diffusion (TRD) [1-2]. An innovative and sustainable processing for that treatment is recycling of titanium chips, generated after machining of ASTM F67 bars for dental implant production, to be applied for TRD. In this work small pieces (20 x 15 x 3mm) of AISI 1513 carbon-manganese steel with composition 0.14C, 1.35Mn, 0.25Si (%wt) were submitted to TRD treatments, using 2.5kW electric furnace, performed in 90-95g KCl-NaCl eutectic mixture added with 5-10g of Ti chips inside 150ml porcelain crucibles. Samples were maintained in molten salt bath at 1000°C up to 4h. After TRD treatments samples were investigated by scanning electron microscopy (SEM), EDS microanalysis and X-ray diffraction (XRD). In all analyzed specimens was formed a titanium-rich coating on the surface of AISI 1513 steel, which thickness have increased with higher content of titanium and longer times. So, coating's thicknesses have changed from 1.1 to 6.1μm. The BSE contrast applied in the SEM micrographs presented in the Fig.1 shows that typical coating is composed by 2 distinctive layers, being visible in the outer layer heterogeneous grooving. The lack of homogeneity of this layer is possibly caused by the rapid growth and/or by the redissolution of Ti into the bath. The BSE contrast could be generated due to chemical partition during diffusion of the titanium from molten bath with the iron and carbon from the steel. EDS analysis presented in Fig.2 confirms that coating is mostly composed by titanium, being iron concentration gradually increase near steel substrate. Presence of carbon and oxygen was observed in higher concentration near to free surface, promoting the formation of titanium carbide in this region. X-ray diffraction results showed in Fig.3 confirms that layer is mainly composed by Ti-α, TiC and Fe-α after Rietveld refinement performed with PROFEX 5 software [3]. The obtained results are consistent with earlier reports [4] and confirm that thermo-reactive diffusion treatment performed using titanium chips is a reliable, sustainable e quite promising metallurgical process to improve surface properties of the non-alloyed steels. The authors are grateful for supporters [5].

REFERENCES

[1] A. Günen et al. Surface and Coatings Technology, 437 (2022) 128280.
[2] N. Lin et al. Journal of Physics and Chemistry of Solids, 129 (2019) 387-400.
[3] N. Döbelin, R. Kleeberg. Journal of Applied Crystallography, 48 (2015) 1573-1580.
[4] B. Kurt et al. Surface and Coatings Technology, 385, (2020) 125332.
[5] This research was supported by CAPES and CNPq (Brazil).

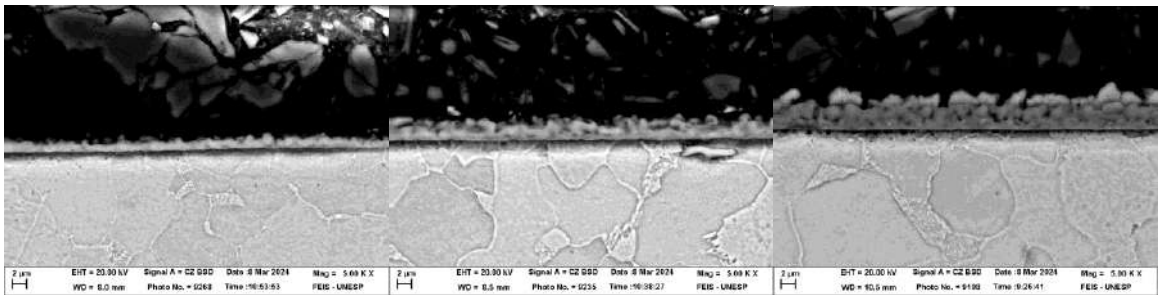

(a) (b) (c)

Fig.1: SEM micrographs showing obtained coating after TRD treatment with 10g Ti molten salt during 1h (a), 3h (b) and 4h (c).

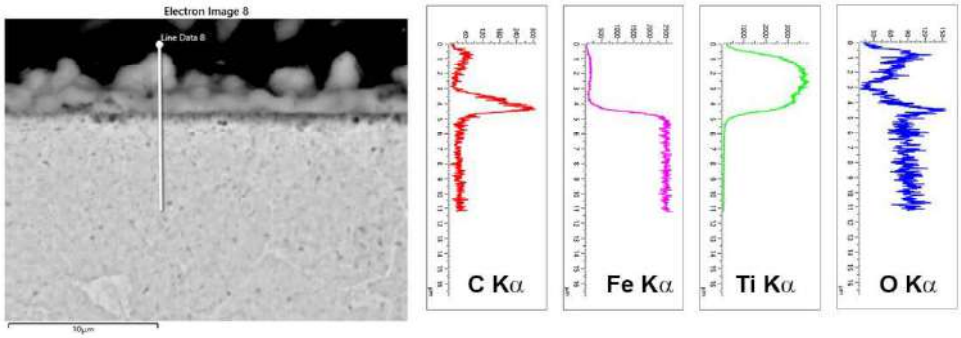

Fig.2: SEM micrograph with BSE contrast of Ti-rich TRD coating, showing EDS elemental line-scan with compositional variation of the C, Fe, Ti and O.

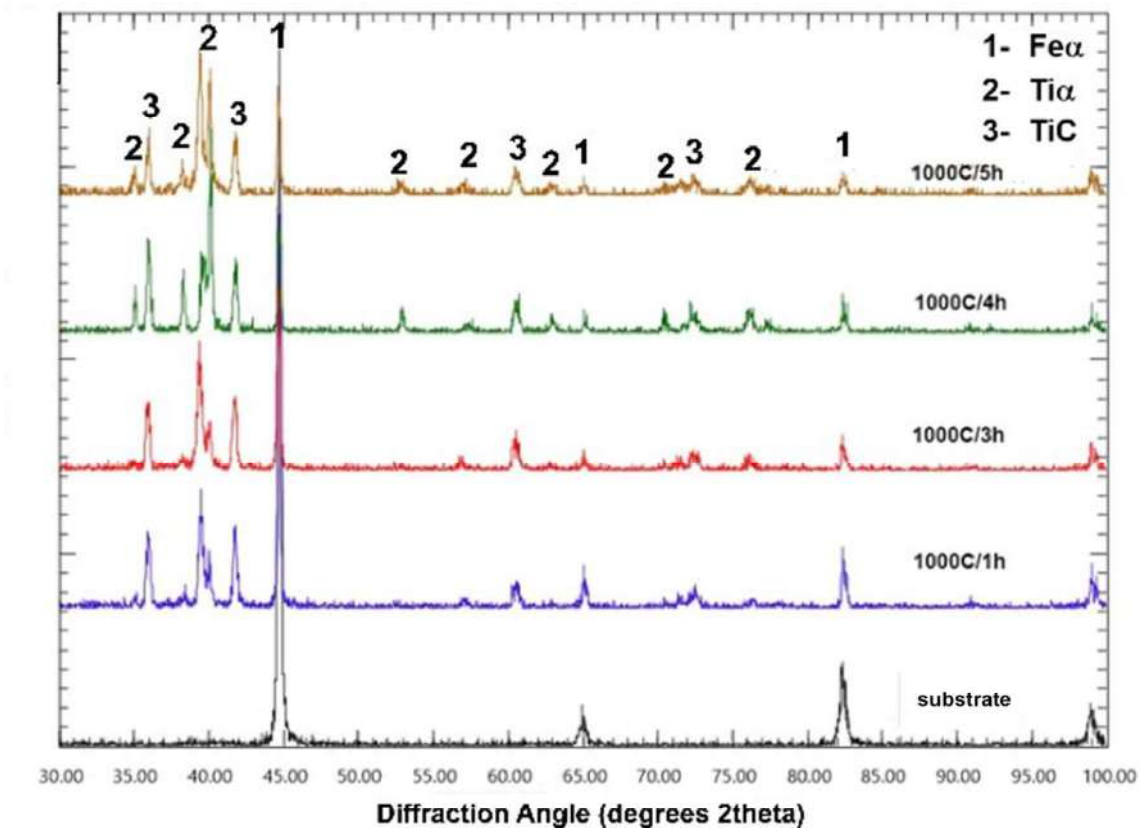

Fig.3: X-ray diffraction pattern of the coating obtained after TRD with 10g Ti chips.

Morphological Characterization of Piperine-loaded polymeric microparticles using Eudragit RS30D and S100

Andressa Novatski[1]*, Patricia Biscaia[2], Guilherme Camargo[2], Jéssica Nadal (PQ)[2], Paulo Farago[2]
[1]Departamento de Física, Universidade Estadual de Ponta Grossa, PR, Brasil.
[2]Departamento de Ciências Farmacêuticas, Universidade Estadual de Ponta Grossa, PR, Brasil.
*anovatski@uepg.br

Piperine (PIP), an alkaloid from *Piper nigrum* and *Piper longum* species, exhibits multiple pharmacological effects, including anti-inflammatory, analgesic, antidepressant, cytoprotective, antileukemic, and antioxidant activities, along with enhancement of drug bioavailability. Its thermogenic and fat-reducing properties make it a candidate for anti-obesity treatments; however, its high pungency limits dosing [1-2]. To improve PIP bioavailability and reduce side effects, polymeric microparticles were developed using Eudragit® RS30D and S100 polymers via spray drying. The formulations were prepared in ethanol:water (50:50, v/v). Morphological characterization was conducted using Field Emission Gun Scanning Electron Microscopy (FEG-SEM) (TESCAN, Mira 3, Brno, Czech Republic). Samples were gold-coated (IC-50 Ion Coater, SHIMADZU, Kyoto, Japan), and micrographs were obtained at 15 kV with Electron Optical Design software. Crystallinity was evaluated by X-ray Diffraction (XRD) using a Shimadzu XRD-6000 diffractometer, with a scan rate of 2° min^{-1} over a 2θ range of 5°–80°, Cu Kα radiation (λ = 1.5418 Å), at 40 mA and 40 kV. FEG-SEM analysis showed that RS30D-based microparticles (formulations MRS_P0, MRS_P5, and MRS_P10) displayed rounded shapes, homogeneous appearance, smooth surfaces, and absence of free drug on the surface. In contrast, the MRS_P20 formulation exhibited crystalline structures on the surface, indicating non-encapsulated PIP, which was confirmed by XRD. The micrographs are presented on Fig.1. S100-based microparticles (MS100 formulations) also demonstrated predominantly rounded morphology, with acceptable uniformity (Fig.2). Some particles exhibited surface roughness, concavities, and irregularities, attributed to shrinkage during the drying and cooling stages. These morphological features suggest structural changes resulting from the evaporation of solvents and capillary action on the dry surface, leading to sub-atmospheric internal pressure and consequent particle collapse [3]. Additionally, vacuole formation was observed, possibly related to solvent migration during the drying process. Moisture absorption during storage, combined with the impact of wet particles against the chamber wall during spray drying, further contributed to deformation, resulting in collapsed and agglomerated particles with altered viscosity [4]. Despite these modifications, the presence and increased concentration of PIP did not remarkably affect the size or overall morphology of the MS100 microparticles prepared in ethanol:water (50:50, v/v). The structural integrity of the MS100 systems remained suitable for drug delivery purposes, supporting their potential for modified release applications. These results confirm the successful production of PIP-loaded polymeric microparticles using spray drying, with both RS30D and S100 systems exhibiting promising characteristics for controlled drug release. The encapsulation approach represents a suitable strategy for the therapeutic application of PIP in obesity treatment, with the potential to reduce the adverse effects associated with its pungency.

[1] ASHOUR, E. A. et al. J. Pharm. Pharmacol., (2016) 989.
[2] WANG, L. et al. Mol. Nutr. Food Res., (2017) 61.
[3] KULKARNI, N. B.; NAIK, P. S. W. J. B. Int. J. Pharm. Pharm. Sci., (2013) 5.
[4] PORRAS-SAAVEDRA, J. et al. J. Food Eng., (2015) 105.
This research was supported by Capes, CNPq, FINEP and Fundação Araucária.

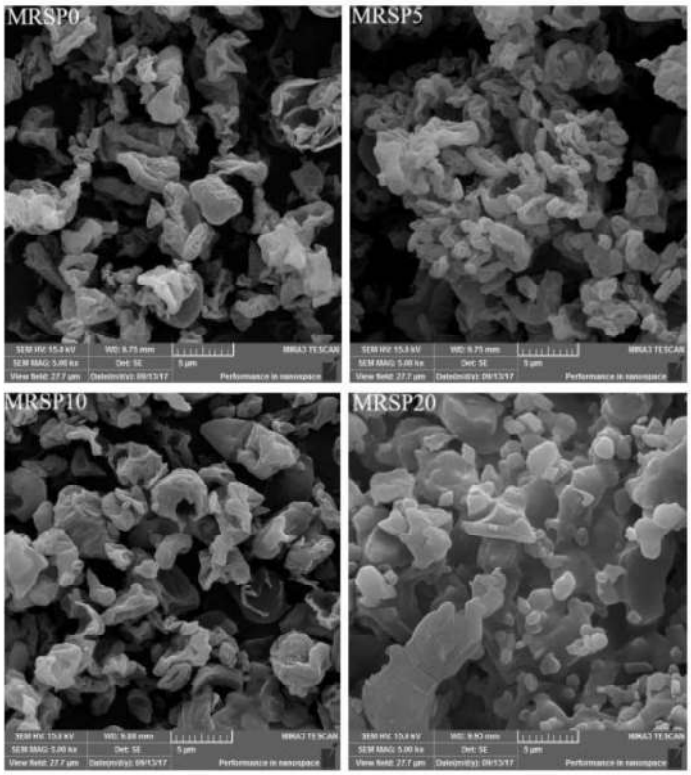

Figure 1. FEG-SEM micrographs of microparticles prepared with Eudragit® RS30D polymer containing or not piperine: MRS_P0, MRS_P5, MRS_P10, and MRS_P20, at 5000× magnification.

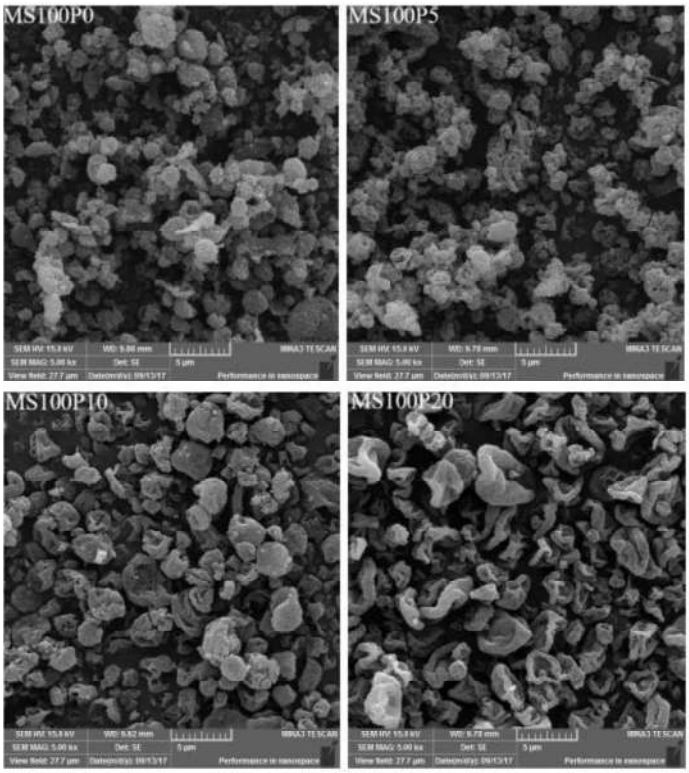

Figure 2. FEG-SEM micrographs of microparticles prepared with Eudragit® S100 polymer containing or not piperine: MS100_P0, MS100_P5, MS100_P10, and MS100_P20, at 5000× magnification.

Morphological Study of ZnO Nanorods Grown on Substrates with Plasma Etching for Spintronic Applications

Johanny Dark Lima de Sousa[1]*, Edycleyson Carlos de Souza[1], Filipe Riberio Rodrigues[1], Eduardo Padrón Hernández [1].

[1]Federal University of Pernambuco, Physics Department, PE, Brazil.
*johanny.dark@ufpe.br, edycleyson.souza.116@ufrn.edu.br,
filipe.ribeirorodrigues@ufpe.br, eduardo.hernandez@ufpe.br

Zinc oxide (ZnO) is a promising material for spintronic applications due to its semiconducting nature, wide bandgap (~3.37 eV), high exciton binding energy, and the possibility of exhibiting diluted magnetic semiconductor (DMS) behavior when doped with transition metals [1]. Among its various nanostructured forms, ZnO nanorods have been widely investigated owing to their high surface-area-to-volume ratio, anisotropic geometry, and ease of synthesis through cost-effective chemical methods. In this study, we investigate the influence of substrate surface preparation on the morphology of ZnO nanorods grown by chemical bath deposition (CBD) [2]. Specifically, we explore the role of plasma etching as a substrate pre-treatment technique. Plasma etching was employed to remove surface contaminants and to modify surface energy, with the goal of improving the adhesion and uniform vertical growth of the nanorods. The cleaned substrates were then used for the deposition of ZnO nanostructures under controlled chemical conditions.The resulting nanostructures were characterized by Scanning Electron Microscopy (SEM) to analyze morphological parameters such as diameter, length, aspect ratio, density, and alignment. The SEM images revealed that plasma-treated substrates led to more homogeneous and vertically aligned nanorods, with improved surface coverage and reduced defect density compared to untreated samples. These characteristics are particularly relevant for spintronic device performance, as structural uniformity and interface quality directly affect spin injection and transport [3]. The results demonstrate that plasma etching is an effective and reproducible method for enhancing the morphological quality of ZnO nanorods. This pre-treatment step can be considered a key factor in optimizing the synthesis process for future spintronic device fabrication, including spin valves, magnetic tunnel junctions, and spin-based sensors. Our findings contribute to the understanding of how surface engineering strategies influence the nanostructure growth and, ultimately, the functional properties of ZnO-based materials in spintronic applications.

[1] Naziba, A.Z., et al., Structural, optical, and magnetic properties of Co-doped ZnO nanorods: Advancements in room temperature ferromagnetic behavior for spintronic applications, *Elsevier B.V.* 134 (2024).
[2] Ruiz-Rojas, C.A., Aguilar-Frutis, M., Ramos-Brito, F. *et al.* Synthesis, characterization, and temperature-dependent electronic properties of ZnO nanorods using CBD techniques. *J Mater Sci: Mater Electron* 32, 8944–8957 (2021).
[3] Younas, I., Mohd, K.M., Chao W., Orientation and actual growth mechanism of ZnO nanorods through hydrothermal method on gold seed layer. *AIP Advances* 11, 125006 (2021).

Figure 1. SEM images of ZnO nanorods grown by chemical deposition on substrates subjected to plasma etching with different powers: (a) 250 W, with morphologically heterogeneous growth; (b) 500 W, showing pointed formation in the nanorods; and (c) 600 W, with well-defined hexagonal structures and vertical orientation.

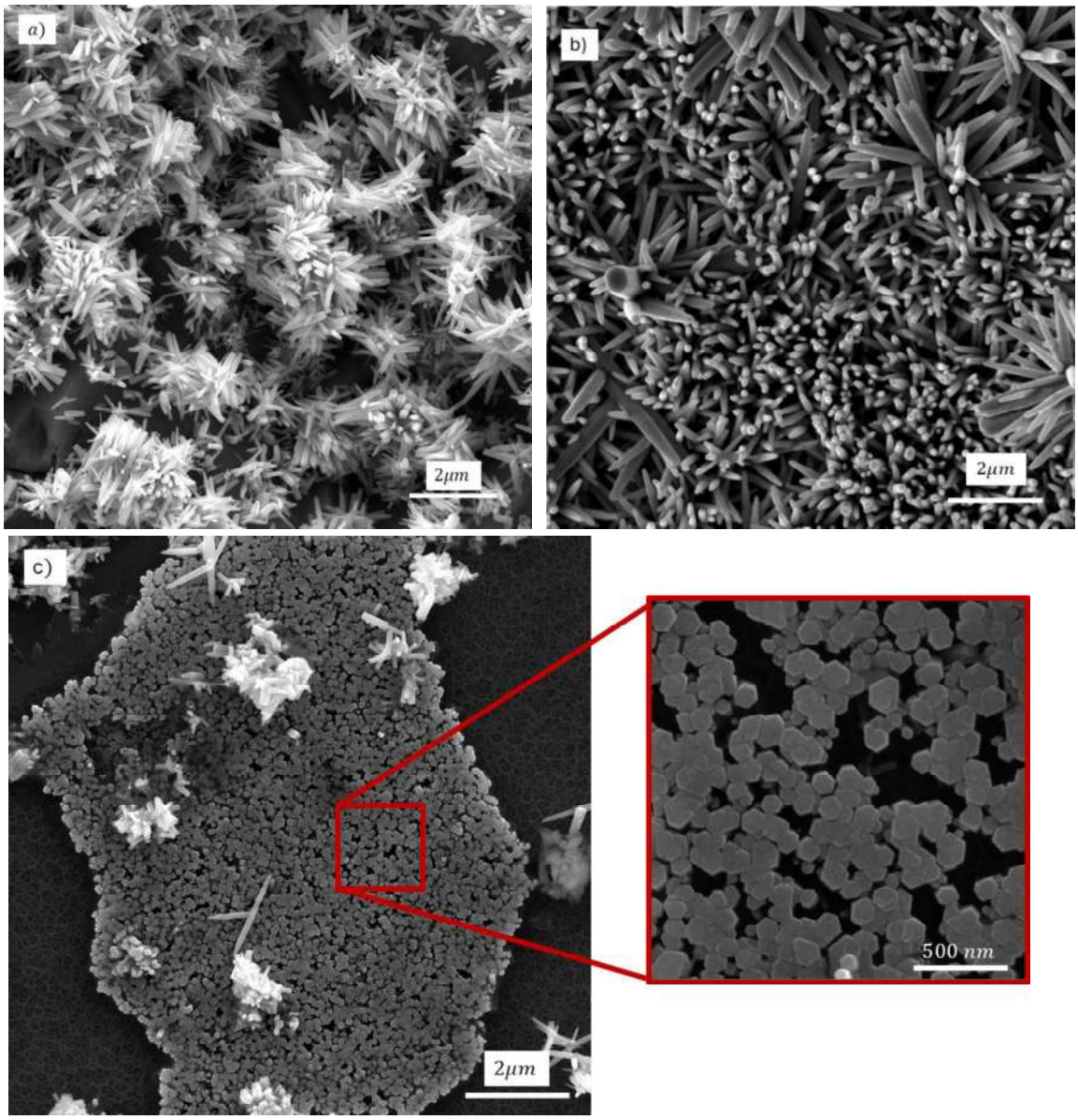

Nitrogen-doped Carbon Dots Analyzed by SEM and STEM with Blue Spectrum Optical Emission

Valéria M.F. Silva[1]*, Ewellyn S. Souza[1], Eduardo P. Hernandez[1], Adriana S. de Carvalho[2].

[1]Federal University of Pernambuco (UFPE), [2] Center for Strategic Technologies of the Northeast (CETENE)
*valeria.mariana@ufpe.br

Carbon dots (CDs) are carbon-based fluorescent nanomaterials, known for their predominantly spherical shape and a size of less than 10 nm. Extensive research has been conducted on these materials due to their distinctive properties, including biocompatibility and photoluminescence. These attributes make CDs promising candidates for a wide range of applications, including biosensing, catalysis, electrochemistry, controlled drug delivery, bioimaging, and other fields. A particularly effective approach to enhancing the performance of CDs is heteroatom doping, capable of tuning their optical and structural properties. Nitrogen doping, in particular, has shown a significant impact on the absorption and photoluminescence emission spectra, which vary according to the structural configuration of the nitrogen atoms incorporated into the carbon network [1]. In this study, nitrogen-doped carbon quantum dots (N-CDs) were synthesized through a hydrothermal method using citric acid and urea as precursors [2,3]. These materials were chosen due to their high availability, biocompatibility, and cost-effectiveness. Raman and FT-IR spectroscopies confirmed the incorporation of nitrogen atoms into the material's structure, as shown in Figure 1, and enhanced crystallinity, as evidenced by the increased intensity of the G band. Additionally, the suspension's colloidal stability demonstrated a zeta potential of -38.57 mV, indicating good electrostatic stabilization. Photoluminescence spectroscopy, shown in Figure 2, revealed an excitation peak at 458 nm and an emission peak at 393 nm, with bands associated with π–π* (C=C) transitions and n–π* transitions related to C–N and C–O bonds. An inset graph showing emission intensity as a function of energy indicated emission around 2.67 eV, corresponding to a blue coloration and a bandwidth of approximately 0.4 eV. The bluish emission was obtained after adjusting the pH of the suspension from 12 to 7, highlighting the significant influence of the medium's pH on the material's photophysical properties. Morphological characterization was performed using Scanning Electron Microscopy (SEM) and Scanning Transmission Electron Microscopy (STEM), revealing particles with estimated diameters ranging from 10 to 20 nm, as ilustrated in Figure 3. The characteristic size of carbon dots is approximately 10 nm, which means that measurements obtained through Scanning Electron Microscopy (SEM) are only preliminary, since this technique generates topographical images based on the return of secondary electrons to the detectors, making it difficult to measure carbon dots accurately. Therefore, techniques such as Transmission Electron Microscopy (TEM) or Scanning Transmission Electron Microscopy (STEM), both of which utilize electrons passing through the sample to generate images. These methodologies deliver superior resolution at the subnanometer level, thereby enabling precise measurements of particle diameters [4]. In the absence of a transmission electron microscope, STEM characterization represents a viable alternative for analyzing such small particles.

[1] S. Munusamy *et al*., Environmental Research, 231 (2023) 116046.
[2] D. Qu *et al*. Scientific Reports, 4 (2014) 5294.
[3] B. Vercelli *et al*., Electrochimica Acta, 387, (2021)138557.
[4] J.I. Goldstein *et al*., Scanning Electron Microscopy and X-ray Microanalysis, Springer, New York, 2017.

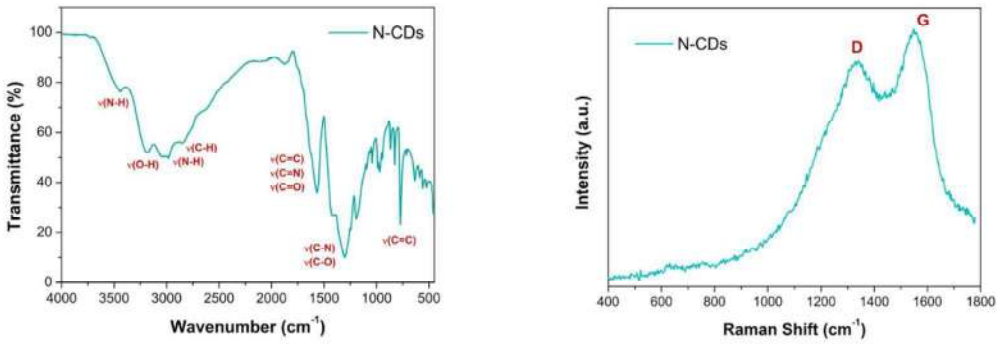

Figure 1. Results of FT-IR and Raman spectroscopies.

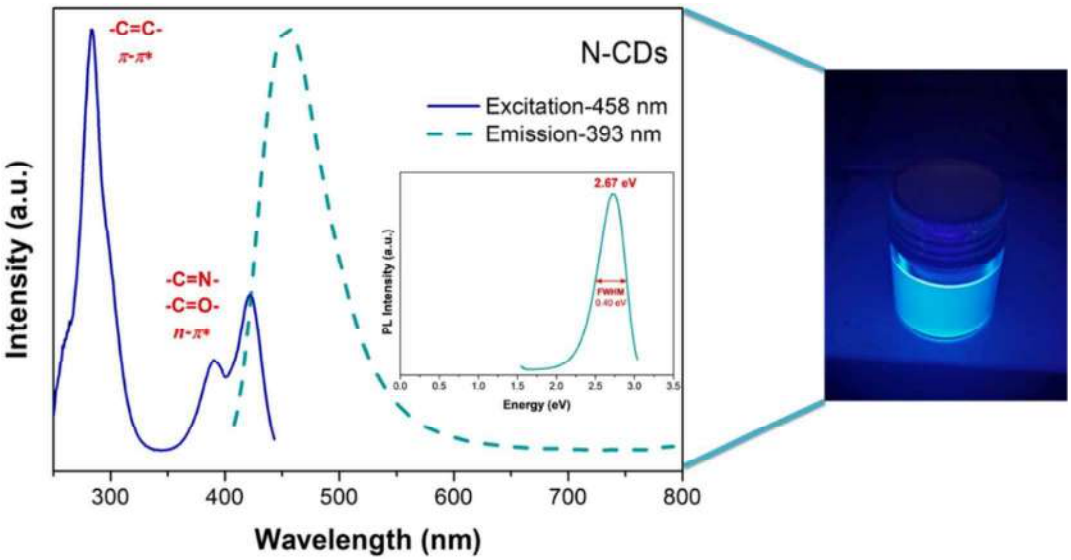

Figure 2. Photoluminescence spectrum and blue light emission under UVA illumination.

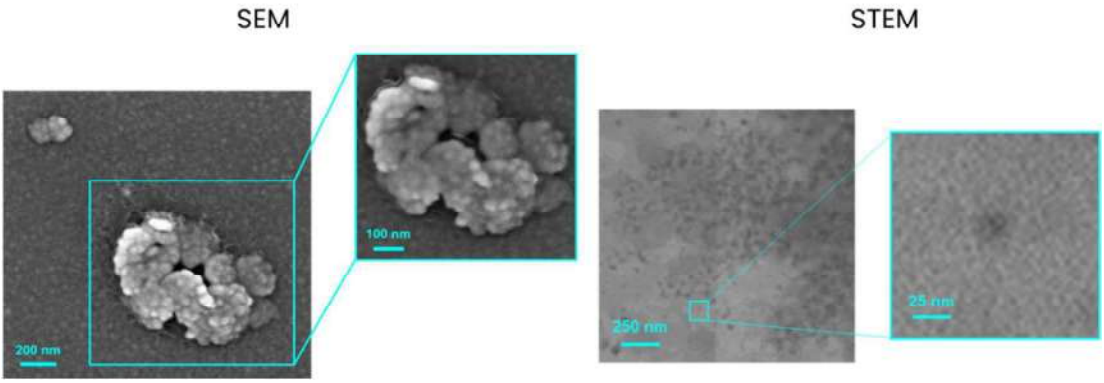

Figure 3. Images of SEM (left) and STEM (right) showing agglomerates of the synthesized *carbon dots*.

Phase Evolution in WAAM Super Duplex Stainless Steel 2594: Thermodynamic Simulation and Microstructural Characterization

Yuri de Abreu Silva Araújo Fleischhauer[1]*, Cesar Giron Camerini[1], Gabriela Ribeiro Pereira[1].

[1]Universidade Federal do Rio de Janeiro – UFRJ, Instituto Alberto Luiz Coimbra de Pós-Graduação e Pesquisa de Engenharia – COPPE, Programa de Engenharia Metalúrgica e de Materiais – PEMM, Rio de Janeiro, RJ, Brasil.
*yuri.abreu@coppe.ufrj.br

Super duplex stainless steels (SDSS) are widely used in offshore, petrochemical, and chemical industries due to their excellent combination of high mechanical strength and corrosion resistance, derived from a balanced ferrite-austenite microstructure [1]. Wire Arc Additive Manufacturing (WAAM) has emerged as a promising technique for producing large metallic components with high deposition rates, minimal material waste, and lower production costs [1, 2]. However, the complex thermal cycles in WAAM can lead to non-equilibrium solidification, microsegregation, and the formation of deleterious phases such as sigma (σ), which severely compromise toughness and corrosion resistance [2]. Since SDSS performance depends strongly on phase balance, thermodynamic simulations are valuable tools for defining suitable post-welding heat treatments. Despite the growing industrial interest in WAAM for SDSS, the behavior of the 2594 grade under these conditions remains poorly explored, especially regarding phase stability and microstructural evolution after heat treatments. This study analyzes the phase evolution in a 2594 SDSS fabricated by WAAM and subjected to post-welding heat treatments defined by Thermo-Calc simulations. The investigated conditions include the as-deposited state, solution-treated (1250 °C for 2 hours), and solution-treated followed by aging at 1040 °C for 2, 5, and 10 minutes. Microstructural characterization was performed using optical microscopy (OM), scanning electron microscopy (SEM), and energy-dispersive X-ray spectroscopy (EDS). Phase quantification was conducted by X-ray diffraction (XRD) with the aid of Bruker EVA software. OM revealed that the as-deposited condition (Figure 1a) shows a highly heterogeneous microstructure due to multiple welding passes and overlapping heat-affected zones (HAZ). The ferritic matrix contains various austenite morphologies, including Widmanstätten, allotriomorphic, and intragranular structures, consistent with Zhang et al. [1]. The solution treatment effectively homogenized the microstructure, producing a ferritic matrix with dispersed austenite islands (Figure 1b). Subsequent aging highlighted the kinetics of the eutectoid transformation $\delta \rightarrow \sigma + \gamma_2$, where delta ferrite is consumed to form sigma and secondary austenite (Figure 1c and d), in agreement with Calliari et al. [3]. SEM-EDS confirmed significant partitioning of chromium and molybdenum into the sigma phase (Figure 2), consistent with Thermo-Calc predictions. XRD confirmed ferrite and austenite in the as-deposited and solution-treated states, as well as sigma formation in the aged samples. The XRD quantification (Table 1) supported the microstructural observations and demonstrated the progressive increase in sigma phase content with longer aging times. The strong agreement between thermodynamic predictions and experimental results demonstrates the effectiveness of an integrated approach to understanding microsegregation, phase stability, and the effects of post-welding heat treatments in WAAM-processed super duplex stainless steels.

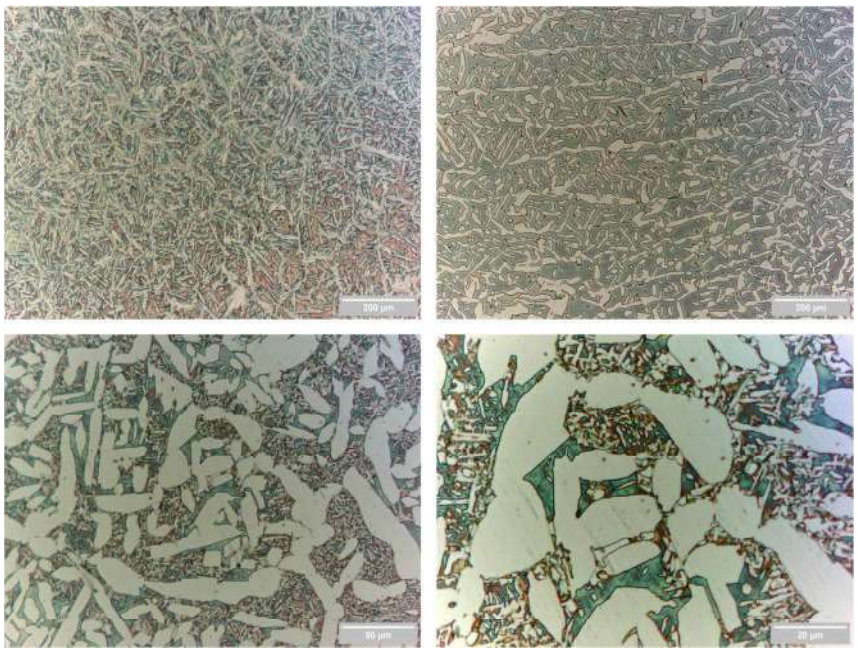

Figure 1. OM micrographs of the as-deposited sample (upper left), showing a heterogeneous microstructure with various austenite morphologies; solution-treated sample (upper right), presenting a more homogeneous microstructure with dispersed austenite islands in ferrite matrix; and sample aged for 5 minutes (bottom), highlighting sigma phase precipitation and secondary austenite formation.

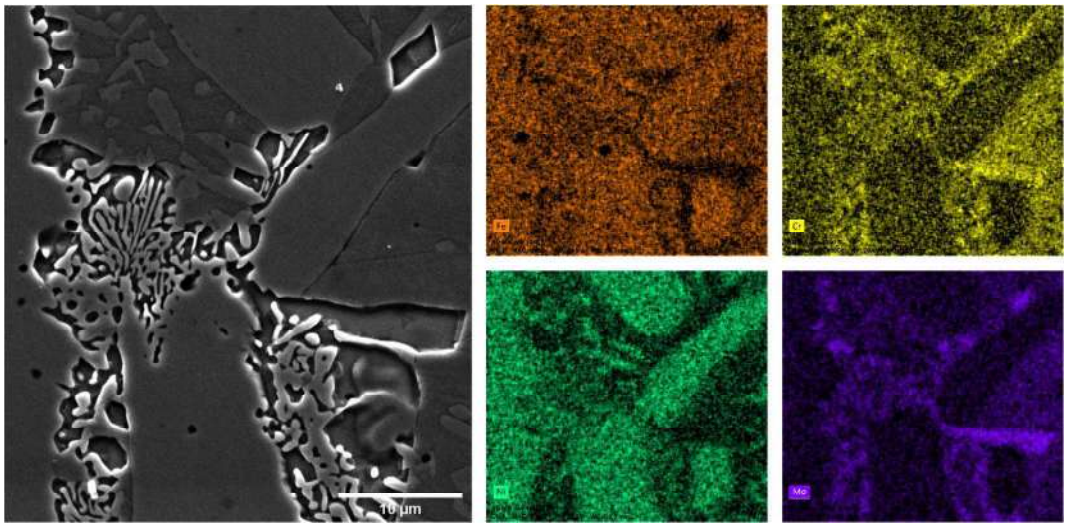

Figure 2. SEM micrograph (left) and corresponding EDS maps (right) for Fe, Cr, Ni and Mo showing element partitioning among ferrite, austenite (Ni rich), and sigma phase (Cr and Mo rich).

Table 1. Phase quantification by XRD.

Sample	Austenite (%)	Ferrite (%)	Sigma (%)
As-deposited	60.2	39.8	
Solution-treated	51.9	48.1	
Aged 2’	69.7	23.9	6.4
Aged 5’	75.2	17.9	6.9
Aged 10’	73.0	13.6	13.3

[1] X. Zhang et al., *Mat. Scien. Eng. A.* 762 (2019) 138097.
[2] X. Huang et al., *Journ. Mat. Res. and Tech.* 27 (2023) 1651.
[3] I. Calliari et al., *Metals.* 107 (2020) 967.
[4] This research was supported by CNPq (Brazil).

Quantitative Phase Analysis of Martensite and Bainite in the Coarse-Grain Heat-Affected Zone of Welded X80 Steel Using EBSD

Gilmar Z. Batista[1,2], Vicente Trindade[3], Matheus C. Mendes[2], Luís Felipe G. de Souza[2], Jorge C. F. Jorge[2].

[1] Petrobras, Rio de Janeiro, RJ, Brazil, [2] Centro Federal de Educação Tecnológica Celso Suckow da Fonseca - CEFET/RJ, Rio de Janeiro, RJ, Brazil, [3] Vallourec, Jeceaba, MG, Brazil
*matheus.mendes@cefet-rj.br

Over the years, the oil industry's increasingly severe operating conditions have driven the development of steel pipes classified by the API 5L standard [1]. X80 steel pipes are favored for oil and gas pipelines due to their excellent properties, and recent advances allow quenched and tempered seamless versions for sour service [2]. However, ensuring performance in onshore and offshore applications requires maintaining these properties after girth welding. Wang et al. [3], suggest that the heat-affected zone (HAZ) is the most critical region in pipes with girth welds due to reduced toughness at lower temperatures. Specifically, the coarse-grain region of the HAZ (CGHAZ) experiences temperatures around 1300°C during welding. This results in the formation of coarse microstructures consisting mainly of a mixture of martensite and bainite. According to Baek et al. [4], the martensite-bainite fraction significantly affects mechanical properties, particularly toughness. Therefore, controlling this ratio is essential for understanding how welded joints behave when subjected to different conditions. Few studies have examined small-diameter seamless tubes that have been treated with quenching and tempering, especially with respect to microstructural transformations in the heat-affected zone (HAZ). This study evaluates the HAZ produced by bead-on-pipe welding using GMAW-RE by comparing it with conventional GMAW. The study focuses on quantitatively measuring martensite and bainite fractions using EBSD characterization. After welding, the samples were metallographically analyzed at the coarse heat-affected zone (CGHAZ), within 0.25 mm from the fusion line (Figure 1a). The extent of the heat-affected zone (HAZ) was measured at three points (Figure 1b) using an optical microscope (OM) with Stream Essentials software. EBSD analysis was performed using band contrast (BC) and misorientation techniques. BC is based on pattern quality, which is sensitive to defects in the crystal lattice. This results in phase contrast because different phases generally have different diffraction intensities. The results showed that martensite and bainite can be quantitatively separated using EBSD. Gaussian fitting with peak deconvolution was performed to achieve this, as shown in Figure 2. A reference point for differentiating between bainite and martensite based on band contrast is visible as a dashed vertical line (Figures 2c and 2d). This value represents where the two curves overlap, similar to the methodology used by Baek et al. [4] and Wang et al. [5]. Table 1 shows the martensite/bainite ratio results obtained using a conventional method and the deconvolution technique for different welding conditions with the GMAW-RE process. Although the results are relevant, it is important to note that EBSD is a useful complementary technique for characterizing the HAZ microstructure and produces results similar to those of SEM analysis. Therefore, this technique is expected to be even more useful in future work on higher-strength steels, where low-carbon martensite and massive morphology can complicate conventional SEM analysis.

[1] J. Jiang et al., Metals. 13, 1530 (2023).
[2] J. Konrad et al., Proc. of the 2010 8th International Pipeline Conference, 2, 423 (2010)
[3] C. Wang et al., J. Mater. Res. Technol. **29**, 3096–3107 (2024).
[4] M.S. Baek et al., Mater. Sci. Eng. A. **785**, 139375 (2020)
[5] Y. Wang, et al., Microsc. Res. Tech. 79(7), 814–819 (2016).

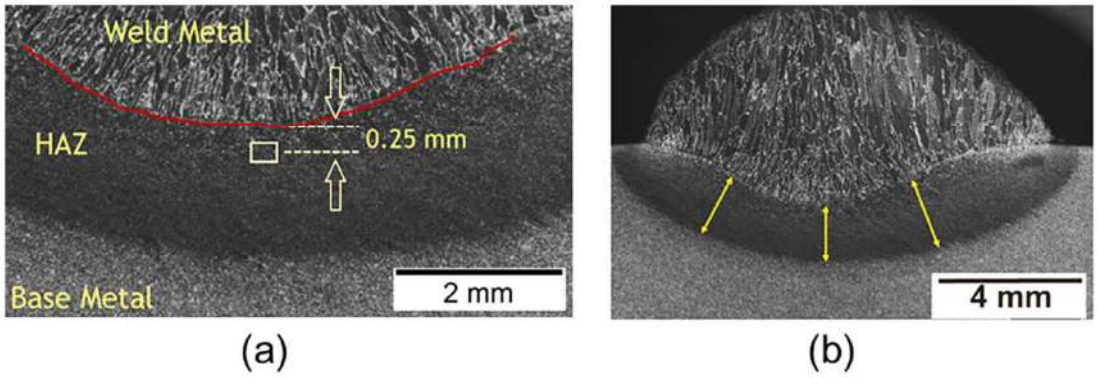

Figure 1. CGHAZ region evaluated in this study (a), and HAZ width measurements indicated by yellow arrows (b)

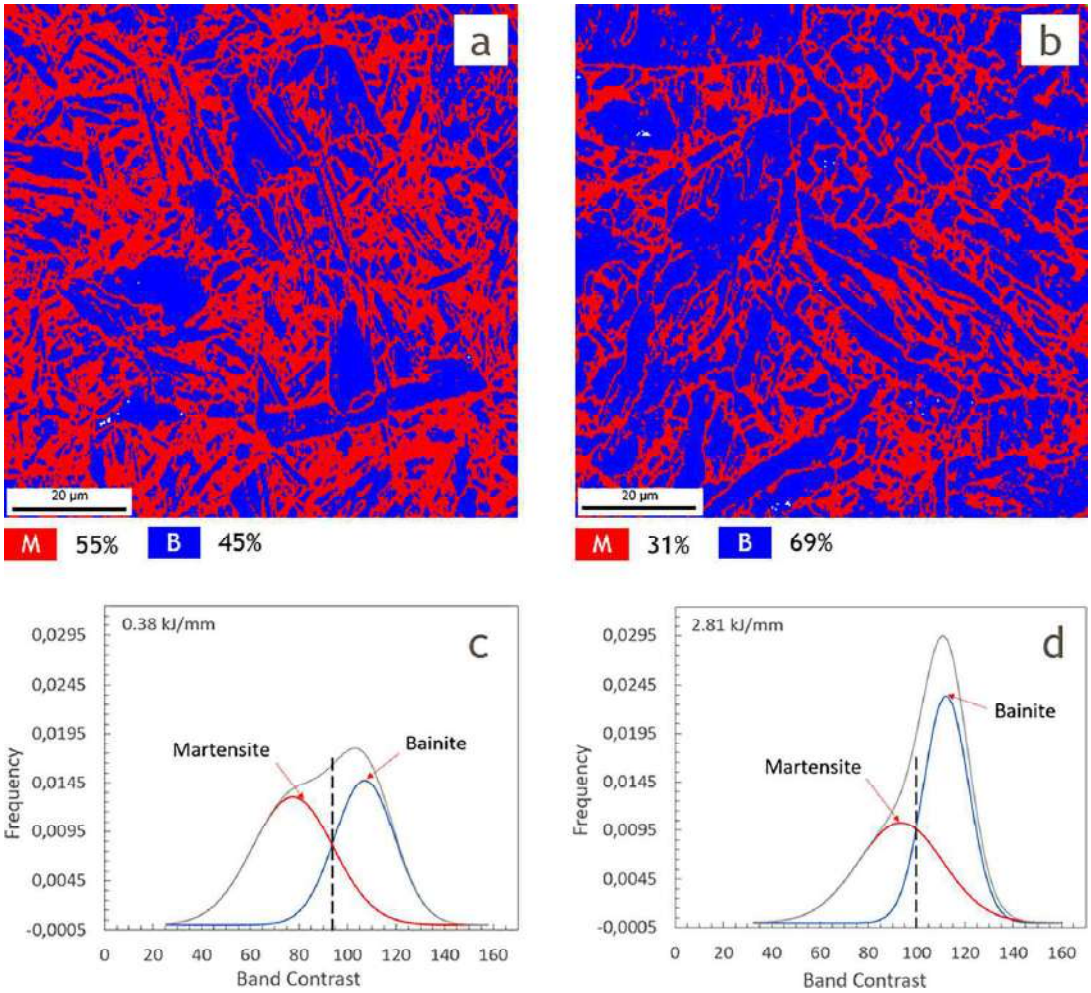

Figure 1. (**a**) and (**b**) Band contrast map: martensite is red and bainite is blue. (**a**) 0.4 kJ/mm and (**b**) 2.8 kJ/mm. (**c**) and (**d**) Band Contrast value frequency and Gaussian fitting. Peaks on the left correspond to martensite and peaks on the right to bainite

Table 1. Fraction of martensite and bainite determined by band contrast and point count methodologies

Rotation speed, rpm	Band Contrast Martensite/ Bainite % (± deviation)	SEM Martensite/ Bainite % (± deviation)
0	52/48 (±6)	51/49 (±17)
1000	58/42 (±2)	53/47 (±5)
2000	51/49 (±1)	58/42 (±6)
3000	55/45 (±7)	57/43 (±9)
Base metal	37/63 (±12)	28/72 (±4)

Recycling of Machining residues in the Production of Welding Fluxes for Hardfacing Coatings

Poliane de Castro Vieira[1], Gabrielle Schultz Braz[1], José Gedael Fagundes Júnior[1]*, Juno Gallego[1].

[1] São Paulo State University "Júlio de Mesquita Filho" (UNESP), Department of Mechanical Engineering. Materials and Process Technology Development and Characterization Group (MaProTec)

* gedael.fagundes@unesp.br

Abrasive wear is the most common and severe wear mechanism in tribological systems, causing significant material loss and premature failure of industrial components. These failures lead to high maintenance and replacement costs, as well as productivity losses due to machine downtime. To mitigate these effects, hardfacing coatings have been widely adopted, allowing the deposition of wear-resistant materials onto critical surfaces, thereby extending component lifespan and reducing operational costs [1]. Hardfacing coatings typically consist of carbides known for their high hardness, melting point, and chemical stability, with tungsten carbide (WC) and titanium carbide (TiC) being among the most effective for abrasive wear resistance. These carbides can be obtained by recycling industrial residues such as hard metal inserts mainly composed of WC and chips from titanium alloys, offering a sustainable approach by reintegrating waste materials into production chains. This study aimed to produce powders from recycled chips and hard metal inserts for use as components in welding consumables applied to deposit for hardfacing coatings. The methodology involved depositing weld beads by GTAW on SAE 1020 steel substrates using two flux compositions: MD (100% inserts of WC powders) and MDTi (50% of inserts WC and 50% titanium chips with graphite addition), under two different welding energy levels, H1 and H2. Welding conditions are presented in Table 1. The results showed that coatings with high TiC content exhibited superior visual uniformity, reduced porosity. Unreacted fragments of WC inserts also were observed in both conditions, Figure 1. A homogeneous distribution of dendritic carbides was observed throughout the microstructure and elevated titanium levels favoured the formation of mixed Ti-W carbides (TiWC), while lower titanium content, derived exclusively from the insert, resulted in the formation of separate TiC and WC carbides, uniformly dispersed within the matrix, Figure 2, [2,3]. The average hardness of the fusion zone ranged from 790 to 1020 HV, representing a four- to five-fold increase compared to the substrate. Dilution levels were relatively high (50% to 75%) across all conditions, exceeding ideal values for hardfacing but still acceptable for industrial applications. Microstructural and X-ray diffraction analyses confirmed the presence of complex Ti and W carbides responsible for enhanced hardness and wear resistance. Regarding the welding energy effect, increasing energy in the MD condition produced wider beads and a reduction in carbide volume fraction without significant changes in grain size or shape, while in the MDTi condition, higher energy promoted grain growth but maintained bead geometry homogeneity. These findings demonstrate the technical and environmental potential of recycling industrial residues for producing hardfacing coatings suitable for demanding industrial applications.

Key-words: Machining inserts. Hardfacing. Tungsten carbide.

[1] H.Holleck, Journal of Vac. Sc. Techn. Vol. 5 (1986) DOI: 10.1116/1.573700.
[2] Y.Yuan et al. Surf. Coat. Technol., v. 378, 2019. DOI: 10.1016/j.surfcoat.2019.124957
[3] X.Zeng et al. *Surf. Coat. Technol.*, v. 427, 2021. DOI: 10.1016/j.surfcoat.2021.127781
[4] This research was supported by CAPES (Brazil), 001 Financial Code.

Table 1. Welding condition

Welding Current, A	Welding Voltage, V	Welding Speed, mm/min	Arc Gap, mm	Argon flow rate, l/min
175 - 200	15 - 17	130 - 140	3	12 - 14

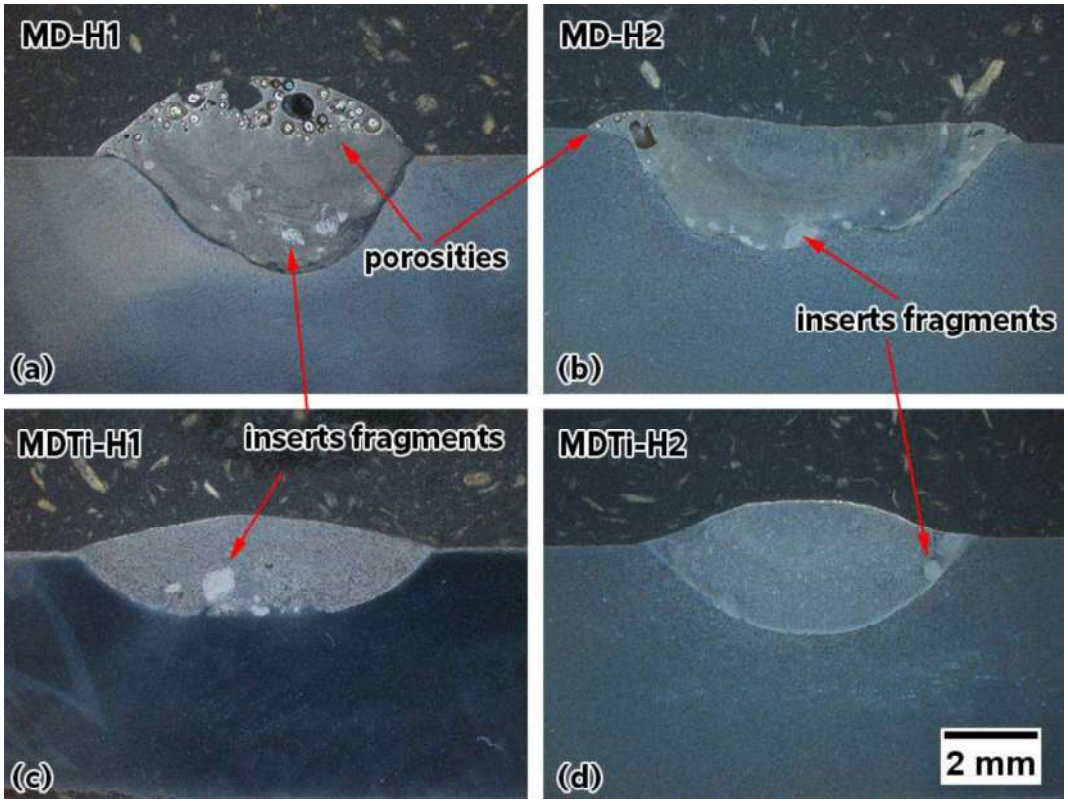

Figure 1. Cross-sectional images of the investigated conditions.

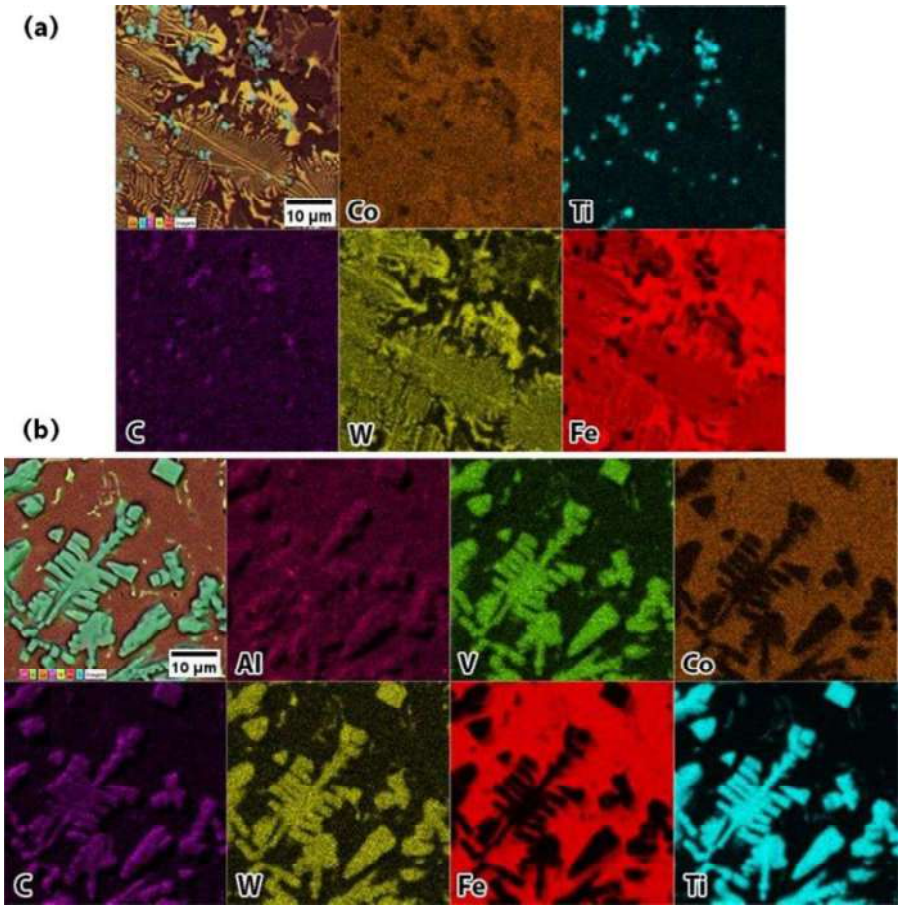

Figure 2. EDS Map Showing Element Distribution. (a). MD and (b) MDTi conditions.

Revealing the microstructural features of cement pastes with limestone filler using SEM-EDS

Liz M. Zanchetta[1]*, Marco Quattrone[1], Vanderley M. John[1]

[1] Polytechnic School, University of São Paulo
*liz@lct.poli.usp.br

The increasing global consumption of cement imposes on the cement industry the need to reduce CO_2 emissions generated in cement production. For this, one of the strategies is the development of binders with low clinker content and different reactive or inert supplementary cementitious materials (SCMs) [1]. Limestone filler, poorly, or not reactive material, has been used as clinker replacement (25% by mass in Brazil) because is interesting from an economic and environmental point of view. Ongoing research has already shown the feasibility of use it with a replacement ratio higher than 50% [2]; however, there is a need to understand the microstructure of these new low carbon cements. In this study, the microstructure of cement pastes containing up to 70% of limestone filler was analyzed by different laboratory techniques such as scanning electron microscopy with energy dispersive X-ray spectroscopy (SEM-EDS), mercury intrusion porosimetry (MIP) and X-ray microtomography (XRM) to obtain a multiscale characterization. The sample preparation protocols for SEM-EDS were detailed to achieve images resolutions that could accurately describe the features of the microstructure and to prove the importance of the sample preparation [3]. Samples were embedded in epoxy resin, grinded and polished using an anhydrous liquid following a multi-step protocol. The unique method of observation of the cement pastes microstructures by SEM-EDS provided detailed analysis (including elemental mapping), with sufficient resolution for the observation of features smaller than 1μm in areas of $1mm^2$ (images acquired at 138 nm pixel size). Surfaces of filler grains and anhydrous cement grains were observed without deep scratches; reliefs between filler particles and cement paste were almost non-existent; and there was very good preservation of hollow shells and delicate features such as hydrated product needles (C-S-H) around anhydrous cement grains, filler grains, and dissolving cement grains. The high quality of the acquired images even enabled the acquisition of quantitative data, such as the porosity of cement pastes. Although the porosities measured by SEM and XRM were significantly lower than the calculated values, the results confirmed the success of the sample preparation, as the porosity calculation is directly dependent on the threshold applied to BSE images, which is strongly influenced by image quality (available gray levels and pixel size). SEM-EDS analyses generated images ensured original results on the effect of clinker substitution by limestone filler.

[1] K.L. Scrivener, V.M. John, E.M. Gartner, Eco-efficient cements: Potential economically viable solutions for a low-CO2 cement-based materials industry, Cement and Concrete Research 114 (2018) 2–26. https://doi.org/10.1016/j.cemconres.2018.03.015.

[2] V.M. John, B.L. Damineli, M. Quattrone, R.G. Pileggi, Fillers in cementitious materials — Experience, recent advances and future potential, Cement and Concrete Research 114 (2018) 65–78. https://doi.org/10.1016/j.cemconres.2017.09.013.

[3] K. Scrivener, R. Snellings, B. Lothenbach, A Practical Guide to Microstructural Analysis of Cementitious Materials, CRC Press, 2016.

[4] This research was supported by INCT CEMTec (FAPESP 2014/50948-3 and CNPq 485340/2013-5), FAPESP (2016/05278-5) and CAPES.

Table 1. Mix proportion of cement pastes and estimated porosity.

Samples	filler (%g/g)	cement (g)	filler (g)	water (g)	admixture (g)	W/C	W/S	Porosity (%vol.)	
								total	capillary
0F-40/16	0	363.73	0.00	180.43	2.40	0.50	0.50	40	16
50F-40/26	50	208.40	212.12	154.12	1.88	0.74	0.37	40	26
70F-40/31	70	136.24	310.69	141.88	1.64	1.05	0.32	40	31
35F-35/16	35	284.72	150.16	151.63	2.24	0.54	0.35	35	16
50F-32/16	50	236.68	240.91	134.32	2.14	0.57	0.28	32	16

W/C = water / cement
W/S = water / solid
Samples identification: **xF-a/b:** x = filler content; a = total porosity; b = capillary porosity

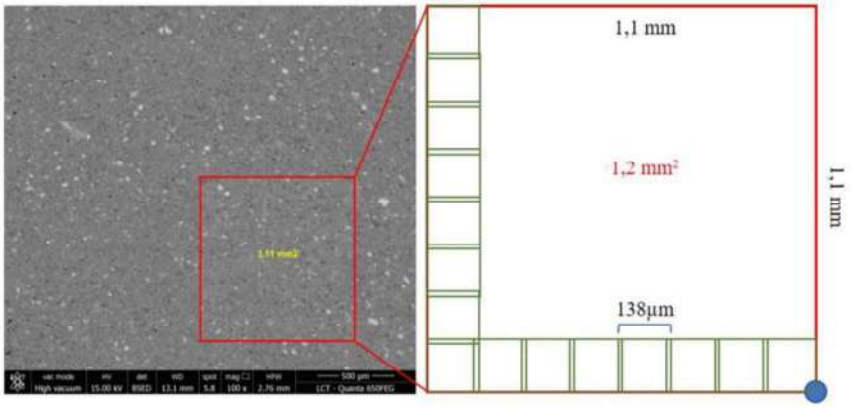

Figure 1. Backscattered electrons image of cement paste with analyzed area (1mm^2) in red consisting of a matrix (8x8) of 64 images, each one with a horizontal field width of 138µm, 5% overlap and resolution of 1000x1000.

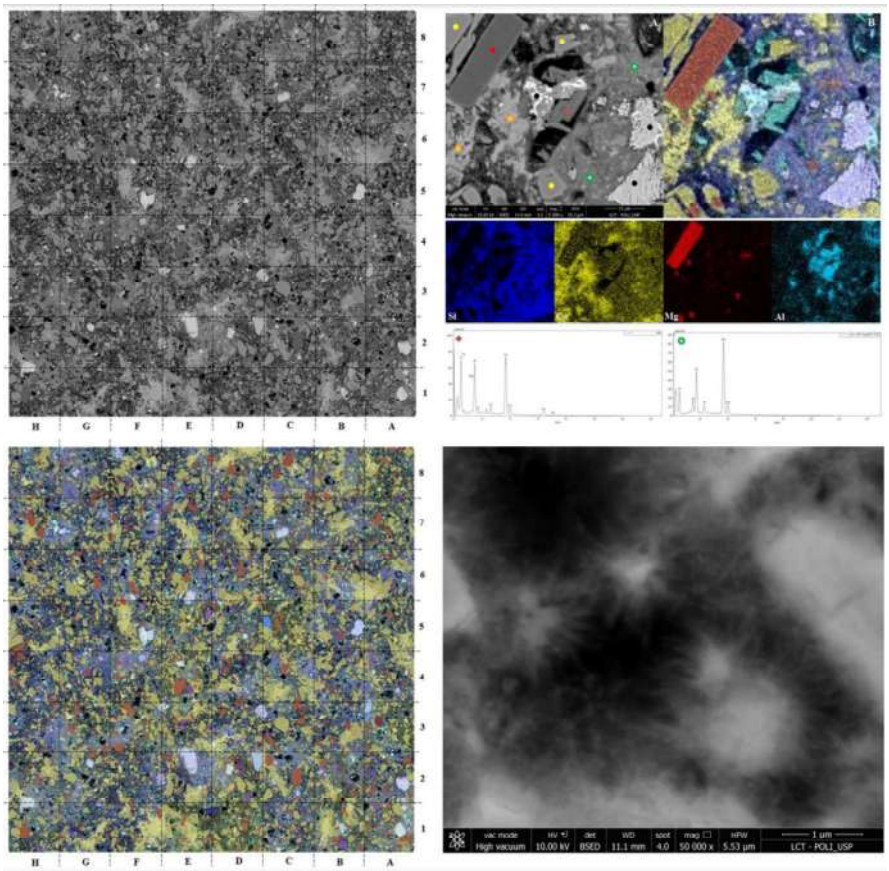

Figure 2. Left: BSE and respective EDS mapping of large area (1mm^2) of cement paste. Right up: microstructure detail from subarea 7F of the large area: BSE, EDS mapping and spectra from point analyses. Right down: BSE image with beam deceleration mode of hydrated product needles (C-S-H) around filler grains.

Scanning Electron Microscopy Analysis of Flocs Formed by Different Coagulation Mechanisms in Kaolinite-Based Raw Water

Diego Gouveia Marques[1], Janaína de Melo Franco Domingos[2], Isaac Jamil Sayeg[3], Valquíria Campos[1]*.

[1]Institute of Science and Technology, São Paulo State University (UNESP), Sorocaba, Brazil,
[2]School of Arts, Sciences and Humanities (EACH), University of São Paulo (USP), São Paulo, Brazil,
[3]Institute of Geosciences, University of São Paulo (USP), São Paulo, Brazil,
*v.campos@unesp.br

Coagulation-flocculation is a key process in water treatment, with charge neutralization and sweep coagulation being the main mechanisms when using iron or aluminum salts. Charge neutralization involves suppressing electrostatic repulsion, allowing particle aggregation with lower chemical consumption and sludge production, typically forming microflocs. Sweep flocculation, in contrast, occurs with higher coagulant dosages and within specific pH ranges that favor the formation of insoluble precipitates such as $Al(OH)_3$, capable of enmeshing particles [1]. In this study, flocs formed by both mechanisms were analyzed using Scanning Electron Microscopy (SEM), after jar test assays and subsequent particle retention through vacuum filtration. Raw water was prepared as a standardized matrix containing kaolinite and humic substances. Coagulation was carried out through jar test experiments under the following conditions: for charge neutralization, 10 mg L^{-1} kaolinite, 5 mg L^{-1} humic substances, turbidity of 18.9 ± 0.5 NTU, 5 mg L^{-1} polyaluminum chloride (PAC), pH 6.5 ± 0.1, and zeta potential of –0.15 ± 0.33 mV; for sweep coagulation, 500 mg L^{-1} kaolinite, 5 mg L^{-1} humic substances, turbidity of 175.3 ± 4.7 NTU, 55 mg L^{-1} PAC, and pH 7.5 ± 0.1. After sedimentation, the samples were vacuum filtered using filter units equipped with a 0.2 µm cellulose acetate (CA) membrane, and dried at 80 °C for 72 hours. Prior to SEM analysis, the dried samples were coated with a thin layer of gold using a sputter coater (Emitech K550). Macroscopically, sweep coagulation produced a thick, clay-like deposit on the filter, while charge neutralization yielded only a thin layer, as observed in Figures 1a and 1b, prior to drying. SEM images at 250× magnification revealed more uniform and smaller particles in the charge neutralization condition, consistent with direct particle aggregation. In contrast, sweep flocculation exhibited fewer microparticles and some larger, irregularly shaped aggregates, suggesting a different floc formation pattern. No large flocs were clearly observed, with a predominance of hexagonal-shaped particles characteristic of kaolinite. The use of vacuum filtration and thermal drying may have altered the original floc structures, limiting the visualization of morphological contrasts expected between the two coagulation mechanisms. Less invasive collection and drying methods are recommended for future studies, such as cryo-SEM or natural air drying [2,3].

[1] D.G. Marques et al., Rev. Virt. Quím. 16 (6) (2024).
[2] M.S. Zbik et al., J. Colloid Interface Sci. 328 (1) (2008) 73–80.
[3] L. Zhou et al., Sep. Purif. Technol. 276 (2021) 119304.
[4] This research was financed by FAPESP (São Paulo Research Foundation, Grant number 2023/12713-3), and by IGTPAN (Granado Polyacrylonitrile Technology Institute).

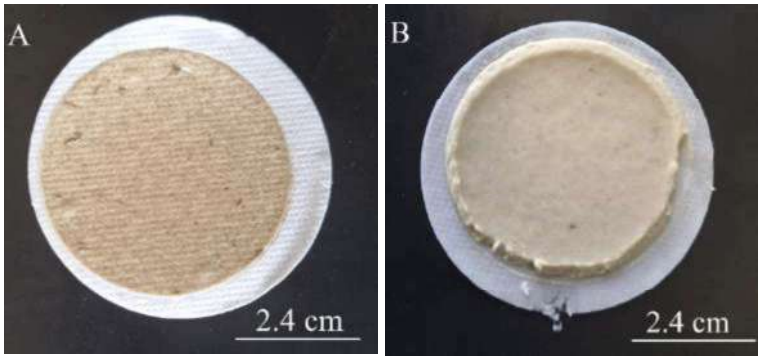

Figure 1. Flocs retained in filters after coagulation by: a) charge neutralization and b) sweep mechanism

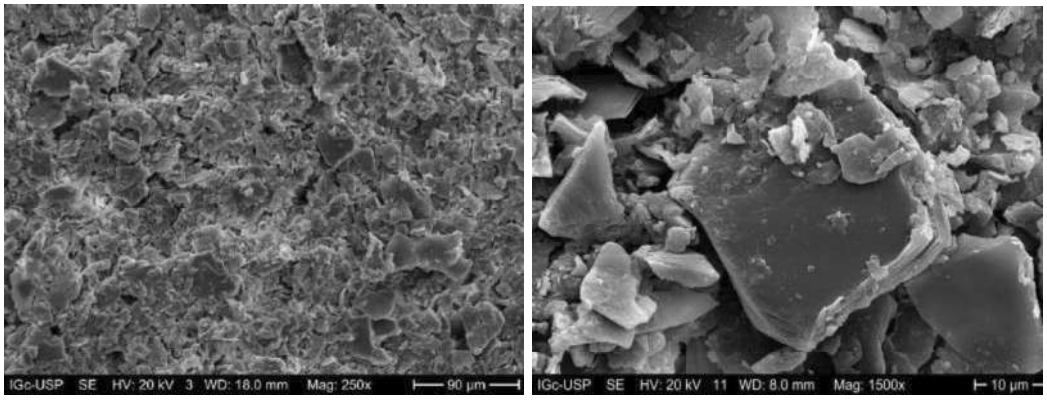

Figure 2. Flocs formed by charge neutralization coagulation observed under SEM (250x and 1500x magnification).

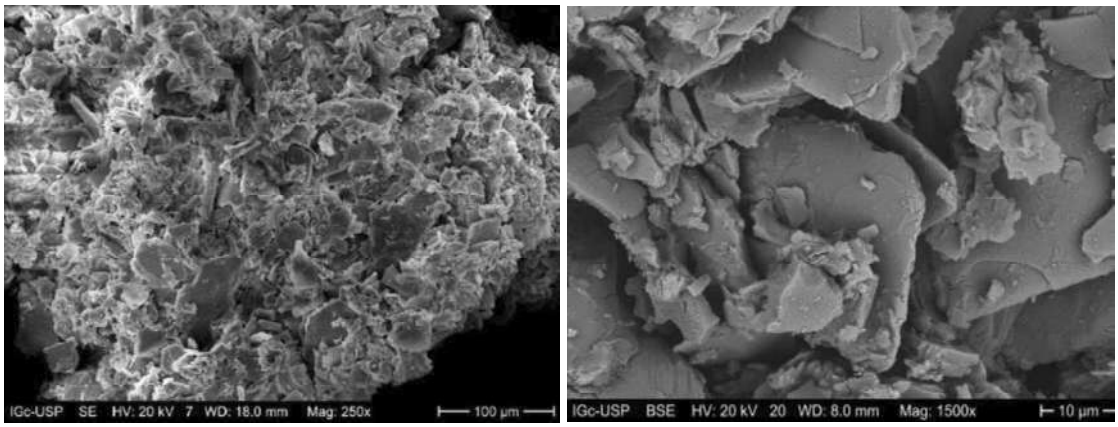

Figure 3. Flocs formed by sweep coagulation observed under SEM (250x and 1500x magnification).

Structural Characterization of Equimolar TiVNbCr Multicomponent Alloy upon Hydrogenation

G. C. Mayer Dias[1], O. A. Pedroso[1], W. J. Botta[1,2] and G. Zepon[1,2,*]

[1] Graduate Program in Materials Science and Engineering, Federal University of São Carlos, São Carlos, São Paulo, Brasil

[2] Federal University of São Carlos, DEMa, São Paulo, Brasil.

Corresponding author: Zepon@ufscar.br

Multicomponent alloys for hydrogen storage have been studied due to their vast compositional field, which allows tuning the hydrogen properties since the thermodynamics of metal-hydride systems are strongly related to both the chemical composition and the crystal structure of the alloy. The hydrogenation of multicomponent body-centered cubic (BCC) alloys leads to the formation of a face-centered cubic (FCC) dihydride, i.e., a hydrogen capacity of 2 hydrogen atoms per metal (H/M) [1]. Depending on the chemical composition, multicomponent BCC alloys can also present an intermediary hydride phase with H/M between 0.5 and 1 [2-3]. These intermediary phases were observed either as distorted BCC or body-centered tetragonal (BCT) structures [2-3] Recently, thermodynamic models to calculate pressure-composition-temperature diagrams of BCC multicomponent alloys have been proposed, aiming to aid the alloy design [4-8]. To improve thermodynamic modelling, it is fundamental to understand the mechanisms of phase transformation through the hydrogenation process in these alloys to accurately describe the thermodynamic magnitudes involved in the phase transition process. For this, the equimolar TiVNbCr alloy was chosen due to the presence of an intermediary hydride [9]. The alloy was processed by arc melting and hydrogenated using a Sievert apparatus until H/M was equal to 1.2, resulting in a powder due to the hydride decrepitation. The microstructure of this powder sample was analyzed using a Phillips XL-30 FEG coupled with an Xplore EDX and cNano+ Oxford EBSD detectors. The EDX mapping indicated that the alloy presented a relatively homogeneous chemical composition, while the EBSD mapping (Figure 1) shows that the alloy microstructure with H/M = 1.2 presents both BCC monohydride and FCC dihydride phases. The dihydride microstructure presents a plate-like growth in the monohydride grains. In addition, the BCC and FCC hydrides presents a Nishiyama-Wasserman crystallographic orientation relationships (OR). The morphology of the FCC dihydride and the OR between the monohydride and dihydride shows that the dihydride formation must take place with a displacive phase transformation mechanism.

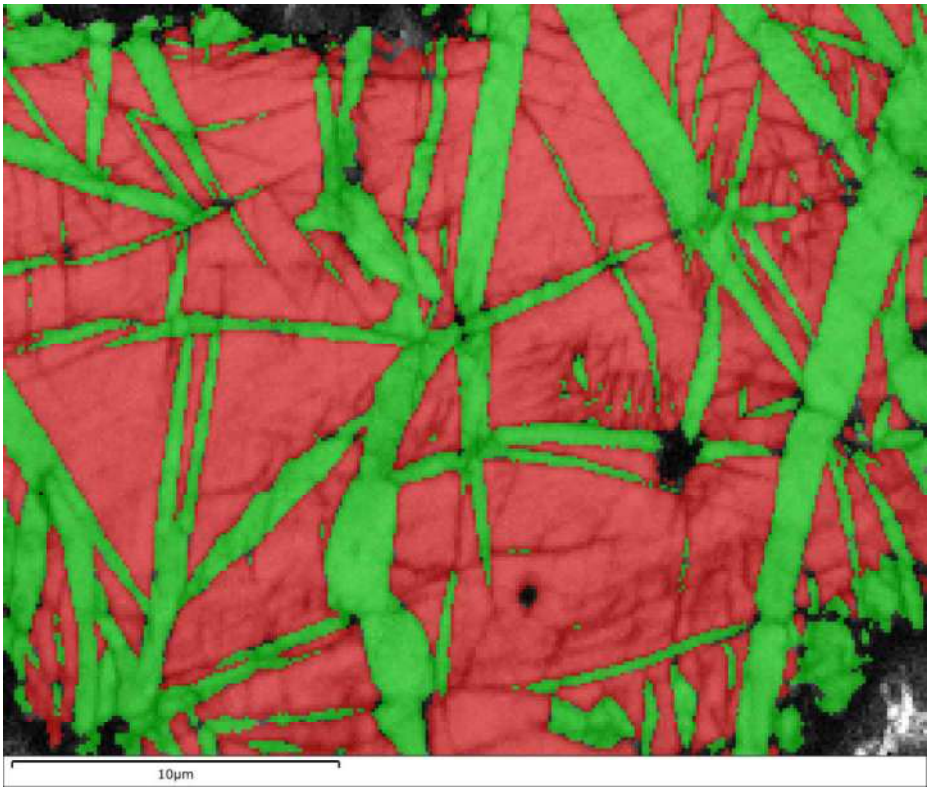

Figure 1: EBSD analysis of TiVNbCr powder, composition of the phase map in which green and red are respectively the dihydride and the monohydride and the band contrast.

[1] F. Marques et al., Energy & Environmental Science 14.10 (2021) 5191

[2] B. H. Silva et al., Journal of Alloys and Compounds 901 (2022) 163620

[3] C. Zlotea et al., Journal of Alloys and Compounds 775 (2019) 667

[4] G. Zepon et al., Acta Materialia 215 (2021) 117070

[5] O. A. Pedroso et al., International Journal of Hydrogen Energy 47.76 (2022) 32582

[6] B. H. Silva et al., International Journal of Hydrogen Energy 48.84 (2023) 32813

[7] R. B. Strozi et al., Journal of Alloys and Compounds 932 (2023) 167609

[8] G. C. M. Dias et al., ACS Applied Energy Materials 7.15 (2024) 6463

[9] R. Strozi et al., Energies 14.11 (2021) 3068

[10] This research was supported by CNPq (Brazil) and CAPES (Brazil). The authors thank the Laboratory of Structural Characterization (LCE/DEM/UFSCar) for the general facilities and support for this research.

Sustainable Hydrogen Storage Using Recycled Ti6Al4V Scraps for Metal Hydride Synthesis

Mariana de Brito Ferraz[1]*, Walter José Botta[1,2], Guilherme Zepon[1,2].

[1] Graduate Materials Science and Engineering Program, Federal University of São Carlos,

[2] Department of Materials Engineering, Federal University of São Carlos.

*marianadebritoferraz@gmail.com

Energy is paramount to providing quality life and assisting the development of society and the economy [1]. There is great potential in using hydrogen as an energy carrier, but achieving the most compact hydrogen storage possible, thereby increasing its volumetric density, is one of the main goals of leveraging the use of hydrogen as an energy carrier [2]. Solid-state storage presents a possibility of elevated hydrogen density at moderate temperatures and a high quantity of hydrogen storage in a small volume [3]. In addition, multicomponent alloys (MCAs) are currently gaining a lot of attention as they can increase the possibility of designing materials with optimized properties. C14 Laves-phase MCAs, a well-known class, has high hydrogen absorption capacity and good reversibility. However, conventional synthesis relies on high-purity elemental feedstock, leading to significant environmental and economic costs due to energy-intensive purification. The $(Ti_{16.67}Zr_{16.67})(Fe_{22.22}Mn_{22.22}Cr_{22.22})$ alloy [4] was selected for synthesis in this study due to its promising hydrogen storage properties and good cycling stability. To promote sustainability, recycled Ti6Al4V (ASTM F136) alloy scraps from the biomedical sector were employed as the Ti source, while high-purity Fe, Mn, and Cr were replaced with commercially pure elements. Zr was the only element used in high purity, as no suitable commercially pure alternative was available. The alloy was produced via arc melting and the final composition was $(Ti_{15}Al_2V_1Zr_{15})(Fe_{22}Mn_{22}Cr_{23})$. X-ray diffraction (XRD) characterization confirmed a dominant C14 Laves phase and about the hydrogen storage capacity, the alloy absorbed about 1.2 wt.% H_2 (only 30% less compared to the purity elements alloy) at room temperature with no activation treatment required. To investigate the alloy's microstructure, elemental distribution, and to confirm its final composition after synthesis, Scanning Electron Microscopy (SEM) combined with Energy Dispersive X-ray Spectroscopy (EDS) was employed. As shown in Table 1, the final composition of the alloy is presented, while Figures 1 display the microstructure and the corresponding color maps illustrating the elemental distribution. These results highlight the potential of industrial scrap recycling as a sustainable and cost-effective strategy for developing next-generation hydrogen storage materials.

[1] B. Seluk. Calculation and Interpretation of the Standard Chemical Exergies of Elements Using the Chemical Reference Species, 2009.
[2] A. Züttel, Materials for hydrogen storage, 2003.
[3] Bilgen S. Structure and environmental impact of global energy consumption, 2014.
[4] Ponsoni JB, Balcerzak M, Botta WJ, Felderhoff M, Zepon G. A comprehensive investigation of the $(Ti_{0.5}Zr_{0.5})_1(Fe_{0.33}Mn_{0.33}Cr_{0.33})_2$ multicomponent alloy for room-temperature hydrogen storage designed by computational thermodynamic tools. J Mater Chem A.
[5] This research was supported by CNPq (Brazil) and CAPES (Brazil). The authors thank the Laboratory of Structural Characterization (LCE/DEM/UFSCar) for the general facilities and support to this research. This study was financed in part by the Coordenação de Aperfeiçoamento de Pessoal de Nível Superior - Brasil (CAPES) - Finance Code 001.

Table 1. Table 1 Chemical composition of the $(Ti_{15}Al_2V_1Zr_{15})(Fe_{22}Mn_{22}Cr_{23})$ alloy as determined by EDS.

Elements	EDS (at. %)
Ti	15.7 ± 0.1
Zr	14.7 ± 0.6
Fe	22.0 ± 0.2
Mn	22.0 ± 0.3
Cr	23.4 ± 0.2
Al	1.7 ± 0.1
V	0.6 ± 0.0

this work.

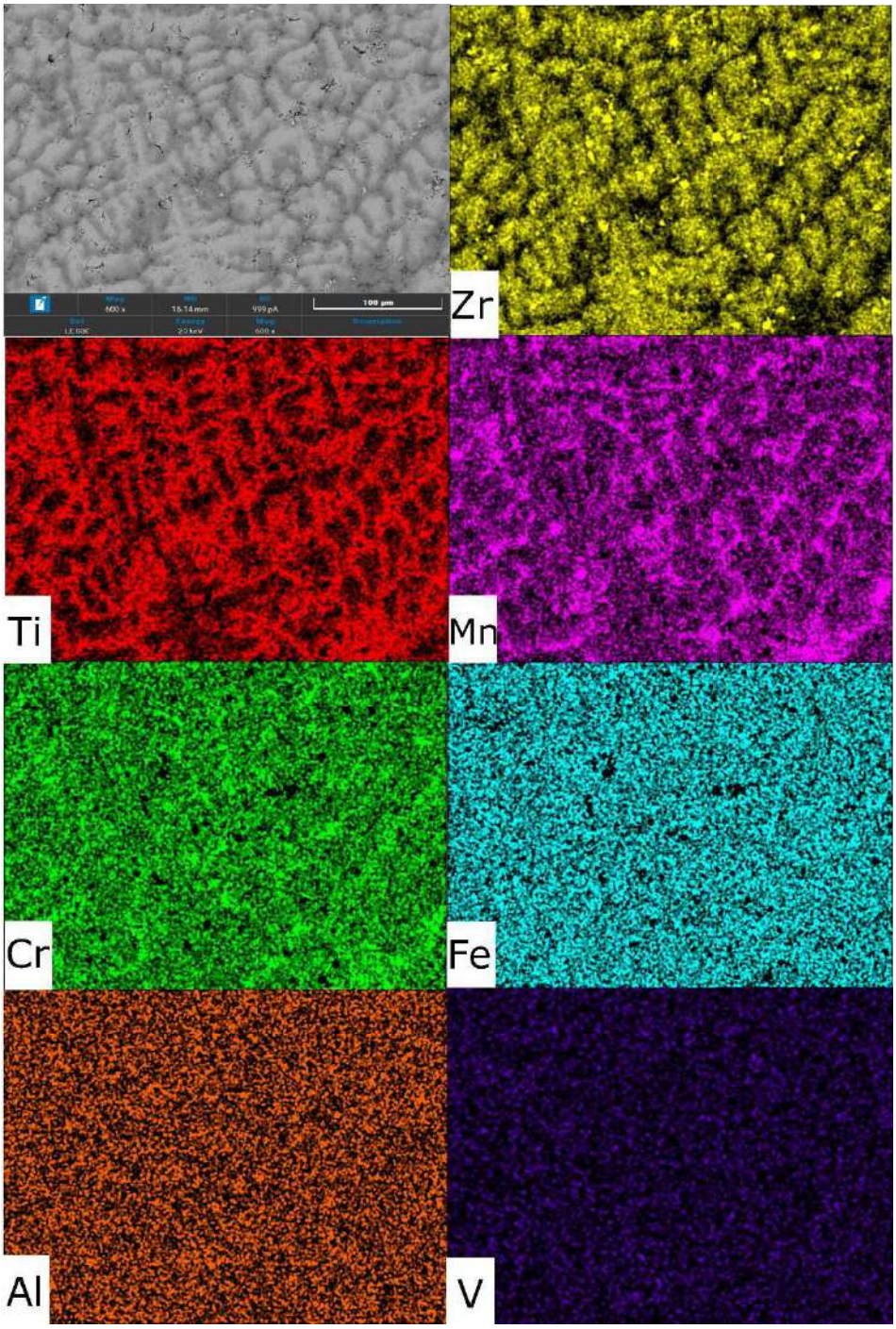

Figure 1. Figure 1 BSE-SEM image and color mapping of the $(Ti_{15}Al_2V_1Zr_{15})(Fe_{22}Mn_{22}Cr_{23})$ alloy.

Sustainable preparation of graphene oxide from sugarcane bagasse via pyrolysis and functionalization for incorporation of Ni nanoparticles

E.S. Souza[1]*, E. R. S. da Paz[2], M.R. de Sá[3], J.E. Kulesza[1], B. S. Barros[4]

[1]Federal University of Pernambuco, Department of Fundamental Chemistry, PE, Brazil, [2]Federal University of Pernambuco, Department of Fundamental Chemical Engineering, PE, Brazil, [3]Federal University of Pernambuco, Department of Physical, [4]Federal University of Pernambuco, Department of Mechanical Engineering, PE, Brazil.

*elibe.souza@ufpe.br

The growing demand for advanced carbon-based materials, such as graphene oxide (GO), has driven research focused on their production through more sustainable routes. Conventional synthesis methods often rely on toxic chemical precursors and environmentally harmful processes, highlighting the need to develop eco-friendly alternatives that reduce the environmental impact associated with the production of these materials [1]. In this context, the use of biomass waste as a raw material represents a promising strategy, not only by mitigating the improper disposal of agricultural by-products, but also by enabling the production of materials with properties similar to those of graphene oxide (GO). This study aims to produce a carbonaceous material derived from biomass with structural and morphological characteristics comparable to GO, promoting a greener synthetic route aligned with the principles of sustainable chemistry. Furthermore, the incorporation of nickel nanoparticles enables excellent electrochemical properties, as observed in nickel–carbon composites, which are widely recognized in the fields of energy storage and catalysis [2,3]. The proposed GO material was obtained through a two-step pyrolysis process using dried sugarcane bagasse (80 °C, 12 h), which had been previously ground and macerated. Initially, 5 g of the biomass were mixed with 0.5 g of ferrocene and calcined at 300 °C for 10 minutes [4]. Subsequently, the material was washed with 5% HCl for 12 hours, rinsed until neutral pH, and dried at 60 °C. For activation, 1 g of the material was treated with 3 g of $ZnCl_2$ in 10 mL of water under stirring for 24 hours, followed by pyrolysis at 750 °C for 1 hour under a nitrogen atmosphere (5 °C/min). The material was then washed with hot water until neutral pH and dried at 100 °C [5]. For functionalization, 300 mg of the activated material was dispersed in 150 mL of DMF by ultrasound (30 min, 30% amplitude, 6 s on/4 s off), 3 mL of APTES was added, followed by reflux at 100 °C for 6 h. The product was then centrifuged, washed with ethanol, and dried at 60 °C for 24 h [6]. Then, 75mg of the functionalized material was dispersed in 20mL of water and sonicated for 30min. $NiCl_2$ solution (0.2mol. L^{-1}) was added, adjusting the pH to 5, and the reduction was carried out with $NaBH_4$ (20mL, 1mol. L^{-1}) at ~0°C for 1h under stirring. The solid was centrifuged (4000rpm, 10min), washed with water and dried at 60°C for 24h [3]. X-ray diffraction (XRD) analysis (Figures 1a and 1b), consistent with the literature [3], revealed that the GO(SB)-APTES material exhibits broad peaks around $2\theta \approx 7°$ and 23°, corresponding to the (001) and (002) planes GO and partially reduced graphene oxide (rGO), respectively. In turn, the diffractogram of GO(SB)-APTES-Ni shows new peaks at 44.5°, 52°, and 76°, attributed to the (111), (200), and (220) reflections of metallic nickel, confirming the successful incorporation of the nanoparticles into the support. Additionally, the peaks marked with dashed lines correspond to boranes, likely residues of the reducing agent used in the synthesis of the Ni nanoparticles. Although activation with $ZnCl_2$ was adopted as a strategy to induce porosity in GO derived from sugarcane bagasse, the results obtained indicate that this process, alone, did not promote a significant increase in the surface area, as evidenced in the N_2 adsorption isotherm (Figure 1 c) for GO(SB)-APTES, which presented an area of only 1.18 $m^2 . g^{-1}$. However, after the incorporation of Ni

nanoparticles, a significant gain in porosity was observed, with the GO(SB)-APTES-Ni sample reaching a surface area of 7.38 $m^2 . g^{-1}$. This increase may be related to structural changes induced during the anchoring of the metal nanoparticles. Thermogravimetric analysis (TGA) (Figure 1 d) indicated greater thermal stability of GO(SB)-APTES-Ni compared to GO(SB)-APTES. The nickel-free material showed a total mass loss of approximately 68%, attributed to dehydration, degradation of oxygenated groups, and thermal decomposition of the APTES functionalizing agent. In contrast, the Ni-containing material showed a total mass loss of only 29%, demonstrating that the metal nanoparticles contributed to increasing the thermal stability of the system. The micrographs obtained by Scanning Electron Microscopy (SEM) (Figures 1 e and f) show that GO(SB)-APTES presents lamellar morphology, with stacked sheets and low visible porosity, compatible with its limited surface area. After Ni incorporation, a rougher and more porous surface with dispersed particles is observed, visible in the higher magnification image (inset in Figure 1 f). These morphological changes confirm the BET results and complement the evidence of metal incorporation provided by XRD. Therefore, the proposed route allowed the production of a Ni-functionalized GO composite from sugarcane bagasse, with improvements in thermal stability and surface area. The results confirm the potential of this approach as a sustainable alternative for the synthesis of carbon-metallic materials.

[1] B. Thangaraj, F. Mumtaz, Y. Abbas, D.H. Anjum, P.R. Solomon, J. Hassan, Molecules 28 (2023) 3329.
[2] L. Wang, X. Gao, D. Wang, H. Shang, Y. Zhao, B. Zhang, Fuel 381 (2025) 133639.
[3] S.J. Martínez, A. Lavacchi, E. Berreti, L. Capozzoli, C. Evangelisti, A. Arranz, J.L. Rodríguez, E. Pastor, Inorganica Chim Acta 566 (2024) 122008.
[4] F.G. da Silva, E.S. Souza, J.D. da Silva Fonseca, S.D. Melo, J.E. Kulesza Barros, B.S. Barros, Materials Research 28 (2025) e20250060.
[5] K. Sun, Q. Huang, Y. Chi, J. Yan, Waste Management 81 (2018) 128–137.
[6] X. Kong, J. Liu, S. Li, M. Yu, Corros Sci 213 (2023) 110966.

[7] This research was supported by CNPq and Facepe (Brazil).

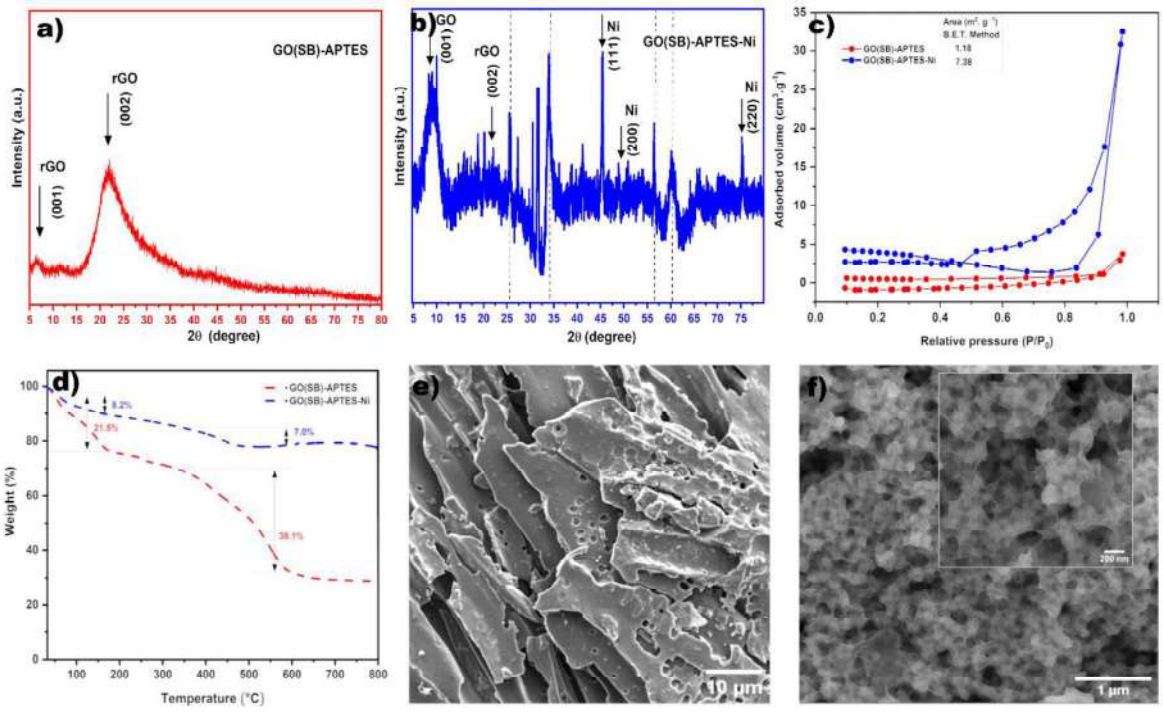

Figure 1. Characterization of GO(SB)-APTES and GO(SB)-APTES-Ni materials: (a, b) XRD diffractograms; (c) N_2 adsorption/desorption isotherms and BET areas; (d) Thermogravimetric analysis (TGA) and (e, f) SEM micrographs.

Synthesis and Characterization of Nickel Selenide Nanowires on Nickel Foam for Green Hydrogen Production: Preliminary Results

Thauane Mayara Silva de Jesus[1]*, Geovane Menezes da Silva Araujo[2], Déboralys Ferreira Passos[3], Ivani Meneses Costa[4], Giancarlo Richard Salazar Banda[5], Amanda de Azevedo Gonçalves[6]*

[1],[2] Federal University of Sergipe, São Cristóvão, SE, Brazil; [3],[4],[5] Tiradentes University, Aracaju, SE, Brazil; [3],[4],[5] Institute of Technology and Research, Aracaju, SE, Brazil; [6] Sergipe Technology Park, São Cristóvão, SE, Brazil
*thauane.mayara@hotmail.com; amanda.goncalves@sergipetec.org.br

Green hydrogen (H_2V), derived from renewable sources, represents a clean and promising energy alternative for the decarbonization of the energy sector. However, its efficient production requires the development of high-performance and low-cost electrocatalysts for water electrolysis. Although noble metals such as platinum and iridium exhibit excellent catalytic activity, their high cost limits large-scale applications. In this context, nickel selenide (NiSe)-based electrocatalysts supported on nickel foam (NF) have emerged as viable alternatives, offering good stability, efficiency, and cost-effectiveness for both the hydrogen evolution reaction (HER) and the oxygen evolution reaction (OER) [1]. This study presents the synthesis of NiSe nanowires supported on porous nickel foam via a hydrothermal process, aiming to contribute to the advancement of green hydrogen production technologies. The nickel foam (1 cm^2) was pretreated through sonication in 3 M HCl, ethanol, and deionized water for 30 minutes in each solvent, followed by vacuum drying at 60 °C for 12 hours [2]. Subsequently, powdered selenium (0.059 g) was added to 1.5 mL of deionized water containing $NaBH_4$. After stirring, a clear NaHSe solution was obtained, to which 30 mL of ethanol was added under a nitrogen (N_2) atmosphere. The mixture was transferred to a Teflon-lined stainless steel autoclave (150 mL) and heated in a muffle furnace at 140 °C for 12 hours. After cooling to room temperature, the sample was washed with water and ethanol and then dried at 60 °C for 8 hours [3]. Figure 1 presents scanning electron microscopy (SEM) images of the NF sample. At 50x magnification (Figure 1a), the typical three-dimensional porous structure of the nickel foam is visible, with uniformly distributed nanowire deposits resulting from the synthesis. At 500x and 1000x magnifications (Figures 1b and 1c), a rougher and more irregular morphology is observed, with greater nanowire adhesion to the surface. This roughness favors electrolyte penetration, increasing the active surface area and, consequently, the efficiency of electrochemical reactions [4]. The strong adhesion of the nanowires may be associated with the drying step and the HCl concentration used during pretreatment. Energy-dispersive X-ray spectroscopy (EDS) analysis, shown in Figure 2, was used to identify and map the elemental distribution on the electrode. Figure 2a shows the SEM-analyzed region, while Figures 2b and 2c demonstrate dense and continuous selenium deposition, evidenced by contrast variations. Figure 2d displays intensity peaks as a function of energy (keV), confirming the significant presence of selenium on the surface. X-ray diffraction (XRD) analysis, shown in Figure 3, identified the presence of metallic nickel from the substrate and an additional peak around 30°, consistent with a selenium diffraction plane, confirming its formation. These results validate the effective surface distribution of selenium on the nickel foam. The porous and rough morphology of the material contributes to an increased active area, enhancing electrocatalytic performance. Therefore, the synthesized material shows strong

potential for application in green hydrogen production via water electrolysis. Further experiments are underway, focusing on the synthesis of the NiSe compound and increasing the selenium surface concentration on the nickel foam [5].

[1] Silva TR et al. *Colloids Surf. A*, 2023, 672.
[2] Cao J et al. *J. Electroanal. Chem.*, 2024.
[3] Tang C et al. *Angew. Chem.*, 2015, 127(32), 9483–9487.
[4] Torres C, Malfatti C. *Estud. Tecnol. Eng.*, 2014, 10(2), 71–76.
[5] This research was supported by CNPq, CAPES, FAPITEC/SE, Sergipe Technology Park (SERGIPETEC), Federal University of Sergipe (UFS), Tiradentes University (UNIT), and the Electrochemistry and Nanotechnology Laboratory (LEN).

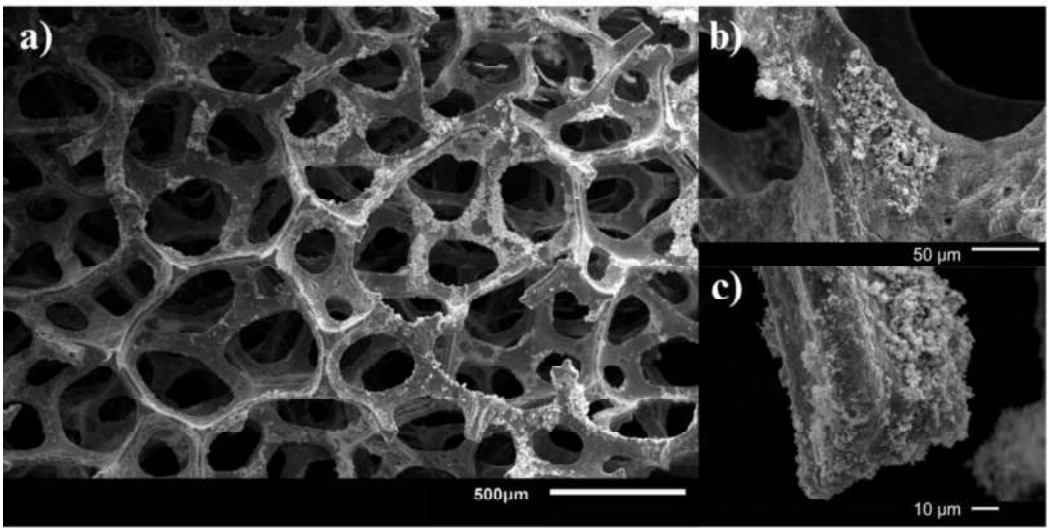

Figure 1. Surface analysis of the NF sample by SEM, showing the same region at three different magnifications: (a) 50x, (b) 500x and c) 1000x.

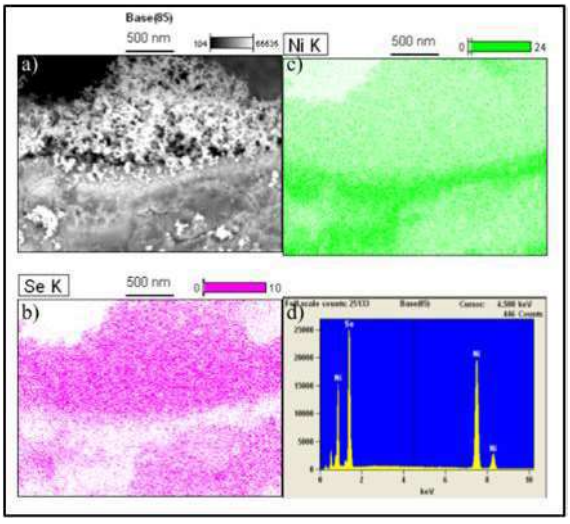

Figure 2. Elemental analysis of the NF sample by EDS: (a) SEM region analyzed, (b) Selenium mapping, (c) Complementary element mapping, and (d) EDS spectrum showing selenium intensity peaks.

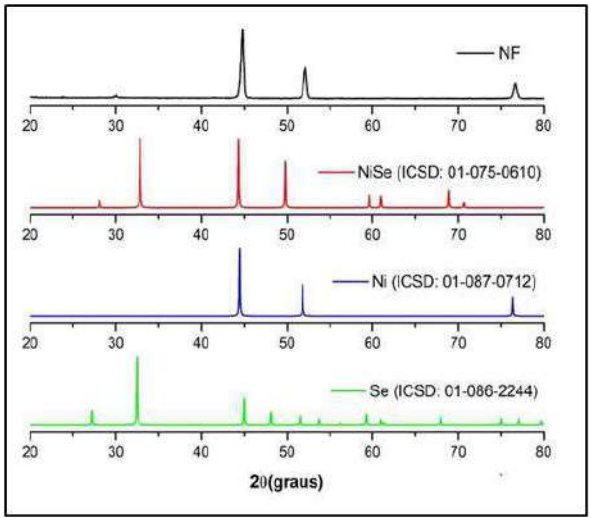

Figure 3. X-ray diffraction patterns of the NF sample, including standard phases (NiSe, Ni, Se).

Synthesis Of Superabsorbent Polymers For Harvesting Atmospheric Water For Human Consumption

Valquiria Campos[1*], Isaac Jamil Sayeg[2], Diego Gouveia Marques[1].

[1]UNESP – São Paulo State University, Science and Technology Institute of Sorocaba, Brazil
[2]USP – University of São Paulo, Institute of Geosciences, Brazil
*v.campos@unesp.br

The goal of this work is to produce drinking water using atmospheric air as a reservoir. Atmospheric humidity and droplets are a significant source of fresh water, especially at low levels of relative humidity typical of arid environments [1]. Synthetic superabsorbent polymers (SAP) are hydrophilic three-dimensionally cross-linked materials characterized by considerable durability and significant water absorption capacity [2,3]. The adsorption of atmospheric water by SAP is highly attractive because its implementation is simple and its operation is low cost. In this study, SAP was synthesized from polyacrylonitrile (PAN) and a device was built for the absorption-desorption of atmospheric water. Polyacrylonitrile, whose general formula is $(C_3H_3N)_n$, is a polymer obtained by polymerization of the vinyl monomer acrylonitrile. The major advantages of this device containing SAP are the easy extraction of water from the air, unlike systems that use metal-organic frameworks and zeolite, and its low cost compared to that of the latter materials. The synthesis of poly(acrylamide-co-acrylic acid) potassium salt was prepared in a 50 mL water sample in a flask equipped with a mechanical device, a thermometer and a nitrogen gas inlet, and placed in a thermostat. After 15 minutes of nitrogen inflow, 20 mL (20%) of potassium persulfate and 12.4 mL (10 mg) of acrylonitrile were added at 40°C in a continuous reaction for two hours. The PAN precipitate was filtered, washed in water and then methanol, and then vacuum dried at 50°C. The polymer was dissolved in DMF and kept at 50°C under a reflux condenser, in a thermostat with constant stirring. A KOH solution (25%) was then added to reach the predetermined degree of hydrolysis, and stirring continued for 240 minutes. Samples were characterized by scanning electron microscopy (SEM) LEO Stereoscan 440I, equipped with an Oxford-LINK ISIS 300 energy dispersive X-ray spectrometer (USP). Finally, the desorption process with the KSAP hydrocell can be monitored using scanning electron microscopy, operated in environmental mode (ESEM), with electron micrographs that record the swelling condition of the hydrocells until their desorption at 30% humidity close to 200 Pa (CNPEM). Macroscopic surface analysis was performed using a stereoscopic magnifying glass equipped with a digital image acquisition system (USP). The capacity of the SAP (hydrocell) plate to absorb atmospheric water was evaluated using a multilayer adsorption-generation device, followed by the modified climate chamber capture process, thus completing the generation-capture cycle. The generation system operated without electricity and could be located in an open or closed environment. Fans were positioned directly over the suspended polymer plates to renew the air. These plates were active during the day and the water was captured by means of a modified climate chamber the following morning. The experimental series indicated that polyacrylonitrile-based KSAP is the better material for harvesting atmospheric water. Its formulation stands out for its high performance in harvesting atmospheric water (1.97 L kg^{-1} of SAP per day), using a constructed device containing polymeric hydrocells [4].

[1] L. Lovis et al., Sustain. Mater. Technol. (2024) 39.
[2] Y. Yang et al., Polymers. 16(4) (2024) 501.
[3] D.G. Marques et al., Rev. Virtual Quim. 16(6) (2024) 844.
[4] This research was financed by FAPESP (Brazil), Grant number 2023/12713-3.

Figure 1. SEM images of the starting materials KSAP (50x and 180x magnification).

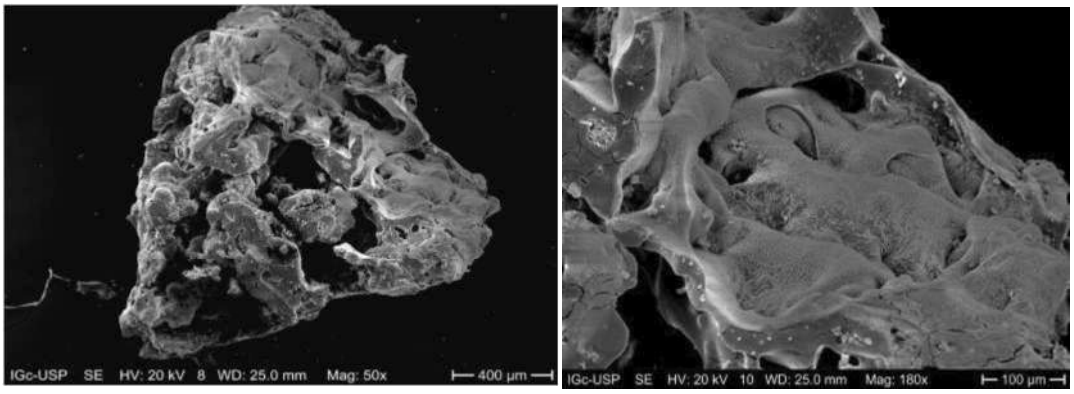

Figure 2. Formation sequence of the KSAP hydrocell: (a) initial adhesion of KSAP grains (1× magnification) and (b) hydrocell (5× magnification).

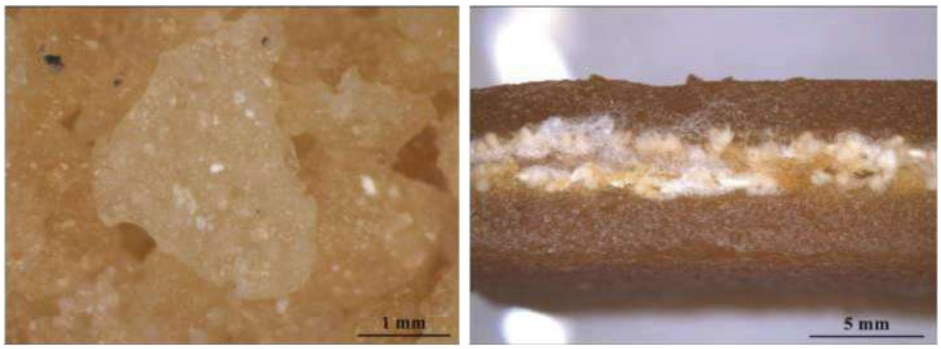

Figure 3. ESEM plate revealing the dehydration sequence of the hydrocells.

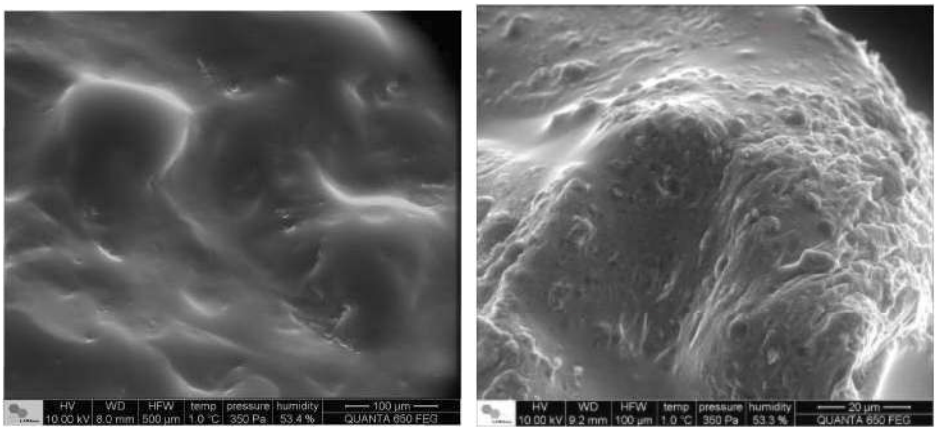

Ti/TiCu Multilayer Composites Fabricated by L-PBF and Functionalized with TiO_2 Nanotubes for Photocatalysis

G.M. Martins[1], L.F. Cremonezzi[1], M. Sangali[2], R. Caram[2], J.A. Dias[1], A. Cremasco[1,2*]

[1]School of Applied Science, University of Campinas, Limeira, SP, Brazil

[2]School of Mechanical Engineering, University of Campinas, Campinas, SP, Brazil

*acremasc@unicamp.br

Ti and its alloys are promising materials for various applications due to their combination of properties, such as high specific strength and excellent corrosion resistance [1]. Laser-based Powder Bed Fusion (PBF-LB) is an additive manufacturing (AM) technology that builds near-net-shape metallic components through layer-by-layer deposition and melting of powder. This technique enables the fabrication of composite multilayer structures using different combinations of metals or alloys [2–3]. When coated with TiO_2 nanotubes, these multilayers samples exhibit enhanced surface properties, opening up potential applications such as reusable photocatalytic filters [4]. The objective of this study is to fabricate a Ti/TiCu multilayer composite using Laser Powder Bed Fusion (L-PBF) and to modify its surface via anodization to create a porous, nanostructured oxide layer for potential use as a photocatalytic filter. The printing parameters included a layer thickness of 30 μm, hatch spacing of 80 μm, laser power of 200 W, and scanning speed of 800 mm/s. After sectioning with a precision cutting machine, TiO_2 nanotubes were formed via anodization in an electrolytic solution containing 0.3% NH_4F and 10% H_2O in ethylene glycol, using two different applied voltages: 20 V and 40 V. The anodized samples were subsequently calcined at 450 °C for 1 hour to induce crystallization to the anatase phase. Morphological and structural analyses of both the substrate and the modified surface were conducted using scanning electron microscopy (SEM) combined with energy-dispersive spectroscopy (EDS), as well as X-ray diffraction (XRD), in the as-built, as-anodized, and heat-treated conditions. The results indicate that surface nanotopography varies depending on the layer's chemical composition and the applied voltage. Heat treatment led to a phase transformation from amorphous to anatase, with minimal changes in surface morphology. The photocatalytic performance of the crystalline nanotube-coated samples was evaluated using a solution containing an emerging contaminant, exposed to a 14 W UVC lamp. Optical absorption analysis, performed with a UV-Vis spectrometer, revealed promising photocatalytic activity.

[1] Li A. et al, Materials Today Communications 42 (2025) 111111.
[2] Dammulla I.N. et al, ACS Omega 9 (2024) 34021.
[3] Sangali M. et al, Vacuum 220 (2024) 112831.
[4] Ji X. et al, Molecular Catalysis 549 (2023) 113463.
[5] This research was supported by Fapesp (Brazil) - Processo nº 2018/18293-8.

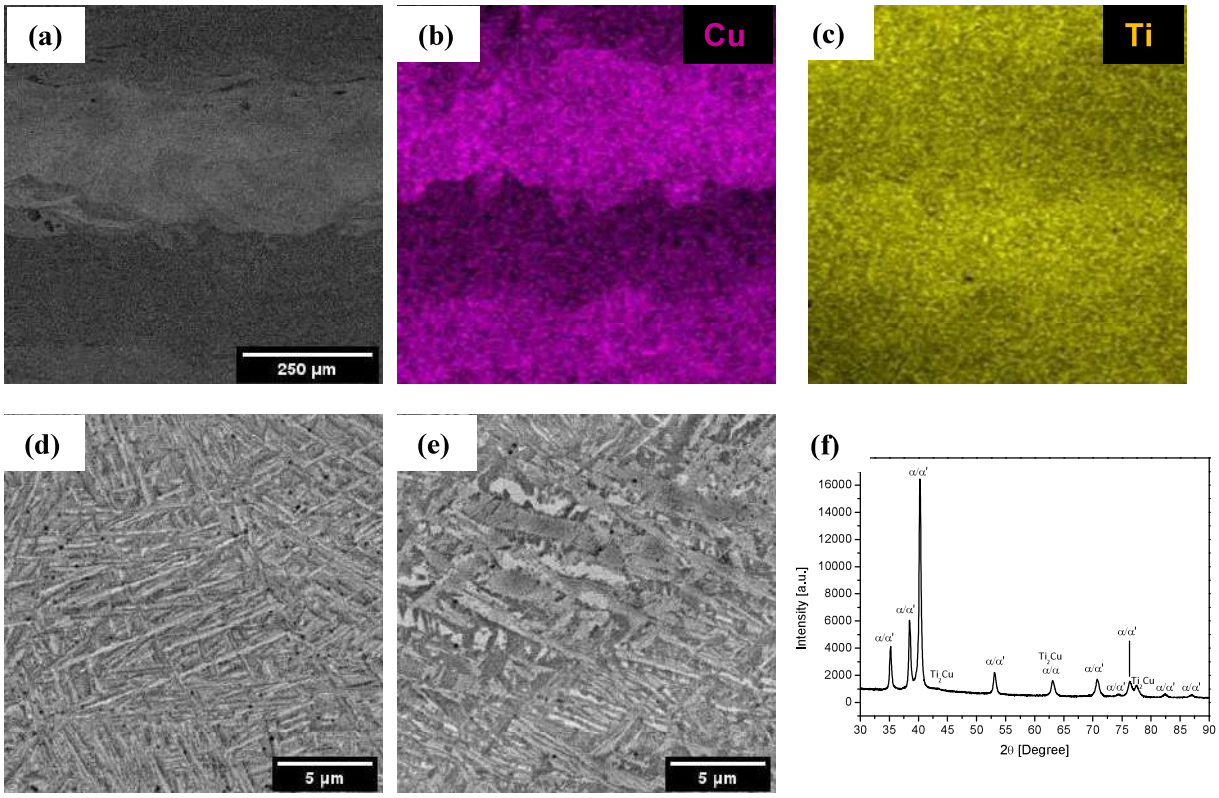

Figure 1. (a) SEM images of the Ti–Ti5Cu multilayer composite produced by Laser Powder Bed Fusion. (b-c) Energy-dispersive spectroscopy (EDS) elemental mapping for Ti and Cu; (d) SEM images of the Ti-5Cu layer region; (e) SEM image of the Ti-CP layer region; and (f) X-ray diffraction (XRD) pattern of the Ti–Ti5Cu multilayer composite

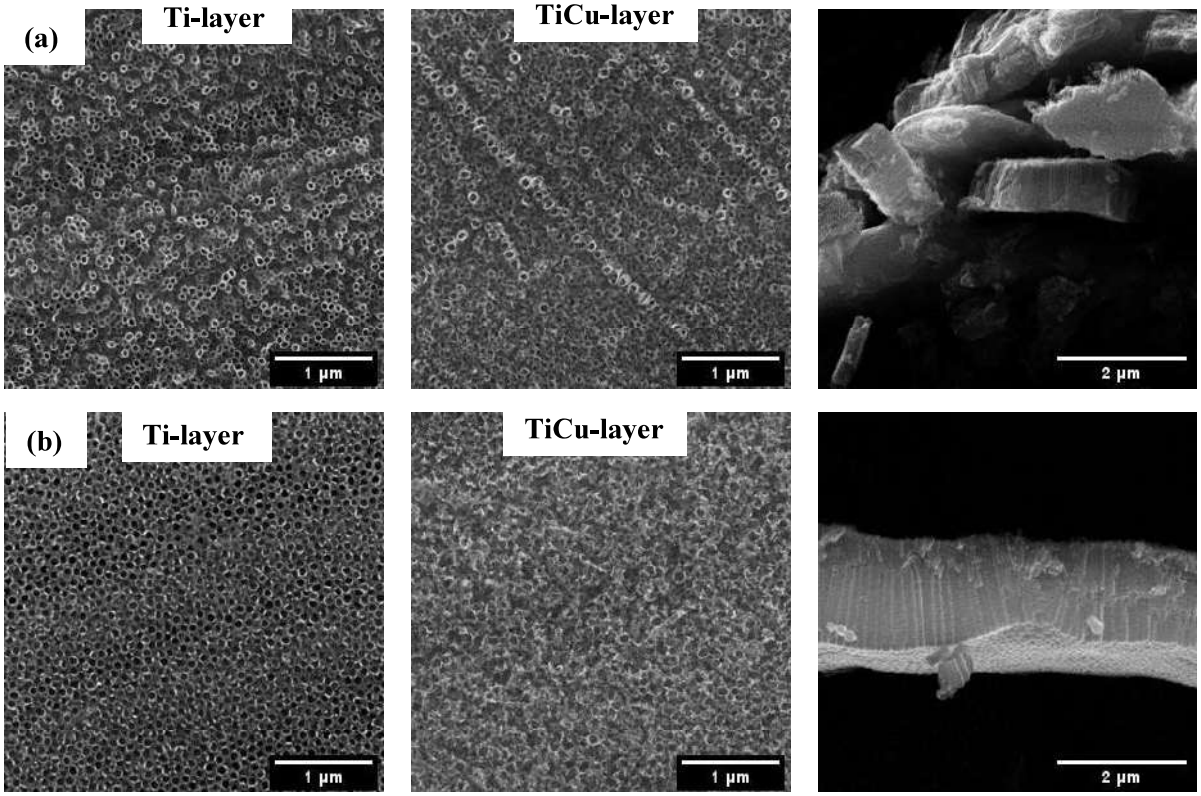

Figure 2. SEM images of TiO_2 nanotubes formed on the surface of the Ti–Ti_5Cu multilayer composite by anodization: (a) anodized at 20 V in an electrolyte containing 0.3% NH_4F and 10% H_2O in ethylene glycol, showing both Ti and Ti–Cu layer regions; and (b) anodized at 40 V in the same electrolyte, also showing both Ti and Ti–Cu layer regions (top-view and cross-sectional views).

Tribological Evaluation of Graphene Coatings on ASTM A36 Steel Synthesized by Low-Pressure Chemical Vapor Deposition

Priscila Carvalho Borba Cardoso[1]*, André do Nascimento Barbosa[2], Marcelo Eduardo Huguenin Maia da Costa[2], Juan Lucas Nachez[3], Fagner Marçal Andrade[3], Suzana Bottega Peripolli[1], José Brant de Campos[1].

[1]Rio de Janeiro State University, [2]Pontifical Catholic University of Rio de Janeiro, [3]Fluminense Federal University
*priborbaengenharia@gmail.com

Graphene has emerged as a revolutionary solid lubricant due to its exceptional mechanical properties and low surface energy, with recent studies demonstrating its effectiveness in reducing friction and wear in steel tribosystems [1,2]. This work was synthesized in a tubular quartz reactor furnace using low-pressure chemical vapor deposition (LPCVD) on ASTM A36 steel substrates at 1000°C and 400 mTorr with an ethanol precursor [3], with growth times of 30, 40, and 60 minutes [1]. The substrate composition was 99% Fe with 0.634% Mn, 0.184% C, 0.0134% Si, 0.0129% P, and 0.011% S. Prior to deposition, substrates were mechanically polished to 0.199 μm roughness and ultrasonically cleaned in acetone and isopropyl alcohol. Tribological characterization was performed using a CTER-UMT Multi-Specimen Test System in ball-on-disk configuration, with an AISI 302 stainless steel ball (6 mm diameter) under reciprocating motion (10 mm stroke length, 10 mm/s sliding velocity). A constant normal load of 0.3 N was applied, corresponding to 398 MPa Hertzian contact pressure. All tests were conducted in a controlled environment (22°C, 55% relative humidity monitored by thermohygrometer) with triplicate measurements for each condition to ensure reproducibility. Figure 1 showed that the uncoated ASTM A36 steel exhibited an initial coefficient of friction (COF) of 0.36 under 0.3 N load, which gradually increased to higher steady-state values, characteristic of unprotected surfaces. In contrast, graphene-coated samples demonstrated superior tribological performance, maintaining stable COF values of 0.11 (30 min growth), 0.12 (40 min), and 0.12 (60 min), representing 67-69% reduction compared to substrate as received [1]. The average 67.42% friction reduction across all coated samples revealed consistency in tribological performance. This performance parallels Singh et al.'s findings for GCr15 steel (COF reduction from 0.59 to 0.15-0.19) [4], attributed to carbon segregation mechanisms. The microscopic analyses in figure 2, starting with optical microscopy of the counterfaces (Fig. 2A, C, E and G), showed no significant film material transfer, confirming the coating's durability. SEM examination of wear tracks (Fig. 2B, D, F and H) revealed smooth, homogeneous surfaces with reduced plastic deformation compared to uncoated samples, demonstrating graphene's effective lubrication mechanism. These results demonstrate the reproducibility and effectiveness of LPCVD-grown graphene coatings for friction reduction in carbon steel applications.

[1] P. C. Borba Cardoso et al., Journal of Materials Research and Technology 36, 9013-9020 (2025).
[2] A. Tomanik et al., Tribology International 198, 109896 (2024).
[3] E. C. Romani et al., Tribology Letters 65, 1-9 (2017).
[4] S. Singh et al., Journal of Tribology 142, 122101 (2020).

Figure 1. Comparison of the tribological performance of CVD graphene coatings on metallic substrates measured with a load of 0.3N.

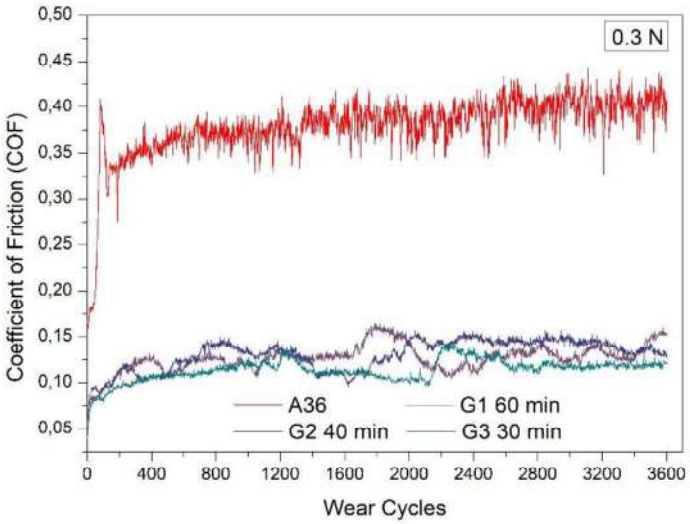

Figure 2. OM and SEM images of the counterbodies and wear tracks of the substrate as received and of the samples with graphene grown by CVD at different synthesis times: (A, B) Substrate A36; (C, D) 30 minutes; (E, F) 40 minutes; (G, H) 60 minutes. (A, C, E, G) Counterbodies; (B, D, F, H) Wear tracks; Magnifications: (A, C, E, G) 10x; (B, D, F, H) 200x.

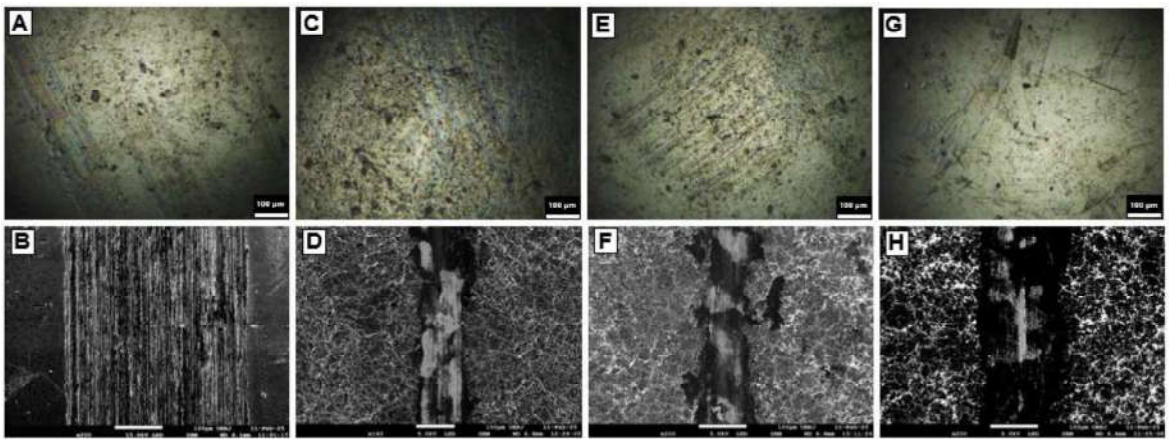

Optical microscopy applied to materials science and related techniques such as fluorescence, confocal, and polarized light microscopy

Dispersion and Stability of CaO Microfluids from Natural Waste in Enhanced Oil Recovery: A Microscopy Study

[1]Késsya J. G. de Araújo Cavalcanti, [1]Jean S. Mafra; [1]Joséfane K. F. de Souza; [1]Valter L. G. da França; [1]Leonardo T. de Almeida; [1]Maria Luiza dos S. Oliveira; [1]Ellen R. de Souza; [1]Giovanna K. C. de Oliveira Lira; [2]José L.S. Duarte, [1]Leonardo M.T.M. Oliveira.

[1]Laboratório de Materiais para Remediação Ambiental (LabMARE), CTEC, UFAL., [2]Departamento de Ingeniería Química y de Materiales, Facultad de Ciencias Químicas, Universidad Complutense de Madrid.

E-mail: goncalves.mk@hotmail.com

In light of the escalating global energy demand and the dwindling conventional oil reserves, the imperative to develop sustainable and efficient Enhanced Oil Recovery (EOR) technologies intensifies. (1) Within this context, nanofluids have emerged as a promising alternative, owing to their unique physicochemical properties like high thermal conductivity, reduced interfacial tension, and the ability to alter rock wettability (2). Nevertheless, the stability of these colloidal suspensions continues to present a major challenge for their practical deployment in oil fields (3). This work aims to analyze the stability of microfluids produced with calcium oxide (CaO) microparticles, obtained from discarded shells of *Mytella charruana*, an abundant food waste in the state of Alagoas, Brazil. The particles were dispersed in distilled water at concentrations (0.05 - 0.5% (w/v), using ultrasonication at different times (1 - 3h). Stability was evaluated through turbidity analysis, optical microscopy (OM), and scanning electron microscopy (SEM). The results demonstrated that the ultrasonication time had a direct influence on particle dispersion. Figure 1a shows that after 1 hour of sonication, large agglomerates were observed. Extending sonication to 2 hours resulted in a more homogeneous dispersion with minimal edge agglomeration, and 3 hours achieved more effective particle separation, particularly at lower concentrations. Stability after 90 minutes of resting was most pronounced in the 0.05% and 0.1% samples (Figure 1b). SEM images (Figure 2) further confirmed the reduction of agglomerates post-dispersion, validating the efficacy of ultrasonication. As presented in Figure 3, the turbidity of calcium oxide nanofluids varies distinctly over time for each concentration, directly reflecting the colloidal stability of the systems. These findings indicate that controlling sonication time is a critical factor for microfluid stability. Achieving such stable dispersions is vital for EOR applications, as it ensures better transport through porous media, minimizes injectant loss, and maximizes effective contact with the crude oil, thereby significantly enhancing recovery efficiency and promoting sustainable solutions.

[1] Ali, Jagar A., et.al. A state-of-the-art review of the application of nanotechnology in the oil and gas industry with a focus on drilling engineering, Journal of Petroleum Science and Engineering, Vol. 191, p. 107118, (2020).

[2] Sandhya, Madderla, et al. Ultrasonication an intensifying tool for preparation of stable nanofluids and study the time influence on distinct properties of graphene nanofluids – A systematic overview.. Ultrasonics Sonochemistry, Vol. 73, p. 105479. 1350-4177, (2021).

[3] Bello, Mohammed Nasiru, et al. A novel green nanocomposite for EOR: Experimental Investigation of IFT Reduction, wettability Shift, and nanofluid stability, Vol. 414. 126187, (2024).

Figure 1: (a) OM of CaO microfluids at different concentrations (0.05, 0.1, and 0.5% w/v) after ultrasonic of 1h, 2h, and 3h. (b) Microfluids stability at different concentrations (0.05, 0.1, and 0.5% w/v) and resting time (T = 0, 30, 60, and 90 min.), via OM**.**

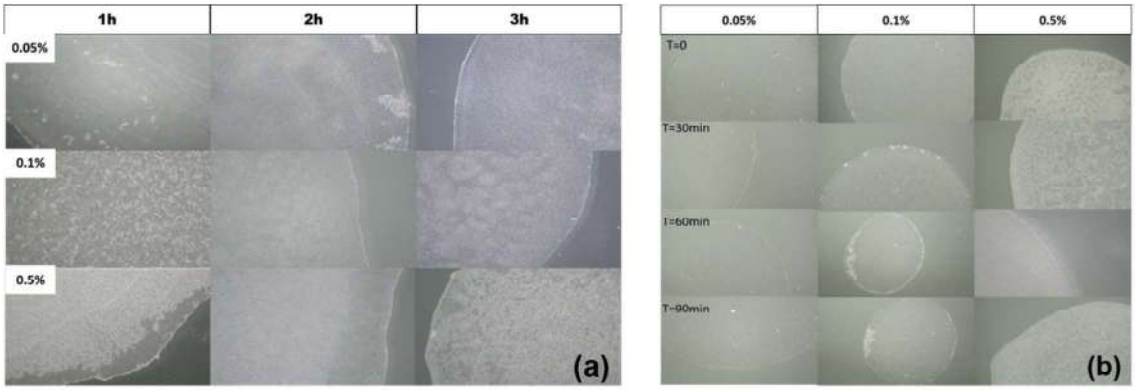

Figure 2: SEM images of CaO particles. Series 1 (1.1–1.3): Powdered particles. Series 2 (2.1–2.3): Particles after dispersion in microfluid and drying.

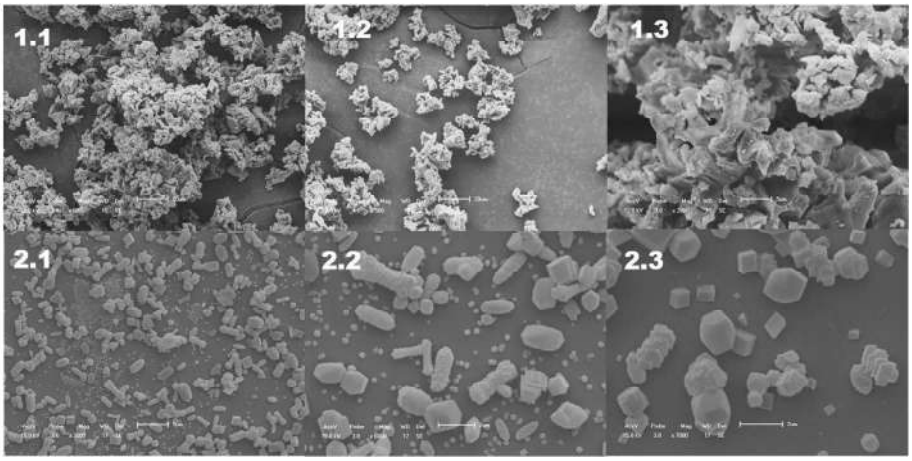

Figure 3: Variation in turbidity over time for calcium oxide nanofluids at different concentrations (0.05%, 0.1%, and 0.5% by weight). Turbidity was monitored as an indicator of the colloidal stability of the systems.

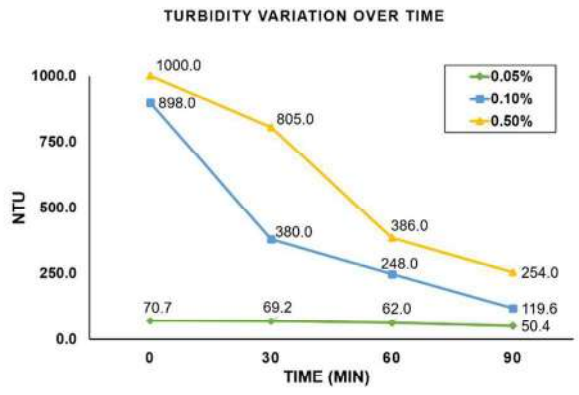

Effect of Cathodic Protection under Alternatives Potentials on the Corrosion Morphology of Carbon Steels

Elisa Kassab[1]*, Eduardo A. de Souza[1], Jefferson R. Oliveira[2], Marcelo Schultz da Rocha[3], José A. Ponciano Gomes[1]

[1] Department of Metallurgical and Materials Engineering, Federal University of Rio de Janeiro (COPPE/UFRJ), RJ, Brazil, [2] Corrosion Engineering, Petrobras, RJ, Brazil, [3]Subsea Engineering, Petrobras, RJ, Brazil
*elisajk@metalmat.ufr.br

Cathodic Protection (CP) stands as a widely adopted method to mitigate corrosion of subsea equipment. International standards, such as ISO-15589-2 [1] and DNV-RP-B401 [2] recommends a Cathodic Protection criteria between -800 and -1,100 mV (Ag/ACl).

In this work, the use of alternative CP potentials was investigated in terms of corrosion morphology of the coupons surface. Laboratory tests were carried out with A36 carbon steel in natural seawater subjected to different CP potentials: conventional CP potential (-800 mV), alternative potentials of -700 and -750 mV and at Open Circuit Potential for 30 days duration time. After immersion tests, the morphology of the corroded surfaces was analyzed using a Smartzoom digital optical microscopy from Zeiss. The images were processed using the MountainsMap 10.0 commercial software for a three-dimensional (3D) scanning and reconstruction of the coupons (Figure 1), which allowed the measurement and quantification of the corrosion events. A minimum depth of 50 μm was established as the criterion for localized corrosion, enabling the measurement of the following parameters: The number of localized corrosion events (N50), the percentage of the area occupied by these events (A50), and the maximum depth of the localized corrosion events. The results showed a significant difference between the non-polarized samples (OCP) and the cathodic polarized samples, with incidence of localized corrosion events only on the group tested at OCP. For the cathodic polarized samples, uniform corrosion was the predominant event and the corrosion morphology was equivalent with the use of standard and alternative potentials.

[1] ISO – INTERNATIONAL ORGANIZATION FOR STANDARDIZATION. ISO-15589-2: Petroleum, petrochemical, and natural gas industries - Cathodic Protection of Pipeline Transportation Systems - Part 2: Offshore Pipelines. 2012-12-01 ed. Switzerland: ISO, 2012. 11 p.

[2] DET NORSKE VERITAS, DNV-RP-B401: 2017 - Cathodic Protection Design

[3] This research was supported by the Fundação Coordenação de Projetos, Pesquisas e Estudos Tecnológicos (Fundação COPPETEC), PETROBRAS, FAPERJ, and CNPq.

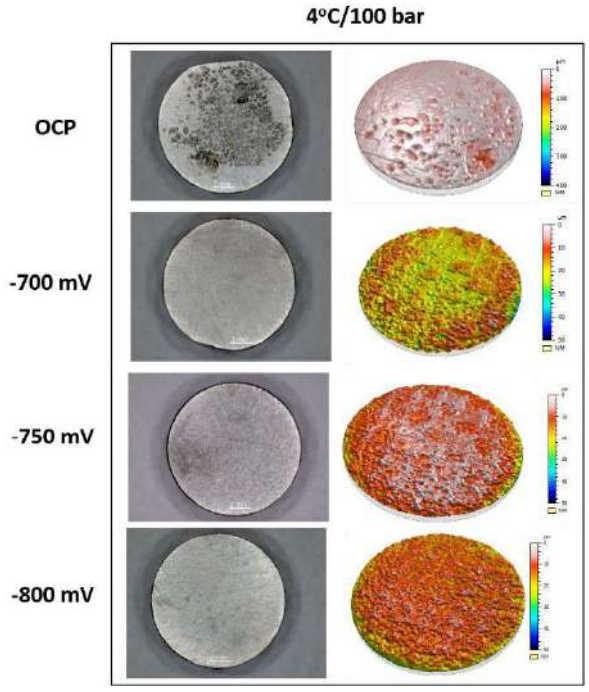

Figure 1. Surface morphology after 30-days immersion in natural seawater. Left: Images obtained by Smartzoom (Zeiss). Right: 3D reconstruction of the test specimen obtained from scanning the surface for the test condition of 4°C/100 bar.

Elemental Characterization of Pigments in a 19th Century Prayer Book Using Portable Milli-XRF

F.T.S. Tsuyama[1]*, H.S. Gama Filho[1], D.S.S. Costa[1], D.O. Mansur[1], R.L. Leitão[1], C.G.L. Canellas[1], M.J. Anjos[1], J. T. Assis[2].

[1] Laboratório de Instrumentação Eletrônica e Técnicas Analíticas, Instituto de Física, Universidade do Estado do Rio de Janeiro, Rio de Janeiro, RJ, Brasil,
[2] Instituto Politécnico, Universidade do Estado do Rio de Janeiro, Nova Friburgo, RJ, Brasil
* tsuyama.fabio@posgraduacao.uerj.br

The prayer book [1] analyzed in this work belongs to the collection of the Imperial Museum/Petropolis/RJ and is part of the Empress Teresa Cristina collection. She was the Empress consort of Emperor Dom Pedro II of Brazil, who reigned from 1831 to 1889. The collection of the museum consists of pieces linked to the Brazilian monarchy (1822-1889). The prayer book was written in French and represents a remarkable work of color lithography. On each margin of the page, there is a golden-colored representation of plants, flowers and a wide variety of insects and small farm animals.

The book was analyzed by XRF technique [2] directly in situ in the Museum Library, using a portable XRF equipment developed in our lab (Figure 1). The milli-XRF system consists of an X-ray tube with a silver target and operates at 50 kV, 200 μA, an SDD detector and 0.5 mm and 1.0 mm X-ray beam collimation. X-ray beam position on the object has been controlled with a CCD micro camera. The mili-XRF system allows spot measurements and mapping. The regions without and with pigments were analyzed (pigments: red, pink, green, blue, silver, golden, brown and white) (Figure 2). The detected elements were: S, Ca, Cr, Fe, Cu, Zn, Ba, Hg and Pb. The results show that Ca, Fe, Cu and Zn were the predominant elements in regions without pigments. Lead (Pb) was detected in all regions with pigments. Correlation tests showed that there is a strong correlation between Pb and S, this may be indicative of the presence of lead white in all regions with pigments. mapping showed the same result. Besides that, the sulfur, chromium and lead mapping in brown pigment showed a high correlation, indicating the presence of chromium red. The red pigment showed a strong correlation between sulfur and mercury, probably indicating the presence of cinnabar. The elements zinc and barium are probably not related to pigments, these elements are known as additives that are used with an extender in lithographs (a mixture of barium sulphate and zinc sulfide). Gold lines L were found only on the book edge, proving to be just an artistic decoration element (Figure 3). It was possible to perform mapping of some regions and the results showed that the pigments found were consistent with the lithographic processes of the 19th century.

[1] A. Agostino et al., *On the Hierarchical Use of Colourants in a 15th Century Book of Hours*, Heritage, 2021.
[2] S. Saverwyns et al., *Macro X-ray fluorescence scanning (MA-XRF) as tool in the authentication of paintings*, Microchemical Journal, 2018.

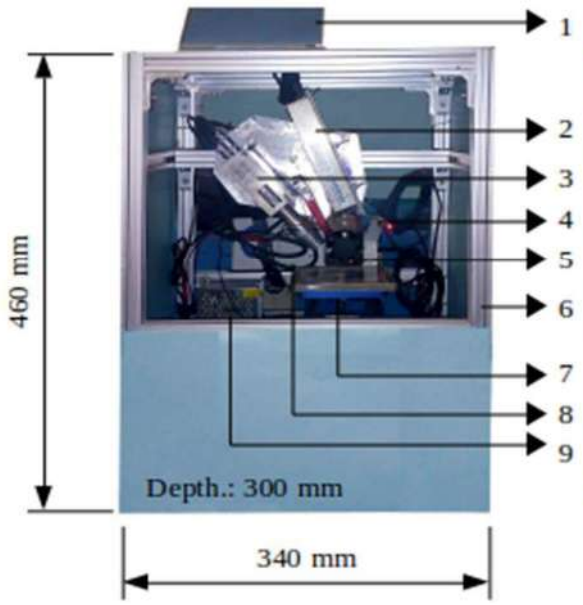

No.	Description
1	Auxiliary screen for local setup. The system command line is displayed since power up.
2	Low-power X-ray tube of 40 kV/200µA. Interfaced with the microcomputer via USB.
3	Photon detector of type SDD with a 16-bit ADC embedded. Interfaced with the microcomputer via USB.
4	7.0 MP monitoring camera. Streaming real-time video to the system web interface.
5	X-ray tube cooler. Automatically triggered by the system when certain critic temperature is reached.
6	Structure of aluminum. Lightweight and sturdy.
7	XYZ stepper motor moved precision stage. Perform the sample alignment and movement. Can achieve minimum step of 50 µm.
8	Raspberry Pi® microcomputer case and control circuit.
9	Power supply. Input: 127-220 V 50-60 Hz AC. Output: 12 VDC and 5 VDC.

Figure 1. mili-XRF system.

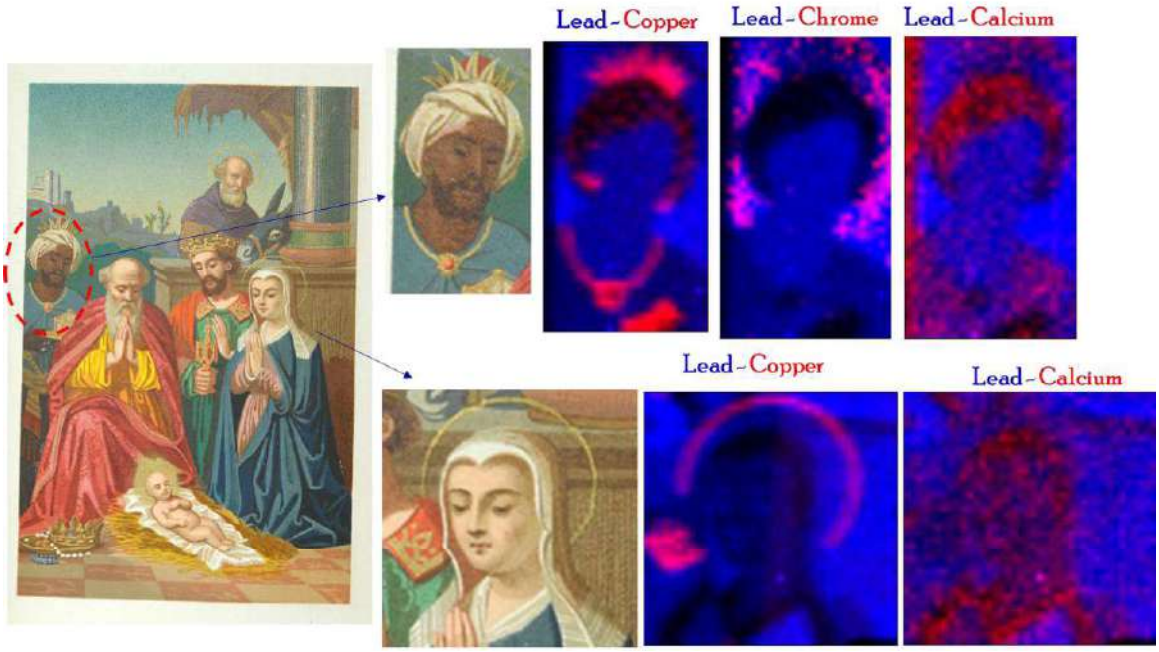

Figure 2. Regions analyzed on a page.

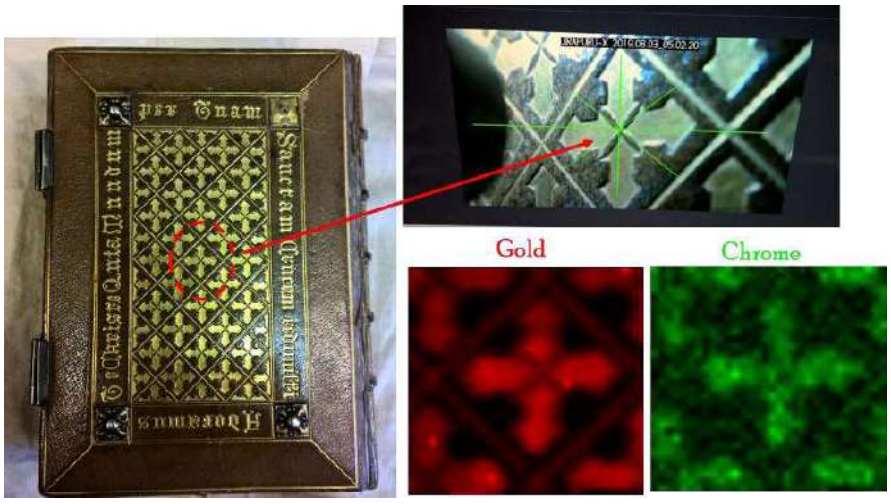

Figure 3. Regions analyzed on the cover.

Immunofluorescence analysis of IL-6 and OPN in the pulp tissue of rats

Evelin Carine Alves Silva[1], Lucas de Andrade Rodrigues[1], Estela Sasso-Cerri[1], Paulo Sérgio Cerri[1]*.

Faculdade de Odontologia de Araraquara, FOAr-UNESP[1].
*paulo.cerri@unesp.br

Calcium silicate-based repair cements have been developed and investigated due to their advantageous physicochemical characteristics and biocompatibility. Upon in contact with tissues, the calcium silicate-based biomaterials release calcium ions, which play a pivotal role in modulating the activity of several cell types, including odontoblasts and fibroblasts [1,2]. Furthermore, the calcium release also promotes the recruitment and activation of progenitor cells capable of differentiating into odontoblast-like cells. In damaged dental pulp, these cells can produce a collagen-rich extracellular matrix, in which calcium and phosphate are deposited, culminating in the formation of a mineralized barrier [3]. Our purpose was to evaluate the pulp dental response to bioceramic cements CIMMO DTA (CM), recently introduced in the market, in comparison with Bio-C Repair (BC) and calcium hydroxide (CH). 60 male Holtzman rats aged 30–35 days were distributed into 4 groups: CM, BC, CH, and a control group (CG; healthy molars). A class I-shaped cavity was performed in the first upper molars with a ¼ carbide round bur at low speed, under constant irrigation. Subsequently, the pulp was exposed using a probe, and the bleeding was controlled with a sterile cotton-pellet. Repair cements were applied to the exposed pulp tissue using disinfected gutta-percha cones, and the cavities were sealed with a light-cured glass ionomer cement. After 7, 21, and 45 days, the rats were euthanized, and the fragments of maxilla were fixed for 48 h in 4% formaldehyde buffered at pH 7.2 with 0.1 M sodium phosphate. Sections of maxilla were stained with Masson's trichrome for morphological analysis and other sections were submitted to immunofluorescence reactions for detection of interleukin-6 (IL-6) and osteopontin (OPN). Statistical analysis was performed using two-way ANOVA followed by Tukey's test ($p < 0.05$). At 7 days, despite a mild inflammatory reaction in the dental pulp, a forming mineralized barrier (Bm) was observed adjacent to the perforated dentine; the "Bm" was associated with a disorganized layer of odontoblast-like cells (Figs. 1a–c). At 45 days, the treated groups exhibited a well-defined mineralized barrier accompanied by a palisade arrangement of odontoblast-like cells (Figs. 1e-g). In contrast, the CG showed healthy pulp tissue at all periods (Figs. 1d,1h). At all periods, the immunofluorescent area for IL-6 in the dental pulp adjacent to the exposed area was significantly greater in the treated groups than in CG (Figs. 2a-h; Table 1). At 7 days, the CM exhibited lower IL-6 immunoexpression than BC whereas significant differences were not observed between CM versus CH, and BC versus CH (Figs. 2a-b; Table 1). However, at 21 and 45 days, significant differences were not observed among CM, BC, and CH (Figs. 2e-g; Table 1). Calcium release by materials may be responsible at least in part for the increased IL-6 in the treated groups [4]. Regarding OPN, at 7 days, significant differences in the immunolabelled odontoblast-like cells layer were not observed among the treated groups, but all treated groups exhibited lower immunoexpression than the CG specimens (Figs 3a-h; Table 1). At 21 and 45 days, the OPN immunoexpression was significantly greater in CM and HC than in BC specimens (Figs. 3e-g; Table 1). Considering that OPN modulates cell adhesion and stimulates the biomineralization [5], our results suggest that CM may promote the mineralization of matrix synthetized by odontoblast-like cells. These results taken together suggest that reduced inflammatory response, initially promoted by CM, favours the production of OPN by odontoblast-like cells allowing the repair of dentine-pulp complex.

[1] L.A. Almeida-Junior et al. J. Endod. 49 (2023) 1329.
[2 M.J.B. Barbosa Silva et al., Oral Surg. Oral Med. Oral Pathol. Oral Radiol. Endod. 105

(2008) e70.
[3] J. Camilleri, Front. Dent. Med. 1 (2020) 9.
[4] A. El-Ghannam, Expert Rev. Med. Devices 2 (2005) 87-101.
[5] K. Suzuki-Barrera et al., Regener. Ther. 21 (2022) 460-468.
[6] This research was supported by CNPq (152717/2024-2) and FAPESP (2024/05041-1).

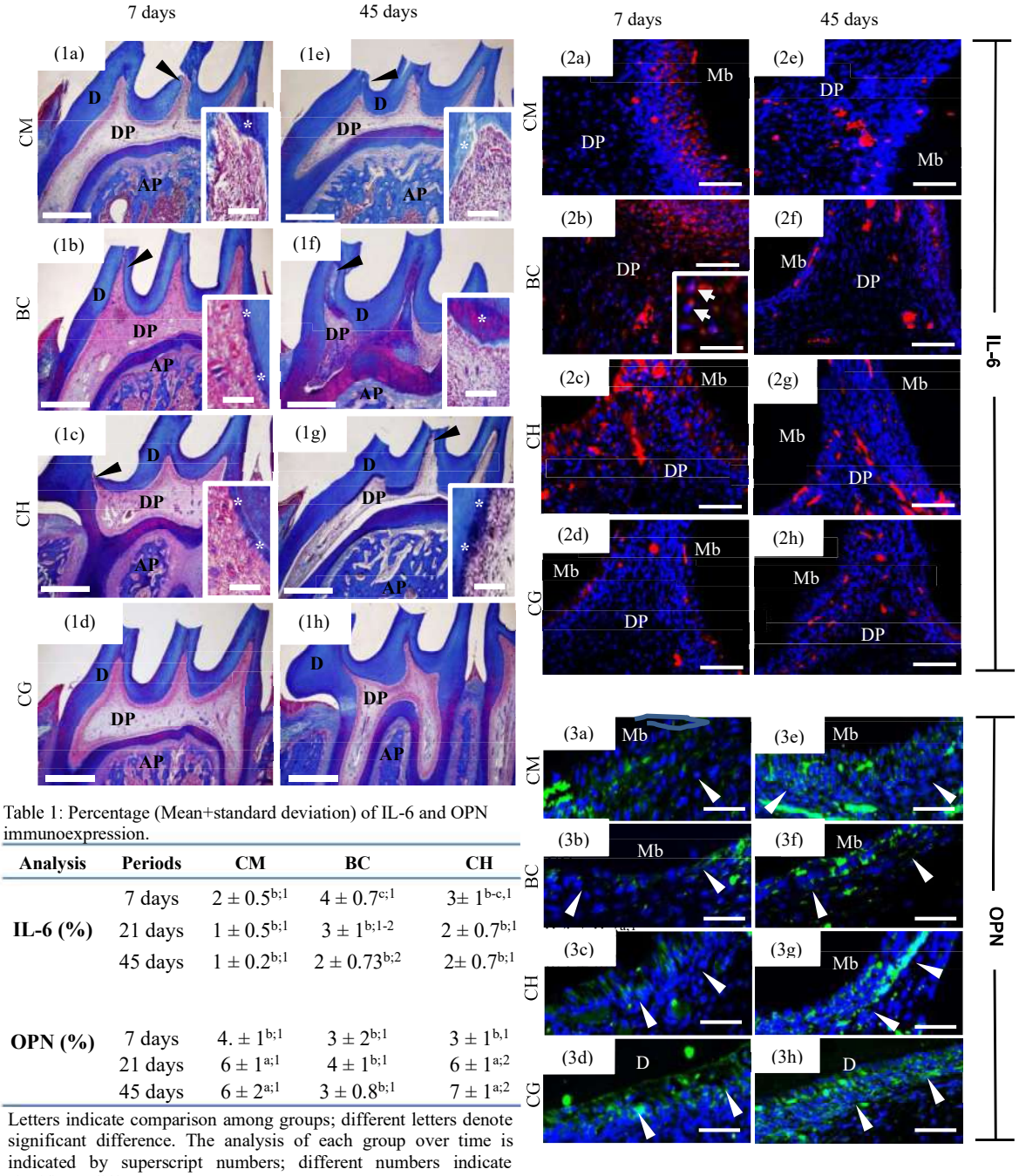

Table 1: Percentage (Mean+standard deviation) of IL-6 and OPN immunoexpression.

Analysis	Periods	CM	BC	CH
IL-6 (%)	7 days	$2 \pm 0.5^{b;1}$	$4 \pm 0.7^{c;1}$	$3\pm 1^{b\text{-}c,1}$
	21 days	$1 \pm 0.5^{b;1}$	$3 \pm 1^{b;1\text{-}2}$	$2 \pm 0.7^{b;1}$
	45 days	$1 \pm 0.2^{b;1}$	$2 \pm 0.73^{b;2}$	$2\pm 0.7^{b;1}$
OPN (%)	7 days	$4. \pm 1^{b;1}$	$3 \pm 2^{b;1}$	$3 \pm 1^{b,1}$
	21 days	$6 \pm 1^{a;1}$	$4 \pm 1^{b;1}$	$6 \pm 1^{a;2}$
	45 days	$6 \pm 2^{a;1}$	$3 \pm 0.8^{b;1}$	$7 \pm 1^{a;2}$

Letters indicate comparison among groups; different letters denote significant difference. The analysis of each group over time is indicated by superscript numbers; different numbers indicate significant difference.

Figure 1: a-h – Sagittal sections of maxillae stained by Masson's trichrome. Perforation site in the first molars is indicated by arrowheads. Insets: show the area adjacent to the perforated dentine. D, dentine; DP, dental pulp; AP, alveolar process; mineralized barrier (asterisks). Scale bars: 546 µm and 72 µm (insets).

Figure 2: a-h – Immunofluorescence reaction for IL-6 (in red colour) showing the dental pulp region adjacent to the perforation site. Inset: immunopositive-cells (arrows). D, dentin; DP, dental pulp; Mb, mineralized barrier. Scale bars: 36 um and 17 µm (inset).

Figure 3: a-h- Immunofluorescence reaction for OPN (in green colour) exhibiting the periphery of the dental pulp adjacent to the perforation site. Immunolabelled odontoblast like-cells layer is delimited by arrowheads. D, dentine; Mb, mineralized barrier. Scale bars: 26 µm.

Impact of top coat thickness on the integrity of thermal barrier coatings

Bianca Costa Rodrigues[1]*, Renata Jesuina Takahashi[1], Leonardo Henrique Fazan[1], Vera Lúcia Othéro de Brito[2], Danieli Aparecida Pereira Reis[1].

[1]Universidade Federal de São Paulo, [2]Instituto de Estudos Avançados - IEAv/DCTA
*bianca.costa@unifesp.br

In the aerospace industry, there is a continuous effort to improve the service life of components and the properties of the materials applied. One of the main focuses is protective coating systems, especially thermal barrier coatings (TBCs), which protect components exposed to high temperatures, such as gas turbines [1]. TBCs are composed of three layers: a metallic bond coat, which is in direct contact with the substrate; an external ceramic layer (top coat); and a thermally grown oxide (TGO) layer between the bond coat and the top coat, which provides chemical protection to the substrate [2-3]. These coatings can be applied by techniques such as atmospheric plasma spraying (APS) and high-velocity oxy-fuel spraying (HVOF), with the production technique influencing the morphology and microstructure of the coating, while the thickness of the layers directly affects their mechanical, thermal oxidation, and insulation properties [4-5]. This work evaluated the impact of using thick top coat layers in TBCs produced with bond coat deposited by APS and HVOF on Ti-6Al-4V substrates, with emphasis on microstructure and coating integrity. The TBCs, with an 8YSZ top coat and NiCrAlY bond coat. The samples were prepared metallographically, cut, hot-mounted in bakelite, ground, polished with silica, and chemically etched with Kroll's reagent. Characterization was performed by optical microscopy (Olympus BX53M), and the layer thicknesses were measured using the ImageJ software. It was found that the manufacturer's parameters resulted in an APS top coat thickness of 1 mm (1000 μm), which is higher than the typical range of 130 to 380 μm [6-7], characterizing it as a thick layer. The bond coat applied by APS showed a thickness of 275 ± 28 μm, exceeding the usual range (60 to 160 μm), while the bond coat applied by HVOF, with 127 ± 11 μm, remained within the expected range [2][7]. Although increasing the top coat thickness can improve thermal insulation, it also raises residual stresses, which may lead to premature coating delamination [8], as evidenced by the cracks observed in the micrographs. Studies showed that top coats up to 300 μm maintain clean and adherent interfaces, while greater thicknesses, such as 400 μm, already present cracks due to high residual stresses, corroborating the results of this analysis [5]. Therefore, the results reinforce that excessively thick top coat layers, although potentially beneficial for thermal insulation, significantly compromise the structural integrity of the TBC system. It is expected that the data obtained may contribute to the development and selection of more effective coatings for applications in the aerospace industry. Furthermore, this study represents a technological advance for the Brazilian aerospace sector by employing national technology.

[1] Y. Zhou *et al. J. Eur. Ceram. Soc.* 44 (5) (2023) 3099–3111.
[2] C.R.C. Lima, R.E. Trevisan, *Aspersão Térmica: Fundamentos e Aplicações*, 2nd ed., Artliber Editora, São Paulo, 2007.
[3] R.J. Takahashi *et al.*, *J. Mater. Res. Technol.* 19 (2022) 4932–4938.
[4] R. Darolia, *Int. Mater. Rev.* 58 (6) (2013) 315–348.
[5] H.R. Abedi, M. Salehi, A. Shafyei, *Ceram. Int.* 44 (6) (2018) 6212–6222.
[6] C.U. Hardwicke, Y.C. Lau, *J. Therm. Spray Technol.* 22 (5) (2013) 564–576.
[7] C.R.C. Limar, *Soldag. Insp.* 19 (2014) 353–363.
[8] J. Zhang, V. Desai, *Surf. Coat. Technol.* 190 (1) (2005) 98–109.
[9] This research was supported by CNPq, CAPES, CNPq, FINEP, FAPES (Brazil), and Alpha Metalização.

Table 1. Thickness measurements of the BC and TC layers deposited by plasma and

HVOF.

Layer	Plasma-Sprayed Bond Coat (µm)	HVOF-Sprayed Bond Coat (µm)
Bond Coat	(274.75 ± 28.22)	(127.54 ± 11.34)
Top Coat	(1062.64 ± 35.06)	(1116.87 ± 15.93)

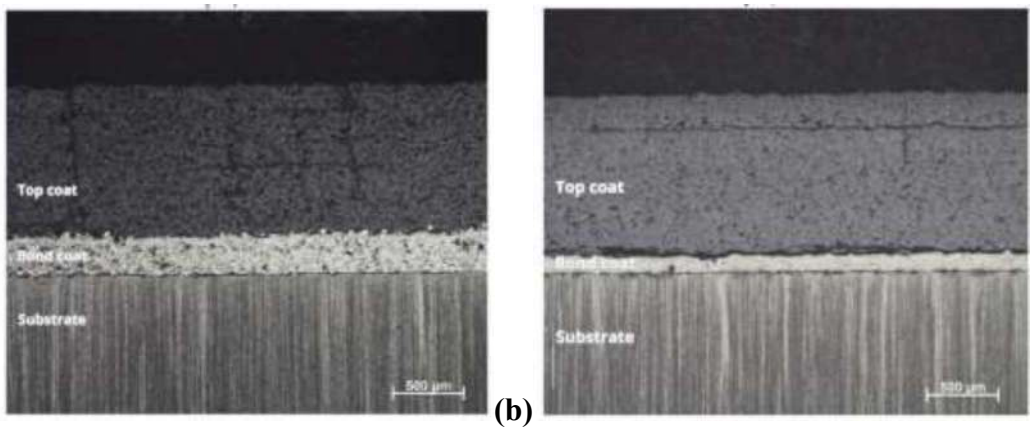

(a) **(b)**

Figure 1. Micrograph of the cross-section of the Ti-6Al-4V specimen with coating obtained by optical microscopy, with bond coat applied by (a) APS and (b) HVOF.

Kapok as an Active Morphological Agent in Emulsion Coalescence: An Optical Microscopy Approach

Noemi Oliveira dos Santos[1]*, Carla Catharine Gomes Brecho[1], Kaline Cavalcante Vasconcelos[2], José Leandro da Silva Duarte[3], Leonardo Mendonça Tenório de Magalhães Oliveira[4].

[1]Federal University of Alagoas [2]Complutense University of Madrid
noemi.santos@ctec.ufal.br

The coalescence of droplets in emulsions is a complex interfacial phenomenon that is not yet fully understood and is often described in classical models based on energetic parameters and simple physical contact between phases [1]. This study proposes a new approach centered on the morphological influence of natural surfaces, using the kapok capsule (Ceiba pentandra (L.) Gaertn) as a model due to its complex microstructures, such as cavities formed by stacked thin plates and cylindrical or spiral elements, which provide high roughness and extensive surface area [2]. The kapok surface was evaluated for its ability to act not only as a physical support but also as an active morphological agent in inducing coalescence. Through assays conducted using optical stereomicroscopy, oil-in-water (O/W) emulsions were analyzed under varying pH conditions (3, 7, and 9), salinity levels, and with/without surfactant, comparing the effects of these variables on coalescence behavior on different surfaces (kapok and glass slide). Salinity promoted coalescence on both materials, though more intensely on kapok. The surfactant stabilized the emulsion on the glass slide, reducing droplet mobility, whereas on kapok, successive coalescence events occurred even in its presence, indicating an active role of the fibrous surface. Under acidic (pH 3) and alkaline (pH 9) conditions, reduced emulsion stability was observed on kapok, with frequent and distributed coalescence, while at neutral pH (7), coalescence frequency was slightly lower. On the glass slide, across all pH ranges, droplets exhibited low mobility and limited coalescence, with only sporadic ruptures. The analysis suggests that the surface heterogeneity of kapok creates preferential collision zones, indicating that coalescence does not depend solely on interfacial energy but is strongly influenced by the local surface conformation. Additionally, the drainage of the film between droplets was accelerated, pointing to selective destabilization beyond mere physical contact with the substrate. This behavior was not replicated on inert surfaces, such as the glass slide, where the emulsion remained more stable, and collisions mostly resulted in sliding. Finally, even at different collision velocities, the frequency of successful coalescence was higher on kapok, reinforcing that its surface does not act merely as a passive support. This work demonstrates the potential of optical microscopy as an effective qualitative tool for revealing critical morphological interactions in coalescence, offering new perspectives for understanding the phenomenon.

[1] R. Cerro, S. Whitaker, J. Colloid Interface Sci. (1971).
[2] K.C. Vasconcelos et al., Sep. Purif. Technol. (2023).

Figure 1. (a) Initial cluster of dispersed droplets in an oil-water emulsion; (b) Redistribution of droplets toward the periphery of the dispersed phase, with no coalescence observed after 7 minutes; (c) Immediate formation of two oil droplets on the fibrous surface of the kapok shell; (d) Complete coalescence, resulting in a single droplet after 18 seconds of contact with kapok.

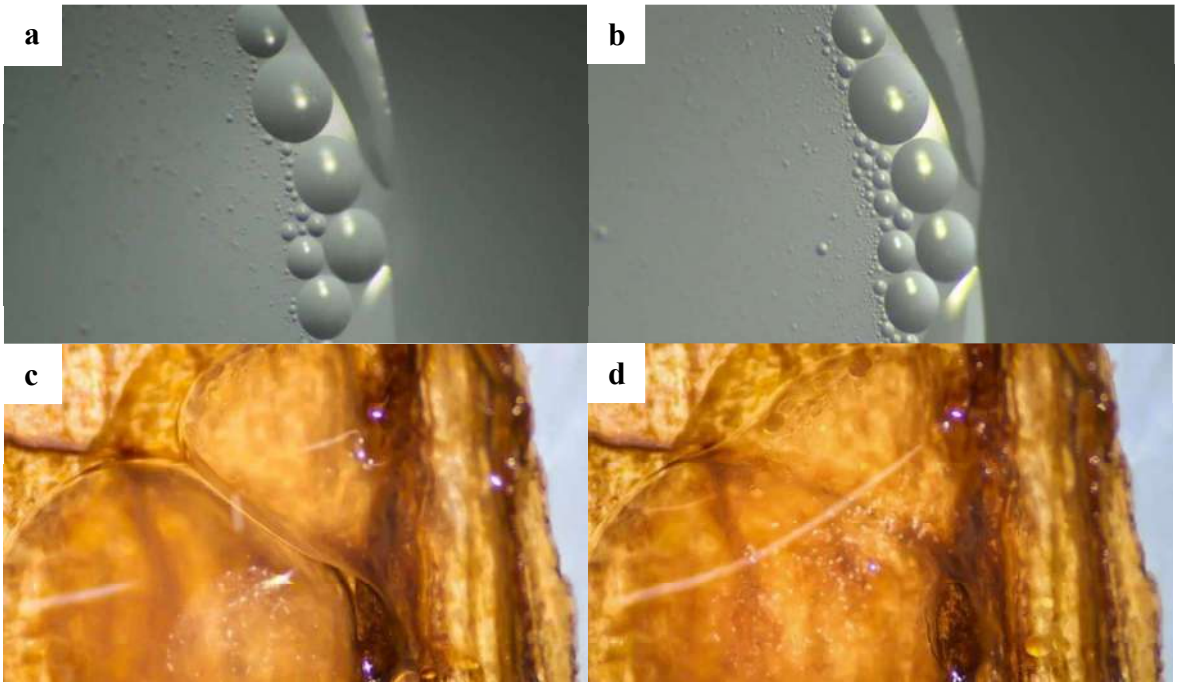

Figure 2. (e) Presence of larger bubbles concentrated at the center of the droplet, with no visible evidence of coalescence; (f) Migration of bubbles toward the periphery, with central coalescence absent or infrequent; (g) Initial formation of two oil droplets on the kapok shell; (h) Single resulting droplet after 6 seconds of contact with the kapok surface.

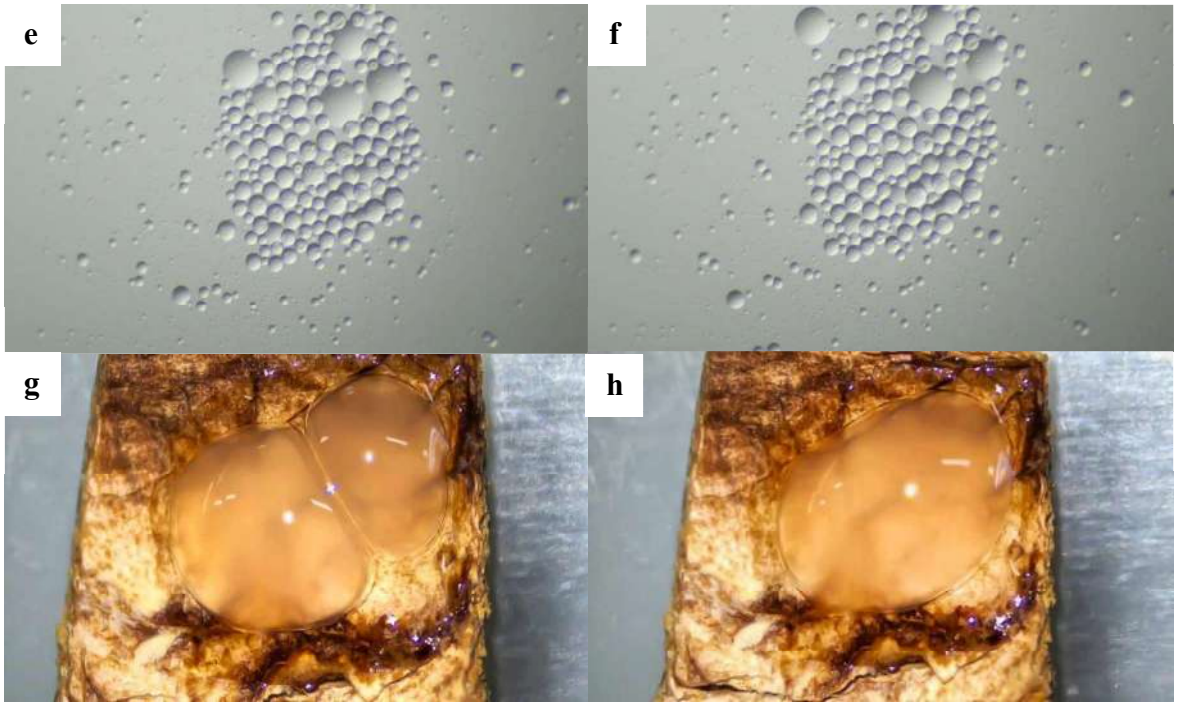

Macrophage-mediated apoptosis in LNCaP cells requires functional p53

Aline Siqueira-Berti* [1] and Hernandes Faustino de Carvalho[1].

[1]State University of Campinas
*alinebt@unicamp.br

Androgens are important for prostate gland development and homeostasis. They are also linked to the pathogenesis of benign prostatic hyperplasia and prostate cancer [1]. Following three days of androgen deprivation, there is a peak of the apoptosis of prostate epithelial cells along with increased infiltration macrophages. Prostatic epithelial cells cultured in the absence of androgenic stimulation secretes soluble factors that influence macrophage polarization towards the classically differentiated phenotype (i.e. increased iNOS expression), general morphology and motility. These macrophages express the ZNF142 gene, a protein-coding gene, and were thus named $M1_{142}$ due to their phenotypic characteristics. Furthermore, the culture medium conditioned by prostate epithelial tumor cell line LNCAP induces the differentiation of RAW 264.7 macrophage cell line to chase and attack epithelial cells and promote their death [2]. Recent unpublished studies from our laboratory have shown that the conditioned medium of prostate epithelial cells in the absence of androgens releases soluble factors, including a progranulin-derived peptide (Pep A), which is capable to mimic the conditioned medium in its capacity to differentiating RAW 264.7 macrophages into killer macrophages. Furthermore, RAW 264.7 cells with LNCAP cells in the presence of peptide A induces the apoptosis of LNCaP prostate epithelial tumor cell and other tumor. Serendipitously we found that tumor cell lines defective in p53 were resistant to macrophage-stimulated cell death. Based on this observation, it was of interest to investigate whether p53 was involved in the mechanism leading to epithelial cell death after the $M1_{142}$ macrophage attacks. Therefore, we treated LNCaP cells with 1nM pifithrin-α, a p53-inhibitor for 2 hours, and then added RAW 264.7 cells and treated the co-culutures with either PepA or scrambled PepA (PepAs). Our results show that pifithrin-α protected LNCaP cells from apoptosis induced by macrophages activated with peptide A, suggesting that p53 is part of the mechanism promoting epithelial cell death (Figure 1). We suggest that the knowledge of the involvement of macrophages in the killing of prostate epithelial cells in response to androgen withdrawal by castration might lead to new ideas for clinical therapy of castration resistant prostate cancer, as well as other tumors.

Keywords: macrophages, prostate, androgen deprivation, p53.

[1] S.E. Rundlett et al., Mol Endocrinol. (1990) 4: 708 – 714.

[2] G.O. Barbosa et al., J Cell Physiol. (2019) Aug 234 (10): 19048-19058.

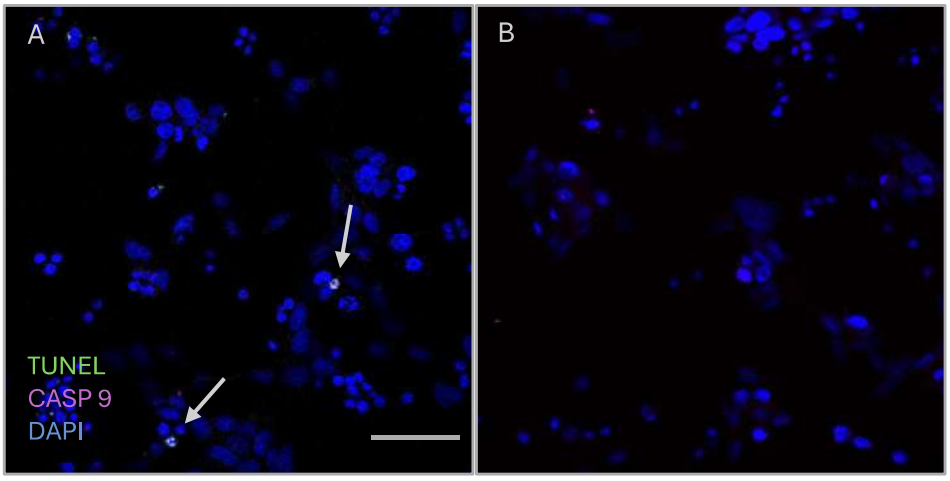

Pep A Pep A+ Pifithrin α

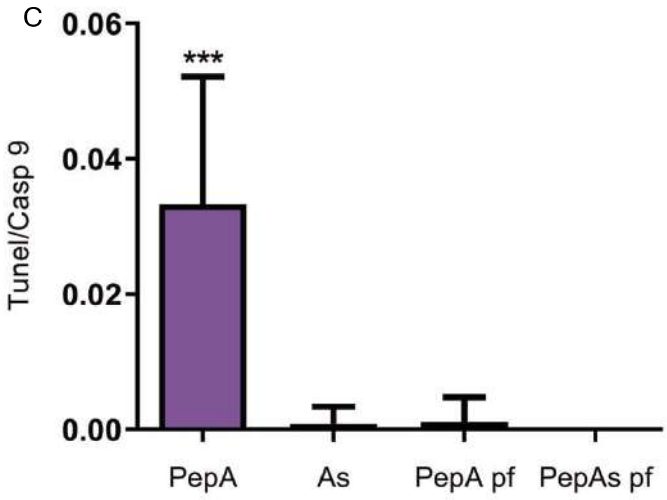

Figure 1: Stimulation of RAW 264.7 cells with peptide A promotes apoptosis in LNCaP tumor cells by activating the intrinsic apoptosis pathway in a p53-dependent manner. A) Image of the co-cultures treated with peptide A. Nuclei were stained with DAPI (blue), cleaved-caspase-9 was identified by immunofluorescence (magenta), and double strand DNA-breaks were identified with TUNEL (green). B) Pre-treatment of LNCaP cells with 1 nM pifithrin-α, a p53 inhibitor, followed by 24-hours coculture with peptide A, abolished apoptosis. C) The presence of peptide A in the co-culture led to an increase in double labeling for TUNEL and caspase-9, while no apoptosis was observed after pre-treatment of LNCaP cells with pifithrin-α. Scale bar: 20 mm.

Microfossil Analysis by Raman Spectroscopy and Confocal Microscopy

Ingrid da Silva Alves[1]*, Neila Nunes Ferreira[2], Carlos Alberto Carbonezi[1], Marcelo Vasconcelos Brandão[1], Igor Augusto Nascimento de Almeida[1].

[1] PETROBRAS Research and Development Center (CENPES), PETROBRAS, Rua Horácio Macedo, 950, Ilha do Fundão, Rio de Janeiro, RJ 21941-915, Brazil, [2] Universidade Federal do Rio de Janeiro (UFRJ), Avenida Athos da Silveira Ramos, 274, Ilha do Fundão, Rio de Janeiro, RJ 21941-916, Brazil

*ingrid.alves@petrobras.com.br

Conventional and routine methods employed in organic-walled microfossil (palynomorph) and inorganic-walled (ostracods) studies mainly involve transmitted light biological microscopy and stereomicroscopy. Complementary and non-destructive optical microscopic techniques for these analyses include Raman spectroscopy and confocal laser scanning microscopy. Confocal laser scanning microscopy is a well-established optical technique allowing for three-dimensional visualization of fluorescent specimens with a resolution close to the diffraction limit of light [1]. Raman spectroscopy is the measurement of the photons arising from inelastic scattering of the light whose spectrum comprises one or more bands that reflect the vibrational energies of the molecules within the analyzed sample [2]. In this work, both techniques were applied in the analysis of palynomorphs and ostracods over 120 million years old. For the analysis of palynomorphs (Table 1, Figure 1), two samples were selected from the Itapecuru Formation (Querru 2 outcrop, Parnaíba Basin) [3]. The analysis of walled-mineralogical microfossils (Table 1, Figure 1) included the identification of five ostracod specimens (well 17348, Campos Mar Basin). Raman spectra of the analyzed palynomorphs and ostracods were performed on a confocal laser Raman spectrometer (Horiba LabRam HR Evolution), while selected palynomorphs and ostracods were analyzed using confocal laser scanning microscopy (Carl Zeiss LSM 700). The chemical treatment of the samples, confocal laser Raman spectrometry, and confocal laser scanning microscopy analysis were performed in the Departments of Biostratigraphy and Applied Paleoecology, and Fluid Technologies - Petrobras Research Center (Rio de Janeiro, Brazil). Raman spectroscopic data of ostracods were compatible with calcite, while phytoclasts showed spectra characteristic of organic matter. The other classes of microfossils presented in this work showed high fluorescence emission, which overwhelmed the Raman signals and prevented the acquisition of Raman spectra. This high fluorescence exhibited by most of the specimens analyzed, except for phytoclasts, resulted in optical sections with submicrometric resolution, allowing for the construction of three-dimensional images (Figure 1). The presence of fluorescence in the analyzed material is a limiting factor for Raman and essential for confocal laser scanning microscopy. The authors thank Petrobras for supporting our participation in the 30*th* Meeting of the Brazilian Society for Microscopy and Microanalysis [4].

[1] A. D. Ball et al., The Paleontological Society Papers. 22 (2017) 29.
[2] M. L. Frezzotti et al., Journal of Geochemical Exploration 112 (2012) 1.
[3] N.N. Ferreira et al., J South Am Earth Sci (2021) 103114.
[4] This research was supported by Petrobras (Brazil).

INTERNA

Table 1. Data from specimens analyzed in this study.

Microfossils		Phytoclast
Palynomorphs	**Ostracods**	
Pteridophytes trilete spores	*Reconcavona*? spp.	Opaque and lath phytoclast
Crybelosporites pannuceus	*Reconcavona*? *camposensis*	
Deltoidospora tenuis	*Reconcavona*? *retrosculpturata*	
Gymnosperm pollen grains		
Classopollis classoides		
Elaterosporites protensus		
Angiosperm pollen grain		
Afropollis jardinus		

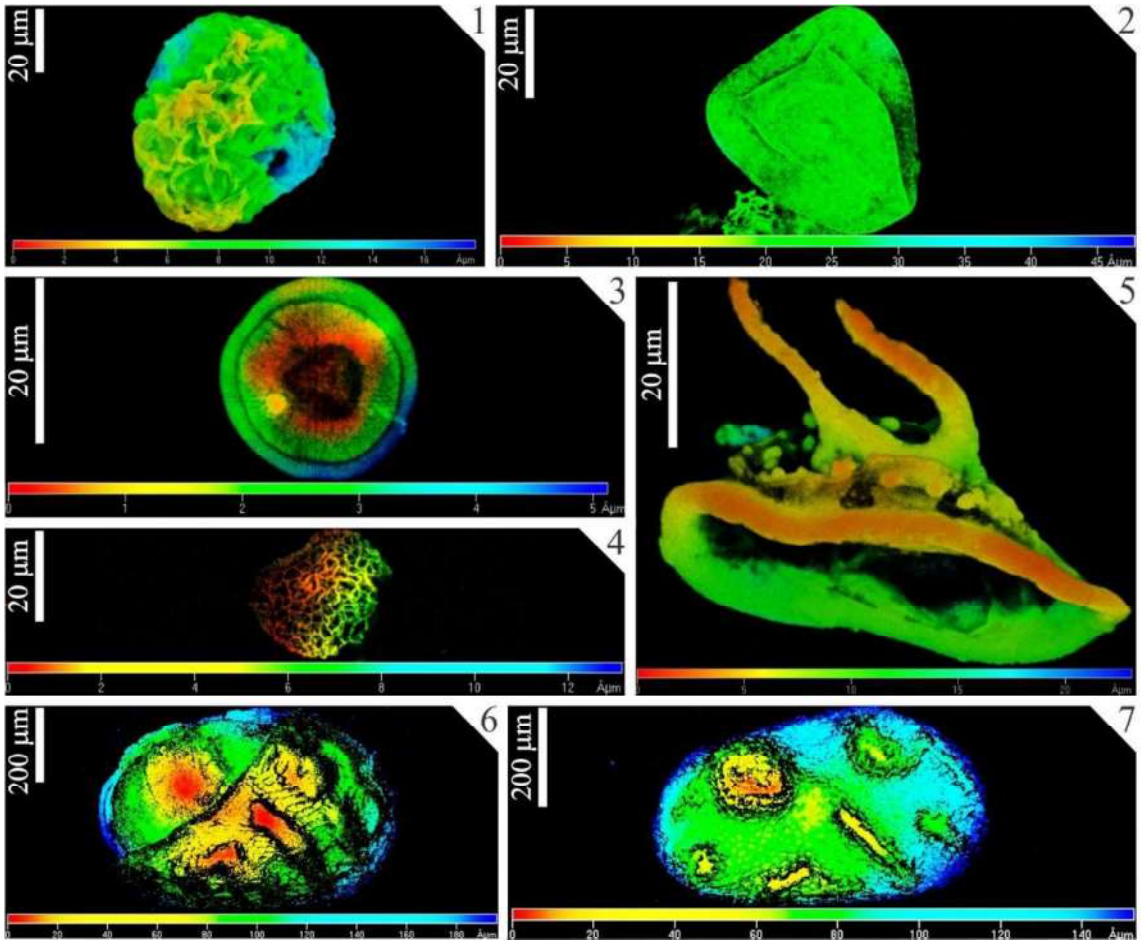

Figure 1. Photomicrographs taken from Confocal-laser-scanning, Depth Codding Mode, of the Palynomorphs (1-5) and Ostracods (6, 7) microfossils. **1**. *Crybelosporites pannuceus*. **2**. *Deltoidospora tenuis*. **3**. *Classopollis classoides*. **4**. *Afropollis jardinus*. **5**. *Elaterosporites protensus*. **6**, **7**. *Reconcavona*? *camposensis*.

INTERNA

Microscopy of Paraffinic Gels: A Comparison Between Bright-Field and Polarized Light Techniques

Letícia Chapeta Vitor de Souza [1]*, André da Silva Guimarães [2], Márcio Nele [1,2].

[1]Universidade Federal do Rio de Janeiro, Escola de Química, [2] Universidade Federal do Rio de Janeiro, Programa de Engenharia Química.
*leticiachapeta@eq.ufrj.br

Deepwater oil exploration faces several challenges related to flow assurance due to the extreme conditions of the marine environment. The seabed temperature, close to 4 °C, is a critical factor in the transportation of paraffinic oils, as cooling of the fluid can induce the precipitation of paraffin crystals. These crystals tend to agglomerate, forming a gel-like structure that can partially or completely obstruct flowlines. Furthermore, the formation of this gel alters the rheological properties of the oil, increasing its viscosity and making transportation more difficult [1]. One of the most commonly used techniques for characterizing the gel formed is cross-polarized light microscopy. However, this technique has limitations, as crystals aligned vertically or horizontally to the x–y plane are not captured, which prevents accurate measurements of crystal length and lattice patterns [2]. In addition, excess light passing through the focal planes distorts the appearance and size of the crystals. To overcome these limitations, image acquisition and processing using bright-field microscopy emerges as an alternative for analyzing the gel formed in model oils and light crude oils. Therefore, this study aims to compare bright-field and polarized light microscopy techniques for the characterization of paraffinic model oil samples and to present processing methods for the generated images. The model paraffinic oil was prepared using liquid petroleum jelly (Isofar, Brazil) and macrocrystalline paraffin SASOL5405 (Sasol, South Africa). The mineral oil and paraffin were heated on an IKAMAG RCT plate and mixed under magnetic stirring at 120 °C for 10 minutes. The paraffin mass fraction was 2.5%. The experimental protocol considered two variables: the sample cooling rate and the microscopy technique used. The cooling rates were 0.5, 1.0 and 1.5 °C/min, and the techniques applied were bright-field microscopy and transmitted cross-polarized light microscopy. The images obtained at 4 °C using both techniques underwent preprocessing and segmentation steps to highlight the paraffin crystals present in the sample. Image processing was performed using the FIJI/ImageJ software [3]. For polarized light images, a methodology adapted from the literature [4] was used, while for bright-field images, a new methodology was developed, inspired by the previous one and based on three steps: (i) preprocessing to remove noise and enhance contrast, (ii) segmentation for binarization, and (iii) post-processing to eliminate artifacts. After processing, it was possible to perform qualitative and quantitative comparisons between the techniques, with particle size and crystal orientation distribution as output variables, both obtained using FIJI/ImageJ [3]. It is expected that bright-field microscopy provides images with greater morphological fidelity and allow more accurate measurements, contributing to advances in flow assurance control.

[1] D.E.V. Andrade, C.O.R. Negrão, *Rheology of waxy oils: a critical review*, Applications In Engineering Science, 21 (2025) 100202.
[2] K. Paso *et al.*, *Paraffin Polydispersity Facilitates Mechanical Gelation*, Industrial & Engineering Chemistry Research, 44 (2005) 7242–7254.
[3] J. Schindelin *et al.*, *Fiji: an open-source platform for biological-image analysis*, Nat Methods, 9 (2012) 676–682.
[4] A.S. Guimarães *et al.*, *Image Processing and Analysis for Fractal Dimension and Lacunarity Calculation of Waxy Oil Gels Using Polarized Light Micrographs*, Crystal Growth & Design, 24 (2024) 7031–7043.

Table 1. Summary of experiments

Experiment	Cooling rate (°C/min)	Microscopy technique
#1	0.5	Bright-field
#2	0.5	Polarized light
#3	1.0	Bright-field
#4	1.0	Polarized light
#5	1.5	Bright-field
#6	1.5	Polarized light

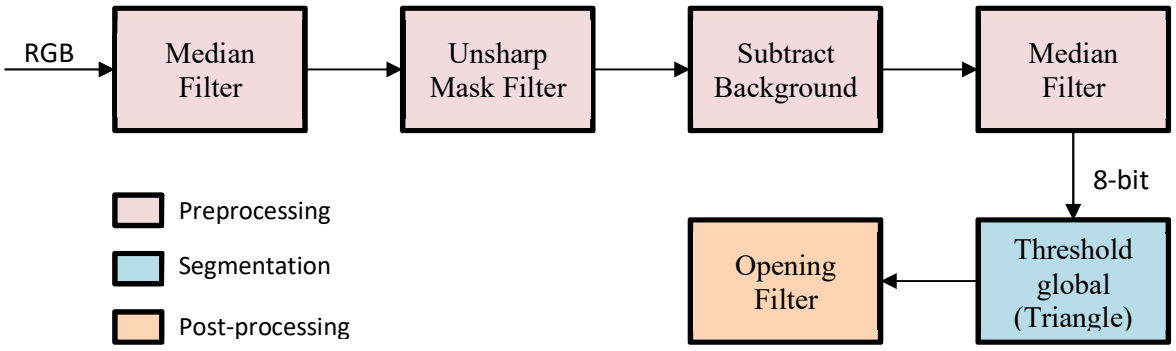

Figure 1. Processing protocol for the images obtained using Bright-Field Microscopy.

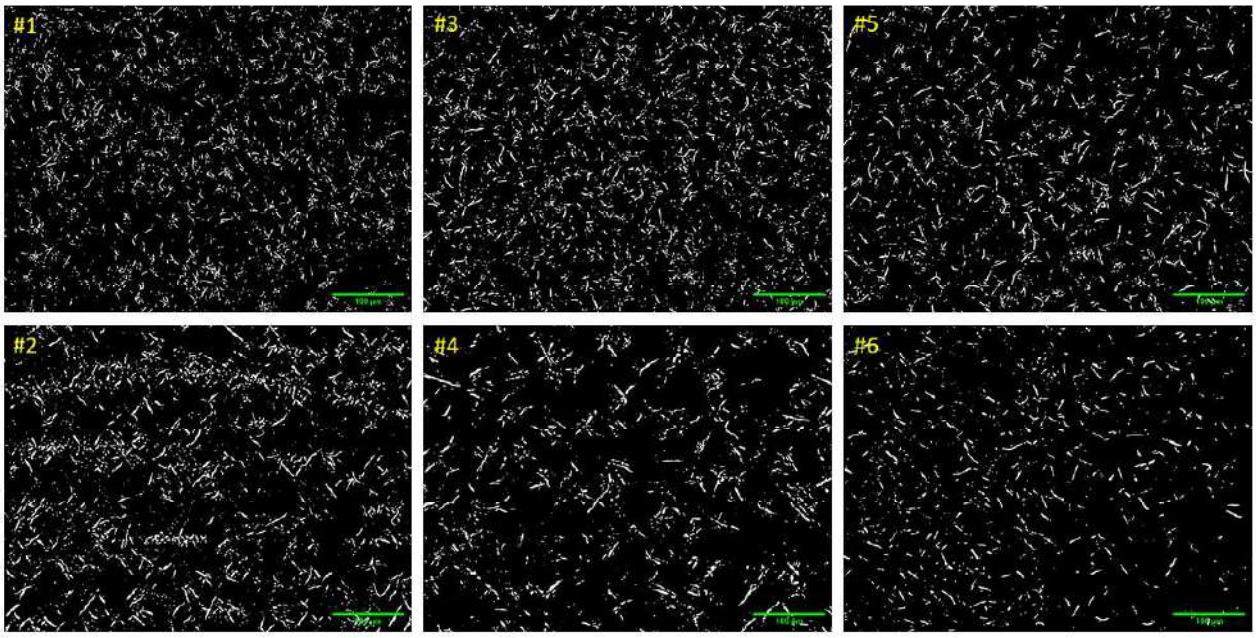

Figure 2. Results of the images obtained at 4 °C after processing

Morphological Influence of Coconut Shell Fiber Composites on Oil Removal: A Sustainable Agribusiness Solution from Alagoas

Rayssa da C. Cabral[1]*, Ingrid dos S. Melo[1], Carla C. G. Brecho[1], Noemi O. dos Santos[1], [2]José L.S. Duarte, [1]Leonardo M.T.M. Oliveira

[1]Laboratório de Materiais para Remediação Ambiental (LabMARE), CTEC, UFAL., [2]Departamento de Ingeniería Química y de Materiales, Facultad de Ciencias Químicas, Universidad Complutense de Madrid.
E-mail:
rayssa.cabral@iqb.ufal.br

Oil spills pose a severe environmental problem, primarily due to their negative impacts on marine ecosystems. In light of this, extensive research has focused on developing efficient methods for pollutant removal in various environments. Within this context, utilizing natural waste materials to produce absorbent compounds emerges as a sustainable, low-cost, and environmentally responsible alternative. This study aimed to evaluate the efficiency of a coconut fiber and cassava starch composite for oil removal, with an emphasis on sorption, retention, and stability under agitation. The developed composite was formulated from crushed coconut shell fiber incorporated into a natural binder based on hydrated cassava starch. The selection of these materials is based on their wide availability, low cost, and biodegradable nature, promoting a sustainable alternative for composite production. Coconut fiber, derived from the fruit of the coconut palm (*Cocos nucifera*), is abundantly found in the state of Alagoas – a prominent region for coconut production and processing – and is typically discarded as agro-industrial waste. In this composite, the fiber acts as a structural element, providing mechanical strength and porosity to the material. Cassava starch, in turn, functions as a binding agent, responsible for particle cohesion and the formation of the composite matrix. The composite's crude oil sorption capacity was quantified using the gravimetric method outlined by Bazargan, Tan, and McKay [1]. Furthermore, to provide a comprehensive analysis, the material's stability and oil retention performance were investigated, adhering to the criteria established by Abdullah, Rahmah, and Man [2], given that in practical applications as an oil absorbent, the composite would inevitably encounter substantial physical agitation. The fabricated composite exhibited an average sorption capacity of 4.7 g of oil per gram of material, a performance comparable to that of commercially available synthetic counterparts. Upon agitation at 180 rpm, oil losses were minimal, recorded at just 1.96% after 5 minutes and 6.50% after 30 minutes, thus indicating robust retention stability even under dynamic conditions. Optical microscopy images prior to sorption (Figure 1) revealed well-defined fibers, significant porosity, and a rough surface, properties conducive to oil uptake via capillarity and adhesion. Post-oil contact, the formation of oily films, pore blockage, and fiber agglomerates were observed (Figure 2), signifying a high affinity for the contaminant. These findings reinforce the critical role of morphological analysis in elucidating the mechanisms governing the sorption and retention of petroleum derivatives. Ultimately, this work demonstrates the composite's substantial potential for applications in environmental remediation systems, thereby underscoring its efficacy and viability as a sustainable alternative.

[1] A. Bazargan, J. Tan, G. McKay, Standardization of oil sorbent performance testing, J. Test. Eval. 43 (2015) 1–6.

[2] M.A. Abdullah, A.U. Rahmah, Z. Man, J. Hazard. Mater. 177 (1) (2010) 683–69

Figure 1. Composite structure before crude oil sorption, at 100x magnification. Images (a) and (b) show different regions of the sample.

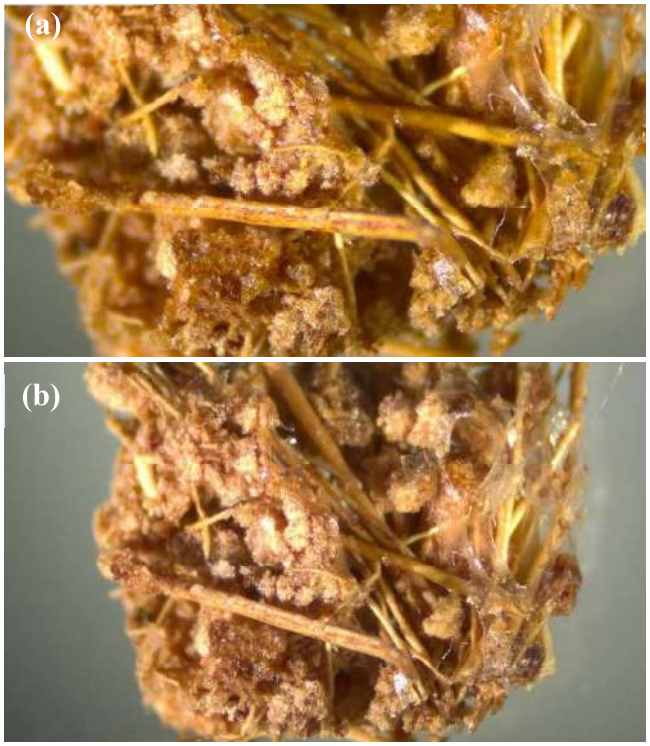

Figure 2. Composite structure after crude oil sorption, at 100x magnification. Images (c) and (d) show different regions of the sample, with oil visibly coating the fiber matrix.

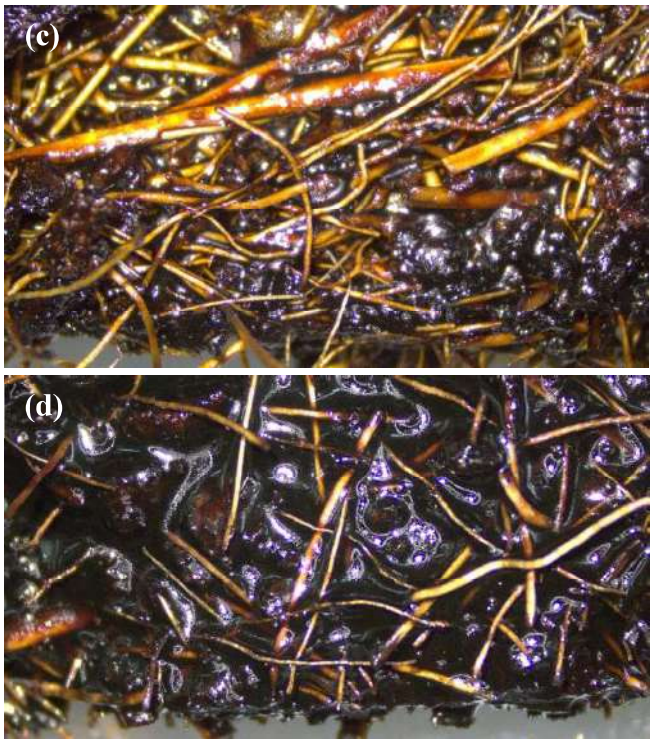

Preclinical Evaluation of the Topical Leishmanicidal Activity of Kojic Acid: An Experimental Study in Non-Human Primates

Brenda Suelen de Oliveira Rocha[1,2*], Lienne Silveira de Moraes[1], Ana Paula Tabaranã Affonso[1], Poliana Dinsam Queiroz de Souza[1], Edilene Oliveira da Silva[1,2]

[1]Structural Biology Laboratory, Federal University of Pará ,[2] Postgraduate Program in Biology of Infectious and Parasitic Agents
*brenda.oliveiracel@gmail.com

Cutaneous leishmaniasis (CL) is an infectious disease with significant public health concern, particularly in the Amazon region. Although conventional therapies are available, they have several limitations, including high toxicity, variable efficacy and increasing parasite resistance. In this context, there has been a growing interest in developing new therapeutic agents, especially those of natural origin [1,2]. Kojic acid (KA), a secondary metabolite produced by fungi, is known for its antimicrobial, antioxidant, immunomodulatory, and antiparasitic properties [3]. Given this potential, the present study aimed to evaluate the leishmanicidal efficacy of KA in an *in vivo* experimental model using non-human primates (*Callimico goeldii*) infected with *Leishmania (Leishmania) amazonensis*. The experiment involved eight young adult *C. goeldii* monkeys, infected intradermally in the tail. After the development of cutaneous lesions, the animals were divided into three groups: a control group (n=2), a group of three animals treated for 30 days (n=3), and a group of three animals treated for 45 days (n=3). All groups received daily topical applications of a KA-based emulsion (100 mg/g). The lesions were monitored weekly for seven weeks. Histopathological analyses were performed on tissue sections stained with Hematoxylin & Eosin and Picro Sirius Red to assess general inflammatory features and collagen deposition and polarized light optical microscopy to characterize collagen fibers. Quantitative collagen analysis was conducted using ImageJ software. Analysis of the collected tissue samples revealed that treatment with the KA resulted in a significant reduction in lesion size and induced tissue remodeling in the affected areas. In the treated groups, a significant decrease in the number of amastigote forms was observed, along with a reduction in the size and structural organization of granulomas. This suggests a more efficient inflammatory response and cicatrization process . In contrast, the control group exhibited well-defined granulomas containing numerous amastigotes. This histological pattern differs from that observed in other animal models of *L. (L.) amazonensis* infection, suggesting that *C. goeldii* shows a distinct inflammatory response, characterised by increased granuloma formation in the absence of treatment. Analysis of collagen fibers showed physiological wound healing in the treated groups, with type I/type III ratios of 1.67 after 30-day treatment group and 1.29 after 45-day treatment group, compared to 3.60 in the control group. These findings suggest that KA not only exerts a leishmanicidal effect but also promotes a more efficient and functional tissue repair process.

[1] Burza S et. al. *Leishmaniose*. Lancet. 392(10151):951–970, 2018.

[2] Croft S L et. al. *Drug resistance in leishmaniasis*.Clin Microbiol Rev, 19:111-126, 2006.

[3] Soujanya N et. al. *Review on Kojic Acid—A Secondary Metabolite From Aspergillus Fungi.* Asian J Pharm Health Sci, 12: 2707–2712, 2022.

[4] This research was supported by CNPq (Brazil) and SECTET/PA (Grant No. 011/2018)

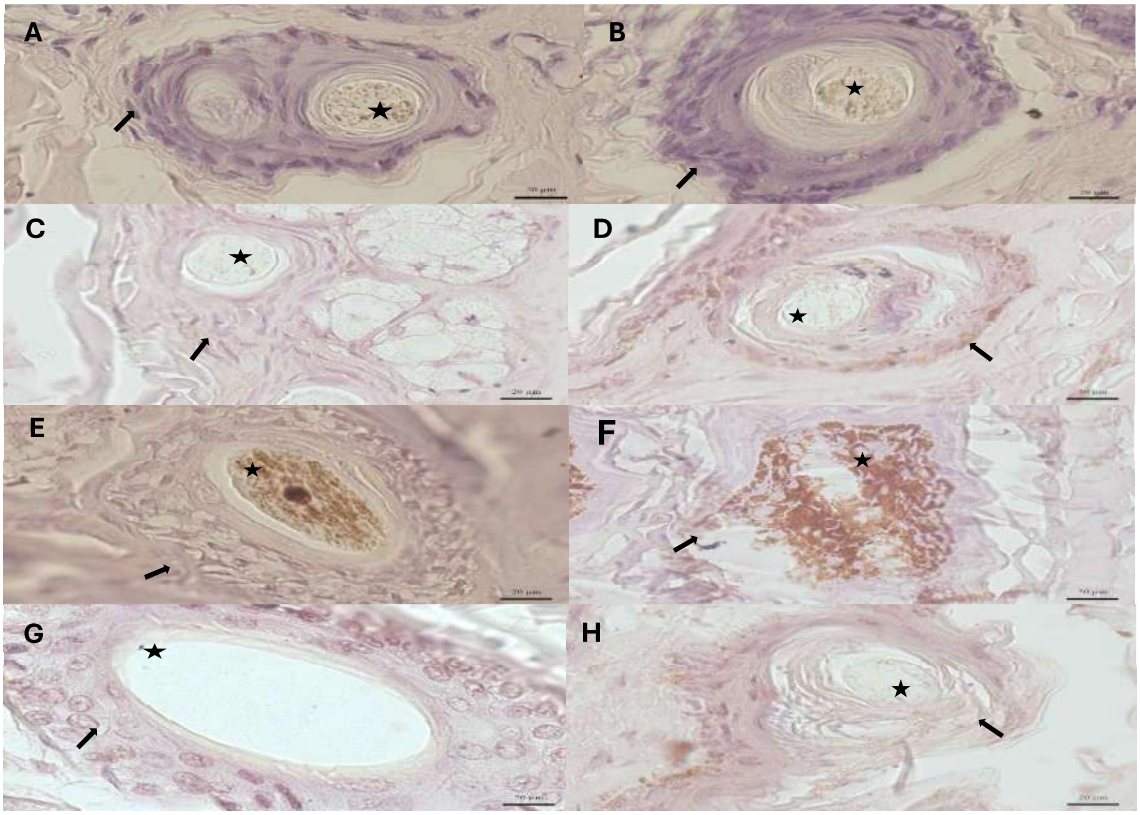

Figure 1: A-B: Control group without treatment, showing the presence of inside granulomas (star). C-D: Control group treated with the vehicle. Note the presence of amastigotes (star) within the granulomas (arrow). E-F: Group treated with the KA emulsion for 30 days. Note the reduction in granulomas and slight tissue remodeling. G-H: Group treated with KA emulsion for 45 days. Observe the decrease in the number of amastigotes, as well as the reduction in granulomas and remodeling of the tissue (arrow). **Scale bars:** 20µm.

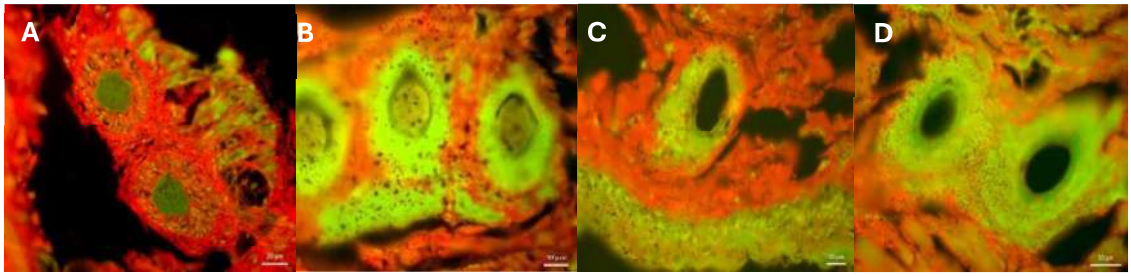

Figure 2: Collagen deposition was analyzed in histological sections stained with Picrosirius Red and examined using polarized light microscopy. (A) control group; (B) vehicle; (C) 30 days and (D) 45 days after treatment. The staining distinguishes between type I collagen fibers, which appear bright red or orange, and type III collagen fibers, which appear greenish. The variations in the distribution and organization of collagen fibers among the groups suggest different stages of extracellular matrix remodeling. **Scale bars:** 20 µm (A), 10 µm (B-D).

Protective Effects Of Resistance Exercise On The Histomorphology Of Retroperitoneal Fat Tissue in a Rheumatoid Arthritis Model

Diego Francis Saraiva Rodriguez[1]*, Emanuelle Santos Camargo Pratti[1], Flávia Heloisa Da Silva[1], Mikael Gerson Kuhn[1], Gabriella Lopes Cappellaro[1], Márcia Miranda Torrejais[1], Gladson Ricardo Flor Bertolini[1], Lucinéia de Fátima Chasko Ribeiro[1].

[1] Programa de Pós-Graduação em Biociências e Saúde - CCBS - Universidade Estadual do Oeste do Paraná (Unioeste) - Cascavel, PR, Brasil.
*diefran.rodriguez@gmail.com

Rheumatoid arthritis (RA) is a chronic inflammatory autoimmune disease that affects the joints, causing pain, stiffness, and functional loss [1]. In addition to local symptoms, patients with RA may experience changes in body composition, including loss of body mass, and in some cases rheumatoid cachexia [2]. In this scenario, complementary and integrative approaches, such as physical exercise, have been explored as promising strategies to mitigate the effects of RA [3]. Thus, the present study was developed with the objective of analyzing the effects of high-intensity stair climbing resistance exercise as a preventive and therapeutic strategy to reduce the tissue effects caused by induced RA. This project was approved by the Ethics Committee on Animal Use, protocol No. 13-22 (CEUA/UNIOESTE). For this study, 20 male Wistar rats were randomized into four groups of five animals each: CTL: unexercised animals, not induced to RA; RA: unexercised animals, induced to RA; EX: exercised animals, not induced to arthritis; EXA: exercised animals, induced to arthritis. Due to its mode of action and history in autoimmune disease induction protocols, Complete Freund's Adjuvant (CFA) was used to induce RA. RA induction was performed in two stages: intradermal inoculation of CFA at the base of the tail; and after one week, intra-articular injection into the right tibiofemoral joint. A vertical wooden ladder was used for exercise, totaling 31 sessions over 9 weeks. At the end of the experimental period, the retroperitoneal fat pads were collected. The material was weighed and processed for histological analysis. The adipose tissue was embedded in paraffin and sectioned into 7 µm thick slices. The histological slides obtained were subsequently stained using Hematoxylin and Eosin (HE) dyes, then the best section from each animal was photomicrographed and analyzed using the Image Pro Plus 6.0 program. Measurements of the area and total number of adipocytes per animal were performed in 10 visual fields. Statistical analysis was performed using two-way ANOVA with Tukey's post hoc test. The results showed that the animals in the EX group had a significantly lower adipocyte area ($p = 0.0175$) compared to the CTL and RA groups. Similarly, regarding cell quantification, only the EX group had a higher number of adipocytes than the CTL group ($p = 0.0104$). Regarding the relative retroperitoneal fat mass, both exercised groups EX ($p = 0.0058$) and EXA ($p = 0.0074$) had lower values than CTL. Still on the analysis of tissue morphology, it was found that both arthritic groups RA and EXA showed marked morphological changes compared to the other groups. The marked presence of poly- and mononuclear inflammatory cells was observed in the connective tissue adjacent to the blood vessels, evidencing the presence of local inflammatory exudate in this region. Thus, this study concluded that early practice of the proposed exercise was effective in promoting important structural changes, but not sufficient to modify the number and area of adipocytes in arthritic animals. The arthritis induction protocol, in turn, was effective in promoting important morphological changes, especially in leukocyte recruitment and tissue inflammation. This study is relevant because it demonstrated that the exercise protocol produces crucial changes in the total retroperitoneal fat mass in arthritic animals, but not in histological parameters, which may provide evidence for future research and clinical trials aimed at preventing chronic inflammatory diseases such as RA [4].

[1] T.F. Andrade et al., Braz. J. Health Rev., 2 (4) (2019) 3698–3718.

[2] J. Calvo Alén et al., Reumatol. Clin., 16 (5P1) (2020) 324–332.
[3] L.N.C. Costa et al., Saúde Pesqui., 14 (1) (2021) e8638.
[4] This research was supported by CAPES (Brazil).

Figure 1. Graphical representation of body adiposity in animals, total adipocyte area, and quantification of total adipocytes per field of view. Two-way ANOVA analysis with Tukey's post hoc test. $p < 0.05$. Photomicrographs of retroperitoneal fat from Wistar rats, stained with hematoxylin and eosin. A, C, E, and G final magnification of 100×. B, D, F, and H final magnification of 400×. Star: Unilocular adipose tissue. Arrow: Connective tissue with the presence of inflammatory cell exudate around blood vessels.

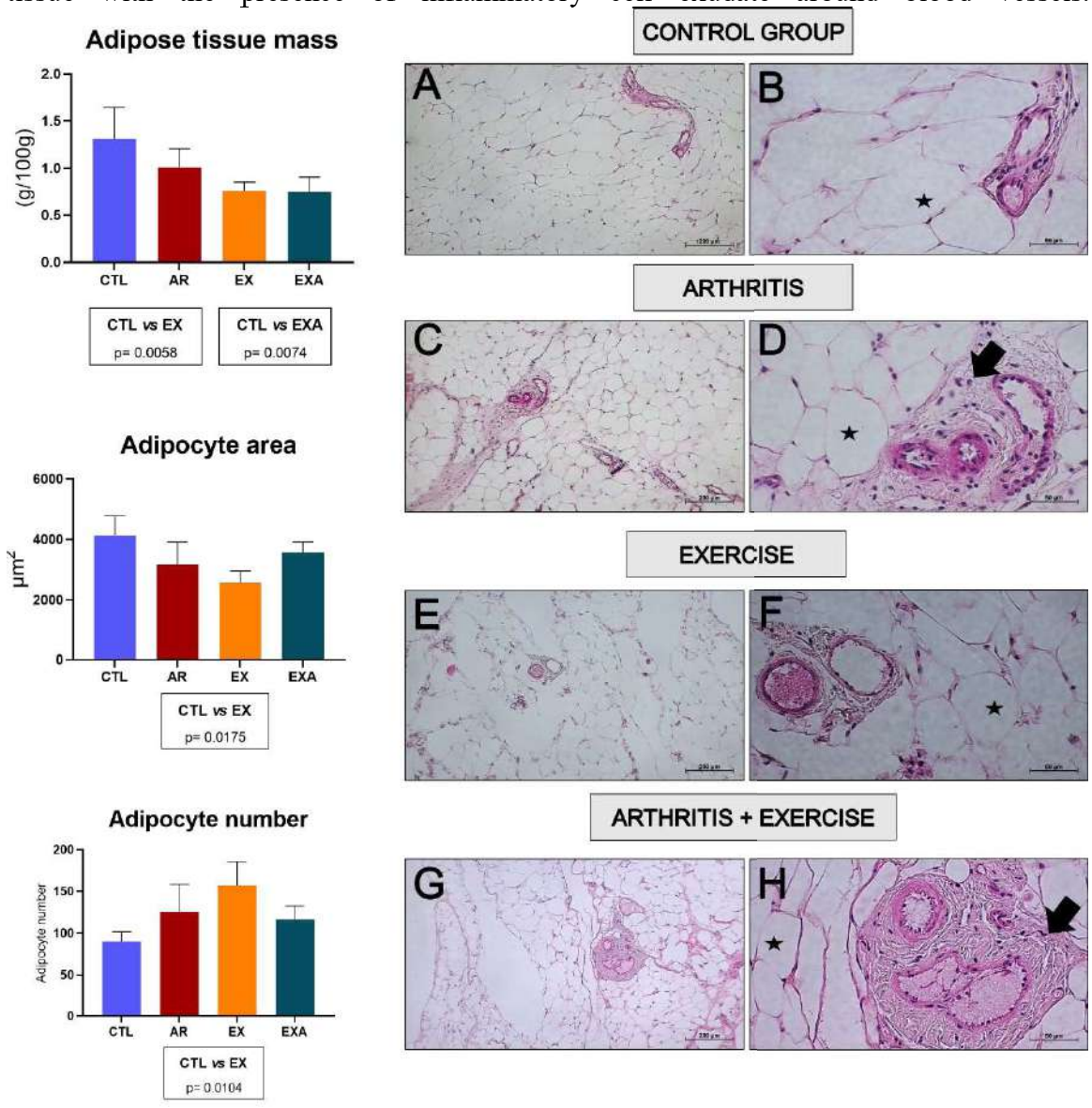

The overlooked impact of N-terminal acetylation on biomolecular condensation

Mayra T. S. Silva[1], Luís F. S. Mendes[1]

[1] Sao Carlos Institute of Physics, University of Sao Paulo, IFSC – USP, 13566-590, Sao Carlos, SP, Brazil.

mayra.tamires@ifsc.usp.br

N-terminal acetylation is one of the most prevalent post-translational modifications (PTMs) in eukaryotes, affecting over 80% of the human proteome [1,2]. Catalysed by N-terminal acetyltransferase (NAT) complexes, this irreversible modification transfers an acetyl group from acetyl-CoA to the free α-amino group of a nascent polypeptide as it emerges from the ribosome [2]. By neutralising the positive charge of the N-terminal amine and introducing a chemically distinct cap, N-terminal acetylation can subtly influence protein polarity, N-terminal conformation, and interaction potential [2]. Biomolecular condensates, formed through protein phase separation, play key roles in cellular organisation by compartmentalising biochemical reactions without membranes [3]. Although multiple PTMs have been implicated in modulating biomolecular condensation, the role of N-terminal acetylation remains largely unexplored. [4,5,6]. Here, we use the Golgi-associated protein Grh1 as a model to systematically compare the condensation behaviour of its acetylated and non-acetylated forms under controlled conditions. Based on microscopy techniques and image analysis, we find that N-terminal acetylation increases the saturation concentration required for condensation, reduces droplet size and number, attenuates pH responsiveness, and diminishes dependence on electrostatic interactions. These effects are linked to acetylation-induced dimerisation and structural rearrangements, including an increase in α-helical content at high protein concentrations. Furthermore, co-condensation assays reveal the formation of core-shell architectures, suggesting that acetylation modulates interfacial tension between condensate components. Together, our findings establish N-terminal acetylation as a potent, yet previously underappreciated, regulator of condensate material properties, mesoscale organisation, and interaction networks. We propose that N-terminal acetylation represents a conserved mechanism for fine-tuning protein phase behaviour across eukaryotic systems.

[1] S. Deng, R. Marmorstein, Protein N-Terminal Acetylation: Structural Basis, Mechanism, Versatility, and Regulation. *TRENDS IN BIOCHEMICAL SCIENCES* **46**, 15-27 (2021).
[2] N. Mctiernan, I. Kjosås, T. Arnesen, Illuminating the impact of N-terminal acetylation: from protein to physiology. *NATURE COMMUNICATIONS* **16**, (2025).
[3] M. Fuxreiter, M. Vendruscolo, Generic nature of the condensed states of proteins. Nature Cell Biology **23**, 587-594 (2021).
[4] Y. Liu, *et al.* Crosstalk between protein post-translational modifications and phase separation. *CELL COMMUNICATION AND SIGNALING* **22**, (2024).
[5] I. Owen, F. Shewmaker, The Role of Post-Translational Modifications in the Phase Transitions of Intrinsically Disordered Proteins. *INTERNATIONAL JOURNAL OF MOLECULAR SCIENCES* **20**, (2019).
[6] S. Rhoads, Z. Monahan, D. Yee, F. Shewmaker, The Role of Post-Translational Modifications on Prion-Like Aggregation and Liquid-Phase Separation of FUS. *INTERNATIONAL JOURNAL OF MOLECULAR SCIENCES* **19**, (2018).

This work was supported by *Fundação de Amparo à Pesquisa do Estado de São Paulo* (FAPESP - Grants No. 2022/06006-0, 2023/04532-9, 2023/17294-9, 2023/12516-3, and 2015/16812-0).

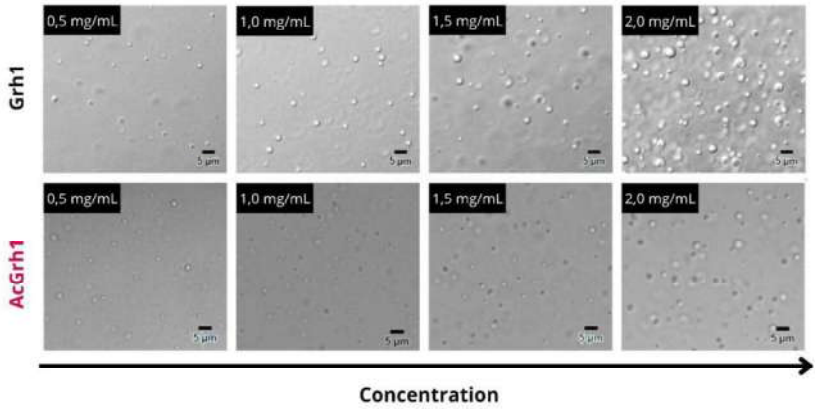

Figure 1: Grh1 and AcGrh1 biomolecular condensation analyses. Differential interference contrast (DIC) microscopy images of condensates formed by Grh1 and AcGrh1 at increasing protein concentrations (0.5 to 2.5 mg/mL). Both proteins form condensates under crowding conditions (10% PEG 8000, pH 5.4), though Grh1 exhibits a higher number and larger condensate size than AcGrh1.

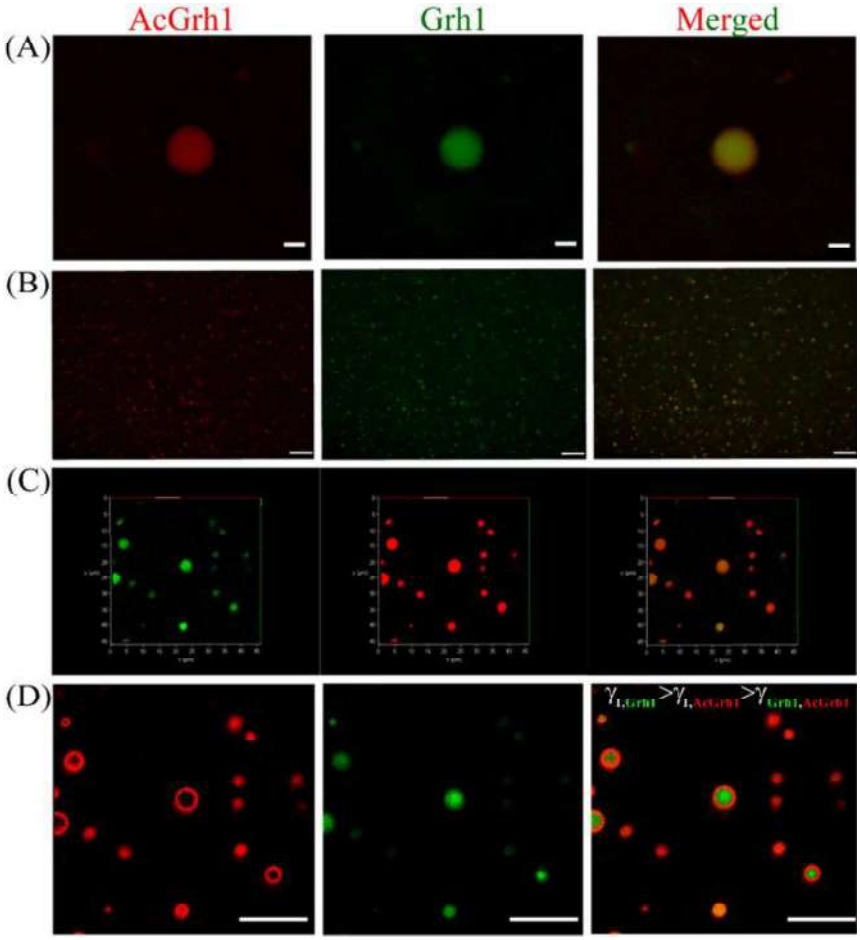

Figure 2. Co-condensation of Grh1 and AcGrh1 reveals the formation of multiphase condensates with core-shell organisation. (A) Fluorescence microscopy images of Grh1 (Alexa Fluor 488, green) and AcGrh1 (Alexa Fluor 546, red), both at 1 mg/mL in 20 mM sodium phosphate buffer (pH 5.4) with 10% PEG-8000. Under these conditions, both proteins form condensates, with substantial signal overlap in the merged image, indicating co-condensation. Scale bar: 5 µm. (B) Wide-field fluorescence microscopy image showing a larger population of condensates. Colocalisation remains prominent, suggesting miscibility between Grh1 and AcGrh1 across multiple droplets. Scale bar: 20 µm. (C) Confocal microscopy Z-stack cross-section of representative condensates, highlighting the internal spatial organisation. A core-shell architecture is observed, with Grh1 localised to the condensate core and AcGrh1 enriched at the periphery. Scale bar: 20 µm. (D) Confocal 3D reconstruction of representative condensates, with fluorescence intensity visualised using Look-Up Tables (LUTs) in ImageJ. This analysis confirms the spatial segregation between Grh1 and AcGrh1 and supports the presence of multiphase organisation. The observed core-shell structure reflects differences in interfacial tension: three interfacial energies are relevant: between Grh1 and the bulk phase ($\gamma_{1,Grh1}$), AcGrh1 and the bulk ($\gamma_{1,AcGrh1}$), and Grh1 and AcGrh1 ($\gamma_{AcGrh1,Grh1}$). Scale bar: 10 µm.

X-ray tomography applied to materials science, including lab and synchrotron-based tomography, new equipment setups, improved AI-based reconstruction methods, and 3D image analysis.

Applications of microCT in Industry and Archaeometry: Case Studies

Davi Ferreira de Oliveira

Laboratório de Instrumentação Nuclear/COPPE/UFRJ

davifoliveira@coppe.ufrj.br

X-ray computed microtomography (microCT) is a high-resolution, non-destructive imaging technique that enables the three-dimensional characterization of internal structures across a wide range of materials. This presentation discusses specific case studies illustrating the analytical capabilities of microCT in industrial and archaeometric applications. In industrial contexts, microCT is applied to assess microstructural features such as porosity, inclusions, and interfaces in metals, polymers, and composites, supporting quality assurance and process optimization. In archaeometry, the technique provides quantitative information on manufacturing methods, internal stratigraphy, and degradation phenomena in cultural heritage materials, including ceramics, pigments, and metallic artifacts. The methodological approach integrates 3D reconstruction, segmentation, and quantitative image analysis to extract structural parameters relevant to both technological and conservation studies. The results highlight the potential of microCT as a cross-disciplinary diagnostic tool, bridging material science, engineering, and heritage conservation through advanced imaging and data processing workflows.

Keywords: computed microtomography (microCT); non-destructive analysis; 3D imaging; microstructure characterization; quantitative image analysis.

Evaluation of Magnetic Nanoparticle Dispersion in NVT Epoxy Adhesive

Kauê C. de Lima[1]*, Eduardo M. Sampaio[1], Joaquim T. de Assis[1], Marcelino J. dos Anjos[2], Catarine C. G. Leitão[2] and Fábio T. S. Tsuyama[2]

[1] Graduate Program in Materials Science and Technology, State University of Rio de Janeiro – Polytechnic Institute, Brazil.
[2] Laboratory of Electronic Instrumentation and Analytical Techniques, State University of Rio de Janeiro, Brazil.
*kaue.lima@iprj.uerj.br

In recent years, the growing demand for structural adhesives as a joining method has attracted attention across various industries. This interest is due to their advantages over traditional mechanical fasteners, including better stress distribution along the bonded area, vibration damping, and reduced impact loads [1]. In particular, the offshore sector has adopted structural adhesives combined with reinforcing fibers for the repair of metallic pipelines, replacing conventional welding techniques. This approach improves the strength-to-weight ratio and reduces the risk of sparking in flammable environments [1,2]. Despite numerous advancements in structural adhesive technologies, further development is necessary due to the harsh service conditions often encountered, such as high temperatures and pressures, corrosive environments, and complex loading like creep and fatigue. Additionally, a portion of the raw materials used in adhesive formulations is imported, creating various logistical and economic challenges. Given these issues, research and development of high-performance, nationally produced structural adhesives are essential to meet industry demands. In this context, nanostructured materials have been investigated as modifying agents for epoxy resins, with magnetic nanoparticles (MNPs) standing out as a promising solution for enhancing mechanical properties [3]. Therefore, this study aims to evaluate the dispersion and homogenization of MNPs within an epoxy matrix as a function of the added nanoparticle content and the dispersion methods employed. An epoxy-based structural adhesive was used, along with iron oxide (Fe_3O_4) nanoparticles with an average diameter of 10 nm. Due to the adhesive's high viscosity, the initial incorporation method involved manual mixing with a glass rod until homogenization was achieved. Samples were prepared with MNP contents of 0.5 wt%, 1.0 wt%, and 1.5 wt% Fe_3O_4, in addition to a pure adhesive sample. A total of 15 specimens were produced for each composition: 5 for tensile testing, 5 for flexural testing, and 5 for single-lap shear testing of bonded metal joints. The pure adhesive and nanocomposites were characterized using Scanning Electron Microscopy (SEM), X-ray Fluorescence (XRF), and X-ray Microcomputed Tomography (MicroCT). The results indicated that the mechanical properties were affected by the formation of agglomerates, which acted as stress concentrators. This hypothesis was confirmed through characterization techniques. SEM images revealed that fracture surfaces were altered by the addition of MNPs (Figure 1), showing a smoother surface in the pure sample and a rougher morphology in the sample with 1.0 wt% MNPs. However, the SEM technique was unable to locate the agglomerates. XRF was used to confirm the presence of MNPs within the samples, while MicroCT imaging revealed agglomeration due to inefficient dispersion during specimen fabrication (Figure 2). To address this issue, a new dispersion method was implemented using an ultrasonic sonicator applied to the base epoxy resin, which has lower viscosity and thus facilitates more effective MNP dispersion. The quality of this dispersion technique was analyzed via MicroCT, both in the liquid MNP-modified epoxy resin and in the cured specimens. In both cases, dispersion was found to be effective, with only small and barely visible agglomerates, which could only be observed at higher magnifications (Figure 3).

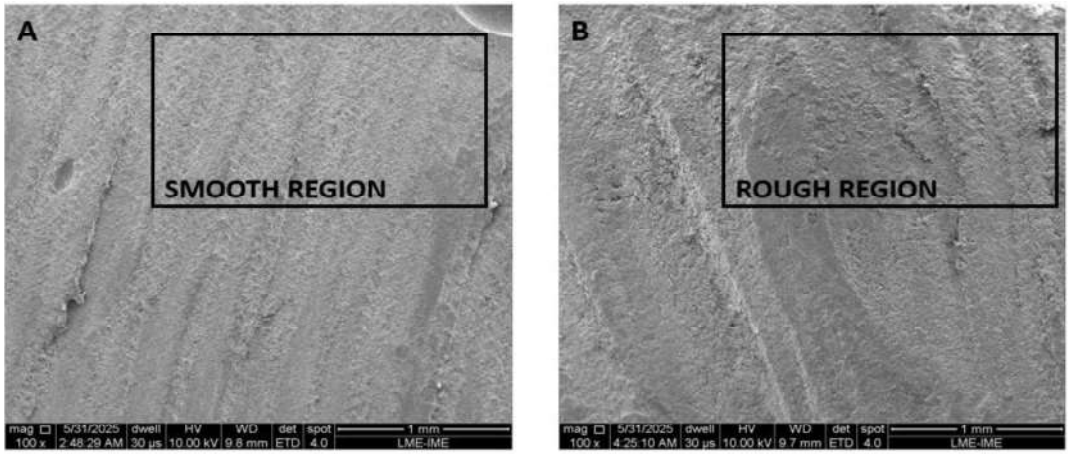

Figure 1. SEM Analysis: A) Pure and B) 1.0 wt% MNPs.

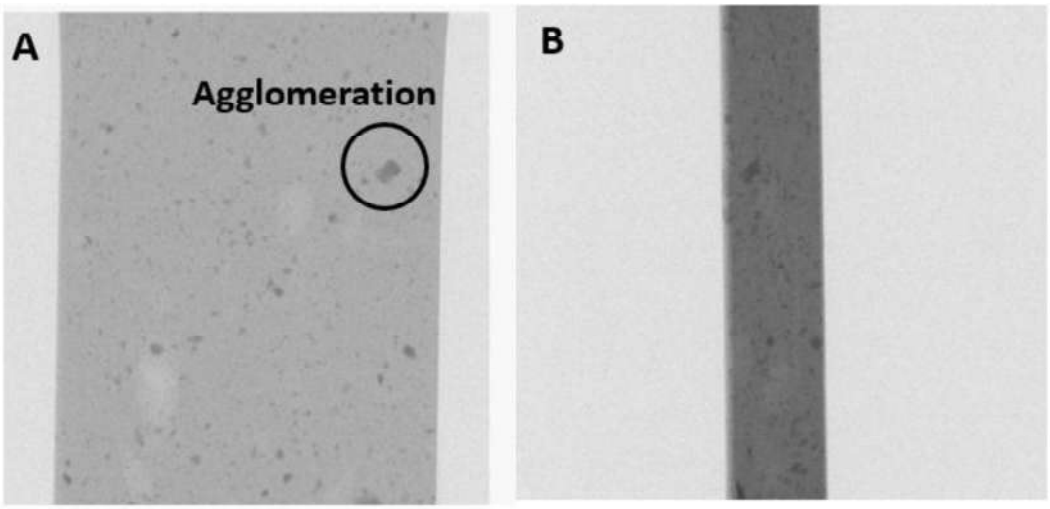

Figure 2. MicroCT analysis of the manual dispersion process for the 1.0 wt% MNP sample: A) Front view and B) Side view.

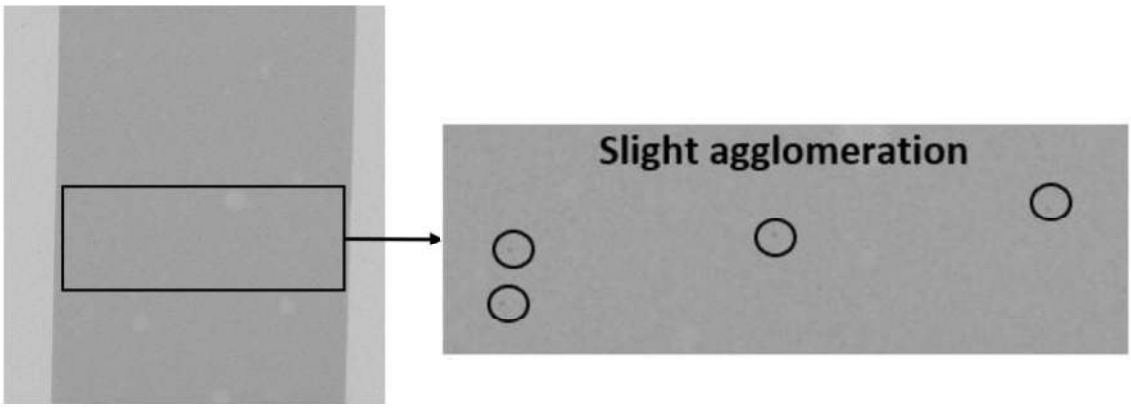

Figure 3. MicroCT analysis of the new dispersion process for the 1.0 wt% MNP sample.

[1] Lamberti et al., *Accelerated aging procedure of epoxy structural adhesive for marine offshore applications*, 9 (2024).
[2] Qin et al., *Effect of continuous high temperature exposure on the adhesive strength of epoxy adhesive, CFRP and adhesively bonded CFRP-aluminum alloy joints*, 154 (2018).
[3] Wan et al., *Effect mechanism of the Fe3O4 nanoparticles on mechanical properties and anticorrosion performances of epoxy coatings*, 173 (2022).
[4] This study was financed by the Coordenação de Aperfeiçoamento de Pessoal de Nível Superior – Brasil (CAPES) – Finance Code 001. The authors also acknowledge FINE COMPOSITES and MAGTECH Brasil.

Multimodal Imaging of Silica Nanoparticle Distribution: Impact of Concentration and Cell Doubling Time

Isabella Scarpa[1,2*], Maiara Ferreira Terra[1], Carla Cristina Pólo[1], Flavia Elisa Galdino[1], André Alexandre de Thomaz[2], Maria Harkiolaki[3], and Mateus Borba Cardoso[1,2]

[1]Brazilian Synchrotron Light Laboratory (LNLS-CNPEM), [2]"Gleb Wataghin" Institute of Physics (IFGW-UNICAMP), [3]Diamond Light Source; Campinas, Brazil.
*isabella.scarpa@lnls.cnpem.br

Silica nanoparticles (SiNPs) have emerged as promising nanoplatforms for diagnosing and treating diseases [1]. Understanding the interactions between SiNPs and cells is crucial for advancing nanomedicine and among the many factors that influence cellular uptake of SiNPs, protein corona formation plays a key role. This corona—an adsorbed layer of proteins that spontaneously forms around nanoparticles upon contact with biological fluids—dramatically alters nanoparticle–cell interactions [2]. In this study, we consider the effects of the protein corona on SiNPs, building on previous findings that demonstrated a significant reduction in cytotoxicity associated with its formation [3]. Here we show that both nanoparticle concentration and cell doubling time influence the spatial distribution of SiNPs within cells. This phenomenon was investigated through three-dimensional imaging techniques, including cryo-soft X-ray tomography (cryo-SXT) and cryo-structured illumination fluorescence microscopy (cryo-SIM), using the advanced imaging infrastructure at the B24 beamline of Diamond Light Source, as illustrated in Figure 1. Data obtained from these techniques revealed that SiNPs consistently enter cells via vesicular transport at all tested concentrations, ultimately localizing within the cytosol. Notably, at higher nanoparticle concentrations, SiNPs were also detected within the cell nucleus—an event not observed at lower concentrations (Figure 1a). Furthermore, after two cell doubling times, nanoparticle aggregation was predominantly observed in the perinuclear region (Figure 1b). Additional imaging methods were employed to deepen our understanding of these phenomena. Confocal fluorescence microscopy was employed to validate and complement the observations from cryo-SXT and cryo-SIM, as shown in Figure 2. A clear variation in the fluorescence intensity of ATTO-633, associated with SiNPs, was observed across different concentrations (Figure 2b, 2c, 2d). A progressive increase in fluorescence intensity and signal clustering was detected over time (Figures 2e, 2f), indicating nanoparticle aggregation. After two doubling times (Figure 2f), the fluorescent signal was predominantly located in the perinuclear region, suggesting targeted accumulation, possibly mediated by late endocytic processes or vesicle maturation, as previously reported in the literature [4]. Moreover, to specifically assess nanoparticle localization within the nucleus, as observed by cryo-SXT and cryo-SIM (Figure 1a), ptychographic imaging was performed at the Cateretê beamline of the Sirius synchrotron to complement and validate these findings. This multimodal approach provides high-resolution three-dimensional and ultrastructural insights into cell–nanoparticle interactions, with significant implications for developing targeted nanomedicine strategies.

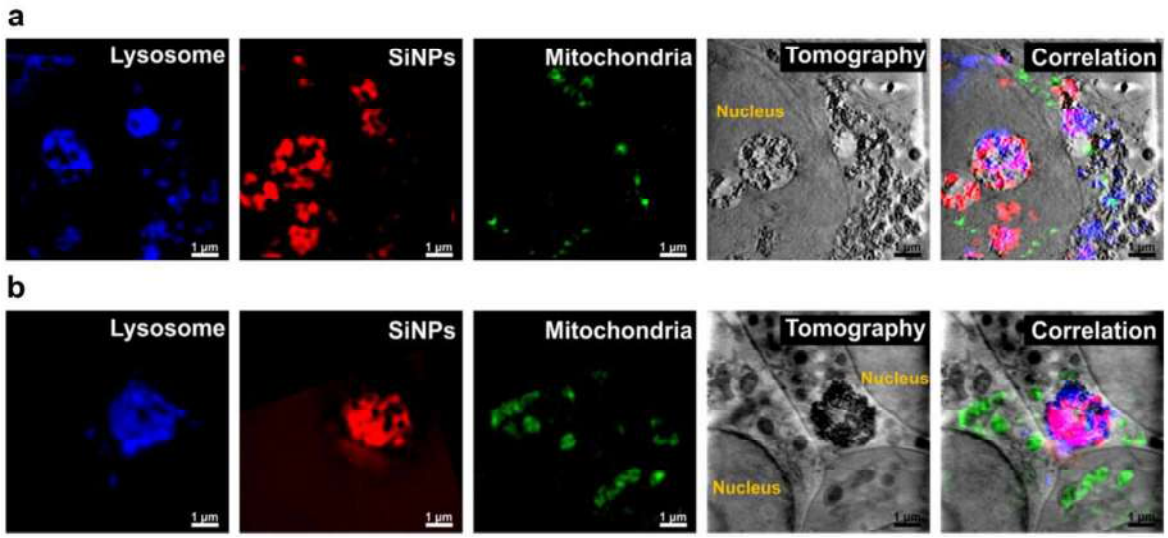

Figure 1. Correlation of tomographic slice images obtained by cryo-SIM and cryo-SXT from the same region: a) RAW 264.7 cell incubated with 0.3 mg/mL of SiNPs for 1 hour, and b) 0.3 mg/mL of SiNPs after 32 hours**.**

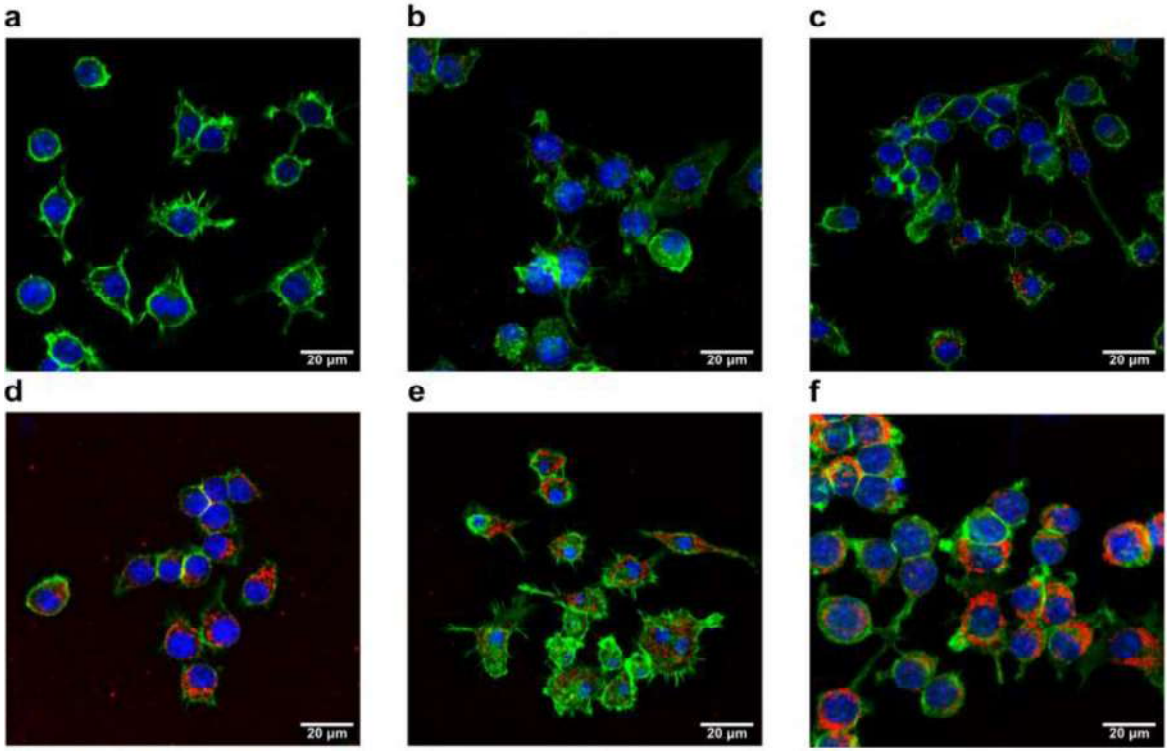

Figure 2. Fluorescence micrographs of RAW 264.7 cells (green: actin; blue: nucleus; red: SiNP@ATTO). a) control, b) 0.003 mg/mL of SiNPs after 1 h of incubation, c) 0.03 mg/mL of SiNPs after 1 h of incubation, d) 0.3 mg/mL of SiNPs after 1 h of incubation, e) 0.3 mg/mL of SiNPs after 9 h (first doubling time), and f) 0.3 mg/mL of SiNPs after 18 h (second doubling time).

[1] Tang, L., et al. Nano Today 8, 290-312 (2013).
[2] Monopoli, M. P., et al. Nat. Nanotechnol. 7, 779-786 (2012).
[3] Cardoso, M. B., et al. Langmuir, 36(39), 11442-11449 (2020).
[4] Galdino F.E., et al. Small, 21, 2409065 (2024)
[5] This research was supported by FAPESP-2023/00103-6 and 2021/12071-6 (Brazil).

Multi-Scale and Multi-Technique microscopy approaches for material characterization: From energy resources to cultural heritage

Jhonatan Jair Arismendi Florez[1]*, Ana Maria Afonso Sena[1], Liz de Mello Zanchetta[1], Daniel Uliana[1], Carina Ulsen[1].

[1]Escola Politécnica da Universidade de São Paulo – Departamento de Engenharia de Minas e Petróleo, Av. Professor Mello Moraes, 2603,05508-030, São Paulo, Brazil
*jhonatanarismendi@usp.br

Microscopy-based material characterization plays a key role across multiple industrial and scientific fields, including mining, petroleum engineering, geology, pharmaceuticals, and cultural heritage preservation [1][2]. By enabling high-resolution 2D and 3D visualization of material structures, often with minimal or no sample preparation, these techniques provide both destructive and non-destructive insights into physical and chemical heterogeneities [3][4]. The diversity of sample types and specific objectives demands innovative, multi-scale, and multi-focus experimental strategies, integrating complementary imaging modalities under a cohesive framework [5][6]. In this sense, this work presents a snapshot of ongoing and recently completed projects at the Technological Characterization Laboratory (LCT) at the University of São Paulo (USP), highlighting how microscopy and microanalysis tools contribute to solving complex problems in different areas of knowledge, as well as future laboratory strategies, aimed at better understanding the physical and chemical heterogeneities of samples. One example focuses on the correlation between mineralogical composition and rock wettability, a key parameter affecting fluid flow in porous media. Using Scanning Electron Microscopy coupled with Mineral Liberation Analysis (SEM/MLA), it was characterized the mineral distribution on carbonate rock surfaces and correlated these findings with contact angle measurements to assess wettability behavior. This study, demonstrated how mineral-specific surface properties can shift reservoir wettability, refining fluid-flow simulations for enhanced oil recovery [7]. Another project focused on constructing synthetic carbonate rock plugs with controlled physical and chemical properties using a novel 3D printing approach. X-ray micro-computed tomography (microCT) allowed for non-destructive 3D characterization of the resulting pore structures, providing insights into how tailored pore geometries impact petrophysical behavior [8]. Additionally, efforts to upscale 2D mineralogical information to 3D spatial models led to the integration of SEM data with microCT through automated image registration using computer vision techniques (currently under patent protection). A similar approach was applied in the study Mineral liberation by 3D X-ray microtomography and SEM-based image analysis in low-grade iron ores with different mineralogy and texture, demonstrating the potential of combining 2D and 3D datasets for detailed mineral liberation analysis [9]. Beyond petroleum and mineral industries, microanalysis techniques also support cultural heritage conservation. The project Microanalytical investigation of Brazilian coat of arms paintings on paper employed SEM-EDS to identify microscale metal alloys and pigments used in historic artworks, providing insights into artistic techniques while preserving fragile samples through non-destructive analysis [10]. Complementary techniques currently being implemented at LCT, such as micro X-ray fluorescence (microXRF), plasma-assisted FIB-SEM for 3D trenching, dual-energy and time-resolved 4D microCT for dynamic fluid displacement studies, and medical CT for full-core rock analysis, further enhance this integrated, multi-scale experimental framework (see Figure 1). Altogether, these strategies advance our understanding of complex materials, from pre-salt carbonate reservoirs to historically significant artworks.

Keywords: Microscopy and Microanalysis, Multi-scale Characterization, 2D and 3D Imaging, Material Heterogeneity.

[1] Ali, A., Zhang, N., Santos, R. M. Mineral characterization using scanning electron microscopy (SEM): a review of the fundamentals, advancements, and research

directions. *Applied Sciences*, *13*(23), 12600. 2023. https://doi.org/10.3390/app132312600
[2] Prats-Mateu, B., Gierlinger, N. Tip in–light on: Advantages, challenges, and applications of combining AFM and Raman microscopy on biological samples. Microscopy Research and Technique, 80(1), 30-40. 2017. https://doi.org/10.1002/jemt.22744
[3] Mizutani, R., Suzuki, Y. X-ray microtomography in biology. *Micron*, *43*(2-3), 104-115. 2012. https://doi.org/10.1016/j.micron.2011.10.002
[4] Bazylewski, P., Ezugwu, S., Fanchini, G. A review of three-dimensional scanning near-field optical microscopy (3D-SNOM) and its applications in nanoscale light management. *Applied Sciences*, *7*(10), 973. 2017. https://doi.org/10.3390/app7100973
[5] Rousselle, S. D. Digital 3D topographic microscopy: bridging the gaps between macroscopy, microscopy and scanning electron microscopy. *Toxicologic Pathology*, *49*(4), 963-970. 2021. https://doi.org/10.1177/0192623320979908
[6] Matheus, G.F., Basso, M., de Carvalho Mendes, L., Winter, A., Sol Paiva de Medeiros, R., da Ponte Souza, J. P., Chinelatto, G. F., Camargo, M. M., Vidal, A.C. Integrated Multiscale Pore Characterization of Carbonate Rocks in the Barra Velha Formation, Santos Basin, Brazil. *SPE Journal*, 1-24. 2025. https://doi.org/10.2118/228310-PA
[7] Ferrari, J. V., de Oliveira Silveira, B. M., Arismendi-Florez, J. J., Fagundes, T. B., da Trindade Silva, M. A., Skinner, R., Ulsen, C., de Carvalho Carneiro, C. Influence of carbonate reservoir mineral heterogeneities on contact angle measurements. *Journal of Petroleum Science and Engineering*, *199*, 108313. 2021. https://doi.org/10.1016/j.petrol.2020.108313
[8] Florez, J. J. A., Ulsen, C., Ferrari, J. V. Investigation of petrophysical properties of synthetic carbonate plugs: Adding a novel 3D printing approach to control pore networks. *Petroleum Research*, *9*(4), 514-540. 2024. https://doi.org/10.1016/j.ptlrs.2024.06.006
[9] Uliana, D., Ulsen, C. Mineral liberation by 3D X-ray microtomography and SEM-based image analysis in low-grade iron ores with different mineralogy and texture. *Minerals Engineering*, *222*, 109150. 2025. https://doi.org/10.1016/j.mineng.2024.109150
[10] dos Santos, I. F. S., de Faria, D. L. A., Marins, P. C. G. Microanalytical investigation of brazilian coat of arms paintings on paper. *Microchemical Journal*, *201*, 110633. 2024. https://doi.org/10.1016/j.microc.2024.110633

Figure 1. Multi-Scale and Multi-Technique microscopy approaches for material characterization

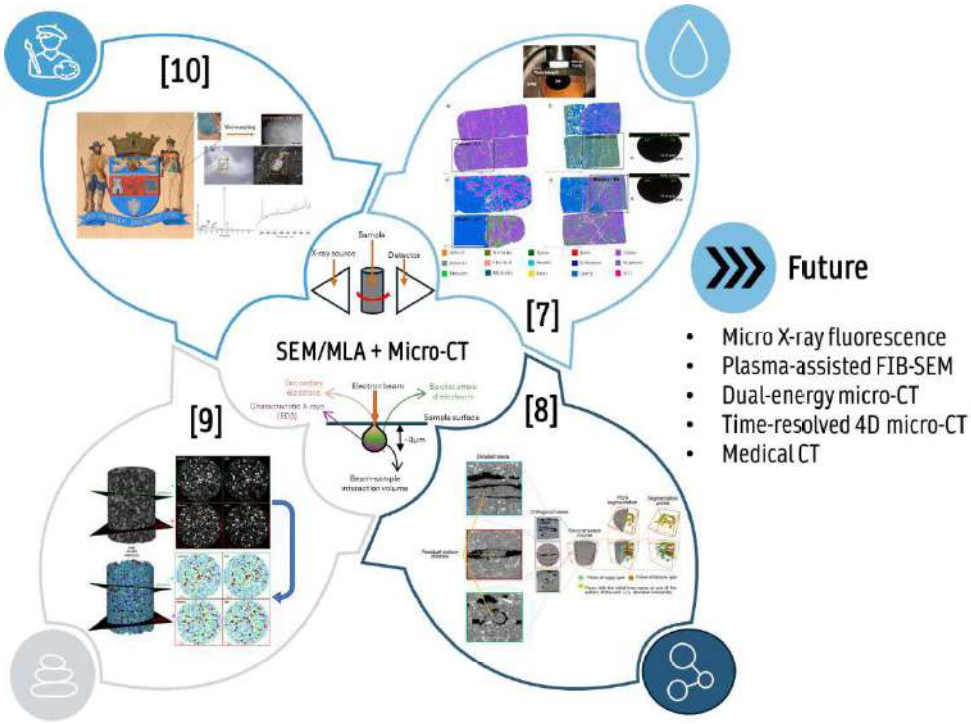

Whole-Tissue X-ray Microtomography Reveals 3D Attachment Patterns of *Trichuris muris* in Murine Intestine

Brunna Vianna Braga[1,3]*, Renato Menezes de Oliveira[2], Eduardo José Lopes-Torres[3]

[1]Programa de Pós-Graduação em Microbiologia, Faculdade de Ciências Médicas, Universidade do Estado do Rio de Janeiro, Brazil, [2]Programa de Pós-Graduação Profissional em Tecnologias de Bioimagem e Bioestrutura, Universidade Federal do Rio de Janeiro, Brazil, [3]Laboratório de Helmintologia Romero Lascasas Porto, Departamento de Microbiologia, Imunologia e Parasitologia, Faculdade de Ciências Médicas, Universidade do Estado do Rio de Janeiro, Brazil
*bviannabraga@gmail.com

Human trichuriasis is a neglected tropical disease caused by *Trichuris trichiura*, affecting approximately 500 million people worldwide [1,2]. Infection occurs through the ingestion of embryonated eggs present in contaminated soil and food. Once inside the host, these infective forms pass through the digestive system and reach in the small intestine, where they interact with the host's microbiota, enabling the hatching of the first-stage larva (L1). The L1 larva invades the intestinal tissue intracellularly and undergoes several molts until it reaches the adult stage. The mature worm reaches the caecum, in the large intestine, embeds its anterior end in the intestinal mucosa, while its posterior end remains free in the lumen [3]. This attachment process is complex and has been the subject of increasing scientific interest over the past decade [3,4,5]. However, questions such as "how does the attachment occur?" and "what are its consequences?" remain largely unanswered. In this study, we aim to investigate in detail the attachment mechanism of *Trichuris muris* – a well-established murine model for trichuriasis – using X-ray microtomography and 3D reconstruction techniques. For this, intestinal tissues from mice previously infected with 150 embryonated eggs (chronic phase) were fixed 4% formaldehyde (EMS®) with a pH 7.4 for 24 h, followed by washing cycles with 0.1 M Cacodylate buffer. Post-fixation was performed using 2% osmium tetroxide for 2 hours, followed by three washes in distilled water. Samples were embedded in 10% agarose in microtubes to ensure stability during analysis. Serial images were acquired using an Xradia 510 Versa MICRO-CT system (Zeiss, Germany), and 3D reconstruction was performed using Amira software 5.3.3, following the steps: alignment, segmentation, 3D reconstruction, smoothing, and model generation. The serial images and 3D reconstruction (Fig. 1A and B) offered a detailed view of the attachment process of *T. muris* in the cecum. The nematode was observed mostly in flat intestinal areas, suggesting it prefers to explore these regions than the curved ones. In addition, the use of Amira's voltex tool - which allowed to turn the intestinal tissue transparent - permitted the observation of the parasite's anterior end inserted in syncytial tunnels, mainly in the mucosa layer, while its posterior end remained free in the lumen (Fig. 1D and E). The intestinal tube format allowed the observation of a thickening process of the submucosa layer, suggesting an inflammatory infiltrate (Fig. 1B). These data provide a basis for a detailed three-dimensional understanding of the parasite's interaction with host tissue and contribute to elucidating the still poorly understood attachment process. The authors acknowledge the financial support for the present work [6].

[1] JOURNAN, P. M. et al., The Lancet. 391(10117) (2018).
[2] BEHNIAFAR, H. et al., Infect. Public Health. 17 (5) (2024).
[3] DUQUE-CORREA, M. A. et al., Nat. Commun. 13 (1725) (2022).
[4] O'SULLIVAN, J. D. B. et al., Exp. Zoo. 303 (11) (2005).
[6] This research was supported by CAPES, FAPERJ, and FINEP (Brazil).

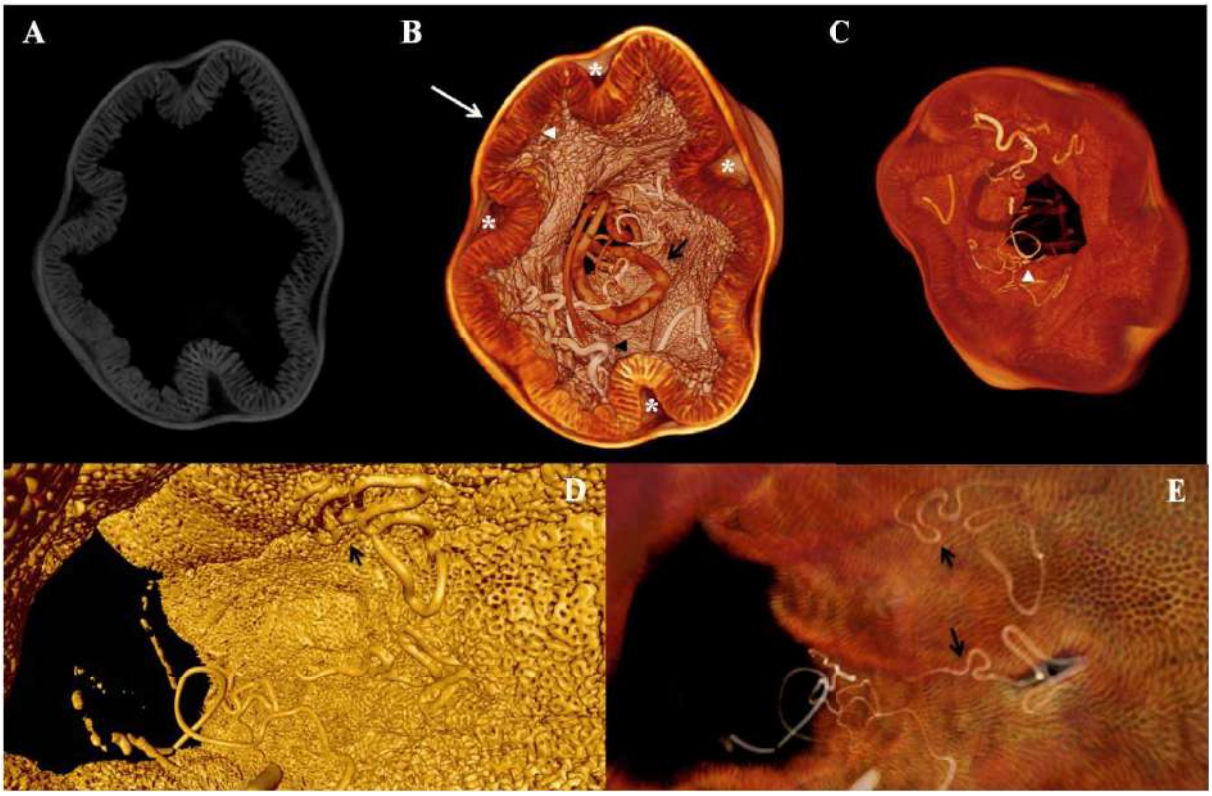

Figure 1. [A] A representative serial image obtained using MICRO-CT; [B] 3D reconstruction of intestinal tube infected by *Trichuris muris*, where it is shown the muscular layer (white arrow), a swollen submucosa layer (asterisks), and the mucosa layer (white arrowhead); [C] Adult helminths attached to the intestinal mucosa layer (white arrowhead); [D and E] Anterior end of the adult helminth of *T. muris* submerged in the mucosa layer through syncytial tunnels (black arrows).

3D Characterization of pericarp laticifers in *Swartzia langsdorffii* using synchrotron X-ray nanotomography

Juliana Villela Paulino[1], Dalton Guimarães Veloso[1], Talita Rosas Ferreira[2], Vidal de Freitas Mansano[3], Simone Pádua Teixeira[4], Igor Almeida Rodrigues[1].

[1]Faculdade de Farmácia, Universidade Federal do Rio de Janeiro, Brazil, [2] Centro Nacional de Pesquisa em Energia e Materiais, Brazil. [3] Instituto de Pesquisas Jardim Botânico do Rio de Janeiro, Brazil, [4] Faculdade de Ciências Farmacêuticas de Ribeirão Preto, Universidade de São Paulo, Brazil.
* jvillelapaulino@yahoo.com.br

Synchrotron X-ray computed nanotomography (SXRCT) is a non-destructive three-dimensional imaging technique that enables high spatial resolution visualization of the internal organization of plant tissues in their natural state [1]. This approach is particularly valuable for studying secretory structures, such as laticifers, which may display a complex and branched distribution within tissues, and for which continuous three-dimensional observation is essential to understand their organization and function [2]. In this context, *Swartzia langsdorffii* (Fabaceae) presents laticifers distributed along the stem [3], and its pericarp exudes a salmon-colored liquid when injured. The structures responsible for this secretion have not yet been properly characterized. Thus, the aim of this study was to analyze, using SXRCT, the secretory structures present in the pericarp of *S. langsdorffii*. For this purpose, pericarp sections of *S. langsdorffii* were treated with a 1% phosphotungstic acid solution in 70% ethanol (contrast agent) for 30 consecutive days [4], dehydrated in an ethanol series, dried using a Bal-Tec CPD 030 critical point dryer (Bal-Tec AG, Liechtenstein), and mounted on metal stubs with the aid of a thermoplastic polymer. Scanning was carried out at the MOGNO beamline (Sirius) [5]. Projection data were acquired using a 2048 × 2048-pixel sCMOS detector equipped with a 3× objective lens. Samples were scanned in fly-scan mode, with projections collected over a 360° rotation and an exposure time of 0.6 s. The average scanning time for both configurations was approximately 15 minutes. Images were reconstructed using an in-house implementation of the FDK algorithm [6]. Amira-Avizo 3D 2024.2 software was used for visualization and quantification of the scan data. Nanotomography revealed that the laticifers are of the articulated non-anastomosing type, forming a network of interconnected cells throughout the mesocarp. These structures occupy approximately 12% of the total volume of the sample analyzed. Analysis of laticifer density by organ may provide valuable insights into adaptive defense and resource allocation strategies, particularly in ecologically relevant structures such as flowers and fruits [7].

Key-words: image reconstruction, 3D image, plant anatomy, plant science, secretory structure,

[1] S. Dierickx, et al. Non-destructive wood identification using X-ray µCT scanning: which resolution do we need?. *Plant Methods* 20.1 (2024): 98.
[2] M. Wang, et al. Three-dimensional reconstruction and autophagy process analysis reveal development pattern of articulated laticifers in Taraxacum kok-saghyz Rodin. *Industrial Crops and Products* 228 (2025): 120857.
[3] C. A. de Oliveira,et al. Bloodwood: the composition and secreting-site of the characteristic red exudate that gives the name to the *Swartzia* species (Fabaceae). *Journal of plant research* 134.1 (2021): 127-139.
[4] M. Y. Staedler, et al. Plant tissues in 3D via X-ray tomography: simple contrasting methods allow high resolution imaging. *PloS one* 8.9 (2013): e75295.
[5] N. L. Archilha, et al. MOGNO, the nano and microtomography beamline at Sirius, the Brazilian synchrotron light source. *Journal of Physics: Conference Series*. Vol. 2380. No.

1. IOP Publishing, 2022.
[6] E. X. Miqueles, et al. "Fast image reconstruction at a synchrotron laboratory." *Proceedings of the 2020 SIAM Conference on Parallel Processing for Scientific Computing*. Society for Industrial and Applied Mathematics, 2020.
[7] This research was supported by CAPES and FAPERJ (Brazil).

Figure 1. Three-dimensional rendering of *S. langsdorffii* pericarp laticifers. Scale bars: A–D = 100 μm.

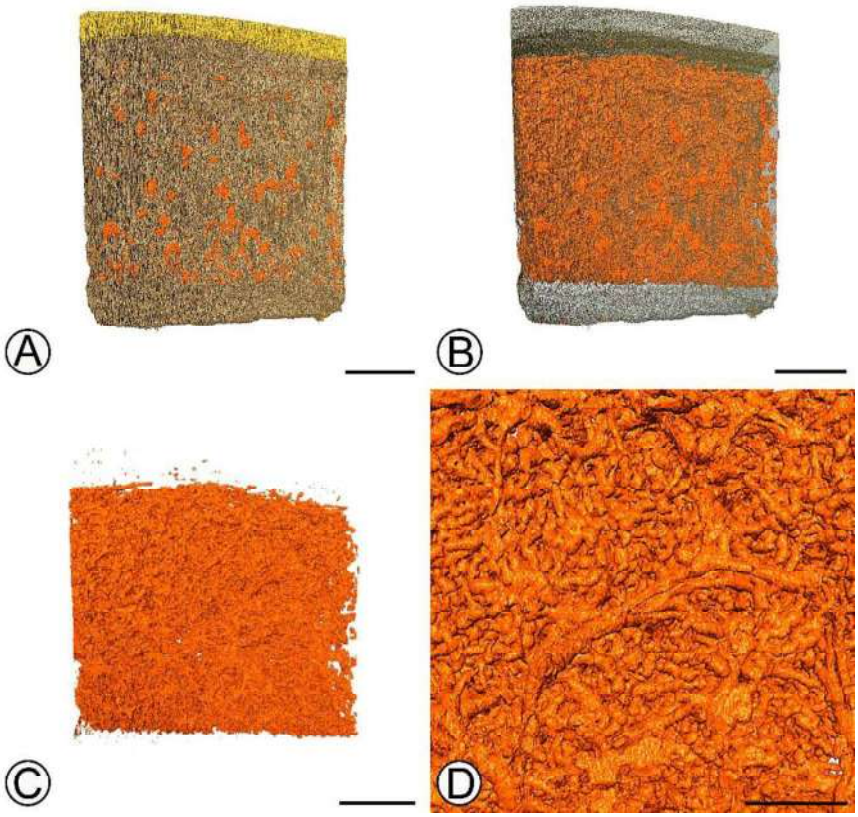

Application of X-ray MicroCT for the Characterization of Defects in Flexible Risers

Adriana J. P. Moreira*, Olga Maria O. de Araújo, Alessandra S. Machado, Ricardo T. Lopes, Davi F. de Oliveira.

Nuclear Instrumentation Laboratory/PEN/COPPE, Federal University of Rio de Janeiro, 21941-914, Rio de Janeiro, RJ, Brazil
*adrianajpmoreira@coppe.ufrj.br

The structural integrity of flexible risers is critical for the safety and performance of offshore systems, as these concentric structures - composed of metallic and polymeric layers - operate under severe tensile, pressure, and bending stresses. Flexible risers possess a complex internal architecture, consisting of external and internal tensile armor layers, a pressure containment layer, and an interlocked carcass [1]. Among these, the tensile armor layers are particularly vulnerable to crack initiation and fatigue failure due to wire imperfections [2,3]. Conventional non-destructive testing (NDT) techniques, while widely employed for riser inspection, exhibit limitations in detecting internal defects and show limited sensitivity to early-stage microcrack formation [4,5]. In this context, X-ray computed microtomography (microCT) emerges as a powerful non-destructive technique capable of producing high-resolution three-dimensional images that accurately reveal the internal microstructures of flexible risers [6]. This study applied microCT to inspect defects in small sections of flexible riser segments removed from an offshore operational environment. Two samples, designated riser 1 and riser 2, were scanned using a Phoenix V|tome|x M microtomography system (Baker Hughes), integrating control of the X-ray source, digital detector, and sample manipulation to ensure high-quality data acquisition. The system employs a high-power microfocus X-ray tube operating up to 300 kV and 500 W, paired with a GE PXR250RT detector featuring a 2024 × 2024-pixel matrix and 200 μm pixel size. Projections were collected over a full 360° rotation and reconstructed with Phoenix Datos|x Reconstruction software. The scanning settings are shown in Table 1. The post-processing of the images, including 2D and 3D visualization, sectional analysis, and segmentation of metallic layers, was performed using VGStudio Max, CTAn, and Avizo software [7,8]. Results showed that riser 1 (Figure 1) presented multiple cracks within the pressure layer, measuring 4.80 mm, 11.05 mm, and 11.19 mm in length, along with misalignment of tensile armor wires. An additional crack of 5.97 mm was detected in another region of the same layer. In riser 2 (Figure 2), microCT revealed defects distributed across both internal and external tensile armor layers, including discontinuities caused by abnormal spacing between armor wires. These defects varied in size up to 2 mm, indicating structural irregularities throughout the armor. These findings confirm that microCT is an effective and reliable tool for high-resolution inspection of flexible risers, enabling the detection and detailed characterization of internal discontinuities often undetectable by conventional NDT methods. The application of microCT contributes to enhanced predictive maintenance and improves the structural reliability of flexible risers in offshore operational settings [9].

[1] X. Li *et al*., *Applied Ocean Research* 80 (2018) 1-10.
[2] Y. Bai, Q. Bai, *Subsea Pipeline Design, Analysis, and Installation*, Gulf Professional Publishing, 2014.

[3] N. J. R. Nielsen *et al*., *Proc. Offshore Technol. Conf.* (2008).
[4] M. Ho *et al*., *Structural Health Monitoring* 19 (2019) 606-645.
[5] E. Cheilakou *et al*., *e-J. Nondestruct. Test.* 24(5) (2018).
[6] D. F. Oliveira *et al*., *Applied Radiation and Isotopes* 151 (2019) 247-255.
[7] O. Araújo *et al*., *e-J. Nondestruct. Test.* 25(2) (2020).
[8] R.C. Gonzalez, Z. Faisal, *Digital Image Processing*, 2nd ed., Pearson, 2019.
[9] This research was supported by CNPq and Capes (Brazil).

Table 1. Scanning settings – Phoenix V|tome|x M microCT system

Parameters	Riser 1	Riser 2
voltage (kV)	240	240
current (µA)	340	340
acquisition time (ms)	333	333
effective pixel size (µm)	94	94
projections	1200	1200

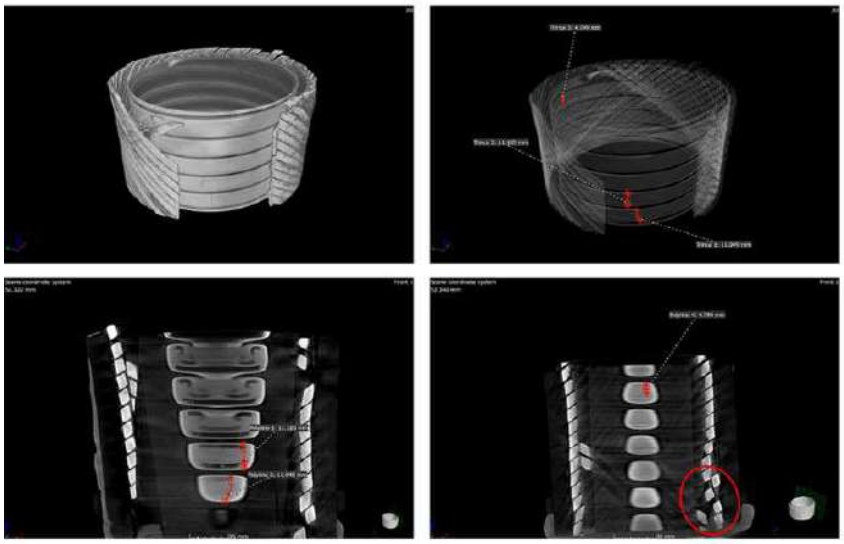

Figure 1. 3D and 2D microCT images showing cracks in the pressure layer of riser 1 and misalignment between tensile armor wires.

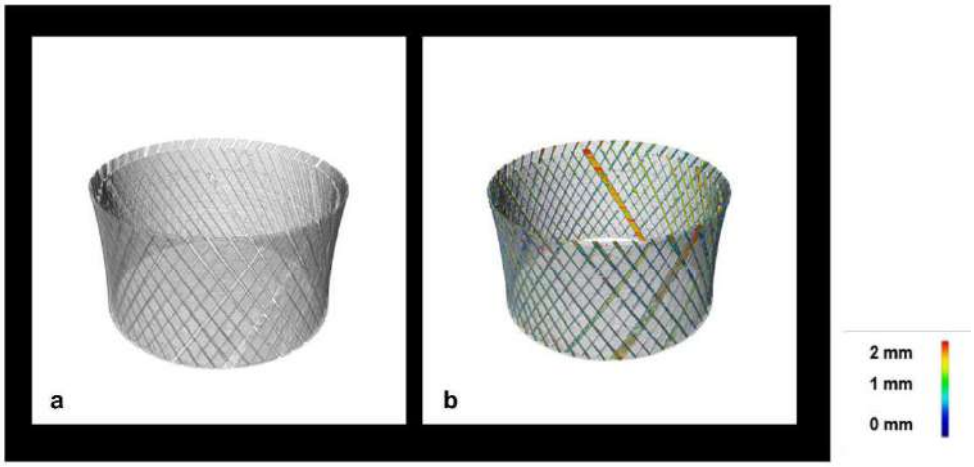

Figure 2. 3D microCT images of riser 2: (a) image of the internal and external tensile layers; (b) image of defects distributed along the internal and external tensile layers.

Microstructural Tailoring of HYTA Alloys: A Metallographic Investigation of Functionally Graded Titanium Processed by PBF-LB

Gilberto Vicente Prandi[1]*, Marcio Sangali[1], João Felipe Q. Rodrigues[1], Matheus Valentim[1], Virginie Roche[5], Alberto M. Jorge Junior[3,4,5], Alessandra Cremasco[1,2], Rubens Caram[1].

[1]School of Mechanical Engineering – University of Campinas (UNICAMP) - Brazil,
[2]School of Applied Sciences – University of Campinas (UNICAMP) - Brazil,
[3] Graduate Program of Materials Science and Engineering, Federal University of São Carlos - Brazil.
[4] Univ. Grenoble Alpes, Univ. Savoie Mont Blanc, CNRS, Grenoble INP, Institute of Engineering and Management, SIMAP – France
[5] Univ. Grenoble Alpes, Univ. Savoie Mont Blanc, CNRS, Grenoble INP, Institute of Engineering and Management Univ. Grenoble Alpes, LEPMI – France
*g242664@dac.unicamp.br

Titanium alloys are known for their remarkable microstructural flexibility, which enables the design of components with tailored mechanical responses, including stiffness gradients or compositional heterogeneity through processing or thermal strategies. In particular, Ti-42Nb exhibits complete β-phase retention upon cooling and avoids the formation of the ω phase, resulting in a ductile structure with low elastic modulus (~62 GPa) and excellent biocompatibility [1]. In contrast, Ti-5Al-5Mo-5V-3Cr shows significant strengthening after aging due to α-phase precipitation, being widely employed in aerospace and marine applications due to its toughness and corrosion resistance [2]. This work explores the combination of these alloys to fabricate Hybrid Titanium Alloys (HYTA) using the powder bed fusion with laser beam (PBF-LB) process. Pre-alloyed powders of Ti-42Nb and Ti-5553 were mixed at 80:20 wt.% under an inert atmosphere using a mechanical eccentric mixer. Fabrication was performed on an OmniSint-160 system equipped with a Yb:YAG fiber laser. Uniform and functionally graded cylindrical samples were fabricated; the latter involved progressive increases in laser power (200, 300, and 400 W) and adjustment of scanning speed every 33 layers (1 mm), to intentionally promote microstructural variation. Samples were metallographically prepared by conventional grinding and polishing and the microstructural characterization was performed by high-resolution field-emission scanning electron microscopy (FE-SEM), including focused ion beam (FIB) cross-sections, energy-dispersive spectroscopy (EDS), and electron backscatter diffraction (EBSD), as shown in Figure 1. After fabrication, the cylinders were cut by wire electrical discharge machining (EDM) and analyzed by X-ray microtomography (EBM system). The tomographic and microstructural analyses confirmed the presence and integrity of spatially distinct regions (Figure 2), with Ti-5553-rich domains displaying increased strength even in the as-built state, while Ti-42Nb preserved its β-phase stability and low modulus. By tailoring the laser parameters, it was possible to produce both fully homogenized microstructures and sharply hybridized zones within the same geometry, validating the potential of this hybrid additive approach for the precise engineering of functionally graded titanium components with biomedical and structural relevance [3].

[1] C. Schulze, M. Weinmann, C. Schweigel, O. Keßler, R. Bader. Materials 11 (2018) 124.
[2] P. Yang, K.L. Johnson, J.D. Carroll, J.L. Buckner, M.A. Blea-Kirby, C. Groves, E.N. Coker, Addit. Manuf. 76 (2023) 103769.
[3] G.V. Prandi, J.F.Q. Rodrigues, M. Valentim, M. Sangali, L.F. Starck, J. Soyama, R. Caram, J. Mater. Res. Technol. 27 (2023).

This research was supported by FAPESP (Sao Paulo Research Foundation, Grant 2022/10049-6 and 2018/18293-8).

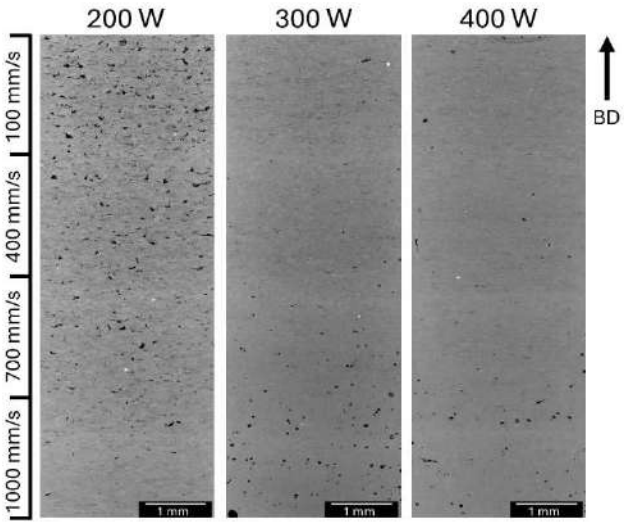

Figure 1. SEM showing the gradient formed and its microstructural differences.

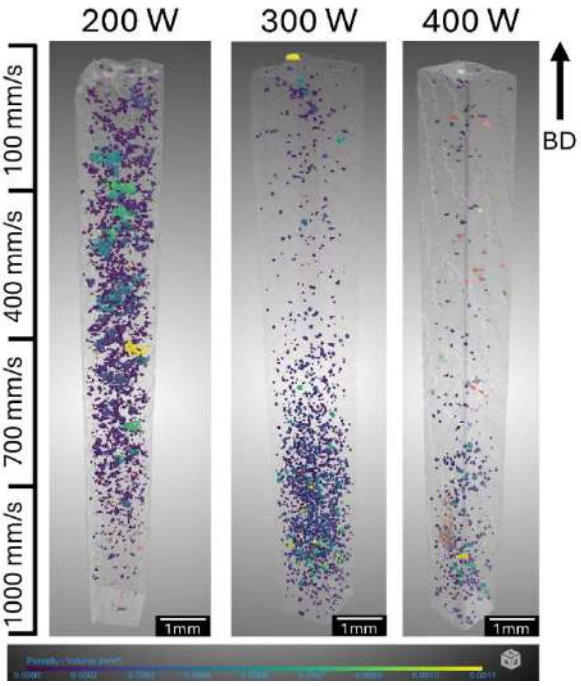

Figure 2. Microtomography shows the porosity formed and also unfused Nb particles.

Study of the Anti-Caries Action of Silver Nanoparticles by X-ray Microtomography with FIB Sample Preparation

Fernanda Karoline da Silva[1]*, Maria Clara Muller de Andrade[1], André Galembeck[1].

[1]Departamento de Química Fundamental, Universidade Federal de Pernambuco (dQF/UFPE), Recife-PE, Brasil
*fernanda.karolines@ufpe.br

Silver nanoparticle (AgNP) based formulations have proven effective in controlling dental caries [1]. Caries begins with the exposure of dentin, a structure composed of dentinal tubules, small canals approximately 2.5 μm in diameter that connect to the dental pulp. The exposure of these tubules allows bacterial penetration, such as *Streptococcus mutans*, which aggravates the lesion. Our group develops AgNP-based formulations with proven antibacterial activity against *S. mutans* and clinical efficacy, with 67% of cases showing lesion arrest after a single application and one year of follow-up [1]. Recently, we demonstrated using focused ion beam (FIB) microscopy that AgNPs also penetrate the tubules (Figure 1), and the amount of silver detected in the intratubular dentin allowed us to estimate a dose exceeding the minimum inhibitory concentration for *S. mutans* [2]. Based on these results, further experiments were conducted to investigate the association between AgNP penetration and the inhibition of bacterial invasion into the tubules. For this purpose, human dentin samples, both treated and untreated with AgNPs, were inoculated with *S. mutans* for seven days. Preliminary analysis by scanning electron microscopy (SEM) revealed that bacterial invasion occurs heterogeneously among the tubules within the same sample (Figure 2). This observation justified the use of X-ray microtomography (MicroCT), which allows the simultaneous analysis of a large number of tubules to obtain more conclusive results. For MicroCT analysis, regions of interest identified by SEM were prepared using FIB, enabling precise and targeted sectioning of 2×2×2 mm^3 blocks. This ensured proper exposure of the tubules for tomographic acquisition while minimizing artifacts commonly introduced by mechanical preparation. Samples were scanned at the MOGNO beamline (Sirius/CNPEM), with resolution up to 300 nm, enabling the visualization of bacteria (~1 μm) inside the tubules. The reconstructed images allowed visualization of the tubular dentin structure (Figure 3), opening the possibility of identifying morphologies compatible with bacterial colonies along the interior of the tubules, in alignment with other reconstruction parameters. The combined methodology of SEM, FIB, and MicroCT proved efficient and reproducible for studying systems composed of both hard and soft components, as is the case of dentin colonized by *S. mutans*. The use of FIB as a targeted preparation method for tomography was a key factor in achieving controlled cuts and proper spatial orientation.

[1] DOS SANTOS, V.E. et al, A new “silver-Bullet” to treat caries in children - Nano Silver Fluoride: A randomised clinical trial, J. Dent. 42 (2014) 945–951.
[2] ANDRADE, M. C. M. et al, Silver nanoparticles penetration in dentin: Implications for long-term caries arrestment, Materialia. 24 (2022)

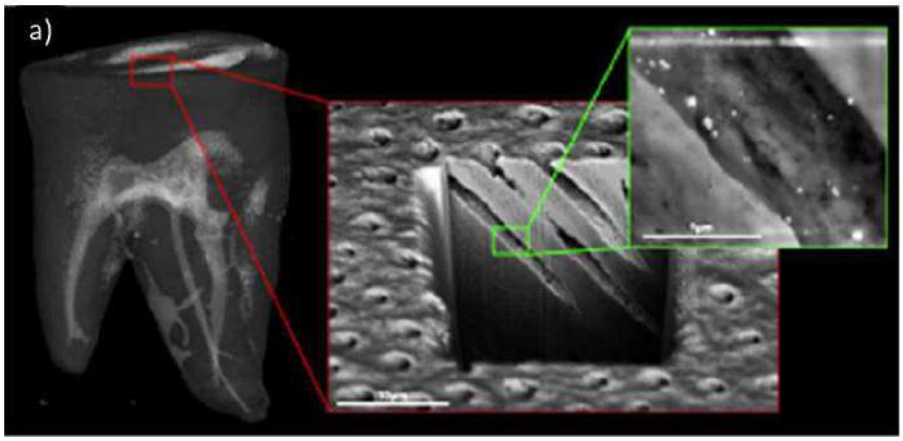

Figure 1. Low-resolution tomography and FIB-SEM of the internal tooth structure and AgNP penetration into the dentinal tubules.

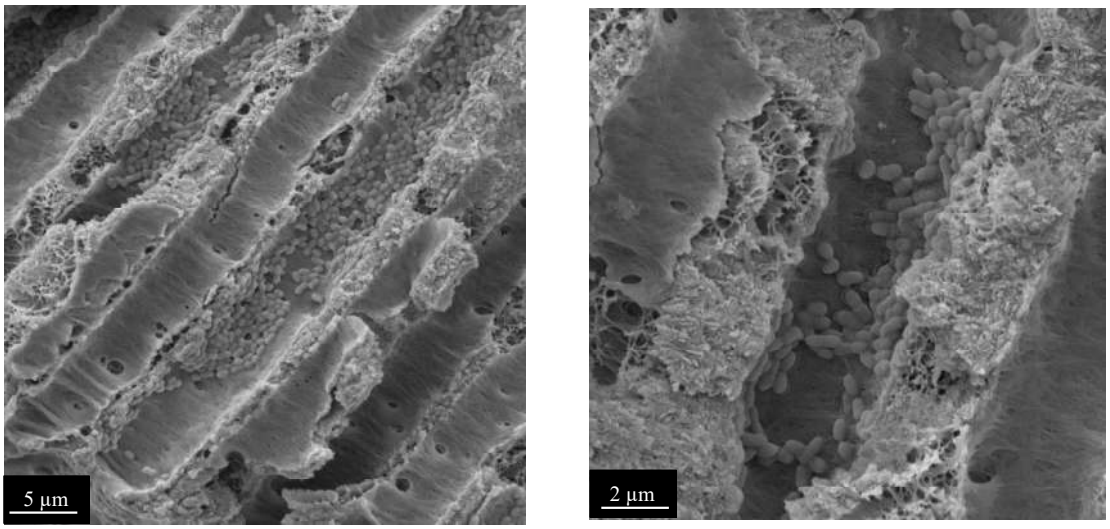

Figure 2. SEM showing heterogeneous penetration of *S. mutans* into the dentinal tubules after 7 days of inoculation.

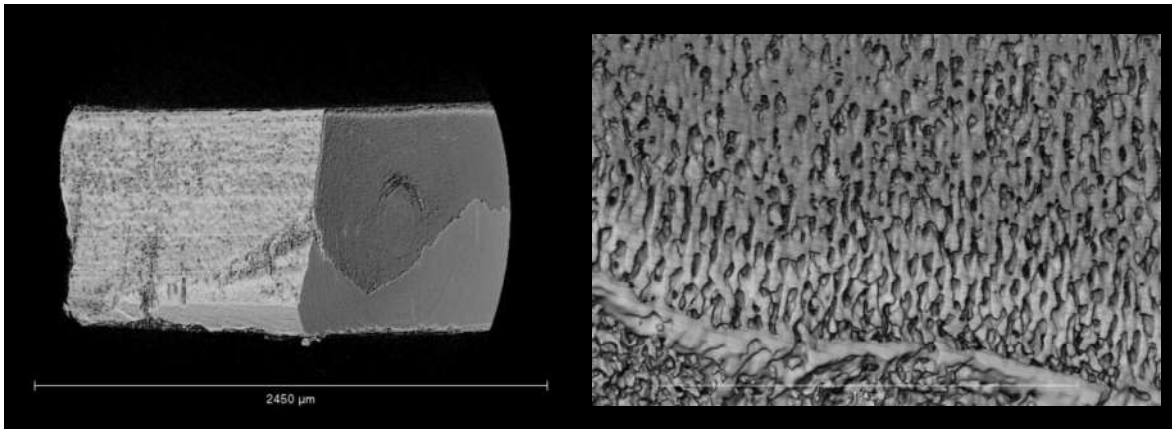

Figure 3. 3D MicroCT reconstruction of dentin samples treated with AgNPs after *S. mutans* inoculation for 7 days.

Scanning electron microscopy (SEM) applied to biological samples, including all techniques associated with SEM, such as EDS and FIB

Creative views of *Toxoplasma gondii* in the feline host by SEM and Serial Block Face

Marcia Attias[1,2], Wanderley de Souza[1,2] Jitender P. Dubey[3]

1. Universidade Federal do Rio de Janeiro. Instituto de Biofísica Carlos Chagas Filho
2. Centro Nacional de Biologia Estrutural e Bioimagem- CENABIO
3. US Department of Agriculture, Beltsville Agricultural Research Center, Animal Parasitic Diseases Laboratory, Beltsville, MD 20705-2350, USA
E-mail address: mattias@biof.ufrj.br

Needless to say, *Toxoplasma gondii* is an important parasite of humans, domestic and wild animals. However, only in feline enterocytes sexual reproduction occurs. In cats primoinfection, whether by tissue cysts or oocysts, the parasites invade and proliferate in enterocytes, where they convert to merozoites, multiply by schizogony and, eventually convert to micro or macrogametes that gives origin to an oocyst that will later be shed with the cat feces and sporulate, giving rise to sporozoites. Today, we are going to look on the intestinal forms of *T. gondii* in the cat using two cutting edge techniques: High resolution field emission scanning electron microscopy (FE-SEM) (**Figures A-D**) and 3-D models in series obtained by Serial block face scanning electron microscopy, and see, how much progress could and can be achieved with these methods (**Figs E and F**). **Methods**: two cats, infected with *Toxoplasma gondii* were euthanized and Scraps, consisting of villi of the lining of the ileum were fixed in 2.5% glutaraldehyde in 0.1M cacodylate buffer. were also fixed. All biosafety and ethical procedures followed approved protocols **012-3 and #12-016** by the Beltsville Area Animal Care and Use Committee (BAACUC), United States Department of Agriculture, Beltsville, MD. **FE-SEM**: the scrapped villi were rinsed in buffer, post fixed in 1% OsO_4, rinsed again and were embedded in a gelatin-chitosan mixture, cut in small pieces with a razor blade and dehydrated. When in ethanol 100%, the fragments were frozen by immersion in liquid nitrogen, cleaved with a razor blade to expose internal features, thawed, macerated in 0.1% OsO4 for 2 days, dehydrated in ethanol and dried by critical point of CO2, mounted and sputtered with Platinum [1] (Fukudome and Tanaka, 1986). Observations were made with an AURIGA 40 (Zeiss) Field emission Scanning electron microscope. **Serial block-face scanning electron microscopy (SBF):** Serial block face series were obtained from a chemically fixed sample embedded in EPON, as for classical TEM. A ZEISS Volutome fitted on a GeminiSEM 360 was used for the slice and view acquisition of the series and 3-D models were rendered with the IMOD package [2] (Kremer et al., 1996). The combination of these two approaches provided new insights on the distribution of parasite stages along the intestinal cells with greater resolution, volume and area coverage that could be achieved before.

Acknowledgements: To ZEISS Oberkochen, DM

[1] Fukudome, H., Tanaka, K., 1986. J. Microsc. 141, 171–8.
[2] Kremer, J.R., Mastronarde, D.N., McIntosh, J.R., 1996. J. Struct. Biol. 116, 71–6.

This research was supported by FAPERJ, CAPES, FINEP and CNPq (Brazil).

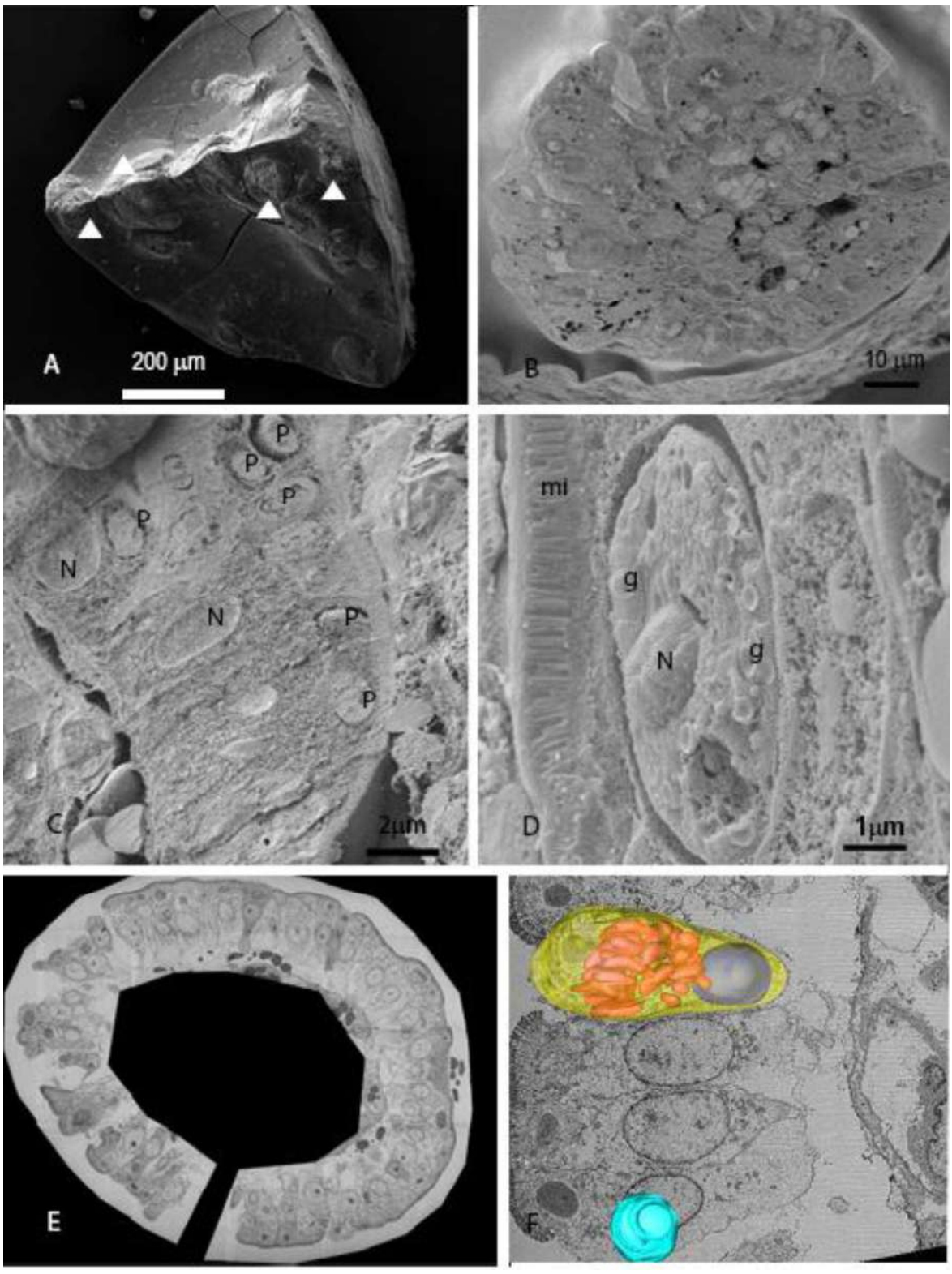

A-D: Intestinal villi embedded in gelatin-chitosan, frozen and cleaved. (A) Several fractured profiles (arrowhead) in a single piece. (B) Cross section of a single villus (C) Zoom view showing parasites (P), (N) nucleus. (D) A cleaved macrogamont exposing internal granules (g), microvilli (mi). E-F. SBF-F- section showing a large area that can be covered and in E the resolution that allows the individualization of several parasites (orange) in a single cell (Yellow). CyanBlue: developing macrogamete.

Cryo-Preparation and In Situ Cooling Strategies for Electron Beam-Sensitive Samples in VPSEM

Fabiano Emmanuel Montoro[1*], Arthur Francisco Carrapato Assis[1], João Marcos da Silva[1], Ana Beatriz Sorana de Araujo[1].

[1]Laboratório de Microscopia Eletrônica de Varredura e Duplo Feixe - Laboratório Nacional de Nanotecnologia (LNNano/CNPEM), Campinas-Brazil.
*fabiano.montoro@lnnano.cnpem.br

Low-temperature scanning electron microscopy (cryo-SEM), combined with variable pressure operation (VPSEM), provides a powerful approach for minimizing dehydration artifacts in biological sample analysis. Organic and polymeric materials are often highly sensitive to the electron beam, exhibiting significant degradation due to radiolysis effects [1]. Conventional preparation methods for such beam-sensitive samples involve cryofixation, controlled transfer for conductive coating, and subsequent mounting in a cryo-stage within the SEM. These protocols also rely on in situ cooling systems to maintain low temperatures during imaging. However, due to the high cost and complexity of the equipment involved, alternative methodologies have been explored in recent literature [2]. The analysis of delicate biological structures, such as the absorptive root hairs of plants, shown in Figure 1, is particularly challenging using standard preparation techniques. These fragile features do not withstand traditional drying and conductive coating steps. While cryo-fixation helps preserve ultrastructure during imaging, the poor electrical conductivity of frozen hydrated samples often results in charging artifacts under electron beam scanning. Nonetheless, when chamber temperature and pressure are finely tuned, it is possible to take advantage of the intrinsic conductivity of ice to achieve high-quality imaging [3]. This study aims to review and evaluate key methodologies for the in-situ preparation and cooling of electron beam-sensitive samples for SEM analysis, with a particular focus on VPSEM modalities such as low vacuum (LV-SEM) and environmental scanning electron microscopy (ESEM). A commercial cryo-transfer and cooling system (Figure 2) will be used to assess performance in comparison with a low-cost, custom-built device developed at the Scanning Electron and Dual Beam Microscopy Laboratory at LNNano/CNPEM. A comprehensive set of sample preparation techniques will be explored, including methods with and without conductive coating and pre-cooling procedures prior to chamber insertion. The study also includes the evaluation of imaging stability over time and mitigation of charging artifacts without the need for metallic coatings. By comparing different strategies and evaluating performance under realistic laboratory conditions, this study contributes to the development of a practical workflow for high-fidelity SEM imaging and FIB processing of delicate samples, enabling future studies that require structural preservation at the micro- and nanoscale. This workflow will be tailored for biological specimens and other electron beam-sensitive materials, aiming to preserve fine structural details while ensuring compatibility with downstream analytical methods such as TEM or EDS.

[1] Goldstein, J. I. et all, Scanning Electron Microscopy and X-Ray Microanalysis, Plenum Press, 1992.

[2] Ensikat, H. J., & Weigend, M. (2013). Microscopy and Analysis, 27(6), 7-10.

[3] Stokes, Debbie J., Principles and practice of Variable Pressure/Environmental Scanning Electron Microscopy (VP-ESEM), John Wiley & Sons Ltd, RMS, 2008.

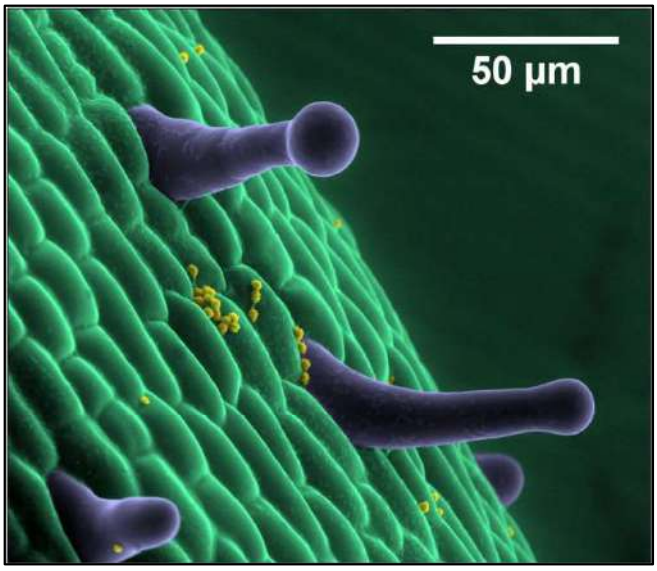

Figure 1 *– Absorptive root hairs on a tomato root imaged under low temperature and atmospheric pressure conditions using a scanning electron microscope. False colors were applied to distinguish the root, the hairs, and associated microorganisms.*

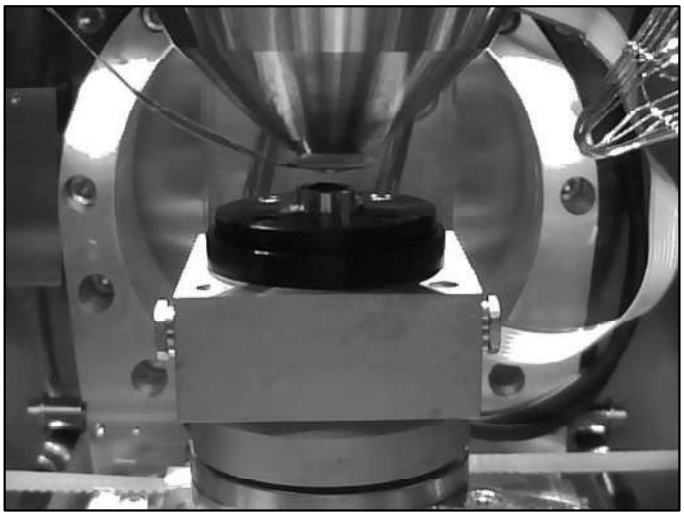

Figure 2 *- FEI/Thermo Fisher in situ cooling device and GSED detector (Gaseous Secondary Electron Detector) for image acquisition in variable pressure and low temperature experiments.*

Internal organization patterns of trabeculae in long bones

Carlos A. Menezes[1], Simão C. Albuquerque Neto[1], Camila Wendt[1], José Brito Neto[1], Matthias Guillo[1], Mair M. M. de Oliveira[1], Alexandre M. Rossi[2], Ovidiu Ersen[3], Marcos Farina[1]*

[1]Institute of Biomedical Sciences, UFRJ - Brazil, [2] Brazilian Center for Research in Physics, [3]Strasbourg Institute of Materials Physics and Chemistry – IPCMS - France.
*marcos.farina.souza@gmail. Marcos Farina

Trabeculae make part of the internal region of the extremities of tibia and femur, the inner region of other long bones like ribs, as well as of spongy cancellous bones as the diploe [1]. Forming trabeculae in tibia and femur of chicken embryo, initiate in the cortex of the mid shaft of the bones (Figs. 1, 2). In diploe bones, they are rod or pillar shaped, while in porcine and bovine ribs, they form repeated patterns, relatively well organized in parallel, with topographies like a sheet swinging in the wind. Besides, in porcine, it is possible to find a substructure, composed of repeated small concave areas, with an approximately circular whole in the center (Figs. 3a, 3b). In this work we focus on the organization patterns and inner appearance of trabeculae in chicken embryo, and in bovine and porcine ribs. In the initial process of bone healing upon an injury, trabeculae are formed growing towards the center of the bone defect. In this case they have a morphology similar to rods or pillars [2]. Few works discuss the topographical arrangement of inner components of trabecula, i.e., the type I collagen molecules [1]. Broadly speaking, we could classify trabeculae as bone structures whose morphology varies from rods to plates. It has been considered that the periphery of rod shaped trabeculae is formed by concentric bone lamellae (i.e. mineralized tissue presenting type I collagen organized in concentric layers [1]. Here we show that, in the trabeculae from bovine ribs type I collagen organization in the bulk of the trabeculae follows the same orientation of the collagen in the cortical bone from where the trabeculae originate (Fig. 4a). Additionally, trabeculae from a bovine origin may present a particular morphological feature which is the presence of Havers systems, running parallel to the longer dimension of the original bone (Fig. 4). In several cases it is possible to see also, clearly, two distinct types of mineralizing regions, with a discernible interface. This type of regions in chicken embryo are easily identified by the different contrasts obtained upon staining (Fig. 1, inset) in this case, represented by the mineralized bulk and the external region containing recently entrapped osteocytes.

Medullary bone in the epiphyses of femur, tibia or inside ribs, contains also trabeculae in the shape of spicules or plates, surrounded by osteoid tissue. The outer region presents also a distinct appearance when compared to the highly mineralizer bulk region, similarly to the forming trabeculae from the mid shaft.

In summary, we showed in this work that trabeculae from bovine rib have type I collagen fibrils oriented similarly to those in the contiguous cortical bone (Fig. 4a), and that they may contain also Havers systems with the longer axis oriented in the same direction (Fig. 4b). In tibia and femur of chicken embryo it was found two patterns of bone tissue, after staining with toluidine blue, distinguishable due to the presence of a clear interface (Fig. 1a and inset). The reason that defines the initial condition for the appearance of this interface is a subject that deserves more studies.

Acknowledgements

[1] N. Reznikov et al. Bone 71 (2015) 189–195.
[2] Victor R. Martinez-Zelaya et al. Acta Biomaterialia 120 (2021) 181–193.
[3] This research was supported by CNPq and FAPERJ Brazilian agencies and International Research Project (IRP-CNRS-France).

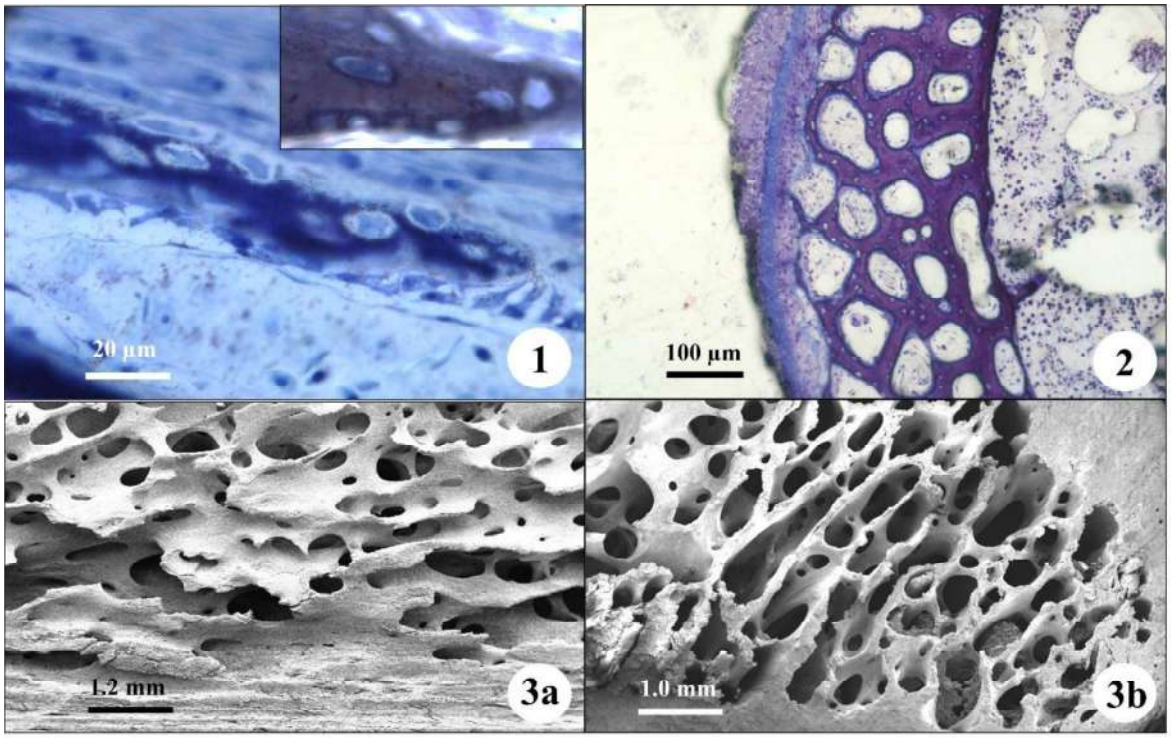

Figure 1. Longitudinal section of a femur of a 14-day-old chicken embryo, stained with toluidine blue, showing the beginning of a trabecula formation (dark blue) containing osteocytes. Inset: detail of an equivalent region; brown: bone tissue with osteocytes; dark blue contour: tissue in the initial process of mineralization with just trapped osteocytes. Magnification like Fig. 1.

Figure 2. Transversal section of a 19-day-old chick embryo tibia. Trabeculae form a network (purple) being attached laterally.

Figure 3a. Scanning electron microscopy (SEM) image of a longitudinal section of a porcine rib. Note that trabeculae are like undulated sheets. **Figure 3b.** SEM image of a transverse section of a rib similar to the one in the previous figure. Note that trabeculae are organized in roughly paralell sheets.

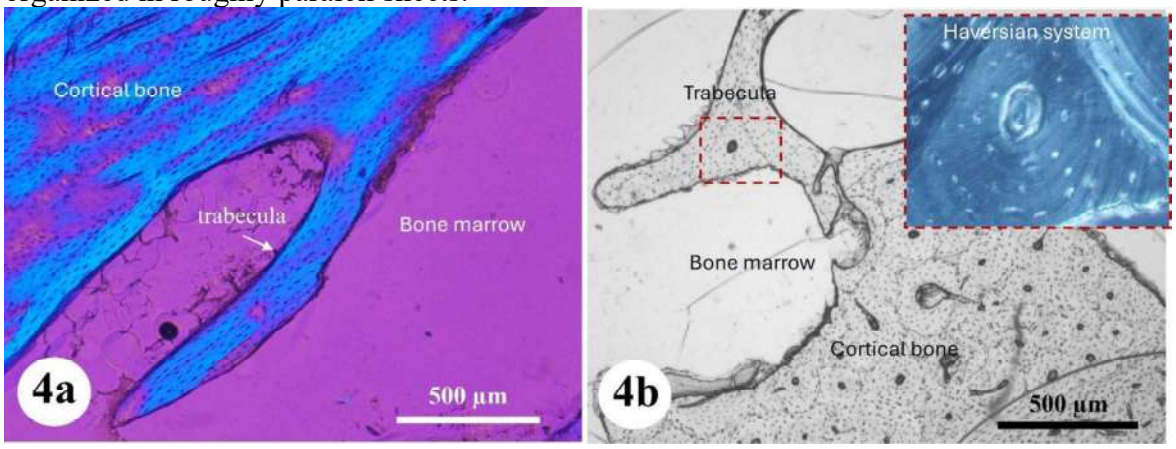

Figure 4a. Longitudinal non-stained section of a bovine rib observed by polarization light microscopy, showing part of a cortical bone (top left) and a trabecula. Note that the orientation of type-I collagen is similar in these two regions (blue in the image). **Figure 4b.** Transversal non-stained section of a bovine rib showing a trabecula in the endosteal region (left), that presents a Haversian system also cut transversely (dashed rectangles). Bar in Fig. 4b corresponds to 125µm in the inset.

3D reconstruction by slice-and-view FIB-SEM of oriented cell monolayers

Vânia Vieira[1]* , Márcia Attias[1,2],

1- Unidade de Microscopia Avançada, Centro Nacional de Biologia Estrutural e Bioimagem, CENABIO, Universidade Federal do Rio de Janeiro, RJ, Brasil

2- Instituto de Biofísica Carlos Chagas Filho. Laboratório de Ultraestrutura Celular Hertha Meyer. Centro de Pesquisas em Medicina de Precisão, Universidade Federal do Rio de Janeiro, RJ, Brasil

*vaniavieiracenabio@gmail.com

This study proposes a modification to the conventional biological sample preparation protocol for Focused Ion Beam Scanning Electron Microscopy (FIB-SEM) in order to improve the precision in localizing structures of interest, thereby reducing series acquisition time. In the FIB-SEM method, biological sample preparation typically follows the same steps used in traditional transmission electron microscopy (TEM) protocols [**1, 2**]. As a result, the orientation of cells and target structures is often suboptimal for 3D reconstruction, leading to extensive milling through resin before reaching a region of interest. This not only extends instrument time but significantly increases the cost per series and decreases the life time of the gallium ion source, which is significantly consumed during this non-productive milling phase. To optimize structural orientation and localization, this study recommends the use of cellular monolayers [2] whenever feasible. Accurate knowledge of the sample's position enables a reduction in the number of slices required to cover the volume of interest, decreasing acquisition time. This positively impacts not only in cost but also increases the amount of samples to be processed for serial acquisition of images by FIB-SEM saving time and increasing throughput. For this purpose, monolayers of LLCMK2 cells infected with *Toxoplasma gondii* (7 hours post-infection) were employed. Samples were chemically fixed, dehydrated, and embedded in Epon resin [2]. The culture dish was then removed, leaving only the cellular monolayer. This slide of resin containing the monolayer was reembedded and polymerized in a sandwich configuration: Epon–monolayer–Epon (Figure 1), then trimmed into a pyramid shape and coated with platinum to prevent charging during FIB-SEM series acquisition in Zeiss Dual-beam - AURIGA 40. Figure 2 shows the secondary electron image acquired prior to volume acquisition, demonstrating that trenching can be performed tangentially to the monolayer. Figure 3 presents a reconstructed parasite by segmentation identified in the sample, first appearing at slice number 28, indicating that image acquisition of the structure of interest could begin immediately following trench milling using the slice-and-view technique. This approach minimizes gallium usage and acquisition time, resulting in improved frequency and precision in targeting the structures of interest (in this case, intracellular parasites), requiring a reduced number of slices, and not less important, lowering acquisition costs.

[1] Augusto, I. Miranda, K. Quantitative assessment of the nanoanatomy of the contractile vacuole complex in Trypanosoma cruzi, Life Sci Alliance. 2024 Jul 29;7(10):e202402826. doi: 10.26508/lsa.202402826. Print 2024 Oct.

[2] Souza, Wanderley de. Técnicas de Microscopia Eletrônica Aplicadas às Ciências Biológicas. Rio de Janeiro: SBMM, 3ª edição. 2007

[3] Goldstein, J.I. et al., Scanning Electron Microscopy and X-ray Microanalysis, Plenum Press, New York, 1992.

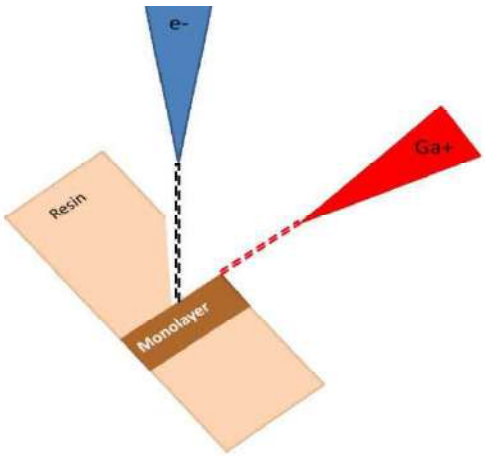

Figure 1: Lateral view illustrating the correct orientation of the monolayer in relation to the FIBSEM system.

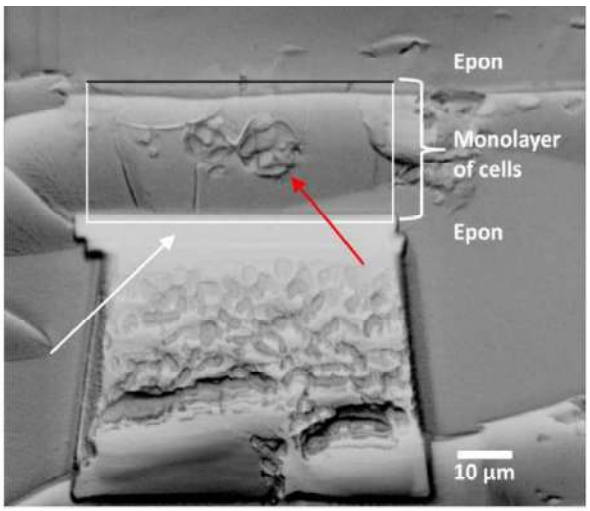

Figure 2: SEM image of the block face showing the precise location of the cell monolayer (red arrow) and the areas with epon resin. Note that the trench (white arrow) must be made tangent to the monolayer.

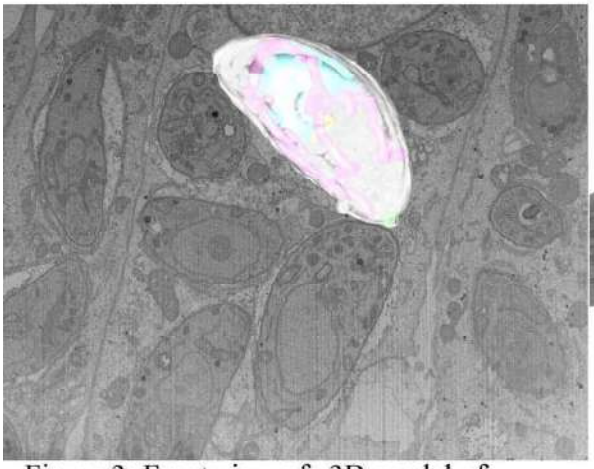

Figure 3: Front view of a3D-model of Toxoplasma gondii rendered from the FIB-SEM series.
Pellicle-White,
Mitochondrion-magenta
Nucleus cyan
apicoplast: yellow

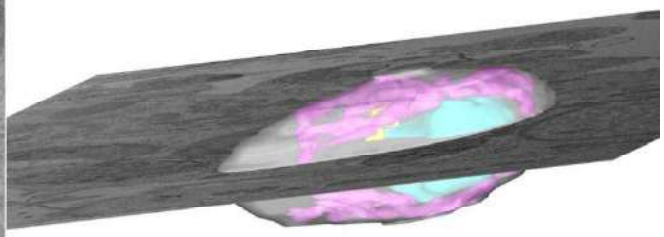

Figure 4: Slice and view of the model shown in Fig. 3. With fewer slices, the whole volume of the parasite was reconstruct.

A modified SEM protocol for studying plant secretions

Viviane Gonçalves Leite[1,2], Vidal Freitas Mansano[2], Simone Pádua Teixeira[1,*]

[1]Department of Pharmaceutical Sciences, Faculty of Pharmaceutical Sciences of Ribeirão Preto, University of São Paulo, Av. do Café, s/n., Ribeirão Preto, SP, 14040-903, Brazil
[2]Rio de Janeiro Botanical Garden Research Institute, DIPEQ. Rua Pacheco Leão, 915, Rio de Janeiro, RJ, 22460-030, Brazil
*Corresponding author. E-mail: spadua@fcfrp.usp.br

Scanning electron microscopy (SEM) is widely used in plant science to investigate the surface morphology of various plant organs and structure, including plant glands. However, conventional sample preparation protocols often compromise the integrity of delicate secretory regions and frequently result in the loss of exudates during chemical processing. In this study, we present a modified SEM protocol specifically optimized for the study of plant exudates. The protocol is based on passive dehydration with silica gel, followed by controlled acclimation at room temperature, and is designed to preserve natural exudates secreted by plant glands in different organs. Immediately after field collection, fresh samples are stored in hermetically sealed glass containers with silica gel and a paper towel at −18 °C for seven days, followed by ten days at room temperature. This prompt and controlled preservation step is critical for maintaining both the integrity of surface structures and the natural exudates. The method was successfully applied to at least five legume species (*Alexa grandiflora, Camoensia scandens, Dipteryx alata, Myroxylon peruiferum,* and *Pterodon pubescens*), allowing detailed observation of glands and their exudates, composed of oils, resins, nectar, and polysaccharides. These species, all within Fabaceae and chemically diverse in their exudates, served as effective test models. In *Dipteryx alata* and *Pterodon pubescens*, anther glands contained viscous oleoresins and polysaccharides involved in pollen aggregation and adhesion to floral visitors [1] (Fig.1a-c). In *Myroxylon peruiferum*, secretory ducts in sepals, petals, ovary, and anthers released oleoresin droplets that hardened upon air exposure, facilitating a novel form of secondary pollen presentation [2] (Fig. 1d-g). In *Alexa grandiflora*, both nectar and oleoresins were released through modified stomata or large epidermal pores [3] (Fig. 1h-j), while in *Camoensia scandens*, the long hypanthium secreted translucent, viscous nectar through large pores [4] (Fig.1k-n). Structures such as glandular trichomes, papillae, modified stomata, and pores were well preserved without dehydration artifacts. These findings demonstrate the effectiveness of the modified SEM protocol in preserving both the surface morphology and secretory contents of plant glands without chemical fixation. The ability to visualize secretory structures and exudates *in situ*, without morphological distortion, provides valuable insights into plant–pollinator interactions and the spatial distribution, composition, and release mechanisms of floral exudates.

[1] Leite et al., Plant Biol 21: 1016–1023, 2019
[2] Leite et al., J. Plant Res. 138: 469–482, 2025
[3] Silva et al., J. Plant Res. 2025
[4] Leite et al., J. Plant Res. 134: 823–839, 2021
[5] This research was supported by CNPq (process numbers 304029/2023-8 and 304193/2022-4), CAPES (finance code 001) and the FAPERJ (process number E-26/204.177/2021; E-26/201.090/2021)

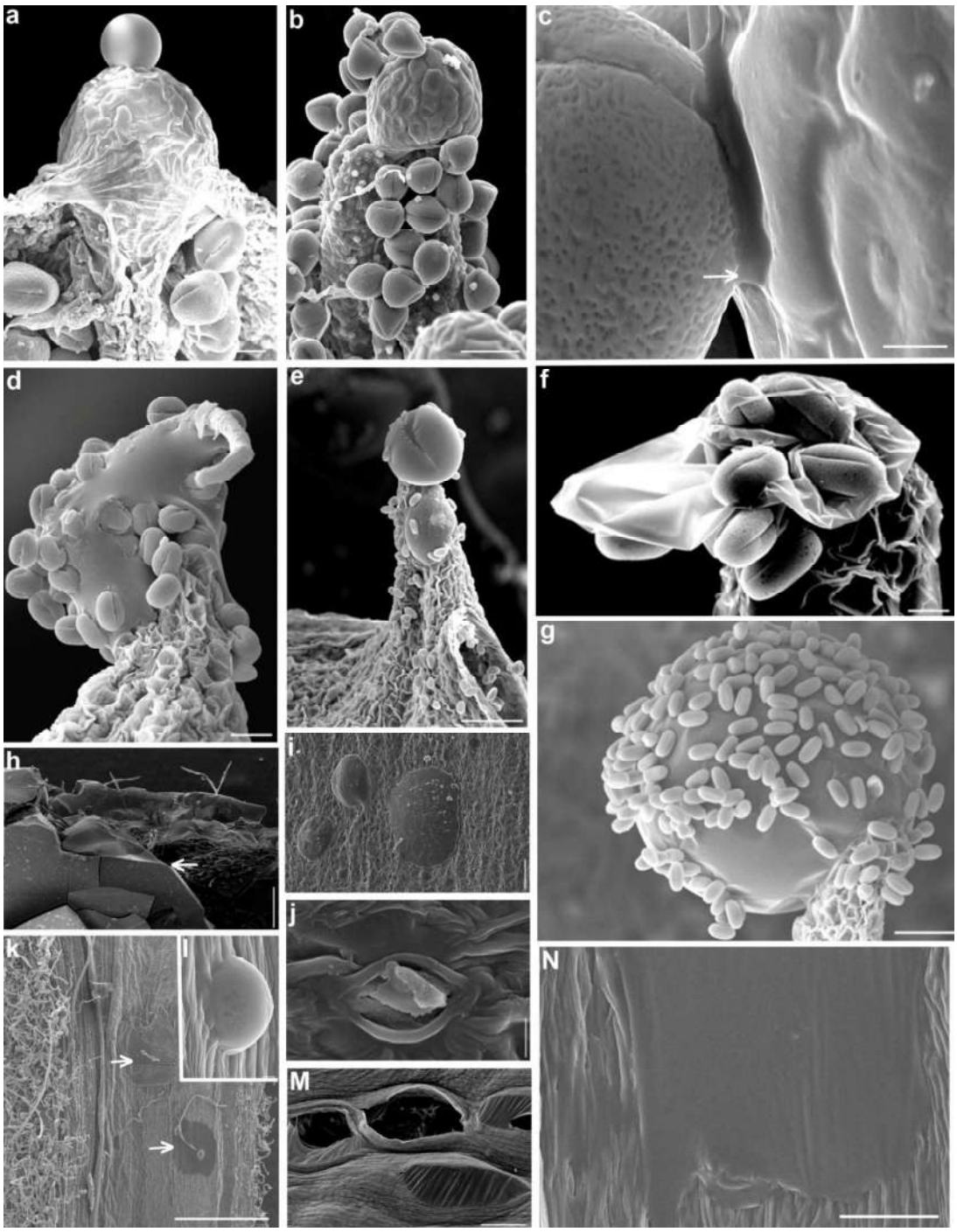

Figure 1. SEM images obtained using the modified protocol, showing floral glands and exudates of *Dipteryx alata* (a), *Pterodon pubescens* (b, c), *Myroxylon peruiferum* (d–g), *Alexa grandiflora* (h–j), and *Camoensia scandens* (k–n). (a–b) Pollen grains adhered to the anther apex by sticky exudates (oleoresins and polysaccharides). (c) Close contact between a pollen grain and the anther gland surface. (d–g) Pollen grains adhered to the anther apex by an oleoresin drop produced by the anther gland. (h) Crystalline deposits and brittle plates of sugar on the sepal surface. (i–j) Sugar plates on petal surfaces (i) and their release through a modified stoma (j). (k–l) Sugar drops (arrow) on the nectary surface. (m) Epidermal pores. (n) Sugar deposits on the nectary surface. Scale bars: a, d, e = 20 μm; b, g, j = 50 μm; c = 5 μm; f, i, l = 10 μm; h = 200 μm; k = 1 mm; m, n = 100 μm.

"In Vivo Evaluation of the Osseointegration of Nanostructured Biomaterials"

Diego Ferreira Regalado[1,2] Camila Wendt[2,3], Kildare Miranda[1,2,], Alexandre Malta Rossi.[3]

[1]CMABIO/UEA Multiuser Center for Analysis of Biomedical Phenomena of the State University of Amazonas, [2] CENABIO/IBCCF/UFRJ The National Center for Structural Biology and Bioimaging, Carlos Chagas Filho Institute of Biophysics, Federal University of Rio de Janeiro, [3] Brazilian Center of Physics Research,. *camilawendt@biof.ufrj.br

Bone tissue regeneration using biomaterials reresents a rapidly developing field in tissue engineering and biomedicine. Osseointegration is the biological process by which an implant—typically made of titanium—forms a direct bond with bone, creating a stable and long-lasting connection [1]. It is a crucial step for ensuring the success of bone implant treatments, allowing the implant to bear load and maintain tissue integrity. Hydroxyapatite graft material is a synthetic substance used in bone regeneration procedures. Hydroxyapatite is a hydrated calcium phosphate compound and is the primary mineral component of human bone and teeth [2]. That similarity to natural bone structure makes hydroxyapatite biocompatible and well-suited for integration with bone tissue [3]. Modifying hydroxyapatite via carbonation and doping with elements such as strontium (Sr) has been explored to enhance its bioactivity, promote bone formation, and modulate material resorption. In this context, detailed physicochemical characterization of these biomaterials is essential for understanding their in vivo performance. In this study, we evaluated carbonate-doped hydroxyapatite microspheres doped with strontium, aiming to investigate their elemental composition, morphology, and fragmentation after implantation in an animal model. Elemental composition of the samples was assessed before and after implantation. Samples included pure carbonated hydroxyapatite and carbonated hydroxyapatite doped with Sr. These samples were implanted into surgically induced n,.,on-critical bone defects in the tibiae of adult rats. After 21 days, the animals were euthanized, and the tibiae containing the implants were harvested, fixed, dehydrated, embedded in Spurr resin. The samples were then sectioned using a diamond saw, polished, metalized, and analyzed by scanning electron microscopy (SEM) coupled with energy-dispersive X-ray spectroscopy (EDS). The results provided morphological and elemental characterization of the nanostructured biomaterial. Microanalysis for the detection of chemical elements revealed the characteristic constituents of the material, including C, O, Ca, P, and in Sr-doped samples, strontium. Other elements such as Si and Al were also observed—likely due to process-related contaminants (Figure 1). The Ca/P ratio was estimated at 1.95, which is higher than the reference range observed in bone tissue (1.7–1.8). Point detection of Sr by EDS served as a marker for dopant incorporation, enabling differentiation between remaining biomaterial and areas of newly formed bone. This combined approach added valuable parameters to the morphological analysis, contributing to the evaluation of material fragmentation, resorption, and osseous integration of the implant. The findings demonstrate that combining SEM with EDS is a powerful multimodal tool for biomaterial characterization, enabling both quantitative and qualitative assessment of composition and interaction with bone tissue.

[1]Brånemark, P. I. Osseointegration and its experimental background. J Prosthet Dent; 1983 Sep;50(3):399-410.
[2] Passi, P. et al Ultrastructural findings on the interface between hydroxylapatite and oral tissues. Quintessence Int. 1991 Mar;22(3):193-7.
[3] Isa Majluf, M. The use of hydroxyapatite in modern dentistry Rev Dent Chile. 1991 Apr;82(1):30-5.

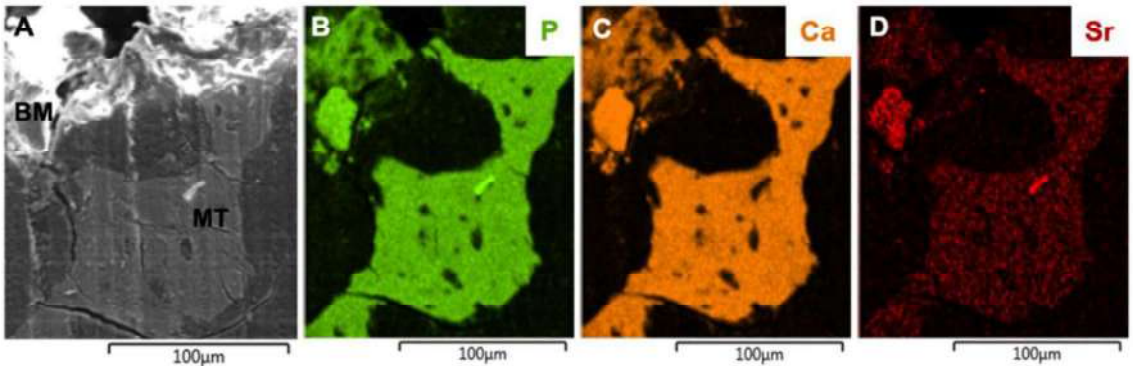

Figure 1. Scanning electron microscopy (SEM) and energy-dispersive X-ray spectroscopy (EDS) elemental mapping of a strontium-doped carbonated hydroxyapatite microsphere after 21 days of implantation in a rat tibia defect. (A) Secondary electron image showing the biomaterial (BM) and surrounding mineralized tissue (MT). (B–D) Elemental maps of phosphorus (P, green), calcium (Ca, orange), and strontium (Sr, red) reveal the distribution of key components within the sample.

Application of SEM-EDS for detecting metallic nanoparticle incorporation in the shell matrix of *Perna perna* due to bioaccumulation.

Luisa Helena Pimenta[1], Thales Augusto Nordi[1], Luis Felipe de Almeida Duarte[2], Camilo Dias Seabra Pereira[2], Iara da Costa Souza[1], Marisa Narciso Fernandes[1]*.

[1] Departamento de Ciências Fisiológicas, Universidade Federal de São Carlos (DCF/UFSCar), Ave. Washington Luiz, Km 235, 13565-905, São Carlos, São Paulo, Brasil,
[2] Departamento de Ciências do Mar, Universidade Federal de São Paulo, Edifício Mariângela Duarte, Rua Silva Jardim, n° 136, 11015-020, Santos, São Paulo, Brasil. *dmnf@ufscar.br

Metallurgical industries are among the main sources of atmospheric particulate matter (PM) emissions in coastal areas [1]. Previous studies have shown that settleable particulate matter (SePM) composed of metallic nanoparticle (MNP) components with an ideal aerodynamic diameter has a high potential for deposition in shell layers (SePM > 10 μm) [2, 3]. To demonstrate this contamination, the mussel species *P. perna*, a bioindicator species, had its biomineral matrix exposed to four different treatments (0, 0.01, 0.1 and 0.1 g/L) for 30 days. This was followed by a 30-day depuration phase to demonstrate the shell's capacity to absorb the MNPs present in SePM [4]. After the exposure phase, shell fragments were extracted, placed on aluminum stubs and fixed with carbon tape. The samples were then stored in Petri dishes (n = 7 samples per plate). The samples were analyzed using a scanning electron microscope (SEM) equipped with an energy dispersive X-ray spectroscopy system and an electron backscatter diffraction system (EDS-EBSD). Microanalyses of the biomineral matrix were then performed to detect metals within the shell layers. SEM measurements revealed that Bi-NP, Ba-NP and Al-NP were incorporated into the matrix samples within the calcite crystals [5]. The biomineral matrix, which is mainly composed of calcium carbonate and is rich in Ca^{2+} ions, suggests partial ionic substitution for Ba^{2+} [5]. Additionally, previous studies suggest that the integration of Bi into calcium-based matrices may occur due to its retention via surface adsorption during shell formation [6]. This process is therefore likely facilitated by their similar ionic charges, allowing incorporation through direct structural substitution or charge-compensated occupancy of structural vacancies [6, 7]. In summary, the results suggest that there is a high potential for metals to bioaccumulate within the biomineral matrix of the species. This was evidenced by SEM analysis, which showed that the metals were intrinsically associated with the shell layers.

[1] I.C. Souza et al. *Metallic nanoparticle contamination from environmental atmospheric particulate matter in the last slab of the trophic chain: Nanocrystallography, subcellular localization and toxicity effects.* Sci. Total Environ. 814:152685–5 (2021).
[2] F. L. A. Duarte et al. *Settleable atmospheric particulate matter harms a marine invertebrate: Integrating chemical and biological damage in a bivalve model.* Sci. Total Environ. 881:163380–0 (2023).
[3] E. S. Galvão et al. *Trends in analytical techniques applied to particulate matter characterization: A critical review of fundaments and applications.* Chemosphere. 199:546–68 (2018).
[4] I.C. Souza et al. *Integrating chemical and biological data by chemometrics to evaluate detoxification responses of a neotropical bivalve to metal and metalloid contamination*. Chemosphere 340:139730–0 (2023).
[5] R. N. Ulrich et al. *Patterns of Element Incorporation in Calcium Carbonate Biominerals Recapitulate Phylogeny for a Diverse Range of Marine Calcifiers*. Front. Earth Sci. 9:641760 (2019).
[6] Y. Shen et al. *Facile synthesis of in situ bismuth-doped calcium phosphate nanocomposite integrated injectable biopolymer hydrogel slurry for bone regeneration*. J Colloid Interface Sci.679:760–71 (2025).

[7] S. M. Paula et al. *Studies on molluscan shells: Contributions from microscopic and analytical methods*. Micron 40:669–90 (2009).
[8] This research was supported by Fundação de Amparo à Pesquisa do Estado de São Paulo (FAPESP) (Brazil) (Proc. 2019/08491-0, 2024/13340-9).

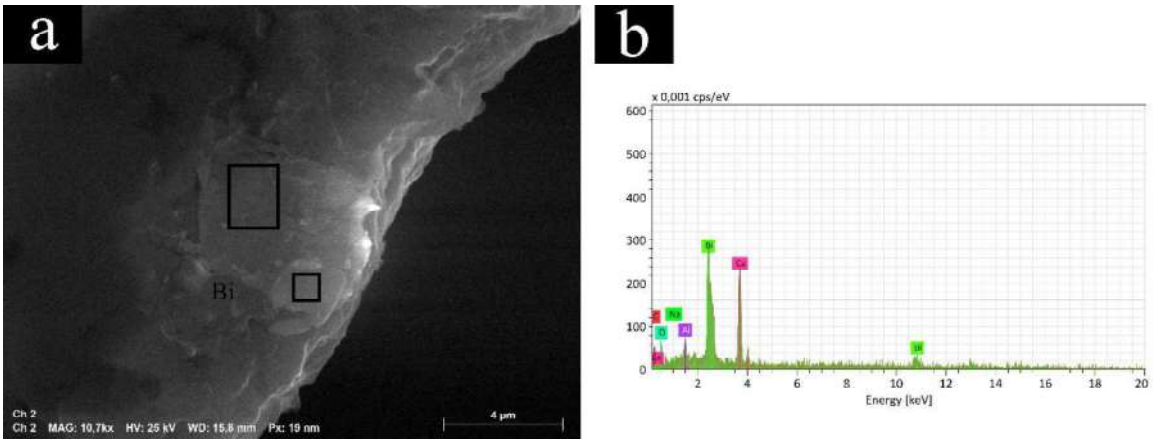

Figure 1. Scanning Electron Microscopy (SEM) of *P. perna* shell after exposure to SePM. (a) Micrograph showing a Bi nanoparticle after exposure to 0.01 $g \cdot L^{-1}$ of SePM. (b) Energy dispersive X-ray spectroscopy (EDS) spectrum indicating the presence of Bi, Al, Ca, C, O, and Na.

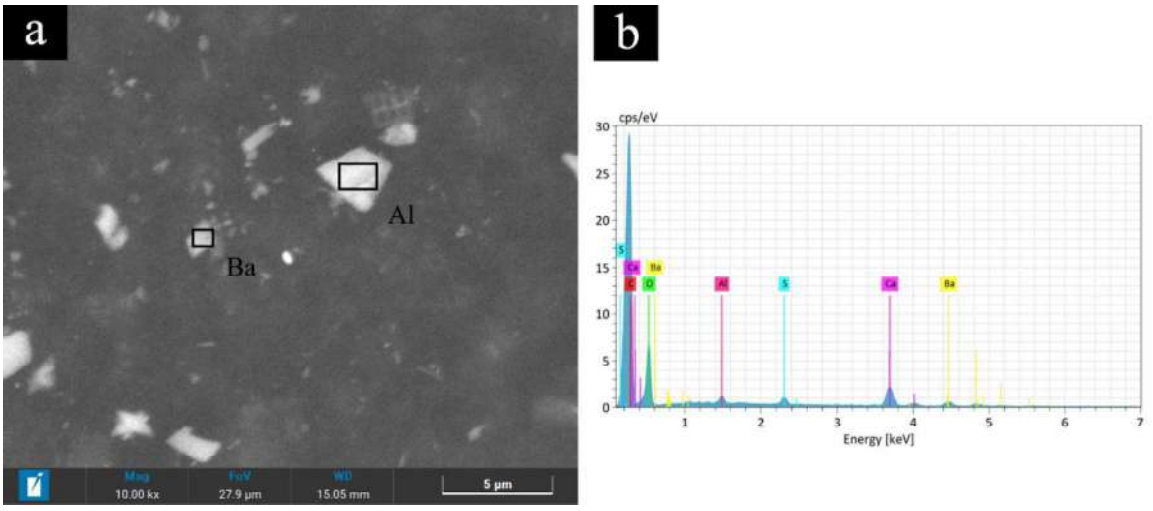

Figure 2. Scanning Electron Microscopy (SEM) of *P. perna* shell after exposure to SePM. (a) SEM image of Ba and Al nanoparticles after exposure to 0.1 $g \cdot L^{-1}$ of SePM. (b) EDS spectrum indicating the presence of Ba, Al, Ca, S, C, and O.

Application of SEM/EDS in the Assessment of Heavy Metals in Marine Cyanobacteria

Márcio Ferreira dos Santos[1*], Helen Michelle de Jesus Affe[2] & Taiara Aguiar Caires[3]

[1]Instituto Gonçalo Moniz, Fiocruz Bahia; [2]Universidade do Estado do Rio de Janeiro;
[3]Universidade Estadual do Sudoeste da Bahia.
*marciodossantos@fiocruz.br

The discharge of domestic and industrial effluents, mining, agriculture, and port activities leads to the organic enrichment of coastal environments and the introduction of various chemical substances, including heavy metals, which are considered highly toxic, non-biodegradable, and capable of significant bioaccumulation in the trophic chain [1–4]. The presence of these pollutants is associated with biodiversity reduction, favoring more resistant species while eliminating sensitive organisms [5]. This study aimed to analyze the chemical composition of the biomass of benthic filamentous cyanobacteria present in two coastal environments with different levels of anthropogenic impact on the coast of Bahia, Brazil: Sítio do Conde Beach, located on the northern coast of Bahia and characterized by lower anthropogenic influence, and Tubarão Beach, located in the Metropolitan Region of Salvador, which is characterized by a higher degree of urbanization and anthropization. Samples were analyzed using optical and electron microscopy for taxonomic identification, and energy-dispersive X-ray spectroscopy (EDS) for heavy metal detection. Morphological analysis revealed 14 cyanobacterial species at Sítio do Conde Beach and only four species at Tubarão Beach, indicating greater species diversity in less impacted environments. In total, 14 distinct heavy metals were detected across both sites. At Tubarão Beach, all of them were identified (As, Ba, Br, Cd, Co, Cr, Cu, Fe, Hg, Mo, Ni, Se, Ti, Zn). In contrast, at Sítio do Conde Beach, only four heavy metals were found (As, Fe, Mo, Ti). Images obtained from EDS coupled with scanning electron microscopy (SEM) Figure 1, and transmission electron microscopy (TEM) Figure 2, evidenced the accumulation of heavy metals in the trichomes of cyanobacteria, confirming their capacity to absorb and concentrate these metals. These findings indicate that the presence of heavy metals acts as an ecological selective factor, shaping the structure of cyanobacterial communities and reducing their diversity in more contaminated environments. Therefore, the data obtained in this study reinforce the potential of benthic cyanobacteria as bioindicators of heavy metal contamination in coastal areas. Their application in environmental monitoring programs can contribute to assessing environmental quality and supporting public policies aimed at pollution mitigation, especially in urbanized areas such as Tubarão Beach.

[1] E.L. Johnston et al., Contaminants reduce the richness and evenness of marine communities: A review and meta-analysis, Environmental Pollution 157 (2009).
[2] H.E.K. El Bahgy et al., Heavy metals bioaccumulation in marine cultured fish and its probabilistic health hazard, Environmental Science and Pollution Research 28 (2021).
[3] S. Meng et al., Interactions between heavy metals and bacteria in mangroves, Marine Pollution Bulletin 172 (2021).
[4] M. Abdou et al., New insights into trace metal speciation and interaction with phytoplankton in estuarine coastal waters, Marine Pollution Bulletin 181 (2022).
[5] H. K. Lotze, et al., Depletion, Degradation, and Recovery Potential of Estuaries and Coastal Seas, Science 312 (2006).

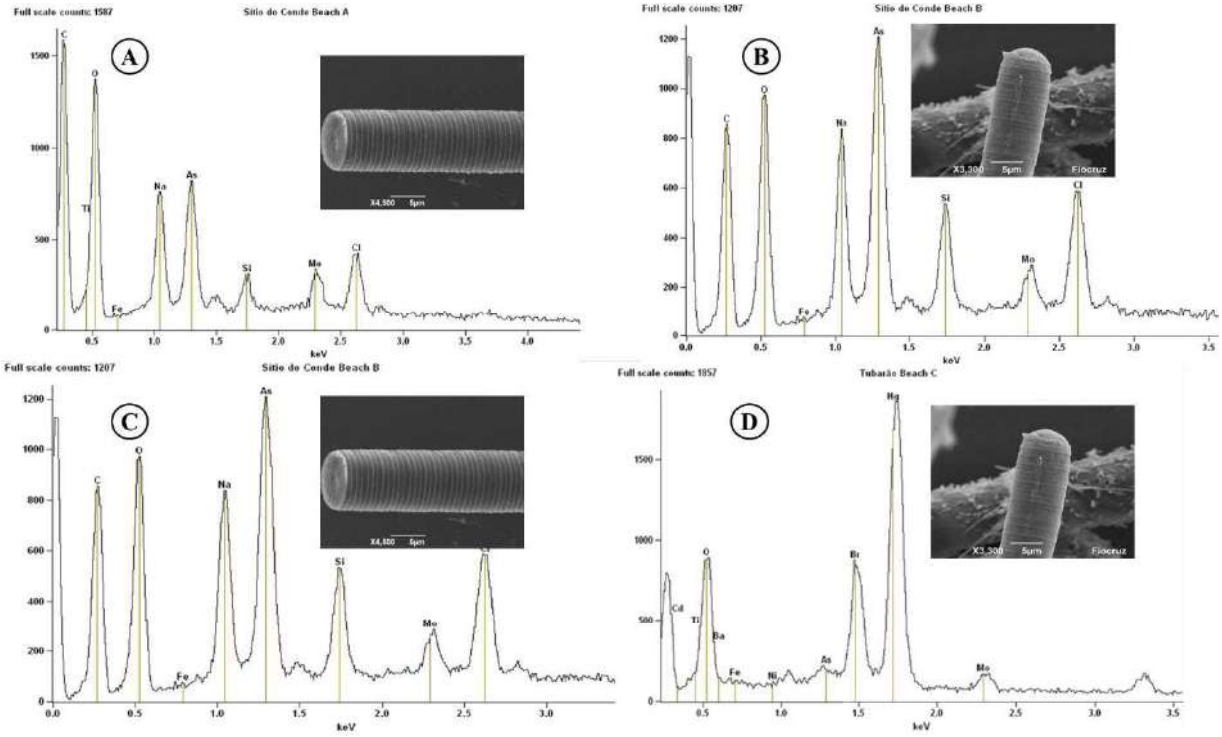

Fig. 1. Scanning Electron Microscopy coupled with Energy Dispersive Spectroscopy (SEM/EDS) microanalysis of samples from Sítio do Conde Beach (A, B) and Tubarão Beach (C, D) samples. (A) *Lyngbya aestuarii* **containing As, Fe, Mo, Ti ; (B)** *Lyngbya confervoides* **containing As, Fe, Mo, Ti; (C)** *Lyngbya aestuarii* **with As, Ba, Br, Cd, Fe, Hg, Ni, Mo, Ti)**; **(D)** *Lyngbya confervoides* **with As, Ba, Br, Cd, Fe, Hg, Ni, Mo, Ti.**

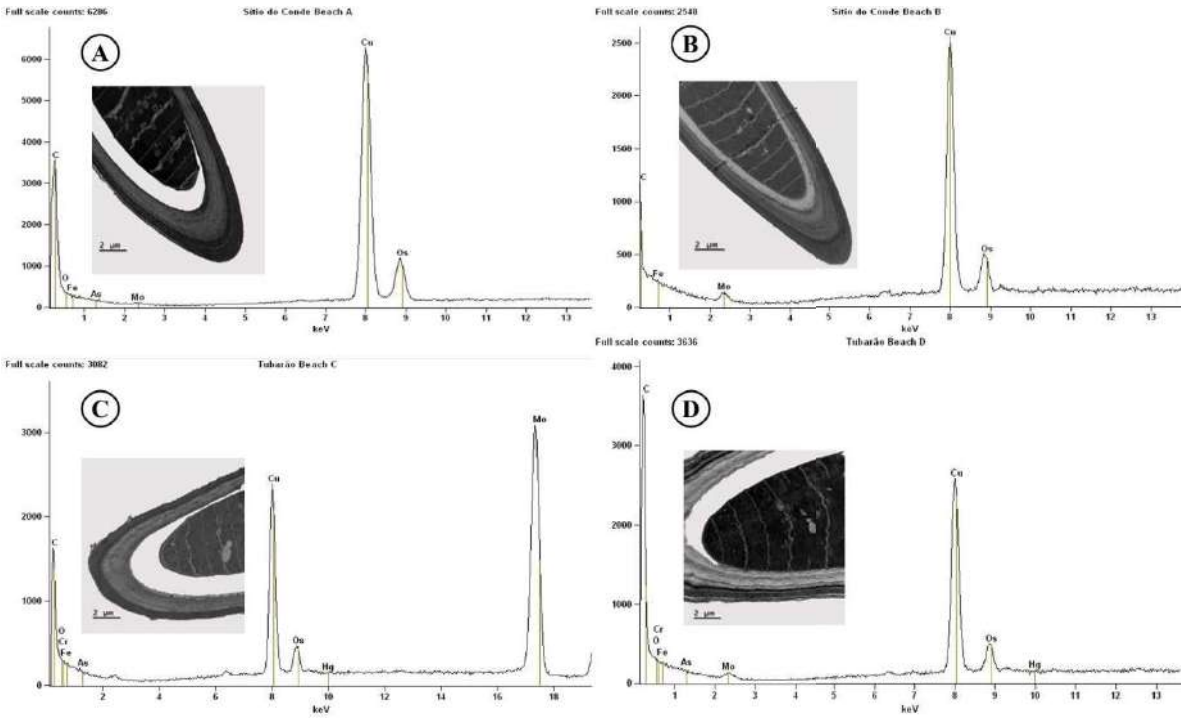

Fig.2. Transmission Electron Microscopy coupled with Energy Dispersive Spectroscopy (TEM/EDS) microanalysis of samples from Sítio do Conde Beach (A, B) and Tubarão Beach (C, D) samples. (A) *Lyngbya aestuarii* **containing As, Fe, Mo; (B)** *Lyngbya confervoides* **containing As, Fe, Mo; (C)** *Lyngbya aestuarii* **with As, Ba, Br, Cd, Fe, Hg, Ni, Mo, Ti; (D)** *Lyngbya confervoides* **with As, Fe, Cr, Hg, Mo. Os and Cu metals originated from grid preparation.**

Calcium Hydroxyapatite Nanoparticles Functionalized with Luteolin: A Microstructural Approach for Cutaneous Biostimulation

Paulo Vitor Farago[1]*, Amanda Jansen[1], Guilherme dos Anjos Camargo[2], Jessica Mendes Nadal[1], Andressa Novatski[1]

[1]State University of Ponta Grossa, [2]Federal University of Paraná
*pvfarago@uepg.br

Skin aging is a complex biological process influenced by intrinsic factors, such as genetics and hormonal regulation, and extrinsic factors, including UV radiation, pollution, and lifestyle. These processes lead to oxidative stress, reduction in collagen synthesis, degradation of the extracellular matrix, and progressive structural deterioration of the skin [1]. One promising approach to mitigate these effects involves the use of bioactive dermal biostimulators capable of promoting neocollagenesis. Calcium hydroxyapatite (HAp) is a synthetic, biocompatible material widely used in facial aesthetics due to its ability to stimulate fibroblast activity and collagen production. Luteolin (LUT), a naturally occurring flavonoid, exhibits potent antioxidant and anti-inflammatory properties and can neutralize reactive oxygen species by reducing oxidative damage and contributing to skin homeostasis [2]. This study aimed to develop and characterize calcium hydroxyapatite nanoparticles (n-HAp) functionalized with luteolin for potential application in dermal biostimulation. The n-HAp was synthesized by precipitation using a stoichiometric Ca/P molar ratio of 1.67, followed by lyophilization. Moisture content was determined (mean 10.47%) to adjust the incorporation of LUT at concentrations of 1, 10, and 20% (w/w). The composites (Table 1) were homogenized using a SpeedMixer and dried at 35 °C for 48 hours. Morphological characterization by field emission gun scanning electron microscopy (FEG-SEM) revealed irregular agglomerates with increased surface roughness and heterogeneity in LUT-containing composites (Figure 1). X-ray powder diffraction analysis indicated that the HAp maintained its crystalline structure, while the LUT diffraction peaks decreased in the composites, suggesting partial amorphization [3]. This transformation may improve aqueous solubility and enhance the release of luteolin. The microstructural and physicochemical data confirmed the successful formation of a hybrid system with potential dual action: mechanical stimulation of fibroblasts and biochemical protection against oxidative stress. These findings support further investigation of HAp-LUT composites for advanced anti-aging strategies in dermatological and biotechnological applications. This research was supported by CNPq (Brazil) [4] and CAPES (Brazil).

[1] Smith, C.D. et al., PRS Global Open 12 (2024) e4689.
[2] Rocchetti, M.T. et al., Int. J. Mol. Sci. 24 (2023) 8824.
[3] Nadal, J.M. et al., Drug Dev. Ind. Pharm. 42 (2016) 1963.
[4] This research was supported by CNPq (Brazil), grant number 310806/2025-9.

Table 1. Composition of HAp-LUT formulations with mass corrected according to the moisture content present in the n-HAp (10.47%)

Formulation	HAp (%)	LUT (%)	HAp (mg)	LUT (mg)
L0	100	0	111.69	–
L1	99	1	110.57	3.33
L2	90	10	100.52	33.3
L3	80	20	89.35	66.6

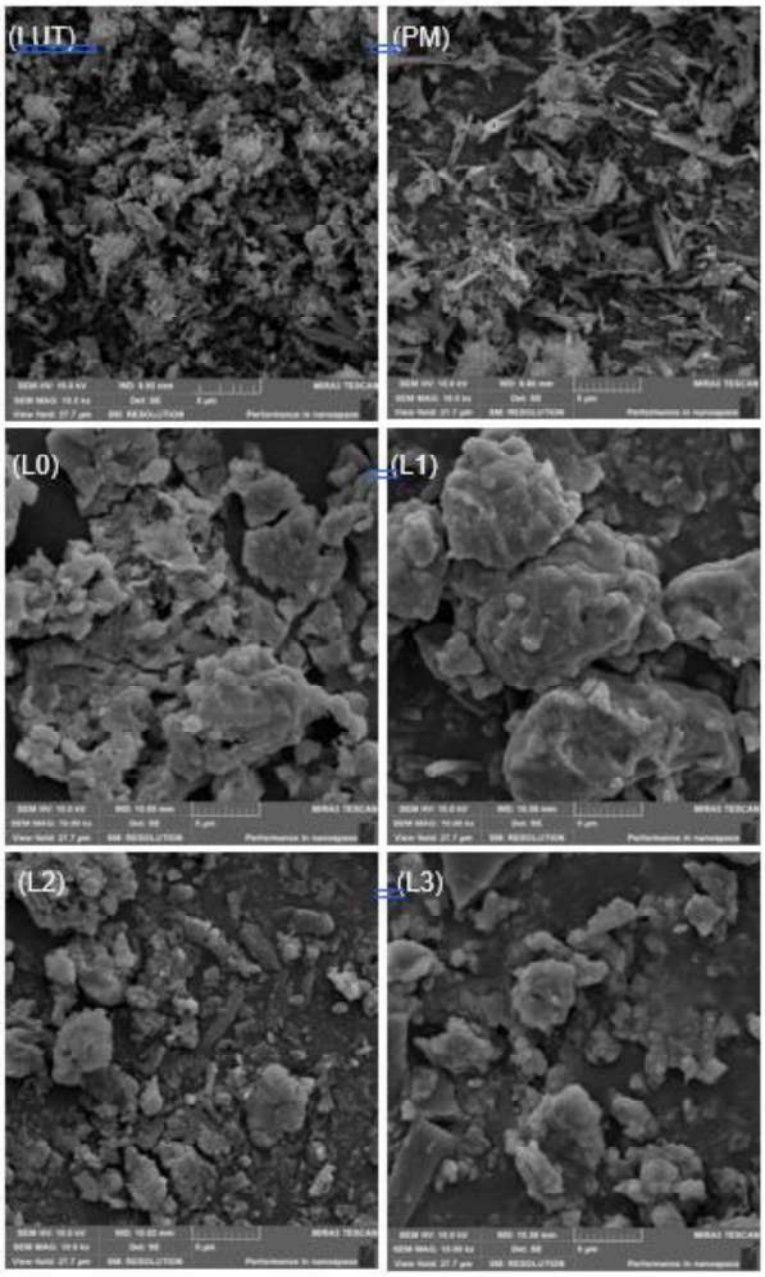

Figure 1. FEG-SEM micrographs of the obtained formulations. LUT: luteolin; PM: physical mixture (calcium hydroxyapatite+luteolin); L0; L1; L2; and L3

Characterization of Zinc Oxide Nanoparticles Functionalized for Biomedical Applications

José Vinícius Melo da Silva[1,2]*, Davi Porfirio da Silva[1,2,3], Fabianny Torres de Oliveira[1,2], Anielle Christine Almeida Silva[1]

[1] Strategic Materials Laboratory, Institute of Physics, Federal University of Alagoas, Maceió, Alagoas, Brazil
[2] Wound Treatment Research Laboratory, School of Nursing, Federal University of Alagoas, Maceió, Alagoas, Brazil
[3] Faculty of Medicine, Federal University of Alagoas, Maceió, Alagoas, Brazil
*E-mail: jose.melo@eenf.ufal.br

Nanotechnology has become a key driver of innovation across numerous scientific and industrial fields, enabling the manipulation of matter at the atomic and molecular levels to create materials and devices with novel properties [1]. Zinc oxide nanoparticles (ZnO NPs) have gained significant attention in the biomedical field due to their unique physicochemical properties. These include high chemical stability, photostability, strong antimicrobial activity, and biocompatibility [2-3]. Additionally, their high surface can be easily modified to improve targeting and interaction with biological systems, further enhancing their potential biomedical applications [3-4]. This study reports the synthesis-and characterization of ZnO nanoparticles functionalized with *Syzygium cumini* (L.) Skeels leaves extracts and evaluates their potential as antimicrobial agents. To this end, the synthesis of these nanoparticles was conducted using a method currently under patent application (BR10201800771) [5], and subsequently functionalized with aqueous and ethanolic extracts of *Syzygium cumini* (L.) Skeels leaves. The characterization techniques of Scanning Electron Microscopy (SEM), Energy Dispersive X-ray Spectroscopy (EDS) and Fourier Transform Infrared Spectroscopy (FTIR) were conducted to analyze the physicochemical and morphological properties of nanoparticles. The antimicrobial efficacy was evaluated against *Staphylococcus aureus* (ATCC 25923) using disk diffusion, minimum inhibitory concentration (MIC), and minimum bactericidal concentration (MBC) assays. From the results, the MEV images showed a uniform, monodispersive pattern (Fig. 1), while EDS confirmed the presence of the element Zn (Fig. 2). Additionally, FTIR analysis confirmed the functionality of ZnO nanoparticles through the formation of complexes between ZnO and functional groups present in the extracts (Fig. 3). The functionalized ZnO NPs exhibited significant antimicrobial effects, indicating their potential as effective antimicrobial agents. Further studies are necessary to evaluate their biocompatibility, safety, and therapeutic effectiveness in living systems. The proposed approach of functionalized ZnO NPs presents a promising alternative to conventional antibiotics, offering potential in overcoming bacterial resistance challenges in future biomedical applications.

References:

[1] Modi S, Prajapati R, Inwati GK, Deepa N, Tirth V, Yadav VK, Yadav KK, Islam S, Gupta P, Kim D-H, et al. Recent Trends in Fascinating Applications of Nanotechnology in Allied Health Sciences. Crystals. 2022; 12(1):39.
[2] Lebaka VR, Ravi P, Reddy MC, Thummala C, Mandal TK. Zinc Oxide Nanoparticles in Modern Science and Technology: Multifunctional Roles in Healthcare, Environmental Remediation, and Industry. Nanomaterials. 2025; 15(10):754.
[3] Faisal S, Jan H, Shah SA, et al. Green Synthesis of Zinc Oxide (ZnO) Nanoparticles Using Aqueous Fruit Extracts of Myristica fragrans: Their Characterizations and Biological and Environmental Applications. ACS Omega. 2021;6(14):9709-9722.
[4] Kumari N, Kumar M, Chaudhary N, et al. Exploring the Chemical and Biological Potential of Jamun (Syzygium cumini (L.) Skeels) Leaves: A Comprehensive Review.

Chem Biodivers. 2023;20(9):e202300479.
[5] Silva ACA et al., inventors; Instituto Nacional da Propriedade Industrial, assignee. Processo de fabricação de nanocristais de óxido de zinco puros e dopados com prata ou cálcio, nanocristais e aplicações. Brazil patent BR 10201800771. 2018, Sep 14.
[6] This research was supported by FAPEAL, CNPq and CAPES.

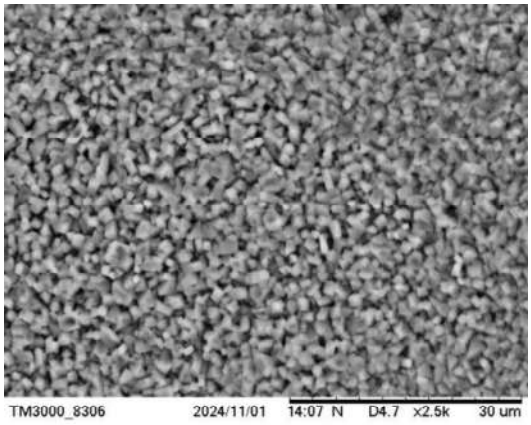

Figure 1. SEM (scanning electron microscope) image of the ZnONPs.

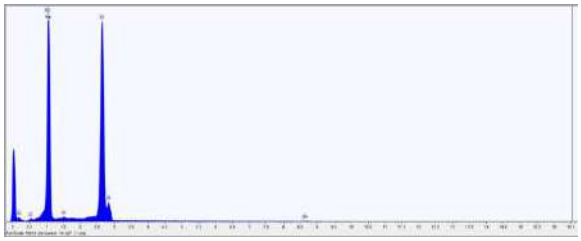

Figura 2. ZnONPs EDS (energy dispersive X-ray spectroscopy).

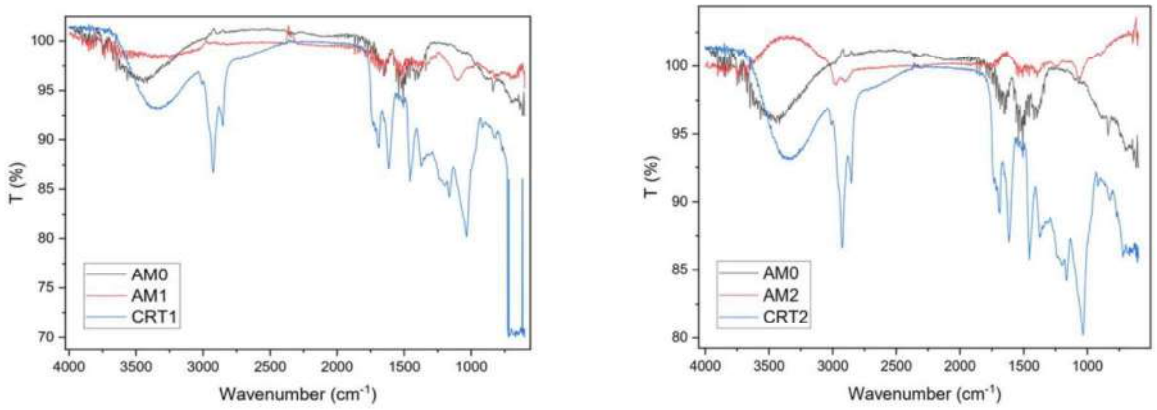

Figura 3. Functionalized ZnONPs FTIR (Fourier transmission infrared spectroscopy).

Decellularized Plant Scaffold: A Sustainable Approach to 3D Cell Culture

Daniela Carolina Almeida dos Santos[1,2*], Rebecca Thereza Silva Santa Brígida[1,2], Arthur Gonçalves Garcia[1,3], Adeniele Lopes da Cruz Carneiro[1,2], Jackeline Figueira da Silva[1], Ana Paula Drummond Rodrigues[1].

[1] Multiuser Laboratory of Cell Biology and Ultrastructure, Evandro Chagas Institute, [2] Postgraduate Program in Biology of Infectious and Parasitic Agents, Federal University of Pará, [3] University of State of Pará.
[*]dancrlina@gmail.com

In vitro cell culture has been widely used to understand the mechanisms underlying cellular behavior *in vivo*, including cell differentiation, migration, growth, and mechanical responses. Traditionally, two-dimensional (2D) systems have been used in this context, but they have some significant limitations, including a uniform distribution of nutrients and stimuli, in addition to restricted interactions between cells and the extracellular matrix (ECM) [1,2]. To overcome these limitations, three-dimensional (3D) cell culture models have been emerging as sophisticated platforms that mimic the structural and functional complexities of *in vivo* tissues. 3D cell culture has several applications in different areas, such as oncology research, stem cell studies, drug development, and investigations related to degenerative and infectious diseases. Numerous techniques can be used to establish three-dimensional (3D) cell cultures, such as the use of hydrogel-based supports, rigid polymeric materials, hydrophilic glass fibers, magnetic levitation, and spheroids grown on surfaces with ultra-low adhesion coatings [3], among others. The use of scaffolds, which act as three-dimensional support structures, providing a suitable matrix for cell adhesion, proliferation, and differentiation, is widely used. In this context, decellularized scaffolds stand out, obtained by removing cellular components from tissues or organs, preserving the native ECM structure [4,5]. Recently, tissues of plant origin have evoked great interest as an alternative to animal sources in the production of decellularized scaffolds, especially for tissue engineering applications. Because they present a highly organized ECM, in addition to a vascularized and naturally interconnected structure, decellularized plants can function as promising perfusion platforms in graft bioengineering. Furthermore, these plant-based scaffolds have been gaining prominence in biomedical applications due to their low production cost, scalability and lower immunogenicity compared to animal sources [6]. In this study, our objective was to develop a scaffold for 3D cell culture from an Amazonian plant. For this purpose, small fragments of a typical leaf from the region were subjected to the decellularization process using detergent. After removal of the cellular components, the plant matrix was cultured with human fibroblasts (HFF-1). Cell viability in this model was evaluated through the MTT assay and ultrastructural analysis through the Scanning Electron Microscope (SEM). SEM analyses demonstrated that, even after the decellularization process, the natural architecture of the plant was preserved, evidencing the effectiveness of the applied protocol. It was also observed that the fibroblasts were able to adhere to the surface of the decellularized scaffold, as indicated by the presence of typical cell adhesion structures (Figure 1-white arrows), which suggests good cell-matrix interaction. The biocompatibility of the model was confirmed by the MTT assay, where no reduction in cell viability occurred. In summary, this study validates the use of scaffolds derived from Amazonian plants as an efficient and biocompatible platform for three-dimensional cell culture, enabling future investigations in tissue regeneration and engineering of complex biological structures.

[1] K. Duval, H. Grover, L.H. Han, Y. Mou, A.F. Pegoraro, J. Fredberg, et al., Physiology 32 (2017) 266–277.
[2] W.H. Abuwatfa, W.G. Pitt, G.A. Husseini, J. Biomed. Sci. 31 (2024).
[3] C. Jensen, Y. Teng, Front. Mol. Biosci. 7 (2020).

[4] R.J. Hickey, D.J. Modulevsky, C.M. Cuerrier, A.E. Pelling, ACS Biomater. Sci. Eng. 4 (11) (2018) 3726–3736.
[5] C. Berry-Kilgour, I. Oey, J. Cabral, G. Dowd, L. Wise, J. Funct. Biomater. 15 (12) (2024).
[6] L.J. Couvrette, K.L.A. Walker, T.V. Bui, A.E. Pelling, Bioengineering 10 (11) (2023).
[7] This research was supported by Evandro Chagas Institute – Ministry of Health, Health Surveillance Secretariat; Emílio Goeldi Museum of Pará; Federal University of Pará (UFPA); Coordination for the Improvement of Higher Education Personnel (CAPES)

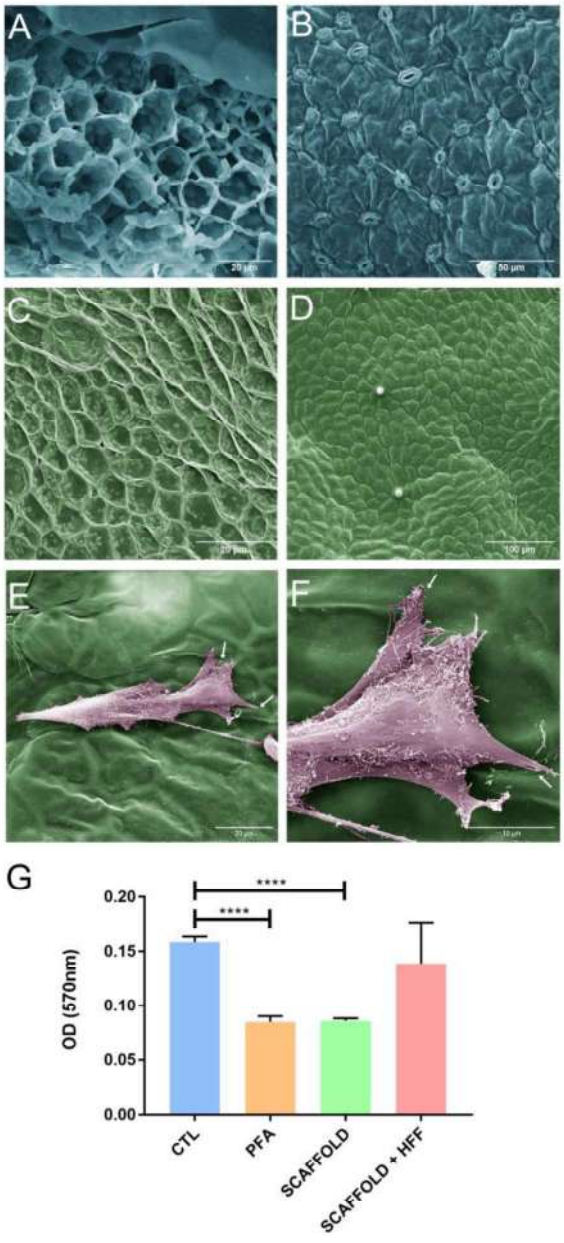

Figure 1: Analysis of natural, decellularized and recellularized leaves with human fibroblasts (HFF-1). (A–B) Images of the natural leaf obtained by Scanning Electron Microscopy (SEM), evidencing its original architecture (scale bar: 20µm and 50µm, respectively. (C–D) Leaf after the decellularization process, demonstrating the preservation of the three-dimensional structure of the matrix (scale bar: 20µm and 50µm, respectively). (E–F) Leaf recellularized with human fibroblasts (HFF-1), indicating cell-matrix adhesion and interaction (scale bar: 10µm and 20µm, respectively). (G) Evaluation of cell viability by MTT assay, comparing the different experimental groups. The optical density (OD) was measured at 570 nm.

Development and Characterization of Buriti Oil Microparticles (*Mauritia flexuosa*) Obtained by Complex Coacervation

Leonardo Correa Gomes da Silva[1]; Janaína Teles de Faria[1]; Andréia Luiza Oliveira Costa[2]; André Luiz Sena Guimarães[2]; William James Nogueira Lima[1*]

[1] Instituto de Ciências Agrárias (ICA), Universidade Federal de Minas Gerais (UFMG), Campus Montes Claros, Minas Gerais, 39404-547, Brazil
[2] Laboratório de Microscopia Avançada (LMA), Instituto de Pesquisa em Saúde (IPS), Universidade Estadual de Montes Claros, Montes Claros, Minas Gerais, 39401-089, Brazil
[*]Corresponding author, Email: william@ica.ufmg.br

The growing demand for healthy, high-quality foods has led to the exploration of products that meet nutritional needs and provide additional health benefits [1]. Functional foods with bioactive compounds have emerged as a key development [2,3]. Food fortification, initially a public health strategy, is now widely used to serve consumers seeking healthier diets. Among the main technologies, encapsulation stands out, allowing the protection and controlled release of bioactive compounds. The choice of encapsulating material is essential, requiring flexibility, rigidity, low reactivity, and film-forming ability at low cost. Natural polymers like gums and gelatin are often used due to their availability and technological properties. Natural hydrocolloids from plants, algae, animals, and microorganisms act as emulsifiers, thickeners, and controlled release agents. Microencapsulation of bioactive compounds from vegetables, marine sources, and essential oils has been widely studied to protect them from chemical reactions and improve storage stability. Techniques include emulsification, spray-drying, freeze-drying, and complex coacervation, the latter being widely applied for lipophilic compounds. This process also enables controlled release and masking of undesirable flavors, meeting the demands of food, pharmaceutical, and cosmetic industries [1, 2, 3]. The present study aimed to develop and characterize microencapsulated buriti oil (*Mauritia flexuosa*) using complex coacervation and evaluate the influence of formulation and encapsulating materials on yield and efficiency. Six formulations were produced with gum arabic and gelatin. The highest yield reached 87.60% (treatment 2) and the highest encapsulation efficiency 89.50% (treatment 4). The best-performing microcapsules underwent characterization for particle size, morphology via SEM, moisture, color, hygroscopicity, solubility, apparent density, and water activity. SEM revealed particles smaller than 89 µm with irregular shapes. Carotenoid content and antioxidant activity were also evaluated, revealing 28.26 mg/mL of carotenoids in the encapsulated oil. The results demonstrated the efficacy of complex coacervation for buriti oil microencapsulation, showing high encapsulation efficiency, good yield, and suitable particle size, confirming the potential of the technique. Vitamin A and its precursor β-carotene are often targeted by microencapsulation for their biological importance and vulnerability to degradation. Vitamin A deficiency is a public health issue affecting low-income populations, especially children and pregnant women. Microencapsulation helps preserve vitamin A stability and improve bioavailability in functional foods. Buriti stands out for its high carotenoid content and antioxidant properties. Despite buriti oil's potential in the food industry, its sensitivity limits commercial application. The present study explored buriti oil microencapsulation by complex coacervation with gum arabic and gelatin, aiming to expand its technological and nutritional application in food matrices.
Keywords: Microencapsulation. *Mauritia flexuosa.* Complex Coacervation.

[1] P. Thorakkattu et al., Crit. Rev. Biotechnol. 45 (1) (2025) 48–68.
[2] A. Al-Hamayda et al., Ind. Crops Prod. 205 (2023) 117556.
[3] T.G. do Nascimento et al., J. Therm. Anal. Calorim. 138 (2019) 3559–3569.
[4] This research was supported by CAPES (Brazil).

Table 1. Microparticle production tests.

Experimental Tests	Gelatin Type A (g)	Gum Arabic (g)	Óleo de buriti
Assay 1	2.5	2.5	1.875 (75%)
Assay 2	2.5	2.5	1.250 (50%)
Assay 3	2.5	2.5	0.625 (25%)
Assay 4	5.0	5.0	3.750 (75%)
Assay 5	5.0	5.0	2.500 (50%)
Assay 6	5.0	5.0	1.250 (50%)

Source: Author's, 2025.

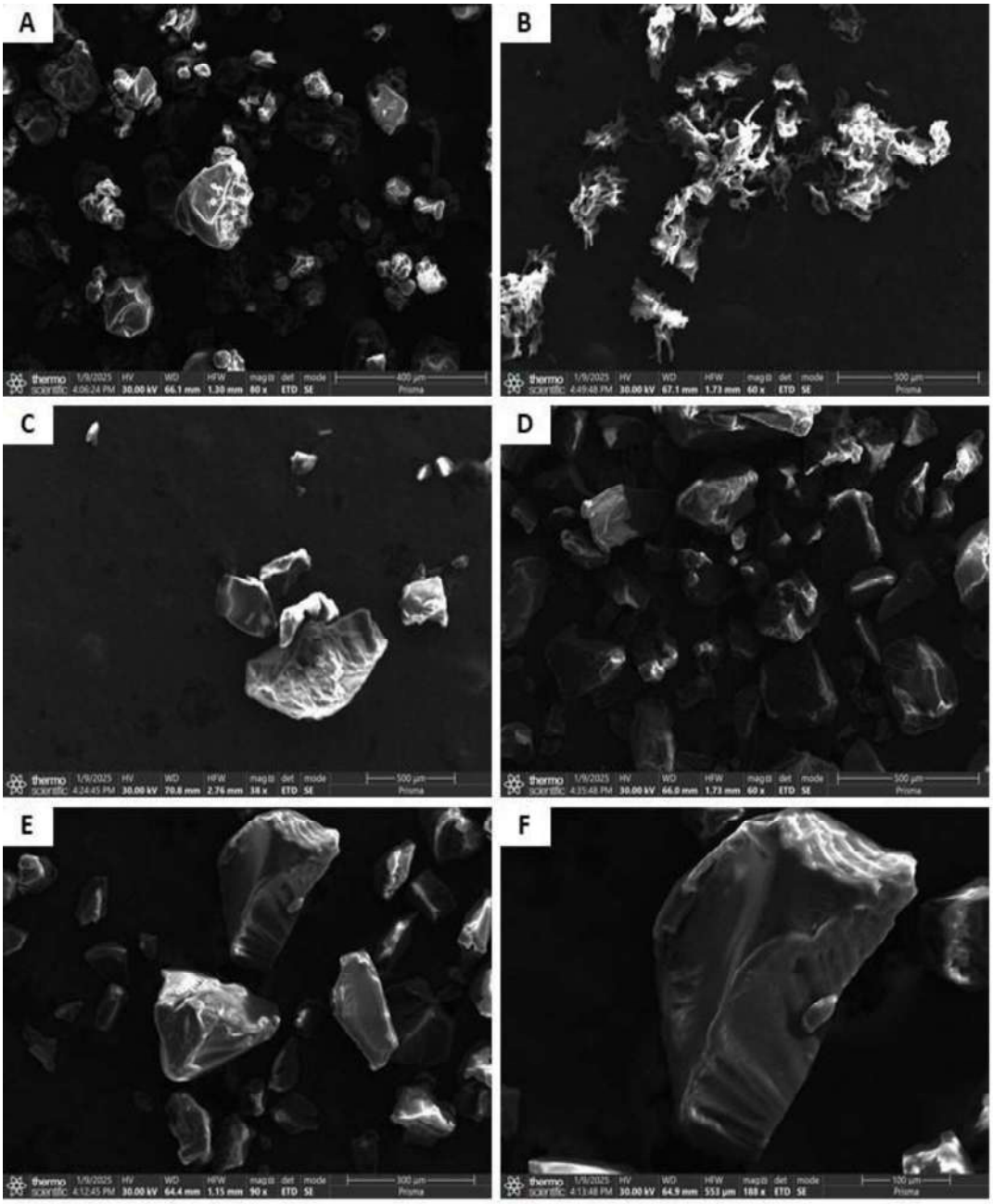

Figure 1. Analysis of buriti oil microcapsules by Scanning Electron Microscopy (SEM). (A) Gelatin type A. **(B)** Gum arabic. **(C-F)** Buriti oil microcapsules, with magnifications of 38x, 60x, 90x and 188x, using spot size of 4.0 and 30 kV, and detection by ETD (electron emission detector). Source: Author's, 2025.

Development, Physicochemical and Morphological Characterization by Scanning Electron Microscopy of Alginate-Based Microspheres Containing Red Propolis and Metallic Nanoparticles via Ionic Gelation for Nutraceutical Applications

Jéssica Maria Pereira[1]*, Lívia Maria Santos de Lima[1], Kathleen Gomes Lins Silva[1], Melissa Rosa Silva[1], Ilza Fernanda Barboza Duarte Rodrigues[1], Orlando F. S. Moura[2], Jeniffer Mclaine Duarte de Freitas[2], Johnnatan Duarte de Freitas[2], Irinaldo Diniz Basílio Júnior[1], Anielle Christine Almeida Silva[1].

[1]Universidade Federal de Alagoas, [2]Instituto Federal de Alagoas.
*jessica.mariapereira.12@gmail.com

Encapsulation methods for bioactive compounds are being commonly used due to their ease in applying substances with bioavailability problems, in addition to promoting improvements in the processing and dispersion capacity of different materials [1]. Therefore, microencapsulation is seen as an alternative to increase stability during processing and biotechnological and, mainly, food application, combined with metallic nanoparticles, aiming to enhance encapsulation [2]. Therefore, the objective of the project was to develop microspheres with a bioactive compound (red propolis - PV) and nanocomposites (ZnO and ZnOAg), using the ionic gelation technique, evaluating their physicochemical characteristics, with possible applications in the nutraceutical area [3]. Nanoencapsulated nanoparticles were synthesized with six different formulations, from F1 to F6, as shown in Table 1, by ionic gelation and encapsulated with sodium alginate as a polymer. Characterization analyses were performed by investigating morphological and physicochemical properties using scanning electron microscopy (SEM), encapsulation efficiency by UV/UV-VIS spectrometry, and thermogravimetric analysis (TGA). The encapsulation analyses showed encapsulation values greater than 80%, according to flavonoid quantification analysis. Furthermore, the nanoparticles showed greater encapsulation of red propolis in the formulations Alginate + PV + ZnO and Alginate + PV + ZnOAg, which contain ZnO and ZnOAg nanoparticles, respectively, as shown in Table 2. The SEM analysis, shown in Figure 1, revealed variations in morphological characteristics, mainly roughness. The formulations showed no significant cracks or openings, which is essential to ensure reduced gas permeability, greater protection, and retention of the active ingredient. These data corroborate the good encapsulation efficiency of natural products. Furthermore, this information suggests that the temperatures used in the microencapsulation processes were adjusted to the coating material used. In the TGA analysis, as shown in graph 2, all formulations presented two thermogravimetric events up to 600°C. The first is due to water loss and the second is due to degradation of the components and wall materials. The formulations containing alginate/propolis and alginate/propolis/nanoparticles presented better stability than the formulations without propolis. When comparing the formulation containing alginate/propolis with those containing alginate/propolis/nanoparticles, it is observed that those containing ZnO and ZnOAg nanoparticles provide greater stability to the formulation, respectively. Encapsulation using the ionic gelation method was successful, with results greater than 80%. The flavonoid method demonstrated good encapsulation efficiency for red propolis and nanoparticles. However, variations in morphological characteristics, particularly roughness, and physicochemical characteristics occurred as the formulations changed. Thermogravimetric analysis (TGA) concluded that formulations containing propolis combined with ZnO and ZnOAg nanoparticles presented better stability.

[1] J. I. Griesang, A. C. Rosso, F. C. Kuzniewski, *et al*; *Microencapsulação de compostos bioativos em alimentos*, BTC, vol. 5, no. 2, Aug. 2019, doi:10.26669/2359-2664.2019.227.
[2] P. T. D. Silva, L. L. M. Fries, C. R. de Menezes *et al*., *Microencapsulation: concepts, mechanisms, methods and some applications in food technology*, Cienc. Rural, vol. 44, no 7, p. 1304–1311, jul. 2014, doi: 10.1590/0103-8478cr20130971.
[3] Du, P., Song, L., Xiong, J. *et al. Photocatalytic degradation of Rhodamine B using electrospun TiO2 and ZnO nanofibers: a comparative study*. *J Mater Sci* 48, 8386–8392 (2013). https://doi.org/10.1007/s10853-013-7649-2
[4] This research was supported by CNPq, FAPEAL, CAPES, LME-UFAL.

Table 1. Formulations

Formulações	
F1	Alginato
F2	Alginato + ZnO
F3	Alginato + ZnOAg
F4	Alginato + Própolis Vermelha
F5	Alginato + Própolis Vermelha + ZnO
F6	Alginato + Própolis Vermelha + ZnOAg

Source: Author.

Table 2. UV/UV-VIS Spectrometry - Encapsulation Efficiency

Amostra	[1]Flavonoides totais	Eficiência de encapsulação (%)
F4*	86,8 ± 2,23	92,51
F5*	110,6 ± 0,92	94,12
F6*	159,5 ± 0,70	95,92

Média ± CV = Coeficiente de Variação

1 - mg EQ.g- 1 Expressos como equivalente de quercetina, por g de própolis vermelha

Source: Author

Figure 1. Scanning Electron Microscopy Analysis (SEM).

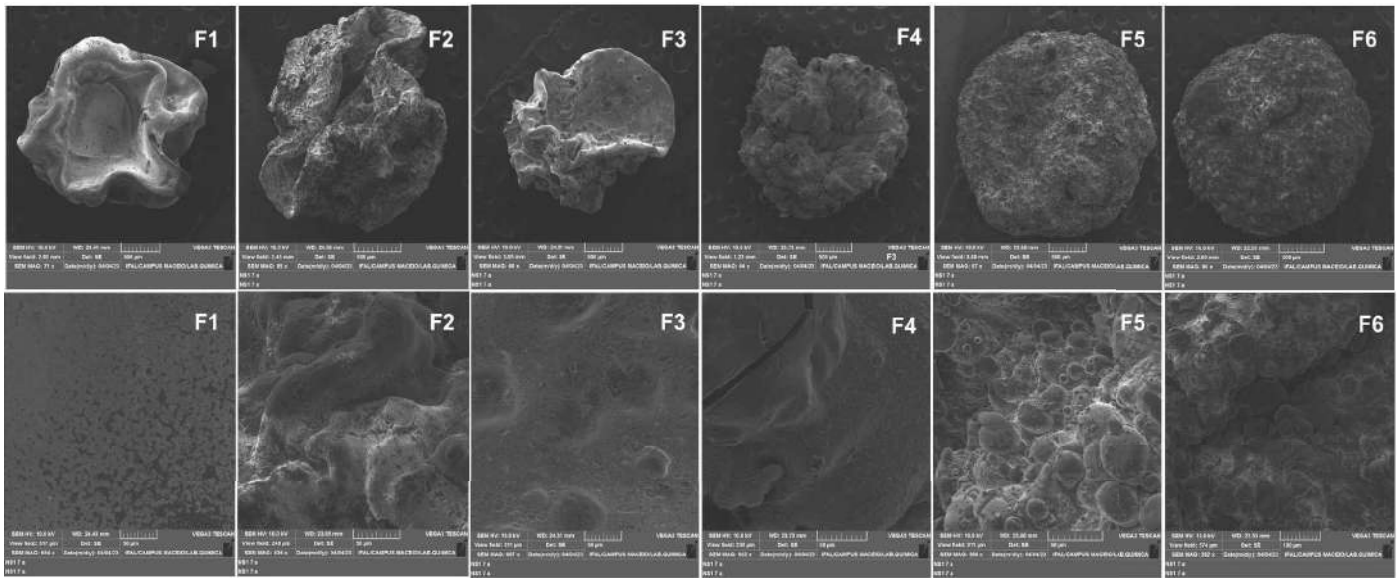

Source: Author

Figure 2. Thermogravimetric Analysis (TGA)

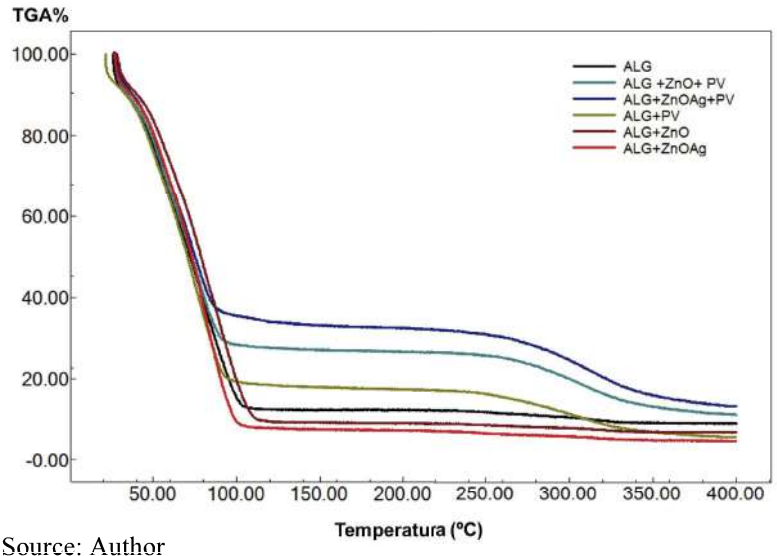

Source: Author

Evaluation of Antileishmanial Activity of Silver Nanoparticles via Cassava Starch

Ana Flávia da Silva Chagas[1]*, Glenda Quaresma Ramos [1,2], Wanderley de Souza[2], Yutao Xing[3], Henrique Duarte da Fonseca Filho[4]

[1] Centro Multiusuário para Análise de Fenômenos Biomédicos, Universidade do Estado do Amazonas, Manaus-AM
[2] Programa de Pós-Graduação em Ciências Biológicas (Biofísica), Instituto de Biofísica Carlos Chagas Filho, Rio de Janeiro, Universidade Federal do Rio de Janeiro, Rio de Janeiro-RJ
[3] Laboratório de Microscopia Eletrônica de Alta Resolução, Centro de Caracterização Avançada para Indústria de Petróleo (LaMAR/CAIPE), Universidade Federal Fluminense, Niterói, RJ, Brazil
[4] Universidade Federal do Amazonas, Departamento de Física de Materiais, Manaus-AM
*chagas.afs@gmail.com

Cutaneous leishmaniasis is an endemic disease in the state of Amazonas, and the species *Leishmania* (Viannia) *guyanensis* and *Leishmania* (Viannia) *naiffi* stand out due to their epidemiological importance and records of resistance to standard drugs. The aim of this study was to evaluate the antileishmanial activity of silver nanoparticles and the morphological changes in promastigote forms. Promastigote forms (10^6 promastigotes/mL) of L. (V.) guyanensis and L. (V.) naiffi were incubated with AgNPs (NP200, NP300, NP400 and NP500) and Glucantime® at concentrations of 0.25 to 4 mg/mL, using untreated parasites as control. The cultures were maintained at 25°C for 24, 48 and 72 hours, with viability quantification under an optical microscope (400x), and the data expressed as CI_{50} [1]. For morphological analysis, the samples were prepared and observed under a SEM (JEOL MEV-JSM-IT500HR). The results obtained demonstrated that in *L. naiffi*, NP200 showed IC_{50} of 1.59 mg/mL at 24 h and <0.125 mg/mL at 48 and 72 h, while for *L. guyanensis*, the values were 2.21 mg/mL (24 h), 0.28 mg/mL (48 h) and <0.125 mg/mL (72 h). In both species, these values were lower than those observed for Glucantime®, whose IC_{50} for L. naiffi was 3.42 mg/mL (24 h), 1.76 mg/mL (48 h) and 1.22 mg/mL (72 h); and for *L. guyanensis*, 7.14 mg/mL (24 h), 2.02 mg/mL (48 h) and 1.21 mg/mL (72 h). In the SEM analysis, the promastigote forms of *L. guyanensis* and *L. naiffi* in the untreated control groups presented preserved morphology, with an elongated body and intact flagellum. In the treatment with Glucantime®, changes such as indentations in the plasma membrane and a slight reduction in body size were observed. In the treatments with NP200 (1 and 2 mg/mL), both species exhibited marked morphological changes, such as a rounded body, membrane deformations and cell rupture, suggesting lysis or apoptosis with leakage of cytoplasmic content, with greater intensity at the concentration of 2 mg/mL. These results are in line with previous studies [2,3] that demonstrated the efficacy of silver nanoparticles against different species of Leishmania, with dose-dependent action and changes in cell integrity suggesting that this damage is associated with programmed cell death. Thus, the data obtained corroborate the literature, highlighting NP200 as a promising formulation against cutaneous leishmaniasis. In addition, the present study expands knowledge about the effect of these particles specifically on *L. naiffi* and *L. guyanensis*, species relevant in the Amazonian scenario and with few published morphological studies.

[1] A. F. Chagas et al., Acta Amaz. 51 (2021) 260 – 269.
[2] A. M. Allahverdiyev et al., Int J Nanomedicine 6 (2011) 2705-14.
[3] A. B. Alves et al., Patógenos 12 (2023) 660.
[4] This research was supported by FAPEAM and CNPq.

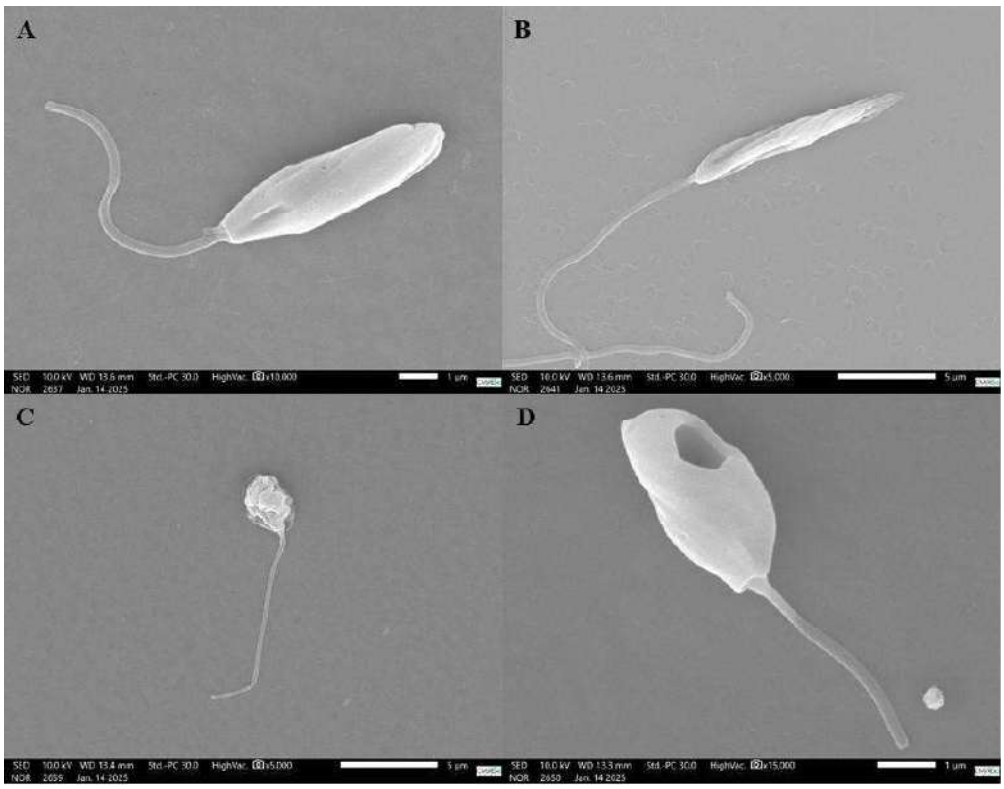

Figure 1. Scanning Electron Microscopy of promastigote forms of Leishmania (Viannia) guyanensis. (A) Parasite from the untreated control group; (B) Parasite treated with Glucantime®; (C) Parasite treated with 1 mg/mL of NP200; (D) Parasite treated with 2 mg/mL of NP200.

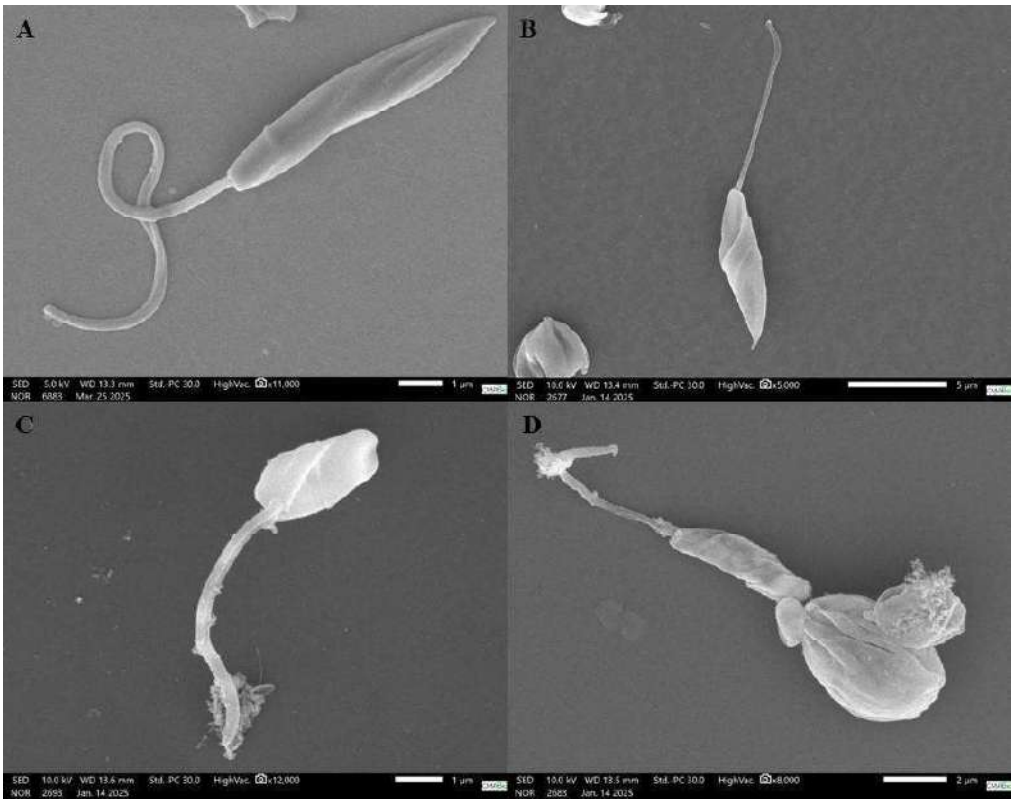

Figure 2. Scanning Electron Microscopy of promastigote forms of Leishmania (Viannia) naiffi. (A) Parasite from the untreated control group; (B) Parasite treated with Glucantime®; (C) Parasite treated with 1 mg/mL of NP200; (D) Parasite treated with 2 mg/mL of NP200.

Extracellular Vesicle Secretion by Ependymal Cilia in Rat Brain Ventricles Following Experimental Brain Ischemia: uncovering new roles for a neglected structure

Rita Sinigaglia[1]*, Aline dos Santos Santana[1,] Andréa Aurélio Borges[2], Rafael Pedro Madeira[3], Ana Claudia Trocoli Torrecilhas[3].

[1]Centro de Microscopia Eletrônica, Escola Paulista de Medicina, UNIFESP, [2] Departamento de Psicobiologia, Escola Paulista de Medicina, UNIFESP. [3]Departamento de Ciências Biológicas, Campus Diadema, UNIFESP
*rita.sinigaglia@unifesp.br

The intricate role of extracellular vesicles (EVs) in neuronal function and disease has emerged as an essential focus in neuroscience research due to their role as mediators in intercellular communication and contributing to brain function [1, 2]. On the other hand, the cellular elements composing the lining of brain ventricles have drawn much attention from neuroscientists, especially the role of subependymal cells in neurogenesis [3]. It is noteworthy that while a considerable body of research has shed light on the regenerative potential of mesenchymal stem cell-derived extracellular vesicles in the nervous system [4, 5], there remains a critical gap in our understanding of the broader landscape of EV functions in the context of brain physiology and neurological conditions such as ischemia. Recent studies revealed the presence of extracellular vesicles in the cerebrospinal fluid of patients and animal models of neurological diseases [6,7]. These studies focused on EV secretion by choroid plexus while our study focused on EV secretion by other structures composing the brain ventricles.

Male Wistar rats were subjected to 10 minutes of global brain ischemia [8] and divided into two groups: sham-operated and saline-treated ischemic animals. Animals were allowed to survive for seven days after ischemia. All procedures were approved by the ethics committee of the Federal University of São Paulo (2018/7633081117). We performed transmission electron microscopic analysis at 80 kV (TEM) (JEOL 1200 EXII) and field emission scanning electron microscopic analysis (FESEM) (FEI Quanta 250) of brain ventricles. Cerebrospinal fluid (CSF) was collected from cisterna magna, ultracentrifuged according to the International Society of Extracellular Vesicles Task Force [9] for nanoparticle tracking analysis (NTA) by NanoSight and morphology analysis through negative staining.

Morphological characterization of brain ventricle through FESEM revealed a slight rarefaction of ciliary tufts of ischemic animals when compared to sham animals. A profuse secretion extracellular vesicle was visualized through FESEM and TEM, revealing EV secretion by ependymal cilia in all animal groups. As seen by FESEM, ischemic animals presented more EVs on the cell cillia sham animals. TEM analysis confirmed EV budding from the cilia membrane. NTA and TEM confirmed the size and concentration of nanoparticles in the CSF.

Our results are unprecedented and bring innovative potential regarding the role of EVs in the nervous system. Further studies are needed to elucidate the mechanisms underlying EV-mediated cellular communication in the pathophysiology of neurological diseases, providing novel insights for theranostic strategies in neurological diseases.

[1] S. Ahmad et al., Frontiers Mol. Sci., 15 (2022) 844194.
[2] M. Gabrielli et al., Cells 12 (Suppl. 1) (2023) 63.
[3] F. H. Gage, J. Neurosc. 22 (Suppl. 3) (2002) 612.
[4] Y. Li, B. Fang, Biomedicine & Pharmacotherapy, 165 (2023), 115092.
[5] Z. Yang et al., Neural Regen. Res. 18(Suppl. 11) (2023) 2406.
[6] C. Vandendriessche et al., Acta Neuropathol. Comm. 9 (2021), 143.
[7] F. Delgado-Peraza et al., Cells 10 (Suppl. 5) (2021), 993.
[8] M-L. Smith et al., Acta Neurol. Scand. 69 (1984) 385.
[9] U. S. Sandau et al., J. Extracell. Vesicles 13 (2024) 12397.
[10] This research was supported by CAPES and FAPESP (Brazil).

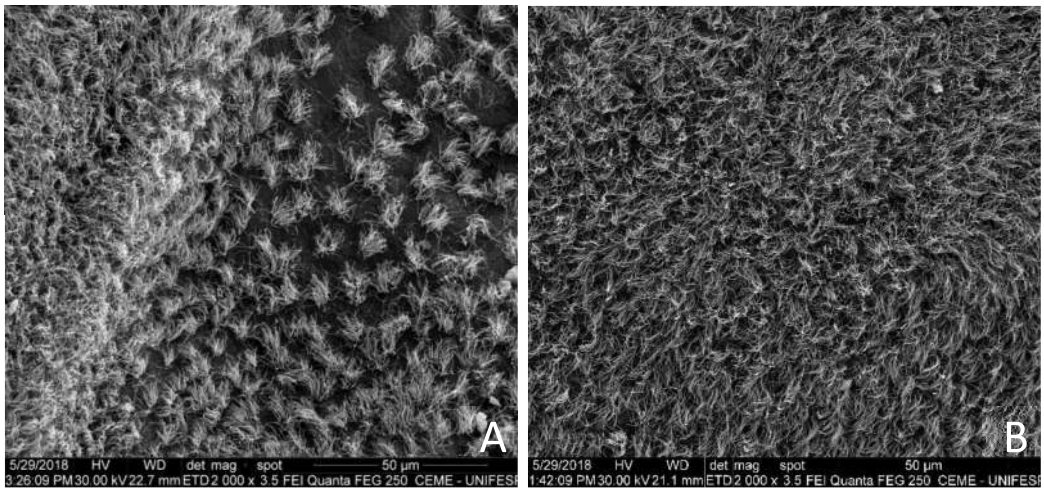

Figure 1. Field emission Scanning microscopic analysis revealed ependymal cilia rarefaction in saline-treated ischemic animals (A) as compared to sham operated animals (B).

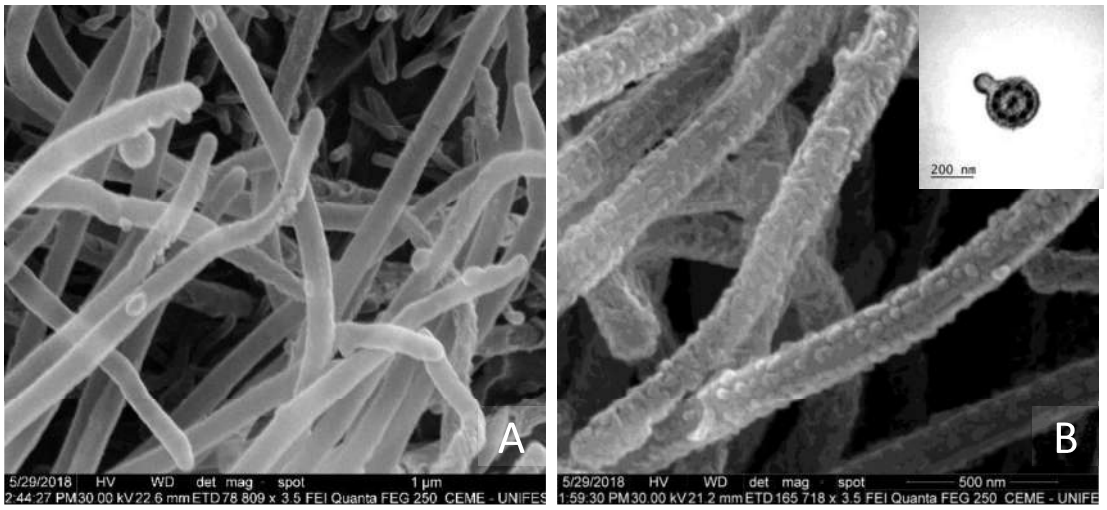

Figure 2. Higher magnification of FESEM analysis revealed that ependymal cilia can release considerable amounts of vesicles of various sizes (from nano to microscale) even under physiological conditions (A, sham animals). Saline-treated ischemic animals presented profuse extracellular vesicles secretion from ependymal cilia (B). TEM analysis confirmed extracellular vesicle secretion from ependymal cilia (insert in B).

Floral meristem size influences androecium ontogeny in *Bauhinia* L. (Fabaceae): Insights from scanning electron microscopy

Flora Siqueira de Moraes[1]*, Andrews V. dos Santos Silva[2], Vidal de Freitas Mansano[2], Louis P. Ronse De Craene[3], Juliana Villela Paulino[4]

[1] Universidade Estadual Paulista "Júlio de Mesquita Filho", Brazil; [2] Instituto de Pesquisas Jardim Botânico do Rio de Janeiro, Brazil; [3] Royal Botanic Garden Edinburgh, United Kingdom; [4] Faculdade de Farmácia, Universidade Federal do Rio de Janeiro, Brazil.

*flora.moraes@unesp.br

Scanning electron microscopy (SEM) allows for the high-precision study of micromorphological structures with minimal deformation. In addition, it has been widely used in studies of floral development [1]. The study of floral ontogeny, which examines the developmental trajectory of flowers from the initial formation of organs to their mature state, provides valuable insights into the evolutionary history of angiosperms [2]. Among these, the Fabaceae family stands out for its remarkable floral diversity, exhibiting a wide array of modifications that deviate from the typical pattern [3]. A typical Fabaceae flower comprises 21 organs, distributed among the calyx (5), corolla (5), androecium (10), and gynoecium (1). *Bauhinia* L. (Fabaceae, Cercidoideae) exemplifies such diversity, displaying striking variation in the number of fertile stamens and staminodes, ranging from 1 to 10 stamens and 0 to 9 staminodes [4]. This study aimed to understand the ontogenetic processes underlying these variations. Seven species representing this diversity were examined, including *B. monandra* and *B. erythrocalyx* (one stamen and nine staminodes), *B. purpurea* (3/7), *B. bauhinioides* and *B. variegata* (5/5), and *B. forficata* and *B. longifolia* (10/0). Floral buds at various developmental stages and mature flowers were collected, fixed in FAA 70 [5], dissected under a stereomicroscope, dried using a critical point dryer, mounted on metal stubs with carbon adhesive tape, sputter-coated with gold, and examined under a scanning electron microscope (LEO Supra 55VP; Hitachi Regulus 8230 and JEOL - JSM-6490LV). In all species, the floral whorls initiated in a mixed acropetal sequence, with the calyx developing in a helical pattern and both the corolla and androecium initiating unidirectionally. Interestingly, species with staminodes exhibited a distinctive carpel morphology, characterized by an expanded basal region that appeared to physically constrain stamen development, primarily on the adaxial side. This suggests that spatial constraints within the floral meristem influence stamen abortion and staminode formation in *Bauhinia*. Species with larger floral meristems tended to develop the full complement of floral organs, while those with more restricted meristematic space exhibited stamen abortion and staminode development. In *Bauhinia*, successful stamen development appears to depend on the spatial availability within the floral meristem. Petal pressure and early carpel development may limit this space, particularly on the adaxial side due to the carpel's shape, resulting in stamen abortion and staminode formation. Notably, species with ten fertile stamens lack the restrictive carpel morphology, reinforcing the hypothesis that physical constraints during development play a critical role in determining the final floral structure in this genus [6,7].

[1] S.C. Tucker, *Floral initiation and development in legumes*, Advances in legume systematics, part 3. Royal Botanic Gardens, Kew, UK, 1987.
[2] P.S. Soltis et al., *Floral variation and floral genetics in basal angiosperms*, 96 (2009) 110-128.
[3] S.C. Tucker. *Floral development in legumes*, 131 (2003) 911-926.

[4] A.M.S. Vaz, A.M.G. Tozzi, *Bauhinia* ser. *Cansenia (Leguminosae: Caesalpinioideae) no Brasil*, 54 (2003) 55-143.
[5] D.A. Johansen, *Plant microtechnique*, McGraw-Hill Book Company, New York, 1940.
[6] L.P. Ronse De Craene, *Understanding the role of floral development in the evolution of angiosperm flowers: clarifications from a historical and physico-dynamic perspective*, 131, (2018) 367-393.
[7] This research was supported by CAPES and FAPERJ (Brazil).

Figure 1. Flower ontogeny with focusing in development of carpel, stamen and staminode formation. (A-C) *B. monandra* development emergence of antesepalous and antepetalous stamen primordia and growth of the carpel (A); intermediate morphology of the carpel during development (B); distinction of carpel cleft and differentiation of abaxial stamen and petal primordia (C); (D) initiation of carpel cleft and expansion of the carpel both adaxially and upwardly in *B. purpurea* (E) intermediate morphology of the carpel during development in *B. variegata*; (F) upwards expansion of the carpel and differentiation of antesepalous stamen and petals in *B. bauhinioides*; (G) emergence of antesepalous stamen primordia and growth of the carpel in *B. forficata*; (H-I) *B. longifolia*; Basal expansion of the carpel (H); elongation and differentiation all organs (I); (J) stamen development and staminode formation in *B. erythrocalyx*; (K) Development of the carpel and growth of stamens in *B. bauhinioides*; (L) differentiation of petals, carpel and outermost stamens in *B. longifolia*. Abbreviations: AN = anther; AP = antepetalous stamen; AS = antesepalous stamen; C = carpel; F= filament; P = petal; ST = staminode. Scale bar: (A, G) = 10 μm; (B-C) = 20 μm; (D-E, H-I) = 50 μm; (F, L) = 100 μm; (J) = 500 μm; (K) = 200 μm.

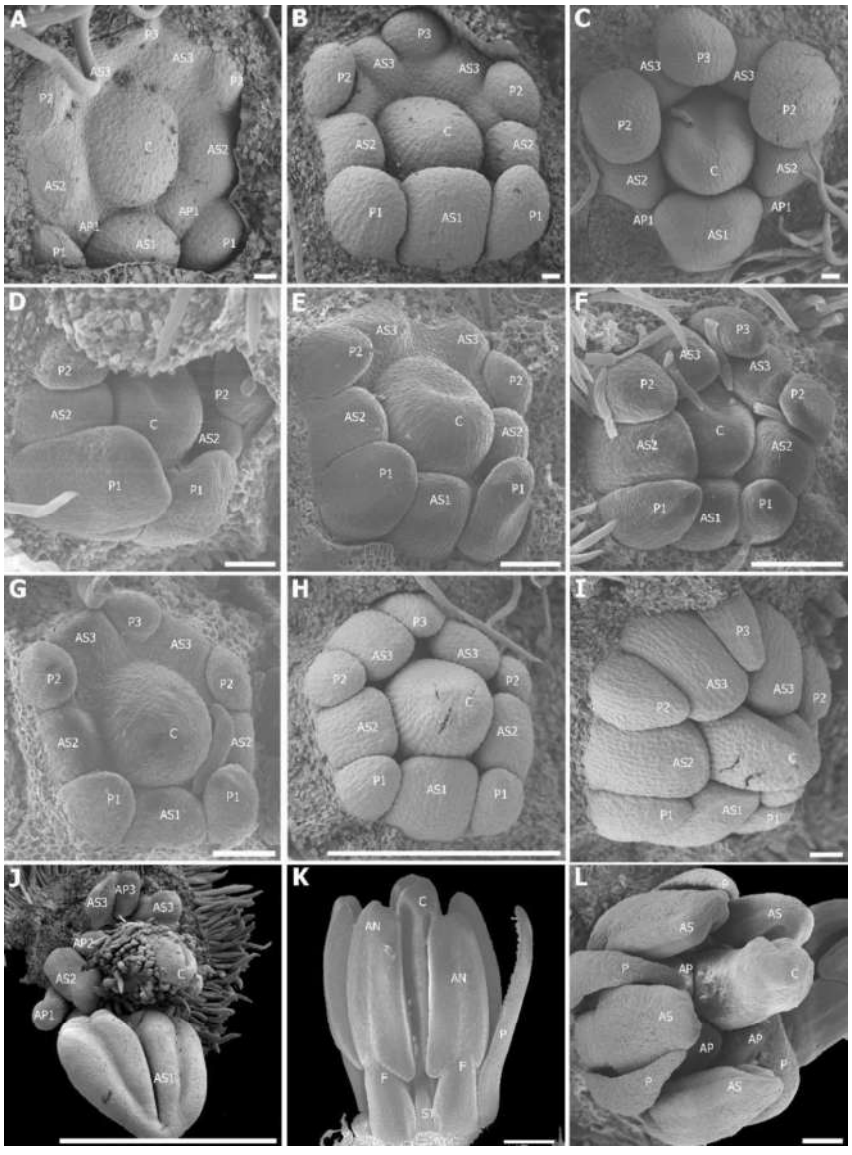

Induction and Experimental Characterization of Extracellular Vesicles from *Trypanosoma cruzi* Epimastigotes

Ana Carolina Gonzaga[1,2]*, Wanderson de Souza[1], Wanderley de Souza[2], Emile Barrias[1,2]

[1] National Institute of Metrology, Quality and Technology (INMETRO), RJ, Brazil.
[2] Hertha Meyer Cell Ultrastructure Laboratory, IBCCF, UFRJ, RJ, Brazil
ac.anagonzaga@gmail.com

Electron microscopy was employed as the main tool to investigate the secretion of extracellular vesicles (EVs) in *Trypanosoma cruzi*, the etiological agent of Chagas disease. These vesicles participate in processes such as intercellular communication, immune modulation, and infection dissemination. Although basal secretion has already been described, little is known about the influence of chemical stimuli on this process. In this study, we evaluated the induction of EV secretion by epimastigotes of the DM28c strain through calcium stimuli: calcium chloride ($CaCl_2$) and calcium ionophore (A23187). In order to evaluate parasite morphology and to verify the presence of vesicles adhered or not to their surface, after induction the parasites were fixed in glutaraldehyde, post-fixed with osmium tetroxide and potassium ferrocyanide, dehydrated in a graded ethanol series, critical point dried, and sputter-coated with platinum (10 nm). Analyses were carried out in a Quattro S scanning electron microscope (Thermo Fisher Scientific, CENABIO/UFRJ), operated at 10 kV in high vacuum mode. The supernatant was subjected to ultracentrifugation, and the isolated EVs were processed for transmission electron microscopy (TEM) by negative staining on copper grids coated with Formvar film, using 5% uranyl acetate, with the aim of analyzing the structure of the secreted vesicles. Observations were conducted in a Hitachi HT7800 transmission electron microscope (CENABIO/UFRJ). Additionally, EVs were characterized by DLS and NTA, enabling the determination of hydrodynamic diameter, size distribution, and particle concentration. Cell viability was monitored using the MTS/PMS assay, revealing that $CaCl_2$ promoted increased metabolic activity, whereas the ionophore exhibited progressive toxicity. SEM revealed a higher density of EVs adhered to the parasite surface in the combined treatment ($CaCl_2$ + ionophore), without significant morphological alterations. TEM revealed abundant spherical vesicles, and NTA showed a significant increase in particle concentration after 20 minutes of exposure to the ionophore, with an average diameter of 150–170 nm. DLS data corroborated these findings, with subtle variations depending on time and type of stimulus. The proposed protocol is reproducible, follows metrological standards (ISO/IEC 17025:2017; DOQ-CGCRE-008), and contributes to the standardization of EV induction and characterization in protozoa, reinforcing the role of intracellular calcium in vesicular secretion and establishing a basis for functional and diagnostic studies involving *T. cruzi* EVs.

References:

[1] J. C. Santana de Andrade *et al.*, Stimulation of microvesicle secretion in *Trichomonas vaginalis*, *Experimental Parasitology*, San Diego, v. 259, p. 108722, 2024. DOI: 10.1016/j.exppara.2024.108722.

[2] J. B. Aggio *et al.*, Trypanosomatid extracellular vesicles as potential immunogens for Chagas disease, *International Journal of Molecular Sciences*, v. 26, n. 4, p. 1544, 2025. DOI: 10.3390/ijms26041544.

This research was supported by a CAPES scholarship (Brazil) and developed at the Hertha Meyer Cell Ultrastructure Laboratory (IBCCF/UFRJ), under the coordination of Professor Wanderley de Souza.

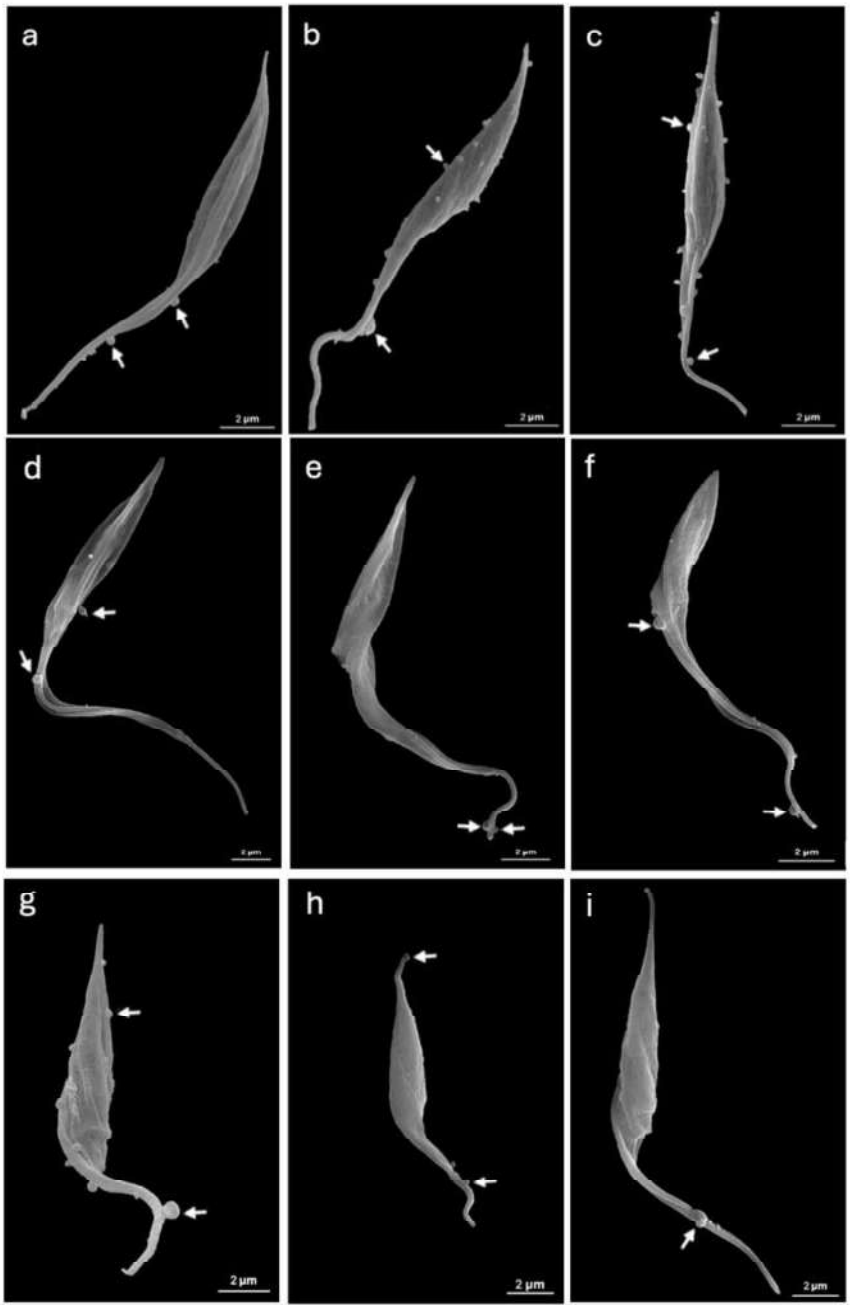

Scanning electron micrographs of *Trypanosoma cruzi* epimastigotes with induction of extracellular vesicles (EVs). Images (a), (b), and (c) correspond to parasites incubated for 5, 10, and 20 minutes, respectively, in the presence of 1 mM $CaCl_2$ and 4.5 µM calcium ionophore, in serum-free medium. Images (d), (e), and (f) correspond to treatment with 1 mM $CaCl_2$ alone, and images (g), (h), and (i) correspond to treatment with 4.5 µM calcium ionophore alone. Arrows indicate extracellular vesicles in the micrographs.

Investigation By Microscopy of The Biological Effects of Topoisomerase Inhibitors in Anti-*Giardia intestinalis* Chemotherapy

Dalilla Oliveira[2,3*], Marlene Benchimol[1,3], Ana Paula Gadelha[2]

[1] Lab. de Ultraestrutura Celular Hertha Meyer, IBCCF, UFRJ, RJ, Brazil.
[2] Lab. de Células Eucariontes, Cobio, Dimci, Inmetro, RJ, Brazil. Electronic address: dalillaoliveirasz@gmail.com
[3] Universidade do Grande Rio (UNIGRANRIO), RJ, Brazil.

Parasitic diseases, especially protozoa, constitute one of the main public health problems in underdeveloped countries, including Brazil. Among them, giardiasis stands out, an infection of the digestive tract that is caused by the protozoan *Giardia intestinalis*. Giardiasis is one of the most common parasitic diseases worldwide, and in 2004, it was included in the Drugs for Neglected Diseases Initiative of the World Health Organization (DNDi/WHO). Children are the main risk group, since this disease can lead to severe malnutrition, impairing physical and intellectual development [1]. Giardiasis has a wide range of clinical manifestations, such as diarrhea, nausea and weight loss. The treatment of the disease is based on drugs from the class of nitroimidazoles and benzimidazoles, which, in addition to having a series of side effects, can even be teratogenic or carcinogenic. In addition, reports of resistance to prescribed drugs grow every year [2]. Thus, the search for new compounds that are more efficient and safe for the patient is extremely important. Topoisomerase inhibitors are part of a new class of drugs with antiparasitic activity. In view of this, our group evaluated the potential of these inhibitors as promising agents for giardiasis chemotherapy using different microscopy modalities. The growth curves indicated that the compounds used in this study have a dose-dependent effect. The compound that had the highest inhibition rate was Nalidixic Acid Sodium Salt, with an IC_{50} value of 4.3μM at 72 h. Scanning electron microscopy showed that the compounds altered trophozoite morphology, with a decrease in externalized flagella and cell rounding. By transmission electronic microscopy, we observed internalized flagella and the presence of vacuoles with cytoplasmic material inside, in addition to myelin figures.Cell cycle assays indicated an increase in the percentage of cells in the G2/M phase after drug exposure. These results show that Topoisomerases Inhibitors can be potential targets for Giardia intestinalis chemotherapy, for this, more studies need to be carried out in order to elucidate the results obtained.

[1] BURET, A.G. Pathophysiology of enteric infections with Giardia duodenalis. Parasite, 15, 261-265, 2008. DOI: 10.1051/parasite/2008153261.
[2] Upcroft P, Upcroft JA. Drug targets and mechanisms of resistance in the anaerobic protozoa. Clin Microbiol Rev. 150-64, 2001. DOI: 10.1128/CMR.14.1.150-164.2001.

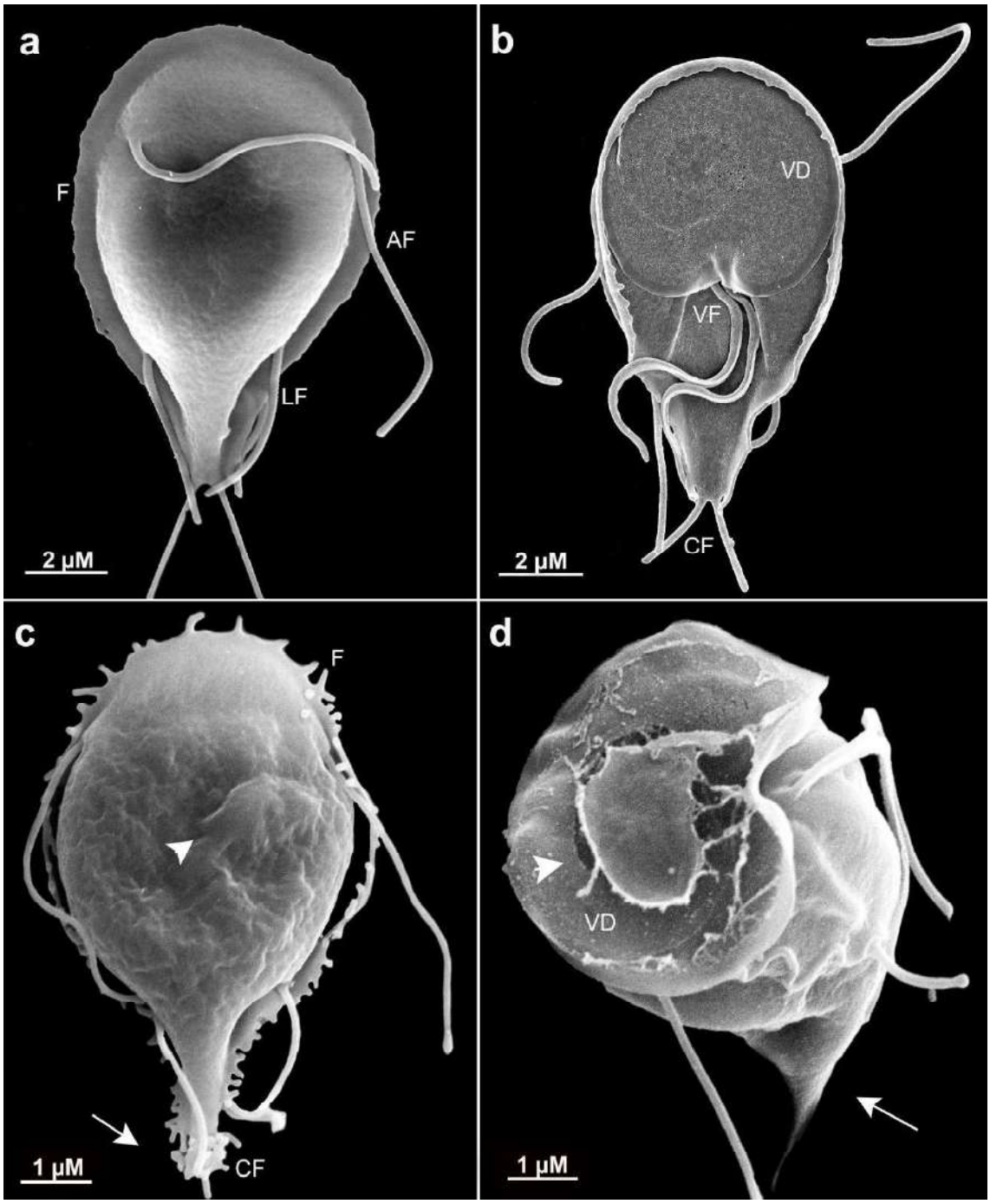

(a) Dorsal surface of the Giardia intestinalis trophozoite. Note the characteristic pear shape, as well as the intact dorsal surface, continuous ventro-lateral flange, and the three pairs of flagella (anterior, posterior-lateral, caudal).**(b)** Ventral surface Note the spiral shape of the ventral disc and the anterior, ventral, and caudal flagella. **(c)** Trophozoite was exposed to the sodium salt of nalidixic acid at a concentration of 5 µM. Note that there are irregularities in the flange and roughness in the cell surface (arrow head), in addition to a reduction in the caudal flagella (CF) (arrow) **(d)** Trophozoite exposed to the sodium salt of nalidixic acid at a concentration of 10µM. Note that the surface corresponding to the ventral disc presents areas with membrane extraction (arrow head) and a modified caudal portion (arrow). **VD,** Ventral Disc; **F,** Flange; **AF,** anterior flagella; LF, lateral flagella; VF, ventral flagella; CF, caudal flagella.

Microscopy Techniques for Investigating the Phytoremediation Potential of Iron by *Isoëtes cangae* Assisted by Mycorrhizal Fungi

Aline Karl Araujo[1*], Naiara Viana Campos[1], Ocimar Ferreira de Andrade[2], Cintia Monteiro de Barros[1], Breno Chaves de Assis Elias[3], Rodrigo Lemes Martins[1]

[1] Federal University of Rio de Janeiro, Institute of Biodiversity and Sustainability (NUPEM), Macaé, RJ, Brazil
[2] Fluminense Federal Institute of Education Science and Technology, Laboratory of Ecotoxicology and Environmental Microbiology (LEMAM), Cabo Frio, RJ, Brazil
[3] Vale S.A., Belo Horizonte, MG, Brazil
* alinekarl.ufrj@gmail.com

Mycorrhizal fungi play an important role in improving tolerance to and accumulation of heavy metals in plants. Several studies relate the presence of mycorrhizal associations in plant roots to the extraction, translocation, and reduction of metal bioavailability in contaminated soils [1,2]. Mycorrhizal fungi, particularly arbuscular mycorrhizal fungi (AMF), effectively immobilize metals(loids) in the soil through a combination of intra- and extracellular mechanisms. Intracellularly, they sequester metals within vacuoles and vesicles [3] and extracellularly, they use cell wall components and extracellular polymeric substances (EPS), including glomalin, to trap metals [4]. They can also enhance the effectiveness of phytoremediation by promoting symplastic and apoplastic pathways in plants [5]. This study addresses the evaluation of the fungus–plant interaction in *Isoëtes cangae* J.B.S. Pereira, Salino & Stützel, a narrow endemic lycophyte recently described in a permanent lagoon in Serra dos Carajás, Pará State, Brazil. To assess the role of mycorrhizae in this remediation process, we used optical and electron microscopy techniques associated with microanalysis. The main goal is to identify the presence of iron and other metals within the roots and fungal structures such as spores, hyphae, and vesicles. We used optical microscopy with Perl's staining technique, also known as Prussian blue staining. Cross-sections of roots fixed in 2.5% glutaraldehyde in sodium phosphate buffer (0.1 M; pH 7.2) and subsequently embedded in historesin were immersed in 4% (v/v) HCl and 4% (w/v) potassium ferrocyanide (Perl's Prussian Blue [6]). Excess stain was washed off with distilled water, and the slides were observed under an Olympus BX51 light microscope. Fungal structures were investigated using trypan blue stain. Iron internalization was investigated using scanning electron microscopy (SEM) followed by EDX for elemental analysis. Fresh root segments (10 mm from the apex) were fixed in 2.5% glutaraldehyde in sodium phosphate buffer (0.1 M; pH 7.2), then washed in phosphate buffer, dehydrated in an ascending acetone series, and embedded in epoxy resin [7]. After polymerization at 70°C for 24 hours, samples were trimmed using an ultramicrotome to expose the tissue, mounted on stubs, and coated with carbon [8]. The samples were then observed under a THERMO FISCHER QUATTRO S SEM with EDS. Preliminary results showed the presence of fungal structures resembling arbuscular mycorrhizal fungi, such as non-septate hyphae and vesicles (Figure 1a). Perl's staining revealed a high concentration of iron on the root exterior and in some structures within the plant cells (Figure 1b). SEM-EDS analysis showed a more dispersed distribution of iron within the plant cell (Figure 2). The next steps will involve analyzing more samples using scanning electron microscopy in search of vesicles with potentially higher metal accumulation, and the use of transmission electron microscopy to investigate the presence of iron within fungal structures.

[1] S. Silva et al., Pesquisa Agropecuária Brasileira, v. 41, p. 1749-1757, 2006.

[2] A. Tariq et al., *Stress Biology* 5, 4 (2025).

[3] B. Chen et al., Microbes Environ 29;33(3) 2018.

[4] Y. Li et al., Int J Environ Res Public Health 21;19(9) 2022.

[5] Q. Zhen et al., Adv Appl Microbiol. 129:171-187 (2024).

[6] M. G. Stacey et al., Plant Physiol. 146, 589–601(2008).

[7] A. R. Spurr, Journal of Ultrastructure Research 26: 31-43 (1969).

[8] A. Chabbi, *New Phytol.* 144, 133–142 (1999).

[9] The authors acknowledge financial support from Vale S.A.

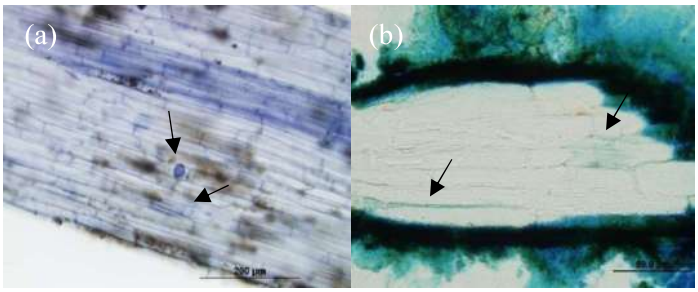

Figure 1: Light microscopy (LM) of *Isoëtes cangae* roots. (a) Presence of structures characteristic of arbuscular mycorrhizal fungi in the root tissue. (b) Cross-section of *I. cangae* root showing intense blue staining on the outer surface and some internal regions, indicating iron deposition via Perl's Prussian blue method.

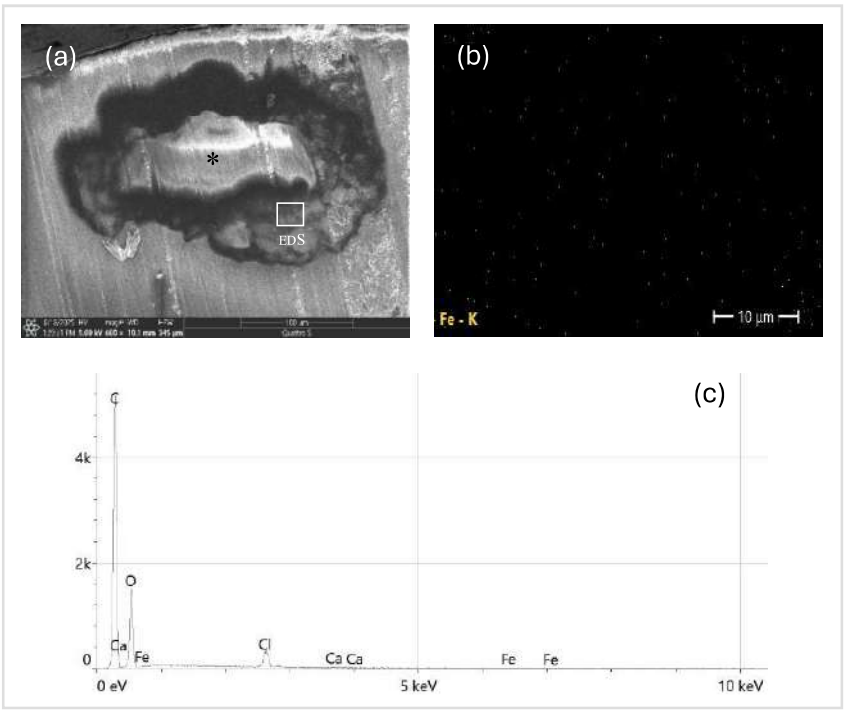

Figure 2: Scanning electron microscopy with energy-dispersive X-ray spectroscopy (SEM-EDS) of *Isoëtes cangae* roots. (a) SEM image of a *I.cangae* root cross-section. The lighter central araea marked by na asterisk consists of the lacunar system characteristic of the species. The rectangle represents the area selected for EDS analysis. (b) Elemental mapping by EDS showing intracellular iron localization. (c) EDS spectrum obtained from selected region.

Morphological Characterization of Terminalia and Spermatozoon of *Ornidia obesa* (Fabricius, 1775) (Diptera: Syrphidae)

Ingrid Gracielle Martins Silva[1], Karine B. Barros-Cordeiro[1]and Sônia N. Báo[1]

[1]Laboratório de Microscopia Eletrônica, Depto. Biologia Celular, IB, UnB, Brasília, Brasil
*gracilias@gmail.com

The Syrphidae family has approximately 6,000 described species, organized into 202 genera. The Neotropical region has one of the greatest diversity of species, with approximately 1,600 known species [1]. This family consists of flies with floral habits, playing an important ecological role as pollinators. The subfamily Eristalinae is a highly diverse group of flower flies, with adult forms that vary greatly in appearance—from small to large, slender to robust, smooth to hairy, opaque to shiny, and plain to colorful [2]. Adult flies of the subfamily Eristalinae often visit flowers, where they consume nectar and pollen. Among the genera that comprises Eristalinae is the genus *Ornidia* Lepeletier & Serville, 1828 - which includes medium to large flies (2.3-4.2 mm) characterized by their metallic green or purple coloration [3]. The morphology of the male genitalia and the ultrastructure of the sperm are used as auxiliary characteristics in the identification of species. The use of scanning electron microscopy (SEM) and transmission electron microscopy (TEM) as tools can contribute to the recognition and characterization of structures that are normally represented by drawings and diagrams, facilitating species identification. The objective of this study was to characterize the morphology of the male terminalia and the ultrastructure of the spermatozoa of *Ornidia obesa* (Fabricius). Preparation for SEM: The specimens were fixed in Karnovsky's for 24 hours. The samples were then rinsed and immersed in osmium tetroxide for one hour, followed by washing in distilled water. Dehydration was performed using different concentrations of acetone (30-100%) for 15 minutes at each concentration. Subsequently, the material was subjected to critical point drying with CO_2, mounted on supports, coated with gold, and viewed under a SEM (JEOL JSM-7001F). The terminology of the genital structures follows Cumming et al., 1995 [3]. For TEM, the protocol is the same until dehydration. After this step, the testes were embedded in Spurr's resin, cut using an ultramicrotome, and analyzed under a TEM (Jeol 1011). It was possible to observe the main morphological structures that compose the male genitalia. In *O. obesa*, the surstylus is cylindrical in shape, with short hair (Fig. 1A and B - blue). The cerci have long hair along their entire length and are surrounded by the epandrium. The epandrium is completely covered with small hair (Fig. 1 A and B – green and purple). The aedeagus is wide and inserted between the hypandrium, which have a small spike on the external margin (Fig. 1 A - orange and light blue). In TEM, it was possible to observe structures such as centriole adjuncts, axonemes in a 9+9+2 pattern, rounded mitochondrial derivatives, with the presence of paracrystalline material. Nucleus with compact chromatin (Fig. 1 C-D). Electron microscopy allowed the recognition and characterization of some morphological structures of the terminalia and the ultrastructure of the spermatozoon of *O. obesa,* providing data and contributing to a better understanding of the morphology of the species.

References:
[1] Thompson, F. C. NRC (2010) v.2.
[2] Carvalho Filho, F.S. *Zootaxa* (2009).
[3] Cumming, J. M. *et al.* Ent.Scand. (1995) v.26
[4] Financial Support: CAPES, CNPq, FAPDF, FINEP

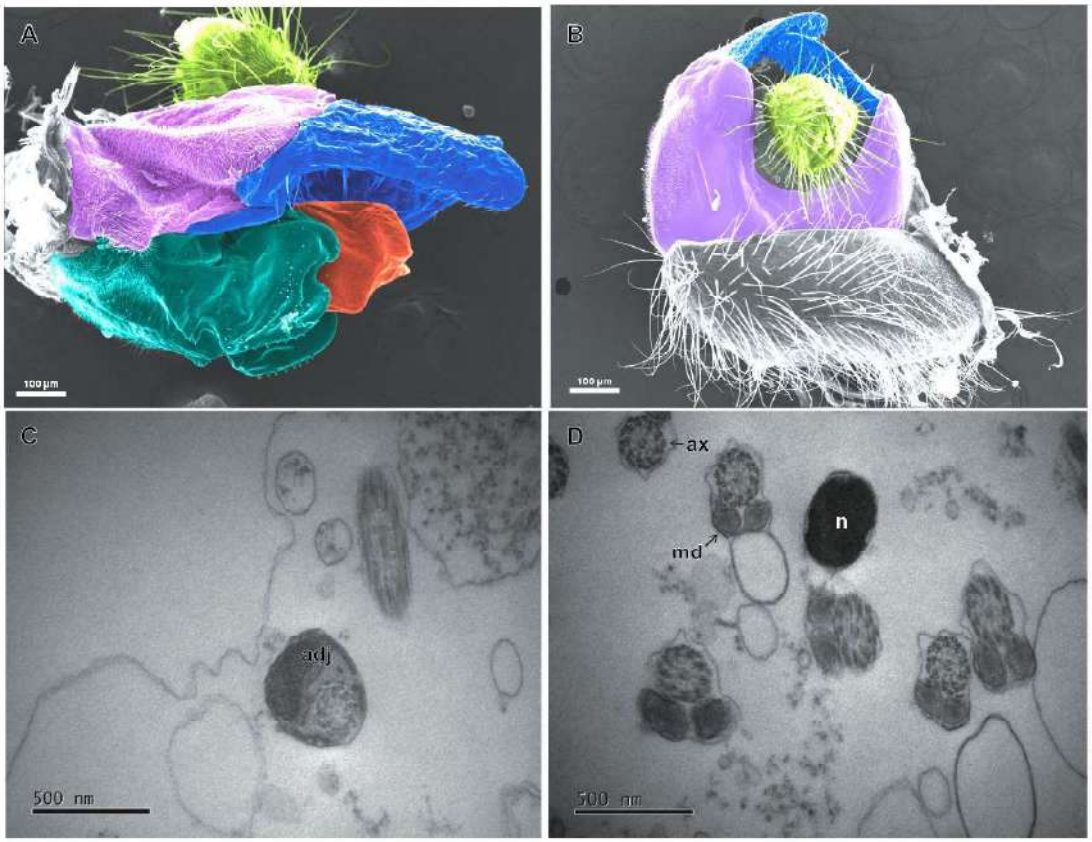

Figure 1. SEM micrographs of male genitalia (A and B) and TEM micrographs of sperm cells (C and D) of ***Ornidia obesa.*** The terminalia region is shown in lateral view (A) and dorsal view (B). **Abbreviations/colors:** In Blue: surstylus; Green: cercus; Purple: epandrium; Light Blue: hypandryum; Orange: aedeagus; adj: centriole adjunct; ax: axoneme; md: mithocondrial derivative and n: nucleus.

Nanostructured Mn-Co Silicates Synthesized via Coprecipitation for Biomedical Applications

Thallys Mendes da Silva[1]*, Mônica Rodrigues de Sá [1,] Eduardo Padrón Hernández[1].

[1]Universidade Federal de Pernambuco, Departamento de Física, PE, Brazil.
*thallys.mendes@ufpe.br

Metallic silicates have gained prominence due to their functional properties and broad versatility in advanced applications, especially in the biomedical field, owing to their biocompatibility, tunable porosity, and controlled ion release capacity [1–4]. In this study, cobalt silicate ($CoSiO_3$), manganese silicate ($MnSiO_3$), and a mixed manganese–cobalt silicate with a 70:30 ratio ($Mn_{0.3}Co_{0.7}SiO_3$) were synthesized via coprecipitation, a simple, reproducible, and cost-effective method that allows precise control over particle morphology and chemical composition. The process involved controlled pH and temperature conditions, followed by washing, drying, and calcination. Scanning electron microscopy (SEM) and energy-dispersive X-ray spectroscopy (EDS) were employed for morphological and elemental characterization. SEM micrographs revealed nanostructured materials for all compositions. Manganese silicate ($MnSiO_3$) exhibited relatively uniform nanoparticles with average sizes of 145 ± 32 nm. Cobalt silicate ($CoSiO_3$) displayed larger, more agglomerated particles averaging around 450 ± 27 nm. The mixed silicate ($Mn_{0.3}Co_{0.7}SiO_3$) showed heterogeneous particle sizes ranging from 250 to 500 nm, indicating a nanometric distribution favorable for biological interactions. These particle size ranges are particularly advantageous for biomedical use, as they enhance cellular uptake, surface activity, and compatibility with biological systems. EDS analysis confirmed the presence of the expected elements Mn, Co, Si, and O in all samples. In the mixed silicate, the relative intensities of the cobalt and manganese signals corresponded closely with the intended 70% Co and 30% Mn ratio, confirming the successful incorporation of both metal ions into the silicate matrix. The use of a 70% cobalt and 30% manganese ratio in the mixed silicate formulation is particularly significant. Cobalt ions are known to stimulate angiogenesis and osteogenesis, while manganese plays a role in enzymatic activity and antioxidant defense. By combining both elements in this specific proportion, it is possible to tailor the physicochemical properties of the particles such as crystallinity, ion release rate, and surface reactivity to optimize their performance for applications in tissue engineering and therapeutic delivery. The cobalt-rich composition ensures robust biological stimulation, while the addition of manganese enhances overall biocompatibility and functional stability. The result is a hybrid silicate with balanced biological stimulation and improved chemical stability. Additionally, the mixed composition may influence ion release kinetics and surface reactivity in a way that enhances therapeutic performance. Overall, the coprecipitation method proved effective in producing nanostructured metallic silicates with tunable properties. The structural and compositional characteristics observed in the SEM and EDS analyses support the conclusion that these materials, particularly the $Mn_{0.3}Co_{0.7}SiO_3$ system, have significant potential for advanced biomedical applications. Their multifunctionality, controllable features, and compatibility with biological environments position them as promising platforms for future development in areas such as tissue engineering, targeted drug delivery, biosensing, and regenerative medicine.

[1] M.R. de Sá et al., Chem. Select 10 (2025) 138168.
[2] X. Tan et al., J. Colloid Interface Sci. 699 (2025) 138168.
[3] H. Zhao et al., Int. J. Nanomed. 18 (2023) 2359.
[4] A. Hoppe et al., ACS Appl. Mater. Interfaces 6 (2014) 2865.

Figure 1. Micrograph of $MnSiO_3$ nanostructures (a) of $CoSiO_3$ (c) $Mn_{0.3}Co_{0.7}SiO_3CoSi$ (e) and map of elements (Mn, Co, O, Si) (b),(d), (f).

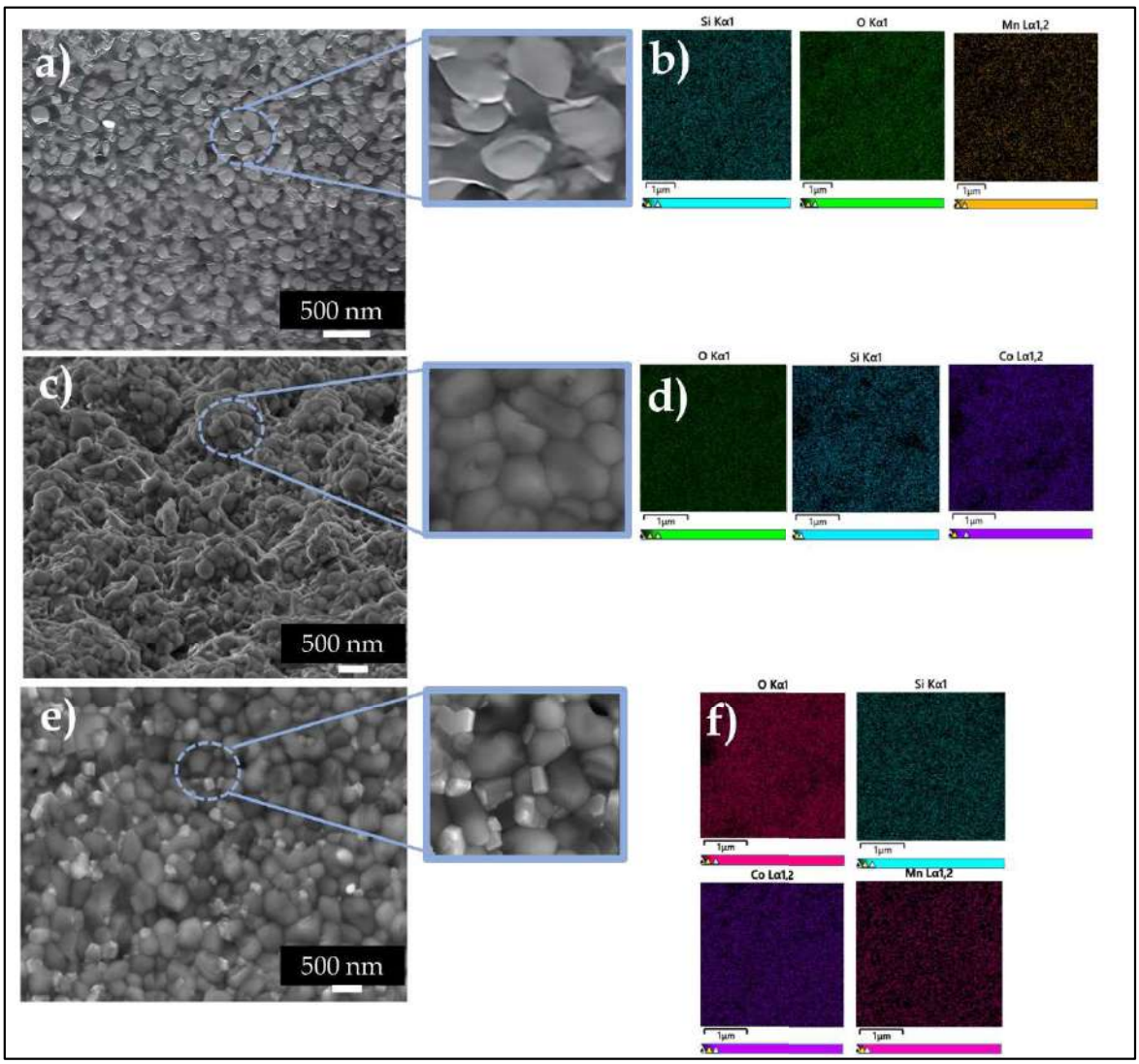

Temperature-Controlled Strategies for In Situ Analysis in Scanning Electron Microscopy

Arthur Francisco Carrapato Assis[1]*, Ana Beatriz Sorana de Araujo[1], João Marcos da Silva[1], Fabiano Emmanuel Montoro[1].

[1]Laboratório de Microscopia Eletrônica de Varredura e Duplo Feixe – Laboratório Nacional de Nanotecnologia (LNNano/CNPEM), Campinas-Brazil
*arthur.assis@lnnano.cnpem.br

The use of variable pressure and temperature in scanning electron microscopy (SEM) has become essential for analyzing specimens that are sensitive to high-vacuum environments and electron beam damage, particularly biological and polymeric samples. These conditions help minimize common artifacts associated with conventional SEM preparation [1]. Precise control of sample temperature and water content is critical not only for improving image quality and controlling relative humidity, but also for enabling or inhibiting water condensation and evaporation during analysis [2]. This capability allows the observation of dynamic processes, including chemical reactions and biological phenomena, such as stomatal movement in plant tissues, as demonstrated in Environmental SEM (ESEM) studies [3]. Low-temperature conditions aid in sample dehydration and help preserve structural integrity by preventing collapse. Moreover, temperature modulation during SEM analysis can reveal material behavior, making it especially valuable for studies involving soft matter. However, one of the main challenges in low-temperature SEM is the condensation of water on the sample surface during preparation, which can obscure fine structures or introduce artifacts. This study aims to develop and assess practical methodologies for implementing temperature variation in SEM analysis, focusing on both passive (e.g., thermal insulation and precooled holders) and active (e.g., Peltier and liquid nitrogen stages) cooling approaches. A key advantage of the proposed methods lies in their low cost and accessibility, in contrast to the high investment required for commercial cryo-SEM systems. Among the evaluated techniques is the Extended Low Temperature Method (ELTM) [4], which simultaneously lowers temperature and pressure, from atmospheric levels to ~200 Pa, enabling biological specimens to freeze in situ without structural collapse, thus preserving their native morphology. A Peltier cooling stage (Figures 1 and 2) is used to sustain low sample temperatures during SEM analysis, enabling subsequent metal coating and high-vacuum imaging without compromising structural integrity. An alternative cooling strategy uses a liquid nitrogen-cooled sample holder, where the specimen is immersed in a cryogenic bath followed by transfer into the SEM chamber. This method maintains low sample temperatures for sufficient durations to enable SEM imaging. As a future direction, this work proposes the design and implementation of a custom-built liquid nitrogen stage with temperature control capabilities, aiming to reach lower and more stable temperatures to expand the range of accessible materials and applications.

[1] Ensikat, H. J., & Weigend, M. (2013). Microscopy and Analysis, 27(6), 7-10.
[2] J.I. Goldstein et al., Scanning Electron Microscopy and X-ray Microanalysis, Plenum, New York, 1992.
[3] McGregor, J. E., & Donald, A. M. (2010, July). In Journal of Physics: Conference Series (Vol. 241, No. 1, p. 012021). IOP Publishing.
[4] Tihlaříková, E. et al. (2019). I. Scientific Reports, 9(1), 2300.
[5] This work was supported by LNNano/CNPEM.

Figure 1 – Thermo Fisher Peltier stage available in Scanning Electron Microscopy Laboratory in LNNano.

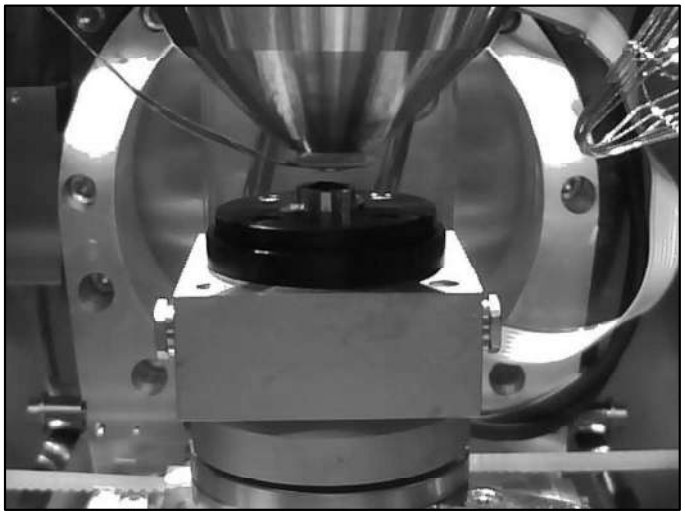

Figure 2 - Peltier stage and GSED (Gaseous Secondary Electron Detector) installed inside a Thermo Fisher Quanta 650 FEG Scanning Electron Microscope.

Toxicity of cold plasma processed coconut water *in vivo* models of *Artemia salina* and *Danio rerio*.

Jorge Henrique de Andrade Vieira[1]*, João Vinicus Sousa Fernandes[1], Ana Kamila Medeiros de Lima[1], Emilio de Castro Miguel[1], Thaiz Batista Azevedo Rangel Miguel[1].

[1]Biomaterials Laboratory, Department of Metallurgical Engineering and Materials and Analytical Center, Federal University of Ceará, Fortaleza, CE, Brazil.
*jorge.henriquejdd@alu.ufc.br

Conventional thermal methods can lead to undesirable changes in color and flavor, problems not observed in non-thermal processing such as cold plasma. Despite this, little is known about the molecular changes caused by cold plasma and its potential toxicity. This study aimed to evaluate the toxic potential of cold plasma-processed coconut water using *Artemia salina* and *Danio rerio* as *in vivo* models. Coconut water was processed by cold plasma at frequencies of 200, 400, 550, and 730 Hz, all for a duration of 15 minutes and 20 kV. The samples were exposed to the biological models at three concentrations: 10, 100, and 1000 $\mu g.mL^{-1}$. For *A. salina*, samples were exposed for 48 h to instar II nauplii, and statistical data were collected during the acute toxicity assay. For *D. rerio*, the OECD protocol No. 236 [1] was followed, embryos were exposed to the sample concentrations for 96 h, and their mortality and hatching results were recorded every 24 h. The images were taken in the first 24 h and at the end, 96 h. Additionally, average body and yolk sac sizes of the survivors were measured after the test. The results showed that coconut water at any of the tested concentrations did not cause a statistically significant number of deaths (below 20%), which would indicate toxicity for *A. salina*. This finding is like results seen by Miguel *et al*. (2021) [2], who demonstrated that non-thermally treated coconut water (ozone, cold plasma, and ultrasound) did not cause deaths in *A. salina* nauplii. Regarding the FET, the unprocessed coconut water sample did not show any evident toxic effect. Samples treated at 200 and 550 Hz were not toxic, and at 400 Hz, toxicity was observed only at the concentration of 100 $\mu g \cdot mL^{-1}$. At 730 Hz, toxicity was low at 10 $\mu g \cdot mL^{-1}$ and higher at 1000 $\mu g \cdot mL^{-1}$. The use of *D. rerio* embryos in toxicity testing of various agents is commonly reported in the literature for the investigation of different products; however, it has not yet been applied in toxicity tests of non-thermally processed food matrices. Studies have demonstrated the use of these fish embryos to investigate the toxicity of dyes, as shown by Motta et al. (2019) [3], and preservatives such as tert-butylhydroquinone (tBHQ) (Leonard et al. 2023) [4].

[1] OECD (2013), *Test No. 236: Fish Embryo Acute Toxicity (FET) Test*, OECD Guidelines for the Testing of Chemicals, Section 2, OECD Publishing, Paris, https://doi.org/10.1787/9789264203709-en.
[2] Miguel, T.B.A.R. et al. 2021. "Protective Effect of Natural and Processed Coconut Water by Non-Thermal Technologies Against Oxidative Stress in Brine Shrimp (Artemia Salina)." Food and Bioprocess Technology.
[3] Motta, Chiara Maria et al. 2019. "Effects of Four Food Dyes on Development of Three Model Species , Cucumis Sativus , Artemia Salina and Danio Rerio : Assessment of Potential Risk for the Environment*." *Environmental Pollution* 253(1333): 1126–35. https://doi.org/10.1016/j.envpol.2019.06.018.
[4] Leonard, Emily R et al. 2023. "Dietary Exposure to the Food Preservative Tert-Butylhydroquinone (TBHQ) Impairs Zebrafish (Danio Rerio) Survival , Growth , Organ Development, and Gene Expression in Nrf2a-Dependent and Independent Ways." *Food and Chemical Toxicology* 176(December 2022): 113788. https://doi.org/10.1016/j.fct.2023.113788

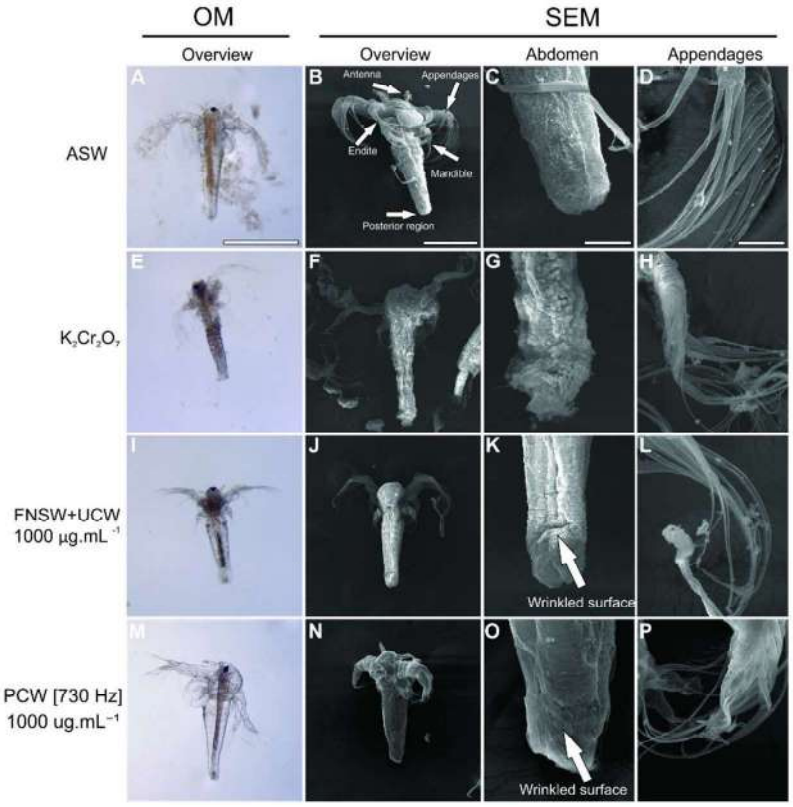

Fig. 1 – Optical Microscopy and scanning electron microscope in *A. salina* within 24h. **A, B, C,** and **D**: Artificial seawater (ASW) - negative control. Note that there is no morphological damage, with preservation of the characteristic structures of the nauplius (Antenna, appendages and abdomen). **E, F, G,** and **H**: Potassium dichromate (0.5 M) - positive control. Caused surface damage. It caused surface damage and deformation of the abdomen and appendages. **I, J, K,** and **L**: Unprocessed coconut water (UCW); similarities were observed with ASW. **M, N, O,** and **P**: Plasma-processed coconut water (PCW) at 730 Hz, with 1000 µg.mL-1; presented density of the digestive tract (Q); abdomen showed deformation on the wrinkled surface, but appendix showed normal development (O and P). Bar A, B, E, F, I, J, M and N - 500 µm. C, D,G, H, K, L, O and P – 50 µm.

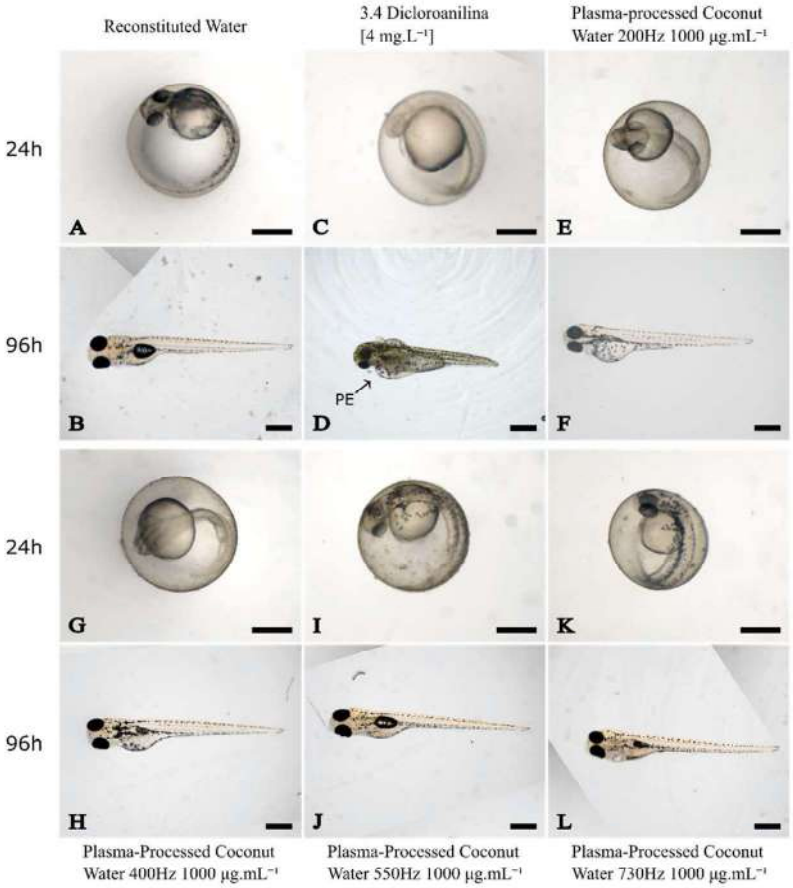

Fig. 2 - Steromicroscope in *Danio rerio* after 24h and 96h of exposition. **A** and **B** Negative Control (Reconstituted Water) in 24 h and 96h. Note that within 24h of exposure, the embryo has coherent development, there is the presence of a somite and a tail detachment. There was no developmental delay. After 96h, it is possible to observe the development of the heart, without the presence of edema. Correct pigmentation and size. **B** and **C.** Positive Control (3,4 dichloroaniline) in 24h and 96h. In the initial 24h, it is possible to observe that there was detachment of the cause and the presence of a somite, however there is a delay in development. However, at 96h, it is observed that the size of the larvae is smaller than that of the negative control, and there is the presence of pericardial edema (PE). **E**, **G**, **I** and **K.** Plasma-processed coconut water 200, 400, 550 and 730 Hz 1000 µg.mL^{-1} in 24 h for exposition; **F**, **H**, **J** and **K.** in 96 h. All plasma-processed coconut water tests resembled the negative control at 24h and 96h. Bar - 500 µm.

Ultrastructural Aspects of Melanosomes in *Sporothrix brasiliensis*

Marcos Vinicius Acylino Duarte Moreira[1]*, Luana Pereira Borba dos Santos[1], Rayane Gonçalves Pereira da Silva[1,2], Marcia Attias[3], Marcel Menezes Lyra da Cunha[1,2], Sonia Rozental[1].

[1]Laboratório de Biologia celular de Fungos, Instituto de Biofísica Carlos Chagas Filho/Universidade Federal do Rio de Janeiro, [2]Nucleo Multidisciplinar de Pesquisa UFRJ - Xerém em Biologia (NUMPEX-BIO) /Universidade Federal do Rio de Janeiro, Campus Duque de Caxias, [3]Laboratório de Ultraestrutura Celular Hertha Meyer, Instituto de Biofísica Carlos Chagas Filho/Universidade Federal do Rio de Janeiro.
*acylinovinicius@gmail.com

Melanin is a biological pigment with a well-established protective role against environmental stressors and is present across a wide range of organisms. In mammalian cells, melanin is synthesized and stored within specialized organelles known as *melanosomes*, which are localized in melanocytes [1]. Interestingly, several pathogenic fungi also exhibit intracellular structures associated with melanogenesis, suggesting the presence of compartments functionally analogous to melanosomes. *Sporothrix brasiliensis*, the principal etiological agent of sporotrichosis in Brazil, displays notable virulence that is closely linked to melanin production. However, the presence and characterization of melanosome-like structures in this fungal species remain insufficiently explored. The present study aimed to identify and characterize intracellular structures related to melanin biosynthesis in *S. brasiliensis*. Yeast-phase cells of *S. brasiliensis* were processed for transmission electron microscopy (TEM) to investigate these structures. Advanced electron microscopy techniques, including transmission electron tomography and focused ion beam-scanning electron microscopy (FIB-SEM), were employed for volumetric cellular analysis. TEM, in conjunction with tomography, enabled the visualization of cytoplasmic structures containing electron-dense material consistent with melanin, suggesting the existence of organelles analogous to mammalian melanosomes (Figure 1). FIB-SEM facilitated the sequential acquisition of entire cells, allowing three-dimensional reconstruction of the observed electron-dense organelles using IMOD software (Figure 2). This approach enabled detailed visualization of the structures, including their spatial distribution and organization. The structures exhibited an average diameter of 113.7 nm. These high-resolution techniques revealed not only the morphology of the electron-dense compartments but also their spatial relationships and potential interconnectivity, indicating a coordinated intracellular trafficking system. Our research group has extensive experience in the study of melanin in pathogenic fungi. These new findings are consistent with previous observations of melanin-producing and storing compartments in *Sporothrix schenckii* and *Fonsecaea pedrosoi* [2]. The data suggest that *S. brasiliensis* possesses regulatory mechanisms for melanogenesis that resemble those observed in mammalian cells. In conclusion, our study demonstrates that *Sporothrix brasiliensis* possesses intracellular organelles with both morphological features and size parameters comparable to those of human melanosomes, supporting the hypothesis that complex intracellular processes regulate fungal melanogenesis [3]. The integration of transmission electron microscopy (TEM), electron tomography, and focused ion beam-scanning electron microscopy (FIB-SEM) was instrumental in uncovering these structures, significantly advancing our understanding of fungal cell biology and opening new avenues for research into the mechanisms underlying fungal virulence.

[1] Le L et al. *Integr Comp Biol*. 2021.
[2] Franzen AJ et al. *J Struct Biol*. 2008.
[3] This research was supported by FAPERJ, CNPq and CENABIO/UFRJ (Brazil).

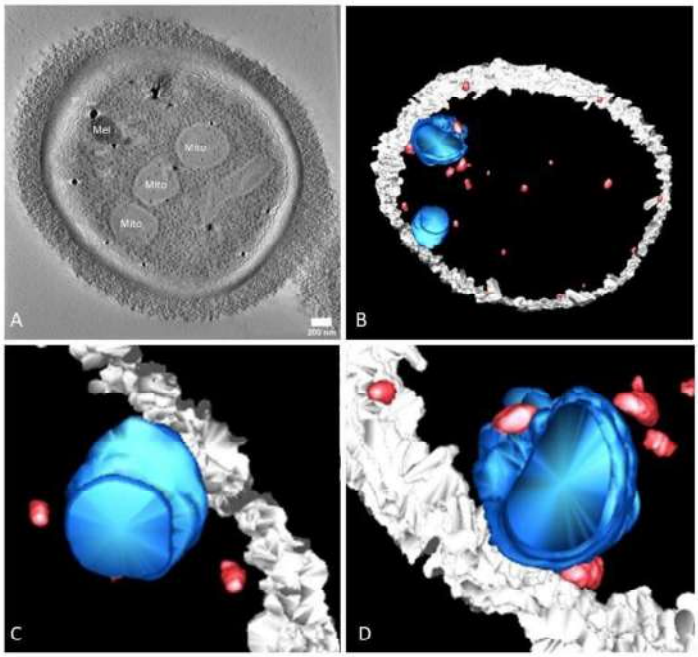

Figure 1. TEM analysis and 3D reconstruction of *S. brasiliensis* using IMOD software. (A) Tomography showing fibrillar cell wall, plasma membrane (MP), melanosome (Mel) and mitochondrion (Mito). (B) 3D reconstruction with melanosomes (blue), vesicles (red), and plasma membrane (white). (C–D) Magnifications of melanosomes near the membrane, highlighting spherical shape, the relationship with the membrane invaginations, and interaction with vesicles. Scale bar: 200 nm.

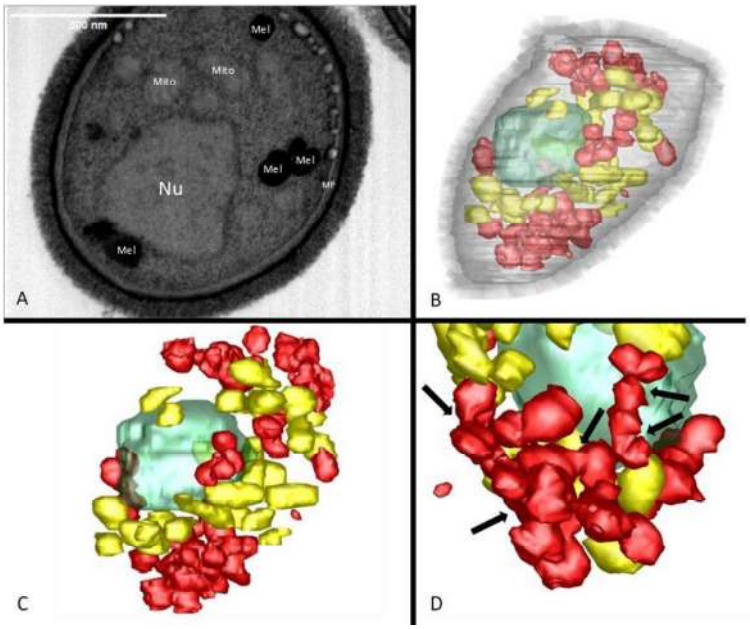

Figure 2. FIB-SEM analysis with 3D reconstruction using IMOD. (A) Ultrathin slice of *S. brasiliensis* showing melanosomes (Mel), mitochondria (Mito), nucleus (Nu) and plasma membrane (MP). (B) 3D model highlighting melanosomes (red), mitochondria (yellow), and translucent nucleus (green) and external contour in gray (plasma membrane and fibrillar wall). (C–D) Views of the 3D model without membrane and wall, emphasizing organelle organization around the nucleus, proximity between melanosomes and possible connections among them indicated by the black arrows. Scale bar: 200 nm.

Use of Hexamethyldisilazane (HMDS) in the Preparation of *Podocnemis expansa* Embryos for Scanning Electron Microscopy

Marcela dos Santos Magalhães[1,3]*, Lucas Castanhola Dias[2], Carlos Eduardo B. de Moura[3].

[1]Universidade Federal do Amazonas, [2]Instituto Nacional de Pesquisas da Amazônia, [3]Universidade Federal Rural do Semi-árido
*marcelasmbio@gmail.com

Preparation of a biological sample for scanning electron microscopy (SEM) involves chemical fixation, dehydration, and drying prior to coating the sample with a thin layer of conductive material, such as gold [1]. Critical point drying is the commonly used drying technique, which involves the passage of liquid CO_2 through the sample at a determined temperature and pressure. Although it reduces the chance of distortion in cell morphology, it can pose a potential physical risk to small and fragile samples [1]. As an alternative, hexamethyldisilazane (HMDS) has been employed as a chemical drying agent, offering advantages such as simplicity, speed, lower cost, and reduced need for specialized equipment [2, 3]. There are reports that HMDS drying is preferable for amphibian embryos, as it effectively preserves fragile structures such as gills and cilia [4]. In this context, we used HMDS as a drying agent to describe the early embryonic development of *Podocnemis expansa*, using embryos collected at the Research and Conservation Center for Aquatic Mammals and Chelonians, Amazonas (CEUA approval nº 025/2013-INPA). *Podocnemis expansa* embryos up to 12 days of incubation were fixed in 2.5% glutaraldehyde solution, post-fixed in 4% osmium tetroxide solution, washed in buffer, and dehydrated in a graded ethanol series. The embryos were dried in HMDS for 30 seconds (twice), then mounted on aluminum stubs, coated with a 60 nm gold layer (Figure 1), and imaged using a LEO 435 vP scanning electron microscope. At three days of incubation, it was possible to clearly identify the amniotic and vitelline membranes, head process, and presumptive pericardial region (Figure 2A). At 7 and 12 days of development, the head region appeared wrinkled, but denser regions such as developing limbs, pericardial region, somites, and tail were well preserved morphologically (Figures 2B, C). Chelonian embryonic tissues are softer, with lower tissue stiffness and little mineralized extracellular matrix in the early stages, making them susceptible to deformation during drying [5]. However, the use of HMDS as a drying technique proved to be an efficient alternative to critical point drying, as it was faster and more economical, while preserving the morphological integrity of important regions for complementing the description of *Podocnemis expansa* embryonic development.

[1] N.H. Hazrin-Chong, M Manefield, J Microbiol Methods. (2012) 90(2):96-9.
[2] P. Oshel, Microscopy Today. (1997) 16.
[3] J. Araújo et al., Journal of electron microscopy. (2003) 52 4, 429-33.
[4] D. Zurita-Paredes et al., J. Morpho. (2025) 286.
[5] J. Gibbons et al., J. Vis. Exp. (2019) 150.
[6] This research was supported by CNPq (Brazil).

Figure 1. Embryo mounting on aluminum supports after chemical drying, showing the embryo coated with gold sputtering.

Figure 2. Scanning electron micrographs of *Podocnemis expansa* embryos prepared by chemical drying. A- 3 days of incubation, ventral view. B- 7 days of incubation, lateral view. C- 7 days of incubation, lateral view. am: amniotic membrane; vm: vitelline membrane; hp: head process; pr: pericardial region; h: head; y: eye, arrow: pharyngeal slits, arrowhead: alb: anterior limb bud; s: somites; t: tail; lb: limb.

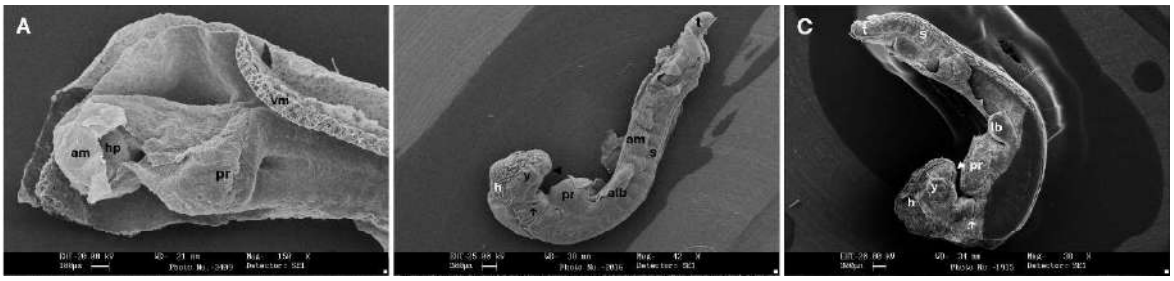

Use of Natural Deep Eutectic Solvents (NaDES) in the Cryopreservation of Fibroblast Cells in the L-132 Cell Line

Pedro Almeida de Jesus da Rocha[1,2]*; Lívia Marques Ferreira[1,2] ;Marina Arantes Radicchi[1,2] :Victor Carlos Mello[1,2,] ; Sônia Nair Báo[1].

[1] Laboratory of Microscopy and Microanalysis, Department of Cell Biology, Institute of Biological Sciences, University of Brasília, Brasília 70910-900, DF, Brazil;

[2] Cooil Cosmetics LTDA, Brasília, DF, Brazil;

*rocha.ajrpedro@gmail.com

Cryopreservation has proven to be effective for long-term cell storage. However, the preservation of tissues and organs remains a significant challenge, mainly due to cellular damage caused by low temperatures, which can result in deep subzero injuries [1]. The use of dimethyl sulfoxide (DMSO) as a cryopreservation agent is an established model, particularly for cell cryopreservation. However, this compound presents high rates of cytotoxicity and ecotoxicity [2,3,4]. To overcome such challenges, the search for less toxic and more sustainable alternatives has led to the exploration of solvents, such as those belonging to the Natural Deep Eutectic Solvents (NaDES) class[5,6]. This category includes compounds mimicking those produced by organisms adapted to extreme environmental conditions and consists of a solution involving a hydrogen bond donor and acceptor species [7]. They exhibit tunable properties such as pH, melting and boiling points, and viscosity. Among their advantages, NaDES presents low ecotoxicity, high versatility, and remarkable innovative potential [8]. Human fibroblast cells of the L-132 lineage were used as the experimental model. Cells were divided into two groups: one frozen with 5% DMSO and 95% fetal bovine serum -FBS- (control), and the other with a 0.4% betaine–levulinic acid –Bet LeA- solution in a 1:2 ratio (treated). After thawing, cells were cultured in DMEM supplemented with 10% fetal bovine serum, incubated at 37°C with 5% CO_2 for 7 days. Subsequently, samples were seeded on 18×18 mm coverslips and fixed with Karnovsky fixative, post-fixed using osmium tetroxide, then dehydrated with serial growing solutions of acetone (30%-100%) for 15 minutes, dried to critical point, and finally, metallized for observation under a scanning electron microscope (SEM-JEOL JSM 7001F). As seen in the micrographs (Figure 1A and 1B), after thawing, cells in the control group exhibited cytoplasmic extensions, epithelial-like morphology, and certain axis symmetry. In contrast, the following micrographs (Figure 1C and 1D) reveal a markedly different morphology in treated cells, with fewer extensions, and asymmetric axes. Furthermore, treated group images show a more flattened morphology, possibly indicative of compromised original cell functions, such as metabolism and resistance to external agents, along with loss of anchorage dependence, contact inhibition, colony formation in semisolid media, and reduced growth factor dependence [9]. Therefore, these

findings suggest unsuitability for experimental applications, as the morphology of the treated group diverged significantly from the control group. The freezing method tested here is not viable and the underlying cause of the altered morphology should be investigated—whether due to environmental adaptation, membrane or cytoskeletal damage, or intracellular accumulation of compounds that drive such changes. These findings emphasize the need to refine and optimize cell cryopreservation techniques to achieve better efficiency and more sustainable protocols in biomedical applications.

References:

[1] Khaydukova IV et al. Int J Mol Sci, 2016.
[2] CF Brayton, *Cornell Vet.*, 76 (1986) 61.
[3] K Kim, SE Lee, *Chemosphere*, 270 (2021) 129405.
[4] J Galvao et al., *FASEB J.*, 28 (2014) 1317.
[5] M Vieira Sanches et al., *Environ Sci Pollut Res Int.*, 30 (2023) 17268.
[6] FJ Gomez et al., *Anal Chim Acta*, 936 (2016) 91.
[7] L Schuh et al., *Molecules*, 28 (2023) 7653.
[8] E Chevé-Kools et al., *Green Chem.*, (2025) Epub ahead of print.
[9] PK Gupta et al., *Fundamentals of Toxicology*, Academic Press, San Diego, 2016.
[10] This research was supported by FAPDF, CNPq, and FINEP.

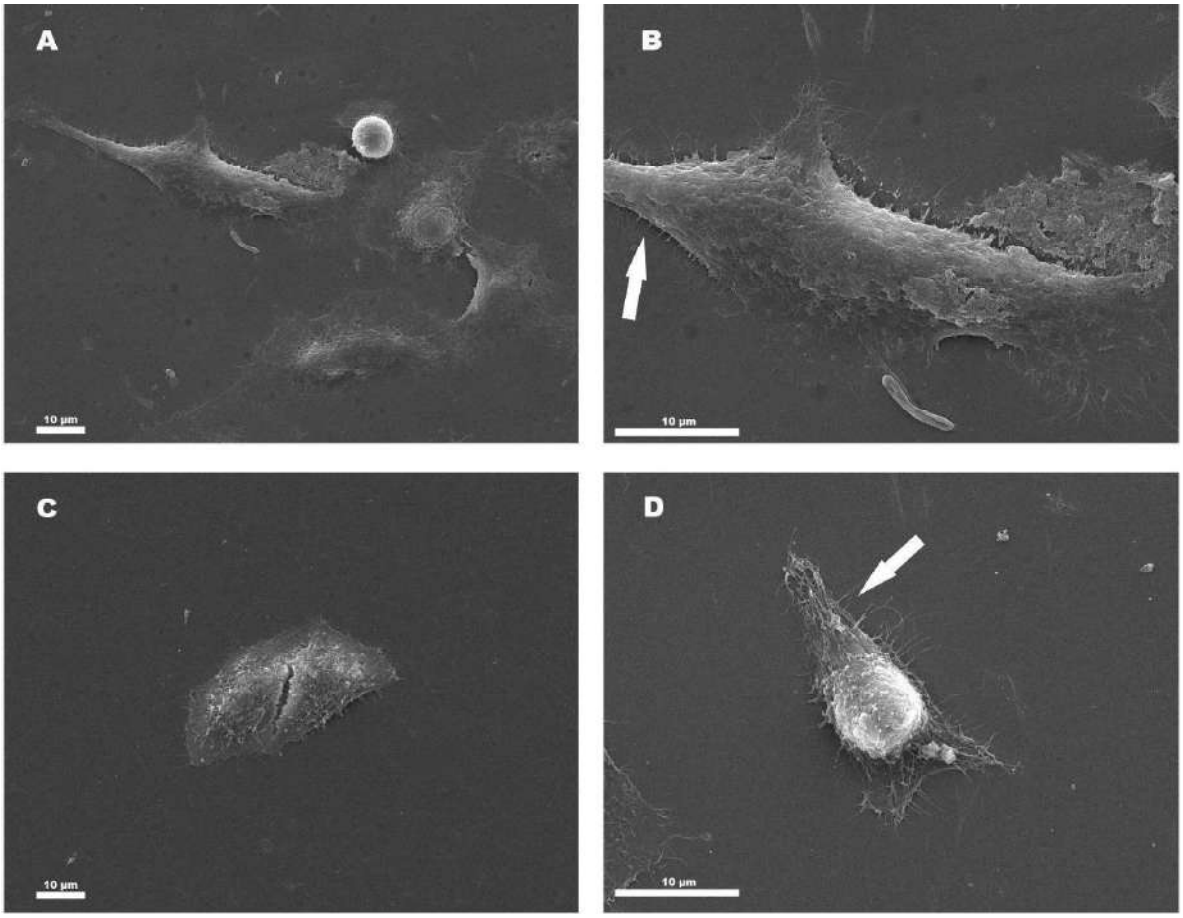

Figure 1. Human fibroblast cells of the L-132 cell line, 7 days after thawing. From left to right, top to bottom, there are: A, B- Control 1,000x and 1,500x; C, D- Treated 1,000x and 1,500x. Arrows indicate cellular extensions.

Use of Scanning Electron Microscopy in the Investigation of Atmospheric Particulate Material Contamination in *Crassostrea rhizophorae* Shells

Thales Augusto Nordi [1], Luisa Helena Pimenta [1], Mariana V. Carvalho [1], Luis Felipe de Almeida Duarte [2], Camilo Dias Seabra Pereira [2], Helen Sadauskas-Henrique[3], Juliana dos Santos Pereira[3], Iara Costa Souza [1], Marisa Narciso Fernandes [1]

[1] Department of Physiological Sciences, Federal University of São Carlos, São Carlos, São Paulo, Brazil, [2] Department of Marine Sciences, Federal University of São Paulo, São Carlos, São Paulo, Brazil. [3] Laboratory of Ecophysiology and Biochemistry of Aquatic Organisms, Santa Cecília University, Graduate Program in Environmental Science and Technology, R. Oswaldo Cruz, 277, Boqueirão, 11045-907 Santos, São Paulo, Brazil.

E-mail: thalesnordi@gmail.com

Atmospheric pollution generated by steel industries contains aerosols with particulate metallic material which, upon settling in soils and aquatic ecosystems, contaminates natural habitats and threatens ecosystem integrity [1]. Oysters, through their biomineralization capacity producing calcium carbonate polymorphs, such as aragonite and calcite, incorporate these metals into their shell matrix, thus functioning as bioindicators of environmental quality [2]. In Vitória (ES), the Tubarão Industrial Complex is a significant source of such emissions, with potential impacts on benthic organisms inhabiting nearby coastal and estuarine areas [3]. This study aimed to investigate the presence and incorporation of metals and metalloids in the shells of *C. rhizophorae* after chronic exposure to different concentrations of settleable atmospheric particulate matter (SePM). Additionally, the study evaluated the potential of this species' shells as sensitive bioindicators of environmental contamination by SePM, highlighting their ecological relevance in environmental monitoring programs. The SePM was collected at Ilha do Boi, located in Vitória (ES), while specimens of *C. rhizophorae* (n = 360) were obtained from red mangrove roots in Cananéia, São Paulo (SP). After an acclimation period under controlled conditions, oysters were exposed to SePM for 30 days at four experimental concentrations (0; 0.01; 0.1; 1.0 $g \cdot L^{-1}$), followed by a 30-day depuration period in particle-free seawater. Structural and elemental characterization of the shell layers was performed using scanning electron microscopy (SEM) equipped with backscattered electron diffraction (EBSD), low field detector (LFD), and energy-dispersive X-ray spectroscopy (EDS). SEM analysis confirmed the incorporation of metallic elements such as Al, Mn, Ba, Zn, and Fe. These elements, known to substitute Ca^{2+} during biomineralization or to naturally occur in shell composition, were found at elevated levels [4]. Time-to-compression tests indicated that oyster shell structure was affected and became more fragile with increasing exposure. The results strongly reinforce the effectiveness of *C. rhizophorae* shells as bioindicators of environmental pollution associated with SePM [5].

[1] Kumar P, Imam B. Air quality and its impact on the urban environment. Urban Ecol. 2020;185–200.

[2] Duarte L, Pereira CD, Silva M, et al. Settleable atmospheric particulate matter harms a marine invertebrate: integrating chemical and biological damage in a bivalve model. Sci Total Environ. 2023;881:163380.

[3] Souza RC, Machado EC, Ferreira TO, et al. Different trophodynamics between two proximate estuaries with differing degrees of pollution. Sci Total Environ. 2021;770:144651.

[4] Stewart BA, Roper DS, Atalah J, et al. Metal pollution as a potential threat to shell strength and survival in marine bivalves. Sci Total Environ. 2021;755:143019.

[5] Financial support: FAPESP Proc 2019/08491-0; Proc 2024/17923-9.

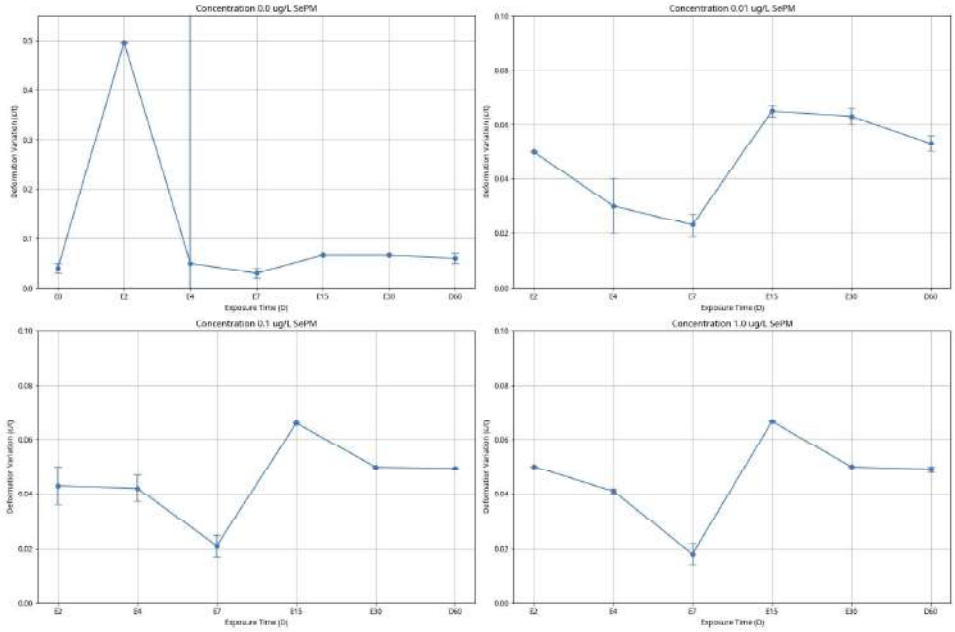

Figure 1. Graphics deformation over time (ε/t) during the exposure periods in days (D) to SeMP at different concentrations 1, 2, 3, 4

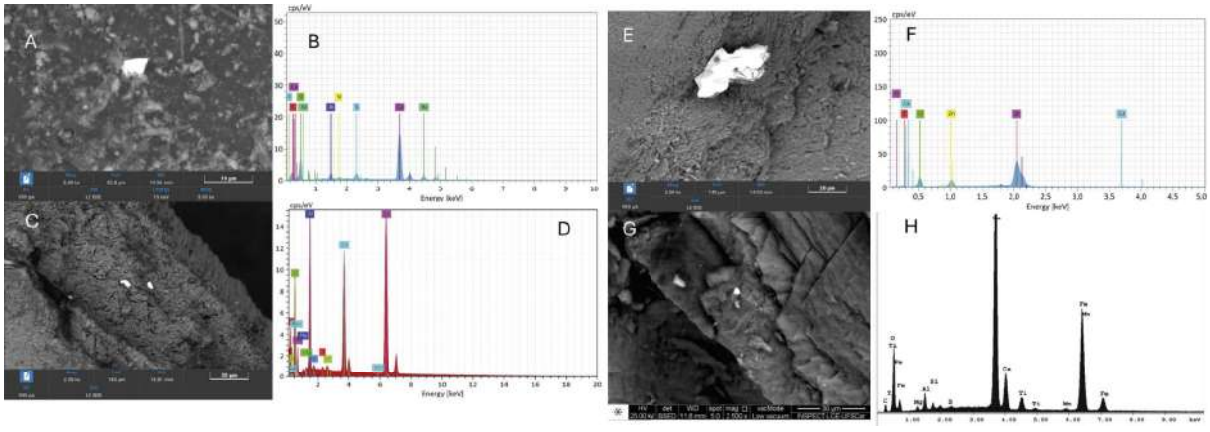

Figure 2. Scanning Electron Microscopy (SEM)of the *C. rhizophorae* oyster shell. (A) Micrograph of an SePM particle, T60, exposure to 1 g·L−1 ; (B) EDS spectrum of Al, Ba, Ca, C,O, S and Si. (C) Micrograph of an SePM particle, T30, exposure to 0.1 g·L−1; (D) EDS spectrum of Al, Fe, Mn, Mg, Ca, Cl, O, S, Cl and Na. (E) Micrograph of an SePM particle, T7, exposure to 1 g·L−1; (F) EDS spectrum of Zn, Zr, Ca, C and O. (G) Micrograph of an SePM particle, T4, exposure to 1 g·L−1; (H) EDS spectrum of Al, Fe, Mn, Ti, Ca, C, O, S and Si.

Use Of The New Experimental Model *Metarhabditis blumi* In *In Vitro* Assays To Test New Anthelmintic Drug Candidates

Aline Ferreira Santos Delmondes[1]*, Ander Castello-Branco Santos[1], Julia Rodrigues Genuncio[1], Silvia Amaral G. Da-Silva[2] and Eduardo José Lopes-Torres[1]

[1] Romero Lascasas Porto Helminthology Laboratory, Department of Microbiology, Immunology and Parasitology, State University of Rio de Janeiro, Rio de Janeiro, Brazil.
[2] Laboratory of Parasitic Immunopharmacology, Department of Microbiology, Immunology and Parasitology, State University of Rio de Janeiro, Rio de Janeiro, Brazil.
* alinedelmondes90@gmail.com

Helminth infections represent a significant global health challenge, particularly due to the increasing resistance to currently available anthelmintic drugs. On the other hand, these organisms have garnered growing scientific interest as potential sources of promising therapies for dysregulated inflammatory diseases [1,2]. Nematodes of the genus *Metarhabditis* are associated with parasitic otitis in cattle breeds such as Gir and Indubrasil, a condition that can severely affect the animal's nervous system, potentially leading to death [3]. In addition, a case of parasitic otitis in humans has been reported in a rural worker in Germany [4]. Current treatment and control strategies for this pathology remain limited. In light of the above, our study aimed to establish *Metarhabditis blumi* as a potential in vitro model for the investigation of novel compounds with anthelmintic activity. To this end, L3 larvae and adult worms were treated with albendazole (16 µM) and ivermectin (2.5 µM) in liquid NGM culture medium for 24 hours. Parameters such as motility and mobility were assessed through video microscopy. Morphological and ultrastructural analyses were performed following chemical fixation, using light microscopy (LM) and scanning electron microscopy (SEM). Results demonstrated that ivermectin was more effective than albendazole in treating both L3 and adult stages. LM images revealed structural changes in adult nematodes, including alterations in the isthmus, esophageal bulb (Fig. A-B), testicles (C-D) and cuticle. SEM images showed drug-induced ultrastructural changes (Fig. E-F). No significant morphological or ultrastructural alterations were observed in L3 larvae. When compared to previous studies using the established *Caenorhabditis elegans* model, *M. blumi* exhibited higher resistance to both albendazole and ivermectin. We conclude that *M. blumi* is a promising experimental model for a variety of biological studies and is feasible for future drug discovery assays. The use of *M. blumi* as a parasitic nematode model may offer a more representative alternative to the conventional free-living *C. elegans* model, particularly for evaluating anthelmintic drug efficacy. In addition, we are conducting complementary analyses, such as the use of resazurin to evaluate the redox potential in order to assess the viability of the nematode at different concentrations of the reference drugs, as well as histological evaluations and transmission electron microscopy (TEM), following exposure of the experimental model, in order to further characterize the therapeutic and toxic effects. We acknowledge the funding support for this research [5].

[1] A.R. Burns et al. Nat. Commun. 2015;6: 7485.
[2] K. E. Lothstein et al., Trends Mol Med. 2021;27(4): 345-64.
[3] M.E. Caracciolo et al. Rev Bras Parasitol Vet. 2024;33(4): e019024.
[4] M. Teschner et al., J. of Clin. Microbiol. 2014;52(5):1793-5.
[5] This research was supported by CAPES - Scholarship; Faperj – JCNE; CNPq (Brazil) - Universal.

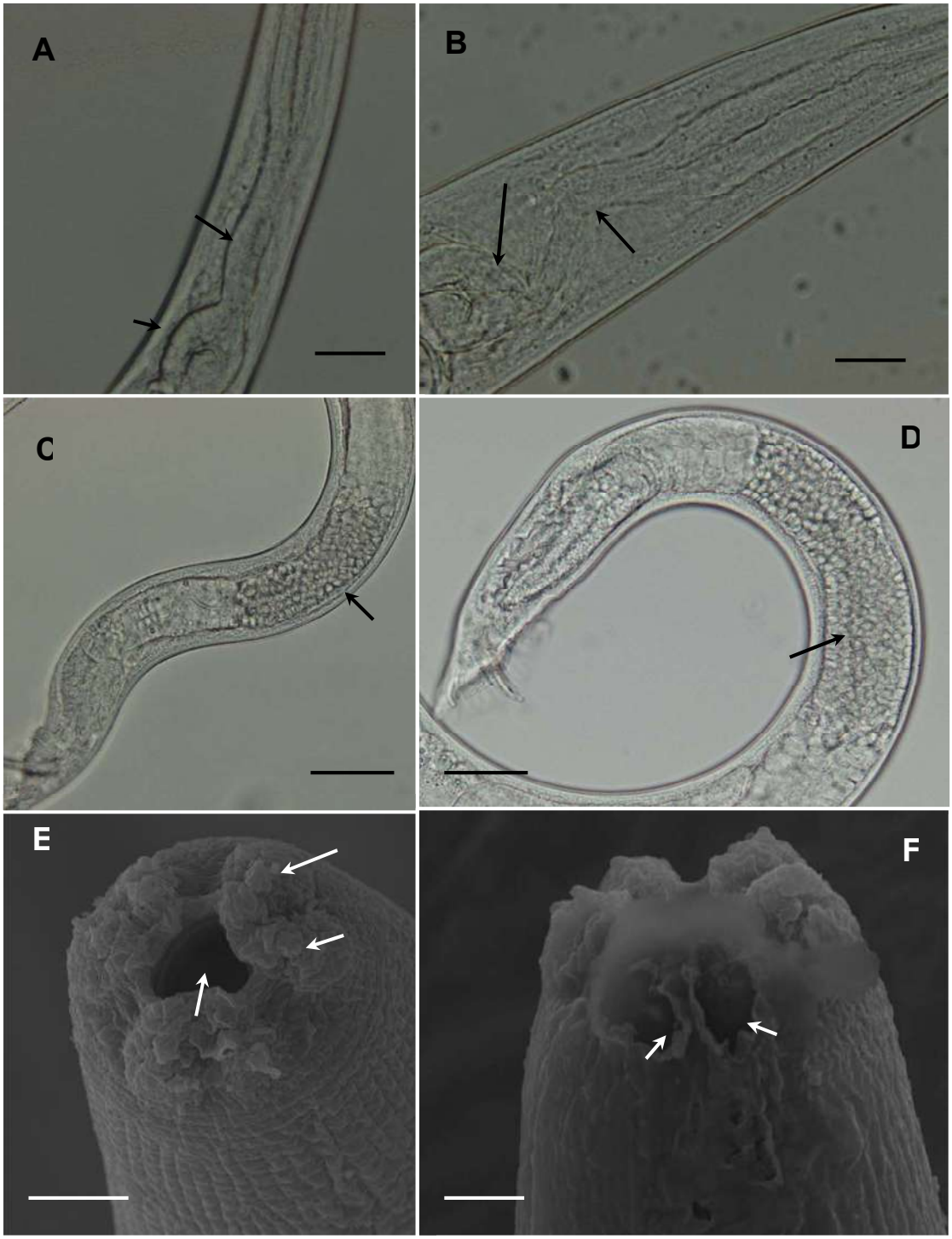

Figure: Light microscopy of Metarhabditis blumi after 24 hours of treatment. **A -** Control group showing the anterior region of the body, with a normal esophageal bulb and isthmus (arrows). **B -** Nematodes treated with ivermectin, showing alterations in the anterior region of the body, including the esophageal bulb and isthmus (arrows). **C -** Control group showing normal testicles of nematodes males, in the mid-body region (arrow). **D -** Nematodes treated with albendazole, highlighting alterations in the testicles, in nematodes males, in the mid-body region (arrow). Scanning Electron Microscopy of adult *M. blumi* worms after 24 hours of treatment. **E -** Control group showing the anterior region, including the oral opening and cephalic papillae (arrows). **F -** Treated with albendazole, showing changes in the anterior region, particularly in the cephalic papillae (arrows).

Scale bars: A-B: 20 µm; C-D: 50 µm; E: 3 µm; F: 2µm.

Transmission electron microscopy (TEM) applied to biological samples, including all techniques associated with TEM, such as STEM, EDS, in situ experiments, and electron tomography

Morphological Changes in Vero Cells Infected with Mayaro Virus: An Electron Microscopy Approach

Igor Pinto Silva da Costa[1*], Maycon Douglas do Nascimento Garcia[1], Marcos Alexandre Nunes da Silva[1], Vivian Neuza dos Santos Ferreira[1], Debora Ferreira Barreto-Vieira[1]

[1] Laboratory of Viral Morphology and Morphogenesis, Oswaldo Cruz Institute, Oswaldo Cruz Foundation – Fiocruz, Rio de Janeiro, RJ, Brazil.
*igorcosta@aluno.fiocruz.br

The Mayaro virus (MAYV), a member of the *Togaviridae* family and *Alphavirus* genus, is responsible for causing Mayaro fever, a disease characterized by fever, headache, myalgia, and persistent arthralgia that can last for months post-infection [1]. MAYV measures approximately 70 nm in diameter, with a positive-sense single-stranded RNA genome encapsulated within an icosahedral nucleocapsid [2]. Transmitted primarily by *Haemagogus* mosquitoes, the virus has the potential to infect *Aedes* spp. mosquitoes, raising concerns about its urbanization, particularly in the Brazilian Central-West region, where increased contact between sylvatic vectors and humans has been observed [3]. This study employs transmission electron microscopy (TEM) to investigate the ultrastructural features of Vero cells infected with MAYV. The aim is to elucidate viral morphology, replication cycle stages, and cellular modifications during infection. Infected Vero cells were analyzed at various post-infection time points (24, 48, and 72 hours), including the application of negative staining techniques to visualize viral particles with high resolution. For TEM analyses, the samples were prepared in accordance with the standard protocol [4]. Results demonstrated prominent cytopathic effects beginning at 48 hours post-infection, with subtle morphological alterations observed as early as 24 hours. As infection progressed, a significant increase in cell death was evident. TEM images revealed changes in cell morphology, organelles, and membrane integrity, along with the presence of viral particles in intercellular spaces (Figure 1). At 72 hours, notable features included clusters of nucleocapsids, alterations in the cytoskeleton, accumulations of virus-like particles at membrane sites suggestive of budding zones, and an important increase in both the number and size of lipid droplets in the cytoplasm was observed compared to uninfected controls. The characteristic icosahedral shape and the viral envelope were confirmed through negative staining, providing clear morphological confirmation of the virus. These findings provide detailed ultrastructural insights into MAYV infection in Vero cells, highlighting the virus's morphological features, replication sites, and induced cellular modifications, thereby contributing significantly to a better understanding of its pathogenic mechanisms and cellular interactions during infection [5].

[1] R.E. Marques et al., Current challenges in the Discovery of treatments against Mayaro fever. Expert. Opin. Ther. Targets. (2024), 28(5):345-56.
[2] R. Chen et al., ICTV Virus Taxonomy Profile: Togaviridae. J. Gen. Virol. (2018), 99(6), 761-2.
[3] L.L.L. Wei, R. Tom, Y.C. Kim, Mayaro Virus: An Emerging Alphavirus in the Americas. Viruses. (2024), 16(8), 1297.
[4] O.M. Barth, M.A.N.d Silva, D.F. Barreto-Vieira, Low Impact to Fixed Cell Processing Aiming Transmission Electron Microscopy. Mem. Inst. Oswaldo Cruz (2016), 111, 411-3.
[5] This research was supported by CNPq and FAPERJ (Brazil).

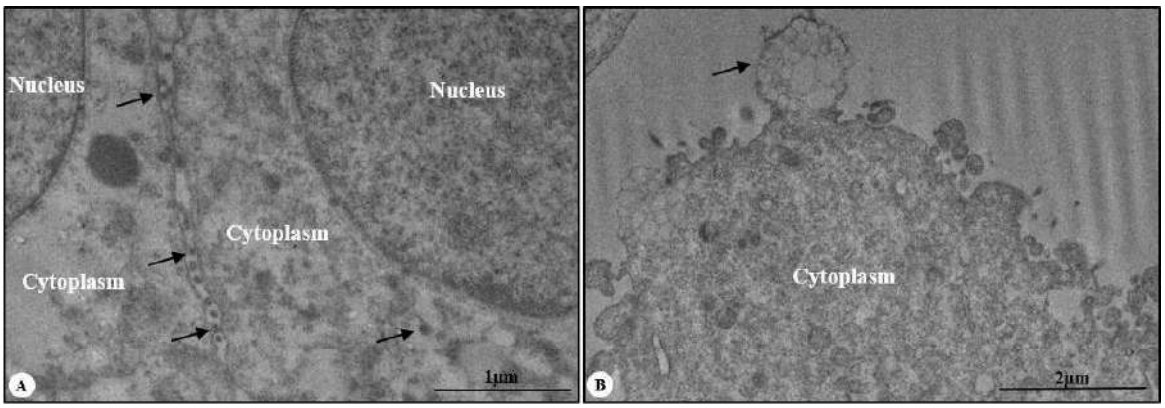

Figure 1. TEM image of Vero cells at 48 hours post infection. A) Viral particles (arrows) located in the space between the membranes of two adjacent cells, an event necessary for the formation of syncytia. B) Cytopathic effects manifested as deformations in the cellular membrane (arrow). (MOI = 0.01)

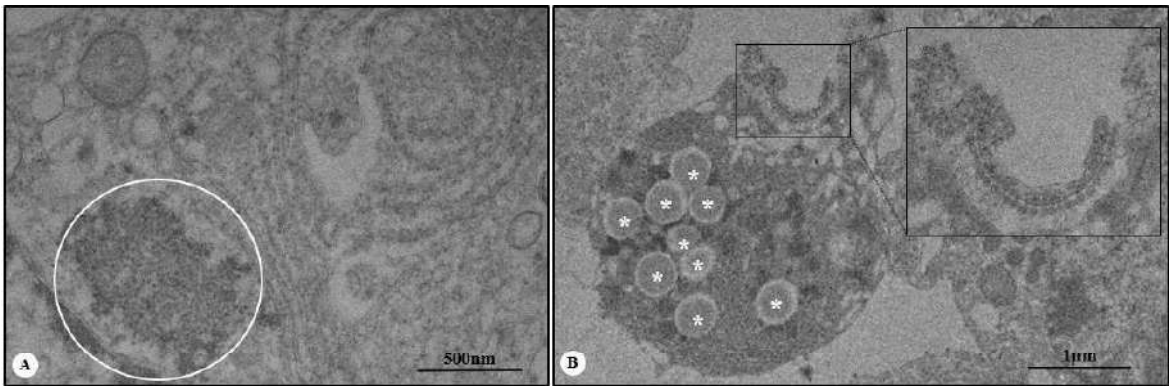

Figure 2. TEM image of Vero cells at 72 hours post infection. A) Area with a high number of nucleocapsids (circle). B) The infected cell displays numerous lipid bodies (*) and a possible membrane domain responsible for viral particle budding (inset). (MOI = 0.01)

Transmission Electron Microscopy Applied to the Study of Eosinophilic Diseases

Rossana C. N. Melo

Laboratory of Cellular Biology, Department of Biology, Federal University of Juiz de Fora, UFJF, Juiz de Fora, MG, Brazil. Email: rossana.melo@ufjf.br

Eosinophils, cells from the innate immune system, have central functions in the pathogenesis of numerous diseases. Eosinophilic diseases or eosinophil-associated diseases (EADs) are characterized by the presence of eosinophil-rich inflammatory infiltrates and/or extensive extracellular deposition of eosinophil-derived proteins, resulting in clinically relevant organ pathology. EADs encompass a broad spectrum of diseases of different etiologies including allergies, gastrointestinal disorders, dermatoses, hematological malignancies, infections, and tumors. Herein, I will discuss how the application of conventional transmission electron microscopy (TEM), in combination with quantitative assessments (quantitative TEM), molecular imaging (immunoelectron microscopy), and three-dimensional electron tomography, has generated important insights into the functional activity of eosinophils during EADs. I will discuss basic eosinophil biology addressing the main processes involved in the release of eosinophil products and how to distinguish between different modes of secretion with the application of TEM. The ultrastructural changes of activated eosinophils undergoing secretion as well as how these alterations can be quantitated will be presented.

Grant support: CNPq (Brazil) 307270/2022-0 and 409301/2023-0; and Fapemig APQ-00754-23 (Brazil).

Beyond Diffraction: EELS as a Quantitative Probe for Electron Beam Damage in Protein Crystals

Marcelo A. de Farias[2], Luelc S. Costa[1*], Marin van Heel[1], Jefferson Bettini[1], Rodrigo V. Portugal[1]

[1] Brazilian Nanotechnology National Laboratory / CNPEM, Campinas, SP, Brazil
[2] Oregon Health & Science University (OHSU), 3181 S.W. Sam Jackson Park Road, Portland, Oregon.
*rodrigo.portugal@lnnano.cnpem.br

Transmission electron microscopy (TEM) inherently subjects specimens to radiation damage caused by the interaction with the electron beam. While this damage is often negligible for hard materials, it imposes a fundamental limitation for achieving atomic resolution in organic and biological samples[1]. Similar to other organic compounds, biological macromolecules suffer irreversible changes after beam exposure, as the excitation of electrons can lead to permanent chemical bond breakage and alterations in molecular structure. Electron-beam damage in proteins has been studied for over 40 years, and various strategies have been proposed to mitigate it, including low-dose imaging techniques, cryogenic conditions, specimen encapsulation, and optimization of beam parameters such as energy, diameter, and imaging mode. Electron diffraction in TEM has been widely used to assess radiation damage in protein crystals by tracking the decay of diffraction spot intensities over time[2]. These patterns arise from Bragg diffraction, which depends on the periodicity of the crystal lattice. As irradiation progresses, damage manifests as fading of diffraction spots, which reflects a loss of crystallinity and long-range order. As a result, electron diffraction may not be sufficient as a standalone or standardized method for quantifying radiation damage, especially because it convolves multiple damage mechanisms. In this study, we propose the use of electron energy loss spectroscopy (EELS) as a complementary approach to evaluate electron beam-induced damage in proteins. EELS is a powerful technique capable of probing both atomic structure and, more importantly, the chemical and electronic properties of a sample. It is highly sensitive to light elements such as carbon, nitrogen, and oxygen. The development of new substrates for TEM grids is fundamental not only to propose new methodologies but also to achieve new results. The production of ultra-thin TiSi films as substrate for TEM grid opens a new scenario to the spectroscopy of carbon using TEM. Once these grids are carbon free, EELS measurement is free from the carbon information of the TEM carbon substrates. Besides that, common carbon spectrum with no carbon information from TEM carbon substrates must be acquired in holes, implying that the sample must present at least one dimension large enough to be found on the hole. For this reason, the use of TiSi films on Cu grids (Cu/TiSi) as TEM grid for spectroscopy of carbon enables the analysis of samples as small as proteins due the presence of continuous TiSi film throughout the grid. Through EELS, it becomes possible not only to directly detect damage to protein molecules but also to quantitatively assess changes in specific chemical bonds. We also introduce a protocol for quantifying radiation damage in three-dimensional protein crystals and discuss the limitations of relying solely on electron diffraction. Catalase was selected as a model biological crystalline sample. Our methodology includes acquisition of electron diffraction patterns, spot selection, and data normalization, enabling comparison between different crystals. Diffraction data were obtained for accumulated doses up to 100 e^{-} $Å^{-2}$, with resolution spots ranging from 1.0 to 3.4 Å.

[1] Garman EF, Weik M. Curr Opin Struct Biol. 82 (2023):102662.
[2] K. Naydenova, A. Kamegawa, M. J. Peet, R. Henderson, Y. Fujiyoshi, C. J. Russo Ultramicroscopy 237 (2022) 113512

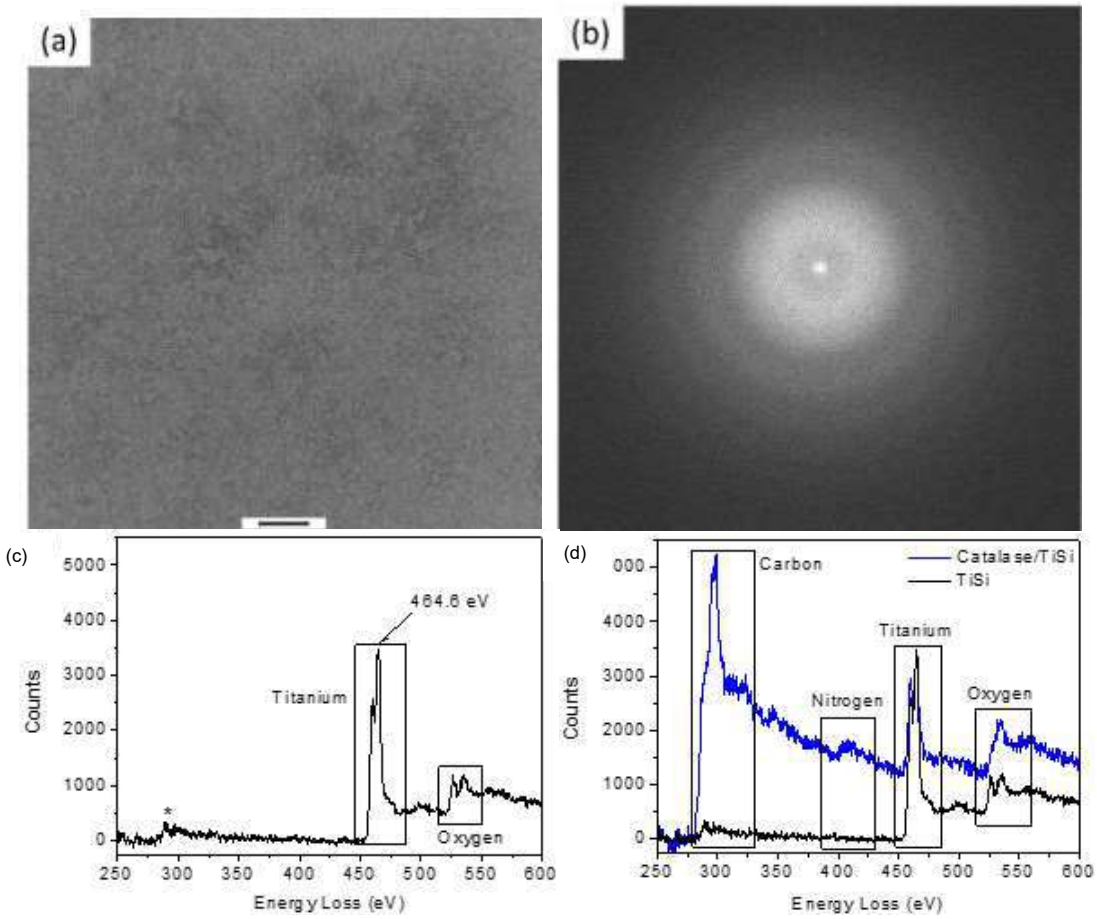

Figure 1. a) Carbon free Cu/TiSi grid with catalase deposited on it showing the uniformity of the deposited protein film and (b) the amorphous character of the substrate highlighted by the thon rings. Scale bar is 100 nm. (c) Spectrum of the ultra-thin TiSi film deposited on Cu grid. The background of carbon K-edge was extrapolated and subtracted showing the remaining energy loss characteristic of titanium and oxygen. Carbon from column contamination or environmental gas is indicated by (*). The arrow highlights the second Ti energy loss peak (464.6 eV) used as reference to align all spectra acquired. (d) Comparative spectra of the catalase deposited on the ultra-thin TiSi film (blue line) and the ultra-thin TiSi film (black line). The background of carbon K-edge was extrapolated and subtracted showing the remaining energy loss characteristic of carbon, nitrogen, titanium and oxygen.

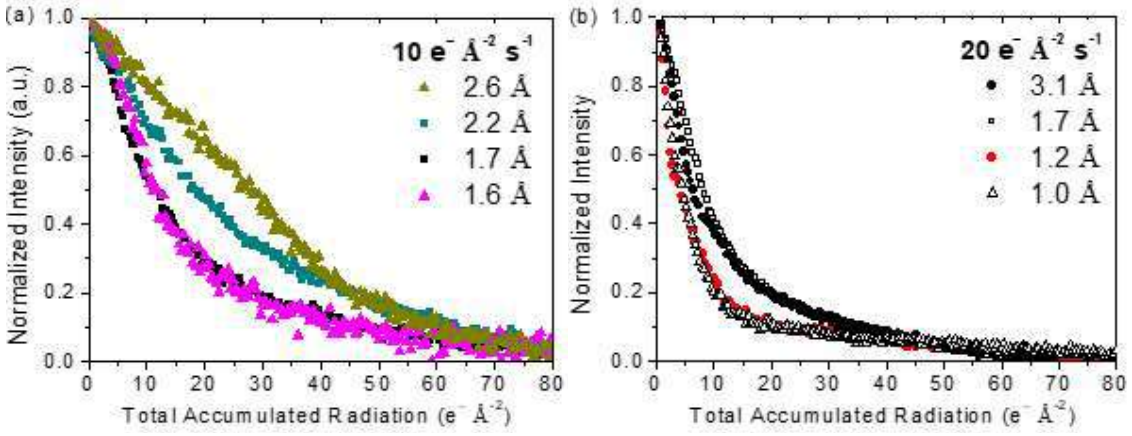

Figure 2.: Normalized intensities vs accumulated dose graph of different catalase crystals. (a) Comparison between crystals A and B identified with triangles and squares, respectively, acquired at 10 e^{-} $Å^{-2}$ s^{-1} dose rate. Comparison between crystals C, D and E identified with open squares, circles and open triangles, respectively, acquired at 20 e^{-} $Å^{-2}$ s^{-1} dose rate.

Cytopathological effects of a new *Lysinibacillus sphaericus* isolate from Pernambuco, Brazil, on the midgut of *Culex quinquefasciatus* larvae susceptible and resistant to biological larvicides.

Marcelo Soares de Barros[1]*, Karina Lidiane Alcântara Saraiva[1], Cláudia Maria Fontes de Oliveira[1], Tatiany Patrícia Romão[1]*.

[1]Instituto Aggeu Magalhães – IAM/ FIOCRUZ-PE
*marcelo.fiocruzpe@gmail.com; tatiany.romao@fiocruz.br

Population control of mosquito vectors is a critical strategy for interrupting the transmission cycle of various pathogens. Bacteria of the genus *Bacillus*, known for their insecticidal activity against dipterans, have been widely used in mosquito control programs targeting the Culicidae family due to their specific larvicidal action, long persistence in organic-rich mosquito breeding sites, and ease of large-scale production and application. However, the emergence of resistant mosquito populations has created a concerning scenario. In this context, bioprospecting for new entomopathogenic bacteria offers an alternative approach to identify novel agents capable of overcoming resistance. The discovery of a new *Lysinibacillus sphaericus* isolate (Ls-PE) from Pernambuco has prompted interest in investigating its larvicidal potential against resistant mosquitoes. This isolate produces a complex of at least six toxins involved in its entomopathogenic activity, including the binary toxin Bin (BinA/BinB). Therefore, the objective of this study was to evaluate the cytopathological effects of this toxin complex on the midgut epithelium of *Culex quinquefasciatus* larvae that are susceptible or resistant to the Bin toxin. For this purpose, fourth-instar larvae from the CqSLab (susceptible colony) and REC-2 (laboratory-resistant strain selected with the reference larvicide Ls2362, RR ~4000-fold) colonies were exposed for six and twelve hours to the LC90 (concentration that kills 90% of larvae) of sporulated bacterial suspensions from the Ls-PE isolate and the Ls2362, with LC90 values determined separately for each colony. After exposure to the bacteria, the larvae midguts were dissected and processed for transmission electron microscopy (TEM). Exposure of the CqSLab colony (Figure 1-A) to the LC90 of Ls-PE (0.006 mg/L) for six hours caused mitochondrial alterations and complete destruction of the microvilli, whereas exposure to the LC90 of Ls2362 (0.015 mg/L) for the same period resulted only in initial fragmentation of the microvilli. After twelve hours, damage from Ls-PE intensified, including destruction of the endoplasmic reticulum (ER), while Ls2362 exposure induced only mitochondrial swelling and ER fragmentation. For the REC-2 colony (Figure 1-B), exposure to Ls2362 for six and twelve hours did not cause observable cellular damage, as expected for a resistant strain. In contrast, exposure of REC-2 larvae to the LC90 of Ls-PE (0.39 mg/L) for twelve hours resulted in severe destruction of microvilli, mitochondrial swelling, and ER alterations. This distinctive cytotoxic effect in the resistant REC-2 colony may be related to the multiple toxins produced by the Ls-PE isolate, which are absent in the Ls2362. These findings suggest that the Ls-PE isolate has significant biotechnological potential for use in developing new biolarvicides capable of overcoming resistance mechanisms.

[1] M. H. N. L. Silva-filha et al. Bacterial toxins active against mosquitoes: Mode of action and resistance. Toxins, v. 13, n. 8, p. 523, 2021.
[2] J. V. de Melo. Caracterização ultra-estrutural dos efeitos citopatológicos causados por toxinas de *Bacillus sphaericus* no instestino de larvas de *Culex quinquefasciatus*. 2008. Tese de Doutorado.
[3] K. D. M. Chalegre et al. Co-selection and replacement of resistance alleles to *Lysinibacillus sphaericus* in a *Culex quinquefasciatus* colony. The FEBS Journal, v. 282, n. 18, p. 3592-3602, 2015.
[4] This research was supported by PROEP – FIOCRUZ, CAPES and FACEPE.

Figure 1. Cytopathological effects on the midgut of mosquito larvae from the CqSLab (A) and REC-2 (B) colonies.

A

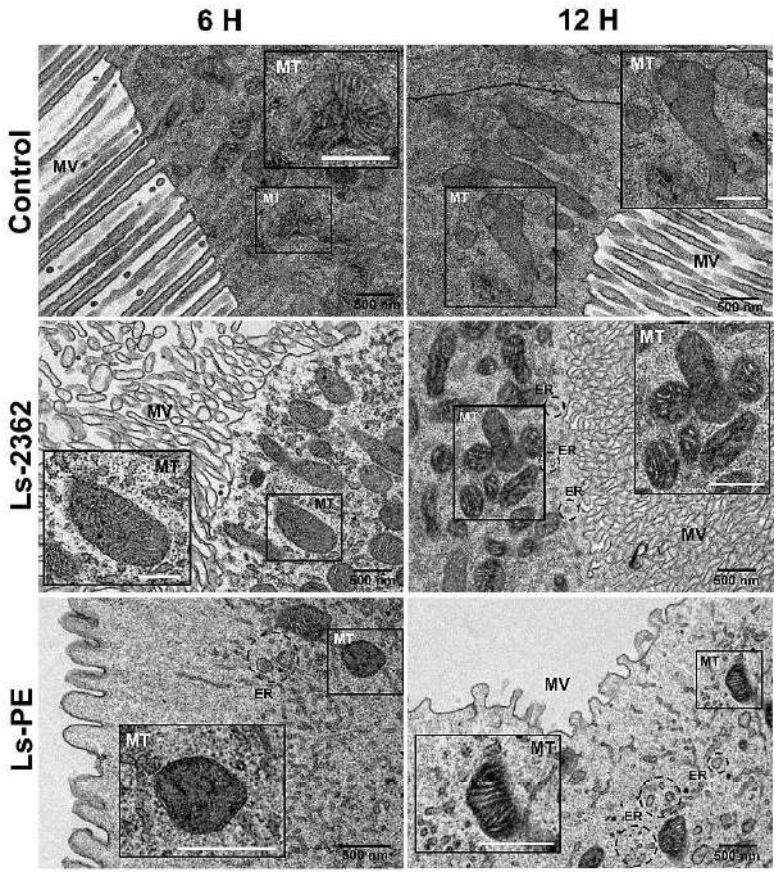

B

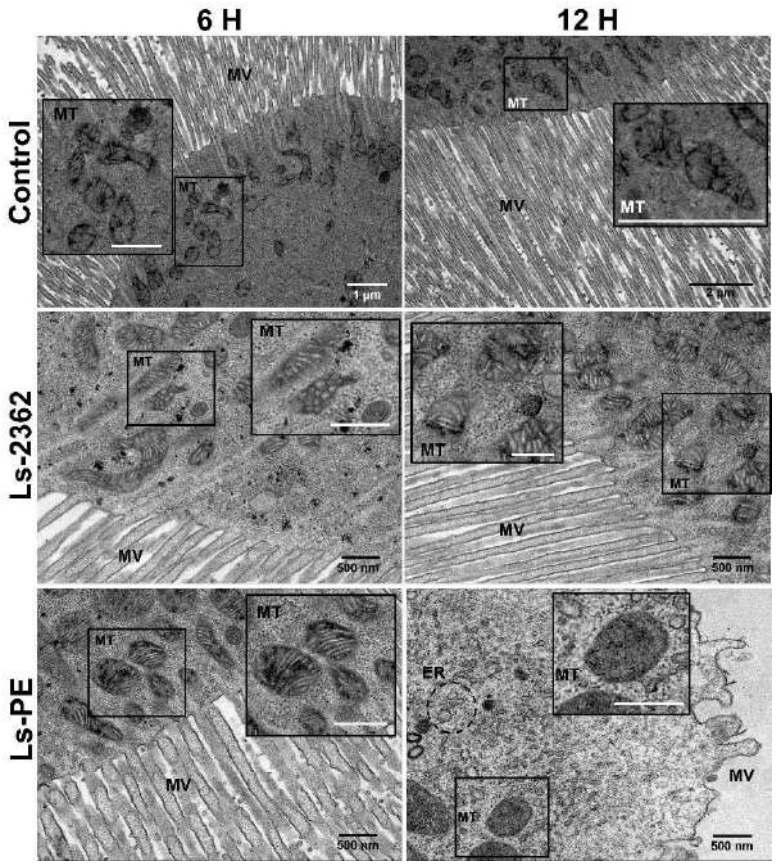

Legend: Cytopathic effects in the larval midgut of the CqSLab (A) and REC-2 (B) colonies after exposure to the LC90 of Ls-PE for 6 hours and 12 hours, visualized by transmission electron microscopy (TEM). (MV) microvilli; (MT) Mitochondria; Endoplasmic reticulum fragmentation (ER). CqSLab – *Culex quinquefasciatus* susceptible colony and REC-2 - *Culex quinquefasciatus* resistant colony.

Human Lung Cells Toxicity And Detoxification Follow-Up After Internalization Of Environmental Metallurgical Nanoparticles

Iara da C. Souza[1]*, Mariana Morozesk[2], Caroline M. Souza[1], Leticia S. Andrade[1], Vitor A.S. Mendes[3], Vinicius C. Azevedo[4], Rafaella Monteiro[1], Silvia T. Matsumoto[5], Magdalena V. Monferrán[67], Daniel A. Wunderlin[7], Michael Elliott[89], Marisa N. Fernandes[1]*.

[1] Departamento de Ciências Fisiológicas, Universidade Federal de São Carlos (DCF/UFSCar), São Carlos, São Paulo, Brazil.
[2] Departamento de Ciências Ambientais, Universidade Federal de São Carlos (DCA-So/UFSCar), Sorocaba, São Paulo, Brazil.
[3] Departamento de Engenharia de Materiais, Universidade Federal de São Carlos (DEMa/UFSCar), São Carlos, São Paulo, Brazil.
[4] Department of Biological Sciences, Simon Fraser University, Burnaby, BC, Canada.
[5] Departamento de Ciências Biológicas, Universidade Federal do Espírito Santo (DB/UFES), Vitória, Espírito Santo, Brazil.
[6] Departamento Bioquímica Clínica, Facultad de Ciencias Químicas, Universidad Nacional de Córdoba, Argentina.
[7] ICYTAC, Universidad Nacional de Córdoba, Córdoba, Argentina.
[8] Department of Biological and Marine Sciences, University of Hull, Hull, UK.
[9] International Estuarine & Coastal Specialists Ltd., Leven, UK.

*iara@ufscar.br, dmnf@ufscar.br

Atmospheric particulates (PM_{10}) originating from metallurgical industrial activities represent a significant environmental health risk due to the presence of potentially toxic metals and emerging metallic contaminants. Despite the growing concern about their toxicological impact, limited information exists regarding the cellular bioavailability, internalization mechanisms, and subsequent detoxification pathways of these particulates within human lung cells. In this pioneering study, we investigated the detailed cellular response of adenocarcinoma human alveolar epithelial lung cells (A549) exposed to metalliferous PM_{10} collected near a smelting region in Vitória, Espírito Santo, Brazil. Cells were subjected to various concentrations of PM_{10} (0, 1, 5, 10, 20, and 40 μg mL^{-1}) over a 24-hour exposure period, with comprehensive time-course ultrastructural analyses conducted at multiple time points (0, 1, 3, 6, 9, 12, and 24h). The results revealed rapid internalization of nanoparticles (NP) within the first hour of exposure, with notable localization in both cytoplasmic compartments and nuclei, suggesting significant cellular uptake and potential for nuclear interaction. Subsequent analyses indicated the initiation of a cellular detoxification process within 3 hours post-exposure, characterized by the formation of vesicles encapsulating internalized nanoparticles. Peak vesicular activity was observed between 6 and 12 hours, corresponding to the substantial sequestration of NP clusters. Importantly, this intracellular containment process culminated in exocytosis-mediated removal of these nanoparticle-loaded vesicles after 24 hours. Chemical analyses identified a dose-dependent bioaccumulation of critical elements including aluminum (Al), titanium (Ti), yttrium (Y), iron (Fe), and cerium (Ce), with Ce, Y, and Ti exerting the most pronounced cytotoxic, genotoxic, and mutagenic effects. Cytotoxicity assays indicated an increasing incidence of necrotic cell death in response to higher concentrations of PM_{10}, highlighting the significant health implications associated with prolonged or high-level exposure. Genotoxic and mutagenic indices further confirmed the hazardous potential of these emerging metallic contaminants, underscoring the critical need for updated regulatory frameworks to mitigate their public health impact. This comprehensive study significantly enhances our understanding of the internalization dynamics, intracellular processing, and detoxification mechanisms of metalliferous nanoparticles. Furthermore, it emphasizes the importance of continuous monitoring and stringent regulation of atmospheric emissions from metallurgical industries, contributing essential insights into potential cellular and health outcomes associated with nanoparticle pollution.

[1] I.C. Souza et al., Sci. Total Environ. 753 (2021) 141976.

[2] M. Morozesk et al., Environ. Adv. 6 (2021) 100125.
[3] I.C. Souza et al., J. Hazard. Mater. 408 (2021) 124424.
[4] I.C. Souza et al., Sci. Total Environ. 814 (2022) 152685.
[5] WHO, Air Quality Guidelines: Global Update 2023.
[6] This research was supported by FAPESP (2019/08491-0, 2023/01356-5), ANPCYT (FONCyT/PICT-2019 N1743, PICT 2021 N002), and CONICET (PIP 2022-11220210100480CO). I.C. Souza received scholarship support from FAPESP (2023/09730-3) and CNPq (151291/2023-3).

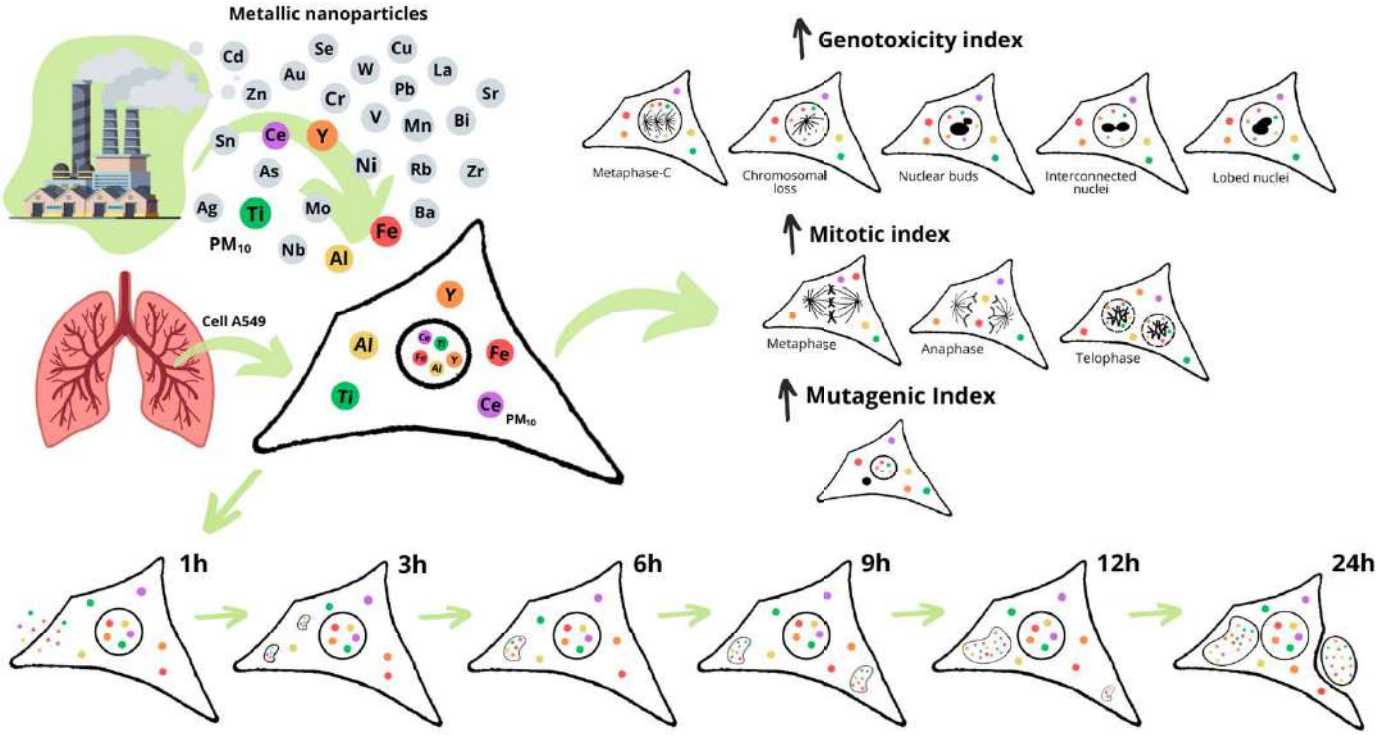

Figure 1. Graphical abstract summarizing the internalization, detoxification pathways, and cytotoxic effects of metallurgical nanoparticles (NP) in human alveolar epithelial lung cells (A549).

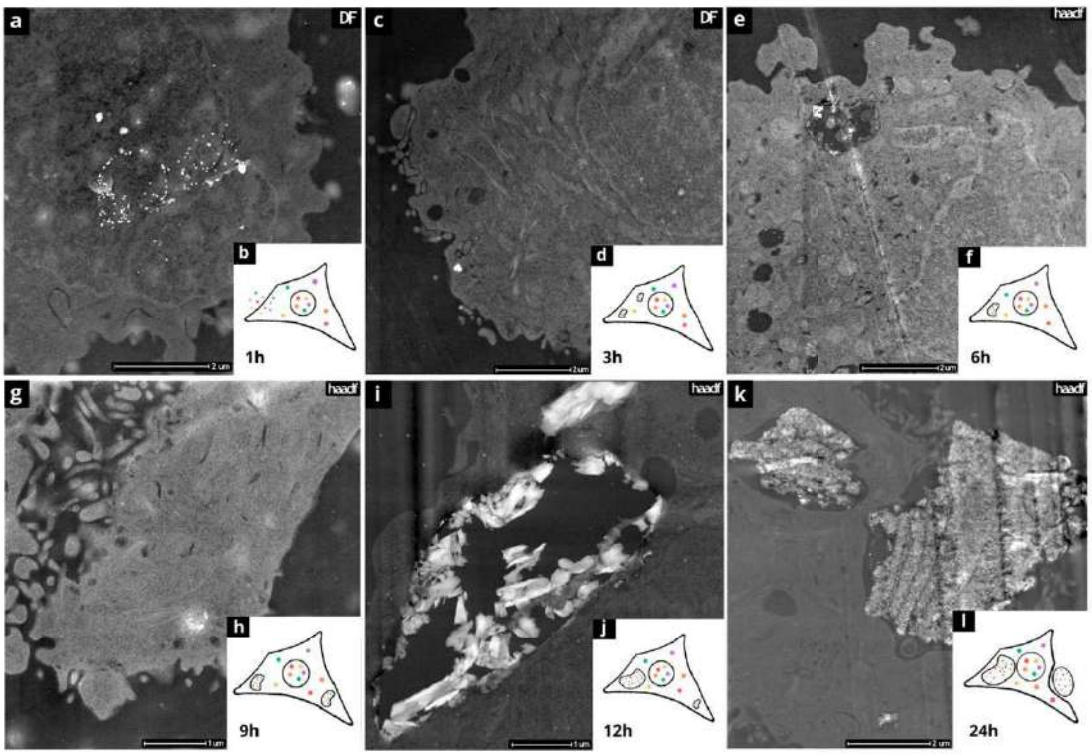

Figure 2. Sequence of events of NPs internalisation and detoxification by A549 cells. Time-1149 course TEM image of A549 lung cells exposed to 20 µg mL-1 of PM10. (a) 1h, (b) 3h, (c) 6h; 1150 (d) 9h, (e) 12h and (f) 24h after exposure.

Integrative Microscopy Techniques Reveal Floral Reproductive System in *Bauhinia uruguayensis* Benth. (Fabaceae)

Andrews V. S. Silva[1]*, Vidal F. Mansano[2], Louis P. Ronse De Craene[3], Fernando I. Carneiro[1], Juliana V. Paulino[4]

[1]Postgraduate Program in Botany, National School of Tropical Botany - Rio de Janeiro Botanical Garden, Rua Pacheco Leão 2040, Rio de Janeiro, RJ, 22460-036, Brazil. [2]Rio de Janeiro Botanical Garden Research Institute, DIPEQ, Rua Pacheco Leão 915, Rio de Janeiro, RJ, 22460-030, Brazil. [3]Royal Botanic Garden Edinburgh, 20a Inverleith Row, Edinburgh, Scotland, EH3 5LR, UK. [4]Department of Natural Products and Food, Faculty of Pharmacy, Center for Health Sciences, Federal University of Rio de Janeiro (UFRJ), Rio de Janeiro, RJ, 21941-902, Brazil.

*andrews.silva@jbrj.gov.br

Andromonoecy, the coexistence of staminate and monoclinous flowers on the same individual, is a rare sexual system investigated here in *Bauhinia uruguayensis* Benth. (Cercidoideae, Leguminosae), a promising model for this phenomenon [1, 2]. This study provides a detailed account of floral ontogeny, an anatomical comparison of carpels, an ultrastructure examination of pollen grains from both floral morphotypes – including details of the exine and cytoplasmic contents –, as well as pollen grain quantity evaluation and nectar availability assessment as a key resource in the reproductive process. Floral buds and flowers at various developmental stages were analyzed using a combination of Scanning Electron Microscopy for surface morphology (using a LEO Supra 55VP, a Hitachi Regulus 8230, and a JEOL - JSM 6490LV at 5, 10, and 15 kV), Transmission Electron Microscopy for ultrastructural details using a FEI Morgagni at 80 kV, and Light Microscopy for anatomy using a Leica DM 750. The SEM analysis revealed that in both morphs, the elliptical floral meristem gives rise to sepals in a helical order, while petals and stamens emerge unidirectionally. The critical divergence occurs during later development, where LM sections and TEM micrographs confirm that the carpel aborts in staminate flowers, a process characterized by the malformation of ovules at the cellular level. This structural differentiation is correlated with functional differences; pollen from staminate flowers, observed via TEM, contains a significantly higher quantity of starch reserves. While nectar volume is greater in staminate flowers, its concentration is similar between morphs. Sexual expression in *B. uruguayensis* is therefore determined by late-stage carpel abortion, making its structure the key trait distinguishing the flower morphs. The evolutionary success of this system is supported by functional trade-offs in resource allocation between the two morphs [3, 4]. In conclusion, andromonoecy in *B. uruguayensis* represents a complex reproductive strategy where morphological differentiation, elucidated through electron and light microscopy, facilitates a functional balance between reproductive roles.

[1] Pedersoli, G.D., Teixeira, S.P. 2016. Floral development of *Parkia multijuga* and *Stryphnodendron adstringens*, two andromonoecious mimosoid trees (Leguminosae). Int. J. Plant Sci. 177 (1), 60-75.
[2] Tucker, S.C., 1991. The role of floral development in studies of legume evolution. Can. J. Bot. 69, 1465-1476.
[3] Bertin, R.I., 1982. The evolution and maintenance of andromonoecy. Evol. Theory 6, 25-32.
[4] Cuevas, J., Pinney, K., Polito, V.S., 1999. Flower differentiation, pistil development and pistil abortion in olive (Olea europaea L.). Acta Hortic. 474, 293-296.

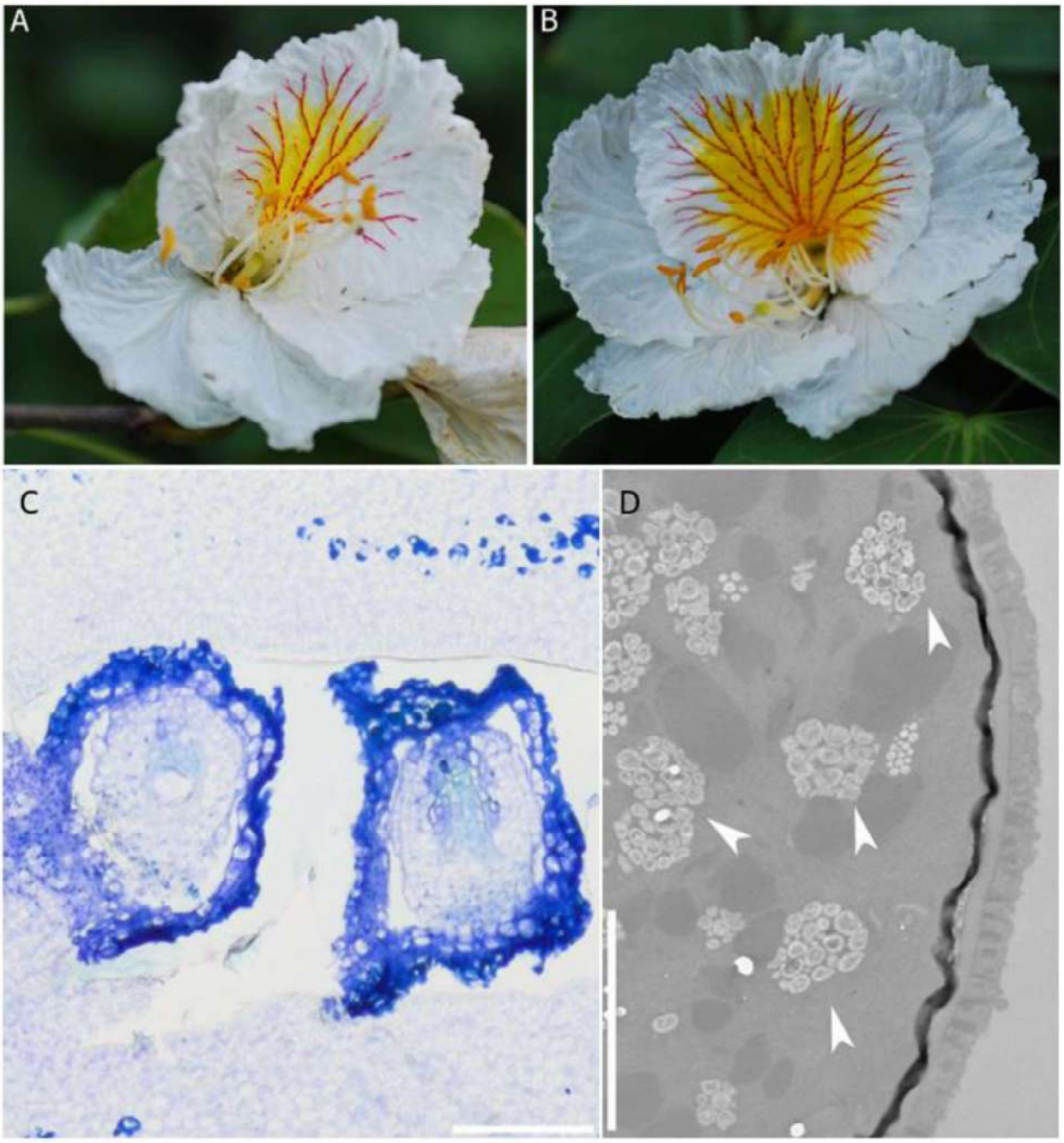

Figure 1. A. Mature staminate flower. Note the length of the carpel. **B.** Mature monoclinous flower. Note the length of the carpel. **C.** Aborted ovules in staminate flower showing underdeveloped tissues. **D.** Detail of amyloplasts (arrowheads) aspect in the staminate floral morphotype.

Interfaces in cortical regions of long bovine bones

Carlos A. Menezes[1], Camila Wendt[1], Tom Ferté[2], Jacques Werckmann[2,3], André L. Rossi[4], Ovidiu Ersen[2], Marcos Farina[1]*

[1] Federal University of Rio de Janeiro (UFRJ) - Brazil, [2]Strasbourg Institute of Materials Physics and Chemistry (IPCMS) - France, [3]Institute of Materials Science of Mulhouse (IS2M) - France, [4]Brazilian Center for Research in Physics.
*marcos.farina.souza@gmail. Marcos Farina

Cortical region of long bones in general contains a bulk middle region surrounded by a cortical area named circumferential lamella composed of concentric layers that can vary in structure as a function of the dimension of the organism and the specific type of bone [1]. It can be formed by layers of type I collagen fibrils or by complex conjugates composed of haversian-like systems running in orientations not completely defined. In bovine radius bone circumferential lamellae are composed of complex structures following vessels. These structures resemble those arrangements present in the havers systems, with not well defined orientation inside each layer. In transverse sections they form concentric layers surrounding the peripheral surface of the bone. This arrangement gives these types of compact bones a unique appearance. In this work, we analyzed the morphological arrangement of the interface region in cortical bone of bovine radius by optical and electron microscopy methods. Sample preparation methods of non-decalcified bones prior to analysis were: - "tripod polishing"; - mechanically fracturing the samples at the interface, and - ultrathin sectioning in an ultramicrotome with a diamond knife. Bright-field and polarization-light optical microscopies, were used to characterize morphologically the interface between the bulk of the compact bone (non-decalcified bovine radius) and the peripheral circumferential lamellae (Figs. 1a, 1b) for further studies by Transmission Electron Microscopy (TEM) methods (see Fig. 3, 4).

In figures 1a and 1b it is possible to identify the interface region, of non-decalcified transversal sections, showing some important features as the outer layer (left in Fig.1a) corresponding to "circumferential lamellae" that represents a significant thickness of the total cortical bone section area in the diaphysis, and that the organization of the bone matrix changes abruptly from one side of the interface, to the other (red arrows in Figs. 1a).

Tripod polished sections observed by reflection light optical microspopy (Fig.2a) showed clearly the interface region, which allowed direct observation of this region by TEM (Figs. 3a, 3b and 4a). Figure 4a showed the presence of micrometer-sized ellipsoidal mineralized granules [2], recently described as essential components of growing bone regions [2], at the interface between the bulk and the circumferential lamella. Figure 4b, obtained by ultrathin sectioning of a region similar to the one shown in figure 4a, confirmed the presence of extensive regions reach in ellipsoidal granules of mineral-organic composites. The observation of mechanically fractured surfaces by reflection microscopy allowed the access of the organization pattern of vessels in each layer (Figs.2b, 2c). In conclusion, we observed that layer of the circumferential lamellae are composed of a network of vessels that most probably define the orientation of the haversian-like structures, and that the interface region in the compact bone is rich in ellipsoidal mineralized granules, suggesting that this region presents different mechanical properties relatively to the surroundings as well as hardness and remodeling dynamics. New studies will be necessary to clarify these points.

Acknowledgements
[1] Ekaterina Novitskaya, Acta Biomaterialia 7 (2011) 3170–3177.
[2] Marc D. McKee et al., J. Struc. Biol. 214 (2022) 107823
[3] This research was supported by CNPq (Brazil) and IRP from CNRS-France.

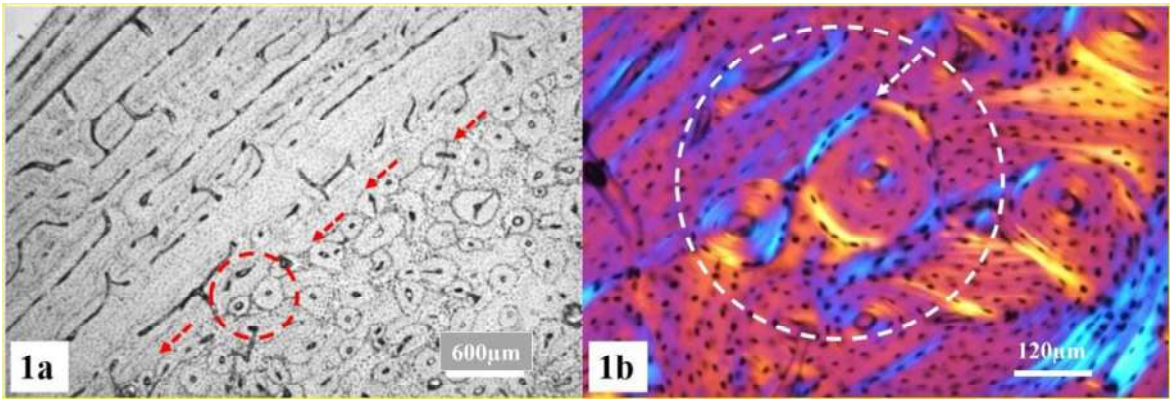

Figure 1a. Non-stained transversal polished section of a cortical region form a bovine radius. Red arrows: interface between the haversian rich region (right) and "circumferential lamellae" (left). **Figure 1b.** Polarization light microscopy image showing details of figure 1a. Blue and yellow regions: distribution of collagen fibrils in the sample. White arrow: interface.

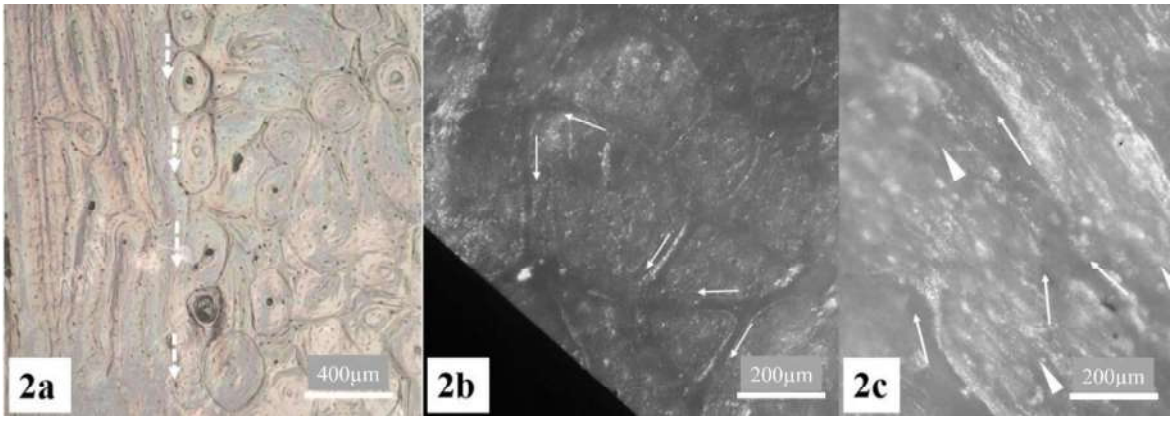

Figure 2a Transverse section of a region similar to figure 1, obtained by "tripod Polishing". White arrows: interface; Bottom: thinnest sample region; **Figure 2b and 2c:** Top view of the interface region (arrows in figures 1a and 2a) after fracture. Vessels (arrows) and mineralized regions (arrowheads) are seen by optical reflexion microscopy.

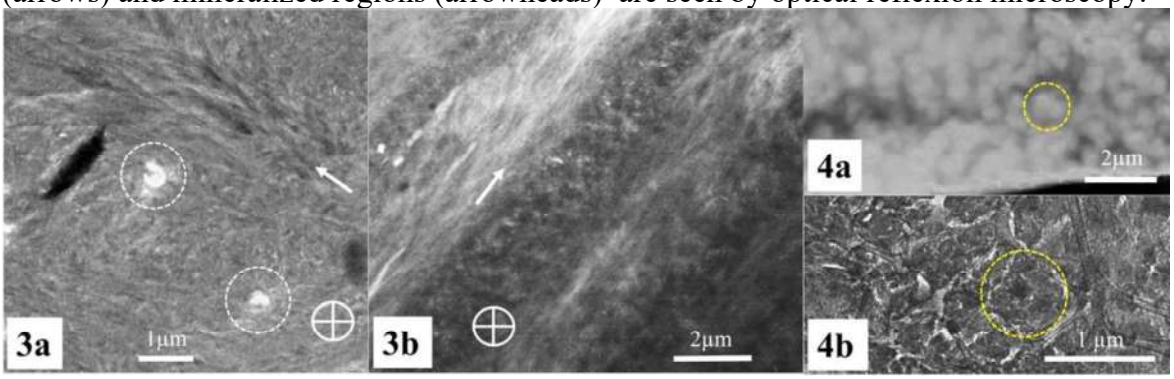

Figure 3a. TEM image showing bundles of collagen fibrils in crossed orientations ("arrow" and "circle with cross"); **Figure 3b.** Thick sample obtained by "tripod polishing" showing organization pattern similar to the previous figure (arrow and circle with cross) although with a different contrast; **Figure 4a.**TEM image of the interface region (see figure 1a) showing discrete mineralized ellipsoidal regions. **Figure 4b.** TEM ultrathin sections of a region similar to the one presented in figure 4a, confirming that the interface region is particularly rich in this type of structures.

Multimodal microscopic and spectroscopic analysis of iron contamination effects on macroalgae from a Brazilian Marine Environmental Protected Area affected by the Fundão dam collapse

Luis Junior Hurtado Ordinola[1], Rodrigo Tomazetto de Carvalho[1], Claudia Santiago Karez[1], Luis Alfredo Simões Rodrigues de Marques Baptista de Leão[1], Camila Hubner Costabile Wendt[2], Renato Crespo Pereira[3], Paulo Sérgio Salomon[4], Alex Cardoso Bastos[5], Rodrigo Leão de Moura[6], Leonardo Tavares Salgado[1*]

[1] Laboratório de Algas, Instituto de Pesquisa Jardim Botânico do Rio de Janeiro, Brazil
[2] Instituto de Ciências Biomédicas, Universidade Federal do Rio de Janeiro, Brazil
[3] Departamento de Biologia Marinha, Universidade Federal Fluminense, Brazil
[4] Instituto de Biologia, Universidade Federal do Rio de Janeiro, Brazil
[5] Departamento de Oceanografia, Universidade Federal do Espírito Santo, Brazil
[6] SAGE-COPPE, Universidade Federal do Rio de Janeiro, Brazil

*lsalgado@jbrj.gov.br

Rhodoliths are calcareous nodules formed by free-living, non-geniculate coralline algae that, in Brazil, cover extensive areas of the seabed and support rich marine biodiversity, including many macroalgae [1]. These structures are sensitive to variations in seawater's physical and chemical parameters, incorporating environmental signatures into their calcareous skeletons over time [2]. In early 2016, marine protected areas near the Doce River mouth, such as the Costa das Algas Environmental Protection Area (EPA), were impacted by the arrival of millions of cubic meters of iron ore tailings released after the Fundão dam collapse in Mariana (MG), transported by the Doce River [3]. While the effects of this disaster on other marine organisms have been widely studied, its impact on rhodoliths and macroalgae remains unclear. This study evaluated the effects of iron ore tailings on annual growth rate, microparticle incorporation, and trace metal accumulation in coastal rhodoliths formed by *Lithophyllum sp*. and the macroalgae *Padina gymnospora*. We applied a range of microscopy and spectroscopy techniques—including optical microscopy scanning electron microscopy (SEM), transmission electron microscopy (TEM), selected area electron diffraction (SAED), energy dispersive X-ray (EDS) and X-ray fluorescence spectroscopy (XRF)—to analyze growth bands from 2013 to 2020. Results showed a 42.5% reduction in growth rate during the two years following the disaster (2016–2017), with signs of recovery from 2018 onward. Elevated concentrations of Fe, Co, Si, and Al were observed in the coralline structures during the post-disaster years, and iron oxide microparticles were incorporated into the calcareous matrix only after 2016, with Fe ions also detected within $CaCO_3$ crystals. In *P. gymnospora,* iron granules were seen adsorbed in the cell walls. These findings suggest that the reduced rhodolith growth rates are linked to the iron-rich plume, underscoring the environmental risks posed by iron ore tailings to rhodolith beds, with potential consequences for carbon burial, future trace metal remobilization and macroalgae citotoxicity.

[1] W.A. Nelson,Mar. Freshw. Res. 60(8), 2009 – 787-801.
[2] S. McCoy & N. Kamenos, J. Phycol. 51(1), 2015 – 6-24.
[3] G.O. Cardoso et al., Sci. Total Environ. , 807, 2022 - 150880.
[4] This research was supported by FEST.

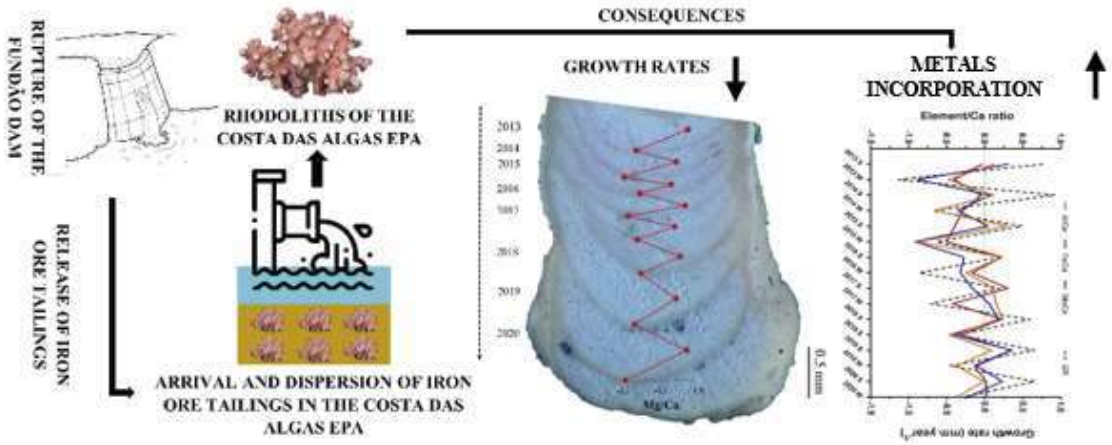

Figure 1. Schematic abstract of the rhodolith metal incorporation after the disaster.

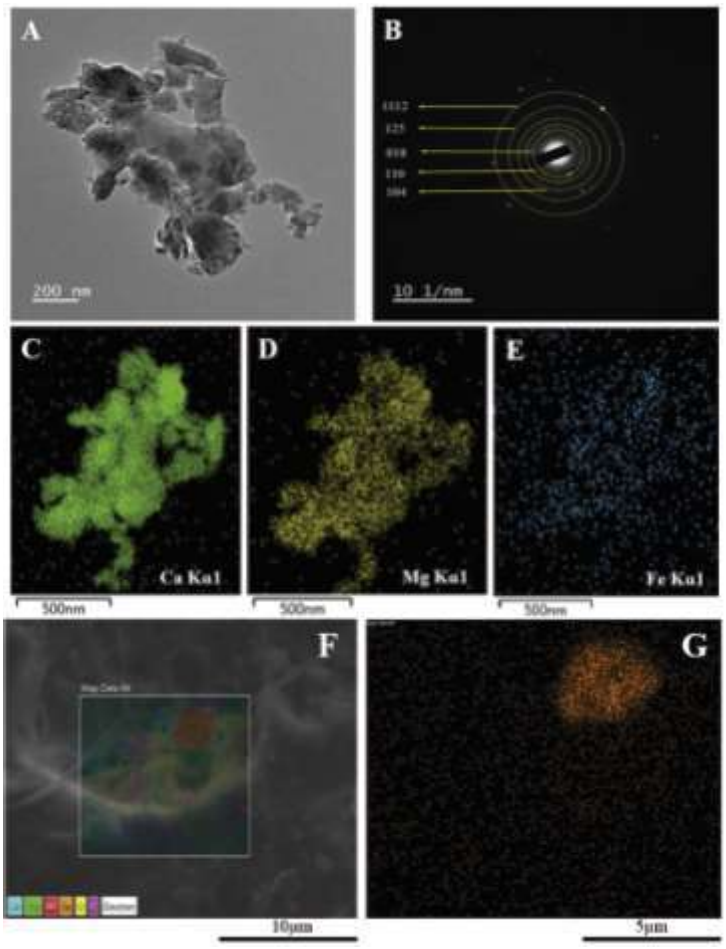

Figure 2. Metal incorporation in $CaCO_3$ crystals from rhodolith cell walls showed by TEM and SEAD and EDS (A, B, C, D, E) and MEV-EDS of micrometric iron particles adsorbed in the rhodolith matrix (F, G).

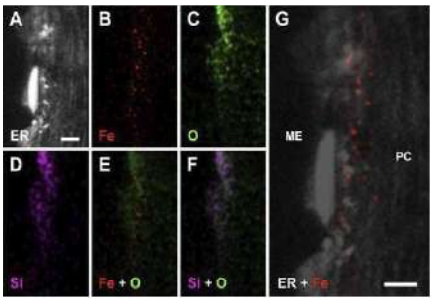

Figure 3. EDS analysis of *Padina gymnospora* cell walls revealing the incorporation of elements, including iron (red) which is an indicative of iron absorption from the surroundings.

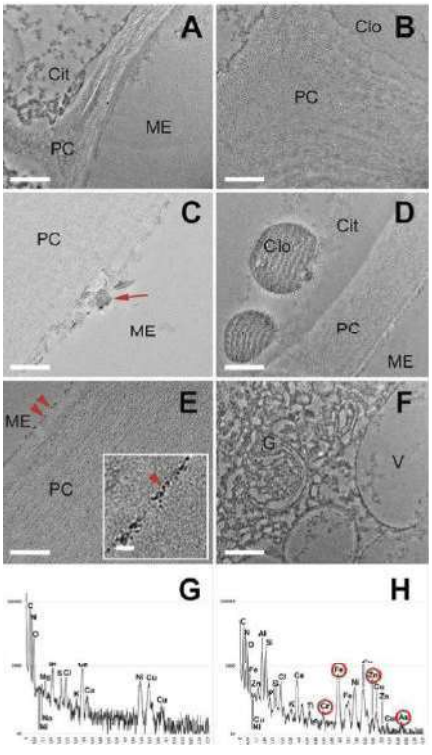

Figure 4. Iron granules adsorbed in cell walls.

A C-type lectin from *Bothrops leucurus* snake venom kills *Leishmania infantum* by inhibiting cell division and mitochondria-dependent pathway cell death

[1,2]Aranda-Souza, M. A.; [2]Borges, A. R.; [1]Correia, M. T. S.; Figueiredo, [2]R. C. B. Q.;

[1]Universidade Federal de Pernambuco - UFPE, [2] Instituto Aggeu Magalhães – IAM/FIOCRUZ
*mary.aranda@ufpe.br

Lectins are proteins of non-immune origin that recognize and reversibly bind to carbohydrates with high affinity and specificity [1]. A C-type lectin, isolated from *Bothrops leucurus* snake venom (BLL), has demonstrated relevant biological activities such as antibacterial and antitumoral activities and also demonstrated an effect against species causing Tegumentary Leishmaniasis [2; 3; 4]. In this work, we aimed to study the effect of BLL against *Leishmania infantum*, which causes visceral leishmaniasis. Thus, the effect of BLL on the promastigote viability and the cytotoxicity in VERO cells was evaluated by MTT assay. Hydrogen peroxide (H_2O_2) production and alterations in mitochondrial transmembrane potential ($\Delta\Psi m$) were also analyzed using H_2DCFDA and JC-1, a cationic mitochondrial vital dye, respectively. Mitochondrial damage was confirmed by Rhodamine 123 staining and ultrastructural analysis. The results showed that BLL inhibited the growth of promastigotes and the IC_{50} value corresponding to 2.1 ± 0.59 μM. On the other hand, the CC_{50} value for mammalian cells was 37.44 ± 1.62 μM after 48 h of cultivation. The lectin proved to be 17.82 times more selective against the promastigote forms of *L. infantum* than VERO cells, as demonstrated by the Selectivity Index (SI) (Table 1). Our data demonstrate that incubation of L. infantum in the presence of BLL ($2xIC_{50}$) was able to promote a threefold increase in cytosolic ROS production (Fig.1A). Interestingly, the increase in ROS levels was accompanied by a loss of $\Delta\Psi m$, with a 42.7 ± 2.2% decrease in $\Delta\Psi m$ (Fig.1B). The confocal microscopy analysis by Rhodamine 123 binding demonstrated a fluorescence intensity decrease in BLL-treated parasites, indicating an effect on mitochondrial bioenergetics (Fig. 2A). Previous studies have demonstrated that, after binding to glycoproteins on the cell membrane of the protozoa *Trypanosoma cruzi*, a lectin isolated from seeds of *Cratylia mollis* was subsequently internalised. Thus, the lectin colocalized with parasite mitochondrion, where it impaired the functioning of the organelle and lead to cell death by necrosis [5]. Corroborating this idea, we showed that the mitochondrial membrane potential was inhibited by BLL treatment on promastigote forms of *Leishmania braziliensis* and *Leishmania amazonensis* [4]. Ultrastructural analysis of BLL-treated promastigotes revealed intense cellular disorganization, with the appearance of large electron-lucent spaces in the cytoplasm. Multiple flagella were also observed in several cells, indicating a loss of cell division efficiency in the parasite (Fig. 2B). Taken together, our results shed light on the understanding the different mechanisms of lectins against each Leishmania species, contributing to the discovery of new drug targets in *Leishmania* spp. [6]

[1] K. Ganguly, T. Madan. *Adv Exp Med Biol.* 1476 (2025) 107-119.
[2] E. S. Nunes et al. *Comp Biochem Physiol B*. 159 (2011) (1):57-63.
[3] E. S. Nunes et al. *Toxicon* 1 (2012) 59 (7-8):667-71.
[4] M. A. Aranda-Souza. *International Journal of Biological Macromolecules* 120 (2018) 431-439
[5] M.P. Fernandes et al. *J. Bioenerg. Biomembr.* 42 (2010) 69–78.
[6] This research was supported by CAPES and FACEPE (APQ/FACEPE 0584-2.13/15).

Table 1. Evaluation of leishmanicidal and cytotoxic effects of *Bothrops leucurus* lectin..

***L. infantum* Promastigotes IC_{50} (µM)**	**VERO cells CC_{50} (µM)**	**Selectivity Index (IS)**
2.1 ± 0.59	37.44 ± 1.62	17.82

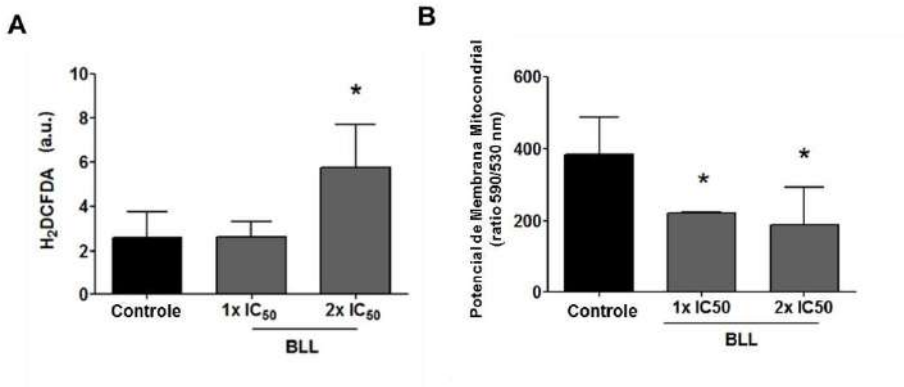

Figure 1. Effect of BLL on ROS production and on mitochondrial membrane potential. (A) Promastigote ROS production is expressed in columns. (B) Alterations in relative ΔΨm values are expressed as the ratio of the fluorescence measurements at 590 nm (for J-aggregate) versus 530 nm(for J-monomer). The values are presented as mean ± S.D. from three independent experiments carried out in triplicate and *p b 0.001.

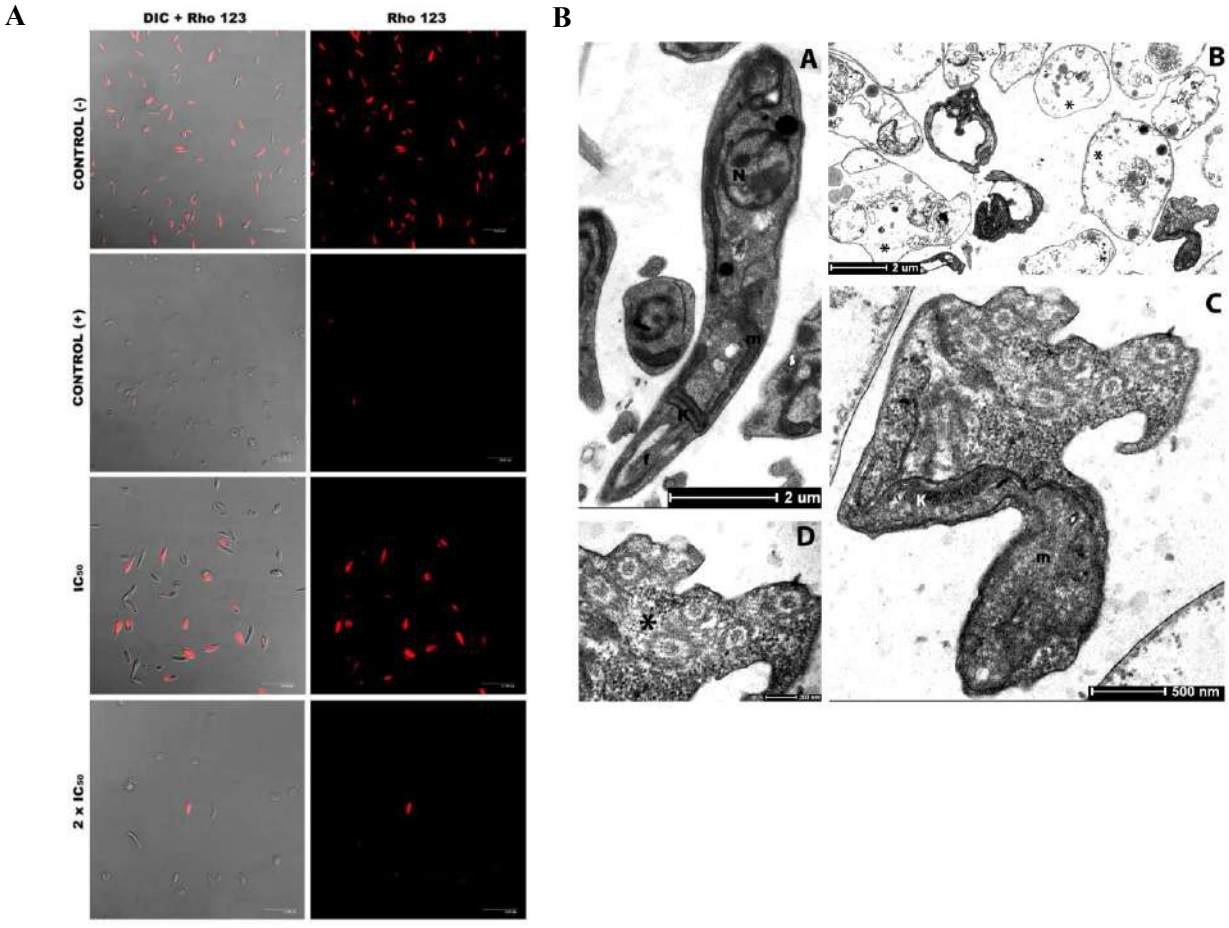

Figure 2. Effects of BLL on promastigote ultrastructure as observed by transmission electron microscopy. (A) Low magnification of control *L. infantum* without treatment, (B, C and D) *L. infantum* BLL-treated.

Aldosterone Excess Alters Mitochondrial Biogenesis and Apoptosis in the Adrenal Gland.

Nascimento A.L.R[1,2,3*], Andrade C.B.V. [1,2,3], Aiceles V.,[1,2,3], Moraes A.C.N. [1,3,4], Alves, L.L. [1,2,3] Ciambarella B.T. [1,2], Silva J.F.R[1,2], Carvalho J.J.[1,2,3]
[1]State University of Rio de Janeiro - UERJ
[2]Ultrastructure and Tissue Biology Laboratory
[3]Electron Microscopy Laboratory – LABMEL
[4]Fluminense Federal University.

Aldosterone, the main mineralocorticoid hormone, is vital for maintaining the homeostasis of body fluids and electrolytes, vascular resistance, and therefore blood pressure (1). Inadequate chronic elevations in aldosterone can increase pro-inflammatory cytokines and cause oxidative stress, which in the long run leads to tissue damage (2). Excess production of aldosterone significantly induced a decrease in mitochondria number and mitochondrial dysfunction in vitro and in vivo in heart and endothelium (3). The present study aims to evaluate possible morphofunctional changes in the adrenal gland of spontaneously hypertensive rats (SHR). A total of 14 wistar rats (with 7 animals from the control group - WKY and 7 animals from the spontaneously hypertensive group - SHR), male, adult, 20 weeks old, were used in this experiment. The blood was collected for subsequent measurement of aldosterone by the ELISA method, and the adrenal glands were processed and analized by light microscopy, transmission electron microscopy and western blotting for and cytochrome c PGC1-a. Results suggest changes such as increased aldosterone synthesis (Figure 1) and apoptosis in SHR animals compared to the normotensive group (WKY).The results of protein expression analyses (Figure 2) showed that the expression of was significantly lower in the hypertensive group, suggesting decreased mitochondrial biogenesis in this group. An increase in PGC1-a expression was observed in the SHR group, suggesting an increase in intrinsic apoptosis in this group. Semi-thin sections, stained with toluidine blue, show the zona glomerulosa containing lipid droplets in the cytoplasm of the cells, which appear in greater numbers in the SHR group when compared to the WKY group. Ultrastructural analysis (Figure 3) shows the presence of numerous mitochondria in the WKY group with tubular cristae,, and electron-dense matrix. Lipid vesicles (L) associated with fused mitochondria (M) are also observed. Some still contain their lipid content and many have already emptied, likely due to hormone release. In the SHR group, we observed numerous lipid vesicles, still containing droplets, and mitochondria with a thinner matrix and more elongated cristae. These images suggest an lipid accumulation resulting from increased aldosterone production. In conclusion, aldosterone excess induced mitochondrial dysfunction, reducing mitochondrial biogenesis and increasing apoptosis in the adrenal gland.

[1] Pauzi, FA and Azizan EA., Front Endocrinol (2021) 12.
[2] Lim, JS and Rainei, WE., Horm Metab Res.(2020) 52.
[3] Tsai, C.H., Biomedicines (2021) 9.
[4] This research was supported by CNPq, CAPES, FAPERJ and UERJ.
[5] Acknowledgments to the Electron Microscopy Laboratory of the Biology Institute of the Fluminense Federal University.

Figure 1

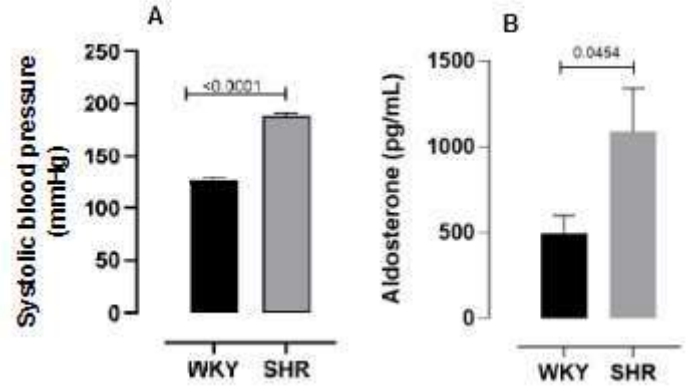

Figure 1. (A) Blood pressure of animals from WKY and SHR groups .(B) Serum levels of Aldosterone in animals from WKY and SHR groups. The biochemical analysis by the ELISA method revealed a significant difference in the synthesis of Aldosterone, which was higher in hypertensive.

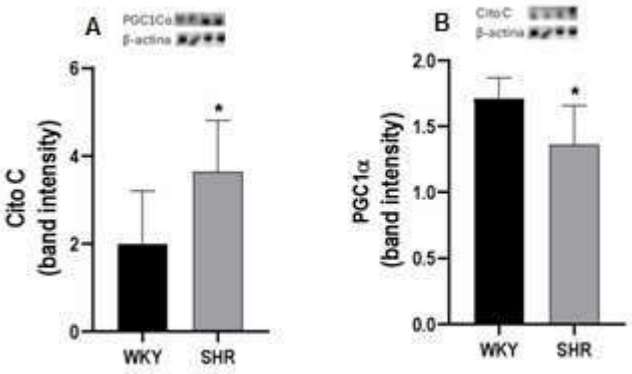

Figure 2. Protein expression by western blotting technique for Cytochrome C (A) and PGC1α (B) significantly different in WKY and SHR groups.

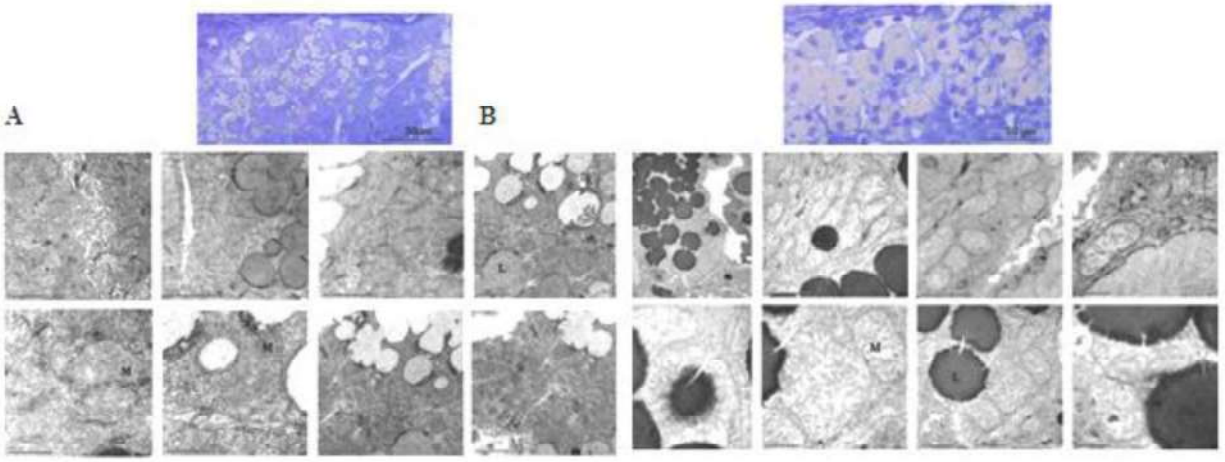

Figure 3. Representative images of the Toluidine Blue technique and transmission electron microscopy of animals from the WKY group (A) and SHR group (B), showing mitochondria (M) and lipids droplets (L). Scale bar = 30μm.

Amazonian Essential Oil Exhibits Antileishmanial Activity and Induces Morphological Alterations in *Leishmania* spp

Amanda Caroline da Silva Barbosa[1, 3]*, Macley Silva Cardoso[1,2], Adeniele Lopes da Cruz Carneiro[1,2], Anderson de Santana Botelho[4], Eloísa Helena de Aguiar Andrade[4], Ricardo Jorge Leal Silvestre[5], José Antonio Picanço Diniz Junior[1], Ana Paula Drummond Rodrigues[1].

[1]Multiuser Laboratory of Cell Biology and Ultrastructure, Evandro Chagas Institute, [2]Postgraduate Program in Biology of Infectious and Parasitic Agents, Federal University of Pará, [3]University of State of Pará, [4]Adolpho Ducke Laboratoty, Emilio Goeldi Museum, [5]Life and Health Sciences Research Institute, University of Minho.
*amandabbiomed@gmail.com

Cutaneous leishmaniasis (CL) is a neglected disease characterized by skin wounds because of the host immune response to the parasite and the infectious form of the *Leishmania* species. Available treatments include intralesional administration of pentavalent antimonials [1, 2]. However, prolonged use of these medications can lead to side effects and the development of parasite resistance. Biomaterials incorporated with essential oils (EO) are being searched for the treatment of lesions resulting from parasitic infection and potential activity against *Leishmania amazonensis* [2, 3]. Therefore, this research aims to investigate the direct action of EO on the *Leishmania* parasite to develop a topical formulation for the treatment of CL. For the tests, RAW 264.7 macrophages and *Leishmania (Leishmania) amazonensis* parasites (MHOM/BR/26361) were used. Cell viability was assessed using MTT bromide (3-(4,5-dimethylthiazol-2-yl)-2,5-diphenyltetrazolium bromide). To define the inhibitory concentration, each treatment condition (EO-10, 100, 200, 300, 400, and 500 µg/mL) was performed in independent experiments in triplicate, with growth monitored daily by counting in a Neubauer chamber for nine days. For morphological and ultrastructural analysis, promastigotes incubated with EO at a concentration of 300 µg/mL, were processed for scanning electron microscopy (SEM) and transmission electron microscopy (TEM), according to the protocol established in the laboratory. The cytotoxic effect was not observed in RAW cell line for the concentrations tested compared to the controls (Fig. 1). For the EO concentrations tested against *L. amazonensis* promastigotes, an antiproliferative effect was demonstrated from 300 µg/mL, where daily counts showed a decrease in parasite density over time (Fig. 2). The treated parasites presented morphological and ultrastructural changes indicative of apoptosis, with marked exposure of cytoplasmic content, rounding of the cell body, enlargement of the kinetoplast, significant increase in lipid vesicles, and organelles disorganization (Fig. 3). These findings support the potential of EO-based formulation as a promising therapeutic alternative for the treatment of CL.

Keywords: Cutaneous leishmaniasis; Antileishmanial activity; Ultrastructure.

Aknowledgments: Instituto Evandro Chagas – Ministério da Saúde, Secretaria de Vigilância em Saúde, Laboratório de Microscopia Eletrônica de Varredura - Museu Paraense Emilio Goeldi, CAPES and CNPq [4].

[1]WORLD HEALTH ORGANIZATION, W. Leishmaniasis. Available in: <https://www.who.int/health-topics/leishmaniasis>. Acess in: 06 may 2025.
[2] N. C. Brito et al. *Efficacy of pentavalent antimoniate intralesional infiltration therapy for cutaneous leishmaniasis: A systematic review*. PLOS ONE, 2017.
[3] C. E. L. Silva et al. *Effect of essential oils on Leishmania amazonensis: a systematic review*. Parasitology, 2020.

[4] This research was supported by Instituto Evandro Chagas – Ministério da Saúde, Secretaria de Vigilância em Saúde, CAPES and CNPq (Brazil).

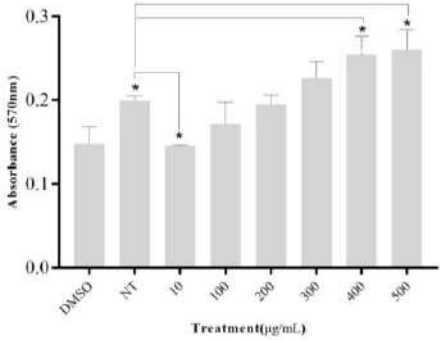

Figure 1. Cell viability of macrophages submitted to EO treatment conditions. MTT test. DMSO: dimethyl sufoxide.

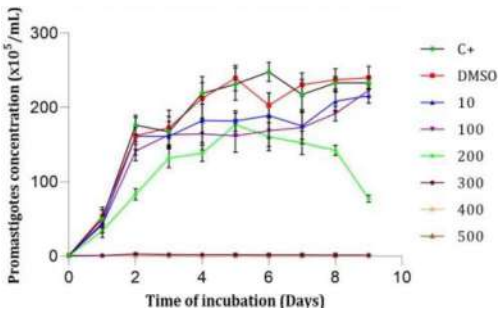

Figure 2. Growth curve of *Leishmania amazonensis* promastigotes treated for nine days with different concentrations of EO. C+: promastigotes treated with amphotericin B; DMSO: dimethyl sufoxide.

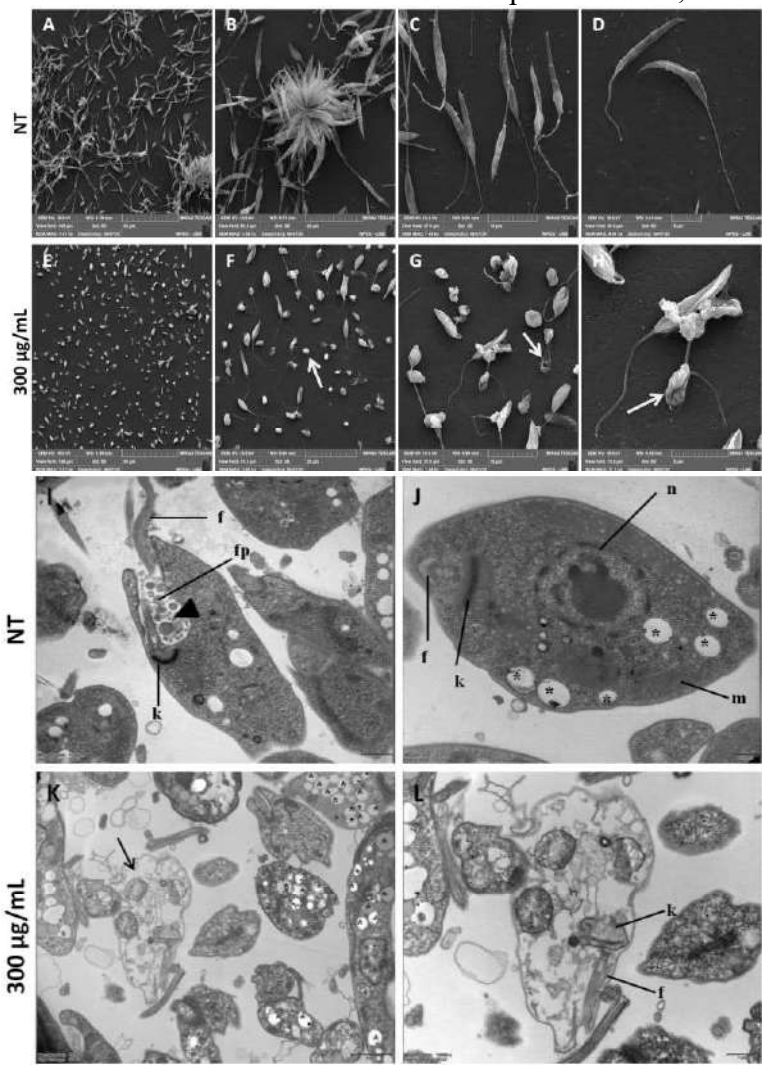

Figure 3. Morphological and ultrastructural analysis of *Leishmania amazonensis* promastigotes untreated and treated with 300 µg/mL for three days with EO. **SEM: A-D:** untreated parasites showed normal structure; **E-H**: promastigotes treated showed exposure of the cytoplasmic content (G), rounding of the cell body (F, H). Scale bars: 50 µm (A, E,), 20 µm (B, F), 10 µm (C, G), and 5 µm (D, H). **TEM:** I-J: untreated parasites showed typical morphology, with mitochondria (m), nucleus (n), flagellum (f), and presence of vesicles (Head-arrow) inside the flagellar pocket (fp), kinetoplast (k), and lipid vesicles (*); K-L: promastigotes treated showed enlargement of the kinetoplast (k), significant increase in lipid vesicles (K - asterisks), and disorganization of organelles and complete loss of morphology (L). Scale bars: 500 nm (J), 1 µm (I, L), 2 µm (K).

Three-dimensional Architecture of Basal Bodies and the Mastigont System in *Trichomonas vaginalis*

Sharmila Ortiz[1], Raphael Verdan[1] and Marlene Benchimol [2,3]

[1] Laboratório de Ultraestrutura Celular Hertha Meyer, Instituto de Biofísica Carlos Chagas Filho, Centro de Pesquisa em Medicina de Precisão, Universidade Federal do Rio de Janeiro, Rio de Janeiro 21941-901, Brazil
[2] BIOTRANS-CAXIAS, Universidade do Grande Rio. UNIGRANRIO, Rio de Janeiro 96200-000, Brazil
[3] Instituto Nacional de Ciência e Tecnologia em Biologia Estrutural e Bioimagens e Centro Nacional de Biologia Estrutural e Bioimagens, Universidade Federal do Rio de Janeiro, Rio de Janeiro, RJ, Brazil

Trichomonas vaginalis is a parasite that is sexually transmitted (STI) that affects more than 156 million people worldwide and can lead to reproductive tract inflammation, adverse pregnancy outcomes, and an increased risk of HIV, virus infections, cervical and prostate cancer. *T. vaginalis* has five flagella, which emerge from the basal bodies. Many common and uncommon organelles are present in this parasite. The most peculiar and uncommon is the hydrogenosome, a producing ATP and molecular hydrogen organelle, and a complex and elaborate mastigont system which comprises the pelta-axostylar complex, formed by microtubules and the pelta that has a role of reinforcing the wall of the flagellar canal which is the flagellar exit [1]. Among these, the basal bodies give rise to not only flagella but also poorly understood filaments and fibers, forming an intricate architecture whose organization and function remain largely unexplored [2, 3]. Advanced imaging techniques—including ultra-high-resolution scanning electron microscopy (UHR-SEM) (Fig. 1, Fig 2b), transmission electron microscopy (TEM) (Fig. 2), electron tomography, and immunolabeling—were employed to investigate the three-dimensional arrangement of the basal body region (Fig. 3). This study reveals novel rootlet fibrils, details of the transitional zone, and the localization of centrin within the basal body triplets and lumen, particularly at the distal ends. These findings shed light on the architecture of the basal apparatus in *T. vaginalis*, contributing to a more comprehensive understanding of its cytoskeletal organization.

1. Honigberg BM *et al*. *Journal Protozoology* (1971) **18**(2),183-98. doi: 10.1111/j.1550-7408.1971.tb03306.x.
2. Fiama das Neves Ortiz S. *et al. Journal Structural Biology X*. (2024) **6**;9:100099. doi: 10.1016/j.yjsbx.2024.100099.
3. Ortiz S *et al Journal Structural Biology* (2024) **6**;216(4):108127. doi: 10.1016/j.jsb.2024.108127. Epub ahead of print. PMID: 39244171.

The authors acknowledge funding from the Conselho Nacional de Desenvolvimento Científico e Tecnológico (CNPq), Financiadora de Estudos e Projetos (FINEP), and Fundação Carlos Chagas Filho de Amparo à Pesquisa no Estado do Rio de Janeiro (FAPERJ).

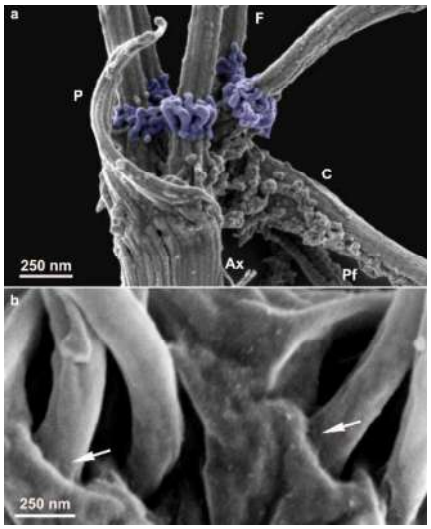

Figure 1. Flagellar externalization region of *T. vaginalis*, shown (a) without the plasma membrane and (b) with the plasma membrane intact. In (a), a proteinaceous structure associated with the basal bodies, in the transitional region is highlighted in blue. In (b), white arrows indicate this structure just beneath the plasma membrane. F, flagellum; P, pelta; C, costa; Ax, axostyle; Pf, parabasal filaments.

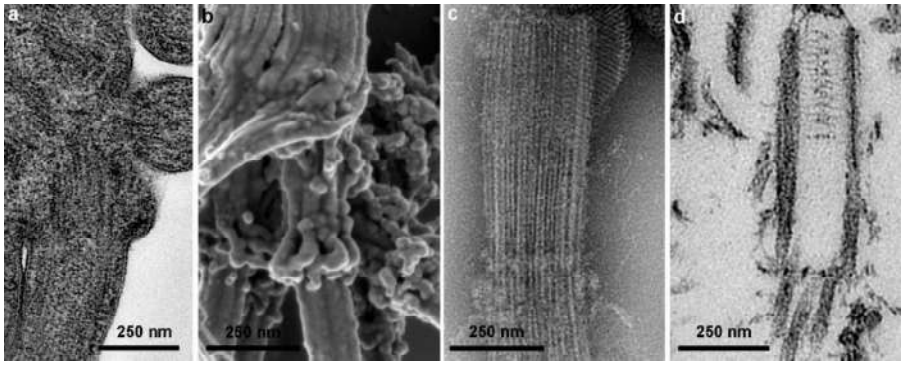

Figure 2. Basal bodies region and flagellar exit zone of *T. vaginalis*. (a) Conventional transmission electron microscopy (TEM), (b) high-resolution scanning electron microscopy (HR-SEM) of isolated cytoskeleton, highlighting the proteinaceous structure at the flagellar exit zone, (c) negative staining of the isolated cytoskeleton and (d) ultrathin section of isolated cytoskeleton embedded in LR White resin.

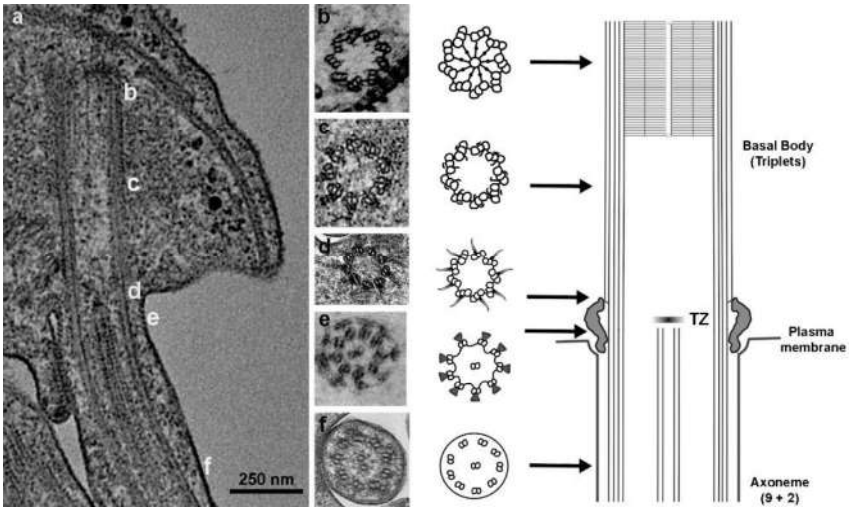

Figure 3. Ultrastructure of the basal body and flagellum of *T. vaginalis* revealed by TEM.
(a) Longitudinal section. Arrow heads indicate the corresponding transverse sections shown in panels (b–f). In (b) cross-section showing a 9+0 arrangement of peripheral triplets, radial spokes, pinheads, and electron-dense material within the lumen, (c) 9+0 triplets with less electron-dense luminal content, (d) transition zone containing electron-dense material surrounding the outer region of the peripheral microtubule triplets, (e) region with a 9+2 microtubule arrangement and structures between microtubules and the plasma membrane region and (f) cross-section of the flagellum.

Characterization of Acidocalcisomes in *Plasmodium vivax* Transmission Stages

Glenda Q. Ramos[1,2,3*], Jander M. Guimarães[1], Rosa A. G. Santana[2], Wanderley de Souza[1,3], Kildare R. Miranda[1,3]

[1] Centro Multiusuário para Análise de Fenômenos Biomédicos da Universidade do Estado do Amazonas, Universidade do Estado do Amazonas, Manaus-AM, Brazil.

[2] Unidade de Entomologia Médica Nelson Ferreira Fé, Fundação de Medicina Tropical Doutor Heitor Vieira Dourado, Manaus-AM, Brazil.

[3] Programa de Pós-Graduação em Ciência Biológicas (Biofísica), Instituto de Biofísica Carlos Chagas Filho and Centro Nacional de Biologia Estrutural e Bioimagem, Universidade Federal do Rio de Janeiro, Rio de Janeiro –RJ, Brazil.

* E-mail: gq.ramos01@gmail.com

Acidocalcisomes are electron-dense organelles rich in polyphosphate complexed with a number of cations [1]. Their functional role involves ion storage and homeostasis, energy metabolism, and osmoregulatio. *Plasmodium vivax* is the leading malaria-causing species worldwide [3], and severity and mortality have been reported in endemic regions. *Plasmodium* sporozoite is the infective form transmitted to the vertebrate host by *Anopheles* mosquitoes, considered one of the major bottlenecks for the control and elimination of malaria. This study aimed to image and chemically characterize acidocalcisomes in *P. vivax* sporozoites by transmission electron microscopy. Sporozoites were isolated from salivary glands by dissecting infected *Anopheles darlingi* mosquitoes 14 days after feeding with infected blood. Sporozoites were washed and resuspended in PBS. Droplets were applied on a Formvar-coated 200-mesh copper grid allowed to adhere for 10 min, carefully blotted dry, and observed in a JEOL-JEM1400 FLASH scanning transmission electron microscope operating at 80 kV. Energy-dispersive X-ray spectra were recorded from the acidocalcisomes present in whole cells. X rays were collected for 100 s with an ultrathin window in a 0–10-keV energy range with a resolution of 10 eV/channel. Elemental analysis was carried out using the Oxford Instruments Aztec Live software 4.3 (Aztec Live, UK). Our results showed that acidocalcisomes of *P. vivax* sporozoite have similar morphological and chemical characteristics to acidocalcisomes found in other protozoa (Figure 1), including those previously described in other species of *Plasmodium* [3]. In conclusion, these data showed the presence of acidocalcisome in sporozoites, providing new information on parasite biology and generating insights for the development of new strategies for blocking transmission.

REFERÊNCIAS

[1] K. Miranda *et al.*, Acidocalcisomes in Apicomplexan parasites. Exp. Parasitol., 1 (2008) 118.
[2] WHO. World malaria report (2021).
[3] F. A. Ruiz, S. Luo, S. N. J. Moreno, and R. Docampo, “Polyphosphate content and fine structure of acidocalcisomes of *Plasmodium falciparum.* Microsc. Microanal. 5 (2004) 10.
[4] This research was supported by FAPEAM, CNPq and MS.

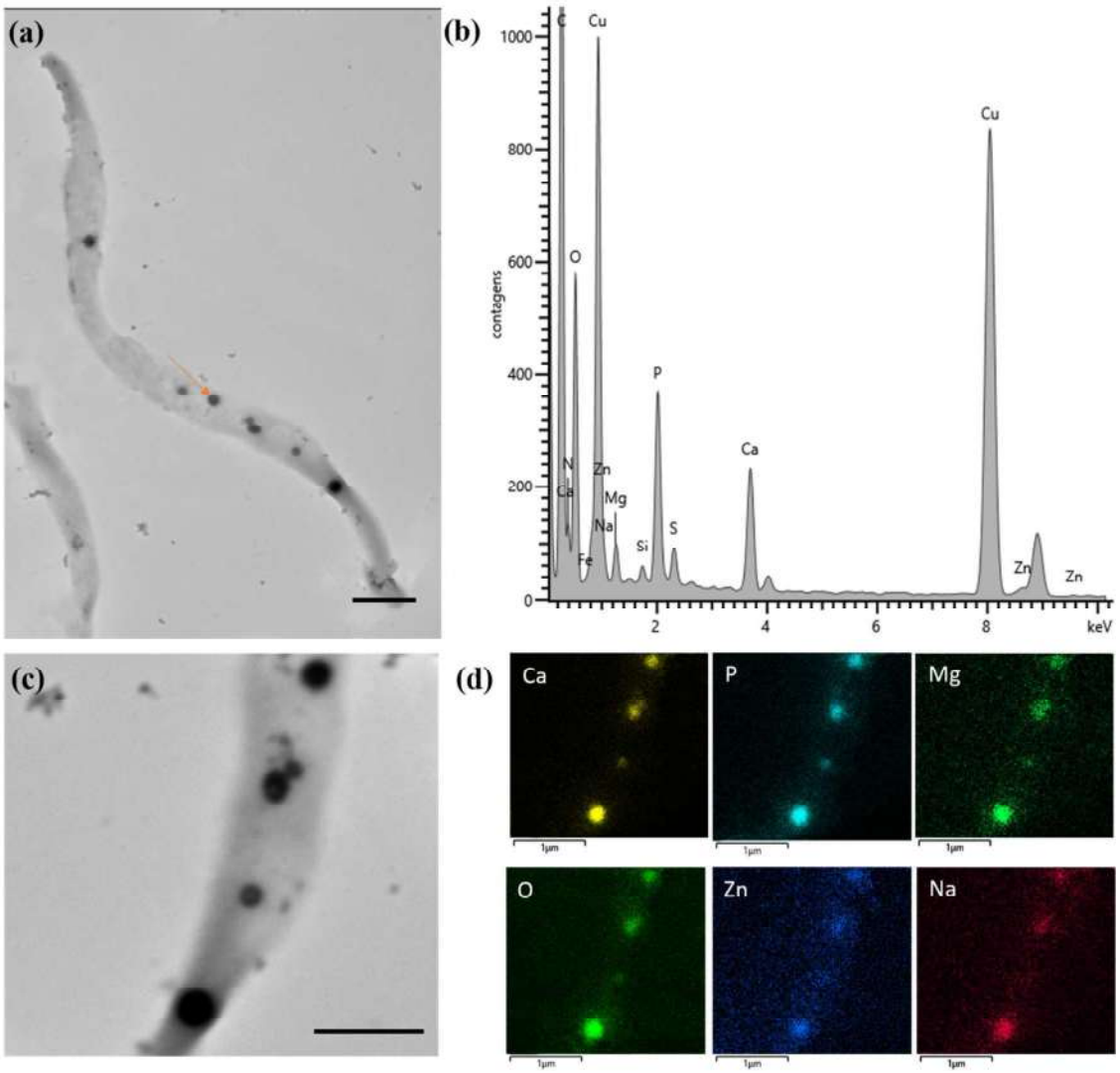

Figure 1 Presence of acidocalcisomes in sporozoites of *P. vivax*. (a) Scanning-transmission electron microscopy image of whole unstained cells showing distribution of acidocalcisomes (arrows) in a sporozoite Bar: 1µm. (b): Typical X-ray spectrum of an acidocalcisome, showing the presence of Na, Mg, P, Ca and Zn. (c) High magnification showing dense organelles that correspond to acidocalcisomes. Bar: 500nm and (d) Elemental maps showing that the typical acidocalcisome elements are concentrated within the acidocalcisome

Characterization of Chikungunya Virus (CHIKV) Infection in Human Neuroblastoma IMR-32 Cells.

Isadora Helena Freitas da Silva[1, 2]*, Maria Ester da Cunha Monteiro[1], Murilo Augusto Ribeiro de Lacerda[1], José Antônio Picanço Diniz Junior[1].

[1]Instituto Evandro Chagas, [2]Centro Universitário Metropolitano da Amazônia

*isadorafs_92@hotmail.com

Infectious diseases remain major contributors to global mortality, with arboviruses such as Dengue, Zika, and Chikungunya virus (CHIKV) representing a significant public health burden [1]. CHIKV has been implicated in severe neurological manifestations, including encephalitis and Guillain-Barré syndrome [2]. Although recent advances have shed light on the pathophysiology of CHIKV infection—particularly regarding viral tropism, replication kinetics, and host inflammatory responses [3]—its interactions with the central nervous system (CNS) are still insufficiently characterized, especially in *in vitro* systems employing human neuroblastoma cell lines. This study aimed to investigate the cytopathic effects and ultrastructural alterations induced by CHIKV infection in IMR-32 neuroblastoma cells. Cells were cultured in Dulbecco's Modified Eagle Medium (DMEM) supplemented with 10% fetal bovine serum (FBS) and maintained at 37 °C in a humidified 5% CO_2 incubator until reaching 80% confluence. Cultures were infected with the CHIKV strain H855964, kindly provided by the Arbovirology Section of the Evandro Chagas Institute. Phase-contrast microscopy (PCM) was used for daily monitoring of cytopathic effects (CPE), photodocumentation, and sampling for ultrastructural analysis. The supernatant of infected cultures was analyzed for the presence of viral particles using immunoelectron microscopy [4]. Cells were fixed in 2% formaldehyde and 2.5% glutaraldehyde in sodium cacodylate buffer [5] and processed using standard protocols for transmission electron microscopy (TEM). CHIKV infection led to a marked reduction in cell viability, with pronounced CPE observed from 48 hours post-infection (h.p.i.) and affecting over 50% of the cell population by 72 h.p.i. TEM analysis revealed extracellular viral particles with morphology consistent with CHIKV, indicating active viral release. Intracellular changes included dilation of rough endoplasmic reticulum cisternae containing viral particles, disorganization of the Golgi apparatus, increased cytoplasmic vacuolization, and formation of myelin figures—suggesting active involvement of these organelles in viral replication, maturation, and intracellular trafficking. IMR-32 cells were permissive to CHIKV infection, exhibiting characteristic cytopathic and ultrastructural alterations. These findings support the use of this cell line as a relevant *in vitro* model to investigate the neuropathogenic mechanisms of CHIKV and to explore the virus's potential applications as a viral vector in therapeutic strategies, including oncolytic virotherapy [6].

[1] Y. Fang et al., Epidemiology of Mosquito-Borne Viruses in Egypt: A Systematic Review. Viruses, 14(7), (2022) 1577.
[2] T. Cerny et al., The Range of Neurological Complications in Chikungunya Fever. Neurocritical care, 27(3), (2017) 447–457.
[3] A.A. Bettis et al., The global epidemiology of chikungunya from 1999 to 2020: A systematic literature review to inform the development and introduction of vaccines. PLoS Negl Trop Dis, Jan 12;16(1) (2022).
[4] J. D. Almeida. The preparation of viruses for electron microscopy. In: R. Harris et al., Techniques in microbiology. New York, 1980.
[5] M.J. Karnovsky. A formaldehyde-glutaraldehyde fixative of high osmolality for use in electron-microscopy. Journal of Cell Biology, 27, (1965) 137-138.
[6] This research was supported by CNPq (Brazil) and the Electron Microscopy Laboratory of the Evandro Chagas Institute (SEMIE/IEC).

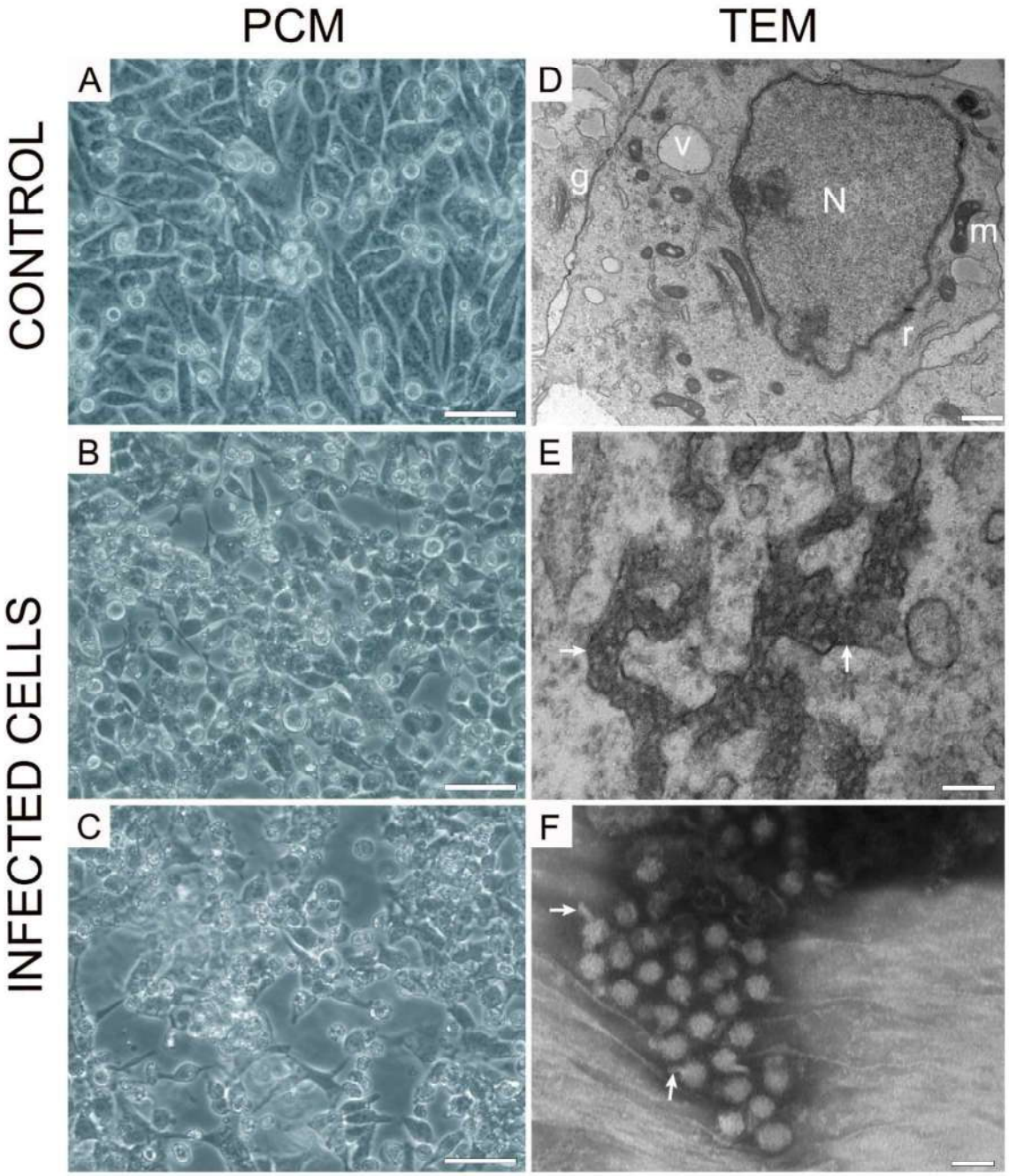

Figure 1. (A), (B), and (C): Phase-contrast micrographs of human neuroblastoma IMR-32 cells (scale bar: 50 µm). (A) Control group showing no morphological alterations; (B) CHIKV-infected cells at 48 h.p.i., displaying disruption of the monolayer, cell rounding, cytoplasmic vacuolization, and evidence of necrosis; (C) Infected cells at 72 h.p.i., with exacerbation of cytopathic effects. (D), (E), and (F): Transmission electron micrographs. (D) Control group (scale bar: 1 µm); (E) CHIKV-infected cell at 72 h.p.i. (scale bar: 200 nm), with arrows indicating dilated rough endoplasmic reticulum cisternae containing viral particles; (F) Immunoelectron micrograph showing immunoprecipitated viral particles (scale bar: 100 nm), with arrows indicating projections extending from the surface of the viral particles.

Characterization of Foamy Macrophages in Oral Inflammatory Lesion: A Microscopic and Ultrastructural Analysis

Marcos Alexandre nunes da Silva[1,2*], Adriana Terezinha Neves Novellino[1], Ana Flávia Schueler de Assumpção Leite[1], Josiane Costa Rodrigues deSá[1], Debora Ferreira Barreto- Vieira[2], Simone de Queiroz Lourenço[1]

[1] Laboratório de Pesquisa Clínica Aplicada em Odontologia, Faculdade de Odontologia, UFF, Niterói, Brasil
[2] Laboratório de Morfologia e Morfogênese Viral, IOC, Fiocruz Rio de Janeiro, Brasil.
*marcossilva@aluno.fiocruz.br.

Mucoceles of the oral mucosa are benign lesions arising from the minor salivary glands, most frequently occurring in the labial mucosa. They typically result from a rupture in the glandular epithelium, leading to saliva extravasation into the surrounding connective tissue and the formation of a pseudocyst (extravasation mucocele) [1]. Multiple treatment options are available, with traditional surgical excision being the most effective due to its low recurrence rate. Although mucoceles predominantly affect young patients, they can occur in individuals of any age. Clinically, they present as soft, bluish, translucent cystic swellings that often exhibit a history of spontaneous rupture, temporary resolution, and recurrent refilling [2]. Microscopically, these lesions are characterized by mucus extravasation surrounded by granulation tissue containing numerous foamy macrophages [3]. This study aimed to evaluate the ultrastructural features of foamy macrophages in oral mucus extravasation lesions, specifically in a lower lip mucocele from a young patient with no identifiable cause. The surgery was uneventful, the lesion was completely removed, revealing an oval lesion with well-defined limits, with liquid inside. Tissue samples were fixed in 2% glutaraldehyde (in 0.1 M sodium cacodylate buffer), post-fixed in osmium tetroxide, dehydrated through a graded acetone series, and embedded in epoxy resin before polymerization at 60°C for transmission electron microscopy (TEM) analysis. Additional samples were fixed in Carson's formalin [4], embedded in paraffin, and stained with hematoxylin and eosin (H&E) for light microscopy. Macrophages containing mucus accumulations were identified and characterized, displaying electron-dense material consistent with mucopolysaccharide and carbohydrate deposition. These macrophages, which internalize material via endocytosis, were closely associated with the internal cavity of the mucus extravasation site. The patient was successfully diagnosed and treated using conventional methods. TEM provided enhanced ultrastructural detail of the vesicular contents within macrophages, contributing to the translational understanding of oral pathologies that are often under investigated.

REFERENCE:

[1] Neville BW, et al *CA Câncer J Clin*. 52:195-215;2016
[2] Nallasivam K U, et al J *Pharm Bioallied Sci* . Aug;7:S731-3, 2015.
[3] Piña AR, *J Oral Maxillofac Pathol.* May;17(2):318. 2013.

[4] Carson FL, *American J of Clinical Pathology* 59:365-373, 1973.

[5] This research was supported by CNPq (Brazil);

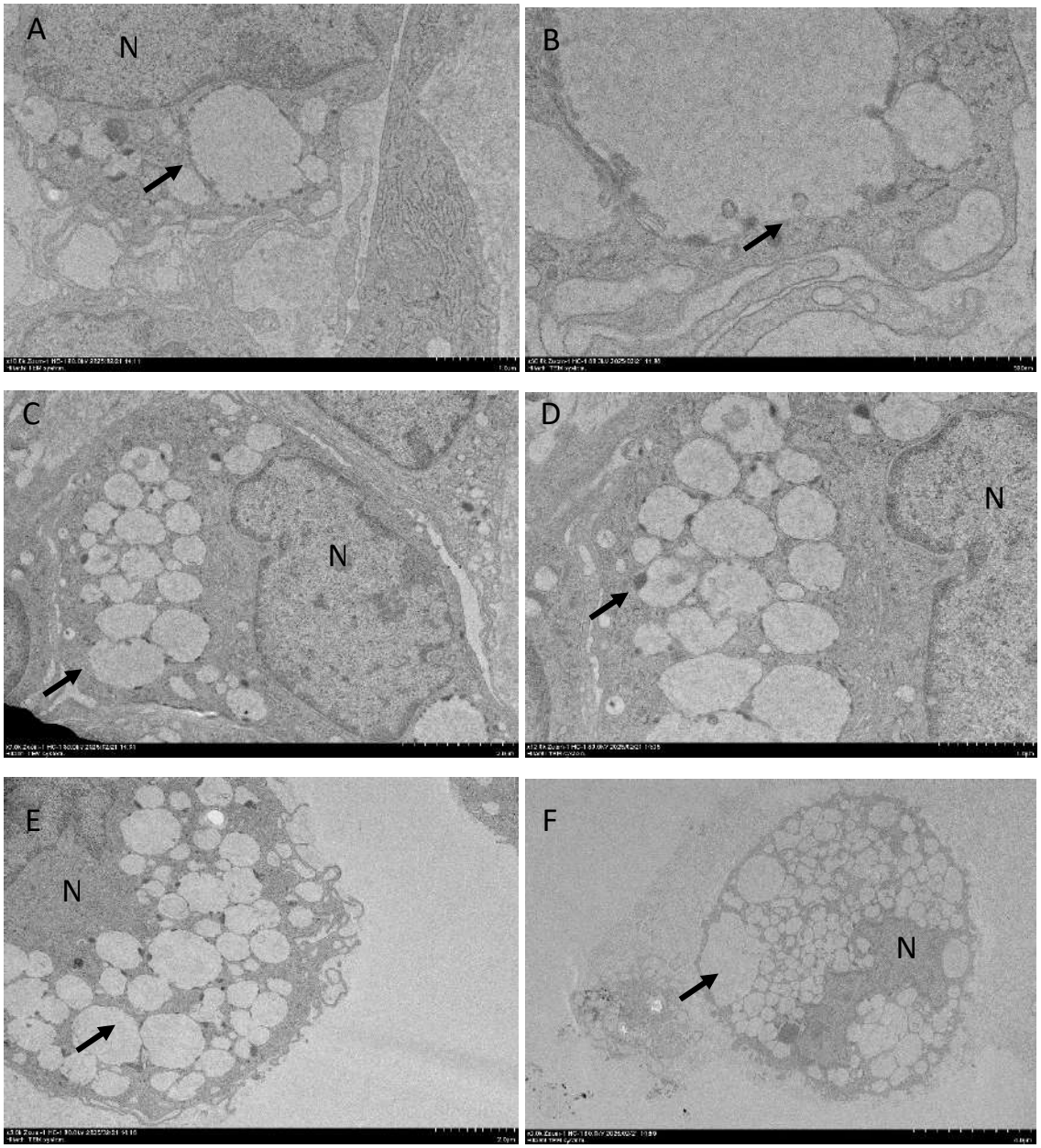

Figures 1: A to F: Electron micrographs of a non-neoplastic inflammatory lesion of the lower lip, mimicking the phenomenon of mucus leakage, mucocele exhibiting vesicles, with amorphous content like free mucin endocytosed by macrophages, Nuclei [N] Endocytosed mucin [black arrows]

Characterization of the structural transition for functional amyloid formation in the context of neuropeptide Y hormone cellular secretion

Murilo de Oliveira Souza[1]*, Luis Felipe Santos Mendes[1].

[1]Sao Carlos Institute of Physics, University of Sao Paulo, IFSC-USP, Sao Carlos, SP, Brazil.
*murilodeoliveira8@usp.br

Amyloid biology investigates how proteins assemble into highly organized, stable structures that play crucial roles in both disease and normal biological processes. These protein aggregates can be divided into pathological amyloids, which are associated with neurodegenerative disorders, and functional amyloids that organisms use for essential processes, such as hormone storage and cellular communication. The precise cellular mechanisms that permit controlled amyloid formation without triggering the cytotoxic effects typically associated with protein aggregates remain incompletely understood. A particularly interesting example is neuropeptide Y (NPY), a hormone involved in stress regulation that can form reversible amyloid structures. This ability enables NPY to achieve high concentration storage while maintaining the capacity for rapid release when needed [1].

Functional NPY amyloids display transient stability, with formation and dissolution occurring within hours rather than the years-long timescale characteristic of pathological aggregates. This rapid kinetic behavior may involve specific structural features common to functional amyloid systems that enhance dynamic flexibility [2], which is essential for maintaining system homeostasis and physiological equilibrium. Our investigation focuses on elucidating these dynamic structural transitions using heterologously expressed NPY under physiologically relevant incubation conditions. Particular attention was given to pH variations along the secretory pathway, where the hormone progresses from the endoplasmic reticulum (pH 7.4) through the Golgi apparatus (pH 6.0-6.7) to secretory granules (pH 5.5) before ultimately being released into the bloodstream (pH 7.4).

Through comprehensive biophysical characterization, we observed NPY's structural transition from predominantly α-helical conformation, evidenced by characteristic circular dichroism minima at 208 nm and 222 nm, to β-sheet-rich amyloid aggregates showing increased intensity at ~200 nm and a new minimum at ~230 nm, confirmed by Thioflavin T fluorescence (Figure 1, A and B). The amyloid nature of these aggregates was confirmed by their resistance to SDS denaturation (Figure 1C), a hallmark feature that distinguishes organized amyloid structures from disordered aggregates. Microscopy studies revealed distinct morphological differences depending on environmental conditions. In the absence of heparin, NPY formed dynamic oligomeric assemblies that evolved into flexible fibrillar structures (Figure 2A and 2B). In contrast, the addition of heparin promoted the formation of more rigid, well-defined fibrils approximately 10 nm in diameter, as visualized by transmission electron microscopy (Figure 3). These findings suggest that under physiological conditions, NPY maintains a dynamic equilibrium of fragmented, short and flexible fibril states that can be concentrated into oligomeric packages optimized for rapid monomeric release. At the same time, heparin addition induces the formation of more rigid, long and stable amyloid-like fibrils that may be less suitable for the rapid disaggregation required for proper hormonal function. This delicate balance between structural stability and reversibility appears crucial for NPY's biological activity within the secretory pathway.

[1] Maji, S. K., Perrin, M. H., Sawaya, M. R., Jessberger, S., Vadodaria, K., Rissman, R. A., Singru, P. S., Nilsson, K. P., Simon, R., Schubert, D., Eisenberg, D., Rivier, J., Sawchenko, P., Vale, W., & Riek, R. (2009). Functional amyloids as natural storage of peptide hormones in pituitary secretory granules. Science (New York, N.Y.), 325(5938), 328–332. https://doi.org/10.1126/science.1173155
[2] Sawaya, M. R., Hughes, M. P., Rodriguez, J. A., Riek, R., & Eisenberg, D. S. (2021). The expanding amyloid family: Structure, stability, function, and pathogenesis. Cell, 184(19), 4857–4873. https://doi.org/10.1016/j.cell.2021.08.013
* This work was supported by Fundação de Amparo à Pesquisa do Estado de São Paulo (FAPESP), process number 2023/09930-2 and 2022/06006-0, and used facilities of the Brazilian Nanotechnology National Laboratory (LNNano)- BAG number: 20233136.

Figure 1. A) Circular dichroism measurements used to characterize the formation of NPY [20 µM] amyloid fibrils, incubated at 37ºC in 100 mM Sodium phosphate buffer, pH 5.4, for up to 72 hours. B) Thioflavin T [40 µM] fluorescence in different PB [100 µM] pH's, excitation 440 nm and emission 485 nm. C) SDS resistance assay, Lane 1: Molecular weight marker; Lane 2: Purified sample of NPY (~ 4.11 kDa); Lane 3: 50 µM of NPY incubated during 48h in Tris Buffer pH 8.0 [50 mM] and treated with Urea [6M]; Lane 4: 50 µM of NPY incubated during 48h in Phosphate Buffer pH 6.0 [50 mM] and treated with Urea [6M].

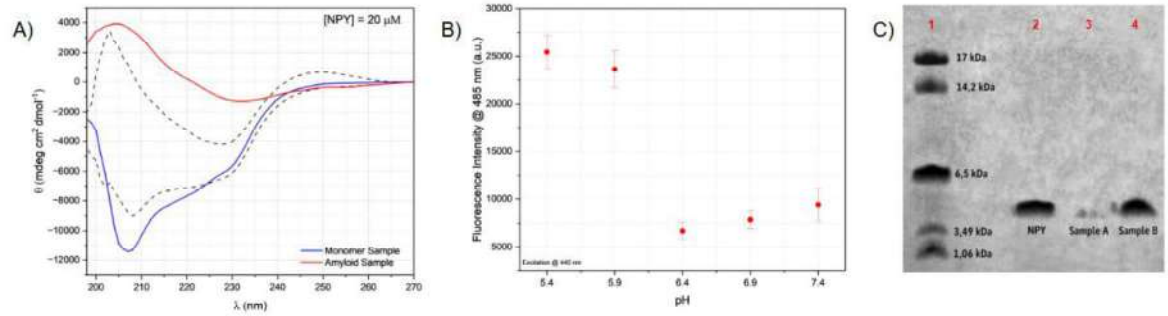

Figure 2. Atomic force microscopy (AFM) images of NPY incubated samples during 12h (A) and 72h (B) in PB pH: 5.4, 37 ºC and 250 r.p.m. Showing an evolution from oligomeric structure with ~10 nm of diameter to a fibrillar structure with ~10 nm of diameter.

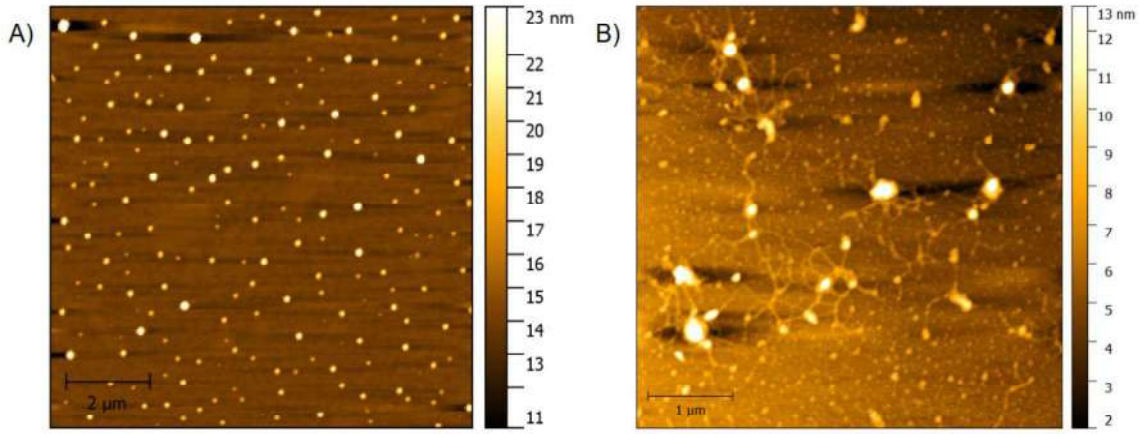

Figure 3. Transmission electron microscopy (TEM) images of NPY samples incubated for 30 days in phosphate buffer (pH 5.4) at 37 °C and 250 r.p.m, in the absence (micrographs 1 and 2) and presence (micrographs 3 and 4) of 10 mg/mL heparin. The images show a transition from oligomeric structures (~10 nm in diameter) to fibrillar structures (~10 nm in diameter).

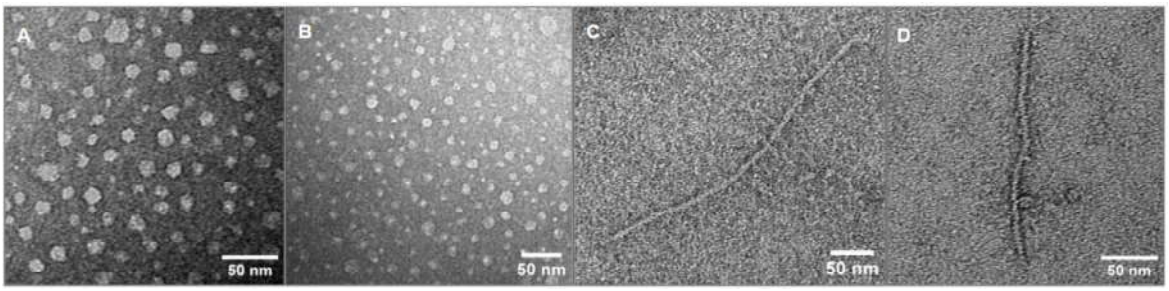

Convergent Microscopy Techniques Confirm the Occurrence of Callose in Laticiferous Cells of a Legume Species

Tatiane Maria Rodrigues[1]*, Stefany Cristina de Melo Silva[1], Yasmin Massimino Sampaio de Souza[1], Yve Canaveze[2], Silvia Rodrigues Machado[1]

[1]São Paulo State University- UNESP, Institute of Biosciences of Botucatu- IBB, [2] Universidade Federal de São Carlos (UFSCar)
*tatiane.rodrigues@unesp.br

Latex is a biological fluid produced in more than 40 phylogenetically distant plant families and present high economic importance, being the raw material for rubber production [1]. Latex remain storaged inside laticifers and is only released after injuries [2]. Laticifers are highly specialized cells forming a system that permeates the plant body [3] and are crucial in the defence against herbivores and pathogens attacks [2]. The protoplast of the laticiferous cell itself can constitute the latex [4], which is characterized as a milky emulsion constituted of a complex mixture of compounds, such as alkaloids, terpenes, resins, gums and proteins, in addition to inorganic components [1, 3]. The walls of laticiferous cells can present some important modifications that contribute to the cell function, such their increased thickening, accumulation of enzymes and impregnation by special substances [5, 6]. In this sense, substances as callose and suberin have been detected impregnating the laticifer cell walls in some plants [6], but not in legumes. *Mimosa caesalpiniifolia* Benth. (Fabaceae, Caesalpinioideae) is one of the few legume species known to produce latex. In this study, we investigated the occurrence of specialized impregnations in the walls of laticiferous cells of this species. Young stem portions were processed according to standard techniques in plant anatomy and transmission electron microscopy. In addition, samples were treated with Sudan IV for detection of lipids, Ruthenium Red for polysaccharides, Periodic Acid/Schiff Reagent (PAS) for neutral polysaccharides and analyzed under a light microscope in bright field. Sections were treated with aniline blue for callosed marking and analyzed under a confocal microscope. Large laticifer cells occured immersed in the stem phloem of *M. Caesalpiniifolia*. Mature laticifers exhibited irregularly thicked pectin-cellulosic cell walls and both the nucleus and organelles were absent. The protoplast was filled with flocculent latex. A discontinuous additional inner layer was observed in the walls of mature laticifer cells. This cell wall portion tested positive for polysaccharides and reacted under the fluorescent marker for callose. To our knowledge, this is the first report of the occurrence of callose impregnations in laticiferous cell walls in a legume species. In contrast to cellulose, callose is found only in specific cell walls [7]. Callose found in the laticifers of *M. caesalpiniifolia* may act as a protective barrier, restricting the infiltration of pathogens into the laticifer system, as suggested for other plants [7]. This protection helps preserve the proper function of secretory cells and maintain the typical composition of the latex. Furthermore, callose may avoid the efflux of latex outside the laticifer cells, thereby avoiding potential self-toxicity caused by the secretion [8]. Given the cytotoxic nature of many latex compounds, researches have proposed that laticifers developed as specialized compartments for isolating these substances, allowing their storage independently of the vascular system [1]. This study, using a legume species as model, highlights potential avenues for investigating the production and distribution of callose in the walls of laticifers, as well as its relevance to the proper functioning of this secretory structure.

[1] J. Gracz-Bernaciak et al., Int J Mol Sci. 22 (2021) 12427.
[2] B.D. Farrel et al., Am. Nat. 138 (1992) 881-900.

[3] R.F. Evert, Esau's plant anatomy, Wiley, New York, 2006.
[4] P. Matile,New Phytol. 105 (1987) 1-26.
[5] Y. Canaveze et al., Protoplasma 256 (2019) 131-146.
[6] M.C. Medina et al, Front. Plant Sci. 18:11 (2021) 612985.
[7] B. Wang et al., Heliyon 8 (2022) e09248.
[8] J.M. Hagel et al., Trends Plant Sci. 13 (2008) 631–639.
[9] This research was supported by CNPq (312900/2021-0), PROPe/UNESP and Capes (001), Brazil.

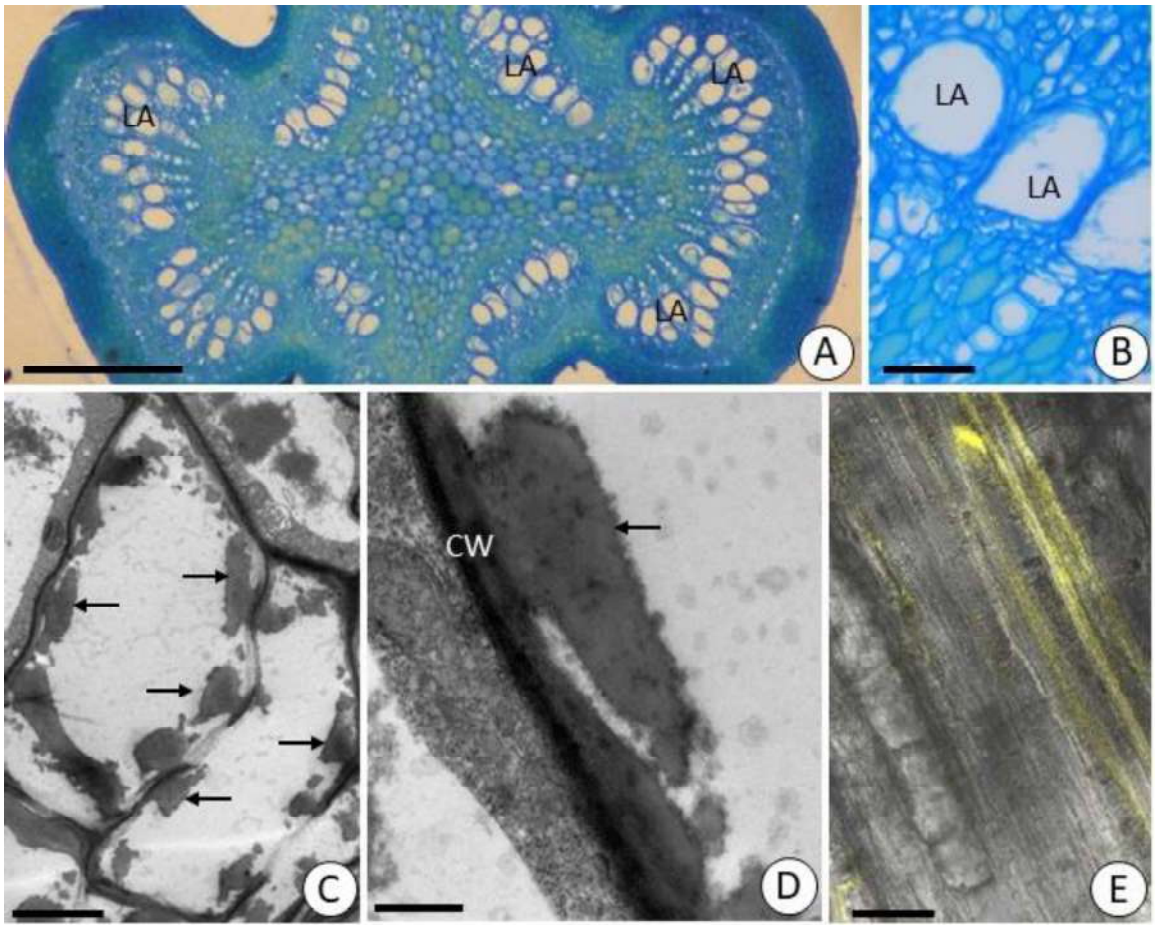

Figure 1. Laticifers in the stem of *Mimosa caesalpiniifolia* (Fabaceae). A, B. Ligh micrographs showing laticifers (LA) in cross sections stained with toluidine Blue. C, D. Transmission electron micrographs showing mature laticifers containing a discontinuous additional inner in the cell wall (arrows). CW = cell wall. E. Longitudinal section treated with aniline blue showing callose deposition (marked in yellow) in the walls of laticifer cells under confocal microscopy. Scale bars : A= 500µm ; B= 50 µm ; C= 5 µm ; D= 0.5 µm ; E= 30 µm.

CULTURE MEDIA IMPACTS HYPHAL DEVELOPMENT IN THE PATHOGENIC FUNGUS *Candida albicans*

Rayane Gonçalves Pereira da Silva[12]*, Pedro Henrique Sampaio[2], Luana Pereira Borba dos Santos[2], Sonia Rozental[2], Marcel Menezes Lyra da Cunha[12]

[1]Núcleo Multidisciplinar de Pesquisa UFRJ-Xerém em Biologia (NUMPEX-BIO)/Universidade Federal do Rio de Janeiro Campus Duque de Caxias Professor Geraldo Cidade.

[2]Laboratório de Biologia Celular de Fungos, Instituto de Biofísica Carlos Chagas Filho/Universidade Federal do Rio de Janeiro.

*rayanegoncalves@biof.ufrj.br

Candida albicans is the most prominent medically important fungus [1]. It exhibits multiple morphological phenotypes of critical importance to its pathogenicity, such as the transition of yeast to pseudohyphae and hyphae [2]. *C. albicans* is commonly found in the microbiota of most healthy individuals, colonizing areas such as the skin, oral and respiratory mucosa, gastrointestinal tract, and genitourinary system. However, under conditions of host immunosuppression, *C. albicans* adopts a filamentous form capable of tissue invasion, leading to infections ranging from superficial to systemic. Our ultimate goal is to characterize the ultrastructure of the hyphal apical region and to analyze the spatial organization, volume, and interactions of subcellular components associated with the pathogenicity of *C. albicans*. Yeast cells were cultured in YNB medium or RPMI 1642 supplemented with 2% (w/v) glucose for up to 24 hours at 37 °C with 5% CO_2 to induce filamentation. Cells were lysed using lysis buffers and enzymes for the isolation of internal organelles. Samples were collected at various time points and processed for scanning electron microscopy (SEM), transmission electron microscopy (TEM), and light microscopy. Electron microscopy preparation was based on fixation with aldehydes, post-fixation with osmium tetroxide, dehydration, critical point drying and metal sputtering for SEM or embedding in Spurr resin for TEM. Hyphae cultured in RPMI medium exhibited increased size and a higher frequency of bifurcated budding structures, which became prominent after 3 hours of incubation, as observed by SEM (Figure 1). Moreover, hyphae of *C. albicans* grown in RPMI showed a larger size after 3 hours of incubation. Cell wall thickness was examined by TEM, and the inner layer (glucan and chitin) appeared slightly thicker compared to cells grown in YNB. Additionally, and as a starting point for the study of isolated organelles of this pathogen, we've established a protocol for fungal lysis, enabling the isolation of integral organelles such as mitochondria (Figure 2). Fungal growth in different media is a valuable approach to understand how growth conditions found in hosts, laboratories and nature affect *C. albicans* virulence determinants and ultrastructural organization. Preliminary results indicated that cells grown in nutrient-poor (YNB) and nutrient-rich (RPMI) media display distinct hyphal growth and polarized patterns. These differences may influence key virulence traits, such as biofilm formation. After the establishment of an efficient cell lysis protocol for fungi, following experiments will be performed to understand the impact of growth conditions over organelles. Our findings will provide new insights into morphogenetic transitions linked to pathogenicity.

[1] World Health Organization (2022) WHO fungal priority pathogens list to guide research, development and public health action. Genebra: WHO Press.
[2] D'ENFERT, C. *et al.* FEMS Microbiol Rev, v. 45, n. 3 (2021)
[3] This research was supported by FAPERJ, CAPES, PMBqBM and CENABIO (Brazil)

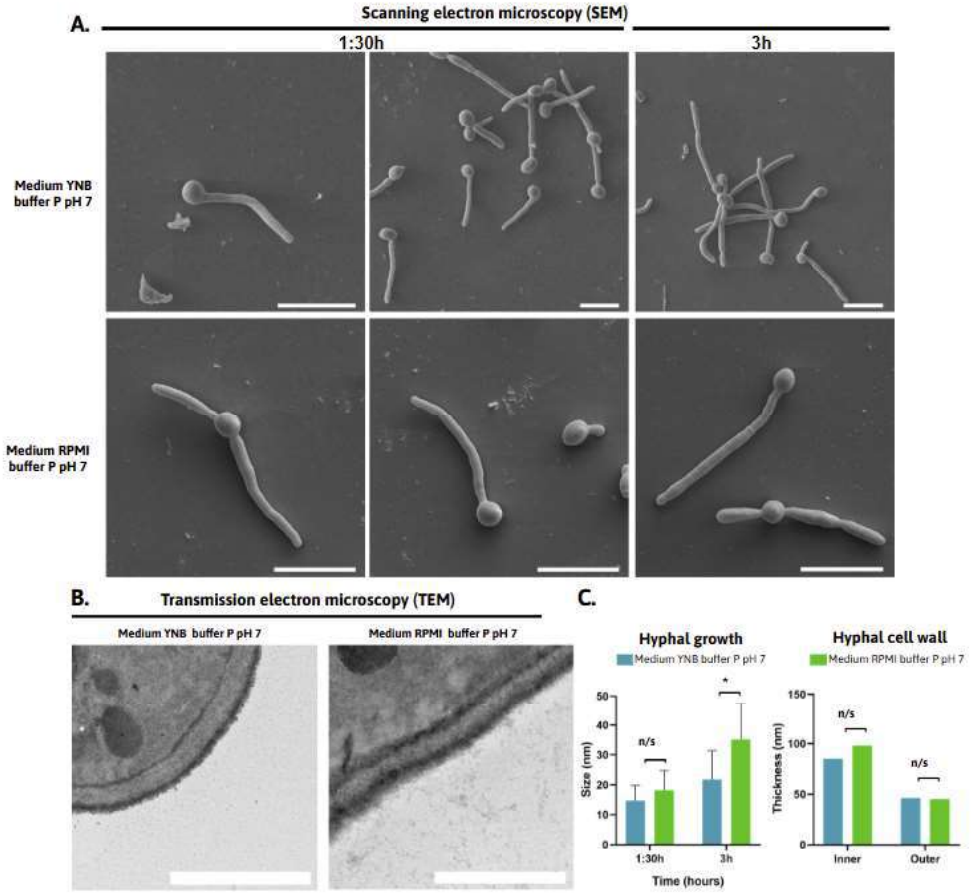

Figure 1. *C. albicans* grown in Medium YNB or RPMI 1640 supplemented with 2% glucose buffered in buffer P pH 7 for 1:30h and 3h at 37ºC 5% CO2 was examined by SEM. Scale bar represents 10 μm in SEM, and 1 μm and 2 μm in TEM (*p<0.05).

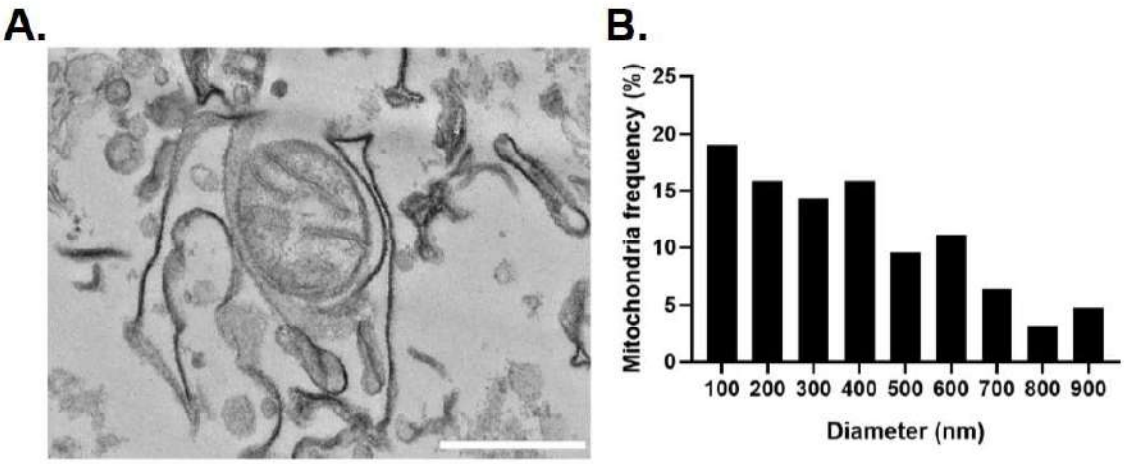

Figure 2. TEM of isolated mitochondria and measurements obtained using an optimized lysis protocol for *C. albicans*. A total of 63 mitochondria were measured. Scale bar: 500 nm.

Effect of Cold Rolling on the Kinetics of Spinodal Decomposition in a Lean Duplex Stainless Steels

Isadora Reis de Souza[1], Dagoberto Brandão Santos[1*]

[1] Metallurgical and Materials Engineering Department, Universidade Federal de Minas Gerais, Belo Horizonte, MG-31270-901, Brazil. * dsantos@demet.ufmg.br

Duplex stainless steels (DSS) are a crucial class of engineering materials known for their optimal corrosion resistance and superior mechanical properties. These iron-based alloys feature a microstructure of equal volume fraction of austenite and ferrite phases. Their optimum balance between mechanical strength and corrosion resistance in harsh environments has made them prominent in the industry [1,2]. The appearance of deleterious phases in DSS is closely linked to their processing. Element segregation during the steel solidification can result in the formation of harmful phases such as the sigma and chi ones. Furthermore, high-temperature heat treatment can also lead to the apparition of these unwanted phases [3,4]. Plastic deformation processes, such as cold rolling, can induce significant microstructural modification, such as the formation of secondary phases. Conversely, the austenitization process can dissolve these existing secondary phases, reducing their concentration and its effect on these steels [5]. According to Ornek et al. [4], aging of DSS above 400ºC can induce embrittlement because of the precipitation of the sigma phase, carbides and nitrides, later leading to a reduction in the material's ductility and toughness. Spinodal decomposition is a clustering reaction in which a homogeneous, supersaturated, solid solution separates spontaneously into two phases with distinctly different chemical compositions and physical properties. These couple phases produced by the spinodal decomposition differ in composition from the parent phase. However, they both have essentially the same crystal structure, occurring uniformly throughout the material or in a specific phase of α-ferrite in DSS [6-7]. This work analyzed the effects of cold rolling and aging treatment at 500°C on lean duplex stainless steel 2304 lean duplex stainless steel (LDSS), Table 1. Microstructural analyses were conducted using scanning electron microscopy (SEM), transmission electron microscopy (TEM), and X-ray diffraction (XRD). The mechanical behavior was assessed through Vickers microhardness and tensile tests. The samples were subjected to different ageing periods ranging from 0.5 h to 48 h at 500°C, both in the as-received condition and after cold rolling with 74% thickness reduction. The primary objective was to detect spinodal decomposition in the samples and understand its influence on mechanical behavior. Deformation-induced martensite formation and spinodal decomposition were observed in the cold-rolled sample. The characterization of spinodal decomposition was based on the mottled appearance under TEM examination, which became more evident for longer aging times, Figure 1. During aging heat treatment, both hardness and tensile strength increased significantly, although there was a corresponding reduction in ductility, Table 2. For cold-rolled samples, the increase in mechanical properties was higher concerning undeformed steels. The spinodal decomposition in deformed steels slows down the ferrite recovery process throughout dislocations anchoring .

[1] Francis R, Byrne G. *Duplex Stainless Steels - Alloys for the 21st Century*. Metals (Basel) 2021; 11:836.

[2] Alvarez-Armas I. *Duplex Stainless Steels: Brief History and Some Recent Alloys.* Recent Patents on Mech Eng. 2008; 1:51–57.

[3] Silva R, Baroni LFS, Silva MBR, Afonso CRM, Kuri SE, Rovere CAD. *Effect of thermal aging at 475°C on the properties of lean duplex stainless steel 2101*. Mater Charact. 2016; 114:211–217.
[4] Örnek C, Burke MG, Hashimoto T, Lim JJH, Engelberg DL. *475°C embrittlement of duplex stainless steel. A comprehensive microstructure characterization study*. Mater Perform Charact. 2017; 6(3):409-436.
[5] Chan KW, Tjong SC. *Effect of Secondary Phase Precipitation on the Corrosion Behavior of Duplex Stainless Steels.* Mater. 2014; 7:5268-5304.
[6] Sahu JK, Krupp U, Ghosha RN, Christ H-J. *Effect of 475ºC embrittlement on the mechanical properties of duplex stainless steel.* Mater Sci Eng A. 2009; 508:1–14.
[7] The authors thank CNPq (Process Number: 305290/2022-3) and CAPES for their support in the research. We thank SENAI Institute of Innovation in Metallurgy and Special Alloys - CIT SENAI - for their support in TEM. Thanks, are also extended to the UFMG Microscopy Center for support in the SEM-FIB and TEM analysis.

Table 1. Chemical composition (% by mass) of duplex stainless steel used

Steel	C	Mn	P	S	Si	Cr	Ni	Mo	Cu	N
2304	0,011	1,45	0,037	0,0004	0,20	22,8	4,2	0,3	0,45	0,10

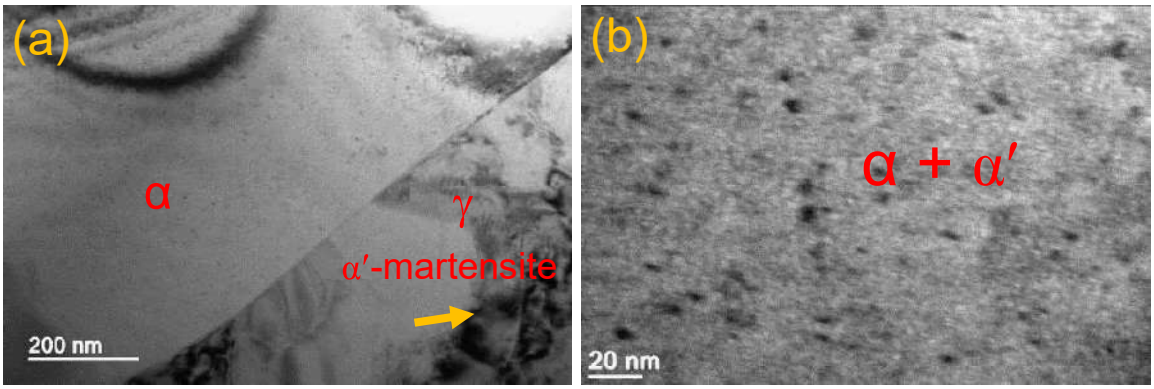

Figure 1. TEM micrographs of the 2304 LDSS sample without deformation aged at 500°C for 24 h. In (a) the α + α'(BCC) and γ (FCC) substructure are illustrated. In (b) a higher magnification of the α region indicated in (a) shows the mottled substructure in ferrite due to spinodal decomposition. Dark globules are rich in Fe and light gray or white are rich in Cr.

Table 2. Mechanical properties of the 2304 DSS after aging at 500ºC for different times obtained by tensile and hardness tests

Sample Identification	**Yield Strength**	**Tensile Strength**	**Total Elongation**	**Hardness Vickers**
	(MPa)	(MPa)	(%)	HV
As-received	642	749	59	246
Aging at 500°C – 0.5 h	630	740	43	279
Aging at 500°C – 2 h	690	787	38	297
Aging at 500°C – 24 h	681	777	32	331
Aging at 500°C – 48 h	694	789	32	281
Cold-rolled	1391	1534	4.6	405
Aging at 500°C – 0.5 h	1166	1293	4.3	442
Aging at 500°C – 24 h	1335	1470	4.7	425
Aging at 500°C – 48 h	1308	1454	4.5	457

Effect of quinazoline derivatives on *Toxoplasma gondii* tachyzoites mitochondrion

Mike dos Santos[1*], Mariana M. Cunha[1]; Carla M. Tecchio; Rosana Freitas[2]; Simon J. Garden[2], Érica dos Santos Martins-Duarte[1].

[1]Departamento de Parasitologia—ICB, Universidade Federal de Minas Gerais, Brasil
[2] Instituto de Química – IQ, Universidade do Estado do Rio de Janeiro
[3]Departamento de Química—IQ, Universidade Federal do Rio de Janeiro, Brasil
*mikesantos@ufmg.br

Toxoplasmosis is a zoonotic disease with a global distribution, and its symptoms are associated with the host's immune status [1]. Congenital toxoplasmosis and toxoplasmosis in immunocompromised patients can be severe, whereas most immunocompetent patients are asymptomatic [2]. One of the problems related to toxoplasmosis is the limited therapeutic arsenal available in clinical practice. The standard treatment is a combination of sulfadiazine and pyrimethamine, which has adverse events that reduce treatment adherence, does not lead to parasitological cure, and acts only statically on tachyzoites (during the acute phase), with no effect on bradyzoites (in the chronic phase) [3]. Therefore, the discovery of new anti-*Toxoplasma gondii* molecules is urgent. In previous studies, our group demonstrated promising activity in the treatment of toxoplasmosis with other quinazoline derivatives [4]. Thus, using the chemical metamorphosis technique, this study tested 24 quinazoline derivatives (six anilinoquinazolines and eighteen pyridyl-anilinoquinazolines) [4]. Cytotoxicity was evaluated using the MTS/PMS assay and the antiproliferative assay (24h) to determine the Selectivity Index (SI). Derivatives with an SI greater than 10 and proliferation inhibition greater than 50% were chosen for analysis by transmission electron microscopy (TEM). For TEM analysis, culture flasks containing NHDF monolayers were infected at a 10:1 parasite-to-cell ratio with the RH strain and then treated for 24 hours with quinazoline derivatives. At the end of this time, the cultures were fixed with 2.5% glutaraldehyde diluted in 0.1M sodium cacodylate buffer (pH 7.4) for 2 hours. and post-fixed for 60 in the dark) with 1% osmium tetroxide, in 0.1 M sodium cacodylate buffer (pH 7.4). Samples were dehydrated in ethanol solutions of increasing concentrations (30–100%) and embedded in PolyBed (Polyscience Inc., Warrington, PA, USA). Ultrathin sections of 70 nM were stained with uranyl acetate and lead citrate, and then observed in a Fei Tecnai Spirit 120 kV transmission electron microscope [4]. Mitochondrial diameter measurement was performed using ImageJ 1.54e software. Data and statistical analysis were performed using GraphPad Prism 8.0.1 software. Of the 24 derivatives, only 3A, 4A, 6A, 1P, 6P, 8P, 12P, 16P, 17P, and 18P were chosen for TEM analysis. After analyzing the TEM images of these best derivatives, morphological changes were observed in the mitochondria in tachyzoites treated with derivatives 3A, 4A, 6A, 12P, 16P, 17P, and 18P (Figures 1 and 2). Thus, anilinoquinazolines and pyridyl-anilinoquinazolines act on *T. gondii* mitochondrion and are viable candidates for future treatments for toxoplasmosis. This research was supported by FAPEMIG and CNPq (Brazil) grants. Authors also thank the BioImaging Network of Minas Gerais (BioIMG Net) and UFMG Microscopy Center.

[1] Molan, A; et al., *Global status of Toxoplasma gondii infection: systematic review and prevalence snapshots.* Trop Biomed (2019),
[2] Saadatnia,G; Golkar, M. *A review on human toxoplasmosis*. Scandinavian Journal of Infectious Diseases (2012)
[3] Dunay, I. D; et al., *Treatment of Toxoplasmosis: Historical Perspective, Animal Models, and Current Clinical Practice*. Clinical Microbiology Reviews (2018)
[4] Duarte-Martins, E.S.; et al., *In vitro activity of N-phenyl-1,10-phenanthroline-2-amines against tachyzoites and bradyzoites of Toxoplasma gondii*. Bioorganic & Medicinal Chemistry (2021).

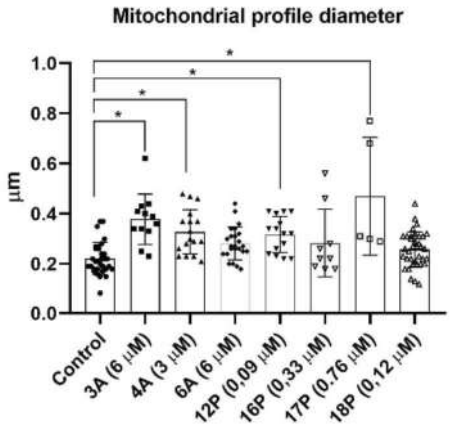

Figure 1. Mitochondrial profiles diameter. Mitochondrion profiles of tachyzoites of *T. gondii* treated with seven derivatives were measured. The results showed that four derivatives induced a significant alteration. *p < 0.05

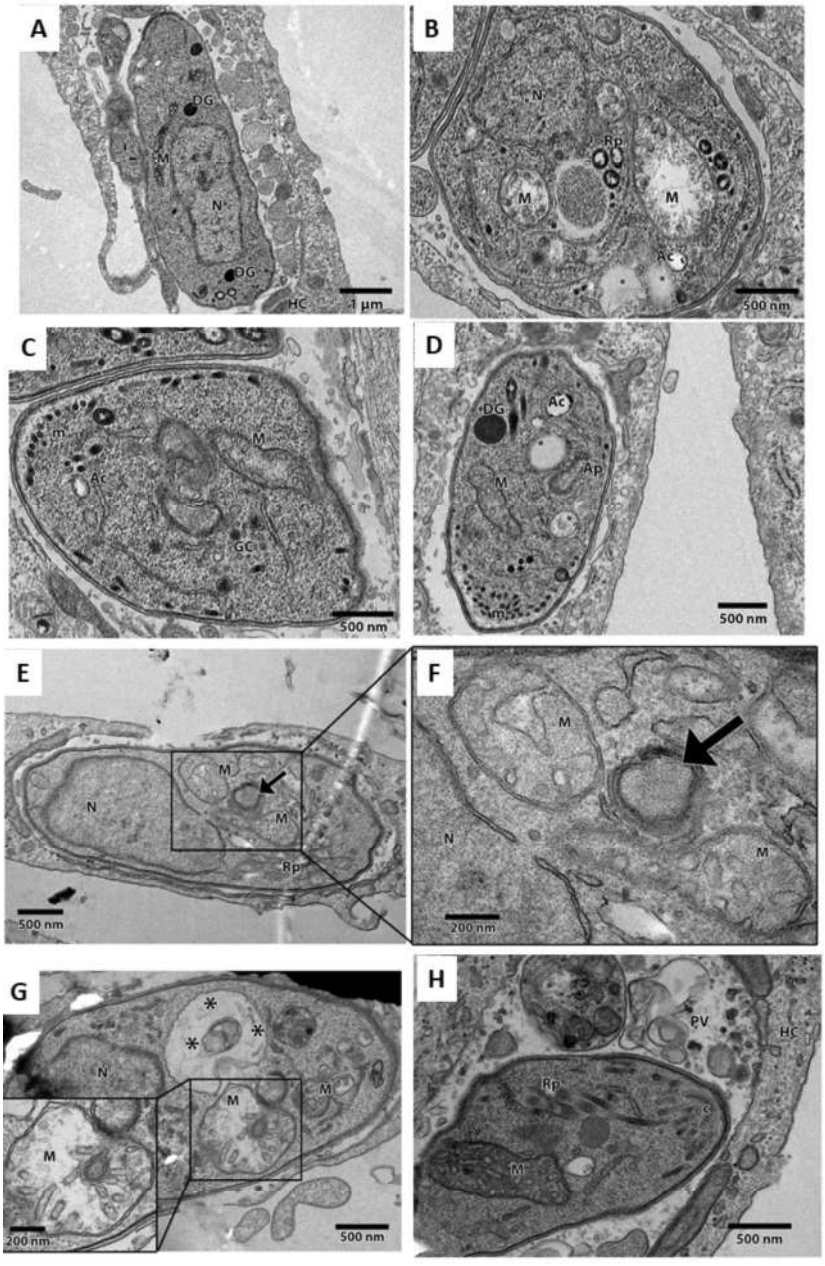

Figure 2. Transmission electron microscopy micrographs of intracellular tachyzoites after treatment with quinazoline derivatives for 24h.
(A) Control. (B) 3A 6 µM. (C) 4A 3 µM. (D) 6A 6 µM. (E-F) 12P 0,09 µM. (G) 17P 0,76 µM. (H) 18P 0,12 µM. (Arrow) autophagic process.; (asterisks) excessive vacuolization of the tachyzoite. DG - Dense granules; GC - Golgi complex; HC - Host cell; M - Mitochondrion; N - Nucleus; Nu - Nucleolus; PV - Parasitophorous vacuole; Rp - Rhoptries.

Effects of settleable atmospheric particulate matter on cardiac function and metal nanoparticle uptake in bullfrog (*Aquarana catesbeiana*) tadpoles

Regiane L. da Costa[1], Iara da C. Souza[1], Magdalena V. Monferrán[2], Daniel A. Wunderlin[3], Cleoni dos Santos Carvalho[4], Marisa N. Fernandes[1], Diana Amaral Monteiro[1]*

[1]Departamento de Ciências Fisiológicas, Universidade Federal de São Carlos (DCF/UFSCar), São Carlos, São Paulo, Brazil, [2]Departamento Bioquímica Clínica, Facultad de Ciencias Químicas, Universidad Nacional de Córdoba, Argentina, [3]ICYTAC, Universidad Nacional de Córdoba, Córdoba, Argentina, [4]Departamento de Biologia (DBio), Universidade Federal de São Carlos, *campus* Sorocaba, Sorocaba, São Paulo, Brazil.

*dianamonteiro@ufscar.br

Airborne particulate matter (APM), especially settleable forms (SePM), has emerged as a pervasive environmental contaminant in industrialized regions, posing threats to both terrestrial and aquatic ecosystems. SePM can carry a complex mixture of metals and metalloids, including iron, aluminum, and titanium, many of which can exist as nanoparticles and penetrate biological barriers. Amphibians, particularly in their aquatic larval stages, are highly vulnerable to such contamination due to their permeable skin and extensive water contact during early development. Previous studies using *Aquarana catesbeiana* (syn. *Lithobates catesbeianus*) tadpoles demonstrated neurotoxicity (Fernandes et al., 2024) and alterations in erythrocyte morphology and blood oxidative stress (da Costa et al., 2023) following exposure to SePM. Building upon this established model and dataset, the current study investigates cardiac function and structural integrity in the same experimental cohort of tadpoles exposed to environmentally relevant concentrations of SePM collected from an industrial region. Given the sensitivity of amphibian hearts to environmental stressors and their utility as vertebrate models in ecotoxicology, we hypothesized that SePM exposure could disrupt cardiac contractility and ultrastructure, with implications for systemic circulation and developmental health. Bullfrog tadpoles at Gosner stage 25 were exposed to 1 $g.L^{-1}$ of SePM under controlled laboratory conditions for 96 hours in a static system. Following exposure, cardiac contractility parameters were evaluated in accordance with the methodology described by Adorno et al. (2023), which includes assessment of heart rate and myocardial performance in isolated ventricles, specifically measuring contractile force and the rates of contraction and relaxation. For ultrastructural analysis, ventricular samples were fixed in glutaraldehyde and processed for transmission electron microscopy (TEM), with microanalysis using an electron dispersive spectroscope (EDS) to detect the presence and subcellular localization of metallic nanoparticles in the myocardium. SePM-exposed tadpoles displayed significant cardiac alterations, including tachycardia, increased contractile force, and contraction/relaxation rates, coupled with reduced relative ventricular mass compared to controls. Microanalysis detected nanoparticulate forms of Fe, Sn, Ni, Ti, and W, frequently localized within the cytoplasm and nuclei of cardiomyocytes. These cardiac adjustments likely represent compensatory mechanisms to maintain cardiac output and tissue perfusion during metal exposure. However, the associated energetic costs may divert resources from critical behaviors like foraging and swimming, potentially impacting fitness. The findings highlight the urgent need for emission controls to protect amphibian populations.

[1] H.A. Adorno et al., Sci. Total Environ. 856 (2023) 159168.
[2] R.L. Costa et al., Environ. Pollut. 340 (2024) 122846.
[3] I.C. Souza et al., Sci. Total Environ. 753 (2021) 141976.
[4] This research was supported by FAPESP (2019/08491-0, 2023/01356-5, 2023/09730-3), ANPCYT (FONCyT/PICT-2019 N1743, PICT 2021 N002), and CONICET (PIP 2022-11220210100480CO).

Figure 1. (A) Heart rate (f_H, bpm) of bullfrog tadpoles in the control (Ct) and SePM-exposed (SePM) groups. **(B)** Isometric force (Fc, mN·mm^{-2}) generated by ventricular strips from Ct and SePM tadpoles during stepwise increases in stimulation frequency. Data are presented as mean ± SEM. Asterisks (*) denote statistically significant differences ($p < 0.05$).

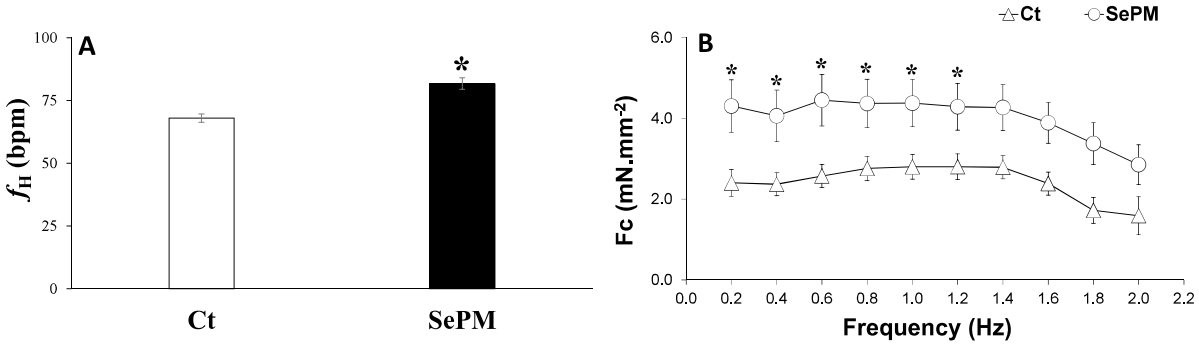

Figure 2. (A–C) Representative transmission electron microscopy (TEM) images of ventricular tissue from bullfrog tadpoles exposed to 1 g.L^{-1} SePM for 96 h. Higher-magnification images reveal tungsten (W) nanoparticles localized within the myocardial trabeculae. (D) Corresponding energy-dispersive X-ray spectroscopy (EDS) analysis confirms the elemental composition of the nanoparticles. Scale bars: (A) 2 µm, (B) 500 nm, (C) 200 nm.

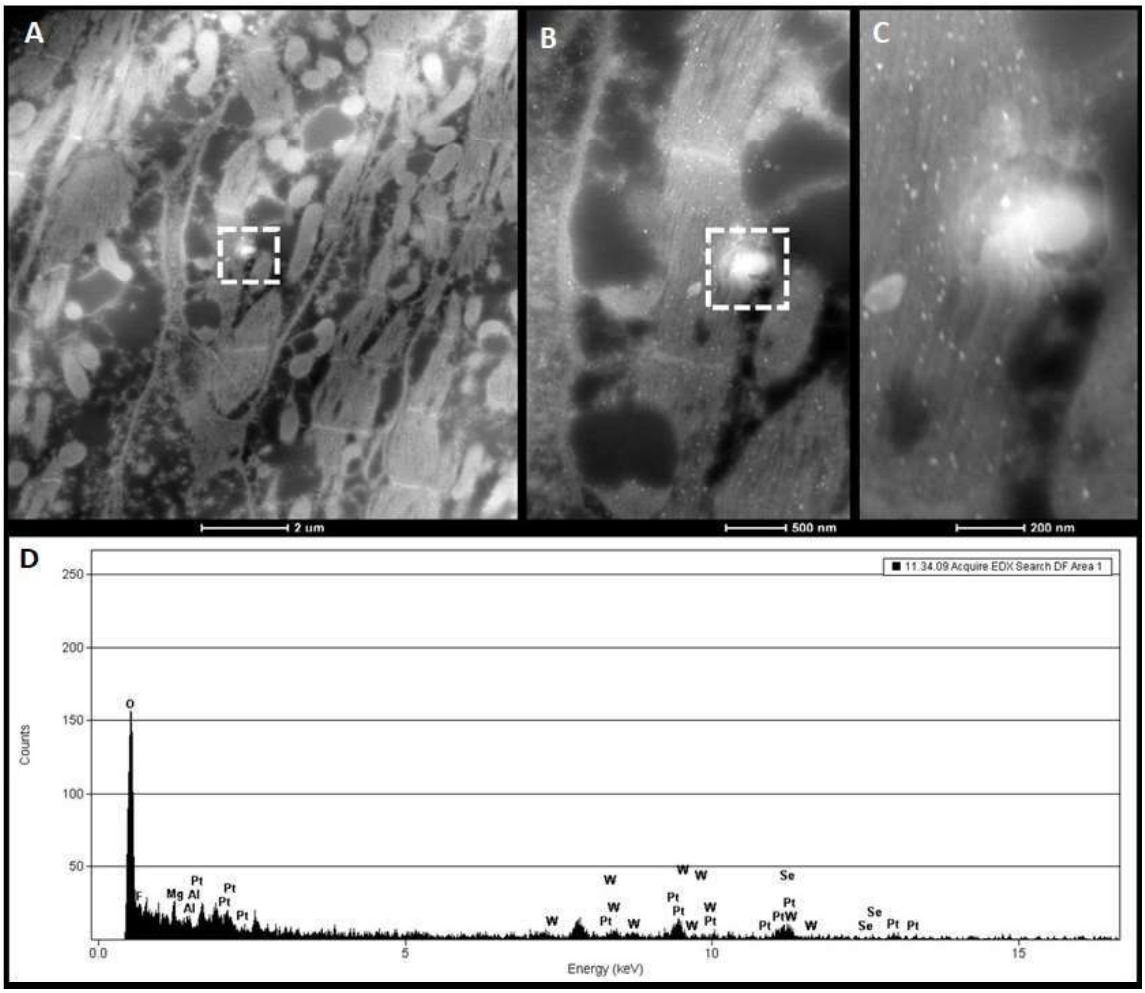

Impacts of settleable atmospheric particulate matter on bullfrog tadpole (*Aquarana catesbeiana*) gills: morphological and metal bioaccumulation

Iara da C. Souza[1]*, Gabriel Martins[1], Regiane L. da Costa[1], Magdalena V. Monferrán[2], Daniel A. Wunderlin[3], Cleoni dos Santos Carvalho[4], Marisa N. Fernandes[1], Diana Amaral Monteiro[1]*

[1]Departamento de Ciências Fisiológicas, Universidade Federal de São Carlos (DCF/UFSCar), São Carlos, São Paulo, Brazil.
[2]Departamento Bioquímica Clínica, Facultad de Ciencias Químicas, Universidad Nacional de Córdoba, Argentina.
[3]ICYTAC, Universidad Nacional de Córdoba, Córdoba, Argentina.
[4] Departamento de Biologia (DBio), Universidade Federal de São Carlos, Campus Sorocaba, Sorocaba, São Paulo, Brazil
*iara@ufscar.br, dianamonteiro@ufscar.br

Settleable atmospheric particulate matter (SePM), predominantly emitted by metallurgical industrial activities, represents a significant environmental risk due to its complex composition, including a variety of metals, emerging metallic contaminants, and nanoparticles. Given their permeable skin and delicate respiratory structures, amphibians—particularly tadpoles – are highly susceptible to environmental pollutants. This study aimed to comprehensively evaluate the sublethal impacts of SePM exposure (1 g L^{-1}) on the gills of bullfrog tadpoles (*Aquarana catesbeiana*) over a 96-hour exposure period, simulating environmental conditions similar to those observed in Vitória-ES, a region significantly impacted by SePM deposition from the Tubarão Industrial Complex. Morphological analyses conducted via histopathology revealed substantial structural damage to the gill tissue of exposed tadpoles. Key findings included hypertrophy and hyperplasia of gill, vacuolization of epithelial cells, and disorganization of supporting structures. These alterations suggest impaired respiratory function and increased vulnerability to environmental stressors. Electron microscopy coupled with X-ray microanalysis confirmed the presence of metallic nanoparticles composed of iron (Fe), titanium (Ti), and aluminum (Al) (Figure 1). These nanoparticles were detected both within the cytoplasm and nuclei of gill cells, indicating intracellular accumulation and potential direct interference with critical cellular functions. Additionally, chemical analyses using Inductively Coupled Plasma Mass Spectrometry (ICP-MS) detected marked bioaccumulation of several metals and emerging metallic contaminants, including aluminum (Al), titanium (Ti), iron (Fe), lead (Pb), and rare earth elements such as cerium (Ce), yttrium (Y), and lanthanum (La). The correlation between metals and biomarkers show the high affinity and vulnerability of tadpole gill tissues to SePM exposure, highlighting potential risks of prolonged contamination in aquatic ecosystems. These comprehensive findings show the sensitivity and susceptibility of amphibian to atmospheric pollutants, emphasizing that morphological damage from SePM exposure could critically impair respiratory function and overall health, ultimately affecting their survival and ecological role. The study implies in stringent environmental regulations aimed at mitigating industrial particulate emissions and highlights the need for ongoing monitoring and management efforts to safeguard vulnerable aquatic ecosystems.

[1] R.L. Costa et al., Environ. Pollut. 340 (2024) 122846.
[2] I.C. Souza et al., Sci. Total Environ. 753 (2021) 141976.

[3] This research was financially supported by FAPESP (2019/08491-0, 2023/01356-5) and ANPCYT (FONCyT/PICT-2019 N1743, PICT 2021 N002), and CONICET (PIP 2022-11220210100480CO). I.C. Souza received scholarship support from FAPESP (2023/09730-3) and CNPq (151291/2023-3).

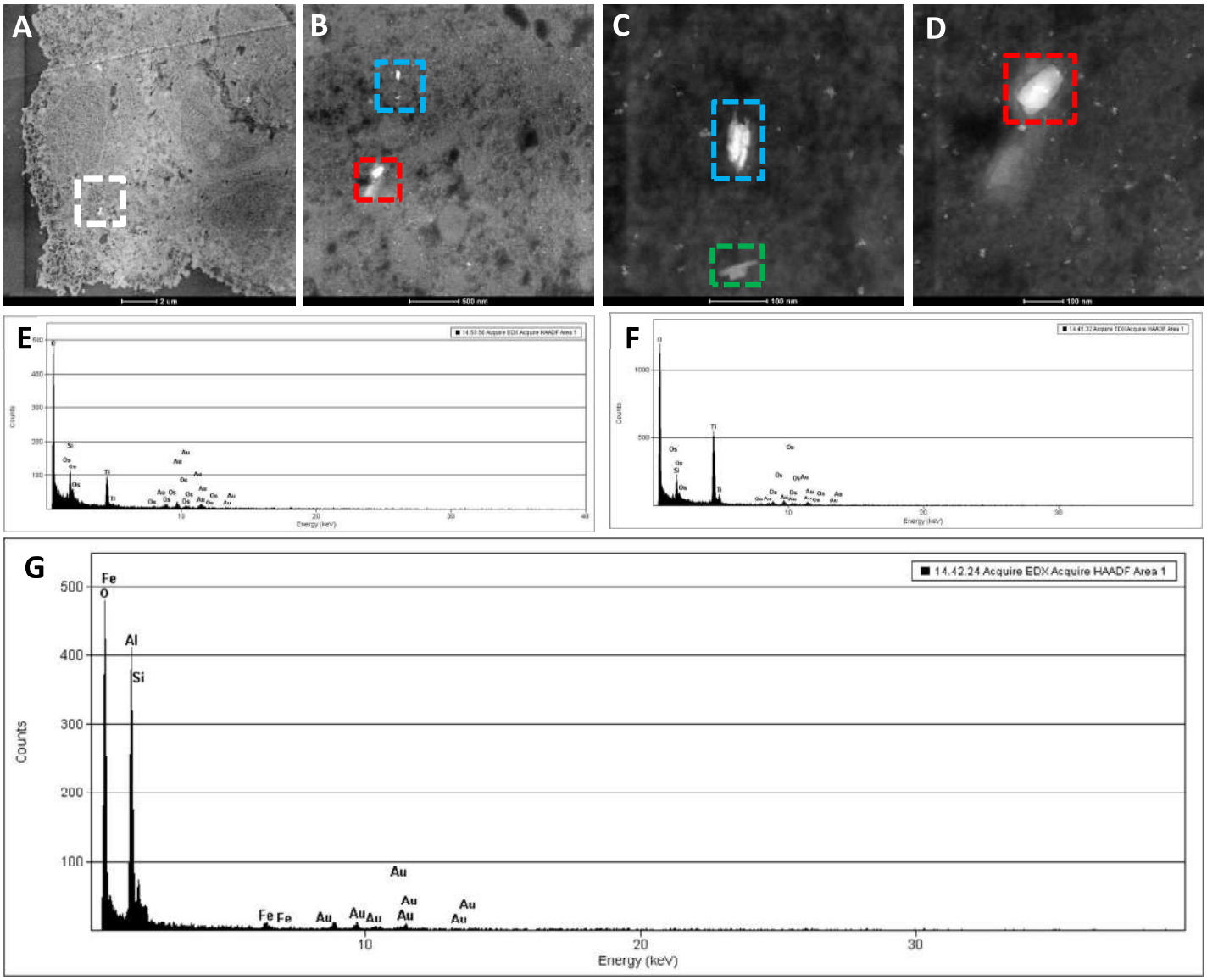

Figure 1. Representative transmission electron micrographs (TEM) of *Aquarana catesbeiana* gills after 96h exposure to 1.0 g SePM L^{-1}. (A) TEM showing nanoparticles (NP) in gills (white square); (B) High magnification of NP in (A); (C) High magnification of NPs in blue square of (B); (D) High magnification of NP in red square of (B); (E) Energy dispersive X-ray spectrum (EDS) of NP composition present in blue rectangle of (C) showing Si and Ti; (F) EDS of NP composition present in green rectangle of (C) showing Si and Ti; (G) EDS of NP composition present in red square of (D) showing Al, Si and Fe. Au is from the gold grid.

Mapping latex compounds *in situ* and their secretory machinery in figs (*Ficus,* Moraceae)

Isabel Cristina Nascimento[1], Sílvia Rodrigues Machado[2] & Simone Pádua Teixeira[1,*]

[1]Faculdade de Ciências Farmacêuticas de Ribeirão Preto, Universidade de São Paulo (USP), Ribeirão Preto, Brazil; [2]Centro de Microscopia Eletrônica, Insituto de Biociências, Universidade Estadual Paulista (UNESP), Botucatu, Brazil.

*For correspondence. spadua@fcfrp.usp.br

Latex is a complex suspension of chemically diverse compounds, including terpenes, alkaloids, proteins, polysaccharides, and phenolics, produced and stored in specialized secretory structures called laticifers [1]. Due to its complex composition, isolating and identifying latex components remains a challenging task. Consequently, *in situ* analyses have become one of the most effective approaches to advance research in this field. Fig trees (*Ficus*, Moraceae) are a latescent group of plants with well-characterized laticifers, described as articulated, branched, and widely distributed across both vegetative and reproductive organs [2]. In this study, we investigated the *in situ* localization of the main chemical constituents of latex within the figs of three Brazilian species of *Ficus*: *F. pertusa*, *F. montana*, and *F. obtusiuscula*. These species represent distinct lineages within the genus and are characterized by abundant latex production in their figs, making them suitable models for cytological studies of laticifers. Histochemical, cytochemical, and ultrastructural analyses were conducted on differentiating laticifers in very young figs. Our results show that the laticifer network originates early during fig formation and becomes highly branched, with latex accumulation observed even in immature laticifer cells. Ultrastructural observations revealed metabolically active laticifer cells, with thickened pecto-cellulosic walls, numerous mitochondria, dictyosomes, extensive rough endoplasmic reticulum, and large vacuoles containing electron-dense inclusions (Fig. 1). Histochemical (Figs. 2, 3) and cytochemical analyses (Fig. 4) demonstrated that latex from all three species contains lipids (identified with imidazole-buffered osmium tetroxide) [4], proteins (confirmed by silver proteinate reaction) [5], and carbohydrates (evidenced by ruthenium red staining) [6]. The lipids identified should represent the precursors or components of the rubber commonly found in fig latex, while the proteins may correspond to enzymes responsible for degrading terminal cell walls during laticifer differentiation, facilitating the formation of the articulated laticifer system. The abundance and diversity of organelles associated with biosynthetic and secretory activity observed at the ultrastructural level further support the complexity of latex composition revealed by the histochemical and cytochemical analyses. By integrating cytological, histochemical, and ultrastructural approaches, this study provides new insights into latex secretion and laticifer differentiation in fig reproductive structures.

[1] A. Fahn, Secretory Tissues in Plants. Academic Press, London, 1979.
[2] C.R. Marinho et al., Acta Oecol 90 (2018) 160–167.
[3] C.D. Souza et al., Am. J. Bot. 102 (2015) 1–14.
[4] S.Angermüller & D. H. Fahimi, Histochem. J. 14 (1982) 823-825.
[5] E. K. Macrae & G. D. Meetz, J. Cell Biol. 45 (1970) 235-245.
[6] C. R. Marinho & S. P. Teixeira, Protoplasma 256 (2019) 1093-1107.
[7] This research was supported by Fapesp and CNPq (Brazil).

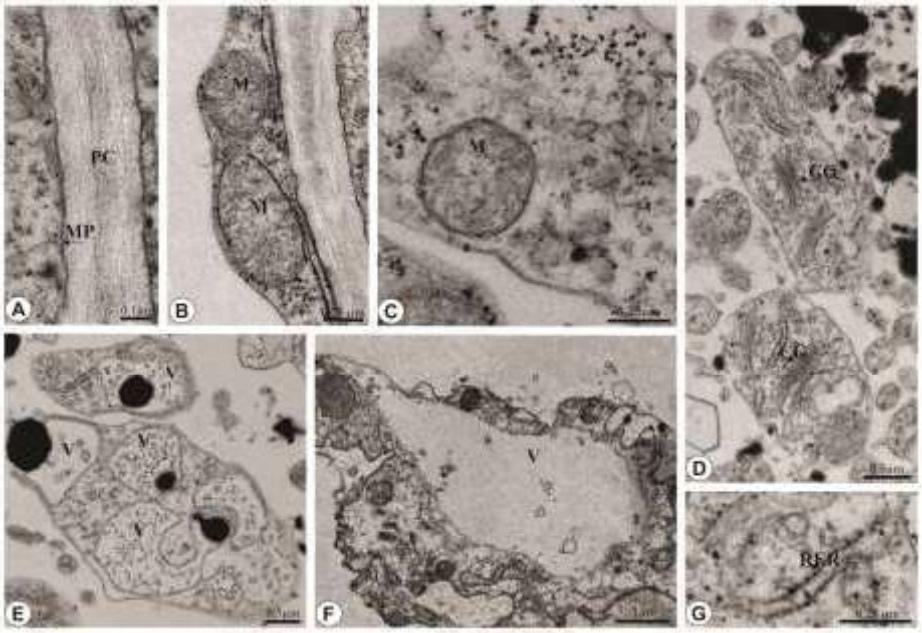

Fig. 1. Ultrastructure of the laticifer in *Ficus pertusa* (A–E, G) and *F. obtusiuscula* (F). A. Detail of the thick cell wall and plasma membrane. B–C. Mitochondria. D. Dictyosomes. E–F. Vesicles with osmiophilic inclusions. G. Rough endoplasmic reticulum. CG = Dictyosome; PM = Plasma membrane; M = Mitochondria; RER = Rough endoplasmic reticulum; V = Vesicle.

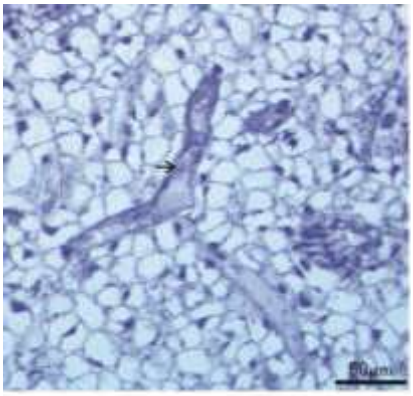

Fig. 2. Detection of proteins with aniline blue black.

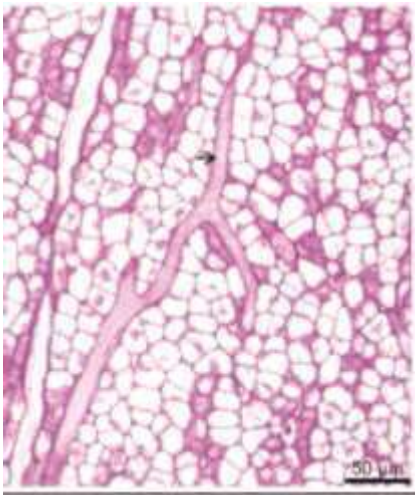

Fig. 3. Detection of polysacharides with PAS.

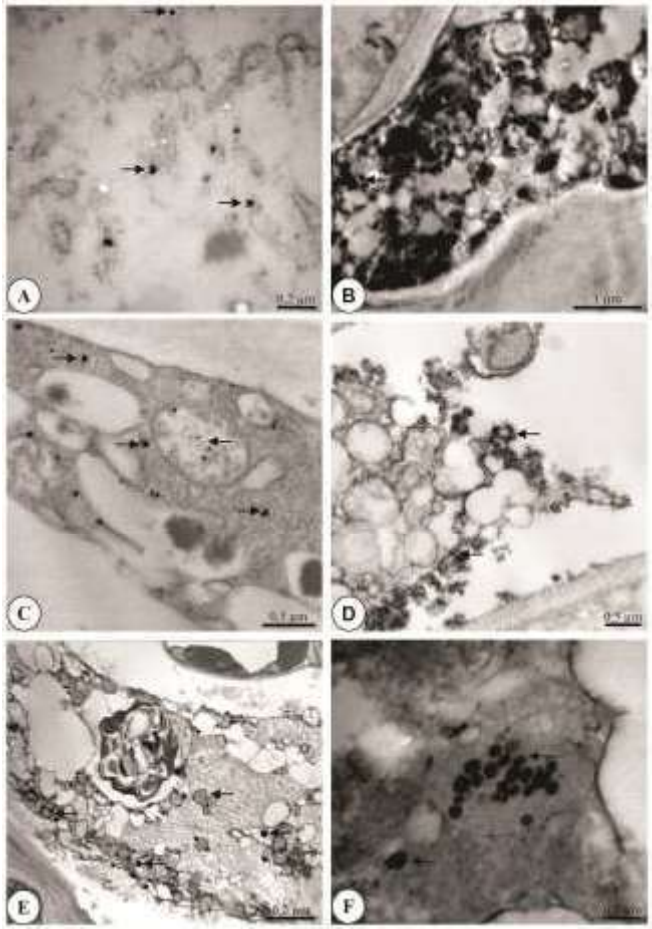

Fig. 4. Cytochemistry of the laticifer in *F. montana* (A, C, E) and *F. pertusa* (B, D, F). A–B. Imidazole-buffered osmium tetroxide for lipid detection (arrows). C–D. Ammoniacal silver for protein detection (arrows). E–F. Ruthenium red for polysaccharide detection (arrows).

Morphological and Ultrastructural Insights into Nuclear Degeneration Patterns in Oral Squamous Cell Carcinoma

Marcos Alexandre nunes da Silva[1,2*], Adriana Terezinha Neves Novellino[1], Ana Flávia Schueler de Assumpção Leite[1], Josiane Costa Rodrigues deSá[1], Simone de Queiroz Lourenço[1], Debora Ferreira Barreto- Vieira[2],

[1] Laboratório de Pesquisa Clínica Aplicada em Odontologia, Faculdade de Odontologia, UFF, Niterói, Brasil
[2] Laboratório de Morfologia e Morfogênese Viral, IOC, Fiocruz Rio de Janeiro, Brasil.
*marcossilva@aluno.fiocruz.br.

Oral Squamous Cell Carcinoma (OSCC) is a malignant neoplasm originating from the epithelium lining the oral cavity, accounting for approximately 90% of all malignant lesions in this region [1]. In Brazil, the oral cavity ranks as the fifth most common cancer site in men and the seventh in women [3]. The tumor microenvironment plays a critical role in tumor migration and invasion, gaining increasing attention due to its ability to promote facilitated tumor growth. This process is driven by a synergistic interplay of factors, including the phenotypic heterogeneity of the cells within this environment [2,4]. The aim of this study was to evaluate the ultrastructural profile of OSCC, with a focus on the cellular ultrastructure of carcinoma basal cells and the characteristics of pyknotic nuclei. Tissue samples were fixed in 2% glutaraldehyde (in 0.1 M sodium cacodylate buffer), post fixed in osmium tetroxide, dehydrated in graded acetone baths, and embedded in epoxy resin and polymerized at 60 °C, for transmission electron microscopy (TEM) analysis. Additional samples were fixed in Carson's formalin, paraffin embedded and stained with hematoxylin and eosin (H & E) for bright field microscopy. Histopathological examination revealed basal cells displaying moderate epithelial dysplasia, keratin pearls, teardrop-shaped extensions of the basal layer, and a prominent inflammatory infiltrate. Ultrastructural analysis identified cells with a basaloid profile, characterized by high protein synthesis activity, centralized nuclei, and pyknotic nuclei exhibiting chromatin condensation and occasional loss of membrane continuity. Immune cells within the microenvironment also displayed an altered profile, along with the absence of GAP junctions. In contrast, the control group exhibited an intact basal layer with no significant abnormalities, resembling normal gingival tissue. Both bright-field microscopy and electron microscopy confirmed alterations in the ultrastructural profile of tumor cell nuclei, with enhanced detail resolution in TEM.

REFERENCE:

[1] Neville BW, et al *CA Câncer J Clin*. 52:195-215;2016
[2] Tanaka N, *J Med Electron Microsc.* (3):127-38, Sep; 2002.
[3] Ministério da Saúde. Instituto Nacional De Câncer (INCA). Estimativa 2025

[4] Hanahan D, *Cancer Discov.* (1):31-46.Jan;12; 2022.

[5] This research was supported by CNPq (Brazil);

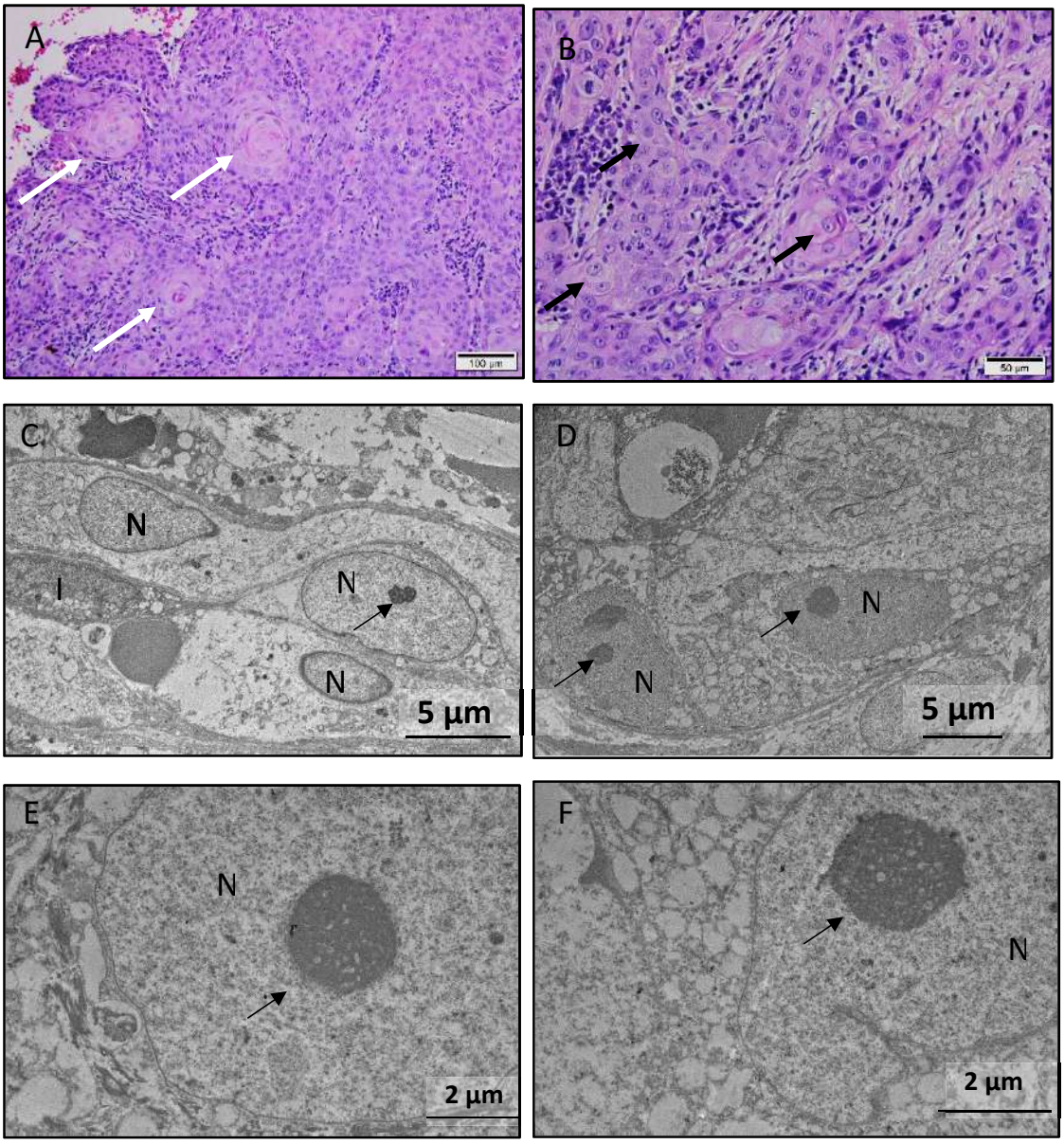

Figures 1: A and B: Brightfield micrographs, altered epithelium, moderate dysplasia, with tumor islands and cords [white arrows], keratin pearls. Figures C to F: Electron micrographs of the squamous cell carcinoma profile, circulating inflammatory cells in the tumor tissue [I], Nuclei [N] chromatin densification [black arrows]

Multiscale Evaluation of Bone Regeneration Using Granular Hydroxyapatite in an Ovine Model

Gisele M. L. Dalmônico[1], Marcos Farina[2], André L. Rossi[1]

[1]Brazilian Center for Physics Research, Rio de Janeiro, Brazil.
[2]Federal University of Rio de Janeiro

The treatment of bone defects remains a significant challenge in regenerative medicine, requiring interdisciplinary approaches involving engineering, chemistry, biology, and biomedicine. Calcium phosphates, particularly hydroxyapatite (HA), have demonstrated excellent performance as bone substitutes due to their biocompatibility and structural similarity to the mineral phase of human bone [1]. This study aimed to evaluate the osseointegration of granular HA using a comprehensive set of characterization techniques, including Raman spectroscopy, scanning and transmission electron microscopy, electron diffraction, atomic force microscopy, confocal and optical microscopy, polarized light microscopy, and Ptychography at the Cateretê beamline (Sirius, Brazil). In vivo experiments were conducted in 16 twelve-month-old Texel sheep. Standardized 4 mm tibial defects were surgically created and filled with HA granules hydrated with autologous arterial blood. Analyses were performed at intervals from 90 days to 12 months. Following implantation, HA gradually disaggregated, releasing Ca^{2+} and PO_4^{3-} ions, thereby promoting osteoconduction and progressive bone growth [1,2]. Histological and ultrastructural analyses revealed early bone formation within the microporous structure of the biomaterial, with nearly complete bone regeneration observed after one year. Electron diffraction confirmed the transformation from the crystalline phase of the bone mineral, accompanied by increased collagen fibrils and surface roughness indicators of biomaterial resorption and tissue remodeling [3,6]. The interconnected porosity of HA played a crucial role in facilitating cell adhesion, proliferation, and mineral deposition. It also served as a nucleation site for amorphous calcium phosphate, which is critical in the early stages of biological apatite formation [5]. These findings highlight the efficacy of granular HA as a scaffold for bone regeneration and provide valuable insights into the multiscale dynamics of mineralized tissue formation [1–6].

REFERENCES

[1] G. M. L. Dalmônico, et all. Biomaterials Science, 2017. 10.1039/c7bm00162b.
[2] V Zelaya, et all. ACTA BIOMATERIALIA Online Version 1 (2020) Beamlines/Facilities: IMX,IMX,IMX,IMX
[3] V Zelaya, et all. International Journal of Nanomedicine 14 3471 (2019) Beamlines/Facilities: IMX,IMX,XRF,XRF
[4] V R. Martinez-Zelayaa, et all Acta Biomaterialia 120 (2021) 181-193.
[5] N Reznikov, et all. Science 360, 507 (2018).
[6] Rossi, A. L.; et all. J. Biomed. Mater. Res. - Part A 2018, 106 (2), 428-439.

ATTACHMENTS

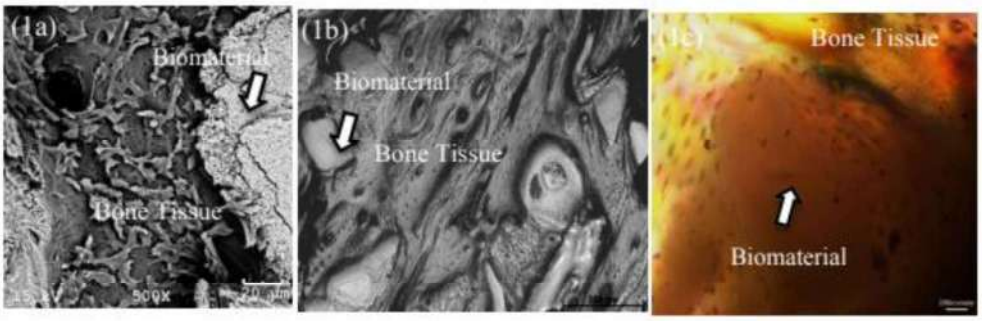

Figure 1. Characterization of biopsies by: scanning electron microscopy HA (1a), optical microscopy HA(1b), polarized light microscopy HA(1c), biomaterial, new bonetissue, osseointegration, biomaterial/bone tissue interface at 180 days.

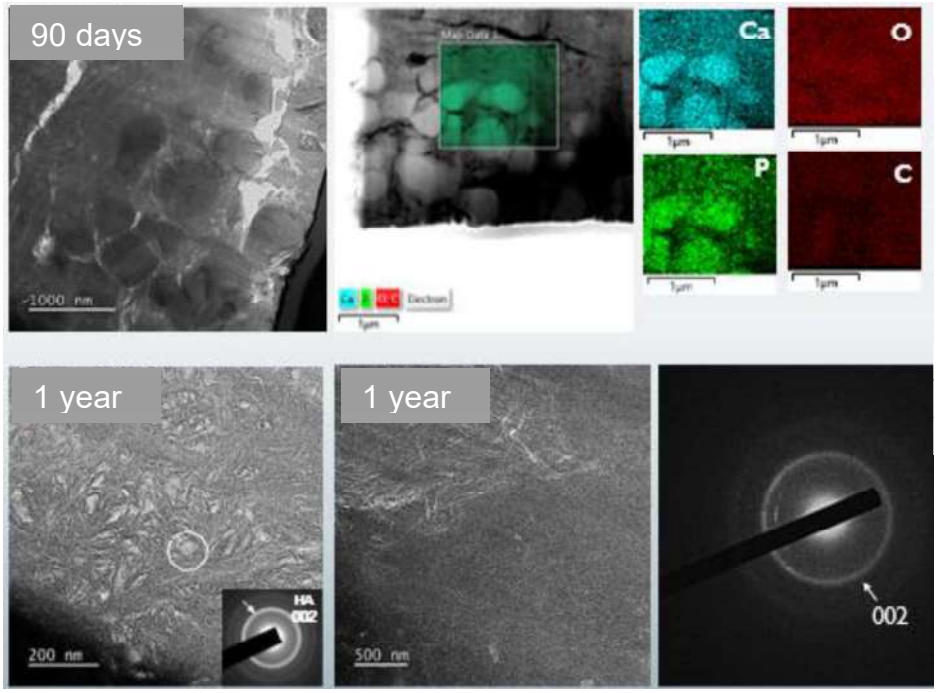

Figure 2. BF and DF TEM images and EDS espectroscopy of HA implanted afther 90 days and 1 year obtained over FIB sample

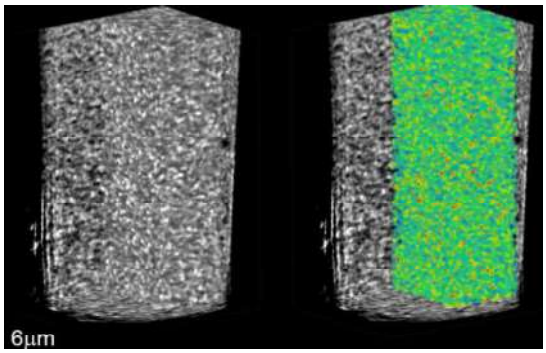

Figure 3. Reconstructed images obtained HA implanted afther 60 days over Xray imaging microtomography

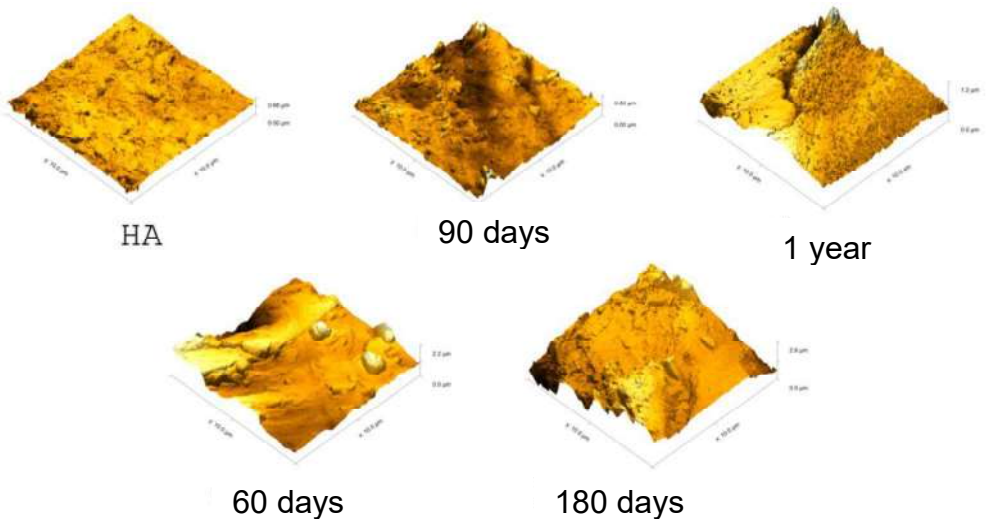

Figure 4. AFM images HA and HA implanted afther 60, 90, 180 days and 1 year to evaluate degradation and osseointegration

Nanoencapsulation of Baculoviruses Using NaDES-Stabilized Lipid Nanocarriers for Enhanced Agricultural Biocontrol

Mariana Tigano Magalhães[1]*, Victor Carlos Mello da Silva[2] , Nicole Santana Alves[2], Thalita do Espírito Santo de Jesus[2], Luis Janssen Maia[1] , Andrews Alexander Fredéric Monvoisin Santos Fisch[1], Sônia Nair Báo[2], Bergmann Morais Ribeiro[1].

[1] Universidade de Brasília - Laboratório de Baculovírus , [2] Universidade de Brasília - Laboratório de Microscopia e Microanálise
*mari.tigano@gmail.com

Climate change, natural resource scarcity, biodiversity loss, and the growing demand for food necessitate more sustainable and regenerative technological solutions. Among these, baculovirus-based bioinsecticides offer a promising alternative for agricultural pest control due to their high specificity, low toxicity, and reduced environmental impact compared to conventional pesticides. However, their field application is still constrained by instability under UV radiation, temperature fluctuations, and pH variations. This study proposes the encapsulation of baculoviruses in lipid nanocarrier systems (NLCs) stabilized with natural deep eutectic solvents (NaDES) to enhance their stability, performance, and longevity in field conditions. The formulation was based on circular lipids, using murumuru butter as the solid lipid phase, soybean oil as the liquid phase, and tomato hydrolate as the aqueous matrix, enriched with a NaDES composed of glycerol, citric acid, and choline chloride. *Spodoptera frugiperda* multiple nucleopolyhedrovirus (SfMNPV) virions and occlusion bodies were produced in SF9 cells cultured in Erlenmeyer flasks under agitation. Occlusion bodies were purified via SDS washing, and DNA from budded virions and polyhedra was extracted using a phenol-chloroform protocol [1]. Amplification was performed via rolling circle amplification (RCA), and viral genome integrity was verified using Nanopore next-generation sequencing [2]. Encapsulation was achieved through hot emulsification followed by rapid cooling, generating nanoparticles with an average diameter of 188 ± 4 nm, a PDI of 0.21, and uniform spherical morphology. Bioassays using *S. frugiperda* are currently underway. The inclusion of NaDES enhanced not only viral solubilization and protection but also the thermal and colloidal stability of the system, particularly relevant in tropical field environments. This approach exemplifies the integration of bioeconomy, virology, and green nanotechnology and aligns with Sustainable Development Goals related to sustainable food production (SDG 2), industrial innovation (SDG 9), and responsible consumption (SDG 12). It highlights how NaDES-based nanoformulations can enable more effective and accessible bioinsecticides for large-scale agricultural use [3]. Transmission Electron Microscopy (TEM) images underscore the critical role of NaDES in nanostructure formation and stabilization. The absence of NaDES (FIg 1A) led to aggregation and loss of spherical morphology, indicating colloidal instability. With NaDES addition (B), well-defined, stable, and homogeneously dispersed particles were observed, suggesting that the solvents act as co-stabilizers by reducing interfacial tension and enhancing system robustness. The DNA-loaded formulation (Fig 1C) retained structural integrity and showed compatibility with genetic material complexation, indicating that NaDES may also facilitate bioactive interactions. The baculovirus-loaded formulation (Fig 1D) demonstrated successful encapsulation and preserved viral morphology, essential for bioinsecticidal efficacy. These findings reinforce the

potential of NaDES as structural modulators in sustainable nanoparticles, improving their stability, functionalization, and biotechnological applications. This work was supported by CNPq and FAPDF [4].

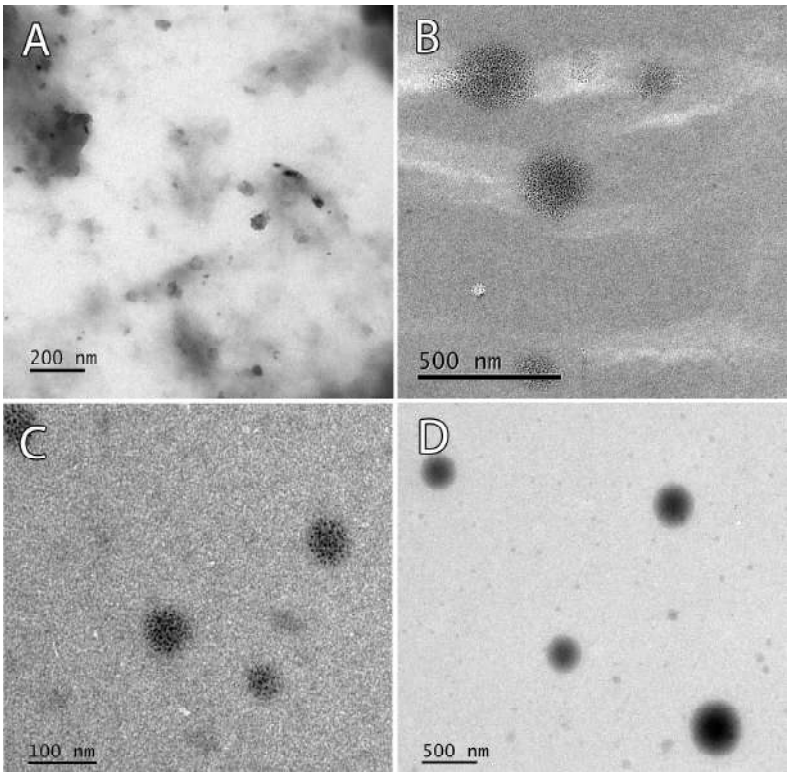

Figure 1. Representative Transmission Electron Microscopy (TEM) images of different nanostructured formulations.

A) Lipid nanoparticle without NaDES, showing severe aggregation, structural collapse, and undefined morphology, indicating colloidal instability and inability to withstand thermal and mechanical stress.

B) Nanoparticle containing NaDES (blank system), exhibiting well-defined spherical morphology, homogeneous dispersion, and preserved structural integrity.

C) Nanoparticles functionalized with NaDES and DNA, maintaining regular structure and organization compatible with genetic material complexation.

D) Nanoparticle encapsulating baculovirus, showing well-individualized particles with uniform contours, consistent with the size of budded virions.

[1] D.R. O'Reilly, L.K. Miller, V.A. Luckow, Baculovirus Expression Vectors: A Laboratory Manual, W.H. Freeman and Co., Salt Lake City, 1992.

[2] M. Kearse, R. Moir, A. Wilson et al., Bioinformatics, 28 (2012).

[3] H. Vanda et al., Deep Eutectic Solvents: Synthesis, Properties, and Applications, 2019, pp. 61–81.

[4] This research was supported by CNPq and FAPDF (Brazil).

Oropouche Virus: In Vitro Isolation and Ultrastructural Study from a Human Case in Rio de Janeiro

Ana Luisa Teixeira de Almeida[1]*, Igor Pinto Silva da Costa[1], Maycon Douglas do Nascimento Garcia[1], Marcos Alexandre Nunes da Silva[1], Yasmim Gonçalves Lazzaro[1], Ana Maria Bispo de Filippis[2], Fernanda de Bruycker Nogueira[2], Debora Ferreira Barreto-Vieira[1]

[1] Laboratory of Viral Morphology and Morphogenesis, Oswaldo Cruz Institute, Oswaldo Cruz Foundation (IOC/Fiocruz), Rio de Janeiro, Brazil
[2] Laboratory of Arboviruses and Hemorrhagic Viruses, IOC/Fiocruz, Rio de Janeiro, Brazil.
*anaalmeida@aluno.fiocruz.br

The Oropouche virus (OROV), a segmented negative-sense RNA arbovirus of the *Peribunyaviridae* family [1], is a significant etiological agent responsible for recurrent outbreaks of Oropouche fever across Central and South America [2]. Although traditionally endemic to northern Brazil, recent evidence indicates its expanding geographical distribution, including non-endemic regions such as Rio de Janeiro [3]. This study reports the isolation and comprehensive characterization of an OROV strain from a human clinical sample collected in Rio de Janeiro, employing in vitro infection model using Vero cells. Viral inoculation at a low multiplicity of infection (MOI=0.01) resulted in prominent cytopathic effects (CPE), including morphological alterations, membrane projections, vacuolization, and cell detachment, observable through bright-field microscopy at 48–96 hours post-infection (hpi). Based on our initial evaluation of the CPE through bright-field microscopy, the time of 48 hpi was selected for ultrastructural evaluation. Cell monolayers were trypsinized and the suspended cells were first fixed in 2% glutaralde-hyde in 0.1 M sodium cacodylate buffer, followed by post-fixation in 1% buffered osmium tetroxide. The samples were dehydrated in increasing concentrations of acetone. Subsequently, the cells were embedded in epoxy resin and polymerized at 60°C for three days. Ultrathin sections were then obtained from the resin blocks using an ultramicrotome, collected on uncoated copper grids (300 mesh) and examined using a Hitachi HT 7800 transmission electron microscope. Ultrastructural analysis (Figure 1) revealed extensive cellular remodeling: apoptotic bodies, mitochondrial swelling and clustering, and significant endoplasmic reticulum (ER) stress manifested as membrane thickening, cisternal dilation, and myelin-like figures. Notably, membrane-bound organelle alterations, multilamellar bodies, multivesicular bodies (MVBs), and autophagic components were prevalent, indicating active trafficking pathways. Viral particles (~80 nm diameter), displaying classic *Orthobunyavirus* morphology, were identified both within cytoplasmic compartments, such as MVBs and Golgi-associated regions, and extracellularly, suggesting ongoing morphogenesis and egress. Quantitative analysis of mitochondrial morphology demonstrated significant pleomorphism and stress responses in infected cells. These detailed ultrastructural insights advance our understanding of OROV's replication cycle and cytopathogenic mechanisms, providing a basis for future antiviral development efforts against this emerging public health threat. We gratefully acknowledge the financial support provided by CAPES and FAPERJ for this study [4].

[1] H.R. Hughes et al. ICTV Virus Taxonomy Profile: Peribunyaviridae. J. Gen. Virol. (2020), 101, 1–2.
[2] R. Sah et al. Oropouche fever outbreak in Brazil: An emerging concern in Latin America. Lancet Microbe. (2024), 5, 100904.
[3] G.C. Scachetti et al. Re-emergence of Oropouche virus between 2023 and 2024 in Brazil: An observational epidemiological study. Lancet Infect Dis. (2025), 25, 166–175.
[4] This research was supported by CAPES and FAPERJ (Brazil).

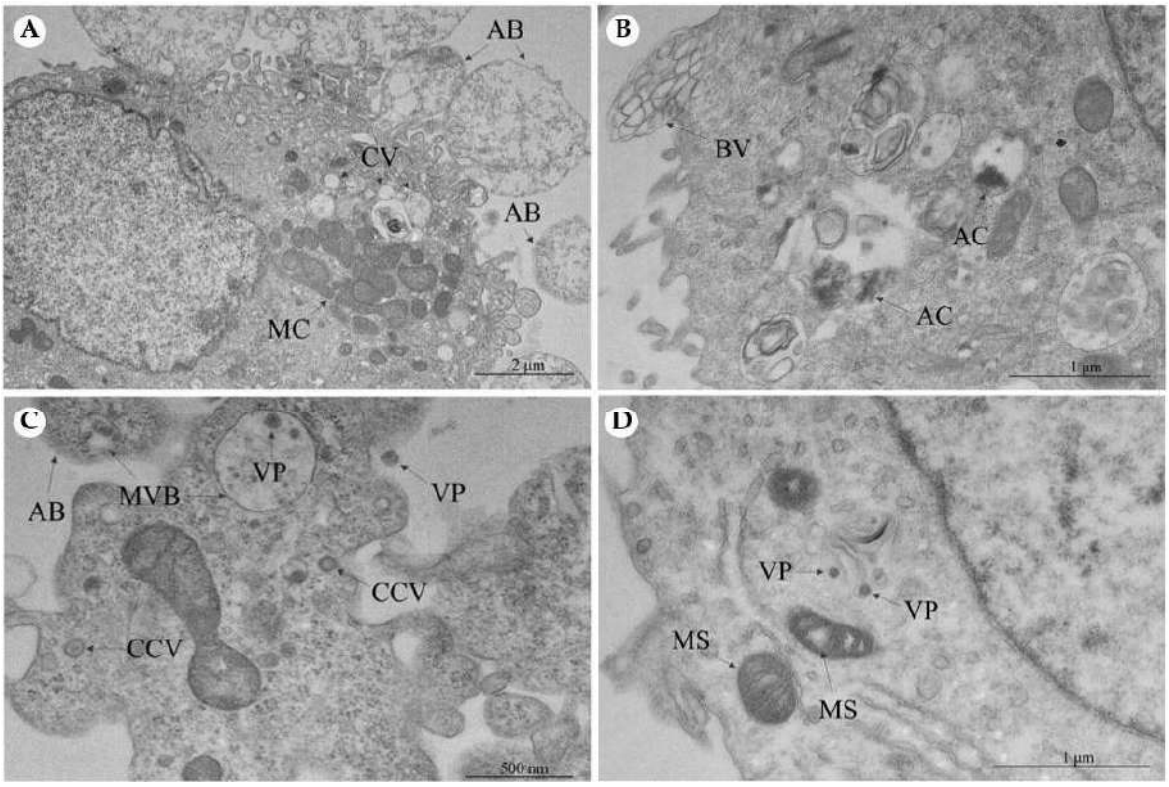

Figure 1. Cytopathic effects in Vero cells infected with Oropouche virus. (A) Apoptotic bodies (AB), cytoplasmic vacuoles (CV), mitochondrial clustering (MC). (B) Autophagy components (AC), budding vesicles (BV). (C) Multivesicular body (MVB), viral particles (VP), clathrin-coated vesicles (CCV), apoptotic body (AB). (D) Viral particles (VP), mitochondrial swelling (MS).

Seminiferous tubules ultrastructure after testicular nanoparticle-mediated hyperthermia

Bruna N. Costa[1]*, Louiz G. dos Santos[1], Juliana L. M. Brito[1], Julyane S. D. Pacheco[1], Vanessa N. Lima[1], André L. S. Mariano[2], Paulo E. N. Souza[2], Andris F. Bakuzis[3], Ingrid Gracielle M. da Silva[1], Sônia N. Báo[1], Carolina M. Lucci[1].

[1] Institute of Biological Sciences, University of Brasília, Brasília/DF, Brazil, [2] Institute of Physics, University of Brasilia, Brasilia/DF, Brazil, [3] Institute of Physics, Federal University of Goiás, Goiânia/GO, Brazil.
*brunabio2015@gmail.com

Overpopulation of stray animals is a global public health concern. Stopping reproduction is the most effective method for population control, but surgical castration procedures have logistical limitations for large-scale application [1]. Therefore, alternative methods are needed to reduce costs and postoperative care. Since testicular cells are sensitive to elevated temperatures, heat-based methods have emerged as viable alternatives to cause infertility [2]. Our research team developed a castration protocol based on nanoparticle-mediated photohyperthermia (PHT) that showed promising results in producing infertility [3]. However, little is known about the ultrastructural damage caused to testicular cells following this procedure. Understanding these effects is crucial for elucidating the mechanisms of cellular damage. This study aimed to evaluate the ultrastructural damage in testicular tissue from animals subjected to the testicular PHT protocol. Twelve adult rats (Rattus norvegicus – Wistar) were divided into two main groups: Control (CTL) and treated. Animals from the treated group received an intratesticular injection of nanoparticles followed by exposure to a light energy source (LED) at 808 nm, heating the testicles. The temperature of 45 °C was maintained for 15 minutes. The treated group was then subdivided based on time points of 24 hours (G24h), 72 hours (G72h), and 7 days (G7d) post-PHT. After euthanasia, testicular samples were collected and processed for transmission electron microscopy. The results showed preserved seminiferous tubules with a uniform basement membrane in CTL (Figure 1A). The germinal epithelium was well-organized, containing normal cells at various stages of spermatogenic development, including spermatozoa, in both the CTL (Figure 1B) and G24h (Figure 1C) groups. Basement membrane wrinkling was observed in the treated groups, particularly in G7d (Figure 1G). Numerous vacuoles were observed within germ cells and Sertoli cells, smaller in G24h (Figure 1D) and larger in G72h (Figure 1E) and G7d (Figure 1G). Additionally, mitochondria appeared larger, with more cristae and increased electron density in the G72h group (Figure 1D). The G7d group exhibited more pronounced damage, including extensive vacuolization in cells from the basal region of the seminiferous tubules (Figure 1G) and desquamation of the germinal epithelium. In these regions, only the nuclei of affected cells remained, with a markedly darkened appearance (Figure 1H). No late spermatids or spermatozoa were observed in G7d samples. In conclusion, this study demonstrates that testicular PHT triggers ultrastructural damage to spermatogenic cells, starting with mild changes as early as 24h after treatment and progressing to severe damage within seven days [4].

[1] M. Cathey, M.A. Memon, Vet. Med. 105 (2010) 12–17.
[2] M.S. Fahim et al., Contraception 11 (5) (1975) 549–562.
[3] V.N. de Lima, Desenvolvimento de um protocolo de fotohipertermia mediada por nanopartículas para promoção de infertilidade de animais machos (Tese de doutorado), Univ. Brasília, Brasília (2024).
[4] This research was supported by CNPq (Brazil) and FAPDF.

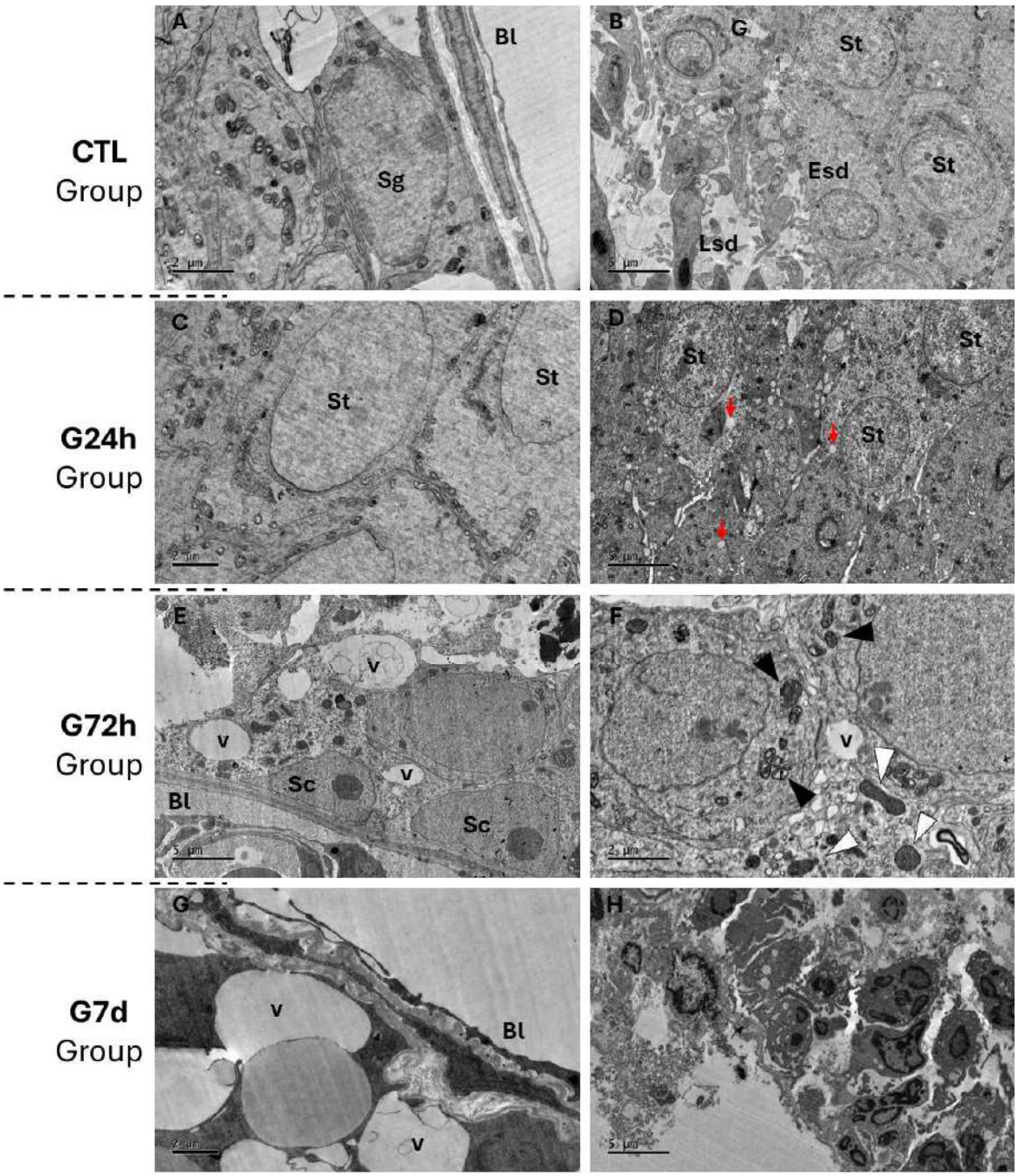

Figure 1. Electronmicrographs of seminiferous tubules. **A:** Control group showing a basal lamina (Bl) with a uniform appearance and spermatogonia (Sg) exhibiting a prominent nucleus. **B:** Control group displaying spermatocytes (St), early spermatids (ESd), and late spermatids (LSd) with distinct nucleus and a visible Golgi Complex (G). **C:** G24h group with organized germinal epithelium. **D:** Germinal epithelium of the G24h group, presenting small vacuoles (red arrow). **E:** G72h group exhibiting large vacuoles (v) distributed throughout the epithelium. **F:** Dense mitochondria with increased cristae observed in germline cells (black arrowhead) and Sertoli cells (white arrowhead). Sertoli cell cytoplasm is heterogeneous, containing numerous small vesicles. **G:** G7d group is characterized by a markedly wrinkled BL and numerous big vacuoles. **H:** G7d showing ruptured cells, with only darkened nuclei remaining.

Telemicroscopy: integrating transmission electron microscopy and medical diagnosis in Brazil

Laila Asth[1,2*], Ingrid Augusto[1,2], Moara Lemos[1,2], Eduardo Resende[1,2], Brenda Fachetti[1,2], Camila Gonçalves[1,2], Jander Guimarães[3], Eduardo Torres[4], Kildare Miranda[1,2,3]

[1]Laboratório de Ultraestrutura Celular Hertha Meyer, Centro de Pesquisa em Medicina de Precisão, Instituto de Biofísica Carlos Chagas Filho, Universidade Federal do Rio de Janeiro, Brasil.
[2]Centro Nacional de Biologia Estrutural e Bioimagem, Universidade Federal do Rio de Janeiro, Brasil.
[3]Centro Multiusuário para Análise de Fenômenos Biomédicos, Universidade do Estado do Amazonas, Manaus, Brasil.
[4]Laboratório de Helmintologia Romero Lascasas Porto e Laboratório Multiusuário de Parasitologia, Departamento de Microbiologia, Imunologia e Parasitologia, Universidade do Estado do Rio de Janeiro, Brasil.

*lailasth@gmail.com

Telemicroscopy is a technique that enables remote access to microscopy platforms, allowing the analysis of samples at distance [1]. It has great potential in aiding medical diagnosis and could be used to reduce geographic distance between pathologists and microscopy centers. Nowadays, there are more than 700 electron microscopes in Brazil, most of them are concentrated in the South and Southern regions [2]. The aim of this work is to establish a sustainable model for integrating transmission electron microscopy tools into the medical diagnostic portfolio through the implementation of telemicroscopy hubs applied to ultrastructural pathology. Methodologies based on protocols from international reference centers were adopted to structure a workflow adapted to be applied at the National Center for Structural Biology and Bioimaging (CENABIO), a multiuser facility of the Federal University of Rio de Janeiro (UFRJ), with an investment of Health Ministry of Brazil. It was evaluated the feasibility of each step in the workflow (i.e. reception of the material, preparation for transmission electron microscopy analysis, and interaction between the microscopy center and the pathologist responsible for the diagnosis) for five different pathologies, PIT1-pituitary adenoma (AH), thrombotic microangiopathy (MAT), membranous glomerulonephritis (GM), focal segmental glomerulosclerosis (GESF), and Crohn's disease (DC). The electron microscopes used for data collection were Hitachi HT 7800 and Tecnai Spirit iCorr 120 kV (D1326, BioTwin). The first step of the workflow was to establish a system to receive and organize samples preserving the anonymity of each patient. For this purpose, an excel spreadsheet was shared between pathologists and microscopy center where proper patient codes and relevant information such as the pathology and hospitals were included. The preservation of the sample's structure was evaluated when prepared directly by pathologists trained by other institutes or by the electron microscopy specialists. Better preparation was achieved by the when performed in the microscopy center highlighting the importance of using standardized protocols. Three strategies of interaction between the microscopy center and the pathologists were tested: asynchronous telemicroscopy, on-site visits, and synchronous telemicroscopy. Overall, synchronous telemicroscopy allowed a precise diagnosis by the pathologist although few pathologies, such as GESF (Figure 1), required one on site visit of the pathologist to train the researchers to recognize the ultrastructural characteristics used to diagnose the disease. The results demonstrated the operational feasibility of the proposed model and highlighted that continuous interdisciplinary communication is essential for better telemicroscopy outcomes. In addition, an initial digital image bank has been created aiming to use machine learning and artificial intelligence techniques to favor the differential tele-diagnostic of specific pathologies. This model has the potential to democratize access to electron

microscopy, reduce regional inequalities, and consolidate a collaborative network within the country.

[1] Prieto-Egido I, González-Escalada A, García-Giganto V, Martínez-Fernández A. Design of New Procedures for Diagnosing Prevalent Diseases Using a Low-Cost Telemicroscopy System. Telemed J E Health. 2016 Nov;22(11):952–9.
[2] Albuquerque PC, de Paula Fonseca E Fonseca B, Girard-Dias W, Zicker F, de Souza W, Miranda K. Mapping the Brazilian microscopy landscape: A bibliometric and network analysis. Micron. 2019 Jan;116:84–92.

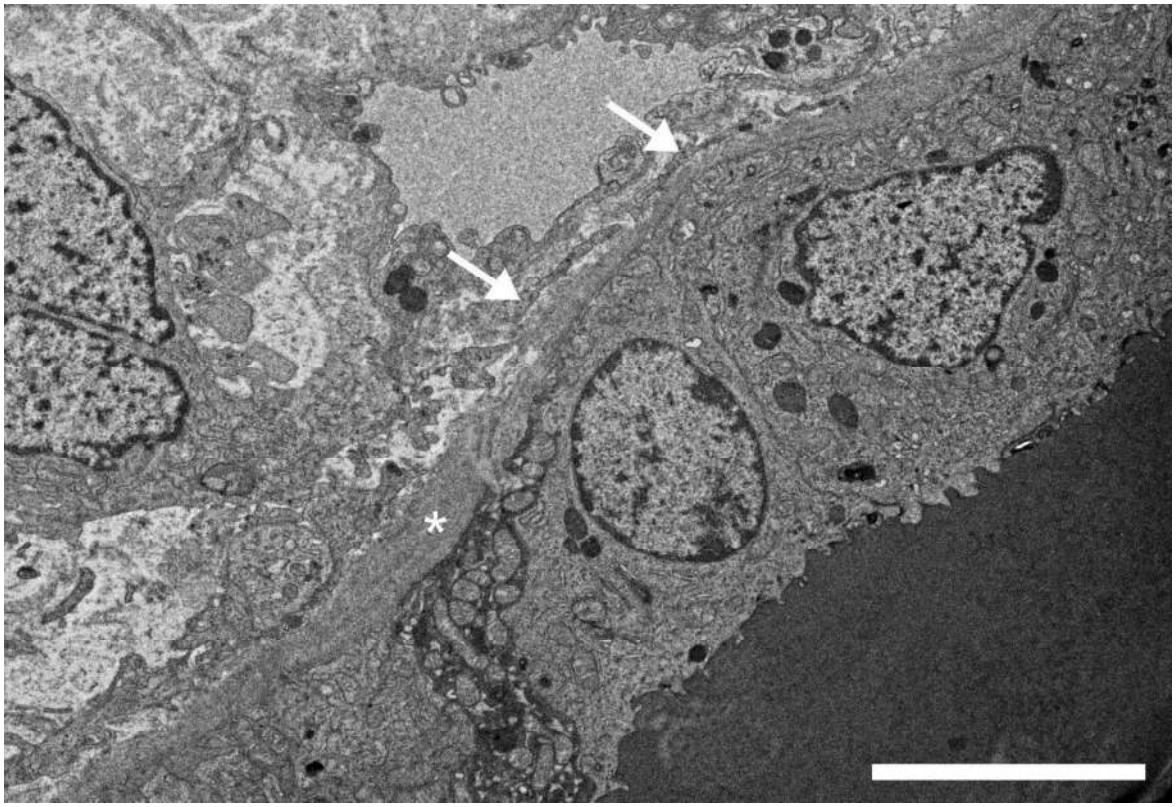

Figure 1: Transmission electron microscopy image of ultrathin section of focal segmental glomerulosclerosis (GESF) showing extensive foot process effacement of the podocytes (arrow) and glomerular basement membrane thickening (*). Scale bar: 5µm.

Temperature Interference on ZIKV and CHIKV Cycles in Mosquitoes and Mammalian Cells

Tiago Souza Salles[1,2], Erica Santos Martins-Duarte[3], Marcelo Damião Ferreira de Meneses[4], Monica Ferreira Moreira[1], Davis Fernandes Ferreira[5], Renata Campos Azevedo[4], Wanderley De Souza[6,7], Lucio Ayres Caldas[6,8]*

[1]Department of Biochemistry, Institute of Chemistry, Federal University of Rio de Janeiro, Rio de Janeiro 21941-909, Brazil; [2]Fiocruz Biodiversity and Health Biobank, Oswaldo Cruz Foundation, Rio de Janeiro 21040-361, Brazil; [3]Department of Parasitology, Federal University of Minas Gerais, Belo Horizonte 31270-901, Brazil; Department of Virology, Institute of Microbiology, Federal University of Rio de Janeiro, Rio de Janeiro 21941-902, Brazil; [4]Department of Virology, Institute of Microbiology, Federal University of Rio de Janeiro, Rio de Janeiro 21941-902, Brazil; [5]Department of Pathology, Duke University Medical Center, Durham, NC 27710, USA; [6]Precision Medicine Research Center, Institute of Biophysics, Federal University of Rio de Janeiro, Rio de Janeiro 21941-904, Brazil; [7]National Centre for Structural Biology and Bioimaging (CENABIO), Federal University of Rio de Janeiro, Rio de Janeiro 21941-902, Brazil; [8]Multidisciplinary Research Centre (Numpex-Bio), Federal University of Rio de Janeiro, Rio de Janeiro 25265-970, Brazil, email: lucio@biof.ufrj.br

Zika virus (ZIKV, Flavivirus, *Flaviviridae*) and Chikungunya virus (CHIKV, Alphavirus, *Togaviridae*) are arboviruses of significant public health concern, particularly in tropical and subtropical regions where their mosquito vectors are prevalent [1,2]. Although they belong to different viral families, both viruses share epidemiological and clinical features. In this study, we investigated the morphogenesis of ZIKV and CHIKV in mammalian (Vero) and insect (C6/36) cells. Both infected cells were incubated at 37 °C and 28 °C, and observed through transmission electron microscopy. These temperatures were chosen because they represent optimal in vitro culture conditions for mammalian and mosquito cells, and by exchanging these conditions, we aimed to impose thermal stress to evaluate its impact on the viral cycle. Infection times were 24, 48 and 72 h. Our results showed that the structural organization of host cells influences and reflects their competence for viral production under varying temperature conditions. Vero cells incubated at 28 °C exhibited pronounced cytoplasmic vacuolization and loss of cell clustering, indicating that suboptimal temperature compromises cellular integrity. Similarly, C6/36 cells exposed to 37 °C also showed vacuolization, suggesting that thermal stress affects both cell lines, albeit in distinct ways. Regarding viral morphogenesis, abundant virus surfing and formation of giant structures were observed in CHIKV-infected Vero cells at 37 °C, while CHIKV particles were detected in membrane projections of C6/36 cells at 28 °C but not at 37 °C, where few viruses adhered to the cell surface. For ZIKV, replication in Vero cells at 37 °C resulted in densely packed viral factories, whereas at 28 °C there was a reduction in vesicle formation and delayed virion maturation. These findings demonstrate that temperature stress significantly affects not only cellular morphology, but also the efficiency of the replication, highlighting the importance of environmental conditions in viral transmission dynamics and pathogenesis. This study advances understanding of viral adaptation mechanisms and may support future strategies for arbovirus control and prevention [3].

[1] Dick et al., Trans. R. Soc. Trop. Med. Hyg. 46 (1952) 509–520.
[2] Gubler et al., History and Emergence of Zika Virus. J. Infect. Dis. 216 (2017) S860–S867.
[3] Funding: Financiadora de Estudos e Projetos—FINEP, grant No. 01.19.0144.00.

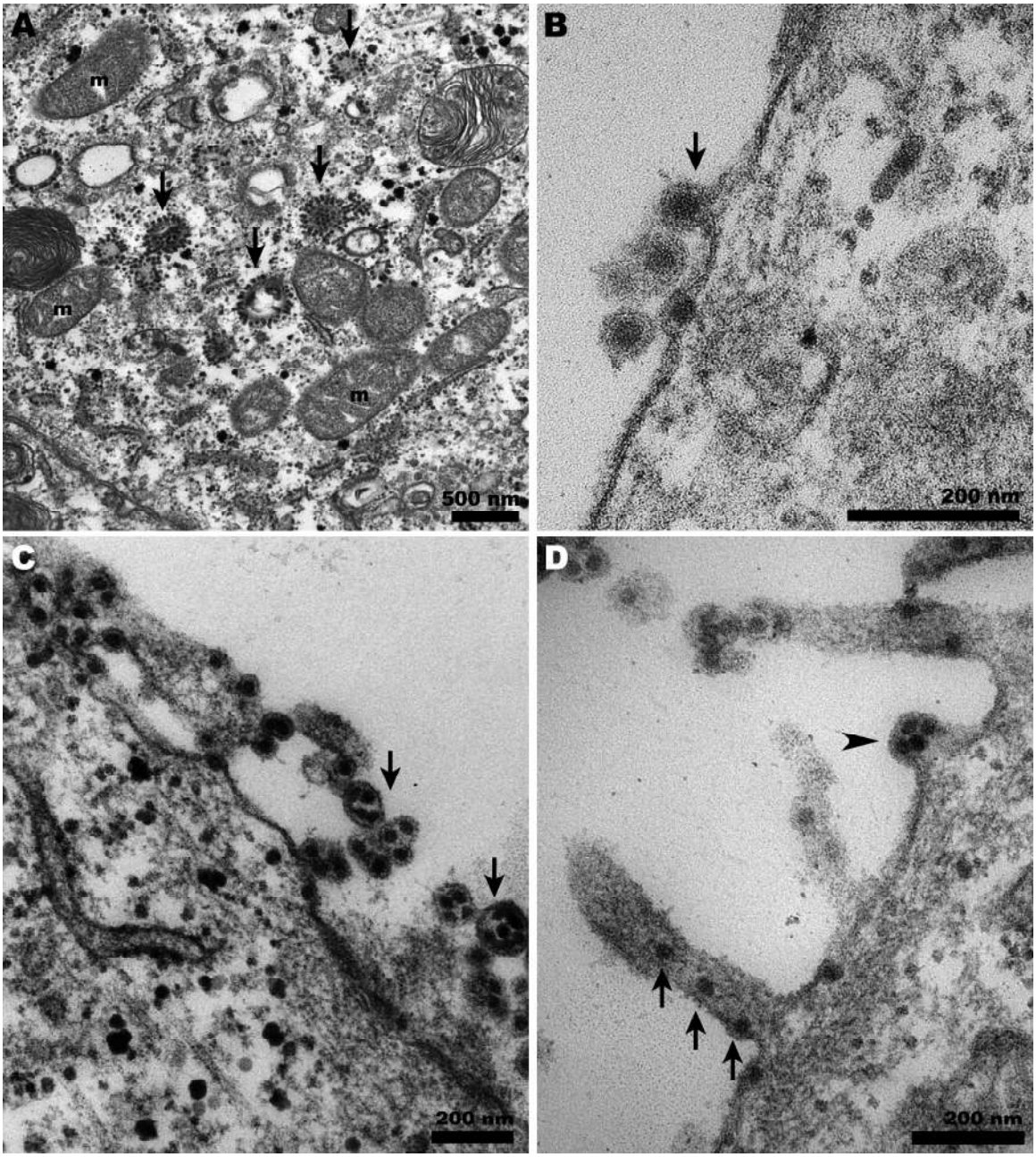

Figure 1: Transmission electron microscopy of CHIKV-infected Vero cells at 37 °C. **(A)** CHIKV-induced CPV-II (arrows) surrounded by clusters of mitochondria (m) were abundant in the cytosol; **(B)** characteristic budding of CHIKV at the plasma membrane (arrows); **(C)** giant forms adjacent to the cell surface (arrows); **(D)** budding of giant forms (arrowheads) and cell membrane projections carrying CHIKV (arrows).

Three-dimensional reconstruction reveals distinct organizational patterns of the intravacuolar network in *Cyrilia lignieresi*

Brenda S. Fachetti [1,3,4], Maíra Turiel-Silva [1,3], Camila Wendt [4], Edilene O. Silva [2], Ana Paula D. Rodrigues [3], Wanderley de Souza [4], Kildare Miranda [4], José A. P. Diniz [3*]

[1] Universidade do Estado do Pará, Departamento de Morfologia e Ciências Fisiológicas, Centro de Ciências Biológicas e da Saúde, Marabá, Brasil;
[2] Universidade Federal do Pará, Instituto de Ciências Biológicas, Belém, Brasil;
[3] Instituto Evandro Chagas, Seção de Hepatologia, Belém, Brasil.
[4] Universidade Federal do Rio de Janeiro, Instituto de Biofísica Carlos Chagas Filho and Centro Nacional de Biologia Estrutural e Bioimagem, Rio de Janeiro, Brasil.
*joseantonio@iec.gov.br

Cyrilia lignieresi (Adeleina: Haemogregarinidae) is a protozoan parasite of the phylum Apicomplexa that infects the erythrocytes of the fish Synbranchus marmoratus, commonly known as "muçum" [1]. The genus Cyrilia was proposed by Lainson [1], based on the description of the parasite's developmental stages in S. marmoratus and the leech Haementeria lutzi. In 2002, Diniz et al. analyzed the ultrastructure of C. lignieresi trophozoites using transmission electron microscopy (TEM), identifying apical organelles typical of apicomplexans such as conoids, rhoptries, and micronemes and reported the unusual presence of spherical bodies within the parasitophorous vacuole (PV). These structures are rarely described in other members of the phylum [2]. Recent studies have reported a tubulovesicular network and cleft-like structures associated with host cell remodeling in gamonts [3]. However, the three-dimensional organization and morphometric analysis of these PV-associated structures had not yet been explored through electron tomography. In this study, we used electron tomography with three-dimensional reconstruction (3D-EM) to characterize the spherical bodies and their spatial organization within the PV of infected erythrocytes.Five parasites were analyzed, with an average of eight serial tomograms per specimen. Manual segmentations and reconstructions were performed using IMOD™ software (v. 4.11.8, University of Colorado, USA), enabling quantitative analysis of volume (nm^3), as well as maximum, minimum, mean, and standard deviation values. Three-dimensional reconstruction revealed that the spherical bodies described by Diniz et al. (2002) are not isolated vesicles, but rather components of a complex intravacuolar tubulovesicular network (IVN) in C. lignieresi (Fig. 1). Two distinct IVN morphologies were identified: (1) a branched network of interconnected tubules and heterogeneous, electron-dense structures distributed between the PV membrane (PVM) and the parasite surface (Fig. 1A–E); and (2) a linear arrangement of unidirectional, electron-dense tubules aligned parallel to the PVM (Fig. 1F–J). Morphometric data for these structures are presented in Table 1. The observed differences suggest potential plasticity of the IVN in C. lignieresi, the implications of which for host-parasite interactions remain poorly understood. These findings improve our understanding of the parasite's ultrastructural organization and suggest that IVN morphology may reflect distinct evolutionary or functional stages of the infection.

REFERENCES

[1] Lainson, R., 1981. Society of Protozoologists, London, Canning EU ed, pp 150–158.
[2] Diniz, J.A., et al., 2002. Parasitology Research, 88(7), 593–597.
[3] Turiel-Silva et al., 2022. Journal of Eukaryotic Microbiology, 00, e12894.

This work was supported by IEC, UEPA, CNPq, FAPERJ e FINEP.

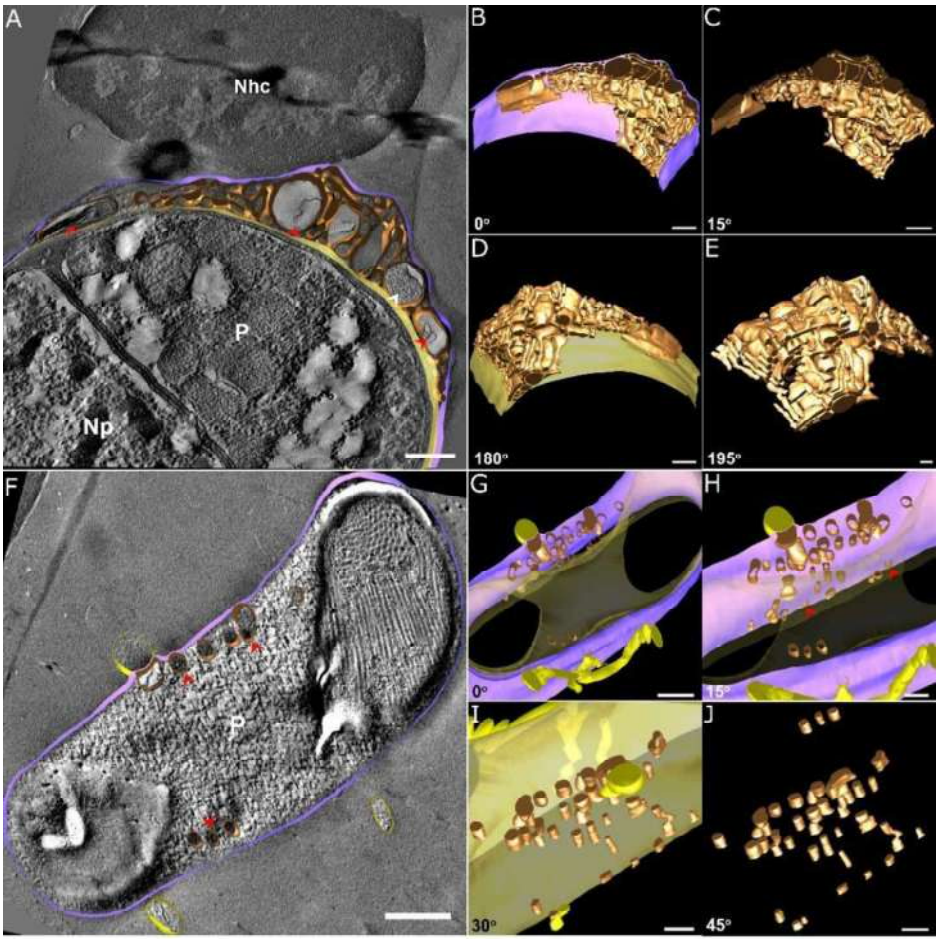

Figure 1. Three-dimensional morphology of the intravacuolar tubulovesicular network (IVN) in two distinct *Cyrilia lignieresi* parasites, analyzed by serial-section electron tomography and 3D reconstruction. **(A-E)** Parasite 1 with a branched IVN. **(A)** Tomographic slice showing the parasite (P), parasite nucleus (Np), host cell nucleus (Nhc), outer membrane (OM, yellow), parasitophorous vacuole membrane (PVM, purple), and the IVN (gold). Red arrowheads indicate vesicles with membrane profiles; White arrowheads indicate vesicles with granular profiles. **(B-E)** 3D models rotated at the indicated angles, highlighting the branched and interconnected morphology of the IVN. **(F-J)** Parasite 2 with a linear IVN. **(F)** Tomographic slice showing the parasite (P), PVM (purple), OM (yellow), and the IVN composed of electron-dense unidirectional tubules. **(G-J)** 3D views at different angles showing the linear organization of the IVN and its parallel distribution along the PVM. Red arrowheads mark contact points with tubulovesicular structures (TVS, yellow). **Scale bars:** 500 nm.

Table 1: Morphometric analysis of the Intravacuolar Tubular Network (IVN) in the Parasitophorous Vacuole (PV) of *C. lignieresi* based on electron tomography scans

Specimens	*Total PV volume (nm3)*	*Quantity of Components*	*Maximum (nm3)*	*Medium (nm3)*	*Minimum (nm3)*	*Standard Deviation (nm3)*	*Occupied Volume (nm3)*	*Occupied Volume (%)*	*Morphology*
P3 (9AJ)	$1{,}17 \times 10^{10}$	118	$1{,}20 \times 10^{12}$	$7{,}75 \times 10^{10}$	$8{,}10 \times 10^{8}$	$1{,}64 \times 10^{11}$	$4{,}82 \times 10^{9}$	41,1%	Branched
P4 (C7)	$2{,}82 \times 10^{9}$	36	$3{,}53 \times 10^{11}$	$6{,}23 \times 10^{10}$	$7{,}71 \times 10^{9}$	$6{,}09 \times 10^{10}$	$2{,}25 \times 10^{8}$	7,96%	Linear
P6 (1AI)	$2{,}11 \times 10^{10}$	14	$6{,}93 \times 10^{9}$	$4{,}95 \times 10^{7}$	$1{,}00 \times 10^{4}$	$1{,}85 \times 10^{9}$	$2{,}67 \times 10^{9}$	12,66%	Branched
P8 (6AG)	$6{,}80 \times 10^{8}$	17	$5{,}44 \times 10^{10}$	$1{,}08 \times 10^{10}$	$7{,}50 \times 10^{8}$	$1{,}51 \times 10^{10}$	$1{,}84 \times 10^{7}$	2,70%	Linear
P10 (3AE)	$9{,}44 \times 10^{9}$	8	$5{,}51 \times 10^{9}$	$6{,}89 \times 10^{8}$	$1{,}00 \times 10^{4}$	$6{,}89 \times 10^{8}$	$9{,}06 \times 10^{7}$	0,96%	Linear

Quantitative data from the morphometric analysis of the IVN in the PV of five *C. lignieresi* specimens. For each specimen, the following are presented: the total volume of the PV (in nm^3); the number of tubular structures identified; the maximum, mean, and minimum volumes, and the standard deviation of the structures (in nm^3); the total volumetric occupation of the IVN, expressed in absolute values (nm^3) and percentages in relation to the PV volume; and the morphological classification of the structures according to shape (branched or simple tubular).

Titanium Nanotopography Modified by Cold Atmospheric Plasma Influences Mitochondrial Dynamics of Osteoblastic Cells

Janine Karla França S. Braz*[1], Moacir Franco de Oliveira[2], Gabriel Moura Martins[3], Jussier Oliveira Vitoriano[4], Marcos Paulo B Viana[5], Bruno Caio Chaves Fernandes[2], Thalita Souza Arantes[6], Clodomiro Alves Júnior[2], Carlos Eduardo Bezerra de Moura[2]

[1]Departamento de Morfologia, Centro de Biociências, Universidade Federal do Rio Grande do Norte, Natal, RN, Brazil.
[2] Departamento de Ciência Animal, Centro de Ciências Agrárias, Universidade Federal Rural do Semi-Árido,Mossoró, RN, Brazil.
[3]Centro de Ciências da Saúde, Universidade Federal do Rio Grande do Norte, Natal, RN, Brazil
[4]Departamento de Física, Universidade Federal do Rio Grande do Norte, Natal, RN, Brazil
[5]Escola Multicampi de Ciências Médicas do RN, Universidade Federal do Rio Grande do Norte, Caicó, RN, Brazil.
[6]Centro de Microscopia, Universidade Federal de Minas Gerais, Belo Horizonte, MG, Brazil.
*janine.braz@ufrn.br

Cold atmospheric plasma (CAP) has been widely used in plasma medicine to promote nanometric modifications on biomaterial surfaces, including titanium [1]. These plasma-nanostructured titanium surfaces accelerate osteogenesis and can improve bone regeneration in dentistry and orthopaedics [2]. Thus, the process of bone cell differentiation on surfaces can induce modifications in cellular ultrastructure, especially of mitochondria. Mitochondria are dynamic organelles that perform fission and fusion in response to microenvironmental changes to maintain cellular homeostasis [3]. Therefore, our study aimed to investigate the differences in mitochondrial dynamics produced by the nanotopography of the titanium surface modified by CAP in osteoblastic cells. For this, we prepared titanium discs (Grade 2), polished (control) and treated (CAP) with 1 L/min of helium, 13 Kv; 600 Hz; a distance of 20 mm for 15 min. Osteoblastic cell line MC3T3-E1 (ATCC CRL-2594) cells were cultured at a concentration of $1x10^4$ cells per disk in DMEM supplemented with 10% fetal bovine serum and 1% streptomycin/penicillin at 37°C in an incubator with 5% CO_2 for 24 h. The samples (cells on discs) were then washed and fixed with 2.5% glutaraldehyde for 24 hours, postfixed with 1% osmium tetroxide for 30 minutes, and stained in a block with 2% uranyl acetate for 20 minutes and 0.5% lead citrate for 10 min. They were dehydrated through an ethanol gradient. The samples were soaked in Spurr's resin and embedded in Eppendorf centrifuge tubes. Analyses were performed using a Transmission Electron Microscopy (Jeol-120Kv). We observed that osteoblastic cells on polished surfaces had shorter and more divided mitochondria, characterising fission. Cells cultured on titanium surfaces treated with CAP presented more elongated and fused mitochondria, in an interconnected manner, indicating improved osseointegration (cell-titanium). Thus, in this work, we demonstrated that the titanium nanotopography produced by CAP can modulate the mitochondrial dynamics of osteoblastic cells. Therefore, future studies require understanding the molecular processes involved in these dynamics for osteogenic modulation.

[1] G.M Martins et al., ACS Biomater Sci Eng. 10 (2024) 1765.
[2] C.E.B. Moura et al., Thin Soli Films, 43 (2019) 764-772.
[3] L. Wang et al., Biochem Biophys Res Commun, 535 (2021) 33-38.
[4] The authors would also like to thank Centro de Microscopia staff of UFMG and the supported by CNPq (Brazil, process nº 402536/2021-5) and BioImaging Network of Minas Gerais (BioIMG Net)

Figure 1. TEM images of MC3T3-E1 cells cultured for 24 hours on titanium discs with different surface treatments. On polished titanium surfaces (A), mitochondria appear shorter and more fragmented, suggesting a predominance of mitochondrial fission. In contrast, cells on titanium treated with cold atmospheric plasma (B) exhibit elongated and interconnected mitochondria, consistent with mitochondrial fusion.

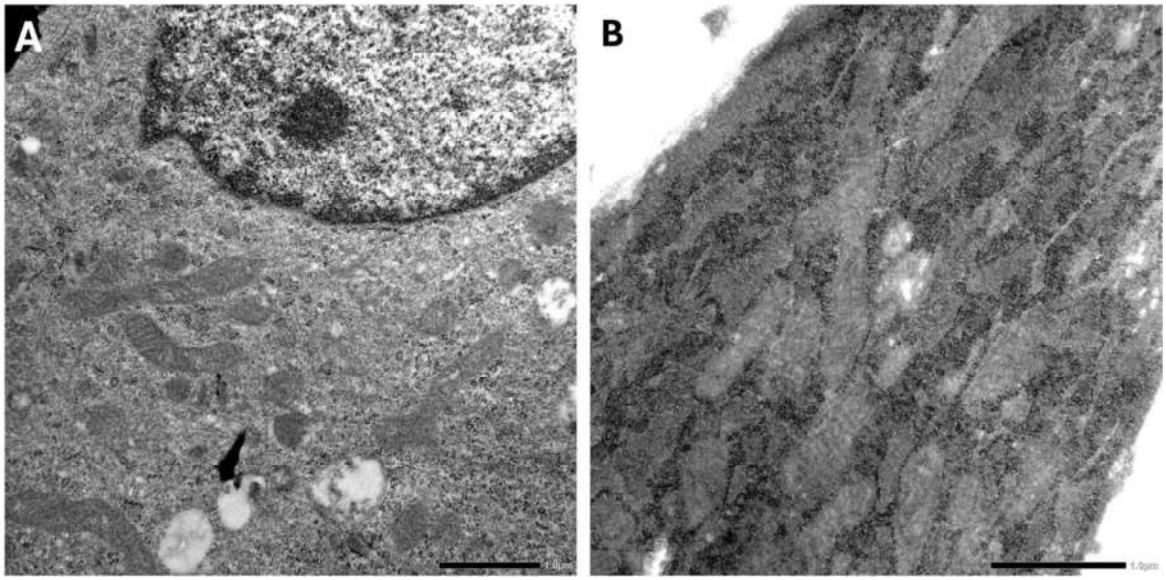

Ultrastructural Analysis of the Tegument of *Schistosoma mansoni* Using High-Pressure Freezing and Freeze Substitution (HPF/FS)

Juliana de Lima Ferreira[1], Jose Roberto Machado-Silva[1.] and Eduardo José Lopes-Torres[1*]

[1]. Romero Lascasas Porto Helminthology Laboratory, Department of Microbiology, Immunology and Parasitology, FCM/UERJ, Rio de Janeiro, Brazil.
*eduardo.torres@uerj.br

Schistosomiasis, a neglected tropical disease caused by *Schistosoma mansoni*, affects millions globally. The parasite's tegument plays a crucial role in nutrient absorption, immune evasion, and host interaction, making it a central focus for drug and vaccine development. High-resolution imaging of the tegumental surface is essential for understanding its structure–function relationships (1,2). This study aimed to examine the ultrastructure of the tegument in adult *S. mansoni* using high-pressure freezing. Adult worms were recovered from Swiss Webster mice after 60 days of infection with the LE strain and cryofixed using a Bal-Tec 010 HPM. Samples were mounted in aluminum carriers types A and B containing 1-hexadecene, rapidly frozen, and then submitted to freeze substitution in the substitute medium composed by 1% osmium tetroxide, 0.5% glutaraldehyde, 0.5% uranyl acetate, and 1% water in acetone at -85°C, for electron microscopy analysis (3). TEM revealed marked ultrastructural differences between male and female parasites. The tegument of females showed a smooth and homogeneous (Fig 1 A-D), lacking the prominent dorsal tubercles and spines observed in males (Fig 2 A-D). The female reproductive system was clearly visible, including vitelline glands, ovaries containing oocytes at various developmental stages, and the oviduct (Fig 1 B, C, D). In contrast, males exhibited a more complex tegumental surface, characterized by large dorsal tubercles, spines, cytoplasmic inclusions, and well-defined muscle layers (Fig 1 A-D). Numerous secretory vesicles were identified on the males tegument, suggesting intense interaction with the host (Fig 2 A, D). The presence of large vacuoles and nuclei within the tegument was also observed. Cryofixation preserved the fine structures of these elements, minimizing the artifacts commonly associated with chemical fixation. These findings highlight the sexual dimorphism of the tegument in *S. mansoni* and demonstrate the effectiveness of cryofixation in preserving ultrastructural integrity. This method enhances our understanding of parasite biology and supports future strategies for identifying novel therapeutic targets.

1. McManus DP, Bergquist R, Cai P, Ranasinghe S, Tebeje BM, You H. *Schistosomiasis—from immunopathology to vaccines*. Semin Immunopathol. 2020 Jun 19;42(3):355–71.

2. Machado-Silva JR, Pelajo-Machado M, Lenzi HL, Gomes DC. *Morphological study of adult male worms of Schistosoma mansoni Sambon, 1907 by confocal laser scanning microscopy*. Mem Inst Oswaldo Cruz. 1998;93(suppl 1):303–7.

3. Lopes-Torres EJ, Girard-Dias W, de Souza W, Miranda K. *On the structural organization of the bacillary band of Trichuris muris under cryopreparation protocols and three-dimensional electron microscopy*. J Struct Biol. 2020 Nov 1;212(2).

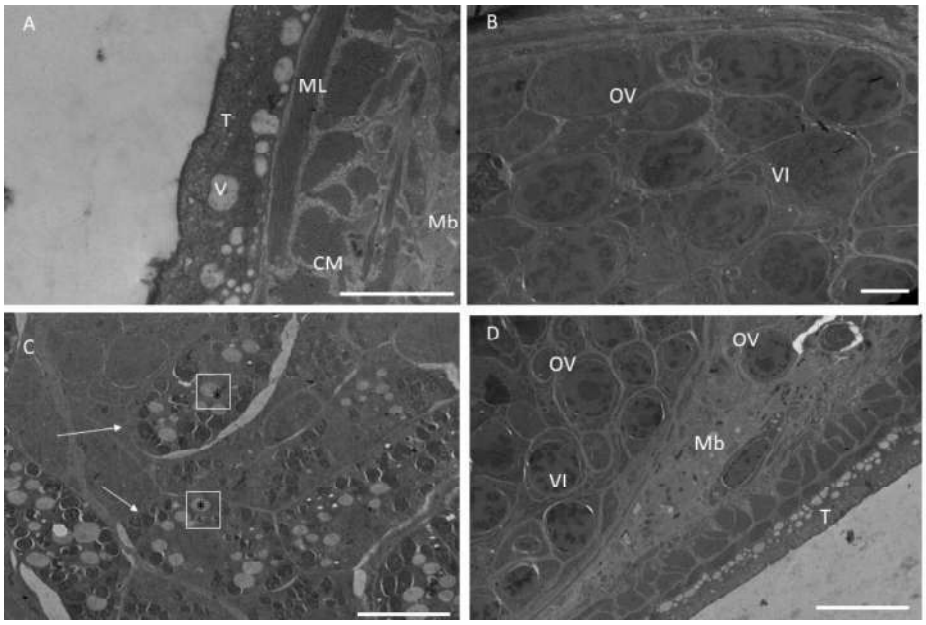

Figure 1. Transmission electron microscopy (TEM) of adult female *Schistosoma mansoni* worms (A, B, C, D). Images (A and D) show the basement membrane and tegument (T) containing vesicles (V). A detailed view reveals circular (CM) and longitudinal (ML) muscle fibers. Images (B and D) show the vitelline duct (VI) and oviducts (OV) with oocytes at different stages of development. Image (C) highlights vitelline cells (indicated by the arrow) containing yolk globules (*). Scale bars: 2 µm (A, B); 5 µm (C, D).

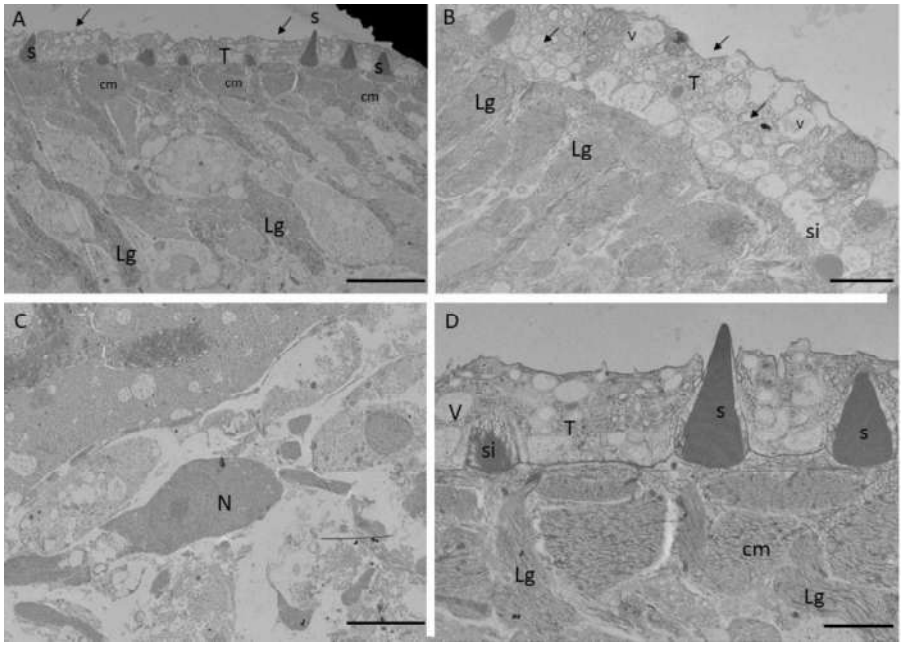

Figure 2. Transmission Electron Microscopy (TEM) of adult male *Schistosoma mansoni* worms (A, B, C, D). Images (A, B, D) show tubercles (T) with spines (S), vesicles (ARROW), and vacuoles (V). A detailed view of the tubercles reveals circular (cm) and longitudinal (Lg) muscle fibers. Image (B) also shows internalized spines (Si), while (C) highlights the nucleus (N). Scale bars: 2 µm (A, C); 2 µm (B); 1 µm (D).

Ultrastructural and Cytochemical Analysis of Secretory Trichomes in Syconia of *Ficus citrifolia*

Giseli Donizete Pedersoli[1], Rodrigo Augusto Santinelo Pereira[2] & Simone de Pádua Teixeira[1]

[1]Universidade de São Paulo, Faculdade de Ciências Farmacêuticas de Ribeirão Preto, Av. do Café, s/n, 14040-903, Ribeirão Preto/SP, Brazil
[2]Universidade de São Paulo, Faculdade de Filosofia, Ciências e Letras de Ribeirão Preto, Av. Bandeirantes, 3900, 14040-901, Ribeirão Preto/SP, Brazil
* Author for correspondence: giselipedersoli@gmail.com

Species of the genus *Ficus* (Moraceae) produce enclosed inflorescences called syconia, which harbor a highly specialized mutualistic interaction with pollinating wasps from the family Agaonidae [1,2]. Various secretory structures are present within these organs, particularly secretory trichomes, whose morphology and chemical composition remain poorly understood [3,4]. While latex has been extensively studied, other secretory glands exhibit potential for the biosynthesis of bioactive compounds with antimicrobial, anti-inflammatory, and wound-healing properties [5]. This study aimed to locate and characterize secretory trichomes in the syconia of *Ficus citrifolia*, with a particular focus on cytochemical and ultrastructural analysis using transmission electron microscopy (TEM). TEM provided high-resolution imaging of the cellular architecture, allowing the identification of organelles involved in secretion, as well as the production, storage, and release sites of secreted compounds. Isolated trichomes were subjected to cytochemical protocols: acidic polysaccharides were detected using the Ruthenium Red method [6]; proteins via the Ammoniacal Silver method [7]; and lipids using the Osmium-Imidazole technique [8]. Secretory trichomes were predominantly found at the base of the receptacle. TEM analysis revealed secretory cells with extensive vacuolization, abundant rough endoplasmic reticulum, lipid bodies, and electron-dense materials within the cytoplasm and associated with the cell walls. Cytochemical tests confirmed the presence of acidic polysaccharides, proteins, and lipids within vacuoles and in the exudate. The integration of cytochemical techniques and TEM was essential to elucidate the dynamics of secretion in *F. citrifolia* trichomes, suggesting ecological roles such as floral tissue protection, lubrication, and pollinator attraction. These findings highlight the relevance of TEM in advancing our understanding of plant secretory structures and contribute to the functional and evolutionary interpretation of glandular tissues in *Ficus*, particularly within the fig-wasp mutualistic system.

[1] Weiblen, G.D. 2002. How to be a fig wasp. Annual Review of Entomology 47: 299-330.
[2] Cook, J. M. & Rasplus, J.Y. 2003. Mutualists with attitude: Coevolving fi g wasps and fi gs. Trends in Ecology & Evolution 18: 241-248.
[3] Machado, A.F.P., Souza, A.M. & Leitão, C.A.E. 2013. Secretory structures at syconia and flowers of *Ficus enormis* (Moraceae): A specialization at ostiolar bracts and the first report of inflorescence colleters. Flora 208: 45-51.
[4] Souza, C.D., Pereira, R.A.S., Marinho, C.R., Kjelberg, F. & Teixeira, S. P. 2015. Diversity of fig glands is associated with nursery mutualism in fig trees. American Journal of Botany 1-14.

[5] Marinho, C.R. & Teixeira, S.P. 2019. Cellulases and pectinases act together on the development of articulated laticifers in *Ficus montana* and *Maclura tinctoria* (Moraceae). Protoplasma 256: 1093-1107.
[6] Luft, J.H. 1971. Ruthenium red and violet. II. Fine structural localization in animal tissues. The Anatomical Record 171: 369-376.
[7] Macrae E.K. & Meetz G.D. 1970. Electron microscopy of the ammoniacal silver reaction for histones in the erythropoietic cells of the chick. Journal of Cell Biology 45: 235-245.
[8] Angermüller S. & Fahimi D.H. 1982. Imidazole-buffered osmium tetroxide: an excellent stain for visualization of lipids in transmission electron microscopy. The Histochemical Journal 14: 823-825.
[9] This work was supported by FAPESP (São Paulo Research Foundation, Brazil).

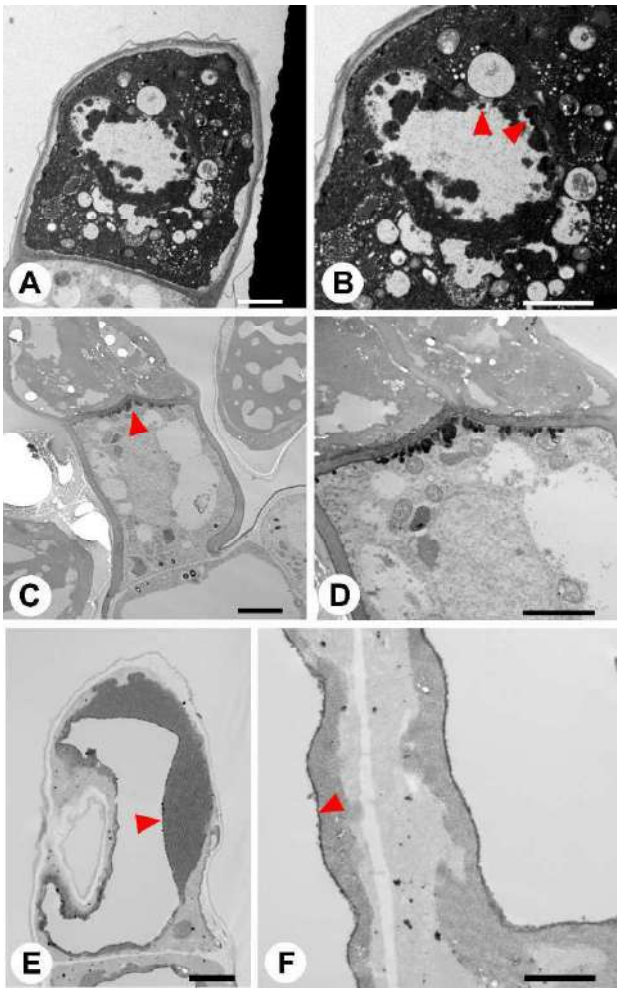

FIGURE 1 - Transmission electron micrographs of secretory trichome cells from *Ficus citrifolia* syconia showing positive cytochemical reactions. A-B: Positive staining for acidic polysaccharides using the Ruthenium Red method. Electron-dense precipitates are observed within vacuoles (arrowheads). C-D: (C-D) Positive protein localization by the ammoniacal silver method. Electron-dense granules are visible in the cytoplasm near the cell wall (arrowheads). E-F: Positive lipid detection using the osmium-imidazole technique. The lipid bodies exhibit intense electron density (arrowheads), indicating lipid accumulation. Scales: A-F: 2 μm.

Ultrastructural characterization of spores and crystals from a new isolate of *Lysinibacillus sphaericus* from Pernambuco (Ls-PE) with larvicidal activity against mosquito vectors.

Marcelo Soares de Barros[1]*, Maria Eduarda de Lima Rocha da Silva[1], Yuri Mouzinho Ramos Tanaka[1], Thaíse Yasmine Vasconcelos de Lima Cavalcanti[1], Karina Lidiane Alcântara Saraiva[1], Cláudia Maria Fontes de Oliveira[1], Tatiany Patrícia Romão[1]*.

[1]Instituto Aggeu Magalhães – IAM/ FIOCRUZ-PE
*marcelo.fiocruzpe@gmail.com; *tatiany.romao@fiocruz.br.

Lysinibacillus sphaericus is a cosmopolitan, Gram-positive bacterium that produces crystalline inclusions containing protein protoxins with larvicidal activity against certain mosquito species during its sporulation phase. This species exhibits insecticidal activity against mosquitoes of the Culicidae family and has been widely used in vector control programs. The binary toxin (Bin) is the primary toxic factor present in all *L. sphaericus* (Ls) strains, responsible for larvicidal activity against mosquitoes of the genera *Culex*, *Anopheles*, and *Aedes*. Traditional bioprospecting studies conducted in our department led to the isolation of a wild strain, Ls-PE, from the state of Pernambuco, identified as a new isolate of *L. sphaericus*. This bacterium's genome contains genes encoding Cry toxins in addition to the Bin toxin, distinguishing it from previously described strains of this species. Therefore, the aim of this study was to characterize the toxin crystals produced by this new isolate during its sporulation phase. To achieve this, the Ls-PE isolate was first cultivated in sporulation medium and subjected to heat shock. After 144 hours, sporulated aliquots were fixed in Karnovsky's solution and processed for transmission electron microscopy (TEM) as well as scanning electron microscopy (SEM). The TEM results showed endospores with a pattern of multiple toxin crystals within the sporangia, generally three (Figure 1A). The toxin crystals displayed a textured polyhedral morphology and were electron-dense (Figure 1B). The sporangium exhibited a rough surface texture under SEM (Figure 1C). For crystal characterization by SEM, the Ls-PE powder, based on lyophilized spore biomass, was germinated in Luria-Bertani medium for 48 hours. The material was washed in the presence of NaCl and Triton X-100 followed by sonication and crystal preparation and adhesion to poly-L-lysine-coated slides. Three-dimensional SEM images revealed crystals with well-defined spatial features of different geometric formats. These differences may be related to the molecular composition of the proteins since these bacterial isolates are capable of synthesizing a complex of protein toxins. In conclusion, the Ls-PE isolate produces additional toxin crystals not commonly found in *L. sphaericus*, which may contribute to its enhanced entomopathogenic potential against insects of the Culicidae family.

[1] M. H. N. L. Silva-filha et al. Bacterial toxins active against mosquitoes: Mode of action and resistance. Toxins, v. 13, n. 8, p. 523, 2021.
[2] J. R. Mounsef et al. A simple method for the separation of *Bacillus thuringiensis* spores and crystals. Journal of Microbiological Methods, v. 107, p. 147-149, 2014.
[3] V. C. P. de Lima et al. Pesquisa e desenvolvimento de formulações para proteção de protoxinas de *Bacillus* e outras bactérias esporuladas entomopatogênicas. Archives of Health, v. 1, n. 5, p. 346-350, 2020.
[4] This research was supported by PROEP – FIOCRUZ, CAPES and FACEPE.

Figure 1. Transmission Electron and Scanning Electron Micrographs of sporulated *Lysinibacillus sphaericus* isolate Ls-PE. (A) TEM image of sporulated Ls-PE; (B) Toxin Crystals produced by Ls-PE; (C) Spores visualized by SEM.

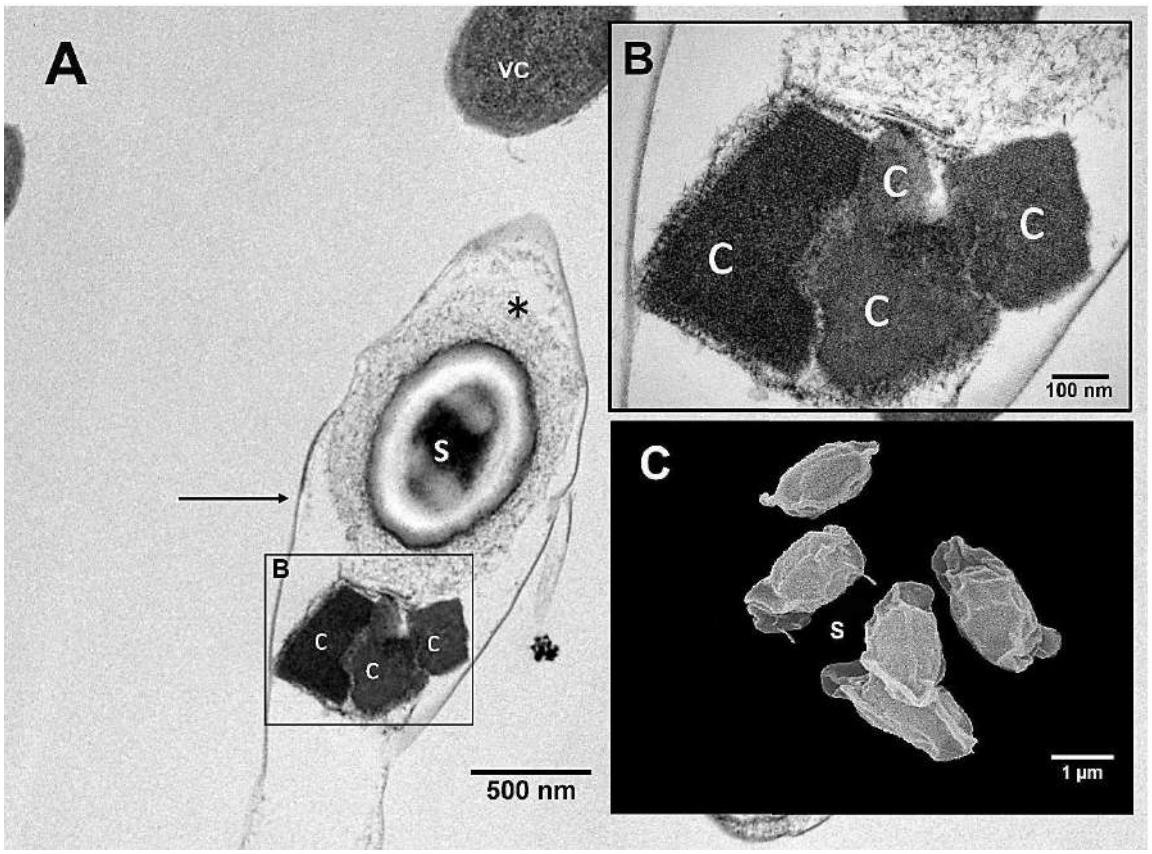

Legend: (S) Spore; (C) Crystals; (VC) Vegetative cell; Arrows (→) Exospore; Asterisk (∗) Endospore.

Figure 2. Scanning Electron Micrograph of Crystals purified from sporulated *Lysinibacillus sphaericus* Ls-PE. Crystals of varying sizes are shown: (A) scale bar = 2 µm; (B and C) scale bar = 1 µm.

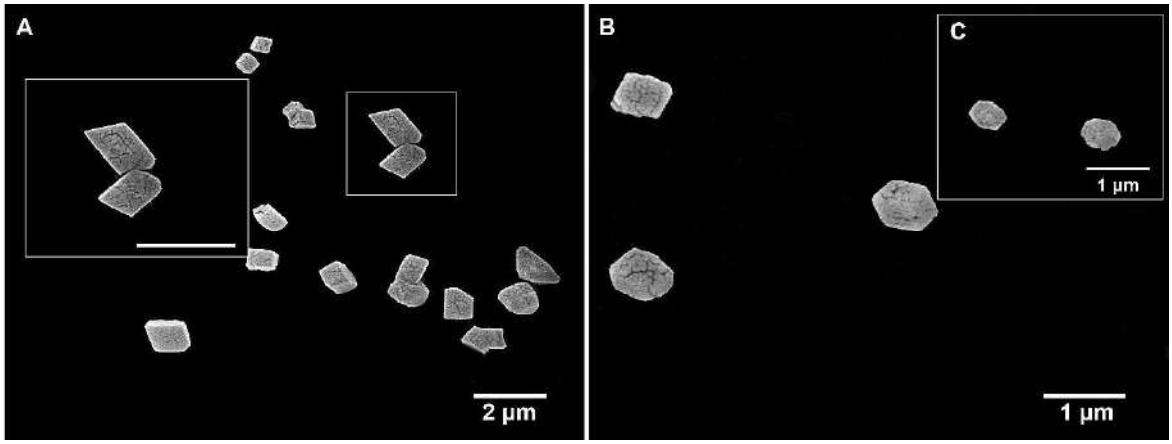

Ultrastructural effects of the interaction between titanium dioxide (TiO_2) microparticles and *Lactuca sativa*.

Ana Kamila Medeiros Lima[1]; João Vinicius Sousa Fernandes[1]; Fernanda Gomes Trindade[2]; Antje Biesemeier[3]; Emilio de Castro Miguel1*[2].

[1] Biomaterials Laboratory, Department of Metallurgical Engineering and Materials and Analytical Center, Federal University of Ceará (UFC), Fortaleza, CE, Brazil.

[2] Cell and Tissue Biology Laboratory, State University of Norte Fluminense Darcy Ribeiro (UENF), Campos dos Goytacazes, Brazil.

[3]Luxembourg Institute of Science and Technology (LIST), Materials Research and Technology (MRT), Advanced Instrumentation for Ion Nano-Analytics (AINA), Esch-sur-Alzette, Luxembourg.

* emiliomiguel@ufc.br

Titanium dioxide (TiO_2) is a chemically stable and insoluble compound widely used in cosmetics, food, and agriculture. It is among the most produced nanomaterials globally, with an estimated production of 2.5 million metric tons by 2025. TiO_2 nanoparticles have attracted attention due to their widespread applications; however, their influence on plant physiology and the environment remains complex [1]. Although considered inert, growing evidence shows that nano-TiO_2 can induce cellular and physiological damage in plants, even at environmentally relevant concentrations. This study aimed to investigate the ultrastructural and metabolic effects of TiO_2 exposure in *Lactuca sativa*, a model species for phytotoxicity studies. Rutile-form TiO_2 nanoparticles (ζ-potential: −17.36 ± 0.11 mV; size: 297.46 ± 3.66 nm) were prepared at 50 mg/L and sonicated for 15 minutes prior to exposure. Seedlings were exposed for 16 h after seven days of germination. Analytical techniques included light microscopy, transmission electron microscopy (TEM), and secondary ion mass spectrometry (SIMS) [2]. Figure 1 illustrates the ultrastructural disorganization observed after 16 h of exposure (1A, 1D, 1F), particularly when compared to control cells. Damage was found in the radicle, hypocotyl, and leaf tissues. In the radicle (1A–1C), cells showed alterations such as disorganized cell walls, ruptured membranes, electron-dense bodies adhered to the inner wall, and vesicles of varying sizes in transit, suggesting vesicular trafficking or exocytosis related to detoxification. Previous studies [3] reported similar injuries: disruptions in cell walls, membranes, chloroplasts, thylakoids, changes in peroxisomes, swollen mitochondrial cristae, abnormal nuclei, and altered mesophyll cells. Although Ti uptake wasn't confirmed in this study, electron-dense deposits near cell walls suggest interaction between NPs and plant cells. These inclusions may also reflect protein aggregation or autophagic activity, indicative of cellular stress. Structural, ultrastructural, and metabolic changes were evident and intensified with exposure duration, even in the absence of confirmed Ti absorption, emphasizing the toxic potential of nanoparticle contact alone. This research was supported by CAPES.

[1] TRELA-MAKOWEJ, Agnieszka; et al. Less is more: The hormetic effect of titanium dioxide nanoparticles on plants. Sci. of the Total Environment, v. 910, 2024

[2] OST, Alexander D. et al. The Ionmaster magSIMS: An Innovative Multi-Ion Species FIB Platform for Correlative High-resolution Ion Microscopy and SIMS Analyses. 2024.

[3] VISHNU, D. et al. Structural and Ultrastructural Changes in Nanoparticle Exposed Plants. (2019). 281-295. doi: 10.1007/978-3-319-97852-9_13

[4] This research was supported by Coordenação de Aperfeiçoamento de Pessoal de Nível Superior - CAPES (Brazil).

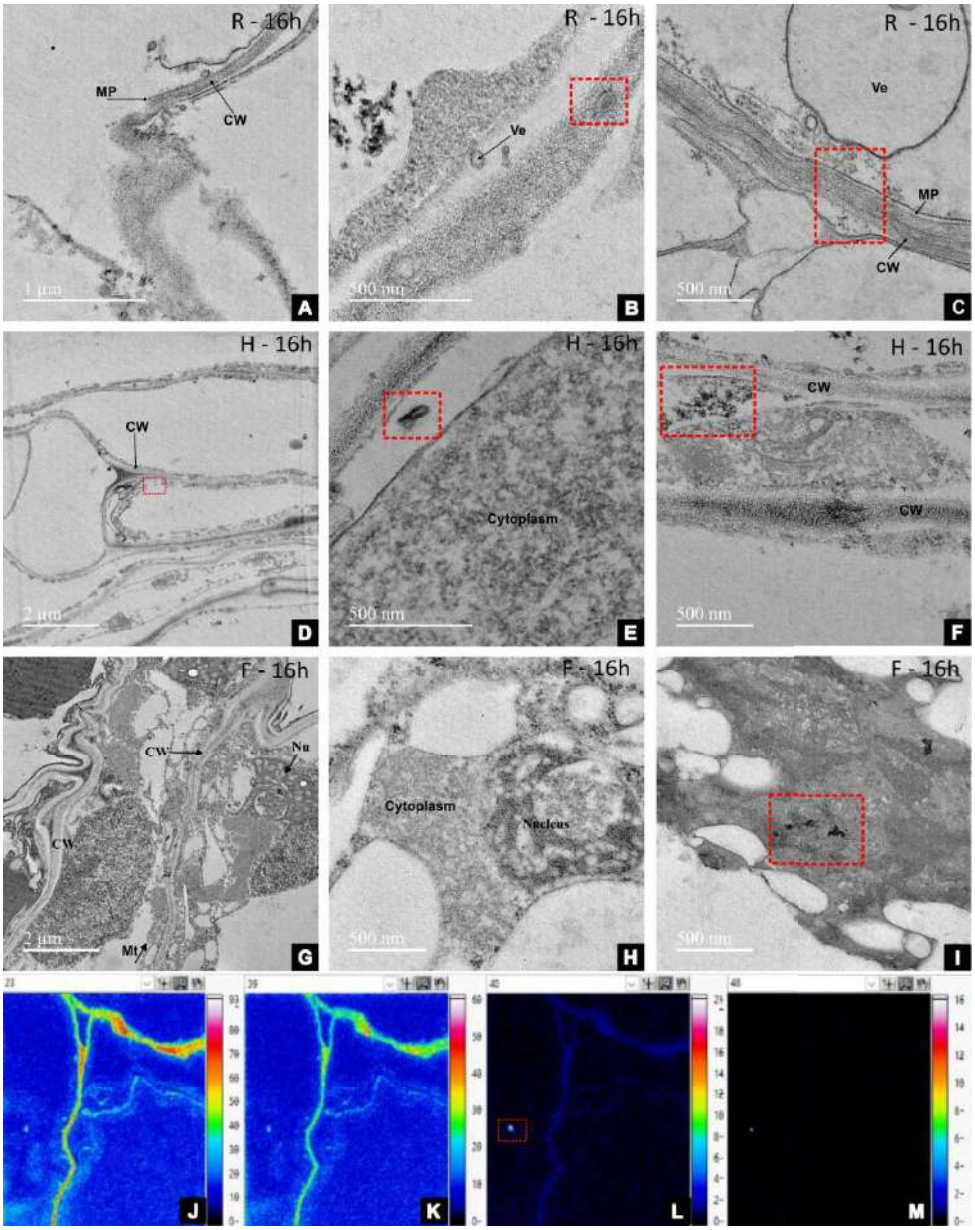

Figure 1. Transmission electron and SIMS micrographs of *Lactuca sativa* radicle, hypocotyl, and leaf cells after 16-hour exposure to 50 mg/L TiO_2. A: Radicle cell showing a disorganized cell wall (CW) and ruptured plasma membrane (PM). B: Radicle cell with a slightly electron-dense body adhered to the inner side of the cell wall. C: Radicle cell containing vesicles (Ve) of different sizes, apparently in transit through the cytoplasm. D: Hypocotyl section displaying multiple structurally damaged cells, with vacuole and cytoplasm rupture highlighted (red square). E: Hypocotyl cell showing dense cytoplasm and the presence of a myelin-like figure. F: Hypocotyl cell exhibiting small electron-dense inclusions near the cell wall. G: Leaf tissue severely damaged, with organelles no longer distinguishable and a nucleus (Nu) showing signs of degeneration. H: Leaf cell with nucleus and cytoplasm containing small electron-dense inclusions. I: Leaf cell presenting a large, amorphous electron-dense body without identifiable organelles. J: SIMS image of the radicle showing high sodium (Na^+) concentration in the cell wall region (red area). K: SIMS image of the radicle revealing a potassium (K^+) gradient (green to red) concentrated in the cell wall region. L, M: SIMS images of the radicle detecting a small titanium (Ti) peak inside the cell. Abbreviations: CW – cell wall; PM – plasma membrane; Ve – vesicle; Nu – nucleus.

Ultrastructural evidence of metal/metalloid nanoparticle internalization in brain and muscle of *Oreochromis niloticus*

Mariana Vitorino de Carvalho[1], Iara da Costa Souza[1], Julieta Griboff[2], William Manuel Pereira Antunes Fortes[1], Luana Beserra de Carvalho[1], Magdalena Victoria Monferrán[2], Daniel Alberto Wunderlin[3], Marisa Narciso Fernandes[1,*]

[1] Departamento de Ciências Fisiológicas, Universidade Federal de São Carlos (DCF/UFSCar), Ave. Washington Luiz, Km 235, 13565-905, São Carlos, São Paulo, Brazil, [2] Centro de Investigaciones en Bioquímica Clínica e Inmunología (CIBICI), Consejo Nacional de Investigaciones Científicas y técnicas (CONICET), Facultad de Ciencias Químicas, Universidad Nacional de Córdoba, Córdoba, Argentina, [3] ICYTAC, Instituto de Ciencia y Tecnología de Alimentos Córdoba, CONICET, Dpto. Qca. Organica, Facultad Ciencias Químicas, Universidad Nacional de Córdoba, Ciudad Universitaria, 5000, Córdoba, Argentina.
*dmnf@ufscar.br

Particulate matter (PM) emitted by metallurgical industries can be transported by wind and deposited in aquatic ecosystems such as lagoons and mangroves [1]. In these environments, settleable PM (SePM > 10 μm) releases metal/metalloid elements and nanoparticles (NPs), which may become bioavailable in the water column or accumulate in sediments, posing risks to aquatic organisms like fish [2]. Free metal ions can interact with biomolecules and cause neurotoxic effects, such as altering acetylcholinesterase (AChE) activity [3]. Metals like Cd, Ni, Cr, and Pb may increase or inhibit AChE depending on their concentration, leading to physiological dysfunctions [4]. This study used *Oreochromis niloticus* as a bioindicator species to investigate the internalization of metal/metalloid NPs and neurotoxic effects after 96-hour exposure to different concentrations of SePM (0.0, 0.01, 0.1, and 1.0 g L^{-1}), as well as in fish collected in 2021 and 2022 from two lagoons near metallurgical industries (Carapebus and Maembá) and a reference aquaculture site (Alegre), in Espírito Santo, Brazil [5]. A total of 27 metals/metalloids were quantified in brain and muscle using Inductively Coupled Plasma Mass Spectrometry (ICP-MS), and ultrastructural analyses were performed with Transmission Electron Microscopy (TEM) to detect NPs. The most abundant elements in the brain were Fe > Zn > Rb > Sn > Al, and in the muscle Fe > Al > Zn > Ni > Cu. AChE activity was reduced in fish exposed to 0.01 and 0.1 g L^{-1} SePM and was also lower in the muscle of fish from Carapebus Lagoon (2021), indicating neurotoxic effects. TEM analysis revealed the presence of Fe, Al, Si, S, Sn, Cl, K, Ca, Na, P, and Ti NPs in muscle tissue, and Fe, Ti, Cu, Si, and Cl NPs in brain tissue. These results suggest that the accumulation of metals in soft tissues occurred due to the saturation of excretory pathways [6]. The detection of emerging metals such as Sn and Ti in fish tissues highlights their bioaccumulation potential and associated health risks, including impaired cholinergic function. The findings emphasize the need for regulatory measures to control atmospheric emissions from metallurgical activities and protect aquatic ecosystems [7].

[1] L.B. Carvalho et al., *Metal/metalloids concentrations and multi-biomarkers in blood of Nile tilapia living in coastal lagoons near metallurgical industrial areas: an integrated evaluation.* Environ. Toxicol. Chem. (2025).
[2] I.C. Souza et al., *Atmospheric particulate matter from an industrial area as a source of metal nanoparticle contamination in aquatic ecosystems*. Sci. Total Environ. 753, 141976–141976 (2021).
[3] D. Lima et al., *In vitro and in vivo inhibition of acetylcholinesterase and carboxylesterase by metals in zebrafish (Danio rerio)*. Mar. Environ. Res. 91, 45–51 (2012).
[4] G. Atli et al., *The evaluations of oxidative stress and neurotoxicity in threatened*

endemic fish Barbus meridionalis from Osor River (Spain). Aquat. Toxicol. 276, 107099–107099 (2024).
[5] C.S. Cleoni et al., *Biomarker responses as indication of contaminant effects in Oreochromis niloticus.* Chemosphere 89(1), 60–69 (2012).
[6] S. García-Medina et al., *Bioaccumulation and oxidative stress caused by aluminium nanoparticles and the integrated biomarker responses in the common carp (Cyprinus carpio).* Chemosphere. 288, 132462 (2021).
[7] This study was supported by Fundação de Amparo à Pesquisa do Estado de São Paulo (FAPESP, Grant, 2019/08491-0, 2023/01356-5), Conselho Nacional de Desenvolvimento Científico e Tecnológico (CNPq, Grant 306818/2020-5, CNPq/INCT-Peixes, Proc. 405706/2022-7), National Agency for Scientific and Technological Promotion (ANPCYT, FONCyT/PICT-2019 N 1743, PICT Aplicado 2021 N 002) and National Council of Scientific and Technical Research (CONICET PIP 2022- 11220210100480CO).

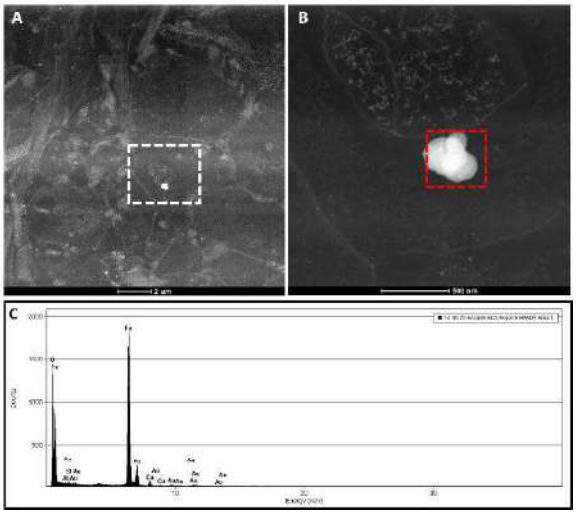

Figure 1: Representative transmission electron micrographs (TEM) of *Oreochromis niloticus* brain after 96 h exposure to 1.0 g SePM L^{-1}. (a) TEM showing Fe nanoparticles (NP) in brain cells; (b) High magnification of white square in A showing Fe NP size; (c) Energy dispersive X-ray spectroscopy (EDS) spectrum of NP composition in A (white square) and B (red square) showing Fe, Si and Cu. Au is the gold grid.

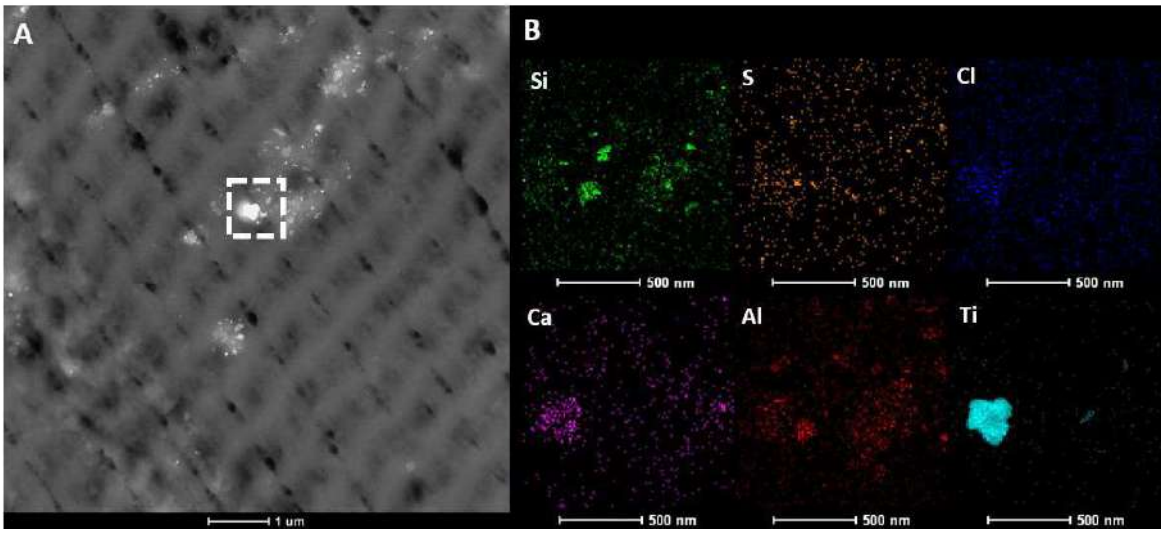

Figure 2: Transmission electron microscopy (TEM) of *Oreochomis niloticus* muscles after 96h of exposure to 1.0 g SePM L^{-1}. (a) Micrograph showing NPs in muscle fiber. (b) Map showing the distribution of elements in the NP: Si, S, Cl, Ca, Al and Ti.

Ultrastructural Features of Ilhéus Virus Replication and Cytopathology Using In Vitro System

Maycon Douglas do Nascimento Garcia[1,*], Igor Pinto Silva Da Costa[1], Marcos Alexandre Nunes da Silva[1], Vivian Neuza dos Santos Ferreira[1,2], Ana Luisa Teixeira de Almeida[1], Andressa Santos de Almeida[1], Ana Maria Bispo de Filippis[3], Natalia Fintelman-Rodrigues[4,5], Aline de Paula Dias da Silva[4,5], Marcelo Alves Ferreira[5], Thiago Moreno L. Souza[4,5], Alex Pauvolid-Corrêa[6], Debora Ferreira Barreto-Vieira[1]

[1] Laboratório de Morfologia e Morfogênese Viral, Instituto Oswaldo Cruz (IOC), Fundação Oswaldo Cruz (Fiocruz), RJ, Brazil, [2] Laboratório de Biologia Estrutural de Vírus, Instituto de Bioquímica Médica, Universidade Federal do Rio de Janeiro, RJ, Brazil, [3] Laboratório de Arbovírus e Vírus Hemorrágicos, IOC, Fiocruz, RJ, Brazil, [4] Laboratório de Imunofarmacologia, IOC, Fiocruz, RJ, Brazil, [5] Centro de Desenvolvimento Tecnológico em Saúde, National Institute for Science and Technology on Innovation on Diseases of Neglected Populations, Fiocruz, RJ, Brazil, [6] Laboratório de Virologia Veterinária de Viçosa, Departamento de Veterinária, Universidade Federal de Viçosa, MG, Brazil.
* maycongarcia@aluno.fiocruz.br

lhéus virus (ILHV), classified within the *Orthoflavivirus* genus of the *Flaviviridae* family, is a neglected arbovirus with significant epidemiological relevance in Latin America, particularly in Brazil, which reports the highest incidence [1,2]. Despite the known pathogenic potential of orthoflaviviruses, detailed insights into ILHV's replication mechanisms and associated cellular alterations remain limited. This study aims to elucidate the primary ultrastructural modifications induced in Vero cells upon ILHV infection, and to characterize the virus's replication cycle, particle morphology, and genomic organization. The ILHV strain was originally isolated from mosquitos Culex sp. in the state of São Paulo, Brazil, in 1994. For clarification, Vero CCL81 cell monolayer was infected with a multiplicity of infection (MOI) of 0.01, and the supernatant was collected 72 h post-infection (h p.i.). The titration of the supernatants was performed using the Plaque-Forming Unit (PFU)/mL technique. Aiming at morphological analysis, infection kinetics (MOI of 0.01) was performed on the Vero CCL81 cell line (1, 2, 3, 24, 48, 72, and 96 h p.i.). Bright-field microscopy analyses were performed at time intervals between 24 and 96 h p.i and compared with the control condition (uninfected monolayer and with the same culture time). For ultrastructural analyses for TEM, monolayers of all points were collected and processed [3]. Supernatants were collected from all points and titrated using the PFU/mL technique. All experimental procedures were performed in a BSL-3 laboratory. Results demonstrated that ILHV prompts the formation of characteristic replication structures, including double-membrane vesicles, convoluted membranes, and vesicular packets, similar to those observed in other orthoflaviviruses such as Zika and Dengue (Figure 1). These formations are indicative of viral replication complexes that facilitate efficient viral proliferation within host cells. Preliminary findings suggest that ILHV induces cytopathogenic effects akin to those documented for other arboviruses, highlighting conserved pathogenic features within the *Orthoflavivirus* genus. These insights contribute to a deeper understanding of ILHV's cytopathological effects on host cells [4].

[1] B.H.G.A Milhim et al. Arboviral Infections in Neurological Disorders in Hospitalized Patients in São José Do Rio Preto, São Paulo, Brazil. Viruses. (2022), 14, 1488.
[2] T.S. Postler et al. Renaming of the Genus Flavivirus to Orthoflavivirus and Extension of Binomial Species Names within the Family Flaviviridae. Arch. Virol. (2023), 168, 224.
[3] O.M. Barth, M.A.N.d Silva, D.F. Barreto-Vieira, Low Impact to Fixed Cell Processing Aiming Transmission Electron Microscopy. Mem. Inst. Oswaldo Cruz (2016), 111, 411-3.

[4] This research was supported by CNPq and FAPERJ (Brazil).

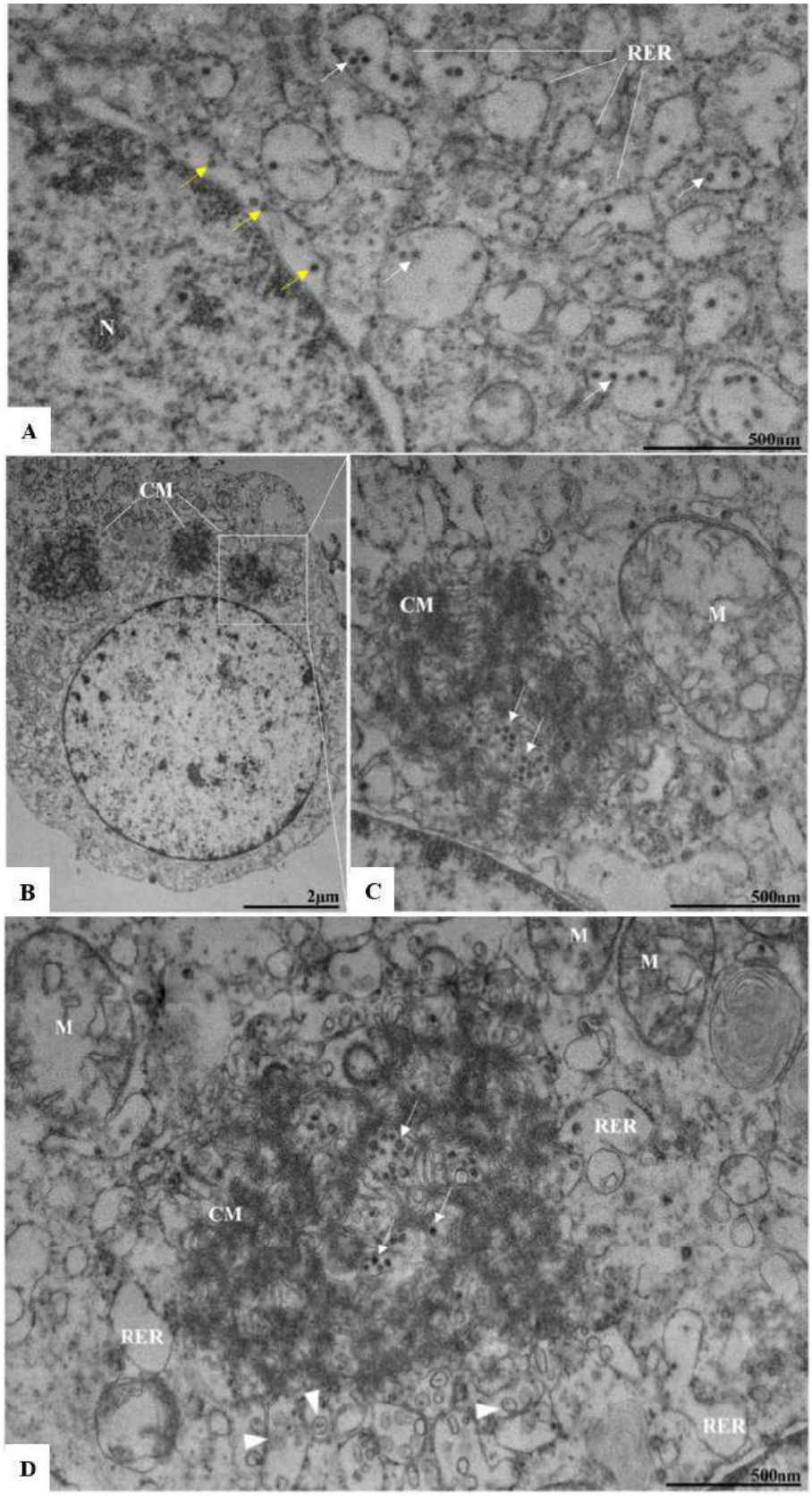

Figure 1. (A) Proliferation of the rough endoplasmic reticulum (RER) in ILHV-infected Vero cells (48 h post-infection). Note: several virus particles inside RER cisternae (white arrow) and in perinuclear space (yellow arrow). (B-C) Convoluted membranes (CM) in Vero cells 72 h post-infection with ILHV with incomplete virus particles (arrow), mitochondria (M). (D) Presence of vesicle packages (arrowhead) near convoluted membrane, mitochondria (M), rough endoplasmic reticulum (RER).

X-ray Microtomography to understand target organs morphology of *Aedes aegypti*

João Marcos de Lima Faria[1], Juliana Martins da Silva[1], Thalita Souza Arantes[2], Isaque João da Silva de Faria[3], Rubia Figueredo Gouveia[1], Maisa Carla Pereira Parra[4], Cecília Artico Banho[4], Karine Lima Lourenço[4], Maurício Lacerda Nogueira[4]; João Trindade Marques[3], Gregory Kitten[2], Rodrigo Villares Portugal[1]

[1]Brazilian Nanotechnology National Laboratory (LNNano), Brazilian National Center for Research in Energy and Materials (CNPEM), Campinas-SP, Brazil, [2]Microscopy Center, Federal University of Minas Gerais (UFMG), Belo Horizonte-MG, Brazil, [3]Institute of Biological Sciences, Federal University of Minas Gerais (UFMG), Belo Horizonte-MG, Brazil, [4]Medical School of São José do Rio Preto (FAMERP), São José do Rio Preto-SP, Brazil.

The *Aedes aegypti* mosquito is a well-known vector responsible for transmitting the viruses of Dengue, Zika, Chikungunya, and Yellow Fever. The replication and transmission cycle of these viruses primarily occur within the mosquito's midgut and salivary glands [1]. Consequently, investigating the morphology and anatomical context of these structures is critical for understanding their role in the vector's biology. This study is integrated into the commissioning techniques for Orion project and employs X-ray microtomography to initiate CLEXM research capable of characterizing the spatial relationship of the midgut and salivary gland. The resulting information can contribute to developing public health strategies to mitigate virus transmission by *A. aegypti*. In this context, head, thorax, and midgut samples of female *A. aegypti* were collected at UFMG and FAMERP, fixed in a solution of 2.5% glutaraldehyde, 4% paraformaldehyde in sodium cacodylate buffer overnight, post-fixed in 1% OsO4 for two hours, in some cases contrasted in block with 2% uranyl acetate solution in acetone, dehydrated in acetone gradients, and infiltrated in epon resin. For X-ray tomography, a Skyscanner 1272 (Bruker, Belgium) tomograph from LNNano was used, with a voltage of 25 kV, a current of 180 µA, and a CMOS camera with 2048x2048 pixels, achieving a pixel size of 0.8 µm. In the head samples, initial efforts to reconstruct the specimen without contrast were unsuccessful; therefore, reconstruction was performed on a sample post-fixed with OsO4. This approach allowed for visualization of the head's anatomy, highlighting the proboscis with an evident division of the tubes derived from the salivary gland and the midgut. Additionally, other anatomical structures of the animal such as eyes, antennae, and pedipalps were also observed. In the thorax and head samples, a block contrasting with uranyl acetate was performed. This allowed the visualization of the tube derived from the midgut, but the salivary gland and its respective anatomical and morphological relationship with the midgut were still not identifiable. Additional results were obtained with isolated midgut samples that were post-fixed with OsO4, enabling the observation of the organ's morphology. However, since the animals remained fasting, the walls of the organ were flattened, making the assessment of volume difficult. Next steps involve improving contrasting methodologies to better highlight the salivary gland and accurately determine the morphology of the isolated gland. New attempts will consider aspects such as incubation time and concentration of reagents during post-fixation and block contrasting. In summary, this study demonstrates that X-ray microtomography can effectively locate and characterize the morphology of biological structures and can be used as a correlative methodology alongside electron microscopy.

[1] S. C. Weaver, W. K. Reisen, Antiviral Research, 85 (2010) 328-345.
[2] This research is founded by Brazilian National Center for Research in Energy and Materials (CNPEM) (Brazil)

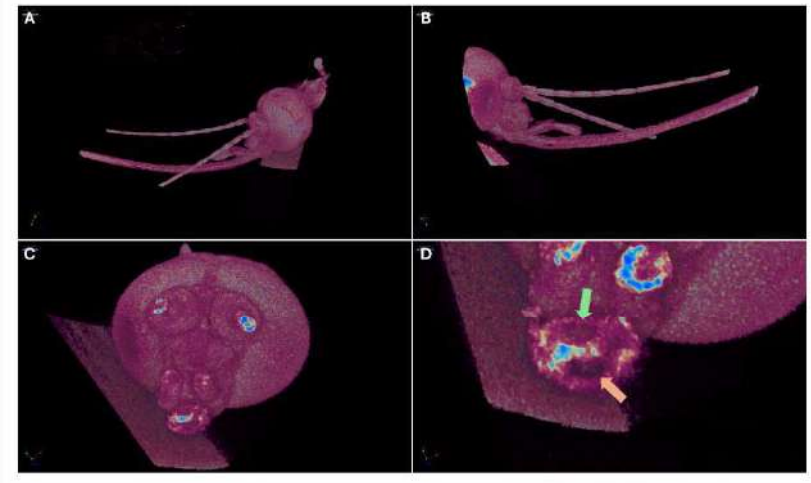

Figure 1: X-ray microtomography of the head of a female Aedes aegypti mosquito. Figures A and B: lateral views; Figure C: frontal view; Figure D: internal view of the proboscis, green arrow: channel derived from the midgut, orange arrow: channel derived from the salivary gland.

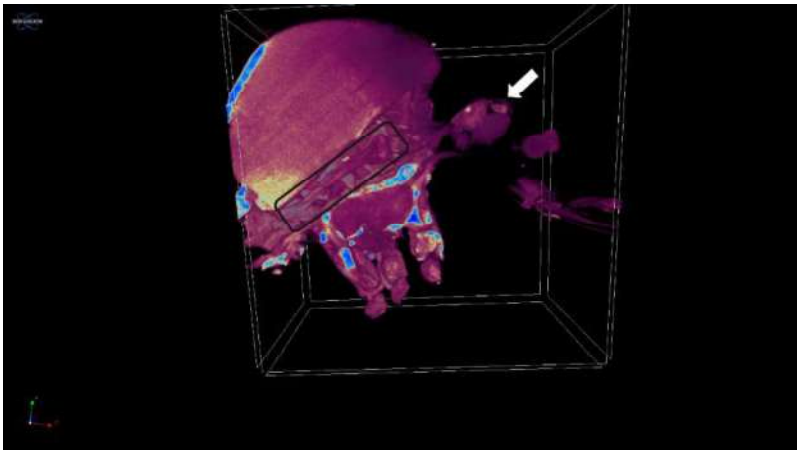

Figure 2:X-ray microtomography of the head and thorax of a female Aedes aegypti mosquito. The highlighted region indicates the tube derived from the midgut. The white arrow indicates the position of the head.

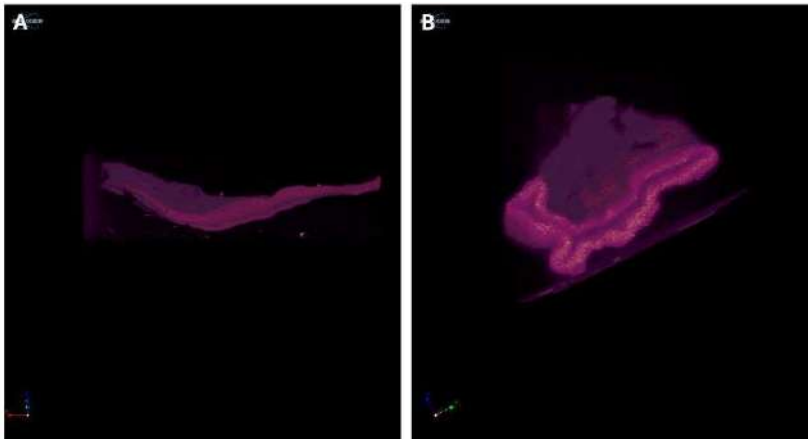

Figure 3: X-ray microtomography of the midgut. A) lateral view; B) cross-sectional view of the organ.

Zika Virus Infection Induces Neurodegeneration and Inflammatory Process During Retinal and Optic Nerve Lesions

Laís Alves de Araújo[1*], Jonas Rodrigues dos Santos[1], Carlos Eduardo Pires Ferreira Rodrigues[1], Celso Martins QueirozJúnior[2], Vivian Vasconcelos Costa[2], Felipe Ferraz Dias[1]

[1]Laboratory of Inflammation Research, Department of Biological Sciences, State University of Minas Gerais, Ibirité, MG, Brazil.
[2]Center of Research and Drug Development, Department of Morphology, Institute of Biological Sciences, Federal University of Minas Gerais, Belo Horizonte, MG, Brazil.
*lais.1397227@discente.uemg.br

Zika is a well known human infectious disease transmited by *Aedes* genus flies, characterized by the Zika congenitus syndrome (ZCS) symptons spectrum, such as microcephaly [1]. During the Brazilian epidemic breakthrough of 2015, many cases of microcephaly and other newborn permanent brain damages were comproved by virus transmission through matern placents [2]. While ZCS have been accompanied by other pathologic symptons, recent studies have found young children with disphagia and, motor, auditive and visual outcomes without microcephaly [3]. Visual deficiencies were corroborated by high intraocular pression and the presence of the virus in the optic nerve (ON) during experimental models' infection [4]. Lesion of the retinal ganglionar axons bundle is responsible to disturb the conection of visual capture to the brain image former centers, leading to considerable and progressive levels of visual blindness [5]. Pathological lesions in both retina and ON may be triggered by neurotoxic factors, leading to tissue neurodegeneration by different cell death processes, which may play key events of the ZIKV immunepathogenesis. Although knowledge of eye alterations by Zika infection, little is known about their pathogenesis, mainly concerning the optic nerve neurodegeneration intracellular ways. Here, we used light to transmission electron microscopy approachs to evaluate the ocular and optic nerve lesion extension induced by Zika virus (ZIKV) infection. Pregnant C57BL/6 mice were inoculated with $1x10^6$/mL ZIKV clinical isolate (HS-2015-BA-01) PFU [N = 6-8; 5.5 *days post-coitum* (dpc)], with or without pan-flavivirus antibodies (hibridoma D1.4G2.4.15) and the whole eyes and optic nerves of the offspring (12 weeks) were processed for histology, immunohistochemistry (IHC) and transmission electron microscopy (TEM). Histopathology of infected eyes showed an increase of apoptotic and necrotic cells as many empty ganglionar cells areas in the retinal layer compared with non-infected littermates (Fig. 1A, B). IHC for Iba-1 and S-100β identifyed tissue areas indicative of microgliosis and astrocytosis (Fig. 2). TEM of the optic nerve showed irregular axons, with myelin sheath detachment (Fig. 3A), nerve fibers demyelinization (Fig. 3B) as autophagosomes formation (Fig. 4). Ultrastructural analyses of ON from infected and 4G2 animals evidenced areas with reduced number of axons (Fig. 5, 6A) and increasing in size compared with control ones (Fig. 5, 6B). Our recent studies ilustrate, for the first time, the main cell death processes and ultraestructural events involved with optical pathogenesis of ZIKV infection. What these cellular changes represent for understanding the disease requires further investigation.

References:

[1] Alvarado et al., *Arch Pathol Lab Med* 141 (2017) 26.
[2] Brasil et al., *N Engl J Med* 375 (2016) 2321.
[3] Faiçal et al., *BMJ Paediatr Open* 3(1) (2019) e000486.
[4] Costa e Del Sarto et al., *mBio* 8 (2017) e00350.
[5] J. Selhorst, Y. Chen, *Seminar Neurol* 29 (01) (2009) 029.
[6] This research was supported by FAPEMIG, CNPq (Brazil) and PAPq - UEMG.

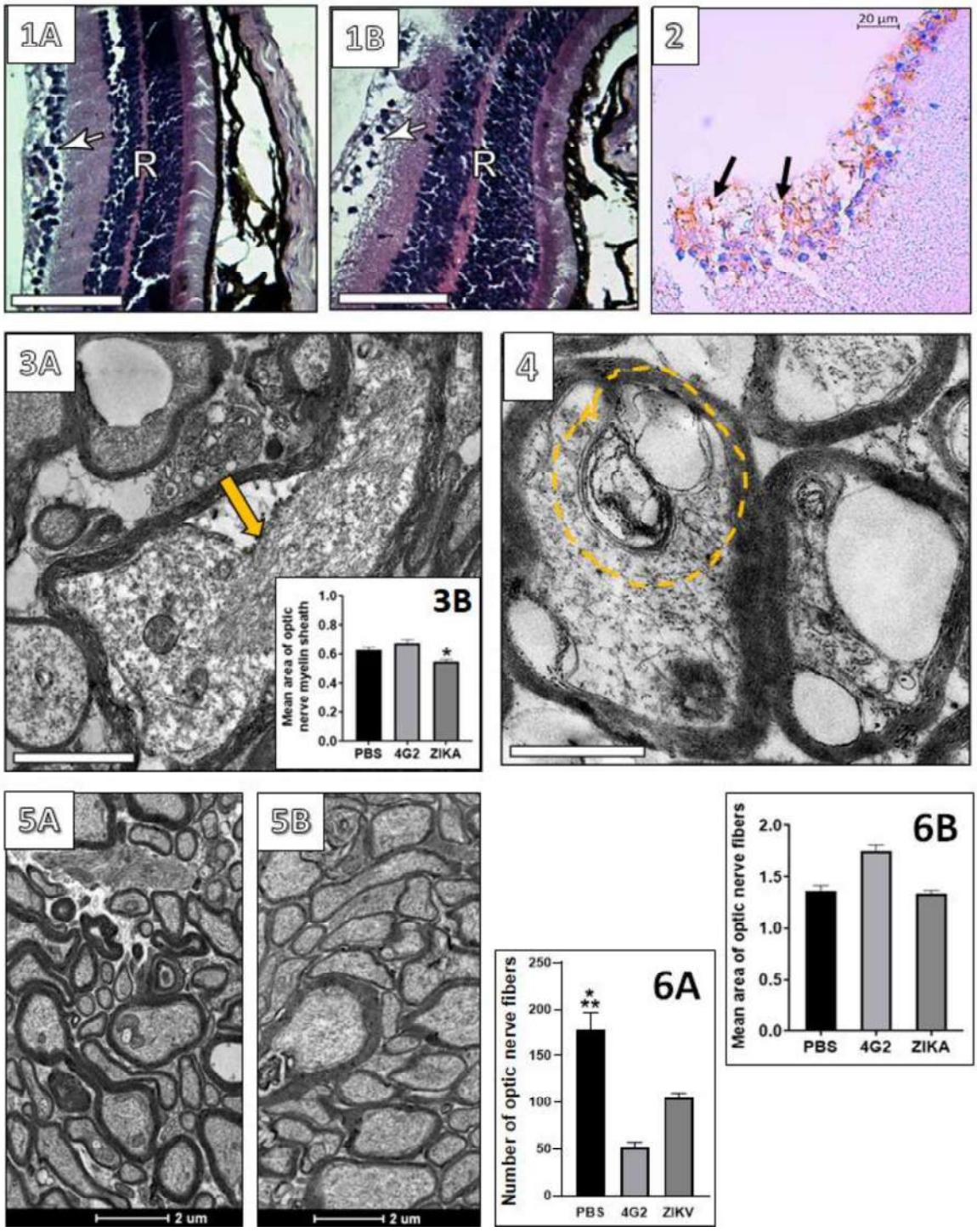

Histopathological and ultrastructural analyses of ZIKV-infected retina and optic nerve. **Figure 1**: Retinal (R) ganglionar cells layer from non-infected (A) and ZIKV-infected mice (B) showing many empty areas (white arrows), indicative of tissue lesion. **Figure 2**: Iba-1 IHC for microglia (black arrows) indicates tissue areas of microgliosis. **Figure 3**: (A) Ultrastructure of irrregular aspect of infected axons with myelin sheath detachment (yellow arrow) and mean area (µm²) of nerve fibers myelin sheath (B), indicative of nerve fibers demyelinization. **Figure 4**: Ultrastructure of autophagosomes formation (yellow dashed area) within infected axons, indicative of cell death process. **Figure 5**: Ultrastructure of ON section showing myelinated axons from control (A) and ZIKV-infected mice (B). **Figure 6:** Morphometric analyses of ON sections showing mean number (A) and mean area of nerve fibers (B). Bars (1A, B): 500 um; (2): 20 µm; (3A, 4): 5000 nm; (5A, 5B): 2 µm.

Cryo-EM and Cryo-ET applied to biological samples

30º Congresso da Sociedade Brasileira de Microscopia e Microanálise

Structural Diversity and Dynamic States of Acidocalcisomes in *Trypanosoma cruzi* Revealed by In Situ Cryo-EM

Ingrid Augusto[1*], Moara Lemos[1], José de Anchieta de Oliveira Filho[2], Pedro G. Pascutti[2], Wanderley de Sousa[1] and Kildare Miranda[1*]

[1] Laboratório de Ultraestrutura Celular Hertha Meyer, Instituto de Biofísica Carlos Chagas Filho & Centro Nacional de Biologia Estrutural e Bioimagem, Universidade Federal do Rio de Janeiro, Rio de Janeiro, Brazil.
[4] Laboratório de Modelagem e Dinâmica Molecular, Instituto de Biofísica Carlos Chagas Filho, Universidade Federal do Rio de Janeiro, Rio de Janeiro, Brazil

*kmiranda@biof.ufrj.br

Trypanosoma cruzi, the etiological agent of Chagas disease, relies on sophisticated mechanisms for survival across diverse environmental conditions, with acidocalcisomes (Accs) being central to its cellular physiology. Acidocalcisomes are multifunctional organelles that play crucial roles in osmoregulation, pH control, cellular homeostasis, calcium signaling, and cell bioenergetics [1]. Known as organelles rich in polyphosphates (polyP), calcium, and other cations organized in nanodomains, Accs also serve as the primary reservoir for intracellular Ca2+, with their calcium uptake and release directly influencing mitochondrial activity, cellular bioenergetics, and parasite infectivity [1, 2]. While the fundamental composition and some functions of Accs are recognized, specific mechanisms of ion dynamics within their matrix, biogenesis, and interactions with other organelles are still not fully understood. Traditional chemical fixation methods often introduce artifacts due to their impact on membrane integrity and ion content, leading to an artificial representation of these organelles. To unveil the molecular and structural architecture of the acidocalcisomes of Trypanosoma cruzi closer to its native state, we analyzed epimastigote cells using high-performance cryo-microscopy (cryo-EM) and cryo electron tomography (cryo-ET). Cells were applied onto Quantifoil 1.2/1.3R grids and cryofixed by plunge freezing. Whole cells were directly observed in a 300 kV Titan Krios G4 or transferred to a Cryo-FIB SEM Aquilos 2 microscope to lamellae production. Cryo Ets were acquired with a maximum dose of 120 electron e-/Å2 s on the 300 kV Titan Krios G4 equipped with a Selectris energy filter and a Falcon4i Direct Electron Detector camera. The acidocalcisomes (Accs) exhibited distinct structural organization patterns: i) fully loaded with an electron-dense core, ii) displaying varying electron densities, potentially representing ionic phase transition, iii) partially filled, iv) multiple cores and v) merging cores (Figure 1). These patterns suggest different elemental clustering or native physiological states of ion mobilization, moving beyond the prevalent assumption that only fully electron-dense acidocalcisomes represent the native state. [3]. The electron-dense core also revealed a unique texture characterized by fiber-like structures measuring between 15Å and 75Å in diameter, consistent with polyphosphate aggregates interacting with ions, as suggested by molecular dynamic simulations (Figure 1A). Furthermore, Accs were observed connected to the mitochondria via electron-dense elements (Figure 2A, B) and close interacting with endoplasmic reticulum (Figure 2C). Mitochondria also displayed random dense granules in their matrix, similar to granules found in mammalian mitochondria, which have been shown to contain phosphorus and calcium [4]. In summary, cryofixation techniques, especially when combined with cryo-electron tomography and Cryo-FIB SEM, are allowing a review of acidocalcisomes by visualization at molecular level of its structural architecture in a state much closer to their native one, revealing their complex composition, different functional states, and dynamic interactions with other organelles and cell structures. Further advanced processing as subtomogram averaging is being applied to enable a deeper understanding of survival mechanisms and *T. cruzi* physiology [5].

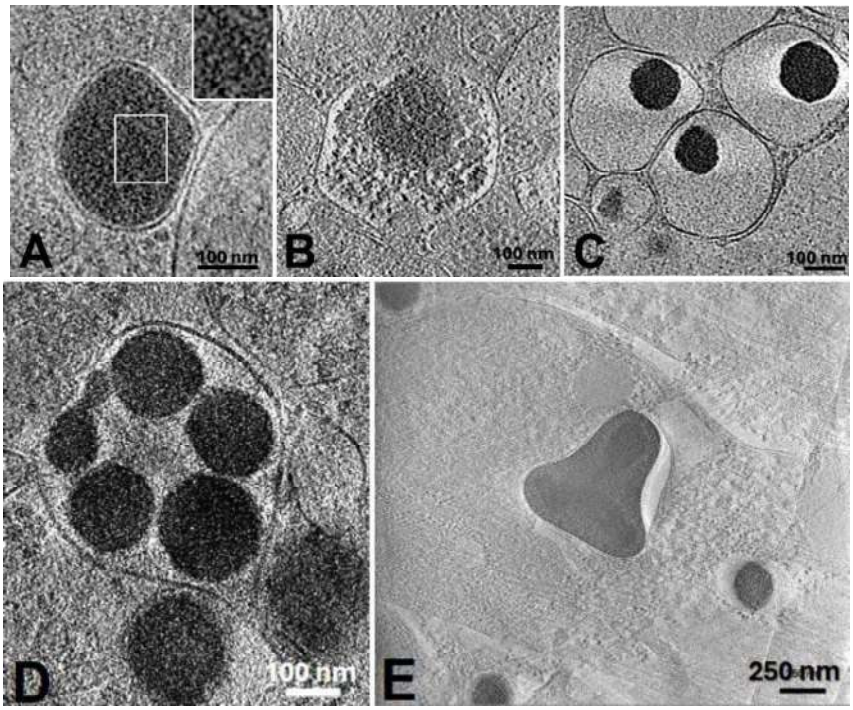

Fig. 1. Cryo-ET virtual sections show various acidocalcisome ultrastructures in *T. cruzi*. (A) Acidocalcisome with a fully loaded matrix, with fiber-like structures in the core (inset). (B) Acidocalcisome with varying electron density in the matrix. (C) Partially filled acidocalcisomes. (D) Multiple electrodense cores into one membrane. (E) Merged core.

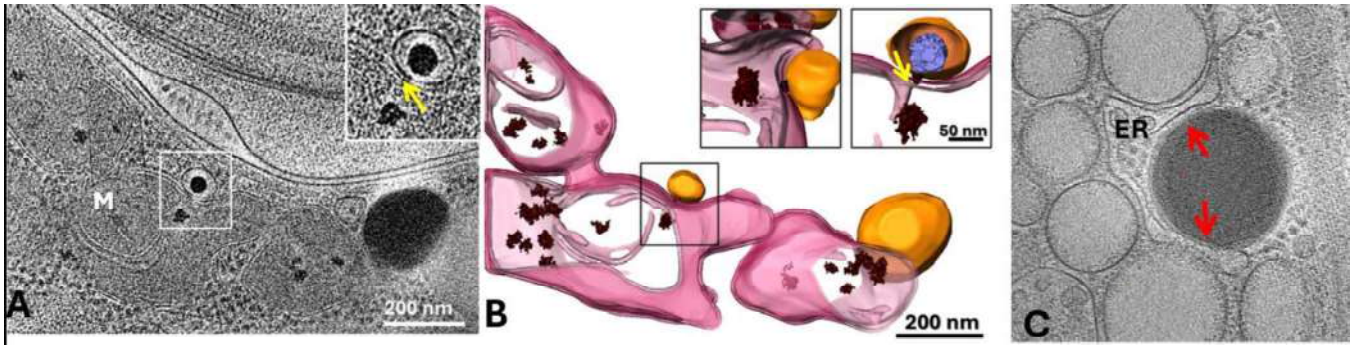

Fig. 2. Cryo-Ets revealing acidocalcisomes interactions in T. cruzi. (A) Acidocalcisome mitochondria contact. In the inset, the yellow arrow points to a structure traversing both membranes. (B) Three-dimensional model of the cell in (A). The electron-dense granules (dark red) are dispersed inside the mitochondrial matrix, mainly close to the membrane (pink) and cristae. (C) Acidocalcisome membrane in close contact with endplasmic reticulum (ER, red arrow).

References

[1] R. Microbiol Docampo https://doi.org/10.1128/mmbr.00042-23
[2] W. Girard-Dias et al. Mol Biol Rev. (2024) 88:e0004223. Proc Natl Acad Sci USA (2023) 120 https://doi.org/10.1073/pnas.2300942120.
[3] Augusto I. et al. mBio. (2025) 16:e01662-24. https://doi.org/10.1128/mbio.01662-24
[4] S.G. Wolf, et al. Elife (2017) 6. https://doi.org/10.7554/eLife.29929.
[5] This research was supported by CNPq, CAPES, FAPERJ, and FINEP

When viruses hunt bacteria: unveiling the *E. coli* phage O86α

Germán G. Sgro
Faculdade de Ciências Farmacêuticas de Ribeirão Preto
Universidade de São Paulo
ggsgro@usp.br

Bacteriophages (phages) are viruses that infect bacteria and are the smallest and most abundant biological entities on Earth. To replicate, they rely on the bacterial host machinery to either i) immediately produce new progeny after infection, leading to the death of the infected cell (lytic pathway), or ii) integrate into the bacterial chromosome as a prophage, establishing a symbiotic relationship between both parties (lysogenic pathway). The interaction begins with the recognition and adsorption of the phage to specific receptors on the bacterial surface, which determines its host range and infection specificity. Most known phages display narrow host ranges, typically infecting particular strains or isolates of a given bacterial species. For such recognition, virions possess specialized proteins that bind to bacterial receptors such as LPS, EPS, outer membrane proteins, fimbriae, pili, and flagella. In recent decades, the interest in using phages as therapeutic agents (phage therapy) for the biological control of infections caused by multidrug-resistant bacteria has increased considerably. In this context, understanding the molecular mechanisms underlying phage-bacteria interactions is crucial to elucidate how phages impact microbial populations and how they can be harnessed for clinical and biotechnological applications. The *Escherichia coli* phage O86α is a lytic member of the *Myoviridae* family that specifically targets *E. coli* O86 strains, a group associated with intestinal and extraintestinal infections in humans. Using cryo-electron microscopy, we determined high-resolution structures of O86α, revealing the intricate architecture of its icosahedral capsid and contractile tail, the molecular machinery responsible for DNA injection into the host. These structural insights, combined with genomic and functional data, contribute to a deeper understanding of the infection mechanisms employed by lytic phages, providing valuable information for the development of phage-based strategies to combat multidrug-resistant *E. coli* infections and to expand their use in biotechnology and therapeutic applications.

This work was supported by Fundação de Amparo à Pesquisa do Estado de São Paulo (FAPESP #2020/11189-0 and FAPESP #2022/03018-7).

ACE2 nanoparticles block infection by SARS-CoV-2 variants

Moara Lemos[1,2*], Cécile Sauvanet[3], Armel Bezault[4], Borja Rodríguez de Francisco[4], Michael CW Chan[5,6], Kenrie PY Hui[5,6], Ka-chun Ng[5], John M Nicholls[7], Niels Volkmann[4,8] and Dorit Hanein[4,8]

[1]Centro Nacional de Biologia Estrutural e Bioimagem, Universidade Federal do Rio de Janeiro, Brasil.First Institution.
[2]Laboratório de Ultraestrutura Celular Hertha Meyer, Centro de Pesquisa em Medicina de Precisão, Instituto de Biofísica Carlos Chagas Filho, Universidade Federal do Rio de Janeiro, Brasil.
[3]Université Paris-Saclay, CEA, CNRS, Institute for Integrative Biology of the Cell (I2BC), 91198, Gif-sur-Yvette, France.
[4] Structural Studies of Macromolecular Machines in Cellulo Unit, Department of Structural Biology and Chemistry, Institut Pasteur, Université Paris Cité, CNRS UMR3528, Paris, France.
[5]School of Public Health, Li Ka Shing Faculty of Medicine, The University of Hong Kong, Pokfulam, Hong Kong SAR, China.
[6]Centre for Immunology and Infection (C2i), Hong Kong Science Park, Hong Kong SAR, China.
[7]Department of Pathology, School of Clinical Medicine, Li Ka Shing Faculty of Medicine, The University of Hong Kong, Pokfulam, Hong Kong SAR, China

The severe acute respiratory syndrome coronavirus 2 (SARS-CoV-2) is the causative agent of the COVID-19 pandemic. SARS-CoV-2 enters human cells via interactions between its spike protein and the human angiotensin-converting enzyme 2 (hACE2) [2]. The virus can enter through membrane fusion, which requires the Transmembrane Serine Protease 2 (TMPRSS2) [3], or through the clathrin-mediated endocytic pathway [4]. In either case, the presence of hACE2 on the cell surface is obligatory for viral entry. Several vaccines and treatment approaches have been developed against SARS-CoV-2. Most of these options rely on the actions of antibodies that prevent cell entry. A major concern with this strategy has been the appearance of different naturally evolving variants of SARS-CoV-2 that cause not only enhanced transmissibility but also tend to decrease susceptibility to antibody neutralization or therapeutics. The delta and omicron variants are particularly problematic in this regard. There is a continuing need for effective therapeutics, especially as new variants are expected to escape natural and vaccine-induced antibodies at least to some extent. One viable strategy to combat viral escape is to make use of the obligatory entry receptor, in this case hACE2, to prevent viral entry. Here, we targeted SARS-CoV-2 cell entry by constructing carrier system based on murine leukemia virus (MLV), with native hACE2 on its surface. To monitor the effect of these hACE2 nanoparticles on SARS-CoV-2 entry was used luciferase activity assays, composed of control MLVs pseudotyped with wild-type SARS-CoV-2 spike, delta-variant spike, or omicron-variant spike. Following pseudovirus infection, we used cellular cryogenic electron tomography (cryo-ET) to verify the morphology of hACE2 nanoparticles (Figure 1A and B), pseudoviruses

expressing the spike protein (Figure 1 D and E) and to independently confirm infection of kidney cells lines expressing endogenously ACE2. The presence of SARS-CoV-2 spikes in both the pre- and post-fusion configurations protruding from the pseudovirus surface were shown by cryo-ET (Figure 1A and B). Our analysis of pseudoviruses inside kidney cells revealed that pseudovirus entry in these cells via the clathrin-mediated endocytic pathway (Figure 1). Our results indicate that the blockage of virus entry occurs not only via competition of membrane-embedded hACE2 receptors in the nanoparticles with hACE2 cell receptors but also via aggregation through the engagement of hACE2 receptors on the same nanoparticle with spike proteins of multiple SARS-CoV-2 viruses. Our studies suggest that hACE2 nanoparticles provide a potent and effective viral entry neutralization effect and thus present a promising opportunity to develop new COVID19 treatment options that are less prone to viral escape.

[1]. P. Zhou *et al.*, *Nature* **579**, 270 (2020).

[2]. J. Shang *et al.*, *Nature* **581**, 221 (2020).

[3]. J. Koch *et al.*, *EMBO J* **40**, e107821 (2021).

[4]. A. Bayati, R. Kumar, V. Francis, P. S. McPherson, *J Biol Chem* **296**, (2021).

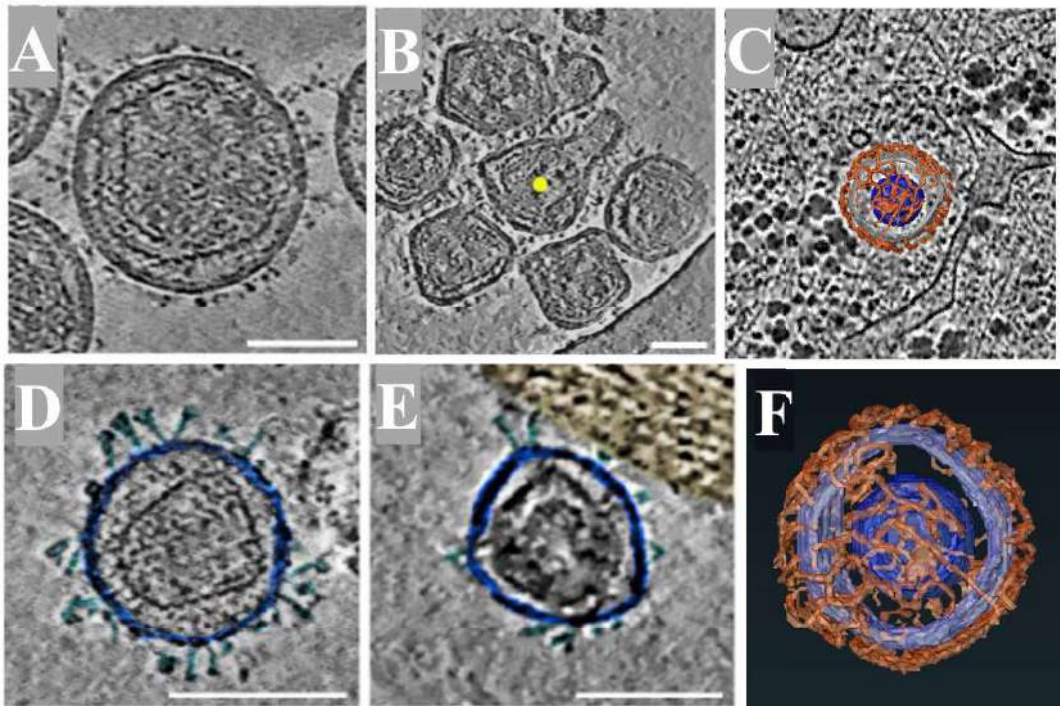

Figure 1 Cryo-ET of hACE2 nanoparticles and pseudovirus infecting VEROE2 cell lines. (A) hACE2 decorating nanoparticles. (B) Aggregation pseudovirus by hACE2 nanoparticles (yellow dot). (D) Pseudovirus expressing spike protein in pre and post-fusion conformation (E). (C) Pseudovirus infecting VERO E2 cells via (F) clathrin-mediated endocytosis.

Comparative Characterization of the Three-Dimensional Morphology of *P. serpens* Using Cryo-Electron Tomography

Julia Miralha R. M. Leite[1], Beatriz Santana Borges[1*], Luelc S. da Costa[1], Rodrigo Villares Portugal[1].

[1]Laboratório Nacional de Nanotecnologia,
*Corresponding Author: beatriz.borges@lnnano.cnpem.br

Trypanosomatidae family includes parasitc species of medical and veterinary importance, such as *Leishmania sp.*, *Trypanosoma brucei*, and *Trypanosoma cruzi (T. cruzi)*, as well as non-pathogenic species like *Phytomonas serpens (P. serpens)* [1]. Among the Trypanosomatidae, one of the main protozoa of medical relevance is *T. cruzi,* the etiological agent of Chagas disease, which affects more than 7 million people worldwide, mainly in Latin America. In contrast, *P. serpens* is non-pathogenic and infects tomatoes, which makes it a suitable model for study due to its similarities with *T. cruzi* [2]. Little is known about *P. serpens*, other than the fact that its life cycle consists of a single form (promastigote) that involves a plant and an insect [3]. Due to its genetic similarity to *T. cruzi* and lack of pathogenicity in humans, suggesting this model promising for vaccine development [4]. Indeed, previous studies have shown that it's extracellular vesicles reduce parasitemia and generate antibodies that recognize *T. cruzi* [2, 5]. The aim of this work is to reconstruct and compare the 3D morphology of the main ultrastructures (flagellum, nucleus, and kinetoplast) of *P. serpens* and *T. cruzi*, using cryo-electron microscopy as the main technique. Initially, an *in silico* analysis of proteins related to *T. cruzi* metacyclogenesis was performed, since *P. serpens* has only one evolutionary form. These proteins are known to be involved in autophagy, nuclear modulation, post-transcriptional regulation, host cell invasion, and immune evasion, and were found to be absent in *P. serpens*. Subsequently, to initiate the characterization of the protozoan, a growth curve and cell cycle analysis were performed compared with *T. cruzi*. Both the proliferation and cell cycle pattern of *P. serpens* were consistent with other trypanosomatids of the same family, as reported in the literature. For cryo-tomography, a protocol was optimized for preparing grids with *P. serpens* using a manual plunger for sample vitrification. The cryo-electron tomography (cryoET) datasets are currently under analysis (Figure 1) and will be segmented and reconstructed using Amira 5® software. However, electrondense organelles were already found in cryoET images, consistent with acidocalciosomes, which are also described in medically important species not only from the Trypanosomatidae family but also from Apicomplexa phylum [6]. EDS and STEM analysis revealed that these organelles' composition corroborates with other described protozoa showing Ca, Mg, P and Zn as the main concentrated ions (Figure 2) [7]. Thus, this study contributes to the comparative morphological characterization of *P. serpens* and *T. cruzi*, not only elucidating the features of this poorly explored protozoan but also highlighting its potential as a non-pathogenic model for investigating ultrastructures relevant to medically important parasites.

REFERENCES

[1] A. Kaufer et al., A review of the systematics, species identification and diagnostics of the Trypanosomatidae using the maxicircle kinetoplast DNA: from past to present, Int. J. Parasitol. 50(6-7) (2020) 449.
[2] J.W. Breganó et al., Phytomonas serpens, a tomato parasite, shares antigens with Trypanosoma cruzi that are recognized by human sera and induce protective immunity in mice, FEMS Immunol. Med. Microbiol. 39(3) (2003) 257.
[3] J.V. Jankevicius et al., Life Cycle and Culturing of Phytomonas serpens (Gibbs), a Trypanosomatid Parasite of Tomatoes, J. Protozool. 36 (1989) 265.
[4] A.L. Santos et al., Phytomonas serpens: immunological similarities with the human trypanosomatid pathogens, Microbes Infect. 9(8) (2007) 915.
[5] J.B. Aggio et al., Trypanosomatid Extracellular Vesicles as Potential Immunogens for Chagas Disease, Int. J. Mol. Sci. 26(4) (2025) 1544.
[6] L.C. Soares Medeiros et al., A proton pumping pyrophosphatase in acidocalcisomes of Herpetomonas sp., Mol. Biochem. Parasitol. 140(2) (2005) 175.
[7] W. Girard-Dias et al., A spatially resolved elemental nanodomain organization within acidocalcisomes in Trypanosoma cruzi, Proc. Natl. Acad. Sci. U. S. A. 120(16) (2023) e2300942120.

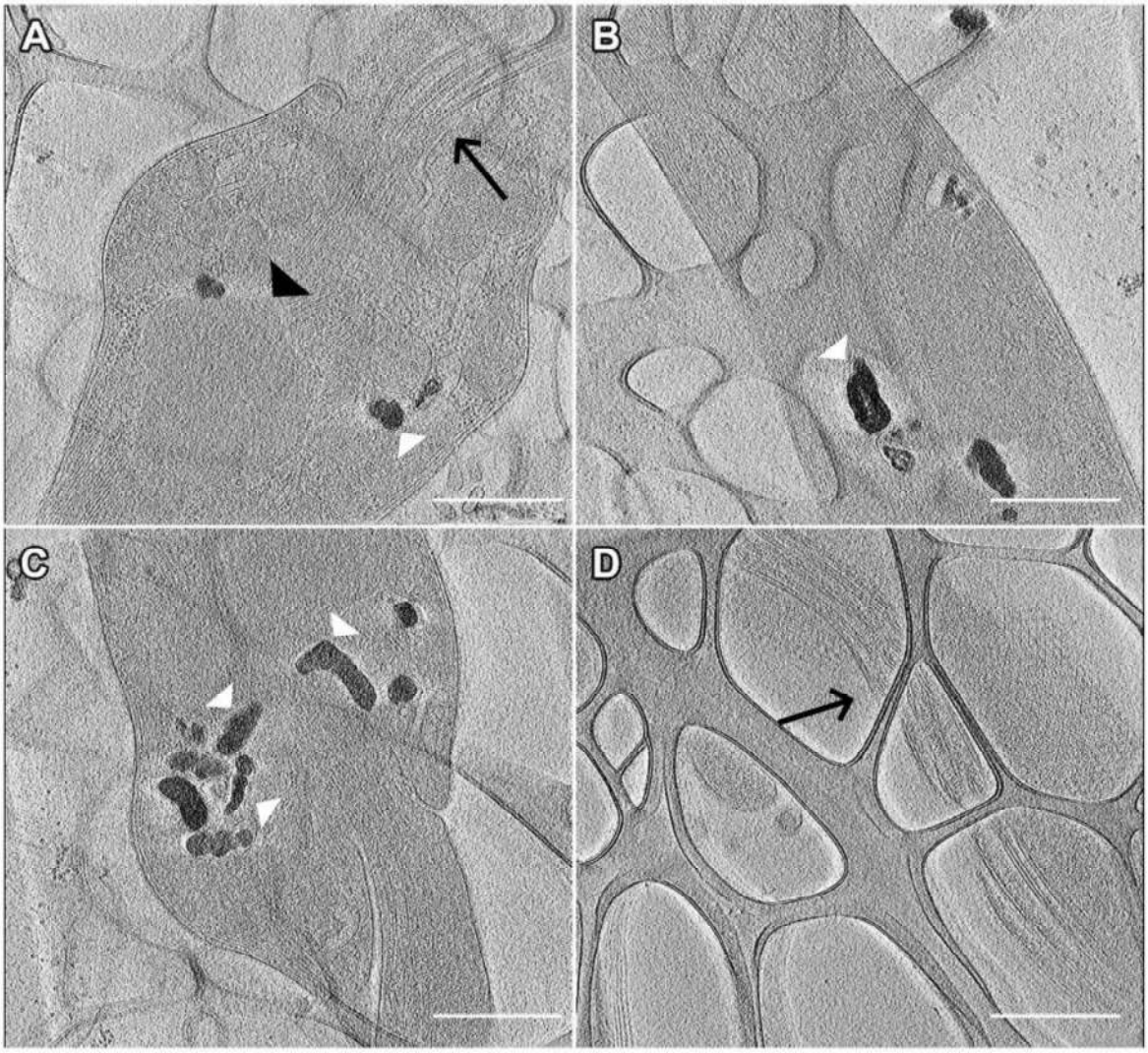

Figure 1. Cryo-electron tomography of *P. serpens*. (A-D) Tomographic slices of a cell indicating the nucleus (black arrowhead), the acidocalcisomes (white arrowhead), and the flagellum (black arrow). Scale bar: 1 µm.

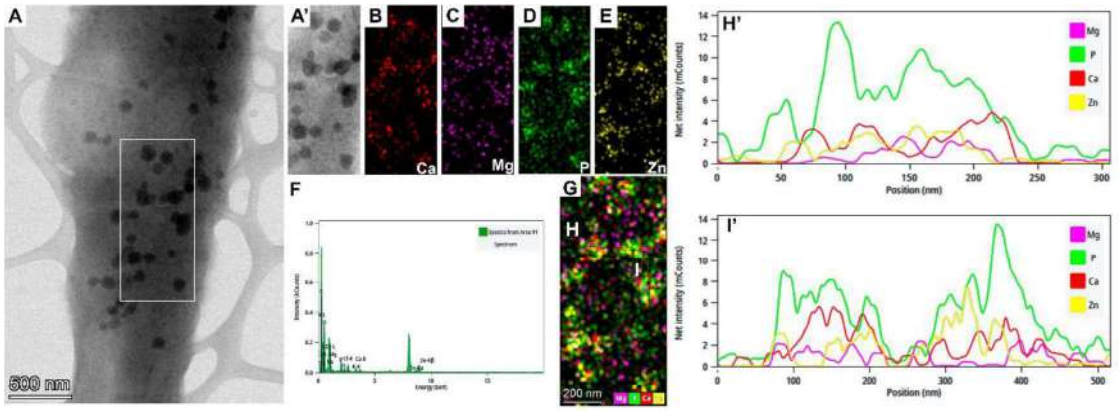

Figure 2. *In situ* elemental characterization of acidocalcisomes by STEM-EDS. (A) HAADF-STEM image of low magnification. (A') HAADF-STEM image of area selected for EDS analysis. (B-E) EDS elemental maps showing the accumulation of elements in acidocalcisome. (F) EDS spectrum of the organelle's composition. (G) Merge image of elements - P, Ca, Mg, and Zn (H-H' and I-I') Line scan profile highlighting the spatial correlation of the elements.

Using cryoEM to study ribosome biogenesis in yeast

Gabriel G. Araujo[1]*, Bruno R. S. Queiroz [2], Carla C. Oliveira[2], Cristiane R. Guzzo[1].

[1] Department of Microbiology, Institute of Biomedical Sciences, University of São Paulo,
[2] Department of Biochemistry, Institute of Chemistry, University of São Paulo
*g.araujo@usp.br

Ribosomes have a long history of being studied by electron microscopy, not only due to their fundamental importance in biology but also because of their abundance and relatively large size [1,2]. More recently, advances in cryoEM made it the leading technique to structurally investigate these ribonucleoprotein complexes [1,2,3]. Nevertheless, the considerable conformational and compositional heterogeneity that these samples often have represent a challenge for data processing. Here we are applying cryoEM to examine ribosomes from mutants of the model yeast *Saccharomyces cerevisiae* with depleted assembly factors that participate in their biogenesis, where additional proteins can bind the defective particles, such as the cytoplasmic ribosome quality-control complex (RQC) [4]. This analysis is complicated by the presence of both full 80S ribosomes and free 60S large subunits, plus multiple conformations of the 40S small subunit and the varying occupancy of tRNAs. The software package cryoSPARC is being used for the diverse reconstruction and classification strategies employed to differentiate these multiple states. Our experimental approaches include data collection at different microscopes: the 200 kV Talos Arctica (preliminary tests) and 300 kV Titan Krios at LNNano-CNPEM, as well as the Tundra at IFSC-USP. Interestingly, our data demonstrates the capabilities of this 100 kV dedicated cryogenic TEM, being able to reach resolutions better than 4 Å for these asymmetric complexes (Figure 1). At the moment, this is a work in progress. More data should be collected and the processing scheme is being optimized [5].

[1] S.M. Webster et al., Cryo-Electron Microscopy in Structural Biology (pp. 305-318), CRC Press, 2023.
[2] A. Brown & S. Shao, Curr Opin Struc Biol, 52 (2018), 1-7.
[3] A. Razi et al., Nucleic Acids Res, 45 (2017), 1027-1040.
[4] A. Sarkar et al. (2017), Nat Struct Mol Biol, 24 (2017), 1107-1115.
[5] This research was supported by FAPESP (Brazil).

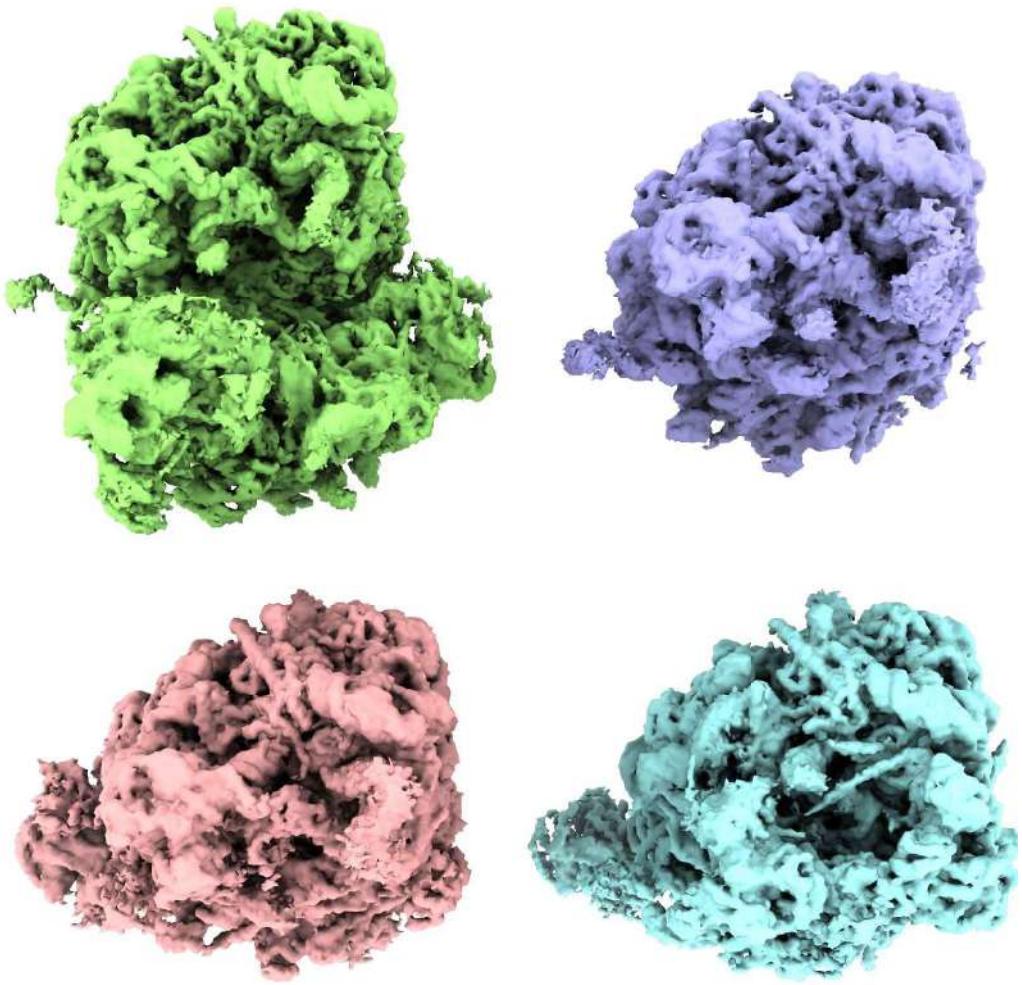

Figure 1. Some ribosome structures obtained from the Tundra dataset: 80S in green (3.27 Å resolution, small subunit presents blurring due to flexibility), 60S in purple (4.07 Å), and 60S particles with different binding partners in pink and blue (3.94 Å and 3.98 Å resolutions, respectively).

Adaptation of a Time-Resolved Vitrification System for (cryo) electron microscopy

Vânia Vieira, Ingrid Augusto, Kildare Miranda*

[1] Unidade de Microscopia Avançada, Centro Nacional de Biologia Estrutural e Bioimagem, Universidade Federal do Rio de Janeiro, Rio de Janeiro, Brasil

[2] Laboratório de Ultraestrutura Celular Hertha Meyer, Centro de Pesquisa em Medicina de Precisão, Instituto de Biofísica Carlos Chagas Filho, Universidade Federal do Rio de Janeiro, Rio de Janeiro, Brasil

*kmiranda@biof.ufrj.br

Conventional methods of sample preparation for biological electron microscopy involve several steps aimed to preserve cell structure that are also known to generate artifacts such as sample shrinking, mobilization of ions and osmolytes and displacement of membranes and minor structures. Physical fixation methods, collectively known as cryofixation, are known to reduce such artifacts [1] although formation of ice crystals remains a limitation when it comes to structural preservation. To cope with that, physical fixation methods that modify the colligative properties of water are able to solidify the cellular environment without forming ice crystals, a process known as vitrification [2]. Several devices of cryofixation have been developed alongside advancements in microscopy. Among these, spray freezing techniques have proven effective for freezing samples confined within small volumes. With this method, a suspension of the cells (stimulated or not) is sprayed, and the resulting droplets are directly projected into a cryogenic liquid, such as ethane or propane liquid, instantly freezing the cells. In 1987, Plattner and Knoll developed the first time-resolved spray freezing prototype to study *Paramecium* cells. The authors used analytical electron microscopy to map calcium ions after triggering the cells with time resolution of 30 ms [4]. This work aims to develop a spray freezing device with temporal resolution, inspired by Plattner's design, for the rapid freezing of small biological samples. In addition, we propose a low-cost, portable version adapted for the vitrification of microorganisms up to 20 μm in size. To achieve this, we designed a mixing chamber capable of accommodating one or two syringes, with gaseous nitrogen injection to facilitate efficient atomization. For this purpose, a device consisting of a stainless-steel piston was machined and coupled to a motor equipped with adjustable speed control and a millisecond-scale timer. Once the speed is selected, the arm is actuated to depress the syringe in a downward motion. The syringe contents are discharged into a mixing chamber pressurized with nitrogen gas at a predefined pressure. The gas-sample system then passes through a sieve with 50 μm holes, forming a spray of micrometric droplets that are launched directly into liquid ethane. These sieves were fabricated from solid stainless steel cylinders that were sliced and laser-drilled. Thus, various samples in solution such as protozoa, viruses, bacteria, fungi, and organelles can be frozen using a time-resolved, portable and low-cost device. The system was first tested with water to define better parameters such as piston movement speed (10u), gaseous N_2 pressure (0,2 bar), and sample volume (0,5 μl). The quality of the freezing process will be evaluated using cryo-scanning EM or diffraction, after which tests will be repeated using epimastigotes cells of *Trypanosoma cruzi*. After vitrified sample spheres are produced, they may be subjected to further protocols, including freeze substitution and cryolamella preparation, to enable advanced time-resolved structural studies via cryo-electron tomography (cryo-ET).

[1] Girard et. al, Histochem Cell Biol (2012) 138:821–831

[2] Dubochet, M. Adrian, J. Lepault, A.W. McDowall, Emerging techniques: Cryo-electron microscopy of vitrified biological specimens, Elsevier Science Publishers B.V., Amsterdam, 1985

[3] Gilkey and Staehelin, Advances in Ultrarapid Freezing for the Preservation of Cellular Ultrastructure, Journal Of Electron Microscopy Technique 3~177-210, 1986
[4] Hardt and Plattner Eur J Cell Biol 79:642-652, 2000.

Figure 1: spray freezing

Figure 1: Structure of the prototype of a spray freezing apparatus, showing the motorized arm and the mixing chamber where syringes containing the samples are discharged.

Figure 2: mixing chamber

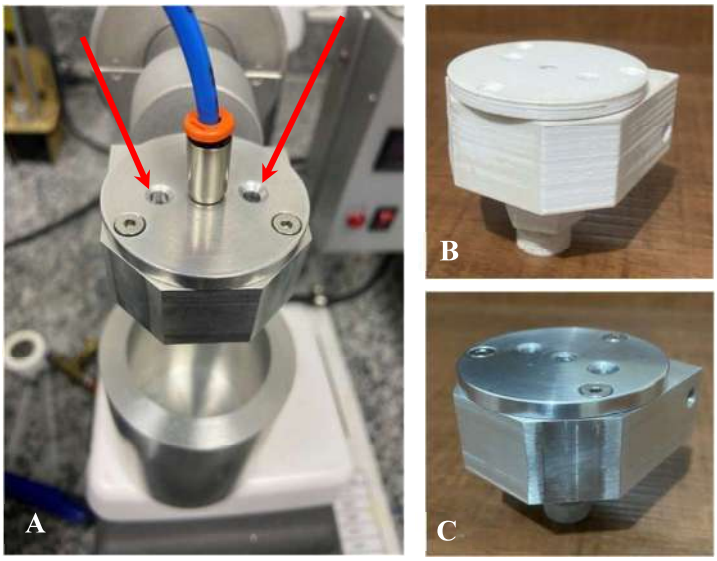

Figure 2: Detail showing the mixing chamber (A) where samples and nitrogen gas are inserted. The red arrows indicate the insertion site of the syringe containing the sample and/or stimulus, whose volumes will be injected into the mixing chamber. (B) Prototype in 3D printer (C) machined chamber

Figure 3: water droplets freezing

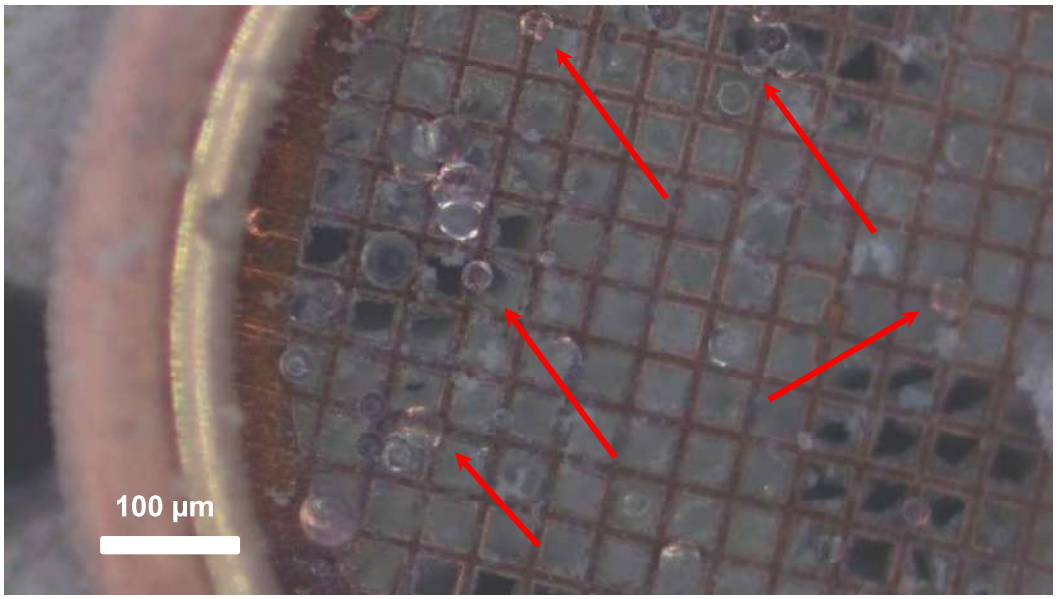

Figure 3: The red arrows indicate the results of the initial tests, showing frozen water droplets.

Cryo-EM Structure of VgrG4 from the T6SS of *Klebsiella pneumoniae* Reveals a Nucleotide-Binding Site

Thaiza G. de Paula [1]; Jairo H. D. Antty[2]; Gabriela D. Noske[3]; Mariana A. A. Aleixo[3]; Rodrigo V. Portugal[3]; Marcel M. L. Cunha[1] and Gisele C. de Amorim[1]*

[1]BIOS H+, Numpex-Bio, Universidade Federal do Rio de Janeiro - Campus Duque de Caxias Geraldo Cidade, Duque de Caxias, RJ, Brazil;
[2]Universidade de São Paulo - Faculdade de Medicina de Ribeirão Preto;
[3]Nanotechnology National Laboratory (LNNano), Center for Research in Energy and Materials (CNPEM), Campinas, SP, Brazil.
***gisele.amorim@caxias.ufrj.br**

Abstract

Klebsiella pneumoniae is a bacterium of medical importance and part of the ESKAPE group of pathogens, known for their resistance to antibiotics and their role as major causes of nosocomial infections. Secretion systems (SSs) are instrumental structures of bacteria for the development of antimicrobial resistance and virulence. SSs are needle-like structures that allow effector molecules to be exported to the extracellular environment or directly injected into host cells. Among the SSs, the Type VI Secretion System (T6SS) stands out as a system found only in Gram-negative bacteria, such as *K. pneumoniae*, characterized by the presence of a VgrG protein at its tip [1]. Evolved VgrGs assemble into trimers, each formed by ~100 kDa monomers containing non-conserved C-terminal domains (CTDs). Our group, BIOS H+, focuses on understanding potential virulence mechanisms in pathogens, and, by NMR spectroscopy, we previously determined that the CTD of the VgrG4 protein from *K. pneumoniae* kp52.145 hypervirulent strain is intrinsically disordered [2]. To further characterize VgrG4, we used cryo-electron microscopy/single particle analysis for the structural determination of the VgrG4 complex. Here, we present the cryo-EM structure of VgrG4 (PDB ID 9O2V, EMDB ID EMD-70023). Samples were prepared immediately after purification over glow-discharged Quantifoil 200 mesh Cu R2/2 grids and plunge-frozen in liquid ethane on a Thermo Fischer's Vitrobot Mark IV. Data acquisition was performed on a 300 kV Titan Krios G3i (Thermo Fisher Scientific) at LNNano/CNPEM by a K3 detector in counted mode equipped with a BioQuantum energy filter, at a nominal magnification of 105kx corresponding to a calibrated pixel size of 0.88 Å at the specimen level. 6428 movies were collected, dose-weighted and aligned using full frame motion correction. The contrast-transfer-function (CTF) was estimated using Patch CTF. Micrographs were filtered to 5901, 3.198.982 particles were detected and 596.857 used for the *ab-initio* models which, after processing, yielded a refined three-dimensional structure at 2.8 Å resolution (figure 1, figure 2). The resolved structure revealed a nucleotide molecule bound to a GKT motif, known as Walker A, a canonical phosphate-binding site (figure 2B, figure 3). As expected, the CTD was not defined, further supporting its characterization as an intrinsically disordered region. To our knowledge, this is the first report of nucleotide binding to the conserved region

of an evolved VgrG protein, providing new insights into the structural and functional complexity of the T6SS machinery.

References:
[1] Cherrak Y, Flaugnatti N, Durand E, Journet L, Cascales E. 2019. Structure and activity of the type VI secretion system. Microbiol Spectrum 7(4):PSIB-0031-2019. doi:10.1128/microbiolspec.PSIB-0031-2019.
[2] do Nascimento Soares T, Silva Valadares V, Cardoso Amorim G, et al. The C-terminal extension of VgrG4 from Klebsiella pneumoniae remodels host cell microfilaments. Proteins. 2022;90(9):1655‑1668. doi:10. 1002/prot.26344

[3] This research was supported by FAPERJ, UFRJ, PMBqBM/SBBq, LNNano and CNPEM.

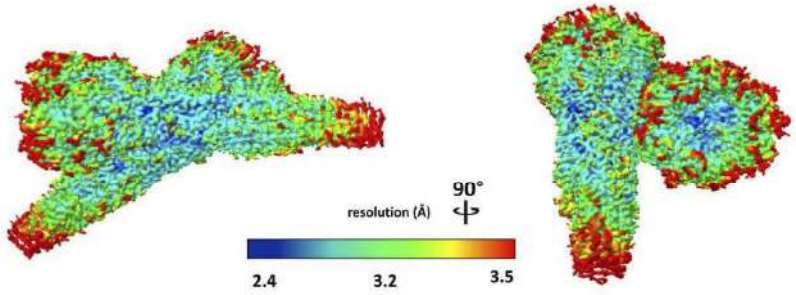

Figure 1. Resolution map of the refined structure of VgrG4.

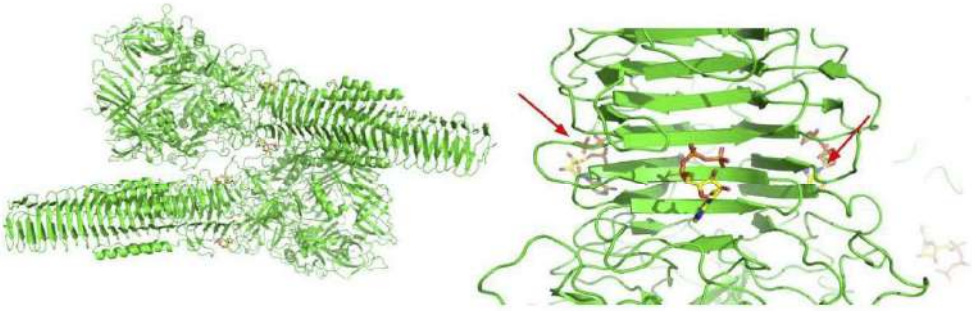

Figure 2: (**A**) Final structure of the VgrG4 protein at 2.8 Å resolution (**B**) ATP-binding region. VgrG4 is colored in green and ATP is represented in sticks.

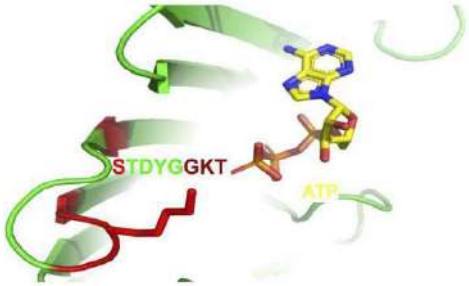

Figure 3: Walker A domain (SXXXXGKT), a canonical ATP phosphate-binding site, presented in VgrG4. The lysine side chain is represented in red sticks and the phosphate groups are in orange.

Structural and Functional Studies of the Bacteria-Phage Interface by Cryoelectron Tomography

Guilherme Oliveira Silva[1,2*]; Germán Gustavo Sgro[1,2]

[1] Medical School of Ribeirão Preto, Postgraduate Program in Cell and Molecular Biology
[2] Pharmaceutical Sciences School of Ribeirão Preto, Department of Biomolecular Sciences
guii.olvr@usp.br

Bacteriophages are viruses that thrive by infecting bacteria. Deciphering molecular mechanisms underlying their replication is the basis for controlling the infection [1]. In this sense, cryoelectron tomography (cryoET) emerges as an alternative to study phage infection overcoming some limitations associated with other imaging methods [2]. Recent advances in cryoET have uncovered several key aspects of phage biology, including mechanisms of host recognition, anchoring, and genome ejection [3,4]. Therefore, this project applies cryoET to study early infection steps by ΦXacm4-11, ZC01, ZC03 and LafX, all modern isolates of lytic phages against *Xanthomonas citri* (Xac) or *Pseudomonas aeruginosa* (PA14 or PASM). Phages were propagated by double-layer plaque assays and purified by CsCl gradient ultracentrifugation. Titrations by small drop plaque assay were performed to phage quantification and yield control. One-step growth trials were used to determine the optimal time to fixate the infection in early stages. Samples of infection were disposed on perforated carbon grids and fast-frozen in liquid ethane using a Vitrobot, and further collected using a Titan Krios microscope. Data processing will be carried out using a standard pipeline directed for tomographic approaches in Scipion framework. The phages were successfully purified, showing three bands on the CsCl gradient each, representing populations with distinct structural qualities. Although the purification tends to keep less than 1% of viable phages, the final concentration is still suitable for cryoET. Growth curves conducted with ΦXacm4-11 suggested adsorption and burst times of 20 and 90 minutes, respectively, and adsorption assays at 4° C reveal that around 80% of LafX particles adsorbs in the first 15 minutes. Other models are still being evaluated. Cryo-grids for Xac infection were prepared, but the MOI was not ideal, so new parameters are being tested. Images of several tilts of ZC03 infecting PA14 were captured, revealing phages attached to the bacterial type 4 pilus, however, the final reconstruction is not yet viable due to the limited number of entities. LafX grids showed a heterogeneity in terms of phage populations, a result from the unintended co-purification of membrane-derived fragments and vesicles, which acted as nucleation sites for particle activation. This points to the lack of specific receptors required to trigger this phage (other than LPS). CryoET is proving to be a great alternative for structural biology. Future steps involve optimizing sample preparation and performing the proper reconstructions for detailed structural insights [5].

[1] Rodrigues RAL, *et al*. An Anthropocentric View of the Virosphere-Host Relationship. Front Microbiol. 2017 Aug;8:1673. doi: 10.3389/fmicb.2017.01673.
[2] Cheng Y. Single-particle cryo-EM-How did it get here and where will it go. Science. 2018 Aug;361 (6405):876-880. doi: 10.1126/science.aat4346.
[3] Quemin ERJ, *et al*. Cellular Electron Cryo-Tomography to Study Virus-Host Interactions. Annu Rev Virol. 2020 Sep 29;7(1):239-262. doi: 10.1146/annurev-virology-021920-115935.
[4] Guerrero-Ferreira RC, Wright ER. Cryo-electron tomography of bacterial viruses. Virology. 2013 Jan 5;435(1):179-86. doi: 10.1016/j.virol.2012.08.022.
[5] This research was supported by CAPES and FAPESP (Brazil).

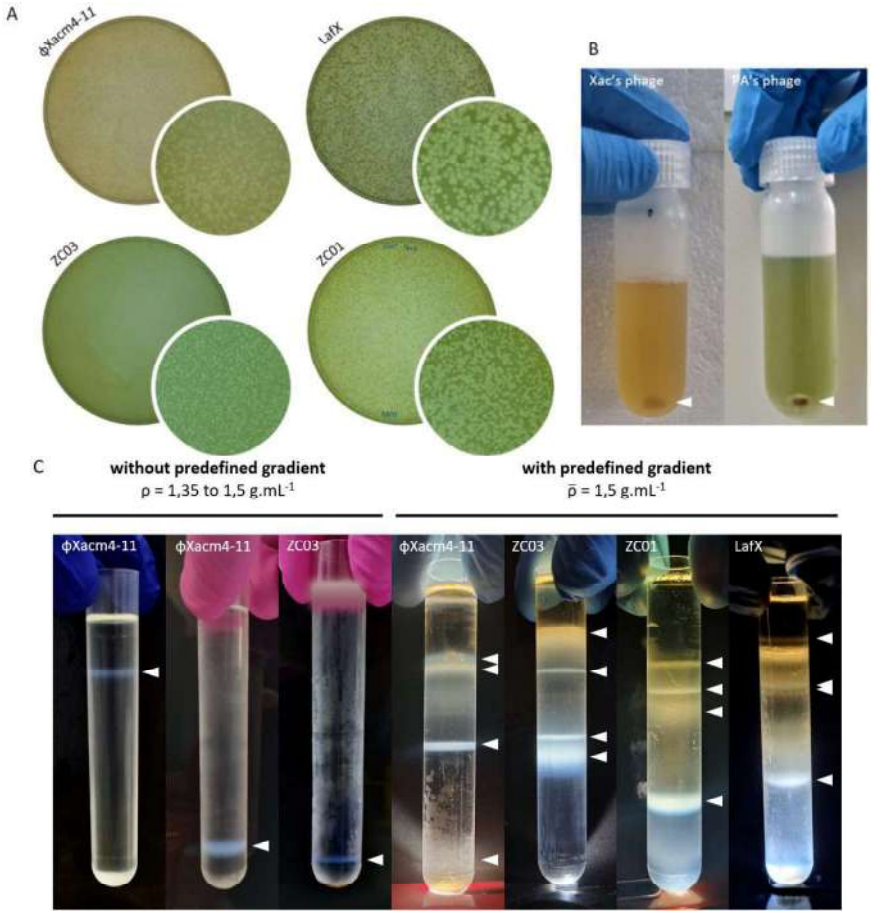

Figure 1. Phage propagation and purification workflow. (A) Culture plates of Xac, PASM and PA14 showing the lysis profiles induced by φXacm4-11, LafX, ZC03 and ZC01, respectively. Phages were then extracted and subjected to (B) precipitation using PEG/NaCl, followed by (C) purification through a CsCl gradient. White arrows indicate the phage-enriched regions. Author, 2025.

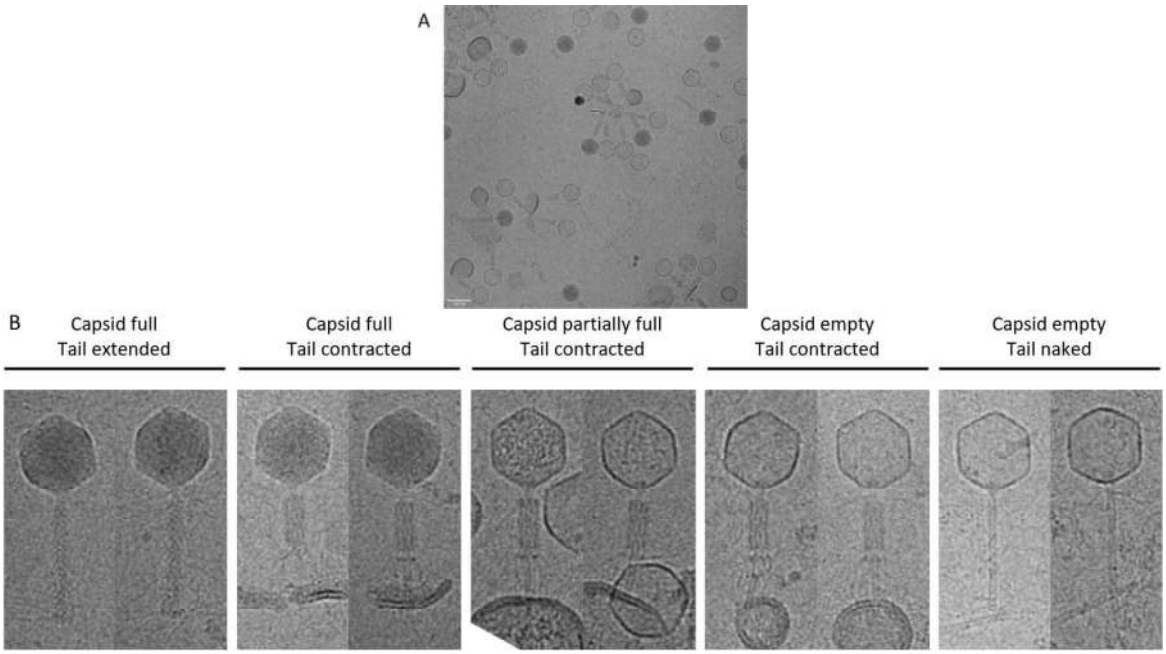

Figure 2. Cryoelectron micrographs of LafX co-purified with membrane fragments. (A) Different representatives of LafX particles can be seen in one single field. Particle concentration could be improved but is already suited for data collection. Grid not prepared with fiduceals. (B) States of LafX particle encountered on the sample. Capsids were found either entirely or partially full, or empty, and tails were extended, contracted or even naked, showing just the inner tube. Author, 2025.

Optical microscopy applied to biological samples, including confocal and super-resolution microscopy (STED, PALM, STORM) and its applications in bioimaging

Effects of Amoxicillin and Calcium/Vitamin D Supplementation on Incisor Enamel in Fluorotic Rats: A Morphological, Biochemical, and Immunohistochemical Study

Isabel Maria Porto[1*], Julia Vargas Alves dos Santos[1], Betânia Mansor Silva[1], Enzo Bacelar Giacomin[1], Gabrielle Sampaio da Fonseca[1].

[1] São Paulo State University (UNESP), Department of Morphology and Pediatric Clinic, School of Dentistry, Araraquara, Brazil.

*isabel.porto@unesp.br

The process of dental enamel formation is called amelogenesis. Initially, an organic matrix is secreted, which subsequently undergoes mineralization, making enamel the most mineralized tissue in the body, with 97% mineral content [1]. The entire amelogenesis process depends exclusively on specialized epithelial cells called ameloblasts. Although it is under genetic control [2,3], external factors such as exposure to high levels of fluoride and excessive use of antibiotics can interfere with enamel mineralization, making it less resistant [6-10]. Thus, this study associates fluoride exposure with antibiotic use. Additionally, a group was tested in which, besides co-exposure, calcium and vitamin D supplementation was administered, since some studies have shown that this treatment may reduce the damage caused by dental fluorosis [11,12]. Therefore, the aim of this study is to analyze the effects of fluoride and amoxicillin, alone or combined, on ameloblasts, and whether these effects are reduced when calcium and vitamin D supplementation is provided. To this end, 80 Holtzman rats were used, divided into 8 groups of 10 animals each: control group, vitamin D + calcium group (Vit D + Ca), fluoride group, amoxicillin group (Amx), fluoride + vitamin D + calcium group (F + Vit D + Ca), amoxicillin + vitamin D + calcium group (Amx + Vit D + Ca), and fluoride + amoxicillin + vitamin D + calcium group (F + Amx + Vit D + Ca). The project was approved by the CEUA of FOAr/UNESP, Araraquara (protocol number 01/2023). After 60 days of treatment, animals were euthanized and hemimandibles were collected for histological processing. Analysis was performed using light microscopy (hematoxylin and eosin), scanning electron microscopy (SEM), immunohistochemistry for caspase-3, and the TUNEL assay. Phosphorus content was also measured after enamel surface etching. SEM results showed no differences in the mineralized enamel matrix among the groups. However, light microscopy revealed the presence of apoptotic bodies, particularly in the fluoride + amoxicillin group, which was confirmed by the TUNEL assay. Immunostaining for caspase-3 also revealed increased ameloblast cell death in the fluoride + amoxicillin group. Although phosphorus measurements indicated that calcium and vitamin D supplementation made the enamel surface more resistant to demineralization, the damage caused to ameloblasts was not reduced. In conclusion, exposure to a high fluoride concentration (45 ppm) or prolonged use of amoxicillin (500 mg/kg/day) during enamel formation impairs ameloblasts, and their combined use increases the harmful effects of these substances.

[1] C. Robinson et al., Int. J. Dev. Biol. 39 (1995) 145.
[2] C.W. Gibson, J. Oral Biosci. 53(3) (2011) 248.
[3] Y. Lu et al., Biol. Chem. 389(6) (2008), 695.
[4] G.W. Suckling et al., Adv. Dent. Res. 3(2) (1989) 219.
[5] R.W. Evans, J.W. Stamm, J. Public. Health Dent. 51(2) 1991 91.

[6] V.E. Beentjes et al., Eur. J. Paediatr. Dent. 3(1) (2002) 9.
[7] T. Aoba, O. Fejerskov, Crit. Rev. Oral Biol. Med. 13(2) (2002)155.
[8] I. Ciarrocchi et al., Pediatr. Med. Chir. 34(3) (2012) 148.
[9] S. Kameli et al., Front. Dent. 16(2) (2019)130.
[10] B. Gottberg et al., Med. Oral Patol. Oral Cir. Bucal 19(1) (2014) 38.
[11] P.P. Patel et al., Indian J. Endocrinol. Metab. 21(1) (2017)190.
[12] A.D. Bhowmilk et al., Biol. Trace Elem. Res. 199 (2021) 3035.
[13] This research was supported by FAPESP (process 2023/08752-3) (Brazil).

Table 1. Enamel mass (mg) removed by acid etching.

Group	Mean ± SD
Control	27.67 ± 13.74**
Vit D + Ca	21.01 ± 9.91
Amx	22.75 ± 11.25
Amx+ Vit D + Ca	13.73 ± 8.81**
Fluoride	31.36 ± 13.90*
F + Vit D + Ca	14.04 ± 6.83*
F + Amx	25.88 ± 11.60
F + Amx + Vit D + Ca	25.42 ± 11.99

* $p \leq 0.05$; ** $p \leq 0.03$.

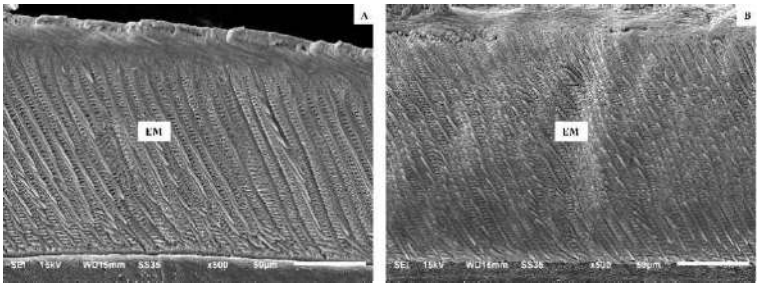

Figure 1. Scanning electron microscopy (SEM) of enamel. **A.** Control group. **B.** Fluoride + amoxicillin + vitamin D + calcium (F + Amx + Vit D + Ca) group. No differences were observed between the groups. Magnification: 500×. **Em:** enamel matrix.

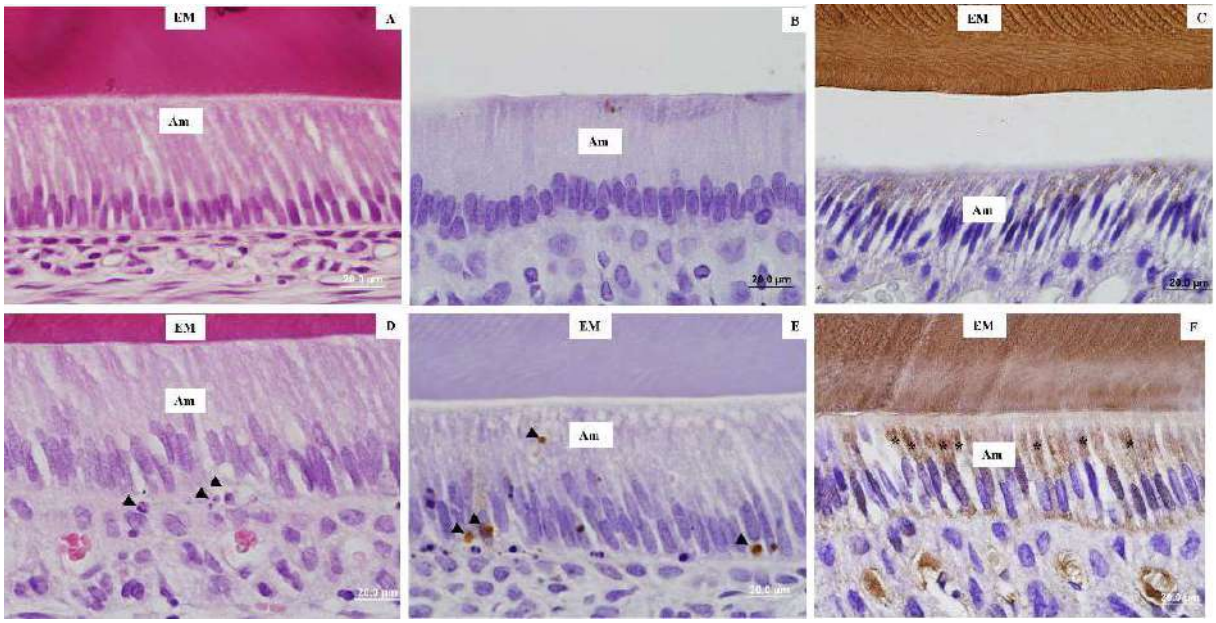

Figure 2. Lower incisor enamel. Control group: (A) H&E staining. (B) TUNEL assay. (C) Caspase-3 immunohistochemistry. No alterations were observed in the control group. **Fluoride + amoxicillin + vitamin D + calcium (F + Amx + Vit D + Ca) group:** (D) Hematoxylin and eosin (H&E) staining showing apoptotic bodies (black arrowheads). (E) TUNEL assay demonstrating TUNEL-positive apoptotic bodies (black arrowheads). (F) Caspase-3 immunohistochemistry revealing positive caspase-3 expression in ameloblasts (asterisk). **Magnification:** 1000×. Em, enamel matrix; Am, ameloblast layer.

Integrated Microscopy and Spectroscopy Approaches for Intracellular Localization of a Bioactive Alkaloid in the cyanobacterium *Moorena bouillonii*

Leonardo Tavares Salgado[1], Rodrigo Tomazetto de Carvalho[1], Wladimir Costa Paradas[1], Taiara Aguiar Caires[2], Felipe de Vargas Ribeiro[3], Omar Ginoble Pandoli[4], Davyson de Lima Moreira[1], Ygor Jessé Ramos[5], Paulo Sérgio Salomon[6], Renato Crespo Pereira[3*]

[1]Instituto de Pesquisas Jardim Botânico do Rio de Janeiro, [2] Universidade do Estado da Bahia, [3]Universidade Federal Fluminense,[4]Pontificia Universidade Católica do Rio de Janeiro, [5]Universidade Federal da Bahia, [6]Universidade Federal do Rio de Janeiro
*lsalgado@jbrj.gov.br

The genus *Moorena* comprises tropical marine cyanobacterial species rich in secondary metabolites, which can be used as allelopathic agents against constructor organisms, thereby threatening the health of coralline reefs [1]. This opportunistic organism is growing in one of the most biodiverse Brazilian marine habitats, the Abrolhos Continental Shelf [2]. Nevertheless, few studies have addressed the cellular localization and extracellular secretion of these crucial chemicals in chemically mediated ecological interactions involving these organisms. We combined spectroscopy, microscopy, chromatography, and chemical analyses to localize and characterize the major secondary metabolite in *Moorena bouillinii*. A crude extract of *M. bouillonii* was fractionated by HPLC, and the purified fraction in the FT-IR spectroscopy presented stretching bands of a potential pyridine ring as major peaks (1.320 cm^{-1} for C-N, 1567 cm^{-1} for -COO^- and 1.590 for C=C), which can be associated with nitrogen phenolic compounds or a pyridine alkaloid. Laser Scanning Confocal Microscopy and Raman Microspectroscopy images showed a bluish excitation/emission pattern in the mucilaginous sheath around the cyanobacterial trichome, inside the vesicles, between the cells, and in the necridia. Scanning Electron Microscopy evidenced the reticulated structure of the chloroplast thylakoid membrane across the cell and the mucilaginous sheath. Raman map revealed the highest concentration of the compound in the intracellular region (above the thylakoid membranes), decreasing from the center outward to the mucilaginous sheath. The location of the compound within *M. bouillonii* cells reveals a dynamic chemical defense system in which the compound is biosynthesized in the thylakoid membranes and transported to the mucilaginous sheath in an analogous process known for marine macroalgae species that exhibit defensive ecological roles. Using Raman Microscopy, FT-IR Spectroscopy, Scanning Electron Microscopy, and Confocal Microscopy analysis allows for comprehensive chemical and morphological insights, often crucial in research focused on natural product discovery, bioengineering, and environmental monitoring.

[1] E. Curren et al., Environ Sci Pollut Res Int. 29(52), 2022 - 78178-78206.
[2] Z.M.A.N. Leão, Corals and coral reefs in Brazil, Elsevier Science, Amsterdam, 2003.
[3] F.V. Ribeiro et al., Front Mar Sci. 8, 2022 - 790277.
[4] This research was supported by CAPES, FAPERJ and CNPq.

Table 1. FT-IR spectra peaks of the cyanobacteria extract and the assigned functional groups.

Wavenumber (cm^{-1})	Functional Groups
722	$(CH_2)_n$
959	C=C
1040, 1043, 1084, 1112, 1171	C-O
1377	CH_3
1408, 1462	CH_3,CH_2
1651, 1656	N-H
1711	C=O
2837	C-H
2853, 2923	C=O
3337, 3372	O-H

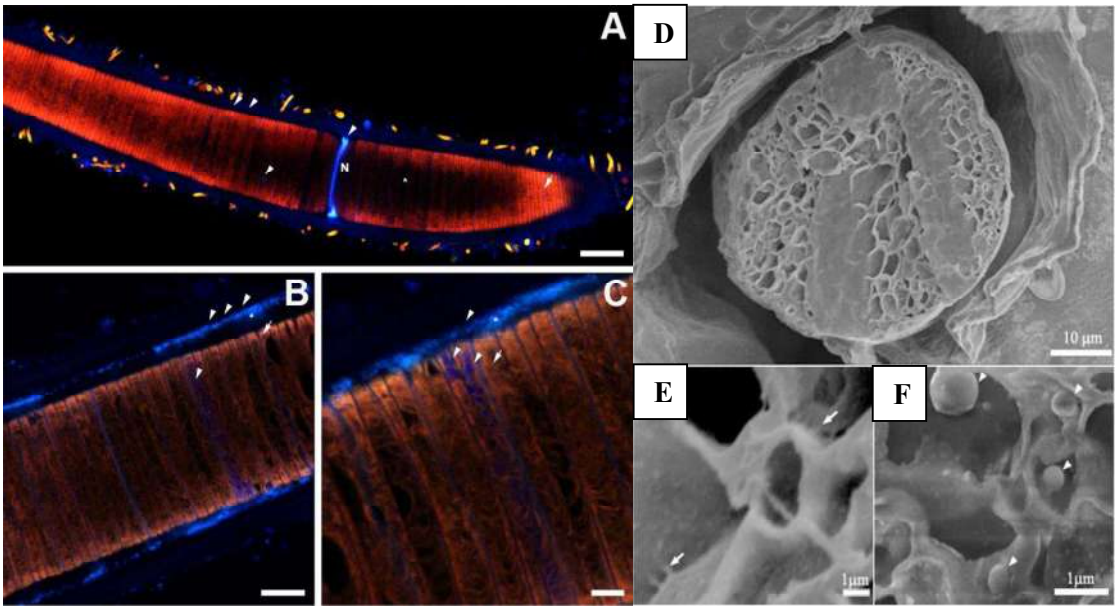

Figure 1. Fluorescence (LSCM) and HRSEM analysis of live *M. bouillonii* filaments. (A) LSCM image showing bluish emission at 465 nm (arrowheads) from the alkaloid after 405 nm excitation. Orange and red emission at 590/690 nm (arrows) are phycobilins and chlorophyll *a*. Scale bar = 20 µm. (B–C) Higher magnification shows it dispersed between the sheath and cytoplasmic membrane (asterisks). Scale bars = 8 µm (B), 1 µm (C). (D) HRSEM showing general thylakoid membrane structure. (E) Filaments (arrowheads) associated with thylakoids are visible after cell wall removal. (F) Membrane-related vesicular structures (arrowheads).

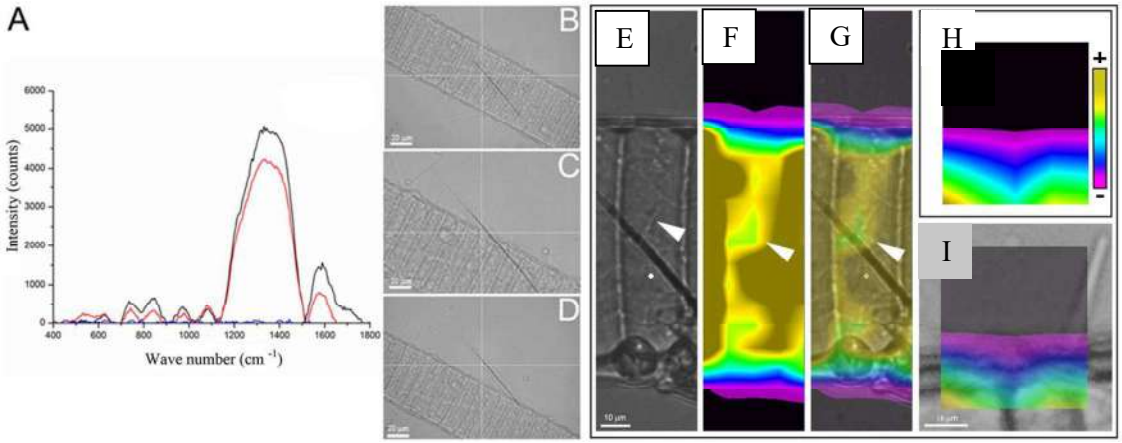

Figure 2. Raman spectra of *M. bouillonii* filament regions. (A) Bright-field image with analyzed points (B, C, D). Laser excitation: 532 nm. Raman mapping of *M. bouillonii* alkaloid (E) Bright-field image highlighting thylakoid membranes (arrowheads). (F) Raman map shows highest alkaloid levels in intracellular regions, particularly cell centers. (G) Optical microscopy and Raman map confirms alkaloid concentration in thylakoid zones, decreasing toward the sheath and absent extracellularly (black). (H) High magnification reveals a color gradient representing alkaloid concentration from the cell center to the sheath. (I) Overlay shows cell interior (mustard/green), cytoplasmic membrane (blue), and mucilaginous sheath (pink).

Protective Role of an Annexin A1-Derived Peptide in Oxidative Stress Models of Human Retinal Organoids

Rafael André da Silva[1,2], Cristiane Damas Gil[2,3], M. Natalia Vergara[1*]

[1]*CellSight* Ocular Stem Cell and Regeneration Research Program, Sue Anschutz-Rodgers Eye Center, University of Colorado School of Medicine, Aurora, CO, United States. [2]Biosciences Graduate Program, Institute of Biosciences, Letters and Exact Sciences, UNESP, São José do Rio Preto, SP, Brazil. [3]Department of Morphology and Genetics, Escola Paulista de Medicina, Universidade Federal de São Paulo, São Paulo, SP, Brazil. *rafael.andre@unesp.br

Oxidative stress is a central mechanism in several retinal diseases, including age-related macular degeneration, diabetic retinopathy, and glaucoma, driving cellular damage and apoptosis [1]. Annexin A1 (ANXA1), known for its roles in inflammation and apoptosis [2], has been identified as a key regulator of oxidative stress and mitochondrial homeostasis [3], highlighting its therapeutic potential in retinal degeneration [4]. This study aimed to evaluate the effects of its mimetic peptide, ANXA1pep, on oxidative stress and apoptosis in retinal organoids (ROs). Transcriptomic datasets from human ROs and embryonic retinas (GSE229682, GSE104827) were analyzed to evaluate ANXA1 gene expression. Protein levels of ANXA1, FPR1, and FPR2 were assessed by Western blot in ROs [5] (A18945 hiPSC line) collected at multiple time points (days 37–382). At day 180, ANXA1 localization and coexpression with CRALBP were examined by immunofluorescence and confocal microscopy. To test ANXA1pep effects, ROs derived from the ILC62.6 hiPSC line were challenged with H_2O_2 or high glucose and treated with the peptide (25 or 50 ng/mL). Apoptosis and ROS levels were measured using PSVue380 and DHE, respectively, and apoptotic signaling pathways were analyzed via Milliplex assay. The results of the transcriptomic and protein analyses revealed a dynamic expression of ANXA1, with elevated levels at early developmental stages, a decline at intermediate time points, and re-elevation at later stages. A similar pattern was observed in embryonic human retina samples. FPR1 and FPR2, receptors for ANXA1, showed low expression in early stages and peaked at more advanced phases. Based on these findings, day 180 organoids were selected for functional analysis, as they present a more mature retinal stage and confirmed receptor expression. At this stage, coexpression of ANXA1 with CRALBP, a Müller glial cell marker, was observed. RO challenge with oxidative and metabolic stressors increased reactive oxygen species levels and apoptosis, as shown by enhanced DHE and PSVue labeling, respectively, confirming the pathophysiological relevance of the model. Notably, treatment of this model with ANXA1pep reduced reactive oxygen species accumulation and apoptotic cell death. Additionally, under metabolic stress, the peptide downregulated pro-apoptotic markers such as p53, BAD, Caspase-8, and Caspase-9, indicating anti-apoptotic activity. Together, these results indicate that ANXA1pep exhibits significant cytoprotective activity by reducing oxidative stress and apoptosis, supporting its potential as a therapeutic agent for retinal degenerative diseases.

[1] W. Wand et al, Oxidative Medicine and Cellular Longevity, 13(2) (2022) 1214-1221.
[2] L.P.S. Ferreira et al., Proteins Struct. Funct. Bioinforma. 91(9) (2023)1191-1204.
[3] J. B. Moreli et al. Int. J. Mol. Sci. 24(12) (2023) 1015524.
[4] R.A. da Silva et al. Drug Discov. Today 27(11) (2022) 103367.
[5] Zhong et al., Nature Communication, 10 (5) (2014) 4047.

[6] This research was supported by FAPESP/BEPE (2024/04275-9) and by a Challenge Grant to the Department of Ophthalmology at the University of Colorado from Research to Prevent Blindness.

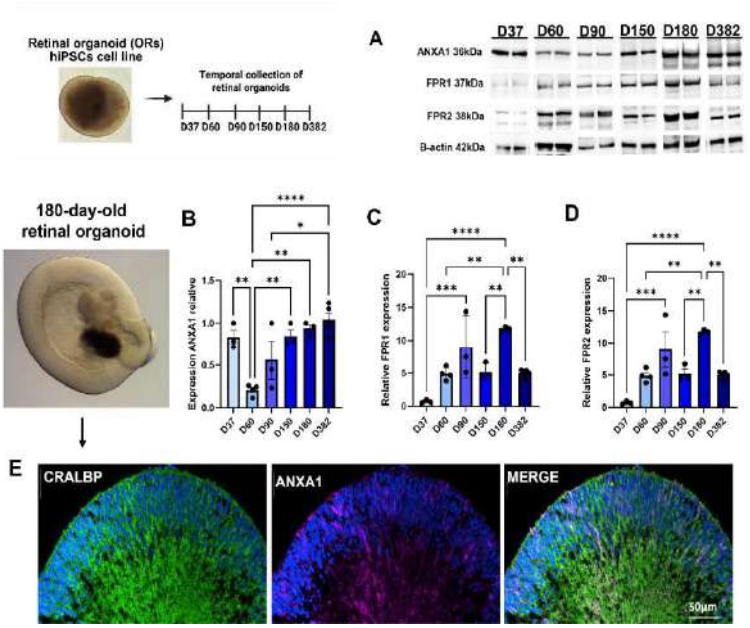

Figure 1. (A) Western blot showing ANXA1, FPR1, and FPR2 expression at different developmental stages. (B-D) Densitometric quantification normalized to β-actin (mean ± SEM). (E) Immunofluorescence of RO cryosections showing ANXA1 (magenta), CRALBP (green), and nuclei (DAPI, blue), with coexpression in inner retinal layers. Scale bar: 50 µm. One-way ANOVA with Tukey's post hoc test: *p < 0.05, **p < 0.01, ***p < 0.001, ****p < 0.0001.

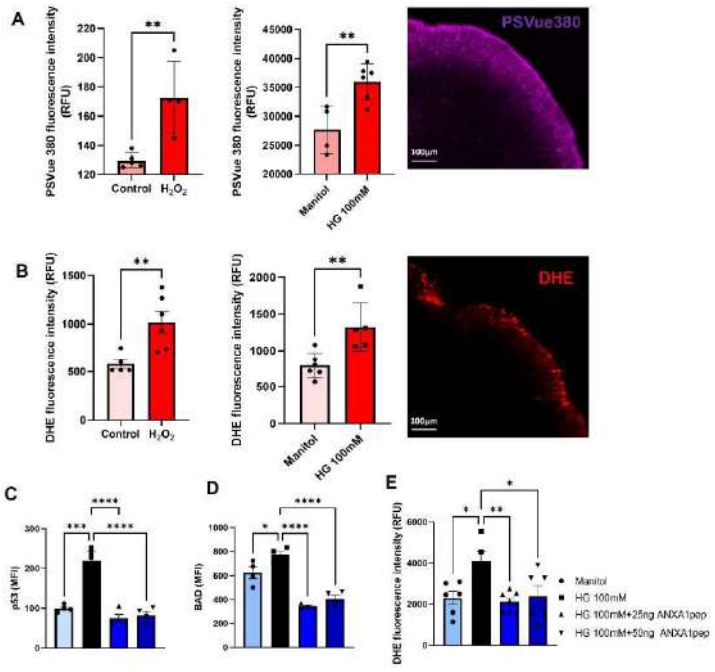

Figure 2. (A) Quantification of apoptosis (PSVue 380) in 180-day-old ROs challenged with high glucose (HG) or H_2O_2. (B) Quantification of ROS levels by DHE fluorescence. (C, D). Protein levels of p53 and BAD under HG conditions with or without ANXA1pep. (E) Quantification of reactive oxygen species modulation by ANXA1pep. Data represent mean ± SEM. One-way ANOVA with Tukey's post hoc test: *p < 0.05, **p < 0.01, ***p < 0.001, ****p < 0.0001.

Proton-secreting clear cells proliferation and CD8 infiltration in epididymis of SARS-CoV-2 infected K18-hACE2 transgenic mice

André Acácio Souza da Silva[1], Stephen Olumide Akinsomisoye[2,3], Paulo Sérgio Cerri[2], Estela Sasso-Cerri[2]*.

Federal Universisty of São Paulo, UNIFESP/EPM[1], São Paulo State University (UNESP) School of Dentistry Araraquara [2], Faculty of Basic Medical Sciences, Obafemi Awolowo University, Ile Ife, Nigeria[3].
*estela.sasso@unesp.br

According to data from the World Health Organization (WHO), men were more frequently infected than women during the SARS-CoV-2 pandemic, and the impact of COVID-19 on human health is still being investigated [1]. The epididymis is, anatomically divided into 4 major segments (initial segment, caput, corpus and cauda), with distinct responses and functions, essential to sperm maturation and storage [2]. The proton-secreting clear cells (CCs) play a role in maintaining the pH homeostasis of the luminal fluid thought recruitment of the proton pump V-ATPase to the apical membrane, and recent studies have shown that these cells play a role in the epididymal immune response [3,4]. Using a transgenic mouse that expresses the human angiotensin-converting enzyme 2 (hACE2), we evaluated the pathogenesis of COVID-19 in this essential organ for male reproductive health. In this study, we evaluated the impact of SARS-CoV-2 infection in the final segment of the epididymis (cauda), responsible for the storage of sperm. 20 male mice were divided into 2 groups: Control group (CG) and the infected group (IG). The CG received DMEM and the IG received 40µL of PFU ($5X10^4$) intranasally. Five days after the infection, the animals were euthanized (CEUA 02-2022). We evaluated the immunoexpression of pro-inflammatory cytokines TNF-α, IL1-β and IL-6, and CD8 (cytotoxic T lymphocytes marker) by immunofluorescence. The mRNA expression of type 1 (INF-α and INF-β) and type 2 interferons (INF-ϒ) were also investigated by RT-qPCR. Spike and actin in the smooth muscle cells (SMCs) layer, responsible for the epididymal contraction and transport of sperm trough the epididymal duct, was detected by double immunolabelling for spike and actin. This layer was also measured, and muscle cells death was detected by TUNEL method and transmission electron microscopy (TEM). Considering the important role of CCs in epididymis, we evaluated the immunoexpression of V-ATPase. The epididymal perimeter containing more than three juxtaposed CCs, forming sequential rows of CCs (a common feature observed in IG), was measured and the incidence of PCNA (cell division marker) was also detected in the rows. The infection with SARS-CoV-2 increased the expression of all pro-inflammatory cytokines as well as the mRNA for the type 1 and 2 interferons (Fig. 1F, G and H), followed by an infiltration of $CD8^+$ lymphocytes in the stroma (Fig. 1A), confirmed by the increased immunolabelling for this marker. The intense expression of pro-inflammatory cytokines observed here corroborates the increased number of macrophages, as previously reported [3]. Since our previous findings showed that the epididymal epithelial cells are infected by SARS-CoV-2 [3], and that cytotoxic T lymphocytes, recruited by interferons, can kill viral infected cells, the recruitment of these lymphocytes is activated by an epididymal immune response to the viral infection, favoring the clarence of infected cells. The colocalization of spike and actin in the smooth muscle layer confirmed that muscle cells were also infected (Fig. 1C). Moreover, this layer was thinner than in CG and exhibited TUNEL-positive cells and ultrastructural features typical of apoptosis under TEM. The SMCs dysfunction could impact the sperm maturation since the contraction of these cells is important to the spermatozoa flow in the epididymis [2]. The rows of CCs in the epididymal cauda increased in IG and a high incidence of PCNA immunolabelling was noted in the CC rows (Fig.1B), confirming that these rows are derived from CCs mitotic activity.

Considering the role of CCs in the immune response [3,4,7], this proliferative activity was probably activated by the immune response to the infection. The immunolabelling for V-ATPase in the clear cells apical portion also increased in IG, suggesting an imbalance in the luminal pH, which is crucial for sperm maturation. In conclusion, the increased number of cytotoxic T cells, associated with the SMCs layer atrophy and the increased V-ATPase, could impair the process of maturation and storage of spermatozoa. The infection also activates the mitotic activity of CCs, forming rows of these cells in the epithelium to provide an effective immune response against the viral infection. Therefore, more attention should be given to the reproductive health of convalescent patients of COVID-19.

[1] World Health Organization (WHO), 2025.
[2] B. Robaire and B. T. Hinton, Knobil and Neill's, Elsevier, New York, 2015.
[3] Da Silva et al., Andrology, 2024.
[4] Da Silva et al., Function, 2025.
[5] F. Carneiro et al., Andrologia, 53 2021.
[6] van de Sandt et al., Am J Respir Cell Mol Biol, 2017.
[7] Battistone et al., Journal of cell science, 2019.
[8] This work was supported by FAPESP (2021/07207-6; 2022/10560-2) and CAPES.

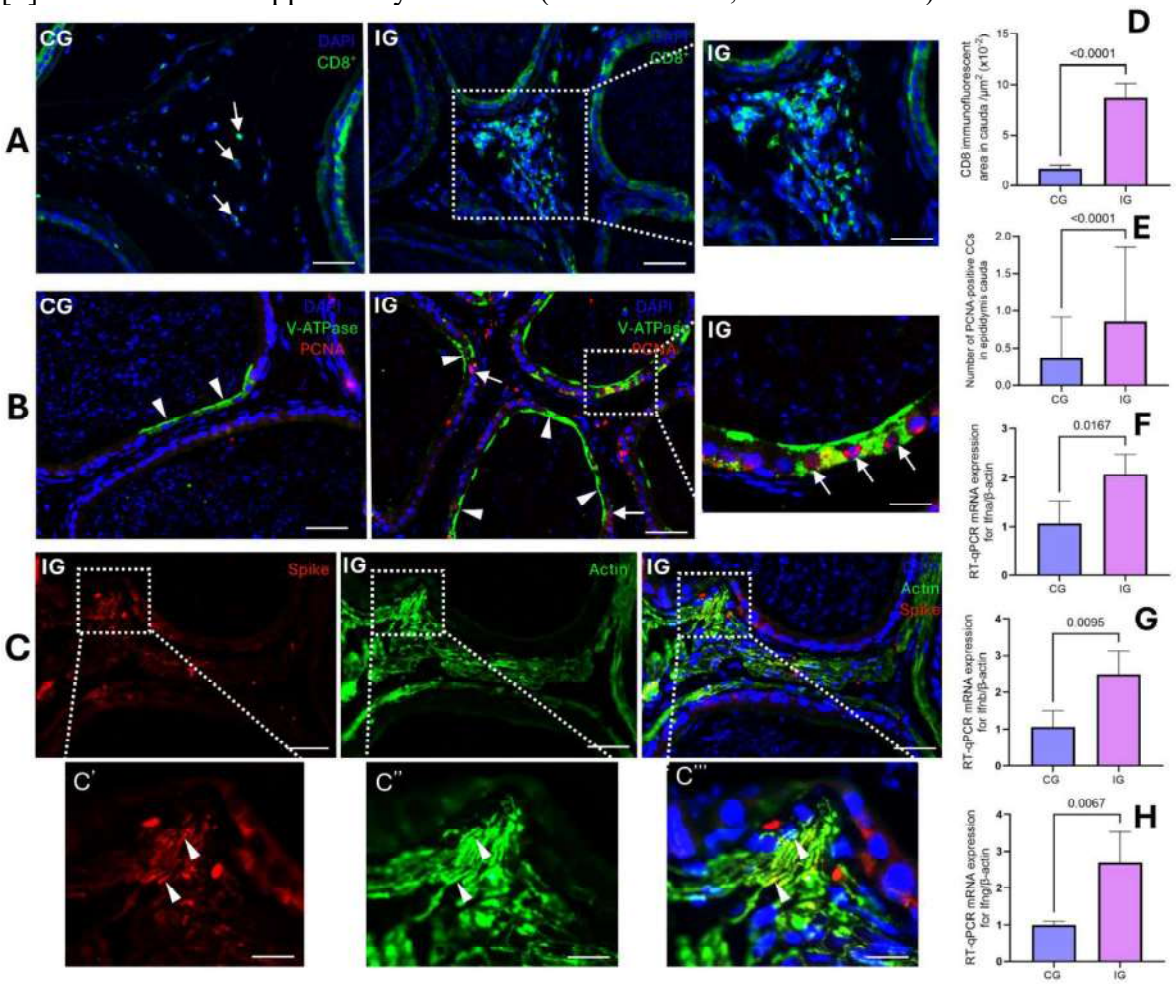

Figure 1. In panel A, CD8 immunofluorescence in cauda. Note immunolabelled cells in the connective tissue (arrows) and the increased number of immunolabeled cells in the IG (inset) compared to CG. In panel B, double immunolabelling for V-ATPase (green, arrowheads) and PCNA (red, arrows). Note several PCNA-positive nuclei in IG (arrows, inset) in comparison with CG. In panel C, double immunolabelling for spike (red) and actin (green). In c', spike immunolabelling (arrowheads), is observed. In c'', note the actin immunolabelling (arrowheads) and in c''', colocalization of spike and actin in yellow (arrowheads). In D, the CD8 immunofluorescent area increased in IG when compared to CG. In E, the number of PCNA+ CCs increased in IG when compared to CG. In F, G and H, the mRNA expression for INF-α, INF-β and INF-ϒ increased in IG when compared to CG. Panel A bars 35 µm, inset 20 µm. Panel B bars 30 µm, inset 10 µm. Panel C bars 30 µm, inset 10 µm.

Acethylcholine Receptors (nAChRs) recovery after neurorrhaphy associated with fibrin biopolymer sealant (BHF) on peripheral nerve injury

Selma Maria Michelin Matheus[1]*, Kevin Silva Muller[2], Felipe Cantore Tiburcio[3].

[1]Department of Structural and Functional Biology, Institute of Biosciences, São Paulo State University (UNESP), Botucatu, SP, Brazil.[2]Institute of Biology, State University of Campinas (UNICAMP), Campinas, SP, Brazil.[3] Faculty of Health Sciences, Federal University of Rondonópolis (UFR), Rondonópolis, MT, Brazil.
*selma.matheus@unesp.br

The neuromuscular junctions (NMJs) are synapses in the peripheral nervous system which transfer information to skeletal muscle fiber. The classic morphology of the NMJ is characterized as a "pretzel" shaped structure, and changes in this structure are closely associated with motor pathologies. At the NMJ, nAChRs are the primary receptors in the muscle to establish neuromuscular motor communication[1]. After denervation obtained by peripheral nerve lesion (PNL) a severe atrophy of the NMJ structure and the associated proteins including the nAChRs takes place [2]. The suture is the gold standard method used after this lesion but the fibrin sealant is an alternative and /or complementary method. The Center for the Study of Venoms and Venomous Animals (CEVAP/Brazil) developed this sealant from the poison of the *Crotalus durissus terrificus* (rattlesnake) that is innocuous and safe [3]. The focus of this study was to verify the potential of the fibrin sealant associated with a single stitch on the nAChRs of the NMJs after ischiatic nerve lesion using scanning confocal microscopy.Twenty male adult Wistar rats (CEUA-FMB: 1402/2021), were divided into 4 groups: Control Group (C): dissection and location of the right sciatic nerve. Denervated Group (D): nerve transection (neurotmesis) and removal of a 6 mm fragment. Neurorrhaphy Group (N): neurotmesis followed by end-to-end neurorrhaphy. Neurorrhaphy + BHF Group (NB): neurotmesis followed by neurorrhaphy, with the addition of BHF. After 120 days the right soleus muscles were removed and prepared for the morphology analysis by confocal microscopy and after for morphometry of the nAChRs that were labeled with α-bungarotoxin conjugated to rhodamine and the nerve terminals were labeled with Anti-neurofilament 200 and FITC. The images were acquired using a Laser Scanning Confocal Microscope (Leica TCS model - SP5) of the CME/IBB/Unesp. Measurements were taken from 50 NMJs per animal of each experimental group: motor endplate area, nAChR area, total area of the motor endplate and the largest orthogonal axis of the nAChR. And based on these measurements, relative planar area, mean diameter of NMJ and density of the motor endplate were calculated [4]. In D group, flattening and fragmentation of the nAChR were observed. In C group, the nAChR presented a distribution compatible with normality as a "pretzel" shaped structure. A similar morphology of nAChR was observed in the NB group (Figure 1). The morphometric analysis of the NMJs and AChR showed that group NB presented results like group C and different from groups N and D about the area of the AChR and motor endplate and number of clusters. In the other parameters, the NB group showed greater proximity to group C (Figure 2). It is important to highlight that the nAChRs area of NB group were similar to C group, so higher are the levels of nAChRs area the lower will be the fragmentation of nAChRs and vice versa reflecting the index of complexity of the NMJ[4,5].These results demonstrate that HFB contributes to partial functional recovery, and morphological restoration of NMJs and AChRs to normal patterns, in addition to promoting reinnervation of motor endplates and regeneration of muscle fibers. These effects contribute to an overall improvement in neuromuscular regeneration. In conclusion, the combination of neurorrhaphy and HFB emerges as an emerging and economically viable medical approach advantageous in peripheral nerve repair.

References
[1] K.S.Muller et al. J Venom Anim Toxins Incl Trop Dis. (2024) Apr 15;30:e20230060.
[2] W.A. Palispis and R. Gupta, Exp. Neurology 290(2017), p.106.
[3] R.S. Ferreira, J. of Venomous Animals and Toxins including Tropical Diseases 20(2014),p. 1.
[4] D.C. Sieck, et al., Respiratory Physiology & Neurobiology 180(2012),p. 88.
[5] C.N.A. Pissulin et al., Journal of Photochemistry and Photobiology B: Biology 167(2017),p. 256.

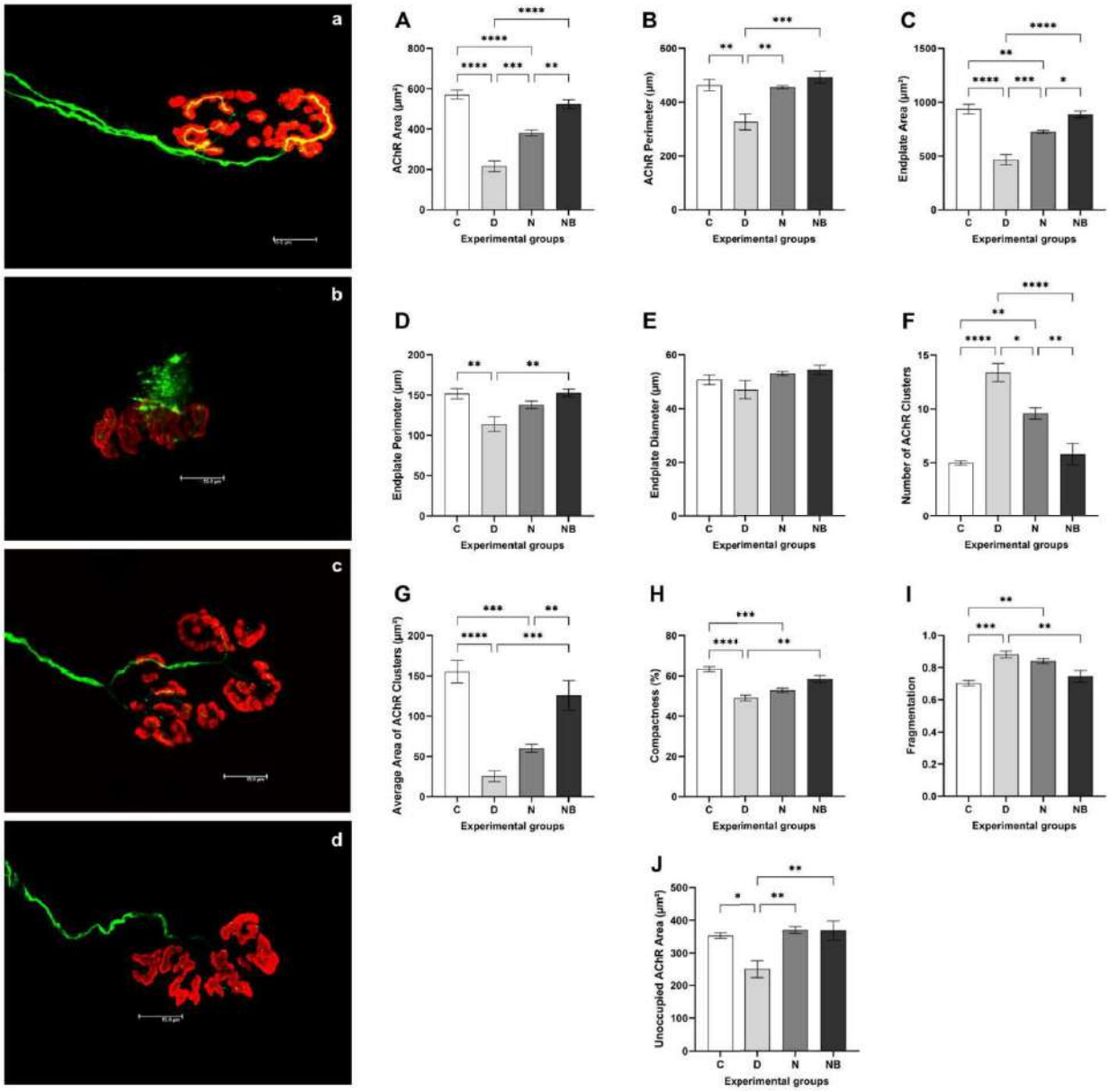

Figure 1. Confocal microscopy of acetylcholine receptors (in red) and nerve terminals (in green), according to experimental groups: a- Control group (C), b- Denervated group (D), c- Neurorrhaphy group (N), d- Neurorrhaphy + fibrin biopolymer group (NB). 63x magnification, zoom 2.

Figure 2. Graphics of NMJ analyses using NMJ-morph. Area (A) and perimeter (B) of AChRs, area (C), perimeter (D) and diameter (E) of the motor endplate, number (F) and average area (G) of AChR clusters, compactness (H) and fragmentation (I) indices, and unoccupied area by AChRs (J). Values expressed as the mean ± standard error of the mean. One-Way ANOVA test followed by post-test of multiple comparisons of Tukey (*p < 0.05; **p < 0.01; ***p < 0.001; ****p < 0.0001).

Analysis Of Oral Supplementation With Turmeric (*Curcuma longa* L.) Associated With Stair Climbing Resistance Exercise On The Connective Tissue Of The Extensor Digitorum Longus Muscle In a Rheumatoid Arthritis Model

Mikael Gerson Kuhn[1]*, Leticia Massochim da Silva[1], Flávia Heloísa da Silva[1], Maiara Cristina Lima de Jesus[1], Michele Gossler[1], Rafaella Cristina Lima da Silva[1], Gladson Ricardo Flor Bertolini[1], Lucinéia de Fátima Chasko Ribeiro[1], Ana Tereza Bittencourt Guimarães[1], Marcia Miranda Torrejais[1]

[1]Graduate Program in Biosciences and Health – Universidade Estadual do Oeste do Paraná, Cascavel, Paraná, Brazil.
*mikaelgerson@hotmail.com

Rheumatoid arthritis (RA) is a chronic, systemic, autoimmune inflammatory disease that affects approximately 1% of the global population [1]. Commonly prescribed treatments include anti-inflammatory drugs, analgesics, glucocorticoids, and disease-modifying antirheumatic drugs (DMARDs) [2,3]. Although these medications help control symptoms, they do not prevent disease progression and may cause adverse effects such as dependency, drowsiness, sensory depression, and gastrointestinal complications, including ulcers and bleeding [4,5]. In this context, complementary therapies such as turmeric supplementation and physical exercise—especially resistance training—have gained attention as integrative strategies in RA management [6]. This study aimed to evaluate the morphological and morphometric effects of turmeric associated with stair climbing resistance exercise (SCRE) on the connective tissue of the extensor digitorum longus (EDL) muscle in *Wistar* rats with induced RA. Thirty-one three-month-old rats were randomly assigned to five groups: Control group (CG, n = 6); RA group (RAG, n = 6); RA group treated with turmeric (RATMG, n = 6); RA group submitted to SCRE (RAEXG, n = 6); and RA group treated with both turmeric and SCRE (RATMEXG, n = 7). RA was induced by intra-articular injection of Complete Freund's Adjuvant [7]. The dry turmeric extract was administered by oral gavage at a dose of 100 mg/kg/day for 14 consecutive days [8]. The SCRE protocol consisted of progressive loads based on body weight (25%, 35%, and 50%) with a fixed training volume of 3 sets of 8 repetitions [9]. Euthanasia was performed on day 24 of the experiment, corresponding to day 15 after RA induction. The EDL muscle was collected, processed, and stained with Masson's Trichrome [10] for morphological and morphometric analysis of connective tissue. Connective tissue was observed in both the perimysium and endomysium across all groups. Although the morphometric analysis did not reveal statistically significant differences in the amount of connective tissue between the groups (Fig. 1F), the morphological evaluation showed structural disorganization in the RAG and RATMG groups (Figs. 1B–1E). In contrast, the RAEXG and RATMEXG groups presented milder alterations, suggesting that SCRE may help mitigate the disorganized deposition of collagen fibers by fibroblasts. It was concluded that, although the amount of connective tissue was not significantly different between groups, morphological disorganization was evident in the muscles affected by RA, and this disorganization was attenuated by SCRE. Turmeric alone did not show a relevant effect on preserving the connective tissue architecture.

[1] World Health Organization, Rev. Panam. Salud Publica, 16 (2004) 218–221.
[2] M.B. Bértolo, Rev. Bras. Reumatol., 47 (2007).
[3] J.M. Torpy et al., JAMA, 305 (2011) 1.
[4] L.F.S. Passos, OPAS/OMS - Representação Brasil, 1 (2016) 1–7.
[5] M. Benucci, J. Inflamm. Res., 11 (2017) 247–252.
[6] C.F. Coelho, R.C. Burini, Rev. Nutr., 22 (2009) 937–946.

[7] R.P. Gomes, E. Bressan, T.M. Silva, M.S. Gevaerd, C.R. Tonussi, C.D. Domenech, Rev. Bras. Reumatol. 54 (2) (2014) 83–89.
[8] N. Nonose et al., Acta Cir. Bras. 29 (11) (2014) 727–734.
[9] C.D.S. Jacob et al., Eur. J. Histochem. 66 (1) (2022) 3356.
[10] J.D. Bancroft, A. Stevens, Theory and Practice of Histological Techniques, 2nd ed., Churchill Livingstone, London, 1990.

Figure 1. Photomicrographs of the ELD muscle of four-month-old *Wistar* rats. Transverse section. Masson's Trichrome staining. Control group (CG); Rheumatoid arthritis group (RAG); RA group treated with turmeric (RATMG); RA group submitted to stair climbing resistance exercise (RAEXG); and RA group treated with both turmeric and exercise (RATMEXG). **A, B, C, D, and E:** Observe the connective tissue in the perimysium (yellow arrow) and endomysium (pink arrow). **F:** Graph showing the estimated percentage of connective tissue.

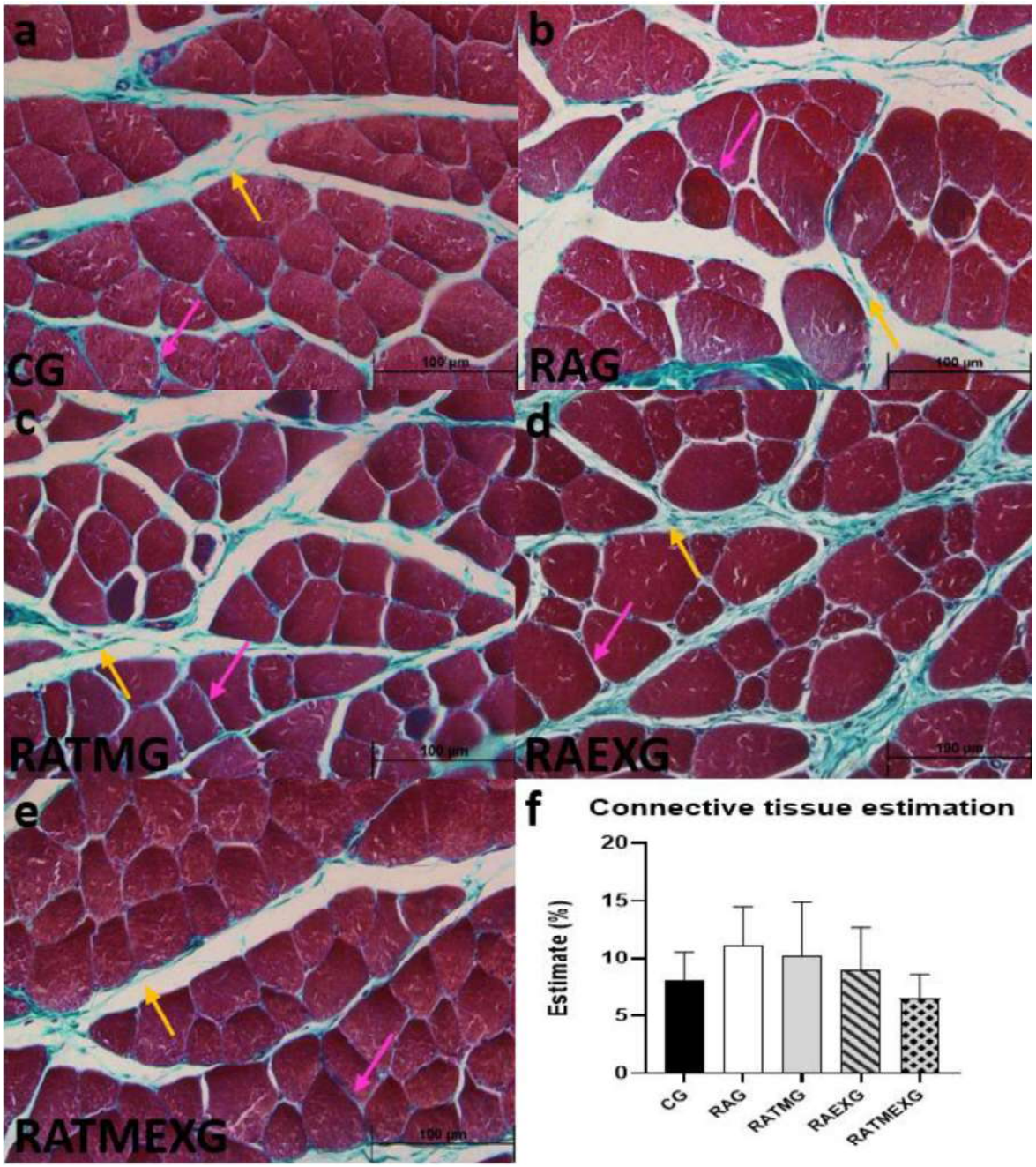

Biochemical analysis and morphometric evaluation of ovaries from diabetic rats treated with lectin from the bark of *Crataeva tapia* (Crata BL)

Ana Vitoria Ferreira dos Santos[1]*, Giovanna Laura de Lima Borba[1], Suellen Rozy da Silva Medeiros[1], Alison Jose da Silva[1], Sara Vitória de Oliveira Costa[1], Raissa Gomes de França[1], Glenison de Rocha Duarte[1], Thaynara Caseli dos Santos[1], Elba Verônica Matoso Maciel de Carvalho[2], Bruno Mendes Tenorio[1], Fernanda das Chagas Angelo Mendes Tenorio[1].

[1] Department of Histology and Embryology, Federal University of Pernambuco (DHE-UFPE)
[2] Department of Biochemistry, Federal University of Pernambuco (DBIOq - UFPE)
* vitoria.fsantos@ufpe.br

Fertility depends on several metabolic, hormonal, and biochemical factors [1]. Type 1 diabetes mellitus is a chronic disease resulting from metabolic defects that can significantly impact the female reproductive system [2]. In parallel, lectin derived from the bark of Crataeva tapia (Crata BL) shows promise in aiding the treatment of diabetes due to its antioxidant, tissue-modulating, anti-inflammatory, and hypoglycemic properties [3]. Therefore, this experimental study aimed to analyze the biochemistry and morphometry of the ovaries of diabetic rats treated with Crata BL. For this study, 20 Wistar albino rats (CEUA-136/2019) were divided into four groups of five animals each: Group I (CG) – Control Rats; Group II (GD) – Diabetic Rats; Group III (GDL) – Diabetic Rats treated with Crata BL; and Group IV (GL) – Non-diabetic rats treated with Crata BL. Diabetes was induced by a single intraperitoneal dose of streptozotocin (50 mg/kg of body weight). Diabetes was confirmed by measuring glucose levels on days 3 and 7 after streptozotocin administration. Lectin treatment involved a single intraperitoneal application on day 1 (5 mg/kg of body weight) on day 8 after diabetes confirmation. On day 15 after treatment, the females were euthanized, blood was collected by cardiac puncture, and their ovaries were harvested, fixed, processed, and stained with hematoxylin-eosin (HE). Photomicrographs of the slides were subsequently taken and analyzed using ImageJ software to quantify corpus luteum cells based on the following parameters: area, perimeter, circularity, cell number, solidity, maximum diameter, and mean diameter. Morphometric analysis of the ovary revealed no significant differences between the experimental groups in terms of perimeter, circularity, solidity, or mean diameter. However, the GD group had a smaller area and a reduced number of cells compared to the other groups, while the GDL group resembled the control group. Regarding maximum diameter, the GD, GDL, and GL groups presented higher values compared to the control group (Table 1). Regarding biochemical parameters, the GD group presented higher blood glucose levels, while the GDL group presented levels similar to the control group. AST, urea, and creatinine levels were significantly elevated in the GD group compared to the control group (Table 2). In conclusion, diabetes mellitus can alter the parameters of ovarian structures crucial for maintaining reproductive balance. Our findings suggest that Crataeva tapia (CrataBL), due to its hypoglycemic properties, may aid in the treatment of diabetes.

[1] DING, Guo-Lian et al. The effects of diabetes on male fertility and epigenetic regulation during spermatogenesis. **Asian journal of andrology**, v. 17, n. 6, p. 948-953, 2015.
[2] Wellons MF et al. Ovarian aging in women with diabetes: An overview. Maturitas [Internet]. 2017 Feb [cited 2022 May 16]; 96:109–13.
[3] da Rocha et al. Lectin from Crataeva tapia Bark Improves Tissue Damages and Plasma Hyperglycemia in Alloxan-Induced Diabetic Mice. *Evidence-based*

complementary and alternative medicine : eCAM. 2013;2013:869305.

Table 1. Mean ± standard deviation of morphometric parameters from the analysis of Corpora Lutea in experimental groups.

Parameters	GROUPS				
	Control	**GD**	**GDL**	**GL**	**P***
Area	757677.7± 642585.5a	342517.8± 13391.4b	592518.1± 283292.8a	626812.4± 194667.0a	0.016*
Perimeter	2999.9± 14449.1	2414.7± 1311.5	2795.6± 696.3	2968.0± 436	0.509
Circularity	754.7± 30.3	868.2± 111.5	879.1± 41.7	885.3± 63.0	0,156
Cell Quantity	266.75± 23.05a	136.75± 25.06b	229.62± 14.70a	227± 14.79a	0,000*
Solidity	0,97±0,01	0,97±0,01	0,96±0,03	0,96±0,03	0,179
Average Diameter	892.63± 448.89	636.09± 381.6	878.90± 240.39	852.09± 202.52	0.216
Maximum Diameter	515.2±231.7a	802.5±129.1b	707.3±319.0b	891.9±128.1b	0,029*

Means followed by different letters within a column differ significantly. This was determined by the non-parametric Kruskal-Wallis test, followed by Dunn's post-hoc test (p≤0,05).

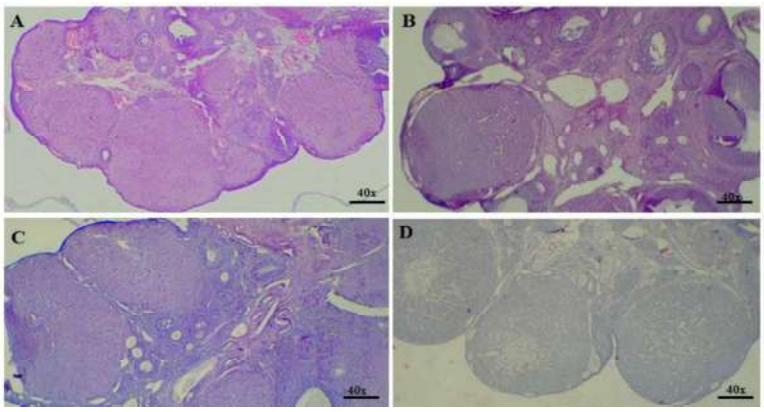

Figure 1: Photomicrograph of the ovary of rats in the experimental groups. A- Control Group; B- Diabetic Group; C- Diabetic Group treated with Lectin; D- Lectin Group. Hematoxylin-eosin staining. AU 40x.

Table 2. Mean ± standard deviation of the morphometric parameters of the analysis of the Corpus Luteum of the experimental groups

Parameters	GROUPS				
	Control	**GD**	**GDL**	**GL**	**P***
Glucose	96.0±5.83a	285.75±77.05a	105.00±12.49a	90.75±7.93	0,01
ALT	61.25±12.28	70.05±6.65	64.66±22.94	59.33±15.50	0,67
AST	23.75±2.21a	211.25±13.74b	112.33±17.39a	30.66±2.51a	0,01
Urea	48.75±5.56a	76.25±9.21b	39.00±3.60a	40.00±5.29a	0,01
Creatinine	0.55±0.05a	1.10±0.08b	0.46±0.15a	0.53±0.05b	0.03

Means followed by different letters within a column differ significantly. This was determined by the non-parametric Kruskal-Wallis test, followed by Dunn's post-hoc test (p≤0,05

Morphometric Analysis of the Lungs of Rats Subjected to Protein Malnutrition during Mid-Gestation and Supplemented with Cannabidiol Nanoemulsion

Maria Eduarda Carneiro de Lima[1*], Weslleyanne Millena da Silva Costa[1], Glenison da Rocha Duarte, Thaynara Caseli dos Santos[1], José Abel Pessôa Neto[1], Raissa Gomes de França[1], Maria Clara Chár Gomes[1], Elba Verônica Matoso Maciel de Carvalho[2], Bruno Mendes Tenório[1], Fernanda das Chagas Angelo Mendes Tenório[1]

[1]Federal University of Pernambuco, Department of Histology and Embryology,
[2]Federal University of Pernambuco, Department of Biochemistry
Corresponding Author's Email: eduarda.carneirolima@ufpe.br[1]*

Nutrition plays an important role in the proper functioning of metabolism [1], and a protein-restricted diet can lead to harmful nutritional disturbances [2]. During pregnancy, protein restriction induces increased oxidative stress and inflammatory responses in the lungs due to decreased bioavailability of amino acids such as glutathione, resulting in the appearance of fibrotic areas in the lungs and thickening of the alveolar septa [3]. Consequently, the integrity of the lung interstitial compartment, essential for adequate gas exchange, is compromised [4]. Given the damage caused by protein deficiency, the use of a phytotherapeutic compound such as cannabidiol (CBD), derived from *Cannabis sativa*, has been widely employed due to its antioxidant and anti-inflammatory properties [5]. It is known that repeated doses of CBD under inflammatory conditions increase glutathione peroxidase and reductase activity, also supporting other antioxidant enzymes, preventing the reduction of microelements that decrease under pathological conditions and are necessary for enzymatic activity [6]. Furthermore, CBD has affinity for other receptors, such as 5-HT1A, increasing AEA levels, acting as a membrane antioxidant by scavenging ROS and neutralizing phospholipid peroxidation [7]. Therefore, the objective of this study was to perform a morphometric analysis of the lungs of rats subjected to protein malnutrition during mid-gestation and treated with cannabidiol nanoemulsion. For this purpose, 24 (n = 8) pregnant Wistar albino rats, with pregnancy induced by natural mating at the beginning of the night, were divided into the following groups after confirmation of day 1 of gestation through the presence of spermatozoa in the vaginal smear: Group I – control rats receiving a normoproteic diet during gestation; Group II – rats subjected to protein restriction during gestation; Group III – rats subjected to protein restriction during gestation and treated with 10 mg/kg/day of cannabidiol nanoemulsion (Ethics Committee: 0053/2024). The females were treated with the nanoemulsion and the hypoproteic diet ad libitum until the 14th day of gestation. At the end of the experiment, the rats were anesthetized, and the lungs were collected, fixed in 10% buffered formalin for 48 hours, then dissected and processed for paraffin embedding. The resulting blocks were cut into 3 µm-thick sections, stained with Hematoxylin-Eosin (H&E), and photographed under a light microscope. Fifteen fields from each slide of each animal were analyzed (120 images per experimental group). The images were processed using ImageJ (National Institutes of Health – NIH, USA) to quantify

pulmonary alveoli based on the following parameters: area, perimeter, width, height, angle, circularity, and solidity. Data were tested for normality using the Shapiro-Wilk test. Subsequently, the non-parametric Kruskal-Wallis test followed by Dunn's post-hoc test was applied, with results expressed as mean ± standard deviation. Differences were considered statistically significant when $p < 0.05$. Analyses were performed using GraphPad Prism 8®. Regarding the parameters analyzed through morphometry, it was observed that the Diet group presented higher mean values for area, perimeter, width, height, circularity, and solidity compared to the Control group. However, the Diet + CBD group, for most parameters, showed a reversal of this pattern, achieving values similar to the Control, except for width and height, which were lower than Control, and solidity, which was similar to the Diet group. Thus, it can be concluded that a protein-deficient diet may affect lung morphometric aspects, potentially altering its function, whereas cannabidiol treatment may be effective in promoting regeneration and restructuring of most morphometric parameters during gestation.

REFERENCES

[1] L.C. Raggi et al., *Am. J. Kidney Dis.* 81 (2023).

[2] A. Ribeiro et al., *Clin. Nutr.* 42 (2023).

[3] N. E. Marshall et al., *American Journal of Obstetrics and Gynecology* 226 (2022).

[4] M. P. Prendecki et al., Eur. J. Clin. Invest. 53 (2023).

[5] A. Kicman, M. Toczek, The effects of cannabidiol, a non-intoxicating compound of cannabis, on the cardiovascular system in health and disease, *Int. J. Mol. Sci.* 21 (2020).

[6] L.C. Raggi et al., Eur. J. Clin. Invest. 53 (2023).

[7] S. Atalay et al., Antioxidants 9 (2020).

Table 01. Alveolar morphometry of the lungs from the experimental groups.

Parameters	Group I	Group II	Group III	p
Area	293.6± 179.6	670.0±186.4*	352.3± 147.0	0.02
Perimeter	291.4± 111.1	311.4±118.9*	277.3±117.2	0.05
Width	44.01±17.8	68.5±22.9*	23.4±5.9*	0.03
Height	45.6±17.9	72.6±12.6*	20.8±7.0*	0.04
Angle	81.80±50.71	77.20±59.31	82.34±45.17	0.81
Circularity	0.133± 0.033	0.169±0.030*	0.110±0.045	0.01
Solidity	0.627±0.042*	0.910±0.054*	0.906±0.033*	0.01

Reference: By the author.
Means followed by different letters within a column differ significantly. This was determined by the non-parametric Kruskal-Wallis test, followed by Dunn's post-hoc test ($p \leq 0,05$).

Annexin A1 Deficiency Attenuates Renal Injury in a Streptozotocin-Induced Model of Diabetic Nephropathy

Larissa Suzuki[1], Diego Dias dos Santos[1], Laura Santana de Chiara[1], Rafael André da Silva[2], Luiz Philipe de Souza Ferreira[1], Caroline Silvério Faria[3], Kátia de Vasconcelos[1], Cristiane Damas Gil[1*].

[1]Department of Morphology and Genetics, Escola Paulista de Medicina (EPM), Universidade Federal de São Paulo (UNIFESP), [2]Biosciences Graduate Program, Instituto de Biociências, Letras e Ciências Exatas, Universidade Estadual Paulista – UNESP, [3]Medical Research Laboratory (LIM03), Hospital das Clínicas (HCFMUSP), Faculdade de Medicina, Universidade de São Paulo (USP).
*cristiane.gil@unifesp.br

Diabetic nephropathy (DN) is one of the most severe complications of diabetes mellitus (DM), in which oxidative stress plays a central pathogenic role. Annexin A1 (AnxA1) is a 37-kDa anti-inflammatory and pro-resolving protein implicated in inflammation resolution and apoptosis; however, its contribution to renal redox balance remains poorly understood. This study investigated the impact of AnxA1 deficiency on renal morphology, function, and oxidative stress using a streptozotocin (STZ)-induced model of type 1 DM. Wild-type (WT) and AnxA1 knockout ($AnxA1^{-/-}$) male C57BL/6 mice received STZ injections for five consecutive days and were analyzed 90 days post-induction [1]. Both diabetic groups developed sustained hyperglycemia; however, $AnxA1^{-/-}$ diabetic mice exhibited significantly lower blood glucose levels and milder weight loss than WT diabetic mice. Renal function parameters revealed increased serum urea and creatinine in WT DM animals, indicating impaired renal clearance. In contrast, these alterations were less pronounced in $AnxA1^{-/-}$ DM mice, possibly due to compensatory glomerular hyperfiltration and hypertrophy [2]. Histological analyses showed tubular degeneration and cytoplasmic vacuolization in both diabetic groups (Figure 1A–H), with significantly elevated histopathological scores in diabetic versus control animals (Figure 1M). Additionally, WT DM mice exhibited a marked increase in glomerular area, perimeter, and Bowman's space. Interestingly, renal fibrosis was more severe in $AnxA1^{-/-}$ DM mice compared to their respective controls and WT DM animals (Figure 1I–L, N), suggesting that the absence of AnxA1 may exacerbate fibrotic remodeling, despite milder functional decline. Oxidative stress analysis revealed that renal levels of superoxide dismutase and catalase were significantly higher in WT DM mice than in $AnxA1^{-/-}$ DM animals. Since reduced antioxidant enzyme levels are associated with progression of renal damage [3,4], this may indicate that $AnxA1^{-/-}$ kidneys have diminished redox defense. Western blotting showed decreased mitochondrial OXPHOS complex I levels in $AnxA1^{-/-}$ DM mice, while complexes III and V were elevated. Among MAPK pathway components, phosphorylated p38 and JNK were upregulated in diabetic mice, with no significant changes in ERK. Regarding formyl peptide receptors, Fpr1 expression was unaltered in Western blotting, while Fpr2 levels decreased in WT DM compared to controls. Immunohistochemistry notably revealed increased cortical expression of both Fpr1 and Fpr2 in $AnxA1^{-/-}$ DM kidneys, in contrast to whole-tissue western blot findings—likely reflecting regional expression differences. Immunofluorescence confirmed coexpression of AnxA1 with both Fpr1 and Fpr2, supporting a possible interaction in renal signaling pathways. Altogether, these findings demonstrate a complex and context-dependent role for AnxA1 in the pathogenesis of diabetic nephropathy. While its absence appears to partially protect against functional impairment and oxidative stress, it may simultaneously enhance fibrotic responses. These dual effects highlight the intricate balance mediated by AnxA1 in the diabetic kidney. Future studies are warranted to dissect the molecular mechanisms underlying these observations and to explore whether modulation of the AnxA1/FPR axis could offer novel therapeutic avenues for diabetic nephropathy.

[1] B.M. Carro et al., International Journal of Molecular Sciences, 24 (2023) 10309.
[2] M.M. Rana et al., Journal of Biomedical Optics, 18 (2013) 087004.
[3] H. Fujita et al., Journal of the American Society Nephrology, 20 (2009) 1303.
[4] Y.A. Hong.; C.H. Park., Antioxidants 10 (2021) 130.
[5] This research was supported by FAPESP (2024/07185-0) and CNPq (308524/2022-5).

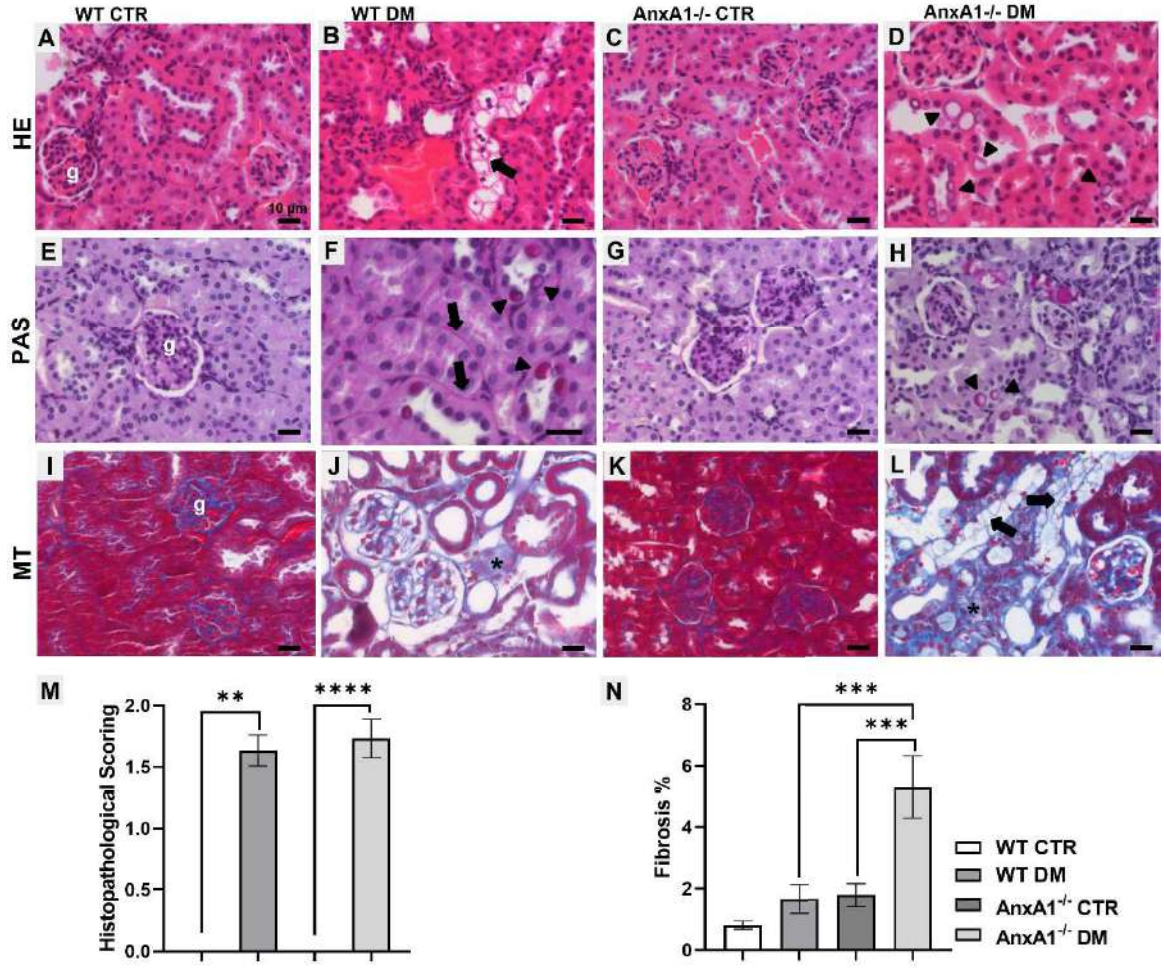

Figure 1. Histopathological renal analysis in wild-type (AnxA1$^{+/+}$) and annexin A1 knockout (AnxA1$^{-/-}$) mice. Morphological alterations in DM kidneys when compared with their respective CTR. Cytoplasmic vacuolization (D, F, H) in tubular epithelial cells, tubular degeneration (B, L), basal membrane thickening (F) and fibrosis (J, L). Analysis of histopathological scoring in renal cortex for vacuolization and degeneration (M) showed that DM had a significance over the CTR, in both genotypes. Fibrosis (%) was significantly higher in AnxA1$^{-/-}$ DM than AnxA1$^{-/-}$ CTR and WT DM (H). Stain: Hematoxylin and Eosin - HE (Figure A-D), Periodic Acid-Schiff – PAS (Figure E-H) and Masson's Trichrome - MT (Figure I-L). Bars: 10 µm. Data are shown as mean ± SEM of histopathological scoring and fibrosis (%). **p<0,01, ***p<0.001, ****p<0.0001 (M: Kruskal-Wallis, Dunn post-test. N: ANOVA, Bonferroni post-test).

Annexin A1 Modulates Cardiac and Reproductive Outcomes in Female Mice with Streptozotocin-Induced Diabetes

Renata Ramos Vieira[1*], Karina Carla de Paula Medeiros[2], Diego Dias dos Santos[1], José Marcos Sanches[3], Sarah Bezerra Brum da Silva[1], Joaquim Soares de Almeida[1], Samara Urban De Oliva[1], Cristiane Damas Gil[1]

(1) Departamento de Morfologia e Genética, Escola Paulista de Medicina, Universidade Federal de São Paulo, SP, Brasil.
(2) Departamento de Morfologia, Centro de Biociências, Universidade federal do rio grande do Norte, Natal, RN, Brasil.
(3) Centro de Ciências Naturais e Humanas, Universidade Federal do ABC, Santo André, SP, Brasil.
*renata.vieira24@unifesp.br

Diabetes mellitus (DM) is a chronic disease that affects millions of people worldwide and is strongly associated with an increased risk of coronary artery disease. DM promotes major hormonal changes, including a decline in estradiol levels, which further contributes to cardiovascular risk [1]. In this context, Annexin A1 (AnxA1) emerges as a protein with well-established anti-inflammatory actions, known to regulate several steps of the inflammatory response and exert cardioprotective effects [2, 3]. However, the role of AnxA1 in DM-associated cardiac dysfunction remains unclear. This study aimed to investigate the role of AnxA1 in diabetic cardiomyopathy using female mice. DM was induced in wild-type ($AnxA1^{+/+}$) and AnxA1 knockout ($AnxA1^{-/-}$) female mice through intraperitoneal administration of streptozotocin (STZ, 65 mg/kg) for five consecutive days. Control animals (Sham) received only vehicle (0.1 M sodium citrate buffer, pH 4.5). Body weight and blood glucose levels were monitored at weeks 4, 8, 12, and 16 after DM induction. Cardiac function was assessed by echocardiography, and heart and blood samples were collected and processed for further analyses. STZ administration effectively induced DM in both $AnxA1^{+/+}$ and $AnxA1^{-/-}$ female mice, as indicated by blood glucose levels above 275 mg/dL from day 30 onwards and reduced body weight in DM groups compared to their respective controls (Figure 1A, B). Estrous cycle analysis revealed that DM impaired reproductive cyclicity, increasing the time spent in diestrus and reducing proliferative phases. These effects were more pronounced in $AnxA1^{-/-}$ mice, suggesting that the absence of this protein worsens DM-induced estrous dysfunction. Cardiac function was impaired only in $AnxA1^{+/+}$ diabetic mice, which exhibited significant reductions in ejection fraction (EF%; 35.10±1.7 vs. 27.32±1.8) and fractional shortening (FS%; 16.63±0.9 vs. 12.62±0.8) compared to controls. These changes were not observed in $AnxA1^{-/-}$ diabetic mice, suggesting that AnxA1 deficiency may attenuate DM-induced cardiac dysfunction. No changes were observed in heart weight relative to body weight (Figure 1G). Histological analysis showed a significant increase in cardiomyocyte perimeter in diabetic mice of both genotypes (Figure 1C–F, H). These findings suggest that although the absence of AnxA1 exacerbates DM-induced reproductive dysfunction, it appears to protect against cardiac contractile impairment, indicating a dual and context-dependent role of AnxA1 in the pathophysiology of diabetes in females. Future studies, including models of estrogen depletion, will help elucidate the endogenous effects of

AnxA1 and its interaction with hormonal status, further defining its potential as a therapeutic target in diabetic cardiomyopathy.

[1] S.R. Mishra et al., BJOG 128(5) (2021) 809-821.
[2] Q. You et al., Adv Sci (Weinh) 11(15) (2024) e2307040.
[3] J. Chen et al., 118(38) (2021) e2020385118.
[4] This research was supported by Capes (Code 001), FAPESP (2024/14322-4), and CNPq (308524/2022-5).

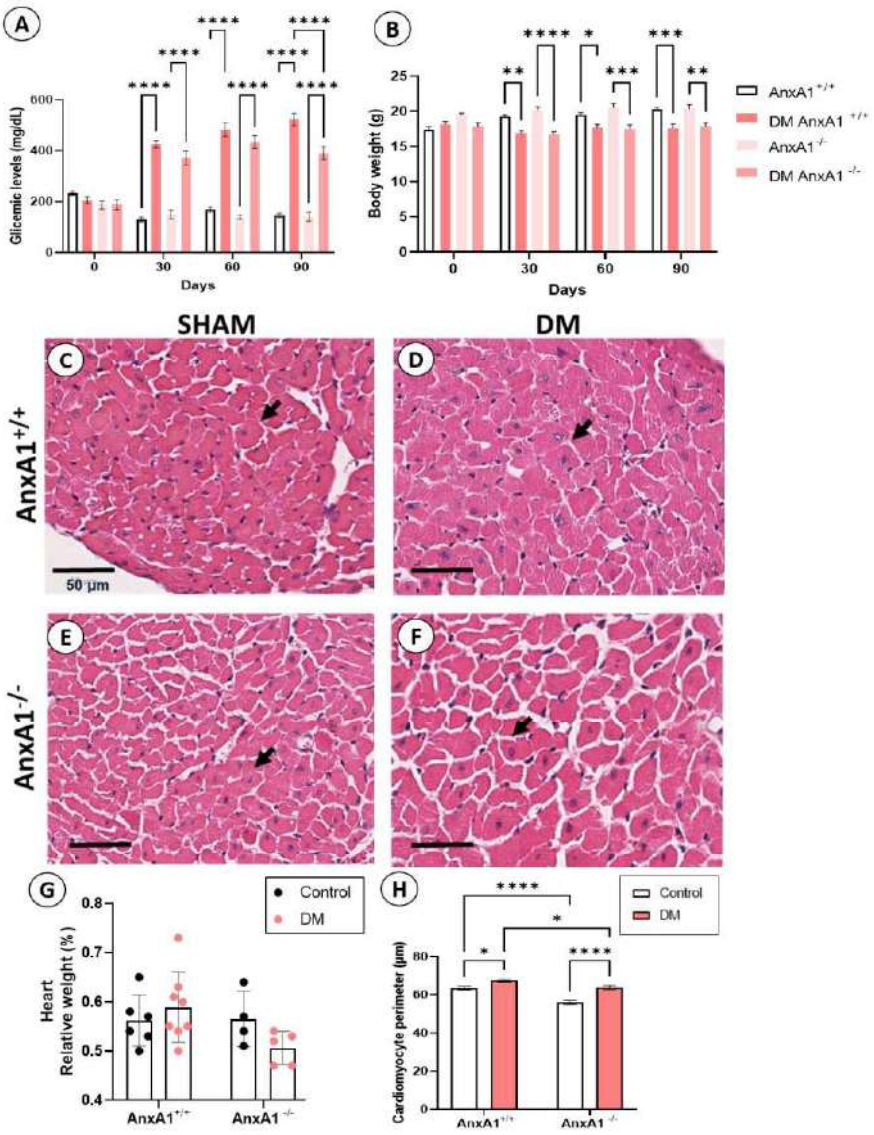

Figure 1. Characterization of the Streptozotocin-Induced Diabetes Mellitus Model. **A:** Blood glucose levels (mg/dL). Both DM AnxA1$^{+/+}$ and DM AnxA1$^{-/-}$ groups showed elevated glycemia compared to their respective control groups on days 30, 60, and 90. **B:** Body weight (g). **C–F:** Representative images of cardiomyocytes (arrows) under different experimental conditions. Staining: hematoxylin and eosin. Scale bars: 50 µm. **G:** Relative heart weight (%). **H:** Cardiomyocyte perimeter (µm). DM AnxA1$^{+/+}$ and DM AnxA1$^{-/-}$ mice exhibited a significant increase in cardiomyocyte size compared to their respective controls. Data are presented as mean ± SEM (n = 5–8 animals/group). *p<0.05, **p<0.01, ***p<0.001, ****p<0.0001 (Two-way ANOVA, Bonferroni post hoc test).

Application of multifractal computational methods in the detection of changes in collagen deposition in glomeruli after renal injury due to ureteral obstruction.

Renan Gabriel da Silva Ferreira[1]*, Jennyfer Martins de Carvalho[2], Jadyel Serdelle Guedes do Nascimento[1], Isaque Bertoldo Santos da Silva[1], Alison Jose da Silva[1], Ana Vitoria Ferreira do Santos[1], Carlos Eduardo da Silva[1], Elba Veronica Maciel Marciel Matoso de Carvalho[2] , Sara Vitoria de Oliveira Costa[1] , Maria Clara Char[1], Ryan Cristian da Silva[2], Fernanda das Chagas Angelo Mendes Tenorio[1], Bruno Mendes Tenorio[1].

[1] Federal University of Pernambuco, Department of Histology and Embryology. Recife, Pernambuco - Brazil.

[2] Federal University of Pernambuco, Department of Biochemistry. Recife, Pernambuco – Brazil.

*renan.gabriel@ufpe.br

Chronic Kidney Disease (CKD) is a progressive and irreversible condition that impairs the structure and function of the kidneys, affecting millions of people worldwide [1]. CKD is characterized by a reduction in glomerular filtration rate (<60 mL/min/1.73 m²) and/or persistent proteinuria, with interstitial fibrosis, glomerulosclerosis, and tubular atrophy, resulting in functional loss [2]. Digital analysis of histological images has emerged as a promising quantitative tool to detect microscopic alterations. In this context, the multifractal method can use algorithms applicable to the development of software and artificial intelligence to quantify the complexity in the spatial distribution of tissue components that are difficult to evaluate by human observation [3]. Thus, the present study aimed to use multifractality to quantify the complexity of collagen deposition in renal glomeruli injured by obstruction. The protocol was approved by the Ethics Committee of UFPE (No. 1152019). Adult rats were subjected to unilateral ureteral obstruction (UUO, n = 5) and compared to the control group (SHAM, n = 5). After 10 days, kidneys were collected, fixed, embedded in paraffin, sectioned (5 μm), and stained with picrosirius red. In each experimental group, 100 images were obtained (20 per animal) with the renal glomeruli centered; these images were cropped to 100×100 pixels. Images of glomeruli were processed using ImageJ software (National Institutes of Health - NIH, USA) with a macro developed in our laboratory, and then analyzed using the FracLac Plugin (A. Karperien, Charles Sturt University, Australia), as described by dos Santos et al. (2025) [3]. The multifractal analysis revealed statistically significant differences between the SHAM and UUO groups in all evaluated parameters: Dq, α, and f(α) for all values from q+1 to q+5 (Table 1). These results indicate an increase in the structural complexity of collagen deposition in the glomeruli of kidneys injured by ureteral obstruction. The parameters Dq, α e f(α) reflect the spatial heterogeneity and structural complexity of collagen deposition in the glomeruli. Kidney damage is commonly assessed using only parameters that measure the amount of space occupied by the glomerulus (area). However, diseases can cause changes in the shape of the structure (how the space is occupied) and not in the total amount of space occupied,

that is, in its area [4]. In conclusion, the multifractal parameters Dq, α and f(α) can be useful markers for software and artificial intelligence to detect changes in collagen deposition in the glomeruli after kidney injury due to ureteral obstruction.

[1] A. Francis et al., *Nat. Rev. Nephrol.* 20 (2024) 473–485. https://doi.org/10.1038/s41581-024-00820-6.
[2] G. Remuzzi, T. Bertani, *N. Engl. J. Med.* 339 (1998) 1448–1456.
[3] A.V.F. dos Santos, R.G. da Silva Ferreira, F. das Chagas Angelo Mendes Tenorio et al., Histochem. Cell Biol. 163 (2025) 1. https://doi.org/10.1007/s00418-024-02336-3.
[4] I.O. Melo et al., *Acta Histochem.* 124(7) (2022) 151949. https://doi.org/10.1016/j.acthis.2022.151949

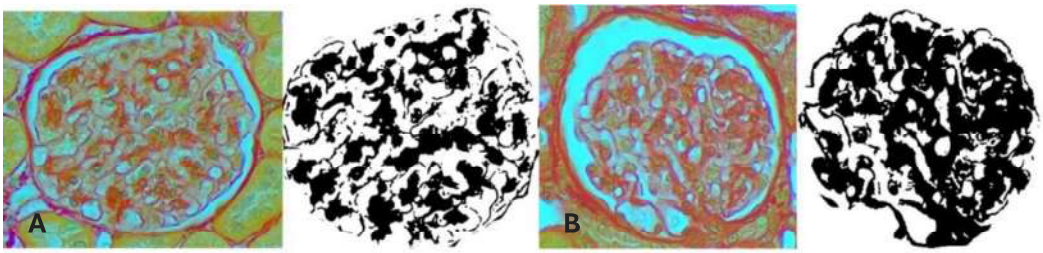

Figure 1. Photomicrographs of the glomerulus in the renal cortex from control rat stained with picrosirius red (A) and glomeruli of rat subjected to ureteral obstruction (B). On the right, binary segmentation of collagen deposition in renal glomeruli performed in ImageJ for multifractal analysis.

Table 1. Multifractal parameters (Dq, α and f(α)) obtained from the analysis of renal glomeruli from control rats (SHAM, n = 5) and rats subjected to ureteral obstruction (UUO, n = 5). Comparisons between groups were performed using the Mann–Whitney test ($p < 0.05$).

Dq	SHAM	UUO	T	p
q+1	1.707	1.777	-5.468	0.0003*
q+2	1.694	1.780	-5.655	0.0002*
q+3	1.687	1.783	-5.793	0.0002*
q+4	1.682	1.784	-5.888	0.0002*
q+5	1.679	1.786	-5.95	0.0002*
Alfa (α)	SHAM	UUO	T	p
q+1	1.707	1.777	-8.002	0.0005*
q+2	1.685	1.783	-5.779	0.0002*
q+3	1.675	1.787	-5.934	0.0002*
q+4	1.670	1.789	-6.011	0.0002*
q+5	1.667	1.791	-6.041	0.0002*
F(α)	SHAM	UUO	T	p
q+1	1.707	1.777	-5.569	0.0003*
q+2	1.676	1.786	-5.838	0.0002*
q+3	1.652	1.795	-5.922	0.0002*
q+4	1.635	1.804	-5.830	0.0002*
q+5	1.617	1.818	-5.672	0.0002*

*Indicates a statistically significant difference.

Beneficial Effect Of Treatment With Capybara Oil Nanoemulsion On Liver Tissue Of Obese Mice

Alves L.L.[1,2]*, Campos M.P.[1], Pereira P.G.[1], Azevedo C.G[1], Ciambarella B.T.[1], Nascimento A.L.R[1,2], Gomes P.F.[1], Andrade C.B.V.[1,2], Moraes A.C.N.[1,2,3], Pereira J.G.[1], Pereira V.L.[1], Ferrarini S.T.[4], Silva J.F.R.[1,2], Rabelo K.[1,2], Carvalho J.J[1,2].

[1]Ultrastructure and Tissue Biology Laboratory, Institute of Biology, UERJ, RJ, Brazil, [2]Electron Microscopy Laboratory of Rio de Janeiro State University, Institute of Biology, UERJ, RJ, Brazil, [3]Electron Microscopy Laboratory of Biology Institute, UFF, RJ, Brazil, [4]Pharmaceutical Nanotechnology Laboratory, UFMT, Sinop, MT, Brazil, *lucianalontro@gmail.com

Obesity is a chronic disease characterized by excess body fat that is harmful to health [1] and may be associated with several diseases, such as non-alcoholic fatty liver disease (NAFLD) [2]. According to the World Obesity Federation (WOF), in 2020, approximately 38% of the global population was overweight or obese, and it is estimated that this value will increase to more than 50% by 2035 [3]. Polyunsaturated fatty acids (PUFAs) are lipid mediators that have anti-inflammatory characteristics and can be found in animals and plants [4], with capybara oil (CO) being a promising source. PUFAs oxidize easily in contact with oxygen and, to avoid this situation, it is necessary to increase their bioavailability through pharmaceutical nanotechnology [5]. The objective of the study was to evaluate the effect of capybara oil nanoemulsion on NAFLD caused by obesity. For this purpose, 30 C57Bl/6 mice with 3-month-old male received a control (CD) or high-fat (HFD) diet for 18 weeks (CEUA UERJ nº 48/2022). From the 15th to the 18th week, the animals received treatment - via orogastric gavage - with placebo, nanoemulsion containing CO (100 mg/kg) (NE-CO), free CO (100 mg/kg) (CO), or white nanoemulsion (NE). The weight of the animals was measured weekly, and at the end of the experiment, the weight gain was determined. In addition, the liver was collected and stored for inclusion and preparation of histological sections with HE, Oil-red-O staining, immunostaining for CD68, TNF-α, IL-1β, IL-6, TGF-β and MMP9, and visualization of the hepatic ultrastructure. The animals fed the HF diet had an increase in body mass and weight gain. Structural damage was observed in the liver tissue, with an increase in lipid droplets and the degree of steatosis, as well as greater expression of CD68, TNF-α, IL-6, indicating an increase in the inflammatory process, and TGF-β and MMP9, indicating tissue remodeling. In addition, we observed a disorganization ultrastructural in the hepatic cytoarchitecture with loss of mitochondrial membrane integrity and the presence of endoplasmic reticulum with well-dilated cisternae. Treatment with NE-CO was not able to alter the animals' body weight, but when we analyzed weight gain, we observed a significant decrease compared to the HFD group. With regard to the other analyses, NE-CO was able to restore the alterations generated by HFD. Thus, showing that treatment with NE-CO has beneficial effects for the treatment of NAFLD [6].

[1] Prospective Studies Collaboration, The Lancet (2009) 373
[2] Marinho, PC et al., Evid Based Complement Alternat Med. (2018) 4956079.
[3] WOF (World Obesity Federation), World Obesity Atlas, 2023.
[4] Molfino A et al., Oxid Med Cell Longev. (2017) 5987082.
[5] Shukla, VK.; Perkins, EG., Lipids. (1991) 23-6.
[6] This research was supported by CNPq, CAPES, FAPERJ, and UERJ.

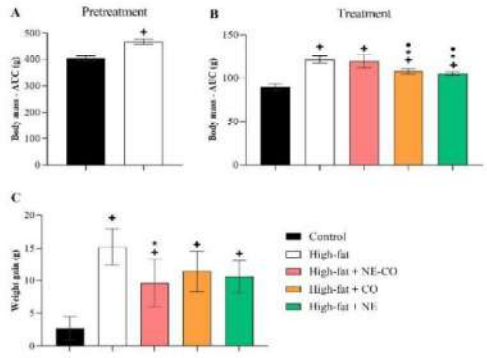

Figure 1. Analysis of body mass and weight gain of the experimental groups. (A) Assessment of the area under the curve (AUC) of body mass in the pre-treatment period (Weeks 0 to 14). **(B)** Assessment of the area under the curve (AUC) of body mass in the treatment period (Weeks 15 to 18). **(C)** Assessment of weight gain of the animals. +: different from CD group; *: different from HFD group; •: different from HFD + NE-CO group. Statistical analysis: Student's t-test in the pre-treatment and one-way ANOVA in the treatment with Tukey's post-test. $p \geq 0.05$. n=6 for all experimental groups.

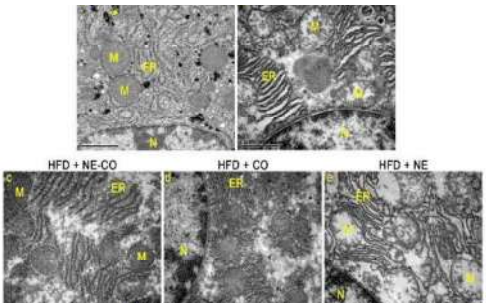

Figure 3. Electron micrographs of liver cross-sections. Electron micrographs of liver cross-sections from control and obese mice with and without treatment. **(A)** CD group. **(B)** HFD group. **(C)** HFD + NE-CO group. **(D)** HFD + CO group. **(E)** HFD + NE group. Abbreviations: M, mitochondria; N, nucleus; ER, endoplasmic reticulum; GL, lipid droplet. Magnification: 20,000x. Calibration bar: 1µm.

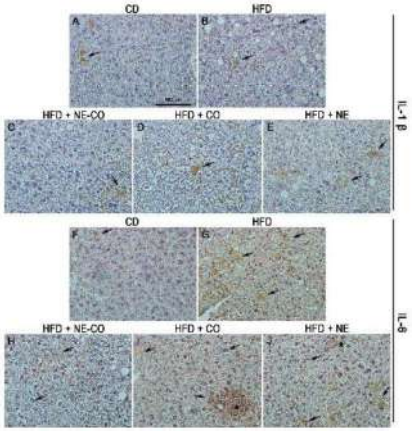

Figure 5. Peroxidase immunostaining for detection of IL-1β and IL-6. Representative photomicrograph of the experimental groups immunostained for interleukins 1 and 6 in the liver tissue of animals fed control and high-fat diets. **(A)** CD Group, **(B)** HFD, **(C)** HFD + NE-CO, **(D)** HFD + CO, **(E)** HFD + NE, all marked for IL1-1β. **(F)** CD, **(G)** HFD, **(H)** HFD + NE-CO, **(I)** HFD + CO, **(J)** HFD + NE all marked for IL-6. (arrow): positive immunostaining. (star) inflammatory infiltrates. Calibration bar: 100 µm.

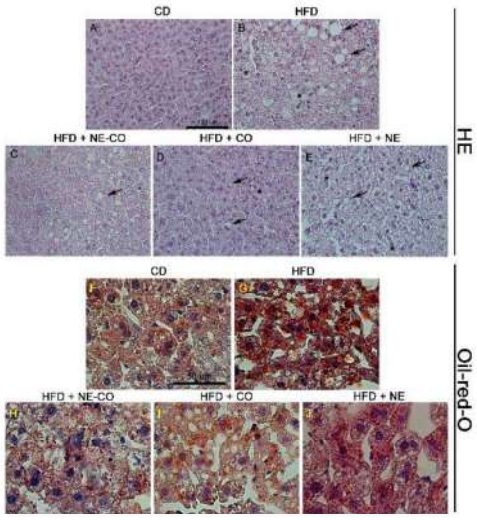

Figure 2. Histopathological analysis of liver tissue. (A) Representative photomicrograph of CD group stained with HE (calibration bar: 100 µm) and Oil-red-O (calibration bar: 50 µm). **(B)** HFD group stained with HE. **(C)** HFD + NE-CO group stained with HE. **(D)** HFD + CO group stained with HE. **(E)** HFD + NE group stained with HE. **(F)** CD group stained with Oil-red-O. **(G)** HFD group stained with Oil-red-O. **(H)** HFD + NE-CO group stained with Oil-red-O. **(I)** HFD + CO group stained with Oil-red-O. **(J)** HFD + NE group stained with Oil-red-O.

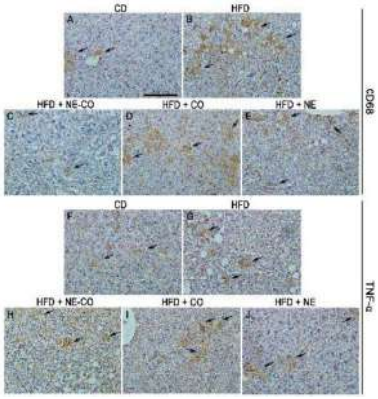

Figure 4. Peroxidase immunostaining for detection of CD68 and TNF-α. Representative photomicrograph of experimental groups immunostained for CD68 and Tumor Necrosis Factor alpha (TNF-α) in liver tissue of animals fed control and high-fat diets. **(A)** CD Group, **(B)** HFD, **(C)** HFD + NE-CO, **(D)** HFD + CO, **(E)** HFD + NE, all marked for CD68. **(F)** CD, **(G)** HFD, **(H)** HFD + NE-CO, **(I)** HFD + CO, **(J)** HFD + NE. all stained for TNF-α. (arrow): positive immunostaining. Calibration bar: 100 µm.

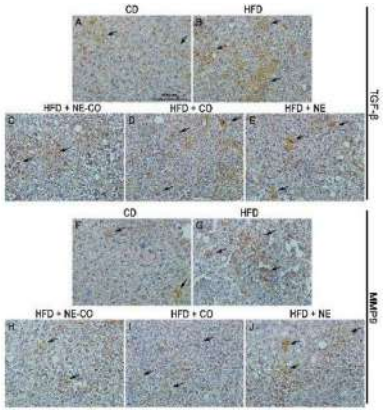

Figure 7. Detection of TGF-β and MMP9, proteins related to hepatic tissue remodeling. Representative photomicrograph of experimental groups immunostained for transforming growth factor beta (TGF-β) and metalloproteinase 9 (MMP9) in liver tissue of animals fed control and high-fat diets. **(A)** CD Group, **(B)** HFD, **(C)** HFD + NE-CO, **(D)** HFD + CO, **(E)** HFD + NE, all stained for TGF-β. **(F)** CD, **(G)** HFD, **(H)** HFD + NE-CO, **(I)** HFD + CO, **(J)** HFD + NE, all marked for MMP9. (arrow): positive immunostaining. Calibration bar: 100 µm.

Can Fractal Methods Detect Spatial Changes in Liver Lipid Macro-droplets of Lactating Rats Subjected to Malnutrition and Physical Activity?

Alison Jose da Silva[1], Ana Vitória Ferreira dos Santos[1], Carlos Eduardo da Silva[1], Maria Gabriela da Silva Mello[1], Weslleyanne Millena da Silva Costa[1], Maria Eduarda Carneiro de Lima[1], Ana Carolina Ribeiro Saraiva da Costa[1], Ryan Cristian da Silva[1], Sara Vitoria de Oliveira Costa[1], Maria Luísa Figueira de Oliveira[2], Bruno Mendes Tenorio[1], Fernanda das Chagas Angelo Mendes Tenorio[1]

[1]Department of Histology and Embryology, Federal University of Pernambuco, Recife-PE. Brazil.
[2]Department of Nutrition, Federal University of Pernambuco, Recife-PE. Brazil.

***Corresponding author:** alison.jsilva@ufpe.br

Protein malnutrition during pregnancy and lactation compromises liver integrity, promoting dysfunctions such as intracellular lipid accumulation, disorganization of hepatic lobules, and impairment of essential functions such as protein synthesis, metabolism, and detoxification [1]. On the other hand, physical activity, even under adverse nutritional conditions, can modulate physiological responses and induce metabolic adaptations with a protective effect on the liver [2]. In this context, non-linear methods such as fractal dimension and lacunarity analyses have been used to identify potential changes caused by adverse effects. Thus, the present study aimed to evaluate, through complex shape methods, possible spatial changes in hepatic lipid macrovesicles of lactating rats subjected to protein malnutrition and physical exercise [3]. For this purpose, the research was approved by the CEUA nº005/2021 and used 32 Wistar rats (n=8), divided into four groups: control, active, highly active, and low active. The rats were mated, and pregnancy was confirmed the following day. Animals were subjected to protein malnutrition and physical activity simultaneously. On the 21st day of lactation, the animals were euthanized for liver collection, which was then submitted to histological analysis and photographed using an optical microscope. Fifteen microscopic fields per animal were analyzed and processed using ImageJ software to obtain outlines in 8-bit images. The FracLac plugin was used to calculate fractal dimension and lacunarity. The results showed that the area of hepatic lipid macrovesicles in the LA and active groups had higher averages, indicating increased lipid accumulation due to malnutrition. In contrast, the HA group presented lower means for this parameter, suggesting a protective effect of intense physical activity, with values similar to the control group. The experimental groups showed significant morphometric liver alterations, with increased area and perimeter in the LA group and a marked reduction in the HA group (Table 1), suggesting a direct impact of the interventions on liver structure. Fractal dimension did not differ significantly between groups. However, lacunarity showed a significant difference between the control and HA groups, indicating changes in the spatial distribution of hepatic lipid macrovesicles (Figure 1). This increase or reduction in lacunarity reflects changes in the heterogeneity and organization of the analyzed structures. Thus, protein malnutrition during lactation caused significant hepatic alterations, with an increase in the area and perimeter of lipid macrovesicles. Intense physical activity mitigated these effects by promoting lower lipid accumulation and better tissue organization. Lacunarity and fractal dimension analyses proved to be sensitive tools for

detecting these changes, showing their efficacy for automated morphological assessment of the liver.

Keyword: Protein malnutrition, Physical activity, Hepatic lipid macrovesicles, Fractal analysis, Lacunarity.

References:

[1] PP Gomes et al., Maternal physical activity on offspring health: a study during pregnancy. Revista Foco (vol. 17), 2024.

[2] J Fragoso et al., Effects of maternal low-protein diet and spontaneous physical activity on the transcription of neurotrophic factors in the placenta and brain of rat mothers and offspring. Journal of Developmental Origins of Health and Disease, (vol. 12), 2021.

[3] AVF Santos et al., Can complex shape markers detect changes in the spatial distribution of cell nuclei in human lung squamous cell carcinoma? A useful tool for automated analysis. Histochem Cell Biol (vol. 163), 2025.

Table 1. Mean ± standard deviation of the morphometric parameters of the Liver analysis between the experimental groups.

	GROUPS				
	Control	**LA**	**Active**	**HA**	**P**
Área	574.5 ± 338.9 a	733.3 ± 373.5 b	658.9 ± 202.5 b	442.6 ± 215.3 c	0.0072*
Perimeter	545.0 ± 261.7 a	1721.1 ± 633.6 b	339.4 ± 387.8 b	201.3 ± 413.3 b	0.0017 *

*Means followed by the same letter do not differ significantly from each other according to the non-parametric Kruskal-Wallis test with Dunn's post-hoc ($p < 0.05$).

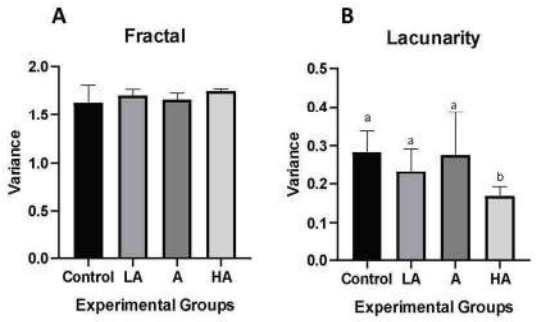

Figure 1. Fractal and lacunarity analysis of hepatic lipid macrovesicles. A: Fractal analysis showed no significant differences between the experimental groups. B: Lacunarity showed a reduction in the spatial distribution of hepatic lipid acrovesicles in the HA group compared to the other groups. *Means followed by the same letter in the lines do not differ significantly from each other using the Kruskal-Wallis test followed by Dunn's post-hoc test ($p > 0.05$).

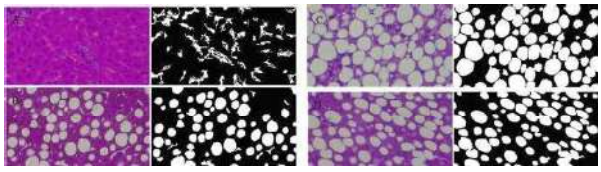

Figure 2. Photomicrographs of the segmentation of lipid macro-droplets in the liver of animals from the experimental groups. A - Control group; B - Active group; C - High activity group; D - Low activity group.

Capybara Oil In Free Form And In Nanoemulsion Improves Morphological Aspects Of Pancreatic Tissue In Obese Mice

Miguel Porto Campos[1*], Priscila Gomes Pereira[1], Bianca Torres Ciambarella[1], Caio Gonçalves Azevedo[1], Stela Regina Ferrarini[3], Jéssica Gomes Pereira[1], Victória Lopes Pereira[1], Kíssila Rabelo[1,2,4], Jemima Fuentes Ribeiro da Silva[1,2], Luciana Lontro Alves[1,2], Jorge José de Carvalho[1,2].

[1]Ultrastructure and Tissue Biology Laboratory, Institute of Biology, UERJ, RJ, Brazil, [2]Electron Microscopy Laboratory of Rio de Janeiro State University, Institute of Biology, UERJ, RJ, Brazil, [3]Pharmaceutical Nanotechnology Laboratory, UFMT, Sinop, MT, Brazil, [4]Interdisciplinar Medical Research Laboratory, Oswaldo Cruz Institute, Fiocruz, RJ, Brazil.
*miguel.porto14@gmail.com

Obesity is a metabolic disease characterized by the excessive accumulation of lipids in the body, leading to an inflammatory state, which causes several chronic conditions in different systems [1]. The pancreas is responsible for the production and secretion of insulin [2] and is of great importance for the study of obesity, considering that this disease is related to the development of insulin resistance, which is a precursor of type 2 diabetes mellitus [3]. Polyunsaturated fatty acids (PUFAs) are lipid mediators that exhibit anti-inflammatory properties [4], present in animals and plants, with a promising new source of these acids being capybara oil (CO) [5]. Despite the health benefits, PUFAs are susceptible to oxidation, compromising the necessary supplementation [6]. An alternative for this problem is pharmaceutical nanotechnology, since studies have already pointed out advantages for its use, such as dose reduction and better absorption [7]. Therefore, the use of CO in its free form or nanoemulsion in the treatment of obesity-related pancreatic diseases emerges as a promising alternative. Our objective was to evaluate the effects of free capybara oil and nanoemulsion on pancreatic changes established by obesity in C57Bl/6 mice. We used 42 3-month-old male C57Bl/6 mice that received a control (CD) or high-fat (HFD) diet for 18 weeks (CEUA No. 048/2022). From the 15th to the 18th week, the animals received the treatment - via orogastric gavage - with placebo of water or white nanoemulsion (NE), or free capybara oil at 100 (CO 100) and 5000 mg/kg/day (CO 5000), or nanoemulsion of CO at 30 (NE-CO 30) and 100 (NE-CO 100) mg/kg/day. Analyses of body mass and glucose tolerance were performed, as well as histological analyses, with HE staining to analyze morphology, and immunohistochemistry for TNF-α, IL1-β, IL6, and TGF-β, in order to observe the inflammatory profile. The high-fat diet was able to establish a case of obesity in these animals, in addition to causing a worsening in the morphological profile and an increase in the inflammatory response. While the free form of CO had some beneficial effects, both NE-OC treatments were able to attenuate the pancreas morphology and inflammation. Therefore, this oil has been shown to be a promising treatment for obesity, as it improves the metabolic symptoms of obesity and its impact on the pancreas. Our findings are relevant and place NE-OC as a great potential for the treatment of obesity and obesity-related diseases [8].

[1] R.M. Lima, Campos dos Goytacazes,2007.
[2] L.C. Junqueira et al., Guanabara Koogan, Rio de Janeiro, 2018.
[3] S. Klein et al., Cell Metab, 2022.
[4] A. Molfino et al., Oxid Med Cell Longev, 2017.
[5] M. Fukushima et al., Lipids, v.32, p.391–395, 1997.
[6] Shukla, VK et al., Lipids. 1991 Jan;26(1):23-6.
[7] Esquerdo, VM et al., J Colloid Interface Sci. 2015 May 01;445:137-42.
[8] This research was supported by CNPq, UERJ and FAPERJ.

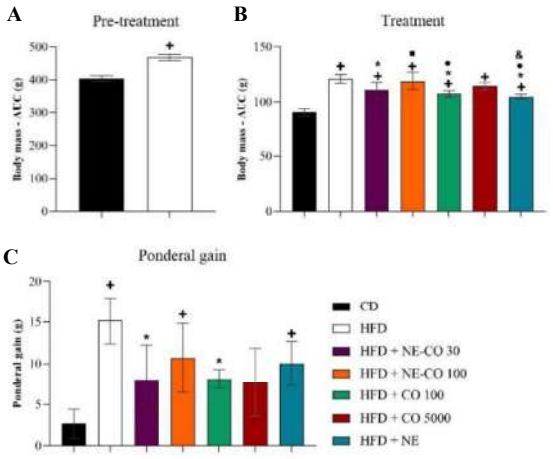

Figure1. Body mass and ponderal gain analysis of the experimental groups. (A) Assessment of area under the curve (AUC) of body mass in the pre-treatment period (Weeks 0 to 14). (B) Assessment of the area under the curve (AUC) of body mass in the treatment period (Weeks 15 to 18). (C) Weight gain evaluation. +: different from the CD group; *: different from the HFD group; ■: different from the HFD + NE-CO 30 group; •: different from the HFD + NE-CO 100 group; &: different from the HFD + CO 5000 group. Statistical analysis: Student's t-test in pre-treatment and one-way ANOVA in treatment with Tukey's post-test. $p \geq 0.05$. n=6 for all experimental groups.

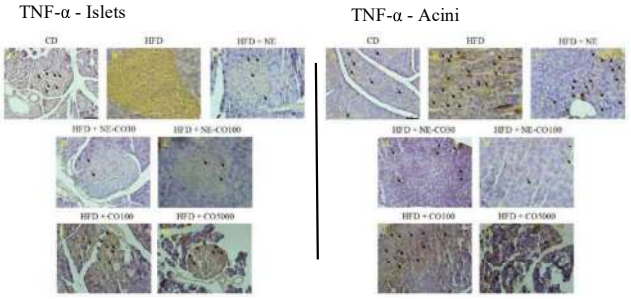

Figure 4. Peroxidase immunostaining for TNF-α detection in islets and acini. Representative photomicrograph of islets and acini of experimental groups immunolabeled for Tumor Necrosis Factor-alpha (TNF-α) in pancreatic tissue of animals fed a control and high-fat diet. (A) CD group. (B) HFD group. (C) HFD + NE group. (D) HFD + NE-CO30. (E) HFD + NE-CO100 group. (F) HFD + CO100 group. (G) HFD + CO5000 group. (arrow): positive immunostaining. Objective: 40x. Calibration bar: 100 µm.

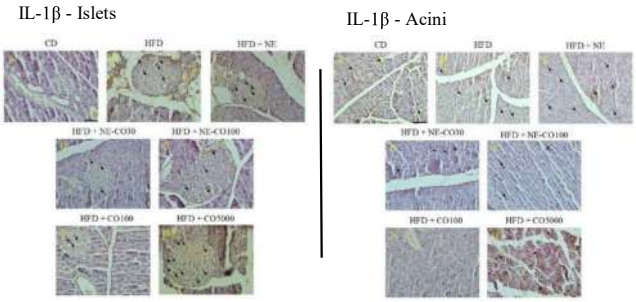

Figure 6. Peroxidase immunostaining for IL-1βdetection in islets and acini. Representative photomicrograph of islets and acini of experimental groups immunolabeled for Interleukin-1 beta (IL-1β) in pancreatic tissue of animals fed a control and high-fat diet. (A) CD group. (B) HFD group. (C) HFD + NE group. (D) HFD + NE-CO30. (E) HFD + NE-CO100 group. (F) HFD + CO100 group. (G) HFD + CO5000 group. (arrow): positive immunostaining. Objective: 40x. Calibration bar: 100 µm.

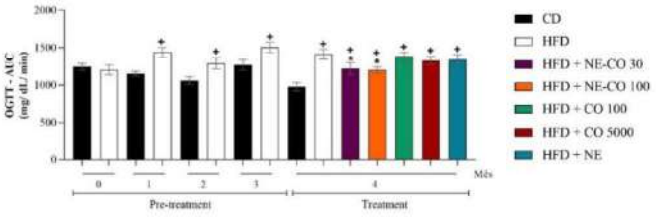

Figure 2. OTTG analysis of the experimental groups. Area under the curve (AUC) evaluation of oral glucose tolerance test (OGTT) in the pre-treatment and treatment period. +: different from the CD group; *: different from the HFD group. Statistical analysis: Student's t-test in pre-treatment and one-way ANOVA in treatment with Tukey's post-test. $p \geq 0.05$. n=6 for all experimental groups.

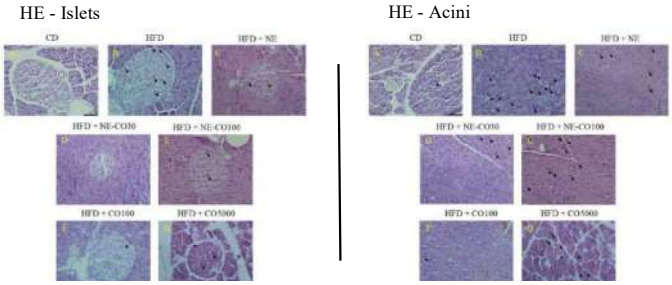

Figure 3. Hematoxylin and Eosin (HE) staining for hepatic steatosis observation. Representative photomicrographs of the islets and acini of the experimental groups for analysis of lipid inclusions in the pancreatic tissue of animals fed a control and high-fat diet. (A) CD group. (B) HFD group. (C) HFD + NE group. (D) HFD + NE-CO30 group. (E) HFD + NE-CO100 group. (F) HFD + CO100 group. (G) HFD + CO5000 group. (arrow): lipid inclusion. Objective: 40x. Calibration bar: 100 µm.

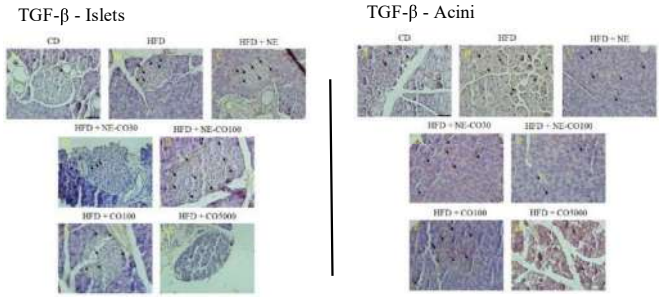

Figure 5. Peroxidase immunostaining for TGF-βdetection in islets and acini. Representative photomicrograph of islets and acini of experimental groups immunolabeled for Transforming Growth Factor-beta (TGF-β) in pancreatic tissue of animals fed a control and high-fat diet. (A) CD group. (B) HFD group. (C) HFD + NE group. (D) HFD + NE-CO30. (E) HFD + NE-CO100 group. (F) HFD + CO100 group. (G) HFD + CO5000 group. (arrow): positive immunostaining. Objective: 40x. Calibration bar: 100 µm.

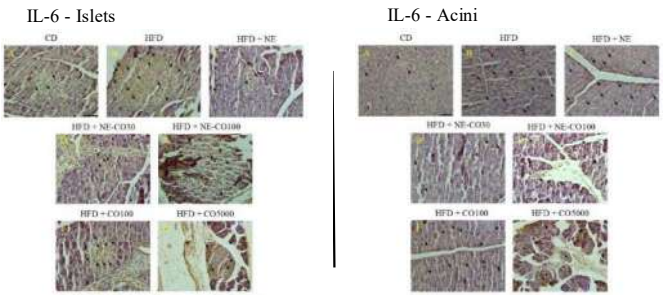

Figure 7. Peroxidase immunostaining for IL-6detection in islets and acini. Representative photomicrograph of islets and acini of experimental groups immunolabeled for Interleukin-6(IL-6) in pancreatic tissue of animals fed a control and high-fat diet. (A) CD group. (B) HFD group. (C) HFD + NE group. (D) HFD + NE-CO30. (E) HFD + NE-CO100 group. (F) HFD + CO100 group. (G) HFD + CO5000 group. (arrow): positive immunostaining. Objective: 40x. Calibration bar: 100 µm.

Characterization of Biochemical Parameters by Raman Spectroscopy in Cutaneous Wound Healing in Mice

Silva EC[1*], Oliveira JNSR[2], Souza ST[2], Ferro JNS[1]

[1] UFAL, Laboratório de Biologia Celular, [2] UFAL, Grupo de Óptica e Nanoscopia
*emilly.silva@icbs.ufal

Raman Spectroscopy (RS) is a quantitative, non-destructive, and non-invasive optical technique that analyzes the chemical composition of samples with high specificity, generating their molecular fingerprint [1]. Widely used in research, RS has gained relevance in diagnostics and biochemical evaluations, including histological analyses such as skin [2]. As the body's interface with the environment, the skin is susceptible to injury and has mechanisms for wound healing that can be impaired in diabetes, leading to complications [3, 4]. This study aimed to evaluate skin biopsies from mice using RS to establish a diagnostic profile. Thus, Swiss mice (male, 20-25g, CEUA-16/2014) were divided into two groups: Non-Diabetic (ND) and Diabetic (DB) (induced by alloxan, i.v., 65 mg/kg). On the 21st day post-diabetes induction, animals with blood glucose levels ≥ 300 mg/dL were considered diabetic, and a model of excisional skin wound was performed. A separate experimental protocol on non-diabetic animals was conducted for comparison using C57BL/6 mice (male, 10-12 weeks, CEUA-12/2023), divided into Healthy Skin (HS) and Non-Treated Wound (NT-C57) groups. Twelve days after wound induction, animals were euthanized, and biopsies were histologically processed, sectioned with a microtome, and analyzed by RS. Principal Component Analysis (PCA) was employed to discriminate between groups based on band intensity. Results included a comparison of different sample preparation and acquisition techniques before analysis. Optimal parameters differed between mouse strains: Swiss mouse biopsies utilized 10 µM thick sections, deparaffinized and unstained, while C57BL/6 biopsies utilized 15 µM thick sections due to increased laser sensitivity. The HS-C57 group exhibited a bands corresponding to organized collagen (853 cm^{-1}, 1453 cm^{-1}, and 1668 cm^{-1}), fibronectin, elastin, and laminin (1090 cm^{-1}, 1247 cm^{-1}, 1307 cm^{-1}, respectively), alongside a phenylalanine peak at 1007 cm^{-1}, a primary melanin precursor. Conversely, the NT group demonstrated attenuated collagen peaks at 1453 cm^{-1} and 1668 cm^{-1}, and emphasized peaks related to collagen precursors, proline, and hydroxyproline (853 and 875 cm^{-1}), as well as keratin (1307 cm^{-1}), indicating wound re-epithelialization. Analysis of Swiss mice revealed that the ND group exhibited differences in fibronectin, elastin, laminin, and keratin peaks with increased intensity, and reduced proline and hydroxyproline peaks compared to the NT group, alongside similar collagen peaks. The DB group displayed increased deposition of fibronectin and elastin in its spectrum, along with significantly intensified proline and hydroxyproline peaks. Both Swiss mouse groups (ND and DB) demonstrated a significant reduction in phenylalanine peak intensity compared to C57BL/6 mice. These findings indicate that Raman spectroscopy has the necessary sensitivity for skin and biopsy analysis under different conditions, marking the first study to demonstrate spectral differences in distinct mouse strains, supporting the use of RS for biological analyses and potential diagnostic applications.

[1] ZUHAYRI, H. *et al.* Journal of Biophotonics, [*s. l.*], 2024.
[2] EGAWA, M. The Analyst, [s. l.], v. 146, n. 4, p. 1142–1150, 2021.
[3] WILKINSON, H. N.; HARDMAN, M. J. Open Biology, [*s. l.*], v. 10, n. 9, 2020.
[4] WANG, H. *et al.* Journal of the Chinese Medical Association, [*s. l.*], v. 81, p. 94–101, 2018.
[5] This research was supported by FAPEAL and CNPq, Brazil.

FIGURES

Figure 1 - Combined analysis of Raman spectroscopy and optical images of non-diabetic and diabetic scar tissue.

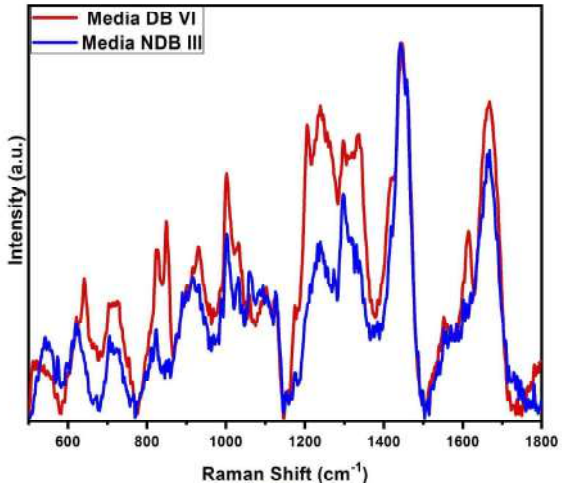

Fig. 1 - Average Raman spectra of diabetic (DB) and non-diabetic (NDB) tissue, highlighting differences in relevant spectral regions (532 nm laser).

Figure 2 - Average Raman spectra of diabetic and non-diabetic scar tissue.

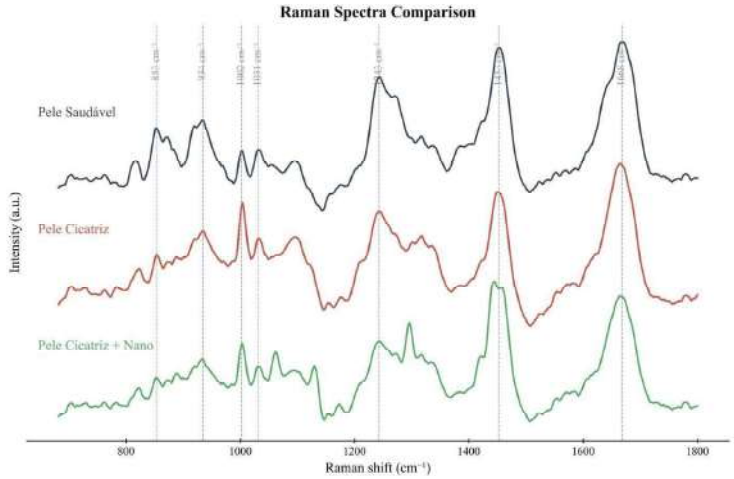

Fig. 2 - Average Raman spectra of healthy skin and scar tissue, highlighting differences in relevant spectral regions (532 nm laser).

Cold Atmospheric Plasma as an Adjunct Therapy in Feline Chronic Gingivostomatitis: Histomorphometric and Immunohistochemical Evidence

Guilherme Ramon Vieira da Silva[1], Samuel Ferreira de França Silvestre[1], Francisco Joelson Correia de Freitas[1], Kilder Dantas Filgueira[1], Marcela Maria de Almeida Amorim[1], Kathryn Nóbrega Arcoverde[1], Layla Ianca Queiroz Rocha[1], Valéria Veras de Paula[1], Clodomiro Alves Júnior[1], Moacir Franco de Oliveira[1], Cibele dos Santos Borges[1], Carlos Eduardo Bezerra de Moura[1]*

[1]Universidade Federal Rural do Semi-Árido, RN, Brazil
*carlos.moura@ufersa.edu.br

Cold Atmospheric Plasma (CAP) can be defined as an ionized gas capable of producing reactive oxygen and nitrogen species (RONS), which are useful in biomedical applications such as disinfection and modulation of wound healing [1, 2]. Feline Chronic Gingivostomatitis (FCGS) is a persistent inflammation of the oral cavity in cats, characterized by severe pain, ulcerations, and other debilitating signs [3, 4]. Conventional treatment involves the use of corticosteroids, immunosuppressants, antibiotics, and primarily surgical management, including partial or full dental extractions—even of healthy teeth [3, 4]. However, these treatments are not always effective [3, 4]. This study aimed to evaluate the effect of direct CAP jet applications combined with prior periodontal treatment in the management of FCGS through histomorphometric and immunohistochemical analyses. Eight cats with FCGS participated in the study, excluding those under immunosuppressive therapy or with retroviral infections, which was approved by the Animal Ethics Committee of the Federal Rural University of Semi-Arid (protocol 27/2023), with owner consent obtained through a written informed consent form. All underwent periodontal treatment (extraction of compromised teeth, scaling, and polishing) and were divided into a treated group (TG, n=5), which received three CAP applications to the affected areas at 7-day intervals, and a control group (CG, n=3), which received only periodontal treatment. CAP was generated using helium flow (2 L/min), power of 2.4 mW, pulsed mode (5 Hz), voltage of 127–230 V, and applied for 30 s/cm². Oral mucosa samples were collected on day 0 (D0) and day 35 (D35) for histological analysis. Sections were processed and examined histomorphometrically using Image Pro Plus software (400x magnification) from five semi-serial sections (20 μm), using a 96-point grid to determine volume densities of inflammatory infiltrate (Vvi), connective tissue (Vvc), and blood vessels (Vvs). Epithelial height was measured in five random regions (100x) using ImageJ software. Samples from D35 were also analyzed by immunohistochemistry for detection of PCNA. Five images per region (400x) were analyzed in ImageJ using the *Color Segmentation plugin*. In the epithelium, only intact regions were considered, and PCNApositive nuclei of epithelial cells were counted. In the lamina propria, analysis focused on positively marked inflammatory cells. The PCNA index was calculated separately for both regions using the formula: (% area of PCNA-positive nuclei / % area of all nuclei) × 100. Data were analyzed using Kruskal–Wallis and Dunn's post-test ($p<0.05$). Epithelial regeneration and reduction of inflammatory infiltrate were observed in the CAP-treated group (TG), while the control group (CG) showed ulcerated epithelium and persistent lymphoplasmacytic infiltrate. TG showed decreased Vvi and increased Vvc and epithelial PCNA index ($p<0.05$). An increase in epithelial height ($p>0.05$) and a low proliferative index in the lamina propria ($p>0.05$) were also detected, indicating inflammatory modulation and tissue architecture reorganization promoted by CAP. The results suggest that CAP is a viable alternative as an adjunct therapy for FCGS, reducing inflammation and promoting mucosal regeneration. This may reduce the need for extraction of healthy teeth and avoid prolonged drug treatments with significant side effects.

[1] N.G. Ibáñez-Mancera et al., Biomedicines 11 (1) (2023).
[2] J. Moszczyńska et al., Int J Mol Sci 24 (16) 12667 (2023).
[3] D.B. Lee et al., Veterinary Clinics of North America: Small Animal Practice 50 (5) 973–982 (2020).
[4] M. Soltero-Rivera et al., J Feline Med Surg 25 (8) (2023).

Table 1. Volume density (Vv) of inflammatory infiltrate (Vvi), connective tissue (Vvc), and blood vessels (Vvs); epithelial height (EH); and proliferation index of epithelial cells (EP PCNA) and lamina propria cells (LP PCNA) in the oral mucosa of cats with feline chronic gingivostomatitis (FCGS), before and after a protocol consisting of either periodontal treatment alone (Control Group) or periodontal treatment combined with cold atmospheric plasma jet applications (Treated Group).

Group/Day	Vvi(%)*	Vvc(%)*	Vvs(%)*	EH (µm)*	EP PCNA(%)*	LP PCNA(%)*
Treated – D0	50,45 (± 6,1)	21,36 (± 4,90)	7,82 (± 3,26)	22,37 (± 17,082)	-	-
Treated – D35	16,34 (± 14,14)**	40,93 (± 7,85)**	6,50 (± 4,99)	72,85 (± 24,42)	56,08 (± 10,88)**	5,89 (± 8,37)
Control – D0	44,57 (± 17,17)	30,41 (± 16,96)	17,70 (± 14,12)	27,95 (± 33,32)	-	-
Control – D35	57,15 (± 1,26)**	17,22 (± 3,32)**	9,50 (± 2,84)	34,52 (± 10,47)	6,16 (± 6,34)**	18,59 (± 8,24)

*Mean (± standard deviation). **Statistical significance (p<0,05).

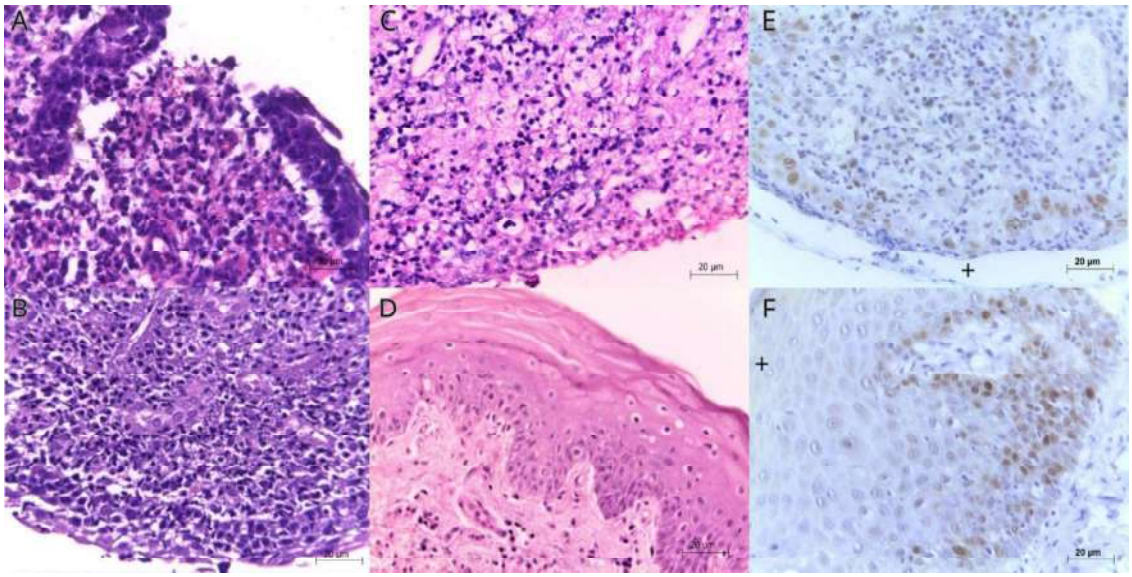

Figure 2. Photomicrographs of the oral mucosa of cats with gingivostomatitis subjected to the experimental protocol. (A, B) Control group on days 0 and 35, respectively, showing intense inflammatory infiltrate, ulceration, epithelial degeneration, and disorganization of the lamina propria. (C, D) Treated group on days 0 and 35, respectively; in D, epithelial regeneration, reorganization of the lamina propria, and reduction of the inflammatory process are observed. (E, F) Immunohistochemistry for PCNA on day 35 in the control and treated groups, respectively ("+" indicates the epithelial surface); In "F," tissue reconstruction and basal epithelial cell proliferation are evident, whereas in "E," few proliferating epithelial cells fail to reorganize into an intact epithelium. Moreover, staining intensity in the lamina propria is more pronounced.

Comparative Analysis of *Leishmania braziliensis* Infection in Phagocytic and Non-Phagocytic Cells Using 2D and 3D Culture Models

Adeniele Lopes da Cruz Carneiro[1,2*], Rebecca Thereza Silva Santa Brígida[1,2] , Daniela Carolina Almeida dos Santos[1,2*], Felipe Tuji de Castro Franco[1], Brenda Furtado Costa[1,2],Ana Paula Drummond Rodrigues[1].

[1] Multiuser Laboratory of Cell Biology and Ultrastructure, Evandro Chagas Institute, [2] Postgraduate Program in Biology of Infectious and Parasitic Agents, Federal University of Pará.
*caneiroadeniele@gmail.com

Leishmaniases are neglected diseases caused by protozoa of the genus *Leishmania*, with the cutaneous form being the most prevalent. Although macrophage infection is well described, *Leishmania* can also invade non-phagocytic cells, such as fibroblasts, especially in two-dimensional (2D) models [1][2]. However, studies using three-dimensional (3D) models, which more realistically mimic the *in vivo* microenvironment, remain scarce[3] [4]. This study aimed to compare the adhesion index of *Leishmania braziliensis* in RAW 264.7 macrophages and 3T3 fibroblasts cultured in 2D and 3D models, as well as to investigate the involvement of actin and the early endosomal marker Rab5 in the invasion process. Cells were infected with promastigotes for 18 hours. In the 2D model, cells were cultured on coverslips; in the 3D model, they were embedded in a type I collagen matrix (1.3 mg/mL). Analyses of adhesion, actin, and Rab5 were performed by immunofluorescence and confocal microscopy. Statistical differences were assessed using the *t*-test ($p < 0.05$). Results showed that the adhesion index was significantly higher in the 2D model compared to 3D (Figure 1 A and B) for both macrophages and fibroblasts ($p = 0.0225$; $p = 0.0248$, respectively). Rab5 labeling was evident in the 2D model, more pronounced around the parasite, but absent in 3D after 18 hours of infection (Figure 1 E and I). Actin displayed rearrangements around the parasites in both models, suggesting active participation in endocytosis. We conclude that *L. braziliensis* modulates its entry process differently in 2D and 3D environments, and that the tridimensional model imposes barriers to adhesion and internalization. These findings highlight the relevance of 3D models for studying host–pathogen interactions and for developing new therapeutic strategies targeting *Leishmania* infection.

[1] V.S. Cavalcante-Costa et al. J Cell Sci. 132 (6) (2019) jcs226183.

[2] B.S. McGwire et al. Infect Immun. 71 (2) (2003) 1008-1010.

[3] J.K Verma et al. PLoS Pathog. 13 (6) (2017) e1006459.

[4] K. Duval et al. Physiology (Bethesda). 32 (4) (2017) 266-277.

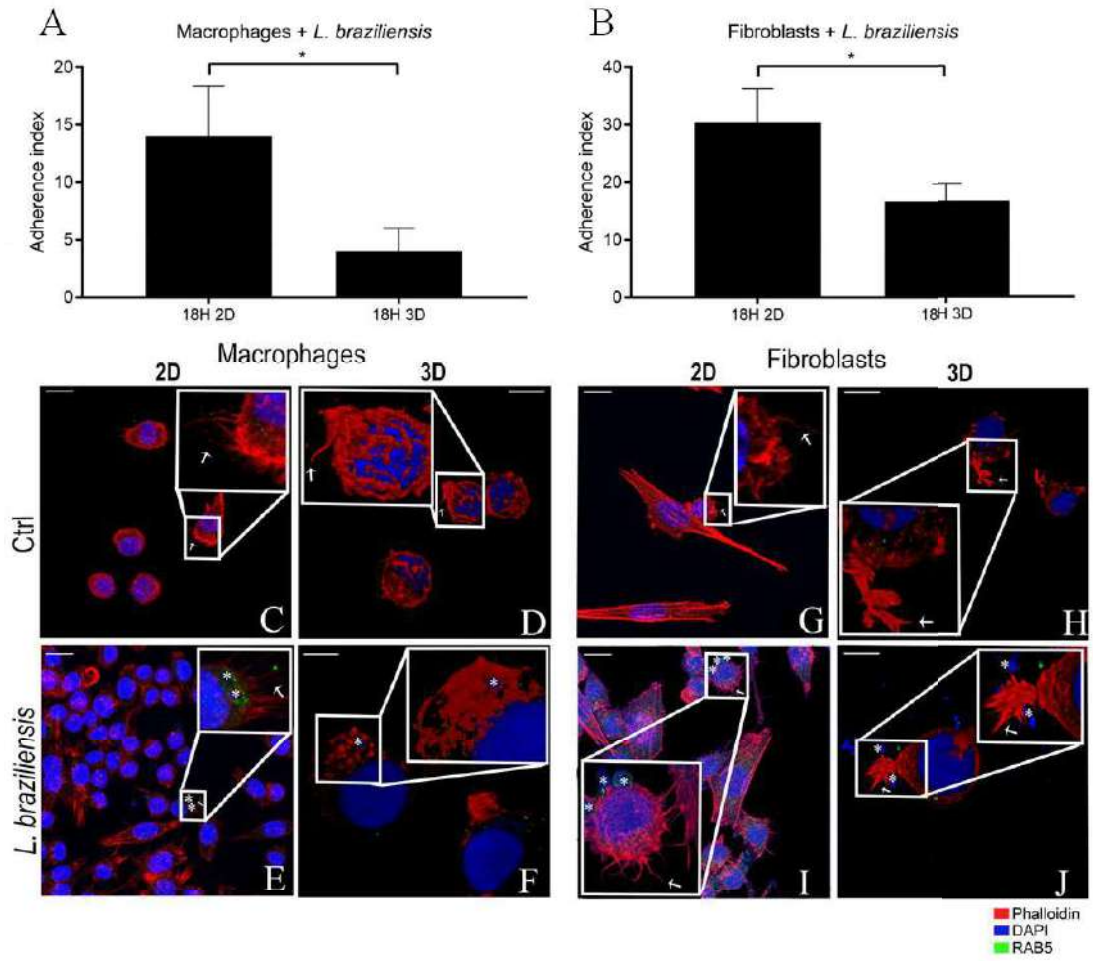

Figura 1: Adherence index and fluorescence endocytosis analysis of macrophages and fibroblasts incubated with *L. braziliensis* for 18 hours in 2D and 3D models. Adherence index (A and B); t-Student test was applied, with significant statistical difference being considered when $p < 0.05$ (*). Macrophages and Fibroblasts without infection - CTL in 2D (C and G) and 3D (D and H). Macrophages and Fibroblasts incubated with *L. braziliensis* in 2D (E and I) and 3D (F and J). Scale bar= 10 µm (C, E, G and I); 20 µm (D, F, H and J). Thin arrows= filopodia; Asterisks= *Leishmania*.

Comparative Histopathology of Vital Organs from Acute Oral Toxicity Induced by Ethanolic Extract of *Rhipsalis baccifera* in Swiss Albino Mice

Karla Mikaelly dos Santos Bezerra[1*], Cláudia Fernanda da Cruz Gouveia Paes[2], Jeymesson Raphael Cardoso Vieira[3], Ivone Antonia de Souza[4].

[1]Department of Histology and Embryology – Morphotechnology Laboratory – Federal University of Pernambuco – UFPE, Pernambuco, Recife.
*karla.mikaelly@ufpe.br

The histopathological analysis is an essential tool in the evaluation of morphological changes in tissues, allowing the identification of lesions and the understanding of toxicity mechanisms induced by experimental agents. Hematoxylin and eosin (H&E) staining is the method used for this type of investigation, as it efficiently highlights nuclear and cytoplasmic components, facilitating the visualization of structural alterations. Histopathological changes in organs such as the liver, kidney, spleen, and lung are frequently used as biomarkers of toxicity and organ dysfunction in animal models, being fundamental for the safety assessment of chemical substances and drugs [1]. The choice of the experimental animal was based on its heterogeneous lineage, high genetic similarity to humans, ease of reproduction, and short life cycle [2]. Thus, according to the biodiversity cataloged in the Brazilian territory, the genus *Rhipsalis* includes several species with therapeutic potential, among them *Rhipsalis baccifera*, popularly known as "macaroni cactus." The aim of the present study was to investigate the acute oral toxicity using the crude Ethanolic Extract of *Rhipsalis baccifera* (cEERb). The animals used were female Swiss albino mice (*Mus musculus*) weighing between 25 and 35 g and aged between 8 and 10 weeks, under approval number 0043/2024. Adult mice were divided into two groups (control and treated). The animals in the treated group received 2000 mg/kg of EERb, and the control group received only saline solution orally. On the 15th day, the animals were anesthetized with a solution of ketamine (75 mg/kg) and xylazine (10 mg/kg) intraperitoneally and euthanized. Subsequently, the liver, kidney, and spleen of the animals from the control and cEERb-treated groups were removed, sectioned, fixed in buffered formalin (10% v/v), and later dehydrated through a graded series of ethanol (70–100%), cleared in xylene, and embedded in paraffin blocks. Sections of 5 µm were mounted on glass slides and stained with hematoxylin-eosin (Merck, Germany). Analyses were performed by optical microscopy using an inverted microscope (Nikon, TS2-FL), and findings were classified according to their intensity and transformed into quantitative variables for each histological finding. Histopathology recorded nuclear vacuolization in the liver of the treated group, with slight disorganization of hepatocyte cords and slight obstruction of hepatic sinusoids. In the kidneys, the morphological alterations were categorized as compatible with moderate glomerular and tubular injury. The renal tubules showed diffuse cytoplasmic vacuolization and epithelial disorganization, loss of cuboidal morphology, and slight lumen dilation; renal corpuscles appeared disorganized, evidenced by the lack of delimitation between the capsular space and capillary loops, indicating glomerular filtration barrier impairment, along with interstitial edema. The spleen maintained preserved tissue architecture; the white pulp, composed of lymphoid nodules and periarteriolar lymphoid sheath, was well-defined; diffuse lymphoid tissue with a structured thymus-dependent area and intact lymphoid follicles were observed. The lungs showed thin and delicate interalveolar septa; aerated alveoli without exudate; bronchioles with preserved epithelium and smooth muscle, without lesions; distributed alveolar sacs, spongy architecture, and thin alveolar walls. The study concluded that, among the analyzed organs, only the kidneys and

liver showed mild to moderate toxicity; the spleen and lungs exhibited intact and preserved tissue architecture, consistent with that of healthy organs.

[1] H. Karimi et al., Histopathological Changes of Organs (Lungs, Liver, Kidney, and Brain) After Using Two Types of AgiCoat and Acticoat Nanosilver Dressings on Deep Second-Degre Burn in Rat, (2019)
[2] G.S Santana et al., Clinical hematological and biochemical parameters in Swiss, BALB/c. C57BL/6 and B6D2F1 Mus musculus, (2020)

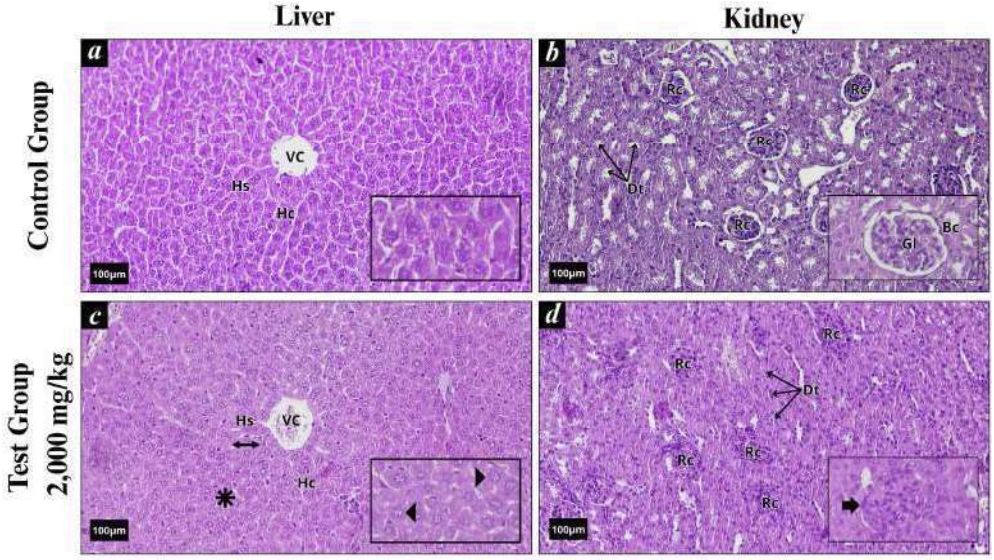

Figure 1.: Photomicrographs of renal and hepatic tissues stained with H&E. Control group (a and b), respectively: VC: Central vein; Hc: Hepatocyte cords; Hs: Hepatic sinusoids; Rc: Renal corpuscles; Dt: Distal tubules; Gl: Glomerulus; Bc: Bowman's capsule. Treated group (c and d), respectively: Arrowhead: nuclear vacuolization; Asterisk: disorganized hepatocyte cords; Double arrow: obstructed hepatic sinusoids; Thin arrow: renal tubules with marked diffuse cytoplasmic vacuolization; Thick arrow: glomerular exudate.

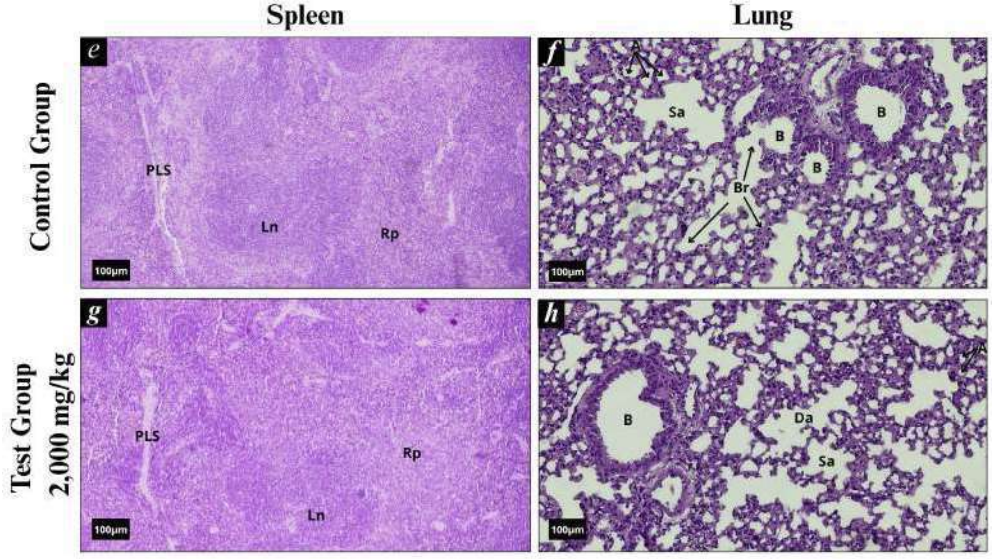

Figure 2.: Photomicrographs of splenic and pulmonary tissues stained with H&E. Control group (e) and treated group (f): Rp: Red pulp; Ln: Lymph node; PLS: Periarteriolar lymphoid sheath. Control group (g) and treated group (h): B: Bronchiole; Br: Respiratory bronchiole; Sa: Alveolar sac; Da: Alveolar duct; A: Alveolus.

Comparison of Synovitis in Arthritis Models

Karoline Calichio Medeiro Pereira[1]*, Lais Panno[1], Ana Caroline Barbosa Retameiro[1], Diego Francis Saraiva Rodriguez[1], Emanuelle Santos Camargo Pratti[1], Gladson Ricardo Flor Bertolini[2], Lucinéia de Fátima Chasko Ribeiro[1]

[1] Struct. & Funct. Bio Lab, CBHS, UNIOESTE, Cascavel, PR, Brazil
[2] Injuries & Physio Res. Lab, CBHS, UNIOESTE, Cascavel, PR, Brazil
*karolcalichio@gmail.com

Inflammatory joint diseases exert a substantial impact on individuals' functional capacity and quality of life, ranking among the leading causes of physical disability within the working-age population. As these conditions progress, they impose increasing limitations on daily and occupational activities and are often associated with reduced life expectancy [1]. Among the affected anatomical structures, synovial joints are particularly vulnerable to chronic inflammatory processes, which lead to intra and periarticular tissue degradation, ultimately compromising joint structural and functional integrity [2,3]. In this context, the application of standardized experimental models is essential for elucidating the underlying pathophysiological mechanisms and for supporting the development of effective therapeutic strategies [4,5]. The present study aimed to comparatively assess the histomorphological alterations of the intimal and subintimal layers of the synovial membrane in three distinct experimental models of joint disorders induced in Wistar rats: rheumatoid arthritis, reactive arthritis, and osteoarthritis [5–9]. A total of twenty male Wistar rats (approximately 3 months old) were randomly allocated into four groups (n = 5): control (CON), induced rheumatoid arthritis (ART), reactive arthritis (ARE), and osteoarthritis (OAR). Following disease induction, animals were euthanized by anesthetic overdose on day 28 of the protocol. The knee joints were harvested, processed, and stained with hematoxylin and eosin (H&E) for subsequent histological evaluation under bright-field light microscopy. In the control group (CON), the synovial membrane displayed preserved morphology, with clearly defined intimal and subintimal layers, comprising two to three layers of synoviocytes and a subintima rich in adipocytes (Figure 1A). In contrast, the ART and ARE groups exhibited similar pathological features, including architectural disorganization, marked synovitis, and replacement of adipocytes by connective tissue (Figures 1B and 1C). The OAR group demonstrated milder synovitis, characterized by sparse inflammatory infiltrate, reduced adipocyte content, and mildly congested blood vessels (Figure 1D). This study provides a comparative histomorphological analysis of synovial alterations in experimentally induced arthritis models, supporting the refinement and selection of pathophysiologically relevant experimental models for future research.

[1] B. Bai et al., *Health Qual Life Outcomes* 18 (2020).
[2] Y. Takeuchi et al., *Front Immunol* 10 (2019).
[3] L. Bai et al., *Front Immunol* 2022.
[4] J. Li et al., *Rheumatic Disease Clinics of North America* 51 (2025) 325–346.
[5] R. Gomes et al., *Einstein* 11 (2013) 76–82.
[6] P. Brandão et al., *Brazilian Applied Science Review* 4 (2020) 2258–2268.
[7] E. Bressan et al., *Life Sci* 87 (2010) 481–489.
[8] D. Kalbhen . *J Rheumatol* 14 (1987) Spec No:130–131.

[9] This research was supported by CNPq (Brazil).

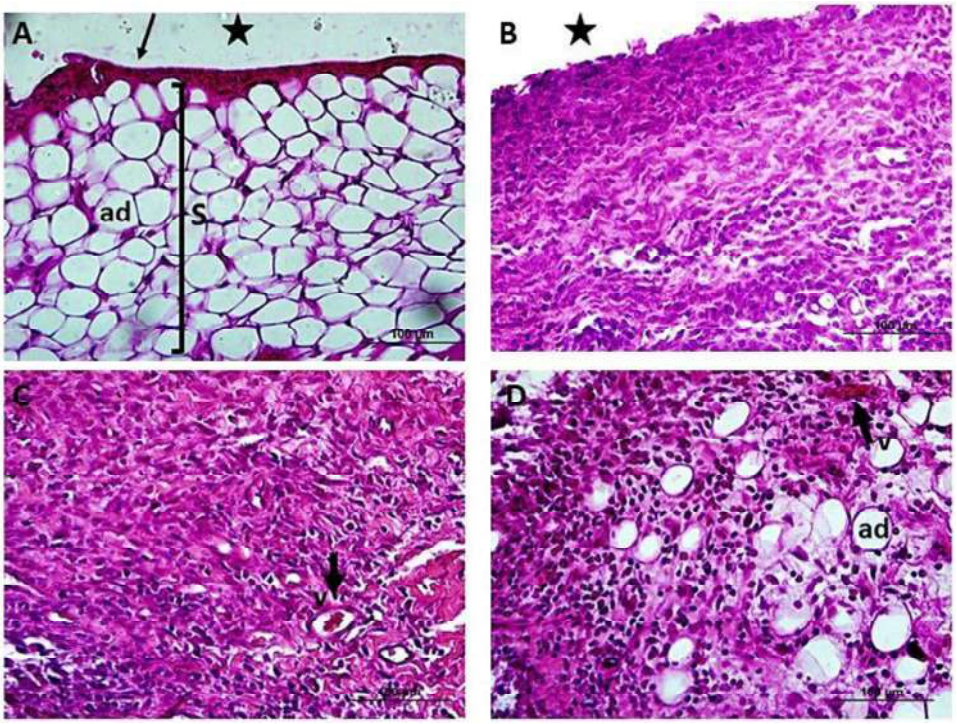

Figure 1. Photomicrographs of synovial membranes from CON (A), ART (B), ARE (C), and OAR (D) groups in sagittal sections stained with Hematoxylin and Eosin. **A:** Synovial membrane intima (arrow), subintimal layer (S), and adipocytes (ad), showing preserved architecture with clearly defined layers. **B:** Disorganization of synovial layers, presence of connective tissue, marked synovitis, and reduced adipocyte content. **C:** Histomorphological features similar to the ART group, with congested blood vessels (arrow-v). **D:** Inflammatory infiltrate and decreased adipocyte density. **(Star)**: Joint cavity.

Confocal Microscopy Analysis of TiO_2 Nanoparticle-Induced Cellular Damage in Zebrafish Embryos

Roberta Laiz Bezerra Santos Albano[1], Ana Kamila Medeiros Lima[1], Luiz Gustavo Vieira Oliveira[1], Emilio de Castro Miguel[1]*

[1]Federal University of Ceara
*emiliomiguel@ufc.br

Titanium dioxide nanoparticles (TiO_2 NPs) are widely used in cosmetics, paints, food additives, and pharmaceuticals, raising concerns about their environmental impact, especially on aquatic organisms [1]. Zebrafish (*Danio rerio*) embryos are an established model for nanotoxicity studies due to their transparency and the presence of the chorion, which may act as a protective barrier. This study evaluated cellular damage in zebrafish embryos exposed to TiO_2 NPs using confocal laser scanning microscopy (CLSM). Embryos were exposed for 96 hours to TiO_2 at 1, 10, and 100 mg/L, with and without the chorion [2]. Acridine orange staining, a marker of apoptosis [3], was used at 24 and 96 hours post-fertilization (hpf). Stained embryos were euthanized and imaged by CLSM (488 nm excitation, 532–580 nm emission). Negative (reconstituted water) and positive (3,4-dichloroaniline) controls were included. At 24 hpf (image omitted), embryos with intact chorion showed no significant apoptotic signal, except at 100 mg/L, where green fluorescence appeared in the yolk sac region. Dechorionated embryos exhibited fluorescence at all concentrations, indicating early cellular damage even at 1 mg/L, demonstrating the partial barrier role of the chorion. At 96 hpf (Figure 1 and 2), increased fluorescence was observed in all exposed groups. Dechorionated embryos showed more intense and widespread apoptotic signals, particularly in the yolk sac and tail, with damage intensifying at higher TiO_2 concentrations. Controls confirmed that the observed fluorescence was specific to acridine orange staining. These results suggest that while TiO_2 NPs may not cause visible mortality at tested concentrations, they induce sublethal cellular damage detectable through high-resolution imaging. The difference between embryos with and without chorion highlights the importance of considering physical barriers in toxicity assessments. CLSM revealed subtle intracellular effects not visible by bright-field microscopy, underscoring the value of advanced imaging for nanotoxicology studies. Overall, this work demonstrates the effectiveness of zebrafish embryos as biosensors for nanoparticle toxicity and supports using confocal microscopy with vital dyes to detect early toxicological effects. Our findings reinforce the need for integrative approaches combining imaging techniques in environmental risk assessments of nanomaterials and emphasize that evaluating cellular-level responses is crucial, beyond traditional survival and developmental endpoints. This research was supported by CAPES, CNPq and Funcap [4].

[1] Srivastava, A., Kumar, A., & Mishra, M. (2020). Titanium dioxide nanoparticles in food and personal care products—What do we know about their safety? Nanomaterials, 10(7), 1339.
[2] OECD (2025), *Test No. 236: Fish Embryo Acute Toxicity (FET) Test*, OECD Guidelines for the Testing of Chemicals, Section 2, OECD Publishing, Paris, https://doi.org/10.1787/9789264203709-en.
[3] Darzynkiewicz, Z., Juan, G., & Bedner, E. (2001). Acridine orange in analysis of cell cycle and cell death. Methods in Cell Biology, 64, 247-270.
[4] This research was supported by CAPES, CNPq and Funcap (Brazil).

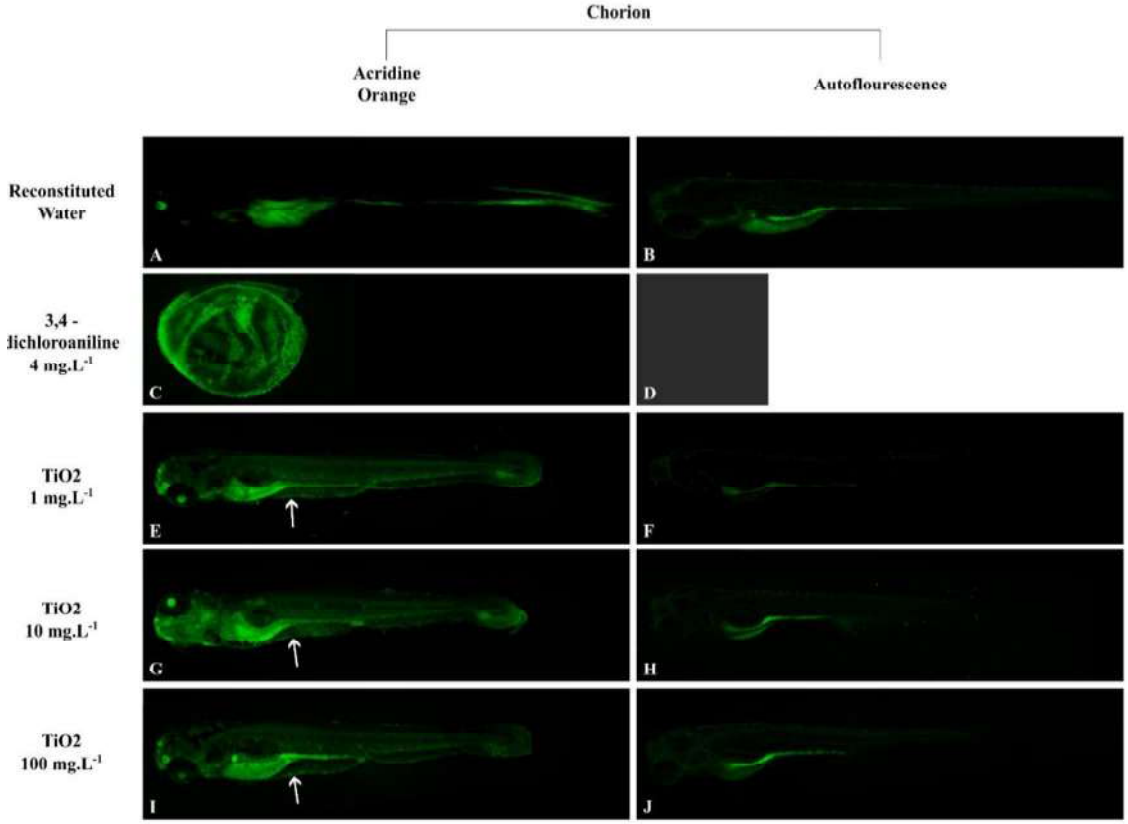

Figure 1. Images of fluorescence of 96 hpf zebrafish (*Danio rerio*) embryos with chorion exposed to varying concentrations of TiO_2, with and without acridine orange staining. Positive and negative controls included.

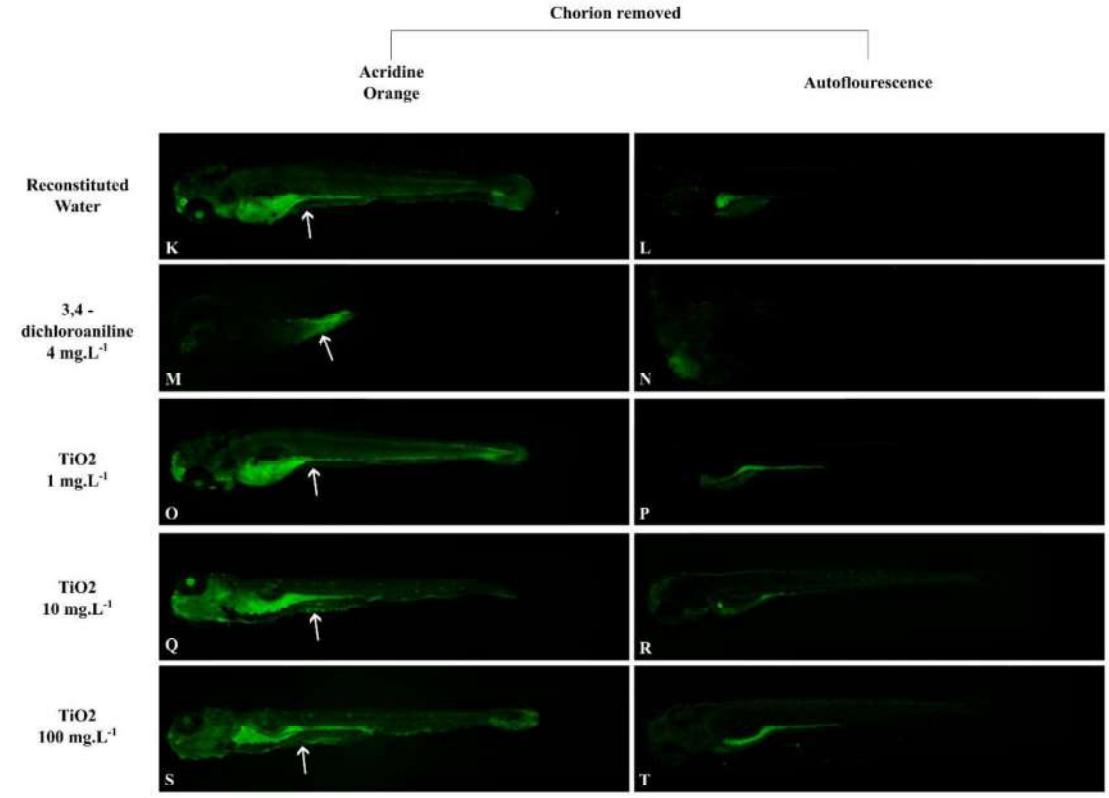

Figure 2. Images of fluorescence of 96 hpf zebrafish (*Danio rerio*) dechorionated embryos exposed to varying concentrations of TiO_2, with and without acridine orange staining. Positive and negative controls included.

Distinct Inflammatory and Metabolic Patterns Associated with Auditory Recovery in Sudden Sensorineural Hearing Loss

Jônatas B. do Amaral[1*],Marina C. Passarelli Scott[1], Tracy L.Tavares Soeiro[1], Kelly Abdo Peron[1], Flávia Tatiana P. Hortense[1], Claudia Maria do Nascimento[1], Miriam Anraku[1], Luiz Henrique da Silva Nali[2], André Luis Lacerda Bachi[2], Carolina Nunes França[2], Elizabeth Cristina Perez[3], Gláucia Maria Machado-Santelli[4], Norma de Oliveira Penido[1]

[1] ENT Research Lab., Department of Otorhinolaryngology- Head and Neck Surgery, Federal University of Sao Paulo (UNIFESP), Sao Paulo, Brazil, [2] Post-Graduation Program in Health Sciences, Santo Amaro University (UNISA), Sao Paulo, Brazil. [3]Graduate Program in Enviromental and Experimental Pathology, Paulista University (UNIP), Sao Paulo, Brazil. [4]Institute of Biomedical Sciences, Department of Cell and Developmental Biology, University of Sao Paulo (USP), Sao Paulo, SP, Brazil.

*jbamaral@unifesp.br

Sudden sensorineural hearing loss (SSNHL) is an otologic emergency affecting 5–20 per 100,000 individuals annually, with an idiopathic etiology in 85–90% of cases [1]. In this study, all patients had SSNHL, were treated equally in the acute phase with oral corticosteroids, and were prospectively followed. They were categorized based on auditory outcomes into two biologically distinct groups: complete or significant recovery (n=38, 58.5%) and partial or no recovery (n=27, 41.5%). Audiometric assessments, including four-frequency pure tone average (4fPTA) and word recognition score (WRS), and blood tests were performed at three time points: V1 (7 days), V2 (30 days), and V3 (120 days). Cytokines and biomarkers (GM-CSF, IFN-λ1, IFN-β, IL-6, IL-10, IP-10, IFN-α2, Klotho) and metabolic parameters (triglycerides, LDL cholesterol) were measured using ELISA and colorimetric assays. Peripheral blood mononuclear cells (PBMCs) were isolated, fixed in 4% formaldehyde, stained with DAPI and Phalloidin 555, and analyzed via LionHeart fluorescence microscopy for cellular morphology and cytoskeletal integrity. Patients in the recovery group showed marked improvement in both 4fPTA and WRS ($p < 0.001$). This improvement was associated with dynamic modulation of inflammatory and repair biomarkers: significant decreases in GM-CSF, IFN-λ1, IFN-β, IL-6, and IL-10 over time indicated active resolution of inflammation. Late-phase increases in IFN-α2 and Klotho suggested roles in tissue repair. IP-10 levels rose early ($p = 0.007$). Metabolically, triglycerides increased ($p = 0.028$) while LDL cholesterol decreased ($p = 0.042$). In contrast, patients in the non-recovery group showed minimal audiometric gains, with only a delayed improvement in 4fPTA ($p = 0.018$) and no significant WRS recovery. Their inflammatory profiles remained largely static, except for a late increase in IP-10 ($p = 0.018$). Metabolic changes included a progressive decline in glucose levels ($p = 0.001$), a late increase in triglycerides ($p = 0.023$), and a reduction in total cholesterol ($p = 0.035$). Immunofluorescence analysis of PBMCs revealed no cellular atypia in either group. Recovery from SSNHL was associated with active resolution of systemic inflammation and metabolic adjustment, while non-recovery was marked by stagnant inflammatory profiles and less favorable metabolic changes. These findings highlight the importance of coordinated cytokine modulation and metabolic balance in auditory recovery and suggest that resolution-based therapies may improve outcomes in SSNHL.

[1] Chandrasekhar SS et al. Otol Head Neck Surg. 161(1 Suppl) (2019) S1–S45.
[2] Amaral JB et al. Front Neurol. 15 (2024): 1382096.
[3] Supported by Fapesp number: 2021/07346-6.

Table 1: Demographic data and clinical characteristics

Characteristic	*Value*
Total Patients	65 (100%)
Age (mean ± SD)	46.3 ± 14.5
Age Range	22–78 years
Female	42 (60.9%)
Male	27 (39.1%)
Hearing Loss: Unilateral	62 (89.9%)
Hearing Loss: Bilateral	7 (10.1%)
Initial Hearing Loss: Mild (≤40 dB HL)	22 (31.9%)
Moderate: (41–70 dB HL)	19 (27.5%)
Severe/Profound: (>70 dB HL)	24 (34.8%)
Tinnitus	58 (84.1%)
Aural Fullness	43 (62.3%)
Dizziness/Vertigo	22 (31.9%)
Auditory Improvement (120 days)	38 (58.5%)
No Significant Improvement	27 (41.5%)

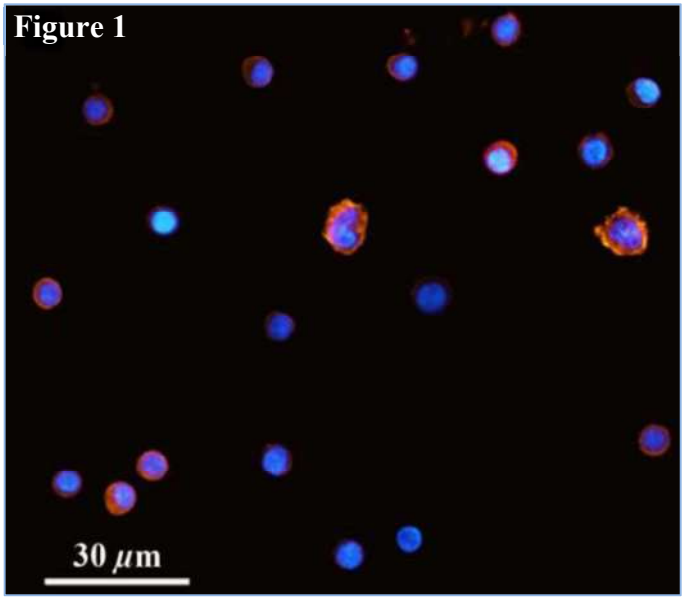

Table 2: Statistically significant variables: Group 1 (G1): Complete/significant recovery. Group 2 (G2): Partial and no recovery

Category	Variable	Significant Comparisons	*p*-values	Interpretation
Audiometry	4fPTA (dB)	V1 vs. V2; V1 vs. V3	<0.001; <0.001 **(G1)**	Strong audiometric improvement (G1); mild late change **(G2)**
Audiometry	WRS (%)	V1 vs. V2; V1 vs. V3	<0.001; <0.001 **(G1)**	Improvement in speech discrimination **(G1 only)**
Inflammatory Cytokines	GM-CSF, IFN-λ1, IFN-β, IL-6, IL-10, IP-10, IFN-α2	Multiple	<0.05 **(G1)**	Dynamic reductions (G1); IP-10 only in **(G2)**
Metabolic Parameters	Triglycerides	V1 vs. V3	0.028 **(G1)**; 0.023 **(G2)**	Late increase in both groups
Metabolic Parameters	LDL Cholesterol	V1 vs. V3	0.042 **(G1)**	Late reduction **(G1)**
Metabolic Parameters	Glucose, Total Chol	V1 vs. V2; V1 vs. V3	<0.001; 0.035 **(G2)**	Progressive reduction **(G2 only)**
Other Markers	Klotho	V1 vs. V3	0.042 **(G1)**	Late repair-related changes **(G1)**
Other Markers	IP-10	V1 vs. V2 **(G1)**; V1 vs. V3 **(G2)**	0.007; 0.018	Initial rise **(G1)** late increase **(G2)**

V1 = 7 days, V2 = 30 days, V3 = 120 days post-diagnosis. Only variables with p < 0.05 are shown.

Figure 1. Immunofluorescence microscopy of peripheral blood mononuclear cells (PBMCs) from patients with Sudden Sensorineural Hearing Loss. Nuclei were stained with DAPI, and actin filaments were labeled with phalloidin-555 (Abcam).

Statistical analyses were performed using repeated-measures ANOVA (nonparametric Friedman test), with multiple comparisons adjusted by the Durbin–Conover test. Statistical significance was defined as $p < 0.05$. Results are presented as medians and interquartile ranges (25–75).

Abbreviations: 4fPTA: Four-Frequency Pure Tone Average; **WRS:** Word Recognition Score; **IL:** Interleukin; **IFN:** Interferon; **IP-10:** Interferon Gamma-Induced Protein 10; **GM-CSF:** Granulocyte–Macrophage Colony-Stimulating Factor; **Klotho:** Anti-Aging Protein Involved in Tissue Repair**; LDL:** Low-Density Lipoprotein; **SD:** Standard Deviation.

Effect of Cannabidiol Nanoemulsion on the Histopathological Integrity of the Myocardium of Rats Subjected to Protein Malnutrition During Pregnancy

Maria Manuela dos Santos Rodrigues[1]*, Suellen Rozy da Silva Medeiros[1], Glenison da Rocha Duarte [2], Thaynara Caseli dos Santos[1], Paloma Vitória Melo da Silva[1], Maria Clara Chár Gomes[1], Ryan Cristian da Silva[3], Elba Verônica Maciel Matoso de Carvalho[1], Bruno Mendes Tenório[1], Fernanda das Chagas Angelo Mendes Tenório[1] Juliana Pinto de Medeiros[1]

Department of Histology and Embryology, Federal University of Pernambuco[1],
Department of Medicine, Faculty of Medicine of Olinda2,
Department of Biochemistry, Federal University of Pernambuco 3,
*manuela.rodrigues@ufpe.br

Gestational protein malnutrition can compromise maternal myocardial integrity, favoring inflammatory and structural alterations [1]. Cannabidiol (CBD), especially in nanoemulsions, has shown neuroprotective and tissue-modulating effects [2]. Recent studies suggest that CBD may also influence cardiac histological parameters [3], justifying the investigation of its effects in pregnant females subjected to malnutrition. This study investigates the effect of this intervention on the myocardium of malnourished pregnant rats, exploring the impact of CBD on myocardial histological integrity in models subjected to this type of diet, which may reveal potential cardioprotective benefits. With prior approval from the Ethics Committee for Animal Use (CEUA: No. 0053/2024) of the Federal University of Pernambuco, Wistar rats from the aforementioned educational institution were used. Adult female rats (n=30) underwent mating, which was confirmed by the presence of sperm in vaginal smears. The experiment began on the first day of pregnancy, in which the rats were divided into three groups: Group I – pregnant rats fed a normocaloric diet for 14 days of pregnancy; Group II – pregnant rats subjected to protein restriction for 14 days of pregnancy; Group III – pregnant rats subjected to protein restriction and treated with 10.0 mg/kg/day of cannabidiol for 14 days of pregnancy. The protein restriction adopted in this study was from RHODES. The CBD was from Aliança Medicina, registered under CNPJ no. 43.178.635/0001-96, and the nanoemulsion was prepared in the nanoparticle laboratory of UFPE. The rats were weighed daily throughout the experiment, and on day 14 of pregnancy, they were anesthetized for heart collection, which was fixed in 10% buffered formalin. The hearts were cleaved, histologically processed, and embedded in paraffin. The resulting blocks were subjected to 3-μm sections for subsequent hematoxylin-eosin (HE) staining. The stained slides were analyzed under a Nikon® NIS Elements light microscope and photographed with a Nikon Eclipse 80 photomicroscope. Thus, the results of this study demonstrated that histological analysis of the hearts of females in the experimental groups at day 14 of pregnancy showed well-defined cardiac septum and endocardial, myocardial, and pericardial layers. In the diet group, the presence of mononuclear infiltrate and vacuolation of cardiomyocytes was observed. In the diet+CBD group, the myocardium showed the presence of mononuclear infiltrate (Figure 1). The data obtained indicate that protein malnutrition during pregnancy significantly compromises the histological integrity of the myocardium, promoting inflammation and cellular degeneration. Although CBD treatment did not completely prevent the inflammatory infiltrate, it appears to have minimized the extent of the damage, suggesting a possible cardioprotective effect, consistent with previous studies on its antioxidant and anti-inflammatory properties. The cannabidiol nanoemulsion demonstrated therapeutic potential by partially attenuating cardiac histopathological changes in rats subjected to gestational protein malnutrition. Although the inflammatory infiltrate persisted, the reduction in cardiomyocyte vacuolization indicates that CBD may exert protective effects on cardiac tissue, representing a promising alternative to mitigate the adverse effects of gestational malnutrition on the maternal heart. Further

studies are needed to elucidate the molecular mechanisms involved.

[1] Lim K, Zimanyi MA, Black MJ (2006) 60(1):83-7.
[2] A.V. Oliveira, Fed. Univ. Ceará, Master's Diss. (2024).
[3] Hao, Enkui, et al. Molecular medicine 21 (2015): 38-45.
[4] This research was supported by CNPq (Brazil).

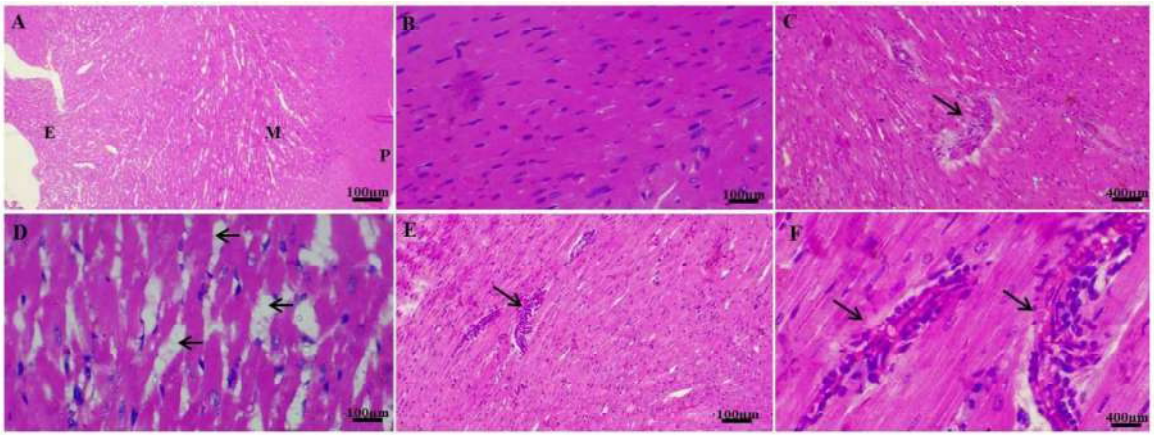

Figure 01: Photomicrograph of the hearts of rats in the experimental groups. A, B – Control group showing well-defined layers of endocardium (E), myocardium (M), and pericardium (P), in addition to transverse myocardial striations; C – Diet group showing mononuclear infiltrate (arrow); D – Diet group showing cardiomyocyte vacuolization (arrow); E, F – Diet+CBD group showing mononuclear infiltrate (arrows). HE

Effect of Cannabidiol Nanoemulsion on Cardiac Morphometry of Rats Subjected to Protein Malnutrition During Pregnancy

Maria Manuela dos Santos Rodrigues[1]*, Suellen Rozy da Silva Medeiros[1], Glenison da Rocha Duarte [2], Thaynara Caseli dos Santos[1], Paloma Vitória Melo da Silva[1], Maria Clara Chár Gomes[1], Ryan Cristian da Silva[3], Elba Verônica Maciel Matoso de Carvalho[1], Bruno Mendes Tenório[1], Fernanda das Chagas Angelo Mendes Tenório[1] Juliana Pinto de Medeiros[1]

Department of Histology and Embryology, Federal University of Pernambuco[1],
Department of Medicine, Olinda School of Medicine2,
Department of Biochemistry, Federal University of Pernambuco 3,
*manuela.rodrigues@ufpe.br

Protein malnutrition during pregnancy compromises the cardiovascular health of the female, potentially causing morphometric changes in the maternal heart, such as myocardial atrophy and ventricular remodeling [1]. Cannabidiol (CBD), in nanoemulsion form, has demonstrated cardioprotective effects due to its antioxidant and anti-inflammatory actions [2]. Studies indicate that CBD can preserve the integrity of tissues sensitive to metabolic stress [3]. This study evaluates the potential of CBD to protect the hearts of malnourished pregnant rats. With prior approval from the Ethics Committee for Animal Use (CEUA: No. 0053/2024) of the Federal University of Pernambuco, Wistar rats from the aforementioned educational institution were used. Adult female rats (n=30) underwent mating, which was confirmed by the presence of sperm in vaginal smears. On the first day of pregnancy, the experiment began, dividing the rats into three groups: Group I – pregnant rats fed a normocaloric diet for 14 days; Group II – pregnant rats subjected to protein restriction for 14 days; Group III – pregnant rats subjected to protein restriction and treated with a concentration of 10.0 mg/kg/day of cannabidiol for 14 days. The protein restriction adopted in this study was from RHODES. The CBD was from Aliança Medicina, registered under CNPJ no. 43.178.635/0001-96, and the nanoemulsion was prepared in the nanoparticle laboratory at UFPE. The rats were weighed daily throughout the experiment, and on the 14th day of pregnancy, the rats were anesthetized for heart collection, which was fixed in 10% buffered formalin. The heart was cleaved, histologically processed, and embedded in paraffin. The obtained blocks were subjected to 3-μm sections for subsequent hematoxylin-eosin (HE) staining. The stained slides were analyzed under a Nikon® NIS Elements light microscope and photographed under a Nikon Eclipse 80 photomicroscope. For morphometric analysis, the parameters of nuclear area and perimeter, and the volumetric proportion of the nucleus, red blood cells, and myocardial cytoplasm were evaluated. For this purpose, point counting was performed by systematic allocation using a 169-point grid, using the freehand tool in ImageJ software. After analysis, the results were subjected to the Kolmogorov-Smirnov normality test, followed by the nonparametric Kruskal–Wallis test with Dunn's post-hoc test at a significance level of 5% ($P < 0.05$). Thus, the result of this study demonstrated that there was no significant change in organ weight and organosomatic index (Table 1). However, in animal weight, there was a statistically significant difference between the groups. The diet group showed a significant increase in nuclear area ($p = 0.0055$) and perimeter ($p = 0.0431$) compared to the control group, indicating cardiac cellular remodeling associated with malnutrition (Table 2). The diet + CBD group showed a significant reduction in these parameters compared to the diet group, suggesting that CBD had an attenuating effect on cellular remodeling induced by protein restriction. Regarding nuclear volume, the diet + CBD group showed a significant increase ($p = 0.0001$), which may indicate an effect of CBD on modulating cellular/nuclear volume.

[1] Y. Wang et al., Sci. Rep. 7 (1) (2017) 12064.
[2] C.P. Stanley, W.H. Hind, S.E. O'Sullivan, Br. J. Clin. Pharmacol. 75 (2) (2013) 313–322.
[3] A. Kicman, M. Toczek, Int.J.Mol.Sci. 21 (18) (2020) 6740.
[4] This research was supported by CNPq (Brazil).

Table 1. Mean ± Standard Deviation of Organ Weight and Organosomatic Index (OSI = {heart net weight/body weight} x 100) of the experimental groups.

Experimental Groups/Parameters	Control	Diet	Diet + CBD	p
Animal Weight	262,6 ±18,27 a	249,2 ±18,02 b	198,8 ±17,04 c	0.0026*
Organ Weight	0,384 ±0,055	0,401 ±0,054	0,364 ±0,069	0,88
Organosomatic Index	0.384±0.05	0.398±0.05	0.358±0.06	0,69

* Means followed by the same letter do not differ significantly from each other according to the non-parametric Kruskal-Wallis test with Dunn's post-hoc ($p < 0.05$).

Table 2. Mean ± standard deviation of morphometric parameters of heart analysis between experimental groups.

	Control	Diet	Dieta + CBD	p
Area	846,1 ± 22650 a	1368 ± 217,0 b	707,0 ± 176,4 c	0,0055*
Perimeter	114,3 ± 74,82 a	195,4 ± 21,92 b	130,7 ± 25,17 c	0,0431*
Air	1.44±0.80a	1.52±0.77a	2.54±1.65b	0.0001*
Circle	0.73±0.18	0.74±0.13	0.79±0.16	0.46
Around	0.41±0.20	0.55±0.17	0.41±0.20	0.63
Solidity	0.90±0.10	0.93±0.04	0.91±0.04	0.52
Cytoplasm	143.6±4.88	146.5±5.27	146.8±4.19	0.16
Nucleus	11.13±3.833a	8.42±3.41b	6.53± 2.38b	0.005*
Red Blood Cell	4.20±3.27	4.14±1.79	6.13± 4.64	0.320

* Means followed by the same letter do not differ significantly from each other according to the non-parametric Kruskal-Wallis test with Dunn's post-hoc ($p < 0.05$).

Effect Of Maternal Glyphosate Exposure On Neuromuscular Junctions In The Extensor Digitorum Longus Muscle Of Mice

Gabriella Canan Kiekiss[1]*, Eduarda Soligo[2], Ariadne Barbosa[1], Sandra Lucinei Balbo[1], Maria Lucia Bonfleur[1], Marcia Miranda Torrejais[1].

[1]Graduate Program in Biosciences and Health – Universidade Estadual do Oeste do Paraná, Cascavel, Paraná, Brazil, [2] Degree in Biological Sciences, Center for Biological and Health Sciences – Universidade Estadual do Oeste do Paraná, Cascavel, Paraná, Brazil
*gabick2012@hotmail.com

Glyphosate, the active compound in various commercial herbicides such as Roundup®, is currently the most widely used pesticide in Brazil [1,2]. Obesity is defined as the excessive accumulation of body fat, characterized as an endocrine, nutritional, and/or metabolic disease that can cause health problems over time [3]. Maternal exposure to pesticides like glyphosate may induce metabolic programming in the offspring, as these compounds affect metabolism and tissue development over prolonged periods [4,5]. In this context, the present study aimed to evaluate the morphology and morphometry of the neuromuscular junctions (NMJs) of the extensor digitorum longus (EDL) muscle in mouse offspring exposed to glyphosate during pre- and postnatal periods, as well as to assess whether a high-fat diet could intensify the effects of this exposure. The experiment used 20 pregnant C57BL/6 mice divided into groups: Control Group (CTL, n=10), receiving pure water during pregnancy and lactation, and Glyphosate-Based Herbicide Group (GBH, n=10), receiving water containing 0.5% glyphosate herbicide [1]. After weaning, male offspring were fed standard chow and water *ad libitum* for 30 days, then separated into four experimental groups (n=6): Control Group (CG-F1); High-Fat Diet Group (HFD-F1); Glyphosate-Based Herbicide Group (GBH-F1); and Glyphosate-Based Herbicide and High-fat Diet Group (GBH-HFD-F1). Offspring were euthanized at 150 days of age. The EDL muscle was collected, and left antimeres were fixed in Karnovsky's fixative [6] and subjected to nonspecific esterase histochemical technique [7] for analysis of 100 NMJs per animal. The HFD-F1 group showed a 28% increase ($p=0.0003$) in body weight and a 455% increase ($p<0.0001$) in retroperitoneal and periepididymal fat compared to CG-F1. The GBH-HFD-F1 group showed a 35% reduction ($p<0.0001$) in these same fats compared to HFD-F1. Regarding NMJs, all groups displayed polymorphic shapes (oval, round, or elliptical) without evident morphological alterations. Morphometric analysis showed that GBH-F1 exhibited a 32% increase in NMJ area ($p=0.0111$) and a 15% increase in major diameter ($p=0.0138$) compared to CG-F1. The combination of glyphosate with a high-fat diet did not induce additional changes in NMJs. In conclusion, glyphosate exposure combined with a high-fat diet reduced retroperitoneal and periepididymal fat accumulation, while glyphosate alone increased the area and major diameter of NMJs in the offspring.

[1] Monsanto, Safety Data Sheet (SDS) – Roundup, 2008.
[2] Brazil, Ministry of Agriculture, Livestock and Supply, AGROFIT: Phytosanitary Pesticide System, 2013.
[3] Ministry of Health, Fact Sheet: Obesity, Government of Brazil, 2020.
[4] K.C.S. Oliveira et al., Multidisciplinary Journal of Health, 2 (2021) 92.
[5] S. Cvitic et al., Diabetologia, 61 (2018) 2398–2411.
[6] M.J. Karnovsky, Journal of Cell Biology, 27 (1965) 1–149.
[7] G.M. Lehrer, L. Ornstein, Journal of Biophysical and Biochemical Cytology, 6 (1959) 399-406.
[8] This research was supported by Fundação Araucária and Unioeste (Brazil).

Table 1. Macroscopic parameters and morphometric evaluation of the neuromuscular junctions of the extensor digitorum longus muscle in 150-day-old mice from the following groups: control group (CG-F1), high-fat diet group (HFD-F1), glyphosate-based herbicide group (GBH-F1), and glyphosate-based herbicide and high-fat diet group (GBH-HFD-F1). Values expressed as mean ± standard deviation. n = 6. Different letters indicate statistically significant differences ($p < 0.05$). [1]Kruskal–Wallis test followed by Dunn's post hoc test. [2]One-way analysis of variance (ANOVA) followed by Tukey's multiple comparison post hoc test.

Groups Parameters	CG-F1	HFD-F1	GBH-F1	GBH-HFD-F1
[1]Body weight (g)	25 ± 1.2[a]	32 ± 4.5[b]	23 ± 1.8[a]	28 ± 2.0[a]
[1]EDL muscle weight (mg)	9.8 ± 0.001	10.8 ± 0.002	9.3 ± 0.002	9.8 ± 0.002
[1]Naso-anal length (cm)	9.3 ± 0.27	9.5 ± 0.32	8.9 ± 0.49	9.3 ± 0.26
[2]Retroperitoneal and periepididymal fat (mg)	301 ± 71[a]	1670 ± 46[b]	298 ± 11[a]	1082 ± 53[c]
[2]EDL muscle length (mm)	7.2 ± 1.10	7.02 ± 0.72	7.6 ± 0.91	6.9 ± 1.05
[2]Lee index (g/cm³)	318 ± 10.4	331 ± 9.2	318 ± 13.3	326 ± 11.4
[2]NMJ area (µm²)	403 ± 63.7[a]	394 ± 49.3[a]	531 ± 62.7[b]	487 ± 108[a]
[2]NMJ major diameter (µm)	31.7 ± 2.87[a]	32.1 ± 2.78[a]	36.7± 3.44[b]	36.1 ± 2.84[a]
[2]NMJ minor diameter (µm)	16.9 ± 1.48	16.7 ± 1.22	18.8 ± 0.896[a]	19.4 ± 3.1

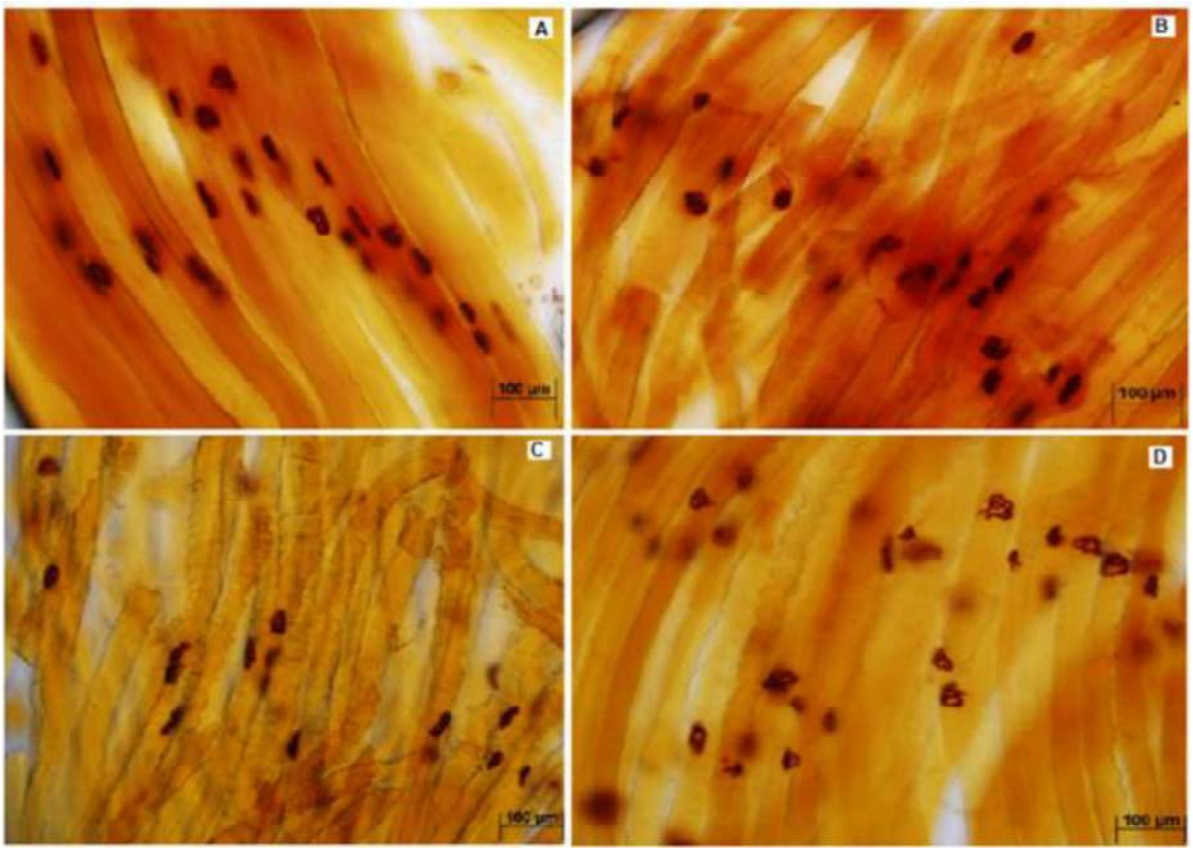

Figure 1. Photomicrographs of neuromuscular junctions in the extensor digitorum longus muscle of 150-day-old mice. Longitudinal section. Nonspecific esterase reaction. **A:** Control group; **B:** Glyphosate-based herbicide group; **C:** High-fat diet group; and **D:** Glyphosate-based herbicide and high-fat diet group.

Effects of Perinatal Exposure to Phthalates on the Extracellular Matrix of Mongolian Gerbil Ovaries

Eloá Alves Bento[1], Isabella Barbosa Melvin[1], Isabella Barreto de Souza[1], Bárbara Costa Malmann Medeiros[1]*, Manoel Francisco Biancardi[2], Fernanda Cristina Alcântara dos Santos[2], Jodi A Flaws[3], Ellen Cristina Rivas Leonel[4].

[1]Programa de Pós-Graduação em Ciências Biológicas, Universidade Federal de Goiás (UFG), [2] Departamento de Histologia, Embriologia e Biologia Celular, Instituto de Ciências Biológicas, Universidade Federal de Goiás (UFG), [3]Department of Comparative Biosciences, University of Illinois at Urbana-Champaign, [4]Louvain Institute of Biomolecular Science and Technology, Université Catholique de Louvain
*eloaalves@discente.ufg.br

Ovaries are dynamic organs subject to significant morphological changes throughout reproductive life. Normal ovarian function depends on the cyclic remodeling of the extracellular matrix (ECM), which is essential for structural support and cell signaling [1]. For folliculogenesis, primordial follicles are recruited and activated under hormonal stimulation, progressively advancing through the primary, secondary, and antral stages until reaching the preovulatory stage [2]. These processes comprise oocyte growth and development, proliferation of granulosa cells and formation of its additional layers, and establishment of an antral cavity [3, 4]. This involves intense ECM remodeling, where localized degradation in the preovulatory follicular wall is important for ovulation and subsequent formation of the corpus luteum [1]. However, endocrine-disrupting compounds (EDCs), such as phthalates, can interfere with ovarian morphophysiology [5], especially when exposure occurs during critical windows such as the perinatal developmental stage. Thus, the objective was to evaluate the effects of a phthalate mixture (PM), administered during gestation and lactation, on the composition and organization of ovarian ECM in Mongolian gerbils at different postnatal (PN) time points. The experiment was approved by the Ethics Commission for Animals Use of the Federal University of Goiás (CEUA-UFG), protocol no. 080/22. The PM consisted of 35.22% DEP, 21.03% DEHP, 14.91% DBP, 15% DiNP, 8% DiBP, and 5.13% BzBP [6]. Pregnant females were sorted into experimental groups: low dose of the PM (200 µg/kg/day), high dose (200 mg/kg/day) or control. Female offspring were euthanized at three different PN days (6, 12, and 18), totaling five animals per age for each group, and had their ovaries collected. Gomori's trichrome and Gomori's reticulin stains were used to analyze collagen fibers and reticular fibers (type III collagen), respectively. For this, the percentage of fibers relative to other tissue components in the ECM was considered. Stereological data were expressed as mean ± standard deviation. Results showed no significant changes in collagen fibers at PN6 (6.895 ± 0.3522; 9.003 ± 0.5304; 7.308 ± 0.8919 for control, low dose, and high dose, respectively). At PN12 and PN18, collagen levels increased in animals exposed to the high dose (22.73 ± 0.5460; 14.08 ± 0.5835, respectively) compared to the low dose (17.44 ± 1.536; 10.80 ± 0.9293). No differences were found between the control group and the others (PN12: 21.11 ± 0.5220; PN18: 12.77 ± 0.5550). Figure 1 displays the results for collagen fibers. For reticular fibers, as per Figure 2, no differences were observed at PN6 (186.8 ± 5.615; 184.6 ± 5.818; 191.8 ± 4.707 for control, low, and high dose, respectively). At PN12, results showed a reduction in type III collagen in the high dose group (148.3 ± 10.17) compared to the control (185.5 ± 3.354). There were no differences between the control and low-dose groups (172.5 ± 5.268) or between the two doses. At PN18, both exposed groups showed a significant increase compared to the control (high dose: 188.9 ± 3.331; low dose: 185.7 ± 1.662; control: 168.0 ± 4.385), with no difference between doses. Our findings suggest that phthalates can interfere with the ECM remodelling that occurs in the ovary during the early postnatal days, leading to morphophysiological alterations in

structures associated with follicular activation and cell migration. Both factors, altered by exposure to these EDCs, may be critical determinants of the animal's reproductive health and fertility, since it is known that alterations in a developing organ may impact its organization and function in adulthood, due to developmental plasticity [7]. Therefore, our research highlights the importance of investigating long-term repercussions of such exposure. [8]

[1] M.F. Smith et al., Mol. Cell. Endocrinol. 191 (2002) 45-56.
[2] J. Griffin et al., J. Exp. Clin. Assist. Reprod. 3 (2006).
[3] J.E. Fortune, Anim. Reprod. Sci. 78 (2003) 135-163.
[4] E.A. Ford et al., Reproduction 159 (2020) 15-29.
[5] E.R. Fletcher et al., Toxics 10 (2022) 251.
[6] E. Brehm, J.A. Flaws, Environ. Epigenet. 7 (2021).
[7] D.J.P. Barker, J. Intern. Med. 261 (2007) 412.

[8] This research was supported by CAPES and FAPEG (Brazil).

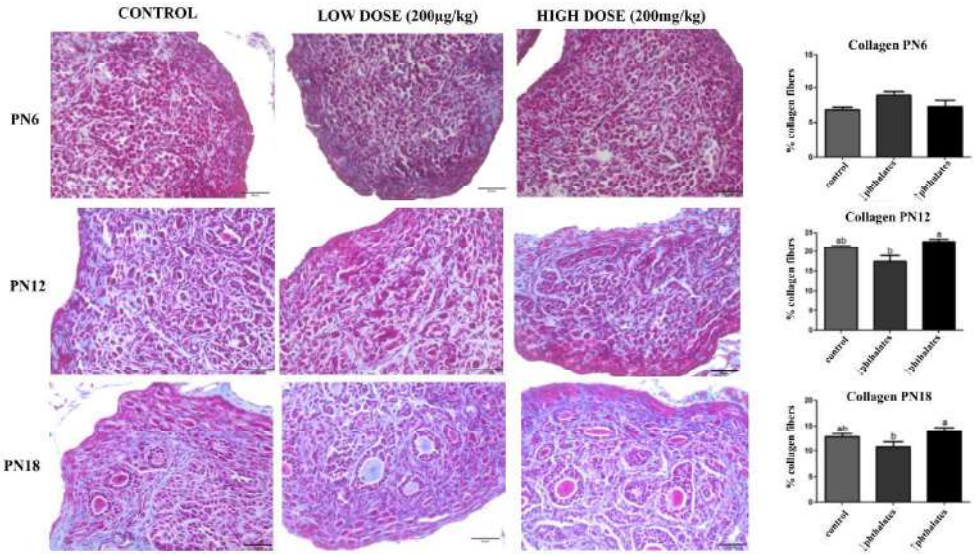

Figure 1. Photomicrographs of ovarian tissue stained with Gomori's trichrome. Collagen fibers in the ECM are stained in light blue. Scale bars: 20µm. Graphs display statistical relations among groups at different PN days for collagen fibers. Data were analyzed using ANOVA followed by Tukey's test ($p<0.05$).

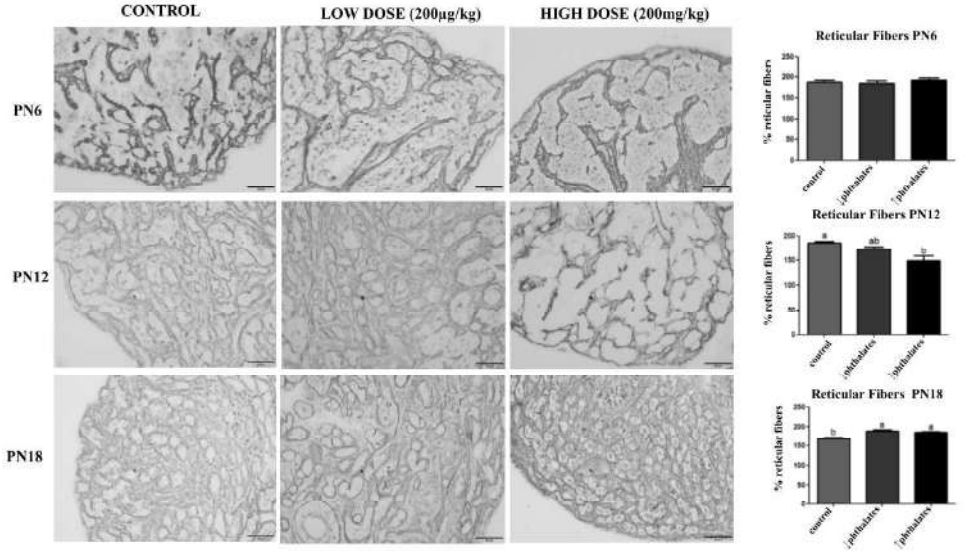

Figure 2. Photomicrographs of ovarian tissue stained with Gomori's reticulin. Reticular fibers in the ECM are stained in dark grey. Scale bars: 20µm. Graphs display statistical relations among groups at different PN days for reticular fibers. Data were analyzed using ANOVA followed by Tukey's test ($p<0.05$).

Estradiol-Induced Changes In The Prostatic Extracellular Matrix In Spontaneously Hypertensive Rats And The Effects Of The Combination With Naringenin

Bárbara Costa Malmann Medeiros[1]*, Max Vinicius Malmann Medeiros[1], Isadora Garcia Fernandes[1], Fernanda Cristina Alcântara dos Santos[1], Manoel Francisco Biancardi[1].

[1]Universidade Federal de Goiás
*bmalmann@discente.ufg.br

The prostate is a gland in the reproductive system of mammals that produces secretions that are important for the survival and maintenance of sperm [1]. Among the diseases that affect it are benign prostatic hyperplasia (BPH), common in men over 60 years of age and characterized by abnormal growth of the gland, and prostate cancer (PCa), the second most common type of cancer among men, according to the Global Cancer Observatory. Estradiol is an important sexual steroid that acts in the prostate from the development to the later stages. In men, permanently elevated estrogen hormones during old age have been associated with an increased risk of prostate diseases, such as PCa [2]. Naringenin, a flavonoid found in the peel of citrus fruits such as orange, grapefruit, and lemon, has anti-inflammatory, anticancer, antioxidant, and antiproliferative properties [3]. Therefore, it has proven to be an excellent therapeutic alternative for the treatment of prostate disorders, although very little is known about the direct action of this substance on the development of lesions in the gland. Studies using spontaneously hypertensive rats (SHR) have shown that these animals develop BPH between the 15th and 29th week of life, a lesion that may precede PCa, although the mechanisms involved in this transition are not yet fully elucidated [4]. Thus, the present study aimed to evaluate the effects of naringenin on estradiol-induced prostate lesions in SHR. For this purpose, 60 male rats (CEUA/UFG - 047/2021) were divided into 6 experimental groups, which were treated for 70 consecutive days starting at the sixth month of life. The rats received doses of estradiol every other day and/or doses of naringenin every day. The control animals received doses of mineral oil, following the same protocol as their respective treated groups. After the end of the treatment, the animals were euthanized and the tissues dissected out, collected, and sent for immunohistochemical analysis, picrosirius staining, and zymography. Through these analyses, we observed an increase in collagen in the prostates of animals treated with estradiol and also in those treated with estradiol and naringenin, in relation to their respective control groups (Figure 1). In addition, we observed an increase in the activity of matrix metalloproteinases (Figure 2) and an increase in the marking of tumor necrosis factor, also in the group treated with estradiol and estradiol in combination with naringenin when compared to their respective controls (Figure 3). Therefore, the evidence suggests that estradiol promoted stromal remodeling, and naringenin did not protect the prostate against these changes. I would like to thank CAPES for the financial support of this research.

[1] L.T. Aaron, O.E. Franco, S.W. Hayward, Urol. Clin. North Am. 43 (3) (2016) 279.
[2] A.F. Al-Domairy, Aust. J. Basic Appl. Sci. 5 (2) (2011) 59.
[3] A. Chanet et al., J. Agric. Food Chem. 60 (36) (2012) 8809.
[4] J. Zhang, M. Zhang, J. Tang, et al., Prostate Cancer Prostatic Dis. 24 (1) (2021) 49.
[5] This research was supported by Capes (Brazil).

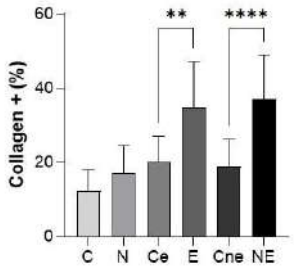

Figure 1. Relative frequency of collagen in the prostate stroma. Values correspond to mean ± standard deviation. Asterisks indicate statistically significant differences between experimental groups (** = $p < 0.01$; **** = $p < 0.0001$).

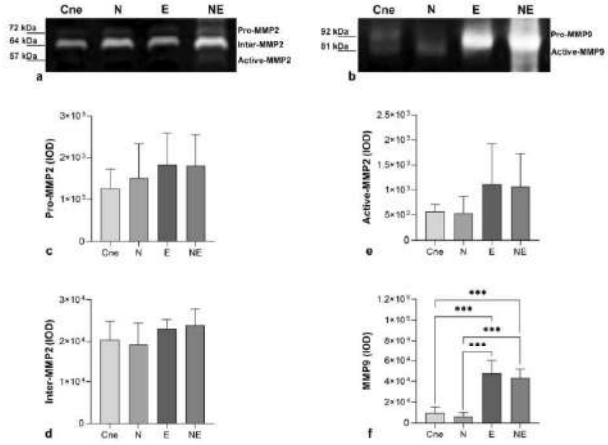

Figure 2. Zymogram analysis. (a-b) Zymography gel showing the typical clear bands of MMP2: proenzyme (72 kDa), intermediate (64 kDa), and active (57 kDa); and MMP9: proenzyme (92 kDa) and active enzyme (81 kDa). Due to the overlap of the pro-MMP9 and active MMP9 bands, they were quantified together. Groups Cne, N, E, and NE are represented. (c-f) Quantification of MMP gelatinase activity was expressed as integrated optical density (IOD). Values represent the mean and standard deviation. ANOVA/Tukey test, *** = $p < 0.0001$.

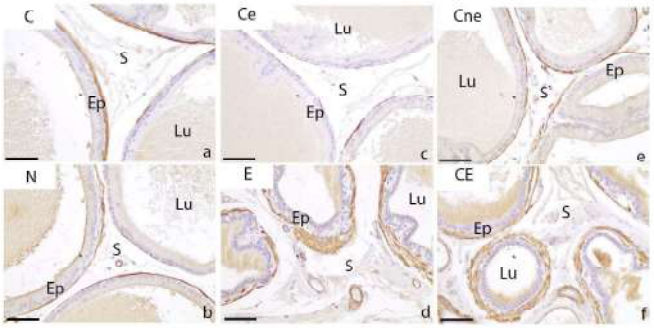

Figure 3. Distribution of TNF-alpha positive cells. The presence of TNF-alpha in the stroma was observed in all experimental groups, with a significant increase in groups treated with estradiol. Scale bar = 50 µm. Ep: epithelium, L: lumen, S: Stroma.

Estrogenic and antiandrogenic effects of atrazine on the ventral prostate of adult gerbils

Ariany Angéllica Caballero Corrêa[1]*, Jane Sousa Naves[1], Gabriel dos Santos Lima Sardinha[1], Danilo da Silva Lima[1], Sebastião Roberto Taboga[2], Manoel Francisco Biancardi[1], Fernanda Cristina Alcantara dos Santos[1]

[1]Institute of Biological Sciences (ICB), Federal University of Goiás (UFG)
[2]Department of Biological Sciences, Institute of Biosciences, Humanities and Exact Sciences, São Paulo State University (UNESP)
*ariany.angellica@discente.ufg.br

The prostate is a gland frequently affected by lesions such as benign prostatic hyperplasia (BPH), prostatitis, and cancer [1]. Several substances are capable of inducing morphophysiological alterations in this organ, such as endocrine-disrupting chemicals (EDCs), for example, plasticizers and pesticides [2]. Atrazine (ATZ) belongs to the class of herbicides and is an organic nitrogen compound that acts as a photosynthesis inhibitor in plants [3]. ATZ is one of the most widely used pesticides in Brazil, one of the world's largest producers of corn, wheat, and soybeans [4,5]. Notably considered an endocrine disruptor, research has highlighted its toxicity to various systems [6], including the reproductive system [7]. Considering this, the present study aimed to investigate the effects of ATZ on the prostate of adult gerbils (*Meriones unguiculatus*). This research received prior approval from the Animal Ethics Committee (CEUA/UFG) under protocol number 112/23. The animals (21ATZ) were exposed to a low dose (0.02 mg/kg/day) of ATZ diluted in 0.2 mL of saline solution for 21 days, characterizing a subchronic exposure. Meanwhile, the control group (21C) received only saline solution (0.2 mL) for the same period. Hematoxylin-eosin (HE) staining was used for histopathological evaluation. Imuno-histochemical techniques were performed to detect positive labeling for AR, PCNA, ERα and ERβ. The statistical analysis employed the Student's t-test for parametric data and the Mann–Whitney U test for non-parametric data. According to the findings, morphological analysis indicated that exposure to atrazine caused epithelial hyperplasia with the formation of papillary projections extending into the glandular lumen. Peri-alveolar inflammatory foci were detected, as well as hypertrophic alveoli with atrophic epithelium. Exposure to atrazine caused a reduction in the immunostaining of AR and ERβ, and an increase in PCNA and ERα. All these findings highlight the ability of ATZ as a potent endocrine disruptor, to affect hormonal balance and induce morphological alterations in the prostate of adult gerbils. These findings reinforce the necessity of conducting research on the toxicological effects of agricultural compounds, given their widespread exposure to humans and animals and their potential to cause adverse health outcomes. Acknowledgment to CAPES and FAPEG for funding the research [8,9].

[1] R. Cannarella et al., Endocrinology of the Aging Prostate: Current Concepts. Frontiers in Endocrinology, 12, 2021.
[2] V. Osadchiy et al., Endocrine disruptors and male sexual health. The Journal of Sexual Medicine, 21(1),2023.
[3] S. Singh et al. Toxicity, degradation and analysis of the herbicide atrazine. Environmental Chemistry Letters, 16, 2017.
[4] IBAMA. Brazilian Institute of the Environment. Pesticide Sales Reports, 2021.
[5] P.E.A. Salomão et al., Herbicides in Brazil: a brief review. Research, Society and Development, Research, Society and Development, 9(2), 2020.
[6] T.B Hayes. et al., From silent spring to silent night: Agrochemicals and the anthropocene. Elem Sci Anth. 29;5(57),2017.

[7] Zhu, S. et al. Meta-analysis and experimental validation identified atrazine as a toxicant in the male reproductive system. Environmental Science and Pollution Research, 28, 2021.
[8] This research was supported by the Coordination for the Improvement of Higher Education Personnel - Brazil (CAPES).
[9] This research was supported by the Research Support Foundation of the State of Goiás- Brasil (FAPEG).

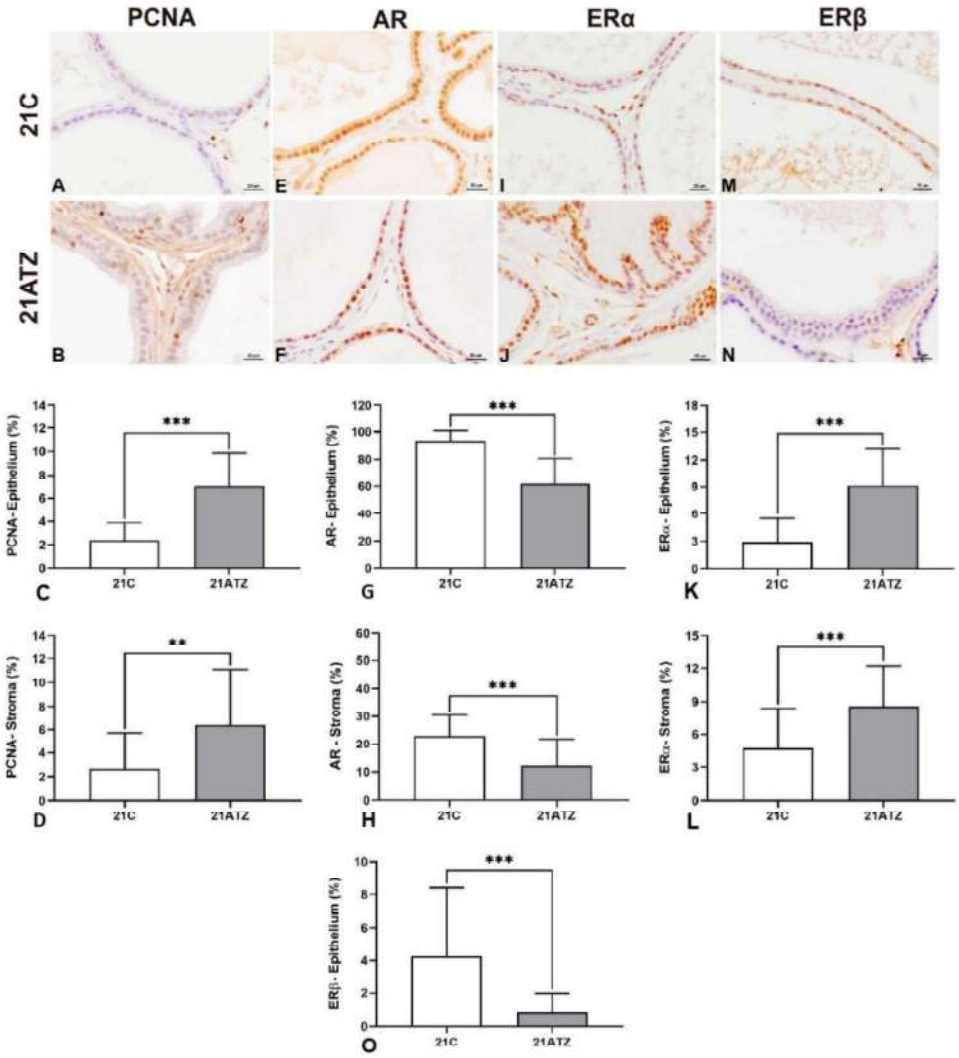

Figure 1. Immunohistochemical staining for PCNA (a–b), AR (e–f), ERα (i–j), and ERβ (m–n) in the ventral prostate of gerbils. Counterstaining: hematoxylin. Positive staining (in brown) is observed in epithelial cells (arrow) and stromal cells (arrowhead). Percentage of PCNA-positive epithelial and stromal cells (c–d), AR (g–h), ERα (k–l), and epithelial ERβ (o). All data are presented as mean ± standard deviation. ** = 0.001; *** = 0.0001.

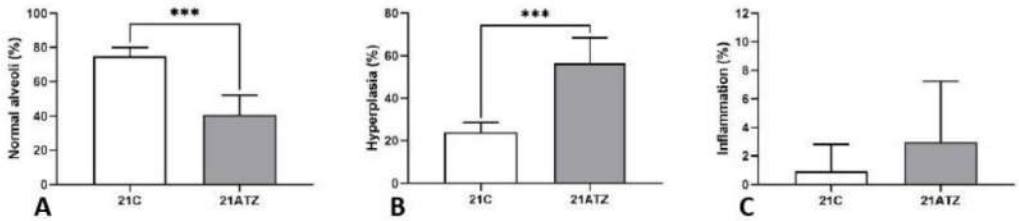

Figure 2. Relative frequency (%) of normal, hyperplastic, and inflammation-associated acini. All data are presented as mean ± standard deviation. ** = 0.001; *** = 0.0001.

Evaluation Of Cell Proliferation and Histopathological Analysis Of Ovaries From Diabetic Rats Treated With Lectin From The Bark Of *Crataeva tapia* (Crata BL)

Ana Vitoria Ferreira dos Santos[1]*, Giovanna Laura de Lima Borba[1], Suellen Rozy da Silva Medeiros[1], Alison Jose da Silva[1], Sara Vitória de Oliveira Costa[1], Raissa Gomes de França[1], Glenison de Rocha Duarte[1], Thaynara Caseli dos Santos[1], Elba Verônica Matoso Maciel de Carvalho[2], Bruno Mendes Tenorio[1], Fernanda das Chagas Angelo Mendes Tenorio[1].

[1] Department of Histology and Embryology, Federal University of Pernambuco (DHE-UFPE)
[2] Department of Biochemistry, Federal University of Pernambuco (DBIOq - UFPE)
* vitoria.fsantos@ufpe.br

Brazil ranks 4th worldwide in the ranking of type 1 diabetes mellitus, with approximately 499,000 individuals affected, according to data from the International Diabetes Federation (IDF) Atlas [1]. Consequently, as a chronic disease triggered by a metabolic disorder, uncontrolled diabetes can impair the Female Reproductive System and, consequently, fertilization. This occurs because follicular development is sensitive to endocrine, autocrine, and paracrine factors [2]. In individuals with diabetes, menstrual cycle abnormalities are common, including alterations in follicular development and corpus luteum formation, delayed menopause, and, in more severe cases, amenorrhea [2]. Lectins also stand out as a strategy to combat diabetes. They are beneficial, non-enzymatic proteins that bind specifically and reversibly to carbohydrates without chemical modifications. The Crata BL lectin, in particular, exhibits tissue-protective, antioxidant, anti-inflammatory, and hypoglycemic properties [3]. Thus, this experimental study aims to analyze the cellular routine and evaluate the histopathology of ovaries of diabetic rats treated with Crataeva tapia bark lectin (Crata BL). For this purpose, 20 Wistar albino rats (CEUA-136/2019) were divided into 4 groups of 5 animals, namely: Group I (CG) - Control rats; Group II (GD) - Diabetic rats; Group III (GDL) - Diabetic rats treated with Crata BL; and Group IV (GL) - Non-diabetic rats treated with Crata BL. Diabetes was induced with a single intraperitoneal dose of streptozotocin (50mg/kg of body weight). Diabetes confirmation was performed by measuring glucose on the 3rd and 7th day after streptozotocin administration. Lectin treatment consisted of intraperitoneal administration on day 1 (5mg/kg of body weight) on day 8 after diabetes confirmation. On day 15 after treatment, females were euthanized, and their ovaries were collected, fixed, processed, and stained with hematoxylin-eosin (HE). Furthermore, for the cellular control test (PCNA), histological sections were placed on silanized slides, which were processed, culminating in an antigen-antibody staining, observed as a brown precipitate. Subsequently, photomicrographs of the slides were used to calculate the area of cellular regulation, selecting PCNA-positive areas using ImageJ software. The PCNA graph was constructed in Excel with high values. Subsequently, the data were subjected to the Shapiro-Wilk normality test and then the nonparametric Kruskal-Wallis tests, followed by Dunn's test. Data were expressed as mean and standard deviation. Differences were considered statistically significant when $p < 0.05$. Analyses were performed using GraphPad Prism8® software. Histopathological analysis revealed that all experimental groups had a connective tissue capsule covering the organ, well-defined medullary and cortical regions, and the presence of developing follicles. However, Group II (diabetic rats) showed decreased ovarian size, a reduced number of corpora lutea, and the presence of larger vessels when compared to the other groups. In this sense, increased angiogenesis served as a compensatory mechanism for supplying energy and nutrients to the organ. However, despite the increased vascularization, the reduced number of corpora lutea

indicates lower ovulation compared to the other groups, which can be explained by the pathophysiology of diabetes (Figure 1). Furthermore, the Cell Proliferation test revealed lower cellular regulation in the Diabetic Group, the Lectin-treated Diabetic Group, and the Lectin Group when compared to the control group. This indicates a reduction in the number of ovarian cells resulting from a decrease in cell division, a fact that, in the diabetic and lectin-treated diabetic groups, can be explained by insulin resistance. However, the lectin-treated diabetic group showed predominantly higher PCNA expression compared to the diabetic group, possibly due to the hypoglycemic properties of the lectin (Figure 2). The non-diabetic lectin-treated group also showed decreased PCNA, which can be explained by a rebound effect, commonly found with current medications. In conclusion, it is possible to state that type 1 diabetes can somehow alter the restrictions on the structures that maintain reproductive balance, and that Crataeva tapia has hypoglycemic properties that can aid in the treatment of diabetes, mitigating the damage the disease can cause to fertility.

[1] Iezzi M. Brazil is the 4th country in the world ranking for type 1 diabetes; 499 thousand live with the condition, says IDF [Internet]. Um Diabético. 2025 [cited 2025 Jun 1].
[2] Wellons MF et al. Ovarian aging in women with diabetes: An overview. Maturitas [Internet]. 2017 Feb [cited 2022 May 16]; 96:109–13.
[3] da Rocha et al. Lectin from Crataeva tapia Bark Improves Tissue Damages and Plasma Hyperglycemia in Alloxan-Induced Diabetic Mice. *Evidence-based complementary and alternative medicine : eCAM*. 2013;2013:869305.

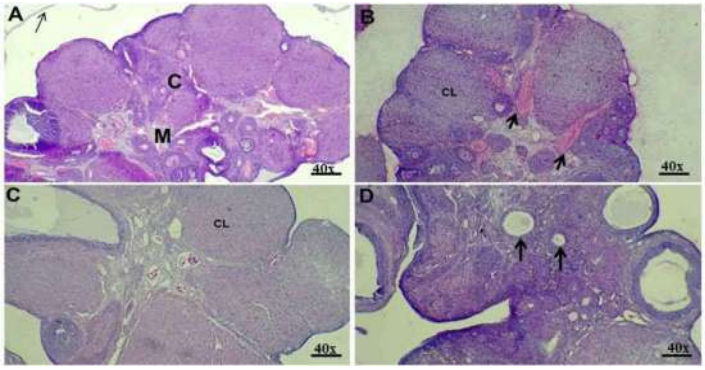

Figure 1: Photomicrographs of the ovaries from the experimental groups. Panel **A** shows Group I, displaying the cortical region (C), medullary region (M), and the connective tissue capsule covering the organ (arrow). Panel **B** depicts Group II, illustrating a reduction in corpora lutea and the presence of larger caliber vessels (arrow). Panels **C** and **D** represent Groups III and IV, respectively, appearing similar to Group I with the presence of corpora lutea (CL) and follicles at various stages of development (arrow). All images are stained with Hematoxylin-Eosin (HE). 40x magnification.

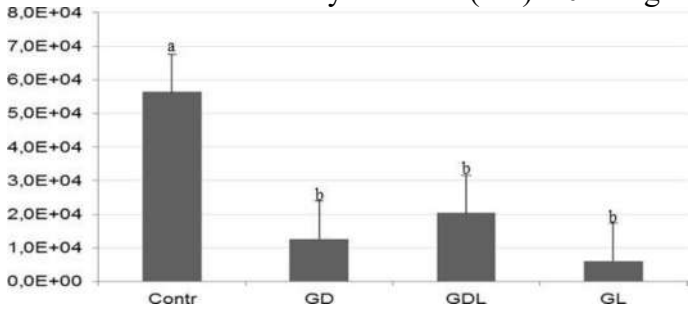

Figure 2: PCNA analysis in the ovaries of experimental groups (p=0.000). Means followed by different letters within a column differ significantly. Kruskal–Wallis non-parametric test followed by Dunn's post-hoc test ($p \leq 0.05$). E(raised).

Evaluation of the Effects of Aspartate-Arginine Dipeptide on the Ventral Prostate of SHR: Analysis of Metalloproteinase Activity and Incidence of Collagen Fibers in the Prostatic Stroma

Isadora Garcia Fernandes[1]*, Bárbara Costa Malmann Medeiros[1], Carlos Henrique de Castro[1], Helen Cristian Marques Tomaz[1], Fernanda Cristina Alcântara dos Santos[1], Manoel Francisco Biancardi[1].

[1] Universidade Federal de Goiás

isadora_395@discente.ufg.br

The prostate gland is located below the bladder and is part of the male reproductive system [1]. Its main function is to produce prostatic fluid, which protects and nourishes sperm [2]. The prostate is susceptible to diseases such as benign prostatic hyperplasia (BPH). BPH is characterized by epithelial and stromal enlargement of the prostate, affecting a large part of the elderly population and potentially causing lower urinary tract symptoms that affect the quality of life of most individuals [3]. The increase in collagen fibers contributes to the primary development of fibrosis, and increased muscle tone and stiffness, compromising the functioning of this organ and aggravating the symptoms of the disease [4]. Therefore, treatments that seek to improve this condition are necessary. Currently, many peptides are showing promising results in therapy. The dipeptide aspartate[1]-arginine[2] (Asp-Arg), obtained from the cleavage of angiotensins in the renin-angiotensin system (RAS), has been studied for its biological activities, exerting opposite effects to the classical angiotensin II pathway responsible for pro-fibrotic and proliferative effects [5][6]. Metalloproteinases (MMPs) play an important role in collagen degradation and tissue remodeling during the development of diseases [7]. Therefore, the present study aimed to evaluate the effects of Asp-Arg on collagen fibers and metalloproteinase activity. For this purpose, 15 male SHR (Rattus norvegicus) rats aged 20 weeks were divided into a control group (SHRC) and treated groups (SHRD 1 and 2) with the dipeptide (1st dose: 7.8 µg/kg/h, and 2nd dose: 15.6 µg/kg/h) for 4 weeks via osmotic minipump (CEUA/UFG - nº 013/2021). The animals were euthanized, and the materials were then collected, processed, and subjected to zymography for metalloproteinases 2 and 9, and picrosirius staining. The results showed that the intermediate form of MMP2 had a significant increase in its activity in the SHRD 1 group (Fig. 1), indicating effects in stromal collagen reduction. For picrosirius staining, it was possible to observe a statistically significant decrease in collagen frequency in the stroma of the SHRD 1 and SHRD 2 groups compared to the SHRC group (Fig. 2). Therefore, the treatment with Asp-Arg was capable of remodeling the prostatic stroma by increasing MMP 2, which increased collagen degradation, contributing to stromal remodeling. I would like to thank the CNPq (National Council for Scientific and Technological Development) for the financial support that encouraged and supported this research [8].

[1] B.G. Timms, Differentiation 76 (6) (2008) 565–577.

[2] G. Untergasser, et al., Exp. Gerontol. 40 (3) (2005) 121.
[3] B. Chughtai et al., Nat. Rev. Dis. Primers 2 (1) (2016) 1–15.
[4] E. Golomb et al., J. Androl. 21 (1) (2000) 58.
[5] R.A.S. Santos et al., Physiol. Rev. 98 (1) (2017) 505
[6] V. Apostolopoulos et al., Molecules 26 (2) (2021) 430.
[7] W. Meng et al., Am. J. Hypertens. 27 (6) (2014) 775–782.
[8] This research was supported by CNPq (Brazil).

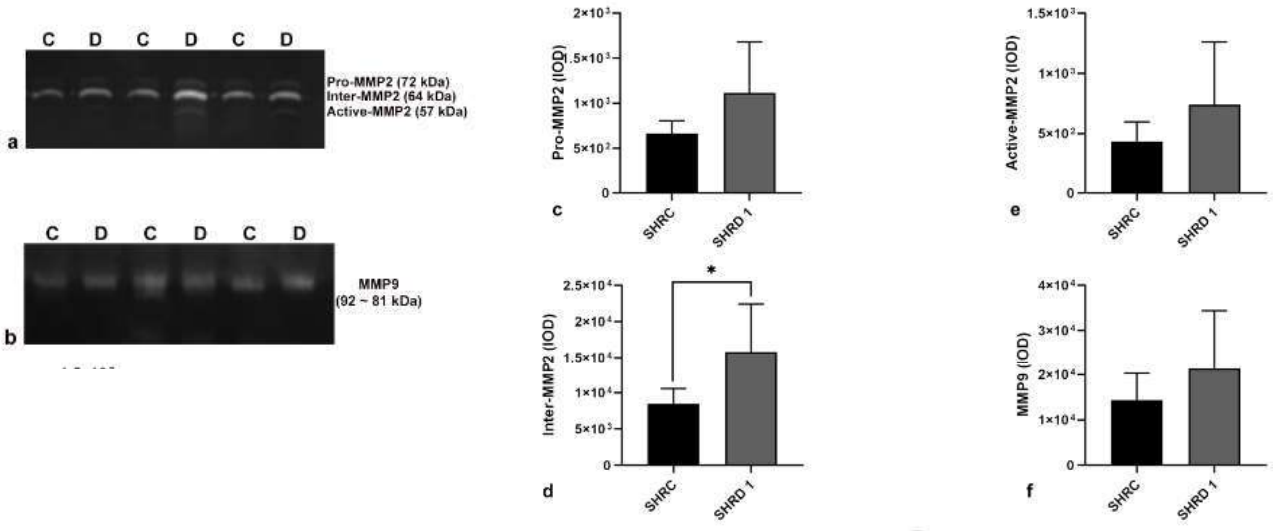

Figure 1. Zymography showing clear bands typical of MMP2 (Fig. 1a): proenzyme (72 kDa), intermediate (64 kDa), and active (57 kDa); and MMP9 (Fig. 1b) (92 kDa - 81 kDa). In the gels, the SHRC (C) and SHRD 1 (D) groups are represented in triplicate. Quantification of MMPs activity was expressed as integrated optical density (IOD) (Fig. 1c-f). Statistically significant difference between groups (*) $p \leq 0.05$.

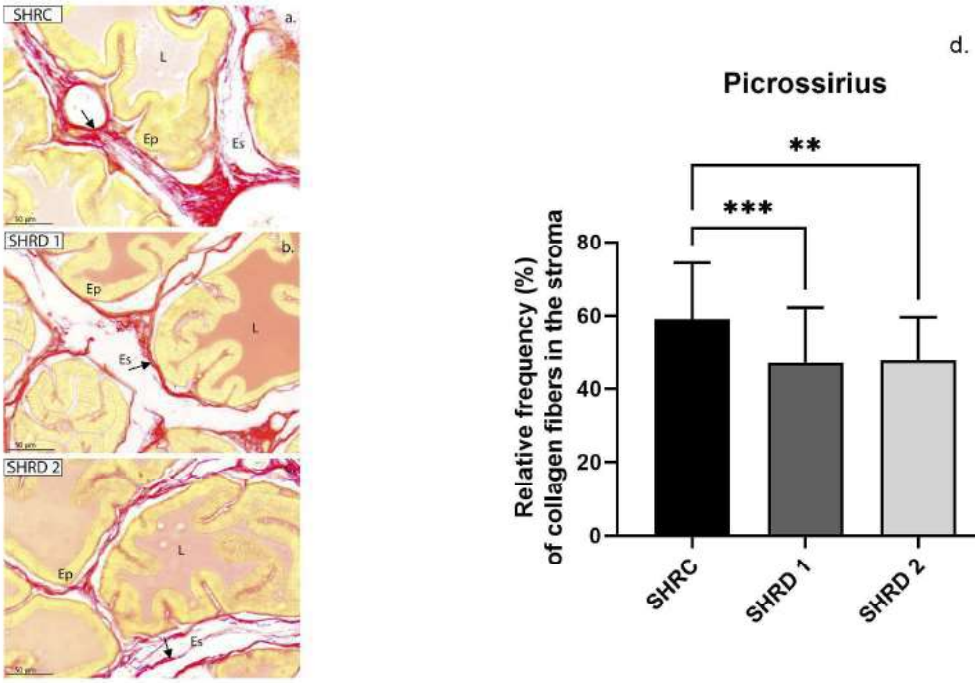

Figure 2: Ventral prostate sections from SHRC, SHRD 1, and SHRD 2 groups (Fig. 2a–c), stained with Picrosirius Red. Relative frequency (%) of collagen in the prostate stroma (Fig. 2d). Statistically significant difference between groups (**) $p \leq 0.01$ and (***) $p \leq 0.001$. Scale bar = 50 µm. (Ep: Epithelium; Stroma; L: Lumen; Arrow: collagen).

Experimental infection of central nervous system cells from mice with CHIKV, in vitro.

Maria Ester da Cunha Monteiro[1,2]*, Adeniele Lopes da Cruz Carneiro[1,3], Felipe Tuji de Castro Franco[1,3], José Antonio Picanço Diniz Junior[1,2].

[1] Multiuser Laboratory of Cell Biology and Ultrastructure, [2] Postgraduate Program in Virology of Evandro Chagas Institute, [3] Postgraduate Program in Biology of Infectious and Parasitic Agents, Federal University of Pará.
*maritemonteiro16@gmail.com

Chikungunya virus (CHIKV) is an arbovirus belonging to the genus *Alphavirus*, family *Togaviridae*. It is composed of a positive-sense single-stranded RNA genome, an icosahedral capsid, and a lipid envelope containing glycoproteins that mediate its entry into the host cell. Infection with CHIKV causes clinical manifestations such as fever, rash, and polyarthralgia, which may progress to chronic joint inflammation [1,2]. In addition, the virus can lead to various central nervous system (CNS) complications, including encephalitis, seizures, meningoencephalopathy, myelitis, and choroiditis, frequently associated with neurological sequelae [3,4]. Murine models have been widely employed to investigate CHIKV pathogenesis and immune responses [5,6]. This study aimed to characterize the cellular alterations induced by CHIKV in co-cultures of glial cells and neurons, as well as to identify the cell types susceptible to infection. Primary cultures of glial cells were established, and after 14 days, embryonic neurons (from gestational day 18) were seeded onto the glial monolayer [7]. After four days, the co-cultures were inoculated with the H855964 viral strain, kindly provided by the Arbovirology Section of the Evandro Chagas Institute. Cultures were photodocumented and fixed at 48, 72, and 96 hours post-infection using 4% paraformaldehyde in PHEM buffer (pH 7.0) at room temperature. Subsequently, cells were subjected to indirect immunofluorescence to detect viral antigens and astrocytes, using anti-CHIKV and anti-GFAP antibodies, respectively [8]. DAPI was employed for nuclear staining. The results demonstrated a progressive cytopathic effect over time, characterized by marked vacuolization in microglia, retraction of astrocytic processes, and decreased cell density, particularly of microglia and neurons. Immunofluorescence revealed intense immunolabeling of the viral antigen predominantly in microglia and neurons, with lower intensity observed in astrocytes. Additionally, perinuclear viral labeling was noted, possibly localized to the endoplasmic reticulum [9], in cells morphologically consistent with mature oligodendrocytes, which were spread across the coverslips and lacked GFAP immunoreactivity. Pyknotic nuclei, indicative of cell death, were also identified. These findings underscore the need for further studies employing specific cellular markers to better characterize the cellular targets of CHIKV in the murine CNS.

[1] L.A. Silva, T.S. Dermody, *J. Clin. Invest.* 127 (3) (2017) 737–749.
[2] B.A. Goupil, C.N. Mores, *Open Rheumatol. J.* 10 (2016) 129–140.
[3] N. Kumar et al., *Front. Cell. Infect. Microbiol.* 14 (2024) 1380736.
[4] K.L. Barr et al., Front. Public Health 6 (2018) 186.
[5] B. Wahid et al., *Int. J. Infect. Dis.* 58 (2017) 69–76.
[6] T. Das et al., *J. Gen. Virol.* 96 (2015) 294–310.
[7] V. Moura Neto et al., *Rev. Bras. Pesq. Méd. Biol.* 16 (4) (1983) 291–294.
[8] J.A.P. Diniz et al., *Rev. Bras. Biociênc.* 6 (Suppl. 2) (2008) 223–225.
[9] T. Inoue, B. Tsai, *Cold Spring Harb. Perspect. Biol.* 5 (1) (2013) a013250.
[10] This research was supported by CAPES (Brazil)

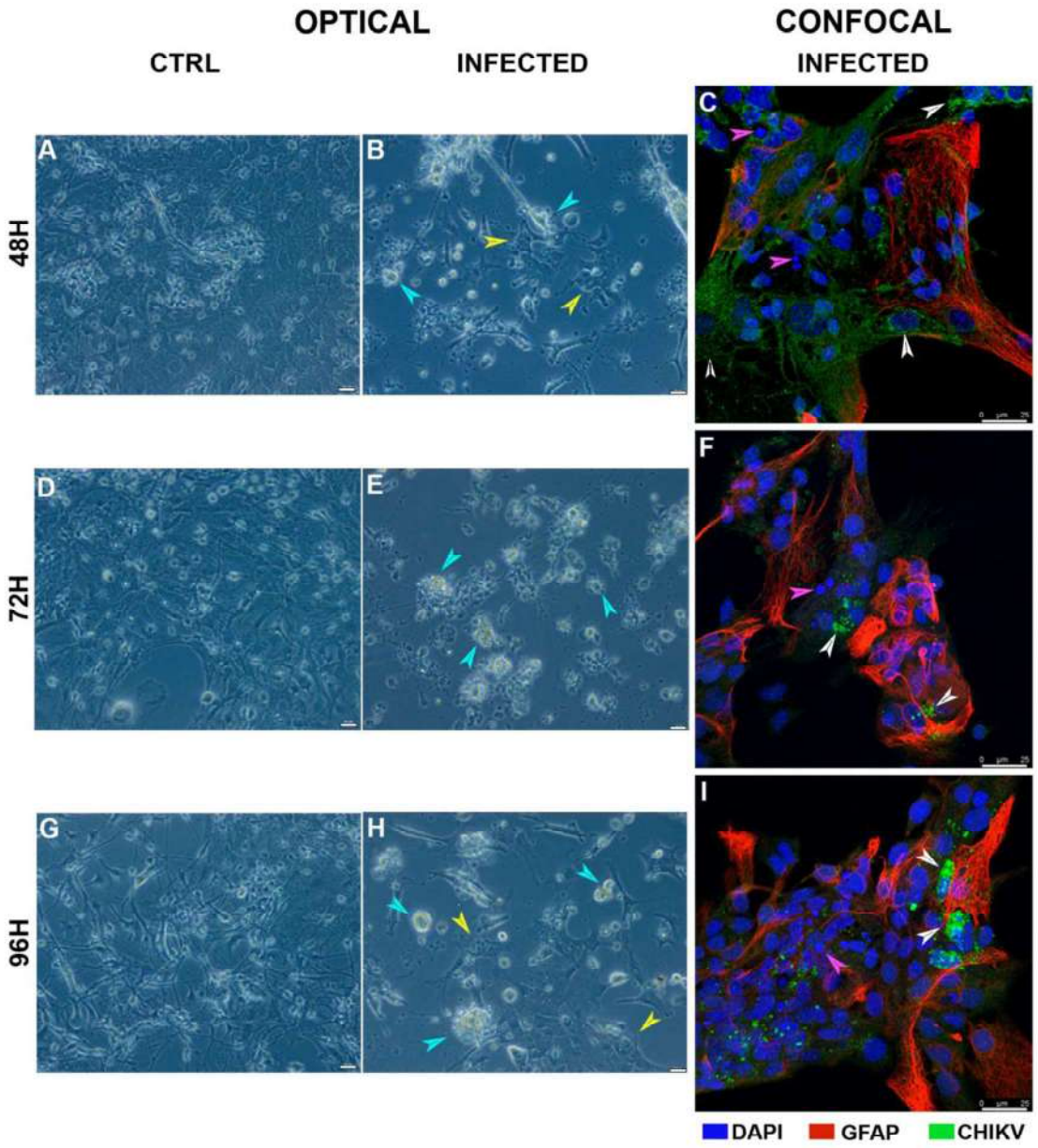

Figure 1: Photomicrographs acquired by phase-contrast microscopy (A, B, D, E, G, and H) and confocal microscopy (C, F, and I). Panels A, D, and G show uninfected control cultures without detectable morphological alterations. Panels B, E, and H correspond to cultures infected for 48, 72, and 96 hours, respectively, in which blue arrowheads indicate highly vacuolated microglia, and yellow arrowheads indicate astrocytes exhibiting retracted processes. Panels C, F, and I display infected cultures at 48, 72, and 96 hours, respectively. In these confocal images, astrocytes are immunolabeled in red for GFAP, CHIKV antigens are labeled in green, and cell nuclei are stained in blue with DAPI. Pink arrowheads indicate pyknotic nuclei, and white arrowheads indicate CHIKV immunolabeling. A, B, D, E, G, and H, scale bar 50 µm; C, F, and I, scale bar 25 µm.

.

Fractal Evaluation Of Myocardial Nuclear Architecture In Neonatal Rats Exposed To Maternal Protein-Energy Malnutrition Treated With Cannabidiol nanoemulsion

Isaque Bertoldo Santos da Silva[1]*, Suellen Rozy da Silva Medeiros[1], Maria Manuela dos Santos Rodrigues[1], José Abel Pessôa Neto[1], Renan Gabriel da Silva Ferreira[1], Jadyel Sherdelle Guedes do Nascimento[1], Elba Verônica Maciel Matoso de Carvalho[2], Sara Vitoria de Oliveira Costa [1], Bruno Mendes Tenorio[1], Fernanda das Chagas Angelo Mendes Tenorio[1]

[1] Department of Histology of Embryology, Federal University of Pernambuco, [2] Department of Biochemistry, Federal University of Pernambuco
*isaque.bertoldo@ufpe.br

The gestational period plays a critical role in the formation and development of embryonic tissues and organs. Adequate maternal nutrition during this stage is essential to ensure proper intake of vital macronutrients, including proteins, carbohydrates, and lipids. Insufficient protein consumption during pregnancy may lead to structural and functional alterations in fetal development, with metabolic consequences in early life and increased risk of cardiovascular and metabolic disorders in adulthood [1]. Oxidative stress, resulting from an inefficient antioxidant system often linked to inadequate availability of amino acids such as glutathione, is a key contributor to these pathologies. When dietary imbalance impairs glutathione synthesis, reactive oxygen species (ROS) accumulate, promoting cellular damage to membranes, proteins, and intracellular components [2]. Cannabidiol (CBD), a non-psychoactive compound derived from Cannabis sativa, has demonstrated significant antioxidant, anti-inflammatory, and analgesic properties. Recent studies suggest that CBD may counteract many of the deleterious effects of protein-energy malnutrition during gestation, potentially through its interaction with CB2 receptors [3]. This study aimed to evaluate the potential protective effects of cannabidiol on the myocardial development of neonatal rats subjected to maternal protein malnutrition (PM), using fractal analysis as a morphometric tool. A total of ten (10) neonatal Wistar rats (Rattus norvegicus) of each group were used in the study (Ethics Committee Protocol: n°0055/2024), allocated into three groups: Group I – offspring from mothers with normal protein intake (control); Group II – offspring from mothers subjected to a PM diet (AIN-93G with 6% protein) for 21 days; Group III – offspring from PM-diet mothers concurrently treated with a CBD nanoemulsion (10 mg/kg/day for 20 days, administered in the morning). After euthanasia, hearts were fixed in buffered formalin, paraffin-embedded, sectioned at 3 µm thickness, and stained with hematoxylin-eosin (HE). Images were captured under an optical microscope (400× magnification), with 15 fields per animal analyzed, totaling 120 images per experimental group. Image processing was conducted in ImageJ (NIH, USA). Images were converted to 8-bit and subjected to the following steps: minimum auto-thresholding, 3-pixel median filtering, LUT inversion, hole-filling, and watershed segmentation. Fractal analysis was performed using the FracLac plug-in (A. Karperien, Charles Sturt University, Australia) to calculate the fractal dimension using the box-counting method (D_{box}) and lacunarity, which describes spatial heterogeneity and the distribution of gaps within the structures (Figure 01). Although no visually apparent morphological differences were observed (Figures 02, 03). The fractal analysis revealed statistically significant differences between the control and PM groups in both fractal dimension and lacunarity, with $p = 0.002$ for both. Furthermore, the group treated with CBD exhibited fractal metrics that closely aligned with those of the control group, indicating a potential restorative effect of cannabidiol against PM-induced structural damage. These findings underscore the relevance of fractal analysis as a robust quantitative tool in biomedical research, capable of detecting

subtle tissue alterations that might not be evident through traditional histological evaluation. By providing precise numerical indicators, such as fractal dimension and lacunarity, this method may enhance diagnostic accuracy and support the development of targeted therapeutic strategies. In conclusion, fractal parameters proved effective in characterizing the myocardial architectural complexity of neonatal rats and demonstrated the therapeutic potential of cannabidiol in mitigating structural impairments caused by gestational protein-energy malnutrition.

[1] H.B. Assalin et al. PLoS One, 14. (2019).
[2] B.C. Masiero et al. Ann Anat, 241. (2022).
[3] K. Lee et al. Cannabis Cannabinoid Res, 9. (2024).

Formula 1:

$$D_{bc} = -\lim_{\varepsilon \to 0}\left[\frac{\log N(r+\varepsilon) - \log N(r)}{\log(r+\varepsilon) - \log r}\right]$$

Formula 2:

$$\Lambda = \left[\sum_{g}\sum_{i}\left(1 + (\sigma|\mu)^2\right)\right] \Big/ n$$

Figure 01. Fractal parameters Formulas

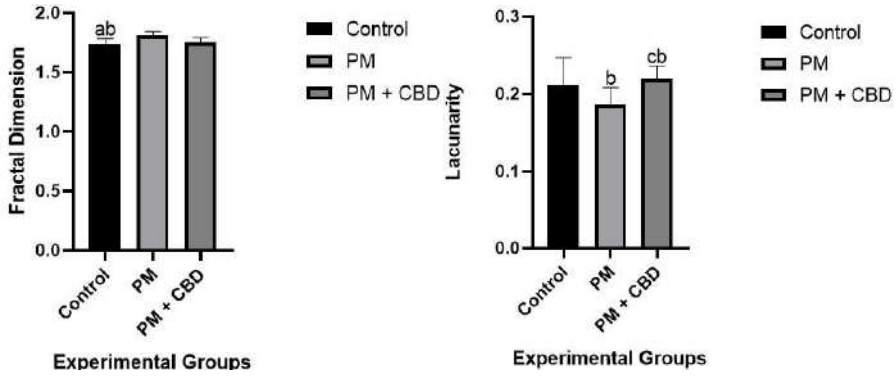

Figure 02. Graphics exhibiting the Fractal dimension and Lacunarity from the Experimental group's images.

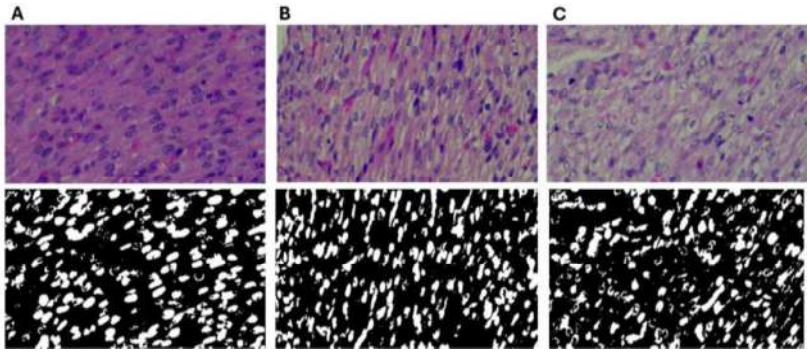

Figure 03. Segmented photomicrographies from the experimental groups - A – Control; B – Protein-energy Malnutrition; C – Protein-energy Malnutrition + Cannabidiol nanoemulsion. 400X.

Galectin-3 as a Modulator of NLRP3 Inflammasome and Ocular Inflammation in Allergic Conjunctivitis

Renata Pereira Lourenço[1*], Diego Dias dos Santos[1], Rebeca Donizete Correia da Silva[1], Gisela Rodrigues da Silva Sasso[1], Kátia de Vasconcelos[1], Cristiane Damas Gil[1]

[1]Department of Morphology and Genetics, Paulista School of Medicine, Federal University of São Paulo – UNIFESP – São Paulo.
*renatapl2002@hotmail.com

The NLRP3 inflammasome is a cytoplasmic receptor complex that, when activated, triggers the release of IL-1β and IL-18, contributing to the pathogenesis of various diseases, including allergic reactions. Studies have shown that the NLRP3/IL-1β axis plays a key role in the development of allergic conjunctivitis (AC) [1]. Additionally, the protein galectin-3 (Gal-3) has been implicated in the activation of the NLRP3 inflammasome and IL-1β production by macrophages [2]; however, its specific role in NLRP3 activation during allergic responses remains unclear. In this study, we investigated the role of Gal-3 in allergic responses and its potential involvement in regulating the NLRP3 inflammasome, using both an experimental model of AC and *in vitro* assays with IL-4-stimulated human keratinocyte cultures. AC was induced in wild-type (WT) and Gal-3 knockout (Gal-$3^{-/-}$) male BALB/c mice immunized with ovalbumin (OVA), followed by topical ocular challenges with OVA on days 14-16. Their palpebral conjunctivae were analyzed under the following conditions (n = 5 animals/group): SHAM (control), which received only sterile saline, and AC. Twenty-four hours after the final challenge, eyelid tissues were collected for analysis (CEUA 2125200323) [3]. AC in both WT and Gal-$3^{-/-}$ mice was characterized by a significant increase in eosinophil numbers (68±10 and 73±9, respectively) in the palpebral conjunctiva compared to their respective controls ($p < 0.05$) (Fig. 1A-D, I). A higher proportion of degranulated mast cells (~60%) was observed in Gal-$3^{-/-}$ AC mice compared to intact cells (~40%), whereas WT AC mice showed more intact (58%) than degranulated (42%) mast cells (Fig. 1J). Transcriptome analysis revealed increased *Il1β* expression in mast cells stimulated with anti-OVA IgE (GSE96696) and in eosinophils stimulated with OVA (GSE57757); however, only mast cells exhibited increased *Lgals3* expression. In WT AC mice, the palpebral conjunctiva showed elevated levels of IL-1β, NLRP3 (Fig. 1E-H, K, L), and phosphorylated p38 compared to both WT SHAM and Gal-$3^{-/-}$ AC groups. *In vitro*, recombinant Gal-3 addition to IL-4-stimulated keratinocytes resulted in increased levels of NLRP3 and ASC, as detected by immunofluorescence, supporting our *in vivo* findings. Moreover, enhanced co-expression of these markers was observed in Gal-3-treated groups compared to control and IL-4-only groups. Overall, our results highlight Gal-3 as a key factor in the pathogenesis of ocular allergy, particularly in modulating mast cell activation and NLRP3 levels, suggesting that these components may serve as potential therapeutic targets in ocular allergic conditions [4].

[1] Y. Xiao et al. *Clinical & Experimental Allergy*, 48 (9) (2018) 1080-1091.
[2] B.S. Markovic et al. *Journal of Crohn's and Colitis*, 10 (5) (2016) 593-606.
[3] F.E.C. Andrade et al. *British Journal of Ophthalmology*, 102 (7) (2018) 1003-1010.
[4] Support: PIBIC/CNPq (143423/2022-3), FAPESP (2022/07848-4) and Capes (Code 001) (Brazil).

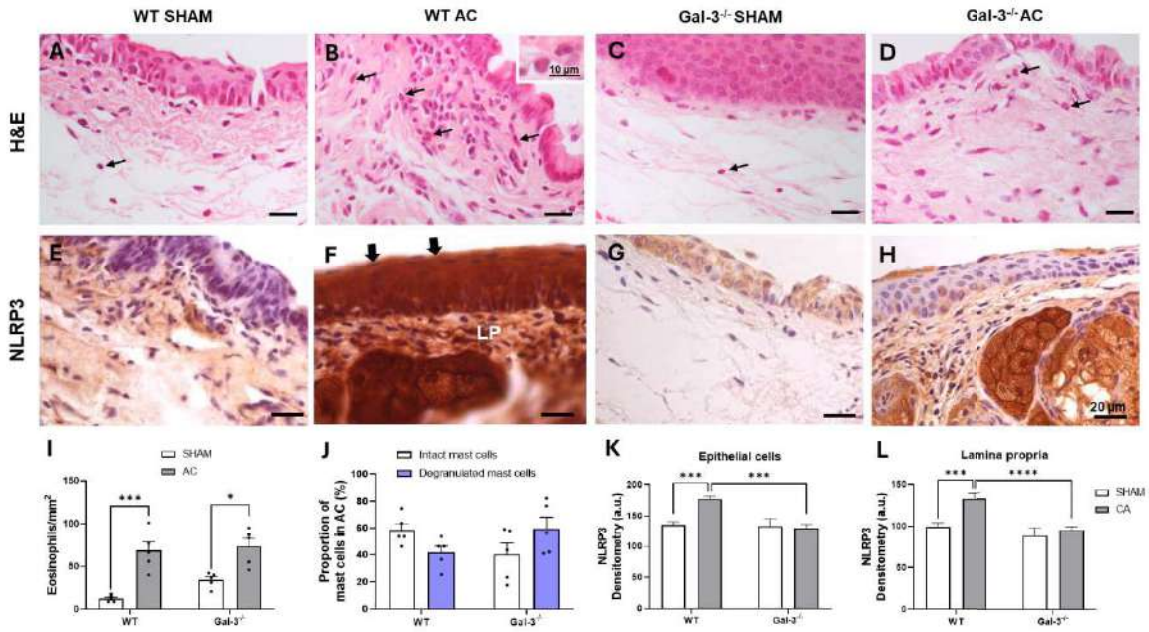

Figure 1. Histopathological analysis of the palpebral conjunctiva in the ovalbumin-induced allergic conjunctivitis (AC) model. **A, E:** WT SHAM group. **B, F:** WT AC group. **C, G:** Gal-3$^{-/-}$ SHAM group. **D, H:** Gal-3$^{-/-}$ AC group. **A–D:** Representative photomicrographs of the palpebral conjunctiva in mice, highlighting eosinophils (arrows) in the groups. Inset (upper right corner) shows two eosinophils in detail. Staining: hematoxylin and eosin. **E–H:** NLRP3 expression in the palpebral conjunctiva. Intense NLRP3 immunoreactivity was detected in the epithelium (arrows) and lamina propria (LP) of the WT AC group compared to the other groups. Counterstaining: Carazzi's hematoxylin. Scale bars: 20 µm and 10 µm (inset in panel B). **I:** Total eosinophil count. **J:** Relative and differential quantification of mast cells in AC. **K, L**: Densitometric analysis of NLRP3 expression in the epithelium and lamina propria. Data are presented as mean ± S.E.M. of cell number per mm² (I), the proportion (%) of intact and degranulated mast cells (J) and arbitrary units (a.u.) (K, L) (n = 5 animals/group). *P < 0.05; ***P < 0.001; ****P < 0,0001 (Two-way ANOVA, Bonferroni post hoc test).

Histochemical, Morphometric, and Fractal Analysis of the Duodenum in Rats Subjected to Early Weaning and Treated with Melatonin

Jadyel Sherdelle Guedes do Nascimento[1]*, Renan Gabriel da Silva Ferreira[1], Weslleyanne Milena da Silva Costa[1], Maria Eduarda Carneiro de Lima[1], Ana Carolina Ribeiro Saraiva da Costa[1], Maria Gabriela da Silva Mello[1], Raissa Gomes de França[1], Elba Verônica Marciel Matoso de Carvalho[2], Bruno Mendes Tenorio[1], Fernanda das Chagas Ângelo Mendes Tenorio[1].

[1]Federal University of Pernambuco, Department of Histology and Embryology. Recife, Pernambuco - Brazil.

[2]Federal University of Pernambuco, Department of Biochemistry. Recife, Pernambuco – Brazil.

*jadyel.sherdelle@ufpe.br

Human breast milk contains hormones and growth factors, such as Epidermal Growth Factor (EGF) and Insulin-like Growth Factor I (IGF-I), which are more concentrated in colostrum and play a crucial role in the development of the gastrointestinal tract [1]. Therefore, the abrupt and premature interruption of breastfeeding may result in harm to the infant's digestive system. However, studies have already demonstrated that exogenous administration of melatonin can reduce microvascular effects in the small intestine during systemic inflammation [2]. This study aims to perform histochemical, morphometric, and fractal analyses of the duodenum in rats subjected to early weaning and treated with melatonin. A total of 40 male Wistar rats were used, in accordance with approval from the Animal Ethics Committee of UFPE (protocol number 0045/2020), and allocated into four experimental groups: Control, Early Weaning (EW), Early Weaning + Vehicle (EW+Vehicle), and Early Weaning + Melatonin (EW+Mel). The animals in the control group were weaned at 21 days of age, while animals in the other groups were weaned on the 15th day of life. Subsequently, the EW+Mel group was treated with intraperitoneal melatonin for 30 days, and the EW+Vehicle group received the vehicle over the same period. After the treatment period, animals were euthanized, and their organs were collected, weighed, and processed for morphometric, histochemical, and fractal analysis. Microscopic images of the duodenum were used to calculate fractal dimension using the box-counting method (Dbox) and entropy-based information dimension (Dinf), as described by Tenório et al. (2017)[3]. Hypothesis testing for morphometric analysis was conducted using the non-parametric Kruskal-Wallis test, followed by Dunn's post hoc test, with a p-value < 0.05 considered statistically significant. Based on the histochemical analysis and statistical results from the experimental animals, significant differences were observed among the groups. The EW and EW+Vehicle groups showed higher PAS staining intensity compared to the Control and EW+Mel groups (Figure 1). Morphometric analysis of the duodenum revealed that the number of goblet cells, epithelial height, and microvilli height were greater in the EW and EW+Vehicle groups compared to the Control group. The EW+Mel group presented values similar to those of the Control group. However, the muscular layer thickness was reduced in the EW and EW+Vehicle groups. It is noteworthy that the EW+Mel group consistently exhibited values tending toward the baseline of the Control group. Fractal dimension and lacunarity parameters were effective in detecting changes in the EW and EW+Vehicle groups compared to the Control and EW+Mel groups. Both fractal dimension and lacunarity were

higher in the EW and EW+Vehicle groups than in the Control and EW+Mel groups (Figures 2 and 3). Again, the EW+Mel group exhibited values approaching those of the Control group, indicating a trend toward normalization. In conclusion, early weaning can lead to disorders in the digestive tract, such as increased goblet cell count. However, melatonin administration can mitigate the effects of early weaning, thereby promoting better gastrointestinal function.

REFERENCES

[1] S. Oguchi et al,. Growth factors in breast milk and their effect on gastrointestinal development. *Zhonghua Minguo Xiao er ke yi xue hui za zhi [Journal]. Zhonghua Minguo Xiao er ke yi xue hui*, *38*(5), 332-337. 1997.

[2] M. Oude Lansink et al., Melatonin reduces changes to small intestinal microvasculature during systemic inflammation. *Journal of Surgical Research*, *211*, 114-125. 2017.

.[3] B.M. Tenório et al,Can fractal methods applied to video tracking detect the effects of deltamethrin pesticide or mercury on the locomotion behavior of shrimps?. *Ecotoxicology and environmental safety*, *142* , 243-249.2017.

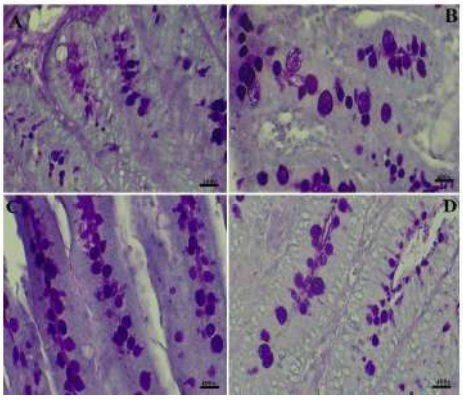

Figure 1 Photomicrograph of the duodenum of animals stained with PAS. The image documents PAS-stained slides to highlight glycoprotein labeling in the histological sections of the following groups: (A) Control Group, (B) EW (Early Weaning), (C) EW+Vehicle, and (D) EW+Melatonin.

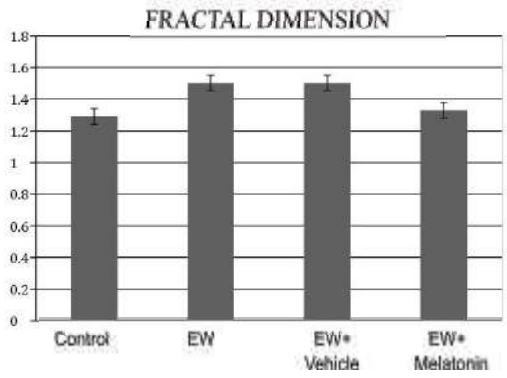

Figure 3 Figure of Fractal Dimension (a rational statistical index of detail and complexity within a pattern). Control Group, EW (Early Weaning) Group, EW + Vehicle Group, EW + Melatonin Group.

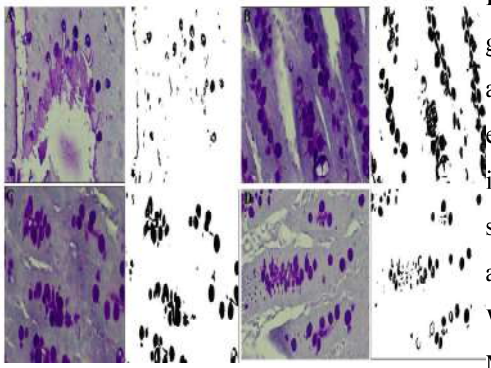

Figure 2 Photomicrographs of the duodenum from the experimental groups, following analysis using the ImageJ software for morphometric assessment.The image illustrates the fractal analysis of goblet cells, with each black dot representing an individual cell. In each image pair, the first image shows the original photomicrograph taken from the histological slides, while the second image presents the segmented version. The groups are as follows: Control Group (A), Early Weaning Group (B), Early Weaning + Vehicle Group (C), and Early Weaning + Melatonin Group (D). Magnification: 400x (AU).

Histological and PCNA Analysis of Pregnant Rats' Ovaries Subjected to Different Intensities of Physical Activity and Protein Malnutrition

Maria Gabriela da Silva Mello[1]*, Isaque Bertoldo Santos da Silva [1,] Alison Jose da Silva[1], Ana Vitoria Ferreira dos Santos[1], Renan Gabriel da Silva Ferreira[1], Raissa Gomes de França[1], José Abel Pessôa Neto[1], Ryan Cristian da Silva[2], Elba Verônica Matoso Maciel de Carvalho[2], Bruno Mendes Tenorio[1], Fernanda das Chagas Angelo Mendes Tenorio[1]

[1]Federal University of Pernambuco, Center for Biosciences, Department of Histology and Embryology, Recife, Pernambuco, Brazil.
[2]Federal University of Pernambuco, Center for Biosciences, Department of Biochemistry, Recife, Pernambuco, Brazil.
*mariagabriela.mello@ufpe.br

Early life stages are crucial for mammals, as the organism becomes more vulnerable to environmental stimuli that can lead to morphological, physiological, and behavioral changes. Processed foods and low-protein diets are contributing factors to excessive gestational weight gain. Consequently, maternal physical activity has been studied to understand how it can influence fetal adaptation and the establishment of growth and development strategies. Studies investigating the impact of low-protein diets on fertility, placental morphology, and fetal development remain scarce. Therefore, it is necessary to explore how these factors affect reproductive health and embryo development, in conjunction with physical activity. Thus, the aim of the present study was to analyze the histology and PCNA expression in the ovaries of pregnant rats subjected to different intensities of physical activity and protein malnutrition. The study was conducted in compliance with the guidelines of the National Council for the Control of Animal Experimentation (CONCEA), and approved by the Ethics Committee on Animal Use of the Center for Biological Sciences at UFPE under protocol number 005/2021. Twenty Wistar rats (n=5 per group) were used, divided into four groups: Group I (Control), Group II (Low activity), Group III (Active), and Group IV (Very active). The rats were subjected to protein malnutrition (AIN-93M diet) and physical activity simultaneously. Voluntary physical activity was conducted in acrylic cages equipped with a cycle ergometer (running wheel) and a sensor monitoring system to evaluate wheel movement, quantifying daily physical activity in terms of distance traveled (km), time of activity (min), and estimated caloric expenditure (kcal). At the end of the experiment, the ovaries were collected, weighed, and subjected to histological and immunohistochemical analysis using PCNA (Proliferating Cell Nuclear Antigen) with a commercial kit (Sigma–Aldrich Brasil Ltda). PCNA data were compiled in Excel and the statistical analyses were performed using the Shapiro-Wilk test for normality, followed by the non-parametric Kruskal-Wallis test and Dunn's post-hoc test. Results were expressed as mean ± standard deviation and considered statistically significant when $p < 0.05$. The analyses were performed using GraphPad Prism8® software. Histological analysis showed that ovaries from Group II (low activity) presented developing primordial follicles and mature follicles. Group III (active) showed a large number of corpora lutea, while Group IV (very active) exhibited greater fat cell deposition. This could be explained by the fact that animals subjected to a high-fat, low-protein diet—despite performing intense physical activity such as swimming—showed impaired oocyte quality, increased lipid droplet accumulation in granulosa cells and oocytes, and alterations in ovulation and fertilization. Regarding PCNA

results, Group III (active) showed the highest average cell proliferation. Group II (low activity) was similar to the control group (Group I), while Group IV (very active) showed reduced proliferation compared to other groups. These results suggest that the combination of protein malnutrition and physical activity during pregnancy in rats influences ovarian morphology and cell proliferation, reinforcing the importance of balanced maternal nutrition and lifestyle for reproductive health.

[1] P.J. Morgane et al., Neurosci. Biobehav. Rev. 17 (1993) 91.
[2] I. Rached de Paoli et al., Arch. Latinoam. Nutr. 51 (2001) 346.
[3] G.P. Lima, H.A.C. Sampaio, Rev. Bras. Saúde Matern. Infant. 4 (2004) 253.
[4] M.S. Martin-Gronert, S.E. Ozanne, Diabetes Obes. Metab. 14 Suppl 3 (2012) 29.
[5] C.G. Leandro et al., Rev. Nutr. 22 (2009) 559.
[6] S. Wu et al., Diabetes 63 (2014) 1270.

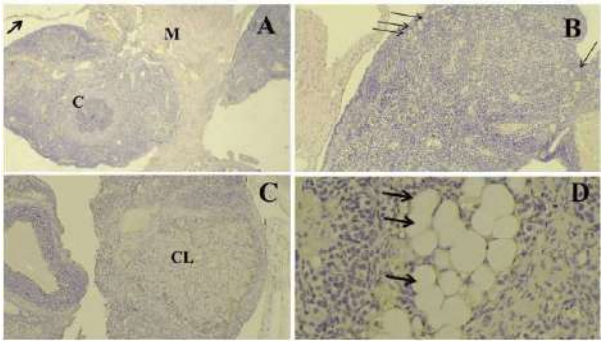

Figure 1. Photomicrograph of the ovaries of rats from the experimental groups. A – Control group showing a connective tissue capsule surrounding the organ (arrow), with well-defined cortical (C) and medullary (M) regions. B – Low activity group, with ovaries showing primordial follicles (arrow). C – Active group presenting corpus luteum (CL). D – Very active group showing fat cell deposition in the cortical region (arrows). Hematoxylin and eosin staining.

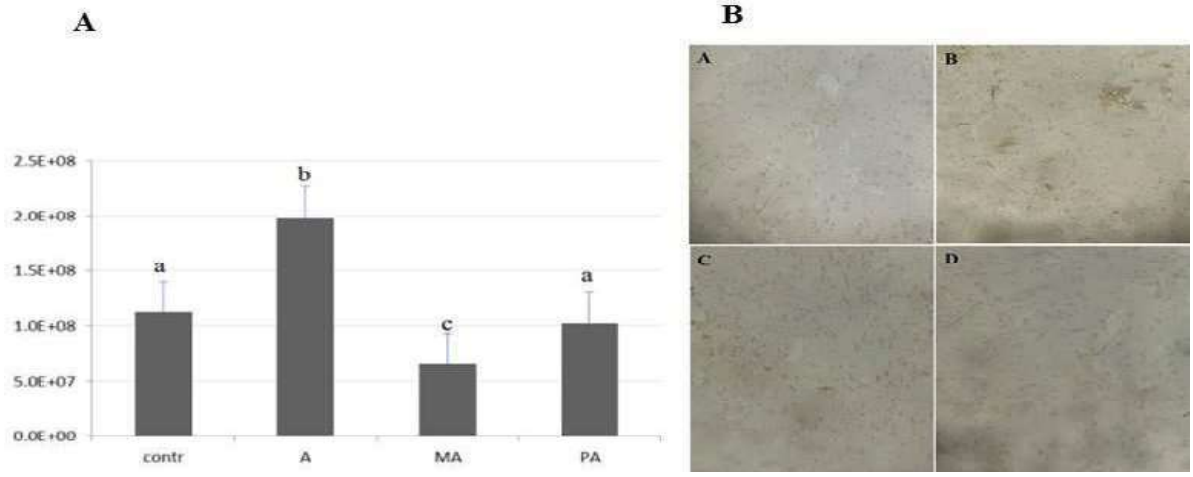

Figure 2. A – PCNA analysis in the ovaries of the experimental groups ($p = 0.02$). The active group (A) showed the highest average rate of cell proliferation. The low activity group (LA) was similar to the control group (C). The very active group (VA) showed reduced proliferation. B – PCNA photomicrograph. *Means followed by different letters in the column differ significantly from each other. Kruskal–Wallis non-parametric test followed by Dunn's post-hoc test ($p \leq 0.05$).

Histopathological Analysis Of The Extensor Digitorum Longus Muscle of Rats Induced With Rheumatoid Arthritis And Supplemented With Turmeric (*Curcuma longa* L.) Associated With Resistance Stair-Climbing Exercise

Mikael Gerson Kuhn[1]*, Leticia Massochim da Silva[1], Flávia Heloísa da Silva[1], Maiara Cristina Lima de Jesus[1], Michele Gossler[1], Gabriella Lopes Cappellaro[1], Gladson Ricardo Flor Bertolini[1], Lucinéia de Fátima Chasko Ribeiro[1], Ana Tereza Bittencourt Guimarães[1], Marcia Miranda Torrejais[1]

[1]Graduate Program in Biosciences and Health – Universidade Estadual do Oeste do Paraná, Cascavel, Paraná, Brazil.
*mikaelgerson@hotmail.com

Rheumatoid arthritis (RA) is a chronic autoimmune disease that can cause widespread alterations in tissues, including impairments in skeletal muscle tissue [1]. Although conventional RA treatment predominantly involves pharmacological approaches, these medications are often associated with adverse effects such as dependency, mood changes, and gastrointestinal complications, including digestive bleeding and peptic ulcers [2]. Consequently, there is growing interest in alternative and complementary therapies. Turmeric (*Curcuma longa* L.), recognized for its anti-inflammatory properties, has emerged as a potential adjuvant in RA management [3]. Additionally, resistance training, especially stair climbing exercise, has been investigated for its beneficial effects in alleviating RA symptoms [4]. Thus, this study aimed to evaluate the morphological effects of turmeric combined with stair climbing resistance exercise (SCRE) on the extensor digitorum longus (EDL) muscle in Wistar rats with induced RA. Thirty-one three-month-old rats were randomly assigned to five groups: Control group (CG, n = 6); RA group (RAG, n = 6); RA group treated with turmeric (RATMG, n = 6); RA group submitted to SCRE (RAEXG, n = 6); and RA group treated with both turmeric and SCRE (RATMEXG, n = 7). RA was induced using the Complete Freund's Adjuvant model [5]. Turmeric was administered by oral gavage at a dose of 100 mg/kg/day for 14 consecutive days [6]. The resistance training followed the SCRE protocol, which involved progressive loading (25%, 35%, and 50% of body weight) and a fixed routine of 3 sets of 8 repetitions performed on alternate days, totaling 14 sessions [7]. Euthanasia was performed on day 24 of the experimental schedule, corresponding to day 15 after intra-articular RA induction. The EDL muscle was collected, processed, and stained with Hematoxylin-Eosin [8] for morphological analysis. The histopathological index proposed by Zazula et al. (2022) [9] was applied, composed of five criteria for assessing alterations in striated skeletal muscle, with a maximum score of 320 points. Morphological analysis revealed focal alterations in muscle fibers resulting from RA, including granulation tissue, amorphous fibers with altered staining, nuclei with basophilic halos, and centralized nuclei (Figs. 1B, 1C, 1D, and 1E). Quantitative histopathological analysis confirmed these alterations with significant differences between groups ($P < 0.0001$). The RAG presented higher scores on the histopathological index when compared to the CG, which quantifies the degree of morphological alterations—higher scores indicate greater muscle degeneration, whereas lower scores indicate muscles with more preserved morphology ($P < 0.0001$). No differences were observed between the RATMG and the RAG. The RAEXG showed significantly lower scores compared to the RAG ($P = 0.0461$). No differences were found between the RATMEXG and the RAEXG (Fig. 1F). It was concluded that SCRE demonstrated a protective effect against muscle degeneration induced by RA, while curcumin supplementation alone did not significantly alter muscle morphology in this experimental model.

[1] J.M. Torpy et al., JAMA 305 (1) (2011) 1.
[2] R. Patel et al., Endocrinology 158 (4) (2017) 1034-1047.

[3] V. Kuptniratsaikul et al., Clin. Interv. Aging 9 (2014) 451-458.
[4] D. Guglielmo et al., MMWR Morb. Mortal. Wkly. Rep. 70 (40) (2021) 1408-1414.
[5] R.P. Gomes, E. Bressan, T.M. Silva, M.S. Gevaerd, C.R. Tonussi, C.D. Domenech, Rev. Bras. Reumatol. 54 (2) (2014) 83-89.
[6] N. Nonose et al., Acta Cir. Bras. 29 (11) (2014) 727-734.
[7] C.D.S. Jacob et al., Eur. J. Histochem. 66 (1) (2022) 3356.
[8] L.C. Junqueira, L.M.M. Junqueira, Técnicas básicas de citologia e histologia, Univ. São Paulo, São Paulo, 1983.
[9] M.F. Zazula et al., Acta Histochem. 124 (4) (2022) 151892.

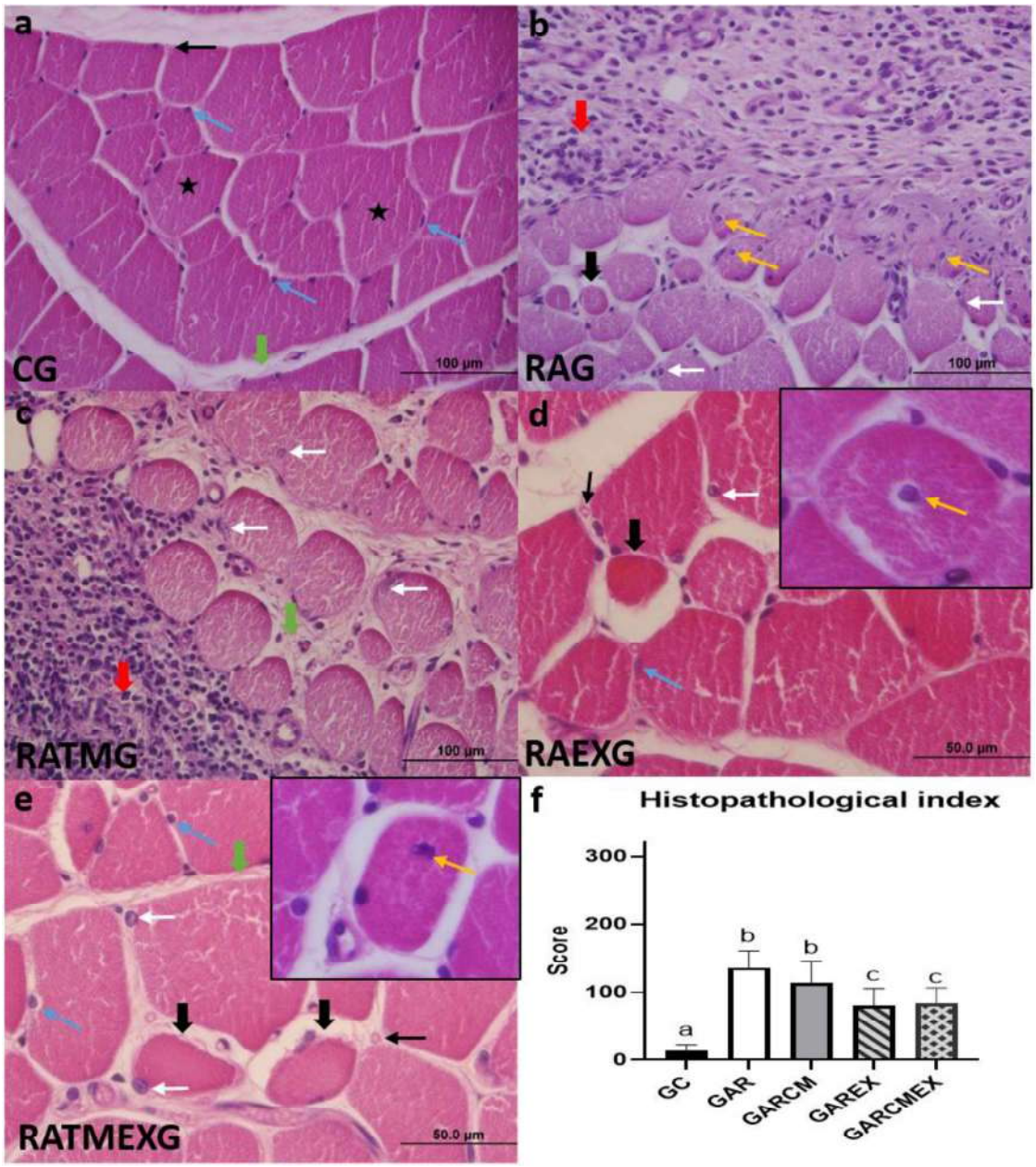

Figure 1. Photomicrographs of the extensor digitorum longus muscle from four-month-old Wistar rats stained with Hematoxylin and Eosin. Transverse sections. Groups: control (CG), rheumatoid arthritis (RAG), RA + turmeric (RATMG), RA + resistance exercise (RAEXG), and RA + turmeric + exercise (RATMEXG). Observe connective tissue (green arrow), peripheral nucleus (blue arrow), capillary (thin black arrow). **A:** Preserved polygonal fibers (star). **B, C, D, and E:** Pathological alterations: amorphous fibers with staining differences (thick black arrow), centralized nuclei (yellow arrow), nuclei with basophilic halo (white arrow), granulation tissue (thick red arrow). Images D and E were taken at 40× objective with magnification **F:** Histopathological index ($P < 0.005$); different letters indicate significant differences.

Histopathological analysis of the liver of rats induced with Diabetes mellitus and treated with *Craetavia tapia* lectin.

Weslleyanne Millena da Silva Costa[1]*, Isaque bertoldo Santos da Silva[1], Carlos Eduardo da Silva[1], Maria Gabriela da Silva Mello[1], Maria Eduarda Carneiro de Lima[1], Ana Carolina Ribeiro Saraiva Costa[1], Suellen Rozy da Silva Medeiros[1], Ryan cristian da Silva[2], Maria Clara Chár Mello[1], Bruno Mendes Tenorio[1], Fernanda das Chagas Angelo Mendes Tenorio[1],.

[1]Federal University of Pernambuco, Department of Histology and Embryology
[2]Federal University of Pernambuco, Department of Biochemistry
*weslleyanne.millena@ufpe.br

Diabetes mellitus (DM) is a class of metabolic disorders characterized by hyperglycemia. This occurs due to the body's inability to produce insulin or to properly use the insulin it produces, resulting in little or no insulin in the body [1,5]. The liver, being a metabolic organ, when affected by DM, shows excessive fat accumulation in hepatocytes, chronic inflammation with activation of macrophages that promotes necrosis, apoptosis, and fibrosis, among other effects [3,4]. In this context, bioactive compounds with anti-inflammatory and hypoglycemic properties have attracted therapeutic interest. The *Crataeva tapia* lectin (CrataBL) consists of glycoproteins that, in the diabetic liver, interact with specific carbohydrates present in cells such as hepatocytes and macrophages, demonstrating its therapeutic potential in treating the disease [2]. Therefore, this study aimed to perform a histopathological analysis of the liver of rats induced with diabetes and treated with *Crataeva tapia* lectin. Fifteen albino Wistar rats were used and divided into three groups: (I) animals without DM (Control); (II) animals induced with DM; and (III) animals induced with DM and treated with lectin. DM was induced by intraperitoneal injection of streptozotocin after a 14-hour fast at a dose of 50 mg/kg diluted in citrate buffer. Streptozotocin was administered in a single dose, and diabetes was confirmed on the 3rd and 7th day after injection. The CrataBL lectin fraction was administered as a single intravenous dose of 5 mg/kg. On the 15th day of treatment, the females from each experimental group were anesthetized using 0.08 ml/100 g body weight of ketamine (Virbaxyl 2%, Virbac do Brasil Ind. Com LTDA) and 0.04 ml/100 g body weight of xylazine hydrochloride via intraperitoneal injection. The liver was then weighed and fixed in 10% buffered formalin for 48 hours. The paraffin embedding process was initiated, and the obtained blocks were sectioned at 3 μm thickness, stained with Hematoxylin-Eosin (H&E), analyzed, and photographed under a light microscope. Based on the above, the results of this study showed that histological analysis of the liver in all experimental groups revealed an externally thin capsule composed of mesothelium and parenchyma with hepatocytes irregularly arranged around the central vein, along with the presence of Kupffer cells. However, the diabetic animals exhibited loss of cytoplasmic content with early vacuolization as well as cellular infiltration. In contrast, the diabetic group treated with *Crataeva tapia* lectin appeared histologically similar to the control group (Figure 1). Thus, it can be concluded that DM may cause cytoplasmic vacuolization and cellular infiltration. However, administration of CrataBL lectin may attenuate the effects of DM in the liver, thereby promoting improved liver function.

[1]Hildefonso I et al. Innovations in the treatment of type 2 diabetes mellitus: emerging therapies and efficacy. *(2025)*
[2] Rocha AA da et al. Lectin from Crataeva tapia bark improves tissue damagens and

plasma hyperglycimia in alloxan-induced diabetic mice. (2013)
[3] Giestas S, Giestas A, Agostinho C. Liver disease and diabetes mellitus – a bidirectional relationship. *Revista Portuguesa de Diabetes (2015)*
[4] Silva JP, Oliveira MR. Relationship between diabetes mellitus and metabolic-associated fatty liver disease: a review. *Revista Brasileira de Endocrinologia* (2025)
[5] Fouad D et al. Hepatoprotective activity of raspberry ketone against streptozotocin-induced type 2 diabetes in male rats. (2025).

Figura 1: Photomicrograph of the liver of experimental animals.

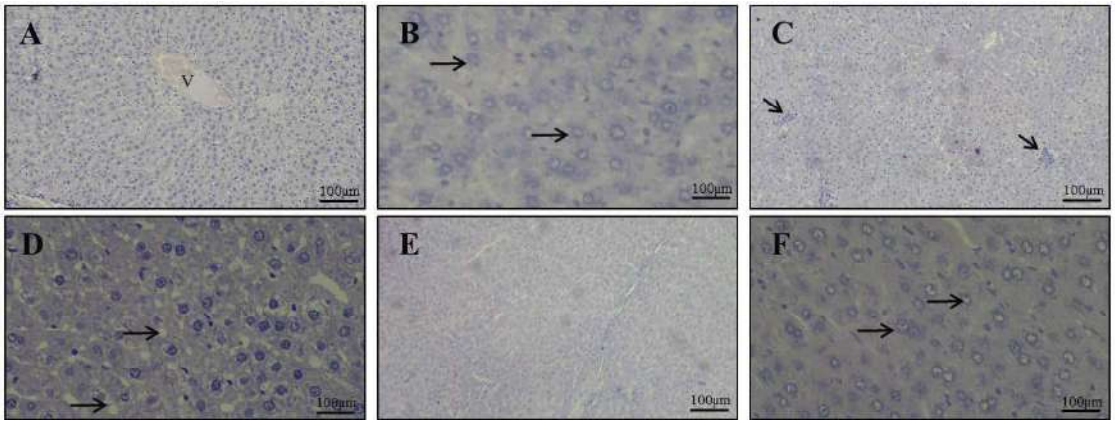

A – Control group showing blood vessels (v). B – Control group showing polyhedral hepatocytes. C – Diabetic group showing cellular infiltration (arrow). D – Diabetic group showing loss of cytoplasmic content with onset of vacuolization (arrow). E, F – Diabetic group treated with *Craetavia tapia* lectin, histologically resembling the control group. Hematoxylin and Eosin staining (H&E).

Histopathological Analysis Of The Mucosa Of The Dorsum Of The Tongue Of Rats Treated With Botulinum Toxin Type A Injection Into The Submandibular Gland

Carlos Eduardo da Silva[1]*, Maria Manuela dos Santos Rodrigues[1], Giovana Siqueira Faustino da Silva[2], Weslleyane Milena da Silva Costa[1], Glenison da Rocha Duarte[1], Maria Gabriela da Silva Mello[1], Maria Eduarda Carneiro de Lima[1], Ana Carolina Ribeiro Saraiva da Costa [1], Suellen Rozy da Silva Medeiros[1], Jaciel Benedito de Oliveira [2], Fernanda das Chagas Angelo Mendes Tenorio[1].

[1]Federal University of Pernambuco, Center for Biosciences, Department of Histology and Embryology, Recife, Pernambuco, Brazil, [2]Federal University of Pernambuco, Biosciences Center, Department of Anatomy, Recife, Pernambuco, Brazil
*eduadocarlos120@gmail.com

Botulinum toxin is a neurotoxin synthesized by the anaerobic bacterium *Clostridium botulinum* and comprising seven serological variants: A, B, C, D, E, F and G, with serotype A (BTX-A) being the most widely used for medicinal purposes [4]. This neurotoxin has proven to be an effective therapeutic option in the treatment of sialorrhea, a common condition observed in patients with neurological disorders characterized by excessive saliva production [3]. However, despite the therapeutic benefits, one undesirable effect is a decrease in salivary production, resulting in hyposalivation or xerostomia [1]. This decrease in saliva compromises both protective and digestive functions, as well as systemic consequences, including dysbiosis of the oral microbiota [2]. The aim of this study was to histopathologically evaluate the mucosa of the dorsum of the tongue of female rats subjected to botulinum toxin injections in the submandibular gland. To this end, thirty Wistar rats were used and divided into five groups with six animals in each: Control Group: without any treatment at the time of collection; BTX-A 12 group: received three injections of BTX-A into the right submandibular gland and samples for analysis were taken 12 days after the last toxin application; BTX-A 35 group: animals with right submandibular glands received 3 injections of botulinum toxin type A (BTX-A) and samples were taken 35 days after the last application of the toxin; GEL 12 group: 6 animals with right submandibular glands treated with an injection of bovine gelatin, a BTX-A stabilizer, and samples were taken 12 days after the last application of the gelatin; GEL 35 group: with right submandibular glands treated with an injection of bovine gelatine, a BTX-A stabilizer, whose samples for analysis were collected 35 days after last gelatine application. The animals were anesthetized to remove the tongue. The collected tongues were sectioned and their middle thirds fixed in 10% formaldehyde for 48 hours. They were then processed using standard histological techniques, embedded in paraffin and the blocks cut to a thickness of 3 micrometers. The sections were stretched in a water bath, mounted on slides coated with Mayer's albumin, and dried in an oven. They were stained with Hematoxylin and Eosin (H&E) and Toluidine Blue, analyzed and photographed using a LEICA ICC50 HD® binocular light photomicroscope (Leica Microsystems, São Paulo, Brazil) coupled to a digital camera, connected to a computer with an image capture card (ATI) using the Leica LAS EZ® capture software (Leica Microsystems, Buffalo Grove, USA). The histopathological analysis revealed, using both H&E and Toluidine Blue staining, showed no significant morphological alterations between the groups. There was also no evidence of inflammatory infiltration in the lamina propria of the study groups. However, the BTX-A 12-day and BTX-A 35-day groups showed a higher incidence of taste corpuscles compared to the other groups (Figures 1 and 2). Therefore, the increase in the number of taste buds in related to BTX-A application suggests a possible compensatory mechanism related to sensory function in response to reduced salivary flow.

[1] T.M. Chung et al., *Dispensing profile of botulinum toxin for the treatment of spasticity: brazilian national data.*. Acta Fisiatr. 23 (1) (2016).
[2] B.J. Franck et al., *Botulinum toxin for the treatment of sialorrhea in patients with Parkinson's disease*. Rev. Bras. Neurol. 54 (3) (2018).
[3] E.D.A. Lima et al., *Saliva and hydration: importance of saliva quantity and quality for maintaining satisfactory oral health in patients with cerebral palsy.* Rev. Campo Saber. 3 (1) (2017).
[4] G. Verma, *Role of Botulinum Toxin Type-A (BTX-A) in the Management of Trigeminal Neuralgia.* Pain Res. Treat. (2013).

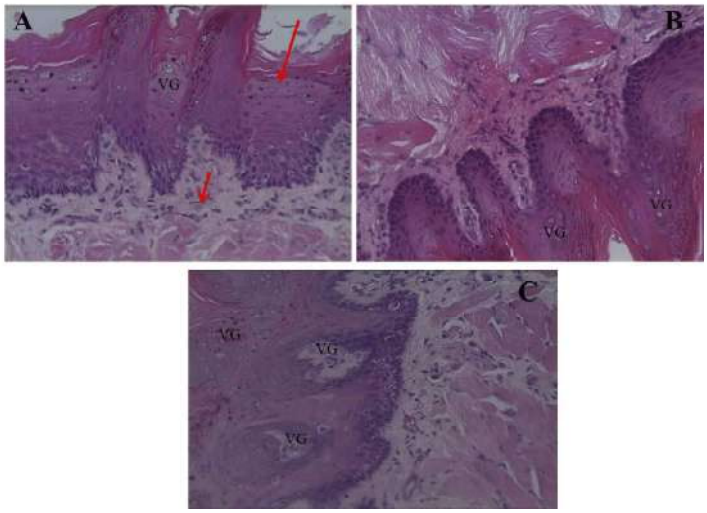

Figure 1. Photomicrograph of rat tongue histology. A, Control Group: observe keratinized stratified sidewalk epithelium (large arrow), loose connective tissue (short arrow) and taste corpuscles (VG); B, Gel 12 days: similar characteristics to the control, also presenting taste corpuscles (VG); C, BTX-A 12 days: observe the presence of a greater number of taste corpuscles (VG). Staining: HE. Magnification: 400x.

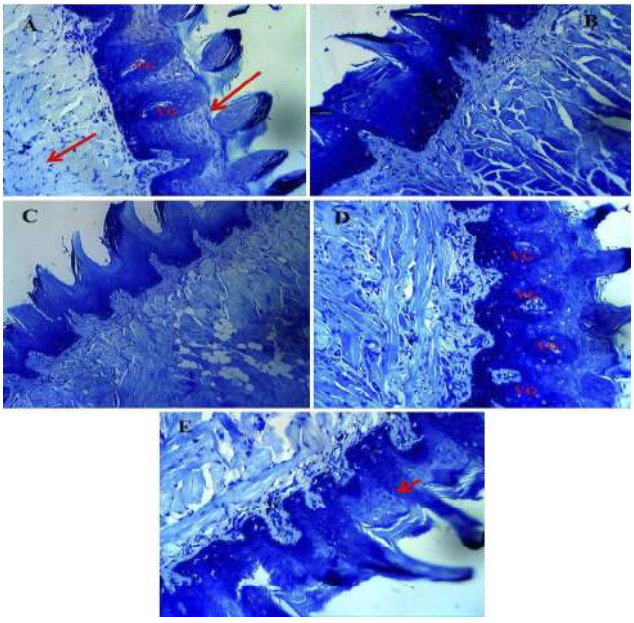

Figure 2. Photomicrograph of the histology of the rat tongue. A, Control Group: observe keratinized stratified sidewalk epithelium (large arrow), loose connective tissue (medium arrow) and taste corpuscles (VG); B, Gel 12 days and C, Gel 35 days: similar characteristics to the control; D, BTX-A 12 days: observe the presence of a greater number of taste corpuscles (VG); E, BTX-A 35 days: observe the presence of taste corpuscles. Staining: Toluidine blue. Magnification: 400x.

Histopathological Analysis Of The Spleen Of Rats Subjected To Protein Malnutrition During Pregnancy And Supplemented With Cannabidiol

Maria Clara Chár Gomes[1]*, Carlos Eduardo da Silva[1], Paloma Vitória Melo da Silva[1], Alison José da Silva[1], Ana Vitoria Ferreira dos Santos[1], Isaque Bertoldo Santos da Silva[1], Renan Gabriel da Silva Ferreira[1], Thaynara Caseli dos Santos[1], Jadyel Sherdelle Guedes do Nascimento[1], Bruno Mendes Tenorio[1], Fernanda das Chagas Angelo Mendes Tenorio[1].

[1]Federal University of Pernambuco, Center for Biosciences, Department of Histology and Embryology, Recife, Pernambuco, Brazil
*mclarachar@gmail.com

The spleen, the largest lymphoid organ in the human body, performs essential immunological roles, including the elimination of bacteria present in the bloodstream and the forming lymphocytes and monocytes [1]. It is also crucial for the phagocytosis of foreign agents such as viruses, bacteria, and leukocytes, and in the production of opsonins, which are substances that facilitate phagocytosis [2]. During pregnancy, the spleen participates in maternal immune adaptation, helping to balance tolerance to the fetus with defense against infections. In the context of a low-protein diet, modulation of the systemic immune response may occur, which highlights the central role of the spleen in sustaining immunity under unfavorable nutritional conditions. Cannabidiol (CBD), due to its anti-inflammatory and immunoregulatory properties, has a proven effect on splenic cells, helping to regulate inflammation and strengthen the immune response, especially in conditions of immunosuppression or inflammation [3]. Thus, the objective of this study was to histologically analyze the spleen of rats subjected to protein-energy malnutrition during pregnancy and supplemented with cannabidiol. To this end, fifteen rats were used, separated into three groups: control, low-protein diet, and diet plus cannabidiol. The rats were mated and subsequently subjected to pregnancy confirmation by vaginal smear. They were then treated with a diet, a low-protein diet, and a low-protein diet supplemented with cannabidiol nanoemulsion at a dose of 10 mg/kg. On the 14th day of pregnancy, the animals were anesthetized for spleen removal, immediately weighed, and then immersed in 10% buffered formalin for 48 hours. Subsequently, the samples were cleaved and subjected to histological impregnation and paraffin embedding. The slides obtained were stained with Hematoxylin and Eosin (H&E), analyzed under a light microscope, and photographed using a Nikon Eclipse 80i photomicroscope. Based on the results obtained, we observed that the histological analysis of the spleen of all experimental groups showed the capsule externally covering the organ, the red pulp, and the well-defined white pulp. The white pulp is defined by the lymphoid nodule consisting of the germinative center and central arteriole. However, animals subjected to a low-protein diet showed changes suggestive of immune compromise, characterized by a possible reduction in lymphoid nodules and migration of lymphocyte cells to the red pulp. Animals subjected to a low-protein diet and treated with cannabidiol were similar to the control group, with no significant proliferation of lymphoid cells from the white pulp to the red pulp (Figure 1). Thus, it is concluded that CBD may have a modulating effect on the damage caused by a protein-poor diet, suggesting its potential as a treatment and the possibility of reversing the damage caused by protein malnutrition during pregnancy.

[1] S.M. Lewis et al., *Structure-function of the immune system in the spleen.* Science Immunology, 4 (2019).
[2] R.G. Marques et al., *The role of the spleen in resistance to infection.* Rev. Bras. Med., 60 (5) (2003).
[3] T.R. Jan et al., *Suppressive effects of cannabidiol on antigen-specific antibody production and functional activity of splenocytes in ovalbumin-sensitizes BALB/c mice. International Immunopharmacology.* 7 (6) (2007).

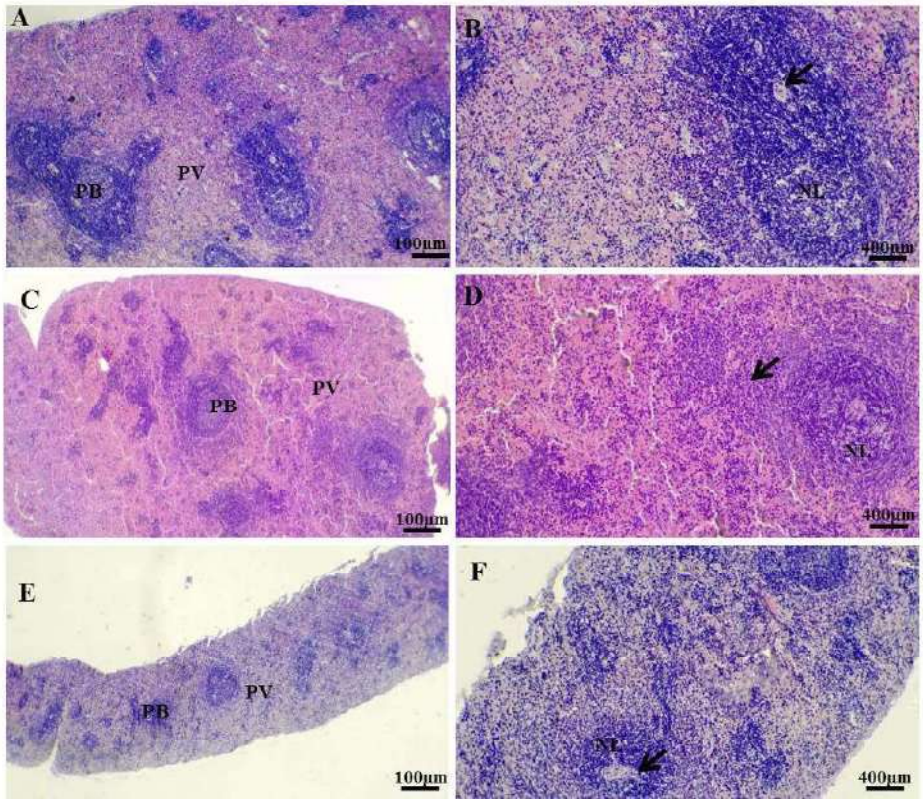

Figure 1. Photomicrograph of the spleen of experimental animals. A, B - Control group showing red pulp (RP) and well-defined white pulp (WP). In addition to lymphoid nodule (LN) consisting of the central arteriole (arrow); C, D - Low-protein diet group showing red pulp (RP) and white pulp (WP), and lymphocyte cells proliferating into the red pulp (arrow); E, F- Low-protein diet + CBD group similar to the control group: red pulp (RP) and white pulp (WP) well defined, lymphoid nodule (LN) consisting of the central arteriole (arrow). H&E.

Histopathological analysis of the uterus of rats subjected to voluntary physical activity and protein malnutrition.

Ana Carolina Ribeiro Saraiva da Costa*[1], Maria Manuela dos Santos Rodrigues[1], Renan Gabriel da Silva Ferreira[1], Jadyel Sherdelle Guedes do Nascimento[1], Isaque Bertoldo Santos da Silva[1], Alison Jose da Silva[1], Ana Vitoria Ferreira dos Santos[1], Ryan Cristian da Silva[2], Bruno Mendes Tenório[1], Fernanda das Chagas Angelo Mendes Tenório [1]

[1]Department of Histology and Embryology, Federal University of Pernambuco, Recife, Pernambuco, Brazil
[2]Department of Biochemistry, Federal University of Pernambuco, Recife, Pernambuco, Brazil 11;

*Carolina.rscosta@ufpe.br

Protein restriction during puberty alters the thickness of the endometrium and the uterine epithelium [2]. In addition, perinatal protein malnutrition impairs serum protein and albumin levels, compromising the structural development of tissues [3]. Studies also report that maternal physical activity has a mitigating effect, improving cardiorespiratory indicators in offspring under malnutrition [1,5]. In pregnancy models, exercise has been shown to positively influence fetal growth markers and expression of trophic factors [4]. However, there are gaps in the literature regarding the combination of these factors in uterine morphology. Thus, this study aims to histopathologically analyze the uterus of rats subjected to physical activity and protein malnutrition. For this purpose, 20 female Wistar albino rats (220–260 g; 85–95 days) were kept in a vivarium with controlled conditions and free access to water and food, in accordance with the ethical standards of COBEA and approved by CEUA-UFPE (n° 005/2021). The rats were distributed into four groups, each consisting of 5 animals: control rats; active rats, very active rats, and slightly active rats. After 30 days of adaptation to the AIN-93M diet, they were classified as slightly active, active, or very active based on the distance and elapsed time. Mating was performed in standard cages, and the rats were redistributed to GAFV for dietary treatment with a normoprotein or hypoprotein diet (8% protein). The uteri were histologically processed: dehydration in alcohol, diaphanization in xylene, paraffin embedding, microtome sectioning (5 μm), slide mounting and staining with Hematoxylin & Eosin. The analysis was performed by light microscopy and Nikon 50E videomicroscopy. The histological analysis of the uterus revealed the presence of well-defined endometrial, myometrial and perimetrium layers in all experimental groups. In the active group, an increase in the density of endometrial connective tissue fibers, epithelial vacuolization and reduction in myometrial thickness were observed compared to the control group. The very active group also presented a higher concentration of endometrial fibers and a marked decrease in myometrial thickness. Similarly, the slightly active group showed an increase in fibers in the endometrial connective tissue, in addition to epithelial vacuolization and myometrial reduction. These findings indicate that different levels of physical activity, even mild ones, can significantly influence uterine morphology. The presence of epithelial vacuoles, associated with connective tissue reorganization and myometrial hypotrophy, suggests structural adaptations possibly related to the physiological demand imposed by voluntary physical activity.

[1] L.D.S. Andrade, Efeitos da atividade física voluntária materna sobre alterações cardiorrespiratórias da prole sob desnutrição proteica perinatal, Dissertação de Mestrado, Universidade Federal de Pernambuco, Recife, 2016. Disponível em: https://repositorio.ufpe.br/handle/123456789/18186..
[2] T.F. Costa, et al., "Protein restriction during puberty alters nutritional parameters and affects ovarian and uterine histomorphometry in adulthood in rats", *J. Dev. Orig. Health Dis.* 12(5) (2021) 678–687. https://www.ncbi.nlm.nih.gov/pmc/articles/PMC7981593/.
[3] M.S. Lima, et al., "Aerobic exercise increases the damage to the femoral properties of growing rats with protein-based malnutrition", *Braz. Arch. Biol. Technol.* 66 (2023).
[4] J.P.F. de Moura, *Efeito da atividade física e dieta hipoproteica sobre expressão gênica trófica fetal*, Dissertação de Mestrado, Universidade Federal de Pernambuco, Recife, 2019. Disponível em: https://repositorio.ufpe.br/handle/123456789/33723.
[5] V.O. Nogueira, *Efeitos da desnutrição proteica e atividade física materna sobre função simpática e ventilação em ratos*, Dissertação de Mestrado, Universidade Federal de Pernambuco, Recife, 2019. Disponível em: https://repositorio.ufpe.br/handle/123456789/339

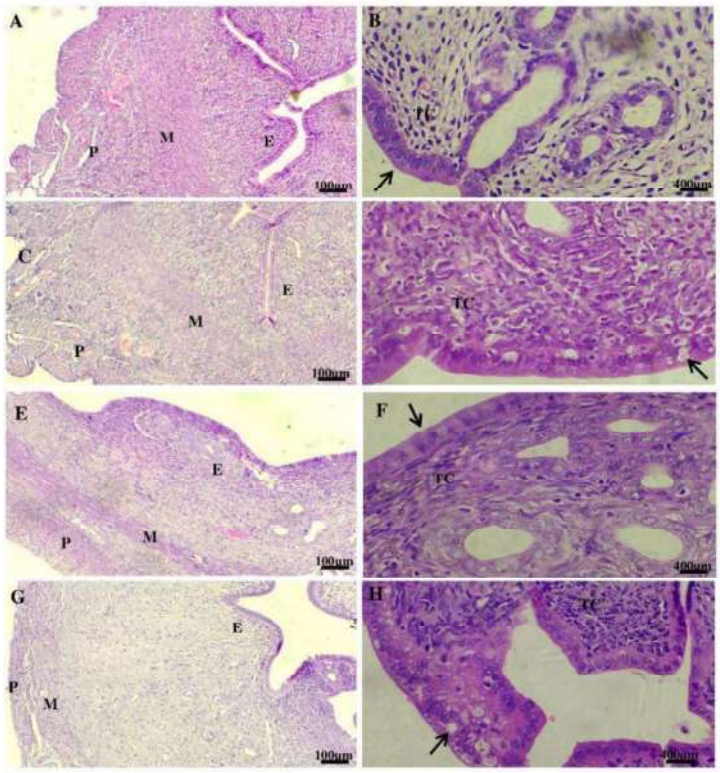

Figure 1.Photomicrograph of the uterus of rats in the experimental groups. A, B- Control group showing well-defined endometrial (E), myometrial (M0) and perimeter (P) layers, in addition to the endometrial epithelium (arrow). C, D- Active group showing a greater thickness of the endometrial connective tissue b, with a denser extracellular matrix and a reduced myometrial layer (M). E, F- Very active group showing an increase in the amount of fibers in the endometrial connective tissue and a reduced myometrial layer (M). G, H- Slightly active group also showing a greater amount of fibers in the endometrial connective tissue, in addition to vacuolization of the endometrial epithelial cells (arrow) and reduction of the myometrial layer (M). H-E staining

Histopathological and Histochemical Analysis of the Uterus of Pregnant Rats Subjected to Protein Malnutrition and Treated with Cannabidiol (CBD)

Suellen Rozy da Silva Medeiros[1]*, Maria Manuela dos Santos Rodrigues[1], Carlos Eduardo da Silva[1], Maria Gabriela da Silva Mello[1], Weslleyanne Millena da Silva Costa[1], Maria Eduarda Carneiro de Lima[1], Ana Carolina Ribeiro Saraiva da Costa[1], Paloma Vitória Melo da Silva[1], Raissa Gomes de França[1], Fernanda das Chagas Angelo Mendes Tenório[1], Bruno Mendes Tenório[1]

[1]Federal University of Pernambuco, Department of Histology and Embryology
*suellen.medeiros@ufpe.br

Protein malnutrition (PM) induces an increase in pro-inflammatory cytokines and oxidative stress, evidenced by elevated thiobarbituric acid reactive substances (TBARS) and a reduction in total sulfhydryl groups, reflecting redox imbalance and activation of the nuclear factor kappa B (NF-κB) pathway. During pregnancy, uterine inflammation compromises arterial remodeling, which is essential for fetal supply, and may lead to endothelial dysfunction and intrauterine growth restriction. The accumulation of reactive oxygen species (ROS) also impairs myometrial contractility, contributing to adverse gestational outcomes. Cannabidiol (CBD) has emerged as a potential therapeutic agent due to its anti-inflammatory and antioxidant properties, acting to protect uterine tissue and maintain gestational homeostasis. Therefore, the aim of this study was to use histological and histochemical methods to detect changes in the endometrium and myometrium of rats subjected to protein malnutrition and treated with CBD. Twenty-four pregnant albino Wistar rats (n = 8) were used and divided into three groups: I – pregnant rats for 14 days (control group, normoprotein diet); II – pregnant rats for 14 days subjected to protein restriction; III – pregnant rats for 14 days subjected to protein restriction and treated with CBD nanoemulsion (ethics committee approval: 0053/2024). The rats were mated naturally, and pregnancy was confirmed by the presence of spermatozoa in the vaginal smear, identifying the first day of gestation. Rats in groups II and III were fed a modified AIN-93G diet containing only 6% protein, starting from the first day of pregnancy, to induce protein malnutrition. Diet and water were offered ad libitum throughout the experimental period. The females in group III were treated with a CBD nanoemulsion at a dose of 10 mg/kg/day, administered from the 1st to the 14th day of pregnancy. The uteri were fixed in 10% buffered formalin, processed for paraffin embedding, and sectioned into 3 μm thick histological slices. The slides were stained with Hematoxylin-Eosin (HE) for general morphological analysis and with Mallory's Trichrome to highlight collagen fibers. Images were obtained using a light microscope (10x and 40x magnification) and digitized for analysis. Fifteen images per animal were selected, totaling 120 images per experimental group, which were analyzed using ImageJ software (NIH, USA), with the Color Histogram tool used to quantify collagen deposition in the uterus and specifically in the endometrial region. Data were analyzed using the Kruskal-Wallis test followed by Dunn's post-hoc test ($p < 0.05$). The results of the present study showed that histopathological analysis of the uterus of the experimental groups revealed well-defined layers of endometrium, myometrium, and perimetrium. The group subjected to PM during pregnancy presented a reduced endometrium and myometrium, in addition to the presence of connective tissue with more compact collagen fibers. In contrast, the group subjected to protein malnutrition and treated with CBD appeared similar to the control group, reversing the possible damage caused by a low-protein diet. Regarding the histochemical analysis of the uterus, it was shown that collagen content in both the endometrium and uterus was higher in the groups subjected to PM during pregnancy, while the group treated during this period showed values similar to the control group. It is concluded that protein malnutrition during pregnancy causes histological and morphological alterations, such as increased

collagen compaction in the uterus, which are attenuated by treatment with CBD.

[1] M. Benabbou et al., Protein vs. Energy Restriction Impact on Rat Testis' Function, Redox Status, and Histomorphometry. 28 (Suplet 1) (2023) 61-68.
[2] T. Cotechini et al., Inflammation in rat pregnancy inhibits spiral artery remodeling leading to fetal growth restriction and features of preeclampsia. 211 (Suplet 1)(2014) 165-79.
[3] S. Ramnarayanan et al., The Unfolded Protein Response Regulates Uterine Myocyte Antioxidant Responsiveness During Pregnancy. 95 (Suplet 6) (2016) 120.
[4] S. Atalay et al., Antioxidative and Anti-Inflammatory Properties of Cannabidiol. Antioxidants. 9 (Suplet 1) (2019) 21

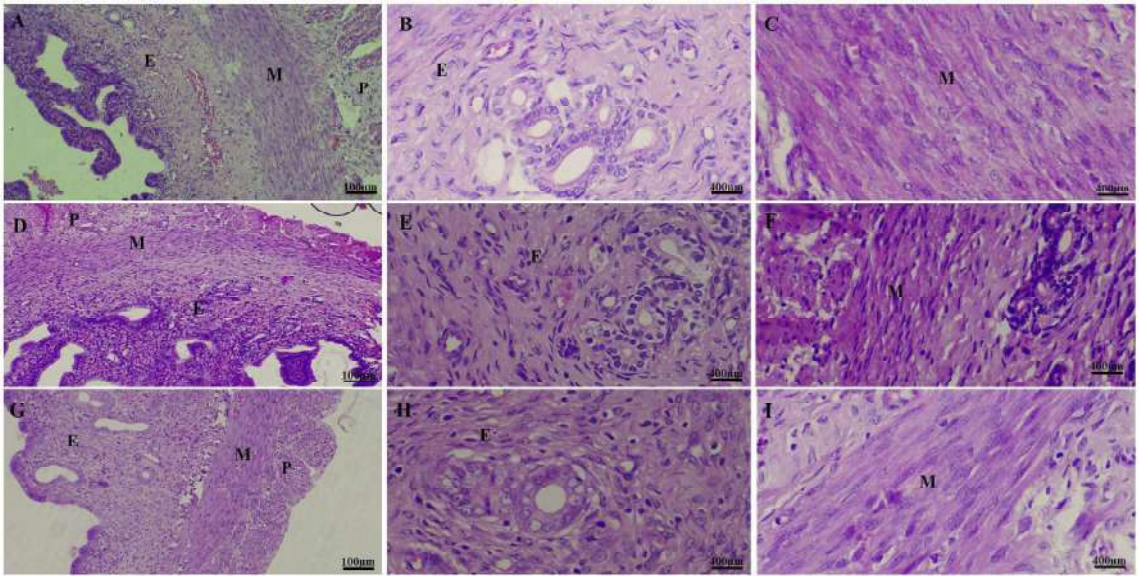

Figure 1. Photomicrograph of the uterus from rats in the experimental groups. A, B, C- Control group showing the layers of the endometrium (E), myometrium (M), and perimetrium (P), as well as the connective tissue of the endometrium (E) and the myometrial layer (M). D, E, F – Diet group presenting a reduction in the endometrium (E) and myometrium (M), with connective tissue in the endometrium showing more compacted collagen fibers (E) and reduced myometrium (M). G, H, I – Diet+CBD group similar to the control, showing the layers of endometrium (E), myometrium (M), and perimetrium (P), as well as the connective tissue of the endometrium (E) and the myometrial layer (M). H&E staining.

Table 1. Quantification of Collagen in the Endometrium and Total Uterus of Pregnant Rats Subjected to a Low-Protein Diet and Treated with Cannabidiol (CBD).

Experimental Groups/Parameters	Control	Diet	Diet+CBD	p
Collagen of the endometrium	**103.3±4.5a**	**142.6±1.7b**	**128.4±3.0c**	**0.001***
Collagen of the uterus	**150.4±8.0a**	**183.9±7.8b**	**161.3±4.7c**	**0.001***

*Means followed by the same letter in the rows do not differ significantly according to the Kruskal-Wallis test followed by Dunn's post-hoc test ($p > 0.05$).

Histopathological aspects of epididymis following chronic infection with a new *Trypanosoma cruzi* strain in mice

André Acácio Souza da Silva[1], Juliana Kaori Ota de Oliveira[2], Jociel Klleyton Santos Santana[2], Bruna Carolina Silva[1], Julia Maria Neves Clemente[3], Paulo Sérgio Cerri[3], João Aristeu da Rosa[2], Isabel Maria Porto[3], Estela Sasso-Cerri[3]*.

Federal Universisty of São Paulo, UNIFESP/EPM[1], São Paulo State University (Unesp), School of Pharmaceutical Sciences, Araraquara[2], São Paulo State University (UNESP), School of Dentistry, Araraquara[3]
*estela.sasso@unesp.br

Considered as a neglected tropical disease by the World Health Organization (WHO), Chagas disease, caused by the protozoan parasite *Trypanosoma cruzi* affects between 6 to 7 million people worldwide (according to WHO 2025) [1; 2]. *Trypanosoma cruzi* has a wide range of strains, and research on this subject becomes challenging due to the variations in clinical manifestations and the biogeographical distribution of the protozoan. The new strain called "Tv" was isolated from an adult triatomine of the species *Triatoma vitticeps* collected in the Grão Mogol region, Minas Gerais, Brazil, 2023. The sperm cells, produced in the testis, acquire the fertilizing capacity and are stored in the epididymis [3]. Strains of *T. cruzi* has already been found in the male reproductive tract [4]; however, considering the variations in clinical manifestations and the recent isolation of this strain, the aim of this study was to evaluate the histopathological alterations, caused by a chronic infection (1 year) with the Tv strain, in the epididymis. Eight 21-day-old male mice were divided into two groups: Control group (CG; n=4) without infection and the TV group (TVG; n=4), which were infected, soon after weaning, using strain passage, and their clinical signs were evaluated for 12 months. After this period, the mice were euthanized, and the epididymis were embedded in paraffin. The histopathological features were analyzed in H.E.-stained sections, and the incidence of cell death was evaluated by TUNEL method. Nests of amastigotes were found in the stroma of the distal region of the epididymis, confirming the epididymal infection by the Tv strain (Fig. 1A). Although the strain passage occurred before puberty and, hence, before the complete epididymal development, the organ displayed the basic histological components, and the lumen was filled with sperm cells. The epididymis from the TVG showed an infiltration of immune cells, mainly lymphocytes and plasm cells. In both proximal and distal regions of the epididymis, numerous lymphocytes were noted in close contact and/or within the epithelium as well as epithelial damage (vacuoles) and apoptotic bodies (confirmed by TUNEL) were found (Fig. 1B1; 1B3; 1C1; 1C3). The presence of lymphocytes clusters, suggesting tertiary lymphoid structures (TLSs), was also observed in the interstitial compartment of the distal region (Fig. 1B2). TLSs are lymphoid aggregates that form in non-lymphoid tissues during chronic inflammation, including autoimmune diseases and infections [5]. These aggregates, composed of heterogenous B and T cells, fibroblasts, and endothelial cells, perpetuate the inflammation and lower the activation threshold for future immune threats [6]. The presence of these structures, together with plasm cells, suggests chronic inflammation in the epididymis due to the *T. cruzi* infection. In conclusion, the new strain of *T. cruzi* strain was able to infect the epididymis, and the infection caused epididymal cells death, epithelial damage and immune infiltration. Taking together, these alterations may impact sperm maturation and storage. Therefore, attention should be given to the reproductive health of patients infected with the *T. cruzi* strain.

[1] WHO, 2025.
[2] Silva et al., Ciência & Saúde Coletiva, 2022.
[3] B. Robaire and B. T. Hinton, Knobil and Neill's, Elsevier, New York, 2015.
[4] Ferreira and Rossi, Am J Trop Med Hyg. 1973.
[5] Dong et al., Front. Immunol, 2024.
[6] Elizagaray et al., bioRxiv [Preprint], 2024.
[7] This work was supported by FAPESP (2022/10560-2; 2021/07207-6; 2022/13607-0) and CAPES (Cod.001).

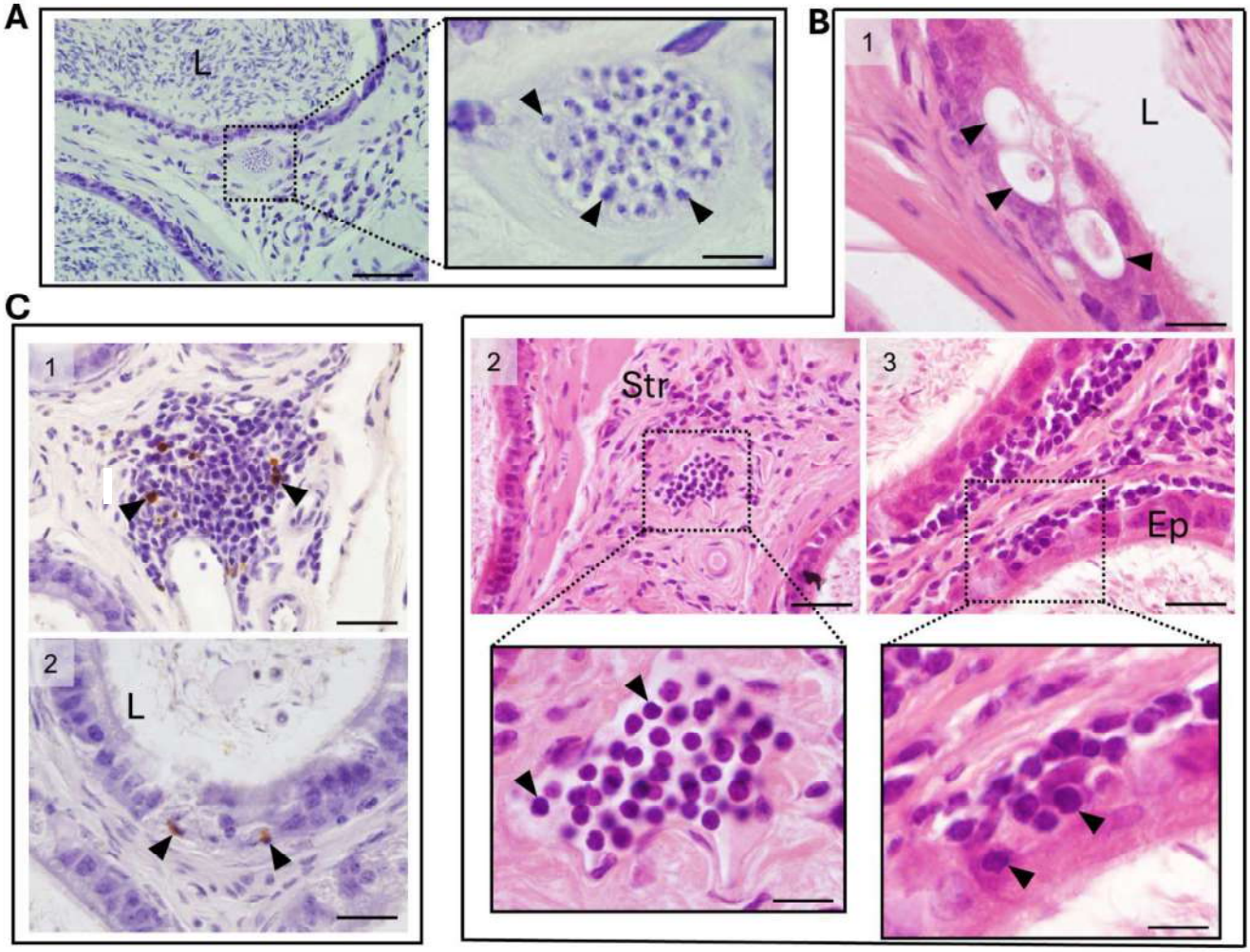

Figure 1. In panel A, the hematoxylin-stained section shows an amastigote nest in the epididymis distal portion (inset, arrowheads). L: lumen filled with sperm cells. **In panel B,** H.E.-stained sections. B1, intracellular vacuoles are observed in the epithelium (arrowheads). L: Lumen. B2, the TLS is observed in the stroma (Str) of distal portion. In the inset, lymphocytes (arrowheads). B3, note the presence of lymphocytes infiltration in the epididymal epithelium (Ep) (inset; arrowheads). **In panel C,** TUNEL method. Note the presence of TUNEL-positive cells in the stroma of the epididymis distal portion (C1, arrowheads) and TUNEL-positive apoptotic bodies in the epididymal epithelium (C2; arrowheads). L: lumen. Bars: A1: 18µm, A1 inset: 2.5µm. B1: 6µm. B2: 18µm, B2 inset: 7µm. B3: 12µm, B3 inset: 5µm. C1: 18µm, C2: 16µm.

Histopathological Evaluation of the Lungs in Wistar Rats Subjected to Early Weaning and Treated with Melatonin

Sara Vitoria de Oliveira Costa[1]*, Renan Gabriel da Silva Ferreira[1], Jadyel Sherdelle Guedes do Nascimento[1], Isaque Bertoldo Santos da Silva[1], Alison Jose da Silva[1], Ana Vitoria Ferreira dos Santos[1], Elba Veronica Matoso Maciel de Carvalho[2], José Anderson da Silva Gomes[1], Luiza Rebeca Soares de Lima[1], Bruno Mendes Tenorio[1], Fernanda das Chagas Angelo Mendes Tenorio[1].

[1]Department of Histology of Embryology, Federal University of Pernambuco, [2]Department of Biochemistry, Federal University of Pernambuco
*sara.vcosta@ufpe.br

Breastfeeding is essential for the development of mammals, providing crucial nutrients and immune protection. Natural weaning occurs gradually, promoting the offspring's nutritional and physiological independence. However, early weaning characterized by the abrupt interruption of lactation can impair development and increase susceptibility to pulmonary infections, primarily due to the activation of inflammatory processes and disruption of lung tissue integrity [1]. In this context, melatonin, a hormone with antioxidant, immunomodulatory, and anti-inflammatory properties, has been identified as a potential therapeutic agent to minimize tissue damage [2]. Therefore, this study aimed to evaluate the effects of melatonin on lung damage induced by early weaning in Wistar rats. Wistar albino rats from the vivarium of the Federal University of Pernambuco were used. The animals were kept in a controlled environment with an inverted light-dark cycle and free access to food and water. After a 16-day acclimatization period, males and females were mated at a ratio of 2 females to 1 male (2:1), with the day of birth considered experimental day zero. The 24 pups were divided into three groups (n=8): control, early weaning (DP), and early weaning treated with melatonin (DP+Mel), with melatonin administered at a dose of 200 µg per 100 g of body weight. Except for the control group, all other animals were weaned on the 16th day after birth. Thirty-five days after weaning, the animals were anesthetized, and their lungs were collected and fixed in 10% formalin. The lungs were dehydrated in increasing concentrations of ethanol, cleared in xylene, embedded in liquid paraffin, and then sectioned using purified histological paraffin. The tissue blocks were cut using a microtome set at 3 micrometers (µm). For histological analysis, the sections were stained with Hematoxylin and Eosin. The slides were examined using a light microscope, and images were captured using a trinocular biological microscope at 10x and 40x magnifications. Histopathological analysis of the lung tissue across all experimental groups revealed alveoli lined by simple squamous epithelium, along with the presence of type I and type II pneumocytes, bronchioles, and alveolar sacs. The DP group exhibited the same structures as the control group; however, an increased number of extravascular erythrocytes was observed. This alteration suggests an inflammatory process characterized by increased blood flow and vascular permeability, resulting from the release of soluble mediators of the inflammatory response [3]. In contrast, the DP+Mel group showed a reduction in vascular leakage, along with alveolar hyperplasia. This finding confirms melatonin's potential to attenuate the inflammatory response by inhibiting the transcription of pro-inflammatory cytokines and influencing vascular adaptation processes, thereby improving pulmonary perfusion [4,5]. Moreover, the observed alveolar hyperplasia indicates melatonin's direct role in tissue regeneration by modulating cellular pathways related to cell proliferation, which is dose-dependent [6]. In conclusion, melatonin exerts a protective effect on the lungs of rats subjected to early weaning, reducing inflammation and promoting beneficial structural adaptations. Although

further studies are necessary to clarify the underlying mechanisms, these findings highlight melatonin's therapeutic potential to minimize lung damage, opening new perspectives for pharmacological interventions in situations that pose a risk to lung development.

[1] R.S. Araújo et al., *Revista Brasileira de Saúde Materno Infantil*, 20 (2020) 348.
[2] J. A. S. Gomes et al., *Revista Eletrônica Acervo Saúde*, 24 (2024), 5.
[3] W.M. Cruvinel et al., *Revista Brasileira de Reumatologia*, 50 (2010) 444.
[4] W. Wang, J. Gao, *Experimental and Therapeutic Medicine*, 21 (2020) 3.
[5] J.A.S. Herruzo, P.S. Munõz, *Revista Espanõla de Enfermedades Digestivas*, 101 (2009) 455.
[6] J.G.M. Silva et al., *Temas em Saúde*, 22 (2022) 317.

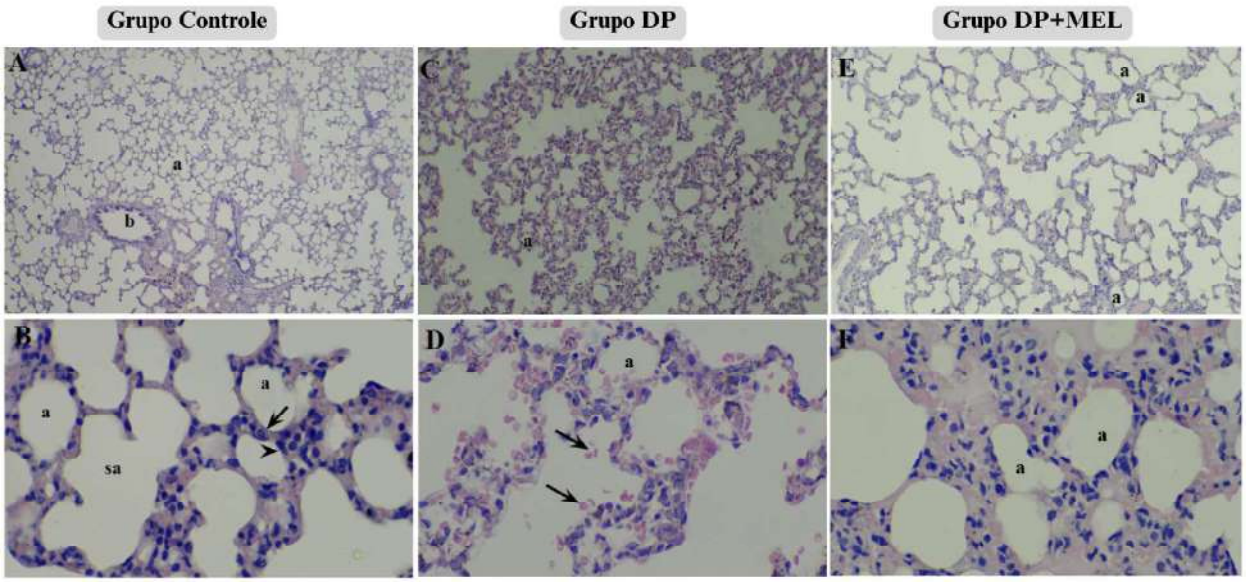

Figure 1. Photomicrographs of lung tissue in experimental animals. A, B – Control group showing alveoli (a), bronchiole (b), alveolar sac (as), type I pneumocyte (arrow), type II pneumocyte (arrowhead); C, D – DP group showing extravascular erythrocytes; E, F – DP+Mel group showing alveolar hyperplasia (a).

Histopathological Evaluation Of The Offspring Lungs Of Rats Subjected To Protein Malnutrition During Pregnancy And Supplemented With Cannabidiol Nanoemulsion

Raissa Gomes de França [1]*, Paloma Vitória Melo da Silva[1], Maria Gabriela da Silva Mello[1], Weslleyanne Millena da Silva Costa[1], Maria Eduarda Carneiro de Lima[1], Ana Carolina Ribeiro Saraiva da Costa[1], Suellen Rozy da Silva Medeiros[1], Maria Manuela dos Santos Rodrigues[1], Ryan Cristian da Silva[2], Bruno Mendes Tenorio[1], Fernanda das Chagas Angelo Mendes Tenorio[1].

[1]Federal University of Pernambuco, Biosciences Center, Department of Histology and Embryology, Recife, Pernambuco, Brazil, [2]Federal University of Pernambuco, Biosciences Center, Department of Biochemistry, Recife, Pernambuco, Brazil
*rg0900665@gmail.com

Protein malnutrition induces an inflammatory condition which, when occurring during pregnancy, can create an unfavorable systemic environment for fetal development by altering the offspring's lung structure and impairing respiratory function [1,2]. In this context, the use of drugs of plant origin, such as cannabidiol (CBD), a bioactive component of *Cannabis sativa*, has been investigated for their anti-inflammatory properties. In models of acute lung inflammation induced by lipopolysaccharide (LPS), administered intraperitoneally of CBD at doses of 20 and 80 mg/kg reduced leukocyte infiltration and pro-inflammatory cytokines production, preserving lung integrity without adverse behavioral effects [3]. These findings suggest its potential as a therapeutic strategy to protect lung function under conditions associated with a low-protein diet. The study aimed to histopathologically evaluate the lungs of offspring from rats subjected to protein malnutrition during pregnancy and supplemented with cannabidiol nanoemulsion. For this purpose, fifteen Wistar rats were used, divided into three groups: control group, low-protein diet group (LPD), and low-protein diet plus CBD supplementation (LPD+CBD). After mating and confirmation of pregnancy by vaginal swab, the females were treated with their respective diets for 21 days: standard diet, low-protein diet, or low-protein diet supplemented with cannabidiol nanoemulsion at a dose of 10mg/kg. On gestational day 21, the offspring were anaesthetized with an intraperitoneal mixture of ketamine and xylazine (0.8:0.6) for lung collection, which were then weighed and fixed in 10% buffered formal liquid for 48 hours. The samples were then cleaved and subjected to the histological technique of impregnation and paraffin embedding. The blocks obtained were cut into 3–5µm sections for subsequent staining with Hematoxylin-Eosin (H&E). The stained slides were analyzed with a Nikon® NIS Elements light microscope and photographed with a Nikon Eclipse 80i photomicroscope. The results of histopathological evaluation revealed that lungs from all the experimental groups displayed alveoli lined by a simple squamous epithelium, as well as bronchi, bronchioles and alveolar sacs (figure 1). The LPD group had the same structures as the control group, but exhibited a reduction in the bronchiolar space and alveolar epithelium thickness compared to controls, despite preservation of basic structures. Conversely, the LPD+CBD group showed evidence of alveolar hyperplasia. Therefore, it can be concluded that a low-protein diet induces histological alterations in the lung, while cannabidiol supplementation may exert regenerative effects on damaged lung tissue.

[1] C.M. Dias et al., *Effects of protein-calorie malnutrition on pulmonary function.* Pulmão RJ, 11 (4) (2002).
[2] T.F. Castro et al., *Protein restriction during pregnancy affects lung development and promotes oxidative stress and inflammation in C57 BL/6 mice offspring.* ScienceDirect 101 (2022).
[3] A. Ribeiro et al., *Effects of cannabidiol, a cannabinoid derived from Cannabis sativa, in a murine model of acute lung inflammation: an immune-neuro-endocrinological evaluation.* Rev. Bras. Terapia Intensiva, 27 (4) (2015).

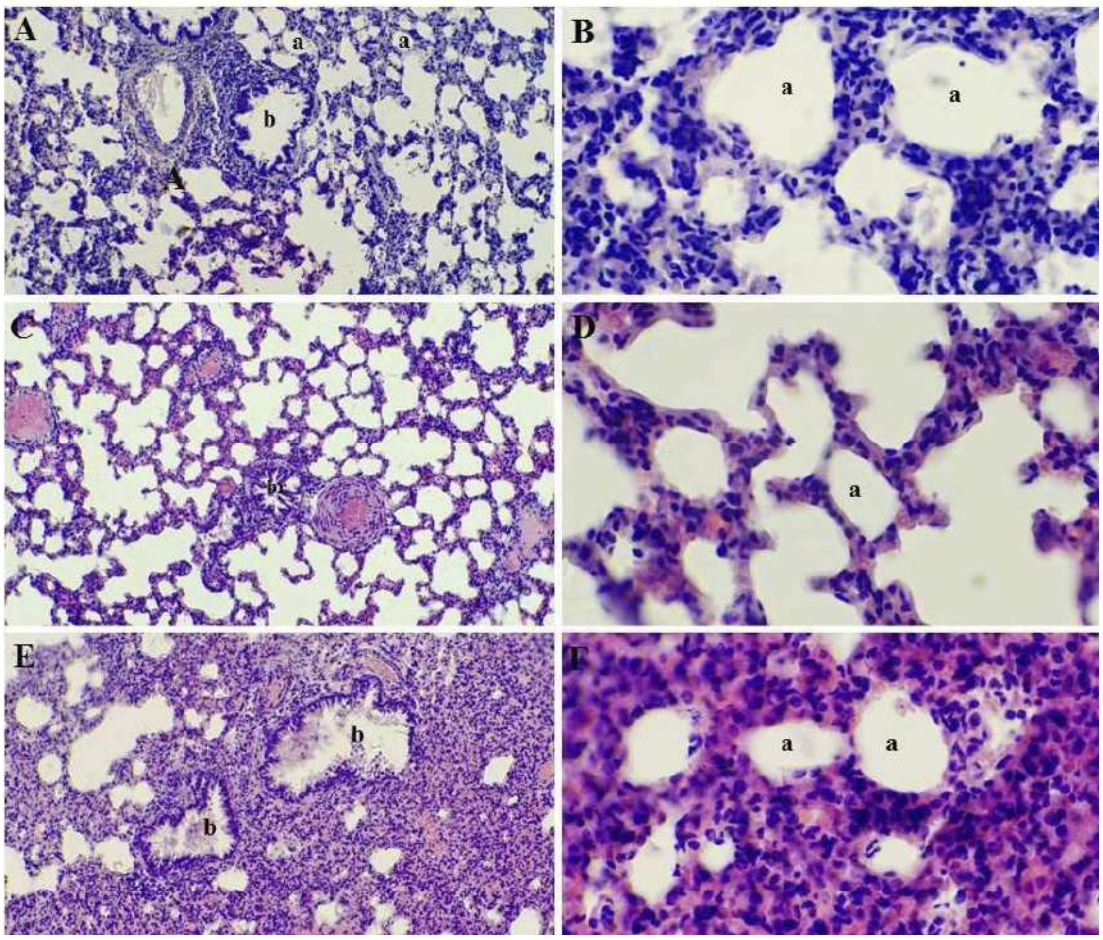

Figure 1. Photomicrograph of the lungs of the offspring of the experimental female animals. Panels A, B- control group showing alveoli (a) and bronchioles (b); C, D- LPD group showing bronchioles and a reduction in the alveolar wall; E, F- LPD+CBD group showing bronchioles (b) and alveolar hyperplasia (a). All images were stained with Hematoxylin-Eosin (H&E) at 100x magnification to A, C, E and the others 400x magnification.

Immunohistochemical Analysis For Caspase-3 Of The Mucosa Of The Dorsum Of The Tongue Of Rats Treated With Botulinum Toxin Type A Injection Into The Submandibular Gland

Carlos Eduardo da Silva[1]*, Maria Manuela dos Santos Rodrigues[1], Giovana Siqueira Faustino da Silva[2], Weslleyane Milena da Silva Costa[1], Glenison da Rocha Duarte[1], Maria Gabriela da Silva Mello[1], Maria Eduarda Carneiro de Lima[1], Ana Carolina Ribeiro Saraiva da Costa[1], Suellen Rozy da Silva Medeiros[1], Jaciel Benedito de Oliveira[2], Fernanda das Chagas Angelo Mendes Tenorio[1].

[1]Federal University of Pernambuco, Center for Biosciences, Department of Histology and Embryology, Recife, Pernambuco, Brazil, [2]Federal University of Pernambuco, Biosciences Center, Department of Anatomy, Recife, Pernambuco, Brazil
*eduadocarlos120@gmail.com

Botulinum toxin is a neurotoxin produced by the anaerobic bacterium *Clostridium botulinum*, which has seven serotypes: A, B, C, D, E, F, G, type A (BTX-A) is the most commonly used [4]. It has been widely used in the treatment of sialorrhea, a common condition in patients with neurological disorders [3]. One of the side effects of this treatment can be hyposalivation or xerostomia [1]. With a reduction in salivary flow, the functions of saliva are compromised, which can have oral and systemic consequences, including causing an imbalance in the oral microbiota [2]. The aim of this study was to investigate possible changes in the mucosa of the dorsum of the tongue of female rats treated with intraglandular injections of BTX-A, checking for the presence of apoptotic figures using immunohistochemistry for the caspase-3 protein. Thirty Wistar rats were used, divided into five groups: Control Group: 6 animals without any treatment at the time of collection; BTX-A 12 Group: 6 animals whose right submandibular glands received 3 injections of botulinum toxin type A (BTX-A) and the samples collected 12 days after the last application of the toxin; BTX-A 35 group: 6 animals whose right submandibular glands received 3 injections of botulinum toxin type A (BTX-A) and the samples for analysis were taken 35 days after the last application of the toxin; GEL 12 group: 6 animals with right submandibular glands treated with injections of bovine gelatin, a BTX-A stabilizer, whose samples for analysis were taken 12 days after the last gelatin application; GEL 35 group: 6 animals with right submandibular glands treated with injections of bovine gelatin, a BTX-A stabilizer, whose samples for analysis were taken 35 days after the last gelatin application. The tongues were sectioned and their middle third was collected for fixation in 10% formalin for 48 hours, and then sent for histological processing and paraffin embedding. Histological sections of approximately 3 µm were obtained, placed on silanized slides and processed for immunohistochemistry to detect caspase-3, a marker of apoptosis. The tongue sections were first deparaffinized with xylene and hydrated with ethanol. They were then incubated with the respective antibodies overnight, then incubated with caspase-3 antibody, then revealed with chromogenic substrate 3, 3'diaminobenzidine (DAB) in brown and counterstained with Harris hematoxylin. It "an increased number of cells expressing of the animals treated with BTX-A 12 days and BTX-A 35 days showed more cells with specificity in the detection of caspase-3, evidenced by the brown cytoplasmic staining, but the BTX-A 35 days group showed less reactivity for this protein when compared to the BTX-A 12 days group. This specificity was not seen in the other groups, control, Gel 12 days and Gel 35 days (Figure 1). We conclude that treatment with botulinum toxin type A (BTX-A) may induce an increase in apoptotic cell activity.

[1] T.M. Chung et al., *Dispensing profile of botulinum toxin for the treatment of spasticity: Brazilian national data.*. Acta Fisiatr. 23 (1) (2016).
[2] B.J. Franck et al., *Botulinum toxin for the treatment of sialorrhea in patients with Parkinson's disease*. Rev. Bras. Neurol. 54 (3) (2018).
[3] E.D.A. Lima et al., *Saliva and hydration: importance of saliva quantity and quality for maintaining satisfactory oral health in patients with cerebral palsy.* Rev. Campo Saber. 3 (1) (2017).
[4] G. Verma, *Role of Botulinum Toxin Type-A (BTX-A) in the Management of Trigeminal Neuralgia.* Pain Res. Treat. (2013).

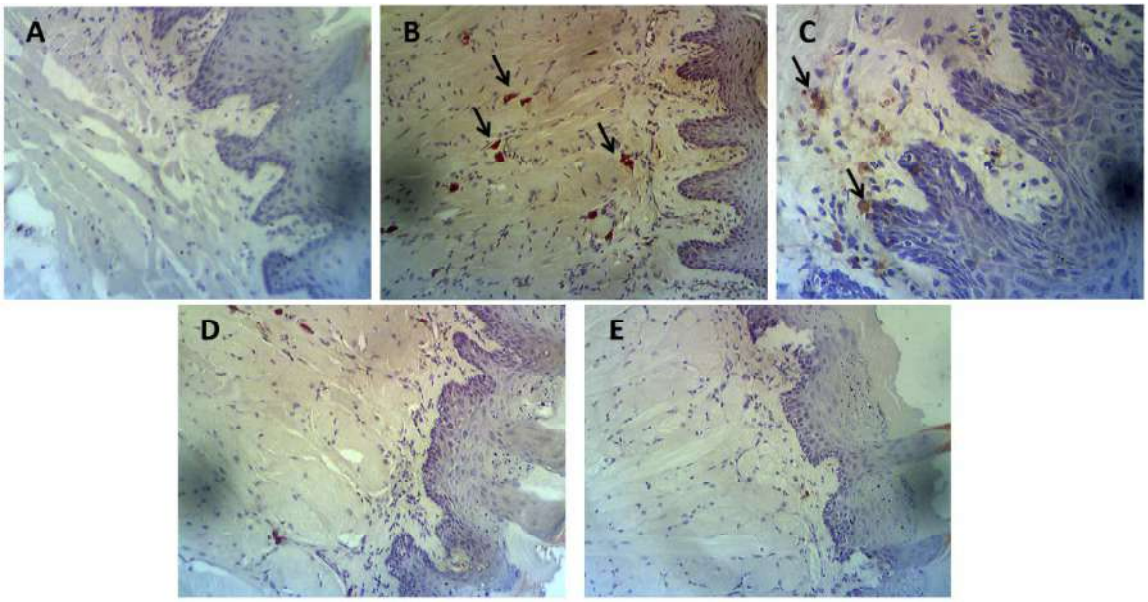

Figure 1. Photomicrograph of the mucosa of the dorsum of the tongue of female rats treated with Botulinum Toxin Type A (BTX-A) injected into the submandibular gland. Immunohistochemistry technique with caspase-3 to analyze apoptosis. In A, we see the control group without caspase-3 labeling. In B, the BTX-A 12-day group, showing cells with specific caspase-3 detection, with brown cytoplasm. C, BTX-A 35 days, showing less specificity for this protein when compared to the BTX-A 12 group. In D and E, groups GEL 12 days and GEL 35 days, respectively, there was no evidence of caspase-3 labeling. A, B, C, D and E, 100x magnification.

Impact of *Trypanosoma cruzi* (Tv Strain) Infection on Incisor Enamel Development in Swiss Mice

Isabel Maria Porto[1*], Juliana Kaori Ota de Oliveira[2], Jociel Klleyton Santos Santana[2], Lucas de Andrade Rodrigues[1], João Aristeu da Rosa[2].

[1] São Paulo State University (UNESP), Department of Morphology and Pediatric Clinic, School of Dentistry, Araraquara, Brazil.

[2]São Paulo State University (UNESP), Department of Biological Sciences, School of Pharmaceutical Sciences, Araraquara, Brazil.

*isabel.porto@unesp.br

Chagas disease, caused by the protozoan *Trypanosoma cruzi*, affects between 6 and 7 million people, mainly in tropical regions, and is classified as a neglected tropical disease [1]. The parasite is transmitted by blood-sucking insects of the Triatominae subfamily and enters the host's bloodstream in the trypomastigote form [2]. Once inside the host, *T. cruzi* invades multiple organs in the amastigote form, leading to chronic damage to the heart, brain, liver, and intestines [3,4]. In 2023, a new strain of *T. cruzi*, designated Tv, was isolated from an adult *Triatoma vitticeps* collected in Grão Mogol, Minas Gerais (Brazil) [5]. Considering the systemic nature of Chagas disease and the absence of studies on dental tissues, this research aimed to investigate the effects of Tv strain infection on ameloblasts and enamel matrix formation. Enamel is highly sensitive to systemic disturbances, as it is formed by specialized epithelial cells known as ameloblasts, which record physiological stress during tooth development [6]. Sixteen *Swiss* mice were used and divided into two groups: control (n=8) and infected with the Tv strain (n=8). The project was approved by the CEUA of FCF/UNESP, Araraquara (protocol number 7977045878). After 12 months of infection, animals were euthanized and hemimandibles were collected for histological processing. Sections were analyzed using light microscopy, caspase-3 immunohistochemistry, and the TUNEL assay to assess apoptotic activity. Results revealed significant impairment in ameloblast viability in the infected group, with a high number of apoptotic bodies, positive caspase-3 expression, and TUNEL-positive labeling, indicating programmed cell death. These findings suggest that chronic *T. cruzi* infection negatively impacts enamel formation, representing a novel observation in the literature. We conclude that dental enamel, particularly during its developmental phase, may serve as a sensitive marker of systemic changes caused by Chagas disease, offering new insights into its pathogenesis beyond traditionally affected organs.

[1] F.S.P Silva et al., Ciência & Saúde Coletiva, 27 (5) (2022) 1939.
[2] A. Herreros-Cabello et al., Genes Basel, 11 (10) (2020) 196.
[3] J. Martín-Escolano et al., *ACS Infectious Diseases*, 8, (6) (2022) 1107.
[4] A.R.L. Teixeira et al., *Clinic Microbiol Rev*, 24 (3) (2011) 592.
[5] G.S. Ferraz. Final Scientific Report – São Paulo Research Foundation (FAPESP), 2022/13607-0.
[6] C.E. Smith. Crit Rev Oral Biol Med., 9 (1998) 128.

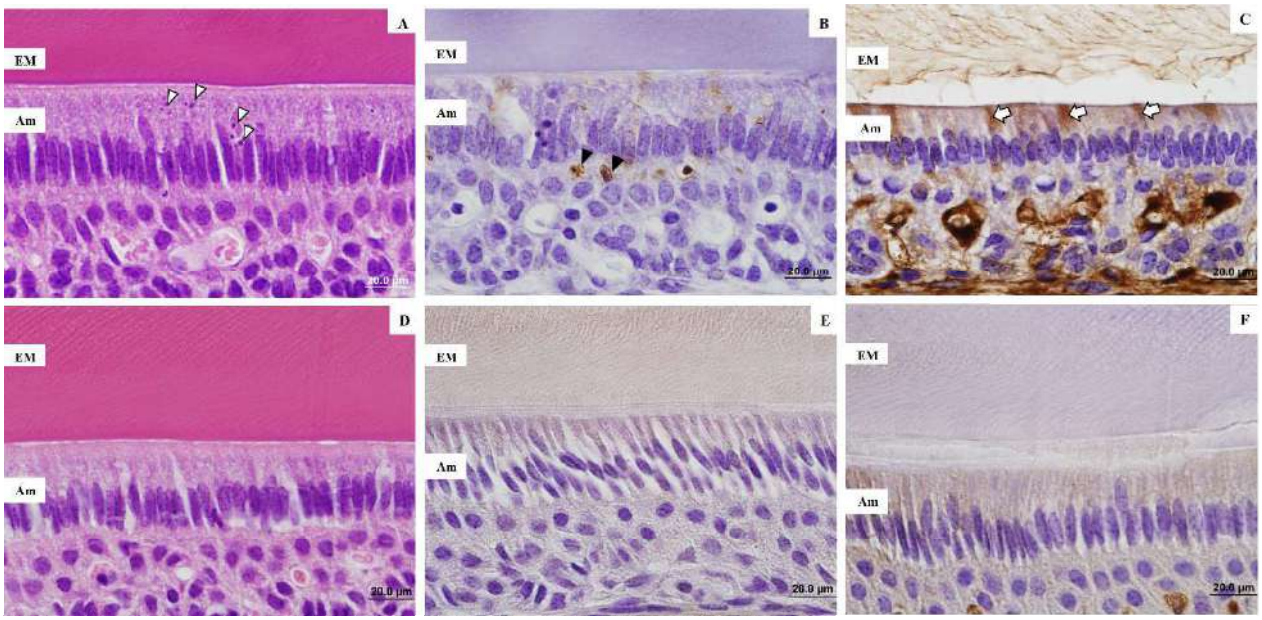

Figure 1. Lower incisor enamel of mice infected with *Trypanosoma cruzi* (Tv strain). (A) Hematoxylin and eosin (H&E) staining showing apoptotic bodies (white arrowheads). (B) TUNEL assay indicating TUNEL-positive apoptotic bodies (black arrowheads). (C) Caspase-3 immunohistochemistry revealing positive caspase-3 expression in ameloblasts (white arrows). **Control group:** (D) H&E staining. (E) TUNEL assay. (F) Caspase-3 immunohistochemistry. No alterations were observed in control group. **Magnification:** 1000×. Em, enamel matrix; Am, ameloblast layer.

Hepatic Impairment in Lactating Rats: Synergistic Effects of Protein Malnutrition and Physical Exercise

Alison Jose da Silva[1*], Ana Vitória Ferreira dos Santos[1], Carlos Eduardo da Silva[1], Maria Gabriela da Silva Mello[1], Weslleyanne Millena da Silva Costa[1], Maria Eduarda Carneiro de Lima[1], Ana Carolina Ribeiro Saraiva da Costa[1], Ryan Cristian da Silva[1], Sara Vitoria de Oliveira Costa[1], Maria Luísa Figueira de Oliveira[2], Bruno Mendes Tenorio[1], Fernanda das Chagas Angelo Mendes Tenorio[1]

[1]Department of Histology and Embryology, Federal University of Pernambuco, Recife-PE. Brazil.
[2]Department of Nutrition, Federal University of Pernambuco, Recife-PE. Brazil.

***Corresponding author:** alison.jsilva@ufpe.br

Protein malnutrition during pregnancy and lactation directly affects the liver, causing changes such as hepatocyte degeneration, inflammation, steatosis and disorganization of the hepatic lobules [1]. This damage impairs essential functions such as plasma protein synthesis, nutrient metabolism and detoxification [2,3]. Furthermore, when associating malnutrition with voluntary physical activity, it is noted that it acts as a natural regulator of the organism, favoring important metabolic adaptations. In the liver, this stimulus can represent a protective key, activating mechanisms that minimize the damage caused by nutritional deficiency, preserving its essential functions even in times of greater physiological vulnerability, such as pregnancy and lactation [4]. Thus, this study seeks to identify whether exercise aggravates or mitigates liver damage caused by nutritional deficiency. To this end, after approval of CEU nº005/2021, 32 Wistar rats (n=8) were divided into 4 groups: control group, active group, very active group and slightly active group. The rats were subjected to mating and pregnancy was confirmed the following day, the animals were subjected to protein malnutrition and physical activity at the same time. Voluntary physical activity was performed in acrylic cages with dimensions of 27 cm, 34 cm and 61 cm in width, height and length, respectively, and having at one of the inner ends of the cage the cycle ergometer (running wheel), together with a sensor monitoring system that was used to evaluate the movement of the cycle ergometer, so that it could be quantified daily by the sensors and recorded in the physical quantities: distance traveled (km), activity time (min) and estimated caloric expenditure (kcal). On the 21st day of lactation, the animals were euthanized for liver collection and subjected to histological analysis. Histological analysis of the liver of animals from all experimental groups showed an externally thin capsule consisting of mesothelium and lobules containing veins of various calibers. In addition, the parenchyma showed hepatocytes arranged in a disorderly manner around vessels of various calibers. And the presence of Kupffer cells. However, the liver tissue of the active, very active and lightly active groups showed accumulation of lipid droplets, hepatocyte hypertrophy and pyknotic nuclei, indicating intense cellular stress and degenerative changes (Figure 1). These findings suggest that, although voluntary physical exercise can offer adaptive benefits under normal physiological

conditions, in a situation of protein malnutrition it can potentiate liver damage, especially at high intensities, due to the metabolic overload in an already weakened organism[2,4]. Thus, the data indicate that protein malnutrition, combined with the practice of physical activity, especially at higher intensities, aggravates histological changes in the maternal liver.

Keywords: Protein malnutrition, Hepatic degeneration, Lactation, Voluntary exercise, Maternal hepatic injury

REFERENCE:

[1] LS Côrtes et al., Maternal protein restriction impairs nutrition and ovarian histomorphometry without changing p38MAPK and PI3K-AKT-mTOR signaling in adult rat ovaries. Life sciences (vol. 264) 2021.

[2] PP Gomes et al., MATERNAL PHYSICAL ACTIVITY ON OFFSPRING HEALTH: A STUDY DURING PREGNANCY. REVISTA FOCO (vol. 17) 2024.

[3] J Fragoso et al., Effects of maternal low-protein diet and spontaneous physical activity on the transcription of neurotrophic factors in the placenta and brain of rat mothers and offspring. Journal of Developmental Origins of Health and Disease , (vol. 12) 2021.

[4] CJ Bautista et al., Effects of maternal protein restriction during pregnancy and lactation on milk composition and offspring development. British Journal of Nutrition (vol. 122) 2019.

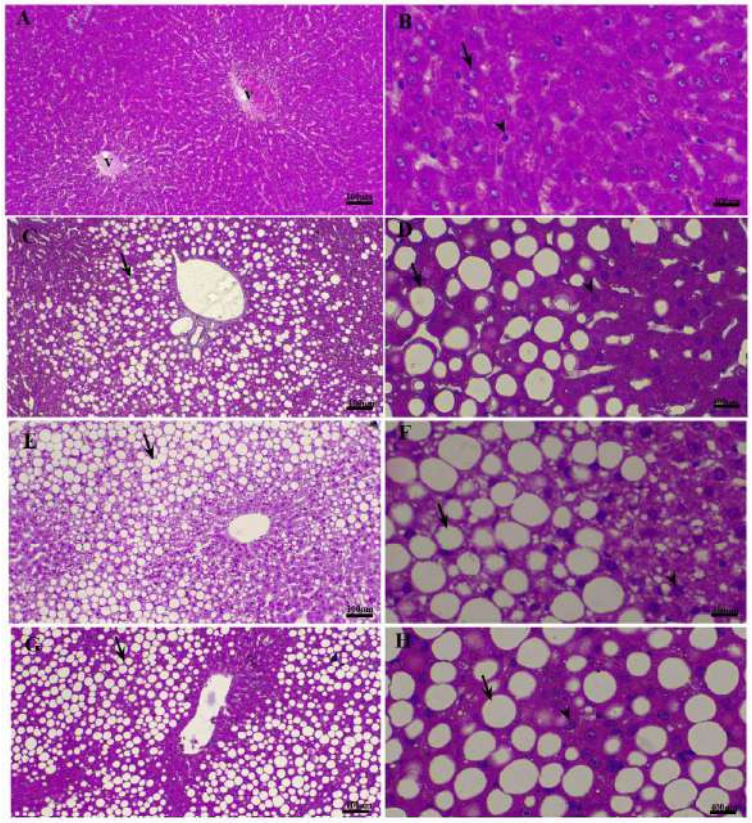

Figure 1: Photomicrograph of the liver of animals in the experimental groups. A, B- Control group showing hepatocytes (arrow) arranged in a disordered manner around vessels (V) in addition to Kupffer cells (arrowhead); C, D- Active group showing lipid droplets (arrow) and hypertrophic hepatocytes and pyknotic nucleus (arrowhead); E, F- Very active group showing lipid droplets (arrow) and hypertrophic hepatocytes and pyknotic nucleus (arrowhead); G, H- Slightly active group showing lipid droplets (arrow) and hypertrophic hepatocytes and pyknotic nucleus (arrowhead). H-E staining.

Internalization Of Carbon Dot Derived From Methyl Red In Yeast Cells Verified Via Confocal Microscopy For Application In Antimicrobial Photodynamic Therapy.

W. Muniz Jr.[1]*, R. L. Ferreira[1], V. P. O. Barros[2], M. F. Landell[2], I. N. de Oliveira[1]

[1]Instituto de Física – UFAL, [2]Instituto de Ciências Biológicas e da Vida – UFAL
*walter.santos@fis.ufal.br

Carbon dots, as carbon-based nanoparticles with outstanding optical and photosensitive properties, stand out among the third-generation drugs used in Antimicrobial Photodynamic Therapy (aPDT) [1]. aPDT is an optical technique used for microbial inactivation, and its mechanism of action is based on the highly oxidizing effect of reactive oxygen species (ROS) on microorganisms [2, 3]. The method takes advantage of the synergistic effect between a photosensitive chemical and light to excite molecular oxygen and subsequently produce ROS, which will induce microbial death. In this study, we analyzed the photoactivity of the carbon dot CD-MR synthesized from azodye methyl red in inactivating pathogenic yeasts *Candida albicans* ATCC 90028 and *Cryptococcus neoformans* ATCC 208821. Microscopy analyses were performed to observe the adhesion and possible absorption of CD-MR by yeast cells. CD-MR is a strong candidate for use as a photosensitizer in aPDT due to its high quantum yield of ROS generation. Biological assays, such as microbial growth curves and the Kirby-Bauer test, indicated that CD-MR has no intrinsic antimicrobial activity. The material, however, exhibits stable photoactivity, with a reduction of 2.25 Log(CFU/mL) in the number of colony-forming units (CFU) of *C. neoformans* compared to the control group (growth without CD-MR and/or light treatment). To understand the interaction of CD-MR with yeast cells, brightfield and confocal microscopy assays were performed. It is possible to verify that the nanoparticle was fully absorbed by both *C. neoformans* and *C. albicans* cells, spreading throughout the cytoplasm but without binding to any specific organelle. Microscopy images revealed that within the fluorescence corresponding to CD-MR, there were dark regions, indicating structures within the cytoplasm that did not absorb the CD-MR. Confirmation of CD-MR presence in the cytoplasm was possible by co-staining the cells with Calcofluor White (CFW) marker, which binds to the chitin of the yeast cell wall. CD-MR fluorescence can be observed throughout the interior of cells, while CFW fluorescence is restricted to the outer perimeter of the yeast, where the cell wall is located. The cells remained intact for a few hours after doping with CD-MR, even exhibiting reproduction by budding, as verified by microscopy. These results, in addition to biological assays confirming the low toxicity of CD-MR, also point to its potential use as a biomarker.

[1] R. Knoblauch, C. D. Geddes, Materials, 13 (18) (2020) 4004.
[2] M. P. Romero et al., Frontiers in Microbiology, 12 (2021) 662149.
[3] S. Jovanović et al., Pharmaceutics, 15 (4) (2023) 1170.
[4] This research was supported by CAPES (Brazil), FAPEAL (AL-Brasil) and INCT-FCx (Brasil).

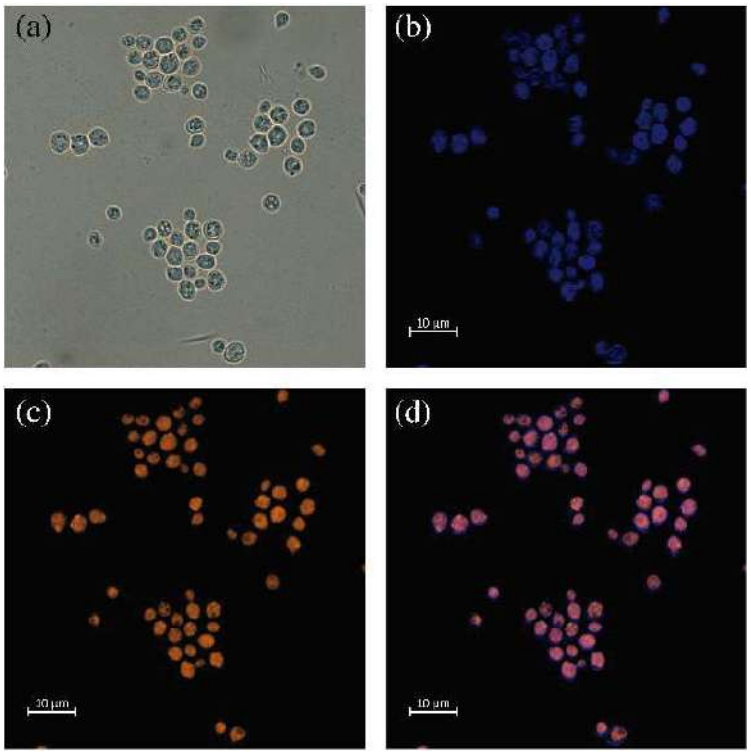

Figure 1. (a) Brightfield and (b), (c) and (d) confocal microscopy of *C. neoformans* stained with CD-MR and CFW.

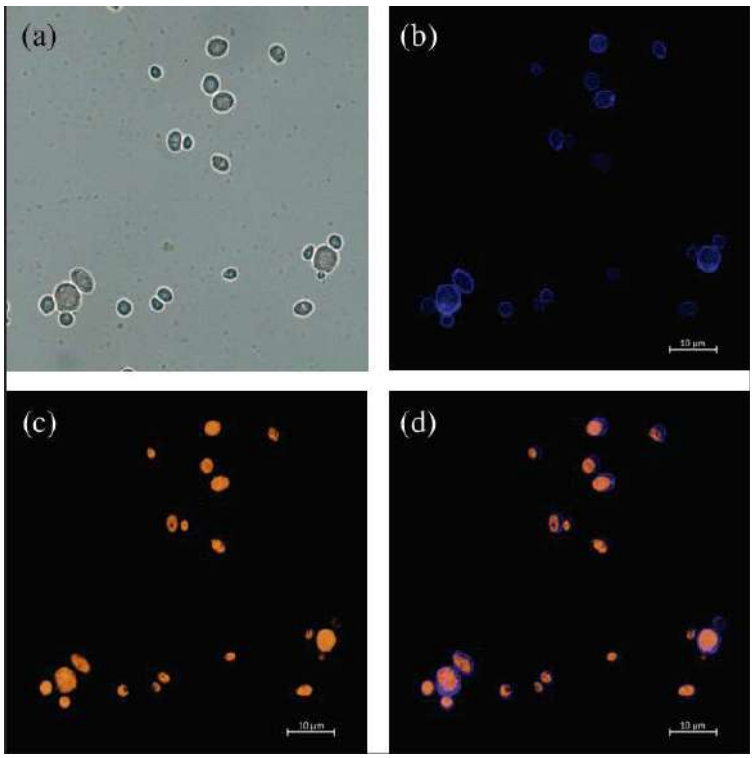

Figure 2. (a) Brightfield and (b), (c) and (d) confocal microscopy of *C. albicans* stained with CD-MR and CFW.

Investigation of the Therapeutic Potential of Mesenchymal Stem Cell-Derived Extracellular Vesicles in a 3D Model of Liver Fibrosis

Tâmysa Ferreira dos Santos[1], Carine Machado Azevedo Cardoso[1]*, Bianca Goés Fialho[1], Milena Botelho Pereira Soares[1,2].

[1] Gonçalo Moniz Institute (Oswaldo Cruz Foundation (IGM-FIOCRUZ/BA), [2] SENAI Institute of Innovation in Health Advanced Systems (CIMATEC ISI SAS), SENAI/CIMATEC
*carine.cardoso@fiocruz.br

Chronic liver diseases represent a serious public health issue, accounting for approximately 4% of global annual deaths [1]. Hepatic fibrosis is the liver's scarring response to chronic injury and is mainly characterized by the accumulation of extracellular matrix produced by hepatic stellate cells (HSCs) [2]. The progression of hepatic fibrosis to advanced stages increases the risk of cirrhosis and hepatocellular carcinoma, potentially leading to chronic liver failure [3]. Currently, the only available therapy is liver transplantation, which is often unfeasible [4]. Mesenchymal stem cell (MSC) therapy has shown therapeutic effects in liver fibrosis due to their self-renewal capacity, multilineage differentiation, and immunomodulatory activity through the secretion of cytokines, growth factors, and extracellular vesicles (EVs) [5]. Furthermore, genetic modification of these cells has been investigated as a strategy to enhance their therapeutic potential [6]. This study aims to evaluate the therapeutic potential of EVs derived from MSC genetically modified to overexpress the growth factor G-CSF in a 3D model of liver fibrosis. Spheroids were generated by co-culturing hepatocyte like cells (HepG2) and hepatic stellate cells (LX2) at different initial densities and ratios. Spheroids were assessed for size, morphology, and cell viability. Immunostaining was performed for α-smooth muscle actin (α-SMA), along with phalloidin and nuclear staining. Expression of GCSF in MSCs was evaluated by RT-qPCR and immunofluorescence. EVs from wild-type MSCs (EV-MSC) and G-CSF-overexpressing MSCs (EV-GCSF) were isolated by ultracentrifugation and characterized by nanoparticle tracking analysis (NTA), transmission electron microscopy (TEM) and dot blot. Spheroids plated at initial densities of 2,000 and 3,000 cells/well with 15% LX2 showed stable morphology and cell viability over 10 days of culture (fig.1). Immunostaining for α-SMA and phalloidin was unevenly distributed, with greater intensity at the outer regions of the spheroids (fig.2). RT-qPCR and immunofluorescence staining confirmed that the genetically modified MSCs maintained both GCSF gene and protein expression (Fig.3). MSC-EVs and GCSF-EVs showed mean sizes of 166.2 ± 11.5 nm and 118.7 ± 4.6 nm, respectively, and exhibited a classical round bilayer membrane structure (Fig.4). Dot blot analysis showed that the EVs expressed exosome-positive markers CD63, CD81, and CD90. Future steps include stimulation of the spheroids with TGF-β to induce fibrotic activation, followed by treatment with the EVs. The treatment effects will be evaluated through cell viability analysis using the Alamar Blue assay, assessment of albumin production, uptake of EVs by the spheroids, and expression analysis of α-SMA, collagen, and TGF-β by immunofluorescence and RT-qPCR. The authors acknowledge the Coordination for the Improvement of Higher Education Personnel (CAPES), Brazil, for funding and support [7].

[1] H. Devarbhavi et al. *Global burden of liver disease: 2023 update*, Journal of Hepatology, 79, (2023) 516.
[2] V. Hernández-Gea, S. L. Friedman, *Pathogenesis of Liver Fibrosis,* Annual Review of Pathology-mechanisms of Disease, 6 (2011) 425.
[3] S. Lemoinne, S. L Friedman*, New and emerging anti-fibrotic therapeutics entering or already in clinical trials in chronic liver diseases,* Current Opinion in Pharmacology, 49 (2019) 60.

[4] X. Wang et al., *Liver transplantation for cirrhosis with chronic liver failure,* Experimental and therapeutic medicine, 11 (2016) 881.
[5] L. Zhang, et al., *Human umbilical cord mesenchymal stem cells inhibit proliferation of hepatic stellate cells in vitro,* International Journal of Molecular Medicine, 41 (2018) 2545.
[6] M. D. Kim et al., *Therapeutic effect of hepatocyte growth factor-secreting mesenchymal stem cells in a rat model of liver fibrosis,* Experimental & Molecular Medicine, 46 (2014) 110.
[7] This research is supported by CAPES (Brazil).

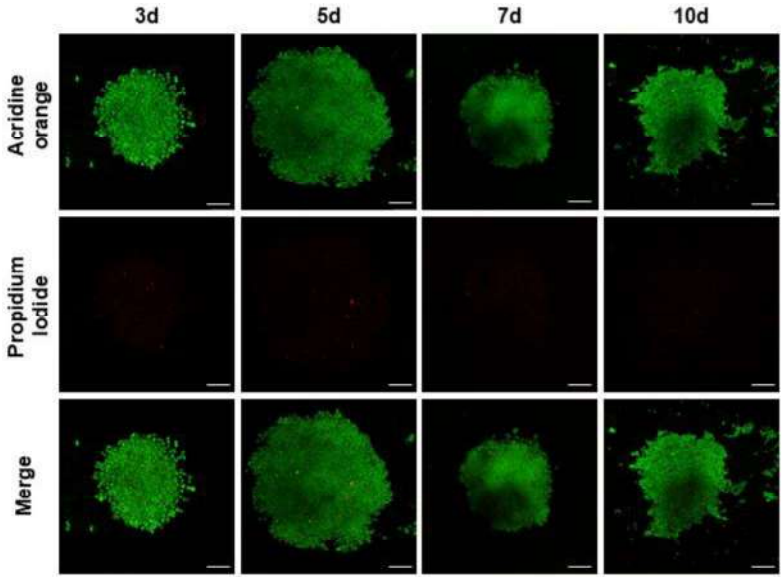

Figure 1. Cell viability in spheroids. Live cells are shown in green, stained with acridine orange, and dead cells in red, stained with propidium iodide. Scale bar = 100 µm. Confocal microscopy.

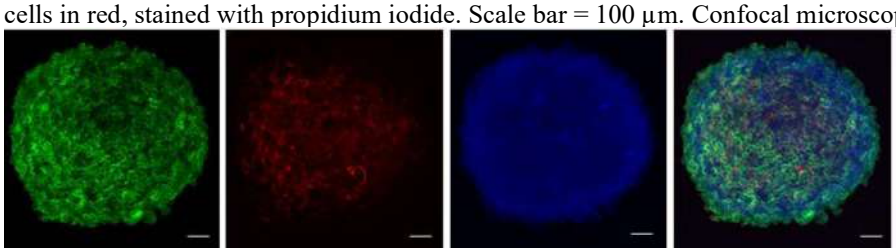

Figure 2. Spheroid immunostaining using phalloidin to visualize the actin cytoskeleton (green), α-SMA (red), and nucleus (blue). Scale bar = 100 µm. Confocal microscopy.

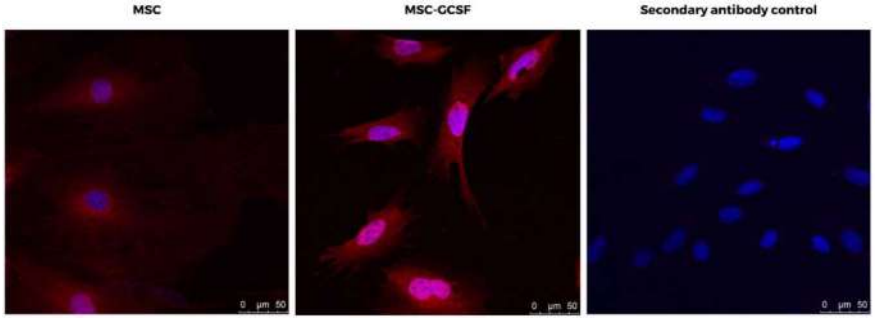

Figure 3. GCSF immunostaining in MSC cells. Scale bar = 50 µm. Confocal microscopy.

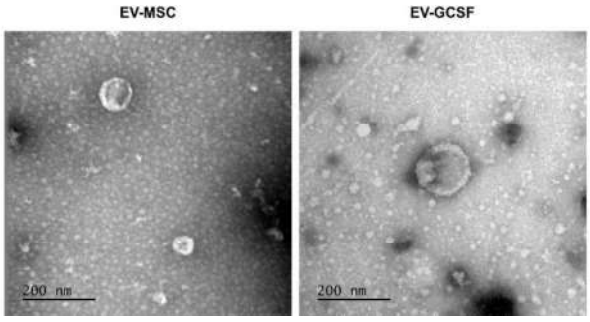

Figure 4. Characterization of EVs by transmission electron microscopy.

In Vitro Analysis of Antioxidant potential in Nanostructured Lipid Carrier Derived from Seriguela Byproducts of the Brazilian Cerrado

Brenda Martins dos Santos [1,2,3]* Leonardo Froes de Azevedo Chang,[1,2,3] Thalita do Espírito Santo Alves[1,2,3], Victor Carlos Mello[1,2,3], Sônia Nair Báo[2].

[1]Cooil Cosmetics, Brasília 72622-401, DF, Brazil, [2]Laboratory of Microscopy and Microanalysis, Department of Cell Biology, Institute of Biological Sciences, University of Brasília, Brasília 70910-900, DF, Brazil, [3]Laboratory of Nanobiotechnology, Department of Genetics and Morphology, Institute of Biological Sciences, University of Brasília, Brasília 70910-900, DF, Brazil

*martinss.brenda06@gmail.com

Seriguela (*Spondias purpurea* L.) is an endemic fruit native to the Brazilian Cerrado, one of the world's most important biodiversity hotspots. Widely recognized and used by local communities, this fruit offers a variety of applications. Recent studies focusing on its byproducts, such as oils and extracts, have revealed significant antioxidant potential, as well as antimicrobial potential [1,2]. However, many of those remain underexplored by both the scientific and industrial sectors, primarily due to challenges associated with the stability and effective utilization of byproducts. To address these issues and enhance treatment delivery, a Nanostructured Lipid Carrier (NLC) was formulated. This NLC incorporates Seriguela extract in conjunction with a Natural Deep Eutectic Solvent (NaDES), thereby facilitating improved stability and targeted delivery of these compounds [3,4]. This study aims to assess the formulation's effects against Reactive Oxygen Species (ROS), free radicals produced by various factors, including ultraviolet radiation. Elevated levels of ROS can lead to DNA damage and are implicated in the pathogenesis of various skin diseases [5]. Human fibroblasts cells (L132) were seeded into a 18x18 slipcover in a 6-well plate at a density of $7x10^4$ and incubated during 24 hours to ensure adhesion. Subsequently, the cells were exposed to the nanotechnology (NLC-Ser 22.5mg/mL), categorized into four distinct groups: Unstimulated (Uns), H_2O_2 500µM treated (exposed for 30 minutes, serving as the positive control); NLC-Ser treatment (H_2O_2 500µM exposure for 30 min, followed by NLC-Ser for 24h); and Preventive treatment (NLC-Ser exposure for 24h, succeeded by H_2O_2 500µM for 30 minutes). Post-treatment, the cells were stained with 5 µM CellROX Green and 0,66 ng/mL DAPI. The analysis was conducted utilizing Leica TCS SP5 Fluorescent Confocal Microscope. Results demonstrated a significant reduction in oxidative stress induced by the NLC. The preventive treatment showed an optimized outcome, leading to a substantial decrease in ROS levels compared to both the untreated and positive control. In conclusion, NLC-Ser demonstrated a significant antioxidant effect, suggesting great potential for new treatments of dermatological conditions, enhancing efficacy and outcomes.

[1] Berni, Plant Foods for Human Nutrition, 2019, https://doi.org/10.1007/s11130-018-0710-1
[2] Oliveira, Journal of Medical Microbiology, 2022, https://doi.org/10.1099/jmm.0.001575
[3] Schuh, Pharmaceuticals, 2024, https://doi.org/10.3390/ph17070855
[4] Schuh, Molecules, 2023, https://doi.org/10.3390/molecules28227653
[5] Bickers, Journal of Investigative Dermatology, 2006, https://doi.org/10.1038/sj.jid.5700340

Acknowledgements
We extend our gratitude to the Laboratory of Microscopy and Microanalysis at the University of Brasília (LMM - UnB) and acknowledge the financial support from CNPq, FAP-DF, and FINEP.

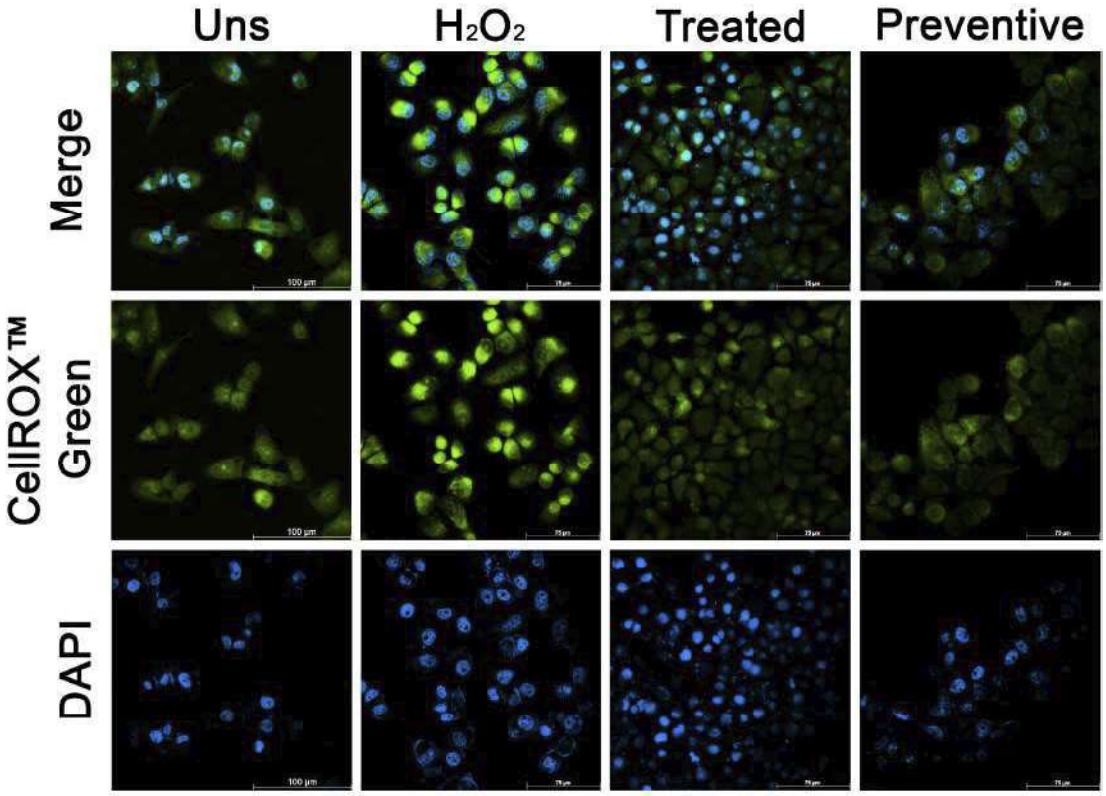

Figure 1. Confocal images of L132 cells in four different groups: UNS, H_2O_2, Treated with NLC-Ser 22.5mg/mL and Preventive treatment. The cells were stained with 5 µM CellROX Green and 0,66 ng/mL DAPI.

Metabolic Programming By Maternal Exposure To Glyphosate And High-Fat Diet: Study Of Neuromuscular Junctions In The Soleus Muscle Of Mice

Rafaella Cristina Lima da Silva[1]*, Ariadne Barbosa[1], Sandra Lucinei Balbo[1], Maria Lucia Bonfleur[1], Marcia Miranda Torrejais[1].

[1]Graduate Program in Biosciences and Health –Universidade Estadual do Oeste do Paraná, Cascavel, Paraná, Brazil.
*rafaella.silva2@unioeste.br

Maternal exposure to toxic compounds such as pesticides can lead to alterations in intrauterine development, resulting in different physiological and/or morphological conditions that may contribute to the onset of diseases [1]. Glyphosate is a widely used pesticide and has been associated with the occurrence of various diseases, including obesity [2], a chronic condition defined as excessive body weight resulting from an imbalance between energy intake and expenditure, and linked to genetic, nutritional, metabolic, and environmental risk factors [3]. However, few studies have investigated its effects on skeletal muscle. Therefore, this study aimed to evaluate the morphology and morphometry of neuromuscular junctions (NMJs) in the soleus (SOL) muscle of offspring from mice exposed to glyphosate during prenatal and postnatal periods, and to determine whether these effects were exacerbated by a high-fat diet. Twenty pregnant C57BL/6 female mice were housed individually and divided into two groups: a control group (CTL, n=10), which received pure water throughout pregnancy and lactation, and a glyphosate- based herbicide group (GBH, n=10), which received water containing 0.5% of the herbicide glyphosate [4] during the same period. After weaning, and for the following 30 days, the male offspring were fed a standard diet and had access to water ad libitum. They were then divided into four experimental groups: Control group (CG-F1); High-fat diet group (HFD-F1); Glyphosate-based herbicide group (GBH-F1); and Glyphosate-based herbicide and high-fat diet group (GBH-HFD-F1). At 150 days of age, the animals were weighed and euthanized, obesity was assessed using the Lee index, the SOL muscle was collected and stored in Karnovsky fixative [5], and subsequently processed using the Non-Specific Esterase histochemical technique [6] for morphological and morphometric analysis of 80 NMJs per animal. The HFD-F1 group showed a 28% increase in body weight ($p = 0.0003$) and a 457% increase in retroperitoneal and periepididymal fat ($p < 0.0001$) compared to the CG-F1 group. The GBH-HFD-F1 group showed a 35% reduction in retroperitoneal and periepididymal fat ($p < 0.0001$) compared to the HFD-F1 group, and a 310% increase ($p < 0.0001$) compared to the GBH-F1 group (Table 1). No morphological differences (Figure 1) or significant morphometric changes (Table 1) were observed in the NMJs. The study of offspring exposed to a high-fat diet and born to mothers exposed to glyphosate showed a reduction in retroperitoneal and periepididymal fat weights, while no changes were found in the NMJ analyses, which may be related to the dosage, method of herbicide administration, and the muscle analyzed.

[1] L.A. Fuiman, K.O. Perez, Proceeding of the Royal Society B 282 (2015) 1-6.
[2] N.M.X. Faria et al., Ciências & Saúde Coletiva, 12 (2007) 25-38.
[3] F.I. Milagro, et al., Molecular Aspects of Medicine, 34 (2013) 782-812.
[4] Monsanto, Safety Data Sheet (SDS) – Roundup, 2008.
[5] M.J. Karnovsky, J Cell Biol. 27 (1965) 1-149.
[6] G.M. Lehrer, L. Ornstein, Biophysical and Biochemical Cytology, 6 (1959) 399-419.
[7] This research was supported by CNPq (Brazil) and Fundação Araucária (Brazil).

Table 1. Macroscopic parameters and morphometry of the neuromuscular junctions (NMJs) of the soleus muscle in 150-day-old mice from the control group (CG-F1), high-fat diet group (HFD-F1), glyphosate-based herbicide group (GBH-F1), and glyphosate-based herbicide and high-fat diet group (GBH-HFD-F1). Values are expressed as mean ± standard deviation. n = 6. Different letters indicate statistically significant differences ($p < 0.05$). [1]Kruskal-Wallis test with Dunn's post hoc test. [2]One-way analysis of variance with Tukey's multiple comparison post hoc test.

Groups	CG-F1	HFD-F1	GBH-F1	GBH-HFD-F1
Parameters				
[1]Body weight (g)	25 ± 1.16^{a}	32 ± 4.52^{ab}	23 ± 1.82^{ac}	28 ± 2.03^{a}
[1]Soleus muscle weight (mg)	9.5± 2.17	11.2 ± 1,33	8.12 ± 3,64	10.8 ± 0.98
[2]Soleus muscle length (mm)	5.7 ± 1.14	4.9 ± 0.44	5.6 ± 0.72	5.9 ± 1.03
[2]Retroperitoneal and periepididymal fat (g)	0.30 ± 0.07^{a}	1.67 ± 0.46^{b}	0.30 ± 0.10^{a}	1.08 ± 0.53^{c}
[1]Naso-anal length (cm)	9.3 ± 0.27	9.5 ± 0.32	8.9 ± 0.49	9.3 ± 0.26
[2]Lee index (g/cm³)	318 ± 10.4	331 ± 9.2	318 ± 13.3	326 ± 11.4
[2]NMJ area (µm²)	255 ± 47.5	231 ± 24.6	270 ± 35	240 ± 54.7
[2]NMJ larger diameter (µm)	16.6 ± 1.48	15.4 ± 1.61	17.3 ± 0.91	16.6 ± 2.68
[2]NMJ smaller diameter (µm)	9.07 ± 1.01	8.95 ± 0.90	9.54 ± 0.91	8.24 ± 0.91

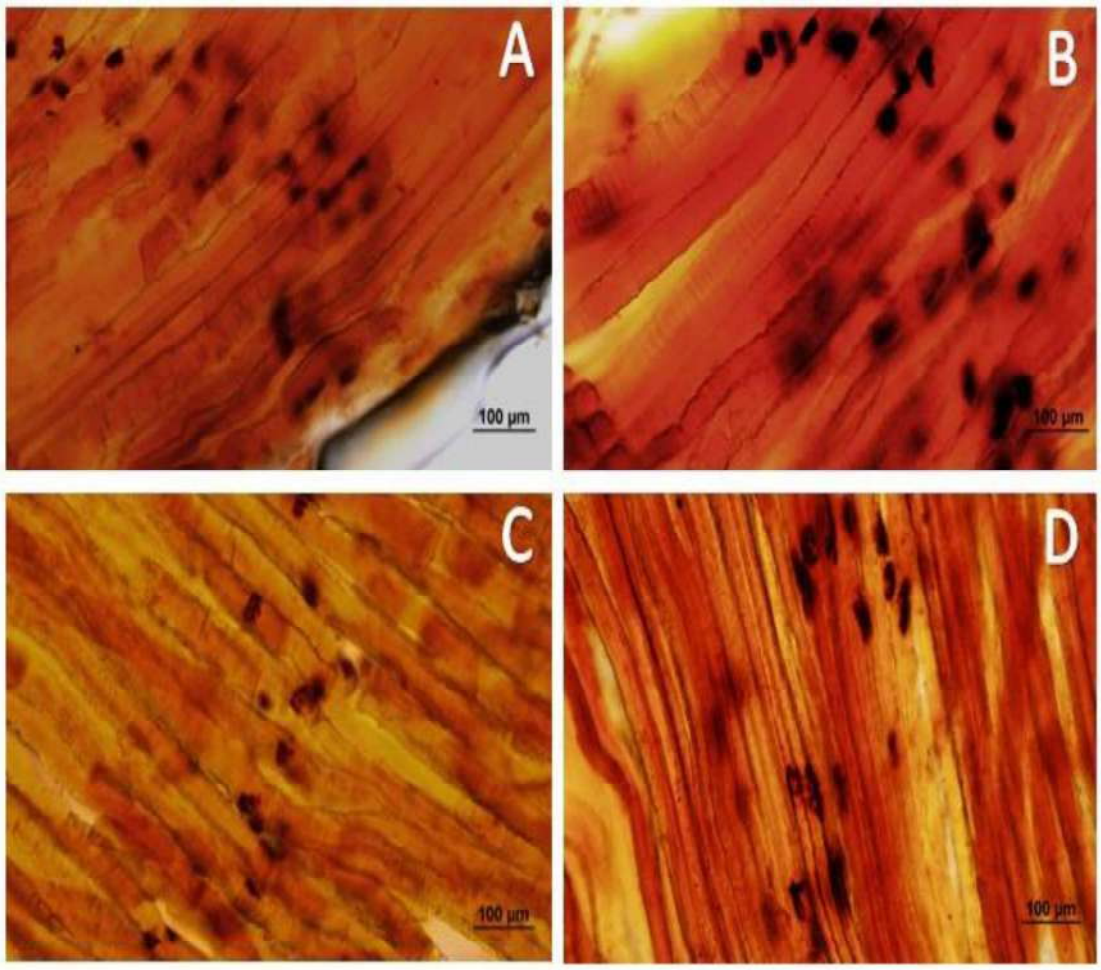

Figure 1. Photomicrographs of neuromuscular junctions in the soleus muscle of 150-day-old C57BL/6 mice. Longitudinal section. Non-specific esterase staining. A: Control group; B: High-fat diet group; C: Glyphosate-based herbicide group; D: Glyphosate-based herbicide and high-fat diet group.

Metabolic Programming By Maternal Exposure To Glyphosate: Morphometric Evaluation Of The Extensor Digitorum Longus Muscle In Mice

Gabriella Canan Kiekiss[1]*, Rafaella Cristina Lima da Silva[1], Ariadne Barbosa[1], Sandra Lucinei Balbo[1], Maria Lucia Bonfleur[1], Marcia Miranda Torrejais[1].

[1]Graduate Program in Biosciences and Health – Universidade Estadual do Oeste do Paraná, Cascavel, Paraná, Brazil.
*gabick2012@hotmail.com

Exposure to pesticides is associated with the occurrence of various diseases and can influence metabolism and tissue development in the long term [1,2]. Studies have shown variations in the uterine and neonatal environment can induce the emergence of different phenotypes. Thus, insults occurring during critical periods of development are linked to the onset of metabolic diseases in adulthood, a biological phenomenon known as Metabolic Programming [3]. This study aimed to evaluate the morphology and morphometry of muscle fibers in the extensor digitorum longus (EDL) muscle of offspring from mice exposed to glyphosate during pre- and postnatal periods, and to determine whether the effects of this exposure were exacerbated by a high-fat diet. Twenty pregnant C57BL/6 female mice were used and divided into: Control Group (CTL, n=10), which received pure water throughout pregnancy and lactation, and Glyphosate-Based Herbicide Group (GBH, n=10), which received 0.5% glyphosate herbicide [4] in the water during the same period. After weaning, male offspring were fed standard chow and water *ad libitum* for 30 days. They were then divided into four experimental groups based on maternal glyphosate exposure and the diet offered to the offspring: Control Group (CG-F1); High-Fat Diet Group (HFD-F1); Glyphosate-Based Herbicide Group (GBH-F1); and Glyphosate-Based Herbicide and High-fat Diet Group (GBH-HFD-F1). Euthanasia was performed at 150 days of age, and obesity was assessed using the Lee index. The EDL muscle was collected and fixed in metacarn for 24 hours, then transferred to 70% alcohol and subsequently subjected to Hematoxylin-Eosin staining [5] for muscle fiber analysis. HFD-F1 showed a 28% increase in body weight ($p=0.0003$) and a 456.7% increase in retroperitoneal and periepididymal fat ($p<0.0001$) compared to CG-F1. GBH-HFD-F1 showed a 35.2% reduction ($p<0.0001$) in both fat depots compared to HFD-F1 (Table 1). Morphological evaluation of the EDL muscle showed preserved fiber morphology in CG-F1, with a polygonal shape and peripheral nuclei (Fig. 1A). HFD-F1, GBH-F1, and GBH-HFD-F1 showed some amorphous fibers (Figs. 1B, 1C, and 1D). Offspring exposed to a high-fat diet and born to glyphosate-exposed mothers showed reduced retroperitoneal and periepididymal fat. Morphological evaluation revealed a greater number of amorphous fibers in the glyphosate-exposed groups, indicating degeneration of some muscle fibers.

[1] N.L. Swanson et al., Journal of Organic Systems, 9 (2014), 6-37.
[2] S. Cvitic et al., Diabetologia, 61 (2018) 2398–2411.
[3] C.G. Leandro et al., Journal of Nutrition, 22 (2009) 559–569.
[4] Monsanto, SDS - Safety Data Sheet: Roundup, 2008.
[5] L.C. Junqueira, L.M.M. Junqueira, Basic Techniques in Cytology and Histology, University of São Paulo, São Paulo, 1983.
[6] This research was supported by Fundação Araucária and the State University of Western Paraná (Unioeste), Brazil.

Table 1. Macroscopic parameters and morphometric evaluation of muscle fibers in 150-day-old C57BL/6 mice from the from the following groups: control group (CG-F1), high-fat diet group (HFD-F1), glyphosate-based herbicide group (GBH-F1), and glyphosate-based herbicide and high-fat diet group (GBH-HFD-F1). Values are expressed as mean ± standard deviation. n = 6. Different letters indicate statistically significant differences ($p < 0.05$). [1]Kruskal–Wallis test followed by Dunn's post hoc test. [2]One-way analysis of variance (ANOVA) followed by Tukey's multiple comparison post hoc test.

Groups Parameters	CG-F1	HFD-F1	GBH-F1	GBH-HFD-F1
[1]Body weight (g)	25 ± 1.16[a]	32 ± 4.52[b]	23 ± 1.82[ab]	28 ± 2.03[ab]
[1]Muscle weight (mg)	9.8 ± 0.001	10.8 ± 0.002	9.3 ± 0.002	9.8 ± 0.002
[1]Muscle length (mm)	7.2 ± 1.10	7.02 ± 0.72	7.6 ± 0.91	6.9 ± 1.05
[1]Retroperitoneal and periepididymal fat (g)	0.301 ± 0.07[a]	1.67 ± 0.46[b]	0.298 ± 0.10[a]	1.08 ± 0.53[c]
[1]Naso-anal length (cm)	9.3 ± 0.27	9.5 ± 0.32	8.9 ± 0.49	9.3 ± 0.26
[1]Lee index (g/cm³)	318 ± 10.4	331 ± 9.2	318 ± 13.3	326 ± 11.4
[1]Muscle fiber area (µm²)	929 ± 93	969 ±13	759 ± 90	859 ± 99
[1]Major fiber diameter (µm)	40 ± 0.9	40 ± 4.2	34.4 ± 1.9	38 ± 2.3
[1]Minor fiber diameter (µm)	28 ± 1.0	27 ± 2.3	24 ± 1.0	26 ± 1.6
[1]Number of muscle fibers	313 ± 49	310 ± 73	262 ± 29	310 ± 60
[1]Number of peripheral nuclei	333 ± 51	328 ± 71	278 ± 27	331 ± 53
[2]Number of central nuclei	1.5 ± 0.83	1.83 ± 1.5	1.7 ± 0.8	1.5 ± 1.5
[2]Nucleus-to-fiber ratio	1.1 ± 0.10	1.1 ± 0.04	1.2 ± 0.21	1.2 ± 0.18

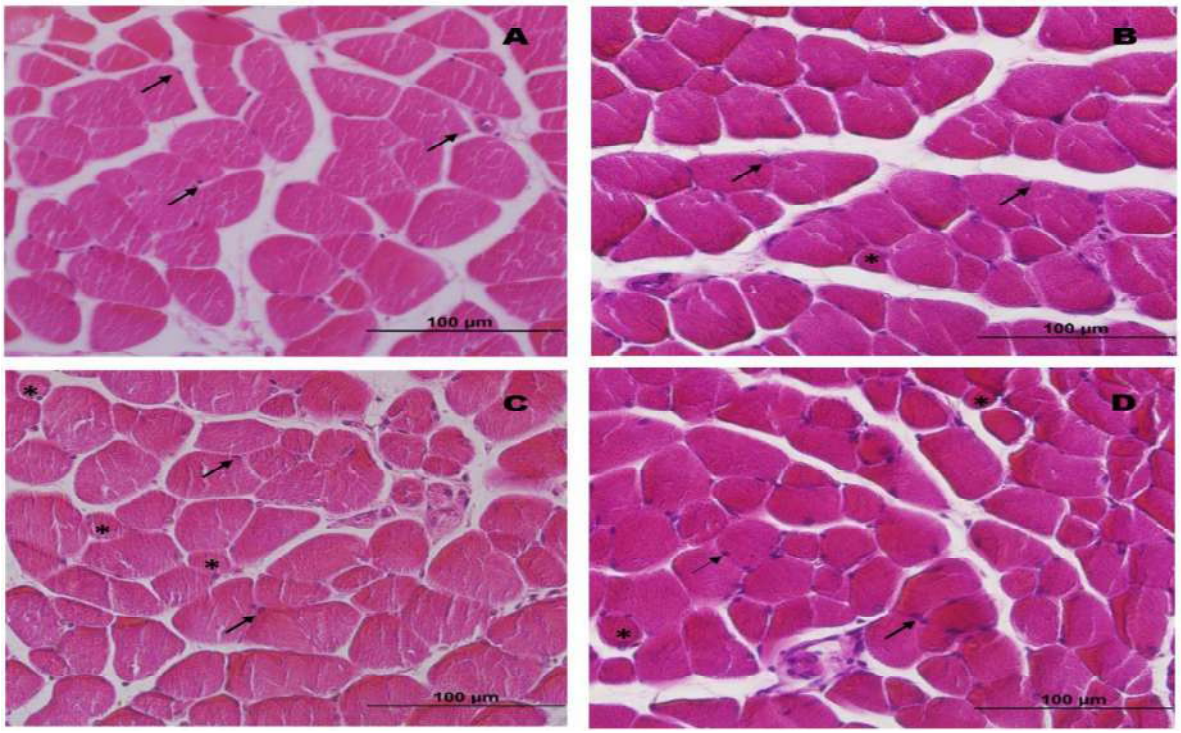

Figure 1. Photomicrographs of the extensor digitorum longus muscle of 150-day-old C57BL/6 mice. Transverse section. Hematoxylin–Eosin staining. Note the muscle fibers with peripheral nuclei (black arrow) and amorphous muscle fiber (asterisk); **A:** Control group; **B:** High-fat diet group; **C:** Glyphosate-based herbicide group; **D:** Glyphosate-based herbicide and high-fat diet group.

Morphological and behavioral adaptations for milk production in amphibian caecilians

Pedro L. Mailho-Fontana[1], Beatriz Mauricio[1], Marta M. Antoniazzi[1], Guilherme R. Coelho[2], Daniel C Pimenta[2], Lígia P. Fernandes[3], Alexander Kupfer[4], Edmund D. Brodie Jr[5], Carlos Jared[1]*.

[1]Laboratório de Biologia Estrutural, Instituto Butantan, São Paulo, Brasil, [2]Laboratório de Bioquímica e Biofísica, Instituto Butantan, São Paulo, Brasil,[3]Laboratório de Desenvolvimento de Alimentos Funcionais, Universidade de São Paulo, [4]Department of Zoology, State Museum of Natural History, Stuttgart, Germany São Paulo, [5]Department of Biology, Utah State University, Logan, USA.*carlos.jared@butantan.org.br

Among vertebrates, the yolk is commonly the only form of nutritional investment offered by the female to the embryo [1]. Some species, however, have developed parental care behaviors associated with parental food provisioning essential for offspring survival, such as milk in mammals [2]. Although lactation is a mammalian attribute, a few non-mammal species have been documented as producing nutrients directed to offspring feeding and functionally similar to mammalian milk [2]. Among amphibians, peculiar parental food provisioning modes have been previously documented in caecilians [3]. These amphibians, members of the Order Gymnophiona, are elongate, limbless, snake- or worm-like living in mostly tropical regions. In live-bearing caecilians, the babies are nourished within the oviducts through a nutritive secretion and fragments of the maternal oviduct epithelium [4]. In oviparous species, post-hatching skin feeding provides the hatchlings periodically lipid-enriched maternal skin [5,6]. While studying the reproductive biology of the South American oviparous caecilian *Siphonops annulatus*, which included a description of skin feeding, we observed that the offspring also consumed a secretion exuded from the maternal vent [6]. This observation led us to hypothesize that this secretion may have an important nutritional function. Here we describe the dynamics of production and provisioning of milk in *S. annulatus*. Females exhibiting post-hatching parental care (N=16) and their respective hatchlings were collected and monitored throughout filming in captivity. To characterize the origin of the milk, we compared the histology of the cloaca, bladder, final portion of the intestine and the oviducts of females, whether performing parental care or not (n=4/group). Milk samples (n=15 extractions) were analyzed by gas chromatography-mass spectrometry (GC-MS) to identify lipids and their relative abundances. During recording (n=242 hours), the mothers remained in a characteristic position, curled up and with the hatchlings distributed over their backs (Fig. 1A). Hatchlings exhibited a marked interest in the distal region of the body and the vent, often touching these areas with their snouts or nibbling them (Fig. 1B), while simultaneously emitting high-pitched sounds. Such behaviors appeared to stimulate the mother to expose the vent (Fig. 1A), from which transparent and highly viscous milk was released (Fig. 1C) and avidly consumed by hatchlings (Fig. 1D). The cloaca, bladder and final portion of the intestine did not show significant morphological and histochemical differences. Conversely, the oviducts of females exhibiting parental care presented hypertrophied epithelial glands (Figs. 2A and 2B) and a significant volume of fluid and cell debris rich in neutral glycoconjugates (Fig. 2C) and lipids (Fig. 2D). GC-MS method revealed that palmitic (C16:0) and stearic (C18:0) acids represented 49.41% and 49.20% of the total lipids, respectively. We demonstrate that the secretion from the oviducts released through the vent is an important food source provided many times a day according to hatchlings' signaling. In *S. annulatus*, beyond the proteins and lipids obtained from skin feeding, hatchlings are also supplied with carbohydrates and lipids from the oviductal milk, turning the maternal food provisioning into a diversified and balanced source of nutrients for the offspring. These nutrients are also present in the oviducts of live-bearing caecilians [4]. Modification of reproductive modes is among the most complex of the great transitions

that vertebrates have achieved in their biology, particularly in morphology [7]. The discovery of oviparous caecilian, *S. annulatus*, providing oviductal milk to hatchlings is a phenomenon that exemplifies how evolution of reproductive modes in vertebrates is more complex than currently recognized.

[1] B.M, Byrne, et al. The evolution of egg yolk proteins. Prog Biophys Mol Biol 53, 33–69 (1989).
[2] Balshine, S. Patterns of parental care in vertebrates. in The Evolution of Parental Care 62–80 (Oxford University Press, 2012).
[3] A. Kupfer, et al. The evolution of parental investment in caecilian amphibians: a comparative approach. Biological Journal of the Linnean Society 119, 4–14 (2016).
[4] M.H. Wake. Evolution of oviductal gestation in amphibians. Journal of Experimental Zoology 266, 394–413 (1993).
[5] A. Kupfer, et al. Parental investment by skin feeding in a caecilian amphibian. Nature 440, 926–929 (2006).
[6] M. Wilkinson et al. One hundred million years of skin feeding? Extended parental care in a Neotropical caecilian (Amphibia: Gymnophiona). Biol Lett 4, 358–361 (2008).
[7] M.H. Wake. "How do homoplasies arise? Origin and maintenance of reproductive modes in amphibians" in Great Transformations in Vertebrate Evolution, k Dial, N. Shubin, B. Brainerd, Eds. (University of California Press, Berkeley, 2015), pp. 373–392.
[8] This research was supported by FAPESP (Brazil) #2017/10488-1 and #2018/03265-9.

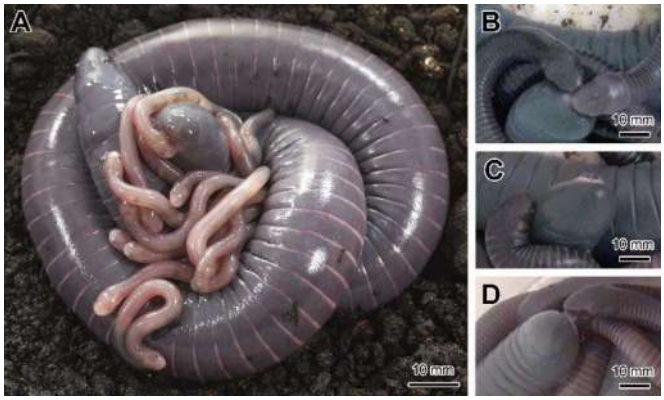

Figure 1. Parental care of *Siphonops annulatus*. (A) Mother and hatchlings. (B) Interest of hatchlings in the maternal vent. (C) Milk releasing. (D) Milk consumption.

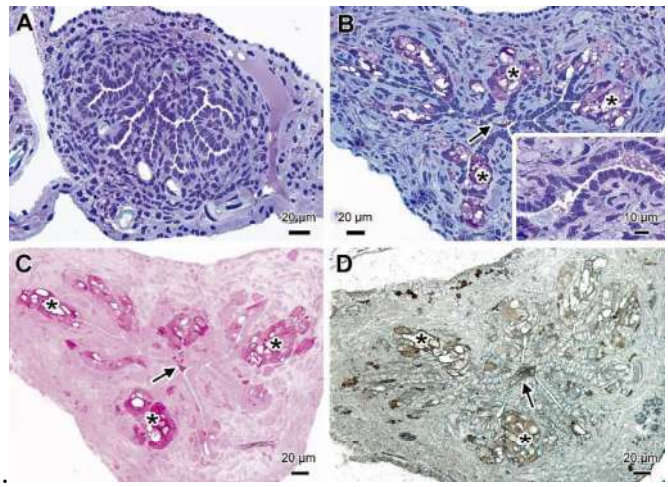

Figure 2. Morphological structure and histochemical composition of oviducts in female *S. annulatus* performing parental care or not. (A) Females out of parental care. (B) Females out of parental care. Hypertrophied oviductal glands (*) and oviductal lumen (arrow). (C) Oviductal glands and milk are rich in neutral mucopolysaccharides. (PAS staining). (D) Lipids were also present within the glands and in the luminal milk. Stains: Toluidine-Fucsin (A and B), PAS (C) and Sudan Black (D).

Morphometric Analysis of Pulmonary Alveoli in Wistar Rats Subjected to Early Weaning and Treated with Melatonin

Sara Vitoria de Oliveira Costa[1]*, Renan Gabriel da Silva Ferreira[1], Jadyel Sherdelle Guedes do Nascimento[1], Isaque Bertoldo Santos da Silva[1], Alison Jose da Silva[1], Ana Vitoria Ferreira dos Santos[1], Elba Veronica Matoso Maciel de Carvalho[2], José Anderson da Silva Gomes[1], Luiza Rebeca Soares de Lima[1], Bruno Mendes Tenorio[1], Fernanda das Chagas Angelo Mendes Tenorio[1].

[1]Department of Histology of Embryology, Federal University of Pernambuco, [2]Department of Biochemistry, Federal University of Pernambuco
*sara.vcosta@ufpe.br

Breastfeeding is a fundamental practice in the lives of mammals, ensuring both immunological and nutritional support in accordance with the needs of their organisms. Natural weaning is the process in which complementary foods are progressively introduced to replace maternal milk, directly influencing the physiological development of the animal [1]. However, due to various factors, weaning may occur prematurely, negatively affecting systemic functioning. Studies have shown that breastfeeding is a preventive factor for pulmonary infections, suggesting a high vulnerability of the respiratory system caused by the early interruption of this activity [2]. Among the treatments aimed at possibly reversing the aforementioned effects, melatonin stands out. It is a hormone produced by the body with chronobiological, antioxidant, immunomodulatory, and anti-inflammatory functions. In its exogenous form, it also has the ability to induce cell proliferation and tissue repair [3]. Therefore, this study aimed to morphometrically analyze the pulmonary alveoli of Wistar rats subjected to early weaning and treated with melatonin. Albino rats of the Wistar lineage, obtained from the animal facility of the Federal University of Pernambuco, were used in this study. The animals were kept in a controlled environment, with an inverted light-dark cycle and free access to water and standard food. After a 16-day adaptation period, mating was conducted using a ratio of two females per male (2:1). The birth of the pups was recorded as day zero of the experiment. Twenty-four pups were selected and divided into three experimental groups (n=8): control group, early weaning group (EW), and early weaning group with melatonin treatment (EW+Mel), with the substance administered at a dose of 200µg per 100g of body weight. The EW and EW+Mel groups underwent abrupt weaning on the 16th day after birth, while the control group maintained natural weaning. Thirty-five days after weaning, the animals were anesthetized for lung collection, which were immediately fixed in 10% formaldehyde solution. Subsequently, the lung tissues underwent progressive dehydration, clearing in xylene, and embedding in histological paraffin after impregnation with liquid paraffin. The resulting blocks were then sectioned with a microtome, set to 3-micrometer (µm) thick slices. The slides were photographed using a Nikon 50E Trinocular Biological Microscope with 10x and 40x objectives. The obtained images were analyzed using ImageJ software for the following parameters: area, perimeter, width, height, angle, circularity, aspect ratio (AR), roundness, and solidity. The data were then subjected to the Kruskal–Wallis statistical test followed by Dunn's post-test, with a significance level of $p < 0.05$. The results showed that in the EW+Mel group, for the parameters of area, perimeter, width, height, and circularity, melatonin was able to reverse the damage caused by early weaning in the EW group, bringing them closer to the values of the control group. This alveolar remodeling is explained by melatonin's ability to promote tissue repair, reduce oxidative stress and inflammation, factors that together contribute to the observed outcome [3]. No significant differences were found between groups for the parameters angle, AR, and roundness. These parameters reflect more the geometric shape of the alveolus than its absolute size; thus, the absence of difference suggests that early weaning and/or melatonin did not substantially alter the shape of the

alveoli, but rather their size and structural integrity [4]. Regarding solidity, the EW and EW+Mel groups had lower values compared to the control. This indicates that even after melatonin treatment, certain aspects of alveolar architecture were not fully restored, suggesting a limiting effect of melatonin or the need for a longer treatment duration for full recovery. These findings demonstrate that melatonin promotes partial repair of alveolar damage caused by early weaning, especially in the parameters of area, perimeter, width, height, and circularity of the alveoli, although complete restoration of tissue architecture has not yet been achieved. However, further investigations are needed to elucidate the underlying mechanisms and optimize therapeutic strategies for post-weaning pulmonary recovery.

[1] C. G. Victora et al., *Lancet*. 387 (2016) 479.
[2] K. M. Silvers et al., *Maternal and Child Nutrition*, 5 (2009) 244.
[3] R. Hardeland, *Journal of Pineal Research*. 65 (2018) e12525.
[4] C. C. W. Hsia et al., *American Journal of Respiratory and Critical Care Medicine*. 181 (2010) 401.

Table 1. Morphometric parameters of pulmonary alveoli in Wistar rats subjected to early weaning (EW) and treated with melatonin (EW+Mel), compared to the control group. Values are expressed as mean ± standard deviation. *Significant difference compared to the control group ($p < 0.05$) and EW+Mel. # Difference between the control group and EW. Kruskal–Wallis test followed by Dunn's post-test ($p < 0.05$).

Parameters	Control	EW	EW+Mel	p
Area	2.17±1.22	1.87±1.82*	3.86±2.85	0.02
Perimeter	246.41±78.68	215.76±142.87*	262.23±211.76*	0.05
Width	62.04±20.60	57.01±31.44*	67.18±41.94*	0.03
Height	61.43±18.41	53.75±23.87*	62.54±49.73	0.04
Angle	81.80±50.71	77.20±59.31	82.34±45.17	0.81
Circularity	0.57±0.15	0.37±0.15*	0.726±0.18	0.01
AR	1.41±0.27	1.59±0.32	1.61±0.42	0.46
Round	0.73±0.12	0.65±0.12	0.66±0.16	0.72
Solidity	0.91±0.05*#	0.84±0.08#	0.72±0.11*	0.01

Reference: By the author.

Morphometric Analysis Of The Neonate Rats' Myocardium Born To Mothers Subjected To Protein Malnutrition Treated With Cannabidiol Nanoemulsion

Isaque Bertoldo Santos da Silva[1]*, Suellen Rozy da Silva Medeiros[1], Maria Manuela dos Santos Rodrigues[1], José Abel Pessôa Neto[1], Renan Gabriel da Silva Ferreira[1], Jadyel Sherdelle Guedes do Nascimento[1], Elba Verônica Maciel Matoso de Carvalho[2], Sara Vitoria de Oliveira Costa [1], Bruno Mendes Tenorio[1], Fernanda das Chagas Angelo Mendes Tenorio[1]

[1] Department of Histology of Embryology, Federal University of Pernambuco, [2] Department of Biochemistry, Federal University of Pernambuco
*isaque.bertoldo@ufpe.br

The gestational period requires significant physiological adaptations, with maternal nutrition playing a crucial role in proper fetal development [1]. Protein restriction during pregnancy impairs the formation of vital organs such as the heart, leading to structural changes in myocardium and potential cardiac dysfunction [2]. Cannabidiol (CBD) has shown cardioprotective properties by regulating inflammation and oxidative stress, suggesting therapeutic potential against malnutrition-induced damage [3]. This study aimed to evaluate the effects of CBD on the myocardium of neonates subjected to protein malnutrition. A total of ten (10) neonate Wistar rats (Rattus norvegicus) of each group were used in the study (Ethics Committee Protocol: n°0055/2024), allocated into three groups: Group I – offspring from mothers with normal protein intake (control); Group II – offspring from mothers subjected to a PM diet (AIN-93G with 6% protein) for 21 days; Group III – offspring from PM-diet mothers concurrently treated with a CBD nanoemulsion (10 mg/kg/day for 20 days, administered in the morning). After euthanasia, the animal and the hearts were fixed in buffered formalin, paraffin embedded, sectioned at 3 µm thickness, and stained with hematoxylin-eosin (HE). Images were captured under an optical microscope (400× magnification), with 15 fields per animal analyzed, totaling 120 images per experimental group. Image processing was conducted in ImageJ (NIH, USA). Assessed parameters included nuclear area, nuclear perimeter, cardiomyocyte diameter, and myocardial thickness. Morphometric analysis was performed through area proportion using systematic point counting with a 180-point grid, and the organosomatic index was calculated as the ratio between heart and body weight. Histology revealed preserved cardiac structure in all groups, but the malnutrition group showed mononuclear infiltration, cardiomyocyte vacuolization, and loss of striations. The PM+CBD group showed expanded fibers and greater vacuolization, with marked perinuclear clearing (Figure 01). Morphometric data indicated significant reductions in cytoplasmic area, nuclear diameter, cardiomyocyte size and myocardial thickness in the malnutrition group (Figure 02), showing the effects caused by the insufficient amount of proteins. Although CBD-treated animals exhibited extensive vacuolization, their cardiomyocyte dimensions approached those of the control group. The Organosomatic index did not show any significant differences statistically (Table 01). Although, the area proportion (Table 02) showed on the PM group a reduction in the cytoplasmic area and an increase in the quantity of nucleus, suggesting that the cells are over stress, and compromising its functions agreeing that there's a loss of striations on the fibers (Figure 01 - D). These findings suggest that protein malnutrition impairs cardiac development, while cannabidiol may exert partial restorative effects, highlighting the need for further research on its use during gestational nutritional deficits.

[1] A.L.M. Rocha, et al. Research, Society and Development, v. 12. (2023).

[2] H.D. Confortim et al. Muscle & Nerve, 55. (2017)
[3] M. Rajesh, et al., J Am Coll Cardiol, 56. (2010).

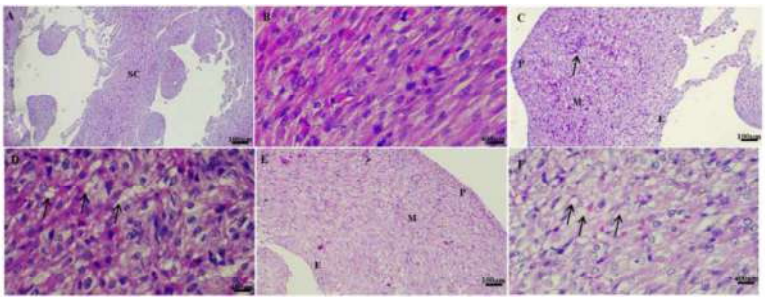

Figure 01: Photomicrograph of the heart from offspring of experimental animals. A, B – Control group showing the cardiac septum (CS) and transverse striations of the myocardium; C – Diet group showing well-defined layers of endocardium (E), myocardium (M), and pericardium (P), as well as discrete interstitial mononuclear infiltrate (arrow); D – Diet group showing cardiomyocyte vacuolization (arrow) and loss of transverse striations; E, F – PEM+CBD group with well-defined layers of endocardium (E), myocardium (M), and pericardium (P), cardiac fibers showing cytoplasmic expansion and vacuolization (arrow), and loss of transverse striations.

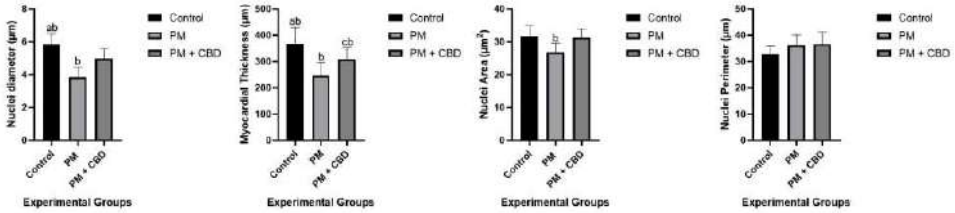

Figure 02. Morphometric parameters of the myocardial neonate's hearts from the experimental groups.

Table 01. Organosomatic Index of neonate hearts from the experimental groups.

Parameters	Control	PM	PM + CBD	p
Organosomatic Index	0.72±0.03	0.76±0.03	0.72±0.02	0.17

Reference: By the author. *Means followed by different letters in the column differ significantly from each other. Nonparametric Kruskal–Wallis test followed by Dunn's post-hoc test ($p \leq 0.05$).

Table 02. Area proportion of neonate hearts from the experimental groups.

Parameters	Control	PM	PM + CBD	p
Cytoplasm	134.1±8.76a	124±11.32b	135.4±6.00a	0.003*
Erythrocytes	3.3±2.94a	3.9±1.37a	5.1±4.38b	0,052*
Nuclei	40±9.29	42.3±10.07	35.6±6.83	0,222

Reference: By the author. *Means followed by different letters in the column differ significantly from each other. Nonparametric Kruskal–Wallis test followed by Dunn's post-hoc test ($p \leq 0.05$).

Morphometric Analysis of the Uterus of Pregnant Rats Subjected to Protein Malnutrition and Treated with Cannabidiol (CBD)

Suellen Rozy da Silva Medeiros[1]*, Maria Manuela dos Santos Rodrigues[1], Carlos Eduardo da Silva[1], Maria Gabriela da Silva Mello[1], Weslleyanne Millena da Silva Costa[1], Maria Eduarda Carneiro de Lima[1], Ana Carolina Ribeiro Saraiva da Costa[1], Paloma Vitória Melo da Silva[1], Raissa Gomes de França[1], Fernanda das Chagas Angelo Mendes[1], Tenório Bruno Mendes Tenório[1]

[1]Federal University of Pernambuco, Department of Histology and Embryology
*suellen.medeiros@ufpe.br

Protein malnutrition (PM), by impairing the synthesis of antioxidant enzymes, reduces the body's ability to neutralize free radicals that damage essential cellular components. Consequently, this nutritional deficiency can profoundly alter uterine morphology, affecting endometrial vascularization, extracellular matrix integrity, and glandular organization. During pregnancy, such structural changes compromise uterine receptivity and embryonic development, particularly because adequate uterine vascularization is essential for the supply of oxygen and nutrients to the fetus. A reduction in this supply jeopardizes the maintenance of pregnancy. Currently, cannabidiol (CBD) has shown promising results due to its anti-inflammatory, antioxidant, and endocannabinoid-modulating effects, potentially protecting uterine tissue against the changes induced by PM and promoting gestational homeostasis. Therefore, the objective of this study was to use morphometric methods to detect alterations in the endometrium and myometrium of rats subjected to protein-energy malnutrition and treated with CBD. A total of 24 pregnant albino Wistar rats (n = 8 per group) were used and divided into three groups: Group I – pregnant rats for 14 days (control group, normoprotein diet); Group II – pregnant rats for 14 days under protein restriction; Group III – pregnant rats for 14 days under protein restriction and treated with CBD nanoemulsion (ethics committee approval: 0053/2024). Pregnancy was induced through natural mating and confirmed by the presence of sperm in the vaginal smear (considered the first day of gestation). Rats in groups II and III were fed a modified AIN-93G diet containing only 6% protein, starting from day one of gestation to induce protein-energy malnutrition. Food and water were provided ad libitum throughout the experimental period. Rats in group III received a CBD nanoemulsion at a dose of 10 mg/kg/day, administered from the 1st to the 14th day of gestation. Uterine tissues were fixed in buffered formalin, embedded in paraffin, sectioned at 3 μm thickness, stained with Hematoxylin-Eosin (HE), and photographed under an optical microscope (10X and 40X magnification). Fifteen images per animal were analyzed, totaling 120 images per experimental group, using ImageJ software (NIH, USA). Morphometric parameters and the uterine volumetric proportion were assessed, focusing on connective tissue cells, extracellular matrix (ECM) of connective tissue, epithelial and glandular lumen, vessel wall, and vascular lumen. Data were analyzed using the Kruskal-Wallis test followed by Dunn's post-hoc test ($p < 0.05$). The morphometric analysis showed that PM significantly reduced the thickness of the endometrium, endometrial epithelium, and myometrium compared to the control group. However, treatment with CBD in the diet group significantly increased the thickness of the epithelium and endometrium, suggesting a restorative effect of CBD on endometrial tissue. In contrast, myometrial thickness did not improve with treatment and remained similar to the diet group. Volumetric analysis revealed that PM did not significantly alter the number of connective tissue cells. However, ECM was reduced in the diet group and significantly increased with CBD treatment. Glandular epithelium was reduced by the diet, with partial recovery in the treated group. Glandular lumen increased in the diet group, possibly due to epithelial atrophy and stromal disorganization, and was normalized with CBD treatment. In uterine blood vessels, the diet reduced both wall and lumen thickness,

alterations that were also reversed with CBD. In conclusion, CBD demonstrated a positive modulatory effect on the morphological changes induced by protein malnutrition.

[1] C.C. Vega et al., Resveratrol partially prevents oxidative stress and metabolic dysfunction in pregnant rats fed a low protein diet and their offspring. 594 (Suplet 5) (2016) 1483-99.
[2] C. Zhang et al., Oxidative stress on vessels at the maternal-fetal interface for female reproductive system disorders. 10 (Suplet 14) (2023) 1118121.
[3] S. Atalay et al., Antioxidative and Anti-Inflammatory Properties of Cannabidiol. Antioxidants. 9 (Suplet 1) (2019) 21.

Table 1. Means ± standard deviation of the uterine morphometric parameters in experimental animals: endometrial epithelium thickness, endometrium thickness, and myometrium thickness. Groups: Control, Diet, and Diet+CBD.

Experimental Groups/Parameters	Control	Diet	Diet+CBD	p
Endometrial epithelium thickness	**144.95±22.7a**	**111.40±21.85b**	**175.35±31.08c**	**0.001***
Endometrium thickness	**465.4±161.2a**	**327.05±148.4b**	**518.3±214.8c**	**0.003***
Myometrium thickness	**326.95±79.1a**	**257.20±40.9b**	**253.25±32.1b**	**0.001***

*Means followed by the same letter in the rows do not differ significantly from each other according to the Kruskal-Wallis test followed by Dunn's post-hoc test ($p > 0.05$).

Table 2. Means ± standard deviation of the volumetric proportion of the uterus in experimental animals: connective tissue cells, connective tissue extracellular matrix (ECM), glandular epithelium, glandular lumen, blood vessel wall, and blood vessel lumen. Groups: Control, Diet, and Diet+CBD.

Experimental Groups/Parameters	Control	Diet	Diet+CBD	p
Connective tissue cells	**70.5±9.00**	**69.6±12.32**	**69.5±5.31**	**0.5259**
Extracellular matrix of connective tissue	**61.3±13.a**	**51.5±19.3b**	**83.7±17.2a**	**0.002***
Glandular epithelium	**37.5±14.4a**	**14.6±11.1b**	**30.0±9.5a**	**0.002***
Glandular lumen	**3.0±2.5a**	**14.3±10.4b**	**5.66±7.0a**	**0.012***
Blood vessel wall	**23.6±12.9a**	**9.2±5.7b**	**22.5±6.7a**	**0.021***
Blood vessel lumen	**16.7±9.2a**	**7.8±3.3b**	**18.2±4.2a**	**0.026***

*Means followed by the same letter in the rows do not differ significantly from each other according to the Kruskal-Wallis test followed by Dunn's post-hoc test ($p > 0.05$).

Morphometric analysis of the uterus of rats subjected to voluntary physical activity and protein malnutrition.

Ana Carolina Ribeiro Saraiva da Costa*[1], Maria Manuela dos Santos Rodrigues[1], Renan Gabriel da Silva Ferreira[1], Jadyel Sherdelle Guedes do Nascimento[1], Isaque Bertoldo Santos da Silva[1], Alison Jose da Silva[1], Ana Vitoria Ferreira dos Santos[1], Ryan Cristian da Silva[2], Bruno Mendes Tenório[1], Fernanda das Chagas Angelo Mendes Tenório [1]

[1]Department of Histology and Embryology, Federal University of Pernambuco, Recife, Pernambuco, Brazil
[2]Department of Biochemistry, Federal University of Pernambuco, Recife, Pernambuco, Brazil 11;

*Carolina.rscosta@ufpe.br

Nutrition and physical activity are determining factors in the development and functioning of organic systems, especially the female reproductive system. Protein malnutrition, prevalent in various social contexts, compromises uterine morphometry and can alter histological parameters essential for reproduction [2,3]. Conversely, physical activity, depending on its intensity and duration, influences uterine morphology, potentially generating adaptive or deleterious effects [1,4,5]. Previous studies demonstrate that maternal physical activity can mitigate some of the negative effects of malnutrition on offspring, but the combined effects of protein malnutrition and physical activity on the adult uterus remain little explored [1,4,5]. Therefore, this study aims to analyze, through morphometric parameters, uterine changes in rats subjected to voluntary physical activity and protein malnutrition, aiming to fill a gap in the current literature. Twenty Wistar rats (220–260 g, 85–95 days old) were kept under controlled conditions, with free access to water and diet, in accordance with COBEA standards and with ethical approval (CEUA-UFPE no. 005/2021). The rats underwent voluntary physical activity in cages with a cycle ergometer monitored by sensors, which recorded distance, time, and caloric expenditure. After 30 days of adaptation to the AIN-93M diet, they were classified as Low Active, Active, or Very Active, according to performance. The groups were mated and fed a normal-protein or low-protein (8% protein) diet during pregnancy and lactation. A control group, without physical activity, was included. The uteri were histologically processed, cut at 5 µm, and stained with Hematoxylin & Eosin. The slides were analyzed using optical microscopy with videomicroscopy, and morphometry was performed using ImageJ software, evaluating tissue thickness and collagen quantification in the uterine layers. The results revealed significant differences between the experimental groups in uterine morphometric parameters. An increase in endometrial epithelial thickness was observed in the Active group, while myometrial thickness decreased in this group and in the very active and slightly active groups compared to the Control group. Endometrial and perimetrium thickness were significantly greater in the Active, very active, and slightly active groups. The amount of collagen in the uterus was higher in the Active, very active, and slightly active groups compared to the Control group. However, a reduction in collagen concentration was observed in the endometrium, myometrium, and perimetrium of these groups compared to the Control group. These data suggest that physical activity, at different intensities, significantly impacts uterine morphometry and collagen metabolism in rats subjected to protein malnutrition.

[1] L.D.S. Andrade, Efeitos da atividade física voluntária materna sobre alterações cardiorrespiratórias da prole sob desnutrição proteica perinatal, Dissertação de Mestrado,

Universidade Federal de Pernambuco, Recife, 2016. Disponível em: https://repositorio.ufpe.br/handle/123456789/18186.
[2] T.F. Costa, et al., "Protein restriction during puberty alters nutritional parameters and affects ovarian and uterine histomorphometry in adulthood in rats", J. Dev. Orig. Health Dis. 12(5) (2021) 678–687. https://www.ncbi.nlm.nih.gov/pmc/articles/PMC7981593/.
[3] M.S. Lima, et al., "Aerobic exercise increases the damage to the femoral properties of growing rats with protein-based malnutrition", Braz. Arch. Biol. Technol. 66 (2023).
[4] J.P.F. de Moura, Efeito da atividade física e dieta hipoproteica sobre expressão gênica trófica fetal, Dissertação de Mestrado, Universidade Federal de Pernambuco, Recife, 2019. Disponível em: https://repositorio.ufpe.br/handle/123456789/33723.
[5] V.O. Nogueira, Efeitos da desnutrição proteica e atividade física materna sobre função simpática e ventilação em ratos, Dissertação de Mestrado, Universidade Federal de Pernambuco, Recife, 2019. Disponível em: https://repositorio.ufpe.br/handle/123456789/339.

Table 1. Means and standard deviations of uterine morphometric parameters in rats subjected to protein malnutrition and different levels of physical activity: Control, Active, Very Active, and Low Active. The parameters analyzed included epithelial thickness, myometrium, endometrium, perimetrium, and collagen quantification in the uterus and endometrium. Values with an asterisk (*) indicate a statistically significant difference in relation to the Control group ($p \leq 0.001$).

Groups Experimental/Parameters	Control	Active	Very Active	Low activity	p
Endometrial Epithelial Thickness	14.33±1.7a	20.50±3.2b	15.50±1.5a	16.60±4.1a	0.001*
Myometrial Thickness	251.8±32.6260a	137.3±25.7b	208.2±7.4c	151.0±26.1b	0.001*
Endometrial Thickness	168.90±45,32a	238.10±36.12 b	400.70±28.74c	321.10±26.68d	0.001*
Perimeter thickness	175.8±52.8a	313±94.5b	275.2±98.4b	268.2±59.6b	0.001*
Uterus collagen	126.5±4.8a	176.3±8.7b	203.8±11.5b	202.0±3.7b	0.001*
Endometrial collagen	180.9±6.4a	95.3±9.5b	125.1±13.6b	130.1±2.68b	0.001*
Myometrial collagen	133.8± 4.56a	78.4±6.31b	103.9±10.25b	109.1±14.08b	0.001*
Perimetrium collagen	138.7± 4.24a	83.2±11.83b	93.5±14.79b	111.1±15.86b	0.001*

*Means followed by the same letter in the rows do not differ significantly from each other using the Kruskal-Wallis test followed by Dunn's post-hoc test ($p>0.05$).

Morphometric And Fractal Evaluation Of The Offspring Lungs Of Pregnant Rats Subjected To Protein Malnutrition And Supplemented With Cannabidiol Nanoemulsion

Raissa Gomes de França [1]*, Paloma Vitória Melo da Silva[1], Maria Gabriela da Silva Mello[1], Weslleyanne Millena da Silva Costa[1], Maria Eduarda Carneiro de Lima[1], Ana Carolina Ribeiro Saraiva da Costa[1], Suellen Rozy da Silva Medeiros[1], Maria Manuela dos Santos Rodrigues[1], Ryan Cristian da Silva[2], Bruno Mendes Tenorio[1], Fernanda das Chagas Angelo Mendes Tenorio[1].

[1]Federal University of Pernambuco, Biosciences Center, Department of Histology and Embryology, Recife, Pernambuco, Brazil, [2]Federal University of Pernambuco, Biosciences Center, Department of Biochemistry, Recife, Pernambuco, Brazil
*rg0900665@gmail.com

A maternal low-protein diet during pregnancy has been shown to induce systemic inflammation, potentially disrupting fetal development by altering the morphology of key organs, including the lungs of the offspring [1,2]. Cannabidiol (CBD), a non-psychoactive compound derived from *Cannabis sativa*, has demonstrated anti-inflammatory properties in various experimental models. In studies of acute lung inflammation induced by lipopolysaccharide (LPS), intraperitoneal administration of CBD at doses of 20 and 80 mg/kg significantly reduced leukocyte migration and the production of pro-inflammatory cytokines, without affecting general behavior in rats [3]. These findings suggest that CBD may represent a promising therapeutic approach to mitigate lung dysfunction associated with maternal protein restriction during gestation. The aim of this study was to perform a morphometric analysis of the lungs of neonatal rats born to mothers subjected to protein malnutrition during pregnancy, with or without supplementation with cannabidiol (CBD) nanoemulsion. Fifteen pregnant Wistar rats were randomly allocated into three groups: Control (no treatment), Low-Protein Diet (LPD), and Low-Protein Diet supplemented with cannabidiol (LPD+CBD; 10 mg/kg). After confirmation of pregnancy via vaginal smear, the animals received the designated dietary treatments for 21 days. On gestational day 21, dams were anesthetized with an intraperitoneal injection of ketamine and xylazine (0.8:0.6) for neonatal lung collection. The lungs were weighed and fixed in 10% buffered formalin for 48 hours. Subsequently, tissues were sectioned, processed by routine histological methods, embedded in paraffin, and stained with Hematoxylin and Eosin (H&E). Slides were examined under a light microscope and imaged using a Nikon Eclipse 80i photomicroscope (Figure 2). Morphometric parameters related to cellular density in the septal and alveolar regions were quantified using histogram analysis in ImageJ software. Microscopic lung images were further analyzed to calculate fractal dimension and lacunarity through the box-counting method using the FracLac plugin. Statistical analysis involved the Kolmogorov–Smirnov test to assess data normality, followed by the non-parametric Kruskal–Wallis test and Dunn's post-hoc test, with a significance level set at $p < 0.05$. All analyses were performed using GraphPad Prism 8®. The results indicated a significant reduction in septal and alveolar areas in the LPD group. In contrast, the LPD+CBD group showed a reversal of this effect, with values approximating those observed in the control group (Table 1). The fractal was reduced in the LPD group and the LPD+CBD group had values similar to the control group, reversing the possible alterations caused by the LPD group. As for lacunarity, the LPD group had a higher average when compared to the control group, while the LPD+CBD group had averages similar to the control (Figure 1). Thus, it can be concluded that CBD has a potential restorative effect on lung tissue when subjected to possible injuries.

[1] D.C. Estrela et al., *Nutritional deficiency in Wistar rats.* Multiscience. 1 (4) (2016).
[2] T.F. Castro et al., *Protein restriction during pregnancy affects lung development and promotes oxidative stress and inflammation in C57 BL/6 mice offspring.* ScienceDirect 101 (2022).
[3] A. Ribeiro et al., *Effects of cannabidiol, a cannabinoid derived from Cannabis sativa, in a murine model of acute lung inflammation: an immune-neuro-endocrinological evaluation.* Rev. Bras. Terapia Intensiva, 27 (4) (2015).

Table 1. Morphometric analysis of the septal area and alveolar area in the lungs of offspring from the experimental groups.

Area	Control	LPD	LPD+CBD	p
Alveolar Septal	1143769.60 ±156635.87a	781867.25± 200332.34b	1299184±198 738.12a	0.001*
Alveolar	954601.60± 701912.90a	774415.13± 102324.16b	1291732.75±2 85721.14a	0.001*

*Means followed by the same letter in the rows do not differ significantly from each other using the Kruskal-Wallis test followed by Dunn's post-hoc test (p>0.05).

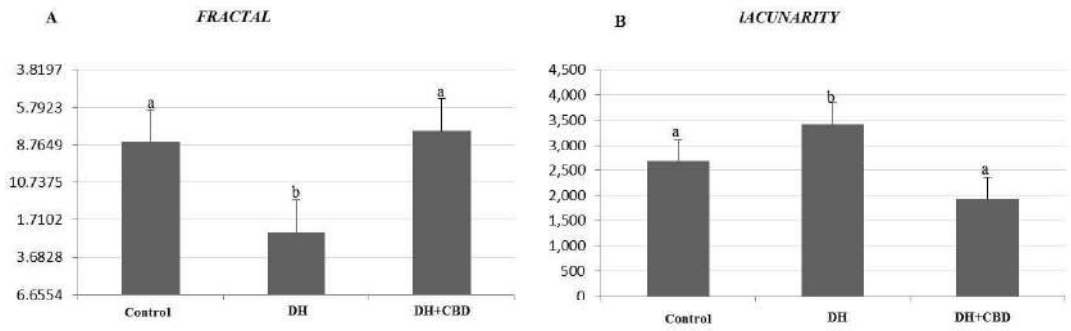

Figure 1. Fractal and lacunarity of the pulmonary alveoli. A: Hypoprotein diet group showing a lower fractal average when compared to the other groups. B: Hypoprotein diet group showing higher mean lacunarity compared to the other groups. *Means followed by the same letter in the lines do not differ significantly from each other using the Kruskal-Wallis test followed by Dunn's post-hoc test (p>0.05).

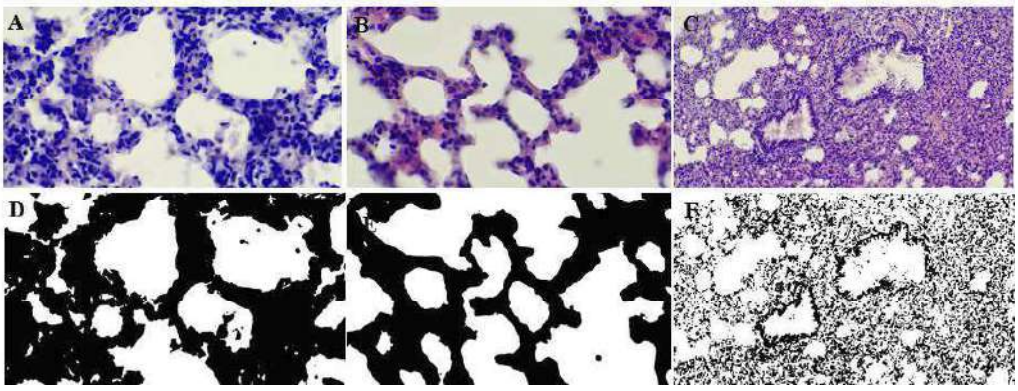

Figure 2. Photomicrographs of the lungs of animals from the experimental groups after using the ImageJ program for fractal and lacunarity analysis. Panels A, B and C are the original photomicrographs stained with H&E, and images D, E and F are the segmented photomicrographs of the control group (A, D), LPD group (B, E), LPD+CBD group (C, F).

Morphometric and Stereological Evaluation in the Ventral Prostate of Spontaneously Hypertensive Senile Rats

Gabriel dos Santos Lima Sardinha[1]*, Nathany Ribeiro Lima dos Santos[1], Max Vinícius Malmann Medeiros[1], Bárbara Costa Malmann Medeiros[1], Fernanda Cristina Alcantara dos Santos[1], Manoel Francisco Biancardi[1]

[1]Institute of Biological Sciences (ICB), Federal University of Goiás (UFG)
*gabrielsardinha@discente.ufg.br

Benign prostatic hyperplasia (BPH) is a common condition in men over the age of 40, characterized by non-cancerous growth of the prostate. In men, prostate growth is related to hormonal changes that occur with aging, especially due to the imbalance between testosterone and estrogen, together with genetic and environmental factors [1-3]. This growth of the gland can compress the urethra, leading to urinary symptoms. Considering the impact of prostatic changes on aging, experimental models such as Spontaneously Hypertensive Rats (SHR), which have a genetic predisposition to hypertension and reduced life expectancy (about 18-24 months), become relevant for comparative studies about age-related prostatic changes and comorbidities, such as hypertension [4,5]. Histologically, the prostate is a branched tubuloalveolar gland composed of ducts lined with pseudostratified columnar epithelium with basal nuclei [2]. In addition to secretory epithelial cells, neuroendocrine cells are also present. It is located just below the bladder, surrounding the initial portion of the urethra, and is surrounded by fibroelastic connective tissue and is rich in smooth muscle. Its main function is to produce and secrete fundamental components of seminal fluid, such as electrolytes, glycoproteins, ions, and enzymes, which are essential for sperm viability and, consequently, for male reproduction [3, 6]. Given the physiological and clinical relevance of the prostate, especially in the context of aging and chronic diseases such as hypertension, this study aimed to evaluate epithelial height and characterize prostatic compartments (epithelium, stroma and lumen) in different strains of elderly rats, as well as to verify whether there was worsening of the hyperplastic condition of these animals. For this purpose, 10 male rats (Rattus norvegicus) aged 18 months were used, five from the Wistar (W) strain and five from the SHR strain. With prior approval from the Animal Use Ethics Committee (CEUA), under protocol number 042/2023, the animals were divided into two experimental groups: W 1.5 and SHR 1.5. After the end of the experimental period, they were weighed and euthanized by intraperitoneal injection of tribromoethanol. Subsequently, the ventral prostate was collected for histological analysis. The results showed that, in the morphometric analysis, the epithelial height of SHR rats increased compared to that of their Wistar control (Figure 1). In the stereological analysis, SHR rats showed a significant increase in the epithelium and muscle layer and a decrease in the lumen (Figure 2). However, the non-muscular stroma did not show statistically significant differences between the two groups analyzed. These findings indicate that SHR rats have significant morphological changes in the ventral prostate compared to Wistar rats, evidenced by increased epithelial height and muscle layer thickness. Such changes suggest that hypertension may directly influence prostate structure during aging. These results provide important insights for future investigations into the pathophysiology of prostate diseases in older individuals, contributing to the understanding of the impact of systemic conditions such as hypertension on male reproductive health.

[1] Junqueira LC, Carneiro J. Histologia básica: texto e atlas. 13ª ed. Rio de Janeiro: Guanabara Koogan; 2017.

[2] Cannarella R, Condorelli RA, Mongioì LM, La Vignera S, Calogero AE. Endocrinology of the aging prostate: current concepts. Front Endocrinol (Lausanne). 2021 Feb 22;12:1–13. doi:10.3389/fendo.2021.554078.
[3] Gasmi A, Peana M, Noor S, Menzel A, Dadar M, Gasmi Benahmed A, et al. Nutritional and surgical aspects in prostate disorders. Crit Rev Food Sci Nutr. 2022;63(21):5138–54. doi:10.1080/10408398.2021.2013158.
[4] Okamoto K, Aoki K. Development of a strain of spontaneously hypertensive rats. Jpn Circ J. 1963;27:282–93.
[5] Fazan VPS, Silva CA, Salgado HC. Ratos espontaneamente hipertensos e neuropatias periféricas. Rev Med (Ribeirao Preto). 2006;:39–50.
[6] This research was supported by the Coordination for the Improvement of Higher Education Personnel - Brazil (CAPES) - Funding Code 001.

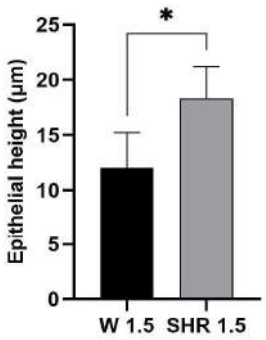

Figure 1. Epithelial height. Values are shown as mean ± standard error of the mean. Asterisks indicate statistically significant differences between experimental groups (* = $p \leq 0.05$).

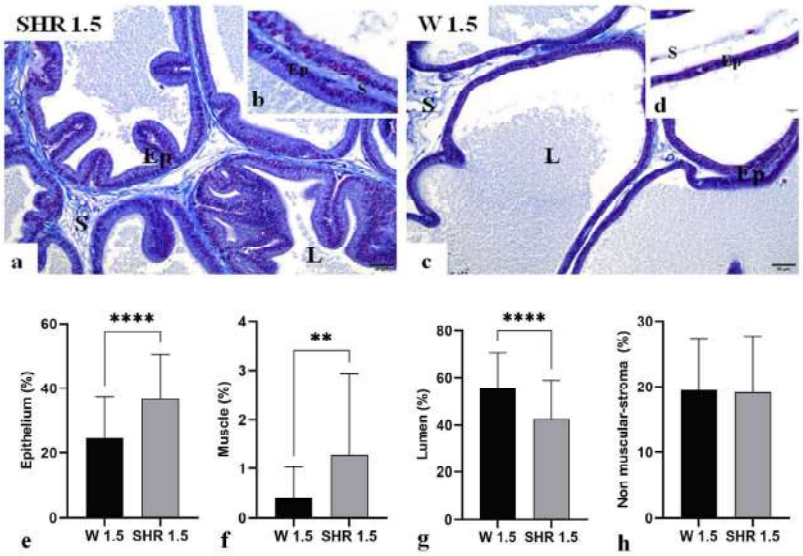

Figure 2. Histological sections of the ventral prostate of male rats of the Wistar (1.5) and SHR (1.5) strains stained using the Gomori trichrome technique (a-d), showing morphological aspects of the gland in the two experimental groups (n = 5 animals/group). Epithelium (Ep), Lumen (L), Stroma (Es). Scale bar (panels a,c - 20 µm scale bar); (panels b,d - 5 µm scale bar). Values are shown as mean ± standard deviation. Asterisks indicate statistically significant differences between the experimental groups (** = $p \leq 0.01$; **** = $p \leq 0.0001$).

Morphometric Study Of The Spleen Of Rats Subjected To Protein Malnutrition During Pregnancy And Supplemented With Cannabidiol

Maria Clara Chár Gomes[1]*, Carlos Eduardo da Silva[1], Paloma Vitória Melo da Silva[1], Alison José da Silva[1], Ana Vitoria Ferreira dos Santos[1], Isaque Bertoldo Santos da Silva[1], Renan Gabriel da Silva Ferreira[1], Thaynara Caseli dos Santos[1], Jadyel Sherdelle Guedes do Nascimento[1], Bruno Mendes Tenorio[1], Fernanda das Chagas Angelo Mendes Tenorio[1].

[1]Federal University of Pernambuco, Center for Biosciences, Department of Histology and Embryology, Recife, Pernambuco, Brazil
*mclarachar@gmail.com

Recognized as the largest lymphoid organ in the human body, the spleen performs essential functions in the immune system, such as eliminating bacteria circulating in the blood and producing lymphocytes and monocytes [1]. It also plays a key role in the phagocytosis of pathogenic microorganisms, such as viruses, bacteria, and leukocytes, in addition to participating in the synthesis of opsonins, substances that facilitate the phagocytosis process [2]. During pregnancy, the spleen helps balance tolerance to the fetus and defense against infections. In situations of low-protein diets, its function strengthens immunity in the face of nutritional challenges, while cannabidiol (CBD) acts on the spleen with anti-inflammatory and immunomodulatory effects, helping to control inflammation and strengthen the immune response, especially in situations of immunosuppression [3]. Thus, the objective of the study was to morphometrically analyze the spleen of rats subjected to protein-energy malnutrition during pregnancy and supplemented with cannabidiol. To this end, fifteen rats were used, separated into three groups: control, low-protein diet, and diet plus cannabidiol. The rats were mated and subsequently subjected to pregnancy confirmation by vaginal smear. They were then treated with a diet, a low-protein diet, and a low-protein diet supplemented with cannabidiol nanoemulsion at a dose of 10 mg/kg. On the 14th day of pregnancy, the animals were anesthetized for spleen removal, immediately weighed, and then immersed in 10% buffered formalin for 48 hours. Subsequently, the samples were cleaved and subjected to histological impregnation and paraffin embedding. The slides obtained were stained with Hematoxylin and Eosin (H&E), analyzed under a light microscope, and photographed using a Nikon Eclipse 80i photomicroscope. Thus, the samples were evaluated using parameters for quantifying the cells present in the white pulp and red pulp regions of the spleen, based on the counting of points by systematic allocation using a grid with 169 points, identifying the components in the microscopic images of the spleen using the freehand tool in the ImageJ software. The results were submitted to the Kolmogorov-Smirnov normality test and then analyzed by the nonparametric Kruskal-Wallis test followed by Dunn's post hoc test with a significance level of 5% ($p < 0.05$). Based on the results obtained through analyses performed using GraphPad Prism8®.4 software, it was concluded that the low-protein diet promoted morphometric changes in the spleen, evidenced by an increase in the number of lymphocytes and a reduction in connective tissue cells compared to the control group. However, supplementation with cannabidiol (CBD) associated with the low-protein diet was able to reverse these changes, presenting values similar to those of the control group. These findings suggest a possible modulatory effect of CBD on the damage induced by a low-protein diet, pointing to its therapeutic potential and likely reversal of the damage caused by protein malnutrition during pregnancy.

[1] S.M. Lewis et al., *Structure-function of the immune system in the spleen.* Science Immunology, 4 (2019).
[2] R.G. Marques et al., *The role of the spleen in resistance to infection.* Rev. Bras. Med., 60 (5) (2003).
[3] T.R. Jan et al., *Suppressive effects of cannabidiol on antigen-specific antibody production and functional activity of splenocytes in ovalbumin-sensitizes BALB/c mice.* International Immunopharmacology, 7 (6) (2007).

Table 1. Mean ± standard deviation of the spleen of experimental animals where the following parameters were analyzed: lymphocytes, connective tissue cells, and splenic cords.

Experimental Groups/Parameters	**Control**	**Diet**	**Diet+CBD**	**p**
Lymphocytes	72.33±32.2a	85.26±25.2b	63.73±32.2a	0.012*
Connective Tissue Cells	51.8±33.7a	39.6±17.2b	62.7±35.9a	0.005*
Splenic cords	45±31.6a	36.2±23.8a	35.2±21.3a	0.865

*Averages followed by different letters in the row differ significantly from each other. Kruskal–Wallis nonparametric test followed by Dunn's post hoc test ($p \leq 0.05$).

Morphophysiological Analysis of Chicken Embryos (*Gallus gallus domesticus*) Subjected to Gradual and Controlled Exposure to Acephate

Jonas Rodrigues dos Santos[1]*, Carlos Eduardo Pires Ferreira Rodrigues[1], Lais Alves de Araújo[1], Felipe Ferraz Dias[1]

[1]Laboratory of Inflammation Research, Department of Biological Sciences, State University of Minas Gerais, Ibirité Campus, Minas Gerais, Brazil.
*jonas.1398361@discente.uemg.br

Brazil occupies a prominent position among the world's leading agricultural producers. To supply the national market with high demand, several strategies are used to maintain agricultural productivity, including the intense use of pesticides [1]. The most widely used compound to expunge bug plagues is acephate ($C_4H_{10}NO_3PS$), an insecticide used in Minas Gerais. Despite its efficacy against bugs proliferation, pesticide is utilized indiscriminately, without proper protective equipment combined with improper handling, entailing serious health risks to both farmers and their families. Recent evidence has linked continuous exposure of acephate to respiratory problems, neurodegenerative disorders, and negative impacts on the reproductive system, such as reduced serum levels of male and female hormones as and congenital malformations [2]. Given this scenario, the present study investigated the teratogenic effects of acephate exposure, using chicken embryos, birds commonly subjected to pesticides at farming places [3], as an experimental model to simulate poisoning during embryonic development. Fertilized *Ross* and *Cobb* strain eggs were incubated in an automatic incubator at 37.9°C and 50% humidity. Morphometric data from 140 eggs (horizontal and vertical diameters, and total weight) were evaluated (30 controls eggs and 110 inoculated with 200mg/kg of acephate) at decreasing concentrations of 50%, 25%, 10%, 5%, and 1%, to determine the minimum exposure to survival. To evaluate the morphophysiological changes, animals (N = 4-5) were euthanized with 200 µl of propofol (1mg/ml), collected from the eggs, at different time intervals of their embryonic development, 2, 4, 7, 11, 14 and 21 days [4] after inoculation, according to ethical recommendations (protocol 001/2023 and 006/2024 UEMG) and, processed for embryologic and histological studies. Stereoscopic evaluation of the embryos pointed to a consistent delay in their body development compared with the development standard for each respective stage (Fig. 1). Survival analyses of intoxicated embryos registered from 30% (50% concentration) to 40% of live animals (1% concentration) (Fig. 2A). At 7-days of development, the survival rate changed from 25% to 75% at 5% acephate concentration (Fig. 2B). Embryo weight of the embryos underwent changes, showing a significant decrease. The average weight of the control group was 11.3g, while the average for the treated embryos was 4g, representing almost 300% of weight decrease (Fig. 3). Histological studies demonstrated embryo germinative as fetal tissues changes compared to control ones, indicative of morphological alterations triggered by direct exposure of germ leaflets to gradual acephate concentrations (Fig. 4). These results highlight the high toxicity of acephate to domestic animals and the need for more in-depth evaluations of the biology of these animals in response to toxic agents, aiming to improve animal health.

References:

[1] W.A. Pignati et al., *Ciênc. Saúde Coletiva* 22(10) (2017) 3281.
[2] T. F. M. Mota et al., *Environ. Res.* 237(2) (2023) 117034.
[3] F. PERES et al. *Veneno ou remédio*, Fiocruz, Rio de Janeiro, 2003.
[4] V. HAMBURGER; H. L. HAMILTON, *Dev Dyn*. 195(4) (1992) 231.
[5] This research was supported by PAPq – UEMG (Brazil).

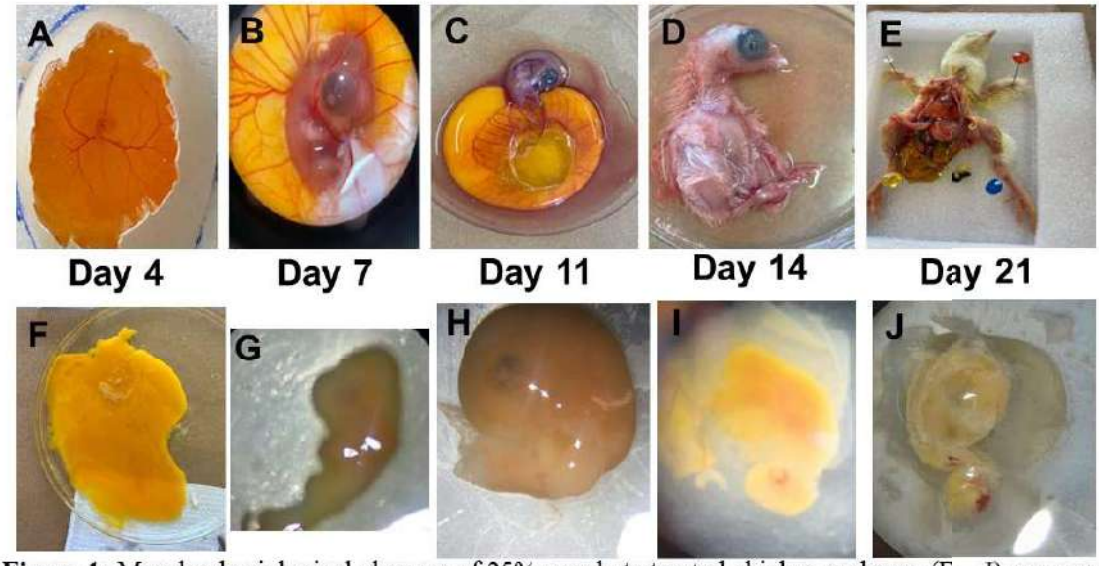

Figure 1: Morphophysiological changes of 25%-acephate treated chicken embryos (F – J) compared to control ones (A – E), along the days of development. 20X ampliation.

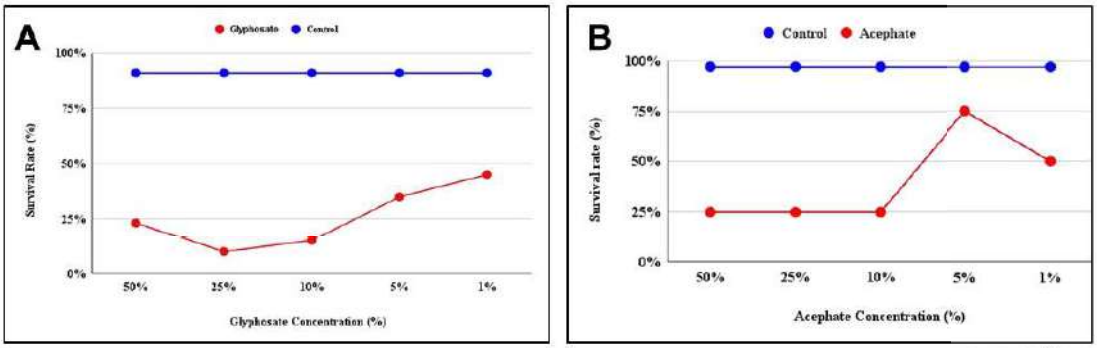

Figure 2: Survival rate of chicken embryos after decrescent acephate concentration administration along whole developmental period (4 to 21 days) (A) and at 7-days of development (B), compared to control ones (0% concentration).

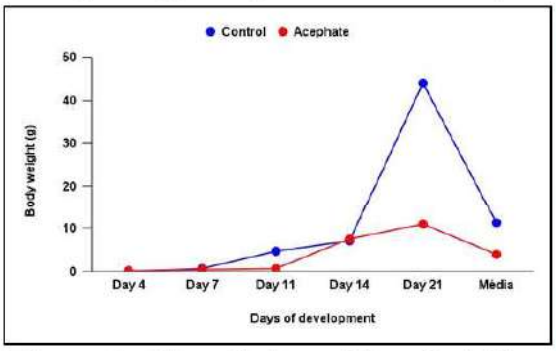

Figure 3: Mean body weight of chicken embryos after decrescent acephate concentration administration along whole developmental period (4 to 21 days) compared to control ones (0% concentration).

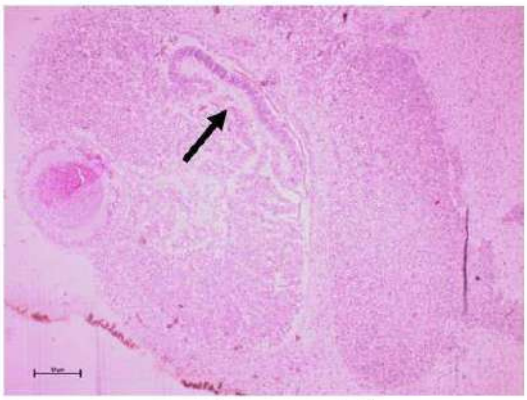

Figure 4: 5%-acephate treated chicken embryo at 4-days of development showing endoderm disarregment (arrow). HE. Bar: 50 µm.

Low Concentrations of Glyphosate Are Responsible to Teratogenic Effects in Chicken Embryos *(Gallus gallus domesticus*)

Carlos Eduardo Pires Ferreira Rodrigues[1]*, Laís Alves de Araújo[1], Jonas Rodrigues dos Santos[1], Felipe Ferraz Dias[1]

[1] Laboratory of Inflammation Research, Department of Biological Sciences, State University of Minas Gerais, Ibirité Campus, Minas Gerais, Brazil.
*carlos.1397347@discente.uemg.br

Family farming employs a variety of techniques for managing rural plots and growing food for the population. The main method is the use of herbicides, like glyphosate, a substance responsible for removing weeds and ensuring efficient agricultural production, but which also degrades the environment where crops are planted and grown [1]. Improper use also causes poisoning in the population exposed to pesticides, such as skin irritation, neuroendocrine, pulmonary, and cardiovascular disorders, such as congenital malformations [2]. Based on this information, this study evaluated the morphophysiological changes in chicken embryos, animals widely subjected to herbicides at farming places [3], subjected to decrescent concentrations of glyphosate throughout their developmental stages. Fertilized *Ross* and *Cobb* strain eggs were incubated in an automatic incubator at 37.9°C and 50% humidity. Morphometric data from 240 eggs (size and total weight) were evaluated, 30 controls and 210 directly inoculated with 200mg/kg of glyphosate at decreasing concentrations of 50%, 25%, 10%, 5%, and 1%, to determine the minimum exposure of herbicide to animal survival. To determine the embryo morphophysiological changes, exposed animals (N = 4-5) were euthanized with 200 µl of propofol (1mg/ml) and taken from the eggs, at different time intervals of their embryonic development, 2, 4, 7, 11, 14 and 21 days [4] after inoculation, according to ethical recommendations (protocol 001/2023 and 006/2024 UEMG) and, processed by conventional histological techniques. Stereoscopic evaluation of the embryos pointed to a body formation impairment as a consistent delay in their development compared with the body development standard for each respective time interval (Fig. 1). Survival analysis over time of intoxicated embryos registered from 23% - for 50% concentration - to 45% - for 1% concentration - of live animals (Fig. 2A). Only after 7 days, the survival rate of glyphosate-treated animals increased to 75% at 5% concentration (Fig. 2B). At concentrations of 50%, 25% and 10%, aspects of delayed development of embryos were observed in the 7 days of development, such as reduced growth and a decrease in the cephalocaudal axis in relation to control group embryos. Embryo weight has changed drastically during the time of development (Fig. 3). While the average weight of the control group was 11.3g, the average weight of the treated group was 0.27 g, representing more than 4,000% of weight decrease (Fig. 3). Embryonic and fetal tissues demonstrated morphological changes in germ leaflets and organs compared with those of the control group, suggesting cellular and tissue alterations triggered by both high to low glyphosate concentrations (Fig. 4). These results bring to light the high toxicity of this herbicide, capable to induce robust changes in the morphophysiology of embryos, even at low concentrations, requiring further studies to elucidate the teratogenic consequences found.

References:

[1] L. M. Bombardi, Geografia do uso de agrotóxicos no brasil e conexões com a união europeia, FFLCH- USP, São Paulo, 2017.
[2] S. M. Bradberry et al., *Toxicol Rev*. 23(3) (2004) 159.
[3] F. Peres et al. *Veneno ou remédio*, Fiocruz, Rio de Janeiro, 2003.
[4] V. Hamburger; H. L. Halmilton, *Dev Dyn*. 195(4) (1992) 231.
[5] This research was supported by PAPq – UEMG (Brazil).

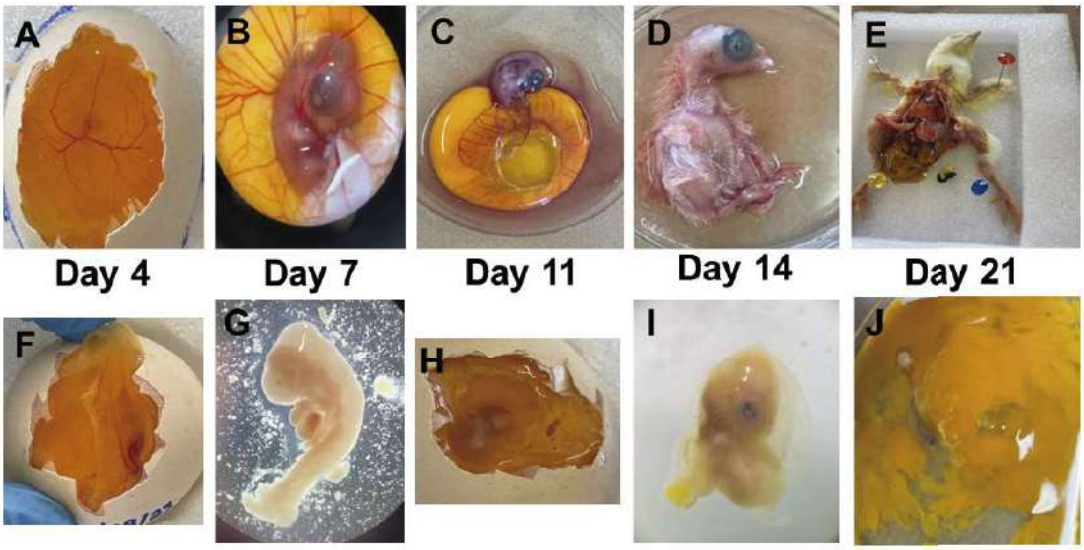

Figure 1: Morphophysiological changes of 25%-glyphosate treated chicken embryos (F – J) compared to control ones (A – E), along the days of development. 20X ampliation.

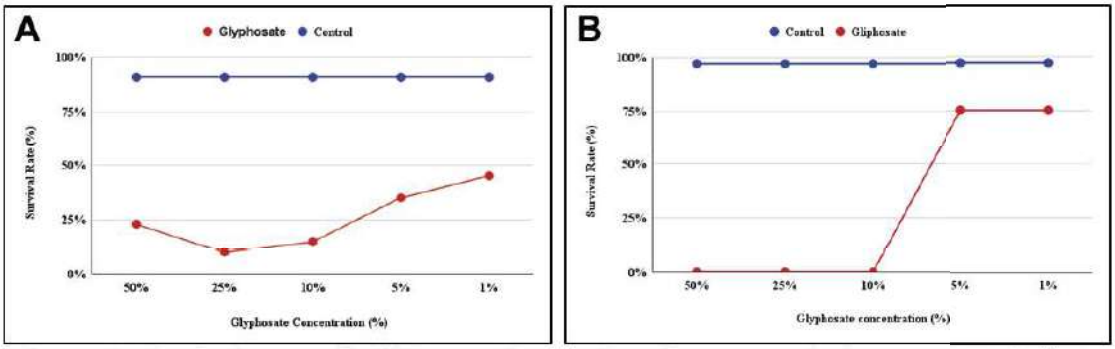

Figure 2: Survival rate of chicken embryos after decrescent glyphosate concentration administration along whole developmental period (4 to 21 days) (A) and at 7-days of development (B), compared to control ones (0% concentration).

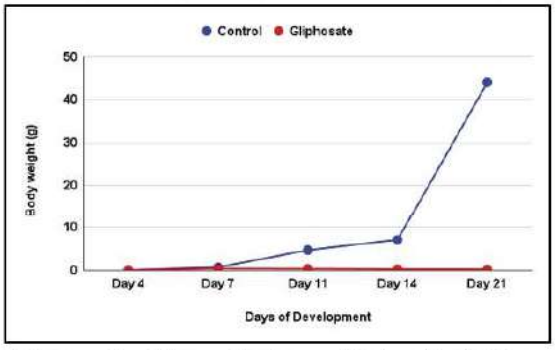

Figure 3: Mean body weight of chicken embryos after decrescent glyphosate concentration administration along whole developmental period (4 to 21 days) compared to control ones (0% concentration).

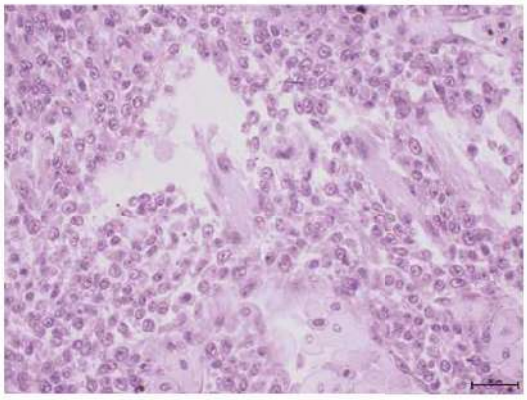

Figure 4: 50%-glyphossate treated chicken embryo at 7-days of development showing mesoderm mesenchymal cells dissociation from each other. HE. Bar: 50 µm.

Nanostructured Lipid Carriers Enhance Antioxidant Delivery of Tapereba's Coproducts in Human Keratinocytes

Leonardo Fróes de Azevedo Chang[1,2]; Isadora F. Souza[1,2] ; Eliana Fortes Gris[3]; Victor Carlos de Mello[1,2]; Sônia Nair Báo[1].

[1] Laboratory of Microscopy and Microanalysis, Department of Cell Biology, Institute of Biological Sciences, University of Brasília, Brasília 70910-900, DF, Brazil;
[2] Cooil Cosmetics LTDA, Brasília, DF, Brazil;
[3] Graduate Program in Health Sciences and Technologies, Faculty of Health Sciences and Technologies, University of Brasilia, Centro Metropolitano, Conjunto A, Lote 01, Brasilia 72220-275, Brazil.

The Tapereba fruit (*Spondias mombin* L.), one of the Cerrado's native fruits, has been getting more attention in the past years. This focus towards tapereba has been not only for its sweet but slightly acidic taste, but also from its promising biological potential, including anti-inflammatory, antimicrobial and antioxidant activities. These properties are due to the high content of phenolic compounds, particularly gallic and ellagic acids [1]. These compounds are not only present in its pulp, but also in its by-products, like seed and peel [2]. According to de Freitas (2024), tapereba contains approximately 1666.18 ± 127.56 mg of total polyphenolic compounds and exhibits strong antioxidant activity in the DPPH assay, with an IC_{50} value of 38.03 ± 0.49 μg/mL. For comparison, ascorbic acid presents an IC_{50} of 24.34 ± 0.09 μg/mL [2,3]. Antioxidant compounds are known for their protective effects against reactive oxygen species (ROS), which can damage intracellular molecules such as DNA, proteins, and sugars [4]. ROS are specially harmful for the skin, inducing pigmentation, decrease of cell density and decline of collagen synthesis [4,5]. To potentialize the antioxidant delivery and effectiveness of tapereba-derived compounds, an extract from its co-products (peel and seed) was incorporated into a nanostructured lipid carrier (NLC), referred to as NLC-TAP-NaDES. In this study human keratinocytes (HaCat) were used to assess the formulation's effects. The NLC was prepared as described by Mello (2025). The cells were seeded into a circular slipcover at 3×10^4 cell per well, treated scoring to which group: Unstimulated (Uns, negative control), H_2O_2-treated (500 μM), NLC-TAP-NaDES (3.612 μg/mL for 24 h), and Preventive treatment (NLC-TAP-NaDES for 24 h followed by 500 μM H_2O_2 exposure). After treatments, cells were stained with 5 μM CellROX Green and 1 μg/mL DAPI, and analyzed using a Leica TCS SP5 confocal microscope. Confocal microscopy (Figure 1) revealed that cells treated with NLC-TAP-NaDES did not exhibit increased ROS formation and showed a reduction in overall ROS levels compared to the unstimulated group. The preventive treatment shows that pre-exposure to NLC-TAP-NaDES mitigated ROS-induced damage following H_2O_2 exposure, relative to the H_2O_2-only group. Morphologically, cells treated with H_2O_2 exhibited an increase in size, consistent with findings by Loo (2011), which suggest activation of the ERK1/2 signaling pathway. In contrast, cells treated with NLC-TAP-NaDES maintained a size comparable to the control groups, further supporting its role in reducing ROS generation and protecting cells from oxidative damage [4,6]. In conclusion, it shows the promising antioxidant potential of Tapereba (*Spondias mombin* L.) by using its co-products, when incorporated into a NLC. The confocal microscopy analysis demonstrated that NLC-TAP-NaDES not only prevented an increase in ROS formation in HaCat cells but also appeared to reduce baseline oxidative stress compared to the untreated group.

[1] KOUADIO IBRAHIME SINAN et al. Antioxidants, v. 10, n. 11, p. 1771–1771, 5 nov. 2021.
[2] NETO, S. et al. Brazilian Journal of Chemical Engineering, v. 39, n. 2, p. 511–525, 3 jan. 2022.
[3] MADHVI, S. K. et al. Research Journal of Pharmacy and Technology, v. 13, n. 4, p. 1701, 2020.
[3] WANG, D. et al. Antioxidants, v. 12, n. 3, p. 609, 1 mar. 2023.
[4] XIAO, L. et al. Antioxidants, v. 10, n. 1, p. 76–76, 8 jan. 2021.
[5] MELLO, V. C. et al. Antioxidants, v. 14, n. 3, p. 290–290, 28 fev. 2025.
[6] LOO, A. E. K.; HO, R.; HALLIWELL, B. Free Radical Biology & Medicine, v. 51, n. 4, p. 884–892, 15 ago. 2011.

Acknowledgements
We would like to thank the Laboratory of Microscopy and Microanalysis at the University of Brasília (LMM - UnB). We also extend our gratitude for the financial support provided by th FAP-DF, CNPq), CAPES, and FINEP.

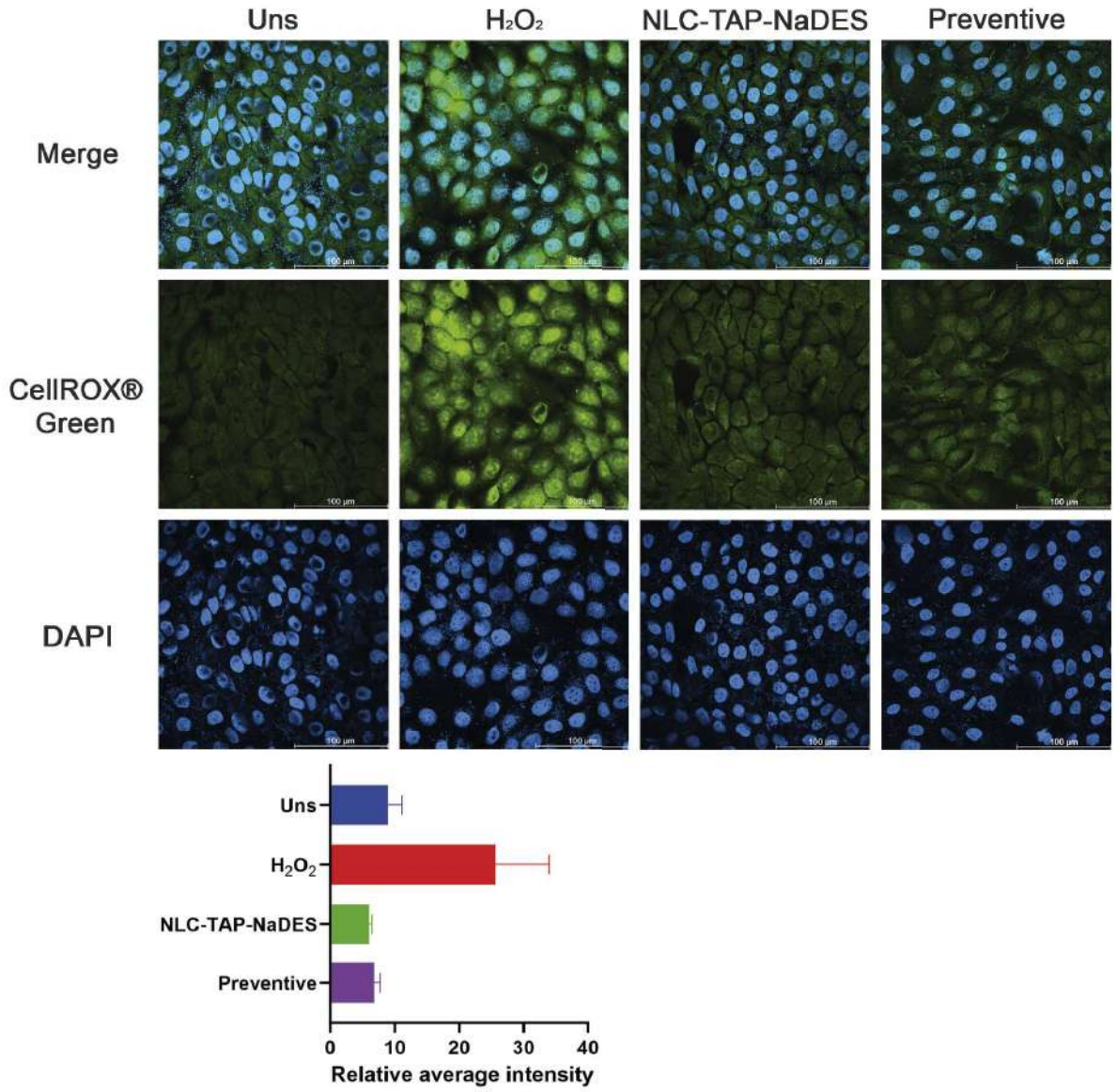

Figure 1. Confocal images of HaCat cells under various treatment conditions: Unstimulated (Uns), exposed to 500 µM H_2O_2, treated with NLC-TAP-NaDES at 3.612 µg/mL, and a preventive treatment with 3.612 µg/mL NLC-TAP-NaDES followed by 500 µM H_2O_2. The cells were stained with 5 µM CellROX Green and 1 µg/mL DAPI. Below the images is a graph showing the relative average intensity of CellROX Green staining in the cells.

Natural Deep Eutectic Systems (NaDES) as Alternative Cryoprotective Agents on the Cryopreservation of SH-4 Melanocytes

Livia Marques Ferreira[1,2]*, Pedro Rocha[1,2], Victor Mello[1,2], Sonia Nair Bao[1].

[1] Laboratory of Microscopy and Microanalysis, Department of Cell Biology, Institute of Biological Sciences, University of Brasília, Brasília 70910-900, DF, Brazil;
[2] Cooil Cosmetics LTDA, Brasília, DF, Brazil.
*marquelivia@gmail.com

The cryopreservation of melanocytes and other cell types cultured *in vitro* is a laboratory necessity and part of the routine of many researchers. Typically, a cryoprotective agent (CPA) is added to minimize damage caused by freezing by inhibiting ice formation and preserving cell membranes. Until now, the most common use has been dimethyl sulfoxide (DMSO) or glycerol as CPAs, but it is known that these compounds require great care during thawing to avoid cell death and other problems in post-thaw cell recovery [1]. Therefore, new solvents have been researched to replace DMSO in freezing solutions, such as natural deep eutectic solvents (NaDES), a new generation of solvents inspired by nature and extracted from plant bioresources [2]. These compounds have shown to be promising as CPAs, in addition to being a more economical and sustainable alternative [3,4]. In this study, two NaDES were used to formulate new freezing solutions: Betaine-Levulinic Acid 1:7 (Bet-LeA) and Betaine-Malic Acid-Water 1:1:7 (Bet-MAc) diluted in fetal bovine serum (FBS) at different concentrations defined after performing cytotoxicity tests. For the efficacy tests of the CPAs, melanocytes of the SH-4 cell line were cultured and frozen in aliquots with 500 µL of freezing solution at 37 ºC. After a period of 5 to 7 days, the aliquots were uniformly thawed at -80 ºC, then cells were resuspended in Dulbelco's Modified Eagle Medium (DMEM with 4.5 g/L glucose) and transferred to cell culture flasks. Post-thaw cell morphology and proliferation were observed for 14 days, when the groups with the highest confluence - control freezing solution (DMSO 5%), Bet-LeA 0.8% and Bet-MAc 0.2% - were seed into a square slide at 3×10^4 cell per well. After fixation they were marked with Phalloidin-TRITC and DAPI, for F-actin filaments and nuclei analysis in Confocal microscope Leica TCS SP5. F-actin tightly follows the cell membrane, allowing for a visual approximation of the entire cell volume [5], targeting its filaments visually elucidates cytoskeletal disruptions or alterations imposed by the stresses and strains experienced by the cells. It was shown in the confocal analysis (Figure 1) that there is no significant cytoskeletal alterations or disruptions in the groups cryopreserved with Bet-MAc 0.2% and Bet-LeA 0.8% when compared to the one cryopreserved with DMSO 5%. In conclusion, by analyzing F-actin filaments, the study shows the promising use of NaDES as alternative cryoprotective agents in the cryopreservation of SH-4 lineage melanocytes.

[1] R. Raju et al, BBA - General Subjects, 1865 (2021) 129749.
[2] Z. Usmani et al, Science of The Total Environment, 881 (2023), 163002.
[3] L. Schuh et al, Molecules, 22 (2023) 7653.
[4] A. R. Jesus et al, Cryobiology, 101 (2021) 95.
[5] M. Hagiyama et al, Frontiers in Physiology, 8 (2017) 997.

Acknowledgements
We would like to thank the University of Brasília (UnB) for the financial support provided, and extend our gratitude to the funding agencies CNPq, FAP-DF and FINEP.

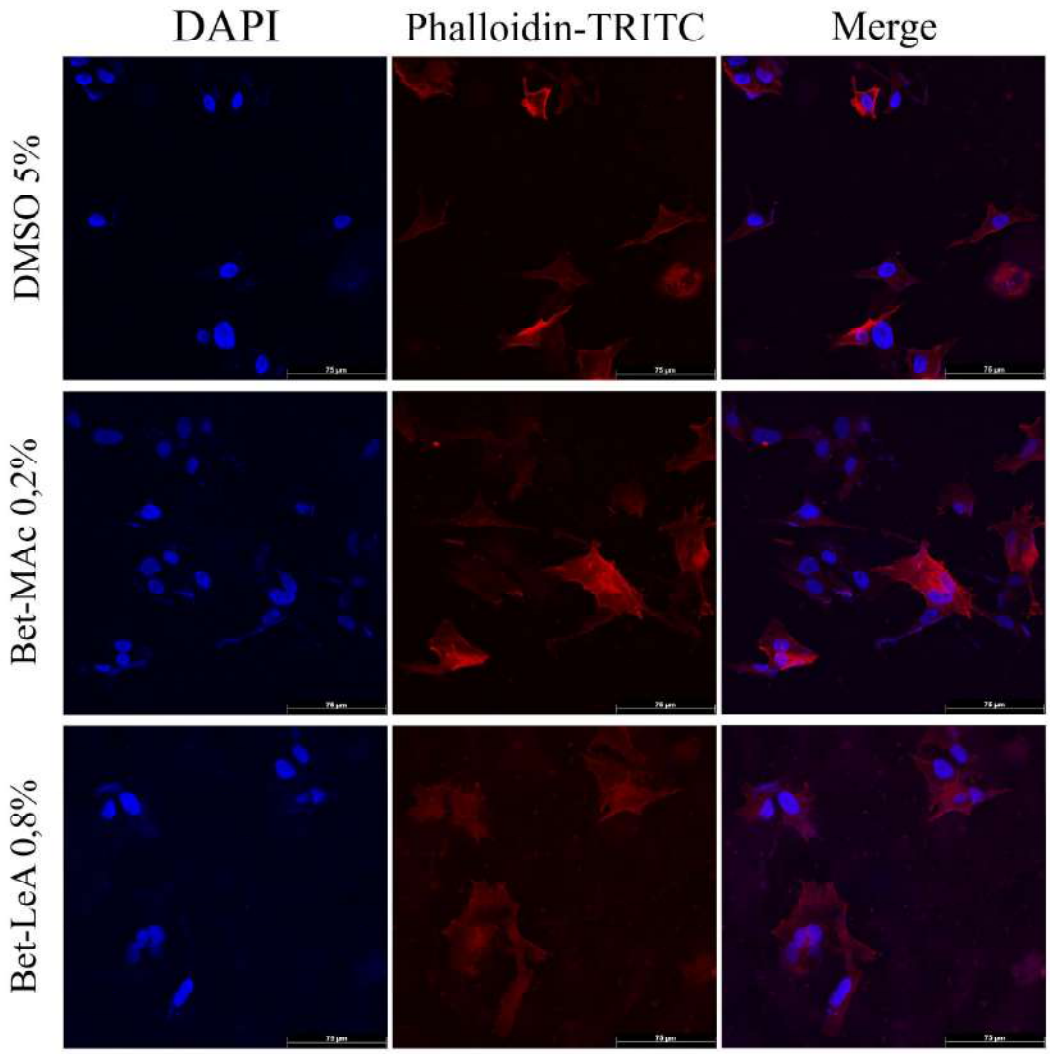

Figure 1. Confocal images of SH-4 cells cryopreserved with different cryoprotective agents: DMSO 5% (Control), Bet-MAc 0.2% and Bet-LeA 0.8%; 14 days after thawing. The cells were stained with 13nM Phalloidin-TRITC and 666,7 mg/mL DAPI.

NET Formation Induced by Cr-LAAO Analyzed by Confocal Microscopy in Human Neutrophils

Mauro Valentino Paloschi[1,2*], Charles Nunes Boeno[1], Milena Daniela Souza Silva[1], Hallison Mota Santana[1], Braz Junior Campos Farias[1], Carolina Pereira da Silva[1], Larissa Faustina Cruz[1], Ketlei Monteiro Tavares[1], Sulamita da Silva Setúbal[1], Ho Phin Chong[3,4], Choo Hock Tan[4,5], Juliana Pavan Zuliani[1,2].

[1]Laboratório de Imunologia Celular Aplicada à Saúde, Fundação Oswaldo Cruz, FIOCRUZ Rondônia, Porto Velho-RO, Brazil; [2]Plataforma de Microscopia - RPT07I, Fundação Oswaldo Cruz, FIOCRUZ Rondônia, Porto Velho-RO, Brazil; [3]Department of Pharmacology, Faculty of Medicine, University of Malaya, Kuala Lumpur, Malaysia; [4]Department of Basic Health Science, Faculty of Pharmacy and Biomedical Sciences, MAHSA University, Jenjarom, Selangor, Malaysia; [5]College of Life Sciences and Medicine, National Tsing Hua University, Hsinchu, Taiwan.
*mauro.paloschi@fiocruz.br

Neutrophil extracellular traps (NETs) are web-like DNA structures released by activated neutrophils as a defense mechanism against pathogens and danger signals. In this study, we investigated the ability of L-amino acid oxidase from *Calloselasma rhodostoma* venom (Cr-LAAO) to trigger NETs formation in human neutrophils, with a focus on DNA and histone H3 release by confocal microscopy analysis. Human neutrophils were isolated from healthy donors and stimulated with Cr-LAAO (50 µg/mL) for 2 hours [1,2]. Cells were fixed, permeabilized, and stained with DAPI (nuclear DNA), SYTOX Green (extracellular DNA), and anti-histone H3 antibodies. High-resolution confocal microscopy revealed extensive release of extracellular chromatin fibers colocalized with histone H3, confirming the formation of NETs. Quantitative analysis of fluorescence intensity showed significantly elevated levels of extracellular DNA and histone H3 signal in Cr-LAAO-stimulated neutrophils compared to RPMI-treated controls. To validate the functional specificity of this process, neutrophils were pre-treated with apocynin, an NADPH oxidase inhibitor. Inhibition of ROS production led to a marked reduction in both DNA release and histone H3 staining, as visualized by confocal microscopy and quantified by image analysis software. Furthermore, extracellular DNA quantification by the Picogreen assay confirmed a significant increase in dsDNA release upon Cr-LAAO stimulation, which was suppressed by apocynin. Importantly, flow cytometry using 7-AAD staining demonstrated that Cr-LAAO did not compromise neutrophil viability, indicating that the NETosis process induced under these conditions was vital and not cytotoxic. Altogether, our findings demonstrate that Cr-LAAO is a potent inducer of vital NETosis in human neutrophils. Confocal imaging provided clear morphological evidence of NETs formation, while fluorescence quantification and viability assays reinforced the specificity and non-lethal nature of the process. These results contribute to the understanding of how venom-derived proteins can modulate immune responses and may have relevance in the context of inflammation, immunity, and potential biotechnological applications.

[1] M.V. Paloschi et al., *Role of L-amino acid oxidase isolated from Calloselasma rhodostoma venom on neutrophil NADPH oxidase complex activation*, *Toxicon* 145 (2018) 48–55.
[2] M.V. Paloschi et al., *Reactive oxygen species-dependent-NLRP3 inflammasome activation in human neutrophils induced by L-amino acid oxidase derived from Calloselasma rhodostoma venom*, *Life Sciences* 308 (2022) 120962.
[3] This research was supported by RPT07I, FIOCRUZ, CNPq and FAPERO.

Figure 1. Neutrophils NETs stimulated by Cr-LAAO.

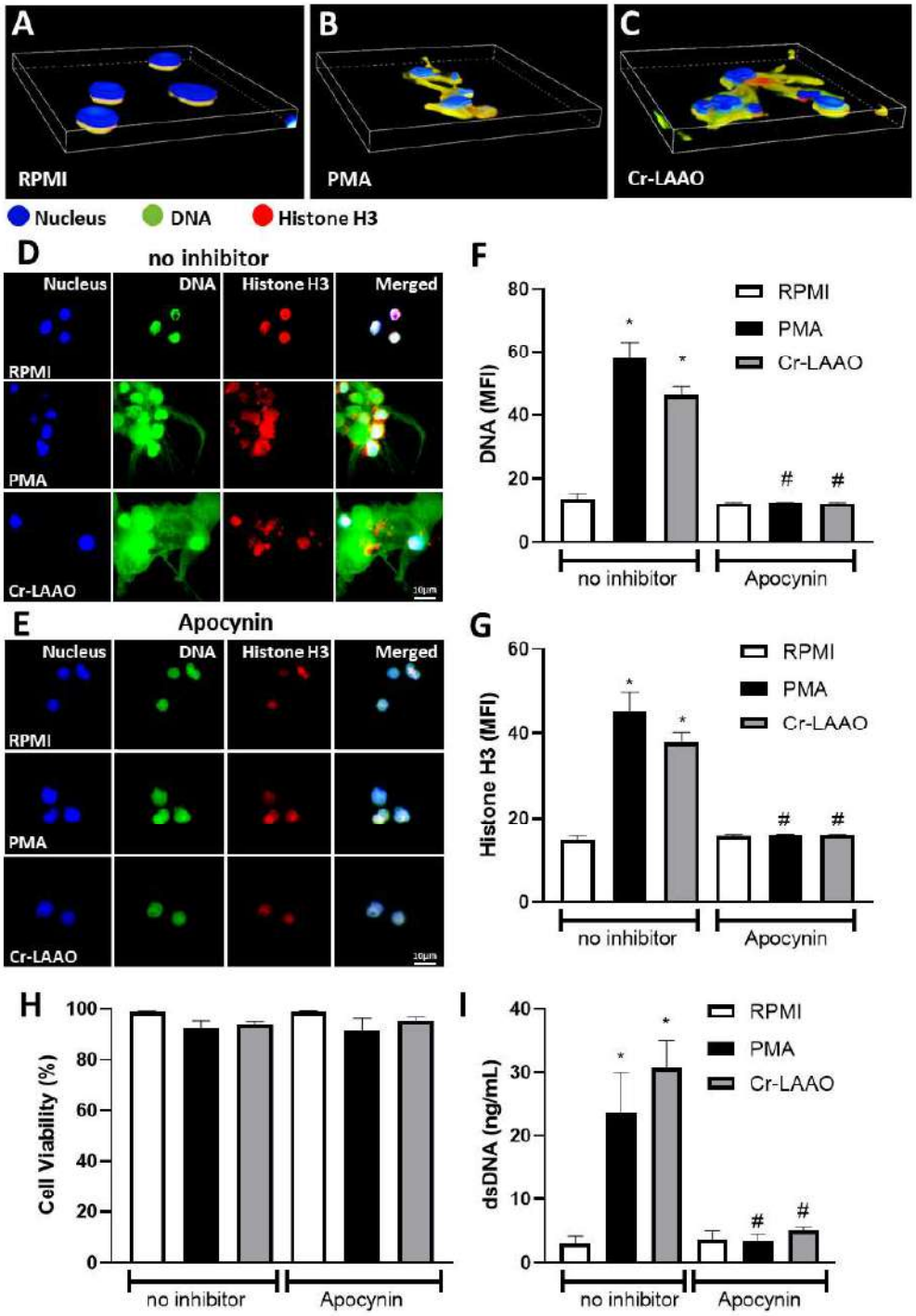

The immunofluorescence assay for the analysis of NETs was performed using human neutrophils (2×10^5) derived from three different donors (three Ns) stimulated with RPMI (negative control), PMA (500 ng/mL; positive control), or Cr-LAAO (50 µg/mL) for 2 h at 37 °C in an atmosphere containing 5% CO_2. Immunofluorescence images were collected with constant automatic gain between samples to quantify differences in absolute levels of fluorescence intensity at 1000x magnification. The slides were analyzed by confocal microscopy for 3D visualization of neutrophils stimulated with RPMI (A), PMA (B), or Cr-LAAO (C). Representative figure of three analyses of independent experiments demonstrating the presence of NETs without inhibitor (D) and using Apocynin (E). The presence of nuclear DNA (blue), released DNA (green), and Histone H3 (red) was analyzed. Analysis of mean fluorescence intensity was performed using 10 fields of view that were observed impartially for each condition for DNA liberated (F) and Histone H3 (G). Cellular viability was assessed by 7-AAD for 15 min at 4ºC and evaluated by flow cytometry (H). The DNA concentrations were measured using the Quant-iT Picogreen dsDNA kit and expressed as ng/mL of dsDNA in the supernatant (I). Values are representative of the mean and standard error of the data of the three donors. *P<0.05 compared to the negative control and #P<0.05 compared to the same condition without pre-treatment with respective inhibitors (data were evaluated with ANOVA followed by Tukey's test).

Nonlinear Analysis through Fractal and Lacunarity of Heterochromatin in Liver Cells of Rats Induced with Diabetes Mellitus and Treated with *Craetavia tapia* Lectin

Weslleyanne Millena da Silva Costa[1]*, Isaque Bertoldo Santos da Silva[1], Carlos Eduardo da Silva[1], Maria Gabriela da Silva Mello[1], Maria Eduarda Carneiro de Lima[1], Ana Carolina Ribeiro Saraiva da Silva[1], Suellen Rozy da Silva Medeiros[1], Ryan Cristian da Silva[2], Maria Clara Chár Gomes[1], Bruno Mendes Tenorio[1], Fernanda das Chagas Angelo Mendes Tenorio[1].

[1]Federal University of Pernambuco, Department of Histology and Embryology
[2]Federal University of Pernambuco, Department of Biochemistry
*weslleyanne.millena@ufpe.br

Diabetes mellitus (DM) is an autoimmune metabolic disorder characterized by hyperglycemia, which occurs when insulin produced by the pancreas is insufficient for the body to properly metabolize glucose [1]. DM can lead to inflammation and fat accumulation in the liver, worsening hepatic conditions [3,4]. In this context, bioactive compounds with anti-inflammatory and glucose-lowering properties emerge as promising therapeutic alternatives. A notable example is CrataBL, a lectin extracted from the plant *Crataeva tapia*, which exhibits antioxidant, anti-inflammatory, and hypoglycemic properties [5]. In the context of diabetes, CrataBL may contribute to glycemic control. Lectins such as CrataBL are glycoproteins that act on the diabetic liver by binding to specific carbohydrates in cells such as hepatocytes and macrophages, showing potential for disease treatment [2]. Thus, the aim of this study was to apply fractal and lacunarity analysis methods to detect possible alterations in heterochromatin distribution in the nuclei of hepatic cells from rats induced to diabetes and treated with *Crataeva tapia* lectin. Fifteen Wistar albino rats were used, divided into three groups: (I) Control; (II) Diabetic-induced (DM); and (III) Diabetic-induced and treated with lectin. DM was induced by intraperitoneal injection of streptozotocin (50 mg/kg) after 14 hours of fasting, diluted in citrate buffer. Three days after streptozotocin induction, postprandial blood glucose was measured using test strips (Accu-Check), and animals with glucose levels ≥ 288 mg/dL were considered diabetic. Fourteen days after diabetes confirmation, the animals were euthanized. Livers were fixed in buffered formalin, embedded in paraffin, sectioned into 3 μm slices, stained with Hematoxylin and Eosin (H&E), and analyzed under a light microscope (40x magnification). The images obtained were processed using ImageJ software (NIH, USA), with threshold adjustment to 8-bit and the application of filters: minimum auto threshold, median (300 pixels), LUT inversion, hole filling, and watershed. The images were analyzed using the FracLac plugin (Charles Sturt University, Australia). The fractal dimension (Db∞) was calculated through cell counting, and lacunarity (Λ) was also measured (Figure 1). Results were statistically analyzed using the non-parametric Kruskal-Wallis test, followed by Dunn's post hoc test ($p \leq 0.05$). Fractal analysis revealed an increase in heterochromatin distribution in the DM group, while the DM+CBL group was able to reverse this increase to levels similar to the control group. In contrast, lacunarity did not show statistically significant differences among the groups (Figures 2 and 3). Therefore, it can be concluded that DM may cause alterations in the nuclear organization of hepatic cells, marked by an increase in heterochromatin distribution, suggesting greater DNA compaction and possible gene repression, which may affect liver function. However, CrataBL lectin was able to reverse these changes, restoring patterns similar to those of the control group. Despite the lack of significant changes in lacunarity, the results indicate that CrataBL holds therapeutic potential in protecting the liver against the effects of diabetes.

[1] F.K.A. Barreto, Antihyperglycemic and Antioxidant Activity of *Bryothamnion seaforthii* Lectin in Diabetic Rats (2016).

[2] Rocha AA da et al. Lectin from Crataeva tapia bark improves tissue damagens and plasma hyperglycimia in alloxan-induced diabetic mice. (2013)
[3]Silva JP, Oliveira MR. Relationship between diabetes mellitusand metabolic-associated fatty liver disease: a review. *Revista Brasileira de Endocrinologia* (2025)
[4]Giestas S et al.. Liver disease and diabetes mellitus – a bidirectional relationship. *Revista Portuguesa de Diabetes (2015)*
[5]M. Opes et al., Anais do XI RAIC e V RAIDTEC, UFRRJ (2023).
[6] This research was supported by CNPq (Brazil).

Formula 1:

$$D_{bc} = -\lim_{\varepsilon \to 0} \left[\frac{\log N(r+\varepsilon) - \log N(r)}{\log(r+\varepsilon) - \log r} \right]$$

Formula 2:

$$\Lambda = \left[\sum_{g} \sum_{i} \left(1 + (\sigma|\mu)^2 \right) \right] \Big/ n$$

Figure 01. Fractal parameters Formulas

Figure 02. Graphics exhibiting the Fractal dimension and Lacunarity from the Experimental group's images.

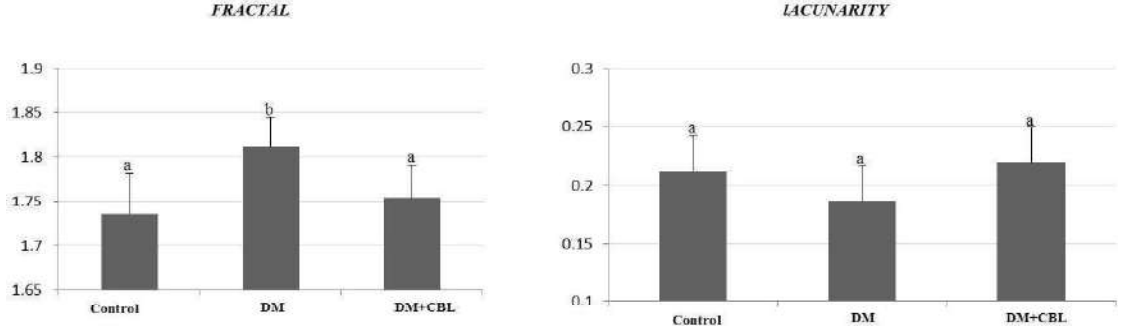

A – Fractal: increased heterochromatin distribution in the DM group. The DM+CBL group was similar to the control. B – Lacunarity: no significant difference among the groups.

Figure 03. Segmented photomicrographies from the experimental groups.

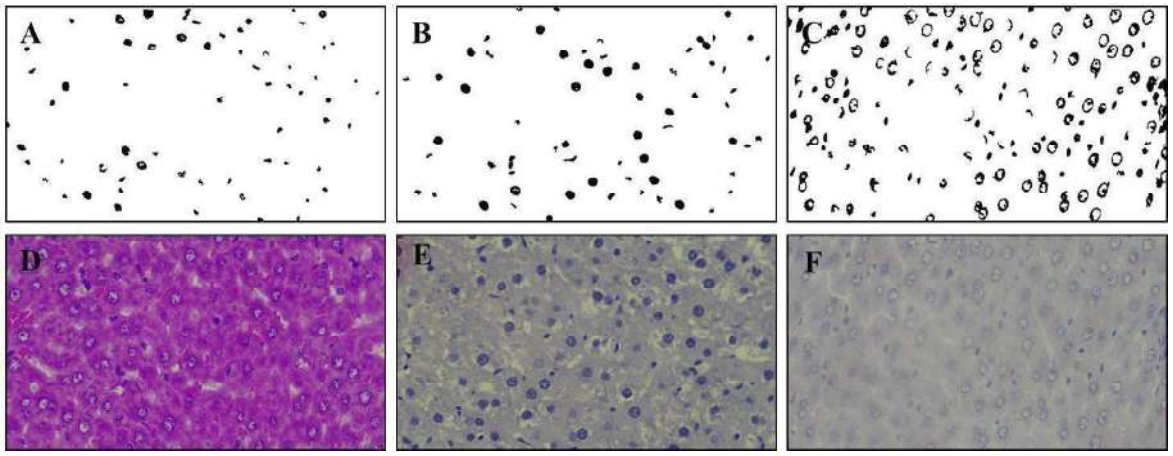

Photomicrograph of the liver from animals in the experimental groups, after using the ImageJ software for fractal and lacunarity analysis. In images A, B, and C are the segmented photomicrographs, and in images D, E, and F are the original photomicrographs stained with H&E. Control group (A, D), DM group (B, E), DM+CBL group (C, F).

Profile Of Prostatic Developmental Markers In Prostate Development Of The Spontaneously Hypertensive Rats

Max Vinicius Malmann Medeiros[1], Nathany Ribeiro Lima dos Santos[1], Barbara Costa Malmann Medeiros[1], Gabriel dos Santos Lima Sardinha[1], Fernanda Cristina Alcantara dos Santos[1], Manoel Francisco Biancardi[1]

[1] Institute of Biological Sciences III, Department of Histology, Embryology and Cell Biology
*vinicius.50@discente.ufg.br

Prostatic organogenesis is a complex process involving intricate signaling pathways, crucial for the proper development and function of the prostate gland [1]. Benign prostatic hyperplasia (BPH) is a common condition, and spontaneously hypertensive rats (SHR) serve as a valuable experimental model to study both hypertension and the spontaneous development of BPH in early life [2]. Understanding the molecular mechanisms underlying prostatic development in SHR rats is essential to elucidate the pathogenesis of BPH. This study aimed to evaluate the expression patterns of key developmental markers, specifically the transcription factor NKX3.1 and fibroblast growth factor 2 (FGF2), during the early postnatal stages of prostatic organogenesis in SHR rats. In this study, 10 experimental groups were created, consisting of 5 Wistar groups and 5 SHR groups, with 10 animals in each. The groups were classified according to ages of 1, 15, 25 days after birth. Euthanasia of the animals was performed according to the protocol defined by CEUA/PRPI/UFG (Protocol nº042/23). Prostatic complexes were collected from male SHR and Wistar rats, at 1, 15, and 25 postnatal days, fixed, processed, and embedded in Paraplast, then cut into 5 μm sections. Immunohistochemistry reactions were performed to analyze the immunostaining pattern of NKX3.1 and FGF2. Optical densitometry was used to quantify the expression of both factors. Our findings reveal a significant differential expression of these factors at the ages studied. For NKX3.1, SHR rats exhibited a significant reduction in expression for the 1 ($p < 0.0001$) (Fig.1 A, B, C), 15 ($p < 0.0001$) (Fig.1 D, E, F), and 25 postnatal days ($p < 0.05$) (Fig.1 G, H, I), compared to control animals (Fig.1 G, H, I). On the other hand, FGF2 expression showed no significant difference between SHR and Wistar rats at 1 postnatal day (Fig.2 A, B, C). However, at 15 postnatal days, SHR rats showed significantly higher levels of FGF2 compared to Wistar rats ($p < 0.01$) (Fig.2 D, E, F), while at 25 postnatal days, FGF2 levels were significantly lower in SHR rats ($p < 0.01$) (Figure 2 G, H, I). These results suggest a dysregulation in the intricate balance between NKX3.1 and FGF2 during early prostatic development in SHR rats, compared to Wistar. The persistent reduction of NKX3.1, a known tumor suppressor and crucial regulator of prostatic differentiation, along with the fluctuating expression of FGF2, a potent mitogen, indicates an altered signaling environment that may predispose SHR rats to prostatic abnormalities, including BPH. This differential expression pattern highlights the importance of these factors in the context of prostate health and disease, providing valuable insights into the initial molecular events that may contribute to the spontaneous development of BPH in this animal model. Further investigations into the precise interactions and downstream effects of these altered expression profiles are

warranted to fully understand their role in prostatic pathology. I would like to thank CAPES for the financial support of this research.

[1] S. Sanches, et al., Microsc. Res. Tech. 77 (6) (2014) 458.
[2] K. Okamoto, K. Aoki, Jpn. Circ. J. 27 (3) (1963) 282.
[3] This research was supported by Capes (Brazil).

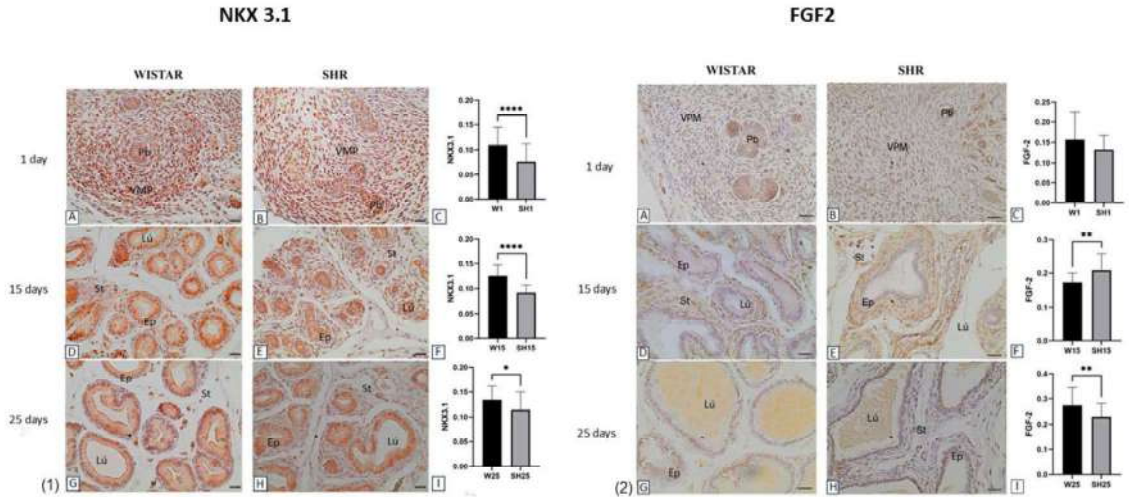

Figures 1 and 2. Expression of NKX3.1 (Fig. 1) and FGF2 (Fig. 2). VMP (Ventral Mesenchymal Pad), Pb (Prostatic Bud), St (Stroma), Lu (Lumen), Ep (Epithelium). The values in the graphs (Figs. 1 and 2 C, F, I) correspond to the mean +/- standard deviation. Asterisks indicate statistically significant differences between experimental groups (*=$p<0.05$; **=$p<0.01$; ** = $p<0.0001$). Photomicrographs at 40X objective. Scale bar = 20 µm.

Protective Role of High-intensity Resistance Training on Neuromuscular Junction in a Rheumatoid Arthritis Rat Model

Karoline Calichio Medeiro Pereira[1]*, Flavia Heloisa da Silva[1], Gabriella Lopes Cappellaro[1], Gladson Ricardo Flor Bertolini[2], Márcia Miranda Torrejais[1], Lucinéia de Fátima Chasko Ribeiro[1]

[1] Struct. & Funct. Bio Lab, CBHS, UNIOESTE, Cascavel, PR, Brazil
[2] Injuries & Physio Res. Lab, CBHS, UNIOESTE, Cascavel, PR, Brazil
*karolcalichio@gmail.com

Rheumatoid arthritis (RA) is an autoimmune disease that primarily affects the joints but also causes systemic chronic inflammation, marked by the release of pro-inflammatory cytokines such as TNF-α, IL-1β, and IL-6 [1]. These cytokines promote muscle catabolism and accelerate motor denervation by impairing the neuromuscular junction (NMJ), leading to muscle atrophy and functional loss [2,3]. In this context, physical exercise has shown promise in the management of RA [4]. However, its effects on NMJs in RA models remain unclear. This study employed 24 male Wistar rats (average age: 12 weeks), randomized into four groups (n = 6): Control Group (CG), non-exercised and non-induced; Arthritis Group (AG), non-exercised and RA-induced; Exercise Group (EG), exercised and non-induced; and Exercise + Arthritis Group (EAG), exercised and RA-induced. The resistance training protocol (ladder climbing) consisted of 31 sessions on alternate days over 9 weeks. The load was progressively adjusted weekly, beginning with 3 sets of 8 repetitions at 25% body weight and culminating in 6 sets of 8 repetitions at 100% body weight. Training ceased one day prior to RA induction. RA was induced using Complete Freund's Adjuvant (CFA) containing Mycobacterium butyricum (0.5 mg/mL, Difco®). A 50 µL subcutaneous intradermal injection was administered at the base of the tail for pre-sensitization, followed seven days later by an intra-articular injection into the synovial cavity of the right knee. Animals were euthanized on days 78 and 79 using carbon dioxide inhalation followed by guillotine decapitation. The medial proximal quarter of the right rectus femoris muscle was fixed in Karnovsky's solution [5], refrigerated, longitudinally sectioned with stainless steel blades, and subjected to a non-specific esterase histochemical reaction [6]. Photomicrographs were captured using an Olympus DP71 camera (Tokyo, Japan) mounted on an Olympus BX60® microscope, under a 20× objective lens, and processed with DP Controller 3.2.1 276 software. NMJ analysis (cross-sectional area, major and minor diameters) was conducted with Image Pro Plus 6.0® software (Media Cybernetics, Maryland, USA) using 100 NMJs per animal. Statistical analysis revealed the following: CSA showed a significant reduction in the AG compared to the CG (11.6% decrease; $F_{3,20} = 7.5$; $p < 0.01$). No significant differences were found between the EAG and the other groups (AG, EG, and CG), suggesting preservation of NMJ morphology (Figure 1A). A significant increase in major NMJ diameter was found in EG (10.5%, $p < 0.001$) and EAG (8.7%, $p < 0.05$) compared to CG ($F_{3,20} = 3.9$; $p < 0.05$). Minor diameter analysis revealed a significant reduction only in AG (9.8% compared to CG; $F_{3,20} = 0.06$; $p < 0.001$) (Figure 1B). Notably, the NMJs of the EAG group were statistically similar to those of the CG across all parameters, indicating that preventive high-intensity resistance exercise preserved NMJ morphology in the presence of RA. These findings support the hypothesis that exercise mitigates the deleterious neuromuscular effects of RA.

[1] S. Ganeshalingam et al., *Molecular Immunology* 184 (2025) 112–122.
[2] M.R. Deschenes et al., *Neuroscience* 316 (2016) 167–177.
[3] N.E. Gilhus, *The Neuromuscular Junction*, Elsevier, Amsterdam, 2025.
[4] M. Gossler et al., *Journal of Bodywork and Movement Therapies* 44 (2025) 138–148.

[5] M.J. Karnovsky, *The Journal of Cell Biology* 27 (1965) 137–138.
[6] G.M. Lehrer, L. Ornstein, *Journal of Biophysical and Biochemical Cytology* 6 (1959) 399–406.
[7] This research was supported by CNPq (Brazil).

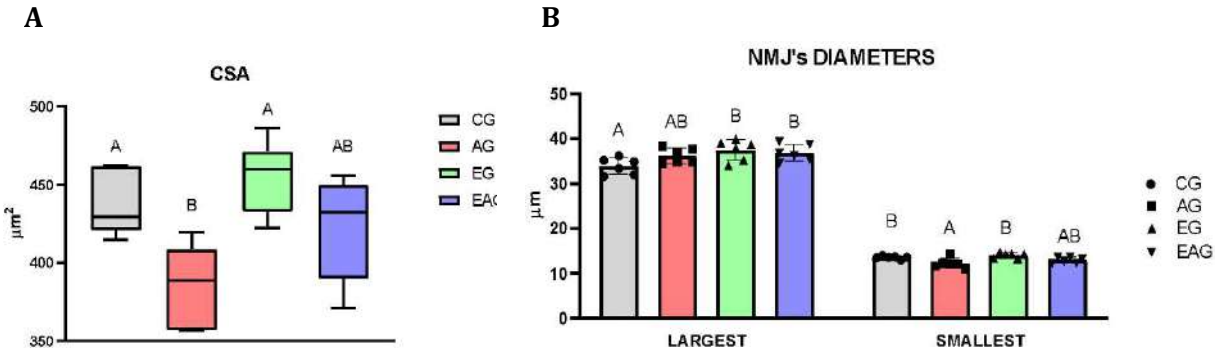

Figure 1. A: Cross-sectional area (CSA) and major diameter of NMJs in the rectus femoris muscle of Wistar rats with or without RA and with or without exposure to high-intensity resistance exercise. **B:** Minor diameter of NMJs across the experimental groups.

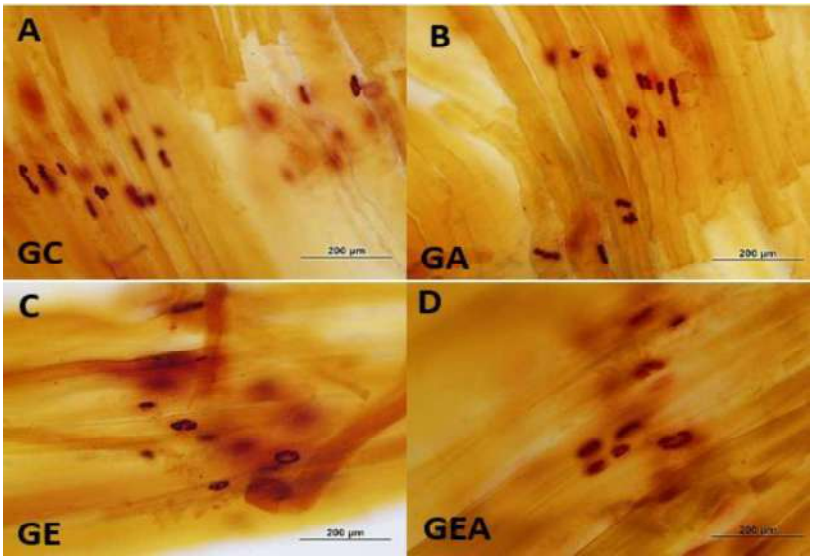

Figure 2. A, B, C and D: Control group (CG), arthritis group (AG), exercise group (EG), and exercise plus arthritis group (EAG), respectively. Neuromuscular junctions (NMJs) with rounded, oval, and elliptical morphologies observed in all groups.

Raman Microscopy for Identification of Chemical Substances with Immunotherapeutic Potential in *Momordica charantia*.

Eduardo Alves[1], José Fábio F. de Souza[2], Rosilene S. Façanha[3], Francileia F. de Souza[4], Diogo S. Couto[5], Isabela A. Marques[6], Fábio N. Reis[7], Hoxana X. L. Kattah[8], Ana P. Peconick[9].

[1] Professor in Plant Patholy department (DFP/UFLA), [2]Ph.D. student in Agronomy/Phytopathology Postgraduate Program – Federal University of Lavras (DFP/UFLA), [3]Federal Institute of Education, Science and Technology of Southern Minas Gerais – Três Corações Campus, [4]Postgraduate Program in Water Resources Management in the Amazon – Federal University of Acre, , [5]Undergraduate Student in Biological Sciences – Federal University of Lavras, [6]Ph.D. student in Agrochemistry – Federal University of Viçosa – Advanced Thermokinetics of Advanced Systems (ATOMS) Group – DEQ/UFV, [7]Undergraduate Student in Veterinary Medicine – Federal University of Lavras / CNPq Scholarship Holder, [8]Master's Student in the Veterinary Sciences Program – Federal University of Lavras – UFLA/DMV, [9] Professora in Department of Veterinary Medicine – Federal University of Lavras – DMV, UFLA.

*email@corresponding.author: ealves@ufla.br

The bitter melon (*Momordica charantia*), a member of the Cucurbitaceae family, is well known for its medicinal and pharmacological chemical properties [1]. In South America, Africa, and Asia, it is widely used as a natural medicine for various diseases [2]. Although its bioactive compounds remain underexplored, the species has demonstrated significant therapeutic potential against cancer. In the present study, Raman Microscopy (RM) was used to analyze and see the preservation of bioactive compounds in fruits and leaves of *M. charantia*, in both fresh and dried states. For RM analysis leaves and fruits were collected directly from plants at the Federal University of Lavras Campus. After harvested, while samples were dehydrated in an oven and later subjected to spectroscopic analysis using a Confocal Raman Microscopy System – Alpha300 model, Witec. A 785 nm laser was used, with 10× and 50× objective lenses. The analysis aimed to identify similarities in characteristic peaks and curves corresponding to phenolic compounds, proteins, and other biomolecules associated with immunological and anticancer activity. The overlapping Raman spectra indicated a high degree of similarity between the fresh and dried fruit and leaf samples. Key peaks related to carotenoid compounds [3 and 4] appeared at approximately 1000 cm^{-1} and 1527 cm^{-1}, with carotenoids and carbohydrates at around 1154 cm^{-1}, and aliphatic compounds near 1387 cm^{-1} (**Figure 1**). The overlapping spectral curves between the samples suggest that certain compounds are preserved in both the fresh and dried fruit and leaves. This spectral stability points to the conservation of active principles with immunotherapeutic potential, even after sample dehydration. The results indicate that bioactive compounds are preserved after leaf drying, maintaining the plant's immunotherapeutic potential in its dried form. RM proved effective in identifying and verifies the stability of compounds, with potential use in formulations of phytotherapics. Further studies will investigate the functional efficacy of these compounds against cancer and RM will be used in studies of the bioavailability of hydroethanolic extracts tested *in vitro* on HeLa cell lines and in nanoencapsulated forms compounds [5].

Figure 1 - Graph showing the spectral quantification results of the compounds and the overlap of the curves obtained for dry and fresh leaves, also in fruit of bitter melon *Momordica charantia*. The values are expressed in wavenumber units.

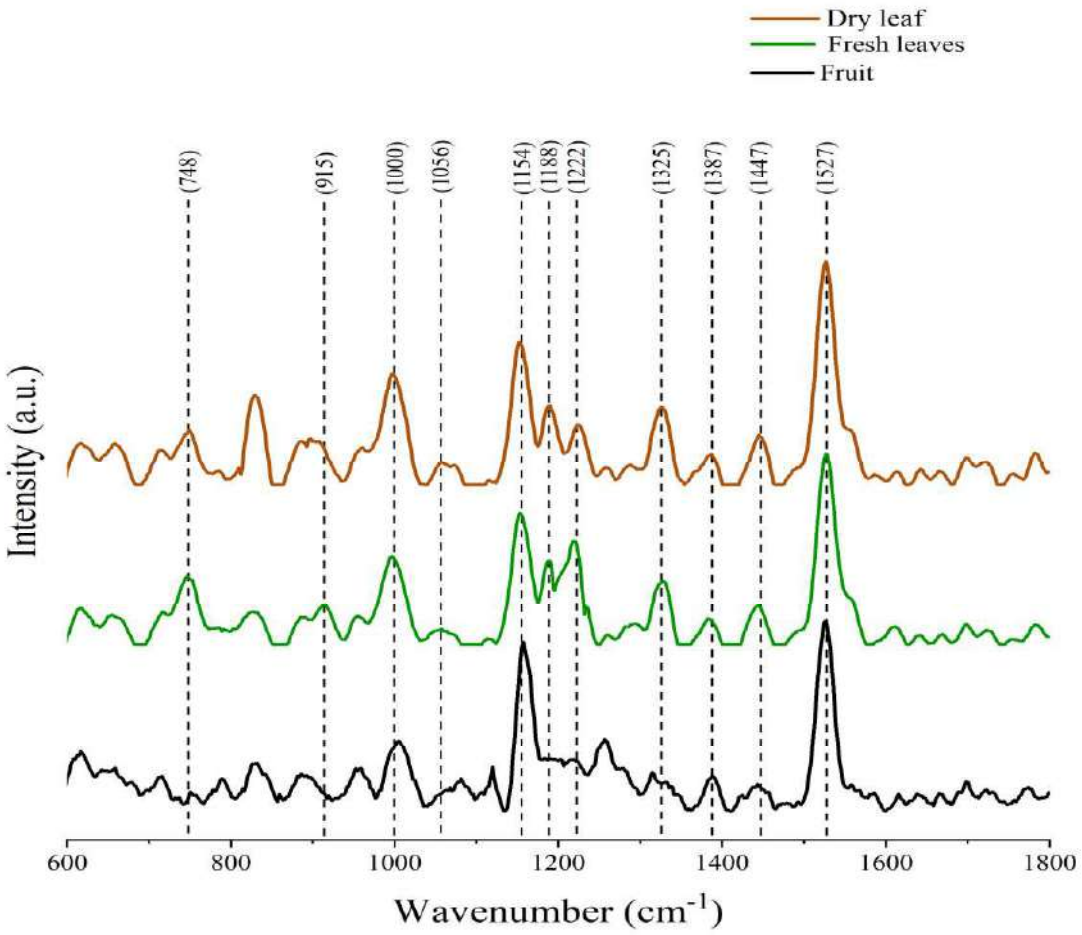

[1] F. Chen et al., Antioxidant activity of *Momordica charantia* polysaccharide and its derivatives. International Journal of Biological Macromolecules, 138, p. 673–680, (2019). doi.org/10.1016/j.ijbiomac.2019.07.129.

[2] Y. Y. Deng et al., Immunomodulatory activity and partial characterization of polysaccharides from *Momordica charantia*. Molecules, v. 19, n. 9, p. 13432-13447, (2014). doi:10.3390/molecules190913432.

[3] T. Dhanani et al., *Raman Spectroscopy Detects Changes in Carotenoids on the Surface of Watermelon Fruits During Maturation*. Frontiers in Plant Science, Lausanne, v. 13, p. 832522, (2022). doi: 10.3389/fpls.2022.832522.

[4] L. Sanchez et al., Raman Spectroscopy Enables Non-invasive and Confirmatory Diagnostics of Salinity Stresses, Nitrogen, Phosphorus, and Potassium Deficiencies in Rice. Frontiers in Plant Science, Lausanne, v. 11, p. 573321, (2020). doi: 10.3389/fpls.2020.573321.

[5] This research was supported by: Laboratory of Electron Microscopy and Ultrastructural Analysis (LME - UFLA, Funding Authority for Studies and Projects (FINEP), Research Support Foundation of the State of Minas Gerais (FAPEMIG), National Council for Scientific and Technological Development (CNPq), and Coordination for the Improvement of Higher Education Personnel (CAPES).

SARS-CoV-2 Induces Morphological Alterations and Inflammatory Responses in Human Placental Tissues

Alves F.A.V.[1,2]*, Salomão N.[2], Portari E.A.[3], Batista M.M.[3], Guedes H.L.M.[4], da Silva J. F. R.[1], Alves, L.L.[1], Carvalho J.J.[1], Rabelo K. [1,2]

[1] Laboratory of Ultrastructure and Tissue Biology, Biology Institute, Rio de Janeiro State University.
[2] Interdisciplinary Laboratory of Medical Research, Oswaldo Cruz Institute, Oswaldo Cruz Foundation.
[3] Pathological Anatomy, Fernandes Figueira Institute, Oswaldo Cruz Foundation.
[4] Laboratory of Clinical Immunology, Oswaldo Cruz Institute, Oswaldo Cruz Foundation.

In late 2019, the emergence of a novel coronavirus led to the development of severe acute respiratory syndrome (SARS), culminating in a global pandemic, which has led to enormous cases of high morbidity and mortality in the world [1]. Previous studies have associated infections caused by various coronaviruses—including SARS-CoV, MERS-CoV, and SARS-CoV-2—with a range of obstetric complications, and even in cases of miscarriage [2-4]. However, morphological and molecular investigations of placental tissue from SARS-CoV-2-infected pregnant women remain limited and inconclusive. This study aimed to characterize histopathological alterations and the local immunological profile in placental samples obtained from five unvaccinated pregnant women infected with SARS-CoV-2. Placental tissues were collected at Casa de Saúde Laranjeiras LTDA and subjected to routine histological staining and special staining protocols to assess morphological changes. Additionally, immunofluorescence and immunoperoxidase techniques were employed to detect the SARS-CoV-2 Spike protein and to evaluate the expression of immune cell markers and pro-inflammatory cytokines. Histopathological analysis revealed the presence of a mononuclear inflammatory infiltrate, extensive fibrin deposition, and trophoblast necrosis. SARS-CoV-2 Spike protein was detected in trophoblasts and CD163+ cells, indicating that infection occurs in activated placental macrophages in addition to the cells that make up the placental membrane. The inflammatory infiltrate was predominantly composed of CD163+, CD68+, CD4+, and CD8+ immune cells, showing that the inflammatory profile is consistent with that of a viral infection with a chronic inflammatory process. Furthermore, elevated expression of pro-inflammatory cytokines—including TNF-α, IL-1β, and IL-6—was observed in both maternal and fetal cells, characterizing the proinflammatory environment characteristic of the cytokine storm caused by covid-19. These findings contribute to the growing body of evidence suggesting that SARS-CoV-2 infection may disrupt placental homeostasis, promote a pro-inflammatory microenvironment, and potentially facilitate vertical transmission. Such alterations may have significant implications for fetal development and pregnancy outcomes [5].

[1] ZHOU, P. et al., Nature, (2020) 270-273.
[2] RICHTMANN, R. et al., Case Reports in Women's Health, (2020) e00243
[3] WONG, S. F. et al., American Journal of Obstetrics and Gynecology, (2004) 292–297
[4] ASSIRI, A. et al., Clinical Infectious Diseases, (2016) 951-953
[5] This research was supported by UERJ, FIOCRUZ, CNPq and FAPERJ.

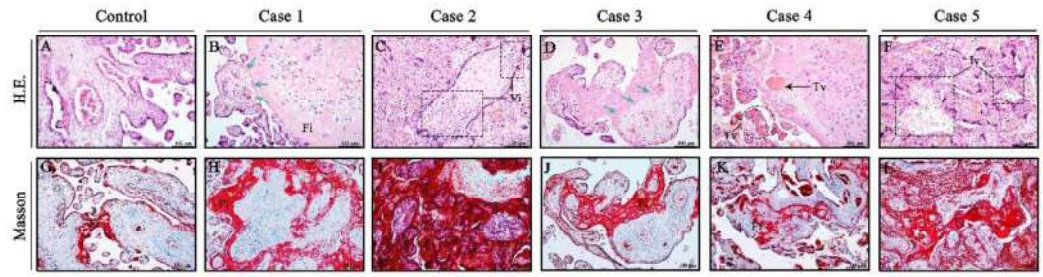

Figure 1. Histopathological changes in placental tissue infected by SARS-CoV-2. (A and G) Pre-pandemic control placenta revealing regular aspect and small fibrin deposits. **(B-F)** Representative microphotographs of SARS-CoV-2 infected placentas stained by Hematoxylin and Eosin. **(H-L)** Extensive fibrin deposits around perivillous areas in SARS-CoV-2 infected placentas. Fibrin (Fi); trophoblastic necrosis (green arrow); villitis (Vi); vessel thrombosis (Tv); and intervillitis (Iv).

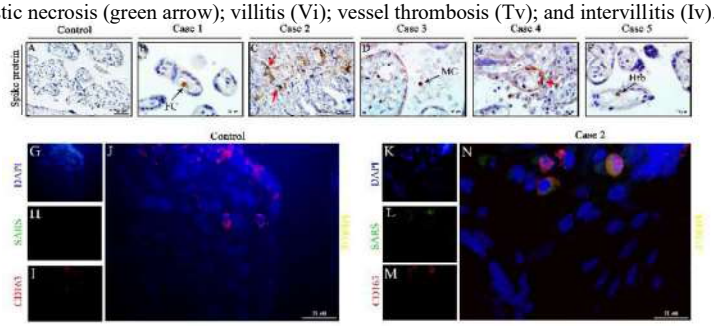

Figure 2. Detection of spike protein in placental cells. (A) Pre-pandemic control placenta. Spike protein detected in **(B)** cells of fetal origins, **(C, E)** trophoblastic cells (red arrows), **(D)** maternal cells and **(F)** Hofbauer cells. **(G-J)** Immunofluorescence showing absent presence of SARS-CoV-2 antigens in Hofbauer cells ($CD163^+$). **(K-N)** Dual staining of spike protein and $CD163^+$ cells in case two unmasking the viral permittivity of Hofbauer cells. Fetal cells (FC); trophoblast cells (red arrows); maternal cells (MC); Hofbauer cells (Hfb).

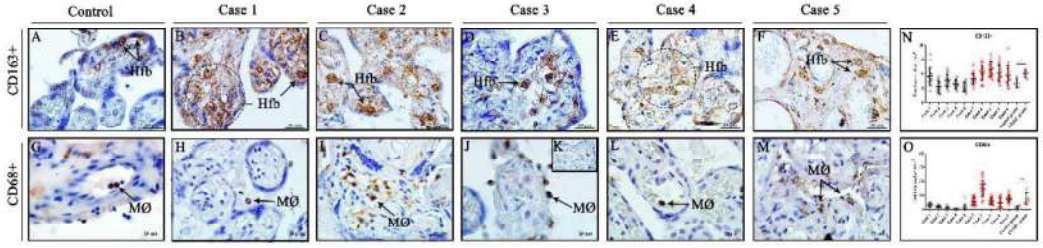

Figure 3. Detection of Hofbauer cells and macrophages. (A and G) Detection of Hofbauer cells and macrophages in chorionic villi in control placenta. **(B-F)** Detection of hyperplasic Hofbauer cells **(H-M)** Detection of hyperplasic macrophages infiltrating chorionic villi, fetal circulation and maternal blood. **(N, O)** Quantitative analysis of $CD163^+$ and $CD68^+$ cells. Hofbauer cells (Hfb); macrophages (MØ). Asterisks indicate significant differences using the T non-parametric statistic test (*$p < 0.05$ and **$p < 0.001$).

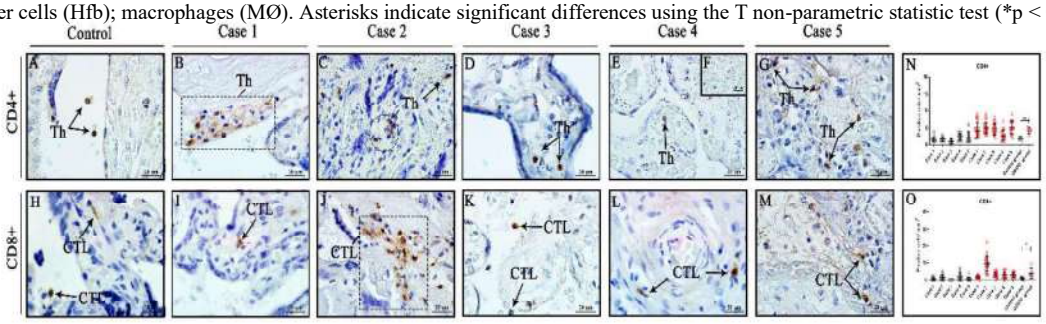

Figure 4. Detection of T helper cells and cytotoxic lymphocytes. (A- G) Detection of T helper cells and cytotoxic lymphocytes in maternal blood and chorionic villi of pre-pandemic control placenta, respectively. **(H-M)** Detection of T lymphocytes circulating in maternal blood and infiltrated in chorionic villi. **(N and O)** Quantitative analysis of $CD4^+$ and $CD8^+$ cells. T helper cell (Th); cytotoxic lymphocyte (CTL). Asterisks indicate significant differences using the F statistic (*$p < 0.05$).

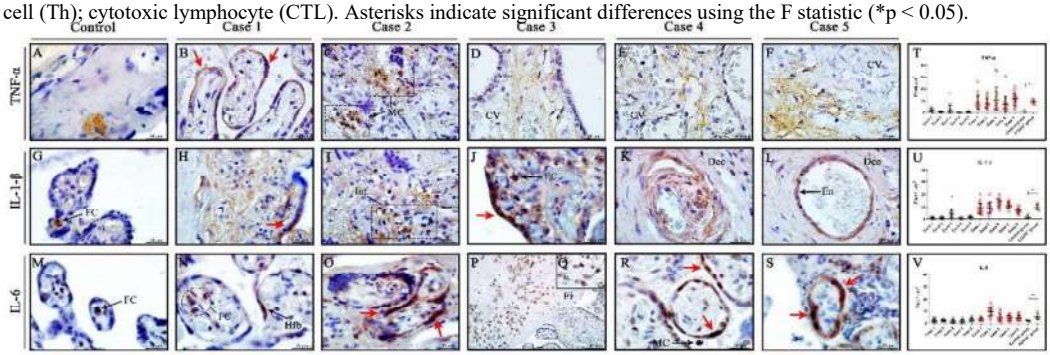

Figure 5. Detection of TNF-α, IL-1-β e IL-6. (A, G and M) Detection of TNF-α, IL-1-β e IL-6 in pre-pandemic control placenta. **(B-F)** Detection of TNF-α expression by trophoblast cells, maternal cells and mesenchymal cells of chorionic villi. **(H-L)** Detection of IL-1-β expression by trophoblast cells, inflammatory infiltrates, fetal cells, cells near decidua vessels and endothelium. **(N-S)** Detection of IL-6 expression by trophoblast cells, fetal cells, Hofbauer cells and cells associated with fibrin deposits. **(T, U and V)** Quantitative analysis of TNF-α, IL-1-β and IL-6 expressions. Trophoblast cells (red arrows); maternal cells (MC); chorionic villi (CV); fetal cells (FC); inflammatory infiltrate (Inf); decidua (Dec); endothelium (En); Hofbauer cells (Hfb); fibrin (Fi). Asterisks indicate significant differences using the T non-parametric statistic test (**$p < 0.001$).

Structural and functional changes in the submandibular gland of rats treated with paroxetine

Bruna Carolina da Silva[1], Paulo Sérgio Cerri[2], Estela Sasso Cerri[2]*

[1]Universidade Federal de São Paulo – Escola Paulista de Medicina (UNIFESP/EPM),
[2]Faculdade de Odontologia de Araraquara – Universidade Estadual Paulista (FOAr/UNESP)
*estela.sasso@unesp.br

In rodents, the submandibular gland (SMG), composed of a secretory portion (serous and/or mucous acini) and a duct system, has a different type of duct, known as the granular convoluted tubule (GCT). Myoepithelial cells, rich in actin, surround the acini and ducts and, due to their contractile capacity, play a crucial role in saliva expulsion [1]. Salivary glands are under serotonergic control. Both 5-HT (serotonin) and its receptor, 5-HT1A, can be found in the acini and ducts [2]. In the SMGs, immune cells such as macrophages and mast cells, express 5-HT receptors, which can induce or inhibit immune responses [3]. Selective serotonin reuptake inhibitors (SSRIs) are the most commonly prescribed antidepressants for the treatment of depression and anxiety disorders [4]. Paroxetine, a frequently prescribed SSRI, exerts some side effects, such as hyposalivation and/or dry mouth [5,6]. The aim of this study was to investigate the effects of paroxetine on the histoarchitecture of acini and GCTs of adult rat SMGs, with emphasis on the myoepithelial cells integrity and incidence of mast cells. Adult male rats were distributed into two groups (n = 10/group): paroxetine - 35 days (PG) and control (CG). PG animals received paroxetine hydrochloride (by gavage) for 35 consecutive days, and the control group received water by the same route (CEUA 20/2017). In the sections stained with H&E, GCT diameters were measured and, in Alcian Blue (A.B.)-stained sections, AB-positive mast cells surrounding the blood vessels were quantified. SMG cell density was assessed by quantifying the number of glandular cell nuclei, and actin immunolabeling in myoepithelial cells was evaluated by immunofluorescence. The histological analyses (H&E) of SMGs showed preserved glandular tissue in CG (Fig. 1A). In contrast, in PG, several glandular cell nuclei showed irregular outline and condensed chromatin, typical of apoptosis (Fig. 1B). This finding was associated with significant reduction of cellular density (Fig. 1F), suggesting glandular atrophy. Curiously, a significant increase of GCT diameter was observed in PG (Fig. 1E). This hypertrophy may be related to a serotonin-modulated response, likely due to mechanisms associated with increased protein secretion in salivary glands [7]. Thus, chronic exposure to paroxetine may have potentiated the secretory activity of GCTs, inducing hypertrophy of these structures. Such structural changes may be caused by a prolonged serotonin stimulation, reinforcing the serotonergic effect in the SMG physiology. The number of mast cells surrounding the blood vessels increased significantly in the stroma of PG (Figs. 1C-D and 1G). As paroxetine influence the immune response [8], and mast cells (immunological cells) express serotonin receptors [3], the increased number of these cells may be related to the paroxetine serotonergic effect. The immunoexpression of actin also reduced (Figs. 2A-2C), indicating dysfunction of myoepithelial cells, a disturbance that may explain xerostomia and/or hyposalivation. In conclusion, the data suggest that the serotonergic action of paroxetine may impair the SMG structure and contractile function, explaining, at least in part, the hyposalivation and/or xerostomia reported by individuals taking this antidepressant [9].

[1] Chibly et al., Physiological Review, 2022;
[2] Huang et al., Journal of Molecular Histology, 2003;
[3] Herr; Bode; Duerschmied, Frontiers in Cardiovascular Medicine, 2017;
[4] Lo et al., Biological Psychiatry Global Open Science, 2025;
[5] Germann et al., Profiles of Drug Substances, Excipients and Related Methodology, 2013;
[6] De Almeida et al., Oral Surgery, Oral Medicine, Oral Pathology, Oral Radiology, and Endodontology, 2008;
[7] Turner et al., Journal of dental research, 1996;
[8] Chen et al., Psychoneuroendocrinology, 2018;
[9] This research was supported by CAPES (001) and FAPESP (2021/07207-6).

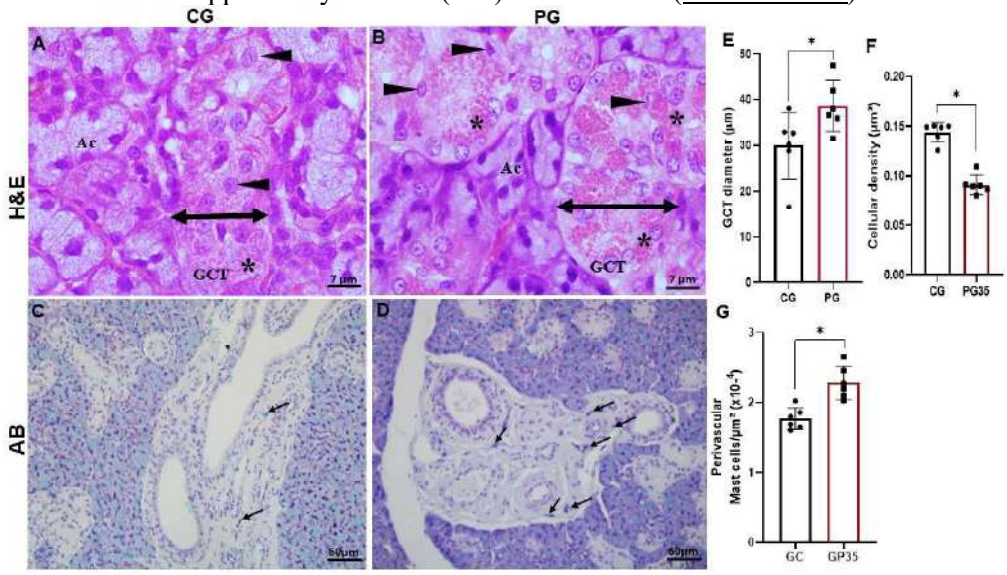

Figure 1: Photomicrographs of SMG sections stained with H&E (A and B) and A.B. (C and D). A and B: Serous acini (Ac), granular convoluted tubules (GCT), nuclei (arrowheads) and cytoplasmic granules (*). The GCTs are larger in B than in A (double headed arrows). C and D: AB-positive mast cells (arrows). E: Significant increase in GCT diameter (*p<0.05). F: The cellular density reduced significantly in PG (*p<0.0001). G: Number of mast cells increased significantly in PG (*p<0.0012).

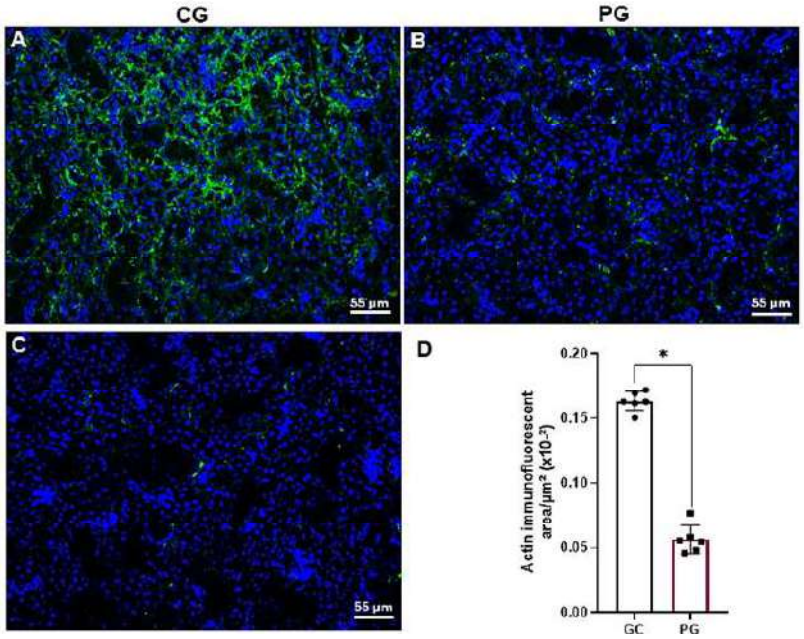

Figure 2: Photomicrographs of SMG sections subjected to actin immunofluorescence and nuclear staining by DAPI. A-B: Weak actin (green) in PG compared to CG. C: Negative control shows only autofluorescence blood red cells in the blood vessels. D: Significant reduction of actin immunofluorescence area (*p<0.0001).

Study of Annexin A1 in Mouse Diabetic Cardiomyopathy Induced by Streptozotocin

Sarah Bezerra Brum da Silva*[1], Diego Dias dos Santos[1], Renata Pereira Lourenço[1], Renata Ramos Vieira[1], Rafael André da Silva[2], Luís Philipe de Souza Ferreira[1], Kátia de Vasconcelos[1], Cristiane Damas Gil[1], [2]

[1] Structural and Functional Biology Graduate Program, Department of Morphology and Genetics, Universidade Federal de São Paulo - UNIFESP, SP, Brazil.
[2] Biosciences Graduate Program, Instituto de Biociências, Letras e Ciências Exatas, Universidade Estadual Paulista (UNESP), São José do Rio Preto, Brazil.
*sarah.brum@unifesp.br

Diabetes mellitus (DM) is a metabolic disorder associated with multisystemic complications, among which cardiovascular dysfunction remains the leading cause of death. Diabetic cardiomyopathy (DCM), a direct consequence of chronic hyperglycemia, is characterized by cardiac inflammation, apoptosis, and accumulation of reactive oxygen species (ROS), all impairing myocardial contractility and cardiac output [1]. Despite the implementation of several therapeutic strategies to mitigate DCM, cardiac complications in diabetic patients remain prevalent. Therefore, identifying new therapeutic targets is essential for developing more effective interventions against DCM. In this context, annexin A1 (AnxA1), a 37-kDa anti-inflammatory protein, stands out for its regulatory roles in various phases of the inflammatory response and its cardioprotective effects in acute myocardial ischemia, including the preservation of contractile function and cardiomyocyte viability [2, 3]. However, its role in regulating cardiac function under diabetic conditions remains poorly understood. To investigate the mechanisms of AnxA1 action in cardiomyocytes under diabetic stress, we established a streptozotocin (STZ)-induced experimental model of DM in male C57BL/6 mice [4], both wild-type ($AnxA1^{+/+}$) and AnxA1 knockout ($AnxA1^{-/-}$). Animals were divided into two experimental groups: the DM group received intraperitoneal STZ injections (65 mg/kg) for five consecutive days, while the control (CTR) group received only vehicle (citrate buffer). Body weight and blood glucose levels were monitored at 15, 30, 60, and 90 days after DM induction. On day 90, cardiac function was assessed by echocardiography, followed by blood and heart collection for further analyses. DM induction was confirmed by hyperglycemia (>350 mg/dL) from day 15 onwards (Figure 1A) and body weight loss from day 60, consistent with a type 1 diabetes phenotype. Echocardiographic parameters revealed that DM $AnxA1^{+/+}$ mice exhibited significantly prolonged ejection time, compensatory bradycardia, and reduced A, A', and S' wave amplitudes in pulsed and tissue Doppler analyses compared to CTR $AnxA1^{+/+}$ and DM $AnxA1^{-/-}$ groups. Histological evaluation showed a reduction in cardiomyocyte perimeter in both DM groups relative to their controls, suggesting possible cardiomyocyte atrophy (Figure 1B-F). In addition, peripheral blood analysis revealed a significant decrease in total leukocyte count in DM $AnxA1^{-/-}$ mice compared to DM $AnxA1^{+/+}$ mice, primarily due to reduced neutrophil counts, indicating a distinct systemic inflammatory profile associated with AnxA1 deficiency. Together, these findings indicate that the presence of endogenous AnxA1 influences key functional and structural alterations in the diabetic heart. While hyperglycemia induced significant cardiac impairment in $AnxA1^{+/+}$ mice, the absence of AnxA1 appeared to mitigate some of these effects, suggesting a complex and context-dependent role of this protein in DCM. Future studies are warranted to elucidate the molecular mechanisms underlying these observations and to determine whether modulating AnxA1 signaling may offer novel therapeutic avenues for the treatment of DCM.

[1] A. Guha et al., Current Opinion in Cardiology 23(3) (2008) 241–248.
[2] M.A. Sugimoto et al., J Immunol Res. (2016) 2016:8239258.
[3] G.S.D. Purvis et al., Front Immunol. 10 (2019) 938.
[4] B. Martín-Carro et al., International Journal of Molecular Sciences 24(12) (2023) 10309.

[5] This research was supported by CAPES (001 Code), FAPESP, and CNPq (308524/2022-5).

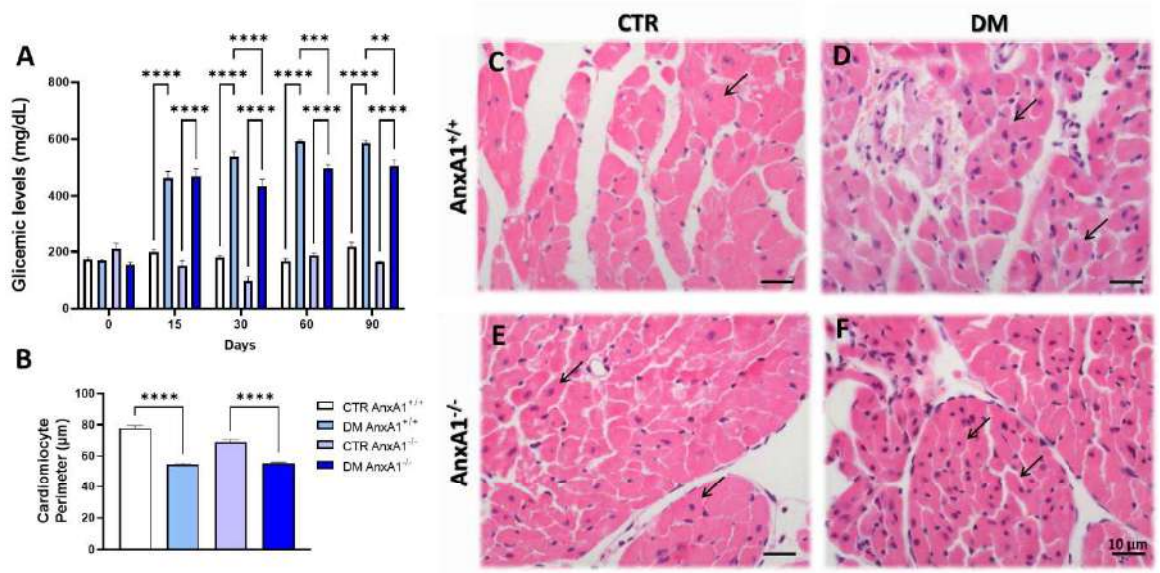

Figure 1. Glycemic levels and cardiomyocyte morphology in diabetic (DM) wild-type ($AnxA1^{+/+}$) and annexin A1 knockout ($AnxA1^{-/-}$) mice. (A) Blood glucose levels (mg/dL) measured at multiple time points during the 90-day experimental period. Persistent hyperglycemia was observed in diabetic (DM) groups compared to controls (CTR). (B) Morphometric analysis of cardiomyocyte perimeter in transverse sections of the left ventricle. Data was shown as mean ± SEM (n = 4-10 mice/group). **p<0.01, ***p<0.001, ****p<0.0001 (Two-way ANOVA, Bonferroni post-hoc test). (C–F) Representative hematoxylin and eosin (H&E)-stained sections of cardiac tissue from $AnxA1^{+/+}$ (C, D) and $AnxA1^{-/-}$ (E, F) mice. DM groups (D, F) show reduced cardiomyocyte perimeter and structural disorganization compared to their respective control groups (C, E). Arrows indicate cardiomyocytes. Scale bars: 10 µm.

Study Of Muscle Fibers In The Soleus Muscle Of Obese Mice Exposed To Glyphosate During The Prenatal And Postnatal Periods

Rafaella Cristina Lima da Silva[1]*, Ariadne Barbosa[1], Sandra Lucinei Balbo[1], Maria Lucia Bonfleur[1], Marcia Miranda Torrejais[1].

[1] Graduate Program in Biosciences and Health –Universidade Estadual do Oeste do Paraná, Cascavel, Paraná, Brazil.
*rafaella.silva2@unioeste.br

Maternal exposure to toxic compounds such as pesticides can influence metabolism and tissue development [1], causing metabolic programming [2]. Glyphosate is a widely used pesticide associated with various diseases, including obesity [3], a multifactorial chronic condition [4]. This study aimed to evaluate the morphology and morphometry of muscle fibers in the soleus (SOL) muscle of offspring from mice exposed to glyphosate during prenatal and postnatal periods, and to determine whether the effects of this exposure were exacerbated by a high-fat diet. Twenty pregnant C57BL/6 female mice were housed individually and divided into: Control Group (CTL, n=10), which received pure water throughout pregnancy and lactation, and glyphosate-based herbicide group (GBH, n=10), which received 0.5% glyphosate herbicide [5] in their water during the same period. After weaning, male offspring were fed standard chow and water ad libitum for 30 days, then separated into four experimental groups based on maternal glyphosate exposure and diet: Control group (CG-F1); High-fat diet group (HFD-F1); Glyphosate-based herbicide group (GBH-F1); and Glyphosate-based herbicide and high-fat diet group (GBH-HFD-F1). At 150 days of age, animals were weighed, euthanized, and obesity assessed using the Lee index; the SOL muscle was collected, fixed in metacarn for 24 hours, then transferred to 70% ethanol. Muscles were embedded in paraffin following embedding in n-butyl alcohol and stained with Hematoxylin-Eosin [6]. The HFD-F1 group showed a 28% increase in body weight ($p=0.0003$) and a 457% increase in retroperitoneal and periepididymal fat ($p<0.0001$) compared to CG-F1. The GBH-HFD-F1 group showed a 35% reduction in retroperitoneal and periepididymal fat ($p<0.0001$) relative to HFD-F1 and a 310% increase ($p<0.0001$) compared to GBH-F1 (Table 1). Morphologically, muscle fibers in HFD-F1 exhibited degeneration (Figure 1B); polymorphic fibers were observed in GBH-F1 (Figure 1C); and rounded muscle fibers were noted in GBH-HFD-F1 (Figure 1D). Morphometric analysis revealed that GBH-HFD-F1 showed a 553.8% increase ($p=0.0211$) in the number of central nuclei compared to GBH-F1 (Table 1). This study demonstrated that glyphosate combined with a high-fat diet altered the number of central nuclei in muscle fibers and fat mass, indicating the influence of the combination of these two factors.

[1] S. Cvitic et al., Diabetologia 61 (2018) 1-14.
[2] C. Eberle, C. Ament, ISRN Pediatr. 2012 (2012) 1-11.
[3] N.M.X. Faria et al., Ciências & Saúde Coletiva, 12 (2007) 25-38.
[4] F.I. Milagro et al., Mol. Aspects Med. 34 (2013) 782-812.
[5] Monsanto, Safety Data Sheet (SDS) – Roundup, 2008.
[6] L.C. Junqueira, L.M.M. Junqueira, Basic Techniques in Cytology and Histology, Univ. São Paulo, São Paulo (1983).
[7] This research was supported by CNPq (Brazil) and Fundação Araucária (Brazil).

Table 1. Macroscopic parameters and morphometry of muscle fibers in the soleus muscle of 150-day-old mice from the control group (CG-F1), high-fat diet group (HFD-F1), glyphosate-based herbicide group (GBH-F1), and glyphosate-based herbicide and high-Fat diet group (GBH- HFD-F1). Values are expressed as mean ± standard deviation. n = 6. Different letters indicate significant differences ($p < 0.05$). [1]Kruskal-Wallis test with Dunn's post hoc test. [2]One-way analysis of variance with Tukey's multiple comparison post hoc test.

Groups Parameters	CG-F1	HFD-F1	GBH-F1	GBH-HFD-F1
[1]Body weight (g)	25 ± 1.16[a]	32 ± 4.52[b]	23 ± 1.82[a]	28 ± 2.03[a]
[1]Soleus muscle weight (mg)	9.5± 2.17	11.2 ± 1.33	8.12 ± 3.64	10.8 ± 0.98
[2]Soleus muscle length (mm)	5.7 ± 1.14	4.9 ± 0.44	5.6 ± 0.72	5.9 ± 1.03
[2]Retroperitoneal and periepididymal fat (g)	0.30± 0.07[a]	1.67± 0.46[b]	0.30± 0.10[a]	1.08 ± 0.53[c]
[1]Naso-anal length (cm)	9.3 ± 0.27	9.5 ± 0.32	8.9 ± 0.49	9.3 ± 0.26
[2]Lee index (g/cm³)	318 ± 10.4	331 ± 9.2	318 ± 13.3	326 ± 11.4
[2]Fiber area (µm²)	801 ± 94.6	863 ± 77.1	728 ± 188	810 ± 84.2
[2]Larger fiber diameter (µm)	38 ± 2.27	39 ± 1.51	36 ± 4.69	37 ± 1.67
[2]Smaller fiber diameter (µm)	25 ± 1.77	27 ± 1.51	24 ± 3.48	26 ± 1.49
[2]Number of fibers	278 ± 27.5	226 ± 27.5	269 ± 79.3	232 ± 17.4
[2]Number of peripheral nuclei	397 ± 39.1	337 ± 45.2	367 ± 75.5	351 ± 36.5
[2]Number of central nuclei	4.3 ± 1.75[a]	5 ± 3.16[a]	1.3 ± 1.21[a]	8.5 ± 6.06[b]
[1]Nucleus-to-fiber ratio	1.4 ± 0.18	1.5 ± 0.19	1.4 ± 0.18	1.6 ± 0.17
[2]Number of capillaries	120 ± 43.3	75 ± 22.2	101 ± 53.3	93 ± 31.2
[2]Capillary-to-fiber ratio	0.44 ± 0.18	0.34 ± 0.13	0.39 ± 0.16	0.40 ± 0.12

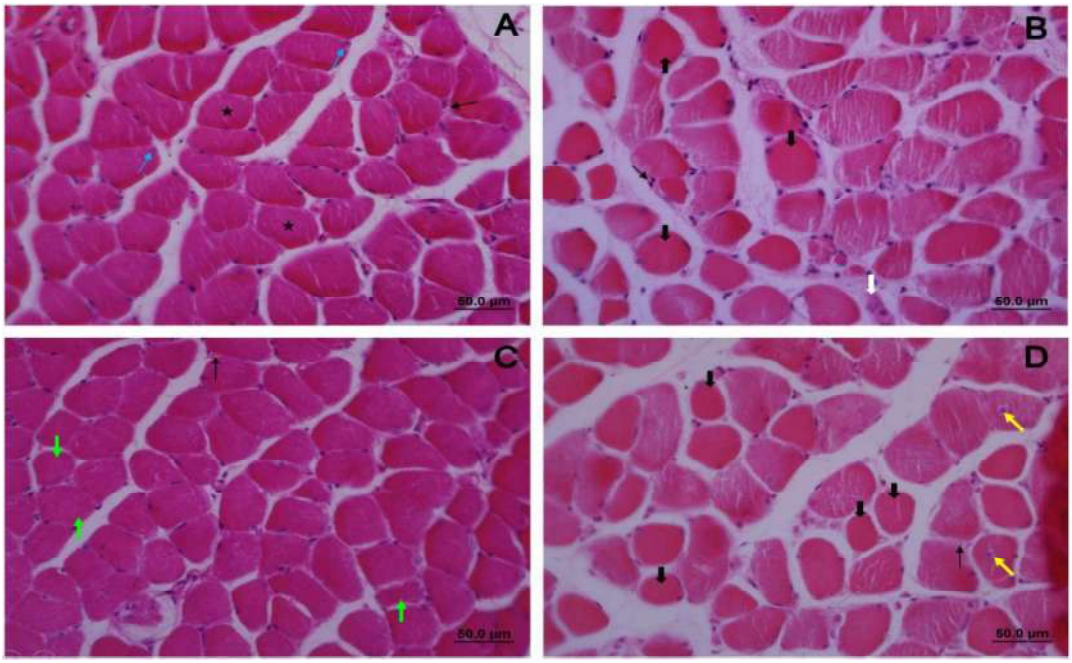

Figure 1. Photomicrographs of the soleus muscle from 150-day-old mice. Cross-section. Hematoxylin-Eosin staining. Capillaries are indicated by thin black arrows. A: Control group, polygonal fibers (star), peripheral nuclei (blue arrow); B: High-fat diet group, amorphous fibers with staining differences (thick black arrow), degenerating fiber (white arrow); C: Glyphosate-based herbicide group, amorphous fibers (green arrow); D: Glyphosate-based herbicide and high-fat diet group, fibers with central nuclei (yellow arrow) and amorphous fibers with staining differences (thick black arrow).

Systemic Morphological Alterations Induced By Secondary Dengue Infection In BALB/cJ Mice

Ana Luisa Teixeira de Almeida[1*], Gabriela Cardoso Caldas[1,2], Arthur da Costa Rasinhas[1], Fernanda Cunha Jácome[3], Debora Ferreira Barreto-Vieira[1]

[1] Laboratory of Viral Morphology and Morphogenesis – Oswaldo Cruz Institute, Oswaldo Cruz Foundation (IOC/Fiocruz), Rio de Janeiro, Brazil
[2] Laboratório de Medicina Experimental e Saúde – IOC/Fiocruz, Rio de Janeiro, Brazil
[3] Laboratório das Infecções Vírus-Hospedeiro – IOC/Fiocruz, Rio de Janeiro, Brazil.
* anaalmeida@aluno.fiocruz.br

In dengue, severe outcomes are often associated with heterologous secondary infections, particularly with dengue virus (DENV) serotypes 2 and 3 [1]. However, most murine models designed to explore these effects rely on neonatal, humanized, or immunodeficient mice and often deviate significantly from natural infection conditions by using neuroadapted strains, lethal virus doses, or invasive inoculation routes, such as intracerebral [2]. Our goal was to develop a model using immunocompetent mice intravenously inoculated with clinical, non-neuroadapted DENV strains. Two-month-old BALB/cJ mice were first infected with 10^4 PFU of DENV-3, followed by infection with 10^4 PFU of DENV-2 two months later. A mock-inoculated group served as the negative control. Mice were euthanized at 3, 7, 10, 14, or 21 days post-infection (d.p.i.) (n=5 per time point). Organs (liver, kidneys, spleen, lungs, heart, brain, and cerebellum) were collected, fixed in formalin, dehydrated in alcohol, cleared in xylene, and embedded in paraffin. Histological sections were stained with hematoxylin and eosin for both histopathological and morphometric analysis. For each histological slide, thirty images were captured using a 40X objective for the liver and lung tissues, a 20X objective for the kidneys, and a 10X objective for the spleen. Variables analyzed included alveolar septa thickness in the lungs, hepatocyte count and classification (uni- vs. bi-/multi-nuclaeated), and the cross-sectional area of sinusoidal capillary lumens in the liver. Additionally, the number and area of renal glomeruli, as well as the areas of the white and red pulp in the spleen, were quantified. These measurements were performed using ImageJ software, version 1.53t. All organs exhibited varying degrees of vascular damage, including congestion and thrombus formation, except for the heart, which showed no significant damage throughout all time points. Hepatocytes and renal tubular cells exhibited pronounced necrosis (Figure 1A-B). In the lungs, inflammatory infiltration led to marked alveolar septa thickening. Other alterations included diffuse alveolar hemorrhage, parenchyma compaction and hyperinflation (Figure 1C). The most notable change in the spleen was the reduction in the white pulp area (Figure 1D). Although some animals presented clot formation within the cranial cavity, histological alterations in the cerebrum and cerebellum were moderate, characterized by focal neuronal death (Figure 1E) and disorganization of Purkinje cells (Figure 1F). These findings highlight the role of morphological studies in DENV infection, as they reveal severe effects through microscopy investigations. We gratefully acknowledge the financial support provided by CAPES and FAPERJ for this study [3].

[1] K.M. Soo et al. Meta-Analysis of Dengue Severity during Infection by Different Dengue Virus Serotypes in Primary and Secondary Infections. PLoS One. (2016), 11(5), e0154760.
[2] S. Zompi, E. Harris. Animal models of dengue virus infection. Viruses. (2012), 4(1), 62-82.
[3] This research was supported by CAPES and FAPERJ (Brazil).

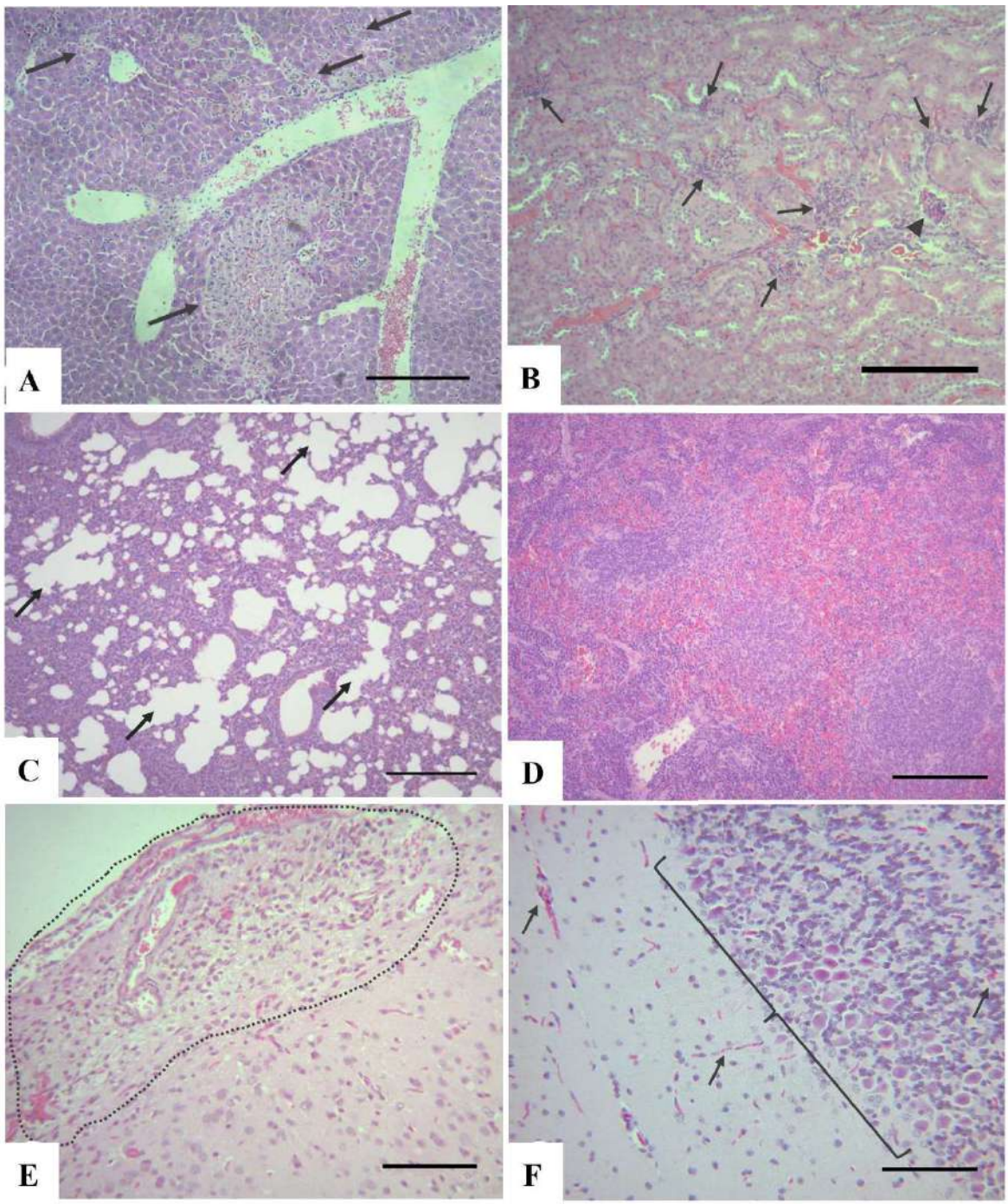

Figure 1: Histopathological analysis of BALB/cJ mice following primary DENV-3 infection and secondary DENV-2 infection. (A) Liver at 10 days post-secondary infection (d.p.i.): necroinflammatory foci and hemorrhagic areas were observed (arrows). (B) Kidney at 7 d.p.i.: inflammatory infiltrate (arrows) and glomerular atrophy (arrowhead). (C) Lung at 3 d.p.i.: regions of alveolar hyperinflation adjacent to areas of thickened alveolar walls. (D) Spleen at 3 d.p.i.: lymphoid follicle atrophy and splenic congestion. (E) Cerebrum at 10 d.p.i.: focal necrosis, inflammatory cell infiltration and hemorrhage in the cortex (dashed area). (F) Cerebellum at 10 d.p.i.: disorganization of the Purkinje layer (brackets), with these cells located in the granular layer that showed reduced cellular density. Additionally, congestion of small vessels is evident (arrows). Scale bars: A–D: 100 μm, E–F: 50 μm.

Toxic effect of silver nanoparticle to *Artemia salina* nauplii I

Alexia Riquet Martins[1]*, Emilio de Castro Miguel[1], Ana Kmila Medeiros Lima[1],Thaiz B. A. Rangel Miguel[2]

[1]Biomaterials Laboratory, Department of Metallurgical and Materials Engineering (DEMM), Federal University of Ceara, Fortaleza, Ceará, Brazil, [2]Biotechnology Laboratory, Department of Food Engineering, Federal University of Ceara, Fortaleza, Ceará, Brazil
*alexiariquet@hotmail.com

Silver nanoparticles (AgNP) have been studied mainly due to their wide application as bactericidal [1], their use in various products increases their disposal, and most of these effluents have the oceans as the final destination [2]. Analysis of the damage caused by AgNPs, to marine organisms, allow toxicity levels to be determined according to the concentration, [2], [3]. Analyses using light microscopy (LM) and scanning electron microscopy (SEM), are utilized for a better comparison of the internal and extensive damage promoted to the animal model, used for toxicological analysis, (*Artemia salina*), in a exposure experiment with 10 specimens in triplicate, and negative control with artificial seawater only and another positive control with potassium dichromate [4]. Statistical analyses of mortality have shown the AgNPs toxicity tests on nauplii, show that mortality increases as the concentration of AgNP increases (6, 12.5, 25, 50 and 100ppm). This increase is also observed in relation to the exposure time, 24 and 48 hours. The eyes, antennae and appendages as well as the digestive tract are well-developed and without any significant visible alterations. In the digestive system, was seen the dark mass present inside the *A.salina* show the entry and agglomeration of the particle in the digestive tract as can be seen in the LM images, not present in other larger samples that also used artemia as a model [4]. It is possible to theorize that the absence of particles in the individuals exposed to the concentration of 6ppm is due to the low concentration of particles in the medium, it would be a very diluted concentration [3]. The absence of particles at 100 ppm, would be due to the agglomeration of particles deposited at the bottom [1]. Considering the particle ingestion process, it is possible to relate the greater death of the arthemias when they reach the NII stage to the ingestion of the particle. It is possible to conclude that exposure to the particle does not directly interfere with the development from nauplius I to nauplius II, and that a mass that can be seen in light microscopy may be related to the consumption of AgNP and the increase in mortality in the nauplius II stage. Acknowledgments FUNCAP, CAPES and CNPq a for supporting the research [5].

[1] P. Bélteky *et al.*, 'Silver nanoparticles: Aggregation behavior in biorelevant conditions and its impact on biological activity', *Int J Nanomedicine*, vol. 14, pp. 667–687, 2019, doi: 10.2147/IJN.S185965.

[2] D. H. Nam, et al., 'Uptake and bioaccumulation of titanium- and silver-nanoparticles in aquatic ecosystems', *Mol Cell Toxicol*, vol. 10, no. 1, pp. 9–17, 2014, doi: 10.1007/s13273-014-0002-2.

[3] H. J. An, et al., 'Comparative toxicity of silver nanoparticles (AgNPs) and silver nanowires (AgNWs) on saltwater microcrustacean, Artemia salina', *Comparative Biochemistry and Physiology Part - C: Toxicology and Pharmacology*, vol. 218, pp. 62–69, Apr. 2019, doi: 10.1016/j.cbpc.2019.01.002.

[4] T. B. A. R. Miguel, et al., 'Protective Effect of Natural and Processed Coconut Water by Non-thermal Technologies Against Oxidative Stress in Brine Shrimp (Artemia salina)', *Food Bioproc Tech*, vol. 14, no. 4, pp. 702–716, Apr. 2021, doi: 10.1007/s11947-021-02600-7.

[5] This research was supported by FUNCAP, CAPES and CNPq (Brazil).

Figure 1. Figure 1 Light microscopy (LM) and scanning electron microscopy (SEM) of *A.Salina* stage I nauplii (NI), exposed to different concentrations of AgNPs for 48 hours. A, C, E, G, I, K, M– Light microscopy; B, D, F, H, J, L, N – Scanning electron microscoply. It should be noted that all the specimens, except those that came into contact with potassium dichromate, reached the next stage of development (NII), without significant structural changes, eye appendages and the digestive tract were well developed and it is possible to see the accumulation of dark colored particles at 12.5, 25 and 50 ppm (I, K, M), 25 ppm has the highest concentration of particles internally (I), as can be seen in light microscopy, in scanning electron microscopy no changes are noted compared to the control with artificial seawater. **Bars: A, C, E, G, I, K, M: 50 µm–; B, D, F, H, J, L, N: 200 µm.**

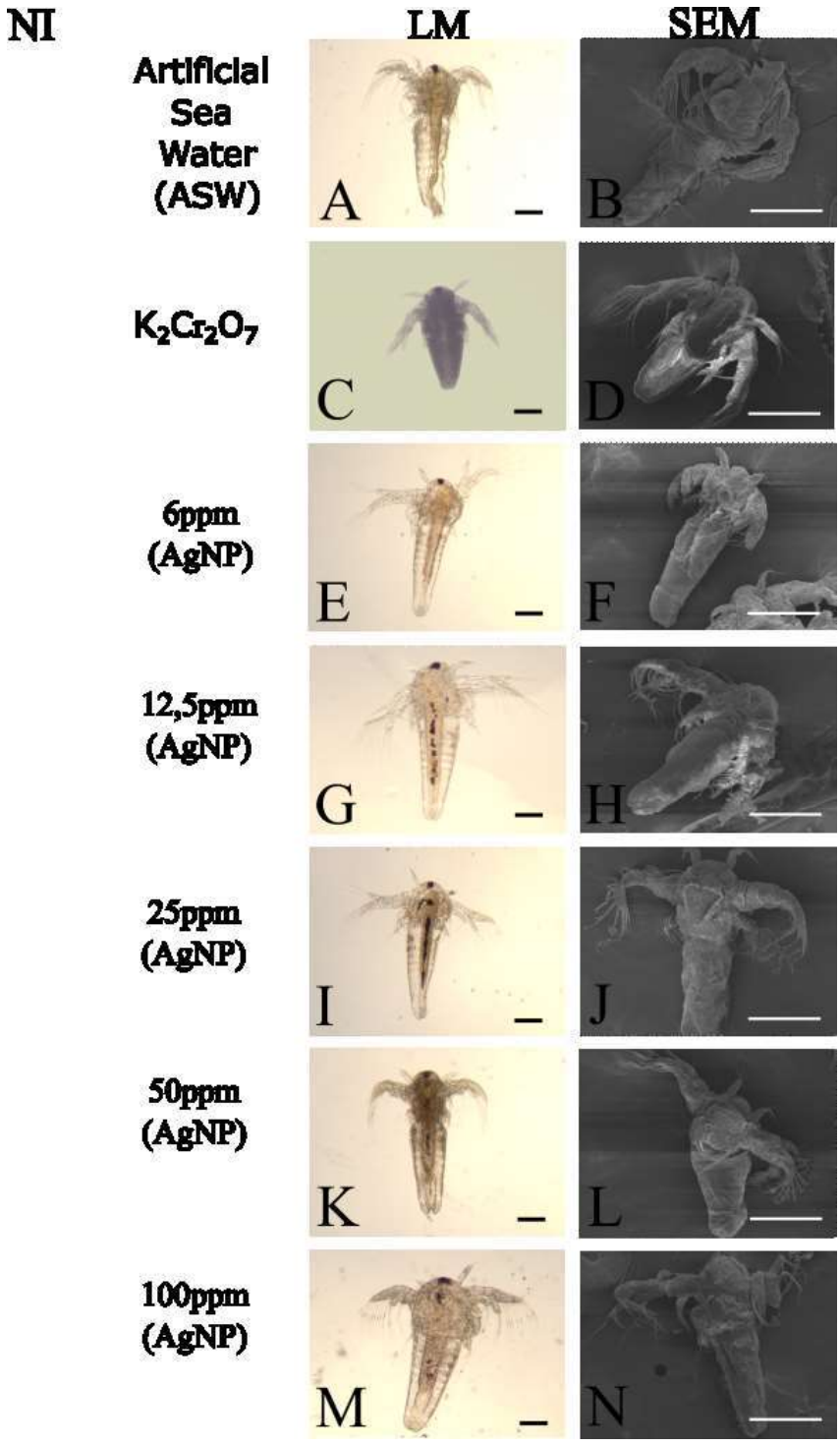

Scanning probe microscopy and applications in physics, materials science, and life sciences.

Mapping the Segregation and Micellization of PEG-*b*-PCL Multiblock Copolymers in PLA/PCL Blends *via* AFM-IR

Lucas H. Staffa[1]*, Sílvia H.P. Bettini[1], Marcelo A. Chinelatto[2].

[1]Department of Materials Engineering (DEMa), Federal University of São Carlos (UFSCar), 13565–905, São Carlos, SP, Brazil
[2]Department of Materials Engineering (SMM), São Carlos School of Engineering (EESC), University of São Paulo (USP), 13563-120, São Carlos, SP, Brazil
*lucas.staffa@ufscar.br

A previous investigation [1] employed AFM-based infrared spectroscopy (AFM-IR) to map the segregation and micellization of two PEG-*b*-PCL (poly(ethylene glycol)-b-poly(ε-caprolactone)) multiblock copolymers—both with similar molar masses but different block sizes—within PLA/PCL (poly(lactic acid)/poly(ε-caprolactone)) (80/20 wt%) polymer blends at 1 and 5 wt%. The tendency of the copolymer to segregate within the PLA matrix after reaching interfacial saturation was investigated using AFM-IR by monitoring IR bands specific to the copolymer, which are absent from both the PLA and PCL phases. Topographical analysis revealed that uncompatibilized blend exhibit reduced interfacial adhesion, as evidenced by pull-out phenomena of PCL droplets. Upon addition of the shorter block-size copolymer, interfacial saturation was observed at 5 wt%, followed by segregation into the matrix without evidence of micellization (see Figure 1). In contrast, the longer block-size copolymer migrates to the PLA matrix at 1 wt%, displaying a self-organized segregation and forming micelles of approximately 20 nm in diameter, which adversely affects the mechanical performance of the blend [2]. The presence of intense specific infrared absorption at 1660 cm^{-1} surrounding the micelle supports the micellar nature of the longer block-size multiblock copolymer, resulting from its surface-activity-driven segregation. Additionally, when analyzing the cryo-fractured cross-section of the blends *via* SEM, a clear correlation is observed between the blend's fracture mode and interfacial saturation. Specifically, when the PLA matrix and PCL droplets fracture along the same plane (see Figure 2), this strongly indicates that the copolymer segregates into the matrix. The correlation was only possible due to the unequivocal identification of the copolymer in the matrix via AFM-IR.

[1] L.H. Staffa et al., Polymer Testing. 138, 108549 (2024).
[2] L.H. Staffa et al, Journal of Polymer Research, 388. 29 (2022).
[3] This study was partly financed by CAPES – Finance Code 001, CNPq – SWE scholarship under Finance Code 202952/2018- 5/SWE, and FAPESP – 2018/23542-7 research was supported by CNPq (Brazil). This research used facilities of the Brazilian Nanotechnology National Laboratory (LNNano), part of the Brazilian Centre for Research in Energy and Materials (CNPEM), a private non-profit organization under the supervision of the Brazilian Ministry for Science, Technology, and Innovations (MCTI). The AFM staff is acknowledged for their assistance during the experiments AFM-25553, AFM-26344, and AFM-27461 experiments

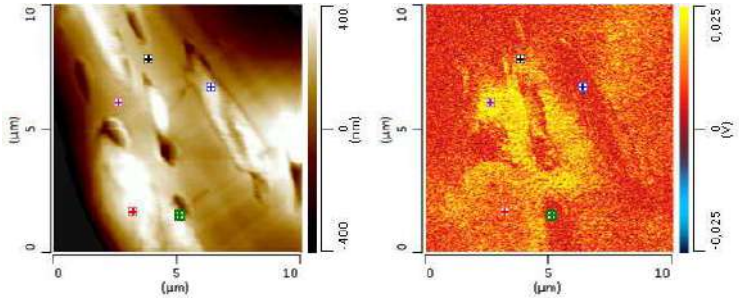

Figure 1. Segregation of the shorter block-size multiblock copolymer at 5wt% into the PLA matrix after interfacial saturation. Scanning at 1660 cm−1.

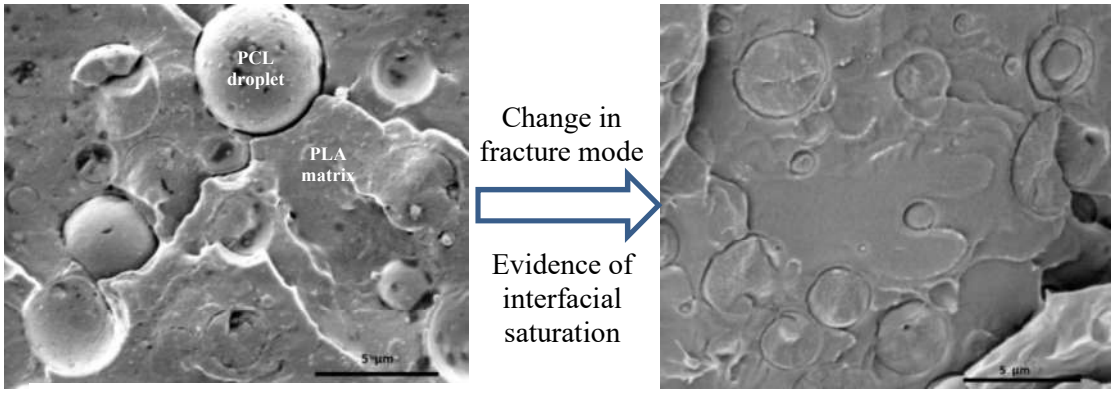

PLA and PCL fracturing along **different planes**

PLA and PCL fracturing along the **same plane**

Figure 2. Demonstration of the change in blend phase fracture mode before and after interfacial saturation.

Revisiting the Microstructural Analysis of ZnO Varistors Using Atomic Force Microscopy and Electron Microscopy

Jefferson Bettini[2], Otavio Berenguel[2], Carlos A. R. Costa[2], Tanna Elyn Rodrigues Fiuza[2], Fabiano Emmanuel Montoro[2], Danilo Biazon Janes[1,2], Edson Roberto Leite[1,2]

[1]Federal University of São Carlos (Graduate Program in Materials Science and Engineering), São Carlos, Brazil
[2]Brazilian Center for Research in Energy and Materials, Campinas, Brazil
e-mail: jefferson.bettini@lnnano.cnpem.br

ZnO varistors are widely used as surge protection devices due to their high nonlinearity current-voltage and energy absorption capabilities [1-2]. Understanding their microstructure is crucial for optimizing their electrical and thermal properties and ensuring operational efficiency.

Existing literature highlights the significance of potential barriers at ZnO varistor grain boundaries and their relationship with dielectric and conductive responses. Previous studies employed conventional techniques for microstructural analysis, but the application of novel methodologies, as utilized in this work, enables a more precise and detailed characterization [2-3].

Despite significant progress in ZnO varistor characterization, gaps remain in understanding the influence of elemental distribution and microstructure on electrical and thermal performance. This work aims to revisit the microstructural analysis of ZnO varistors using scanning thermal microscopy (SThM) and conductive-AFM (c-AFM), see figure 1. The goal is to update knowledge on varistor composition by analyzing its different phases and homogeneous and heterogeneous junctions, as well as the distribution of elements, characterized by scanning electron microscopy with energy-dispersive X-ray spectroscopy (SEM/EDS), and their influence on electrical and thermal properties characterized by scanning Transmission electron microscopy (STEM) with Differential Phase Contrast (DPC).

The AFM characterization revealed detailed information on the electrical and thermal properties across the material's phase distribution. The secondary phases exhibited lower thermal conductivity compared to the primary ZnO phase, and the correlation of these findings with elemental composition, grain boundaries, and morphology provided a comprehensive understanding of the material's performance.

The application of advanced characterization techniques will significantly update knowledge on ZnO varistor microstructure. The results can provide valuable guidelines for developing more stable and efficient devices while fostering further research in this field.

[1] T. K. Gupta, Application of zinc oxide varistors. Journal of the american ceramic society, v. 73, n. 7, 1990, p. 1817-1840.
[2] E. R. Leite, M. A. L. Nobre, E. Longo, J. A. Varela, Microstructural development of ZnO varistor during reactive liquid phase sintering. Journal of Materials Science, v. 31, 1996, p. 5391-5398.
[3] S. Li, J. Li, W. Liu, J. Lin, J. Shengtao, Advances in ZnO varistors in China during the past 30 years—fundamentals, processing, and applications. IEEE Electrical Insulation Magazine, v.31, n. 4, 2015, p. 35-44..

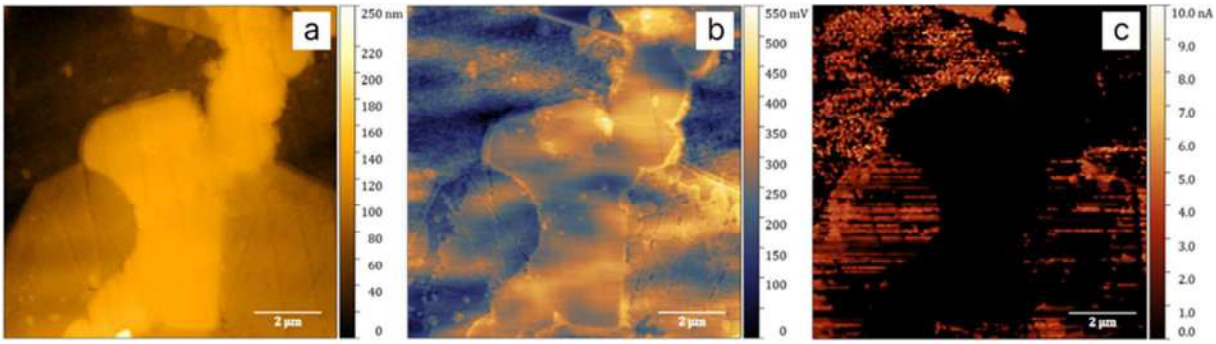

Figure 1: Correlated micrographs of a ZnO varistor: (a) topography, (b) thermal conductivity, and (c) electrical conductivity.

Shedding Light on the Antibacterial Mechanisms of Silver Nanoparticles with Correlative Microscopy

Maria Clara M. de Andrade[1]*, Fernanda K. da Silva[1], Cleyton A. Biffe[2], Otávio Berenguel[2], Carlos Alberto R. Costa[2], Etienne Dague[3], André Galembeck[1].

[1] Departamento de Química Fundamental, Universidade Federal de Pernambuco (dQF/UFPE), Recife-PE, Brasil, [2] Laboratório Nacional de Nanotecnologia (LNNano/CNPEM), Campinas-SP, Brasil, [3] Laboratoire de recherche spécialisé dans l'analyse et l'architecture des systèmes (LAAS-CNRS), Toulouse, France.
*clara.muller@ufpe.br

The antimicrobial activity of silver nanoparticles (AgNPs) has been extensively studied over the past two decades. Recent reviews highlight their applications in oral care [1,2]. Our group was the first to demonstrate that AgNP-based formulations can arrest tooth decay. Clinical trials showed that 67% of dental caries were halted one year after a single application of AgNPs to the affected area [3]. *In vitro* assays confirmed that AgNPs have bactericidal and bacteriostatic action against the highly cariogenic *Streptococcus mutans* (*S. mutans*), among other oral species [1,2]. However, the mechanisms underlying their caries-arresting effect are not fully understood. Nor are the precise antibacterial mechanisms of AgNPs, despite ongoing interest and debate within the scientific community concerning this topic [4,5]. In this work, we used a multimodal microscopy approach to investigate these mechanisms. By combining focused ion beam (FIB), scanning electron microscopy (SEM), energy-dispersive X-ray spectroscopy (EDS), and X-ray microtomography, we assessed the penetration of AgNPs into human dentin after applying the caries-arresting formulation on its exposed surface. We found that the nanoparticles were able to infiltrate and adhere to dentinal tubules—the microchannels beneath the dental enamel that become exposed after caries initiation. The local silver concentration within tubules was estimated to exceed the minimum inhibitory concentration for *S. mutans*. This suggests that AgNPs interact with dentin to create a long-lasting antimicrobial reservoir at the affected site, potentially preventing intratubular infection and the consequent progression of tooth decay (Figure 1) [6]. We also investigated how AgNPs interact with bacteria at the single-cell level, using atomic force microscopy (AFM) and *S. mutans* as our model organism (Figure 2). Within a Bio-AFM platform, we analyzed living *S. mutans* (n = 20) immersed in physiological medium, individually assessing their responses to AgNP exposure. Only 3 minutes of exposure was enough to exert biomechanical and morphological impact on the bacteria. All cells exhibited pronounced stiffening within 15–75 minutes following their treatment (Figure 3). Cell enlargement and morphological deformation were also observed. Additionally, AFM-based infrared spectroscopy (AFM-IR) provided evidence of interactions between AgNPs and cell wall components, along with plasma membrane damage in treated bacteria. Taken together, the results of this study deepen our understanding of how AgNPs prevent tooth decay and affect bacterial cells shortly after contact, the latter with implications that extend beyond the context of dental caries. Moreover, the findings underscore the power of correlative microscopy to address complex questions at the interface of nanomaterials and biological systems [7].

[1] I.X. Yin et al., *Int. J. Nanomedicine* 15 (2020) 2555–2562.
[2] S.K. Mallineni et al., *Bioengineering* 10 (2023) 327.
[3] V.E. dos Santos Jr. et al., *J. Dent.* 42 (2014) 945–951.
[4] H. Wang et al., *Int. J. Mol. Sci.* 23 (2022) 2486.
[5] V. Singh et al., *Biometals* 36 (2023) 483–503.
[6] M.C.M. Andrade et al., *Materialia* 24 (2022) 101489.
[7] This research was supported by FACEPE, CAPES, and CNPq (Brazil)

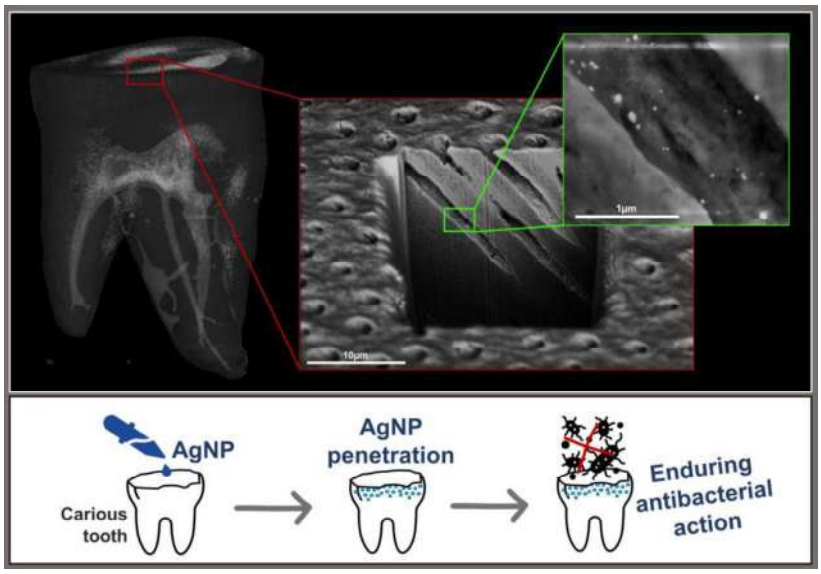

Figure 1. X-ray microtomography and FIB-SEM analysis of a tooth sample treated with silver nanoparticles (AgNPs), showing that the particles can penetrate and adhere to dentinal tubules. These results support the hypothesis illustrated at the bottom of the figure, which explains the previously reported effectiveness of AgNPs as caries-arresting agents.

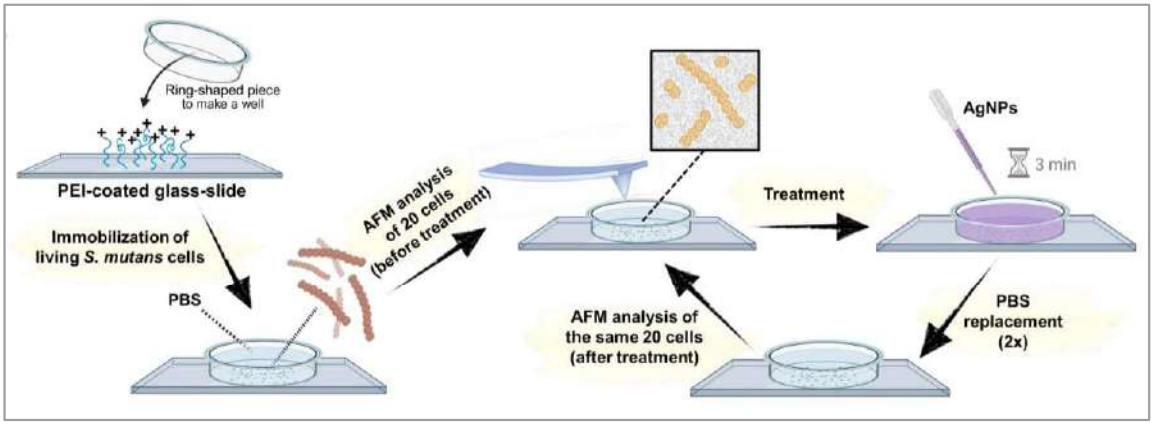

Figure 2. Summary of the bio-AFM experiments performed with cariogenic living *S. mutans*, to assess short-term antibacterial effects of AgNPs at the single-cell level.

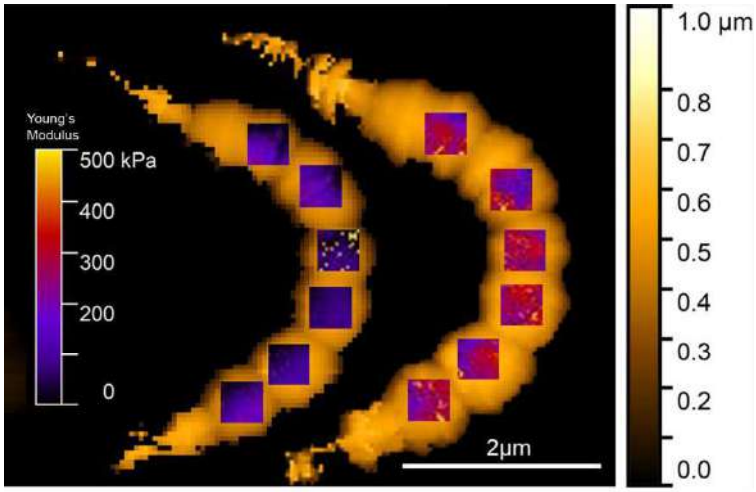

Figure 3. Topography AFM images showing the same *S. mutans* cells before (right) and after (left) contact with AgNP; The inserts at the center of each cell correspond to Young's modulus maps obtained from force spectroscopy measurements (indentations). Rigidity and size increases were observed for the cells following exposure to AgNPs.

Characterization of *Staphylococcus aureus* Biofilm on Glasses Containing Zinc Oxide: A Topographical and Nanomechanical Approach using Atomic Force Microscopy

Adriele Rocha[1], Thalia Delmondes[2], Clovis de Souza[3], Lucas Staffa[1,2]**

[1] Laboratório de Caracterização Estrutural (LCE), Departamento de Engenharia de Materiais (DEMa), Universidade Federal de São Carlos (UFSCar),[2] Departamento de Engenharia de Materiais (DEMa), Universidade Federal de São Carlos (UFSCar),[3] Departamento de Morfologia e Patologia (DMP),Universidade Federal de São Carlos (UFSCar)

*
lucas.staffa@ufscar.br

The formation of bacterial biofilms on biomedical materials poses a major challenge to infection prevention, particularly in implants [1]. This study aims to evaluate the influence of zinc oxide (ZnO) at different mass fractions (5 wt%, 7.5 wt%, and 10 wt%) in glass, with the objective of characterizing its bioactive effects on *Staphylococcus aureus* biofilm formation [2]. Special emphasis was placed on topographical and nanomechanical analyses using Atomic Force Microscopy (AFM) in PeakForce QNM® mode [3]. The surface images reveal that a 5 wt% ZnO concentration increases biofilm roughness, which is directly associated with a thicker extracellular matrix, suggesting an adaptive bacterial defense mechanism [4]. Higher concentrations of ZnO (7.5 wt% and 10 wt%) significantly inhibit biofilm development, markedly reducing its height, density, and surface coverage by bacterial colonization. The nanomechanical properties indicate a progressive reduction in the modulus with increasing ZnO concentration, accompanied by higher adhesion forces, suggesting possible modifications to the biofilm surface [5]. Scanning Electron Microscopy (SEM) images show reduced surface coverage in samples with higher ZnO concentrations, reinforcing the conclusions drawn from AFM analysis. These results highlight the potential of ZnO-containing glass formulations to prevent biofilm formation and contribute to the development of biomaterials with antimicrobial properties. This work highlights the importance of advanced AFM techniques, such as PeakForce QNM®, in elucidating interactions between biomaterials and biofilms, supporting future biomedical and dental applications.

[1] N.K. Archer et al., Virulence 2 (5) (2011) 445–459.
[2] S. Gómez et al., Acta Biomater. 42 (2016) 341–350.
[3] Bruker Nano Surfaces Division, PeakForce QNM, Santa Barbara, CA, 2010.
[4] M.R.M. Ranieri et al., Opin. Microbiol. 45 (2018) 164–169.
[5] D.R. Radford, J.D. Walter, J. Dent. 26 (7) (1998) 577–583.

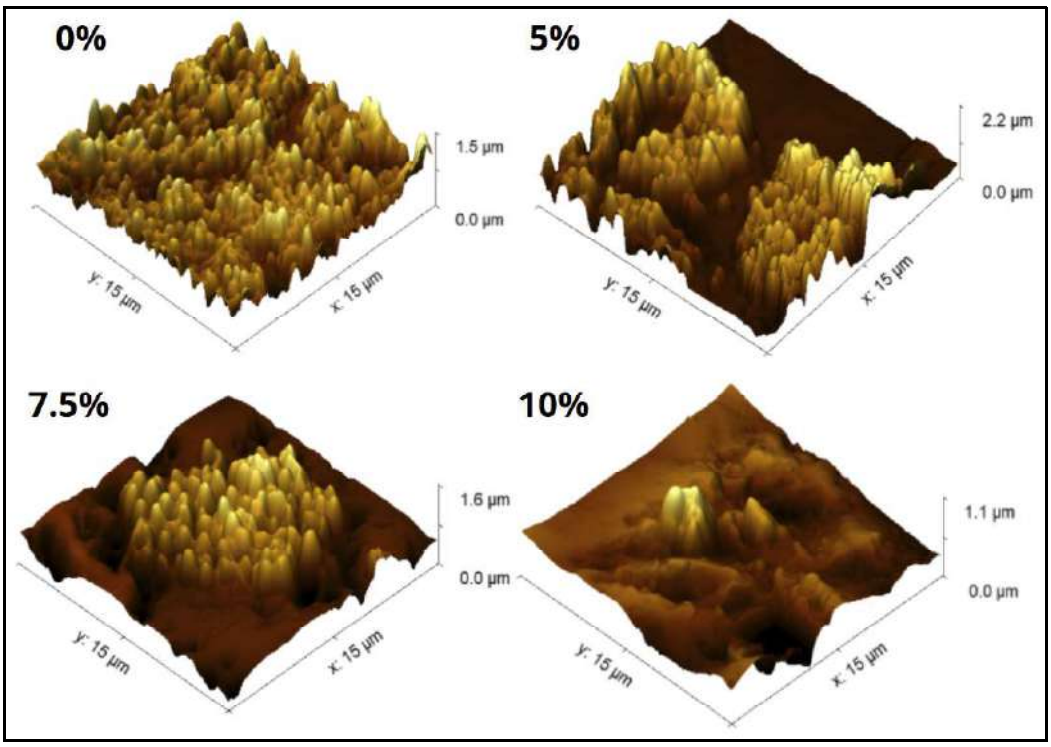

Figure 1. AFM topographic images of a *S. aureus* biofilm grown on glass without ZnO (control) and with 5, 7.5 and 10% ZnO.

Comparative study of porous detection by AFM e FIB-SEM

G. B. Pinheiro[1*], C. A. Senna[1], T. D. P. Caldas[1], E. P. Pinto[1,2], R. Prioli[1], D. C. Dias-Filho[3], M. K. de Souza[3], Y. M. Parizeck[3],

[1]Departamento de Física, Pontifícia Universidade Católica Do Rio De Janeiro, Rio De Janeiro, Brazil

[2]Departamento de Física, Universidade Federal do Amapá, Macapá, Brazil

[3]Petrobras (CENPES), Rio De Janeiro, Brasil

*gabriel.bpinheiro@aluno.puc-rio.br

Pore characterization is crucial for assessing properties like mechanical deformation, porosity, and permeability. While pores are generally defined as empty spaces [1], analyzing them, especially in surface images, can be subjective. Microscopy techniques, particularly scanning electron microscopy (SEM) combined with focused ion beam (FIB-SEM), are commonly used for pore studies [2]. These techniques provide high-resolution analysis and 3D reconstructions but can produce images that represent subsurface volumes rather than just the surface. On the other hand, atomic force microscopy (AFM) offers accurate 3D topography images based solely on surface interactions. These methods can be combine to visualize pores [3]. The present study aims to analyze and compare the pores observed in 2D and 3D FIB-SEM images with those found in 3D AFM images. A sedimentary rock sample, with pores of micro- and nanometric sizes, was used for comparison. A co-localization methodology was developed to align SEM and AFM images taken from the same regions. We tested various operating conditions for both AFM and SEM. Subsequently, 3D FIB-SEM images of a small volume of the rock were obtained using the ion beam. The three methods were then compared (Figure 1). The pore parameters were extracted from the segmented images for comparison between the different techniques (Figure 2). The results indicate that both methods consistently capture most pore populations. Their comparison enables the separation of pores from topographic features, allowing for accurate characterization of the pores. Our observations also revealed that some large pores detected in SEM images were not visible in AFM images. This finding indicates that pores typically shown in SEM may not correspond to surface features but rather represent subsurface volumes, indicating a potential overestimation of the porosity reported with this technique.

[1] Milliken, Kitty L., and Mark E. Curtis. "Imaging pores in sedimentary rocks: Foundation of porosity prediction." *Marine and Petroleum Geology* 73 (2016): 590-608.

[2] Zhao, Jianpeng, et al. "Quantitative characterization of organic and inorganic pores in shale based on FIB-SEM." *Frontiers in Earth Science* 10 (2022): 994312.

[3] Li, Yong, et al. "Nanoscale pore structure and mechanical property analysis of coal: An insight combining AFM and SEM images." *Fuel* 260 (2020): 116352.

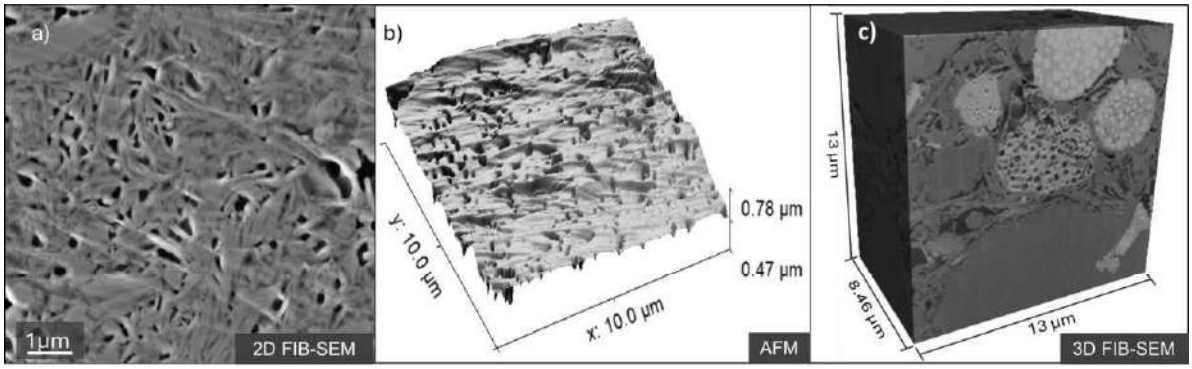

Figure 1. Images observed using a) 2D FIB-SEM, b) AFM and c) 3D FIB-SEM.

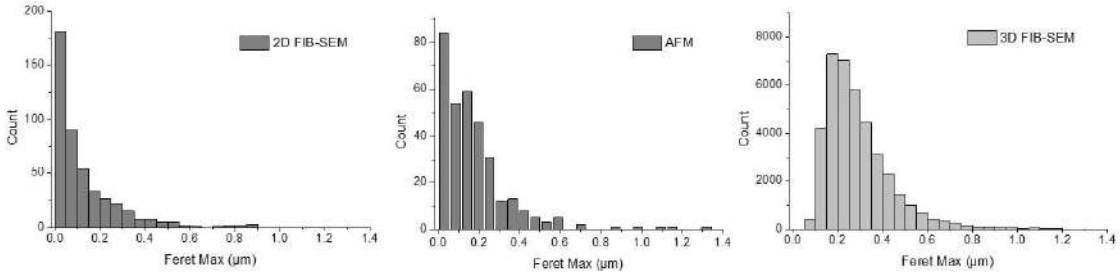

Figure 2. Histogram of pores observed using a) 2D FIB-SEM, b) AFM and c) 3D FIB-SEM.

Exploring Nanomechanical Properties of Pharmaceutical Nanocrystals: An Approach Using Atomic Force Microscopy

Beatriz Ferreira de Carvalho Patricio[1,4]*, Cinira Fandaruff [2], Wellington da Silva Ferreira[3,4], Michelle Alvares Sarcinelli[2], Marcelo Henrique Cunha Chaves[2], Gilberto Weissmuller[3,4], Helvécio Vinícius Antunes Rocha[2]

[1]Universidade Federal do Estado do Rio de Janeiro (UNIRIO), Instituto Biomédico, Laboratório de Inovação Farmacêutica e Tecnológica, Brasil

[2]Fundação Oswaldo Cruz (FIOCRUZ), Centro de Desenvolvimento Tecnológico em Saúde (CDTS), Laboratório de Micro e Nanotecnologia, Brasil

[3]Universidade Federal do Rio de Janeiro (UFRJ), Instituo de Biofísica Carlos Chagas Filho, Laboratório de Física Biológica, Brasil

[4]Universidade Federal do Rio de Janeiro (UFRJ), Centro Nacional de Biologia Estrutural e Bioimagem, Brasil

*beatriz.patricio@unirio.br

Nanotechnology has become an important tool in pharmaceutical research by enabling the reformulation of drugs with low solubility, poor bioavailability, or high toxicity, allowing them to be commercialized [1,2]. Through nanoscale modifications, these molecules gain enhanced therapeutic performance and reduced side effects, making previously discarded compounds viable again [1]. Among the various nanosystems, nanocrystals (NCRs) stand out due to their simple composition and high drug loading (typically over 90%), stabilized by surfactants or polymers with steric and electrostatic properties [3]. NCRs are primarily produced through top-down approaches, such as bead milling, where micron-sized drug particles are broken down into nanoparticles and stabilized in this form during the process [3]. Despite the widespread application of this method in research and commercial formulations, the underlying reasons why some active pharmaceutical ingredients (APIs) exhibit easier size reduction and better dissolution after reaching the nanosized remain' unclear. This study investigates the nanomechanical properties of APIs and their respective nanocrystals using Atomic Force Microscopy (AFM). NCRs of efavirenz (EFV) and ritonavir (RTV)—classified as class II drugs by the Biopharmaceutical Classification System (BCS)—and amphotericin B (class IV, BCS), were prepared via bead milling. Compressed tablets of APIs and NCRs were analyzed using Peak Force Quantitative Nanomechanical Mapping mode in AFM. After adhesion and elastic modulus (DMT Modulus) values were extracted from force–distance curves to compare mechanical behavior. Figure 1 illustrates surface images of RTV API and its nanocrystal tablet. When analyzing the nanomechanical properties of the samples a significant difference in adhesion was observed between NCR and API of RTV, and not in the other samples. In contrast, EFV displayed an apparent variation in DMT Modulus between its API and NCR, and not in the other drug samples. Differences in this property were also noted between the API of EFV and RTV, suggesting that nanomechanical behavior may influence both the grinding efficiency and dissolution rate of NCRs, since the milling process of RTV was easier and its dissolution was almost instantaneous. Understanding these properties provides insight into material processing and may guide the rational design of nanocrystal-based formulations with improved pharmaceutical performance.

[1] Shegokar, R. et al. Int J Pharm, **399**(1-2) (2010) 129-39.
[2] Rizzo, L.Y., et al.. Curr Opin Biotechnol, **24**(6) (2013) 1159-66.
[3] Verma, S., Int J Pharm, **380**(1-2) (2009) 216-22.
[4] This research was supported by CNPq, FAPERJ, Capes (Brazil).

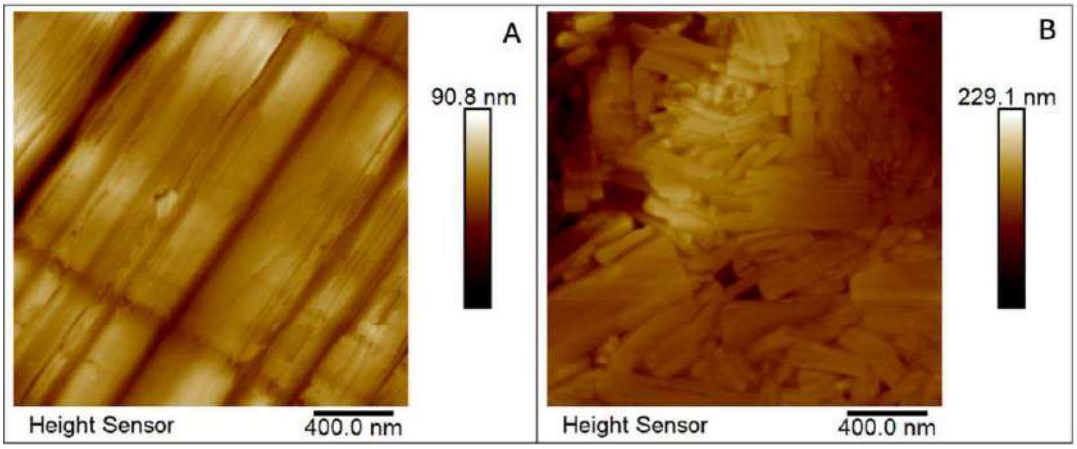

Figure 1: Topography image acquired by atomic force microscopy in PFQNM Mode of ritonavir in bulk form (A) and nanocrystal (B).

Hierarchical Nanotopographies and Fractal Fingerprints of Anopheles Mosquito Wing Surfaces

Leandro Caio Correa Pinto[1], Glenda Quaresma Ramos[2,3], Carlos Alberto Rodrigues Costa[4], Robert Saraiva Matos[5]Rosa Amélia Gonçalves Santana[3], Silvia Cássia Brandão Justiniano[3], Henrique Duarte da Fonseca Filho[1,*]

[1]Laboratório de Desenvolvimento e Aplicações de Nanomateriais da Amazônia (LADENA) – Departamento de Física de Materiais, Universidade Federal do Amazonas, Manaus, Amazonas, 69067-005, Brazil.
[2]Universidade do Estado do Amazonas - UEA, Centro Multiusuário para Análise de Fenômenos Biomédicos (CMABio), Manaus, Amazonas - 69065-001, Brazil.
[3]Fundação de Medicina Tropical Doutor Heitor Vieira Dourado, Unidade de Entomologia Médica Nelson Ferreira Fé, Manaus, Amazonas – 69040-000, Brazil.
[4]Laboratório Nacional de Nanotecnologia (LNNano), Centro Brasileiro de Pesquisa em Energia e Materiais (CNPEM), Campinas-SP, Brazil.
[4] Grupo de Materiais Amazônicos, Departamento de Física, Universidade Federal do Amapá, Macapá, 68903-419, Amapá, Brazil.

*hdffilho@ufam.edu.br

Insects constitute a highly diverse group, with significant biological importance across various environments. The morphological study of insects plays a fundamental role in taxonomic identification [1], as well as in understanding their relationship with environmental factors. Insect wings exhibit a sophisticated and functional architecture [1], which, in addition to enabling flight, also serves functions in thermal regulation [2], optical properties [2], defense mechanisms [3], and interspecific interactions [4]. Wing morphology consists of a highly organized arrangement of veins, membranes, and micro- to nanostructures. These characteristics and their spatial distribution vary among taxonomic groups, making insect wings one of the most important structures in taxonomy, supporting identification at the levels of population, sexual dimorphism, and responses to environmental conditions. Moreover, the surface architecture of wings is associated with various physical properties - such as optics and wettability - which have been the subject of studies aimed at assessing their functionality and biological interactions. This study investigates the nanoscale surface morphology of *Anopheles darlingi* and *Anopheles aquasalis* mosquito wings using Atomic Force Microscopy (AFM) and fractal analysis. High-resolution 3D AFM imaging revealed pronounced inter- and intra-species differences, with the ventral surface of *An. darlingi* (V-Ad) exhibiting the greatest roughness (Sq = 45.34 ± 3.20 nm) and height amplitude (Sz = 399.17 ± 65.46 nm), compared to the smoother dorsal surface of *An. aquasalis* (D-Aa, Sq = 23.54 ± 3.47 nm, Sz = 157.80 ± 17.91 nm). Spectral analysis via Fast Fourier Transform (FFT) and Hough transform identified directional anisotropy in *An. darlingi*, suggesting aligned nanostructures possibly related to aerodynamic or ecological adaptations. Monofractal analysis revealed that V-Ad surfaces had the highest Hurst coefficient (H = 0.96 ± 0.02), indicating persistent roughness, while dorsal surface of *An. aquasalis* (D-Aa) showed lower spatial correlation (H = 0.82 ± 0.03). These findings highlight functional nanostructural divergences among malaria vectors and underscore the utility of AFM and fractal descriptors in entomological and bioinspired materials research.

[1] R.J. Wootton. Rev. Entomol. 37 (1992) 113–140.
[2] A. Krishna, X. Nie, A.D. Briscoe, J. Lee, Sci. Rep. 11 (2021).
[3] E.P. Ivanova, et al, J. Colloid Interface Sci. 603 (2021) 886–897.
[4] F.O. Lehmann, S.P. Sane, M. Dickinson, J. Exp. Biol. 208 (2005).

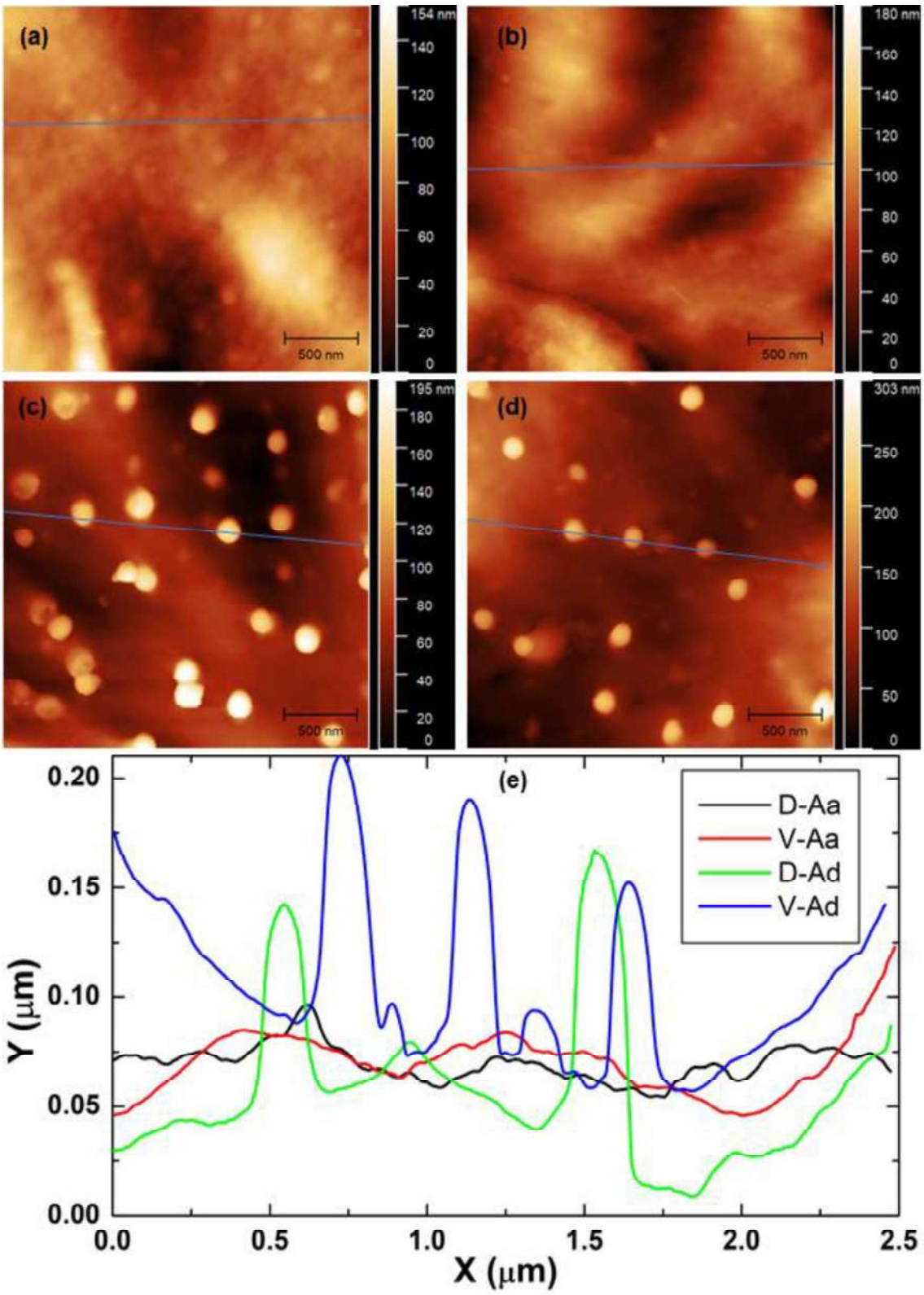

Figure 1. 3D AFM topographical maps of wings: (a) D-Aa, (b) V-Aa, (c) D-Ad, and (d) V-Ad sides. (e) Profiles from the line shown in AFM images.

Kapok Fiber Modifications (*Ceiba pentandra* (L.) Gaerth) for Oil Spill Remediation

Laís F.A.M. Oliveira[1]*, Leonardo M.T.M. Oliveira[2], Eduardo J.S. Fonseca[1], Vanderson B. Bernardo[3], Carmem L.P.S. Zanta[3], Jennifer N.S.R. de Oliveira[1], Samuel T. de Souza[1] and José L.S. Duarte[4].

[1]Physics Institute, Federal University of Alagoas, Brazil, [2]Laboratory of Materials for Environmental Remediation (LabMARE), Technology Center, Federal University of Alagoas, Brazil, [3]Chemistry and Biotechnology Institute, Federal University of Alagoas, Brazil and [4]Faculty of Chemical Sciences, Complutense University of Madrid, Spain.
*lais.farias@fis.ufal.br

The number of oil spill accidents is high, and their environmental impacts have driven the development of remediation techniques. Physical methods, such as containment barriers and sorbent systems, have stood out [1], especially when associated with naturally derived materials, which offer low cost and sustainability, often being reused residual biomass [2]. To make these materials competitive with synthetic ones, such as polyurethane and polypropylene foams [3], functional and structural modifications are required to improve handling, reduce hydrophilicity, ensure flotation stability, and increase mechanical strength [4]. Such modifications involve thermal treatments and immersion in chemical solutions [5,6]. *Ceiba pentandra* (L.) Gaerth, known as kapok, produces highly lipophilic fibers with a reported sorption capacity of 58 g/g [7,8]. These fibers are composed of cellulose, lignin, and hemicellulose, and have a hollow tubular morphology and a waxy surface composed of alkanes (octane, nonane, decane), aromatic compounds (benzene, o-xylene), and alcohols—as revealed by FTIR analysis (Figure 1). Tests conducted with natural and chemically/thermally modified kapok showed that, despite the induced physicochemical changes, the sorption capacity remained close to that of the natural fiber under most conditions. SEM and AFM images (Figures 2 and 3) demonstrated that more aggressive treatments partially removed the wax layer, increasing surface roughness. Nevertheless, even under these extreme conditions and with evident defunctionalization, the sorption performance was not drastically compromised (Table 1). This suggests that increased roughness acts as a compensatory factor, helping to maintain sorption performance, although it is not the only factor responsible. Therefore, kapok stands out as a renewable, accessible, and effective natural resource for mitigating environmental damage caused by oil spills.

[1] J. Liu et al., *Research on oil boom performance based on Smoothed Particle Hydrodynamics method*. 18 (2023) e0289276.
[2] K.C. Vasconcelos et al., *Application of Agricultural Waste form Main Brazilian Crops as Adorbent fo Wasterwater Treatment*. 15 (2023) 956-983.
[3] A. De Folly d'Auris et al., *A novel polyurethane-based sorbent material for oil spills management.* 11 (2023) 111386.
[4] S. Fürtauer et al., *Current status of cellulosic and nanocellulosic matrerials for oil spill cleanup.* 13 (2021) 2739.
[5] L. Wang, C. Liu, *Hydrothermal treatment and transesterification modification of rice straw for oil spill absorption material.* 36 (2017) 1811-1817.
[6] S.N.C.M. Hussein et al., *Study os acid treated mixed sawdust as natural oil sorbent for oil spill.* 19 (2019) 1382-1389.
[7] K.C. Vasconcelos et al., *Novel kapok pods (Ceiba pentandra (L.) Gaerth) adsorbent and its reusability by transformation on hydrochar with an outstanding adsorptive capacity for Rhodamine B removal.* 326 (2023) 124787.
[8] L.M. Oliveira et al., *Ultrafast diesel oil spill removal by fibers form silk-cotton tree: Characterization and sorption potential evaluation.* 263 (2020) 121448
[9] This research was supported by CNPq (Brazil), CAPES (Brazil) and UFAL (Brazil).

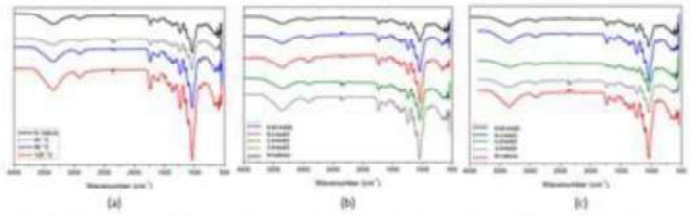

Figure 1. (**a**) FTIR spectra of the kapok samples treated at different temperatures. (**b**) Acid activation and (**c**) alkali activation.

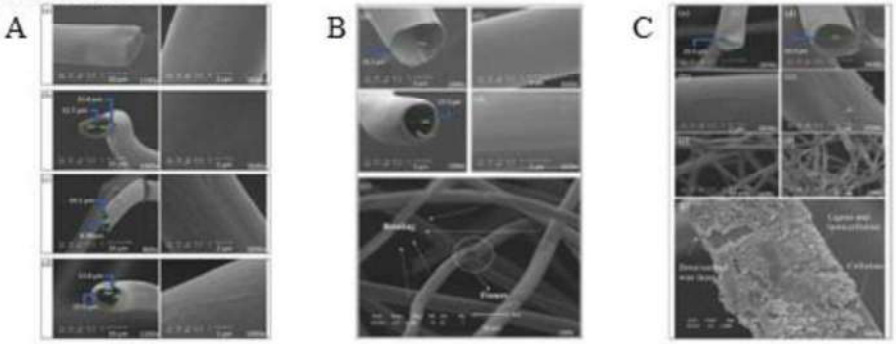

Figure 2. SEM images of kapok fibers under different treatments: (A) Untreated (a) and treated at 60°C (b), 90°C (c), and 120°C (d). (B) Acid-treated fibers with HCl 0.1 mol/L (a), surface—HCl 0.1 mol/L (b), 2.0 mol/L (c), surface 2.0 mol/L (d), fissures on the structure (e). (C) Alkaline-treated fibers with NaOH: 0.1 mol/L – lumen (a), surface (b), and general fiber condition (c); 2.0 mol/L lumen (d), surface (e), (**f**) general fiber condition (f), and evidence of advanced mercerization (g).

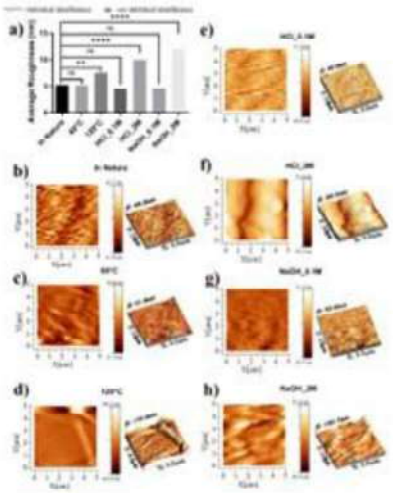

Figure 3. Average roughness (Ra) of natural and post-treatment kapok fibers. (a) Average values of roughness (Ra) of all kapok fibers analyzed. (b–h) Topographical images obtained using AFM of the fibers: (b) in natura, (c) treated at 60 °C, (d) treated at 120 °C, (e) treated with HCl 0.1 mol/L, (f) treated with HCl 2.0 mol/L, (g) treated with NaOH 0.1 mol/L, and (h) treated with NaOH 2.0 mol/L.

Table 1. Relationship between sorption and roughness of kapok fibers in activation processes.

	Sorption (g/g)		Roughness (nm)		Functionalization	
Treatment	**Low Limit**	**High Limit**	**Low Limit**	**High Limit**	**Low Limit**	**High Limit**
Raw	58.5 [8]		4.757		C-C, CHx, C=O [8]	
Thermal	50.29	57.8	5.092	7.267	Slight CHx reduction	C-O increased
Acidic	50.2	50.96	4.470	9.735	Almost constant	C-O increased
Alkali	38.56	56.21	4.404	12.35	Almost constant	OH and C-O increased and C-H, C=O reduced

Nanoscale Characterization of Beta Ti processed by Accumulative Roll Bonding and 3D printing alloy for Application as Biomaterials

Conrado R. M. Afonso[1], Mariana L. Lourenço[1], Vinicius Gonçalvez[1], Marcio Sangali[2], Peter Minarik[3], Danielle C. C. Magalhães[1], Rubens Caram[2]

[1]Department of Materials Engineering (DEMa), Federal University of São Carlos (UFSCar), 13565-905, São Carlos/SP, Brazil, [2] Universidade Estadual de Campinas (FEM/Unicamp), Campinas - SP, 13083-970, Brazil. [3]Charles University (CUNI), Department of Physics of Materials, Ke Karlovu 5, 12116 Prague, Czechia.
*conrado@ufscar.br

β-Ti alloys are considered for biomedical applications due to their mechanical properties, good biocompatibility, corrosion resistance and lower elastic modulus in the range of 42 to 80 GPa [1]. Therefore, Ti and its combinations have been applied as biomedical implants, such as the Ti-6Al-4V combination. However, it presents problems regarding the cytotoxicity of Al and V elements related to neuronal disruption and Alzheimer's disease, even with good mechanical properties. The present study aims to evaluate the feasibility of producing through advanced processing by laser 3D printing by laser power bed fusion (LPBF) and accumulative roll bonding (ARB) of bcc multiprincipal β Ti-33Nb-33Zr (wt.%) alloy. The objective was to define which thermomechanical processing parameters (degree of deformation per pass, intermediate annealing temperature and number of ARB cycles) would produce satisfactory, well-adhered joints with few or no voids/defects. The multiprincipal β Ti alloy was obtained by laser 3D printing (LPBF) according to parameters of Table 1.a and by arc melting, showing a lower Young's modulus (E = 47 GPa). The characterization of the LPBF β Ti alloy was performed by X-ray diffraction (XRD), optical (OM) and scanning (SEM) and transmission electron microscopy (TEM). Vickers microhardness and elastic modulus were used to evaluate mechanical properties. 3D printing of multiprincipal β Ti-33Nb-33Zr alloy formed a refined stable β-Ti microstructure (Figure 1.a to 1.c) with microhardness of 310 HV and low elastic modulus of (E = 62 GPa) suitable for application as biomedical implants avoiding stress shielding. The main results indicated that it is feasible to produce such heterostructured sheets with up to 7X ARB cycles, which were preheated for 5 min at 500 °C. The tests performed at 300 °C indicated that there was not enough adhesion between the layers. Even at 500 °C, the results suggested that an extra pass at the end of the last ARB cycle could increase the adhesion of the last created interface. Results showed increasing of Vickers microhardness of Ti-α (from 212 to 290 HV) and β Ti-33Nb-33Zr (from 231 to 303 HV) before deformation and after 7 passes of ARB (Table 1.b). Figure 1.d to 1.g shows TEM-ASTAR analysis of interface between heterostructure interface of β Ti-33Nb-33Zr alloy (upper part) with cp Ti (bottom part) by ARB showing pancaking nanoscale grains (aligned in the direction of rolling by ARB) from β-Ti phase and sub-micron grain from α-Ti in virtual bright field (VBF) image (Fig. 1.d), Index image (Fig. 1.e), IPF-X combined with Index (Fig. 1.f), and Phase's map with β Ti-33Nb-33Zr alloy bcc phase side (in red) in the upper part, and α-Ti phase (in green) (Fig. 1.g). Regarding elastic modulus, pure materials showed α-Ti (E = 100 GPa) and β Ti-33Nb-33Zr (E = 68 GPa) previously to the deformation, after 4 and 7 passes of ARB the heterostructure showed E = 74 GPa and 66 GPa, respectively, confirming a reduction of nanostructured α-Ti /β Ti-33Nb-33Zr in-situ deformed heterostructure.

[1] Neto., J. V. C. et al. ACS Biomater Sci Eng, 10 (2024) 6029.
[2] De Mattos, F.N. et al. Mater Lett., 358 (2024) 135776.
[3] Silva, R. et al. J. Mater Res Tech. 35 (2025) 2055.
[4] This research was supported by FAPESP and CNPq (Brazil).

Table 1. (a) Laser 3D printing by OmniTek LPBF parameters including laser power of 200 W and scanning speed of 500 to 1000 mm/s using. (b) Theoretical and experimental elastic moduli for Ti and its alloys and for the materials produced in this work by ARB.

a TNZ33 Alloy	Power (w)	Laser speed (mm/s)
AM-500	200	500
AM-750	200	750
AM-1000	200	1000

OmniTek, model OMNISINT-160 with fiber laser Yb:YAG, raycus RFL-C500, and wavelenght λ=1070 nm, spot size of ∅ = 80 µm.

b Material/Alloy (wt.%)	E (GPa)	Phases
Human Bone	30	–
Ti-6Al-4V	110	α + β
c.p. Ti	100 ± 2	α
MEA Ti-33Nb-33Zr	74 ± 1	β
α+β HM (4X)	78 ± 1	α + β*
α+β HM (5X)	89 ± 1	
α+β HM (6X)	66 ± 1	
α+β HM (7X)	65 ± 1	

Note: α + β* is a heterostructured produced in-situ during ARB processing.

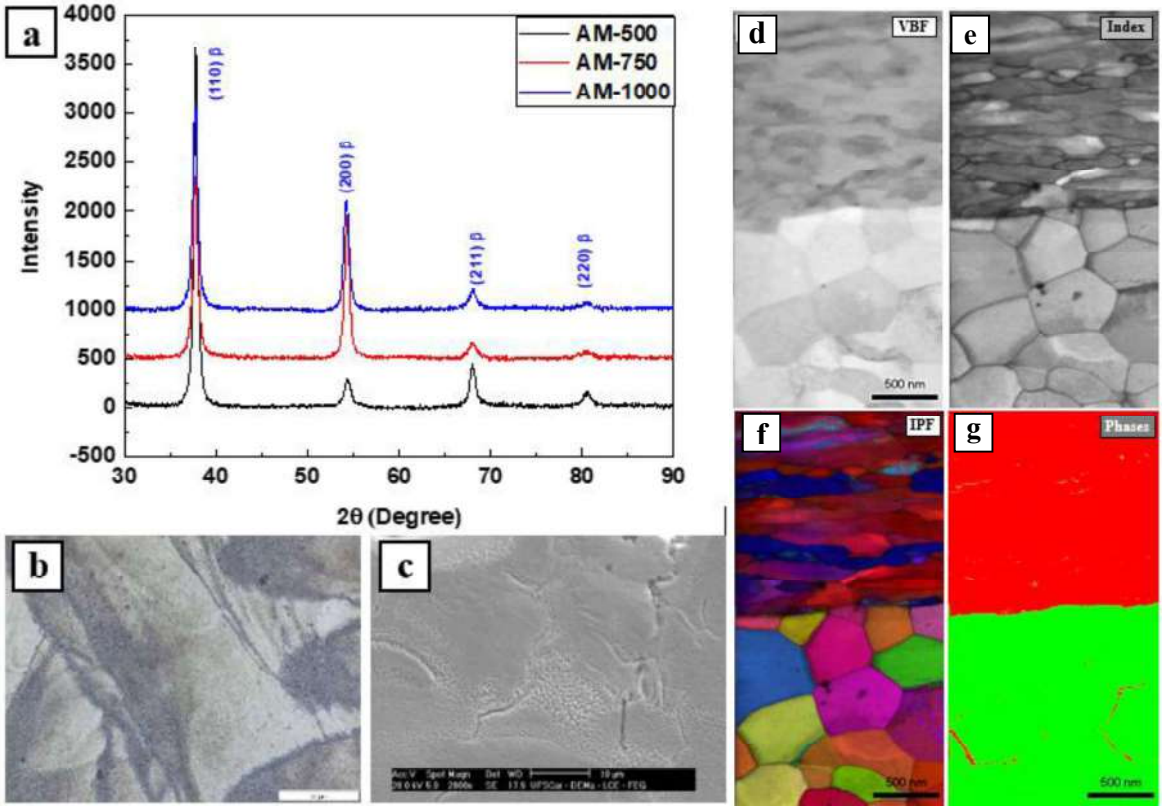

Figure 1. a) XRD of the Ti-33Zr-33Nb array obtained by 3D printing: Power = 200 W and laser speed (v= 500, 750, 1000 mm/s. b) optical and c) LPBF MEB for v= 750 mm/s. TEM-ASTAR analysis of interface between heterostructure interface of β Ti-33Nb-33Zr alloy (upper part) with cp Ti (bottom part) by ARB showing pancaking nanoscale grains (aligned in the direction of rolling by ARB) from β-Ti phase and sub-micron grain from α-Ti in: (a) virtual bright field (VBF) image, (b) Index image, (c) IPF-X combined with Index, and (d) Phase´s map with β Ti-33Nb-33Zr alloy bcc phase side (in red) in the upper part, and α-Ti phase (in green), respectively

Scanning thermal microscopy for nanoscale mapping of thermal properties of epoxy/carbon fiber composite and multiphasic ceramic: a parameters optimization study

Otávio Berenguel[1]*, Danilo Biazon Janes[1], Carlos Alberto Rodrigues Costa[1], Edson Roberto Leite[1].

[1]Brazilian Nanotechnology National Laboratory (LNNano), Brazilian Center for Research in Energy and Materials (CNPEM)
*otavio.berenguel@lnnano.cnpem.br

Scanning thermal microscopy (SThM) is a type of scanning probe microscopy (SPM) that enables the acquisition of high-resolution maps of temperature distribution and thermal conductivity variations at the nanometric level [1]. This technique can be applicable to a broad range of materials and provides thermal contrast that is directly correlated with the topography of the sample analyzed [2]. This technique was first widely recognized through the pioneering work of C. C. Williams and H. K. Wickramasinghe [2]. Despite its early conceptualization, SThM remains a relatively underutilized but powerful SPM technique. In practice, a thermal probe equipped with a resistive element near the tip apex scans the sample surface [3]. The resistive element heats slightly under a small voltage, and its resistance is monitored via a Wheatstone bridge (as the scheme in Figure 1) and reveals local thermal conductivity variations [3]. In this work, we report the optimization of SThM parameters during the analysis of two distinct systems: an epoxy/carbon fiber composite and a multiphasic ceramic (containing zinc and bismuth oxides, and antimony-based spinel phases). Using a nanoIR2-s (Bruker™) system operated in contact mode with a PR-EX-AN2-300 probe (Bruer™), key parameters such as the heating voltage, the setpoint, and the scan rate were systematically varied, in this order, to enhance contrast and improve measurement quality. The results offer guidance for optimizing SThM in different materials with different thermal and topographical features. Figure 2 presents the topography and SThM profiles obtained during the heating voltage variation for the composite and ceramic samples analyses. Figure 3 displays the corresponding topography and SThM profiles acquired during the variation of the setpoint and the scan rate for the ceramic sample. From the obtained data, we could observe that the heating voltage actually must be the first parameter to be optimized to balance sensitivity, and thermal stability, ensuring high-quality, reliable, and accurate SThM maps. It is worth noting that a very low voltage (a few tenths of a volt) results in a weak thermal signal, whereas an excessively high voltage can saturate the sensor or even damage the sample. Following the optimization of the heating voltage, additional thermal maps of the ceramic sample were acquired by systematically varying other acquisition parameters, such as setpoint and the scan rate. The setpoint defines the normal force applied by the probe to the sample and must be carefully adjusted to ensure good thermal contact without damaging either the sample or the probe. An adequately tuned interaction force allows the probe to accurately follow the sample topography while maintaining a stable thermal coupling. In contrast, an improperly adjusted setpoint may lead to thermal drift or loss of contact during scanning, thus compromising the quality of the thermal map. The scan rate must also be optimized to ensure stable thermal contact while preventing potential damage to the sample or the probe.

[1] Y. Zhang et al., Adv. Funct. Mater. 30 (2020) 1900892.
[2] C.C. Williams, H.K. Wickramasinghe, Microelectron. Eng. 5 (1986) 509.
[3] E. Erickson, P. De Wolf et al., *Atomic Force Microscopy: A Comprehensive Guide to Expanding Your Materials Research Capabilities – The Definitive AFM Modes Handbook*, Bruker (2nd ed.).
[4] The authors acknowledge the LNNano/CNPEM facilities supported by the Ministry of Science, Technology and Innovations (MCTI).

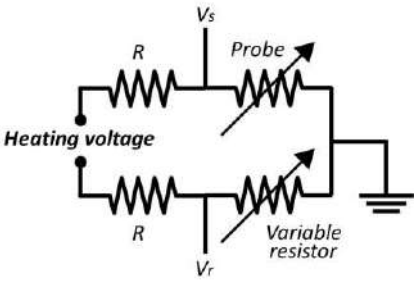

Figure 1. Scheme of Wheatstone bridge setup of SThM instrument. The heating voltage is the voltage applied to both sides of the bridge. The variable resistor needs to be adjusted to the same probe resistance. The SThM signal is obtained from the voltage difference (V_s-V_r). Typically, for measuring small changes in temperature of the probe, this signal must be amplified up to 1000x.

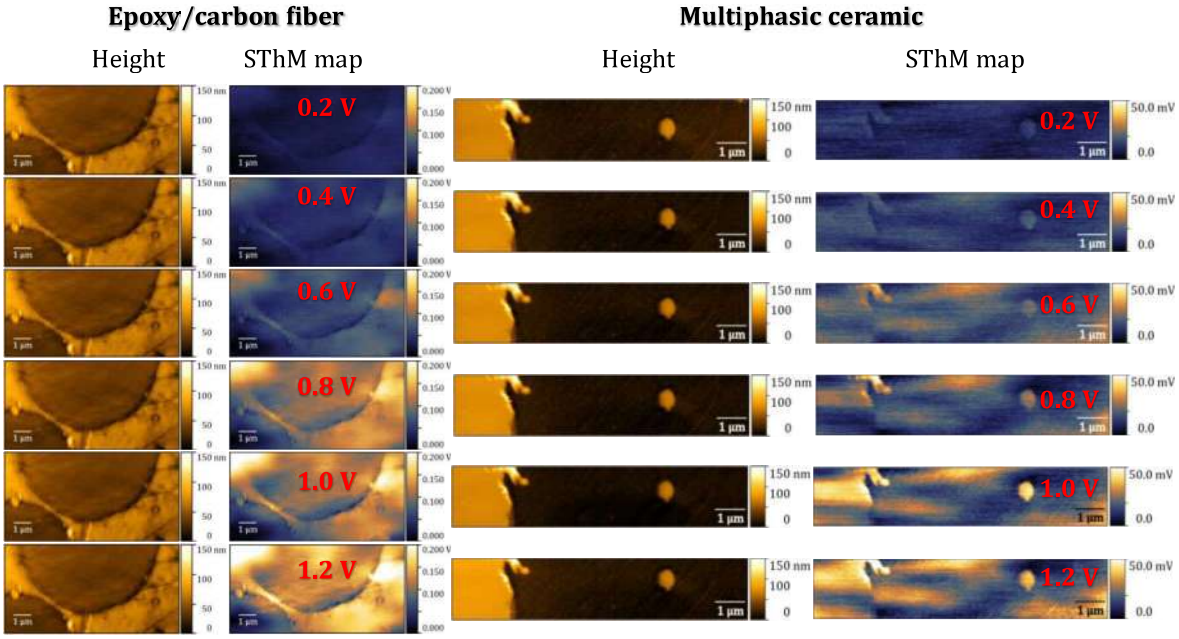

Figure 2. Topography images are shown in orange tones, while SThM maps are displayed in blue/yellow-scale color maps. In the SThM images, the color bar intensity is inversely proportional to the local thermal conductivity of the domains. The heating voltage used in each acquisition is indicated in red above each SThM image. The epoxy/carbon fiber composite sample images correspond to a 10 × 5 µm² are, while the multiphasic ceramic to a 10 × 2 µm² area.

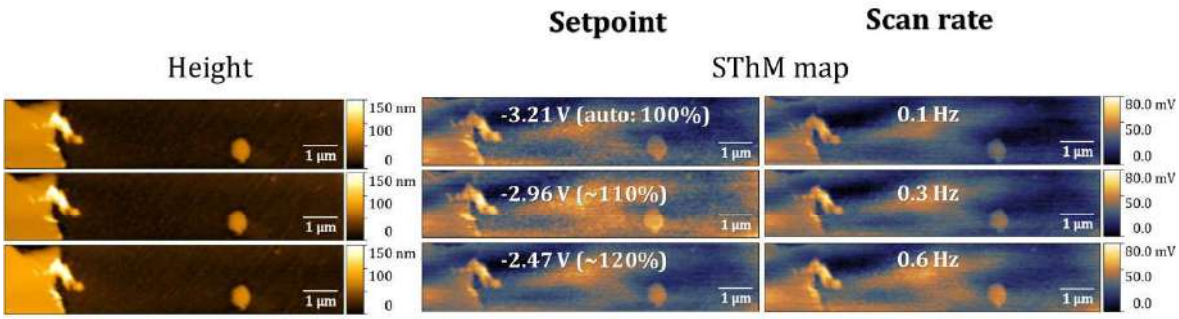

Figure 3. Topography images are shown in orange tones, while SThM maps are displayed in blue/yellow-scale color maps. In the SThM images, the color bar intensity is inversely proportional to the local thermal conductivity of the domains. The setpoint and scan rate used in each acquisition are indicated in white above each SThM image. To achieve optimal SThM contrast, a heating voltage of 1.0 V was applied in the tests of setpoint and scan rate variations. In the tests of scan rate variation, the setpoint was fixed at -2.96 V (~110% comparing to the auto/default system setpoint). The multiphasic ceramic sample images correspond to a 10 × 2 µm² area.

Image processing and alanysis for life science and materials science, including new artificial intelligence, machine learning, and deep learning methods

Automatic Rock Chip Characterization Combining LIBS and the Segment Anything Model (SAM)

Bernardo Amaral Pascarelli Ferreira[1]*, Sidnei Paciornik[1], Melissa Narbey[2], Victor Mota e Nogueira[2]

[1]Departamento de Engenharia Química e de Materiais (DEQM), PUC-Rio, [2]Automated Mineralogy Incubator (AMI) – AXT PTY LTD, WA, Australia
*bernardo.amaral@aluno.puc-rio.br

The Elemission ECORE scanner utilizes Laser-Induced Breakdown Spectroscopy (LIBS), a rapid, versatile, and robust non-destructive technique widely used for quantitative mineral characterization without extensive sample preparation [1, 2]. Accurate segmentation of rock chips in optical images is crucial for correlating LIBS mineral maps with individual particles, enabling detailed phase composition and grain-size analysis within heterogeneous rock samples. However, traditional digital image processing and deep learning-based segmentation methods struggle with the high variability in rock fragment composition and morphology. Moreover, training deep learning models requires extensive annotated datasets, which are laborious and often impractical, especially for fine granulometries. This study proposes the use of the Segment Anything Model (SAM) [3], a state-of-the-art foundation model for image segmentation, to overcome these challenges. SAM's zero-shot generalization capability enables effective segmentation of diverse rock fragments without the need for sample-specific training or manual annotation. We demonstrate that SAM can reliably detect particle boundaries across varied geological samples, providing a generalized segmentation approach robust to compositional heterogeneity, as shown in Figure 1. To address overlapping detections inherent to SAM's predictions, a simple Intersection-over-Union (IoU) thresholding algorithm was applied, refining segmentation outputs. Although quantitative ground-truth data is unavailable, qualitative visual assessment confirms the high accuracy of SAM's segmentation results. Manual spatial alignment of segmented images with corresponding LIBS mineral maps allows integration of particle-level segmentation with elemental analysis, as Figure 2 demonstrates. This integration facilitates the calculation of phase composition and grain-size distribution within individual rock fragments, enhancing LIBS as a practical alternative to more complex techniques such as scanning electron microscopy coupled with energy-dispersive spectroscopy (SEM-EDS). Overall, SAM presents a fast, reliable, and sample-generalizable solution for rock fragment segmentation, advancing mineral characterization workflows that rely on LIBS data.

[1] Rifai, Kheireddine, et al. "Quantification of lithium and mineralogical mapping in crushed ore samples using laser induced breakdown spectroscopy." *Minerals* 12.2 (2022): 253.
[2] Capela, Diana, et al. "Robust and interpretable mineral identification using laser-induced breakdown spectroscopy mapping". Spectrochimica Acta Part B: Atomic Spectroscopy 206 (2023) 106733.
[3] Kirillov, Alexander, et al. "Segment anything." Proceedings of the IEEE/CVF international conference on computer vision. 2023.

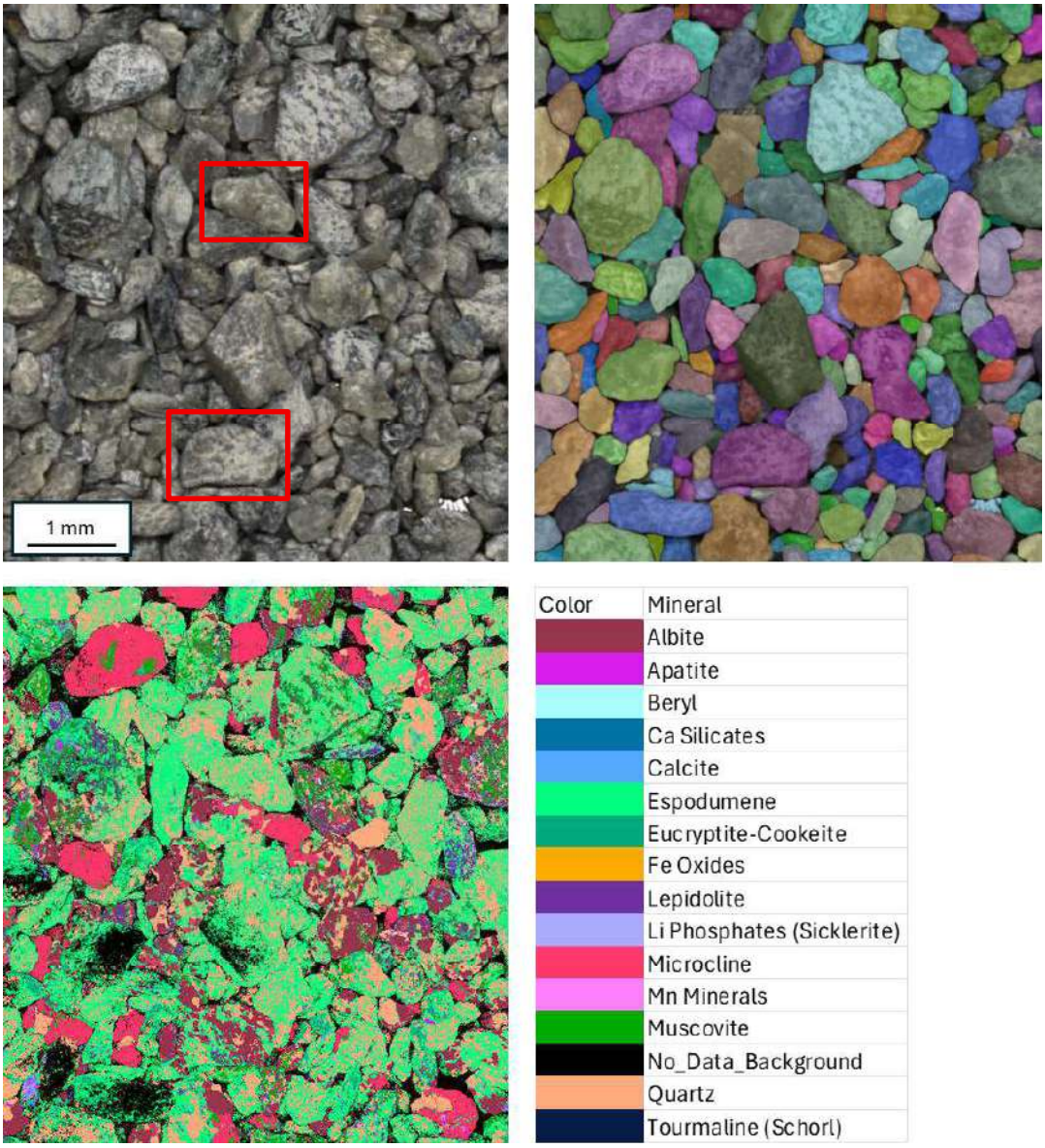

Figure 1. Top row: Left – Original optical image, +2 mm granulometry. Red rectangles highlight two particles analyzed in Figure 2. Right – SAM segmentation result. Bottom row: LIBS mineral map and phase color legend.

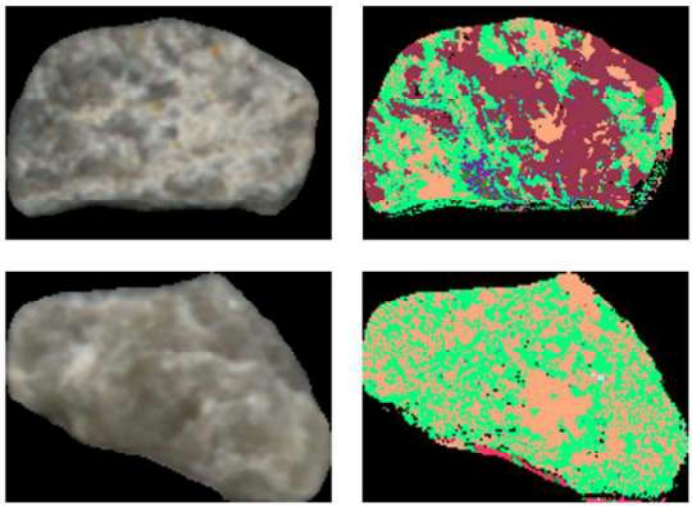

Figure 2. Left Column: Single particles isolated from the optical image after SAM segmentation. Right Column: Same particles analyzed by LIBS.

Automatic Sinter Feed Characterization combining Segment Anything Model and Classification Model

Bernardo Amaral Pascarelli Ferreira[1], Laura Nunes de Menezes[1*], Sidnei Paciornik[1], Marcos H. de P. Mauricio[1], Maria Beatriz Vieira[2], Érica Simões Rodrigues Vinco[3], Lillian Serra de Mello[3], Kamila do Espírito Santo[3], Igor Aniceto Santos[3], Vinicius Thiago Lecco Rampinelli[3], Kioshi Márcio Kaneko[3]

[1]Departamento de Engenharia Química e de Materiais (DEQM) da Pontifícia Universidade Católica do Rio de Janeiro (PUC-Rio), [2]BV Mineral Consultoria, [3]ArcelorMittal Brasil
*laura.nunes@aluno.puc-rio.br

Sinter feed characterization is a critical step in optimizing sintering processes in the steel industry, where accurate phase composition analysis directly impacts product quality. Many companies still rely on visual classification by a trained operator, with well-known limitations. In previous works, traditional image processing routines were developed with successful results. However, these methods still struggle to segment opaque and complex multi-phase particles, such as quartz and iron oxides, limiting their applicability [1]. Deep learning-based instance segmentation methods offer improvements but require extensive annotated datasets and complex training procedures, which are often impractical due to the labor-intensive nature of data labeling and the variability of sinter feed samples [2]. This study proposes a novel two-step approach to automate sinter feed particle segmentation and phase classification by leveraging the Segment Anything Model (SAM) [3] combined with the YOLOv11 classification head [3]. SAM was employed to detect particles across eight 4×4 mosaic optical microscopy images from four chemically distinct sinter feed samples sourced from different mines. Despite the absence of ground-truth annotations, qualitative visual assessment demonstrated that SAM effectively delineates particle boundaries, including challenging opaque and multi-phase particles, as shown in Figure 1. Following segmentation, a small, manually curated training set comprising seven mineral phases (Compact Hematite, Porous Hematite, Magnetite, Martite, Quartz, Goethite, and Terrous Goethite) was generated from SAM-detected particles (Figure 2). The classification model within YOLOv11 was trained on this dataset and evaluated on a separate test set, achieving recall and precision metrics exceeding 88% for most phases, as shown in Table 1. These results highlight the potential of combining SAM's generalizable segmentation capabilities with targeted classification to circumvent the need for large-scale annotated datasets and complex segmentation model training. While this research is ongoing and minor segmentation inaccuracies by SAM are being addressed, the approach demonstrates a promising direction for efficient, scalable, and accurate sinter feed characterization using optical microscopy and deep learning. [5]

[1] Amaral Pascarelli Ferreira, Bernardo, et al. "Instance segmentation of quartz in iron ore optical microscopy images by deep learning." Minerals Engineering 211 (2024): 108681.
[2] Caldas, Thalita Dias Pinheiro, et al. "A methodology for phase characterization in pellet feed using digital microscopy and deep learning." Minerals Engineering 212 (2024): 108730.
[3] Kirillov, Alexander, et al. "Segment anything." Proceedings of the IEEE/CVF international conference on computer vision. 2023.
[4] https://docs.ultralytics.com/pt/models/yolo11/.
[5] This research was supported by CNPq (Brazil), CAPES (Brazil), FAPERJ (Brazil), and ArcelorMittal Brazil.

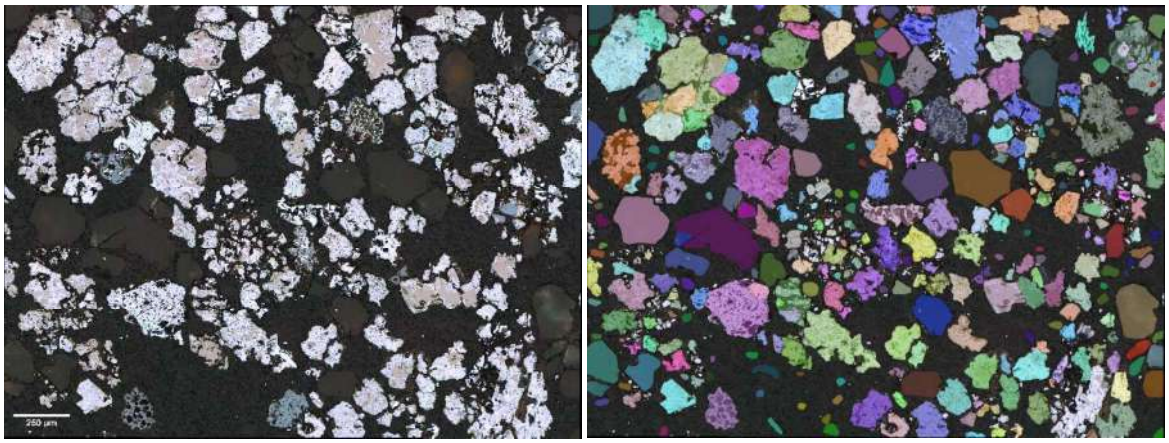

Figure 1. Left- Original sinter optical image. Right – SAM segmentation result. Notice the detection of hard-to-segment quartz particles.

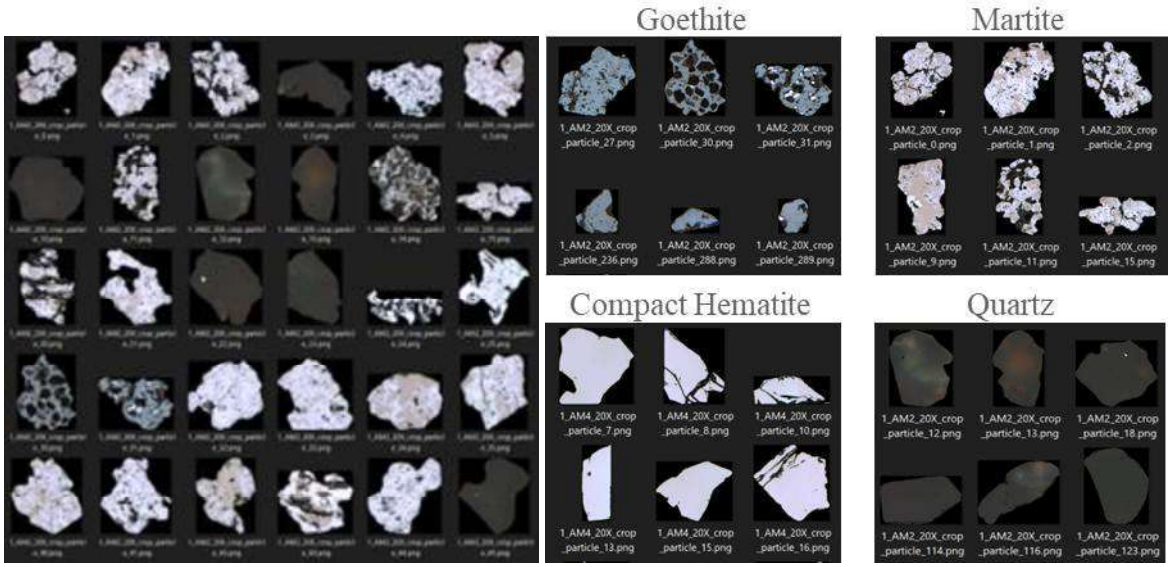

Figure 2. Left- Automatically extracted particles. Manual separation of some particle classes to create a training set for YOLO.

Table 1. Metrics for the YOLO classification of seven particle classes

	Goethite	Terrous Goethite	Compact Hematite	Porous Hematite	Magnetite	Martite	Quartz
True Positive	99	5	98	72	3	119	102
False Negative	10	5	8	9	9	5	1
False Positive	4	5	4	5	0	20	9
Recall	90.8%	50.0%	92.4%	88.9%	25.0%	96.0%	99.0%
Precision	96.1%	50.0%	96.0%	93.5%	100.0%	85.6%	91.9%

Development of a Convolutional Neural Network-Based Platform for the Classification of Force Curves Acquired by Atomic Force Microscopy in Pharmaceutical Inputs

Wellington Silva Ferreira[1]*, Beatriz Ferreira Patricio[2], Gilberto Weissmüller[1].

[1] Institute of Biophysics Carlos Chagas Filho, Federal University of Rio de Janeiro,
[2]Biomedical Institute. State University of Rio de Janeiro
*wellington.silvaferreira@biof.ufrj.br

Atomic Force Microscopy (AFM), a member of the Scanning Probe Microscopy (SPM) family, was first demonstrated in 1986 and revolutionized surface visualization by enabling the analysis of both conductive and non-conductive materials at atomic resolution in a non-destructive manner [1]. Among its modes of analysis, force curve (FC) acquisition stands out, since it allows the quantification of tip–sample interactions and the investigation of specific molecular interactions through probe functionalization [2]. In the pharmaceutical context, this approach provides valuable insights into the behavior of the interaction of active pharmaceutical ingredients (APIs) and excipients, aiding in the understanding of their processability and the optimization of solid formulations [3]. However, the large volume of curves acquired poses a significant challenge for manual data curation, interpretation, and consistent processing. Although machine learning has advanced in several AFM applications, its use in force curve analysis remains incipient, particularly regarding the classification of these curves as “good” or “not suitable” [4]. In this context, this work aims to develop and validate a machine learning-based platform for the automated analysis of force curves obtained by AFM in air, focusing on classifying these curves to optimize data curation. For database construction, samples of APIs and excipients were deposited onto stainless steel disks and compressed to form flat surfaces suitable for force spectroscopy analyses, performed with cantilevers functionalized with active ingredient crystals. Based on these analyses, convolutional neural network (CNN) models with different architectures were trained for force curve classification. In addition to providing relevant information on the behavior of the interaction between APIs and the excipients 36.864 curves were manually classified, and the nanomechanical information of the good ones was extracted (Figure 1). These same curves were used to train 24 distinct CNN models, and one of which showed promising performance, with high accuracy, robust generalization, and no evidence of overfitting (Figure 2). These results pave the way for the expanded use of artificial intelligence in force spectroscopy, enabling faster, more precise analyses applicable to different research contexts involving AFM.

[1] Binning et al., Atomic Force Microscope. 56 (1986) 930.
[2] Butt et al., Force Measurements with the atomic force microscope: Technique, interpretation and applications. 59 (2025) 1.
[3] Eve et al., A study of single drug particle adhesion interactions using atomic force microscopy. 238 (2002) 17.
[4] Laskar and Celano., Scanning probe microscopy in the age of machine learning. 1 (2023) 1.
[5] This research was supported by CNPq (Brazil) and CAPES (Brazil).

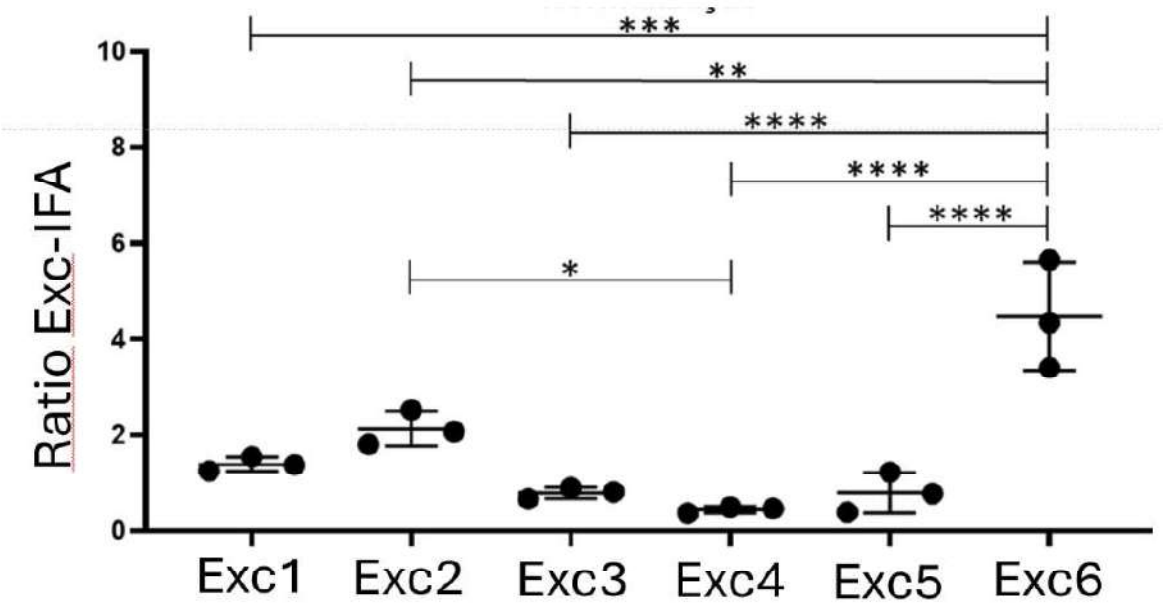

Figure 1. Ratio between the mean interactions of API–Excipient and API–API obtained by force spectroscopy in AFM for each evaluated excipient (Exc). A total of 1,024 curves were analyzed for API–API interactions and 1,024 curves for API–Excipient interactions, resulting in 6,144 curves in triplicate and a total of 36.864 curves across all compounds. Each point in the graph represents the ratio obtained between two AFM interaction images (one referring to the API–Excipient interaction and the other to the API–API interaction), allowing the assessment of the relative difference in adhesion between the samples after normalization. The values were compared using a One-Way ANOVA test with Tukey's post hoc analysis (*p<0.05; **p<0.005; ***p<0.0001).

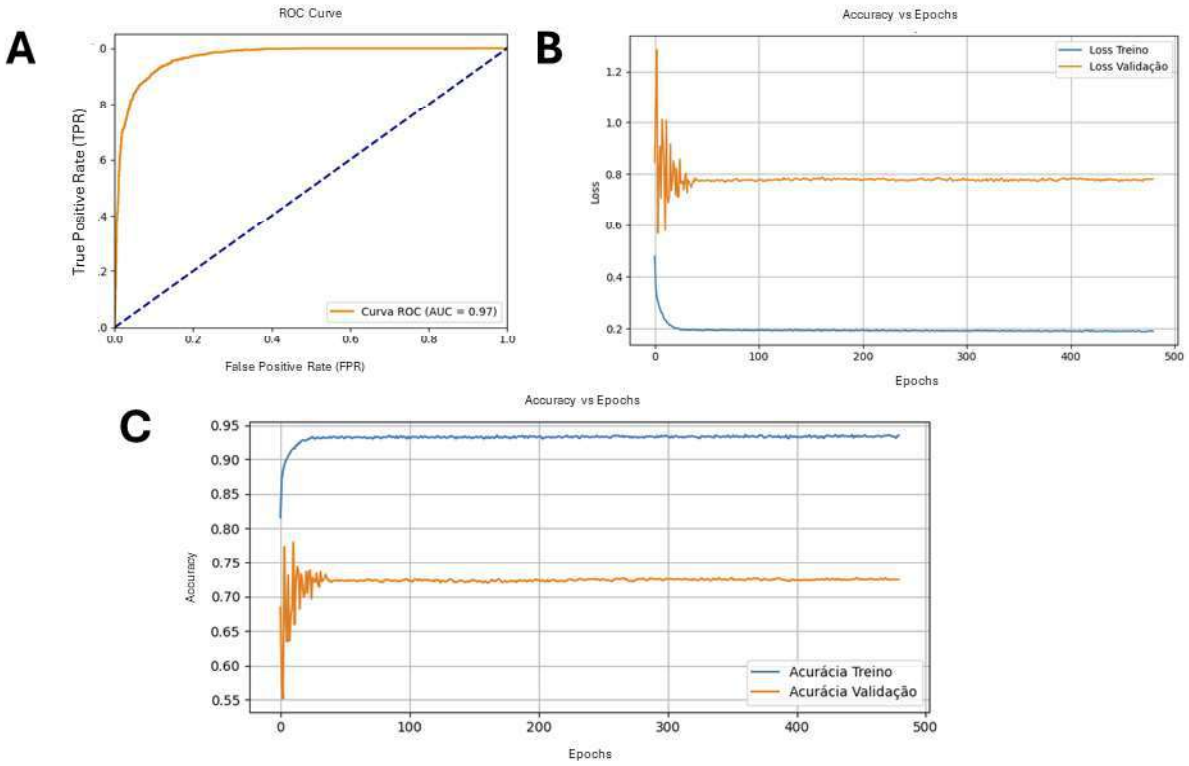

Figure 2. Performance of the convolutional model for classifying AFM force curves. (A) ROC curve with AUC = 0.97, indicating high discriminative capacity. (B) Evolution of the loss function for training and validation over the epochs. (C) Evolution of accuracy for training and validation, showing stability after the initial iterations.

Development of Deep Learning Model for Composition Determination in Mudrocks Using SEM and EDS Images

Thalita Dias Pinheiro Caldas[1]*, Maria Vitoria Torres Finamore[1], Carlos Alberto Senna[1], Gabriel Branco Pinheiro[1], Erveton Pinheiro Pinto[2], Rodrigo Prioli[1], Dorval Carvalho Dias-Filho[3], Marcos Klotz de Souza[3], Yaro M. Parizeck[3].

[1]Departamento de Física, Pontifícia Universidade Católica Do Rio De Janeiro, Rio De Janeiro, Brazil, [2] Universidade Federal do Amapá, [3]Petrobras, Rio De Janeiro, Brazil.
*thalitacaldas@puc-rio.br

Mudrocks are sedimentary rocks with low porosity, with most pores of nanometer size and associated with clay minerals. [1-2] The identification of the non – clay minerals (such as quartz, feldspar, pyrite, plagioclase, calcite, etc.) and clay minerals in these rocks are therefore of significance. Scanning Electron Microscopy (SEM) is one of the most used methods for mineralogical and pore identification in rocks. The classical workflow is based on SEM mosaics, of millimeter sizes, composed of high-resolution backscattering or secondary electron images. The mosaics clearly show each phase of interest. However, quantifying the non – clay minerals, clay minerals, and pore phases is challenging due to the difficulty in segmenting these phases based on pixel hues, as many phases have similar hues, making traditional methods unfeasible. [3] We developed an artificial intelligence (AI) model, based on a U-Net architecture [4] and trained by an expert to recognize, segment, and classify these phases in SEM images. The U-Net was chosen as a Deep Learning network architecture capable of performing semantic segmentation with little input data and preserving essential image details. A total of 150 images were used for labeling. In addition to the "non – clay mineral" and "clay mineral" classes, we noticed that there was a need to label a third class, called "artifacts", consisting of cracks and surface features introduced by the natural physical process of pressure relief during sample acquisition and evidence of the removal of grains during the sample preparation. After labeling the images, the dataset was divided into a training set consisting of 120 images and a validation set with 30 images. Model 1 was trained using the training set. Once the model was developed, it was tested on the validation images to compare its predictions against the ground truth. This process resulted in accuracy rates of 82% for the non – clay mineral class and 85% for the clay mineral class. Subsequently, Model 1 was applied to all images from a set of 14 mudrock samples, from basins in southeastern Brazil, allowing us to determine the proportion of each class within each sample. Figure 1a shows one of the original images from this sample set alongside the model's identification results shown in Figure 1b. Figure 2a illustrates the results for each sample as a function of burial depth. The accuracy rates indicate that the model aligns well with the labeling performed. To improve the labeling process, we incorporated Energy-Dispersive X-Ray Spectrometry (EDS) data from the samples in our analysis. We developed an automated routine to identify the non – clay minerals based on the element maps obtained from the EDS measurements. Using the non – clay minerals identified by EDS, we refined the labeling and selected a set of 37 representative images from the 14 samples for training Model 2. This model was then applied to all samples, and the results are shown in Figure 1c, compared to Model 1 (Figure 1b). Additionally, the fractions of each class per sample were calculated, as shown in Figure 2b. It is evident that with refined labeling, the identification of the classes improved significantly. In Model 2, the boundaries between non- clay minerals and clay minerals are better defined and align more closely with observations from the original images. However, the amount of clay minerals is still overestimated. Despite using much less data than Model 1, Model 2 achieved promising results. Furthermore, Model 2 is considered more reliable because it was validated with the EDS mosaics.

[1] R. G. Loucks, R. M. Reed, S. C. Ruppel, and U. Hammes, “Spectrum of pore types and networks in mudrocks and a descriptive classification for matrix-related mudrock pores,” Am Assoc Pet Geol Bull, vol. 96, no. 6, pp. 1071–1098, 2012, doi: 10.1306/08171111061.
[2] A. Rezaeyan et al., “Compaction and clay content control mudrock porosity,” Energy, vol. 289, Feb. 2024, doi: 10.1016/j.energy.2023.129966.
[3] S. Evsevleev, S. Paciornik, and G. Bruno, “Advanced Deep Learning-Based 3D Microstructural Characterization of Multiphase Metal Matrix Composites,” Adv Eng Mater, vol. 22, no. 4, Apr. 2020, doi: 10.1002/adem.201901197.
[4] O. Ronneberger, P. Fischer, and T. Brox, “U-Net: Convolutional Networks for Biomedical Image Segmentation,” May 2015, [Online]. Available: http://arxiv.org/abs/1505.04597
[5] J. Schindelin et al., “Fiji: an open-source platform for biological-image analysis,” Nat Methods, vol. 9, pp. 676–682, 2012.

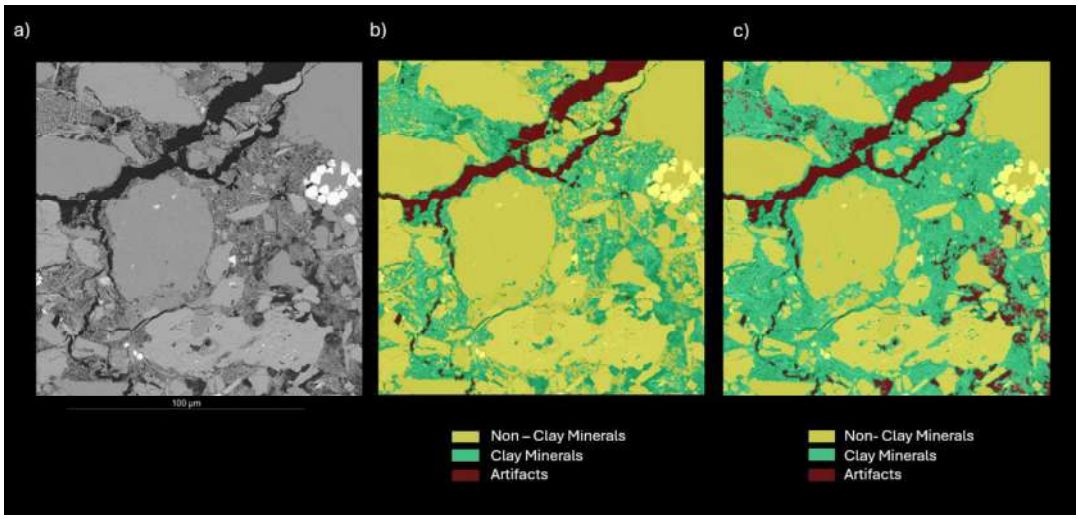

Figure 1 - Comparison between the predictions of the models. In a) the Original SEM image, in b) the prediction of Model 1, and in c) the prediction of Model 2

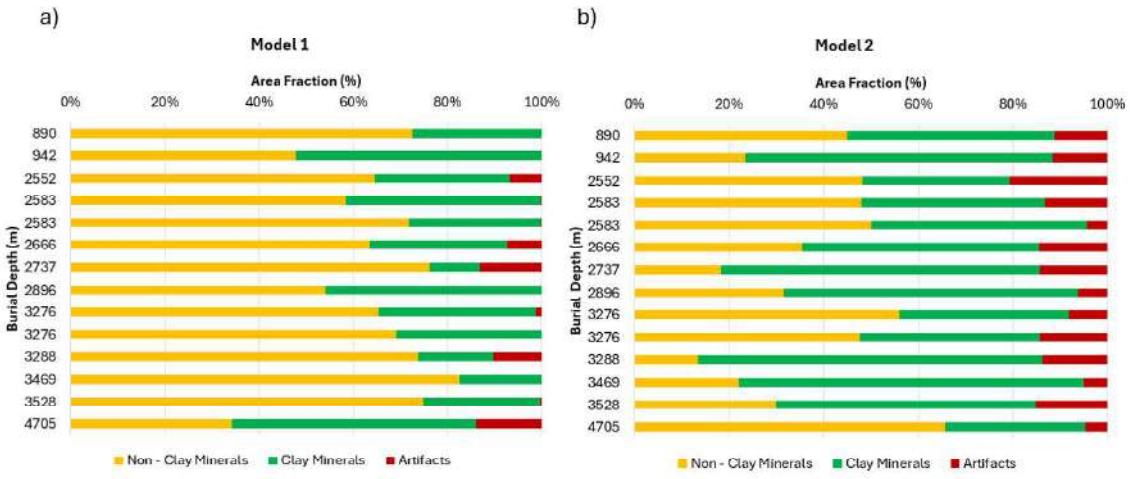

Figure 2 - In a) fractions are calculated from the prediction of Model 1, and in b) from the prediction of Model 2.

Three-dimensional quantification of vacancies through 4DSTEM multislice ptychography

Rodrigo Souza[1]*, Carlos Ospina[1].

[1]Centro Nacional de Pesquisa em Energia e Materiais – Laboratório Nacional de Nanotecnologia (CNPEM – LNNano)
*rodrigo.souza@lnnano.cnpem.br

Electron ptychography is a computational imaging technique aimed to recover information from diffracted probe overlaps in reciprocal space to reconstruct the scattering object phase, providing a "super-resolution" image which could be limited only by the atom's thermal vibrations [1]. Moreover, the method provides efficient dose usage, does not require prior knowledge of symmetry to be used as constraint, and the reconstructed phase image contains monotonic contrast dependence of sample thickness, which allows sub-nanometer depth information to be retrieved from samples with tens of nanometers thanks to the multislice method variation [1]. These advantages significantly broaden its applications both in physical and life sciences, but its usability can be hindered by the necessity of fast-detector technologies and the computational demand for mathematical optimization. The present work uses open-source tools to analyze a simulated 4DSTEM dataset of ZSM-5, an aluminoslicate belonging to the family of zeolites. In this kind of material, compositional and structural inhomogeneities such as oxygen (O) vacancies strongly affect their properties. With it also being sensitive to the beam, it becomes a challenge to study it under conventional TEM, making low dose ptychography one the best technique for high-resolution characterization [2]. Aiming to propose a methodology for analyzing three-dimensional composition and structure of the material, (i) the atomic potential of a 28 nm thick ZSM-5 specimen is calculated with random O vacancies using multislice approach, (ii) the 4DSTEM measurement is simulated and (iii) the phase and probe are then reconstructed through multislice ptychography using batched gradient descent algorithm [3, 4], with results shown in Figure 1. The reconstructed images consist of 7 different slices of 4 nm each, which were then analyzed using in-house scripts to locate O atomic columns and estimate the number of vacancies based on their respective intensity ranges. Figure 2 presents the percentage of O columns with their number of vacancies detected. It is shown that columns with 2 or 3 vacancies are easily identified, while columns with none or 1 vacancy are not easily distinguishable. Ongoing work is focused on applying this methodology to experimental data.

[1] Z. Chen et al., Science, 372.6544 (2021) 826-831.
[2] H. Zhang et al., Science, 380.6645 (2023) 633-638.
[3] B. H. Savitzky et al., Microscopy and Microanalysis, 27.4 (2021) 712-743.
[4] G. Varnavides et al., arXiv, 2309.05250 (2024)

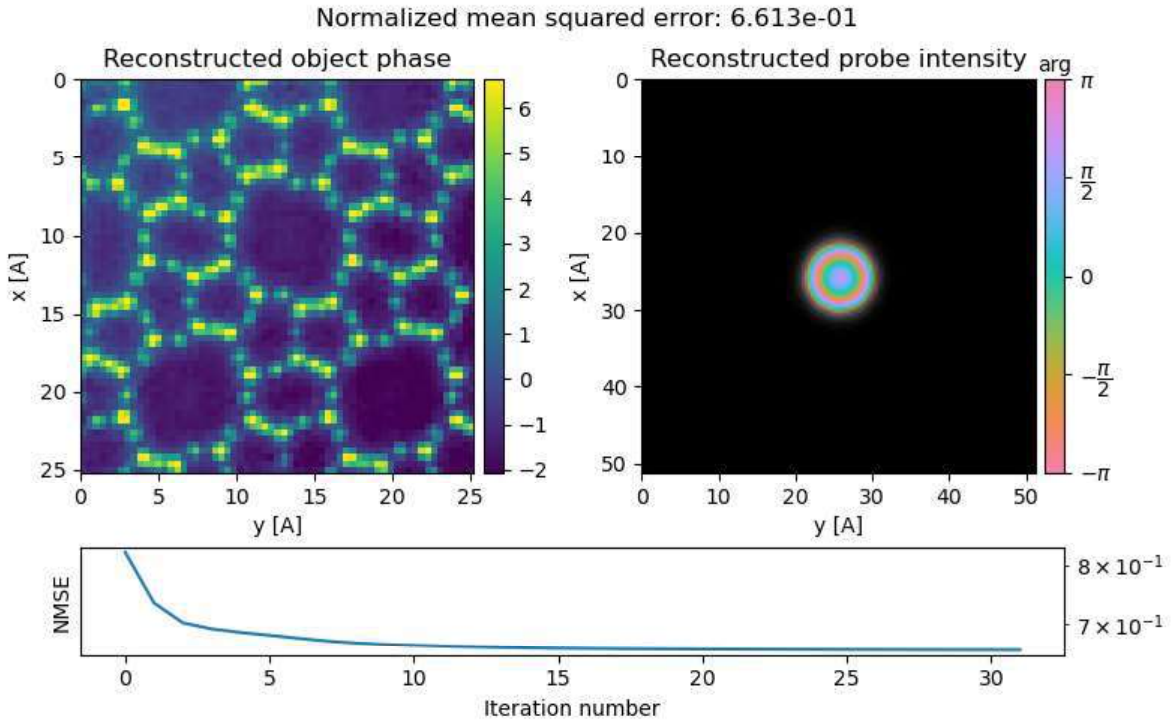

Figure 1. Reconstructed ZSM-5 phase in [010] projection, probe intensity and the normalized mean squared error along the algorithm iterations.

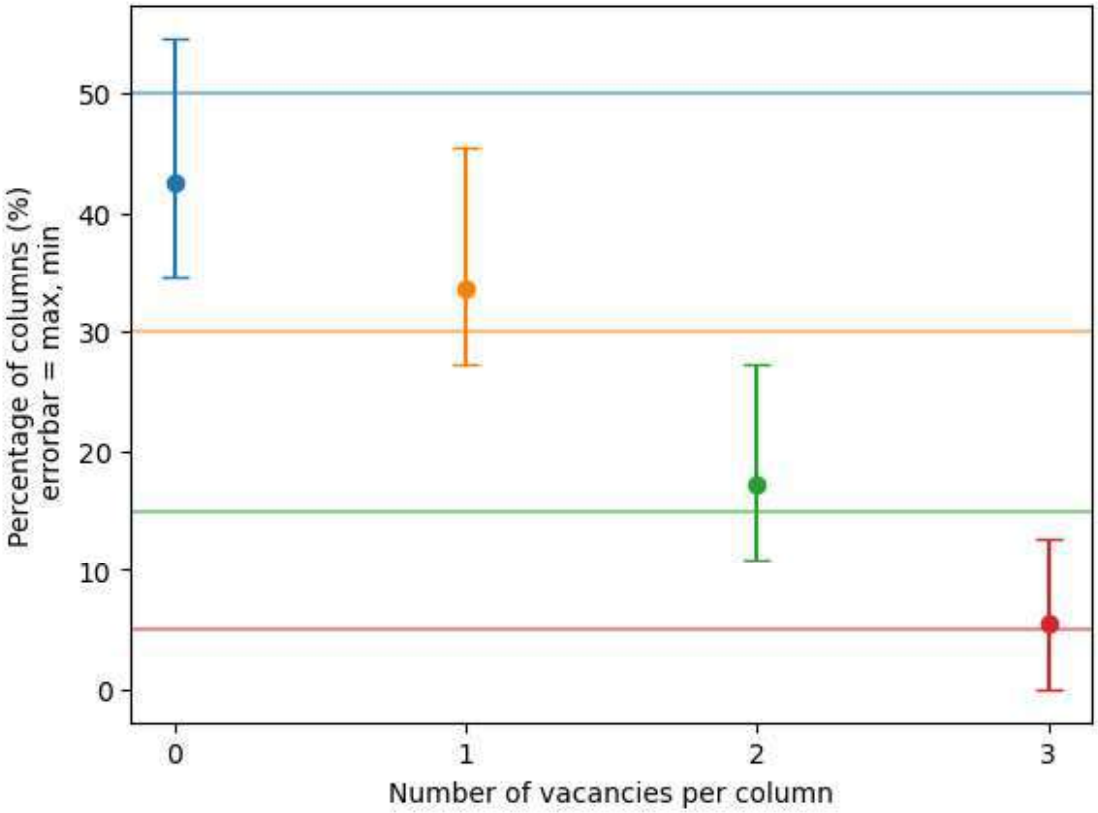

Figure 2. Percentages of O columns in each reconstructed slice identified as having 0 to 3 vacancies (each 4 nm-thick slice contains up to 8 O atoms per column) from a dataset simulated randomly with 50% of O columns with no vacancies, 30% with 1, 15% with 2 and 5% with 3 vacancies. The data points represent the mean percentage identified across all slices and the error bar indicates the range observed (minimum to maximum). Horizontal lines are the expected mean value based on the simulation input.

Advanced Processing of Cryo-EM Data with Modern Mini-PCs

Sayan Bhakta[1], Leandro Leonardo Passarelli[1], Michael Schatz[2], Ralf Schmidt[2], Marin van Heel[1,3,4]

[1]Brazilian Nanotechnology Nat. Lab. (LNNano/CNPEM), Campinas, SP, Brazil.
[2]Image Science Software GmbH, Berlin, Germany.
[3]Emeritus Professor of Structural Biology, Imperial College London, London, UK.
[4]Emeritus Professor, Leiden University, Biology Department (NeCEN), The Netherlands.
[*]marin.vanheel@gmail.com

Cryogenic electron microscopy (Cryo-EM) generates images of biological macromolecules samples, vitrified at LN2 temperatures, which preparation technique preserves a near-native conformation of their structures. 3D Reconstruction have become a routine reality today, even yielding near-atomic resolution results, a true "resolution revolution" [1]. However, modern Cryo-EM relies on processing huge amounts of data (many "terabytes") of hundreds of thousand high-resolution images. Thus, the common opinion in the field is that one needs large computational facility to process such Cryo-EM data. However, technological advancements have brough us very powerful computational resources in the form of ("gaming") mini-PCs. These computational resources are portable and easy to install everywhere, for example, just at the control desk of a microscope, or at a table in a hotel room. In combination with terabytes of high-speed M.2-SSD drives one achieves a powerful interactive computing resource independent of any large external computational facility.

Harvesting meaningful information from terabytes of very noisy and very large Cryo-EM datasets requires efficient, advanced processing algorithms running of very fast computers. 3D-Reconstructions of biological molecules is a multi-step, multi-dimensional image analysis procedure that includes many procedures such as: conversion of image formats, camera corrections, concentrating on the most relevant frequency components, Contrast Transfer Function (CTF) correction, Particle Picking, Particle Alignment, Orientation, unsupervised classification and 3D reconstruction from class-averages of aligned images [2-3]. Direct feedback on the quality of the data, during data-acquisition, not only facilitates further processing, it also reduces the associated resource-costs by optimising the system throughput. IMAGIC-4D is one of the first software packages that was developed to process images from Electron Microscopes [4] and it contains all the necessary algorithms as separate tools for processing Cryo-EM data [5]. This toolbox feature of IMAGIC-4D software package allows one to create flexible pipelines for fast on-the-fly processing of the Cryo-EM data during data collection. In our poster-demo we show that information can be harvested from "big-data" Cryo-EM in a cheap, portable, and compact modern mini-PC. Our results show the proof-of-concept of using a comprehensive custom pipeline for image processing in a portable mini-PC. This project has been developed and realized at the LNNano, CNPEM, SP, Brazil [6].

References:

[1] W. Kühlbrandt, Science 343 (2014) 1443-1444.
[2] S. Bhakta & M. van Heel, Francis & Taylor Publication, CRC Press (2024) 87-109
[3] M. van Heel et al, Quarterly reviews of biophysics, 33(4) (2000) 307-369
[4] M. van Heel & W. Keegstra, Ultramicroscopy, 7 (1981) 113-130
[5] M. van Heel et al., International Tables for Crystallography, Vol. F, Chapter 19.9, (2012) 624–628.
[6] This research was supported by CZI and FAPESP (2020/06062-1).

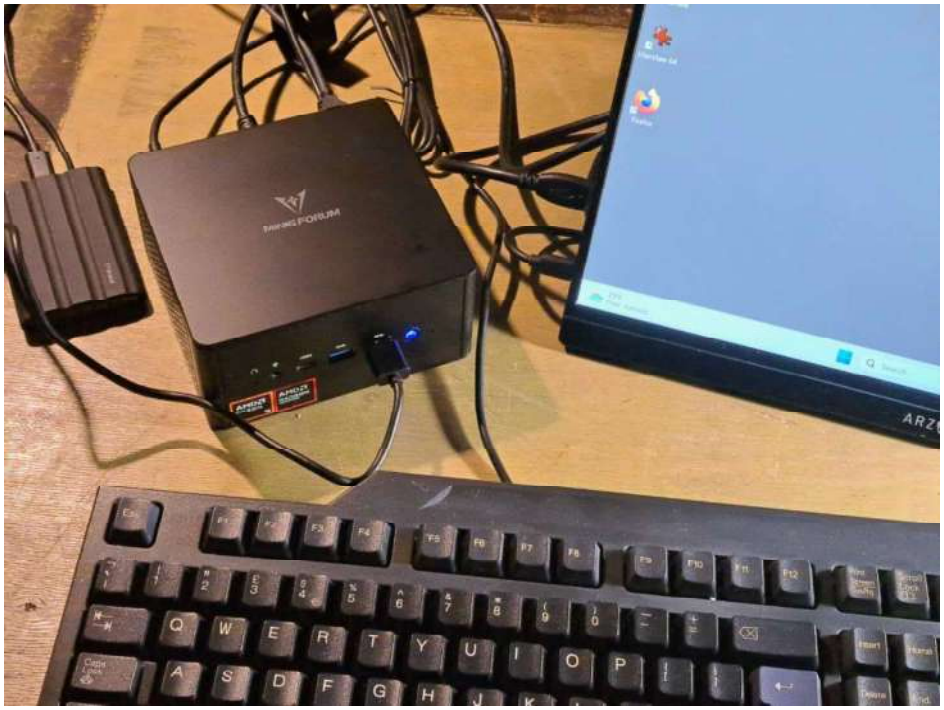

Figure 1: We here demonstrate how the compactness of modern gaming mini-PC facilitates the organisational complexity for Cryo-EM data processing. With the portability of these machines (including accessories like portable monitor and a separate keyboard), one can perform anywhere with a couple of fast external (M.2) SSDs to process the large datasets data, and becomes largely independent of access to large central computing. This little box is powerful enough to perform 1024x1024x1024 voxels 3D reconstructions of large icosahedral viruses. One thing to watch out for in such Mini-PCs is that the memory is often soldered onto the motherboard and therefore cannot be extended later. This particular Mini-PC currently operates with 64Gb memory and can be extended to 96Gb or even 128 Gbyte.

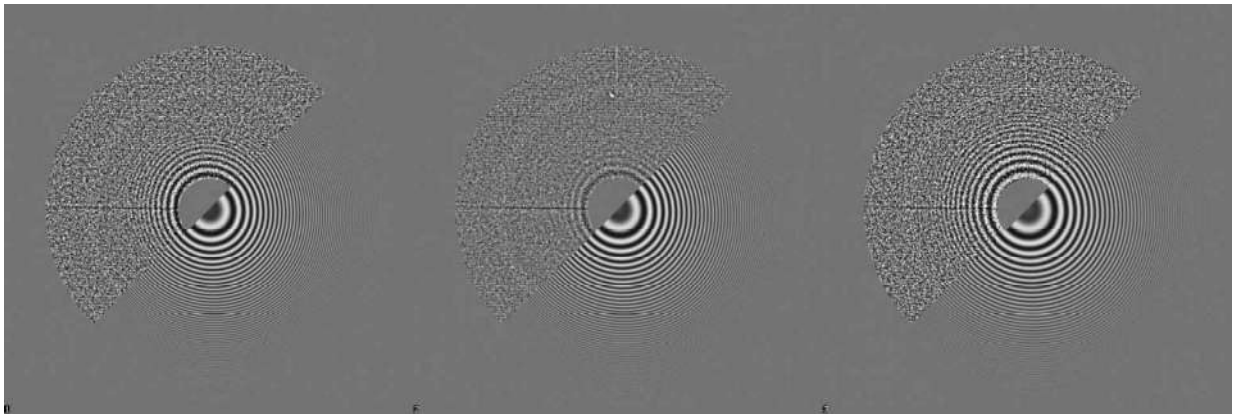

Figure 2: Some averages of movie-spectra classified after the MSA (Multivariate Statistical Analysis) data compression and unsupervised classification of thousands of movie-spectra. CTF fitting all within the possibilities of the mini-PC equipment shown above.

Analysis and Comparison of the Cryo-EM structures of Togaviridae

Katie Cristina Takeuti Riciluca[1,2], Sayan Bhakta[1], Pedro Ismael da Silva Júnior[2], Marin van Heel[1]*.

[1] Brazilian Nanotechnology Nat. Lab. (LNNano/CNPEM), Campinas, SP, Brazil
[2] Laboratório Toxinologia Aplicada (LETA/IBU). Instituto Butantan, São Paulo, SP, Brazil
*marin.vanheel@lnnano.cnpem.br

Alphavirus, a member of the Arbovirus group (**Ar**thropod-**bo**rne **virus** of vertebrates) and a genus which belongs to the Togaviridae family [1], includes Chikungunya virus, Mayaro virus, Encephalitis equine virus, etc. [2]. The virions which are approximately 70 nm in diameter, contain positive-sense, single-stranded RNA genomes (some 10 to 12 kbases) encapsulated in an icosahedral enveloped capsid [3]. These viruses are responsible for many (human) diseases throughout the world [4]. Many Cryo-EM structures of these viruses have been published and deposited in the Electron Microscopy Data Bank (EMDB) [5]. This database serves as a resource for harvesting information about many fundamental viral processes, such as: maturation; evolution; and infection. This harvesting of information from a large pool of Cryo-EM structures is not always straightforward since the various final structures may have been processed by different, possibly sub-optimal Cryo-EM procedures. A unified "4D stack" of Cryo-EM structures of all *Alphavirus* was created to harvest meaningful, novel structural information to understand functional aspects of the viruses (e.g. maturation, evolution and infection) from the deposited structural information. We have collected 42 structures of Alphavirus in our initial 4D stack, out of which 35 could be used effectively. These 35 structures were pre-processed (rotational and translational correction-alignment and harmonized residual magnification) in the IMAGIC-4D software package [6] [***Fig. 1***]. The MSA classification [7] resulted in grouping by species and maturation stage. We used 20 eigenimages to performed the classification into 15 classes [***Fig. 2***]. To check and confirm the size of all Alphavirus, the structural polyprotein sequence of Mayaro virus and the region of E2 glycoprotein was used as a reference to compare with the other virus in our stack. All the sequences showed the same size and the sequences are very similar in composition of amino acid residues [***Fig. 3***]. Our work has the potential to yield new structural insights in the life cycle of arboviruses and help combating such diseases. The work has been realized at LNNANO, CNPEM, Campinas, SP, Brazil [8].

[1] J. CASALS Comparative Virology. pp. 307–333, 1971.
[2] H. V. Ribeiro-Filho et al., Nat. Commun., vol. 12, no. 1, pp. 1–13, 2021.
[3] R. Jones et al., PLoS One, vol. 15, no. 2, pp. 1–17, 2020.
[4] R. Chen et al., J. Gen. Virol., vol. 99, no. 6, pp. 761–762, 2018
[5] K. Lata, S. Charles, V. Mangala Prasad, J. Struct. Biol., vol. 215, no. 3, p. 107993, 2023.
[6] M. van Heel et al. International Tables for Crystallography. Vol. F, Chap. 19.9, 624–628
[7] M. van Heel et al. Open J. Stat., vol. 06, no. 04, pp. 701–739, 2016.
[8] This research was supported by CZI and FAPESP (2020/06062-1).

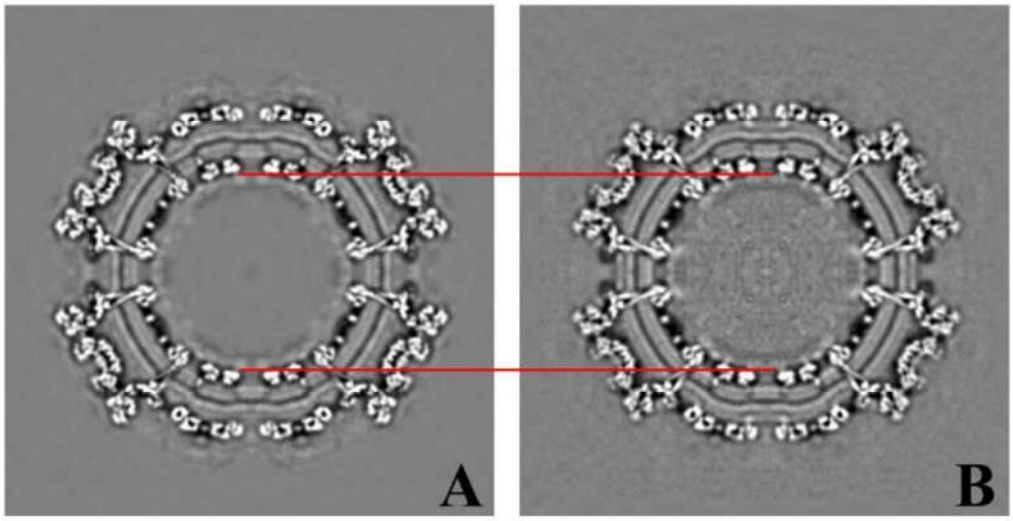

Figure 1. Central sections of Mayaro virus (**A**) and Chikungunya virus (**B**). The red lines indicate that the two viruses have been aligned for subsequent multivariate comparison.

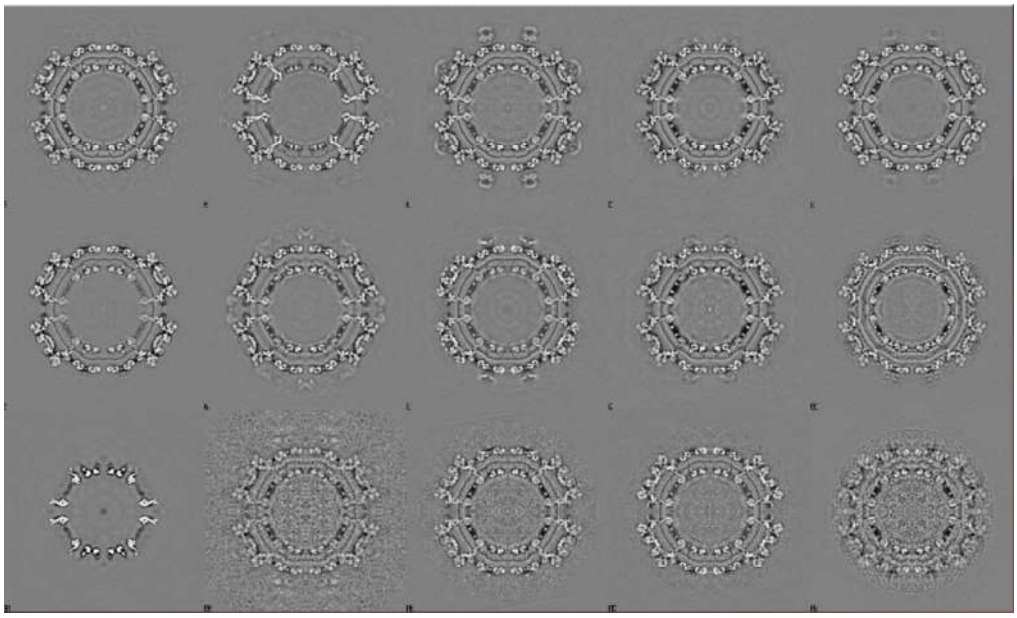

Figure 2. MSA-classification of Alphavirus 4D stack. Each of the image is the average of the members of a class. Different classes were obtained which were species specific.

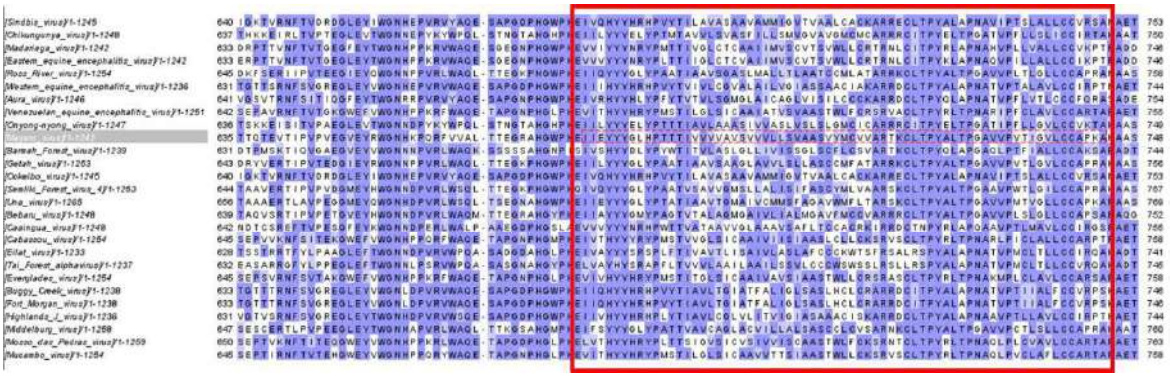

Figure 3. Multiple sequence alignment. The sequence of structural polypeptide of Alphavirus was performed on jalview with Clustal W and Clustal X version 2.0. Dashed red box is showing the E2 sequence. The red box represents all sequence in this region (E2 sequence).

Automated Analysis of Neurons In The Oculomotor Nerve Nucleus In *Artibeus planirostris*

Milena Soares Lustosa[1]*, Andréa Silva de Medeiros Bandeira[1], Wigínio Gabriel de Lira Bandeira[1], Ana Clara de França Gama[2], Expedito Silva do Nascimento Júnior[3], Melquisedec Abiaré Dantas de Santana[3].

[1]Graduate Program in Structural and Functional Biology, Federal University of Rio Grande do Norte, Natal, RN, Brazil.
[2]Federal University of Rio Grande do Norte, Natal, RN, Brazil.
[3]Department of Morphology, Federal University of Rio Grande do Norte, Natal, RN, Brazil.
*milenaslustosa@gmail.com

Frugivorous bats, such as *Artibeus planirostris*, stand out for their visual acuity in distinguishing shapes, which aids in the efficient search for fruit [1]. The oculomotor nerve nucleus (nIII) plays an essential role in the interdependence between binocular visual functions and oculomotor control by regulating the extraocular muscles [2,3]. Understanding the organization of the nIII in bats allows us to relate their sensory demands to foraging behavior, which is vital for their survival [4]. The absence of previous studies on the nIII in chiropterans represents a gap in the understanding of neuroanatomical characteristics within the visual system of these species. Its morphological and organizational description expands knowledge about the neurobiological strategies used to interact with the environment and provides a basis for future investigations regarding the relationship between morphology, functionality, and the evolution of visual and adaptive abilities in bats. This study aimed to describe the cytoarchitecture of the nIII in *A. planirostris*. Five adult males were used, captured on the UFRN campus and maintained in an environment with controlled light, temperature, and humidity, as well as free access to food and water. The protocol was approved by the Ethics Committee on Animal Use (CEUA/UFRN No. 009/2012). The animals were euthanized and transcardially perfused. The brains were removed, post-fixed, and processed into six series of coronal sections 30 µm thick using a freezing microtome. One series from each animal was stained with the Nissl technique. The sections were analyzed under a Nikon microscope, and digital images were captured with a Nikon DS-Ri1 digital camera. The images were processed using ImageJ® software (Figure 1), undergoing steps of preprocessing, normalization, filtering, segmentation, and particle analysis. During preprocessing, the software was calibrated and adjustments of contrast and brightness were made. Normalization involved defining pixel intensity ranges on the grayscale and applying a Gaussian blur filter with sigma 2. During segmentation, colors were inverted, and the image was dilated and eroded once each. Particle analysis was performed using the Watershed separation algorithm, allowing measurement of neuronal bodies in the nIII, generating data tables containing the number of cells counted and the area of each. For statistical analysis, GraphPad® software was used for descriptive statistics (mean, median, and standard deviation). The results indicate that the mean neuronal areas are approximately distributed between 100 µm² and 200 µm² (Table 1). The standard deviation, represented by the error bars, indicates data dispersion. In all animals, the bars are relatively large, indicating specific variation among neuronal areas in the animals. The results demonstrate the effectiveness of using macros created in ImageJ® as tools for quantitative microanalysis, enabling precise visualization and measurement of nIII cells. The use of the custom macro was essential to ensure standardization, reproducibility, and robustness of morphological data, reinforcing its importance in comparative neuroanatomical studies and in investigating sensory adaptations in bats.

[1] C Korine, EKV Kalko, Behavioral Ecology and Sociobiology, 59 (2005) 12.
[2] HEA Bicas, Brazilian Archives of Ophthalmology, 66 (2003) 687.
[3] AKE Horn, RJ Leigh, The anatomy and physiology of the ocular motor system, in: C Kennard, RJ Leigh (Eds.), Handbook of Clinical Neurology. Neuro-ophthalmology, Elsevier, [s.l.], 2011, pp. 21–69.
[4] J Rydell, J Eklöf, Naturwissenschaften, 90 (2003) 481.

Table 1. Descriptive statistics of the five animals used in the study.

Statistic	Animal 1	Animal 2	Animal 3	Animal 4	Animal 5
Mean	172,2	149,7	112	129,6	156,4
Median	140,2	146	90,11	116,4	132,9
Standard Devitation	82,78	56,01	53,6	47,02	66,37

Table 1 Reference: Author (2024).

Figure 1. Analysis of the reading performed by ImageJ® on the photomicrograph.

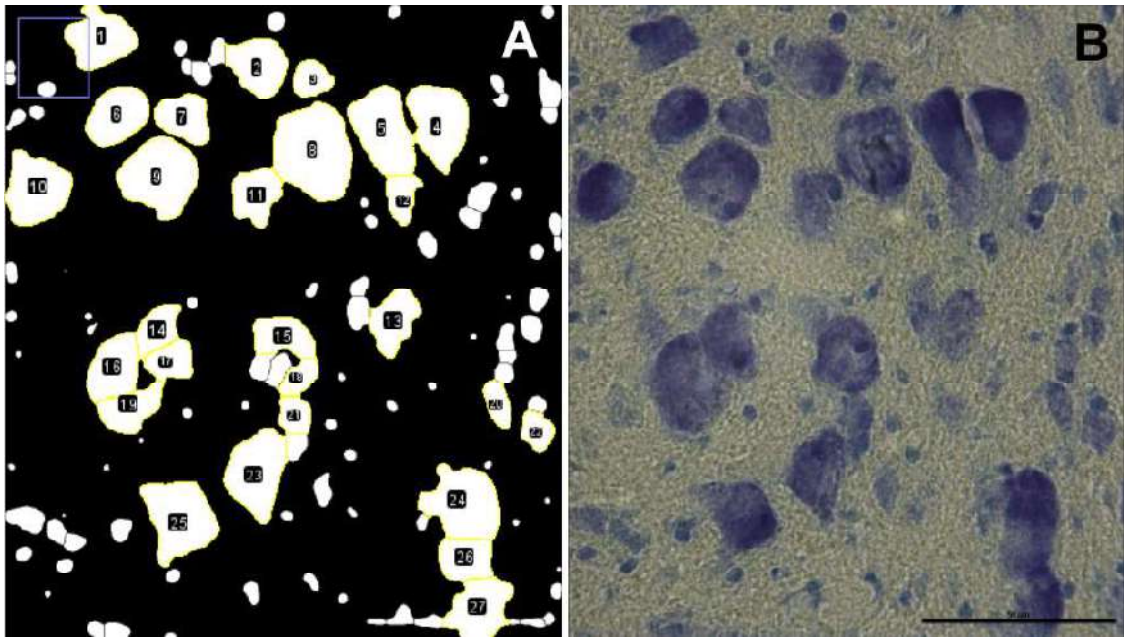

Caption: A) Image showing the effect of the macro created in ImageJ®. B) Photomicrograph of neuronal bodies in the nIII stained with Nissl at 40x magnification, with a 50 µm scale.
Reference: Author (2024).

Automated morphometry of serotonin-immunoreactive neurons in the raphe nuclei of *Artibeus planirostris*

Andréa S. M. Bandeira[1*], Mariana D. Leite[2], Wigínio G. L. Bandeira[1], Milena S. Lustosa[1], Ana C. F. Gama[4], Marília A. S. Barros[3], Melquisedec A. D. Santana[4], Expedito S. Nascimento Jr[4].

[1]Postgraduate Program in Structural and Functional Biology, Federal University of Rio Grande do Norte, Natal, RN, Brazil
[2]Federal Institute of Education, Science and Technology of Rio Grande do Norte, Ipanguaçu, RN, Brazil
[3]BE Bioinsight & Ecoa, Porto Alegre, RS, Brazil
[4]Department of Morphology / Laboratory of Neuroanatomy, Biosciences Center, Federal University of Rio Grande do Norte, Natal, RN, Brazil.
*E-mail: andreamedeirosbandeira@gmail.com

Serotonergic neurons, identified by immunoreactivity to 5-hydroxytryptamine (5-HT), are concentrated in the raphe nuclei of the brainstem, where they influence functions ranging from thermoregulation and circadian rhythms to motor and cognitive behavior [1]. Although this system's morphology has been extensively described in rodents, primates and monotremes, its organization in neotropical bats remains poorly explored [2]. *Artibeus planirostris*, a widely distributed South American mammal, provides a valuable comparative model for neuroanatomical investigations [3]. This study was designed to develop and apply a standardized, ImageJ-based protocol for quantifying the cell-body area of 5-HT-immunoreactive neurons across subdivisions of the raphe nuclei, in order to assess morphometric homogeneity. Six adult male *A. planirostris* (body mass 40–47 g), captured on the Federal University of Rio Grande do Norte campus (Natal, Northeast Brazil) under ICMBio permit no. 25233-2, were deeply anesthetized and transcardially perfused with 150 mL phosphate-buffered saline (pH 7.4) containing 500 IU heparin, followed by 300 mL of 4 % paraformaldehyde in 0.1 M phosphate buffer (pH 7.4). Brains were post-fixed in the same solution for 24 h, cryoprotected in 30 % sucrose (0.1 M phosphate buffer, pH 7.4), and coronally sectioned at 30 µm on a cryostat into six series. One series was processed for 5-HT immunohistochemistry (primary anti-5-HT antibody, 1:5000; ABC Elite kit; DAB), with negative controls omitting the primary antibody to confirm specificity. Mounted sections were imaged under bright-field illumination on a Nikon Eclipse/Ni-U microscope (20×) with a DS-Ri1 camera. Initial image preparation minimal brightness/contrast adjustments and anatomical schematics in Canvas 12® using a bat atlas [4] and stereotaxic coordinates—was followed by import into ImageJ/Fiji®. There, images underwent preprocessing (contrast and brightness enhancement), normalization (noise reduction, gray-scale pixel interval equalization, Gaussian blur $\sigma = 2$), segmentation (thresholding, color inversion, single erosion and dilation), and Watershed separation. The "Analyze Particles" function then quantified neuronal cell-body areas; ~100 neurons were sampled per nucleus per animal. Cell bodies were classified as small (< 60 µm²), medium (60–69 µm²) or large (> 70 µm²), and results are presented as mean ± SD. Normality was assessed with the Shapiro–Wilk test in IBM SPSS 20, and group differences were evaluated by one-way ANOVA with Tukey's post hoc test ($\alpha = 0.05$). No significant differences in cell-body area were observed among raphe subdivisions. In the rostral cluster, the caudal linear nucleus (CLi) averaged 61.3 ± 6.4 µm² versus 61.6 ± 3.9 µm² in the supralemniscal (B9). The median (MnR: 64.2 ± 5.4 µm²) and paramedian (PMnR: 60.6 ± 6.4 µm²) regions showed similar values. In the caudal cluster, raphe magnus (RMg) and pallidus (RPa) measured 64.0 ± 3.4 µm² and 70.3 ± 3.8 µm², respectively; rostral/caudal ventrolateral (rVL/cVL) averaged 68.2 ± 8.5 µm²; and raphe obscurus (ROb) was smallest at 57.4 ± 4.7 µm². All comparisons were non-significant ($p > 0.05$), confirming morphometric uniformity. In summary, this ImageJ-based workflow provides a reproducible, efficient tool for quantitative analysis of immunolabeled neuronal populations in neotropical bats. The absence of soma-size differences supports a conserved structural organization of the serotonergic system in *A. planirostris* and underscores the protocol's applicability to comparative neuroanatomy and image-processing studies across other species and

histological markers.

[1] I Tork, Neuroscience, 6 (1985) 557–618.
[2] JL Kruger, LA Dell, A Bhagwandin, et al., J Chem Neuroanat, 40 (2010) 210–222.
[3] L Hollis, Mammalian Species, (2005) 1–6.
[4] F Scalia, JJ Rasweiler, J Scalia, R Orman, M Stewart, Forebrain atlas of the short-tailed fruit bat, *Carollia perpicillata*, Springer, (2013).

Table 1. Mean and standard deviation of neuronal cell body area of 5-HT-immunoreactive neurons in subdivisions of the raphe nuclei of *Artibeus planirostris.*

Animal	B9	RPa	RMg	ROb	DR	CLi	VL	PnR	MnR	PMnR
	Mean±SD (μm²)	Mean±SD (μm²)	Mean±SD (μm²)	Mean±SD (μm²)	Mean±SD (μm²)	Mean±SD (μm²)	Mean±SD (μm²)	Mean±SD (μm²)	Mean±SD (μm²)	Mean±SD (μm²)
Mean	**61.6** (±3.9)	**70.3** (±3.8)	**64.0** (±3.4)	**57.4** (±4.7)	**65.4** (±6.8)	**61.3** (±6.4)	**68.2** (±8.5)	**52.0** (±6.7)	**64.2** (±5.4)	**60.6** (±6.4)

Figure 1. ImageJ processing workflow for neuron quantification in *Artibeus planirostris*: immunohistochemistry photomicrograph for 5-HT (left); result after ImageJ processing (right). Scale bar 60 μm.

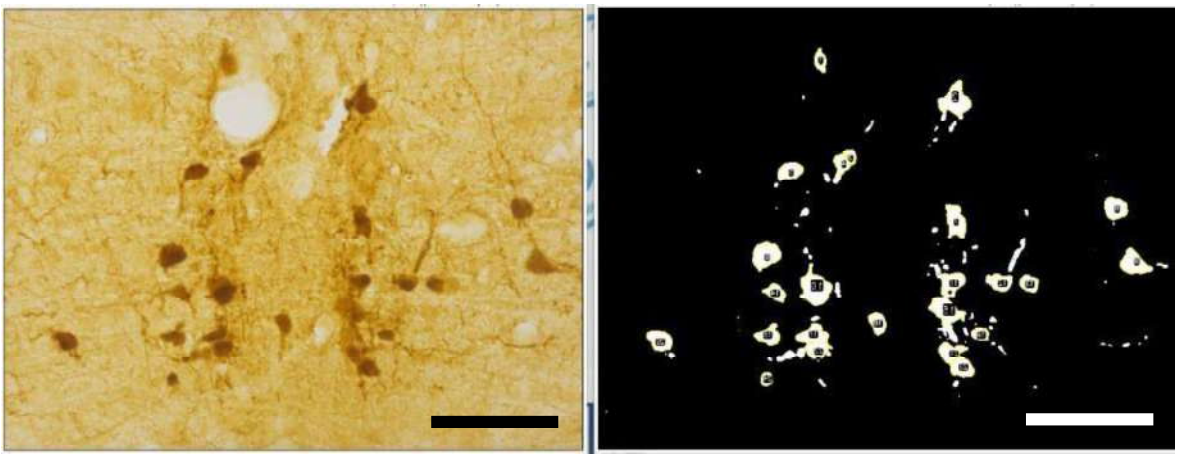

Fractal Methods Applied in Computational Algorithms for Detecting Chromatin Alterations in Basal Cells of Oral Squamous Cell Carcinoma

José Abel Pessôa Neto[1], Maria Manuela dos Santos Rodrigues[1], Renan Gabriel da Silva Ferreira[1], Jadyel Sherdelle Guedes do Nascimento[1], Alison Jose da Silva[1], Isaque Bertoldo Santos da Silva[1], Ana Vitoria Ferreira dos Santos[1], Carlos Eduardo da Silva[1], Paloma Vitória Melo da Silva, Raissa Gomes de França[1], Fernanda das Chagas Angelo Mendes Tenorio[1], Bruno Mendes Tenorio[1*].

[1]Department of Histology and Embryology, Federal University of Pernambuco.
[*]bruno.mtenorio@ufpe.br

Oral squamous cell carcinoma (OSCC) is the most common head and neck carcinoma. Each year, 2.5% of all newly reported cases of carcinoma are OSCC, while the mortality rate is 1.9% [1]. The diagnosis of OSCC is sometimes difficult to establish, mainly due to the heterogeneity of clinical lesions associated with the subjectivity of the histopathological interpretation and differential diagnosis. Therefore, microscopic characterization based on new technologies emerges as an auxiliary tool for interpretation of digital images [2]. Computational algorithms are being developed for research, disease detection and prognosis prediction, supporting the pathologist. Thus, the use of computational algorithms in microscopic images can play a role as a first or second reader to improve the efficiency of pathological detection. These methods can reduce the workload in screening healthy tissues and reduce the rate of false positive and false negative diagnoses. It is worth noting that software usually requires a human operator to review all diagnoses [3]. This research aims to use fractal algorithms applicable in software and artificial intelligence as shape markers to detect changes in basal cell heterochromatin in microscopic images of oral squamous cell carcinoma. The analyzed photomicrographs were based on the NDB-UFES dataset [4]. The dataset provides microscopic images recorded in 40x objectives of a Leica DM500 light microscope coupled to a Leica ICC50 HD digital camera and Leica LAS EZ software (Heerbrugg, Switzerland). Microscopic images (n=15) of oral squamous cell carcinoma (OSCC), oral leukoplakia with epithelial dysplasia (LED) and leukoplakia without epithelial dysplasia (LK, reference control) were analyzed from human patients with one or more lesions in the oral mucosa. The images are presented as Portable Network Graphics (PNG) with 2048 × 1536 pixels. In each photomicrograph, 6 to 15 basal cell nuclei with well-defined chromatin were analyzed in 100 x 100 pixel images. In total, 141 cells were analyzed in the OSCC group, 126 in the LED group and 183 in the LK group. Nuclei positioned up to 400 pixels from the basal lamina were considered basal cells. Images of the nuclei were processed in the imageJ software (National Institutes of Health - NIH, USA) using a macro made in our laboratory, and then analyzed using the FracLac Plugin (A. Karperien, Charles Sturt University, Australia) as described by dos Santos et al. (2025) [3]. Figure 1 shows photomicrographs of basal cell nuclei and their segmentation for heterochromatin binarization aiming at analysis automation. The results are shown in Table 1. The carcinoma OSCC and LED groups showed a larger heterochromatin area compared to the LK group (reference control). Lacunarity also showed changes in the shape of basal cell

heterochromatin in the OSCC and LED groups compared to the LK control. Interestingly, fractal dimension showed no statistical difference between leukoplakia without (LK) or with dysplasia (LED); and both LK and LED showed statistical difference compared to OSCC carcinoma. Chromatin observed under optical microscopy can indicate how DNA and proteins are organized in the cell nucleus, providing information about the patterns of compaction and activity of genetic material in the nucleus. It is worth noting that the present study evaluated basal cells of the oral epithelium; therefore, these cells are still undifferentiated, which may suggest that these algorithms are capable of detecting changes at early stages in still undifferentiated cells. Research is being conducted in our laboratory to verify this perspective. In conclusion, the lacunarity, fractal dimension and heterochromatin area can be useful markers for software and artificial intelligence to detect changes in OSCC carcinoma and dysplasia.

[1] Yasin MM et al., *BMC Oral Health*, 22 (2022) 305.

[2] Pereira-Prado V et al., *Diagnostics (Basel)*, 13 (2023) 2416.

[3] dos Santos AVF et al., *Histochem Cell Biol*, 163 (2025) 1.

[4] Ribeiro-de-Assis MCF et al., *Data Brief*, 48 (2023) 109128.

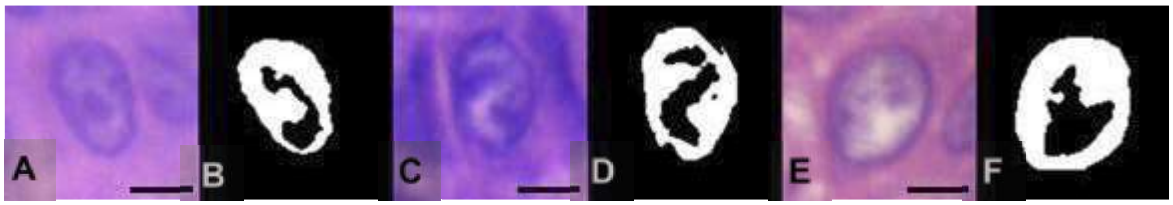

Figure 1. Photomicrograph of basal cell nuclei and its binary segmentation on the right in microscopic images of oral squamous cell carcinoma (A and B), leukoplakia with epithelial dysplasia (C and D) and leukoplakia without epithelial dysplasia (E and F). Scale bar: 8 μm.

Table 1. Analysis of shape markers to detect changes in basal cell heterochromatin in microscopic images (n=15) of oral squamous cell carcinoma (OSCC), leukoplakia with epithelial dysplasia (LED) and leukoplakia without epithelial dysplasia (LK).

	LK	LED	OSCC	F	p
Area (pixel^2)	1385 ± 355^a	1854 ± 543^b	1852 ± 478^b	6.7	0.002^*
Fractal dimension	1.64 ± 0.04^a	1.63 ± 0.03^a	1.59 ± 0.05^b	5.6	0.006^*
Lacunarity	0.34 ± 0.04^a	0.29 ± 0.04^a	0.30 ± 0.04^b	5.7	0.005^*

Different letters on the same line indicate statistical difference between groups (*indicates $p<0.05$).

30ª CSBMM

Identification of interaction sites between the staphylococcal exfoliative toxin complex and desmoglein 1

Angela R. N. Santisteban[1]*, Marin van Heel[1].

[1] Brazilian National Nanotechnology Laboratory – LNNano, National Center for Energy and Materials Research - CNPEM
*angela.santisteban@lnnano.cnpem.br

Staphylococcus aureus is a commensal and opportunistic bacterium that can infect a variety of hosts, including humans and different species of cattle that represents a global public health problem, and causes enormous damage to the livestock industry. Exfoliative toxins (ETs) are a virulence factor that facilitates the spread of the pathogen by inducing the generalized detachment of the granular layer of the epidermis in host [1]. Occasional secondary interactions, which are still unknown in this system, and uncommon between serine proteinases induce specific hydrolysis of the peptide bond between *Glu-Gly* of Desmoglein 1 (Dsg1) [1,2]. A better understanding of the mechanism of action of ETs is necessary to develop strategies to inhibit the pathogen [3]. This work seeks to elucidate the mechanisms and modes of action at the atomic level in the interactions between ETs and the substrate Dsg1, focusing on native ET proteins from *S. aureus*. Four serotypes of ET have been described as produced by this bacterial pathogen, each specific to the host: ETA, ETB, ETD, and ETE. The first three primarily infect humans, while the last one infects ovines and caprines. For this study, the different ETs will be expressed in *E. coli* BL21 (DE3)-T1R, while the ectodomains 3 and 4 (EC3–EC4) of human and ovine Dsg1 will be produced using a baculovirus system [4]. Subsequently, proteins will be purified by gel filtration on a Superdex® 75 10/300 GL column with 20 mM Tris, 150 mM NaCl, pH 7.4. Protein secondary structure will be assessed by circular dichroism (CD), and melting temperature (T_m) along with enthalpy will be determined through differential scanning calorimetry (DSC). ET and Dsg1 samples will be incubated to form the protein-protein complex, which will be analyzed by time-resolved cryo-electron microscopy (cryo-EM) [5] using a Talos Arctica G2 microscope (Thermo Fisher Scientific). Finally, single-particle analysis (SPA) will be applied to reconstruct the high-resolution structure of the complex, following SPA workflows including sample preparation, vitrification, data acquisition, and image processing [6,7] at LNNano (CNPEM, Campinas, Brazil). So far, we have obtained the expression and purification of ETE (Figs. 1 and 2). This protein showed a secondary structure with a predominance of random coil (Fig. 3) and exhibited two-state behavior, transitioning from an initial native folded state to a final unfolded conformation, as evidenced by the regulated heating process from 20 to 90 °C, resulting in irreversible thermal unfolding. The ETE_{wt} thermogram (Fig. 4) shows a Gaussian peak representing the protein unfolding process between 35 and 64 °C, with an endothermic transition at 46.40 ± 1.30 ºC, followed by exothermic aggregation up to 64 °C. Thermal unfolding experiments using CD and DSC allowed us to establish a melting temperature of 49.0 ± 1.4 °C, a calorimetric enthalpy of 220 ± 50 kcal/mol, and a Van't Hoff enthalpy of 270 ± 70 kcal/mol. The other proteins are currently in the process of cloning and expression. Our objective is to resolve the structure of ETD and the EC3–EC4 domains of Dsg1 to characterize their protein–protein interactions and the other ETs with Dsg1. These results will be compared with existing structural like crystal structures and models obtained via X-ray crystallography [8], docking studies, and molecular dynamics simulations [9] to validate the interactions we observe.

Figure 1. Confirmation of the expression of the wild-type ETE (ETEwt) protein from *S. aureus.* **A**. 15% SDS-PAGE gel was performed after Ni-NTA purification of the ETEwt protein, which has a molecular weight of 28.10 kDa. M: Marker (Tag 17044601, GE Life Sciences). Fractions collected: 1 - 40 mM (imidazole), 2 - 60 mM, 3 - 80 mM, 4 - 400 mM. **B.** Western blot analysis. M: Marker. Lane 1: ETEwt protein at 28.10 kDa.

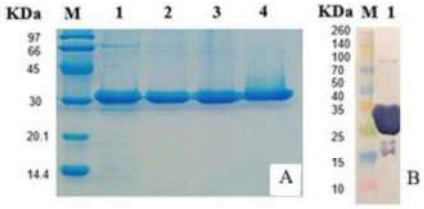

Figure 2. Purification of ETEwt protein from *S. aureus*. **A.** Size-exclusion chromatography (SEC) profile of ETEwt using a Superdex 75 10/300 GL column (GE), following Ni-NTA purification. The y-axis represents absorbance in milli-absorbance units (mAU), and the x-axis represents the elution volume in milliliters (mL). The chromatogram shows absorbance at 230 nm. ETEwt samples were purified in 20 mM MES, 150 mM NaCl, pH 7.4. **B.** 15% SDS-PAGE gel performed after purification of the ETEwt protein, which has a molecular weight of 28.10 kDa. M: Marker (1704460 GE Life Sciences). Fractions collected: lines 1, 2, and 3 correspond to fractions eluted at 10 mL, 11 mL, and 12 mL, respectively.

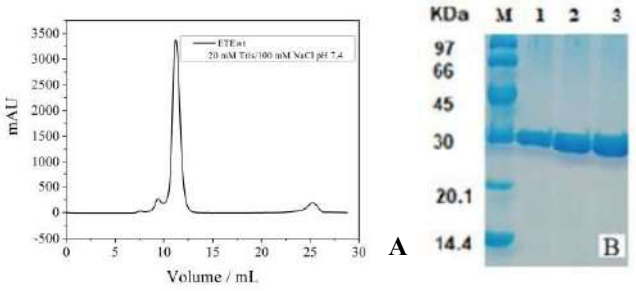

Figure 3. Far-UV-CD spectrum of the ETEwt protein from *S. aureus*, in phosphate buffer (5 mM NaH2PO4, 50 mM NaF, pH 7.40) at 20 °C.

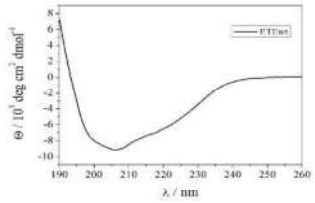

Figure 4. DSC thermogram of the ETEwt protein from *S. aureus*. The apparent excess heat capacity curve was recorded for ETEwt (0.64 mg/mL) in phosphate buffer (10 mM NaH_2PO_4, 100 mM NaF, pH 7.40) at a scan rate of 1 °C/min.

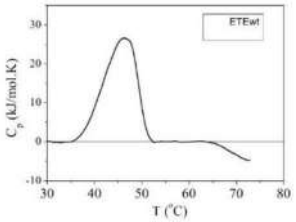

REFERENCES

[1] M. Bukowski et al., Toxins. (2010) 1148.
[2] Y. Hanakawa et al., Journal of Biological Chemistry. (2004) 5268.
[3] S. Ladhani. FEMS Immunol Med Microbiol. (2003) 181.
[4] R.P. Lemaitre et al., BMC Biotechnol. (2019) 20.
[5] Microscopy Australia. Cryo-Electron Microscopy. (2021).
[6] M. van Heel M et al., Quarterly Reviews of Biophysics. (2000).
[7] S. Bhakta and M. van Heel, Ed. K. Appasani., Francis & Taylor Publication. (2024).
[8] R. B. Mariutti et al., Biochem Biophys Res Commun. (2015) 171.
[9] C. Gismene et al., Int J Biol Macromol. (2025) 145784.
[10] This research was supported by FAPESP and CZI (Brazil).

Physicochemical Characterization of Bacterial Cellulose Membrane Functionalized with Strontium Apatite

Vilma Lima[1]*, Samia Jéssica Silva Tavares[2], Érika Patricia Chagas Gomes Luz[3], Ana Lorena Brito Soares3,Fábia Karine Andrade[3], Rodrigo Silveira Vieira[3]*.

[1]Federal University of Ceará, Department of Physiology and Pharmacology,
[2]Federal University of Ceará, Department of Clinical Dentistry,
[3]Federal University of Ceará, Department of Chemical Engineering. Fortaleza, Ceará, Brazil. *vilma@ufc.br ; *rodrigogpsa@gmail.com .

The production of implantable materials has aroused interest in the medical field, mainly for use in bone regeneration [1]. Many developed combinations present important characteristics in bone tissue repair, such as controlled biodegradability, bioactivity, and biocompatibility [2,3]. Therefore, it is important to characterize the intrinsic properties of implantable material, which is essential for human health. Thus, we sought to evaluate the cell viability and physicochemical properties of a bacterial cellulose membrane functionalized with strontium apatite (BM). For experimental procedures, BM was compared to the commercial Bio-Gide® membrane (BG) regarding cell viability by MTT (3-[4,5-dimethylthiazol-2-yl]-2,5 diphenyl tetrazolium bromide) assay with MC3T3-E1 cells and by analytical techniques: strontium ions (Sr^{2+}) were quantified in BM by atomic absorption spectroscopy (AAS). The swelling degree (GI) of BM and BG were compared, as well as their chemical structures were analysed by Fourier transform infrared spectroscopy (FTIR) and their morphologies by scanning electron microscopy (SEM; Figure 1). BM was also analysed by thermogravimetry (TGA). BM presented 32.6±1.7 mg of Sr2+/g of material by AAS. The BM and BG membranes did not alter cell viability ($p>0.05$) compared to the negative controls. The GI between BM and BG were similar up to 12 min ($p>0.05$), becoming different from 22 min to 72 min (BM = 950%; BG = 727% at 72 min; $p<0.05$). The FTIR spectra for BM showed vibrational bands characteristic of bacterial cellulose, and another band around 670 cm^{-1}, corresponding to the Sr2+ content, while BG showed bands with amide groups corresponding to collagen. SEM revealed that BM has micropores and crystals of varied shapes and sizes, consistent with mineralization. BG presented a tangle of nanometric fibers characteristic of collagen. TGA analysis of BM evidenced three events: 1st (~100 ºC) = evaporation of light volatile compounds; 2nd (~300 ºC) = degradation of the matrix; 3rd (320 ºC-350 ºC) = oxidation and breakdown of carbon residues and formation of gaseous products. As a conclusion, BM did not present cellular toxicity and presented good physicochemical characteristics, making it interesting for studies in animals.

[1] M.T. Maia et al., Polym Rev, 61 (4) (2021) 736.
[2] E.P.C.G., Luz et al., Carbohydr Polym, 237 (2020) 116174.
[3] E.P.C.G., Luz et al., Mat Sci Eng, C116 (2020) 1.
[4] This research mas supported by Fundação Cearense de Apoio ao Desenvolvimento Científico e Tecnológico (FUNCAP; Brazil).

Figure 1. Scanning electron microscopy (SEM) images of a bacterial cellulose membrane functionalized with strontium apatite (BM) (A–C) and a commercial Bio-Gide® membrane (BG) (D–F). The images illustrate the macroscopic aspects of the respective biomaterials.

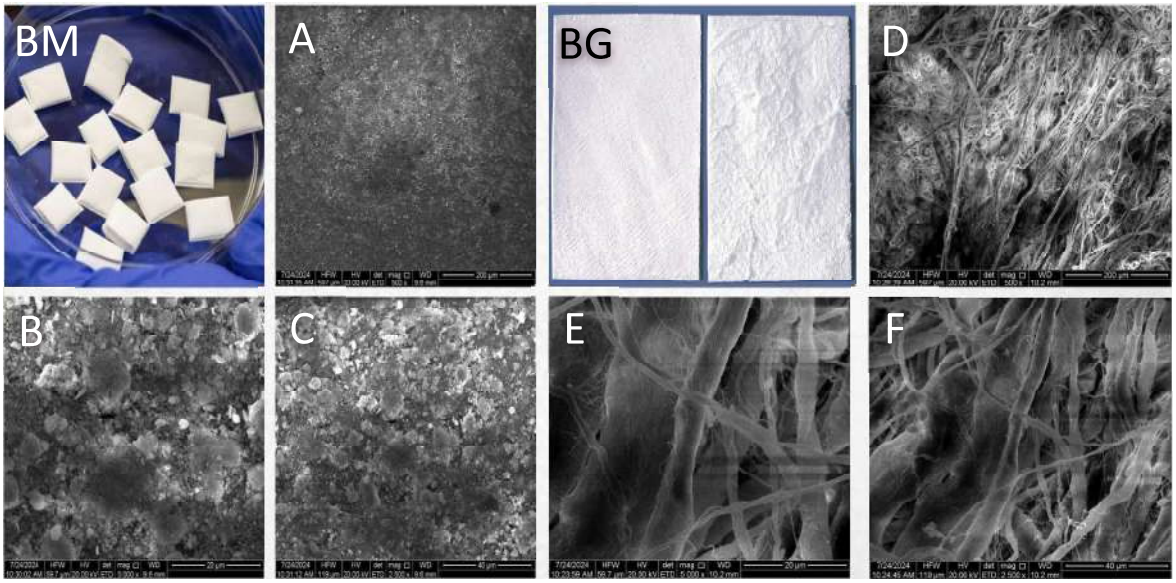

Single-Electron Counting in EM is changing the Foundations of Physics

Marin van Heel [1,2,3,4*]

[1] Brazilian Centre for Research in Energy and Materials (CNPEM/LNNano), Rua Giuseppe Máximo Scolfaro, 10.000, CEP 13083-100, Campinas/SP, Brazil.
[2] Image Science Software GmbH, Berlin, Germany.
[3] Emeritus Professor, Leiden University, Biology Department (NeCEN), Netherlands.
[4] Emeritus Professor of Structural Biology, Imperial College London, London, UK.
* Correspondence: marin.vanheel@lnnano.cnpem.br – marin.vanheel@gmail.com

The detection of **individual electrons arriving in a sensor** has led to impressive resolution improvements in **Cryo-EM** [1, 2]. The approach also helped pinpoint shortcomings in the classical **Laws of Physics (**including **Quantum Mechanics QM)**. **Mathematical Sciences,** preceded the **Physical Sciences** historically, are **explicitly** defined as **deterministic**. A **Mathematical Science** builds upon a few **axioms**, forming a "**bubble**" of mutually consistent of entities. The **bubble exists** irrespective of anything in any **outside universe**. Its entities can therefore not be **scaled** to anything that is not part of the **bubble**. **Mathematics** are thus per-definition **dimensionless**. The **Physical Sciences** do not share that luxury**:** they are **created** to **assess the outside world** from **inside** of a "**Halfway**" **Deterministic Bubble**. **Scaling** the inside of such a **HDB** to **match metrics** of an **outside universe** then becomes **unavoidable**. This **inconsistency** created a **measurement problem** that has hampered the **progress of science**. **Closed-Systems**, or rather, **Halfway Closed-Systems** were **postulated** for studying the **outside universe** from **inside** a **physico-mathematical bubble**. **Closed-system** approximations were nevertheless successfully adopted in **Newtonian Mechanics**, underpinning the concept of a **deterministic Classical Physics.** That success was achieved for **large systems** in an era of imprecise **instruments**. By then also successfully including **Thermodynamics** into **Classical-Physics** its **deterministic** basis was reinforced. **Deterministic Physics** became dominant in the 19th century and even scientists like: **Maxwell**; **Boltzmann**; **Planck**; and **Einstein**, preferred to describe **quantum effects** in a **Deterministic** framework, rather than in a **Discrete Physics** in which **arriving quanta were counted**. **Determinism** became a **dogma**. The new generation of **direct electron-counting** cameras require a **sampling interval in time**, compatible with the **energy spread** of the incoming electrons. That energy spread is expressed as a dimensionless uncertainty principle (**$\Delta t \cdot \Delta \upsilon \approx 1$**) (Fig.2). A new perspective brought on by **Discrete Physics**, is that the **mathematics** of a **measurement** is **dimensionless** and it is the **measuring device** (say, an EM) that provides the energy scale for the measurement of, say, ~300keV per arriving electron.

References:

[1] Van Heel M, Schatz M: ***Fourier Shell Correlation Threshold Criteria***. *J. Struct. Biol*. **151** (2005).
[2] Van Heel M, Schatz M: ***Information: to Harvest, to Have and to Hold***, *arXiv* (2020).
[3] Van Heel M: ***Symmetric Sampling and the Discrete Laws of Physics* (1)**: ***Refuting the Classical Shannon-Nyquist Sampling Theorem*** (2024). researchsquare.com
[4] Van Heel M: ***Symmetric Sampling and the Discrete Laws of Physics* (2)**: ***Measuring Quanta arriving in a Sensor*** (2025) OSFpreprints, https://doi.org/10.31219/osf.io/hcngu.
[5] Van Heel M: ***Symmetric Sampling and the Discrete Laws of Physics* (4)**: ***Heisenberg's Uncertainty Principle is "incomplete"*** (2025c). https://osf.io/preprints/osf/5enwk.
[6] Van Heel M: ***Symmetric Sampling and the Discrete Laws of Physics* (7)**: ***The Measurement Problem*: *A Verbose Postscript***. Submitted

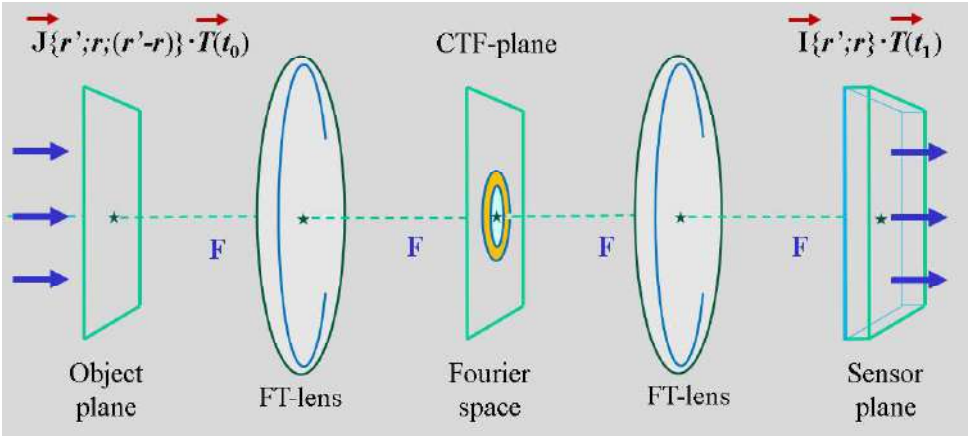

Figure 1. **The 4F symbolic imaging system** ("**4**" ***focal distances*** "***F***") is the generic ***linear imaging system***, symbolically consisting of two ***Fourier transform lenses*** that creates a one-to-one image of the ***Object*** $O_{in}(r)$ in the ***object plane***. This representation is ***deterministic classical physic*** description of a linear imaging device like an electron microscope.

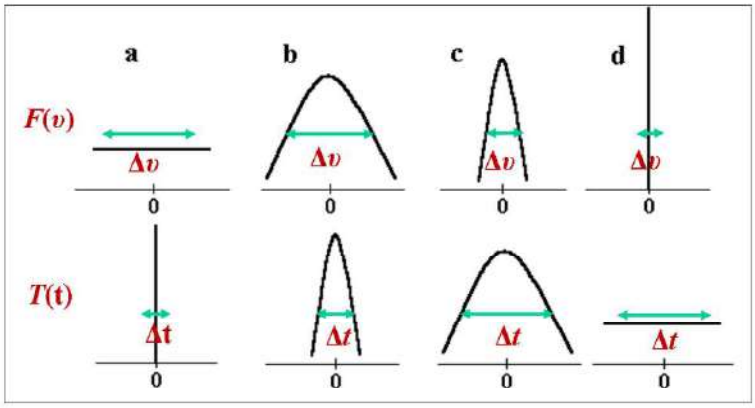

Figure 2. ***Minimal Measurable Unit*** (***MMU***) in the ***Time-to-Frequency domain***. This ***MMU*** is the smallest ***measurable entity*** in the direction of ***energy flow*** or the ***counting of quanta*** in ***a physical measurement***. The ***MMU*** concept is a dimensionless uncertainty principle ($\Delta t \cdot \Delta \upsilon \approx 1$) replaces the "***incomplete***" classical ***energy-time uncertainty*** ($\Delta E \cdot \Delta t \geq h/2$) measured in [$J \cdot s$].

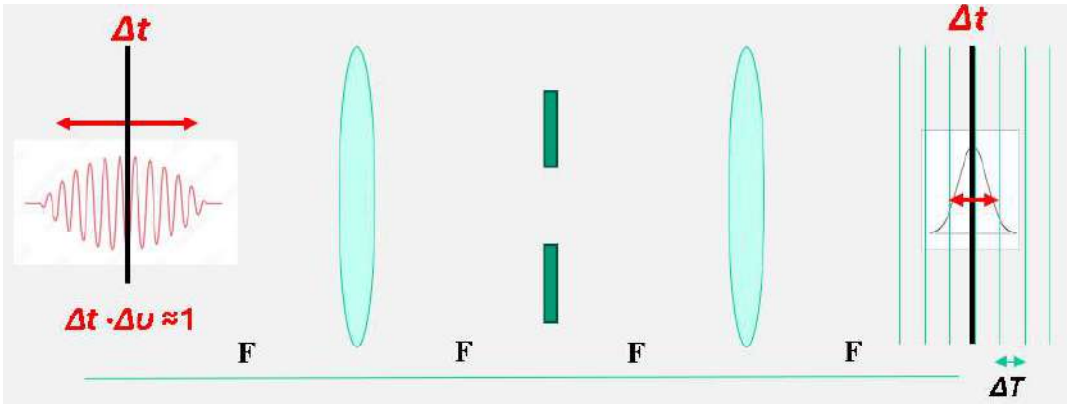

Figure 3. ***Sampling*** in the ***time-to-frequency domain***. The ***MMU uncertainty principle*** in the ***time-to-frequency*** direction determines the ***length of the wave-packets*** in the direction of the ***energy flow*** in a ***measurement***: a ***neglected entity*** in ***QM***. In ***electron-counting EM*** it defines the minimum time (**ΔT**) between frames needed to sample the "***length of arriving electrons***" (**Δt**).

Interface between life and material sciences

30º Congresso da Sociedade Brasileira de Microscopia e Microanálise

Effect of phosphonate molecules in the nucleation and growth of calcium carbonate nanoparticles revealed by cryo-TEM

Fernanda Costa de Medeiros[1], Raquel Pires Gonçalves[2], Gisele Dalmônico[1], Vanessa Pimentel Lages[2], Amaro Gomes Barreto Junior[1], André Linhares Rossi[1]*

[1]Brazilian Center for Physics Research, CBPF, Rio de Janeiro, RJ, Brazil,
[2] Federal University of Rio de Janeiro, Rio de Janeiro, RJ, Brazil
*andrelinharesrossi@gmail.com

The formation of calcium carbonate ($CaCO_3$) scale is a recurring problem in industrial systems, such as heat exchangers, water treatment plants and oil and gas extraction units [1]. The use of chemical inhibitors is one of the most effective strategies to mitigate this phenomenon, acting mainly in the nucleation stage or in the crystal growth [2,3]. The present work investigates the effect of three scale inhibitors — DTPMP (inh-D), HEMPA (inh-H) and Vs-Co (inh-V) — on the nucleation and growth of calcium carbonate ($CaCO_3$). The synthesis was carried out by coprecipitation in aqueous solution, with simultaneous monitoring of pH and calcium concentration. The samples were analyzed by transmission electron cryo-microscopy (Cryo-TEM), energy-dispersive spectroscopy (EDS), electron energy loss spectroscopy (EELS) and nanometer-resolution X-ray fluorescence (nano-XRF) at a synchrotron source. The results showed that all inhibitors significantly delayed calcium consumption and initial nucleation compared to the control. Nano-XRF maps indicated variations in particle density and size, with inhD promoting a smaller density of particles, but with larger particles, while inhH increased the density of small particles. Cryo-TEM evidenced the formation of nanoclusters of 2 nm, which evolved into faceted particles typical of calcite and vaterite. Quantitative analysis of Ca/C by EDS indicated a progressive increase in the atomic ratio as crystal growth. Cryo-STEM revealed distinct morphologies according to the inhibitor, with inhD forming smaller particles organized in line, and inhH promoting agglomeration of intermediate clusters. Finally, Cryo-STEM-EELS analysis confirmed the chemical composition of particles, showing spatial correlation between calcium and carbon and characteristic spectra of calcite.

[1] CRABTREE, M., et al., Oilfield Review. 11 (1999).
[2] Yan Ji, et al, Desalination, 422 (2017).
[3] Heng Wang, et al., Petroleum, 2021.
[4] This research was supported by CNPq (Brazil)

Immunomodulatory Action Of Turmeric Extract (*Curcuma Longa* L.) Diluted In Fish Oil Associated With Resistance Exercise In A Model Of Induced Rheumatoid Arthritis

Diego Francis Saraiva Rodriguez[1]*, Jéssica Suelen Ferreira de Souza[1], Flávia Heloisa Da Silva[1], Mikael Gerson Kuhn[1], Gladson Ricardo Flor Bertolini[1], Lucinéia de Fátima Chasko Ribeiro[1].

[1] Programa de Pós-Graduação em Biociências e Saúde - CCBS - Universidade Estadual do Oeste do Paraná (Unioeste) - Cascavel, PR, Brasil.
*diefran.rodriguez@gmail.com

Rheumatoid arthritis (RA) is a chronic, progressive, systemic inflammatory disease that significantly affects quality of life and imposes high social and economic costs [1]. Animal models that mimic the signs of RA are studied to understand its mechanisms and to find alternatives to current drug treatments. In this sense, the analysis of the functional activity of macrophages isolated from the peritoneal cavity as immunological biosensors of systemic inflammation has not yet been fully explored and may provide a new perspective for monitoring the dynamics of RA, as well as treatment protocols [3]. There is a growing search for non-pharmacological interventions, such as turmeric (*Curcuma longa* L.), which has anti-inflammatory, antioxidant, and immunomodulatory actions but low oral bioavailability, preferably diluted in fish oil. Resistance exercise is another fundamental intervention in the treatment of RA, acting to reduce pain and improve function, as it induces adaptations that favor homeostasis [2]. However, few studies provide information on the association of these two therapies. Thus, the originality of this study lies in the evaluation of the combination of these elements on the activity of peritoneal leukocytes with a simultaneously preventive and therapeutic approach in a model of RA induced by Complete Freund's Adjuvant (CFA). Forty-eight Wistar rats were used, randomized into six experimental groups: control group (CTL); rheumatoid arthritis (AR) group; climbing resistance exercise + RA (EA) group; *Curcuma longa* L. supplementation + RA (SA) group; supplementation + resistance exercise without RA (ES) group; and supplementation + resistance exercise + RA (ESA) group. RA induction was performed in two stages: intradermal inoculation of CFA at the base of the tail; and after one week, intra-articular injection into the right tibiofemoral joint. Supplementation was performed daily by oral administration of 500 mg/kg of turmeric solubilized in 1000 mg/kg of fish oil and lasted 30 days: 21 consecutive days before arthritis induction and 9 days after local induction. The exercise lasted 21 days, with sessions on alternate days, totaling 16 sessions. On the 39th day of the experiment, the animals were euthanized by guillotining, followed by lavage of the peritoneal cavity with buffer solution for isolation and analysis of peritoneal macrophage activity. The cells obtained were incubated in RPMI 1640 culture medium, and in vitro analyses of cell adhesion, phagocytosis, and basal production of reactive oxygen species (hydrogen peroxide and superoxide anion) were performed using a spectrophotometer. Statistical analysis used was two-way ANOVA with Tukey's post-test, with a 5% significance level. The study was approved by the Ethics Committee on Animal Use (CEUA/UNIOESTE), protocol no. 09-24. It was observed that the AR group had a 38% higher production of hydrogen peroxide compared to CTL ($p = 0.0031$), demonstrating that the inflammatory process induced by the arthritis model was effective in modifying systemic leukocyte activity. Conversely, macrophages from the ASE group showed 37% lower peroxide production compared to AR ($p < 0.00001$), in addition to 50.2% lower phagocytic activity ($p = 0.0362$). The ES, AR, EA, and ESA groups showed greater cell adhesion than CTL ($p < 0.05$). Regarding superoxide production, the ES and AS groups had significantly higher levels than CTL ($p < 0.05$). The results demonstrate that the combination of turmeric in fish oil and resistance exercise was effective in preventing and/or reducing the inflammatory activity of macrophages. This study concludes that the combined intervention played a role in modulating systemic inflammation, contributing to the attenuation of the in vitro phagocytic response of peritoneal macrophages in

an experimental model of RA. These findings also reinforce the use of peritoneal lavage and cell culture as tools to detect systemic inflammation in models of induced arthritis [4].

[1] C. Alvarez et al., *Reumatol. Clin.*, 16 (5P1) (2020) 324–332.
[2] K.R. Pertiwi et al., *J. Keolahragaan*, 10 (2) (2022) 247–257.
[3] J. Tu et al., *Front. Immunol.*, 12 (2021) 678456.
[4] This research was supported by CAPES (Brazil).

Figure 2. Graphs showing the mean ± standard error of the mean of in vitro activity of peritoneal macrophages (2×10^6 cells/well). A: Cell phagocytosis. B: Cell adhesion per well. C: Basal hydrogen peroxide production. D: Basal superoxide production. Two-way ANOVA post hoc Tukey test. $p < 0.05$.

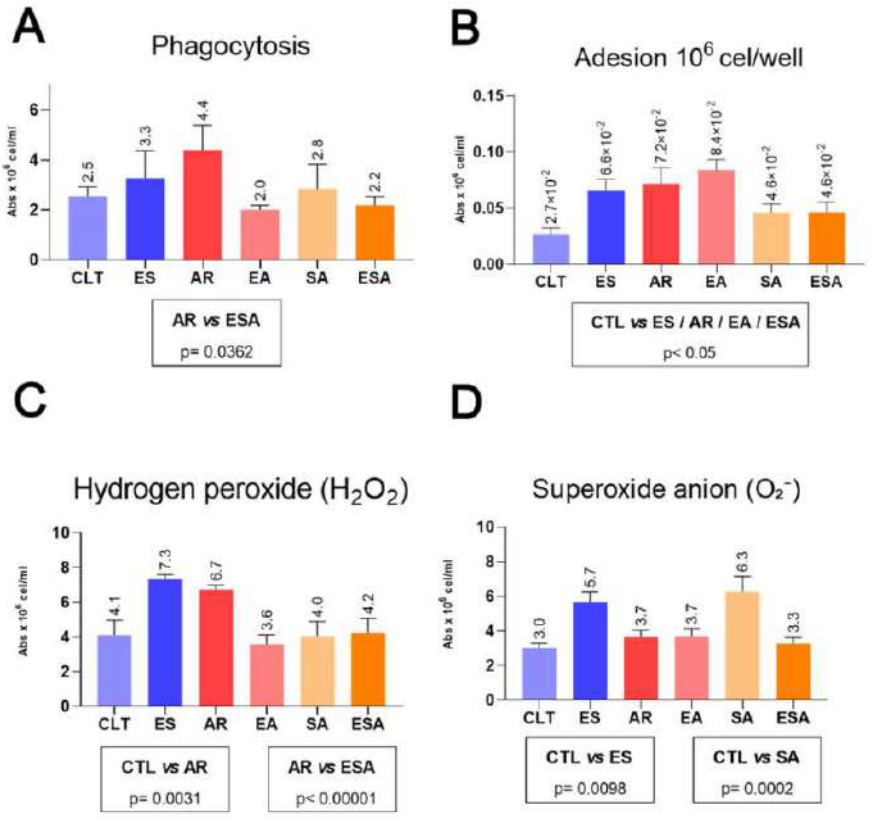

Inside the Placenta: Visualizing Microplastic Internalization with Multimodal Microscopy

Aldilane Lays Marques [1*], Rodrigo Weingrill [2], Stephanie Ospina-Prieto [1], Keyla Pires [1], Isadora Cavalcante [1], Ashelley Kettyllem Sousa [1], Iasmin Cristina Cavalcante [1], Lais Oliveira [3], Samuel Souza [3], Eduardo Jorge Fonseca [3], Johann Urschitz[2], Alexandre Borbely [1]

[1] Cell Biology Laboratory, Institute of Biological and Health Sciences, Federal University of Alagoas, 57072-900, Maceio, Brazil
[2] Institute for Biogenesis Research, Department of Anatomy, Biochemistry and Physiology, John A. Burns School of Medicine, University of Hawaii at Manoa, Honolulu, 96813, Hawaii, USA
[3] Group of Optics and Nanoscopy, Physics Institute, Federal University of Alagoas, 57072-900, Maceio, Brazil
* Laysxavier0398@gmail.com

Microplastics (MPs) are increasingly recognized as widespread environmental pollutants, recently detected in human biological samples, including the placenta. However, little is known about their capacity to cross the placental barrier and their interactions within placental tissue. In this study, we investigated the translocation and intratissue distribution of 5 μm polystyrene microplastics (PS-MPs) in human term placental chorionic villi explants using a multimodal microscopy approach. Placental explants were exposed to 100 μg/mL of fluorescently labeled PS-MPs for up to 72 hours. Microscopy techniques, including optical microscopy, fluorescence confocal imaging, and confocal atomic force microscopy (C-AFM), were used to analyze the internalization and localization of the particles. Our results demonstrate that PS-MPs can traverse the syncytiotrophoblast layer and penetrate up to 120 μm into the mesenchymal core of the villi. Notably, the particles were not simply surface-bound but internalized and distributed within the tissue. High-resolution imaging revealed that PS-MPs were surrounded by a thin actin-rich layer, suggesting active uptake mechanisms. Importantly, no morphological evidence of syncytiotrophoblast membrane disruption or tissue damage was observed, indicating that the barrier remains structurally intact during particle internalization. These findings provide direct evidence of MP translocation across the human placental barrier in vitro and underscore the critical role of advanced microscopy techniques in visualizing subcellular interactions between environmental contaminants and human tissues. The ability of MPs to reach the fetal side of the placenta raises concerns about potential impacts on fetal development. Future investigations should focus on elucidating the molecular pathways of MP uptake and assessing their biological consequences during pregnancy.

This research was supported by Brazilian National Council for Scientific and Technological Development (CNPq).

Integrated analysis of D-galactose-induced cellular senescence in murine thymic epithelial cells

Vanessa de Oliveira Batista[1,2], William Fabrício Lima Cabral[1,2] , Beatriz Souza Santos[1,2], Felipe Lima Porto[1,2], Laís Farias Azevedo de Magalhães Oliveira[3], Samuel Teixeira de Souza[3], Marvin Paulo Lins [2,4],Maria Danielma dos Santos Reis[1,2]

[1]Laboratory of Cell Biology, Institute of Biological and Health Sciences Federal University of Alagoas, Maceió, Brazil; [2]Brazilian National Institute of Science and Technology on Neuroimmunomodulation (INCT-NIM), Rio De Janeiro, Brazil; [3]Optics and Nanoscopy Group, Institute of Physics, Federal University of Alagoas; [4]Federal University of Mato Grosso.
*vanessa.batista@icf.ufal.br

Aging is a biological phenomenon characterized by the progressive accumulation of senescent cells, which can trigger inflammatory processes and promote the development of age-related diseases [1]. This process is directly related to changes in the thymus, the organ responsible for the maturation of T lymphocytes, which are essential cells for the adaptive immune response [2]. The age-related thymus involution is characterized by the loss of lymphoid tissue, accompanied by the appearance of adipose cells and a reduction in T lymphocyte export to the periphery [3]. Studies have indicated an accumulation of senescent thymic epithelial cells (TECs) in the thymus, which could explain the thymic alterations during aging [4]. In this context, investigating the morphological and biochemical alterations associated with thymus involution becomes fundamental for the development of strategies aimed at preserving the integrity and immune efficiency of the thymus throughout life. For this purpose, an in vitro experimental model of TEC senescence induced by D-galactose (D-gal) was used. This sugar is widely used to mimic aspects of cellular senescence, such as oxidative stress, inflammation, and morphofunctional alterations. As results, a significant reduction in cell viability was observed after 48 hours of exposure to D-gal at 40 mg/mL, compared to the control group. Quantitative PCR analysis revealed a marked increase in the expression of the *P16* gene together with an increase in p16 protein expression by immunostaining in D-gal-treated cells, suggesting the activation of the *p16/Rb* pathway and the induction of cell cycle arrest, the main feature of cell senescence. Morphological evaluation by optical microscopy showed notable alterations in treated cells, such as reduced cytoplasm, loss of cellular extensions, and decreased cell-to-cell interaction, contrasting with the elongated and interconnected morphology of control cells. Finally, Raman spectroscopy, combined with PCA analysis, revealed biochemical changes consistent with stress and cellular damage, with alterations in bands related to DNA, proteins, and lipids, confirming the effects induced by D-gal treatment. These results, along with morphological and molecular evidence, demonstrate that the integration of these techniques was essential for a comprehensive characterization of senescence in TEC. This approach contributes to the understanding of the mechanisms associated with thymic involution and may guide future strategies aimed at preserving immune function throughout aging [5].

[1] P.R.C. Lazzarini et al., Cuad. Educ. Desarro. 16 (2) (2024) 378.
[2] A.S. Alves, V. Bueno, Einstein (São Paulo) 17 (2) (2019)
[3] A.W. Dorschner et al., Aging Cell 7 (2) (2008) 158.
[4] A. Barbouti et al., Mech Ageing Dev (2019) 177:88–90.
[5] This research was supported by UFAL, CNPq, FAPEAL e INCT-NIM.

Fig. 1- Effect of D-Galactose on the viability of murine TEC

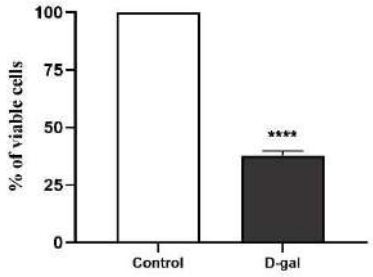

The graph shows the mean±SEM of the percentage of viable cells after treatment with D-galactose at a concentration of 40 mg/mL for 48 hours. (*) $p<0.05$ (*) $p<0.05$ using t-test relative to untreated control.

Fig. 2- Evaluation of *P16* gene expression in TEC after D-galactose-induced senescence.

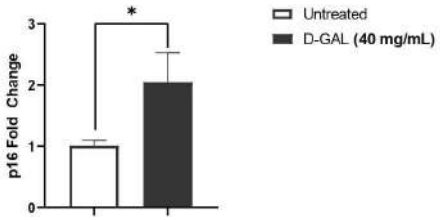

The graph shows the mean±SEM of the relative expression of the P16 gene through comparative Ct. (*) $p<0.05$ using t-test in relation to the untreated control

Figura 4- Assessment of thymic epithelial cell morphology

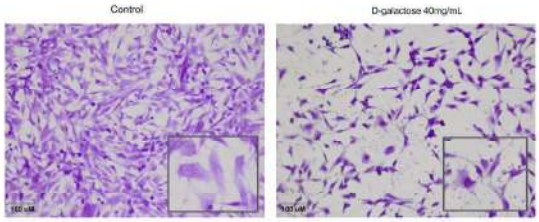

Morphology of thymic epithelial cells stained with crystal violet under 200x magnification, analyzed by optical microscopy.

Figura 5- p16 immunostaining of TEC after D-galactose-induced senescence

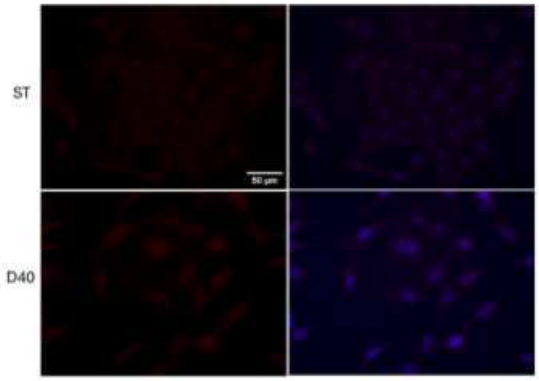

Photomicrographs demonstrating p16 protein expression by immunofluorescence in untreated (ST) and D-galactose-treated (40 mg/mL) groups. Nuclei were stained with DAPI (blue), and p16 is shown in red. Magnification: 400x.

Figura 6- Principal component analysis (PCA).

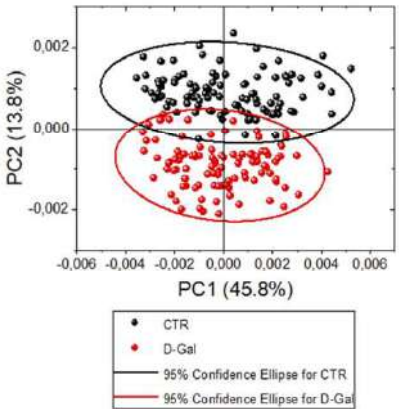

Figura 7- Raman spectrum of thymic epithelial cells after D-galactose-induced senescence

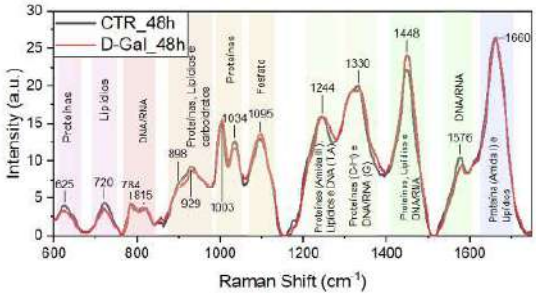

Investigation of Nucleation and Crystallization Mechanisms in Hydroxyapatite–Chitosan Nanocomposites

Raquel Pires Gonçalves[1]*, Fernanda Costa Medeiros[2],
Gisele Maria Leite Dalmônico[2], André Linhares Rossi[2].

[1]Federal University of Rio de Janeiro, Rio de Janeiro, Brazil.
[2] Brazilian Center for Physical Research, Rio de Janeiro, Brazil.

*raquelgoncalves.rp@gmail.com

Hydroxyapatite (HAp) is a widely studied material for bone tissue engineering applications due to its chemical similarity to the mineral phase of natural bone. Composite systems combining HAp and biopolymers have been extensively investigated to improve mechanical and morphological properties compared to pure HAp [1,2]. Among these biopolymers, chitosan, a linear homopolymer with properties such as biodegradability, biocompatibility, non-toxicity, and antibacterial activity, has been used in biomaterials engineering. There are still few studies that fully understand the role of chitosan in the nucleation and crystallization behavior of hydroxyapatite, modulating the morphology and structure [3,4]. In this study, HAp–chitosan nanocomposites were synthesized by a wet chemical coprecipitation. The reaction time was set to 24 h, with a Ca/P molar ratio of 1.67 and chitosan was introduced into the reaction medium at concentrations ranging from 0.5% to 2% (w/v). The resulting materials were characterized by Fourier-transform infrared spectroscopy (FTIR), X-ray diffraction (XRD), transmission electron microscopy (TEM), selected area electron diffraction (SAED). The results showed that increasing chitosan concentration led to a decrease in average particle size (from 12.8 nm to 9.2 nm) and improved morphological homogeneity, suggesting its stabilizing effect during crystal growth. XRD analysis showed a progressive decrease in HAp crystallinity with broader and less intense diffraction peaks in the presence of chitosan. The FTIR spectra confirmed the successful incorporation of the polymer by characteristic vibrational bands, with intensity increasing proportionally to the chitosan content. SAED patterns confirmed the nanocrystalline nature of the particles and showed a decrease in ring sharpness with increasing chitosan content, suggesting increased structural disorder with decrease peak intensities at higher polymer content. TEM imaging revealed improved contrast and particle organization in the presence of chitosan, while EDS analysis confirmed the presence of Ca, P, and N, validating composite formation. Overall, the incorporation of chitosan modulated the morphology, crystallinity, and thermal stability of hydroxyapatite without altering its fundamental chemical composition. These findings highlight the potential of chitosan-modified HAp as a promising strategy for the development of functional biomaterials for bone regeneration and tissue engineering applications.

[1] G.M.L. Dalmônico et al., Mater. Chem. Phys. 237, (2019).
[2] M.-Y. Wu et al., Pharmaceutics. 16, (2024), 730.
[3] A. Harugade et al., React. Funct. Polym, 191, (2023).
[4] T. Szatkowski et al., Physicochem. Probl. Miner. Process. 51, (2015).
[5] This research was supported by CAPES, CNPq and FAPER. This work was performed in the Laboratory of Nanoscience and Nanotechnology (LABNANO) - Brazilian Center for Physical Research (Brazil).

Magnetic Hyperthermia with Iron Oxide: Oncological Theranostic for Osteosarcoma in Alternative Models to Animal Use

Claudiane Santos Maximiano [*] [1], Célio Valente[2,3], Marla Horta[2], Flávio Garcia[3], Victor Midlej[4], Marcel Guimarães Martins[2], Sara Gemini Piperni [1]

1 Laboratório de Biotecnologia, Bioengenharia e Biomateriais Nanoestruturados – UFRJ
2 Magtech Soluções em Nanopartículas Magnéticas – MAGTECH BRASIL
3 Laboratório de Materiais Magnéticos Multifuncionais – CBPF
4 Laboratório de Biologia Estrutural, IOC/FIOCRUZ

* Claudyannesantos22@gmail.com

Osteosarcoma is the most common type of primary bone cancer in adolescents and young adults, with a predilection for long bones and high metastatic potential, especially to the lungs [1], [2]. Despite surgical and chemotherapeutic advances, cancer treatment remains approximately 20 years behind, and associated costs have increased by 400% in the last four years alone. Furthermore, the current therapeutic approach has significant limitations, such as high toxicity, tumor resistance, infertility, and negative impact on patients' quality of life. Given this scenario, the development of more effective and selective therapies becomes urgent [1]. In this scenario, nanotechnology, especially through the use of magnetic iron oxide nanoparticles (IONs), has shown promise for both the diagnosis and treatment of solid tumors [3]. The magnetic hyperthermia technique, which locally raises the tumor temperature through these particles under the action of an alternating magnetic field, has been successfully tested in glioblastoma and prostate cancer, and is in clinical phase II, demonstrating therapeutic potential with fewer side effects [4]. In this context, the objective of this work is to evaluate the formation of protein corona and internalization pathways of the nanosystems, in addition to the effects of the application of an alternating magnetic field in osteosarcoma models, after internalization of pure iron oxide magnetic nanoparticles (NPMp) and doped with Zn/Co/Cr (NPMd). Methodology: Magnetic hyperthermia, XRD, Fluorescence microscopy, Electron microscopy. Results: The characterization confirmed the presence of magnetite and superparamagnetic behavior in both samples, in addition to thermal self-regulation in NPMd. TEM micrographs showed spherical morphology for the pure sample (NPMp) and cubic shape for the doped sample (NPMd). DLS analysis showed a bimodal hydrodynamic diameter distribution around 100 and 1000 nm for both particles, both in water and in culture medium. The decrease in zeta potential in culture medium and FTIR analysis confirmed the adsorption of proteins on the nanoparticles. Mass spectrometry identified 15 proteins common among the nanosystems and 161 adsorbed exclusively on NPMd, which were preferentially internalized by clathrinmediated endocytosis and lipid raft. Before exposure to the magnetic field, MTT analysis demonstrated the safety of the particles up to a concentration of 300 μg/ml. After field exposure, the reduction of spheroids presents a significant cumulative effect with irreversible damage to the cellular ultrastructure after 4 cycles of magnetic field exposure for both particles when compared to the control, but without significant differences between the two samples. However, this effect is anticipated at the 3rd cycle in cells in contact with NPMp, suggesting that doping of self-regulated NPMd enhances the cumulative effects of field application.Conclusions: These advances aim to consolidate the therapeutic application of NPs, optimizing their use in multimodal treatments and in the controlled release of drugs, strengthening their clinical viability.

PRELIMINARY RESULTS

Transmission electron microscopy (TEM) revealed ultrastructural changes in the spheroid cells after contact with magnetic nanoparticles (NPMp and NPMd) and exposure to alternating magnetic fields. In the initial cycles (T1) (Figure 1), both nanoparticles were internalized, evidencing endocytic vesicles and mitochondrial alterations, presenting cellular alterations and cytoplasmic modifications and formation of autophagosomes. After the final cycle (T5) (Figure 2) and cumulative exposure to the magnetic field, the treated spheroids presented significant structural damage, such as cytoplasmic destruction and formation of multivesicular bodies. In contrast, controls without nanoparticles maintained cellular integrity. These findings indicate that magnetic nanoparticles associated with magnetic hyperthermia promote cellular alterations that may be related to the mechanisms of cell death induced by the treatment.

Figure (1). TEM images at T1 time point showing internalization of nanoparticles (NPMp and NPMd) and initial changes in cellular organelles. Figure (2). TEM images at T5 time point demonstrating advanced cellular damage and formation of multivesicular bodies in spheroids treated with nanoparticles and magnetic field.

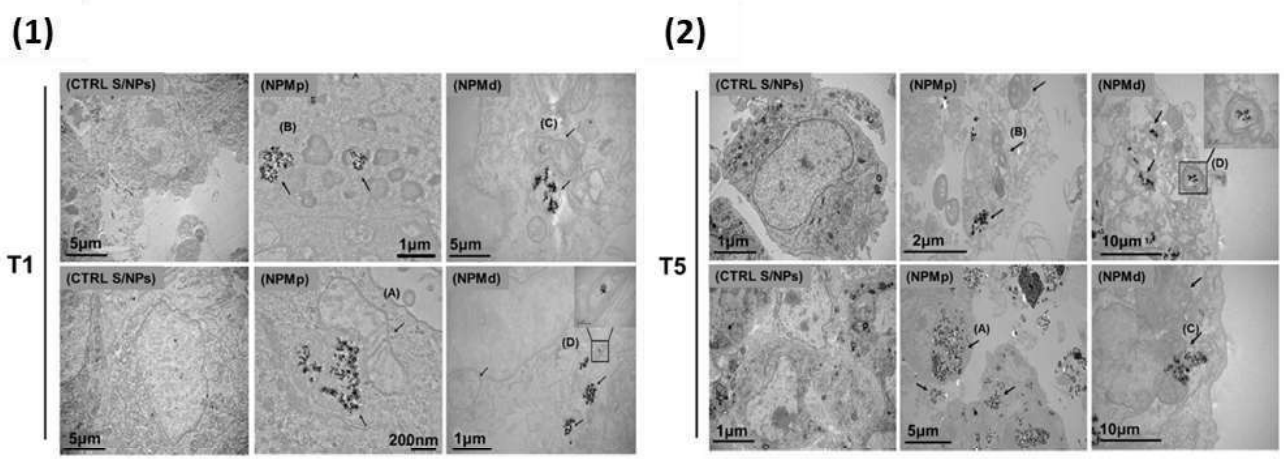

[1] PILAVAKI, P. et al. Osteosarcoma: Current Concepts and Evolutions in Management Principles. v. 12, n. 8, p. 2785–2785, 9., 2023.

[2] ZHANG S, sun k, zheng r, zeng h, wang s, chen r, et al. Cancer incidence and mortality in China, 2015. **J Natl Cancer Center**, 2021

[3] RIVERA, et al. Functional glucosamine-iron oxide nanocarrie. **Journal of Materials Research**, 2020.

[4] GUPTA, ruby; sharma, deepika, Evolution of Magnetic Hyperthermia for Glioblastoma Multiforme Therapy. **ACS Chemical Neuroscience**, 2019

Microbiological Profile of Natural Seawater from the Brazilian Atlantic Coast and Its Influence on Carbon Steel Corrosion

Carolina Garín Correa[1]*, Danielly C. O. Mariano[2], Bianca Cruz Neves[3], José Antônio Da Cunha Ponciano Gomes[1]

[1] Departamento de Engenharia Metalúrgica e de Materiais, Universidade Federal do Rio de Janeiro (UFRJ), Brasil.
[2] Instituto de Biofísica Carlos Chagas Filho, Universidade Federal do Rio de Janeiro (UFRJ), Brasil.
[3] Instituto de Química, Universidade Federal do Rio de Janeiro (UFRJ), Brasil.

*cpgarin@metalmat.ufrj.br

Microbiologically Influenced Corrosion (MIC) is the acceleration of corrosion processes caused by microbial activity, leading to substantial losses in industrial settings [1]. The primary way in which both aerobic and anaerobic bacteria contribute to corrosion [2] involves the development of biofilms on metal surfaces. This begins with the attachment of planktonic cells and is followed by the production of exopolysaccharides (EPS). It is important to note that MIC is not driven by a single type of microorganism; rather, it results from the synergistic effects and interactions among various microbial species within a specific corrosive environment. Seawater, due to its complex biological community, is a naturally corrosive medium where MIC is likely to occur. The analysis of Amplicon Sequence Variants (ASVs) based on 16S ribosomal RNA genes is a widely used approach to study microbial genetic material directly from environmental sources such as soil, freshwater, or marine ecosystems [3,4]. In this study, a molecular methodology was employed to investigate the microbial constituents of seawater samples collected by the Brazilian Navy at specific geographical coordinates, serving as a fundamental step in evaluating their potential involvement in MIC during laboratory-based corrosion experiments on carbon steel A36. The composition of the microbiota was analyzed with a focus on its capacity to initiate or promote MIC. Sequencing analysis revealed remarkable microbial diversity among bacteria and archaea in seawater samples MW02 and MW0. In sample MW02, the most abundant families were Halomonadaceae (62.89%), Flavobacteriaceae (12.27%), and Gimesiaceae (7.77%). In sample MW03, they were Pseudoalteromonadaceae (48.11%), Saccharospirillaceae (9.68%), and Cyanobiaceae (9.35%) for bacteria region, and genera *Candidatus Nitrosopumilus* (51.85%), *Candidatus Nitrosopelagicus* (22.54%), *Woesearchaeales* (16.87%), and *Marine Group II* (8.29%) for archaea region (Figure 1). Scanning Electron Microscopy (SEM-EDS) revealed differences in the thickness and composition of corrosion products for each seawater sample, as well as in the intensity of corrosion on carbon steel after 28 days of study. The figure 2 shows thickness of corrosion products and EDS analysis, indicated that the main components of the corrosion products in all the samples were inorganic compounds based on O, C, and Fe, in contrast to the seawater sample MW02, where a high thickness and percentage of calcium was observed, which could correspond to marine biomineralization processes [5] acting as a protective barrier, coinciding with electrochemical results.

1. J.G. Caporaso, C.L. Lauber, W.A. Walters, D. Berg-Lyons, C.A. Lozupone, P.J. Turnbaugh, N. Fierer, R. Knight, "Global patterns of 16S rRNA diversity at a depth of millions of sequences per sample", *Proc Natl Acad Sci U S A*, *108* (**2011**) 4516–4522.
2. M.J.L. Coolen, E.C. Hopmans, W.I.C. Rijpstra, G. Muyzer, S. Schouten, J.K. Volkman, J.S. Sinninghe Damsté, "Evolution of the methane cycle in Ace Lake (Antarctica) during the Holocene: response of methanogens and methanotrophs to environmental change", *Org Geochem*, *35* (**2004**) 1151–1167.
3. A de S. Pires, G.M. Dias, D.C. de O. Mariano, R.N. Akamine, A.C. Cruz de Albuquerque, C. Groposo, C.M. Soares Ribeiro, L. de Figueiredo Vilela, B.C. Neves, "Molecular diversity and abundance of the microbial community associated to an offshore oil field on the southeast of Brazil", *Int Biodeterior Biodegradation*, *160* (**2021**) 105215.
4. D.C.O. Mariano, G.M. Dias, M.R. Castro, D.A. Tschoeke, F.J.S. de Oliveira, E.F.C. Sérvulo, B.C. Neves, "Exploring the diversity and functional profile of microbial communities of Brazilian soils with high salinity and oil contamination", *Heliyon*, *10* (**2024**) e34336.
5. C. Fang, V. Achal, "Enhanced steel corrosion inhibition through microbially induced carbonate precipitation with facultative anaerobic denitrifying bacterium", Case Studies in Construction Materials, 21 (2024) e03607

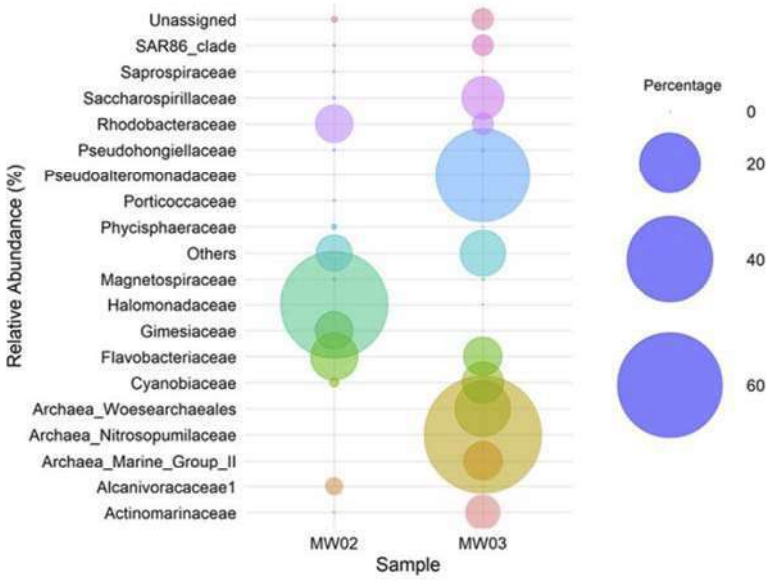

Figure 1: Relative abundance of seawater samples, MW02 and MW03, analyzed by the 16S rRNA amplicon sequencing, based on the primers V4 for bacteria and V4V5 for archaea region. The figure shows the distribution within family level

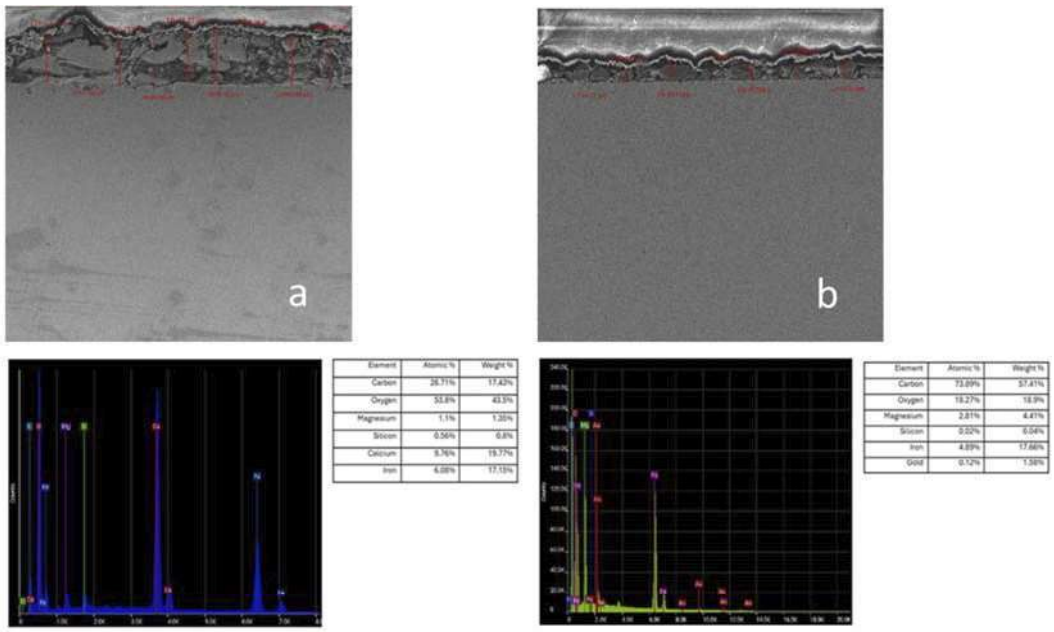

Figure 2: SEM an Energy dispersive X-ray spectroscopy EDS analysis of A36 Carbon Steel in different seawater samples for 28 days: a) MW02 and b) MW03.

Navigating the Bone–Biomaterial Interface: Structural Hierarchy Revealed by Multiscale Imaging

Camila Wendt[1, 4], André Linhares[1], Caio Santos[3], Victor Zelaya[2], Ricardo Lopes[3], Marcos Farina[4], Alexandre Rossi[1]

[1]Centro Brasileiro de Pesquisas Físicas, Rio de Janeiro, Brasil
[2] Laboratório Nacional de Luz Síncrotron, Campinas, Brasil
[3]Coppe, Universidade Federal do Rio de Janeiro, Rio de Janeiro, Brasil
[4]Instituto de Ciências Biomédicas, Universidade Federal do Rio de Janeiro, Rio de Janeiro, Brasil
* camilawendt@cbpf.br

Bone structure has different hierarchical levels from the macroscale to the nanoscale characterized by specific spatial ordering and high complexity [1]. One challenge for producing high-quality biomaterials is understanding how the biomaterial affects bone hierarchical ultrastructure during a bone repair process. In this work we aimed to evaluate the microarchitecture of newly formed bone during a healing of rat tibia defect after a 21-day implant of cHa/alginate microspheres. Analysis of the bone/biomaterial interface was carried out using synchrotron X-ray tomography (SRuCT), focused ion beam-scanning electron microscopy (FIB-SEM), and transmission electron microscopy (TEM/HRTEM). Results showed that microsphere fragmentation improves osteoconduction, and the newly trabecular bone-like network grows, filling the space between the microsphere fragments and attaching to the fragment surface. Mineral tissue (MT) is nucleated inside micrometer and sub-micrometer pores. FIB-SEM slice and view tomography showed that the trabeculae volume is filled with osteocyte-lacunae and mineralized ellipsoidal structures oriented in different directions (figure 1). TEM/HRTEM images showed that each ellipsoid comprises a packet of non-ordered mineralized collagen microfibril clusters with a mean length of 1.6 μm and width of 0.7 μm. These structures cover the biomaterial interface, but the ellipsoidal morphology is not identified inside sub-micrometer pores. In this confined condition, the mineralized tissue presents a different ultrastructure than woven trabecular ellipsoids but with a similar electron diffraction pattern. Inside sub-micrometer pores, MT organizes in nearly linear arrangements of mineralized collagen microfibril. Altogether, results provide novel details regarding the relationship between synthetic calcium phosphates scaffolds and the mineralized tissue.

[1] Reznikov, N. *et al.*, Acta Biomaterialia, 2014.
[2] This work was supported by Conselho Nacional de Desenvolvimento Científico e Tecnológico (CNPq), Fundação o Carlos Chagas Filho de Amparo à Pesquisa do Estado do Rio de Janeiro (FAPERJ) and INCT REGENERA.

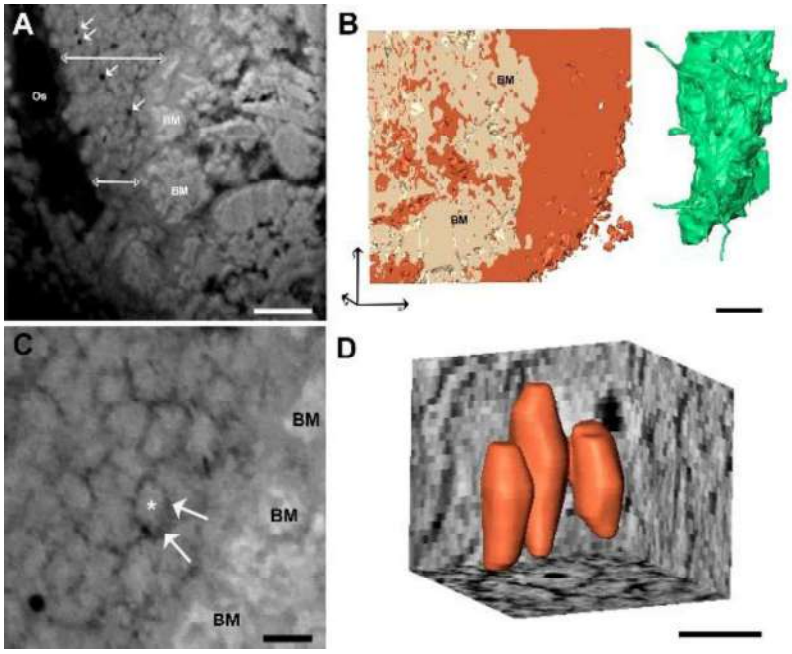

Figure 1: FIB-SEM slice and view analysis. (A) The biomaterial (BM) is observed in close proximity to the neoformed bone, osteocyte lacuna (Os) and the canalicular network (arrows). (B) 3D rendered model shows the complex association between the neoformed bone and the biomaterial. Bone structure is shown in brown, biomaterial in white and osteocyte network in green. (C) Less mineralized collagen fibrils (arrows) are seen at the boundaries of mineralized blocks (asterisk). (D) 3D rendered model showed that the mineral clusters appear as ellipsoidal structures. Scale bar: 4 μm (A-B), 1 μm (C-D).

Raman Spectral Microscopy for the Characterization of 2D and 3D Cultures of Murine Thymic Epithelial Cells

Érica da Silva de Oliveira[1]*, Eduardo Jorge Fonseca da Silva[2], Maria Danielma dos Santos Reis[3], Laís Farias Azevedo de Magalhães Oliveira[2], Jennifer Nathieli da Silva Rotandaro de Oliveira[2], Izabela Pereira dos Santos [2].

[1] Optics and Nanoscopy Group and Cell Biology Laboratory – ICBS – Federal University of Alagoas, Institute of Physics – Federal University of Alagoas, Institute of Biological and Health Sciences – Federal University of Alagoas.
*erica.oliveira@cedu.ufal.br

Two-dimensional (2D) cell cultures are widely used due to their ease of handling; however, they present structural and complexity limitations when compared to three-dimensional (3D) models, such as spheroids [1]. Various 3D culture techniques have been developed to provide cells with an environment more similar to the in vivo condition [2]. Although spheroids bring in vitro cultures closer to in vivo tissue conditions, the available techniques to analyze their chemical alterations have limitations, including changes in biochemical properties and the need for spheroid lysis after the procedures. Raman spectroscopy stands out as a non-destructive technique capable of identifying unique vibrational signatures with minimal sample preparation [3]. In this context, the present study aimed to evaluate the influence of culture time on the biochemical composition of thymic epithelial cells grown in monolayers and 3D spheroids, using Raman spectroscopy as an analytical tool. For this purpose, sample preparation was standardized for live cells in both culture models. Raman measurements were then performed using a 532 nm laser, a 60x oil-immersion objective, and acquisition parameters of 3 seconds per spectrum over 20 cycles. Initial results revealed distinct biochemical profiles between 2D and 3D cultures, with higher intensities in bands associated with proteins, lipids, and genetic material in the 3D cultures, reflecting greater compaction and structural organization (Figure 1). The flattened morphology of 2D cells may have favored spectral overlap. Principal component analysis (PCA) (Figure 2) showed clear separations between the groups, confirming specific metabolic and structural adaptations in spheroid cultures, as indicated by the spectral assignments in the PC1 loading (Figure 2). Raman spectroscopy proved to be an effective tool for identifying and distinguishing biochemical profiles, structural organization, and cellular metabolism between 2D and 3D cultures. The methodology is expected to be extended to evaluate other samples at different culture times and preparation methods, including fixed samples, in order to deepen the understanding of the stability and reproducibility of biochemical profiles in these models [5].

[1] JUAREZ-MORENO, K. et al. Monolayer (2D) or spheroids (3D) cell cultures for nanotoxicological studies? Comparison of cytotoxicity and cell internalization of nanoparticles. Toxicology In Vitro, v. 85, p. 105461, 2022.
[2] SUN, M. et al. 3D Cell Culture—Can It Be As Popular as 2D Cell Culture? Advanced NanoBiomed Research, v. 1, p. 2000066, 2021.
[3] LIAO, H. X. et al. Multifocal Raman Spectrophotometer for Examining Drug-Induced and Chemical-Induced Cellular Changes in 3D Cell Spheroids. Analytical Chemistry, v. 95, p. 14616–14623, 2023.
[4] HASE, D. A. M. K. et al. Thymic epithelial cells co-opt lineage-defining transcription factors to eliminate autoreactive T cells. Cell, v. 185, p. 2542–2558, 2022.

[5] Research supported by CAPES, CNPq, FAPEAL, Federal University of Alagoas (UFAL), Institute of Physics (IF/UFAL), and the Graduate Program in Materials Science (PPGMAT).

LISTA DE FIGURAS

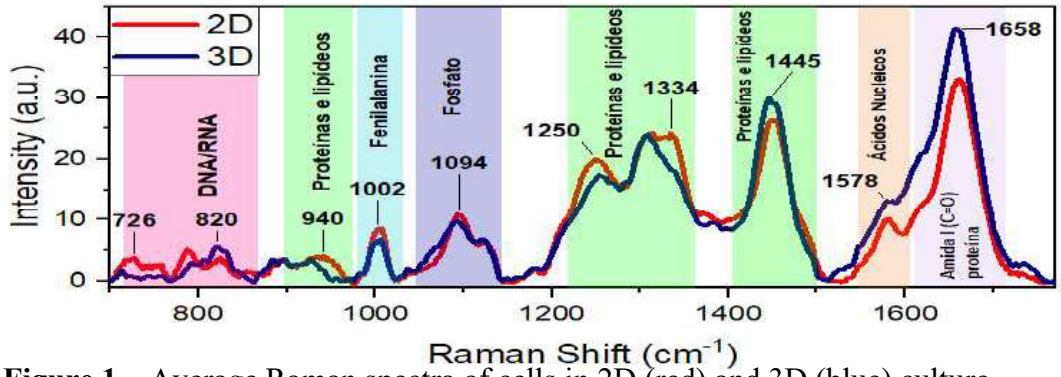

Figure 1 – Average Raman spectra of cells in 2D (red) and 3D (blue) culture conditions.

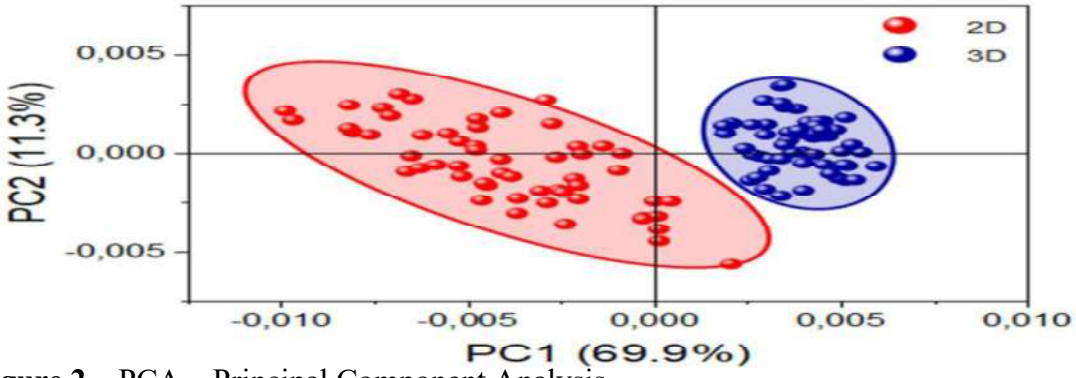

Figure 2 – PCA – Principal Component Analysis.

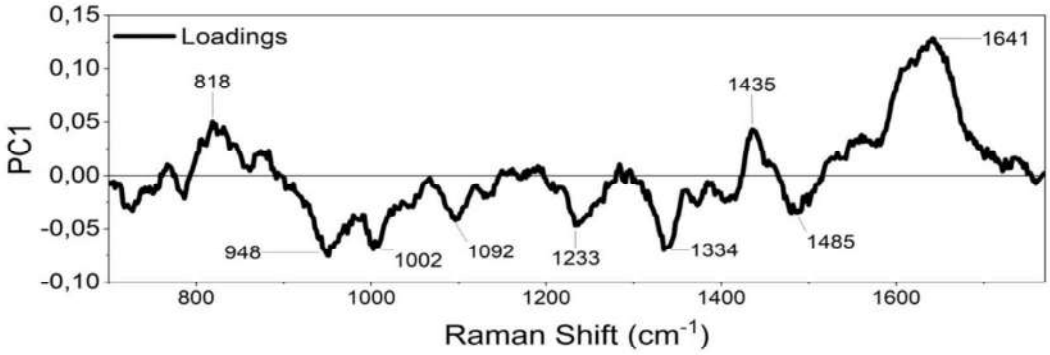

Figure 3 – PC1 Loading – Spectral Assignments

Synthesis and Characterization of Polysaccharide-Nanozyme Biohybrids for Potential Chemodynamic Therapy of Brain Cancer

Herman S. Mansur[1]*, Alexandra A. P. Mansur[1].

[1]Center of Nanoscience, Nanotechnology, and Innovation – CeNano[2]I, Department of Metallurgical and Materials Engineering, Federal University of Minas Gerais, UFMG, Brazil. *hmansur@demet.ufmg.br; herman.mansur2016@gmail.com

Although significant advances have been achieved in cancer therapy in recent years, glioblastoma multiforme (GBM) remains a devastating primary brain tumor with a very unfavorable prognosis for the patient [1-4]. Thus, we report the synthesis and characterization of organic-inorganic biohybrids for the killing of brain cancer cells. These nanohybrids were built based on two different anionic polysaccharide derivatives surrounding cobalt-doped magnetite nanoparticles (Co-MION) mimicking the activity of natural enzymes (i.e., nanozyme) for chemodynamic therapy (CDT) [2,3]. The organic shell, based on carboxymethyl cellulose (CMC, sodium salt, molecular weight, Mw = 90 kDa, degree of substitution = 0.7) or hyaluronic acid (HA, sodium salt, Mw = 80-100 kDa) polysaccharides, behaved simultaneously as a capping macromolecular ligand and passive target molecules. HA is also a membranotropic affinity vector for active targeting of CD-44 receptors overexpressed by glioblastoma cells [4]. These engineered biohybrids (Co-MION@CMC and Co-MION@HA) were produced using a facile, sustainable, green aqueous colloidal process of co-precipitation of metal salts in the presence of ammonium hydroxide at mild temperatures [2]. Morphological features and size distribution of nanoparticles were assessed by transmission electron microscopy at 200 kV accelerating voltage (TEM, Tecnai G2-20-FEI, FEI Company) coupled with energy-dispersive X-ray spectroscopy (EDX, TEM microscope with EDAX detector). Selected area electron diffraction pattern (SAED) analysis was performed to assess the crystallinity aspects of the nanoparticles. X-ray diffraction (XRD, PANalytical Empyrean diffractometer) was also applied to assess the crystalline structure of nanozymes. The catalytic activity was tested through the oxidation of 3,3',5,5'-tetramethylbenzidine hydrochloride (TMB) by H_2O_2 substrate, which was detected by the absorption of TMB oxidized species (TMB_{ox}) in a microplate reader (Bio-Rad®, iMark™ Microplate absorbance reader, λ = 654 nm). TEM images indicated that both nanohybrids were based on an inorganic core of 5-6 nm in diameter with predominant spherical morphology. Moreover, a slight contrast was detected at the nanoparticle surfaces, ascribed to a "dry" polymer shell layer overcoating the nanoparticles. High-resolution (HR) TEM images revealed the presence of interference fringes compatible with the interplanar distances (d, ± 0.1 Å) of the nanosized magnetite according to the JCPDS-89-0691 file. This crystalline cubic spinel structure of ferrites was also depicted in SAED analysis and confirmed by XRD patterns. Regarding elemental analysis, EDX spectra evidenced the incorporation of Co species into the magnetite nanoparticle structure and peaks associated with polymers. Peroxidase-like behavior of Co-MION@CMC and Co-MION@HA was confirmed by the progress of the absorbance of TMB_{ox} with time upon the injection of substrate (H_2O_2) into nanohybrid suspensions at pH 5.0 ± 0.2 (pH characteristic of tumor microenvironment). These results confirmed the potential of nanohybrids for killing GBM cancer cells through biocatalytic CDT, relying on their nanozyme-bearing peroxidase-like activity.

[1] A.C. Tan et al., CA: A Cancer Journal for Clinicians 70 (2020) 299.
[2] S.M. Carvalho et al., Pharmaceutics 15 (2023) 1702.
[3] A.A.P. Mansur, H.S. Mansur, Journal of Nanotheranostics 6 (2025) 4.
[4] M. A. Pibuel et al. The Journal of Biological Chemistry 296 (2021) 100549.
[5] This research was supported by CNPq, CAPES, and FAPEMIG (Brazil).

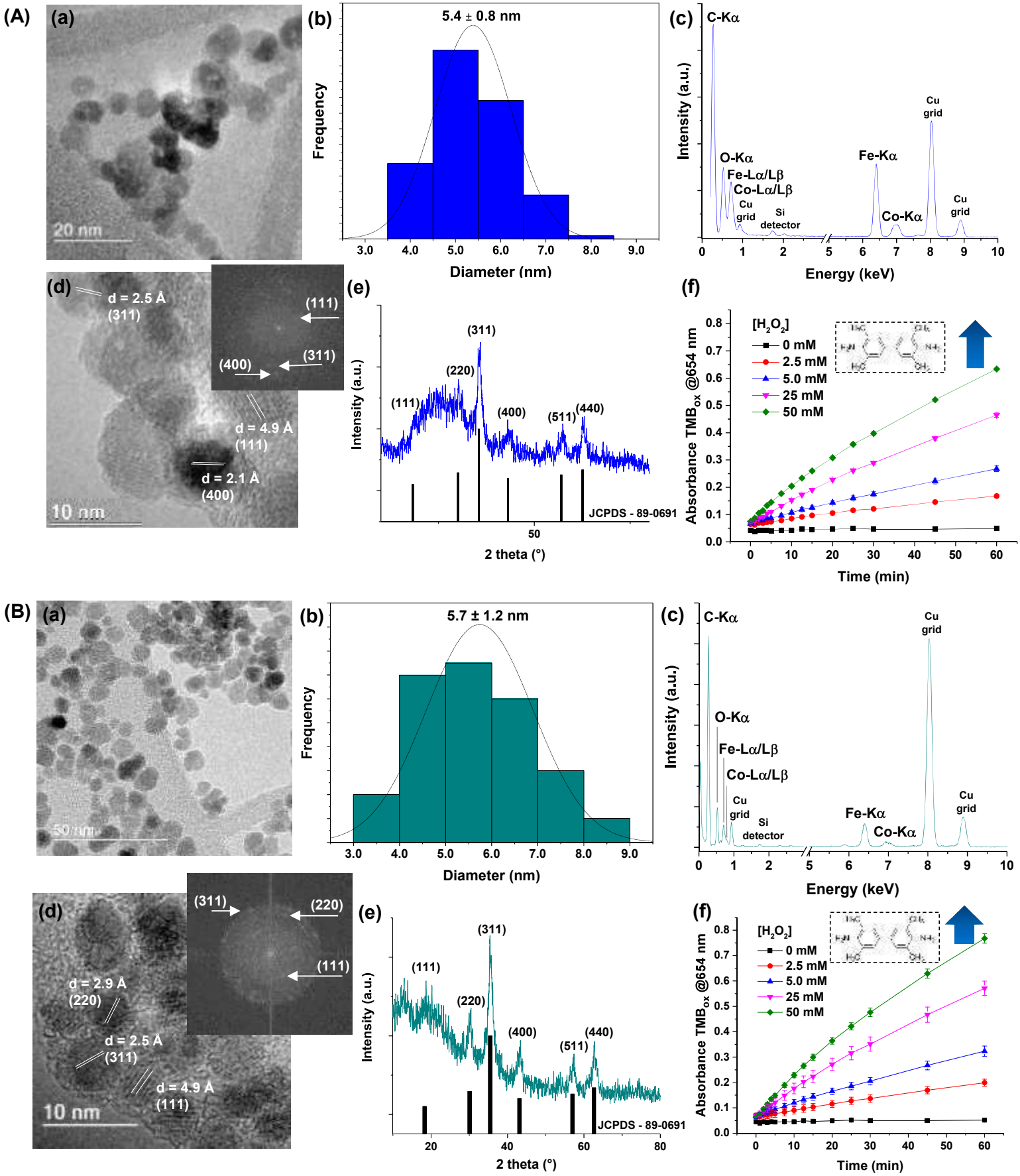

Figure 1. (a) TEM image, (b) Histogram of size distribution, (c) EDX spectrum, (d) HR-TEM image showing lattice fringes and SAED, (e) XRD pattern, and (f) Time-course absorbance curves as a function of H_2O_2 concentration (pH = 5.0; Co-MION = 30 µg/mL) for (A) Co-MION@HA and (B) Co-MION@CMC.